Depositional Pathways and the Post-Depositional History of the Neoarchean Algoma-Type BIF in Temagami, ON

David Diekrup

A thesis submitted to the Faculty of Graduate and Postdoctoral Studies in partial fulfillment of the requirements for the Doctor of Philosophy degree in Earth Sciences

Department of Earth and Environmental Sciences
Faculty of Science
University of Ottawa

© David Diekrup, Ottawa, Canada, 2019

Abstract

Algoma-type banded iron formation is common in Neoarchean greenstone belts, and many of its distinctive features such as the banding of iron-rich and silica-rich material and deposition in volcanic terranes have been ascribed to their deposition related to volcanic-hydrothermal activity and cyclic variability in depositional pathways. The work presented in this thesis tests these assumptions and presents a model for the deposition and post-depositional processes now represented by the petrography and geochemistry of a 2.73 Ga type-locality of Algoma-type BIF in Temagami, ON. Adsorption of components onto the surface of Fe-oxyhydroxides forming in the anoxic Neoarchean water column is the most likely process capable of transferring silica, as well as trace quantities of transition metals, rare earth elements, Ge, P, U and other components to the sediment. The petrogenesis of the Temagami BIF lithologies suggests ongoing recrystallization processes and volume loss reactions leading to the formation of magnetite layers, while jasper is identified as the most pristine lithology best representative of the initially deposited Fe-oxyhydroxide-silica gel. Recrystallization and volume loss reactions are controlled by the ongoing dewatering during compaction and diagenesis, without the influence of external hydrothermal or metamorphic fluids. When corrected for the volume loss and small amounts of clastic contamination, little residual variability can be observed in the composition of jasper and magnetite layers, indicative of an originally homogenous primary precipitate instead of sorted and layered material deposited on the seafloor. This model is in stark contrast to previous interpretations of seasonal variability in biologic activity, cyclical seasonal or hydrothermal events responsible for primary layering in BIF. Instead, very little direct input of hydrothermal components is recorded in the chemistry of the Temagami BIF, and elements abundant in high-temperature hydrothermal fluids such as sulfur are instead sourced from atmospheric sources and deposited by bacterial pathways. Lack of primary chemical variability and non-hydrothermally sourced components captured in BIF argue against a genetic link to local hydrothermal venting, but rather an open ocean depositional setting. As such, the Temagami BIF does not represent a marker horizon related to local or regional hydrothermal venting and potential formation of associated massive sulfide deposits but reflects processes and the chemistry of the open Neoarchean ocean.

Acknowledgements

I would like to acknowledge the support and patience of my supervisor Mark Hannington. This thesis would not be in place for another six years if it were not for your guidance.

Thank you to my thesis committee.

This project would not have been possible without all the help I received over the years, professionally and personally. Many people supported me and influenced this project in one way or another, but I would like to specifically acknowledge the contributions of the late Eric Hoffman at Actlabs, Jack Cornett, and Nic Olivieri.

I appreciate the great work in the laboratories at uOttawa and at the Universitaet Muenster, especially Paul Middlestead, Artur Fugmann, and Sam Morfin.

Thank you to Keiko, Dave, Ingrid and Glenn, for sharing your knowledge and support over the years.

Thanks to Steve, Lily, and Khalhela for your contributions to the project, and assistance in the field.

To my friends and family, thank you for welcoming me to Ottawa and not forgetting about me in Germany. Courtney, thank you for your unfaltering support.

Table of Contents

Title I

Abstract II

Acknowledgements III

Preamble IX

Statement of original contribution XI

Chapter 1: Banded Iron Formations – Significance and Current Issues 1

Abstract 2

1.1 Introduction 5

1.2 Mineralogical and geochemical characteristics of Algoma-type BIF 7

1.3 Outstanding questions 10

1.4 References 14

Chapter 2: Mineralogy and Paragenesis of the Temagami BIF: A Detailed Reconstruction of the Diagenetic History of Neoarchean Algoma-Type BIF 23

Abstract 24

2.1 Introduction 26

2.1.1 The mineralogy of BIF 29

2.2 Geology of the Temagami Greenstone Belt and Sherman Mine 33

2.3 Sampling and methodology 36

2.3.1 Scanning electron microscopy (SEM) 37

2.3.2 Electron probe microanalysis (EPMA) 37

2.3.3 LA-ICP-MS 38

2.4 Description of the BIF samples 39

2.4.1 Grain-scale petrography 39

2.4.2 Oxide-facies BIF 41

2.4.3 Microstructures 44
2.4.4 Other lithologies 46
2.5 Mineral paragenesis 47
2.6 Mineral chemistry 49
2.6.1 Magnetite 49
2.6.2 Chlorite 52
2.6.3 Apatite 53
2.6.4 Monazite and xenotime 54
2.6.5 Other mineral species 55
2.7 Discussion 55
2.7.1 Origin of magnetite, jasper, and chert layers 55
2.7.2 Earliest diagenesis 57
2.7.3 Late-stage diagenesis 60
2.7.4 Metamorphism 61
2.7.5 Magnetite versus hematite growth in BIF 63
2.7.6 Significance of magnetite chemistry 65
2.7.7 Significance of chlorite compositions 69
2.7.8 Apatite-monazite chemistry 71
2.7.9 REE and Y systematics in the host minerals 72
2.8 Conclusions 74
2.9 References 76
Tables 98
Figures 121

Chapter 3: Geochemistry of the Oxide-, Silicate-, Carbonate-, and Sulfide Facies of the 2.73 Ga Temagami Iron Formation: New Evidence of the Depositional Pathways and Diagenetic Processes of Neoarchean Algoma-Type BIF 172
Abstract 173

3.1 Introduction 175
3.2 Algoma-type BIF at Temagami 176
3.2.1 Local stratigraphy 177
3.2.2 Facies distribution and abundance 179
3.3 Previous work 183
3.4 This study 184
3.4.1 Sample preparation 185
3.4.2 Analytical methods 185
3.4.3 Quality assurance 187
3.5 Results 188
3.5.1 Si and Fe 188
3.5.2 Ca, Mg, Na, and K 188
3.5.3 Aluminum 189
3.5.4 Phosphorous 189
3.5.6 C, S, N, LOI 190
3.5.7 Rb, Sa, Cs, Ba 190
3.5.8 Li, Be, B 191
3.5.9 Sc, Ti, Zr, Hf, Nb, Ta 191
3.5.10 Co, Ni, Cu, Zn, As, Ag, Cd, Sn, Sb, Hg, Pb 192
3.5.11 Ge, Ga, Se, In, Te, Tl, Bi 192
3.5.12 Mn, V, Cr, Mo, W, Re, Th, U 192
3.5.13 REE and Y 193
3.6 Discussion 194
3.6.1 Inter-element correlations 194
3.6.2 Clastic versus chemical components of the BIF 196
3.6.3 REE systematics in the whole rock 197
3.6.4 Geochemistry of the primary precipitates 201
3.6.5 Depositional mechanisms and implications for Archean seawater 201

3.6.6 Comparisons with other BIF and modern metalliferous sediments 206
3.6.7 Geochemical mass fluxes 207
3.7 Conclusions 209
3.8 References 213
Tables 230
Figures 257
Chapter 4: Decoupling of Neoarchean Sulfur Sources Recorded in Algoma-type Banded Iron Formation 286
Abstract 287
4.1 Introduction 288
4.2 Samples and Methods 290
4.2.1 Samples 290
4.2.2 Methods 292
4.3 Results and Discussion 294
4.5 Conclusions 299
4.6 References 301
Tables 307
Figures 310
Chapter 5: Summary and Conclusions 315
5.1 Summary 316
5.2 Primary depositional processes 317
5.3 Post-depositional processes 318
5.4 Geochemistry 320
5.5 Sulfur, hydrothermalism, and biology 322
5.6 Implications for BIF-Systems and Conclusions 322
5.7 References 324

Appendices

Appendix A: Sample descriptions 327

Appendix B: EPMA analyses of magnetite 396

Appendix C: LA-ICP-MS analyses of magnetite 403

Appendix D: EPMA analyses of chlorite 411

Appendix E: EPMA analyses of apatite 416

Appendix F: LA-ICP-MS analyses of apatite 418

Appendix G: EPMA analyses of monazite and xenotime 421

Appendix H: EPMA analyses of quartz 423

Appendix I: EPMA analyses of hematite 424

Appendix J: EPMA analyses of Fe-Ti oxides 425

Appendix K: EPMA analyses of carbonates 426

Appendix L: Polyatomic interferences in ICP-MS 427

Appendix M: Geochemistry of Temagami BIF whole rock samples 429

Appendix N: Principal Component analysis 436

Appendix O: Temagami BIF element variable maps 444

Appendix P: Supplementary information for Chapter 5 461

Preamble

Iron Formation is "a chemical sediment, typically thin-bedded or laminated, containing 15 percent or more of iron of sedimentary origin, commonly but not necessarily containing layers of chert." The deceptively simple definition of these lithologies was coined by Harold James in 1954, but its broad nature covers many different types of iron-rich lithologies, including the massive deposits of Precambrian Superior-type iron ore that formed in response to the rise in atmospheric oxygen around the time of the Great Oxidation Event in Australia, Brazil, South Africa and North America. It also encompasses younger deposits of metalliferous sediments and hydrothermal vent precipitates, as well as some of the oldest sediments in the rock record and Algoma-type banded iron formations (BIF) in Archean greenstone belts. This variability of lithologies under the "iron formation" umbrella complicates the identification of common depositional processes. For this thesis, models for depositional and post-depositional processes were tested on a type locality of Algoma-type BIF in Temagami, ON. The generally accepted assumption that these Neoarchean, up to 10 km strike length iron deposits occurring in greenstone belts around the margins of cratons formed in response to local hydrothermal venting and represent deep water deposits marking time breaks in the deposition of volcanic material and potential marker horizons for hydrothermal ore deposits forming along strike was tested in the case of the Temagami BIF. The origin of the banding, sources and depositional pathways of iron and other components, and a characterization of the depositional environment were investigated.

The Temagami BIF is a 2.73 Ga Algoma-type iron formation, hosted in a bimodal volcanic greenstone belt also containing volcaniclastic sediments. The lithologies in the greenstone belt are steeply dipping, allowing for the investigation of a stratigraphic cross-section along the Hwy 11 roadcut outcrop just north of the town of Temagami, ON. Parts of the Temagami BIF were mined for iron ore in the former Sherman Mine, where large ore blocks were left on the rims of the four open pits. The petrography and mineralogy of the Temagami BIF presented in Chapter 2 is based on the detailed study of the magnetite-jasper-chert bands and other BIF facies in the Hwy outcrop, ore blocks in the Sherman mine and samples from its host rocks. Using petrographic and electron microscopy, a petrogenetic reconstruction has been established and jasper layers were identified as best representative lithified product of the initially deposited Fe-oxyhydroxide-silica gel. Movement and escape of pore fluids and volume loss by silicon escape reflected by several

generations of quartz veins and related to the formation of magnetite layers. In-situ analyses by EPMA and LA-ICP-MS were used to track the preferential incorporation or removal of components, reflected in the internal compositional variations in magnetite and other mineral phases. The effect of the mobility of components in the sedimentary package and the reliability of BIF as a geochemical archive recording the conditions in the Neoarchean ocean is tested in Chapter 3, using the whole rock geochemistry of samples from all BIF facies to reconstruct the depositional pathways and characteristics of the Neoarchean seawater from which the Temagami BIF formed. Results from high-precision Fusion-ICP-MS and Total-digestion ICP-MS analyses inform adsorption of components in a hydrothermally influenced water column onto the surface of settling Fe-oxyhydroxides as the main depositional pathway. The initial geochemical signal is overprinted by the post-depositional processes such as volume loss reactions, but reflect a common, homogenous precursor material for the diagenetically formed jasper, magnetite, and chert layers. The depositional environment was anoxic, open to a larger oceanic basin, and allowed for considerable residence time of rare earth elements and the fractionation of transition metals, contrasting the traditional view of BIF deposition related to hydrothermal venting. Influence of hydrothermal venting as a source of components in the Temagami BIF was tested using multiple sulfur isotopes to track its sources and pathways in the environment. The results presented in Chapter 4 indicate that trace amounts of sulfur in the oxide-facies BIF extracted from whole rock samples using wet chemical methods offer no evidence for hydrothermally derived sulfur in sulfide- or oxide-facies BIF. Instead, an atmospheric source signal and biologic turnover of sulfur are captured in BIF.

The emerging picture of the deposition of the Temagami BIF is one of a biologically active open ocean setting, with some components derived from distal hydrothermal venting while others reflect sources such as atmospherically cycled sulfur. Such a model for an open-ocean depositional setting independent of hydrothermal venting contrasts commonly assumed models of Algoma-type BIF formation, summarized in Chapter 5.

Statement of original contribution

This thesis is the summary of original research undertaken at the University of Ottawa by David Diekrup under supervision of Prof. Mark Hannington. The project was planned and executed by D. Diekrup, with primary funding from a NSERC Discovery grant awarded to Mark Hannington and additional funding from a Society of Economic Geologists research fund awarded to D. Diekrup for field work.

Chapter 1: Introduction

Written by D. Diekrup with editorial corrections by M. Hannington.

Chapter 2: Mineralogy

Written by D. Diekrup with editorial corrections by M. Hannington. Field work in the summer seasons of 2013-2017 in collaboration with S. Ginley, L. Streit, and K. Khan. Sampling undertaken in collaboration with S. Ginley and L. Streit. Thin section preparation by D. Diekrup and S. Ginley, as well as L. Streit under supervision of D. Diekrup. Petrographic descriptions and SEM survey by D. Diekrup, in part building on a parallel petrographic study of the same samples by S. Ginley (referenced where applicable). EPMA analyses by D. Diekrup. Chlorite EPMA analyses by L. Streit under supervision of D. Diekrup and by D. Diekrup on an expanded dataset. LA-ICPMS analyses performed by D. Diekrup under technical guidance of S. Morfin. All figures and tables produced by D. Diekrup with the exception of Figure 2.6 b) and c) produced by S. Ginley and modified by D. Diekrup. Figures 2.32 and 2.33 originally produced by L. Streit, reproduced using an expanded dataset by D. Diekrup.

Chapter 3: Geochemistry

Written by D. Diekrup with editorial corrections by M. Hannington. Field work in the summer seasons of 2013-2016 with support from S. Ginley and K. Khan. Sampling undertaken by D. Diekrup with support from S. Ginley and K. Khan. Whole rock sample powder preparation undertaken by D. Diekrup and S. Ginley. Whole rock geochemical results produced by Actlabs –

Activation Laboratories, Ancaster, ON. Statistical analyses of results and interpretations by D. Diekrup. All figures and tables by D. Diekrup.

Chapter 4: Sulfur Isotope Study

Written by D. Diekrup with editorial corrections by M. Hannington. Field work in the summer of 2013 with support from S. Ginley. Sample preparation by D. Diekrup. Wet chemical extractions at the University of Muenster by D. Diekrup. Isotopic analysis by K. Siedenberg and Andreas Lutter. Data analysis and interpretation by D. Diekrup. All figures and tables by D. Diekrup. The manuscript was reviewed by at least two anonymous referees and edited according to reviewers' suggestions.

Chapter 5: Summary and Conclusions

Written by D. Diekrup with editorial corrections by M. Hannington.

Chapter 1

Banded Iron Formations – Significance and Current Issues

Abstract

Banded iron formations (BIF) are ubiquitous chemical sediments in Precambrian greenstone belts and many ancient ocean basins. They are widely regarded as archives of the paleo-ocean conditions in which they formed, including element cycles on Early Earth. BIF contain particularly important records of ocean chemistry without many of the shortcomings of clastic sediments that are affected by highly variable detrital input and reworking. However, many aspects of the primary depositional nature and secondary processes of BIF are still poorly understood. The origin of many components of BIF, including the most abundant elements Fe and Si, as well as the distinctive banding are still a matter of debate. In the absence of a clear understanding of the makeup of BIF, it is not always clear what material should be sampled to study the geochemical record using modern analytical technologies and isotope systems.

To illustrate the potentially diverse geochemical signals in BIF and to address the origins of some of their characteristic features, this project examined the depositional pathways and complex diagenetic history of one of the type localities of Neoarchean Algoma-type BIF in the area of the Sherman Mine in Temagami, ON. The BIF comprises predominantly oxide-facies interlayers of jasper, chert and magnetite. Minor sulfidic cherts, chlorite-rich layers and lenses of siderite represent sulfide-, silicate-, and carbonate-facies BIF in the area.

Detailed paragenetic studies of the mineralogy and mineral chemistry reveal a sequence of formation beginning with primary jasper deposition followed by the growth of microcrystalline magnetite and development of pseudobanding by volume loss and remobilization of primary constituents. The origins of hematite and magnetite layering, historically attributed to changes in redox state of the depositional environment, are considered here to be mainly secondary in nature and controlled by diagenetic reactions. Jasper and magnetite layers formed from a common precursor material consisting of amorphous Fe-oxyhydroxide, a potent scavenging agent that also transported silica to the seafloor. Chert layers formed from Si-rich pore water expelled during diagenetic conversion of amorphous Fe-oxyhydroxide to hematite and magnetite. Certain trace elements, such as Ge, Mn, and As, were enriched in the diagenetic magnetite and depleted in the chert layers, whereas the hematite and jasper layers retained much of the geochemical signature of

the primary Fe-oxyhydroxides. The jasper layers have a uniform geochemistry throughout the BIF, suggesting a spatially and temporally consistent flux of components to the seafloor during the original deposition. Fe-oxyhydroxides are potent scavenging agents, delivering the geochemical fingerprint of Neoarchean seawater to the sediments. Their composition suggests that Temagami seawater was strongly hydrothermally influenced, but rare earth elements and transition metals do not record direct hydrothermal plume-fallout from proximal black smoker-type fluids or post-depositional infiltration in an enclosed basin. Instead, the Temagami ocean, as a whole, was hydrothermally influenced at a large scale, and local conditions (local changes in redox, pH, or biological activity) triggered the deposition of the chemical sediments forming the Temagami BIF. Free oxygen was likely near-absent in the Temagami ocean, buffered by vast amounts of reduced, soluble Fe in the water column. Many elements abundant in the modern ocean as oxyanions, such as Mo and W, are absent in Temagami BIF, although some elements with lower oxidation thresholds or faster oxidation kinetics, such as U, are present in trace quantities.

Trace S-isotope systematics in all facies present in the Temagami BIF tell a similar story: that no significant influence of a local high-temperature vent source for sulfur is recorded in Temagami BIF. Both oxide- and sulfide-facies BIF record the predominance of atmospheric sulfur metabolized by different bacterial pathways. Ultra-trace S in oxide-facies BIF was derived from elemental atmospheric sulfur passively delivered to the sediment and metabolically processed along a bacterial pathway not requiring organic carbon as electron donor. Elemental sulfur disproportionation into a reduced and oxidized sulfur component can yield energy for bacteria without organic carbon involved as reactant, as can bacterial metabolisms reducing elemental sulfur to form sulfide while using ferric iron as electron acceptor. The strong correlation of trace chalcophile elements in the magnetite with isotopically distinct sulfide, suggest biologically mediated deposition of the base metals rather than from direct hydrothermal or volcanic sources. Larger quantities of sulfate were locally reduced to H_2S in the sulfide-facies BIF and converted diagenetically to pyrite, controlled by the availability of organic carbon in the sediments. The more abundant sulfides trapped minor chalcophile elements, such as, Pb, Cu and Zn, that were delivered by low-temperature hydrothermal seawater diffusing through the sediments.

The Temagami BIF formed in a volcanically and biologically active environment but under a well-mixed water column reflective of Neoarchean seawater, rather than in a restricted basin. Anoxic conditions in the water column were buffered by abundant ferrous iron in solution, along with enrichments in transition- and post-transition metals (Cu, Pb, Zn, As, Ni, Cr, and Co). The composition of Temagami seawater reflects lacking mobilization of redox-sensitive elements during oxidative weathering in modern surface environments (Mo, W, U, and Re), but instead dominant supply from hydrothermal sources and weathering of mafic-ultramafic material delivering higher Cr and Ni to Temagami seawater compared to modern oceans. This geochemical fingerprint of the larger Neoarchean ocean was delivered to the seafloor by adsorption processes onto iron-oxyhydroxides and preserved in diagenetic magnetite and local sulfide. Formation under anoxic, open-ocean conditions contradicts the depositional environment usually invoked for Algoma-type BIF: small, enclosed basins and association with hydrothermal venting forming Algoma-type BIF as exhalites. Instead, many characteristics are shared with Superior-type BIF, highlighting the importance of the investigation of depositional mechanisms in addition to the associated lithologies as a basis for BIF classification.

1.1 Introduction

BIF have been in the focus of scientific interest since the ground laying studies by Harold James (1954), Gordon Gross (1965a; 1980; 1983), and Preston Cloud (1973). Renewed interest has focused on BIF as archives of paleoenvironmental conditions and in particular the evolution of the oceans and atmosphere at the time of the Great Oxidation Event around 2.3 Ga (GOE: e.g., Ohmoto, 1996; Farquhar et al., 2000; Farquhar and Wing, 2003; Bekker et al., 2004; Ohmoto et al., 2006; Ohmoto et al., 2008; Guo et al., 2009, Pufahl and Hiatt, 2012). BIFs are also widely considered to record secular changes before the GOE, for example related to early bacterial metabolism and development and erosion of early continental landmasses (Konhauser et al., 2002; Kappler et al., 2005; Konhauser et al., 2005; Bowins and Crocket, 2011; Posth et al., 2013b; Viehmann et al., 2014).

The formation of Algoma-type BIF peaked during the Neoarchean, although they are also present in older (mostly 3.5-2.7 Ga) as well as younger (Paleozoic and Mesozoic) volcano-sedimentary successions (Gross, 1965b). They were deposited in deep marine sub-basins in close association with bimodal volcanism and clastic sedimentary rocks interpreted to have been deposited in a eugeosynclinal environment (devoid of clastic sediments: Gross, 1965a). Algoma-type BIF are thought to have formed by deposition of a primary chemical precipitate from a hydrothermally influenced water body devoid of oxygen (Gross, 1965a; Gross, 1965b; Gross and Donaldson, 1990; Bowins and Heaman, 1991; Ohmoto et al., 2006). Many consider that their formation was at least in part controlled by bacteria, either photosynthetically oxidizing Fe^{2+} to Fe^{3+} directly (reaction [1.1]; Widdel et al., 1993), or producing oxygen that led to Fe oxidation (Konhauser et al., 2002; Kappler et al., 2005; Ohmoto et al., 2006; Konhauser et al., 2007; Bau and Alexander, 2009). Alternative models of iron oxidation involve direct photooxidation or pH-controlled reactions: UV-photooxidation of Fe^{2+} (reaction [1.2]; Cairns-Smith, 1978) may have been involved in the formation of BIF, but was probably a negligible process in Neoarchean surface environments (Cairns-Smith, 1978; Konhauser et al., 2007). Increased mantle plume activity correlating with BIF formation in the Archean (Isley and Abbott, 1999) is the basis for a model of Fe^{3+} production reliant on water column pH changes: Anomalous hydrothermal systems hosted in ultramafic lithologies more common in the Archean can produce alkaline (pH >9.5) fluids with high silica

concentrations. In contact with slightly acidic Archean seawater, silica would have precipitated and Fe^{2+} would have been oxidized abiotically following
reaction [1.3] without the involvement of free O_2 (Shibuya et al., 2010). Another possible mechanism delivering ferrous iron and silicon to the sediments in proximity to hydrothermal venting is the formation of amorphous ferrous iron-silica precipitates or hydrothermal clays in contact of high-temperature hydrothermal fluids with cooler seawater (Lascelles, 2007; Fisher and Knoll, 2009; Rasmussen et al., 2013). Such a process can also form Al-poor phases such as nontronite under anoxic conditions if ferric iron is available in the water column (Harder, 1978; Rasmussen et al., 2017).

$$4Fe^{2+} + HCO_3^- + 10H_2O \underset{h\nu}{\rightarrow} 4Fe(OH)_3 + CH_2O + 7H^+ \quad [1.1] \quad \text{(Widdel et al., 1993)}$$

$$2Fe^{2+} + 2H^+ \underset{h\nu}{\rightarrow} 2Fe^{3+} + H_2 \quad [1.2] \quad \text{(Cairns-Smith, 1978)}$$

$$4Fe^{2+} + 8H_2O \xrightarrow[pH\sim10]{} 4FeOOH + 2H_2 + 8H^+ \quad [1.3] \quad \text{(Shibuya et al., 2010)}$$

The traditional view of different types of Neoarchean BIF and the corresponding facies relations has been that of a restricted sub-basin within a eugeosynclinal environment in which different sedimentary layers are developed in response to changing redox conditions (e.g., from sulfidic to oxidizing bottom waters), although this model is difficult to reconcile with uniformly anoxic conditions inferred for Neoarchean basins (e.g., Bekker et al., 2010). Early research focused on secular variations in the water column chemistry, including seasonality and basin overturn, to explain the banded nature of many iron formations, often seen as analogues to varves (Dimroth and Chauvel, 1973; Trendall, 1973; Walker, 1984; Garrels, 1987; James, 1992; Bekker et al., 2010). Recently, the early models have been refined and fluctuations in temperature have been interpreted as controlling mechanisms (Posth et al., 2008; Bekker et al., 2010). The model after Posth et al. (2008) relies on different responses of silica precipitation and bacterial ferrihydrite production towards seasonal temperature variations. Warmer temperatures lead to more vigorous bacterial activity forming Fe-rich layers while Si-solubility is increased, while colder temperatures have the reverse effect and would produce Si-rich layers (Posth et al., 2008).

Hydrothermal venting and continental runoff are thought to have been the major sources of Fe, Si and other constituents in the enriched bottom waters, with remobilization from marine sediments as potentially an additional important process. Proximity to a volcanic-hydrothermal source has been a common feature of most models, involving either biogenic or abiogenic precipitation (e.g., Bekker et al., 2010). While there may have been many different causes of BIF deposition, the dominant process almost certainly involved initial precipitation of iron oxyhydroxides formed in the hydrothermally-influenced water column (Gross, 1980; Bowins, 1989; Bau and Alexander, 2009), followed by deposition at the seafloor and significant diagenetic changes leading to the different BIF facies (e.g., Klein, 2005; Pufahl and Hiatt, 2012; Posth et al., 2013a). Algoma-type BIF, in particular, provides a unique record of the paleoseafloor conditions of Neoarchean volcanic basins. Those conditions are explored here in a world-class locality for Archean Algoma-type iron formation in the 2.73 Ga Temagami greenstone belt (Figure 1.1). In the first chapter of the thesis, the origin of the remarkable banding in Algoma-type BIF, including different stages of formation of chert, red jasper and magnetite layers, is studied in detail. Diagenetic and metamorphic reactions, in particular volume loss, are traced through the individual mineral phases to explain the geochemical evolution of the layers. In the second and third chapters, the geochemical and isotopic composition of the BIF layers is examined, shedding light on the nature of the depositional environment open to exchange with the ocean, and revealing important aspects of the chemistry of Neoarchean seawater.

1.2 Mineralogical and geochemical characteristics of Algoma-type BIF

Detailed studies of individual mm-scale bands in Temagami BIF reveal a complex depositional and diagenetic history. The chert and jasper layers are early pseudobands formed by silicification of an initial, amorphous Fe-oxyhydroxide precipitate, whereas the magnetite layers formed at a late stage during dewatering and recrystallization associated with significant volume loss, which also upgraded the material to commercially important Fe concentrations. Initial precipitates in chemical sediments of this type can contain up to 90% water (Williams et al., 1985; Gurvich, 2006), which is released during burial. In this study we examine processes that could have contributed to the formation of distinctive layering from these initial precipitates. We consider

whether burial temperatures that rise above ambient Archean seawater temperatures (40-70 ºC: Knauth, 2005; Robert and Chaussidon, 2006) could have caused silica solubility in pore water to increase, dissolving amorphous silica or intermediate silica phases such as opal and resulting in silicification of early-formed hematite and magnetite by less soluble quartz in jasper and black chert layers. We examine to what extent these processes may have sealed and preserved early jasper and black chert layers, with dissolution of silica along the flow path and significant loss of Si during pore water escape, and whether recrystallization was by layer-parallel migration of pore water or the rise of fluids through the sediment column. A similar process of silica expulsion related to diagenetic development of layering and upgrading of BIF to iron ore has been proposed for BIF of the Hamersley basin (Findlay, 1994). Early silicification processes are evident in other BIF, where the formation of cherts as siliceous hardgrounds on the seafloor has been interpreted as hiatus in BIF deposition (Krapež et al., 2003). The process of hardground-formation was linked to export of silica from the water column, similar to the modern seafloor silicification processes (Siever, 1992; Rasmussen et al., 2015). However, pre-compaction silicification processes can also preserve chert pods, lenticular silicified material formed by upwards migration of silica-rich pore waters in some BIF (Fischer and Knoll, 2009).

If diagenesis, and in particular volume loss, are major factors in the evolution of the BIF, these changes should be evident in the mineralogy and chemistry of the BIF layers. We examine whether such changes can be traced through different paragenetic stages of individual mineral phases, such as magnetite, chlorite, and apatite. In particular, we show higher chlorite formation temperatures in magnetite layers and the volcanic-host rocks than in jasper and chert layers. We also examine how different elements are partitioned into the mineral phases formed during diagenesis and recrystallization, especially among the trace elements (e.g., Ge in magnetite, REE in apatite). The effects of volume loss and silica mobility have been previously invoked for models of hypogene and supergene enrichment of BIF to iron ore (e.g., Morris 1985; Taylor et al., 2001). However, this study shows that volume loss reactions need not be linked to external fluid sources, but that the Temagami BIF was upgraded to iron ore by internal fluids similar to a process suggested by Lascelles et al. (2007).

Many previous studies have attributed geochemical variations in the BIF layers to primary enrichment at the time of deposition (e.g.,West Greenland; Appel, 1986), but it remains unclear to what extent geochemical variations are reflective of extensive diagenetic interactions, volume loss, and recycling of elements back into seawater. We show that layers that were minimally altered by post-depositional processes best reflect the element budgets. Most studies focussing on post-depositional element mobility in BIF report limited mobility few selected element groups like REE, Ni-Zn, or U within layers while retaining the general geochemical signal of the original precipitate (Alibert, 2016; Robbins et al., 2019; Oonk et al., 2018). Such studies are commonly based on partition coefficients, direct measurements of elements in mineral host phases, or simulated diagenetic processes (e.g., Posth et al., 2013; Köhler et al., 2013). However, this is the first study quantifying loss or enrichment of 48 elements plus REE during diagenesis, showing a strong control of preferential retention or loss depending on the availability of suitable mineralogic host phases and element mobility.

In particular, layer-by-layer sampling and analysis of the Temagami BIF are compared to BIF-like exhalites, which are commonly viewed as analogs of Algoma-type iron formation. We examine to what extent spatial and temporal variations in geochemical profiles (including REE profiles) are reflective of a varying hydrothermally influenced reservoir versus chemical changes in the sediments after deposition. Hydrothermal pulses into semi-enclosed basis are commonly invoked to explain the composition of exhalites (e.g., Goodwin et al., 1985; Peter and Goodfellow, 1996; Laurila et al., 2014), whereas large, stable reservoirs of the major and trace elements would be expected to produce compositionally homogenous layering with a predominance of hydrogenous components for the entire history of deposition. We address the question of whether BIF deposition was dominated by local hydrothermal sources, or instead mainly reflects the chemistry of the open Neoarchean ocean. We test this by examining multiple isotopes of trace quantities of sulfur preserved in magnetite and chert, which can record the full spectrum of sources (magmatic, biological, atmospheric) and the different pathways to the sediments.

1.3 Outstanding questions

Algoma-type BIF are outwardly similar to Fe-rich chemical sediments (i.e., exhalites) that formed by direct hydrothermal input associated with volcanogenic massive sulfide deposits. A large part of this study aims at the characterization of such a link in the case of the Temagami BIF, where field evidence for local hydrothermal systems is lacking. Lake Superior-type BIF, which formed in response to large-scale upwelling and changes in the redox state of the shallow ocean, similarly do not have an obvious hydrothermal source and are interpreted to reflect mainly open ocean conditions (Gross, 1980). We speculate that regionally extensive Algoma-type BIF in greenstone belts of the Southern Superior Province recorded episodes of mainly open ocean circulation that were affected by large-scale but mainly diffuse rather than focused high-temperature hydrothermal venting. The extent of Algoma-type BIF deposition in the Abitibi greenstone belt, with a cumulative strike length of hundreds of kilometers of BIF (Thurston et al., 2008) suggests that these conditions proliferated in the periods between major volcanic episodes and were possibly related to the cooling of the volcanic pile over millions of years (Goodwin, 1980). Massive sulfide deposits form contemporaneously with volcanism, but the deposition of exhalites and BIF can be more variable before or during, but usually after extrusive volcanism and VMS emplacement (Peter and Goodfellow, 1996; Franklin et al., 2005; Thurston et al., 2008). Heat flow driving hydrothermal systems that form volcanogenic massive sulfide deposits is usually only sustainable for tens of thousands of years, and hydrothermal circulation covering the duration of BIF deposition of one million years or more would require repeated intrusions to replenish the energy required to heat the fluid (Cathles et al., 1997). It remains to be tested if a local hydrothermal system was present in Temagami, and if it could have remained active long enough to form a BIF as large as the deposit in Temagami.

Fe and Si in Algoma-type BIF are generally considered to originate from hydrothermal-seawater sources, whereas younger Superior-type BIF reflect compositions influenced by hydrothermal components that were delivered by upwelling, but also from continental weathering (Isley, 1995). The Temagami BIF captures REE systematics typical of strong hydrothermal influence, but also isotopic Nd-Hf systematics indicative of continental landmasses exposed to subaerial weathering (Viehmann et al., 2014). The time frame around 2.7 Ga may therefore mark a transitional period

from ocean chemistry dominated by mantle-hydrothermal chemistry towards continent-erosion dominated processes. Such a transition from more mantle-ultramafic towards continental-felsic element sources has been invoked for the delivery of nickel to the oceans, its potential effects on methanogenic bacteria, and the accumulation of oxygen in the atmosphere (Konhauser et al., 2009). Active continental weathering would have also influenced the delivery of other components, such as an increase in the delivery of phosphate from continental weathering, compared to a loss of phosphate from seawater during hydrothermal cycling in the crust (Wheat et al., 1996). Phosphate is a major nutrient and possibly a limiting factor for metabolisms such as anoxygenic Fe(II)-oxidizing bacteria in the Archean (Bjerrum and Canfield, 2002). Increased supply of components from newly emerged continental landmasses (including phosphate) will therefore be tested as a potential trigger mechanism for the potentially biologically controlled deposition of BIF.

The major control on facies development within BIF (e.g., hematitic facies versus magnetite facies) has traditionally been considered spatial variation in redox, e.g., between more reduced, euxinic and more oxidized parts of the basin (e.g., James, 1954; Cloud, 1973; Holland, 1973). However, facies changes in Algoma-type BIF commonly occur between individual layers, which is difficult to reconcile with large-scale basin evolution. Isotopic data now strongly suggest that the entire basin was anoxic and therefore redox controls appear to have been less important (see Chapter 4; Diekrup et al., 2018). Therefore, another mechanism is required to explain the rapid changes from hematite-dominant to magnetite-dominant facies. Different diagenetic formation temperatures reflected by oxygen isotope studies in chert and magnetite have previously been suggested (Shimada et al., 2006), and will be tested by chlorite geothermometry. Diagenetic volume loss by silica remobilization in progressively warming pore waters is proposed as a primary mechanism controlling the development of jasper and magnetite from a homogenous precursor material. Temperature as a potent mechanism driving the remobilization of Si is proposed, as an increase from near ambient temperature in the sediment (i.e., 50ºC to 150ºC) can lead to an ~8-fold increase amorphous silica solubility in the pore water (Williams and Crerar, 1984). An additional increase in silica solubility could stem from rising alkalinity in the pore waters due to a reverse of reaction [1.1] during iron reduction. It needs to be shown if increased heat flow under elevated geothermal gradients in a Neoarchean volcanic terrane would be

sufficient to generate the required early diagenetic temperature increase to dissolve and remove sufficient Si from the sedimentary package.

Transitions between oxide facies BIF, and locally abundant sulfide facies in the Sherman Mine sequence appears to be unrelated to higher-temperature hydrothermal venting and may instead be a result of available organic carbon. The availability of organic material is suggested as a controlling factor for the development of sulfide-facies BIF by sulfate-metabolizing bacteria. It remains to be shown what controlled the preferential deposition of organic material in sulfide-facies, while no C_{org} is preserved in oxide-facies.

In previous studies, properties of Neoarchean seawater have been established from fluid inclusions in hydrothermally altered volcanic rocks, geochemical analyses of sedimentary successions as well as modeling of atmospheric CO_2: Neoarchean seawater had a pH of 6.5-7.0 and was probably between 50-70ºC, contained only trace O_2, 40-3000 µM dissolved Fe^{2+}, 670-2200 µM SiO_2, and trace SO_4^{2-} (0.06-0.08 µM; Grotzinger and Kasting, 1993; Saito et al., 2003; Canfield 2005; Ohmoto et al., 2006; Crowe et al., 2014; Halevy and Bachan, 2017). A major outstanding question is the extent to which ambient seawater could have been a source of Neoarchean BIF, and whether changes in the chemistry of that water column (temperature, pH, redox) would have been sufficient to cause widespread BIF deposition. Such changes may have also been induced by the depositional mechanism if it was controlled by bacteria. Anoxygenic photoferrotrophy following equation [1.1] consumes HCO_3^- and releases 1.75 moles of H^+ per mole of $Fe(OH)_3$ produced. The release of protons leads to a pH drop in the environment (Wu et al., 2014). The effects of changing pH on carbonate equilibrium, complexation and metal adsorption onto Fe-oxyhydroxides, solubility of pH-sensitive phases (Si, B), CO_2 consumption on a scale required to deposit BIF by anoxygenic photoferrotrophy, and potential delivery of organic material from primary production to the sediment all need to be evaluated.

In the absence of any enrichments in trace metals observed in other BIF, such as W-Mo-Zn-Co-Pb-Sn enrichments in the Archean Malene BIF, West Greenland (Appel, 1986), we propose that the Temagami BIF records only the background Neoarchean ocean chemistry. Low trace element contents of redox-sensitive elements commonly present as oxyanions in seawater (e.g., Mo, W,

Re), as well as a lack of Ce anomalies, and variable contents of transition metals, support an emerging picture of Neoarchean seawater below the threshold of oxidation for many redox-sensitive elements. It remains unclear to what extent deposition of those elements is controlled by redox, rather than other factors (e.g., adsorption onto Fe-oxyhydroxides; biological formation of sulfides acting as geochemical traps for chalcophile elements). If the BIF record mainly open ocean conditions, as opposed to proximal hydrothermal sources, they may be an important archive of key elements, for example involved in biologic activity (P, Ni, Mo, and possibly other trace elements: Konhauser et al., 2009; Planavsky et al., 2010). The understanding of the geology and geochemistry of volcanic-derived and chemical sediments and their link (or absence thereof) to mineralization in this setting is crucial for targeted exploration for greenstone-hosted ore deposits, and for tracing element cycles in the Earth's early oceans, including the metabolisms of early photosynthesizers.

1.4 References

Appel, P.W., 1986. Strata bound scheelite in the Archean Malene supracrustal belt, West Greenland. Mineralium Deposita 21, 207-215.

Ayer, J.A., Thurston, P.C., Bateman, R., Dubé, B., Gibson, H.L., Hamilton, M.A., Hathway, B., Hocker, S.M., Houlé, M., Hudak, G.J., Ispolatov, V., Lafrance, B., Lesher, C.M., MacDonald, P.J., Péloquin, A.S., Piercey, S.J., Reed, L.E., Thompson, P.H., 2005. Overview of results from the Greenstone Architecture Project, Discover Abitibi Initiative. Ontario Geological Survey Open File Report 6154, 125p.

Ayer, J.A., Chartrand, J.E., Grabowski, G.D.P., Josey, S., Rainsford, D., Trowell, N.F., 2006. Geological compilation of the Cobalt–Temagami area, Abitibi greenstone belt. Ontario Geological Survey, Preliminary Map, 3581.

Bau, M., Alexander, B.W., 2009. Distribution of high field strength elements (Y, Zr, REE, Hf, Ta, Th, U) in adjacent magnetite and chert bands and in reference standards FeR-3 and FeR-4 from the Temagami iron-formation, Canada, and the redox level of the Neoarchean ocean. Precambrian Research 174, 337-346.

Bekker, A., Holland, H.D., Wang, P.L., Rumble, D., Stein, H.J., Hannah, J.L., Coetzee, L.L., Beukes, N.J., 2004. Dating the rise of atmospheric oxygen. Nature 427, 117-120.

Bekker, A., Slack, J.F., Planavsky, N., Krapež, B., Hofmann, A., Konhauser, K.O., Rouxel, O.J., 2010. Iron Formation: The Sedimentary Product of a Complex Interplay among Mantle, Tectonic, Oceanic, and Biospheric Processes. Economic Geology 105, 467-508.

Bennett, G., 1978. Geology of the northeast Temagami area, District of Nipissing. Ontario Ministry of Natural Resources.

Bjerrum, C.J., Canfield, D.E., 2002. Ocean productivity before about 1.9 Gyr ago limited by phosphorus adsorption onto iron oxides. Nature 417, 159-162.

Bowins, R., Crocket, J., 2011. Tungsten in Archean banded iron formation of the former Sherman and Adams mines, Ontario: possible mineralization processes. Canadian Journal of Earth Sciences 48, 11-23.

Bowins, R.J., 1989. Rare earth and other geochemical studies of Archean banded iron formation: Sherman and Adams Mines, Ontario. McMaster University, PhD thesis, 399 pp.

Bowins, R.J., Heaman, L.M., 1991. Age and timing of igneous activity in the Temagami greenstone belt, Ontario: a preliminary report. Canadian Journal of Earth Sciences 28, 1873-1876.

Cairns-Smith, 1978. Precambrian solution photochemistry, inverse segregation, and banded iron formations. Nature 276, 807-808.

Canfield, D.E., 2005. The early history of atmospheric oxygen: Homage to Robert A. Garrels. Annual Review of Earth and Planetary Sciences 33, 1-36.

Cathles, L.M., Erendi, A.H.J., Barrie, T., 1997. How long can a hydrothermal system be sustained by a single intrusive event? Economic Geology 92, 766-771.

Cloud, P., 1973. Paleoecological Significance of the Banded Iron-Formation. Economic Geology 68, 1135-1143.

Crowe, S.A., Paris, G., Katsev, S., Jones, C., Kim, S.-T., Zerkle, A.L., Nomosatryo, S., Fowle, D.A., Adkins, J.F., Sessions, A.L., Farquhar, J., Canfield, D.E., 2014. Sulfate was a trace constituent of Archean seawater. Science 346, 735-739.

Diekrup, D., Hannington, M.D., Strauss, H., Ginley, S.J., 2018. Decoupling of Neoarchean sulfur sources recorded in Algoma-type banded iron formation. Earth and Planetary Science Letters 489, 1-7.

Dimroth, E., Chauvel, J.-J., 1973. Petrography of the Sokoman Iron Formation in Part of the Central Labrador Trough, Quebec, Canada. GSA Bulletin 84, 111-134.

Donaldson, J.A., Garrett, R.G., 1991. Iron-Formation in Temagami and Sherman Mine Area, in: Gross, G.A., Donaldson, J.A. (Eds.), Geological Survey of Canada Open File 2163 - Iron-Formation and Metalliferous Sediments in Central Canada [Field Trip 8], p. 66.

Farquhar, J., Bao, H., Thiemens, M., 2000. Atmospheric Influence of Earth's Earliest Sulfur Cycle. Science 289, 756-758.

Farquhar, J., Wing, B.A., 2003. Multiple sulfur isotopes and the evolution of the atmosphere. Earth and Planetary Science Letters 213, 1-13.

Findlay, D., 1994. Diagenetic boudinage, an analogue model for the control on hematite enrichment iron ores of the Hamersley Iron Province of Western Australia, and a comparison with Krivoi Rog of Ukraine, and Nimba Range, Liberia. Ore Geology Reviews 9, 311-324.

Fischer, W.W., Knoll, A.H., 2009. An iron shuttle for deepwater silica in Late Archean and early Paleoproterozoic iron formation. GSA Bulletin 121, 222-235.

Franklin, J.M., Gibson, H.L., Jonasson, I.R., Galley, A.G., 2005. Volcanogenic Massive Sulfide Deposits, in: Hedenquist, J.W., Thompson, J.F.H., Goldfarb, R.J., Richards, J.P. (Eds.), One Hundredth Anniversary Volume. Society of Economic Geologists.

Garrels, R.M., Perry, E.A., Mackenzie, F.T., 1973. Genesis of Precambrian iron-formations and the development of atmospheric oxygen. Economic Geology 68, 1173-1179.

Goodwin, A.M., Thode, H.G., Chou, C.L., Karkhansis, S.N., 1985. Chemostratigraphy and origin of the late Archean siderite–pyrite-rich Helen Iron Formation, Michipicoten belt, Canada. Canadian Journal of Earth Sciences 22, 72-84.

Goodwin, A., 1980. Archean volcanic studies in the Timmins-Kirkland Lake-Norandsa region of Ontario and Quebec. Geological Survey of Canada Bulletin 278, 51.

Gross, G.A., 1965a. Geology of iron deposits in Canada, Vol. 1 general geology and evaluation of ore deposits: Geological Survey of Canada. Economic Geology Report 22, 81.

Gross, G.A., 1965b. Origin of Precambrian iron formations. Economic Geology 60, 1063-1065.

Gross, G.A., 1980. A classification of iron formations based on depositional environments. The Canadian Mineralogist 18, 215-222.

Gross, G.A., 1983. Tectonic Systems and the Deposition of Iron-Formation, in: B. Nagy, R.W.J.C.G., Schidlowski, M. (Eds.), Developments in Precambrian Geology. Elsevier, volume 7, pp. 63-79.

Grotzinger, J.P., Kasting, J.F., 1993. New Constraints on Precambrian Ocean Composition. The Journal of Geology 101, 235-243.

Guo, Q., Strauss, H., Kaufman, A.J., Schröder, S., Gutzmer, J., Wing, B., Baker, M.A., Bekker, A., Jin, Q., Kim, S.-T., Farquhar, J., 2009. Reconstructing Earth's surface oxidation across the Archean-Proterozoic transition. Geology 37, 399-402.

Gurvich, E.G., 2006. Metalliferous Sediments of the World Ocean. Springer, Berlin, Germany.

Halevy, I., Bachan, A., 2017. The geologic history of seawater pH. Science 355, 1069-1071.

Harder, H., 1978. Synthesis of Iron Layer Silicate Minerals under Natural Conditions. Clays and Clay Minerals 26, 65-72.

Holland, H.D., 1973. The oceans: A possible source of iron in iron-formations. Economic Geology 68, 1169-1172.

Isley, A.E., Abbott, D.H., 1999. Plume-related mafic volcanism and the deposition of banded iron formation. Journal of Geophysical Research 104, 15461-15477.

Isley, A.E., 1995. Hydrothermal Plumes and the Delivery of Iron to Banded Iron Formation. The Journal of Geology 103, 169-185.

James, H.L., 1954. Sedimentary facies of iron-formation. Economic Geology 49, 235-293.

James, H.L., 1992. Chapter 11 Precambrian Iron-Formations: Nature, Origin, and Mineralogic Evolution from Sedimentation to Metamorphism. Developments in Sedimentology 47, 543-589.

Kappler, A., Pasquero, C., Konhauser, K.O., Newman, D.K., 2005. Deposition of banded iron formations by anoxygenic phototrophic Fe(II)-oxidizing bacteria. Geology 33, 865-868.

Klein, C., 2005. Some Precambrian banded iron formations (BIFs) from around the world: Their age, geologic setting, mineralogy, metamorphism, geochemistry, and origin. American Mineralogist 90, 1473-1499.

Knauth, L.P., 2005. Temperature and salinity history of the Precambrian Ocean: Implications for the course of microbial evolution. Palaeogeography Palaeoclimatology Palaeoecology 219, 53-69.

Konhauser, K., Newman, D.K., Kappler, A., 2005. The potential significance of microbial Fe(III) reduction during deposition of Precambrian banded iron formations. Geobiology 3, 167-177.

Konhauser, K., Amskold, L., Lalonde, S.V., Posth, N.R., Kappler, A., Anbar, A., 2007. Decoupling photochemical Fe(II) oxidation from shallow-water BIF deposition. Earth and Planetary Science Letters 258, 87-100.

Konhauser, K.O., Pecoits, E., Lalonde, S.V., Papineau, D., Nisbet, E.G., Barley, M.E., Arndt, N.T., Zahnle, K., Kamber, B.S., 2009. Oceanic nickel depletion and a methanogen famine before the Great Oxidation Event. Nature 458, 750-753.

Konhauser, K.O., 2002. Could bacteria have formed the Precambrian banded iron formations? Geology 30, 1079-1082.

Krapež, B., Barlye, M.E., Pickard, A.L., 2003. Hydrothermal and resedimented origin of the precursor sediments to banded iron formation: Sedimentological evidence from the Early Proterozoic Brockman Supersequence of Western Australia. Sedimentology 50, 979-1011.

Lascelles, D.F., 2007. Black smokers and density currents: A uniformitarian model for the genesis of banded iron-formations. Ore Geology Reviews 32, 381-411.

Laurila, T.E., Hannington, M.D., Petersen, S., Garbe-Schönberg, D., 2014. Early depositional history of metalliferous sediments in the Atlantis II Deep of the Red Sea: Evidence from rare earth element geochemistry. Geochimica et Cosmochimica Acta 126, 146-168.

McBride, D., 2010. Report on the Scholes Township Property, Ontario. Temagami Iron Corporation Exploration Report, p. 37.

Meyn, H.D., 1977. Geology of Afton, Scholes, Macbeth, and Clement Townships, Districts of Sudbury and Nipissing, Ontario Geological Survey Report 170, p. 77.

Morris, R.C., 1985. Genesis of iron ore in banded iron-formation by supergene and supergene-metamorphic processes – A conceptual model. In: Wolff, K.H., ed. Handbook of Strata-bound and Stratiform Ore deposits. Amsterdam, Elsevier 13, 73-235.

OGS, 2001. Airborne magnetic and electromagnetic surveys, residual magnetic field, Temagami South area. Ontario Geological Survey, Map 60 090.

Ohmoto, H., 1996. Evidence in pre-2.2 Ga paleosols for the early evolution of atmospheric oxygen and terrestrial biota. Geology 24, 1135-1138.

Ohmoto, H., Watanabe, Y., Ikemi, H., Poulson, S.R., Taylor, B.E., 2006a. Sulphur isotope evidence for an oxic Archaean atmosphere. Nature 442, 908-911.

Ohmoto, H., Watanabe, Y., Yamaguchi, K.E., Naraoka, H., Haruna, M., Kakegawa, T., Hayashi, K., Kato, Y., 2006b. Chemical and biological evolution of early Earth: Constraints from banded iron formations. Geological Society of America Memoirs 198, 291-331.

Peter, J.M., Goodfellow, W.D., 1996. Mineralogy, bulk and rare earth element geochemistry of massive sulphide-associated hydrothermal sediments of the Brunswick Horizon, Bathurst Mining Camp, New Brunswick. Canadian Journal of Earth Sciences 33, 252-283.

Planavsky, N.J., Rouxel, O.J., Bekker, A., Lalonde, S.V., Konhauser, K.O., Reinhard, C.T., Lyons, T.W., 2010. The evolution of the marine phosphate reservoir. Nature 467, 1088-1090.

Posth, N.R., Hegler, F., Konhauser, K.O., Kappler, A., 2008. Alternating Si and Fe deposition caused by temperature fluctuations in Precambrian oceans. Nature Geoscience 1, 703-708.

Posth, N.R., Köhler, I., D Swanner, E., Schröder, C., Wellmann, E., Binder, B., Konhauser, K.O., Neumann, U., Berthold, C., Nowak, M., 2013a. Simulating Precambrian banded iron formation diagenesis. Chemical Geology 362, 66-73.

Posth, N.R., Konhauser, K.O., Kappler, A., 2013b. Microbiological processes in banded iron formation deposition. Sedimentology 60 (7), 1733-1754.

Pufahl, P.K., Hiatt, E.E., 2012. Oxygenation of the Earth's atmosphere-ocean system: A review of physical and chemical sedimentologic responses. Marine and Petroleum Geology 32, 1-20.

Rasmussen, B., Meier, D.B., Krapež, B., Muhling, J.R., 2013. Iron silicate microgranules as precursor sediments to 2.5-billion-year-old banded iron formations. Geology 41, 435-438.

Rasmussen, B., Krapež, B., Muhling, J.R., 2015. Seafloor silicification and hardground development during deposition of 2.5 Ga banded iron formations. Geology 43 (3), 235-238.

Rasmussen, B., Muhling, J.R., Suvorova, A., Krapež, B., 2017. Greenalite precipitation linked to the deposition of banded iron formations downslope from a late Archean carbonate platform. Precambrian Research 290, 49-62.

Robbins, L.J., Swanner, E.D., Lalonde, S.V., Eickhoff, M., Paranich, M.L., Reinhard, C.T., Peacock, C.L., Kappler, A., Konhauser, K.O., 2015. Limited Zn and Ni mobility during simulated iron formation diagenesis. Chemical Geology 402, 30-39.

Robert, F., Chaussidon, M., 2006. A Paleotemperature curve for the Precambrian oceans based on silicon isotopes in cherts. Nature 443, 969-972.

Saito, M.A., Sigman, D.M., Morel, F.M.M., 2003. The bioinorganic chemistry of the ancient ocean: the co-evolution of cyanobacterial metal requirements and biogeochemical cycles at the Archean–Proterozoic boundary? Inorganica Chimica Acta 356, 308-318.

Shibuya, T., Komiya, T., Nakamura, K., Takai, K., Maruyama, S., 2010. Highly alkaline, high-temperature hydrothermal fluids in the early Archean ocean. Precambrian Research 182, 230-238.

Shimada, Y., Yasumatsu, A., Motomura, Y., Okazaki, R., Nakamura, T., Ohmoto, H., Okaue, Y., Yokoyama, T., 2006. Geochemical Study on Temagami Iron-Formations, Canada. Geochimica et Cosmochimica Acta 70, A585.

Siever, 1992. The silica cycle in the Precambrian. Geochimica Cosmochimica Acta 56, 3265-3272.

Simony, P., 1964. Geology of Northwestern Timagami Area, District of Nipissing, Geological Report No. 28, Map No. 2057. Ontario Department of Mines, p. 30.

Taylor, D., Dalstra, H.J., Harding, A., Broadbent, G.C., Barley, M.E., 2001. Genesis of High-Grade Hematite Orebodies of the Hamersley Province, Western Australia. Economic Geology 96, 837-873.

Trendall, A., 1973. Varve cycles in the Weeli Wolli Formation of the Precambrian Hamersley Group, Western Australia. Economic Geology 68, 1089-1097.

Viehmann, S., Hoffmann, J.E., Münker, C., Bau, M., 2014. Decoupled Hf-Nd isotopes in Neoarchean seawater reveal weathering of emerged continents. Geology 42, 115-118.

Walker, J.C.G., 1984. Suboxic diagenesis in banded iron formations. Nature 309, 340-342.

Widdel, F., Schnell, S., Heising, S., Ehrenreich, A., Assmus, B., Schink, B., 1993. Ferrous iron oxidation by anoxygenic phototrophic bacteria. Nature 362, 834-836.

Williams, L.A., Crerar, D.A., 1985. Silica diagenesis, II. General mechanisms. Journal of Sedimentary Research 55 (3), 312-321.

Wu, W., Swanner, E.D., Hao, L., Zeitvogel, F., Obst, M., Pan, Y., Kappler, A., 2014. Characterization of the physiology and cell–mineral interactions of the marine anoxygenic phototrophic Fe(II) oxidizer Rhodovulum iodosum – implications for Precambrian Fe(II) oxidation. FEMS Microbiology Ecology 88, 503-515.

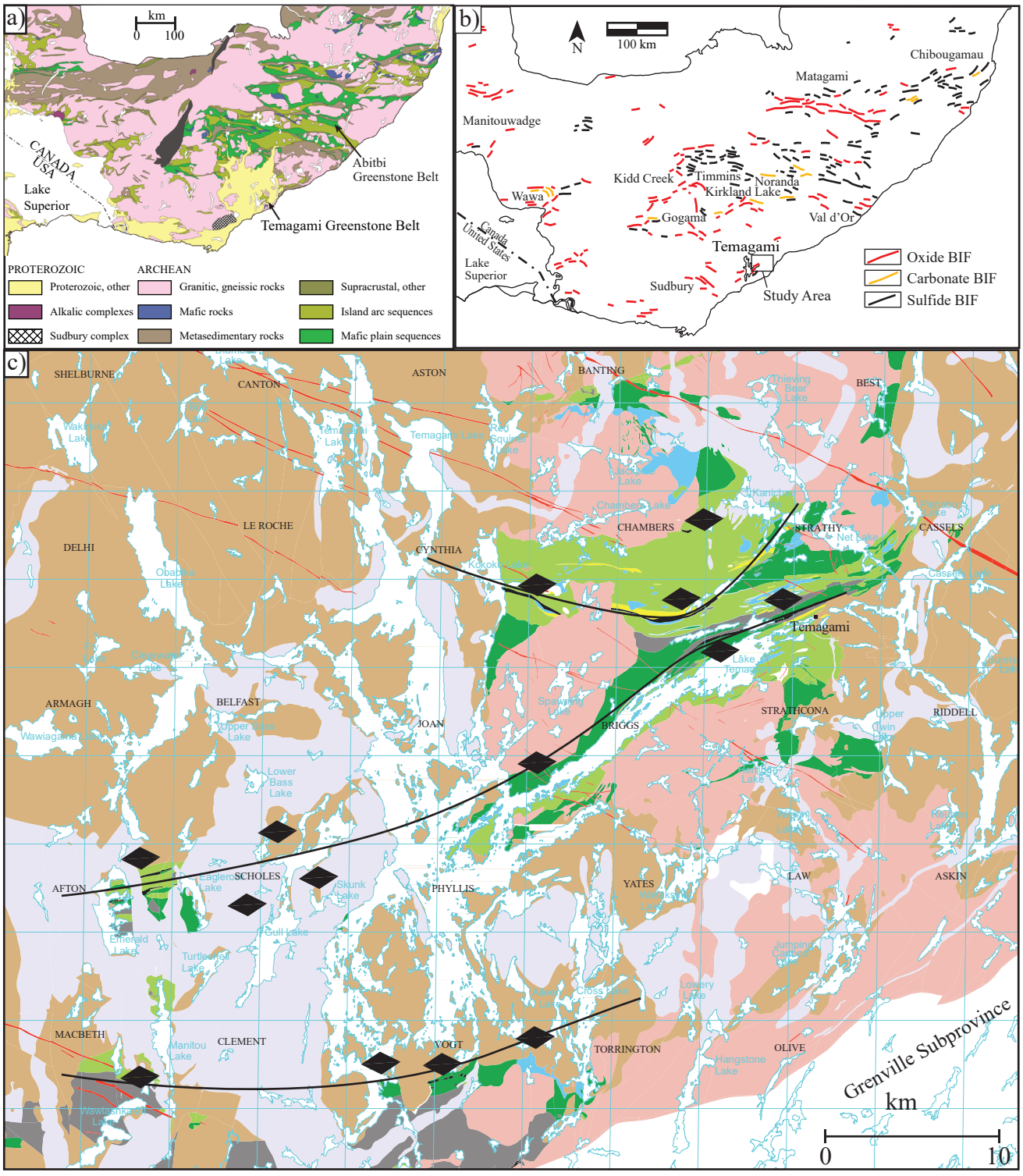

a)
km
0 100
CANADA
USA
Lake Superior
Abitbi Greenstone Belt
Temagami Greenstone Belt
PROTEROZOIC
Proterozoic, other
Alkalic complexes
Sudbury complex
ARCHEAN
Granitic, gneissic rocks
Mafic rocks
Metasedimentary rocks
Supracrustal, other
Island arc sequences
Mafic plain sequences
b)
N
100 km
Chibougamau
Matagami
Manitouwadge
Kidd Creek
Timmins
Noranda
Kirkland Lake
Wawa
Gogama
Val d'Or
Canada
United States
Lake Superior
Temagami
Sudbury
Study Area
Oxide BIF
Carbonate BIF
Sulfide BIF
c)
SHELBURNE
CANTON
ASTON
BANTING
BEST
LE ROCHE
DELHI
CHAMBERS
STRATHY
CASSELS
CYNTHIA
Temagami
ARMAGH
BELFAST
JOAN
BRIGGS
STRATHCONA
RIDDELL
AFTON
SCHOLES
PHYLLIS
YATES
LAW
ASKIN
MACBETH
CLEMENT
VOGT
TORRINGTON
OLIVE
Grenville Subprovince
km
0 10
LEGEND
Inferred BIF horizon
BIF Occurence
VOGT Township
PROTEROZOIC
Diabase Dikes
Nipissing-type Intrusive Rocks
Huronian Sedimentary Rocks
NEOARCHEAN
Felsic Intrusive Rocks
Mafic-Ultramafic Intrusive Rocks
Iron Formation
Clastic Metasedimentary Rocks
Felsic Metavolcanic Rocks
Intermediate Metavolcanic Rocks
Mafic Metavolcanic Rocks

Figure 1.1: Location and geologic overview of the Temagami Greenstone Belt between the Grenville Front in the southwest and the Cobalt embayment in the north. a) Geological overview of the Superior Province (modified after Ayer et al., 2005). b) BIF occurences in the Abitibi Greenstone Belt and wider Superior Craton (modified after Ohmoto et al., 2006b). c) Geological overview of the Temagami Greenstone Belt and reported occurences of BIF and the minimum extend of the Temagami iron formations from Ontario Geological Survey aeromagnetics maps (OGS, 2001). Base geology simplified after Ayer et al. (2006). BIF occurences after Simony (1964), Meyn (1977), Bennett (1978), McBride (2010).

Chapter 2

Mineralogy and Paragenesis of the Temagami BIF:
A Detailed Reconstruction of the Diagenetic History of Neoarchean Algoma-Type BIF

Abstract

Neoarchean Algoma-type Banded Iron Formations (BIF) are chemical sediments deposited from metal-enriched bottom waters in ancient volcanic basins. The precipitation of Fe-oxyhydroxides in the water column and scavenging of silica and other elements as they settle to the seafloor explains many of the mineralogical and geochemical features of the sediments, which record the conditions of their formation including key aspects of the nature of the basin in which they formed. The characteristic banding has been generally interpreted to reflect variability in the mode of deposition. However, a detailed study of the paragenesis of the 2.73 Ga Temagmi BIF, a type locality of Algoma-type iron formation, strongly suggests that the earliest layering was developed during diagenetic recrystallization of an originally homogenous, amorphous Fe-oxyhydroxide-silica precipitate, with no indication of primary heterogeneity in the precipitated material. The jasper layers are the best preserved of the original depositional facies and the preferred archive for Neoarchean oceanic conditions, with early silicification of jasper spherules. The banding, which ranges from microbands in jasper and chert to meter-thick layers at the outcrop scale, is interpreted to be mainly secondary in origin (i.e., pseudobands) caused by grain-scale remobilization of Fe and silica during earliest diagenesis. All developmental stages of banding are observed, with some early jasper bands preserving silica spherules with microcrystalline hematite. Recrystallization and mm-scale deformation introduces microbanding in jasper and chert: pseudobanding, which can be replaced by coarser-grained magnetite in chert bands. This contrasts with models of BIF formation in which the banding is interpreted to have formed in response to cyclical changes in water-column chemistry. Primary depositional features are best observed in sedimentary structures in volcanic-derived clastic layers (now chlorite bands); however, some other features that have previously been interpreted as primary sedimentary structures (e.g., “syneresis cracks”) probably formed in brittle magnetite layers during metamorphism. The purest (white) chert layers of the BIF have been closely studied as archives for Neoarchean ocean conditions, but we present evidence that these layers are mainly produced by silica remobilization related to expulsion of Si-rich pore waters from the sediments recorded by breakout structures and quartz veins,. White chert layers in the BIF may be partly a product of these escaping fluids, and not directly precipitated from the water column, and therefore a questionable archive for seawater chemistry. Instead, the most primitive lithology and preferred archive for Neoarchean oceanic conditions is jasper. Magnetite

crystallization, which has been widely interpreted as a product of changing redox or infiltration of reduced hydrothermal fluids, is interpreted here to reflect mainly increasing temperature during diagenesis. Magnetite formed diagenetically from original Fe-oxyhydroxides or hematite, possibly controlled by increasing temperatures during burial diagenesis (exceeding primary hematite stability). Increasing diagenetic and pore water temperatures lead to higher Si solubility and mobility in the fluid, recorded by oscillatory zonation of Si in the growing magnetite. Rising diagenetic temperature controlling magnetite growth is supported by its chemistry, which shows retention of Mn and Ge during early stages of diagenesis and does not reflect infiltration of hydrothermal fluids (e.g., enrichment in base metals). Preferential retention of some trace elements in magnetite fractionates indicator ratios such as Ge/Si, which are not a reliable proxy of paleoseawater composition in magnetite layers. Likewise, the chemistry of trace minerals such as apatite and monazite reflects processes that are intepreted to be mainly related to BIF diagenesis, such as small but systematic differences in rare earth element (REE) patterns of early and late apatite due to differences in REE mobility. These findings shed light on the composition of Archean seawater and its role in controlling the chemistry of Algoma-type BIF.

2.1 Introduction

The evolution of the early Precambrian deep ocean has been referenced extensively to the geochemistry of Neoarchean Algoma-type BIF (e.g. Barrett and Fralick, 1985; Ohmoto et al., 2006; Alexander et al., 2009; Thurston et al., 2012; Viehmann et al., 2014; Gourcerol et al., 2016b) but often without a clear understanding of the mineralogical control on the chemistry of the sampled lithologies. Detailed mineralogical studies of banded iron formations (BIF) inform the suitability of the Fe-bearing minerals as iron ore but also shed light on the paleoenvironmental conditions of the depositional basin (redox state, nature and extent of diagenesis, evidence for ancient biologic activity: James, 1954; Trendall and Blockley, 1970; Gross, 1972; Beukes, 1973; Cloud, 1973; Holland, 1973; Gross, 1980; Konhauser et al., 2002; Clout and Simonson, 2005; Klein, 2005; Ohmoto et al., 2006; Bekker et al., 2010). However, many investigations of iron formations as archives of the Precambrian oceans and atmosphere do not consider the detailed paragenesis of the ores (e.g. Johnson et al., 2008; Alexander et al., 2009; Thurston et al., 2012; Gourcerol et al., 2016b). Growing evidence suggests that many features of Eoarchean BIF and younger Superior-type BIF, such as mm-scale layering (Dymek and Klein, 1988; Mloszewska et al., 2012; Nutman et al., 2017), are mainly products of late-stage recrystallization of iron minerals by metamorphic or hydrothermal fluids (Trendall and Blockley, 1970; Tsikos et al., 2003; Ohmoto et al., 2006; Bekker et al., 2010; Konhauser et al., 2017), and so the extent to which the dominant mineralogy (quartz, magnetite, and hematite) reflects primary depositional conditions is poorly known. With few exceptions, such as the Superior-type BIF in the Hamersley and Transvaal basins and Eoarchean iron formations from the Isua greenstone belt, (e.g. Pecoits et al., 2009; Heimann et al., 2010; Nutman et al., 2017; Sampaio et al., 2018), the mineralogy is rarely part of the interpretation of detailed isotopic or trace element studies. In this study, we examine the detailed mineralogy and paragenesis of Fe-minerals in one of the type localities of Algoma-type BIF in the 2.73 Ga Temagami BIF of the Superior Province of Canada, and compare the results to a number of the accepted models for the genesis of the iron formations.

Although younger and even modern analogues are known, most banded iron formation, and especially cherty BIF, formed between 2.7 and 1.9 Ga (James, 1983; Isley and Abbott, 1999). The oldest iron formations still preserved are located in the 3.8 to possibly >4.3 Ga Isua and

Nuvvuagittuq greenstone belts of Greenland and Canada (Dodd et al., 2017). These highly metamorphosed supracrustal assemblages contain layered quartz-magnetite-amphibole rocks that are considered to have had a chemical-sedimentary origin and potentially even record ancient bacterial activity (Dymek and Klein, 1988; Frei et al., 1999; Fedo and Whitehouse, 2002; Czaja et al., 2013; Thomassot et al., 2015). In younger greenstone belts, beginning at ~2.9 Ga, BIF is more common, both in terms of the number of occurrences and the sizes of the deposits. While some of this increase in BIF occurrence is undoubtedly due to greater preservation of younger successions there is also a causal link to major episodes of crustal growth and changing styles of tectonics (Goodwin, 1973; Gross, 1983; Isley, 1995; Bekker et al., 2010). Meso- to Neoarchean BIF hosted mostly in greenstone belts (so-called Algoma-type BIF) are found throughout volcanic-dominated provinces such as the Abitibi in the Canadian Shield (Gross, 1983; Thurston et al., 2008). Here, they form regionally important marker horizons and are locally associated with or host synvolcanic massive sulfide deposits, and also later orogenic gold deposits (Gross, 1959; Gross, 1983; Thurston et al., 2008). Several, such as the Temagami BIF and the Adams Mine in Kirkland Lake were primary iron ore deposits.

Algoma-type BIF are associated stratigraphically and genetically with (bimodal) volcanism in tectonically active deep-water depositional environments that were parts of volcanic arcs or spreading centers (Gross, 1983; Donaldson and Garrett, 1991; Klein, 2005; Ohmoto et al., 2006). The dominant Fe mineral is magnetite, although Algoma-type BIF commonly include distinctive iron-rich jasper beds. Where they occur as lateral extensions of volcanic-hosted massive sulfide deposits, cherty iron (-oxide and –sulfide) rich lithologies are commonly referred to as “exhalites”, having formed as local products of the same hydrothermal venting that produced the sulfide ores (Peter, 2003). Such exhalites are not restricted to the Archean but include examples such as the Ordovician Brunswick horizon of the Bathurst mining Camp in New Brunswick and in the Løkken ophiolite complex of similar age in Norway (Scott et al., 1983; Kalogeropoulos and Scott, 1989; Liaghat and MacLean, 1992; van Staal et al., 1992; Peter and Goodfellow, 1996; Grenne and Slack, 2005). The latter are closely linked to nearby volcanic centers and are interpreted to represent direct chemical precipitation or plume fallout from proximal hydrothermal vents (or a hydrothermal brine pool; cf. Peter and Goodfellow, 1996). Other important examples of Algoma-type BIF are known from Bjørnevatn in Norway, at Kostomuksha in the Russian Karelia peninsula,

the Kudremuk and Iron Ore Group (India), Cerro Bolivar (Venezuela), Carajas (Brazil), Suichang (China), and Krivoy Rog (Russia; Gross, 1996; Mukhopadhyay et al., 2012). In Paleozoic and younger analogs, much of the reduced iron vented into the ocean would have been oxidized (the balance deposited locally as Fe-sulfides, -silicates, or -carbonates proximal to hydrothermal vents), whereas Precambrian Algoma-type BIF are thought to have mostly formed less oxygenated or even anoxic conditions and may or may not be sourced by proximal volcanic-hydrothermal vents.

Superior-type BIF, dominant after 2.7 Ga, are commonly larger than Algoma-type BIF (10-100 km in strike length versus 1-10 km, respectively). Unlike Algoma-type BIF, which are interpreted to have formed mainly as cherty chemical sediment in deep water (>200 m, likely >600 m: Klein, 2005; Slack and Cannon, 2009), Superior-type BIF contain abundant granular iron minerals indicative of deposition in higher-energy, shallow continental shelf settings that developed widely during the late Neoarchean and Paleoproterozoic (e.g., in the Hamersley and Transvaal basins and the Labrador trough: Trendall and Blockley, 1970; Beukes, 1973; Trendall, 2002a; Clout and Simonson, 2005). The abundance of clastic sedimentary features, association with clastic and carbonate lithologies, and commonly an absence of volcanic rocks within the host succession are distinctive features of Superior-type BIF. The shift from magnetite-dominated cherty lithologies in Meso- to Neoarchean Algoma-type BIF to much larger and dominantly hematitic Superior-type BIF in the Neoarchean to Paleoproterozoic reflects the emergence of larger stable continents and sediment-starved shelf environments (Clout and Simonson, 2005), changes in the chemistry of the atmosphere around the time of the Great Oxidation Event (~2.3 Ga, Farquhar et al., 2000; Bekker et al., 2004; Guo et al., 2009), the evolution of microbial metabolic pathways (Konhauser, 1998; Kappler et al., 2005), or a combination of all three. Although mostly attributed to very different tectonic settings, examples of BIF transitioning spatially from shelf environments to deep-water deposition have been described (Brandt et al., 1972; Kimberley, 1989). In particular, the Krivoy Rog BIF has been interpreted as transitional from deep-water Algoma-type to shallow-water Superior-type BIF deposition (Gross, 1996).

Other types of BIF, such as the Rapitan-type, formed in enclosed basins during large-scale glaciations in the Neoproterozoic (e.g., the Urucum iron ore system in Brazil), and are commonly associated with interlayers of Mn deposits in sequences of diamictites. Paleozoic oolitic ironstones

(e.g., the Ordovician Wabana Formation on Bell Island in Newfoundland, and the Devonian Nictaux-Torbrook iron formation in Nova Scotia) have a number of similarities to Superior-type BIF, including the abundance of sedimentary oolitic iron oxides and -silicates, but commonly lack the cherty matrix or chert interlayers (Gross, 2009). These deposits, referred to as Clinton-type or Minette-type iron formations, formed in sedimentary basis rather than volcanic basins and closely resemble earlier Superior-type BIF (Gross, 1965a).

Modern iron-rich metalliferous muds found in a number of deep-sea volcanic environments at mid-ocean ridges, in submerged arc volcanic complexes (e.g., Santorini volcano in the Hellenic Arc), and in anoxic basins such as the Atlantis II Deep in the Red Sea (Backer and Schoell, 1972; Cloud, 1973; Puchelt, 1973; Gross, 1980; Hannington et al., 1998; Petersen et al., 2000) are considered to be modern analogs of Algoma-type BIF. Some metalliferous sediments in mid-ocean ridge environments and on volcanoes of submarine volcanic arcs are products of plume fallout or detrital sediments from the collapse of hydrothermal vent complexes; others are products of diffuse, low-temperature hydrothermal venting at the seafloor. Iron-rich metalliferous sediments of the Atlantis II Deep, which have formed in deep restricted basins overlain by anoxic brine pools, have distinctive banding like Algoma-type BIF and have been considered among the best modern analogs (Laurila et al., 2014a,b; Laurila et al., 2015)

2.1.1 The mineralogy of BIF

All iron formations are characterized by a relatively simple mineralogy of magnetite and hematite as the major iron oxides, lesser iron carbonates, iron silicates and iron sulfides, and accessory apatite and other minerals in a matrix of dominantly microcrystalline quartz. Magnetite and hematite are the most abundant iron minerals in oxide-facies BIF, and especially in Algoma-type BIF. Jasper and chert layers contain different proportions of the same minerals (magnetite, hematite, and quartz), with quartz dominant. In carbonate-facies BIF, siderite and ankerite are dominant. Siderite was probably the thermodynamically stable iron-carbonate at the time of deposition (i.e, earliest diagenetic stage or direct precipitation from the water column) but transformed to ankerite, Fe-dolomite, and calcite in many deposits (Ohmoto et al., 2008).

Sulfide-facies BIF contain pyrite or pyrrhotite as the major iron phase, together with quartz (i.e., sulfidic chert). Silicate-facies BIF is common, dominated by Fe-silicate minerals that have been

transformed to chlorite, stilpnomelane, greenalite, and minnesotaite during metamorphism. Primary iron-rich aluminosilicate precipitates (i.e., Fe-rich clay minerals) may be deposits, but many of these phases appear to have formed by alteration of volcaniclastic layers (Klein, 1974; Klein, 2005). Common accessory minerals in oxide-facies Algoma-type BIF are apatite, carbonate, minor pyrite, monazite, and detrital minerals like zircon and the iron-aluminosilicates. In some cases, organic-rich black shale layers are present, often with abundant authigenic sulfide, but the argillaceous component is dominantly clastic in origin (Gross, 1996).

Superior-type BIF contain most of the same minerals, but in different abundances and paragenesis. Pure chert layers are common, but often more thickly bedded than in Algoma-type BIF. Hematite is more abundant than magnetite, probably reflecting the changing oxidation state of seawater and the atmosphere through time (Ohmoto, 2003). A larger input of organic material and phosphates is also consistent with deposition in stable shelf environments, commonly present in metamorphosed BIF as graphite and apatite combined with sulfates (Huston and Logan, 2004; Planavsky et al., 2010).

The origin of Algoma-type BIF from metal-enriched bottom waters is a generally accepted model (cf. Bekker et al., 2010). In this model, a primary precipitate likely formed in the water column from a pool of reduced Fe in solution with high amounts of dissolved silica, possibly close to saturation (Tréguer et al., 1995). The oxidation of Fe^{2+} in solution to form insoluble Fe^{3+} precipitates has been attributed to changing redox conditions in the depositional basin, or with oxidation triggered by UV radiation (or involving microbial metabolisms rather than reaction with free oxygen; James, 1954; Cloud, 1973; Cairns-Smith, 1978; Braterman et al., 1983; Walker and Brimblecombe, 1985; Ohmoto, 2003; Kappler et al., 2005; Konhauser, 2007; Posth et al., 2008; Bekker et al., 2010; Koehler et al., 2010; Nishizawa et al., 2010; Posth et al., 2013a; Posth et al., 2013b; Sun and Li, 2017a). Rapid changes of pH during mixing of anomalous alkaline hydrothermal fluid from ultramafic-hosted systems with neutral to acidic Neoarchean seawater also could have led to the formation of Fe-oxyhydroxides by hydrolysis and oxidation of Fe^{2+} in the absence of oxygen (cf., reaction [2.1] below: Shibuya et al., 2010). Such fluids may have been common in Archean oceans that were largely buffered by the mantle (e.g., by reaction with abundant mafic and ultramafic rocks; Veizer et al., 1982). Co-precipitation of an iron-

oxyhydroxide phase, such as lepidocrocite or ferrihydrite, and amorphous silica is now widely accepted as the primary deposition (Dimroth and Chauvel, 1973; Hamade et al., 2003; Kappler et al., 2005; Fischer and Knoll, 2009; Bekker et al., 2010; Koehler et al., 2010). Some have argued for precipitation of Fe^{2+} with silica (i.e., green rust: Klein, 2005; Beukes and Gutzmer, 2008; Rasmussen et al., 2016; Li et al., 2017), but the majority of iron in Algoma-type BIF is thought to have been precipitated as Fe^{3+}, evident from the prevalence of fine grained hematite formed directly from primary Fe-oxyhydroxide (Bekker et al., 2010). The abundant chert in all BIF was deposited as silica spherules, which are especially well-preserved in Neoarchean and older BIF (Stefurak et al., 2014, this study).

The origin of the two major iron minerals in BIF, hematite (Fe_2O_3) and magnetite (Fe_3O_4), the timing of their formation, and the causative reactions remain the fundamental questions in BIF research. Two different controlling mechanisms have been suggested.

1) A primary control based on the original Fe^{2+}/Fe^{3+} ratio of the deposited material: Initial precipitation of more oxidized iron would preferentially produce hematite during diagenesis; more reduced iron would yield magnetite (or siderite or pyrite depending on the availability of carbonate and sulfide and mineral stability). Changing redox in the depositional environment, for example caused by mixing of different hydrothermally influenced versus seawater-dominated water masses, could then account for the variable hematite and magnetite deposition. Alternatively, different Fe^{2+}/Fe^{3+} ratios of the deposited material could reflect adsorption of Fe^{2+} onto Fe-oxyhydroxide particles as they settled through the reduced water column, possibly influenced by bacterial activity (e.g. dissimilatory Fe-reduction; Klein, 2005; Steinhoefel et al., 2010; Li et al., 2017).

2) Recrystallization of the primary mineralogy under changing physicochemical conditions: Both magnetite and hematite can be produced directly during diagenesis of a primary $Fe(OH)_3$ precipitate (reactions [2.2]-[2.4]), depending on the prevailing postdepositional conditions (Klein, 2005; Sun and Li, 2017a). These reactions are thought to have occurred in both Superior- and Algoma-type BIF during early diagenesis or during later hydrothermal, metamorphic, metasomatic, or supergene alteration (Morris, 1983; Pecoits et al., 2009; Posth et al., 2013b;

Hensler et al., 2015; Hagemann et al., 2016). Nonredox acid-base reactions triggered by infiltration of external, hydrothermal fluids have been suggested as a potential pathway for addition or leaching of Fe^{2+} to form magnetite from hematite or vice versa (Ohmoto, 2003). However, it has been noted that the formation of magnetite from hematite via reaction [2.5] would be accompanied by a large volume change (+47 vol.%) that may be difficult to reconcile with the fine layering of the iron oxides (Mücke and Cabral, 2005).

$$4Fe^{2+} + 8H_2O \rightarrow FeOOH \quad + 2H_2 + 8H^+ \quad [2.1] \quad \text{(Shibuya et al., 2010)}$$

$$Fe(OH)_{3\,(fer)} \underset{<\sim 25℃}{\rightarrow} FeOOH_{(goe)} + H_2O \quad [2.2] \quad \text{(Trolard and Tardy, 1987)}$$

$$2FeOOH_{(goe)} \underset{\sim 60℃}{\rightarrow} Fe_2O_{3\,(hem)} + H_2O \quad [2.3] \quad \text{(Cornell and Schwertmann, 2003)}$$

$$16Fe(OH)_{3\,(fer)} + 8Fe^{2+} + 16OH^- \rightarrow 8Fe_3O_{4\,(mag)} + 32H_2O \quad [2.4]$$

(Koehler et al., 2010)

$$Fe_2^{3+}O_{3\,(hem)} + Fe^{2+} + H_2\,O \rightarrow Fe^{2+}Fe_2^{3+}O_{4\,(mag)} + 2H^+ \quad [2.5] \quad \text{(Ohmoto, 2003)}$$

In this study, we examine the detailed mineralogical relationships in the Temagami iron formation to reveal the fine structure of the oxide-facies BIF, the nature of mineral transformations at the mm-layer scale, and complex paragenetic relationships and chemical zonation of individual minerals. The mineralogy and paragenesis of the BIF were documented using transmitted and reflected light microscopy, scanning electron microscopy (SEM) imaging, electron probe microanalyser (EPMA) techniques, including element mapping, and laser ablation inductively coupled plasma (LA-ICP-MS) analyses to document intra-grain chemical variations at 1 µm resolution and down to ppb levels. These data shed new light on details of BIF mineralogy that directly inform larger questions of whole-rock geochemistry and the origin of banding and the hematite-magnetite transition.

2.2 Geology of the Temagami Greenstone Belt and Sherman Mine

The Temagami Greenstone Belt is a Neoarchean volcanic-sedimentary succession of the Superior Province of the Canadian Shield, spanning roughly 400 km^2 just east of the Ontario-Quebec border and 100 km north of the town of North Bay, Ontario, Canada (Fig. 2.1). The volcanic and sedimentary rocks of the central Temagami Greenstone Belt crop out in a glacially carved window surrounded by regionally dominant younger lithologies of Huronian sedimentary rocks (2.3 Ga) and intrusions of Nipissing diabase (2.2 Ga). The greenstone belt consists of east-west trending bimodal volcanic and sedimentary successions and synvolcanic intrusives (Bennett, 1978; Blum, 1986; Fyon and Crocket, 1986). It is closely spatially and temporally related to the much larger Abitibi Greenstone Belt to the North and shows similar structural and metamorphic history, but the exact nature of their relationship is unclear (Jackson et al., 1994; Ayer et al., 2002). The volcanic and sedimentary rocks of the greenstone belt have been metamorphosed to lower greenschist facies, generally producing a quartz-chlorite-albite-epidote assemblage. All volcanic and sedimentary units in the central part of the greenstone belt are steeply dipping and roughly ESE-WNW trending. The largest synvolcanic intrusions in the area are the Chambers-Strathy Batholith in the central northern part, east of Hwy 11, the Spawning Lake pluton 20 km east of Temagami, and the Iceland Lake pluton southeast of Temagami (Bennett, 1978; Ayer et al., 2002).

The Temagami BIF is located in the central part of the greenstone belt, just north of the town of Temagami, and is exposed as two ESE-WNW-striking members, each ~10 km in strike length and 60-185 m in thickness (Donaldson and Garrett, 1991). The northern and southern BIF members cap volcanic sequences comprising mafic tholeiitic to felsic calc-alkalic volcanic cycles with volcaniclastic sediments (Donaldson and Garrett, 1991; Brons, 1989; Fyon and Crocket, 1986). BIF occurs at the top of the volcanic sequences A and E (see Figs. 2.3 and 2.4), which have been interpreted to represent stratigraphic equivalents on the north and south limbs of the Tetapaga syncline. However, the BIF members are interpreted to be separate deposits and possibly slightly different in age (Fyon and Crocket, 1986; Ayer et al., 2006). Other volcanic sequences (B, C, D, see Fig. 2.3) do not contain substantial BIF.

Reported ages for the volcanic rocks of the central Temagami Greenstone Belt range from 2685 to 2766 Ma (Ayer et al., 2006; see Fig. 2.2), with a general younging of lithologies towards the south in the central part of the greenstone belt, north of the town of Temagami and including the North BIF, and younging to the north in the area south of the Tetapaga Syncline, including in the South BIF (see Fig. 2.4). The ages of the volcanic rocks, as well as sedimentary structures (gradation in turbiditic sequences) and pillow facing directions in the mafic flow sequences support the existence of a steeply dipping, WSW-ENE trending syncline in the map area (see Fig. 2.2; Bennett, 1978; Fyon and Crocket, 1986; Ayer et al., 2006). Although interpretations of features observed when mining was active have varied (Johnston, 1997; Fyon and Crockett, 1990; Donaldson and Garrett, 1991; Ayer, 2006). U-Pb ages of felsic volcanic- and sedimentary rocks bracketing the North BIF are between 2767±1 and 2717 Ma; all ages in the vicinity of the South BIF at <2721.5±1.1 Ma (Ayer et al., 2006). While some uncertainty remains about the exact age of the BIF the best approximation is 2.73-2.72 Ga (Bowins and Heaman, 1991; Ayer et al., 2006).

Both the North and South members contain lenses of BIF of varying strike length, from 500 to 1500 m along distinct horizons; the four largest of these lenses were exploited in open pits of the Sherman mine (Fig. 2.5). The North and West Pits exploited the north BIF member, and the South and East Pits are in the south BIF member. Collectively, 22.6 Mt of iron ore pellets were produced from 82 Mt of ore grade material extracted from the Sherman Mine (Donaldson and Garrett, 1991). The open pits only extracted the shallow parts of the deposit, while the extent of the deposit at depth is undetermined beyond the depth of exploration drilling (>300 m; Blackburn et al., 1990). More BIF occurs along strike of the mined lenses: northwest of the Spawning Lake Pluton and south of it, as well as in Scholes and Afton townships around Eaglerock Lake and Emerald Lake, about 30 km southeast of the Sherman mine, and in MacBeth and Vogt townships (Meyn, 1977; McBride, 2010). Aeromagnetic surveys indicate BIF occurrences along two or more stratigraphic levels under the overburden southeast of the Sherman mine area (Fig. 2.1), and many deposits have been found along strike and in independent horizons during exploration drilling, but their size and extent are poorly constrained (Meyn, 1977; OGS, 2001). Few of those deposits have been studied during exploration activities, and at least one occurrence has been estimated to be as large or larger than the Temagami BIF of the Sherman mine (potentially 2500 Mt of iron ore at >25% Fe at one locality north of Cummings Lake and south of Lower Bass Lake in Scholes township), but the

cover of Huronian sedimentary rocks and diabase intrusions make exploitation unlikely (Meyn, 1977).

Most of the iron in the Temagami BIF is in magnetite. Oxide facies BIF is dominant, but sulfide-, carbonate-, and silicate-facies BIF have been reported in studies from the time of active mining when the pits were accessible (Campbell, 1978; Fyon and Crocket, 1986; Donaldson and Garrett, 1991; Gross, 2009). There is no systematic pattern in the distribution of the different facies in the pits; however, the oxide facies is commonly in contact with pyritic argillites or sulfidic cherts either in the immediate footwall or hanging wall (Fig. 2.5; Boyum and Hartviksen, 1970; Campbell, 1978; Gross, 2009). Semi-massive sulfide and sulfide facies BIF also occur as discontinuous, meter-scale lenses within the oxide facies, and some oxide facies BIF in contact with these lenses contain minor pyrite (Gross, 2009, this study; Diekrup et al., 2018). Carbonate facies is notably absent in the North BIF (Campbell, 1978), but Fe-carbonates were common in the matrix of chert-magnetite in the South BIF (see Fig. 2.5). Jasper layers are more abundant in the North BIF and distinctly bright orange and red in colour compared to less abundant burgundy jasper in the South BIF (Campbell, 1978; this study; Ginley, 2016). The dominant footwall lithologies the individual pits of the Sherman mine vary from volcaniclastic sediments, pyritic argillite, and mafic and felsic volcanic rocks (Fig. 2.5). The volcanic rocks are pervasively hydrothermally altered to quartz, chlorite, and muscovite, but no obvious hydrothermal alteration pipes or base metal sulfide mineralization have been found (Bennett, 1978; Hurley, 1985; Blum, 1986; Fyon and Cole, 1989).

This study involved the collection of a comprehensive suite of BIF samples from a combination of outcrop, archived samples, and more than 600 large ore blocks remaining at the edge of the former open pits. Although the North and South pits were mined out, pit walls were locally accessible, and ore blocks that were too large for the crusher were left on the pit rims (cf., Ginley, 2016). A 200-m long roadcut along Hwy 11, just north of the town of Temagami, is a world-class exposure of the South member and the subject of many studies of the Temagami BIF. It allows the best in-situ access to the typical ore facies (Fig. 2.6; Diekrup et al., 2018). Due to its location at the extreme east end of the South BIF, this part of the south member is considered a “distal” equivalent of the ore material exploited in the Sherman mine. Although the average grade of Fe

along Hwy 11 would not have been high enough to be mined, the exposed units are considered to be the best representation of the Temagami BIF within the Sherman mine area (Ginley, 2016). Figure 2.7 shows a measured section of the south BIF member along Hwy 11, corresponding to a complete stratigraphic section of the subvertically dipping lithologies. The footwall of the south BIF at this location consists of several meters' exposure of volcaniclastic sandstone with cm-thick layers of chlorite-rich material clastic material interlayered with chert. The chert content increases over 20 m towards the north (up-section), until magnetite first appears in volcaniclastic material and then as continuous layers that comprise the main part of the South BIF member. The magnetite-rich BIF comprises 2-5 cm thick black chert and magnetite bands, with few interlayers of chlorite and jasper. The next 30 m are progressively more magnetite- and jasper-chert rich, closely resembling the mined material from the South Pit. Small scale, tight (synsedimentary) folding and quartz veining are abundant in this part of the outcrop. The magnetite-jasper-chert layers are interrupted by more chlorite-rich domains (at 43 m and 60 m: Fig. 2.7), and a 50-m break in outcrop is though to be due to a zone of more recessively weathering altered mafic volcanic material, including a small massive pyrite lens at 110 m. The upper part of the south BIF member is exposed between 120 and 160 m and consists of more chert-magnetite and chert-magnetite-jasper layers. The BIF is overlain by volcaniclastic material containing chert-magnetite clasts and then mafic volcanics at the top of the section.

2.3 Sampling and methodology

Eighty-three samples were collected along the Hwy 11 outcrop (n=50) and from the Sherman mine ore blocks (n=33, see Appendix A). An additional 23 samples were selected from the archive of the Geological Survey of Canada in Ottawa and from the footwall lithologies north of the south BIF. The samples include all facies of the BIF (oxide, carbonate, silicate, and sulfide), as well as intercalated clastic lithologies. 66 thin sections were cut from the samples that were subsequently analyzed for whole rock geochemistry (see Chapter 3). 17 additional thin sections were prepared from samples collected in the Sherman mine and along Hwy 11. Thick sections were prepared from the same sample pucks for LA-ICP-MS analyses.

2.3.1 Scanning electron microscopy

Scanning electron microscopy (SEM) imaging and energy dispersive (EDS) analyses were performed on a JEOL 6610LV at the University of Ottawa on carbon coated thin sections at 20 kV acceleration voltage with a spot size of 56 (no unit) at a working distance of 10 mm and a beam current of ~1 µA. X-ray intensity and energy were measured on an Oxford INCA 30 mm^2 SD detector. Imaging in backscatter mode was typically at lower acceleration voltage, spot size, and working distance to achieve better resolution except when done in combination with EDS analyses. Cathodoluminescence (CL) images were obtained using the Gatan Mini-CL detector at 500 nm wavelength with a working distance of 20 mm (to fit the detector over the sample stage), an accelerating voltage of 20 kV, and a spot size of 57 (no unit).

2.3.2 Electron probe microanalysis (EPMA)

A JEOL 8230 SuperProbe electron microprobe analyzer (EPMA) at the University of Ottawa was used for element mapping and quantitative analysis of magnetite, chlorite, REE-phosphates, and other accessory mineral phases. The EPMA is equipped with five WDS detectors tuned to the x-ray peaks that were calibrated for each element using matrix-matched standard materials before and after each run. Analyses were performed at 20 kV accelerating voltage at variable spot sizes (<1 – 10 µm), beam currents (20-40 nA), and dwell times (20-30 s on peak) appropriate for the elements and different minerals. The standards used for magnetite analyses were diopside (Ca, Si), chromite (Cr, Al, Mg), sphalerite (Zn), hematite (Fe), rutile (Ti), pentlandite (Ni), and vanadinite (V). For chlorite analyses, sanidine (K, Si, Al), diopside (Ca, Mg), gahnite (Zn), hematite (Fe), tephroite (Mn), chromite (Cr), rutile (Ti), albite (Na), tugtupite (Cl), and fluorite (F) were used as standard materials. Apatite, monazite and xenotime were analyzed using standards diopside (Si, Mg), Smithsonian fluorapatite (Ca, P, F), sanidine (Al), YAG Yttrium-aluminum-garnet (Y), REE glass (Sc), $LaPO_4$ (La), $CePO_4$ (Ce), $PrPO_4$ (Pr), $NdPO_4$ (Nd), $SmPO_4$ (Sm), $EuPO_4$ (Eu), $GdPO_4$ (Gd), $TbPO_4$ (Tb), $DyPO_4$ (Dy), $YbPO_4$ (Yb), $HoPO_4$ (Ho), $LuPO_4$ (Lu), $ErPO_4$ (Er), $TmPO_4$ (Tm), ThO_2 (Th), crocoite (Pb), UO_2 (U), albite (Na), celestine (Sr, S), and tugtupite (Cl). Results were processed and interferences corrected for, using the "ProbeForEPMA" software. Details of the analyses, standard materials, detection limits and analytical errors for each run are presented with the full results in Appendices B-H.

2.3.3 LA-ICP-MS

Laser ablation inductively coupled plasma mass spectrometry (LA-ICP-MS) was performed using a Photon Machines Analyte Excite laser connected to an Agilent 7700x quadrupole ICP-MS at the University of Ottawa. The ablation system uses a 193 nm excimer laser at 15 Hz and 4.9 mJ/cm^2 with 1 l/m He and 0.7 l/m Ar carrier gas flow. The beam size for magnetite and apatite analyses was set to 52 µm for line and spot analyses. Element abundances were calculated using Fe as an internal standard for magnetite and Ca as an internal standard for apatite, applying values obtained from EPMA results. GSE-1g and GSD-1g (USGS-synthetic glass) was used for calibration as a primary standard for magnetite analyses, and NIST SRM610 for apatite. Additionally, NIST SRM612, and the internal standard BC28 (Bushveld complex magmatic magnetite) were used for quality control (Dare et al., 2014). Standards were analyzed at the beginning of each run and after every eight sample analyses. Results were considered acceptable if the values for standards measured as unknowns did not exceed +/- 2% of the preferred value for GSE, and +/- 5% of the internal standard BC28 (cf. Dare et al., 2014). 35 elements were quantified by line and spot analyses of magnetite using the following isotopes: ^{25}Mg, ^{27}Al, ^{29}Si, ^{31}P, ^{43}Ca, ^{45}Sc, ^{47}Ti, ^{51}V, ^{52}Cr, ^{55}Mn, ^{59}Co, ^{60}Ni, ^{65}Cu, ^{66}Zn, ^{69}Ga, ^{74}Ge, ^{75}As, ^{89}Y, ^{90}Zr, ^{93}Nb, ^{95}Mo, ^{109}Ag, ^{111}Cd, ^{115}In, ^{118}Sn, ^{121}Sb, ^{133}Cs, ^{137}Ba, ^{139}La, ^{147}Sm, ^{172}Yb, ^{178}Hf, ^{181}Ta, ^{182}W, ^{208}Pb. 47 elements in apatite were quantified by spot analyses of ^{7}Li, ^{11}B, ^{23}Na, ^{25}Mg, ^{27}Al, ^{29}Si, ^{31}P, ^{34}S, ^{35}Cl, ^{39}K, ^{45}Sc, ^{49}Ti, ^{51}V, ^{53}Cr, ^{55}Mn, ^{56}Fe, ^{59}Co, ^{60}Ni, ^{65}Cu, ^{66}Zn, ^{69}Ga, ^{75}As, ^{85}Rb, ^{88}Sr, ^{89}Y, ^{90}Zr, ^{93}Nb, ^{121}Sb, ^{133}Cs, ^{137}Ba, ^{139}La, ^{140}Ce, ^{141}Ce, ^{141}Pr, ^{146}Nd, ^{147}Sm, ^{153}Eu, ^{157}Gd, ^{159}Tb, ^{163}Dy, ^{165}Ho, ^{167}Er, ^{169}Tm, ^{172}Yb, ^{175}Lu, ^{208}Pb, ^{232}Th, ^{238}U. Raw results are rounded to three significant figures in data tables, considering mean relative errors in the range of 5-10% for most elements in magnetite and apatite. Two significant figures are reported for trace elements with abundances within an order of magnitude of the limit of detection and consequently higher mean relative errors. Inclusions (quartz, apatite, chlorite, zircon in magnetite; quartz in apatite) were avoided by choosing sections of each time-resolved analysis void of any peaks in indicative elements (Si – quartz, P – apatite, Al – chlorite, Zr – zircon), and the reported values are interpreted to represent compositions of the pure mineral phases. The GLITTER software (Van Achterbergh et al., 2001) was used for data reduction.

2.4 Description of the BIF samples

The Temagami BIF material is characteristically layered or banded. In this thesis, a layer is considered a >1 cm thick stratum of distinct material. Samples of specific material (e.g., magnetite-rich), are also referred to as samples from a "magnetite layer". A band is broadly used for smaller distinctions, including microbanding within a layer and for general descriptions of the BIF material to give special reference to the "banded" nature of BIF. Thick layers of e.g. magnetite can also contain "bands" or "lenses" of jasper. More generally, the term "layer" is typically used to describe compositional or textural differences bound by interfaces in sedimentary rocks – layer boundaries. In the case of the Temagami BIF, the primary nature of the banded material is questionable, and the term "pseudobanding" to describe the secondary, diagenetic origin of the banding is discussed in the appropriate context. "Diagenesis" is the process of lithification of lose sediment to form a sedimentary rock. In the following discussion, the term "diagenesis" is used also for the initial recrystallization of the deposited material and up to the stage of formation of magnetite and jasper layers.

Five main layer types have been identified in the Temagami BIF: jasper, magnetite, and chert layers within the oxide-facies BIF (Fig. 2.8), sulfidic cherts (described in the literature as sulfide facies BIF), and chlorite layers, which may be true silicate-facies BIF or altered volcanic material. Carbonate facies BIF is rare or absent, represented by <1 cm bands of siderite. The major minerals in all oxide-BIF layers are quartz, magnetite, hematite, and chlorite (Table 2.1). With few exceptions (e.g., refractory minerals, such as zircon, titanite, and monazite in volcaniclastic layers), the minerals constituting the main facies are interpreted to represent original chemical precipitates or their metamorphosed equivalents.

2.4.1 Grain-scale petrography

Detailed petrography of the BIF samples reveals several different generations of hematite, magnetite and quartz. Type 1 hematite consists of ultrafine (<<1 μm) translucent red particles that lack an obvious crystal habit and occur as a fine dusting of the interiors of individual (20-50 μm) quartz grains (Fig. 2.9). Type 2 hematite occurs as larger euhedral to subhedral crystals, 5-20 μm in size, often found along quartz crystal boundaries or in the interstices of larger magnetite grains.

It is commonly (micro-) platy and typically aligned parallel to the banding of BIF, in pockets between layers, or between magnetite crystals aggregates in magnetite-rich layers. Notably, hematite 2 is nonopaque but deep red in colour under plain polarized light.

Five different types of magnetite are recognized (Fig. 2.10). Type 1 magnetite resembles Type 1 hematite, in terms of its distribution as a fine dusting in quartz grains, but it has a clear crystal habit as mainly equant grains, 500 nm to 1 μm in size and slightly larger than Type 1 hematite. Type 2 magnetite resembles Type 2 hematite, occurring as euhedral to subhedral crystals, 5-20 μm in size mainly at quartz crystal boundaries or in the interstices of Type 3 magnetite crystals. Type 3 magnetite crystals are nearly perfectly euhedral and up to 500 μm in diameter. They commonly exhibit poikioblastic textures, with inclusions of Type 1 hematite-bearing quartz, clear quartz, apatite, and rare sulfides. Fragments of jasper are sometimes preserved in the core of Type 3 magnetite and overgrown by zoned Si-rich and Si-poor magnetite. The outer rims of Type 3 magnetite grains contain abundant inclusions of quartz and accessory minerals. Type 4 magnetite consists of aggregates of Type 3 magnetite that have grown together to form a nearly coherent mass of magnetite. Type 5 magnetite is distinguished from Type 3 by its abundant quartz inclusions and highly irregular shapes (anhedral, skeletal, elongated).

Quartz is present as a major phase in all types of BIF in two principal habits: as cryptocrystalline masses of <20 μm poorly defined grains (spherules) with abundant inclusions, and coarsely intergrown subhedral grains of uniform size (50-200 μm) with well-defined crystal interfaces (Fig. 2.11).

The accessory minerals apatite and chlorite are mostly hosted in quartz, in the interstitial spaces between magnetite grains in magnetite-rich layers, and rarely as small inclusions in the outer zones of Type 3 magnetite. Apatite has two distinct habits, as anhedral grains and (sometimes perfectly) euhedral crystals, both of variable sizes up to several hundred μm. Anhedral (Type 1) apatite is elongated and usually oriented parallel to banding. It contains abundant inclusions of Type 1 magnetite and is common among jasper spherules. Larger, euhedral to subhedral (Type 2) apatite crystals are typically intergrown with or overgrow Type 3 magnetite. Type 2 apatite usually does

not contain inclusions. A third type of apatite found in some chlorite layers occurs as irregular, rounded grains (<100 μm) that may be detrital in origin.

Traces of chlorite are widespread in all of the BIF layers as small (1-20 μm) anhedral grains. Where it is more abundant, as in discrete chlorite layers, the grains can be up to 50 μm in size, comprising large intergrown masses (Fig. 2.11). Elsewhere, chlorite is an important alteration product of glass in the volcaniclastic units. Muscovite is present locally in magnetite layers together with chlorite and calcite. Fe-rich dolomite and calcite occur as euhedral crystals with abundant quartz inclusions in interstitial spaces of magnetite and rarely as discontinuous lenses (up to 0.5 cm) in magnetite layers (see Fig. 2.12). Siderite is also present locally as evenly distributed, 20 μm crystals in the chert layers. Monazite and rare barite are also found, mainly in the interstices of Type 3 magnetite aggregates. Notably, radiating blades (>100 μm) of stilpnomelane, together with grunerite and biotite, occur in the interstices of Type 4 and Type 5 magnetite in aluminosilicate-rich layers. The occurrence of the aluminosilicate minerals and carbonate, mainly in the interstices of Type 4 and Type 5 magnetite, suggests that the latter formed by metamorphic recrystallization of the earlier Type 1-3 magnetite. Type 5 magnetite is particularly common in BIF adjacent to mafic intrusions and may be partly a product of contact metamorphism.

Pyrite is the dominant sulfide mineral, occurring visibly as traces in Type 3 magnetite (Fig. 2.12) but also likely present as submicroscopic inclusions in earlier magnetite (see Chapter 4). Where pyrite is more abundant, it occurs in radiating, skeletal, euhedral and nearly massive aggregates. In coarse pyrite masses, traces of chalcopyrite, sphalerite and galena are present as <1 μm inclusions. Pyrrhotite is rare.

2.4.2 Oxide-facies BIF

Jasper layers: The jasper layers comprise fine crystalline (<50 μm) quartz accounting for >70 vol.% of the layers, with 6-18 vol.% hematite. Minor magnetite (2-12 vol.%) is common, and apatite can be locally abundant but is generally less than 1 vol. %. Traces of Fe-carbonates, dolomite, and chlorite are also present. The quartz layers consist of 10-50 μm-sized spheroidal aggregates that closely resemble textures described as “gels” in other cherty sediments (Duhig et al., 1992; Stefurak et al., 2014). Silica spherules of this type are a common feature of Neoarchean

cherts and have been interpreted to represent a primary feature of silica deposition (Stefurak et al., 2014). The shapes of the spherules are consistent with original amorphous silica spheres, preserved as loosely packed botryoidal, or globular structures. The other distinctive feature of the jasper layers is the bright red colour, ranging from a blood red to deep burgundy (Fig. 2.13). This is caused by a fine dusting of nm-scale Type 1 hematite in the quartz spherules. Importantly, the fine hematite inclusions are not homogeneously distributed throughout the quartz but concentrated within the cores of the spherules, giving them a red "cloudy" appearance in the interior with clear rims along boundaries of the spherules.

Microbanding is common in the jasper layers. These mm-scale laminae consist of alternating dark and orange- to burgundy-red couplets in hand sample, but they commonly appear translucent and uniformly red or clear in thin section under transmitted light (Fig. 2.13a,b). The distinction between microbands is similar to the zonation of hematite inclusions observed in the silica spherules, with cloudy Type 1 hematite in the interiors of the red bands and discrete Type 2 hematite and magnetite, between or at the margins of the bands (Fig. 2.13d). The total amount of Fe and Si does not change (Fig. 2.14), but Fe in Type 1 hematite in the interior of the bands is replaced by Fe in Type 2 hematite and magnetite at the margins and in cherty microlayers between the red bands.

Darker colors of jasper are an indication of coarser grained hematite and more abundant disseminated magnetite (Types 1 and 2), transitioning into black chert. The transition from red jasper to black chert is observed at cm- to meter-scale, both laterally along individual bands and between bands (see Fig. 2.8b,c). Lateral transitions from jasper layers into black chert are common in stacks of alternating magnetite and jasper layers. They typically occur at the same lateral position in several parallel jasper layers, consistent with selective replacement of the jasper layers by magnetite and leaving jasper relics in the black chert-magnetite matrix (Fig. 2.8c). Some jasper layers are dominantly hematitic along the upper and lower contacts, while their centers consist mainly of black chert. Jasper also commonly loses its red color in proximity to quartz veins.

Chert layers: Chert layers comprise >65 vol% quartz (up to 98 vol.%) with magnetite abundance not exceeding 35 vol.% and chlorite abundance less than ~2 vol.% (Table 2.1). The chert layers are subdivided in the field between white and black chert (Fig. 2.15). White chert typically consists of coarsely intergrown quartz crystals, 50 to 100 μm in size, whereas the black chert mainly contains finer quartz (< 20 μm). White chert is mostly devoid of magnetite or chlorite but can contain traces of Fe-carbonate, apatite, and pyrite, as the other oxide-facies BIF. White chert bands can sometimes be traced to dewatering and breakout structures in hand sample (Fig. 2.8e,f). Entire ore blocks consisting of white chert (up to 1.5 m) are also found.

Black chert contains 5 to ~30 vol.% magnetite and up to 2 vol.% chlorite. Quartz in black chert layers is commonly cryptocrystalline, with very poorly developed crystal interfaces marked by fine mineral inclusions. Type 2 magnetite is most common, mainly in the interstitial spaces of coarser recrystallized quartz. Type 1 magnetite occurs as fine inclusions in quartz, similar to Type 1 and Type 2 hematite in the jasper layers, but the sizes of Type 1 magnetite grains (>100 nm) are significantly larger than Type 1 hematite in jasper spherules. Hematite is mostly absent in black chert but can be present where jasper layers transition into black chert, as noted above. As in the jasper layers, microbands of white and black chert are common. Ginley (2016) also reported structures in the black chert layers that resemble bacterial filaments. A few samples contain discontinuous lenses (m-scale strike length, <1 cm thickness) of Fe-carbonate but they comprise much less than 1 vol.% of the black chert layers (Fig. 2.15e,f).

Magnetite layers: Magnetite layers contain >30 vol.% magnetite (up to 85 vol.%). The magnetite crystals in these layers are typically between 10 μm and 500 μm in size and much larger than the disseminated magnetite in the chert or jasper layers. The magnetite grains are typically euhedral and commonly show complex internal structures, including oscillatory zoning and zones of abundant inclusions. Uniformly magnetite-rich layers mostly contain Types 3, 4 and 5 magnetite (see Fig. 2.10). The boundaries of the magnetite layers with neighbouring black chert or jasper layers are typically quite sharp in outcrop and hand specimens, but in thin section they are clearly marked by a transition from smaller magnetite grains close to the layer boundaries to larger, more complexly zoned crystals in the center of the layers (Fig. 2.16). The transition from Type 3 through to Type 5 magnetite is gradational over several hundred microns to few mm (Figs. 2.8d, 2.10e),

and appears to be mainly a result of internal recrystallization forming dense, intergrown masses of magnetite in the interiors of the layers. Such transitions are continuous laterally on a meter scale, although they may be interrupted by quartz veins or small offsets (Fig. 2.8d). In the most magnetite-rich layers, quartz (12-52 vol.%) mainly occurs in the interstitial spaces between magnetite grains. The quartz contains rare Type 1 hematite in relict jasper spherules or platy Type 2 hematite ranging in size from 5 to 20 μm. The hematite is mostly found near the transition from chert or jasper layers to more magnetite-rich layers (e.g., where Type 2 magnetite replaces Type 1 hematite). Other minerals in the magnetite layers (in total 10-20 vol.%) include Fe-rich dolomite, calcite, apatite, muscovite, chlorite, and stilpnomelane, with rare pyrite and monazite (e.g., Fig. 2.16b,c), mainly in the interstitial spaces between large magnetite crystals. In a few cases, the magnetite-rich layers contain up to 20 vol.% chlorite with accessory ilmenite, zircon, and monazite. In other cases, the dominant aluminosilicate phase is muscovite instead of chlorite.

Chlorite layers: Chlorite-rich layers are common in the oxide-facies BIF interlayered with magnetite and chert. Most are only 1-5 cm in thickness, commonly finely laminated, and contain between 20-40 vol.% chlorite and 40-60 vol.% quartz. Magnetite can be present up to 20 vol.%. The most common accessory minerals are ilmenite, apatite, monazite, zircon, and locally Fe-carbonate. Most of the chlorite-rich layers in the BIF are interpreted to be volcaniclastic in origin based on the presence of detrital zircon, abundant authigenic Ti-oxides, and CL active quartz. The cathodoluminescence of quartz is an indication of igneous-detrital provenance, while trace Fe in sedimentary or BIF-quartz extinguishes the CL signal (Zinkernagel, 1978; Götze et al., 2001). Few layers consist of alternating, mm-scale microbands of chlorite and quartz. Such layers are likely chemical precipitates since they contain less or no detrital zircon and ilmenite, only CL passive quartz, and more diagenetic magnetite (Fig. 2.17).

2.4.3 Microstructures

In addition to widespread microbanding, a variety of other microstructures are observed in the different layer types, including apparent fluid-escape structures, quartz microveinlets, and features resembling syneresis cracks (Donaldson and Munro, 1982). Some are primary; others are clearly secondary. Fluid-escape structures are particularly common between layers and within individual layers. They are interpreted to represent pore water expelled from the sediments or from the silica

"gels", which could have contained 50->90% water and result in the auto-brecciation of overlying brittle layers (Williams and Crerar, 1985; Williams et al., 1985, Krapez et al., 2003). The fluids escaped along channeled conduits that are often marked by flame-like breakout structures (Fig. 2.18). The breakouts range from diffuse upward flow through the layers to fracture-controlled brecciation of more brittle material.

Several stages of quartz veining are documented (Table 2.2). The earliest stage 1a) veinlets are sub-mm to mm-wide quartz stringers confined to the jasper and chert layers. They are mainly oriented at steep angles to layering and commonly bent, distorted, or deformed (Fig. 2.19). Stage 1a) veins in jasper commonly show stepwise offsets, reflecting deformation along the planes of microbands (Fig. 2.13e). Later stage 1b) veins are similar to but cut the earlier type 1a) and are not deformed. Locally, they can be traced from one jasper layer to the next across magnetite layers in which they are more difficult to see. Quartz-magnetite veins (stage 2) containing Type 3 magnetite are found mainly in chert and jasper layers and also cut the early type 1a) veins. They can be present in the outer parts of magnetite layers but are generally not present in their centre. Stage 3a veins contain quartz, magnetite, and chlorite or stilpnomelane and cut all previous stages. These veins are present mostly in magnetite and chert layers, and never occur in jasper. Stage 3b veins are ~5 mm-wide, quartz-filled cracks in magnetite layers that have been widely interpreted to have been syneresis cracks (Donaldson and Munro, 1982). The cracks, which are always perpendicular or at a steep angle to layering and may widen from one end to the other, are confined to the magnetite layers and do not affect neighboring chert layers (see Figs. 2.8d, 2.19e). Several observations argue against a syn-sedimentary origin; most notably that they occur mainly in massive magnetite layers that are dominated by recrystallized Type 4 magnetite and contain stilpnomelane needles and other minerals interpreted to be mainly metamorphic in origin. They are particularly common where the magnetite layers are in contact with chert, suggesting that the cracks are filled by material remobilized from the chert layers during metamorphism and possibly prograde dewatering reactions of hydrous minerals and associated volume loss in magnetite layers. The latest veins are cm-wide quartz-pyrite-carbonate veins (stage 4), which cut all lithologies. These veins can be traced in outcrop over several metres and are not affected by any deformation (Fig. 2.19f).

Clastic layers in the BIF exhibit local sorting and graded bedding. In the Hwy 11 outcrop, fining from coarse sand to silt is observed in volcaniclastic material at the south end of the outcrop and has been used as a younging direction indicator towards the north (Donaldson and Garrett, 1991). Small, mm-scale clasts of jasper within magnetite layers were also interpreted as rip up clasts (see discussion; Donaldson and Garrett, 1991). In some chert samples, aluminosilicate-rich microbands decrease in thickness from the bottom of the chert layers towards the top (cf. Ginley, 2016), which may be an indication of sorting at the layer scale. Donaldson and Munro (1982) used such features within the south pit of the Sherman mine to infer a younging direction towards the north.

2.4.4 Other lithologies

Sulfidic chert: Sulfidic cherts, formerly present in the Sherman mine have been mined out, but an important sample archive was retained by the Geological Survey of Canada (Gross, 2009). In the west wall of the South Pit (stratigraphically equivalent to the Hwy 11 oxide-facies BIF), lenses of sulfidic cherts were intercalated with volcaniclastic material over 300 m stratigraphically (Riedel, 1969; Boyum and Hartviksen, 1970; Bennett, 1978; Donaldson and Garrett, 1991). Where mapped, the sulfide facies graded into minor carbonate- and oxide-facies BIF over ~100-200 m along strike. The sulfidic portions consisted of up to 60 vol.% pyrite, with ~30 vol.% quartz and minor graphite (5-10 vol.%, see Fig. 2.12). In the archived samples, pyrite occurs as nodular growths, but also euhedral and intergrown masses (Figure 2.12). The graphitic material occurred in anastomosing lenses of finely disseminated graphite in quartz. Accessory minerals include Fe-rich dolomite, chlorite, biotite, and muscovite, but also traces of sphalerite and chalcopyrite as inclusions in the pyrite. The cherty groundmass and lack of detrital minerals (e.g., zircon) is similar to the oxide-BIF and contrasts with volcanic-derived shales elsewhere in the section (see below).

Clastic sediments: Mudstones, greywacke and other volcaniclastic lithologies are present throughout the Sherman mine sequence. Many are preserved as chloritic layers that have distinctive sedimentary features such as graded bedding and erosional contacts. These units are distinct from the chlorite in the magnetite and chert layers of the BIF. Clastic units with abundant graphite are also present throughout the volcanic succession hosting the BIF (e.g., between the north and south BIF units, see below). In contrast to chlorite layers, the volcaniclastic material is

typically devoid of any authigenic magnetite, but contains abundant ilmenite and refractory quartz apatite, zircon, and monazite, which are interpreted to be detrital in origin (Ginley, 2016).

Footwall lithologies: The volcanic rocks hosting the Temagami BIF comprise a bimodal succession of mafic volcanic flows and felsic volcaniclastic units (see Fig. 2.20). In the north BIF, felsic volcanic and volcaniclastic material is predominant in the footwall of the BIF, and sulfidic argillites were present in the immediate footwall to the north of the BIF unit (see Fig. 2.4; Donaldson and Munro, 1991). In the footwall of the south BIF, tholeiitic basalts are dominant, overlain by andesitic and rhyolitic extrusive units (Fyon and Crocket, 1986). The immediate footwall of the south BIF exposed in the Hwy 11 outcrop consists of massive andesite flows and greywacke. The volcanic rocks have been subjected to intense sulfide-carbonate-sericite-epidote-chlorite alteration. Sericitized felsic volcaniclastic units are also well exposed north of the Sherman mine. Pyritic clasts are locally abundant in the rhyolitic breccias, and have been identified by Schwartz (1995) as mainly derived from seafloor mudstones, based on low Co/Ni ratios ($\leq$1) rather than from VMS (Co/Ni ratios >5: Bralia et al., 1979; Hurley, 1985; Blum, 1986).

2.5 Mineral paragenesis

A paragenetic sequence for the different authigenic phases of the oxide-facies BIF has been determined from the petrographic observations (Figure 2.21). The sequence is interpreted to represent mainly chemical precipitation with minor detrital input, with the primary precipitate having consisted of Fe-oxyhydroxides in amorphous silica gel (i.e., jasper precursor). Relics of the initial Fe-oxyhydroxides are preserved as fine-grained Type 1 hematite dust (grains <100 nm in size) in the jasper layers. The early hematite is encapsulated (and protected from further recrystallization) in the earliest fine-grained (20-50 μm) quartz grains. Type 1 magnetite is also preserved in this quartz, but probably formed just after or by replacing Type 1 hematite, as the Type 1 hematite is generally absent in portions of the quartz grains where Type 1 magnetite is present. Coarser-grained Type 2 hematite and Type 2 magnetite increase in abundance and appear to have formed in the quartz at the expense of fine-grained Type 1 hematite (Figure 2.9a). Type 2 hematite resembles the structure of "microplaty hematite" attributed to supergene alteration in Superior-type BIF (cf. Morris, 1983). In the Temagami BIF, "microplaty" hematite occurs as mm-

scale pockets in a coherent rock and likely a product of internal, fluid-driven recrystallization instead of supergene alteration. Originally cloudy quartz with abundant Type 1 hematite gives way to clear quartz with coarser Type 2 hematite and magnetite at the grain boundaries. The implication is that iron from the jasper spherules was mobilized to the outer margins and crystallized as Type 2 hematite and magnetite. This was likely the dominant process by which original jasper layers were replaced by black chert throughout the oxide-facies BIF. The red microbands in the jasper layers preserve an early, poorly recrystallized mineralogy, which may reflect encapsulation of the primary Fe-oxyhydroxides by quartz prior to burial and diagenesis.

Type 3 and Type 4 magnetite represent the progressive growth and recrystallization of magnetite, with complex overgrowths and incorporating locally abundant inclusions. The internal structure of Type 3 magnetite, in particular, reflects fabric destructive growth around a single center of crystallization rather than aggregation of Type 2 magnetite. The ongoing fabric-destructive magnetite recrystallization processes (cf. Sampaio et al., 2018), as well as dissolution and overgrowth documented in Type 3 through Type 5 magnetite indicate substantial mobility of the components of magnetite (Fe^{2+}, Fe^{3+}) and quartz (Si) throughout the diagenetic and later metamorphic history of the oxide-facies BIF. Because apatite and chlorite are located mostly in the interstitial spaces of Type 3 and 4 magnetite, and sometimes as small inclusions in the outer zones of coarse magnetite crystals, they are thought to have formed mainly after Type 3 magnetite crystallization. Locally euhedral crystals of apatite overgrow Type 3 magnetite. Dolomite and ankerite, which grew in open spaces in Type 3 and later magnetite, typically have abundant inclusions of quartz and other late-stage accessory minerals (e.g., monazite). Type 5 magnetite, common in BIF adjacent to mafic intrusions, is skeletal and appears to have undergone partial dissolution during latest stage metamorphism. Stilpnomelane, grunerite and biotite are metamorphic minerals. However, they lack significant porphyroblastic textures and do not deflect any foliation.

The paragenetic sequence is summarized in Figure 2.21:
1) primary precipitation of a Fe-Si gel, relicts of which are preserved in some jasper layers;

2) early (i.e., diagenetic) crystallization of opal/quartz and dewatering with recrystallization of iron-oxyhydroxides to form Type 1 hematite 1 and possibly Type 1 magnetite plus crystallization of Type 1 apatite;
3) diagenetic recrystallization, dewatering, and remobilization of iron to form Type 2 hematite and magnetite;
4) late diagenetic recrystallization and overgrowth of Type 3 and 4 magnetite, trapping inclusions of accessory chlorite, Type 2 apatite and early carbonates, with deposition of interstitial quartz;
5) metamorphic recrystallization, of magnetite and formation of Fe-rich aluminosilicates, including stilpnomelane and metamorphic amphiboles (grunerite);
6) contact metamorphic recrystallization, leading to localized Si- and Fe loss producing skeletal Type 5 magnetite and late quartz veins containing stilpnomelane and grunerite.

2.6 Mineral chemistry

Because of the fine-grained nature of oxide-facies BIF, few data are available on the chemistry of individual minerals. Here we present combined in situ analyses of magnetite, apatite, monazite, and chlorite in the Temagami BIF. We emphasize magnetite as the dominant Fe mineral and a potentially robust archive of trace element enrichment and depletions during BIF formation. Variation in the composition of magnetite [ideal formula: $Fe^{3+}(Fe^{2+}Fe^{3+})O_4$] mainly reflects the ionic charge and radius Fe^{3+} and Fe^{2+} and allows for a range of substitutions in different sites in the magnetite structure, most notably Si, Al, Mg, Ti, Zn, Mn, Cr, Ni, V, Co, Cu, and Ge, making it a useful as a petrogenetic indicator (Fig. 2.22; Dare et al., 2014; Nadoll et al., 2014).

2.6.1 Magnetite

The major and trace element concentrations in magnetite were determined in 395 individual EPMA spot analyses and 137 LA-ICP-MS analyses. Results for 40 elements were obtained: Fe, Mg, Al, Si, P, Ca, Sc, Ti, V, Cr, Mn, Co, Ni, Cu, Zn, Ga, Ge, As, Y, Zr, Nb, Mo, Ag, Cd, In, Sn, Sb, Cs, Ba, La, Sm, Yb, Hf, Ta, W, and Pb. Additionally, Se, Re, Pt, Pd, Te, and Bi were monitored, but not detected (always bdl, <20-100 ppb). Complete results of the EPMA are provided in Appendix B, and LA-ICP-MS data are listed in Appendix C. Although microinclusions could not be avoided in all cases, zones with abundant inclusions were avoided by monitoring time-resolved signal

intensity and deselecting periods of peak indicator elements for inclusions (Zr, P, Si, Al). A transect through inclusion-rich zones of magnetite in Figure 2.23, illustrates the spatial variations in selected trace elements due to microinclusions in the magnetite.

Most of the magnetite in the oxide facies BIF is not stoichiometric Fe_3O_4 (Table 2.3). Even inclusion-free magnetite shows distinct overgrowths and oscillatory zoning, particularly in Type 3 magnetite (see Fig. 2.24). In large, ~500 μm magnetite grains at least 4 distinct growth zones can be distinguished, for example in Fig. 2.24b: 1) at the very center of type 3 magnetite, 1-10 μm jasper spheres or clusters of <1 μm quartz inclusions are common (cf. Fig. 2.10c), 2) oscillatory zonation defined by variable Si (and Mg) in areas without mineral inclusions, 3) outer zones with densely packed 5-10 μm quartz inclusions, and 4) pure magnetite rims. At the thin section scale, all magnetite in a single sample shows the same order of zoning, although this is less obvious with decreasing sizes of the magnetite grains (Fig. 2.24e). The most complexly zoned magnetite occurs in magnetite layers that are interlayered with jasper. The presence of Si and Mg in the magnetite structure is supported by their strong internal zoning and covariation (Fig 2.24c), distinguishable from the presence of quartz nano-inclusions alone. Similar lattice-bound Si in magnetite has been documented in other BIF by micro x-ray diffraction (Huberty et al., 2012). The covariation with Mg likely reflects a coupled substitution (possibly redox controlled) of Si^{4+} with Mg^{2+} or Fe^{2+}, necessary to avoid charge imbalance. LA-ICP-MS data show Si is present in all types of magnetite, ranging from 217 to >90000 ppm, with a median of 3297 ppm. The highest values are undoubtedly due to inclusions of quartz; the maximum Si concentration from EPMA analyses, which more reliably avoid inclusions due to the small spot size, is ~2.78 wt.% (Table 2.3). Median concentrations of Mg are 337 ppm by La-ICP-MS and 0.03 wt.% by EPMA analyses. Aluminum concentrations have a median value of 91 ppm. Al occurs independent of Mg and is therefore likely hosted in the magnetite lattice as opposed to chlorite inclusions.

Magnetite is also the main host for a range of trace elements in the Temagami BIF (Table 2.4). High concentrations of Ca and P above 100 ppm in some magnetite likely indicate the presence of microinclusions of apatite, indicated by a weak co-enrichment of REE, Ca, P, and Ba (e.g., Fig.

2.25). However, concentrations below 100 ppm may be present in the magnetite structure. Concentrations of REE (La+Sm+Yb) up to 1 ppm occur independent of high P concentrations, and therefore are likely hosted independently in the magnetite lattice rather than apatite inclusions. Similarly, about 18 ppm Ti (median value) is likely present in the magnetite, where obvious inclusion-related peaks are absent.

Mn, Ga, and As can substitute for Fe^{3+} in the octahedral site of the magnetite structure; the median concentrations of these elements are 194 ppm Mn (up to 1634 ppm), 0.9 ppm Ga (up to 10 ppm), and 0.63 ppm As (up to 64 ppm). However, the highest concentrations of As (together with high Ag up to 5.1 ppm, Sb up to 8 ppm, and Pb up to 52 ppm) were found in a sample with pyrite inclusions. The correlation between As and Sb (e.g., Fig. 2.26), in particular, may reflect enrichment by adsorption onto primary Fe-oxyhydroxides, which was then inherited by the magnetite (see also Chapter 3). Up to several tens of ppm V, Cr, Co, Ni, Cu, Zn, and Ge also may be present in the magnetite structure (Fig. 2.26), with median concentrations of 14 ppm Zn (up to 88 ppm), 7.6 ppm Ge (up to 88 ppm), 7 ppm V (up to 149 ppm), 5 ppm Ni (up to 165 ppm), 0.9 ppm Cr (up to 248 ppm), 0.8 ppm Co (up to 32 ppm), and 0.3 ppm Cu (up to 505 ppm). The highest values of Cu, Co, Ni and Zn are in one sample with sulfide inclusions. Mo concentrations were mostly below detection limit, and where detected showed time-resolved spikes in the Mo signal typical of inclusions. Slightly higher concentrations of W in some samples (up to 16 ppm) may be related to apatite inclusions, showing weak correlation with Ca, P, and REE (see Table 2.5).

Trace elements in magnetite that are likely hosted in the crystal lattice (i.e., independent of microinclusions) include Ti, V, Cr, Co, Ni, Zn, Ge, Mn, Ga, Mo, W. The concentrations of the trace elements vary independently, arguing against mineral inclusions, and they have rather smooth abundance patterns in time-resolved LA-ICP-MS signals (Fig. 2.27). Ge, Mn, and Pb, and to a lesser degree Si, As, and Sb, are enriched in the cores of Type 3 magnetite (cf. Fig. 2.23). V, Cr, Co, Ni, Zn, and Ga ($\pm$As) show no significant variation across large, Type 3 magnetite crystals. Mg, Al, Ti, and Sc are enriched in the rims of Type 3 magnetite.

Y, Zr, Nb and Hf have highly variable concentrations but are not considered to be present in substitution in the magnetite structure because of their high field strengths (e.g. Nadoll et al., 2014). All show large variations in concentration, between 0.01 ppm and 10s to 100s of ppm, and

covariation of Zr and Hf suggest ultrafine inclusions of zircon in some magnetite. Slightly elevated concentrations of Hf, up to 1.6 ppm, are probably related to zircon inclusions. However, low amounts of Ta (median concentration of 0.04 ppm) occur independently of other HFSE and are probably present in the magnetite structure. Y is most likely associated with minor apatite or monazite inclusions. Concentrations of the REE reach up to 29, 17, and 1.6 ppm, respectively for La, Sm, and Yb; these are most likely present in apatite inclusions, although Yb may also be present in zircon. Values close to the median concentrations (0.06, 0.03, and 0.04 ppm, respectively) are similar to values reported for other BIF-magnetite without apatite inclusions (Gourcerol et al., 2016a). A summary of the inferred host relationships of different trace elements in magnetite from the Temagami BIF is given in Table 2.6.

2.6.2 Chlorite

185 analyses of chlorite were obtained from the BIF samples and host volcanic rocks. In BIF, only the magnetite, chert, chlorite, and sulfide facies contain chlorite; no chlorite was found in the jasper layers, and chlorite associated with the siderite may be late in the paragenesis. Representative analyses of chlorite are provided in Table 2.7, and all results are presented in Appendix D. Fe, Al, Ca, Mg, Na, K, Ti, Mn, Zn, Ni, Cr, F, and Cl have been determined by EPMA. FeO and Fe_2O_3 were calculated based on cation balance and assuming full site occupancy.

In the magnetite layers, chlorite contains 35.2 wt.% FeO (median value), with a maximum of 42.6 wt.% (Table 2.7). The maximum calculated Fe_2O_3 is 2.9 wt.%. MgO ranges from 4.3 to 13.9 wt.%, with a median concentration of 7.3 wt.%. Al_2O_3 varies by only a few wt.%, with a median concentration of 18.2 wt.%. SiO_2 concentrations vary considerably, between 22.8 and 29.5 wt.% in magnetite layers (median concentration of 24.9 wt.%). Trace amounts of TiO_2 (0.03 wt.%), MnO (0.05 wt.%), and ZnO (0.04 wt.%) are also present in chlorite in the magnetite layers. In the chert layers, FeO contents of chlorite are lower (median concentrations of 26.9 wt.%), and Fe_2O_3 generally higher (up to 4.8 wt.%). MgO and SiO_2 concentrations are also higher, with median values of 12 wt.% and 28.3 wt.%, respectively. Al_2O_3 concentrations are similar to those in magnetite layers, with a median value of 19.3 wt.%. TiO_2, MnO and other trace elements in chlorite from the chert layers are low.

FeO concentrations are generally high in the chlorite layers (median value of 32.9 wt.%), and median concentrations of MgO (10.7 wt.%), SiO_2 (26 wt.%), and Al_2O_3 (18.2 wt.%) are similar to those of chlorite in the magnetite BIF. TiO_2 and MnO concentrations are also similar to magnetite BIF (up to 0.05 wt.% and 0.06 wt.%, respectively). Chlorite associated with rare siderite and Mn-dolomite lenses in the chert-magnetite assemblages has the highest FeO concentrations (median value of 40.9 wt.%), with calculated Fe_2O_3 <0.01wt.%. MgO, SiO_2 and Al_2O_3 concentrations are low (median values of 4.7 wt.%, 18.3 wt.% and 23.2 wt.%, respectively) .

Chlorite in the sulfidic cherts has the lowest FeO (18.6 wt.%); MgO, SiO_2 and Al_2O_3 are high, with median values of 14.5 wt.%, 29.6 wt.% and 21.7 wt.%, respectively. This chlorite is also strongly enriched in MnO (0.33 wt.%) and has low TiO_2 (0.03 wt.%). Chlorite in the altered volcanic host rocks (including rhyolite, andesite, basalt and associated volcaniclastics) has a narrow range of compositions, with median concentrations of FeO from 24.3 to 29.0 wt.%. Calculated Fe_2O_3 concentrations are as high as 9.5 wt.%, but median values are 0.35-0.82 wt.%. Median concentrations of MgO range from 8.8 wt.% in the altered volcaniclastic units to 13.5, 11.8, and 15.0 wt.% in rhyolite, andesite, and basalt, respectively. Median concentrations of Al_2O_3 and SiO_2 are 19.0-21.6 wt.% and 23.4-25.9 wt.%, respectively, and MnO concentrations are high (median values of 0.09, 0.12, 0.38, and 0.32 wt.% in volcaniclastics, rhyolite, andesite, and basalt respectively). TiO_2 concentrations are 0.02 and 0.04 wt.%, similar to chlorite in BIF, but several analyses of chlorite in basalt (0.32 wt.%) and andesite (0.21 wt.%) have notably higher TiO_2 than in BIF.

2.6.3 Apatite

EPMA analyses of apatite were obtained in jasper, magnetite, and chlorite facies BIF and are summarized in Table 2.8 (all results reported in Appendix E). Ca and P concentrations in apatite vary minimally around median values of 39.2 wt.% and 18.3 wt.%, respectively. Lower Ca and P concentrations (down to 33.1 wt.% and 15.9 wt.%) are a result of interference from neighboring quartz or magnetite or where inclusions may have been present. For this reason, Fe and Si were monitored, and analyses were discarded if either exceeded few wt.%. Fluorine was present in appreciable concentrations, between 2.23 to 4.06 wt.%; Cl was not present in significant

concentration (for remarks on F analysis reliability in apatite by EPMA, see discussion below and Appendix E).

Trace elements in apatite in the major host lithologies (jasper, magnetite and chert layers) were obtained on 33 spots in four samples by LA-ICP-MS (see Table 2.9, all results listed in Appendix F). As for the magnetite analyses, time-resolved signals for indicator elements Si, Fe, and Zr were monitored to avoid inclusions of quartz, magnetite and zircon.

The most important trace elements in apatite are the REE, Y, and S. The total concentrations of the REE are 1302 ppm (median value). Y concentrations are 913 ppm. Other important constituents are Sr (1916 ppm), Na (844 ppm), S (519 ppm) Mn (322 ppm) and Pb (24 ppm; see Appendix F for full results). Some notable differences in the apatite compositions occur between the BIF facies. The LREE, La, Ce, Pr, Nd, and Sm are two to ten times more abundant in apatite in chlorite layers than in magnetite and chert layers, whereas the concentrations of MREE and HREE are similar in all facies. The exception is Eu, which is more abundant in apatite in jasper and magnetite layers (62 and 105 ppm) than in apatite in chlorite layers (22.5 ppm, see Table 2.9). Arsenic is enriched in apatite in the jasper layers (68.5 ppm) compared to magnetite and chlorite layers (5.13 and 6.06 ppm, respectively), Sr and Pb are enriched in jasper and magnetite layers (1675 and 4188 ppm Sr, and 22.3 and 27.0 ppm Pb) compared to chlorite layers (504 ppm Sr and 4.87 ppm Pb), Th and U are enriched in chlorite layers (8.27 ppm Th and 3.95 ppm U) compared to jasper and magnetite layers (0.12 and 0.027 ppm Th, and 0.35 and 0.32 ppm U).

2.6.4 Monazite and xenotime

Monazite and xenotime were identified petrographically as additional phosphate phases. Because of their small size, ~1 µm, EPMA was used to analyze these minerals, with an emphasis on REE and Y concentrations. The median concentrations of REE and Y in all analyzed monazites are listed in Table 2.10 (all results reported in Appendix G). La, Ce, Pr, Nd and Sm total 53.0 wt.%; all other REE and Y are < 1wt.%. P accounts for the remaining 12.8 wt.%. Measure Fe , (<0.013 to 9.96 wt.%), Si (<0.05 to 6.75 wt.%), and Al (<0.004 to 2.82 wt.%) are highly variable and mainly reflect interference from surrounding magnetite and quartz due to the small grain size of the target minerals. However, high concentrations of Pb (760 ppm), Th (6200 ppm), Ca (1260

ppm), Sr (770 ppm), Cl (420 ppm), and F (5420 ppm) are not attributable to interferences. Monazite in the chlorite layers of the BIF is more than two times enriched in Pb, Th, and Sr, compared to monazite in the chert and magnetite layers but contains only about half the La and Eu.

A single xenotime analysis (Table 2.10) obtained from a magnetite layer yielded major and trace element concentrations similar to monazite, except that Y is the dominant cation (39.8 wt.%) and the heavy REE (e.g., 2-3 wt.% each of Yb, Dy, and Er) have higher concentrations than the LREE (e.g., <0.1 wt.% La and Ce).

2.6.5 Other mineral species

Other mineral species analyzed by EPMA include quartz, hematite, ilmenite, rutile, titanite, ferroan dolomite (ankerite), and siderite (Table 2.11). All results are presented in Appendices H-K. Notable enrichments of the major and trace elements in these minerals include: 1.17 wt.% SiO_2 in hematite in sample 11-41, 1.18 wt.% MnO in ferroan dolomite and siderite in six samples from the Hwy 11 outcrop, and 0.6 wt.% MnO and 0.27 wt.% V_2O_3 in ilmenite, rutile and titanite in nine samples from the Hwy 11 outcrop.

2.7 Discussion

2.7.1 Origin of magnetite, jasper, and chert layers

The most striking feature of Algoma-type iron formations is the characteristic banding, including macro-, meso-, and micro bands (metre-scale, cm-scale, and mm layers: Trendall, 1973; Gross, 2009). The banding has been attributed to a variety of different processes, including changes in the conditions of primary precipitation as well as to post-depositional processes (Trendall and Blockley, 1970; Krapež et al., 2003). These include 1) variation in the physicochemical conditions of the water column, 2) mineral transformations during diagenesis, for example by microbial or abiotic reactions, or 3) metasomatic replacement and alteration caused by hydrothermal fluids (Morris, 1993; Klein, 2005; Ohmoto et al., 2006; Steinhoefel et al., 2009; Satkoski et al., 2015; Li et al., 2017). Banding in Lake Superior-type BIF has been attributed to seasonal variations in the water column producing layers of different composition resembling varves, or sorting of minerals

into discrete layers by density currents (Trendall, 1973; Trendall, 2002b; Krapež et al., 2003; Posth et al., 2008). These processes are considered less important in Algoma-type BIF, which formed in deep marine conditions under relatively stable water masses (Gross, 1996), although primary sedimentary features such as sorting of volcaniclastic material, scour marks, ripples, and erosional contacts in clastic layers have been identified that indicate active sedimentary processes (Gross, 1972; Donaldson and Garrett, 1991; Ginley, 2016). However, these sedimentary structures are much less common in Algoma-type BIF, consistent with mainly chemical sedimentation.

The initial precipitate in Algoma-type BIF is generally thought to have been an Fe-oxyhydroxide-rich silica gel (Gross, 1965b; Clout and Simonson, 2005; Maliva et al., 2005; Ohmoto et al., 2008; Bekker et al., 2014; Stefurak et al., 2014; Sun et al., 2015; Alibert and Kinsley, 2016; Konhauser et al., 2017). In Temagami, relics of this material are preserved in jasper layers, with the original "gel" represented by the jasper spherules. These features are distinct from the hematitic ooids common in Lake Superior-type BIF. Instead, the spherules, which range in size from 20 to 50 μm, are very similar to silica spherules precipitated from solution in modern chert (Ahn and Buseck, 1990; Jones and Renaut, 2007; Stefurak et al., 2015). Experimental and other evidence has shown that silica sols can form with spherules up to 100 μm in size under neutral or slightly acidic conditions, with the sizes and shapes of the spherules controlled by factors such as the silica concentration and pH (Iler, 1973; Williams and Crerar, 1985; Stefurak et al., 2014). The distinctive red colour of the spherules in jasper layers is due to microscopic hematite grains, as also observed in much younger examples (e.g., Løkken Ophiolite in Norway: Grenne and Slack, 2003). In some Eoarchean BIF (e.g. Nuvvuagittuq BIF, cf. Dodd et al., 2017) the red colour is due to larger translucent hematite crystals in the matrix between silica spherules and microfossils (e.g., Fig. 2.28). The latter more closely resemble Type 2 hematite in the Temagami BIF, which formed in the interstices of Type 3 magnetite later in the diagenetic history. In parts of the Løkken BIF and the Nuvvuagittuq BIF, hematite is concentrated along filaments in anastomosing lenses, suggesting the involvement of bacteria in the Fe deposition (Grenne and Slack, 2003; Dodd et al., 2017). Similar filaments have been noted in the Temagami chert (Ginley, 2016), but they are lined by magnetite rather than hematite.

2.7.2 Earliest diagenesis

After initial deposition of the Fe-oxyhydroxide silica gel, stepwise recrystallization resulted in the appearance of the first microcrystalline hematite (Type 1 hematite). This may have started immediately after deposition of the silica gel, as pore water diffused out of the jasper spherules (Duhig et al., 1992; Rasmussen et al., 2013; Stefurak et al., 2014). Internal redistribution of iron and silica in the initially homogenous layers resulted in the fine microbanding that is still preserved in some jasper layers. Similar microbanding developed in the white and black chert layers, with the growth of fine Type 1 and Type 2 magnetite. Thus, the microbands mainly represent changes in grain size and crystallinity rather than bulk composition. The process is thought to be very similar to that observed in the early jasper spherules, where Fe migrated short distances out of the cloudy jasper and into coarser hematite or magnetite at the margins of the spherules. Incipient chemical sorting is common in multicomponent gels (e.g., Liesegang banding and Ostwald ripening), and thus may have been the starting point for the development of the microbands in Algoma-type BIF (Stern, 1954; Morse and Casey, 1988). This early banding also may have resulted in planes of differential strain during initial compaction, as there is evidence of early movement during recrystallization of mineral phases along some microbands. These observations are strong evidence that microbanding does not reflect rhythmic deposition caused by fluctuations in the chemistry of the water column but rather different degrees of recrystallization of a homogeneous Fe-rich silica precursor. The microbanding present in the chlorite layers reflects the authigenic growth of aluminosilicates (initially amorphous clays) in alternating bright and dark bands. In contrast to microbanding defined mainly by iron-oxide crystallinity, the banding of aluminosilicates may represent true chemical variation related to depositional control.

Quartz most likely formed by a stepwise transformation and water loss from initially deposited amorphous silica (opal A or opal CT [christobalite-tridymite]; Wise Jr and Kelts, 1972; Maliva and Siever, 1988). Formation of quartz in this manner is thermodynamically favored over direct precipitation of quartz at near-ambient temperatures (Williams and Crerar, 1985; Williams et al., 1985; Simonson, 1987), and is supported by the preservation of structures resembling opal spherules in the jasper layers (Wise and Kelts, 1972). The initial transformation of amorphous opal A to opal CT occurs at ~50°C, but it has been reported at temperatures as low as 18°C and as high as 56°C in natural systems (Ernst and Calvert, 1969; Pisciotto, 1981). Transformation of opal CT

to microcrystalline quartz takes place at temperatures between 31°C and 165°C (Murata and Larson, 1975; Mizutani, 1977; Pisciotto, 1981). The crystallization steps may involve dissolution-reprecipitation that allowed water to escape and goethite and later hematite to form from the initial amorphous iron-oxyhydroxide (at ~25°C and ~50°C, respectively: Cornell and Schwertmann, 2003; Trolard and Tardy, 1987). The formation of hematite from goethite and transformation of opal CT at about the same temperature provides a first-order estimate of the temperature at which the jasper layers formed. At the elevated temperatures of Archean seawater, thought to be in the range of 26-35°C (from oxygen isotopes in phosphates: Blake et al., 2010) to 50-70°C (from Si isotopes in cherts: Robert and Chaussidon, 2006), these processes could have started in the water column and continued with recrystallization to microcrystalline quartz and hematite on the seafloor.

There is abundant evidence for dewatering shortly after deposition of the Fe-oxyhydroxide-silica gel and formation of the first microbands. Where the hydrostatic pressure in the pore spaces exceeded the integrity of the compacting BIF layers, breakouts like those depicted in Figure 2.18 were common. As newly precipitated amorphous silica gels could have contained as much as 90 vol.% water (Williams and Crerar, 1985), significant volume loss must have occurred when that water was expelled. In addition to porewater, loosely bound water in amorphous silica and Fe-oxyhydroxides also would have been liberated during recrystallization (up to 11 wt.% in the case of the opal-quartz transition: (Jones and Renaut, 2007). The escaping pore water would have been in equilibrium with the originally precipitated material (i.e., Fe and silica saturated), providing a recycling pathway for some of the early-deposited components back to the water column or to recrystallized minerals in the BIF layers. The lack of fluid inclusions in the quartz is consistent with formation accompanied by water loss.

Soon after depositon, recrystallization and silicification by expelled pore water would have transformed the newly formed BIF layers into siliceous hardgrounds (i.e., thought to be the primary lithification process in Algoma-type BIF: Simonson, 1987; Krapež et al., 2003; Pickard et al., 2004; Fischer and Knoll, 2009). Silicification (i.e., precipitation of quartz between spherules) also appears to have protected the jasper spherules from further recrystallization and complete replacement of early hematite by magnetite. Temperature was likely the main control on silica

solubility (Kastner and Siever, 1983; Williams et al., 1985), and warm pore waters would have been enriched in Si (see Fig. 2.29), thus forming hardgrounds from the "bottom-up" upon cooling, rather than by export of Si from the water column as in the formation of normal marine chert (Siever, 1962; Simonson, 1987; Siever, 1992). This process has previously been suggested for the formation of chert pods and nodules in other BIF (Trendall and Blockley, 1970; Murray et al., 1992; Maliva et al., 2005; Fischer and Knoll, 2009), and similar features of the Temagami BIF likely formed in the same way (Fig. 2.20a).

Some silica in expelled pore waters likely escaped the sediment altogether and upon contact with cold seawater reprecipitated as pure amorphous silica (white chert) on top of the Fe-Si sediments. These white chert layers, once covered by more Fe-oxyhydroxide-silica gel, would have become part of the BIF stratigraphy. Thus, there appear to have been several pathways for the formation of the white chert layers: chemical sorting of the original Fe-oxyhydroxide-silica gel into jasper and white chert microbands; expulsion of silica from the sediments forming discrete layers of white chert; a break in Fe deposition allowing deposition of pure silica from the water column. However, it is likely that a break in Fe deposition would also have terminated the export of Si from the water column. Scavenging of Si by Fe-oxyhydroxides is a highly effective process, precipitating Si from seawater even under conditions significantly below silica saturation (Davis et al., 2002), and silica concentrations in Temagami seawater might even have been drawn down by the scavenging processes. This could explain the absence of chert beds outside of BIF strata. In all cases, silica deposition must have been fast enough to avoid any accumulation of clastic material in the white chert.

Early silicification led to some layers becoming more brittle, developing microfractures occupied by quartz veinlets that do not cross the layer boundaries. The quartz veinlets in jasper are among the earliest generation of quartz veins, recording deformation between the semi-brittle jasper microbands (e.g., "deck-of-card"-like movenment: Fig. 2.12e). Fluid movement accompanying this early deformation may have initiated the preferential recrystallization of Type 1 hematite to Type 2 magnetite.

2.7.3 Late-stage diagenesis

While jasper and black chert layers were probably stabilized during very early diagenetic conditions, magnetite layers and specifically growth of Type 3 magnetite mainly formed during later diagenetic stages. This interpretation is supported by higher formation temperatures for magnetite documented in other BIF. For example, oxygen isotope data from the Dales Gorge BIF indicate formation temperatures <140ºC for hematite, whereas magnetite formed between 140ºC and 300 ºC (Becker and Clayton, 1976). The progression from smaller Type 1 and Type 2 magnetite to Type 3 magnetite also follows the Ostwald rule of increasing crystal size and decreasing number of individual crystals with maturation (Morse and Casey, 1988), and suggests that Fe was sufficiently mobile during diagenesis to reach the sites of Type 3 magnetite growth.

The abundance of jasper steadily decreased during diagenesis relative to magnetite layers. The initial "sealing" of the jasper spherules by microcrystalline quartz was due to the low solubility of quartz in the early pore fluids that were in equilibrium with amorphous silica (i.e., oversaturated with quartz). During later diagenesis, when all amorphous silica and opal had been deposited, some dissolution-recrystallization of quartz would have occurred along the boundaries of jasper and magnetite layers. This is supported by the presence of larger Type 2 hematite grains along the boundaries between the jasper and magnetite layers (see Fig. 2.9d,e). As long as diagenetic fluids were still present in the sediments, silica would have continually undergone dissolution-reprecipitation (Williams and Crerar, 1985). Increasing Si mobility also would have been promoted by rising temperatures in the sediment during diagenesis, and increasing alkalinity (especially in the magnetite layers) may have increased its solubility even further (Williams and Crerar, 1985). One mechansim for changing pH in the sediments could have been organic-inorganic reactions, such as bacterial Fe(III) reduction producing dissolved inorganic carbon (Fischer and Knoll, 2009). Such a process also could explain the presence of Fe-rich dolomite and calcite in some magnetite layers (see Fig. 2.16b).

Another indication of the mobility of Si during diagenesis is the incorporation of Si in the crystallizing magnetite. Type 3 magnetite overgrew quartz that was crystallizing at the same time, now preserved as inclusions in the magnetite (Fig. 2.22). The development of siliceous magnetite and oscillatory zoning of Si in larger magnetite crystals is strong evidence for the presence of Si

in contemporary diagenetic fluids. The mechanism of incorporation is likely a coupled substitution of Si^{4+} and Mg^{2+} or Fe^{2+} with $2Fe^{3+}$, possibly incurring an octahedral vacancy (Huberty et al., 2012). Thus, the ability of magnetite to incorporate Si in its crystal lattice may be related to slight variations in redox during magnetite growth (Putnis et al., 1992; Shimazaki, 1998; Huberty et al., 2012). The crystallization of Type 3 magnetite is interpreted to have taken place over a range of temperatures, starting after initial diagenesis (>50°C but <200°C: French, 1973; Klein, 2005) and at temperatures as high as 140-300°C (Becker and Clayton, 1976; Shimada et al., 2006). Different temperatures of formation of magnetite and quartz in different layers are also possible, reflecting the highly variable conditions of diagenesis within the sediment column (e.g., Blum, 1986).

Late-stage veining by quartz in the chert and jasper layers is broadly discordant to layering but randomly oriented. A clear structural control is not evident, suggesting a dominantly pre-metamorphic origin. No obvious alteration is observed in association with the veins, suggesting that they are not related to infiltration of high-temperature hydrothermal or metamorphic fluids. Instead, we interpret them to represent pathways of internal fluid migrations during diagenesis. They are commonly associated with dewatering ("break-out") structures, and the quartz in the veinlets often shows a change in grain size between layers. Some of the quartz veins are broadly layer-parallel and diffuse in chert layers, possibly reflecting a genetic link to expulsion of silica from the different layers (Fig. 2.8e,f).

Some siderite is observed in the oxide-facies BIF of the Highway 11 outcrop. Elsewhere, Fe-carbonate has been interpreted as a primary precipitate from CO_2-enriched bottom water (Ohmoto et al., 2004; Canfield, 2005); however, the majority of Fe-carbonate in the Temagami BIF is of late diagenetic or metamorphic origin.

2.7.4 Metamorphism

The Temagami BIF was affected by regional metamorphism up to lower greenschist conditions (<350 °C), generally below quartz-albite-epidote-biotite stability (Bennett, 1978). Locally, higher temperatures were caused by contact metamorphism in proximity to synvolcanic and later intrusions. Jasper and chert layers, already converted to quartz, were largely unaffected by the regional metamorphism. Differences between the layers, in terms of the oxygen isotopes of quartz

and magnetite, also suggest that these minerals were not affected by regional metamorphism (Blum, 1996).

Magnetite crystallization likely continued to lower greenschist facies (200-300°C: French, 1973; Walker, 1984; Shimada et al., 2006; Koehler et al., 2010), together with chlorite and apatite. Type 2 apatite (and monazite), which occurs both as inclusions in and euhedral overgrowths on Type 3 magnetite, formed during early-stage metamorphism, with the metamorphic remobilization of quartz creating space for crystal growth. Ferroan dolomite, which occurs as late-stage euhedral crystals containing abundant quartz inclusions, was also likely metamorphic in origin. However, none of the metamorphic minerals have chemistry that would reflect infiltrating metamorphic fluids (e.g., Fe/Fe+Mg in chlorite, Si in magnetite, REE in apatite are similar to those of preserved diagenetic phases). Early pyrite occurs mainly as small, anhedral inclusions in magnetite and rarely as diagenetic growths (radial and skeletal textures: e.g., Kalliokoski, 1966) in sulfidic chert. Larger, euhedral pyrite, interpreted to be metamorphic porphyroblasts occur locally in the altered volcanic host rocks but are not observed in the oxide-facies BIF.

In the Highway 11 outcrop, the most obvious metamorphic minerals are related to contact metamorphism caused by late Sudbury-style intrusions (stilpnomelane, grunerite, and some Type 4 and Type 5 magnetite, and mm-sized euhedral pyrite). Original jasper layering is lost in the vicinity of the intrusions, and stilpnomelane needles and amphiboles interpreted to be mainly metamorphic in origin are also common. These minerals would have formed at temperatures of 250-500°C and pressures of 2-5 kb (French, 1973; Klein, 1973; Forbes, 1977; Klein, 2005; McSwiggen and Morey, 2008). Stilpnomelane is also common in fractures within the coarse-grained magnetite (some previously interpreted as “syneresis cracks”). The cracks are most common in the coarse magnetite layers, which may have been more brittle, whereas the adjacent chert layers are only moderately recrystallized. Some volume change and cracking may have occurred due to iron mobility, reaction of original chlorite to amphibole, or possibly thermal expansion of quartz relative to magnetite under metamorphic conditions (Manahan, 1990; Ahrens, 1995).

Contact metamorphism of the oxide-facies BIF was also reported at the west end of the Sherman mine in proximity to the Spawning Lake Pluton (Bennett, 1978; Bowins and Heaman, 1991). Here, temperatures producing garnet were reached, with local recrystallization of magnetite. Apatite is abundant in these layers, together with amphibole (cummingtonite-grunerite), and other aluminosilicates not found in unmetamorphosed oxide facies BIF samples (albite and biotite). These samples also contain pyrrhotite possibly produced by metamorphism of original pyrite.

Metamorphic quartz veins are abundant. They cut across all layers and show no change in crystallinity or grain size between layers. The veins are up to several centimeters in width and include quartz, ankerite, and pyrite. They are continuous at the outcrop scales and not affected by lithologic changes or folding. Locally they have thin, cm-scale alteration halos marked by euhedral pyrite and, if jasper is present, local recrystallization of the hematite to magnetite. Similar quartz-ankerite-pyrite veins, which are common in all lithologies of the greenstone belt, have been targeted locally in gold exploration (Riedel, 1969; Fyon and Crocket, 1986).

2.7.5 Magnetite versus hematite growth in BIF

The earliest views of basin-scale redox control on the deposition of hematite versus magnetite have long been regarded as an oversimplified concept for the origin of BIF layering (James, 1954; Klein, 2005). Instead, the small-scale, alternating layers of hematite and magnetite strongly suggest a more local phenomenon related to diagenesis of primary Fe-oxyhydroxides (Cloud, 1973; Klein, 2005). A variety of reactions have been suggested to explain magnetite versus hematite growth in iron formations: e.g., reaction of primary greenalite with oxidizing diagenetic fluids (Ohmoto, 2006; Rasmussen et al., 2014), selective stripping of Fe^{2+} from magnetite to form secondary hematite (Ohmoto, 2003), supergene alteration resulting in Si-loss and martitization of magnetite to form hematite-goethite iron ore (e.g., Morris, 1983; Hagemann et al., 2016). None of these have been observed in the Temagami BIF.

The dominant pathway for Fe-oxide precipitation in the Temagami BIF was primary deposition of Fe-oxyhydroxide followed by recrystallization, first to hematite, and then to magnetite. Ohmoto (2003) suggested that the conversion of hematite to magnetite might be achieved in the presence

of reducing hydrothermal fluids rising through the sediment column, according to the reaction [2.6]:

$$3Fe_2O_{3(hm)} + H_{2(g)} \rightarrow 2Fe_3O_{4(mt)} + H_2O \quad [2.6] \quad \text{(Ohmoto, 2003)}$$

The direct precipitation of magnetite also has been reproduced under experimental conditions that incubated ferrihydrite with organic material, producing abundant Fe-carbonates and some magnetite (Posth et al., 2013a). However, a non-redox reaction of ferrihydrite or hematite to magnetite (eq. [2.5]) may be more applicable to the diagenetic conditions in the Temagami BIF (Lovley, 1991; Zegeye et al., 2010; Li et al., 2017). This type of reactions has been suggested by (Ohmoto, 2003; Bazylinski et al., 2007; Posth et al., 2014).

An additional possibility for the crystallization of magnetite is presented in Figure 2.30. Calculated stabilities of the iron-oxides under conditions inferred for in a water saturated sedimentary package (e.g., log fO_2= -40 to -50, pH=6, temperature 50-150°C: Ohmoto et al., 2006), a simple increase in temperature can drive the system from early-formed hematite stability to magnetite stability. Additionally, hydrogenous Fe^{2+}-silicates such as greenalite ($Fe_3Si_2O_5(OH)_4$) and related green rust phases may have been directly precipitated from the water column under the most reducing conditions (Klein, 2005; Zegeye et al., 2012; Rasmussen et al., 2013).

The Fe^{2+} to form magnetite from hematite in reaction 2.5 could have originated from the high concentrations of Fe^{2+} inferred for Archean anoxic seawater (~40-3000 μM: Shibuya et al., 2010) or from external hydrothermal or metamorphic fluids. Recycling of organic carbon by dissimilatory iron reducing bacteria or abiogenic metamorphic redox reactions between C_{org} and Fe^{3+} could also provide Fe^{2+} or form magnetite directly, as noted above (Ohmoto, 2003; Johnson et al., 2008; Posth 2013a; Posth 2013b). Higher abundances of carbonates, such as Fe-rich dolomite, in the magnetite layers may be products of original organic carbon, as is the abundant graphite in the sulfidic cherts within the Sherman mine. Negative carbonate-$\delta^{13}C$ values around -5 to -8 ‰ vs PDB in Temagami oxide BIF have been interpreted as evidence for recycling of organic material along such pathways (Bowins and Crockett, 1994). A model involving direct replacement of hematite by magnetite requires nearly 50% volume increase (Mücke and Cabral, 2005) which

would be difficult to accommodate, without significant mobility of Si and ongoing dissolution-reprecipitation of quartz in the BIF layers allowing this reaction to proceed.

In this study a detailed paragenetic sequence has been established showing a much more complex relationship between hematite and magnetite. Both hematite and magnetite are shown to have formed directly from an initially precipitated amorphous Fe-oxyhydroxide phase. Sealed from further recrystallization by early diagenetic silicification, Type 1 hematite and magnetite were preserved in jasper and black chert, respectively. Where the jasper and chert layers were not lithified, recrystallization favoured the growth of magnetite over hematite under rising diagenetic temperatures and supply of Fe^{2+}. The co-existence of Type 1 magnetite and hematite indicates conditions close to the magnetite/hematite equilibrium, or limited supply of Fe^{2+} or electron donors for hematite reduction. If the formation of the Fe-oxyhydroxides was bacterially mediated, then the conditions might have been closer to magnetite stability. The mineral chemistry of the magnetite (see below) also argues against an external hydrothermal fluid having infiltrated the BIF and supplying Fe^{2+} for the hematite-magnetite transition, as suggested by Ohmoto et al. (2008).

2.7.6 Significance of magnetite chemistry

The major geochemical variability in magnetite is in its Si content. Electron backscattered diffraction studies of siliceous magnetite from other types of BIF have shown that silicon is in the magnetite structure (Huberty et al., 2012). Substitution of Si^{4+} for Fe^{3+} in the tetrahedral site creates a charge imbalance and structural contraction because the ionic radius of tetrahedral Si^{4+} (0.26 Å) is too small to fit well into the tetrahedral Fe^{3+} site (0.57 Å; Shannon, 1976). Moessbauer studies of siliceous magnetite from other deposit types also have shown that expulsion of Fe^{2+} from the octahedral site leaves some vacancy to accommodate the imbalance (Shimazaki, 1998). In the siliceous magnetite of the Temagami BIF, a coupled substitution via reaction [2.7] is likely involved in the formation of siliceous magnetite containing ~0.5 wt.% Si and ~0.03 wt.% Mg:

$$Si^{4+} + (Mg^{2+}_{\sim 0.05}\, Fe^{2+}_{\sim 0.95}) \leftrightarrow 2Fe^{3+} \qquad [2.7]$$

A fractional vacancy on the octahedral site as described by Shimazaki (1998) could also allow for the incorporation of other trace elements (Xu et al., 2014). Type 3 magnetite shows the highest Si

content, with well-developed euhedral crystal shapes during all its growth stages showing strong oscillatory zoning of Si. The zoning has been interpreted to reflect a temporal variation in magnetite growth and availability of mobile Si (Putnis et al., 1992; Shore and Fowler, 1996). In this case, termination of oscillatory zoning and the increasing abundance of quartz inclusions in the magnetite may indicate a shift from mobile Si to conditions favouring quartz crystallization (e.g., Fig. 2.24). Alternatively, a self-organizing effect during magnetite crystallization may control the incorporation of Si in the magnetite structure (e.g., Prieto et al., 1990; Reeder et al., 1990; Putnis et al., 1992), possibly related to pH, redox, or temperature (Huberty et al., 2012; Sun and Li., 2017a). The co-crystallization of siliceous Type 3 magnetite and Fe-dolomite (see Fig. 2.16) may be an indication of decreasing oxygen fugacity and rising pH, as noted above, which may influence the incorporation of Si.

Trace element enrichments and depletions in the cores and rims of zoned magnetite reflect some variation in the composition of the pore fluids during diagenesis. Magnetite is the dominant host for Ge, with concentrations of up to 88 ppm. It is particularly enriched in magnetite from chlorite-rich layers. In magnetite layers, Ge is enriched in the core of well-developed Type 3 magnetite compared to the rims, while Type 2 magnetite has a relatively constant Ge content.

The enrichment of Ge, Mn, and Pb, and to a lesser degree Si, As, and Sb, in the cores of Type 3 magnetite suggest increased availability during early stages of magnetite crystallization. The strong partitioning of Ge into the magnetite structure is consistent with the better fit of Ge^{4+} (0.39 Å) substituting for Fe^{3+} (0.49 Å; Shannon, 1976), compared to Si^{4+} (0.26 Å) substituting for Fe^{3+} (0.49 Å; Shannon, 1976; O'Neil and Navrotsky, 1983). Ge/Si ratios in marine sediments are considered a tracer for hydrothermal input, with high values indicative of hydrothermal sources and lower values mainly reflecting detrital or seawater sources (Bernstein, 1985; Pokrovski and Schott, 1998; Hamade et al., 2003). While Ge is preferentially incorporated into the magnetite lattice, other factors may influence the uptake of Si (see above). Therefore, direct application of Ge/Si ratios from analyses of magnetite may not be suitable as a proxy for hydrothermal vs. seawater input. Moreover, the retention of Ge in magnetite implies that any pore fluids escaping during magnetite crystallization would be depleted in Ge compared to Si.

Mn is only present in magnetite in samples that also contain late diagenetic or metamorphic Mn-rich carbonates, suggesting that some Mn in the magnetite could be present as carbonate inclusions. It behaves similarly to Fe in aqueous environments, but the kinetics of oxidation in the water column are typically slower (Hem, 1981; Sato et al., 1989; Lovley, 1991). Once deposited in the sediment, Mn can undergo a range of biogenic and abiogenic redox reactions with organic material or other transition metals and get remobilized in its reduced form Mn^{2+} (Hem, 1981; Lovley, 1991; Burdige, 1993; Canfield et al., 1993; Kowalski et al., 2011). This early remobilization may be reflected by higher Mn abundances in the cores of Type 3 magnetite.

In contrast to Ge, the low concentrations of Mo in magnetite may reflect the initial concentrations in the Fe-oxyhydroxide precipitates and, by extension, in the overlying water column, rather than a mineralogical control on incorporation into magnetite. The ionic radius of Mo in tetrahedral coordination is a good fit in magnetite (0.46 and 0.41 Å at oxidations states of 5+ and 6+: respectively; Shannon, 1976) and seawater is a significant source for Mo scavenging in modern marine sediments (Morford and Emerson, 1999; Siebert et al., 2003; Siebert et al., 2005; Xu et al., 2006). Median concentrations <1 ppm are consistent with limited availability of Mo in the reduced bottom waters. The limited uptake of other transition metals, all of which have a better fit in the magnetite structure than Si or Ge (e.g., Ti, V, Cr, Mn, Co, Ni, Cu, Zn: (Lindsley, 1991; Dare et al., 2012; Nadoll et al., 2014), suggest that they too had very low concentrations in the reduced bottom waters. Zn and Mn ($\pm$Ni) are the only transition metals showing slight enrichment in the magnetite from the Temagami BIF, similar to other Precambrian BIF (e.g., Table 2.12).

V, Cr, Co, Ni, Zn, and Ga ($\pm$As), which show no variation, must have been available for all stages of magnetite crystallization. In contrast, Mg, Al, Ti, and Sc, which are enriched in the rims of Type 3 magnetite may be related to replacement of volcanic-derived material. A similar association of Ti-V-Cr (-Al-Ga-Zr-Nb-Hf) has been noted in magnetite in chlorite-rich layers (see Tables 2.4 and 2.6). The presence of these elements in the magnetite structure probably indicates the decomposition of Ti and Cr-bearing minerals, such as biotite and pyroxene, during late Type 3 magnetite growth and increasing mobility under the highest temperatures experienced by the Temagami BIF.

Table 2.12 compares available LA-ICP-MS data on trace elements in magnetite from different types of BIF (Algoma-type, Lake Superior-type, and VMS exhalites). The compiled data include examples of magnetite from metamorphosed and mineralized Neoarchean Algoma-type BIF in Musselwhite, Ontario: (Biczok et al., 2012; Gourcerol et al., 2016a); Wutai, China: (Wilde et al., 2004; Sun and Li, 2017b), Paleoproterozoic Lake Superior-type BIF (Dales Gorge and Kuruman BIF of the Transvaal Supergroup in South Africa and Luliang in China: Pickard, 2002; Pickard, 2003; Sun and Li, 2017b), mineralized iron formation from the Pipe Mine in the Thompson nickel belt of Manitoba (Hulbert et al., 2005; Dare et al., 2014), and exhalites from the Archean Izok Lake VMS deposits in the Slave Province, Canada (Morrison and Balint, 1993; Makvandi et al., 2016) and the Cambrian Zankan sulfide deposit in Kunlun, China (Zhou et al., 2017). Although limited, the data reveal the generally very low concentrations of trace elements in Algoma-type BIF. Magnetite from Lake Superior-type BIF contains notably higher concentrations of Ca and P, most likely reflecting the role of marine organisms in BIF deposition, and magnetite from Archean exhalites is enriched in Mg, Sc, Ti, V, and Cr, probably reflecting the mafic volcanic host rocks, and also Mn, Co, Ni, Zn and Ga, reflecting proximity to higher-temperature hydrothermal vent sources. From the Izok Lake data, magnetite in VMS have generally high concentrations of Co, Ni, Zn, and Ga (>100 ppm). Magnetite from the large Lake Superior-type BIF that formed in sedimentary systems in continental shelf settings is unexpectedly enriched in Ge compared to Algoma-type BIF and exhalites, which have a much greater hydrothermal influence. Ge is enriched in hydrothermal fluid over seawater and continental runoff (Pokrovski and Schott, 1998), and so should be depleted in the Superior-type BIF. Mo also appears to be enriched in the Proterozoic BIF, possibly reflecting a growing global ocean budget of Mo in increasingly oxygenated oceans (e.g., Kendall et al., 2011).

Dare et al. (2014) and Dupuis and Beaudoin (2011) used Ti-V-Ni-Cr-Mn systematics to discriminate magnetite compositions from different types of hydrothermal ore deposits (Fig. 2.31). The construction of the discrimination diagrams reflects the interpreted abundances and mobility of key elements in different ore-forming systems (e.g., immobile Ti and low Cr and V in magnetite of hydrothermal origin; more abundant Ti, Cr, and V in mafic magmatic systems compared to felsic systems: Nadoll et al. (2014). Mn and Ni are seawater components enriched in magnetite forming in shallow (marine) hydrothermal systems and BIF. Magnetite from the oxide-facies BIF

at Temagami falls in the field of hydrothermal magnetite with very low Ti concentrations expected for chemical sedimentary environments that lack a large detrital component (Fig. 2.31). The most Ti-rich magnetite from Temagami is in the chlorite layers, in which Ti has been incorporated from volcanic-derived material. The large spread of magnetite compositions from Temagami illustrates the need for a review of the discrimination diagrams applied to low-temperature systems such as BIF (and probably VMS) and the expansion of the BIF-magnetite fields.

2.7.7 Significance of chlorite compositions

The chemistry of chlorite can be a sensitive indicator of conditions of formation and the late diagenetic and metamorphic history of the Temagami BIF. The defining substitution in chlorite is Mg-Fe, producing the endmembers clinochlore: $(Mg_{10}Al_2)Si_6Al_2O_{20}(OH)_{16}$, and chamosite $(Fe^{2+}_{10}Al_2)Si_6Al_2O_{20}(OH)_{16}$. A more detailed classification was proposed after Hey (1954), based on the compositional differences in Fe/(Fe+Mg) and Si (Fig. 2.32). Between them, chlorites can host a range of trace elements, most importantly Mn^{2+}, Ni^{2+}, Zn^{2+}, Al^{3+}, and Cr^{3+}.

Volcanic material (especially glass) was likely the precursor for much of the chlorite and other aluminosilicate phases in the BIF lithologies and volcanic footwall. Hydrothermal clays have been proposed as a precursor for trace amounts of low-Ti chlorite in magnetite and chert layers (Streit, 2017), but an expanded data set presented here (Fig. 2.33) confirms that most of the chlorite originated from a volcanic-derived precursor. For example, Ti is present in igneous biotite, a likely detrital precursor for chlorite (Parry and Downey, 1982). In many samples, this chlorite with ~300-500 ppm Ti, occurs with Ti-rich magnetite as well as high-Mn ilmenite (~0.9-1.5 wt.-% Mn; e.g., samples 11-1, 11-4, A028). In contrast, chlorite in magnetite and chert layers with very low chlorite content is notably Ti-poor (<50 ppm, bdl), indicating a different mode of formation, such as metamorphic recrystallization of hydrothermal clays like smectite or montmorillonite (Haymon and Kastner, 1981; Guillaume et al., 2003; Severmann et al., 2004). Such clays can form in the water column around hydrothermal discharge sites and range in composition between Fe-Si rich to Si-Al rich, and typically contain several wt.% of Fe_2O_3, K_2O, MgO, or CaO but very little Al_2O_3 (see Table 2.13; James, 1979; Haymon and Kastner, 1981; Jaynes and Boyd, 1991). Instead, such authigenic clay phases, green rust or greenalite formed in the water column or early diagenesis may be the precursor phases for low-Al, Fe-silicates such as stilpnomelane and minnesotaite found

in some Temagami BIF samples (e.g., samples A028, D015; Gole, 1980; Rasmussen et al., 2016; Rasmussen et al., 2017). The very low Mn, Zn, and F in the chlorite from Temagami BIF also contrast sharply with chlorite in VMS systems (Table 2.13; e.g., Hannington et al., 2003a,b). The highest MnO concentrations are in sulfide facies and the altered volcanic rocks, consistent with chlorite as a preferred host for Mn in the absence of magnetite and fewer carbonates available compared to oxide BIF.

The Fe/(Fe/Mg) ratio of chlorite (in atoms per formula unit, apfu) is a sensitive indicator of the conditions of formation, including temperature, precursor compositions, hydrothermal input and exchange with seawater (Kranidiotis and MacLean, 1987; Kalogeropoulos and Scott, 1989). Higher Fe/(Fe+Mg) ratios are commonly associated with high-temperature upflow of Fe-rich hydrothermal fluids and are found closer to mineralization; lower ratios may reflect entrainment of colder Mg-rich seawater (Spry et al., 2000; Hannington et al., 2003; Galley et al., 2007; Wilkinson et al., 2015). In the Temagami BIF and host rocks, Fe/(Fe+Mg) ratios of chlorite are highly variable (Fig. 2.34), sometimes exhibiting bimodal compositions on the thin section scale between chert and magnetite layers in the same sample. The median value of Fe/(Fe+Mg) is lowest in the volcanic host rocks (basalts, andesites and rhyolites: 0.48-0.58), whereas volcaniclastic units contain chlorite with Fe/(Fe+Mg) ratios of 0.64. A few analyses of chlorite in carbonate-facies BIF have Fe/(Fe+Mg) ratios of 0.83. Within the oxide facies BIF, Fe/(Fe+Mg) ratios are higher in magnetite layers (0.74) than in chlorite layers (0.64), chert layers (0.58), and sulfidic cherts (0.47). The large variations likely reflect the availability of Fe and Mg during chlorite formation. Fe-rich chlorite in magnetite layers and with siderite reflect the availability of Fe at the time of chlorite formation. Fe-poor (Mg-rich) compositions in the sulfide facies and other host rocks are more typical of seawater alteration of volcanic glass (e.g., expected in layers that are essentially shales). However, at low temperatures, an Fe-rich precursor such as nontronite could also explain the Fe-rich chlorite in some layers.

The chemistry of chlorite can be very sensitive to pressure, temperature, and redox state (Inoue et al., 2009; Bourdelle and Cathelineau, 2015) and has been used as a geothermometer (Cathelineau and Nieva, 1985; Bourdelle and Cathelineau, 2015). The calculation of chlorite crystallization temperatures is based on the abundance of tetrahedral Al (Cathelineau, 1988), or combining

tetrahedral Al with the Fe/(Fe/Mg) ratio (Zang and Fyfe, 1995). The most important requirements for the applicability of chlorite geothermometry is the uniform bulk composition of the hydrothermal fluids, crystallization of chlorite in equilibrium with quartz, and, where it is a product of hydrothermal alteration, a uniform host rock. The method of Cathelineau (1988) yields chlorite formation temperatures of 156-394ºC for all chlorites in the Temagami BIF; the method of Zang and Fyfe (1995) yields temperatures in the range of 147-296ºC (all results listed in Appendix D). The calculated temperatures by both methods correlate well (Fig. 2.35) but are interpreted here to reflect mainly recrystallization temperatures, consistent with the regional greenschist facies metamorphism (Bennett, 1978; Hurley, 1985; Blum, 1986).

2.7.8 Apatite-monazite chemistry

Apatite and monazite (and xenotime) are the phosphorous phases in the Temagami BIF and the dominant hosts for rare earth elements and yttrium (REY; Bowins, 1989; Bowins and Crocket, 2011). Three distinct types of apatite, two authigenically grown generations (early Type 1 and late Type 2 apatite) and one of potential detrital origin (Type 3 apatite), were recognized. All are fluorapatites, containing between 2.2-4.1 wt.% F, which compares well with stoichiometric $Ca_5(PO_4)_3F$ (3.8 wt.% F; see Appendix E for results and notes on limitations of quantification by EPMA). Notable chemical differences occur between Type 1 and 2, mainly in oxide-facies BIF, and Type 3 in chlorite BIF. Sr concentrations are high in Type 1 and 2 apatite (1700-4200 ppm). Arsenic is particularly enriched in Type 1 apatite. These enrichments are likely indicators of seawater and hydrothermal geochemical sources, respectively (Elderfield and Gieskes, 1982; Paytan et al., 2002; German and Von Damm, 2006), and are consistent with authigenic apatite forming in sediments of hydrogenous-hydrothermal origin. The range of REY concentrations in Type 1 and 2 apatite is similar to that observed in Superior-Type BIF and hydrogenous apatite, but one order of magnitude lower compared to magmatic and hydrothermal apatite (Table 2.14; Mao et al., 2016; Alibert, 2016; Gadd et al., 2016). Type 3 apatite has generally low Sr (500 ppm) and is characterized by much higher Th and U (8.3 ppm Th versus 0.1-0.03 ppm in Types 1 and 2; 4.0 ppm U versus 0.32-0.35 ppm in Types 1 and 2). High Th and U concentrations, in the range of Type 3 apatite, have been reported for other (Archean) hydrothermal/metamorphic apatite (Table 2.14; cf. Bingen et al., 1996 and references therein). Combined with the rounded habit of Type 3 apatite, it can be confidently identified as being of igneous-detrital origin.

Monazite in chlorite BIF is more enriched in Th (>2 wt.%) compared to oxide BIF (<1 wt.% Th for all but two analyses). The range of Th is similar (<1 wt.%) in other BIF, but much lower in chlorite BIF and magmatic-hydrothermal monazite (Table 2.15; Poitrasson et al., 2000; Smith et al., 2008). Monazite grains in the chlorite BIF are therefore probably of a similar detrital source as Type 3 apatite. Xenotime in Temagami oxide BIF is very similar in composition compared to authigenic xenotime in Archean, Superior-type BIF (Smith et al., 2008).

The concentrations of REY in the phosphate minerals are between three and five orders of magnitude higher than in other phases (Fig. 2.36). Even considering the low abundances of apatite (~0.5-1 vol.% apatite), it is by far the dominant host for REY in the BIF. Monazite and xenotime occur only in trace amounts.

2.7.9 REE and Y systematics in the host minerals

Most studies of the REY systematics of BIF consider only the bulk rock and not the host minerals (Bau, 1991; Murray et al., 1991; Bau, 1993). The reliability of the REY signal of BIF is largely due to the refractory nature of the host minerals during post-depositional alteration and metamorphism (e.g., Gourcerol et al., 2016). In the case of the phosphates, the REE selectivity of the host minerals is likely not an important factor, as the systematics closely reflect the REE geochemistry of the whole rock (see Chapter 3).

Two generations of authigenic apatite, based on petrogenetic relationships, reflect early and late diagenetic REY enrichments and depletions. The early Type 1 apatite shows LREE depletion, normalized to PAAS, with a concave-up pattern between La and Sm and HREE enrichment, forming a slight concave down pattern (Fig. 2.37). This contrasts with Type 2 apatite displaying a more pronounced MREE enrichment and depletions of LREE and HREE. Early Type 1 apatite in jasper displays positive La anomalies and higher Y/Ho ratios than late Type 2 apatite in magnetite layers (median Y/Ho of 38.4 and 31.0, respectively; cf. chondritic Y/Ho = 27). Higher, fractionated Y/Ho, as well as a positive La anomaly develop over long residence times of REY in seawater, allowing the slightly less particle reactive Y and La to accumulate relative to

other REE (Bau, 1996). REY must have previously experienced substantial residence time in the open ocean before they were stabilized in Type 1, and to a degree, Type 2 apatite. Even though Type 2 apatite is more enriched in MREE, the calculated Eu-anomaly is slightly bigger in Type 1 apatite (median 4.23 and 4.37 Eu/Eu^*_{PAAS}, respectively). The smaller Eu anomaly in the paragenetically late Type 2 apatite argues against infiltration of hydrothermal fluids during later stages of diagenesis. Despite these differences, both generations of apatite reflect a similar hydrothermally influenced seawater source of REY, indicated by the LREE depletion and positive Eu anomalies (e.g. Fryer, 1977; Bau and Dulski, 1996).

The REY in Type 1 apatite in jasper and apatite inclusions in Type 3 magnetite in the magnetite layers probably reflect the primary, seawater-dominated signal of the Temagami BIF. Later, Type 2 apatite reflects a later stage of diagenesis or metamorphism influenced by dewatering and desorption of REY from the initial precipitate, with La and Y (and Eu) preferentially lost and other REE retained. The influence of external (hydrothermal) fluids is not supported by the REY profiles of Type 2 apatite, specifically the lower Eu anomalies compared to Type 1 apatite. None of the apatites show a negative Ce anomaly of the type previously reported in whole-rock samples as evidence of an oxygenated water column (Ohmoto et al., 2006). The REY profile of detrital Type 3 apatite in chlorite BIF has an inverted profile compared to Type 1 and 2 apatite, with LREE enrichment and negative Eu/Eu^*_{PAAS}. This is consistent with an igneous source.

Limited REY data for magnetite (La, Sm, Y, and Yb only) are shown in Figure 2.36. The Sm/Yb_{PAAS} ratios (indicating the slope of the REY profile) of Type 3 magnetite and Type 1 apatite in adjacent jasper layers are very similar (median values of 0.49 and 0.55, respectively), indicating a similar early diagenetic fixation of REY in the magnetite and apatite in those layers. The Sm/Yb_{PAAS} ratio is lower in Type 3 magnetite than in Type 2 apatite, indicating a reversed LREE/MREE vs. HREE pattern (medians of 0.49 and 1.66, respectively). The changes between REY in Type 3 magnetite and Type 2 apatite occur over distances of few hundred microns and cannot be explained by heterogeneities in the precursor material. Instead, diagenetic effects and fractionation of the REY (i.e., loss of Y and La anomalies, decreasing LREE and HREE compared to MREE) by desorption of REE from the initial precipitate and loss from the lithologic package

by dewatering was likely. Monazite and xenotime are trace minerals in the BIF and do not appear to influence the REY systematics, except possibly in the chlorite-facies BIF (see Chapter 3).

2.8 Conclusions

A detailed petrographic and mineral-chemcial study of the Temagami BIF has revealed a complex post-depositional history summarized in Figure 2.38. While it remains unclear what triggered the precipitation, it is very likely that the deposited material consisted of Fe-oxyhydroxides that scavenged silica, metals and REY from the water column by adsorption. These features are preserved in jasper layers, which were protected from recrystallization and alteration by early diagenetic silicification. Microbanding in jasper is defined by crystallographic rather than chemical changes. Black chert formed by recrystallization of Fe-oxyhydroxides or hematite to magnetite, the new stable phase under increasing diagenetic temperatures, and possibly lower O_2 activity and/or changes in pore fluid pH. The development of chert pods and quartz veins was due to early remobilization of silica. In outcrop and hand sample, white chert layers can be found as lateral equivalents of large dewatering structures and chert plugs rooted in other BIF lithologies. This observed link to sediment dewatering processes implies that much of the silica that stabilized the jasper and black chert layers was from the sedimentary package itself rather than the water column. A simplified conceptual model for the development of the oxide facies BIF is illustrated in Figure 2.38. Whereas some white chert layers may be products of Si-rich pore fluids expelled from the sediments during diagenesis, the preservation of early jasper suggests that these layers are a more suitable geochemical archive of the conditions of the Neoarchean ocean, as noted in other studies (cf. Alibert and Kinsley, 2016).

Growth of large (>100 μm) magnetite crystals and the eventual formation of magnetite layers occurred throughout the later stages of diagenesis. Relict jasper fragments overgrown by magnetite in magnetite layers and chemically similar apatite in both jasper and early magnetite layers point to the late diagenetic origin of the magnetite and development from a common, homogenous precursor material. Crystallization under high silica concentrations is reflected by distinctly Si-rich zones in Type 3 magnetite, which are overgrown by later, possibly metamorphic, magnetite (Types 4 and 5).

Some elements, such as Ge and Mn, are preferentially incorporated in early magnetite while other elements, such as As, Sb, and B are lost. Most of the element mobilitiy is in diagenetic fluids sourced from pore water. Some fractionation of REY is evident based on the slopes of the profiles in magnetite, and this should be taken into account when comparing the chemistry of early-formed jasper and black chert with samples from magnetite layers. However, neither the magnetite chemistry nor the apatite REY support an overprint of external, hydrothermal fluids. In particular, the lack of significant variations in Ge/Si ratios, low transition metal contents, and REY systematics argue against a late external (hydrothermal) fluid to explain the hematite-magnetite transition as suggested by Ohmoto et al. (2008).

The link between Fe deposition and local synvolcanic hydrothermal activity remains a signficant question. Although few mineralogical or geochemcial features of the BIF point to a direct hydrothermal input, apart from the Fe and some aspects of the REY (e.g., positive Eu anomaly in apatite), the volcanic host rocks are strongly chloritized and sericitized. Reworking of sedimentary sulfides as clasts in brecciated felsic flows support an active, effusive volcanic environment (Schwartz, 1995). Chlorite layers (silicate-facies BIF) intercalated with the oxide BIF were mainly products of volcanic-derived material, including high-Ti chlorite and ilmenite, and detrital phosphates have igneous REY chemistry. Magnetite in chlorite layers also contains more V, Cr, and Zr (clastic-derived) and lower seawater-hydrothermal components, like Mn, than magnetite in oxide BIF. However, the lack of a clear hydrothermal imprint on the oxide-facies suggests a setting in which hydrothermal conditions were insufficient to mobilize signficant transition metals (e.g., Cu, Zn, Ni) into the mixed clastic-hydrothermal-seawater source of the BIF.

2.9 References

Abbott, J.G., Gordey, S.P., and Tempelman-Kluit, D.J., 1986. Setting of stratiform, sediment-hosted lead-zinc deposits in Yukon and northeastern British Columbia. In: Morin, J.A., Ed. Mineral Deposits of Northern Cordillera: Canadian Institute of Mining and Metallurgy, Special Volume 37, 1–18.

Ahn, J.H., Buseck, P.R., 1990. Hematite Nanospheres of Possible Colloidal Origin from a Precambrian Banded Iron Formation. Science 250, 111-113.

Ahrens, T.J., 1995. Global Earth Physics: A Handbook of Physical Constants. American Geophysical Union, Washington, DC.

Alexander, B.W., Bau, M., Andersson, P., 2009. Neodymium isotopes in Archean seawater and implications for the marine Nd cycle in Earth's early oceans. Earth and Planetary Science Letters 283, 144-155.

Alibert, C., 2016. Rare earth elements in hamersley BIF minerals. Geochim. Cosmochim. Acta 184, 311-328.

Alibert, C., Kinsley, L., 2016. Ge/Si in Hamersley BIF as tracer of hydrothermal Si and Ge inputs to the Paleoproterozoic ocean. Geochimica et Cosmochimica Acta 184, 329-343.

Ayer, J., Amelin, Y., Corfu, F., Kamo, S., Ketchum, J., Kwok, K., Trowell, N., 2002. Evolution of the southern Abitibi greenstone belt based on U–Pb geochronology: autochthonous volcanic construction followed by plutonism, regional deformation and sedimentation. Precambrian Research 115, 63-95.

Ayer, J.A., Chartrand, J.E., Grabowski, G.D.P., Josey, S., Rainsford, D., Trowell, N.F., 2006. Geological compilation of the Cobalt–Temagami area, Abitibi greenstone belt. Ontario Geological Survey, Preliminary Map, 3581.

Backer, H., Schoell, M., 1972. New Deeps with Brines and Metalliferous Sediments in the Red Sea. Nature Physical Science 240, 153.

Barrett, T.J., Fralick, P.W., 1985. Sediment redeposition in Archean iron formation; examples from the Beardmore-Geraldton greenstone belt, Ontario. Journal of Sedimentary Research 55, 205-212.

Bau, M., 1991. Rare-earth element mobility during hydrothermal and metamorphic fluid-rock interaction and the significance of the oxidation state of europium. Chemical Geology 93, 219-230.

Bau, M., 1993. Effects of syn-and post-depositional processes on the rare-earth element distribution in Precambrian iron-formations. European Journal of Mineralogy 5, 257-267.

Bau, M., 1996. Controls on the fractionation of isovalent trace elements in magmatic and aqueous systems: evidence from Y/Ho, Zr/Hf, and lanthanide tetrad effect. Contributions to Mineralogy and Petrology 123, 323-333.

Bau, M., Dulski, P., 1996. Distribution of yttrium and rare-earth elements in the Penge and Kuruman iron-formations, Transvaal Supergroup, South Africa. Precambrian Research 79, 37-55.

Bazylinski, D.A., Frankel, R.B., Konhauser, K.O., 2007. Modes of Biomineralization of Magnetite by Microbes. Geomicrobiology Journal 24, 465-475.

Becker, R.H., Clayton, R.N., 1976. Oxygen isotope study of a Precambrian banded iron-formation, Hamersley Range, Western Australia. Geochimica et Cosmochimica Acta 40, 1153-1165.

Bekker, A., Holland, H.D., Wang, P.L., Rumble, D., Stein, H.J., Hannah, J.L., Coetzee, L.L., Beukes, N.J., 2004. Dating the rise of atmospheric oxygen. Nature 427, 117-120.

Bekker, A., Planavsky, N., Rasmussen, B., Krapez, B., Hofmann, A., Slack, J., Rouxel, O., Konhauser, K., 2014. Iron formations: Their origins and implications for ancient seawater chemistry, Treatise on geochemistry. Elsevier 12, pp. 561-628.

Bekker, A., Slack, J.F., Planavsky, N., Krapež, B., Hofmann, A., Konhauser, K.O., Rouxel, O.J., 2010. Iron Formation: The Sedimentary Product of a Complex Interplay among Mantle, Tectonic, Oceanic, and Biospheric Processes. Economic Geology 105, 467-508.

Bennett, G., 1978. Geology of the northeast Temagami area, District of Nipissing. Ontario Ministry of Natural Resources.

Bernstein, L.R., 1985. Germanium geochemistry and mineralogy. Geochimica et Cosmochimica Acta 49, 2409-2422.

Beukes, N.J., 1973. Precambrian Iron-Formations of Southern Africa. Economic Geology 68, 960-1004.

Beukes, N.J., Gutzmer, J., 2008. Origin and Paleoenvironmental Significance of Major Iron Formations at the Archean-Paleoproterozoic Boundary, in: Hagemann, S., Rosiere, C., Gutzmer, J., Beukes, N.J. (Eds.). Society of Economic Geologists 15, pp. 5-47.

Biczok, J., Hollings, P., Klipfel, P., Heaman, L., Maas, R., Hamilton, M., Kamo, S., Friedman, R., 2012. Geochronology of the North Caribou greenstone belt, Superior Province Canada: Implications for tectonic history and gold mineralization at the Musselwhite mine. Precambrian Research 192-195, 209-230.

Bingen, B., Demaiffe, D., Hertogen, J., 1996. Redistribution of rare earth elements, thorium, and uranium over accessory minerals in the course of amphibolite to granulite facies metamorphism: The role of apatite and monazite in orthogneisses from southwestern Norway. Geochimica et Cosmochimica Acta 60, 1341-1354.

Blackburn, C.E., Hailstone, M.R., Storey, C.C., Perrault, M.E., 1990. Kenora resident geologist's district, in: Fenwick, K.G., Newsone, J.W., Pitts, A.E. (Eds.), Report of Activities. Ontario Geological Survey Miscellaneous Paper 152, p. 29.

Blake, R.E., Chang, S.J., Lepland, A., 2010. Phosphate oxygen isotopic evidence for a temperate and biologically active Archaean ocean. Nature 464, 1029.

Blum, N., 1986. Geochemical Studies of Archean Iron Formations and Associated Volcanic Rocks (Kirkland Lake and Temagami/Ont. areas). McMaster, PhD thesis, 410 pp.

Bourdelle, F., Cathelineau, M., 2015. Low-temperature chlorite geothermometry: a graphical representation based on a T–R2+–Si diagram. European Journal of Mineralogy 27, 617-626.

Bowins, R.J., 1989. Rare earth and other geochemical studies of Archean banded iron formation: Sherman and Adams Mines, Ontario. McMaster University, PhD thesis, 399 pp.

Bowins, R.J., Crocket, J.H., 2011. Monazite, Xenotime and REE Minerals in Archean Banded Iron-Formation from the Sherman and Adam Mines, Ontario, Canada. The Canadian Mineralogist 49, 749-763.

Bowins, R.J., Heaman, L.M., 1991. Age and timing of igneous activity in the Temagami greenstone belt, Ontario: a preliminary report. Canadian Journal of Earth Sciences 28, 1873-1876.

Boyum, B., Hartviksen, R., 1970. General Geology and ore-grade control at Sherman-Mine, Temagami, Ontario. Canadian Mining and Metallurgical Bulletin 63.

Bralia, A., Sabatini, G., Troja, F.J.M.D., 1979. A revaluation of the Co/Ni ratio in pyrite as geochemical tool in ore genesis problems. 14, 353-374.

Brandt, R., Gross, G., Gruss, H., Semenenko, N., Dorr, J., 1972. Problems of nomenclature for banded ferruginous-cherty sedimentary rocks and their metamorphic equivalents. Economic Geology 67, 682-684.

Braterman, P.S., Cairns-Smith, A.G., Sloper, R.W., 1983. Photo-oxidation of hydrated Fe2+-significance for banded iron formations. Nature 303, 163-164.

Burdige, D.J., 1993. The biogeochemistry of manganese and iron reduction in marine sediments. Earth-Science Reviews 35, 249-284.

Cairns-Smith, A.G., 1978. Precambrian solution photochemistry, inverse segregation, and banded iron formations. Nature 276, 807-808.

Campbell, G., 1978. Petrography and Stratigraphy of the North Band of Iron Formation, Sherman Mine, Temagami, Ontario. Laurentian University, MSc thesis, 75 pp.

Canfield, D.E., 2005. The early history of atmospheric oxygen: Homage to Robert A. Garrels. Annual Review of Earth and Planetary Sciences 33, 1-36.

Canfield, D.E., Thamdrup, B., Hansen, J.W., 1993. The anaerobic degradation of organic matter in Danish coastal sediments: Iron reduction, manganese reduction, and sulfate reduction. Geochimica et Cosmochimica Acta 57, 3867-3883.

Card, K.D., 1990. A review of the Superior Province of the Canadian Shield, a product of Archean accretion. Precambrian Research 48, 99-156.

Cathelineau, M., 1988. Cation site occupancy in chlorites and illites as function of temperature. Clay and Clay Minerals 23, 471-485.

Cathelineau, M., Nieva, D., 1985. A chlorite solid solution geothermometer the Los Azufres (Mexico) geothermal system. Contributions to Mineralogy and Petrology 91, 235-244.

Cloud, P., 1973. Paleoecological Significance of the Banded Iron-Formation. Economic Geology 68, 1135-1143.

Clout, J.M.F., Simonson, B.M., 2005. Precambrian Iron Formations and Iron Formation-Hosted Iron Ore Deposits, in: Hedenquist, J.W., Thompson, J.F.H., Goldfarb, R.J., Richards, J.P. (Eds.), Economic Geology 100th Anniversary Volume. Society of Economic Geologists, pp. 643-679.

Corfu, F., 1993. The evolution of the southern Abitibi greenstone belt in light of precise U-Pb geochronology. Economic Geology 88, 1323-1340.

Cornell, R., Schwertmann, U., 2003. The iron oxides, 2 ed. Wiley-VCH.

Czaja, A.D., Johnson, C.M., Beard, B.L., Roden, E.E., Li, W., Moorbath, S., 2013. Biological Fe oxidation controlled deposition of banded iron formation in the ca. 3770 Ma Isua Supracrustal Belt (West Greenland). Earth and Planetary Science Letters 363, 192-203.

Dare, S.A.S., Barnes, S.-J., Beaudoin, G., 2012. Variation in trace element content of magnetite crystallized from a fractionating sulfide liquid, Sudbury, Canada: Implications for provenance discrimination. Geochimica et Cosmochimica Acta 88, 27-50.

Dare, S.A.S., Barnes, S.-J., Beaudoin, G., Méric, J., Boutroy, E., Potvin-Doucet, C., 2014. Trace elements in magnetite as petrogenetic indicators. Mineralium Deposita 49, 785-796.

Davis, C.C., Chen, H.-W., Edwards, M., 2002. Modeling Silica Sorption to Iron Hydroxide. Environmental Science & Technology 36, 582-587.

Diekrup, D., Hannington, M.D., Strauss, H., Ginley, S.J., 2018. Decoupling of Neoarchean sulfur sources recorded in Algoma-type banded iron formation. Earth and Planetary Science Letters 489, 1-7.

Dimroth, E., Chauvel, J.-J., 1973. Petrography of the Sokoman Iron Formation in Part of the Central Labrador Trough, Quebec, Canada. GSA Bulletin 84, 111-134.

Dodd, M.S., Papineau, D., Grenne, T., Slack, J.F., Rittner, M., Pirajno, F., O'Neil, J., Little, C.T.S., 2017. Evidence for early life in Earth's oldest hydrothermal vent precipitates. Nature 543, 60.

Donaldson, J.A., Garrett, R.G., 1991. Iron-Formation in Temagami and Sherman Mine Area, in: Gross, G.A., Donaldson, J.A. (Eds.), Geological Survey of Canada Open File 2163 - Iron-Formation and Metalliferous Sediments in Central Canada [Field Trip 8], p. 66.

Donaldson, J.A., Munro, J., 1982. Precambrian geology of the Cobalt area, northern Ontario, Eleventh International Congress on Sedimentology. Field Excursion Guidebook 16B, p. 72.

Duhig, N.C., Stolz, J., Davidson, G.J., Large, R.R., 1992. Cambrian microbial and silica gel textures in silica iron exhalites from the Mount Windsor volcanic belt, Australia; their petrography, chemistry, and origin. Economic Geology 87, 764-784.

Dymek, R.F., Klein, C., 1988. Chemistry, petrology and origin of banded iron-formation lithologies from the 3800 Ma isua supracrustal belt, West Greenland. Precambrian Research 39, 247-302.

Elderfield, H., Gieskes, J.M., 1982. Sr isotopes in interstitial waters of marine sediments from Deep Sea Drilling Project cores. Nature 300, 493-497.

Ernst, W., Calvert, S., 1969. An experimental study of the recrystallization of porcelanite and its bearing on the origin of some bedded cherts. American Journal of Science 267, 114-133.

Farquhar, J., Bao, H., Thiemens, M., 2000. Atmospheric Influence of Earth's Earliest Sulfur Cycle. Science 289, 756-758.

Fedo, C.M., Whitehouse, M.J., 2002. Metasomatic Origin of Quartz-Pyroxene Rock, Akilia, Greenland, and Implications for Earth's Earliest Life. Science 296, 1448-1452.

Fischer, W.W., Knoll, A.H., 2009. An iron shuttle for deepwater silica in Late Archean and early Paleoproterozoic iron formation. Geological Society of America Bulletin 121, 222-235.

Forbes, W.C., 1977. Stability relations of grunerite, Fe7Si8O22(OH)2. American Journal of Science 277, 735-749.

Frei, R., Bridgwater, D., Rosing, M., Stecher, O., 1999. Controversial Pb-Pb and Sm-Nd isotope results in the early Archean Isua (West Greenland) oxide iron formation: preservation of primary signatures versus secondary disturbances. Geochimica et Cosmochimica Acta 63, 473-488.

French, B.M., 1973. Mineral Assemblages in Diagenetic and Low-Grade Metamorphic Iron-Formation. Economic Geology 68, 1063-1074.

Fryer, B.J., 1977. Rare earth evidence in iron-formations for changing Precambrian oxidation states. Geochimica et Cosmochimica Acta 41, 361-367.

Fyon, J., Crocket, H., 1986. Exploration potential for base and precious metal mineralization in part of Strathy Township, Temagami Area. Ontario Geological Survey Open File Report 5591.

Fyon, J.A., Cole, D.R., 1989. Geology of part of the Temagami greenstone belt, District of Nipissing, including relationships between lithologic, alteration and structural features and precious-metal occurences., in: Colvine, A.C., Cherry, M.E., Dressler, B.O., White, O.L., Barlow, R.B., Riddle, C. (Eds.), Summary of fieldwork and other activities. Ontario Geological Survey Miscellaneous Paper 146, pp. 108-115.

Gadd, M.G., Layton-Matthews, D., Peter, J.M., Paradis, S.J.J.M.D., 2016. The world-class howard's pass sedex Zn-Pb district, selwyn basin, yukon. Part I: Trace element compositions of pyrite record input of hydrothermal, diagenetic, and metamorphic fluids to mineralization. 51, 319-342.

Galley, A., Hannington, M., Jonasson, I., 2007. Volcanogenic massive sulphide deposits. Geological Association of Canada, Mineral Deposits Division, Special Publication 5, Mineral deposits of Canada: A synthesis of major deposit-types, district metallogeny, the evolution of geological provinces, exploration methods, pp. 141-161.

German, C., Von Damm, K., 2006. Hydrothermal processes, Treatise on Geochemistry 6, pp. 181-222.

Ginley, S.J., 2016. A Field and Petrological Study of Oxide-Facies Algoma-Type Banded Iron Formation, Sherman Mine, Temagami. University of Ottawa, M.Sc. thesis, 275 pp.

Gole, M.J., 1980. Mineralogy and petrology of very-low-metamorphic grade Archaean banded iron-formations, Weld Range, Western Australia. American Mineralogist 65, 8-25.

Goodwin, A.M., 1973. Archean iron-formations and tectonic basins of the Canadian Shield. Economic Geology 68, 915-933.

Gourcerol, B., Kontak, D.J., Thurston, P.C., Duparc, Q., 2016a. Do Magnetite Layers In Algoma-Type Banded Iron Formations (BIF) Preserve Their Primary Geochemical Signature? A Case Study of Samples From Three Archean BIF-Hosted Gold Deposits. The Canadian Mineralogist 54, 605-624.

Gourcerol, B., Thurston, P.C., Kontak, D.J., Côté-Mantha, O., Biczok, J., 2016b. Depositional setting of Algoma-type banded iron formation. Precambrian Research 281, 47-79.

Götze, J., Plötze, M., Habermann, D.J.M., Petrology, 2001. Origin, spectral characteristics and practical applications of the cathodoluminescence (cl) of quartz – a review. 71, 225-250.

Grenne, T., Slack, J.F., 2003. Paleozoic and Mesozoic silica-rich seawater: Evidence from hematitic chert (jasper) deposits. Geology 31, 319-322.

Grenne, T., Slack, J.F., 2005. Geochemistry of Jasper Beds from the Ordovician Løkken Ophiolite, Norway: Origin of Proximal and Distal Siliceous Exhalites. Economic Geology 100, 1511-1527.

Gross, G., 1965a. Geology of iron deposits in Canada, Vol. 1 general geology and evaluation of ore deposits: Geological Survey of Canada. Economic Geology Report 22, 81.

Gross, G., 1996. Algoma-type iron-formation. Selected British Columbia Mineral Deposit Profiles 2, 1996-1913.

Gross, G.A., 1959. A classification for iron deposits in Canada. Canadian Mining Journal 80, 87-91.

Gross, G.A., 1965b. Origin of Precambrian iron formations. Economic Geology 60, 1063-1065.

Gross, G.A., 1972. Primary features in cherty iron-formations. Sedimentary Geology 7, 241-261.

Gross, G.A., 1980. A classification of iron formations based on depositional environments. The Canadian Mineralogist 18, 215-222.

Gross, G.A., 1983. Tectonic Systems and the Deposition of Iron-Formation, in: B. Nagy, R.W.J.C.G., Schidlowski, M. (Eds.), Developments in Precambrian Geology. Elsevier Volume 7, pp. 63-79.

Gross, G.A., 2009. Iron Formation in Canada, Genesis and Geochemistry. Geological Survey of Canada, Open File 5987, p. 141.

Guillaume, D., Neaman, A., Baronnet, A., Cathelineau, M., Mosser-Ruck, R., Pfeiffert, C., Abdelmoula, M., Dubessy, J., Villieras, F., Michau, N., 2003. Experimental synthesis of chlorite from smectite at 300°C in the presence of metallic Fe. Clay Minerals 38, 281-302.

Guo, Q., Strauss, H., Kaufman, A.J., Schröder, S., Gutzmer, J., Wing, B., Baker, M.A., Bekker, A., Jin, Q., Kim, S.-T., Farquhar, J., 2009. Reconstructing Earth's surface oxidation across the Archean-Proterozoic transition. Geology 37, 399-402.

Hagemann, S.G., Angerer, T., Duuring, P., Rosière, C.A., Figueiredo e Silva, R.C., Lobato, L., Hensler, A.S., Walde, D.H.G., 2016. BIF-hosted iron mineral system: A review. Ore geology reviews 76, 317-359.

Hamade, T., Konhauser, K.O., Raiswell, R., Goldsmith, S., Morris, R.C., 2003. Using Ge/Si ratios to decouple iron and silica fluxes in Precambrian banded iron formations. Geology 31, 35-38.

Hannington, M.D., Galley, A.G., Herzig, P.M., Petersen, S., 1998. Comparison of the TAG mound and stockwork complex with Cyprus-type massive sulfide deposits, Proc. Ocean Drill Program Sci. Results, pp. 389-415.

Hannington, M.D., Santaguida, F., Kjarsgaard, I.M., Cathles, L.M., 2003a. Regional-scale hydrothermal alteration in the Central Blake River Group, western Abitibi subprovince, Canada: implications for VMS prospectivity. Mineralium Deposita 38, 393-422.

Hannington, M.D., Kjarsgaard, I.M., Galley, A.G., Taylor, B.J.M.D., 2003b. Mineral-chemical studies of metamorphosed hydrothermal alteration in the kristineberg volcanogenic massive sulfide district, sweden. 38, 423-442.

Haymon, R.M., Kastner, M., 1981. Hot spring deposits on the East Pacific Rise at 21°N: preliminary description of mineralogy and genesis. Earth and Planetary Science Letters 53, 363-381.

Heimann, A., Johnson, C.M., Beard, B.L., Valley, J.W., Roden, E.E., Spicuzza, M.J., Beukes, N.J., 2010. Fe, C, and O isotope compositions of banded iron formation carbonates demonstrate a major role for dissimilatory iron reduction in ~2.5 Ga marine environments. Earth and Planetary Science Letters 294, 8-18.

Hem, J.D., 1981. Rates of manganese oxidation in aqueous systems. Geochimica et Cosmochimica Acta 45, 1369-1374.

Hensler, A.-S., Hagemann, S.G., Rosière, C.A., Angerer, T., Gilbert, S., 2015. Hydrothermal and metamorphic fluid-rock interaction associated with hypogene "hard" iron ore mineralisation in the Quadrilátero Ferrífero, Brazil: Implications from in-situ laser ablation ICP-MS iron oxide chemistry. Ore geology reviews 69, 325-351.

Hey, M., 1954. A new review of the chlorites. Mineralogical Magazine 30, 277-292.

Holland, H.D., 1973. The Oceans; A Possible Source of Iron in Iron-Formations. Economic Geology 68, 1169-1172.

Huberty, J.M., Konishi, H., Heck, P.R., Fournelle, J.H., Valley, J.W., Xu, H., 2012. Silician magnetite from the Dales Gorge Member of the Brockman Iron Formation, Hamersley Group, Western Australia. American Mineralogist 97, 26-37.

Hulbert, L.J., Hamilton, M.A., Horan, M.F., Scoates, R.F.J., 2005. U-Pb Zircon and Re-Os Isotope Geochronology of Mineralized Ultramafic Intrusions and Associated Nickel Ores from the Thompson Nickel Belt, Manitoba, Canada. Economic Geology 100, 29-41.

Hurley, T.D., 1985. Petrology and Geochemistry of the Volcanic Host Rocks to the West and North Pits of the Sherman Mine Iron Formation, Temagami, Ontario. McMaster University, Hamilton, Ontario, thesis, 154 pp.

Huston, D.L., Logan, G.A., 2004. Barite, BIFs and bugs: evidence for the evolution of the Earth's early hydrosphere. Earth and Planetary Science Letters 220, 41-55.

Iler, R., 1973. Colloidal silica, Surface and Colloid Science. Wiley, New York 6, pp. 1-100.

Inoue, A., Meunier, A., Patrier-Mas, P., Rigault, C., Beaufort, D., Vieillard, P., 2009. Application of Chemical Geothermometry to Low-Temperature Trioctahedral Chlorites. Clays and Clay Minerals 57, 371-382.

Isley, A.E., 1995. Hydrothermal Plumes and the Delivery of Iron to Banded Iron Formation. The Journal of Geology 103, 169-185.

Isley, A.E., Abbott, D.H., 1999. Plume-related mafic volcanism and the deposition of banded iron formation. J. Geophys. Res. 104, 15461-15477.

Jackson, S.L., Fyon, J.A., Corfu, F., 1994. Review of Archean supracrustal assemblages of the southern Abitibi greenstone belt in Ontario, Canada: products of microplate interaction within a large-scale plate-tectonic setting. Precambrian Research 65, 183-205.

James, H.L., 1954. Sedimentary facies of iron-formation. Economic Geology 49, 235-293.

James, H.L., 1983. Distribution of Banded Iron-Formation in Space and Time, in: Trendall, A.F., Morris, R.C. (Eds.), Developments in Precambrian Geology. Elsevier 6, pp. 471-490.

James, R., 1979. Origin of iron-rich montmorillonite from the manganese nodule belt of the north equatorial Pacific. Clays and Clay Minerals 27, 185-194.

Jaynes, W.F., Boyd, S.A., 1991. Clay Mineral Type and Organic Compound Sorption by Hexadecyltrimethlyammonium-Exchanged Clays. 55, 43-48.

Johnson, C.M., Beard, B.L., Klein, C., Beukes, N.J., Roden, E.E., 2008. Iron isotopes constrain biologic and abiologic processes in banded iron formation genesis. Geochimica et Cosmochimica Acta 72, 151-169.

Johnston, M., 1987. Stratigraphy and Geochemistry of a Portion of the Temagami Greenstone Belt, Northeastern Ontario. Laurentian University, MSc thesis, 122 pp.

Jones, B., Renaut, R.W., 2007. Microstructural changes accompanying the opal-A to opal-CT transition: new evidence from the siliceous sinters of Geysir, Haukadalur, Iceland. Sedimentology 54, 921-948.

Kalogeropoulos, S.I., Scott, S.D., 1989. Mineralogy and geochemistry of an Archean tuffaceous exhalite: the Main Contact Tuff, Millenbach mine area, Noranda, Quebec. Canadian Journal of Earth Sciences 26, 88-105.

Kamber, B.S., Moorbath, S., Whitehouse, M.J., 2001. The oldest rocks on earth: Time constraints and geological controversies. 190, 177-203.

Kappler, A., Pasquero, C., Konhauser, K.O., Newman, D.K., 2005. Deposition of banded iron formations by anoxygenic phototrophic Fe(II)-oxidizing bacteria. Geology 33, 865-868.

Kastner, M., Siever, R., 1983. Siliceous Sediments of the Guaymas Basin: The Effect of High Thermal Gradients on Diagenesis. The Journal of Geology 91, 629-641.

Kendall, B., Gordon, G.W., Poulton, S.W., Anbar, A.D., 2011. Molybdenum isotope constraints on the extent of late Paleoproterozoic ocean euxinia. Earth and Planetary Science Letters 307, 450-460.

Khalil, K.I., El-Shazly, A.E., Lehmann, B., 2015. Late neoproterozoic banded iron formation (BIF) in the central eastern desert of egypt: Mineralogical and geochemical implications for the origin of the gebel el hadid iron ore deposit. Ore geology reviews 69, 380-399.

Kimberley, M.M., 1989. Nomenclature for iron formations. Ore geology reviews 5, 1-12.

Klein, C., 1973. Changes in Mineral Assemblages with Metamorphism of Some Banded Precambrian Iron-Formations. Economic Geology 68, 1075-1088.

Klein, C., 1974. Greenalite, stilpnomelane, minnesotaite, crocidolite and carbonates in a very low-grade metamorphic Precambrian iron formation. The Canadian Mineralogist 12, 475-498.

Klein, C., 2005. Some Precambrian banded iron formations (BIFs) from around the world: Their age, geologic setting, mineralogy, metamorphism, geochemistry, and origin. Am. Mineral. 90, 1473-1499.

Koehler, I., Konhauser, K., Kappler, A., 2010. Role of Microorganisms in Banded Iron Formations, in: Barton, L.L., Mandl, M., Loy, A. (Eds.), Geomicrobiology: Molecular and Environmental Perspective. Springer Netherlands, Dordrecht, pp. 309-324.

Konhauser, K.O., 1998. Diversity of bacterial iron mineralization. Earth-Science Reviews 43, 91-121.

Konhauser, K.O., 2007. Decoupling photochemical Fe(II) oxidation from shallow-water BIF deposition. Earth and Planetary Science Letters 258, 87-100.

Konhauser, K.O., Hamade, T., Raiswell, R., Morris, R.C., Ferris, F.G., Southam, G., Canfield, D.E., 2002. Could bacteria have formed the Precambrian banded iron formations? Geology 30, 1079-1082.

Konhauser, K.O., Planavsky, N.J., Hardisty, D.S., Robbins, L.J., Warchola, T.J., Haugaard, R., Lalonde, S.V., Partin, C.A., Oonk, P.B.H., Tsikos, H., Lyons, T.W., Bekker, A., Johnson, C.M., 2017. Iron formations: A global record of Neoarchaean to Palaeoproterozoic environmental history. Earth-Science Reviews 172, 140-177.

Kowalski, N., Dellwig, O., Beck, M., Grunwald, M., Dürselen, C.-D., Badewien, T.H., Brumsack, H.-J.r., van Beusekom, J.E.E., Böttcher, M.E., 2011. A comparative study of manganese

dynamics in the water column and sediments of intertidal systems of the North Sea. Estuarine, Coastal and Shelf Science.

Kranidiotis, P., MacLean, W.H., 1987. Systematics of chlorite alteration at the Phelps Dodge massive sulfide deposit, Matagami, Quebec. Economic Geology 82, 1898-1911.

Krapež, B., Barley, M.E., Pickard, A.L., 2003. Hydrothermal and resedimented origins of the precursor sediments to banded iron formation: sedimentological evidence from the Early Palaeoproterozoic Brockman Supersequence of Western Australia. Sedimentology 50, 979-1011.

Laurila, T.E., Hannington, M.D., Leybourne, M., Petersen, S., Devey, C.W., Garbe-Schönberg, D., 2015. New insights into the mineralogy of the Atlantis II Deep metalliferous sediments, Red Sea. 16, 4449-4478.

Laurila, T.E., Hannington, M.D., Petersen, S., Garbe-Schönberg, D., 2014a. Early depositional history of metalliferous sediments in the Atlantis II Deep of the Red Sea: Evidence from rare earth element geochemistry. Geochimica et Cosmochimica Acta 126, 146-168.

Laurila, T.E., Hannington, M.D., Petersen, S., Garbe-Schönberg, D., 2014b. Trace metal distribution in the Atlantis II Deep (Red Sea) sediments. Chemical Geology 386, 80-100.

Li, Y.-L., Konhauser, K.O., Zhai, M., 2017. The formation of magnetite in the early Archean oceans. Earth and Planetary Science Letters 466, 103-114.

Liaghat, S., MacLean, W.H., 1992. The Key Tuffite, Matagami mining district; origin of the tuff components and mass changes. Exploration and Mining Geology 1, 197-207.

Lindsley, D., 1991. Oxide minerals: petrologic and magnetic significance, Reviews in Mineralogy and Geochemistry. Mineralogical Society of America, Chantilly, VA. 25, p. 509.

Lovley, D.R., 1991. Dissimilatory Fe(III) and Mn(IV) reduction. Microbiol. Mol. Biol. Rev. 55, 259-287.

Makvandi, S., Ghasemzadeh-Barvarz, M., Beaudoin, G., Grunsky, E.C., Beth McClenaghan, M., Duchesne, C., 2016. Principal component analysis of magnetite composition from volcanogenic massive sulfide deposits: Case studies from the Izok Lake (Nunavut, Canada) and Halfmile Lake (New Brunswick, Canada) deposits. Ore Geology Reviews 72, 60-85.

Maliva, R.G., Knoll, A.H., Simonson, B.M., 2005. Secular change in the Precambrian silica cycle: Insights from chert petrology. Geol. Soc. Am. Bull. 117, 835-845.

Maliva, R.G., Siever, R., 1988. Pre-Cenozoic nodular cherts; evidence for opal-CT precursors and direct quartz replacement. American Journal of Science 288, 798-809.

Manahan, M.P., 1990. Thermal expansion and conductivity of magnetite flakes taken from the Oconee-2 steam generator. Journal of Materials Science 25, 3424-3428.

Mao, M., Rukhlov, A.S., Rowins, S.M., Spence, J., Coogan, L.A., 2016. Apatite trace element compositions: A robust new tool for mineral exploration. Economic Geology 111, 1187-1222.

McBride, D., 2010. Report on the Scholes Township Property, Ontario. Temagami Iron Corporation Exploration Report, p. 37.

McSwiggen, P.L., Morey, G.B., 2008. Overview of the mineralogy of the Biwabik Iron Formation, Mesabi Iron Range, northern Minnesota. Regulatory Toxicology and Pharmacology 52, S11-S25.

Meyn, H.D., 1977. Geology of Afton, Scholes, Macbeth, and Clement Townships, Districts of Sudbury and Nipissing, Ontario Geological Survey Report 170, p. 77.

Mizutani, S., 1977. Progressive ordering of cristobalitic silica in the early stage of diagenesis. Contributions to Mineralogy and Petrology 61, 129-140.

Mloszewska, A.M., Pecoits, E., Cates, N.L., Mojzsis, S.J., O'Neil, J., Robbins, L.J., Konhauser, K.O., 2012. The composition of Earth's oldest iron formations: The Nuvvuagittuq Supracrustal Belt (Québec, Canada). Earth and Planetary Science Letters 317, 331-342.

Moghazi, A.M., 2003. Geochemistry and petrogenesis of a high-K calc-alkaline dokhan volcanic suite, south safaga area, egypt: The role of late neoproterozoic crustal extension. Precambrian Res. 125, 161-178.

Morford, J.L., Emerson, S., 1999. The geochemistry of redox sensitive trace metals in sediments. Geochimica et Cosmochimica Acta 63, 1735-1750.

Morris, R.C., 1983. Chapter 14 Supergene Alteration of Banded Iron-Formation, in: Trendall, A.F., Morris, R.C. (Eds.), Developments in Precambrian Geology. Elsevier 6, pp. 513-534.

Morris, R.C., 1993. Genetic modelling for banded iron-formation of the Hamersley Group, Pilbara Craton, Western Australia. Precambrian Research 60, 243-286.

Morrison, I., Balint, F., 1993. Geology of the Izok Lake Massive Sulphide Deposits, Northwest Territories, Canada, Proceedings of the World Zinc'93 Symposium, Hobart, Australia, pp. 161-170.

Morse, J.W., Casey, W.H., 1988. Ostwald processes and mineral paragenesis in sediments. American Journal of Science 288.

Mücke, A., Cabral, A.R., 2005. Redox and nonredox reactions of magnetite and hematite in rocks. Chemie der Erde-Geochemistry 65, 271-278.

Mukhopadhyay, J., Ghosh, G., Zimmermann, U., Guha, S., Mukherjee, T., 2012. A 3.51 Ga bimodal volcanics-BIF-ultramafic succession from Singhbhum Craton: implications for Palaeoarchaean geodynamic processes from the oldest greenstone succession of the Indian subcontinent. Geological Journal 47, 284-311.

Murata, K., Larson, R., 1975. Diagenesis of Miocene siliceous shales, Temblor range, California. J. Res. US Geol. Surv 3, 553-566.

Murray, R.W., Buchholtz Ten Brink, M.R., Gerlach, D.C., Russ, G.P., Jones, D.L., 1991. Rare earth, major, and trace elements in chert from the Franciscan Complex and Monterey Group, California: Assessing REE sources to fine-grained marine sediments. Geochimica et Cosmochimica Acta 55, 1875-1895.

Murray, R.W., Jones, D.L., Brink, M.R.B.t., 1992. Diagenetic formation of bedded chert: Evidence from chemistry of the chert-shale couplet. Geology 20, 271-274.

Nadoll, P., Angerer, T., Mauk, J.L., French, D., Walshe, J., 2014. The chemistry of hydrothermal magnetite: A review. Ore geology reviews 61, 1-32.

Nishizawa, M., Yamamoto, H., Ueno, Y., Tsuruoka, S., Shibuya, T., Sawaki, Y., Yamamoto, S., Kon, Y., Kitajima, K., Komiya, T., Maruyama, S., Hirata, T., 2010. Grain-scale iron isotopic distribution of pyrite from Precambrian shallow marine carbonate revealed by a femtosecond laser ablation multicollector ICP-MS technique: Possible proxy for the redox state of ancient seawater. Geochimica et Cosmochimica Acta 74, 2760-2778.

Nunes, P., Pyke, D., Jensen, L., 1978. Toward an absolute age stratigraphy for the Abitibi greenstone belt, eastern Ontario--zircon ages from the timmins and kirkland lake areas. Journal of the Geological Society of America, Abstract with Programs 10, 464-465.

Nutman, A.P., Bennett, V.C., Friend, C.R.L., 2017. Seeing through the magnetite: Reassessing Eoarchean atmosphere composition from Isua (Greenland) ≥3.7 Ga banded iron formations. Geoscience Frontiers 8, 1233-1240.

O'Neil, H.S.C., Navrotsky, A., 1983. Simple Spinels: crystallographic parameters, cation radii, lattice energies, and cation distribution. American Mineralogist 68, 181-194.

Ontario Geological Survey, 2001. Airborne magnetic and electromagnetic surveys, residual magnetic field, Temagami South area. Ontario Geological Survey, Map 60 090.

Ohmoto, H., 2003. Nonredox transformations of magnetite-hematite in hydrothermal systems. Economic Geology 98, 157-161.

Ohmoto, H., Hoashi, M., Otake, T., Bevacqua, D., Watanabe, Y., 2008. Origins of hematite, magnetite and siderite in banded iron formations. Geochimica et Cosmochimica Acta 72, A699-A699.

Ohmoto, H., Watanabe, Y., Kumazawa, K., 2004. Evidence from massive siderite beds for a CO2-rich atmosphere before ~ 1.8 billion years ago. Nature 429, 395.

Ohmoto, H., Watanabe, Y., Yamaguchi, K.E., Naraoka, H., Haruna, M., Kakegawa, T., Hayashi, K., Kato, Y., 2006. Chemical and biological evolution of early Earth: Constraints from banded iron formations. Geological Society of America Memoirs 198, 291-331.

Parry, W., Downey, L., 1982. Geochemistry of hydrothermal chlorite replacing igneous biotite. Clays and Clay Minerals 30, 81-90.

Paytan, A., Mearon, S., Cobb, K., Kastner, M., 2002. Origin of marine barite deposits: Sr and S isotope characterization. Geology 30, 747-750.

Pecoits, E., Gingras, M.K., Barley, M.E., Kappler, A., Posth, N.R., Konhauser, K.O., 2009. Petrography and geochemistry of the Dales Gorge banded iron formation: Paragenetic sequence, source and implications for palaeo-ocean chemistry. Precambrian Research 172, 163-187.

Peter, J.M., 2003. Ancient iron formations: their genesis and use in the exploration for stratiform base metal sulphide deposits, with examples from the Bathurst Mining Camp. GeoText 4, 145-176.

Peter, J.M., Goodfellow, W.D., 1996. Mineralogy, bulk and rare earth element geochemistry of massive sulphide-associated hydrothermal sediments of the Brunswick Horizon, Bathurst Mining Camp, New Brunswick. Canadian Journal of Earth Sciences 33, 252-283.

Petersen, S., Herzig, P.M., Hannington, M.D., 2000. Third dimension of a presently forming VMS deposit: TAG hydrothermal mound, Mid-Atlantic Ridge, 26°N. Mineralium Deposita 35, 233-259.

Pickard, A.L., 2002. SHRIMP U–Pb zircon ages of tuffaceous mudrocks in the Brockman Iron Formation of the Hamersley Range, Western Australia. Australian Journal of Earth Sciences 49, 491-507.

Pickard, A.L., 2003. SHRIMP U-Pb zircon ages for the Palaeoproterozoic Kuruman Iron Formation, Northern Cape Province, South Africa: evidence for simultaneous BIF deposition on Kaapvaal and Pilbara Cratons. Precambrian Research 125, 275-315.

Pickard, A.L., Barley, M.E., Krapez, B., 2004. Deep-marine depositional setting of banded iron formation: sedimentological evidence from interbedded clastic sedimentary rocks in the early Palaeoproterozoic Dales Gorge Member of Western Australia. Sedimentary Geology 170, 37-62.

Pisciotto, K.A., 1981. Diagenetic trends in the siliceous facies of the Monterey Shale in the Santa Maria region, California. Sedimentology 28, 547-571.

Planavsky, N.J., Rouxel, O.J., Bekker, A., Lalonde, S.V., Konhauser, K.O., Reinhard, C.T., Lyons, T.W., 2010. The evolution of the marine phosphate reservoir. Nature 467, 1088-1090.

Poitrasson, F., Chenery, S., Shepherd, T.J., 2000. Electron microprobe and LA-ICP-MS study of monazite hydrothermal alteration: Implications for U-Th-Pb geochronology and nuclear ceramics. Geochimica et Cosmochimica Acta 64, 3283-3297.

Pokrovski, G.S., Schott, J., 1998. Thermodynamic properties of aqueous Ge(IV) hydroxide complexes from 25 to 350°C: implications for the behavior of germanium and the Ge/Si ratio in hydrothermal fluids. Geochimica et Cosmochimica Acta 62, 1631-1642.

Posth, N.R., Canfield, D.E., Kappler, A., 2014. Biogenic Fe(III) minerals: From formation to diagenesis and preservation in the rock record. Earth-Science Reviews 135, 103-121.

Posth, N.R., Hegler, F., Konhauser, K.O., Kappler, A., 2008. Alternating Si and Fe deposition caused by temperature fluctuations in Precambrian oceans. Nature Geoscience 1, 703-708.

Posth, N.R., Köhler, I., D Swanner, E., Schröder, C., Wellmann, E., Binder, B., Konhauser, K.O., Neumann, U., Berthold, C., Nowak, M., 2013a. Simulating Precambrian banded iron formation diagenesis. Chemical Geology 362, 66-73.

Posth, N.R., Konhauser, K.O., Kappler, A., 2013b. Microbiological processes in banded iron formation deposition. Sedimentology 60, 1733-1754.

Puchelt, H., 1973. Recent Iron Sediment Formation at the Kameni Islands, Santorini (Greece), in: Bernard, A.J. (Ed.). Springer Berlin Heidelberg, Berlin, Heidelberg, pp. 227-245.

Putnis, A., Fernandez-Diaz, L., Prieto, M., 1992. Experimentally produced oscillatory zoning in the (Ba, Sr)SO4 solid solution. Nature 358, 743.

Rasmussen, B., Meier, D.B., Krapež, B., Muhling, J.R., 2013. Iron silicate microgranules as precursor sediments to 2.5-billion-year-old banded iron formations. Geology 41, 435-438.

Rasmussen, B., Muhling, J.R., Suvorova, A., Krapež, B., 2016. Dust to dust: Evidence for the formation of "primary" hematite dust in banded iron formations via oxidation of iron silicate nanoparticles. Precambrian Research 284, 49-63.

Riedel, R.W., 1969. General Geology of the Iron-Formation at Sherman Mine, Temagami, Ontario. Exploration Project Report. p. 6.

Robert, F., Chaussidon, M., 2006. A Paleotemperature curve for the Precambrian oceans based on silicon isotopes in cherts. Nature 443, 969-972.

Sampaio, G.M.S., Pufahl, P.K., Raye, U., Kyser, K.T., Abreu, A.T., Alkmim, A.R., Nalini, H.A., 2018. Influence of weathering and hydrothermal alteration on the REE and δ56Fe composition of iron formation, Cauê Formation, Iron Quadrangle, Brazil. Chemical Geology 497, 27-40.

Satkoski, A.M., Beukes, N.J., Li, W., Beard, B.L., Johnson, C.M., 2015. A redox-stratified ocean 3.2 billion years ago. Earth and Planetary Science Letters 430, 43-53.

Sato, Y., Okabe, S., Takematsu, N., 1989. Major elements in manganese and iron oxides precipitated from seawater. Geochimica et Cosmochimica Acta 53, 1883-1887.

Schwartz, T.C., 1995. Petrology and geochemistry of felsic volcaniclastic rocks along the Sherman Mine Road, Temagami Greenstone Belt, Strathy Township, Ontario. McMaster University, MSc thesis, 180 pp.

Scott, S.D., Kalogeropoulos, S.I., Shegelski, R.J., Siriunas, J.M., 1983. Tuffaceous exhalites as exploration guides for volcanogenic massive sulphide deposits. Journal of Geochemical Exploration 19, 500-502.

Severmann, S., Mills, R.A., Palmer, M.R., Fallick, A.E., 2004. The origin of clay minerals in active and relict hydrothermal deposits. Geochimica et Cosmochimica Acta 68, 73-88.

Shannon, R.D., 1976. Revised effective ionic radii and systematic studies of interatomic distances in halides and chalcogenides. Acta Crystallographica Section A: crystal physics, diffractoin, theoretical and general crystallography 32, 751-767.

Shibuya, T., Komiya, T., Nakamura, K., Takai, K., Maruyama, S., 2010. Highly alkaline, high-temperature hydrothermal fluids in the early Archean ocean. Precambrian Research 182, 230-238.

Shimada, Y., Yasumatsu, A., Motomura, Y., Okazaki, R., Nakamura, T., Ohmoto, H., Okaue, Y., Yokoyama, T., 2006. Geochemical Study on Temagami Iron-Formations, Canada. Geochimica et Cosmochimica Acta 70.

Shimazaki, H., 1998. On the Occurrence of Silician Magnetites. Resource Geology 48, 23-29.

Siebert, C., Kramers, J.D., Meisel, T., Morel, P., Nägler, T.F., 2005. PGE, Re-Os, and Mo isotope systematics in Archean and early Proterozoic sedimentary systems as proxies for redox conditions of the early Earth. Geochimica et Cosmochimica Acta 69, 1787-1801.

Siebert, C., Nägler, T.F., von Blanckenburg, F., Kramers, J.D., 2003. Molybdenum isotope records as a potential new proxy for paleoceanography. Earth and Planetary Science Letters 211, 159-171.

Siever, R., 1962. Silica Solubility, 0º-200ºC., and the Diagenesis of Siliceous Sediments. The Journal of Geology 70, 127-150.

Siever, R., 1992. The silica cycle in the Precambrian. Geochim. Cosmochim. Acta 56, 3265-3272.

Simonson, B.M., 1987. Early silica cementation and subsequent diagenesis in arenites from four early Proterozoic iron formations of North America. Journal of Sedimentary Research 57.

Slack, J.F., Cannon, W.F., 2009. Extraterrestrial demise of banded iron formations 1.85 billion years ago. Geology 37, 1011-1014.

Smith, A.J.B., Beukes, N.J., Gutzmer, J., 2013. The composition and depositional environments of mesoarchean iron formations of the west rand group of the witwatersrand supergroup, south africa. Economic Geology 108, 111-134.

Smith, A., Gutzmer, J., Beukes, N., Reinkie, C., Bau, M., 2008. Rare earth elements (REE) in banded iron formations—link between geochemistry and mineralogy, Proceedings of the 9th international congress for applied mineralogy, Australian Institute for Mining and Metallurgy (AusIMM), Brisbane, Australia, pp. 8-10.

Spry, P., Peter, J., Slack, J., 2000. Meta-exhalites as exploration guides to ore, in: Spry, P., Marshall, B., Vokes, F. (Eds.), Reviews in Economic Geology, Vol. 11, pp. 163-201.

Staudigel, H., Schmincke, H.-U., 1984. The pliocene seamount series of La Palma/Canary Islands. Solid Earth 89, 11195-11215.

Stefurak, E.J.T., Lowe, D.R., Zentner, D., Fischer, W.W., 2014. Primary silica granules—A new mode of Paleoarchean sedimentation. Geology 42, 283-286.

Stefurak, E.J.T., Lowe, D.R., Zentner, D., Fischer, W.W., 2015. Sedimentology and geochemistry of Archean silica granules. GSA Bulletin 127, 1090-1107.

Steinhoefel, G., Horn, I., von Blanckenburg, F., 2009. Micro-scale tracing of Fe and Si isotope signatures in banded iron formation using femtosecond laser ablation. Geochimica et Cosmochimica Acta 73, 5343-5360.

Steinhoefel, G., von Blanckenburg, F., Horn, I., Konhauser, K.O., Beukes, N.J., Gutzmer, J., 2010. Deciphering formation processes of banded iron formations from the Transvaal and the Hamersley successions by combined Si and Fe isotope analysis using UV femtosecond laser ablation. Geochimica et Cosmochimica Acta 74, 2677-2696.

Stern, K.H., 1954. The Liesegang Phenomenon. Chemical Reviews 54, 79-99.

Sun, S., Konhauser, K.O., Kappler, A., Li, Y.-L., 2015. Primary hematite in Neoarchean to Paleoproterozoic oceans. GSA Bulletin 127, 850-861.

Sun, S., Li, Y.-L., 2017a. Geneses and evolutions of iron-bearing minerals in banded iron formations of >3760 to ca. 2200 million-year-old: Constraints from electron microscopic, X-ray diffraction and Mössbauer spectroscopic investigations. Precambrian Research 289, 1-17.

Sun, S., Li, Y.-L., 2017b. Microstructures, crystallography and geochemistry of magnetite in 2500 to 2200 million-year-old banded iron formations from South Africa, Western Australia and North China. Precambrian Research 298, 292-305.

Swanson, E.R., Keizer, R.P., Lyons, J.I., Clabaugh, S.E., 1978. Tertiary volcanism and caldera development near Durango City, Sierra Madre Occidental, Mexico. GSA Bulletin 89, 1000-1012.

Thomassot, E., O'Neil, J., Francis, D., Cartigny, P., Wing, B.A., 2015. Atmospheric record in the Hadean Eon from multiple sulfur isotope measurements in Nuvvuagittuq Greenstone Belt (Nunavik, Quebec). Proceedings of the National Academy of Sciences 112, 707-712.

Thurston, P.C., Ayer, J.A., Goutier, J., Hamilton, M.A., 2008. Depositional Gaps in Abitibi Greenstone Belt Stratigraphy: A Key to Exploration for Syngenetic Mineralization. Economic Geology 103, 1097-1134.

Thurston, P.C., Kamber, B.S., Whitehouse, M., 2012. Archean cherts in banded iron formation: Insight into Neoarchean ocean chemistry and depositional processes. Precambrian Research 214–215, 227-257.

Tréguer, P., Nelson, D.M., Van Bennekom, A.J., DeMaster, D.J., Leynaert, A., Quéguiner, B., 1995. The Silica Balance in the World Ocean: A Reestimate. Science 268, 375-379.

Trendall, A., 1973. Varve cycles in the Weeli Wolli Formation of the Precambrian Hamersley Group, Western Australia. Economic Geology 68, 1089-1097.

Trendall, A.F., 2002a. The significance of iron-formation in the Precambrian stratigraphic record. International Association of Sedimentology Special Publication 33, 33-66.

Trendall, A.F., 2002b. The significance of iron-formation in the Precambrian stratigraphic record. Precambrian Sedimentary Environments: A Modern Approach to Ancient Depositional Systems, Special Publication of the IAS, 33-66.

Trendall, A.F., Blockley, J.G., 1970. The iron formations of the Precambrian Hamersley Group, Western Australia, with special reference to the associated crocidolite. Western Australia Geological Survey Bulletin.

Trolard, F., Tardy, Y., 1987. The stabilities of gibbsite, boehmite, aluminous goethites and aluminous hematites in bauxites, ferricretes and laterites as a function of water activity, temperature and particle size. Geochimica et Cosmochimica Acta 51, 945-957.

Tsikos, H., Beukes, N.J., Moore, J.M., Harris, C., 2003. Deposition, Diagenesis, and Secondary Enrichment of Metals in the Paleoproterozoic Hotazel Iron Formation, Kalahari Manganese Field, South Africa. Economic Geology 98, 1449-1462.

Van Achterbergh, E., Ryan, C.G., Jackson, S.E., Griffin, W.L., 2001. Data reduction software for LA-ICP-MS: appendix, in: Sylvester, P.J. (Ed.), Laser Ablation ICP Mass Spectrometry in the Earth Sciences: Principles and Applications. Mineralogical Association of Canada Short Course Series, Ottawa, ON, Canada, v. 29, pp. 239-243.

van Staal, C.R., Fyffe, L.R., Langton, J.P., MacCutcheon, S.R., 1992. The Ordovician Tetagouche Group, Bathurst Camp, northern New Brunswick, Canada; history, tectonic setting and distribution of massive-sulfide deposits. Exploration and Mining Geology 1, 93-103.

Veizer, J., Compston, W., Hoefs, J., Nielsen, H.J.N., 1982. Mantle buffering of the early oceans. Naturwissenschaften 69, 173-180.

Viehmann, S., Hoffmann, J.E., Münker, C., Bau, M., 2014. Decoupled Hf-Nd isotopes in Neoarchean seawater reveal weathering of emerged continents. Geology 42, 115-118.

Walker, J.C.G., 1984. Suboxic diagenesis in banded iron formations. Nature 309, 340-342.

Walker, J.C.G., Brimblecombe, P., 1985. Iron and sulfur in the pre-biologic ocean. Precambrian Research 28, 205-222.

Wilde, S.A., Cawood, P.A., Wang, K., Nemchin, A., Zhao, G., 2004. Determining Precambrian crustal evolution in China: a case-study from Wutaishan, Shanxi Province, demonstrating the application of precise SHRIMP U-Pb geochronology, in: Malpas, J., Fletcher, C.J.N., Ali, J.R., Aitchison, J.C. (Eds.), Aspects of the Tectonic Evolution of China. Special Publication 226, Geological Society of London, pp. 5-25.

Wilkinson, J.J., Chang, Z., Cooke, D.R., Baker, M.J., Wilkinson, C.C., Inglis, S., Chen, H., Bruce Gemmell, J., 2015. The chlorite proximitor: A new tool for detecting porphyry ore deposits. Journal of Geochemical Exploration 152, 10-26.

Williams, L.A., Crerar, D.A., 1985. Silica diagenesis, II. General mechanisms. Journal of Sedimentary Research 55.

Williams, L.A., Parks, G.A., Crerar, D.A., 1985. Silica diagenesis, I. Solubility controls. Journal of Sedimentary Research 55.

Wise Jr, S.W., Kelts, K.R., 1972. Inferred diagenetic history of a weakly silicified deep sea chalk. GCAGS Transactions 22, 177-203.

Xu, H., Shen, Z., Konishi, H., 2014. Si-magnetite nano-precipitates in silician magnetite from banded iron formation: Z-contrast imaging and ab initio study. American Mineralogist 99, 2196-2202.

Xu, N., Christodoulatos, C., Braida, W., 2006. Adsorption of molybdate and tetrathiomolybdate onto pyrite and goethite: Effect of pH and competitive anions. Chemosphere 62, 1726-1735.

Zang, W., Fyfe, W.S., 1995. Chloritization of the hydrothermally altered bedrock at the Igarapé Bahia gold deposit, Carajás, Brazil. Mineralium Deposita 30, 30-38.

Zegeye, A., Mustin, C., Jorand, F., 2010. Bacterial and iron oxide aggregates mediate secondary iron mineral formation: green rust versus magnetite. Geobiology 8, 209-222.

Zhou, Z.-J., Tang, H.-S., Chen, Y.-J., Chen, Z.-L., 2017. Trace elements of magnetite and iron isotopes of the Zankan iron deposit, westernmost Kunlun, China: A case study of seafloor hydrothermal iron deposits. Ore geology reviews 80, 1191-1205.

Zinkernagel, U., 1978. Cathodoluminescence of quartz and its application to sandstone petrology, in: Füchtbauer, H., Lisitzyn, A.P., Milliman, J.D., Seibold, E. (Eds.), Contributions to Sedimentology 8. Schweizerbart'sche Verlagsbuchhandlung, Stuttgart, p. 69.

Table 2.1: Abundances of major mineral phases in each layer type of the oxide facies of the Temagami BIF

		Mineral phase [vol.-%]			
Layer type		**Quartz**	**Magnetite**	**Hematite**	**Chlorite**
Jasper	Mean	76	9	12	0.2
	Minimum	71	2	6	0.1
	Maximum	92	12	18	0.3
Magnetite	Mean	33	58	1	0.9
	Minimum	12	29	0	0.04
	Maximum	52	85	3	20
Chert	Mean	87	9	0	0.4
	Minimum	66	1.2	0	0.04
	Maximum	98	34	1	2.3

Values from quantitative petrography of 38 thin sections by Ginley (2016) and this study.

Table 2.2: Summary of vein generations in oxide-facies samples of the Temagami BIF

Generation	Mineralogy	Varieties, Effects
1) early diagnetic	Qtz	a) exclusively present in jasper layers, affected by microbanding-related shearing
		b) exclusively present in jasper and chert, not affected by internal shearing
2) late diagenetic	Qtz-mag	present in jasper and chert, sometimes partly annealed in magnetite layers
3) metamorphic	Qtz-mag-chl-stilp	a) veins cutting all oxide-facies layers, commonly containing chlorite and stilpnomelane needles
		b) "syneresis cracks" exclusively in magnetite
4) metamorphic/ post-regional folding	Qtz-ank-py	cm-wide continuous veins, affecting all sedimentary lithologies

Table 2.3: EPMA analyses of magnetite in Temagami BIF facies. All values in wt.%.
Individual results listed in Appendix B.

	SiO_2	TiO_2	Al_2O_3	Cr_2O_3	V_2O_3	Fe_2O_3	FeO	MnO	MgO	CaO	ZnO	NiO	Total
dl	0.01	0.03	0.08	0.01	0.01	0.02	0.02	0.01	0.01	0.01	0.01	0.01	
All (n=395, s=21)													
median	**0.52**	**bdl**	**bdl**	**bdl**	**bdl**	**68.0**	**31.8**	**0.01**	**0.03**	**0.01**	**bdl**	**bdl**	**100.4**
min	bdl	bdl	bdl	bdl	bdl	56.6	30.7	bdl	bdl	bdl	bdl	bdl	97.7
max	2.78	6.68	0.66	0.82	0.06	70.5	37.9	0.20	0.63	0.21	0.11	0.04	102.7
Oxide facies-hosted (n=248, s=16)													
median	**0.41**	**bdl**	**bdl**	**bdl**	**bdl**	**68.3**	**31.7**	**0.01**	**0.02**	**bdl**	**bdl**	**bdl**	**100.5**
min	bdl	bdl	bdl	bdl	bdl	62.9	30.7	bdl	bdl	bdl	bdl	bdl	97.9
max	2.78	0.16	0.30	0.03	0.06	70.5	35.0	0.20	0.29	0.21	0.11	0.03	102.7
Chlorite-hosted (n=137, s=4)													
median	**0.65**	**bdl**	**bdl**	**bdl**	**0.01**	**67.5**	**31.9**	**bdl**	**0.05**	**0.01**	**bdl**	**bdl**	**100.3**
min	0.03	bdl	bdl	bdl	bdl	56.6	31.0	bdl	bdl	bdl	bdl	bdl	97.7
max	2.20	6.68	0.66	0.82	0.05	70.3	37.9	0.08	0.63	0.21	0.09	0.04	102.4
Hwy 11 oxide facies-hosted (n=134, s=12)													
median	**0.62**	**bdl**	**bdl**	**bdl**	**bdl**	**68.0**	**32.0**	**bdl**	**0.01**	**0.01**	**0.01**	**bdl**	**100.7**
min	0.08	bdl	bdl	bdl	bdl	62.9	30.9	bdl	bdl	bdl	0.00	bdl	97.9
max	2.78	0.16	0.30	0.02	0.02	70.5	35.0	0.03	0.23	0.21	0.10	0.03	102.7
Sherman Mine oxide facies-hosted (n=114, s=5)													
median	**0.24**	**bdl**	**bdl**	**bdl**	**bdl**	**68.6**	**31.3**	**0.04**	**0.05**	**bdl**	**bdl**	**bdl**	**100.3**
min	bdl	bdl	bdl	bdl	bdl	64.2	30.7	bdl	bdl	bdl	bdl	bdl	98.6
max	2.21	0.08	0.18	0.03	0.06	70.3	34.0	0.20	0.29	0.18	0.11	0.03	102.3

Notes:

Fe_2O_3, FeO calculated from total Fe assuming stoichiometric Fe_3O_4 composition with all cations present in the mineral structure.

n: number spots analyzed in thin sections of each facies, s: number of thin sections of each facies.

dl: detection limit

Table 2.4: LA-ICP-MS analyses of magnetite in different facies of Temagami BIF. All values in ppm. For individual analyses, see Appendix C.

	Mg	Al	Si	P	Ca	Sc	Ti	V	Cr	Mn	Co	Ni	Cu
dl	**0.7**	**0.3**	**25**	**9.7**	**23**	**0.05**	**0.4**	**0.04**	**0.25**	**0.18**	**0.03**	**0.3**	**0.03**
All (n=137, s=10)													
median	**337**	**91.3**	**3300**	**38**	**81**	**0.2**	**15**	**5**	**1.0**	**200**	**0.7**	**4.3**	**0.21**
min	23.9	9.2	217	11	24	0.06	1.3	0.96	0.29	24	0.033	0.67	0.03
max	21100	30800	92100	9870	9300	2.2	4890	150	250	1630	32	160	500
Oxide facies-hosted (n=119, s=7)													
median	**712**	**219**	**4930**	**35**	**72**	**0.27**	**15**	**4.7**	**0.81**	**190**	**0.750**	**5.4**	**0.30**
min	203	81.0	1170	18	40	0.06	1.3	1.0	0.29	35	0.033	0.67	0.03
max	1109	355	34400	132	175	2.0	1590	20	12.0	1630	7.1	47	8.90
Chlorite-hosted (n=20, s=3)													
median	**712**	**219**	**4930**	**35**	**72**	**0.18**	**360**	**90.0**	**9.8**	**370**	**1.00**	**3.9**	**0.45**
min	203	81.0	1170	18	40	0.08	103	26	0.64	24	0.42	1.8	0.11
max	1110	355	34400	132	175	2.2	4890	150	250	790	32.0	170	500
Hwy 11 oxide facies-hosted (n=26, s=2)													
median	**150**	**65**	**2400**	**58**	**95**	**0.3**	**37**	**4.0**	**1.4**	**210**	**0.72**	**1.5**	**1.82**
min	23.9	9.2	217	11	24	0.09	10	3.7	0.60	62	0.21	0.67	0.34
max	12900	461	92100	9870	9300	0.56	1590	5.6	2.9	290	0.93	3.1	8.92
Sherman Mine oxide facies-hosted (n=89, s=5)													
median	**241**	**76**	**3460**	**42**	**77**	**0.20**	**13**	**8.1**	**0.73**	**180**	**1.2**	**11**	**0.15**
min	24	9.2	217	11	24	0.06	1.3	1.0	0.29	35	0.033	1.8	0.03
max	12900	461	92100	9870	9300	2.0	51	20	12	1630	7.1	47	6.57
Type 2 magnetite (n=3, s=1)													
median	**606**	**478**	**3220**	**23**	**187**	**0.48**	**11**	**18**	**0.52**	**320**	**5.7**	**25**	**0.05**
min	179	25.3	1470	13	39	0.12	1.6	1.0	0.42	62	0.39	20	0.05
max	21100	30800	82200	389	2750	0.51	16	18	0.60	330	5.8	26	0.06
Type 3 magnetite core (n=9, s=2)													
median	**164**	**29.5**	**778**	**30**	**77**	**0.20**	**11**	**1.4**	**0.80**	**190**	**0.092**	**6.5**	**0.05**
min	116	21.0	404	22	54	0.11	5.5	1.1	0.44	160	0.034	3.9	0.03
max	671	91.3	3460	659	548	2.0	19	19	2.0	340	5.8	40	0.11
Type 3 magnetite rim (n=4, s=2)													
median	**130**	**23.0**	**1040**	**23**	**56**	**0.42**	**12**	**18**	**0.68**	**300**	**5.6**	**25**	**0.05**
min	123	19.5	495	22	55	0.11	8.4	1.2	0.46	190	0.043	5.0	0.04
max	147	53.5	7290	24	60	1.0	17	19	1.6	330	5.9	37	0.07

Table 2.4 (continued): LA-ICP-MS analyses of magnetite in different facies of Temagami BIF. All values in ppm. For individual analyses, see Appendix C.

	Zn	Ga	Ge	As	Y	Zr	Nb	Mo	Ag	Cd	In	Sn	Sb
dl	**0.3**	**0.2**	**0.17**	**0.08**	**0.01**	**0.01**	**0.014**	**0.1**	**0.1**	**0.2**	**0.07**	**1.4**	**0.23**
All (n=137, s=10)													
median	**14.1**	**1.1**	**7.5**	**0.39**	**0.22**	**0.38**	**0.24**	**bdl**	**0.2**	**0.4**	**0.13**	**1.70**	**0.99**
min	2.8	0.2	1.4	0.09	bdl	bdl	bdl	bdl	bdl	bdl	bdl	bdl	bdl
max	87.8	9.9	88.2	64.3	301	57	12	4.0	5.1	12	0.13	2.9	8.0
Oxide facies-hosted (n=119, s=7)													
median	**16.4**	**0.8**	**7.3**	**0.65**	**0.28**	**0.12**	**0.075**	**bdl**	**bdl**	**bdl**	**0.03**	**bdl**	**0.76**
min	2.8	0.2	1.4	0.09	bdl	bdl	bdl	bdl	bdl	bdl	bdl	bdl	bdl
max	87.8	1.7	88.2	4.67	9.25	13	3.68	4.0	0.29	12	0.13	2.9	6.7
Chlorite-hosted (n=20, s=3)													
median	**7.23**	**2.3**	**16**	**0.46**	**0.83**	**8.5**	**1.50**	**0.1**	**bdl**	**bdl**	**bdl**	**bdl**	**0.19**
min	3.4	1.1	5.4	0.15	0.05	0.51	0.18	bdl	bdl	bdl	bdl	bdl	bdl
max	64.2	9.9	39	64.3	301	57	12.0	2.1	5.1	0.24	bdl	2.3	8.0
Hwy 11 oxide facies-hosted (n=26, s=2)													
median	**10.5**	**1.0**	**6.4**	**1.20**	**0.22**	**0.75**	**0.29**	**bdl**	**bdl**	**0.12**	**bdl**	**bdl**	**1.9**
min	6.4	0.6	4.5	0.32	0.04	0.19	0.065	bdl	bdl	bdl	bdl	bdl	0.20
max	13.3	1.7	10	3.11	4.55	13	3.7	0.2	0.1	12.0	0.07	2.5	4.5
Sherman Mine oxide facies-hosted (n=89, s=5)													
median	**18.6**	**0.7**	**7.9**	**0.44**	**0.32**	**0.08**	**0.036**	**bdl**	**bdl**	**bdl**	**bdl**	**bdl**	**0.57**
min	2.8	0.2	1.4	0.092	bdl	bdl	bdl	bdl	bdl	bdl	bdl	bdl	bdl
max	87.8	1.5	88	4.67	9.3	6.2	2.5	4.0	0.3	0.62	0.13	2.9	6.7
Type 2 magnetite (n=3, s=1)													
median	**53.4**	**1.2**	**1.6**	**0.32**	**bdl**	**0.05**	**0.020**	**bdl**	**bdl**	**bdl**	**bdl**	**bdl**	**0.20**
min	2.8	0.3	1.4	0.22	bdl	0.02	bdl	bdl	bdl	bdl	bdl	bdl	0.14
max	54.0	1.2	2.7	0.63	0.13	0.14	0.13	0.2	bdl	bdl	bdl	1.6	0.91
Type 3 magnetite core (n=9, s=2)													
median	**20.0**	**0.3**	**7.6**	**0.26**	**0.01**	**0.06**	**0.010**	**bdl**	**bdl**	**bdl**	**bdl**	**bdl**	**0.12**
min	14.2	0.2	1.6	0.21	bdl	0.02	bdl	bdl	bdl	bdl	bdl	bdl	0.11
max	57.0	1.2	18.3	0.46	0.24	0.08	0.089	bdl	0.1	0.26	bdl	2.1	0.47
Type 3 magnetite rim (n=4, s=2)													
median	**55.5**	**1.2**	**5.2**	**0.27**	**0.49**	**0.03**	**0.020**	**bdl**	**bdl**	**bdl**	**bdl**	**bdl**	**0.17**
min	18.3	0.3	1.5	0.22	0.02	0.02	bdl	bdl	bdl	bdl	bdl	bdl	0.12
max	56.3	1.2	15.1	0.50	2.20	3.7	0.079	0.2	bdl	bdl	bdl	2.6	0.76

Table 2.4 (continued): LA-ICP-MS analyses of magnetite in different facies of Temagami BIF. All values in ppm. For individual analyses, see Appendix C.

	Cs	Ba	La	Sm	Yb	Hf	Ta	W	Pb
dl	**0.09**	**0.1**	**0.01**	**0.04**	**0.03**	**0.04**	**0.01**	**0.08**	**0.05**
All (n=137, s=10)									
median	**0.17**	**2.01**	**0.06**	**0.07**	**0.06**	**bdl**	**0.02**	**0.24**	**0.69**
min	bdl	bdl	bdl	bdl	bdl	bdl	bdl	bdl	bdl
max	2.14	28	9.37	28.6	16.6	1.6	0.40	16.3	52.2
Oxide facies-hosted (n=119, s=7)									
median	**bdl**	**1.9**	**0.06**	**bdl**	**0.04**	**bdl**	**0.01**	**0.25**	**0.63**
min	bdl	bdl	bdl	bdl	bdl	bdl	bdl	bdl	bdl
max	0.70	19.0	5.46	1.21	0.37	0.42	0.27	16.3	15.7
Chlorite-hosted (n=20, s=3)									
median	**0.33**	**1.3**	**0.10**	**bdl**	**0.11**	**0.18**	**0.04**	**0.14**	**0.66**
min	bdl	0.1	0.01	bdl	bdl	bdl	bdl	bdl	bdl
max	2.14	27.5	9.37	28.6	16.6	1.58	0.40	3.09	52.2
Hwy 11 oxide facies-hosted (n=26, s=2)									
median	**0.12**	**3.4**	**0.05**	**bdl**	**0.05**	**bdl**	**0.04**	**0.19**	**1.48**
min	bdl	1.1	0.01	bdl	bdl	bdl	0.01	bdl	0.51
max	0.70	13.9	0.92	0.10	0.37	0.42	0.27	16.3	9.50
Sherman Mine oxide facies-hosted (n=89, s=5)									
median	**bdl**	**1.4**	**0.08**	**bdl**	**0.04**	**bdl**	**0.01**	**0.42**	**0.47**
min	bdl	bdl	bdl	bdl	bdl	bdl	bdl	bdl	bdl
max	0.18	19.0	5.46	1.21	0.36	0.06	0.03	9.24	15.7
Type 2 magnetite (n=3, s=1)									
median	**bdl**	**0.1**	**bdl**	**bdl**	**0.02**	**bdl**	**bdl**	**0.09**	**0.05**
min	bdl	bdl	bdl	bdl	bdl	bdl	bdl	bdl	bdl
max	bdl	1.4	0.02	0.03	0.03	bdl	0.01	0.11	0.27
Type 3 magnetite core (n=9, s=2)									
median	**bdl**	**0.1**	**0.01**	**bdl**	**0.02**	**bdl**	**bdl**	**bdl**	**0.05**
min	bdl	bdl	bdl	bdl	bdl	bdl	bdl	bdl	bdl
max	0.11	1.0	0.05	0.06	0.08	bdl	0.01	0.15	3.20
Type 3 magnetite rim (n=4, s=2)									
median	**bdl**	**0.2**	**0.01**	**bdl**	**0.09**	**bdl**	**bdl**	**bdl**	**0.43**
min	bdl	bdl	bdl	bdl	bdl	bdl	bdl	bdl	bdl
max	bdl	3.9	0.21	0.04	0.25	bdl	0.01	0.22	0.64

Notes:
dl - average detection limit, bdl - below detection limit. For analyzed isotope and mean relative error see Appendix C.
n - number of individual analyses in s - number of thin sections.
Median values calculated using 1/2 detection limit where value is bdl.

Table 2.5: Correlation matrix for major and trace elements in Temagami BIF magnetite

	Si	Al	Ca	Mg	P	Ti	Mn	Zn	Cu	Pb	Ag	As	Sb
Si	1	-0.05	-0.04	0.06	-0.01	-0.03	-0.31	-0.08	0.11	-0.01	0.00	0.54	0.60
Al	-0.05	1	0.02	0.20	-0.17	0.34	-0.05	-0.39	0.27	0.25	0.10	0.11	-0.02
Ca	-0.04	0.02	1	0.11	0.74	0.13	-0.02	-0.23	-0.11	-0.09	0.10	0.10	0.13
Mg	0.06	0.20	0.11	1	-0.04	-0.01	0.15	-0.07	0.23	0.03	-0.05	0.22	0.27
P	-0.01	-0.17	0.74	-0.04	1	-0.09	-0.31	-0.25	-0.12	-0.12	0.15	0.08	0.07
Ti	-0.03	0.34	0.13	-0.01	-0.09	1	0.16	-0.18	0.04	0.03	0.01	0.13	0.06
Mn	-0.31	-0.05	-0.02	0.15	-0.31	0.16	1	0.50	0.04	-0.13	-0.18	-0.22	-0.15
Zn	-0.08	-0.39	-0.23	-0.07	-0.25	-0.18	0.50	1	-0.24	-0.18	-0.10	-0.22	-0.19
Cu	0.11	0.27	-0.11	0.23	-0.12	0.04	0.04	-0.24	1	0.18	0.26	0.38	0.30
Pb	-0.01	0.25	-0.09	0.03	-0.12	0.03	-0.13	-0.18	0.18	1	0.16	0.02	0.03
Ag	0.00	0.10	0.10	-0.05	0.15	0.01	-0.18	-0.10	0.26	0.16	1	-0.03	-0.04
As	0.54	0.11	0.10	0.22	0.08	0.13	-0.22	-0.22	0.38	0.02	-0.03	1	0.86
Sb	0.60	-0.02	0.13	0.27	0.07	0.06	-0.15	-0.19	0.30	0.03	-0.04	0.86	1
Cd	-0.03	0.11	-0.06	0.02	-0.05	0.10	0.00	-0.05	0.17	0.17	0.14	0.12	0.15
Co	0.18	-0.33	-0.14	0.27	-0.17	-0.12	0.33	0.69	-0.20	-0.17	-0.20	-0.03	0.05
Ni	0.46	-0.40	-0.08	0.12	-0.12	-0.17	0.06	0.50	-0.25	-0.16	-0.27	0.15	0.27
Mo	-0.04	0.06	0.35	-0.09	0.30	0.04	0.02	-0.03	-0.06	-0.06	-0.03	0.18	0.08
Sn	0.06	0.11	0.08	-0.12	0.03	0.23	-0.04	0.01	-0.13	0.06	-0.02	0.08	0.03
Ge	-0.02	0.25	0.12	0.13	0.00	0.15	0.03	-0.14	-0.12	-0.02	-0.14	0.26	0.05
In	-0.04	0.14	0.22	-0.04	0.25	0.03	-0.12	-0.19	0.17	0.00	0.46	0.17	0.01
W	0.11	-0.07	0.26	-0.04	0.34	0.53	-0.19	-0.16	0.01	-0.08	0.06	0.40	0.41
Cr	-0.08	0.20	-0.04	-0.02	-0.13	0.32	0.12	-0.16	0.07	0.21	0.08	-0.13	-0.14
V	-0.05	0.38	0.10	0.02	-0.19	0.44	0.36	-0.05	-0.09	0.22	0.05	-0.14	-0.16
Ga	-0.10	0.50	0.01	0.21	-0.33	0.41	0.48	0.08	0.02	0.04	-0.02	-0.12	-0.15
Zr	-0.10	0.77	-0.04	0.06	-0.17	0.30	0.04	-0.15	-0.04	0.13	0.00	-0.12	-0.18
Hf	-0.08	0.80	-0.01	0.08	-0.15	0.31	0.03	-0.18	-0.02	0.18	0.03	-0.08	-0.15
Ba	0.50	0.07	0.11	-0.14	0.14	0.22	-0.25	-0.25	0.20	-0.02	0.12	0.49	0.43
Cs	-0.05	0.44	-0.04	0.00	-0.11	0.49	0.27	-0.16	0.03	0.04	0.05	0.11	-0.01
Ta	-0.02	0.37	-0.06	0.14	-0.12	0.55	-0.03	-0.22	0.29	0.10	0.18	0.25	0.19
Nb	0.03	0.46	0.12	0.17	-0.16	0.83	0.15	-0.26	0.05	0.07	-0.01	0.21	0.19
Y	-0.04	0.12	0.35	0.01	0.50	0.01	-0.26	-0.23	-0.08	-0.06	0.19	0.02	-0.02
Sc	0.08	-0.14	-0.18	0.29	-0.16	-0.04	0.27	0.61	-0.02	-0.09	-0.15	0.08	0.03
La	-0.06	-0.07	0.19	-0.09	0.33	0.07	-0.24	-0.22	-0.04	-0.06	0.12	0.00	-0.04
Sm	-0.02	-0.09	0.31	-0.07	0.44	0.02	-0.22	-0.19	-0.05	-0.07	0.14	-0.01	-0.03
Yb	-0.06	0.22	0.27	0.09	0.37	0.03	-0.18	-0.18	-0.01	-0.05	0.17	0.03	0.01

Table 2.5 (continued): Correlation matrix for major and trace elements in Temagami BIF magnetite

	Cd	Co	Ni	Mo	Sn	Ge	In	W	Cr	V	Ga	Zr
Si	-0.03	0.18	0.46	-0.04	0.06	-0.02	-0.04	0.11	-0.08	-0.05	-0.10	-0.10
Al	0.11	-0.33	-0.40	0.06	0.11	0.25	0.14	-0.07	0.20	0.38	0.50	0.77
Ca	-0.06	-0.14	-0.08	0.35	0.08	0.12	0.22	0.26	-0.04	0.10	0.01	-0.04
Mg	0.02	0.27	0.12	-0.09	-0.12	0.13	-0.04	-0.04	-0.02	0.02	0.21	0.06
P	-0.05	-0.17	-0.12	0.30	0.03	0.00	0.25	0.34	-0.13	-0.19	-0.33	-0.17
Ti	0.10	-0.12	-0.17	0.04	0.23	0.15	0.03	0.53	0.32	0.44	0.41	0.30
Mn	0.00	0.33	0.06	0.02	-0.04	0.03	-0.12	-0.19	0.12	0.36	0.48	0.04
Zn	-0.05	0.69	0.50	-0.03	0.01	-0.14	-0.19	-0.16	-0.16	-0.05	0.08	-0.15
Cu	0.17	-0.20	-0.25	-0.06	-0.13	-0.12	0.17	0.01	0.07	-0.09	0.02	-0.04
Pb	0.17	-0.17	-0.16	-0.06	0.06	-0.02	0.00	-0.08	0.21	0.22	0.04	0.13
Ag	0.14	-0.20	-0.27	-0.03	-0.02	-0.14	0.46	0.06	0.08	0.05	-0.02	0.00
As	0.12	-0.03	0.15	0.18	0.08	0.26	0.17	0.40	-0.13	-0.14	-0.12	-0.12
Sb	0.15	0.05	0.27	0.08	0.03	0.05	0.01	0.41	-0.14	-0.16	-0.15	-0.18
Cd	1	-0.08	-0.10	0.00	-0.06	-0.07	0.02	0.07	0.02	-0.06	0.00	-0.02
Co	-0.08	1	0.79	-0.14	0.11	-0.05	-0.15	-0.13	-0.06	0.11	0.20	-0.09
Ni	-0.10	0.79	1	-0.11	0.08	-0.09	-0.22	-0.05	-0.15	-0.01	-0.05	-0.18
Mo	0.00	-0.14	-0.11	1	0.01	0.10	0.06	0.28	-0.04	-0.02	-0.07	0.02
Sn	-0.06	0.11	0.08	0.01	1	0.00	0.45	0.18	0.00	0.04	-0.01	0.11
Ge	-0.07	-0.05	-0.09	0.10	0.00	1	-0.09	-0.04	0.17	0.29	0.19	0.21
In	0.02	-0.15	-0.22	0.06	0.45	-0.09	1	0.12	-0.08	-0.05	-0.01	0.07
W	0.07	-0.13	-0.05	0.28	0.18	-0.04	0.12	1	-0.06	-0.12	-0.21	-0.09
Cr	0.02	-0.06	-0.15	-0.04	0.00	0.17	-0.08	-0.06	1	0.68	0.41	0.21
V	-0.06	0.11	-0.01	-0.02	0.04	0.29	-0.05	-0.12	0.68	1	0.69	0.49
Ga	0.00	0.20	-0.05	-0.07	-0.01	0.19	-0.01	-0.21	0.41	0.69	1	0.51
Zr	-0.02	-0.09	-0.18	0.02	0.11	0.21	0.07	-0.09	0.21	0.49	0.51	1
Hf	-0.01	-0.14	-0.21	0.03	0.23	0.19	0.17	-0.07	0.20	0.49	0.48	0.90
Ba	0.08	-0.13	0.16	0.14	0.04	-0.04	0.10	0.32	-0.11	-0.06	-0.07	-0.09
Cs	0.04	-0.17	-0.21	0.05	0.09	0.13	0.20	0.18	0.03	0.38	0.46	0.38
Ta	0.20	-0.22	-0.30	0.00	0.12	-0.04	0.20	0.36	0.09	0.06	0.22	0.14
Nb	0.08	-0.11	-0.14	0.02	0.24	0.18	0.02	0.41	0.34	0.48	0.52	0.41
Y	-0.06	-0.08	-0.14	0.10	0.19	-0.02	0.37	0.27	-0.07	-0.05	-0.01	0.30
Sc	0.00	0.72	0.49	-0.08	0.18	0.02	0.04	-0.04	-0.11	-0.02	0.16	-0.06
La	-0.01	-0.14	-0.14	0.03	0.01	-0.03	0.14	0.21	-0.06	-0.09	-0.15	-0.07
Sm	-0.03	-0.07	-0.10	-0.01	0.10	-0.04	0.19	0.15	-0.08	-0.09	-0.15	-0.06
Yb	-0.07	-0.02	-0.11	0.14	0.18	-0.01	0.25	0.23	-0.05	-0.02	0.05	0.42

Table 2.5 (continued): Correlation matrix for major and trace elements in Temagami BIF magnetite

	Hf	Ba	Cs	Ta	Nb	Y	Sc	La	Sm	Yb
Si	-0.08	0.50	-0.05	-0.02	0.03	-0.04	0.08	-0.06	-0.02	-0.06
Al	0.80	0.07	0.44	0.37	0.46	0.12	-0.14	-0.07	-0.09	0.22
Ca	-0.01	0.11	-0.04	-0.06	0.12	0.35	-0.18	0.19	0.31	0.27
Mg	0.08	-0.14	0.00	0.14	0.17	0.01	0.29	-0.09	-0.07	0.09
P	-0.15	0.14	-0.11	-0.12	-0.16	0.50	-0.16	0.33	0.44	0.37
Ti	0.31	0.22	0.49	0.55	0.83	0.01	-0.04	0.07	0.02	0.03
Mn	0.03	-0.25	0.27	-0.03	0.15	-0.26	0.27	-0.24	-0.22	-0.18
Zn	-0.18	-0.25	-0.16	-0.22	-0.26	-0.23	0.61	-0.22	-0.19	-0.18
Cu	-0.02	0.20	0.03	0.29	0.05	-0.08	-0.02	-0.04	-0.05	-0.01
Pb	0.18	-0.02	0.04	0.10	0.07	-0.06	-0.09	-0.06	-0.07	-0.05
Ag	0.03	0.12	0.05	0.18	-0.01	0.19	-0.15	0.12	0.14	0.17
As	-0.08	0.49	0.11	0.25	0.21	0.02	0.08	0.00	-0.01	0.03
Sb	-0.15	0.43	-0.01	0.19	0.19	-0.02	0.03	-0.04	-0.03	0.01
Cd	-0.01	0.08	0.04	0.20	0.08	-0.06	0.00	-0.01	-0.03	-0.07
Co	-0.14	-0.13	-0.17	-0.22	-0.11	-0.08	0.72	-0.14	-0.07	-0.02
Ni	-0.21	0.16	-0.21	-0.30	-0.14	-0.14	0.49	-0.14	-0.10	-0.11
Mo	0.03	0.14	0.05	0.00	0.02	0.10	-0.08	0.03	-0.01	0.14
Sn	0.23	0.04	0.09	0.12	0.24	0.19	0.18	0.01	0.10	0.18
Ge	0.19	-0.04	0.13	-0.04	0.18	-0.02	0.02	-0.03	-0.04	-0.01
In	0.17	0.10	0.20	0.20	0.02	0.37	0.04	0.14	0.19	0.25
W	-0.07	0.32	0.18	0.36	0.41	0.27	-0.04	0.21	0.15	0.23
Cr	0.20	-0.11	0.03	0.09	0.34	-0.07	-0.11	-0.06	-0.08	-0.05
V	0.49	-0.06	0.38	0.06	0.48	-0.05	-0.02	-0.09	-0.09	-0.02
Ga	0.48	-0.07	0.46	0.22	0.52	-0.01	0.16	-0.15	-0.15	0.05
Zr	0.90	-0.09	0.38	0.14	0.41	0.30	-0.06	-0.07	-0.06	0.42
Hf	1	-0.06	0.46	0.16	0.44	0.32	-0.07	-0.06	-0.04	0.41
Ba	-0.06	1	0.22	0.20	0.20	0.12	-0.11	0.12	0.11	0.08
Cs	0.46	0.22	1	0.38	0.51	0.05	-0.04	0.00	-0.02	0.05
Ta	0.16	0.20	0.38	1	0.51	-0.03	0.03	0.03	-0.02	0.01
Nb	0.44	0.20	0.51	0.51	1	0.05	-0.08	0.02	-0.03	0.12
Y	0.32	0.12	0.05	-0.03	0.05	1	-0.11	0.27	0.38	0.90
Sc	-0.07	-0.11	-0.04	0.03	-0.08	-0.11	1	-0.13	-0.07	-0.04
La	-0.06	0.12	0.00	0.03	0.02	0.27	-0.13	1	0.93	0.16
Sm	-0.04	0.11	-0.02	-0.02	-0.03	0.38	-0.07	0.93	1	0.24
Yb	0.41	0.08	0.05	0.01	0.12	0.90	-0.04	0.16	0.24	1

Notes:

Pearson correlation coefficient for n=137 individual LA-ICPMS analyses in s=10 thin sections of magnetite in BIF samples from the Hwy 11 outcrop and Sherman Mine.
Correlation coefficients calculated for values reported in Appendix C.
18 outliers omitted.

Table 2.6: Mineralogical host relationships of elements in Temagami BIF-magnetite based on LA-ICP-MS results

Host	Strong association	Weak association
structurally hosted in magnetite	Mg, Al, Si, Ti, V, Cr, Mn, Co, Ni, Cu, Zn, Ge, As Mo, W	Sc, Nb, Ga, Ag, In, Sn Sb, La, Sm, Yb, Re, Pt
quartz inclusion	Si	As, Sb
apatite inclusion	P, Ca, Y, Sb, La, Sm, Yb	
chlorite inclusion	Mg, Al, Si, Ga, Cd, Ti, Cr In, Sn, Cs, Ta	W
sulfide inclusion	Cu, Zn, As, Se, In, Sb, Re Pb	Mo, Ag
zircon inclusion	Zr, Nb, Hf, Ta	
others	Ba, Bi	

Table 2.7: EPMA analyses of chlorite in Temagami BIF and host rocks. Results in wt.-%. All analyses listed in Appendix D.

	SiO_2	TiO_2	Al_2O_3	Cr_2O_3	Fe_2O_3	FeO	MnO	MgO	ZnO	CaO	Na_2O	K_2O	F	Cl	H_2O*	Total	Fe/(Fe+Mg)
dl	0.01	0.03	0.08	0.01	0.02	0.02	0.01	0.01	0.01	0.01	0.01	0.01	0.01	0.01			
BIF - magnetite (n=12, s=4)																	
median	**24.9**	**0.03**	**18.2**	**0.01**	**bdl**	**35.2**	**0.05**	**7.30**	**0.04**	**0.01**	**0.01**	**0.02**	**bdl**	**0.01**	**10.6**	**98.3**	**0.74**
min	22.8	bdl	16.3	bdl	bdl	26.3	0.03	4.34	bdl	bdl	bdl	bdl	bdl	bdl	10.3	97.2	0.55
max	29.5	0.07	19.3	0.02	2.89	42.6	0.19	13.9	0.09	0.29	0.04	0.03	bdl	0.03	11.6	101.9	0.8
BIF - chert (n=19, s=4)																	
median	**28.3**	**0.04**	**19.3**	**0.01**	**1.55**	**26.9**	**0.05**	**12.0**	**bdl**	**bdl**	**0.01**	**0.01**	**bdl**	**bdl**	**11.2**	**101.6**	**0.58**
min	25.1	bdl	17.2	bdl	bdl	21.1	0.01	3.91	0.00	bdl	bdl	bdl	bdl	bdl	10.8	98.4	0.48
max	33.7	0.08	19.9	0.12	4.78	41.7	0.18	15.6	0.08	0.13	0.05	0.05	0.14	0.01	12.2	104.3	0.9
BIF - chlorite (n=13, s=3)																	
median	**26.0**	**0.04**	**18.2**	**0.01**	**bdl**	**32.9**	**0.06**	**10.7**	**bdl**	**0.01**	**0.01**	**0.01**	**bdl**	**0.01**	**10.9**	**98.5**	**0.64**
min	20.2	0.03	13.2	0.00	0.00	25.8	0.01	6.63	bdl	bdl	bdl	bdl	bdl	bdl	9.6	90.8	0.55
max	30.0	0.05	19.9	0.02	3.21	36.6	0.44	12.8	0.05	2.35	0.09	0.11	0.07	0.03	11.7	102.8	0.8
BIF - carbonate (n=3, s=1)																	
median	**23.2**	**0.05**	**18.3**	**bdl**	**bdl**	**40.9**	**0.04**	**4.67**	**bdl**	**0.01**	**0.01**	**0.01**	**bdl**	**0.01**	**10.3**	**98.1**	**0.83**
min	22.8	0.05	18.2	bdl	bdl	40.6	0.03	4.56	bdl	bdl	bdl	bdl	bdl	bdl	10.2	96.8	0.82
max	23.3	0.07	18.4	0.01	bdl	41.8	0.06	5.00	bdl	0.02	0.02	0.01	bdl	0.01	10.3	98.1	0.84
BIF - sulfidic chert (n=23, s=2)																	
median	**29.6**	**0.03**	**21.7**	**bdl**	**4.19**	**18.6**	**0.33**	**14.5**	**bdl**	**bdl**	**bdl**	**0.01**	**0.04**	**bdl**	**11.9**	**101.0**	**0.47**
min	23.6	bdl	19.2	bdl	0.41	9.5	0.25	5.16	bdl	bdl	bdl	bdl	bdl	bdl	10.5	96.0	0.31
max	32.6	0.05	24.0	0.01	5.84	38.1	0.46	19.3	0.07	0.02	0.02	0.06	0.08	0.04	12.4	102.3	0.8
Host rock - volcaniclastic (n=30, s=4)																	
median	**23.4**	**0.04**	**19.8**	**0.01**	**0.58**	**29.0**	**0.09**	**8.84**	**0.03**	**0.01**	**0.01**	**0.01**	**bdl**	**0.01**	**10.5**	**96.8**	**0.64**
min	22.5	bdl	18.9	bdl	bdl	18.3	0.04	3.92	bdl	bdl	bdl	bdl	bdl	bdl	10.1	92.2	0.49
max	29.1	0.11	22.9	0.08	4.47	41.0	0.14	14.3	0.08	0.13	0.10	0.37	0.11	0.03	11.3	98.6	0.85
Host rock - rhyolite (n=40, s=6)																	
median	**25.0**	**0.04**	**21.6**	**0.01**	**0.82**	**24.3**	**0.12**	**13.5**	**0.03**	**0.02**	**0.02**	**0.03**	**bdl**	**0.01**	**11.1**	**97.5**	**0.51**
min	23.4	0.01	18.6	bdl	0.02	15.2	0.06	7.49	bdl	bdl	bdl	bdl	bdl	bdl	10.3	93.4	0.45
max	33.0	0.12	23.2	0.05	9.53	35.4	0.25	15.3	0.08	0.35	0.06	0.99	0.20	0.03	12.1	102.9	0.7
Host rock - andesite (n=13, s=2)																	
median	**25.1**	**0.05**	**18.9**	**0.02**	**0.70**	**28.9**	**0.38**	**11.8**	**0.03**	**0.04**	**0.01**	**bdl**	**bdl**	**0.01**	**11.0**	**97.1**	**0.58**
min	23.2	bdl	17.7	bdl	bdl	24.5	0.11	10.9	0.01	0.02	0.01	bdl	bdl	bdl	10.2	95.2	0.53
max	26.8	0.21	20.6	0.07	4.32	29.8	0.42	12.6	0.07	0.20	0.02	0.27	0.07	0.12	12.5	99.1	0.69
Host rock - basalt (n=32, s=1)																	
median	**25.9**	**0.02**	**19.0**	**bdl**	**0.35**	**24.8**	**0.32**	**15.0**	**0.03**	**0.03**	**0.01**	**0.01**	**bdl**	**0.04**	**11.1**	**96.8**	**0.48**
min	24.5	0.01	18.1	bdl	bdl	17.6	0.27	13.5	bdl	bdl	bdl	bdl	bdl	bdl	10.3	88.7	0.44
max	30.7	0.32	19.4	0.02	4.39	26.1	0.39	15.5	0.05	0.47	0.20	0.21	0.01	0.64	11.4	98.1	0.50

Notes:

Fe_2O_3, FeO and H_2O calculated to achieve cation charge balance on the basis of 28 oxygen, assuming full crystallographic site occupancy.

Fe/(Fe+Mg) calculated as molar ratio from Fe and Mg atoms per formula unit.

dl: detection limit, n: number of spot analyses in s: number of thin sections

Table 2.8: EPMA analyses of apatite. All values in element-wt.%. For individual analyses, see Appendix E.

	Ca	P	Sr	Si	Fe	Al	Mg	Na	S	U	Th	Pb	Sc	Y	La	Ce	Pr
dl	0.006	0.006	0.022	0.005	0.013	0.004	0.005	0.009	0.006	0.036	0.037	0.036	0.011	0.033	0.042	0.036	0.065
All (n=29, s=9)																	
median	**39.2**	**18.3**	**0.14**	**bdl**	**0.56**	**bdl**	**bdl**	**0.05**	**bdl**	**bdl**	**bdl**	**bdl**	**bdl**	**0.04**	**0.02**	**bdl**	**0.03**
min	35.9	15.9	bdl	bdl	0.03	bdl	bdl	bdl	bdl	bdl	bdl	bdl	bdl	bdl	0.02	bdl	0.03
max	40.1	18.7	0.52	1.93	3.35	0.39	0.05	0.35	0.25	0.95	0.79	0.66	0.12	0.17	0.21	0.36	0.14
Oxide facies-hosted (n=25, s=6)																	
median	**39.2**	**18.3**	**0.17**	**bdl**	**0.56**	**bdl**	**bdl**	**0.05**	**bdl**	**bdl**	**bdl**	**bdl**	**bdl**	**0.05**	**0.02**	**bdl**	**0.03**
min	35.9	15.9	0.05	bdl	0.03	bdl	bdl	bdl	bdl	bdl	bdl	bdl	bdl	bdl	0.02	bdl	0.03
max	40.1	18.7	0.52	1.93	3.35	0.39	0.05	0.19	0.06	0.95	0.79	0.66	0.12	0.17	0.11	0.12	0.03
Chlorite BIF-hosted (n=4, s=2)																	
median	**39.3**	**18.1**	**bdl**	**0.07**	**0.56**	**0.02**	**0.04**	**0.18**	**0.12**	**bdl**	**bdl**	**0.07**	**bdl**	**0.03**	**0.08**	**0.21**	**0.03**
min	37.2	16.9	bdl	bdl	0.28	bdl	bdl	0.02	bdl	bdl	bdl	bdl	bdl	bdl	0.02	0.04	0.03
max	39.7	18.7	0.06	0.12	1.35	0.03	0.05	0.35	0.25	0.07	bdl	0.20	0.08	0.15	0.21	0.36	0.14
Sulfide facies-hosted (n=4, s=1)																	
median	**39.1**	**18.0**	**0.07**	**0.62**	**0.06**	**0.14**	**bdl**	**0.08**	**bdl**	**0.12**	**bdl**	**bdl**	**bdl**	**0.03**	**0.02**	**bdl**	**0.03**
min	38.6	17.7	0.05	bdl	0.03	bdl	bdl	bdl	bdl	bdl	bdl	bdl	bdl	bdl	0.02	bdl	0.03
max	40.1	18.7	0.23	1.07	0.13	0.39	bdl	0.19	bdl	0.95	bdl	0.58	bdl	0.14	0.02	bdl	0.03
Hwy 11 oxide facies-hosted (n=8, s=2)																	
median	**39.4**	**18.4**	**0.18**	**bdl**	**0.54**	**bdl**	**bdl**	**0.05**	**bdl**	**bdl**	**bdl**	**bdl**	**bdl**	**0.07**	**0.02**	**bdl**	**0.03**
min	39.2	18.3	0.06	bdl	0.12	bdl	bdl	0.03	bdl	bdl	bdl	bdl	bdl	bdl	0.02	bdl	0.03
max	39.6	18.5	0.52	0.05	1.66	bdl	0.05	0.12	bdl	bdl	0.79	0.66	0.12	0.17	0.02	0.06	0.03
Sherman Mine oxide facies-hosted (n=17, s=4)																	
median	**39.2**	**18.3**	**0.19**	**bdl**	**0.69**	**bdl**	**bdl**	**0.04**	**bdl**	**bdl**	**bdl**	**bdl**	**bdl**	**0.03**	**0.02**	**bdl**	**0.03**
min	35.9	15.9	0.10	bdl	0.09	bdl	bdl	0.02	bdl	bdl	bdl	bdl	bdl	bdl	0.02	bdl	0.03
max	39.6	18.5	0.52	1.93	3.35	bdl	0.04	0.12	0.06	0.60	0.79	0.66	0.12	0.13	0.11	0.12	0.03

Table 2.8 (continued): EPMA analyses of apatite. All values in element-wt.%. For individual analyses, see Appendix E.

	Nd	Sm	Eu	Gd	Tb	Dy	Ho	Er	Tm	Yb	Lu	Cl	F*	O	Total
dl	0.035	0.032	0.031	0.032	0.03	0.059	0.061	0.034	0.032	0.032	0.035	0.006	0.066		
All (n=29, s=9)															
median	**bdl**	**bdl**	**bdl**	**bdl**	**bdl**	**0.03**	**0.03**	**bdl**	**bdl**	**bdl**	**bdl**	**bdl**	**2.99**	**38.6**	**100.9**
min	bdl	bdl	bdl	bdl	bdl	0.03	0.03	bdl	bdl	bdl	bdl	bdl	2.23	36.4	96.3
max	0.07	0.12	0.16	0.33	0.19	0.18	0.36	0.22	0.41	0.33	0.06	0.39	4.06	39.4	103.7
Oxide facies-hosted (n=25, s=6)															
median	**bdl**	**bdl**	**bdl**	**bdl**	**bdl**	**0.03**	**0.03**	**bdl**	**bdl**	**bdl**	**bdl**	**bdl**	**2.96**	**38.6**	**100.9**
min	bdl	bdl	bdl	bdl	bdl	0.03	0.03	bdl	bdl	bdl	bdl	bdl	2.23	36.6	96.3
max	0.07	0.06	0.16	0.33	0.19	0.18	0.36	0.22	0.41	0.33	0.06	0.06	4.06	39.4	103.7
Chlorite BIF-hosted (n=4, s=2)															
median	**0.04**	**0.03**	**bdl**	**bdl**	**0.07**	**0.03**	**0.03**	**bdl**	**bdl**	**bdl**	**bdl**	**0.06**	**3.12**	**38.4**	**100.9**
min	bdl	bdl	bdl	bdl	bdl	0.03	0.03	bdl	bdl	bdl	bdl	bdl	2.78	36.4	96.4
max	0.07	0.12	bdl	0.11	0.15	0.06	0.03	bdl	0.03	bdl	bdl	0.39	3.53	39.3	102.2
Sulfide facies-hosted (n=4, s=1)															
median	**bdl**	**bdl**	**bdl**	**0.03**	**bdl**	**0.03**	**0.03**	**bdl**	**bdl**	**bdl**	**bdl**	**bdl**	**3.77**	**38.6**	**101.6**
min	bdl	bdl	bdl	bdl	bdl	0.03	0.03	bdl	bdl	bdl	bdl	bdl	3.64	37.2	98.5
max	bdl	bdl	bdl	0.33	0.19	0.03	0.03	0.04	bdl	bdl	0.06	0.03	4.06	39.2	103.7
Hwy 11 oxide facies-hosted (n=8, s=2)															
median	**bdl**	**bdl**	**bdl**	**bdl**	**bdl**	**0.03**	**0.03**	**bdl**	**bdl**	**bdl**	**bdl**	**bdl**	**2.55**	**38.8**	**101.3**
min	bdl	bdl	bdl	bdl	bdl	0.03	0.03	bdl	bdl	bdl	bdl	bdl	2.23	38.7	100.1
max	0.06	0.06	0.16	0.24	0.06	0.18	0.10	bdl	0.41	bdl	bdl	bdl	3.14	39.4	102.0
Sherman Mine oxide facies-hosted (n=17, s=4)															
median	**bdl**	**bdl**	**bdl**	**bdl**	**bdl**	**0.03**	**0.03**	**bdl**	**bdl**	**bdl**	**bdl**	**0.03**	**2.69**	**38.5**	**100.6**
min	bdl	bdl	bdl	bdl	bdl	0.03	0.03	bdl	bdl	bdl	bdl	bdl	2.23	36.6	96.3
max	0.07	0.06	0.16	bdl	0.06	0.18	0.36	0.22	0.04	0.33	0.06	0.06	4.00	39.4	101.7

Notes:
dl: detection limit, n: number of spot analyses in s: number of thin sections
F*: See text and Appendix E for details on the limitation of F quantification in apatite.

Table 2.9: LA-ICPMS analyses of apatite in Temagami BIF. All values in ppm. All results in Appendix F.

	Li	B	Na	Mg	Al	Si	P	S	Cl	K	Sc	Ti	V	Cr	Mn	Fe
dl	0.89	2.18	9.9	2.1	0.95	73.7	14.4	49.1	145	2.1	0.19	0.55	0.03	0.68	0.2	1.2
Jasper - hosted (n=20, s=1)																
median	**1.8**	**4.7**	**950**	**66**	**9.1**	**23900**	**201000**	**554**	**325**	**8.8**	**0.30**	**0.83**	**0.06**	**1.1**	**313**	**6950**
min	bdl	2.2	650	26	1.5	1610	160000	427	186	2.1	0.21	0.62	0.04	bdl	105	1450
max	3.3	480	1200	249	87	109000	315000	729	895	34	0.62	1.1	0.15	1.6	875	37000
Magnetite - hosted (n=11, s=2)																
median	**2.2**	**5.5**	**446**	**260**	**13**	**1940**	**225348**	**416**	**331**	**6.8**	**0.77**	**1.2**	**0.07**	**1.0**	**276**	**735**
min	1.5	3.4	97	11	1.1	124	61800	309	178	2.5	0.23	0.55	0.04	0.83	229	76
max	16	6420	1110	130000	684	248000	288000	706	2610	244	14	14	0.87	9.8	45200	55600
Chlorite - hosted (n=2, s=1)																
median	**1.7**	**3.7**	**579**	**769**	**508**	**2700**	**261000**	**422**	**230**	**7.0**	**0.41**	**5.2**	**9.9**	**0.98**	**487**	**9160**
min	0.89	3.2	310	576	1.0	560	253000	401	193	5.2	0.37	0.59	2.82	0.75	463	1750
max	2.6	4.1	848	963	1014	4840	268000	443	266	8.7	0.45	9.7	17	1.2	511	16500

	Co	Ni	Cu	Zn	Ga	As	Rb	Sr	Y	Zr	Nb	Sb	Cs	Ba	La	Ce
dl	0.05	0.26	0.10	0.22	0.02	0.63	0.1	0.01	0.003	0.01	0.01	0.11	0.06	0.06	0.003	0.004
Jasper - hosted (n=20, s=1)																
median	**0.09**	**0.43**	**0.37**	**0.38**	**0.15**	**69**	**0.25**	**1680**	**1040**	**0.09**	**0.010**	**0.41**	**0.09**	**6.1**	**180**	**362**
min	0.06	0.28	0.11	bdl	0.04	43	bdl	1130	803	0.03	bdl	bdl	0.06	2.8	138	291
max	0.17	0.80	1.2	2.3	46	189	0.88	3750	1380	0.42	0.020	1.8	0.18	1970	277	519
Magnetite - hosted (n=11, s=2)																
median	**0.19**	**0.98**	**0.36**	**5.7**	**0.05**	**5.1**	**0.17**	**4190**	**818**	**0.10**	**0.033**	**0.18**	**0.07**	**1.8**	**42.7**	**187**
min	0.05	0.28	0.10	0.22	0.02	3.1	0.11	1120	205	0.02	0.000	bdl	bdl	bdl	25.6	66
max	15	117	4.9	458	0.37	22	1.9	5650	913	30	0.070	1.1	1.1	17	118	355
Chlorite - hosted (n=2, s=1)																
median	**0.35**	**0.55**	**0.82**	**2.8**	**0.43**	**6.1**	**0.12**	**504**	**433**	**1.8**	**0.026**	**0.13**	**0.06**	**4.4**	**624**	**1930**
min	0.31	0.27	0.20	1.2	0.10	4.7	0.11	397	226	0.57	0.024	0.11	0.06	2.2	381	1170
max	0.40	0.83	1.4	4.5	0.75	7.4	0.13	612	640	3.1	0.028	0.14	0.06	6.5	867	2690

	Pr	Nd	Sm	Eu	Gd	Tb	Dy	Ho	Er	Tm	Yb	Lu	Pb	Th	U
dl	0.003	0.02	0.02	0.01	0.03	0.003	0.010	0.003	0.010	0.020	0.010	0.003	0.005	0.005	0.004
Jasper - hosted (n=20, s=1)															
median	**45.5**	**186**	**52.7**	**62.2**	**87.0**	**14.5**	**113**	**26.7**	**79.6**	**10.4**	**57.6**	**8.21**	**22.3**	**0.120**	**0.316**
min	34.8	150	42.6	47.9	66.1	11.9	90.0	21.3	66.0	8.0	45.8	6.40	8.98	0.012	0.058
max	63.4	273	79.8	87.4	129	21.0	157	36.8	115	14.5	77.7	11.3	70.2	0.378	0.796
Magnetite - hosted (n=11, s=2)															
median	**38.9**	**241**	**123**	**105**	**176**	**21.6**	**138**	**25.2**	**58.0**	**6.75**	**36.1**	**4.95**	**27.0**	**0.027**	**0.350**
min	11.4	71.2	30.9	32.0	48.0	6.74	34.4	7.02	15.6	1.90	10.3	1.33	19.1	0.012	0.096
max	55.4	310	128	115	209	29.0	155	27.0	64.6	7.66	42.7	5.89	96.6	0.229	0.573
Chlorite - hosted (n=2, s=1)															
median	**263**	**1094**	**201**	**22.5**	**161**	**18.9**	**100**	**16.8**	**37.1**	**4.08**	**21.1**	**2.52**	**4.87**	**8.27**	**3.95**
min	159	643	115	15.4	90.0	10.2	52.2	8.51	20.7	2.43	12.9	1.74	3.88	7.53	1.92
max	366	1544	286	29.5	231	27.7	147	25.0	53.5	5.72	29.2	3.31	5.86	9.00	5.98

Notes:
dl: detection limit, bdl: below detection limit.
For individual analyses, analyzed isotope, mean relative error, and detection limit see Appendix F.
n: number of spot analyses in s: number of thin sections

Table 2.10: EPMA analyses of monazite and xenotime. All values in element-wt.%. All results in Appendix G.

	Ca	P	Sr	Si	Fe	Al	Mg	Na	S	U	Th	Pb	Sc	Y	La	Ce	Pr
dl	0.006	0.006	0.022	0.01	0.01	0.01	0.005	0.009	0.006	0.036	0.037	0.036	0.011	0.033	0.042	0.036	0.065
All monazite (n=27, s=8)																	
median	**0.13**	**12.8**	**0.08**	**0.35**	**2.46**	**bdl**	**bdl**	**bdl**	**bdl**	**bdl**	**0.62**	**0.08**	**bdl**	**0.26**	**15.0**	**25.0**	**2.20**
min	0.02	10.7	bdl	0.00	0.01	bdl	bdl	bdl	bdl	bdl	0.07	0.02	bdl	0.17	8.28	19.7	1.65
max	0.86	13.4	0.27	6.75	9.96	2.82	1.68	0.01	0.13	0.11	4.45	0.72	0.02	0.64	20.6	26.7	2.68
Oxide facies-hosted monazite (n=25, s= 6)																	
median	**0.10**	**12.9**	**0.07**	**0.11**	**2.46**	**bdl**	**bdl**	**bdl**	**bdl**	**0.02**	**0.45**	**0.07**	**bdl**	**0.26**	**15.1**	**25.3**	**2.17**
min	0.02	11.3	bdl	bdl	bdl	bdl	bdl	bdl	bdl	bdl	0.07	0.02	bdl	0.17	12.9	21.3	1.65
max	0.69	13.4	0.13	6.75	9.96	0.19	0.34	0.01	0.07	0.02	1.62	0.19	0.02	0.44	20.6	26.7	2.38
Chlorite-hosted monazite (n=4, s=2)																	
median	**0.57**	**11.6**	**0.23**	**2.43**	**2.87**	**0.60**	**0.32**	**bdl**	**0.09**	**0.02**	**2.24**	**0.26**	**bdl**	**0.36**	**9.21**	**21.7**	**2.35**
min	0.28	10.7	0.06	0.15	1.23	bdl	bdl	bdl	bdl	0.02	1.27	0.13	bdl	0.22	8.28	19.7	2.09
max	0.86	12.6	0.27	4.26	6.31	2.82	1.68	0.01	0.13	0.11	4.45	0.72	0.02	0.64	11.8	26.2	2.68
Oxide facies-hosted xenotime (n=1)																	
	bdl	**15.89**	**bdl**	**bdl**	**2.80**	**bdl**	**bdl**	**bdl**	**bdl**	**0.02**	**0.02**	**0.36**	**bdl**	**39.78**	**bdl**	**bdl**	**bdl**

Table 2.10 (continued): EPMA analyses of monazite and xenotime. All values in element-wt.%. All results in Appendix G.

	Nd	Sm	Eu	Gd	Tb	Dy	Ho	Er	Tm	Yb	Lu	Cl	F	O	Total
dl	0.035	0.032	0.031	0.032	0.03	0.059	0.061	0.034	0.032	0.033	0.035	0.006	0.066		
All monazite (n=27, s=8)															
median	**9.45**	**1.26**	**0.41**	**0.57**	**bdl**	**0.09**	**bdl**	**0.02**	**bdl**	**bdl**	**bdl**	**0.04**	**0.54**	**27.6**	**99.9**
min	6.49	0.42	0.21	0.19	bdl	bdl	bdl	bdl	bdl	bdl	bdl	0.03	0.42	26.9	96.1
max	11.5	2.10	0.63	1.08	0.06	0.21	0.08	0.09	0.07	0.10	0.02	0.05	0.87	32.9	106.3
Oxide facies-hosted monazite (n=25, s= 6)															
median	**9.38**	**1.18**	**0.48**	**0.55**	**bdl**	**0.09**	**bdl**	**0.02**	**bdl**	**bdl**	**bdl**	**0.04**	**0.54**	**27.6**	**100.2**
min	6.49	0.42	0.21	0.19	bdl	bdl	bdl	bdl	bdl	bdl	bdl	0.03	0.42	27.0	96.1
max	10.3	1.44	0.63	0.86	0.02	0.20	0.08	0.07	bdl	0.10	0.02	0.05	0.61	32.9	106.3
Chlorite-hosted monazite (n=4, s=2)															
median	**9.67**	**1.70**	**0.32**	**0.86**	**bdl**	**0.20**	**bdl**	**0.05**	**bdl**	**bdl**	**bdl**	**0.04**	**0.65**	**27.9**	**99.1**
min	9.41	1.45	0.25	0.79	bdl	0.09	bdl	bdl	bdl	bdl	bdl	0.04	0.42	26.9	96.7
max	11.5	2.10	0.35	1.08	0.06	0.21	0.04	0.09	0.07	0.06	0.02	0.05	0.87	30.8	102.3
Oxide facies-hosted xenotime (n=1)															
	0.11	**0.16**	**0.35**	**0.82**	**0.15**	**2.28**	**0.77**	**2.80**	**0.44**	**2.27**	**0.37**	**bdl**	**bdl**	**34.03**	**103.5**

Notes:
dl: detection limit, bdl: below detection limit. n: number of spot analyses in s: number of thin sections

Table 2.11: EPMA analyses of other mineral species. All values in wt.%. All results in Appendices H-K.

	SiO_2	TiO_2	Al_2O_3	Cr_2O_3	V_2O_3	Fe_2O_3	MnO	MgO	CaO	ZnO	NiO	Total
dl	0.01	0.03	0.08	0.01	0.01	0.02	0.01	0.01	0.01	0.01	0.01	
Quartz (n=15, s=7)												
median	100.1	bdl	bdl	bdl	bdl	0.8	bdl	bdl	bdl	bdl	bdl	101.0
Hematite (n=7, s=1)												
median	1.17	bdl	0.19	bdl	bdl	98.9	0.01	0.14	0.02	0.02	bdl	100.5
Ilmenite (n=27, s=8)												
median	0.14	51.18	0.12	bdl	0.33	46.7	0.72	0.02	0.03	0.04	bdl	99.1
Rutile (n=1)												
median	0.17	98.64	bdl	bdl	0.69	1.5	bdl	bdl	bdl	0.04	bdl	101.1
Titanite (n=3, s=1)												
median	30.5	35.9	1.58	0.02	0.19	1.4	0.02	0.15	27.9	0.02	0.01	97.3
Fe-dolomite (n=12, s=2)												
median	0.08	bdl	bdl	bdl	bdl	10.30	1.78	16.3	28.0	0.01	bdl	56.1
Siderite (n=12, s=4)												
median	0.10	bdl	bdl	bdl	bdl	60.90	0.88	4.72	0.30	0.03	bdl	67.3

Notes:
Results for quartz and carbonates have been obtained under non-mineral specific calibration.
and are for reference only.
dl: detection limit, bdl: below detection limit. n: number of spot analyses in s: number of thin sections

Table 2.12: Compilation of data from the literature for in-situ analyses of magnetite in various BIF and other lithologies. Average values in ppm.

	Temagami	**Musselw.**	**Wutai**	**Dales G.**	**Kuruman**	**Luliang**	**Pipe Fm**	**Sokoman**	**Zankan**	**Izok Lake**	**Izok Lake**
host	Algoma	Algoma	Algoma	Superior	Superior	Superior	Superior	Superior	exhalite	exhalite	VMS
Age (Ma)	2730[a]	2970[b]	2520[c]	2470[d]	2465[e]	2200[f]	1880[g]	1880[h]	536[i]	2700[j]	2700[j]
Mg	241		*90*	*536*	*192*	*384*	40	154	625	738	3914
Al	76.1		*8030*	*1400*	*197*	*1035*	1375	127	1232	751	50.5
Si	3455	44790	*270*	*7853*	*9701*	*2360*				956	1313
P	41.9		*50*	*109*	*47*	*158*					
Ca	77.2		*280*	*192*	*229*	*208*	40	84		421	285
Sc	0.27	1.01	0.06	1.4	0.42	0.29			<1		
Ti	15.1	111	616	178	9	30	441	32	1249	1299	4.4
V	4.69	15.4	2.9	14.4	4.57	5.05	91	23.0	4747	11	
Cr	0.81	10.5	2.04	2.60	3.11	2.11	37	6.1	15.5	147	153
Mn	188	1071	137	641	35	65	469	287	2452	659	1381
Co	0.75	1.74	3.17	0.34	1.58	0.59	11.0	14.1	16.8	1.1	492
Ni	5.40	2.83	6.08	1.87	15.2	3.37	16.0	1.4	19.1	100	111
Cu	0.30	2.06	0.03	0.28	1.29	1.54	0.90	1.30			
Zn	16.4	11.1	60.2	4.54	3.16	4.02	33.8	10.0	24.1	14.4	333
Ga	0.85	2.29	3.47	4.00	0.26	0.33	8.2		44.3	12	102
Ge	7.29		11.9	6.71	42	12.6	11.2		1.57		
As	0.65	0.53									
Y	0.28	3.85					0.33		<1		
Zr	0.12	0.82					0.20			0.6	0.7
Nb	0.07	0.23					0.33			4	0.4
Mo	0.03	0.05	0.10	0.67	0.89	0.81	1.19		0.17		
Ag	0.04	0.01							<1		
Cd	0.11	0.09									
In	0.03	0.01									
Sn	1.07	0.17					1.19		6.6		
Sb	0.76	0.36									
Cs	0.06	0.43									
Ba	1.89	13.0	0.04	242	1.44	3.58			<1		
La	0.06	0.62									
Sm	0.03	0.35									
Yb	0.04	0.36									
Hf	0.02	0.02					0.01				
Ta	0.04	0.01					0.03				
W	0.25	0.31					0.09				
Pb	0.63	0.88					0.41	1.25	0.29		
Ge/Si min	34		78	31	520	49					
Ge/Si max	14000		12000	220	1900	1400					

Table 2.12: Notes

All values from LA-ICP-MS, except EPMA results in italics. Empty cells: no value available

average values for all references, median values for Temagami Oxide facies BIF

Temagami: median of n=119 magnetite analyses in oxide facies BIF, this study

Sokoman: Sokoman Iron Formation, primary magnetite, Superior-type, Canada; results from Chung (2015)

Musselw.: Musselwhite Iron Formation, mineralized, Algoma-type, Canada; results from Gourcerol et al. (2016)

Zankan: Zankan Iron Formation, Algoma type, Kunlun, China from Zhou et al. (2017)

Pipe Fm: Pipe Mine, Thompson Ni belt, Canada Thompson Ni belt from Dare et al. (2014)

Wutai, Dales Gorge, Kuruman, Luliang from Sun et al. (2017)

Izok Lake: VMS and related iron formation from Makvandi et al. (2016)

Ge/Si (in µmol/mol)

Ages: a) Ayer (2002), b) Biczok et al., 2012, c) Wilde et al. (2004), d) Pickard (2002), e) Pickard (2003),
f) Sun and Li (2017b), g) Hulbert et al. (2005), i) Zhou et al. (2017) and references therein, j) Morrison and Balint (1993)

Table 2.13: Compilation of data from the literature for in-situ analyses of chlorite and hydrothermal clay in BIF and other lithologies. Average values in wt.%.

	Temagami	Weld Range	Gebel El H.	Isua	La Palma	Noranda	TAG
mineral	**chlorite**	**chlorite**	**chlorite**	**chlorite**	**chlorite**	**chlorite**	**nontronite**
host	A	A	A-R?	A	H-M	H-M	H-A
Age (Ma)	2730[a]	~2650[b]	717[c]	3740[d]	<5[e]	~2700[f]	0
SiO_2	26.60	23.59	22.65	26.26	28.50	26.13	48.56
TiO_2	0.04	0.04	0.07	0.04	0.01	0.05	0.02
Al_2O_3	18.74	19.09	20.99	20.71	16.90	19.15	0.50
Cr_2O_3	0.01					0.03	
Fe_2O_3	0.77						34.20
FeO	31.04	33.16	40.24	23.78	23.95	23.69	
MnO	0.05	0.13	0.23	0.09	0.31	0.45	0.01
MgO	9.66	9.88	6.27	16.64	18.75	15.25	1.88
ZnO	0.02					0.06	0.26
CaO	0.01	0.07	0.06	0.02	0.35	0.18	0.03
Na_2O	0.01	0.04		0.04	0.03	0.28	0.27
K_2O	0.01	0.01	0.02	0.05	0.05	0.07	0.17
F	<0.01					0.14	
Cl	<0.01					0.04	
H_2O	10.90		10.8				
Total	99.94	86.00	101.31	87.64	88.05	85.57	100.7

Notes:

Temagami: average of 31 analyses of chlorite in 8 samples of chert and magnetite, this study.
H_2O and FeO-Fe_2O_3 calculated based on 28 oxygen assuming full crystallographic site occupancy.

Weld Range: average of n=4 chlorite analyses in 2600-2700 Ga Algoma-type BIF in the Yilgarn Craton; results from Gole (1980)

Gebel El H.: Gebel El Hadid BIF in the central Eastern Desert of Egypt. Average of 2 analyses of chlorite in oxide-facies Algoma-Rapitan intermediate-type BIF; results from Khalil et al. (2015)

Isua: Isua BIF, Greenland, average of 11 analyses of chlorite in magnetite-chert BIF; results from Dymek and Klein (1988)

La Palma: average of 6 chlorite analyses from smectite-derived hydrothermal-metamorphic chlorite in the La Palma hydrothermal seamount; results from Schiffman and Staudigel (1995)

Noranda: average of 61 chlorite analyses from ore-related hydrothermal alteration in andesites of the Blake River Group; results from Hannington et al. (2003)

TAG: average of 12 analyses of Al-poor nontronite (authigenic clay) from the TAG hydrothermal field, results from Severmann et al. (2004). Results for TAG-nontronite also included P_2O_5 (0.55 wt.%), Cu (0.1 wt.%), and LOI (12.45 wt.%; Severmann et al., 2004).

Ages: a) Ayer (2002), b) Gole (1980), c) Moghazi (2003), d) Kamber et al. (2001), e) Staudigel and Schmincke (1984), f) Corfu (1993)
Ages are depositional host lithology ages and may deviate from metamorphic/hydrothermal formation of chlorite

A: Algoma-type BIF, R: Rapitan-type BIF, H-M: Hydrothermal-metamorphic, H-A: Hydrothermal-authigenic

Table 2.14: Compilation of data from the literature for apatite in-situ analyses compared to Temagami BIF apatite.

	Temagami	Temagami	Temagami	Kirkland-L.	Durango	Dales Gorge	Howard's P.
host	**A-oxide**	**A-oxide**	**A-chlorite**	**M**	**H**	**S**	**H-SW**
Age (Ma)	2730[a]	2730[a]	2730[a]	2714[b]	30[c]	2479[d]	442[e]
mineral	Type 1 apatite	Type 2 apatite	Type 3 apatite	apatite	apatite	apatite	apatite
Ca [wt.%]	*39.3*	*39.2*	*39.3*		*39.1*		*38.5*
P [wt.%]	*18.4*	*18.2*	*18.1*		*18.0*		*17.5*
Al [wt.%]	*<0.005*	*<0.005*	*0.022*		*0.003*		
Si [wt.%]	*<0.005*	*0.073*	*0.073*		*0.153*		*0.10*
Fe [wt.%]	*0.17*	*1.23*	*0.56*		*0.08*		
Mg [wt.%]	*<0.005*	*<0.005*	*0.04*	*0.10*	*0.013*		*<0.01*
Na [wt.%]	*0.05*	*0.05*	*0.18*		*0.165*		*<0.04*
K	8.79	6.77	6.96		11.5		
S	554	416	422		1846		*245*
Sr	1675	4188	504	4172	513		361
Mn	313	276	487	181	97.0		
Li	1.83	2.24	1.73				
B	4.75	5.51	3.68		11		
Sc	0.30	0.77	0.41				
Ti	0.83	1.23	5.15				
V	0.06	0.07	9.92	23.1	44.6		
Cr	1.08	1.01	0.98				
Co	0.09	0.19	0.35		1.59		
Ni	0.43	0.98	0.55				
Cu	0.37	0.36	0.82	58.2	1.11		
Zn	0.38	5.68	2.85		1.88		
Ga	0.15	0.05	0.43		0.90		
As	68.5	5.13	6.06	51.7	1242		
Rb	0.25	0.17	0.12		0.30		
Y	1042	818	433	414	670	896	221
Zr	0.09	0.10	1.83	6.91	0.343		
Nb	0.01	0.03	0.03		0.060		
Sb	0.41	0.18	0.13				
Cs	0.09	0.07	0.06				
Ba	6.11	1.82	4.40	32.3	1.81		263
La	180	42.7	624	1971	3879	159	177
Ce	362	187	1933	4085	4773	206	245
Pr	45.5	38.9	263	468	368	23.4	43
Nd	186	241	1094		1174	103	166
Sm	52.7	123	201	273	162	19.4	33.1
Eu	62.2	105	22.5	56.4	15.6	7.94	7.25
Gd	87.0	176	161	198	149	35.6	33.2
Tb	14.5	21.6	18.9		16.6	5.63	4.47
Dy	113	138	99.8	91.0	107	49.3	27.5
Ho	26.7	25.2	16.8		19.3	13.1	5.47
Er	79.6	58.0	37.1		53.4	52.5	15.1
Tm	10.4	6.75	4.08		6.56		1.79
Yb	57.6	36.1	21.1	18.4	39.4	44.6	9.26
Lu	8.21	4.95	2.52		4.89		1.27
Pb	22.3	26.96	4.87	54.1	0.61		
Th	0.12	0.027	8.27	70.1	222		
U	0.32	0.350	3.95	10.2	10.0		
Cl [wt.%]	*<0.006*	*0.02*	*0.06*		*0.40*		*0.025*
F [wt.%]	*2.6*	*2.9*	*3.1*		*4.32*		*4.00*
O [wt.%]	*38.5*	*38.7*	*38.4*				

Table 2.14: Notes

All results from EPMA analyses (italics, wt.% indicated) and LA-ICP-MS (all other results, in ppm).

Average values for all references, median values for Temagami Oxide facies BIF.

Temagami Type 1 apatite: median of n=10 EPMA analyses in 3 samples, and n=20 LA-ICP-MS analyses in 1 sample.

Temagami Type 2 apatite: median of n=6 EPMA analyses in 2 samples, and n=11 LA-ICP-MS analyses in 2 samples.

Temagami Type 3 apatite: median of n=7 EPMA analyses in 2 samples, and n=2 LA-ICP-MS analyses in 1 sample. See text for limitations on F quantification by EPMA.
All Temagami results from this study.

Kirkland L.: averages of 5 LA-ICP-MS analyses in 5 samples of magmatic-hydrothermal apatite in clinopyroxenite and orogenic Au-related and unmineralized igneous lithologies from Kirkland Lake;
results from Mao et al. (2016).

Durango: averages of 218 LA-ICP-MS analyses in 1 sample of apatite standard Durango from Kiruna-type iron ore;
results from Mao et al. (2016)

Dales Gorge: one analysis of apatite in the BIF0 sample of the Dales Gorge member in the Hamersley BIF;
results from Alibert (2016)

Howard's P.: averages of 82 LA-ICP-MS analyses in 10 samples and 51 EPMA analyses in 5 samples from the Howard's Pass SEDEX deposit, samples from the mineralized zone and host lithologies.
Apatite is interpreted as hydrogenous in origin; results from Gadd et al. (2016).

Ages: a) Ayer (2002), b) Corfu (1993), c) Swanson et al (1978), d) Pickard (2002), e) Abbott et al. (1986)

A- Algoma-type BIF, S- Superior-type BIF, M- magmatic, H- hydrothermal, SW- hydrogenous

Table 2.15: Compilation of data from the literature for REE-phosphate in situ analyses compared to Temagami BIF.

host-facies	Temagami A-oxide	Temagami A-chlorite	Adams A-oxide	West Rand S-oxide	Skiddaw M-H	Temagami A-oxide	West Rand S-oxide
Age (Ma)	2730[a]	2730[a]	2711[b]	~2950[c]	~425[d] *	2730[a]	~2950[c]
mineral	monazite	monazite	monazite	monazite	monazite	xenotime	xenotime
Ca	0.10	0.57	0.18	0.24	0.28	<0.01	0.20
P	12.9	11.6	12.5	12.6	12.4	15.9	14.6
Sr	0.07	0.23				<0.02	
Si	0.11	2.43		1.32	0.11	<0.01	0.97
Fe	2.46	2.87		2.04	<0.31	2.80	2.19
U	0.02	0.02		0.01	0.00	0.02	0.01
Th	0.45	2.24		0.71	2.56	0.02	0.01
Pb	0.07	0.26		0.08	0.03	0.36	0.34
Y	0.26	0.36	0.40	0.39	0.25	39.78	34.2
La	15.1	9.21	20.8	13.4	15.8	<0.04	<0.01
Ce	25.3	21.7	23.8	25.6	29.0	<0.04	0.03
Pr	2.17	2.35	2.53	2.80	2.71	<0.07	0.03
Nd	9.38	9.67	7.85	11.1	9.69	0.11	0.17
Sm	1.18	1.70	1.01	1.64	1.37	0.16	0.36
Eu	0.48	0.32	0.57	0.39		0.35	0.28
Gd	0.55	0.86	0.48	0.95	<0.78	0.82	1.78
Tb	<0.03	<0.03		0.11		0.15	0.43
Dy	0.09	0.20		0.33	0.16	2.28	3.58
Ho	<0.06	<0.06		0.01		0.77	0.92
Er	0.02	0.05		0.02	0.01	2.80	3.02
Tm	<0.03	<0.03				0.44	
Yb	<0.03	<0.03	0.02	0.10	0.00	2.27	2.23
Lu	<0.04	<0.04		<0.01		0.37	0.34
Cl	0.04	0.04				<0.006	
F	0.54	0.65	1.08			<0.07	

Notes:

All results from EPMA analyses in wt.%.

average values for all references, median values for Temagami Oxide facies BIF

Temagami oxide facies monazite: median of 21 analyses in 5 samples.

Temagami chlorite facies monazite: median of 5 analyses in 2 samples.

Adams: average of 6 analyses of monazite from the Adams mine central pit; results from Bowins and Crocket (2011).

West Rand monazite: average of 10 monazite analyses in 8 samples from 4 Superior-type BIF horizons in the Witwatersrand- and Pongola Supergroups between ~2985 and ~2914 Ma; results from Smith et al. (2008).

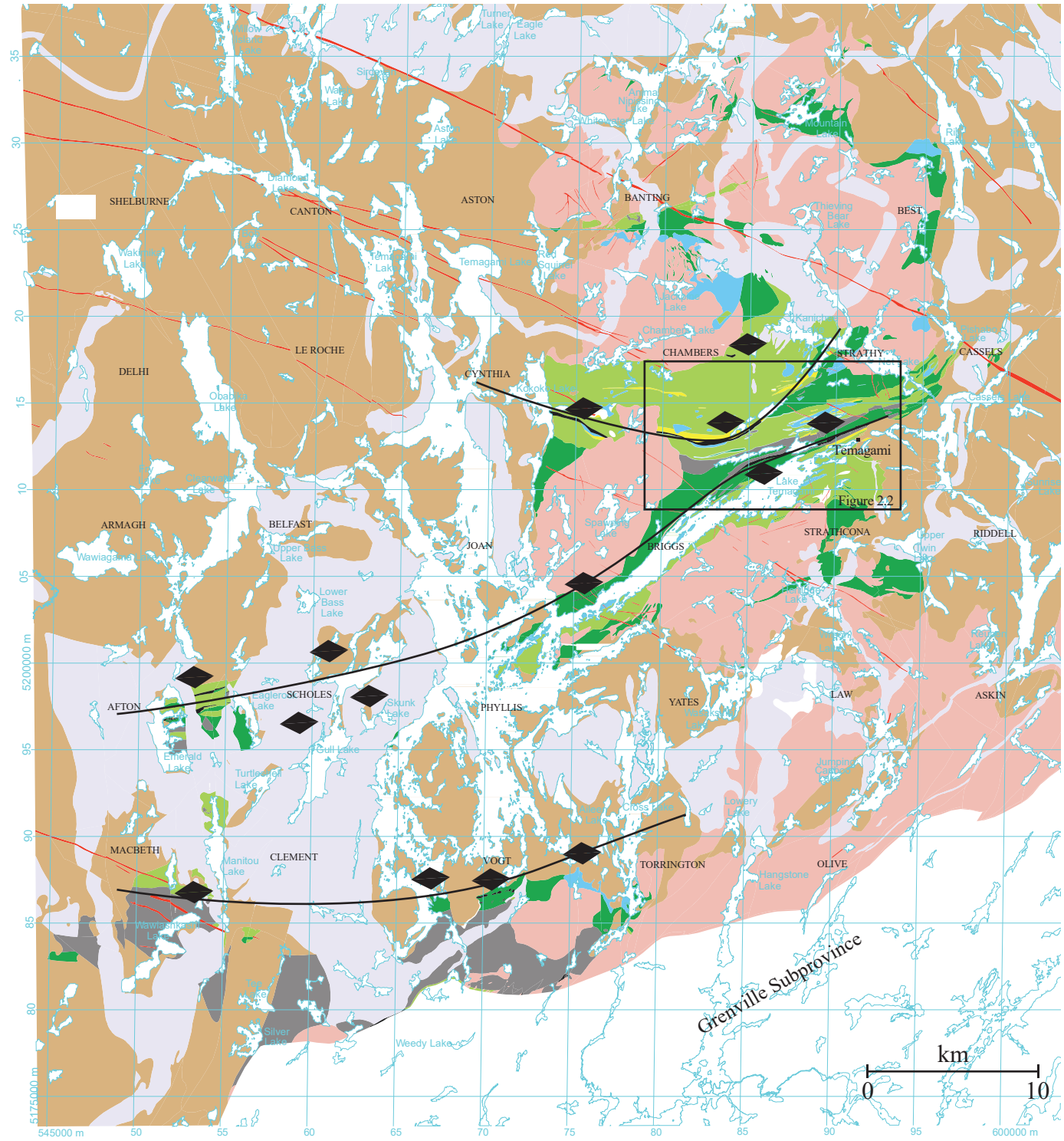
Skiddaw: EPMA and LA-ICP-MS analyses of hydrothermal monazite in one sample of greisenized granite, Lake District, NW England; results from Poitrasson et al. (2000).

Temagami oxide facies xenotime: 1 analysis from oxide BIF; this study.

West Rand xenotime: average of 8 xenotime analyses in 8 samples from 4 Superior-type BIF horizons in the Witwatersrand- and Pongola Supergroups between ~2985 and ~2914 Ma; results from Smith et al. (2008).

Ages: a) Ayer (2002), b) Nunes et al. (1978), c) Smith et al. (2013), d) Poitrasson et al. (2000), approximate alteration age from monazite Th-Pb dating.

A- Algoma-type BIF, S- Superior-type BIF, M- magmatic, H- hydrothermal, SW- hydrogenous



LEGEND

Inferred BIF horizon

BIF Occurence

VOGT Township

PROTEROZOIC

Diabase Dikes

Nipissing-type Intrusive Rocks

Huronian Sedimentary Rocks

NEOARCHEAN

Felsic Intrusive Rocks

Mafic-Ultramafic Intrusive Rocks

Iron Formation

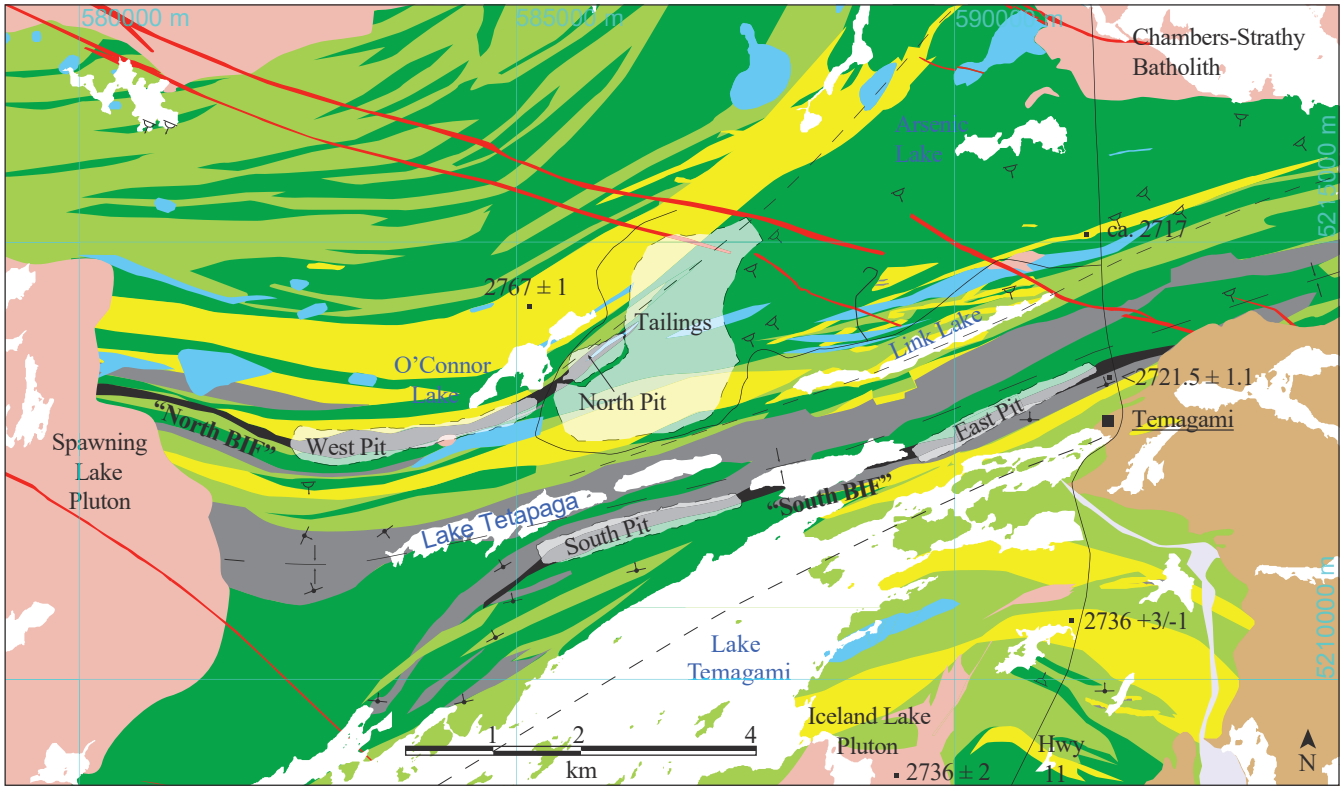
Clastic Metasedimentary Rocks

Felsic Metavolcanic Rocks

Intermediate Metavolcanic Rocks

Mafic Metavolcanic Rocks

Figure 2.1: Location and geologic overview of the Temagami Greenstone Belt between the Grenville Front in the southwest and the Cobalt embayment in the north. Reported occurrences of BIF and the minimum extent of the Temagami iron formations inferred from Ontario Geological Survey aeromagnetics maps (Ontario Geological Survey Map 60090, 2001) are indicated. Base geology simplified after Ayer et al. (2006). BIF occurrences after Simony (1964), Meyn (1977), Bennett (1978), McBride (2010).



LEGEND

PROTEROZOIC

- Diabase Dikes
  Sudbury-type (1238 Ma)
- Mafic Intrusive Rocks
  Nipissing-type: diabase, granophyre (2200 Ma)

INTRUSIVE CONTACT

- Sedimentary Rocks
  Gowganda Formation (2300 Ma)

NEOARCHEAN

- Felsic Intrusive Rocks
  Monzonite, trondhjemite, granodiorite, porphyry
- Mafic Intrusive Rocks
  Diorite, gabbro

INTRUSIVE CONTACT

- Chemical Metasedimentary Rocks
  Iron formation: oxide, sulfide, silicate facies
- Clastic Metasedimentary Rocks
  Argillite, wacke, conglomerate
  Arenitic sandstone, mudstone
- Felsic Metavolcanic Rocks
  Massive rhyolite flows
  Tuff, lapili tuff, pyroclastic breccia
- Intermediate Metavolcanic Rocks
  Massive-, pillowed-, variolitic flows
  Hyaloclastite, flow breccia
  Tuff, lapili tuff, pyroclastic breccia
- Mafic Metavolcanic Rocks
  Massive-, pillowed-, variolitic basaltic flows
  Hyaloclastite, flow breccia,
  Tuff, lapili tuff, tuff breccia

SYMBOLS

- Pillowed flow, with facing
- Sedimentary bedding, with facing
- Syncline, inferred
- Fault, deformation zone
- Road: Highway, mine access road
- ▪2736 Geochronological age in Ma (Ayer et al., 2006)

COORDINATE SYSTEM
UTM zone 17N, NAD27

REFERENCES:

Ayer, J.A., Chartrand, J.E., Grabowski, G.P.D., Josey, S., Rainsford, D., and Trowell, N.F. 2006. Geological compilation of the Cobalt-Temagami area, Abitibi greenstone belt, Ontario Geological Survey, Preliminary Map P. 3581, scale 1:100000

Bennett, G. 1978. Geology of the Northeast Temagami Area, District of Nipissing; Ontario Geological Survey Report 163, 128p. Accompanied by Maps 2323 and 2324, scale 1 inch to 1/2 mile (1:31,680), and 1 chart.

Johnston, M.M. 1987. Stratigraphy and geochemistry of a portion of the Temagami Greenstone Belt, northeastern Ontario. Unpublished MSc thesis. Laurentian University, Sudbury, ON. 123p.

Figure 2.2: Geologic map of the central part of the Temagami Greenstone Belt. Lithologies compiled after Bennett (1978), Johnston (1987) and this study. Ages from Ayer et al. (2006) and references therein. Archean lithologies dip subvertically in all areas of the map (dip angles omitted from bedding symbols, for details see Bennett, 1978), forming two limbs of the isoclinal Tetapaga synform. However, the location of the fold axis and repetition of the units has been poorly documented. BIF horizons are considered independent units, not fold repetitions (Bennett, 1978; see text for discussion and Figure 2.3).

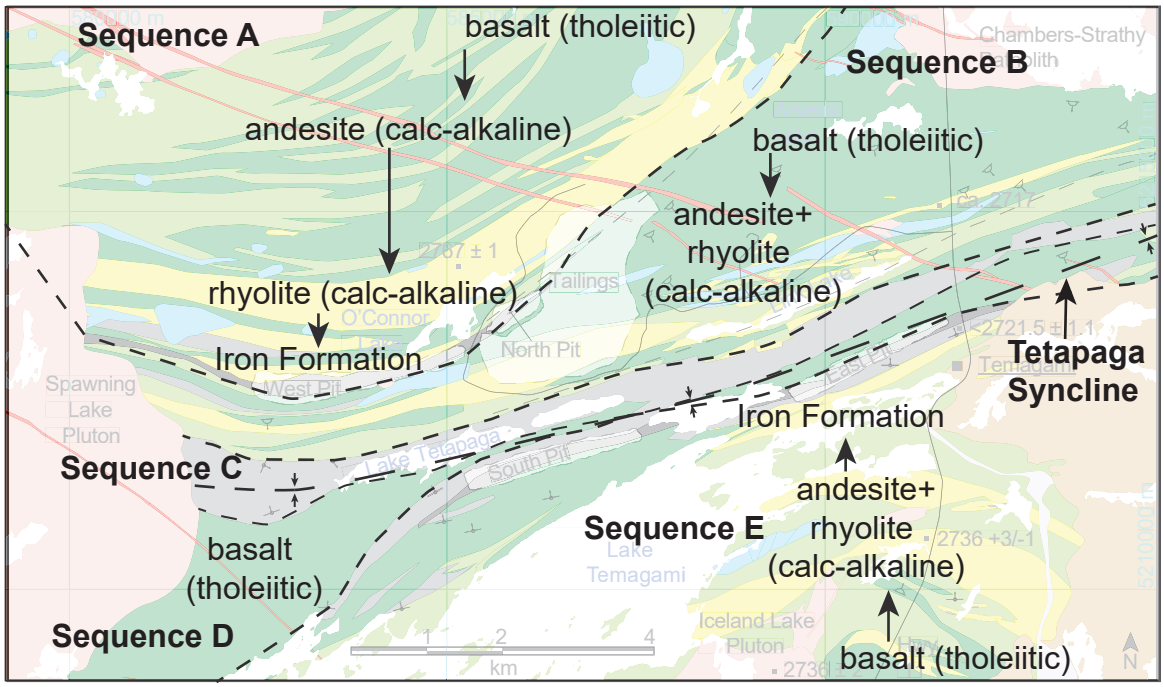


Figure 2.3: Interpreted stratigraphic succession of the Temagami Greenstone Belt A and E are approximately stratigraphically equivalent on opposite sides of the proposed Tetapaga syncline (note the opposing younging directions). Both sequences have tholeiitic, pillowed Fe-rich basalts at their base (partly outside the map area), transitioning to more felsic and calc-alkaline lithologies and capped by BIF on top of the sequence. The younging directions of the middle sequences (B and D) are not as clearly defined but they are dominated by tholeiitic basalts with few felsic rocks. Sequence C is dominated by clastic metasedimentary rocks and partly contained within the Tetapaga Syncline in its central part, but the location of the fold axis is not well constrained. The BIF in sequences A and E are not equivalent on either side of the syncline, but occur in different stratigraphic positions within their sequence. Map overlay modified from Fyon and Crocket (1989).

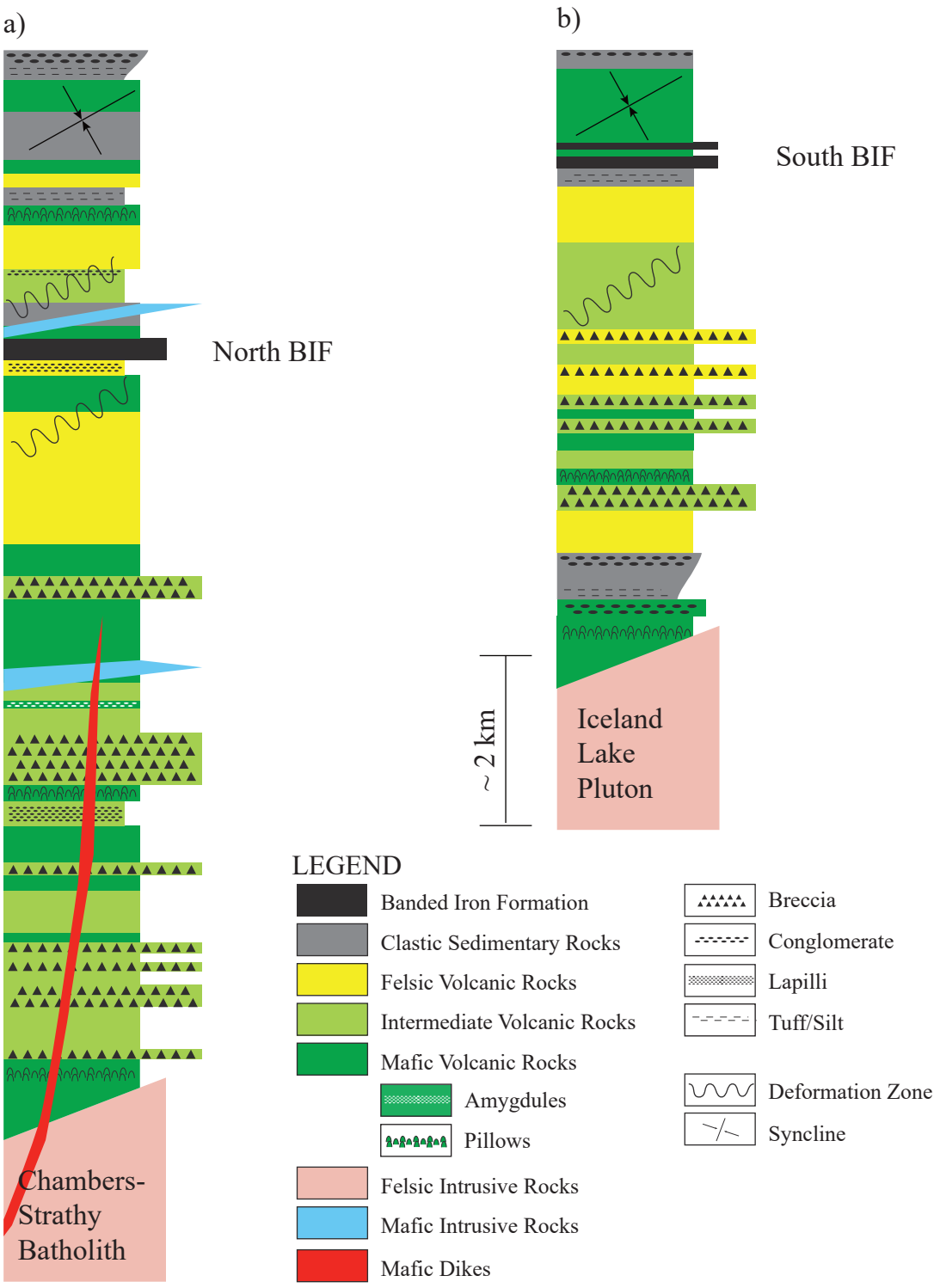


Figure 2.4: Generalized stratigraphic columns containing the North BIF and South BIF of the Temagami Greenstone Belt (cf., North BIF and South BIF horizons in Figure 2.2). a) N-to-S section from the Chambers-Strathy Batholith to the Tetapaga Syncline stratigraphically above the North BIF. b) S-to-N section from the Iceland Lake Pluton to the Tetapaga Syncline stratigraphically above the South BIF. Note the opposing younging directions in the study area. The Chambers-Strathy batholith and Iceland Lake Pluton have intrusive contacts with volcanic lithologies but may be synvolcanic (see text for discussion). The stratigraphic column in a) is based on the geological map by Bennett (1978) and mapping undertaken during this study; the column in b) is based on Bennett (1978) and the stratigraphic study by Johnston (1987).

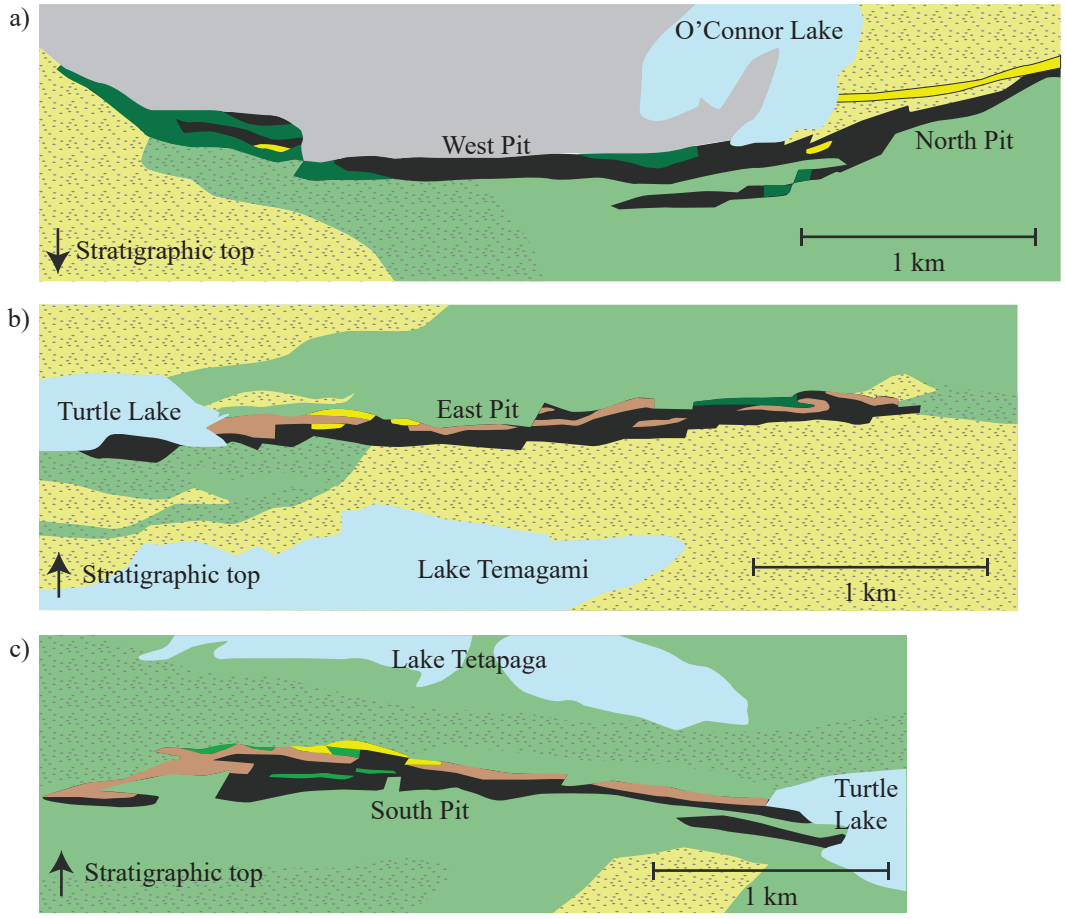


Figure 2.5: Distribution of BIF facies in the Sherman Mine area. a) North BIF in the Sherman Mine North Pit and West Pit, b) South BIF in the Sherman Mine East Pit, c) South BIF in the Sherman Mine South Pit. Oxide facies BIF was dominant, with intercalated silicate (chlorite) and carbonate facies. No systematic changes are evident in the distribution of the BIF facies in the mine area, but sulfide facies BIF and sulfidic shale is mostly present along the contacts between BIF and volcanic host rocks and north of the North BIF. Carbonate facies BIF is almost completely absent in the North BIF. In the South BIF, areas identified as "carbonate facies" are, in fact, mostly chert-magnetite with less Fe-carbonates. North is to the top in all panels. Adapted from Gross (2005) with additions from Bennett (1978), Campbell (1978), and this study.

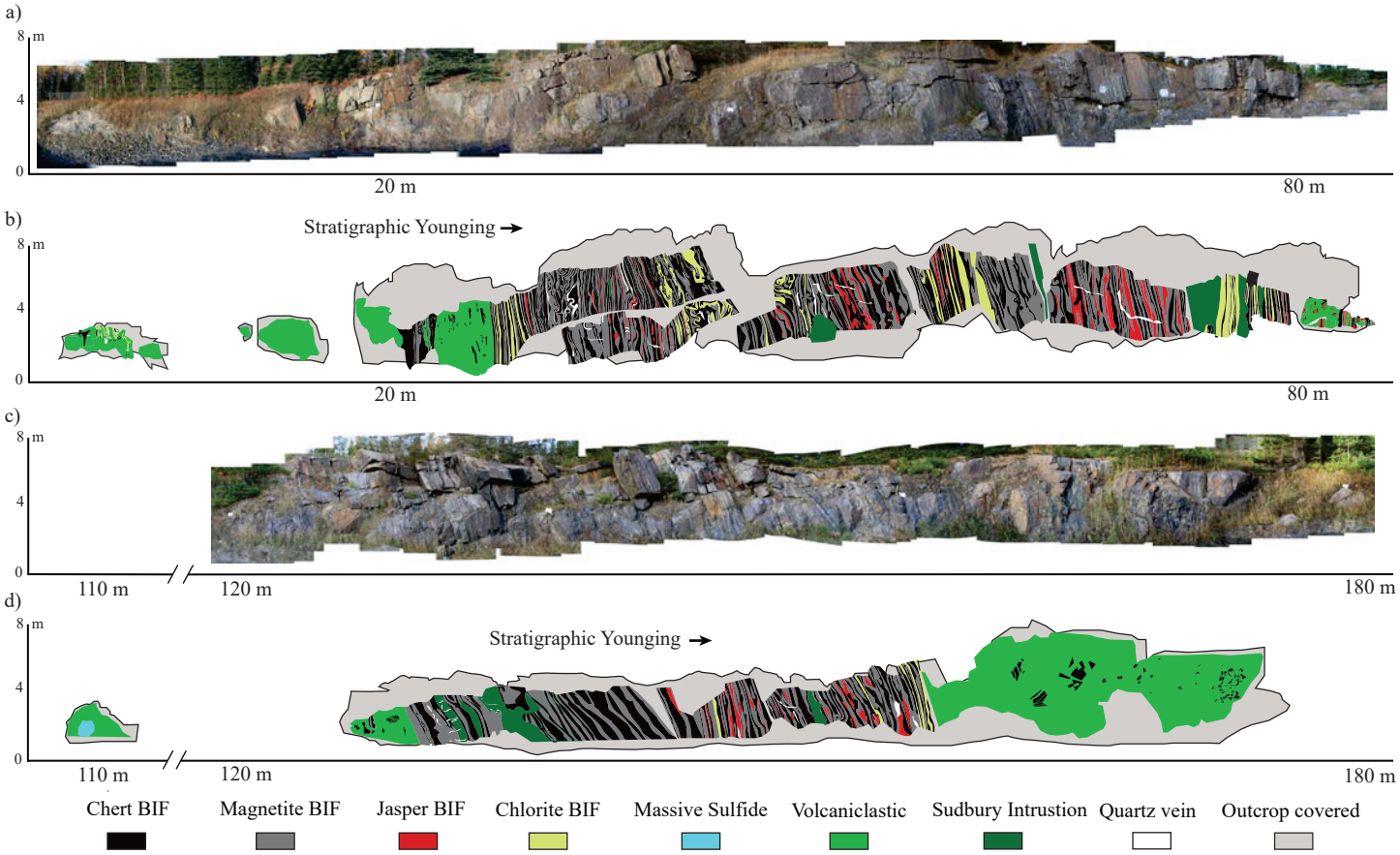


Figure 2.6: Photomosaic and lithological section of the Hwy 11 outcrop of the South BIF north of the town of Temagami. The entire exposure is 180 m in length. a) and b) are the southern, stratigraphically lower part; b) and c) are the northern, stratigraphically higher part. The steeply northward dipping oxide BIF consists of a chert-magnetite-jasper assemblage, interlayered with chlorite layers (silicate BIF). BIF deposition occurred between felsic volcaniclastic units in the footwall and mafic volcanic and volcaniclastic units in the hanging wall. North is towards the right in all panels. From Diekrup et al. (2018).

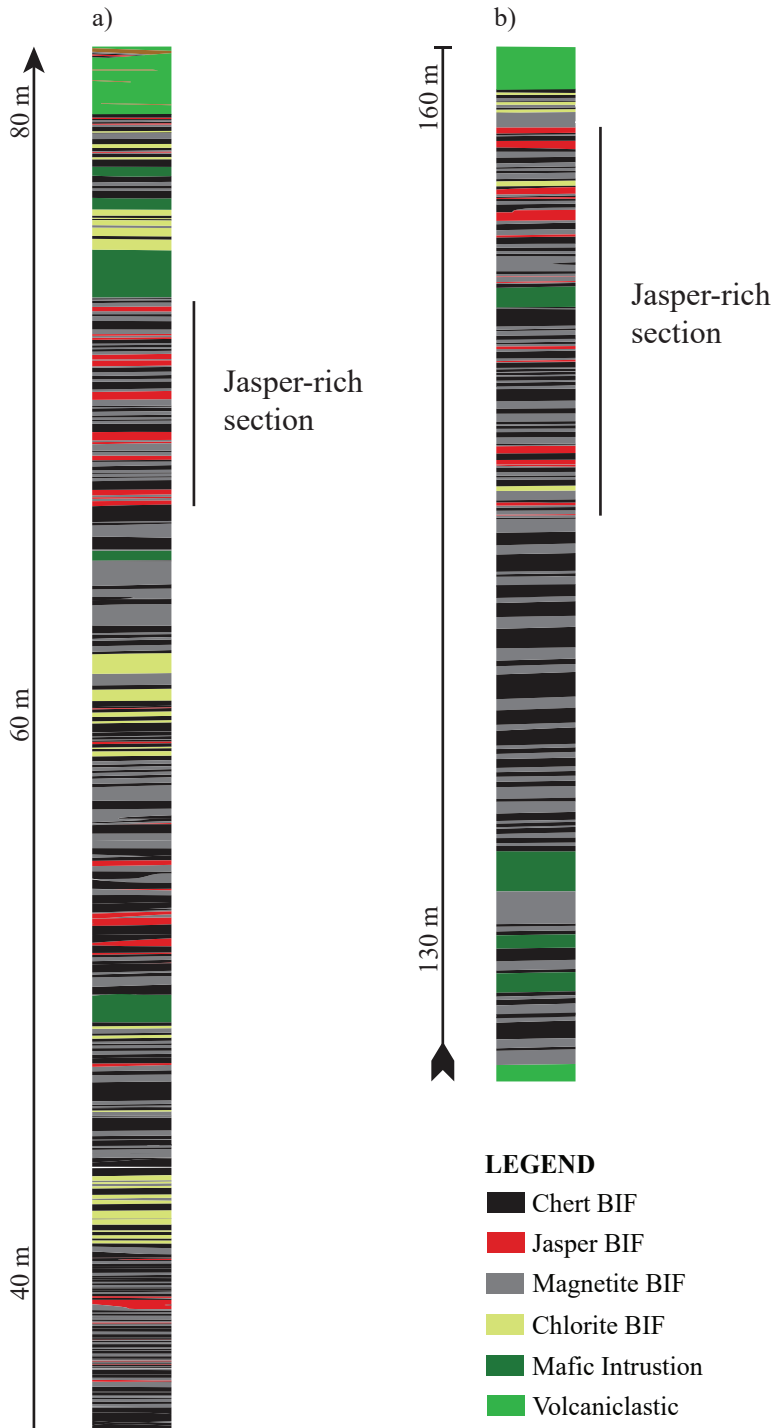


Figure 2.7: Simplified lithostratigraphic column of the South BIF along the S-to-N section of the Hwy 11 outcrop. a) and b) are the northern and southern parts of the South BIF, respectively, shown in Figure 2.6. Only the dominant BIF facies at the m-scale are shown, although individual units contain many cm- and mm-scale interlayers. Note the increase in the abundance of jasper-rich units towards the top of each section. The two sections are interrupted by mafic volcanic rocks for about 60 m in the middle part. From the outcrop map in Diekrup et al. (2018).

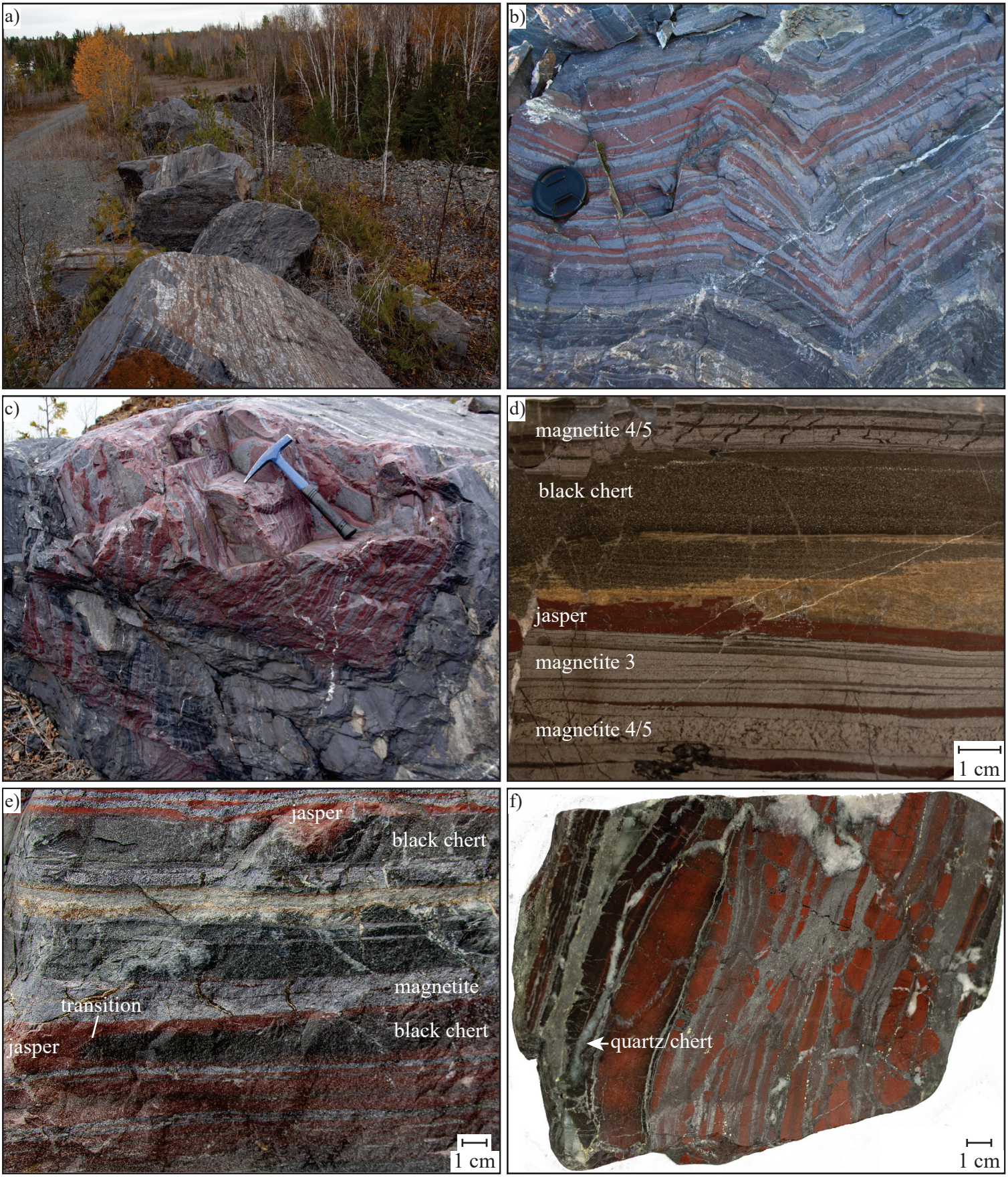

a)
b)
c)
d)
magnetite 4/5
black chert
jasper
magnetite 3
magnetite 4/5
1 cm
e)
jasper
black chert
magnetite
transition
black chert
jasper
1 cm
f)
quartz/chert
1 cm

Figure 2.8: Field and hand sample photographs of different BIF facies represented in the Sherman Mine. a) Some of the nearly 600 blocks of BIF left behind around the rims of the open pits in the Sherman Mine. b) Typical ore block with distinctive cm-scale chert-magnetite-jasper layering. Visible in the layers are synsedimentary deformation features, such as flame structures, boudinage, and partial replacement of jasper layers by magnetite. Lens cap for scale. c) Ore block showing distinctive burgundy-coloured jasper transitioning to black chert. Close inspection of the contact between magnetite and jasper shows that the jasper is everywhere replaced by magnetite, leaving a large relict of jasper at the center of the block. Hammer for scale. d) Polished slab of chert-jasper-magnetite-silicate-BIF. Type 3 magnetite layers show ultrafine, wispy layering, whereas coarser-grained Type 4 and 5 magnetite layers show brecciation and extension. e) Close up photograph of hematite in jasper layers replaced by magnetite, producing black chert. Transitions occur laterally along layers and vertically. f) Polished slab of partially replaced jasper layers in magnetite. Note how magnetite has invaded but not completely replaced the jasper bands. Late-stage quartz veins and pods occur within and cut the layers.

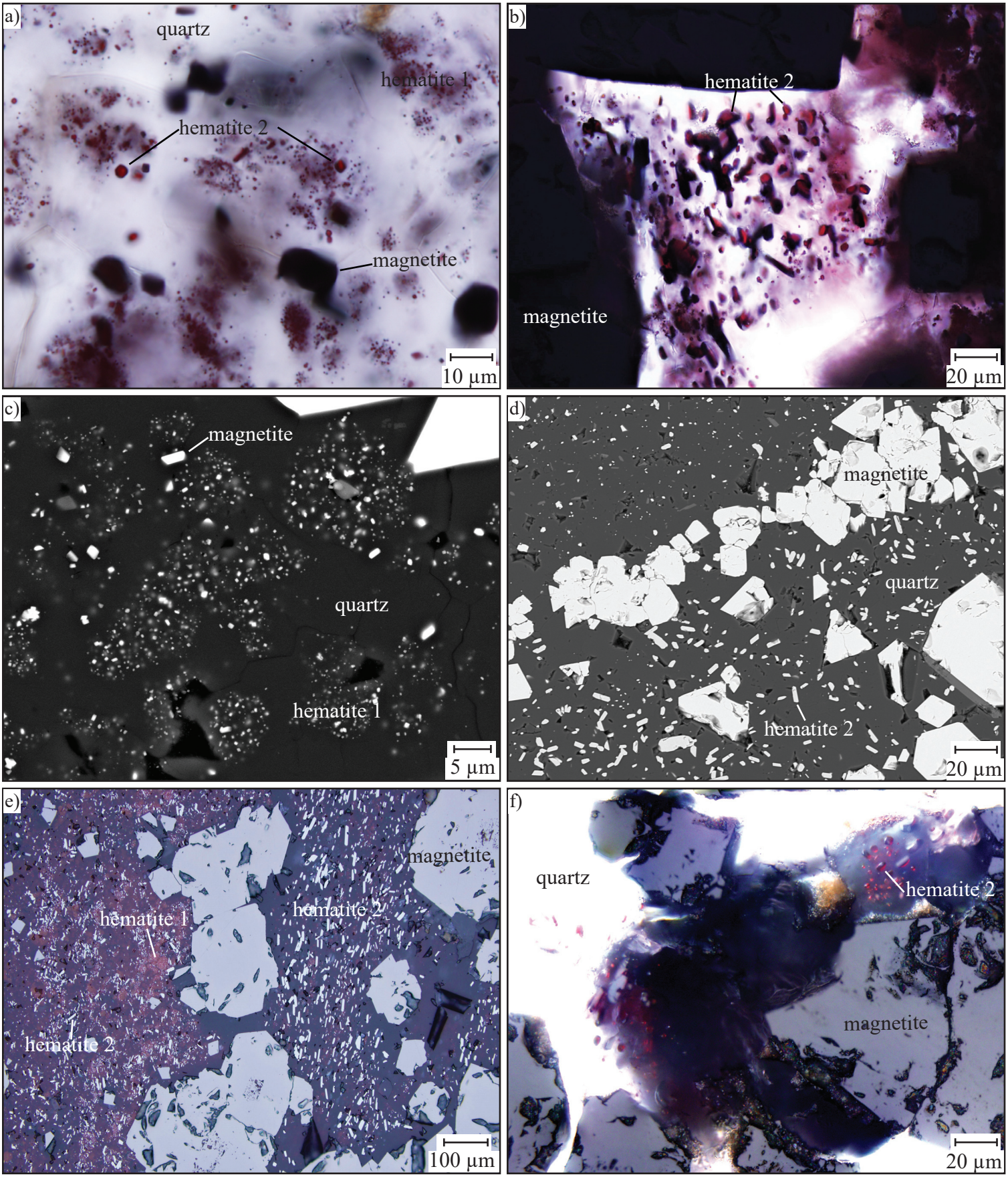

a)
quartz
hematite 1
hematite 2
magnetite
10 µm
b)
hematite 2
magnetite
20 µm
c)
magnetite
quartz
hematite 1
5 µm
d)
magnetite
quartz
hematite 2
20 µm
e)
magnetite
hematite 1
hematite 2
hematite 2
100 µm
f)
quartz
hematite 2
magnetite
20 µm

Figure 2.9: Characteristics of early Type 1 and Type 2 hematite. a) PPL (plane polarized light) transmitted light photomicrograph of fine, dusty Type 1 hematite (sample SM052). b) PPL transmitted light photomicrograph of larger, translucent Type 2 hematite in quartz-filled interstitial spaces of Type 3 magnetite (sample SM18). c) BSE image of nm-scale Type 1 hematite in quartz (sample SM11). Note the lower abundance of Type 1 hematite in domains of more crystalline quartz. d) BSE image of μm-scale Type 2 hematite in the quartz-filled interstitial spaces between Type 3 magnetite (sample 11-11). e) Reflected light photomicrograph of Type 1 and Type 2 hematite (sample SM18). Type 2 hematite crystals are elongated parallel to macroscopic banding (vertical in the image). f) Combined transmitted and reflected light photomicrograph of Type 2 hematite in the quartz-filled interstitial spaces of Type 3 magnetite. Translucent Type 2 hematite occurs in smaller clusters up to ~1 μm. Note: Optics are adjusted to observe a larger depth of field "into" the thin section and not only the surface.

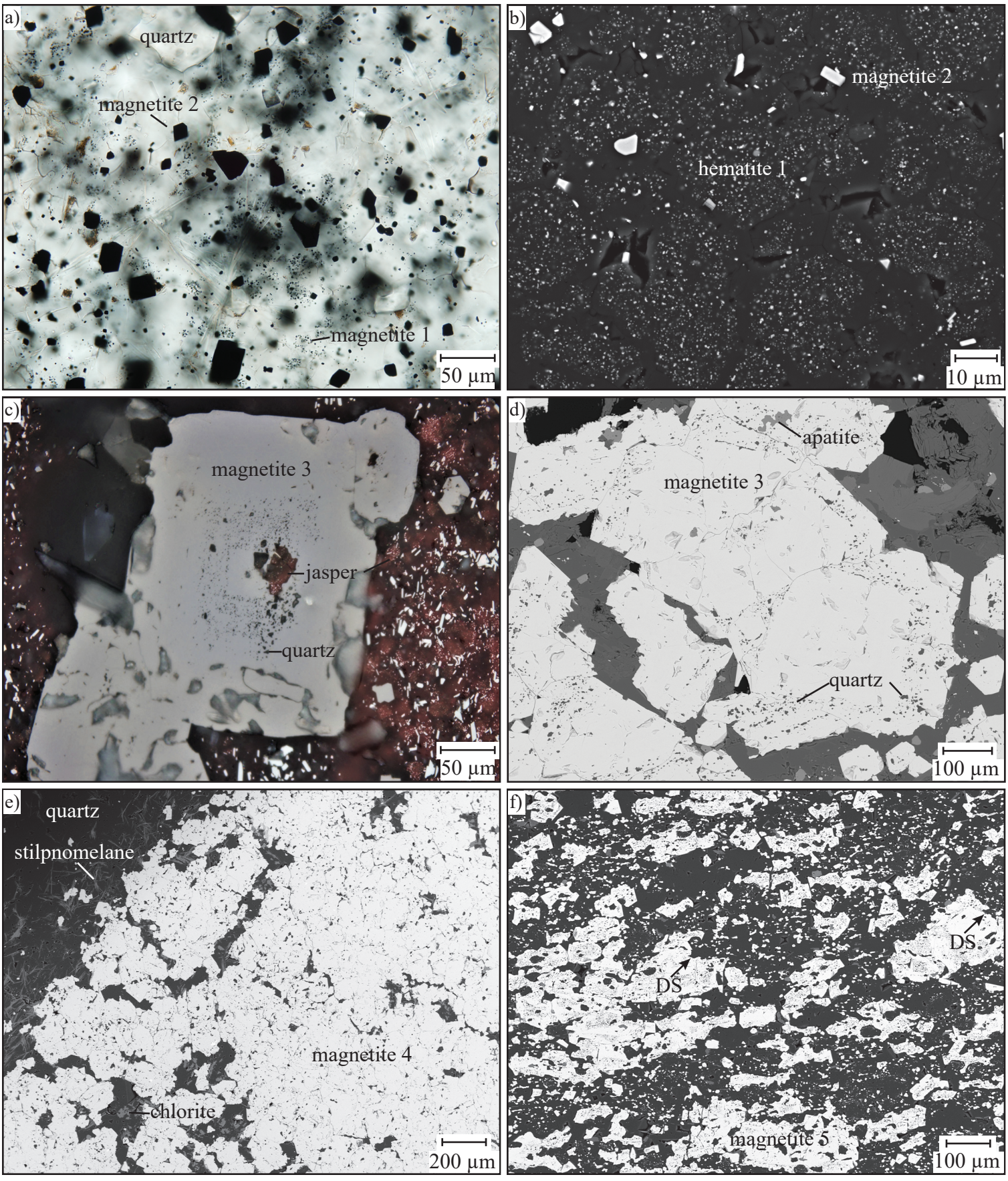

a)
quartz
magnetite 2
magnetite 1
50 µm
b)
magnetite 2
hematite 1
10 µm
c)
magnetite 3
jasper
quartz
50 µm
d)
apatite
magnetite 3
quartz
100 µm
e)
quartz
stilpnomelane
magnetite 4
chlorite
200 µm
f)
DS
DS
magnetite 5
100 µm

Figure 2.10: Characteristics of Types 1, 2, 3 and 4 magnetite. a) PPL transmitted light photomicrograph, showing clusters of fine, dusty Type 1 magnetite and larger Type 2 magnetite in quartz between the clusters. b) BSE image of crystals of Type 2 magnetite in the spaces between jasper spherules containing Type 1 hematite (see text for description). c) Reflected light photomicrograph of a Type 3 magnetite in a jasper layer in sample SM18. Note the complex structure of the magnetite, including abundant inclusions and a core of unreplaced jasper. d) BSE image of a large Type 3 magnetite crystal showing the complex structure, and abundant quartz and apatite inclusions in the outer rim (sample SM11). e) BSE image of massive Type 4 magnetite in contact with chert (sample D015). Chlorite, stilpnomelane, and quartz occur in the pore spaces of the magnetite. f) BSE image of skeletal Type 5 magnetite in sample B013. Note the abundant quartz inclusions and corroded and dissolved grain boundaries (DS). The black matrix consists of quartz with minor stilpnomelane, chlorite, and apatite.

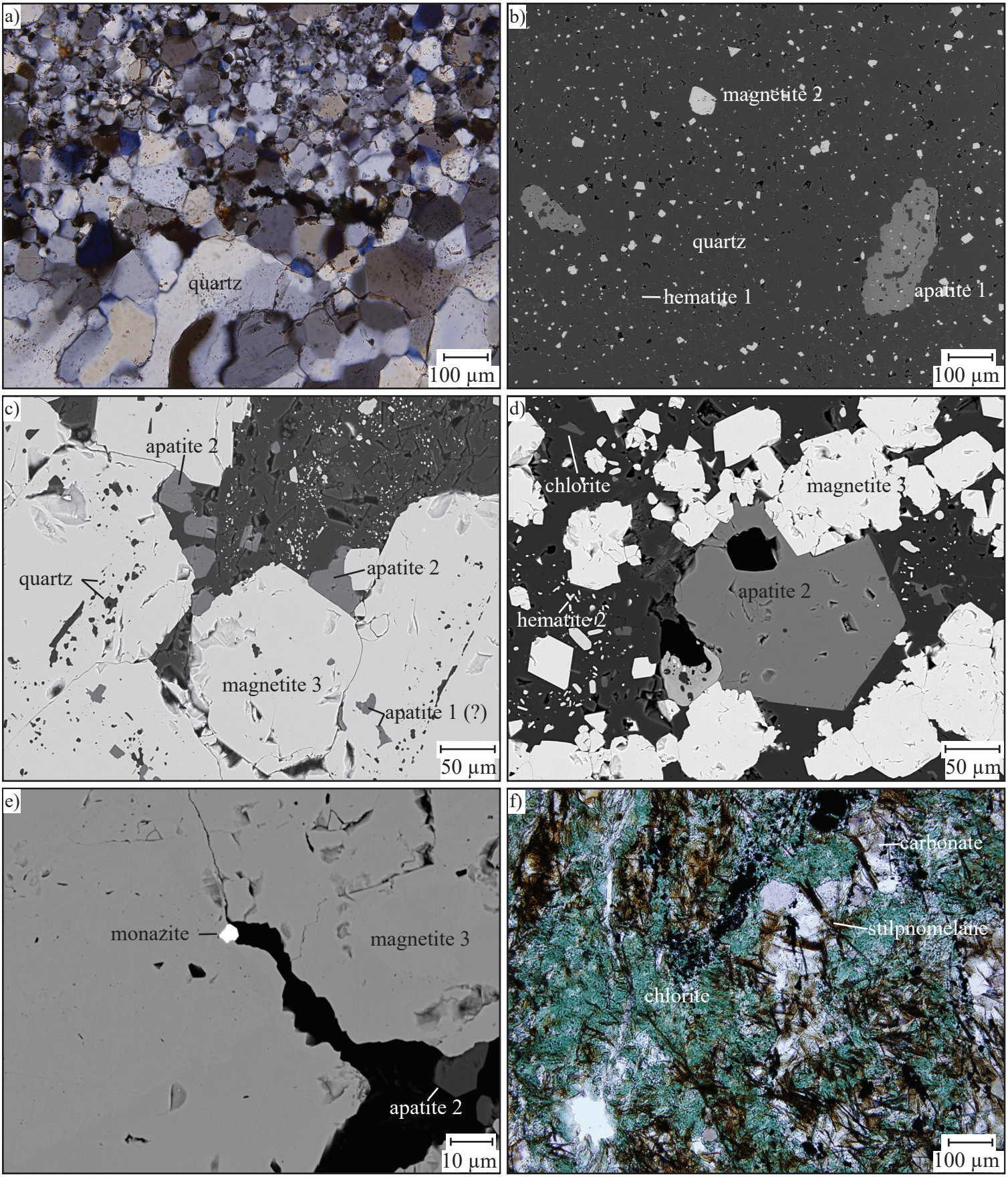

a)
quartz
100 µm
b)
magnetite 2
quartz
hematite 1
apatite 1
100 µm
c)
apatite 2
quartz
apatite 2
magnetite 3
apatite 1 (?)
50 µm
d)
chlorite
magnetite 3
apatite 2
hematite 2
50 µm
e)
monazite
magnetite 3
apatite 2
10 µm
f)
carbonate
stilpnomelane
chlorite
100 µm

Figure 2.11: Quartz and accessory minerals in magnetite, chert, and chlorite layers. a) PPL transmitted light photomicrograph of quartz in a white chert layer, showing its bimodal grain size distribution (sample 11-41). Coarse quartz grains (50-100 μm) are common in white chert; finer quartz is more common intergrown with Type 2 magnetite in black chert. b) BSE image of Type 1 apatite in a jasper layer in sample SM052. c) BSE image of Type 2 apatite in the interstitial spaces of, and overgrowing Type 3 magnetite. Apatite inclusions in Type 3 magnetite may be earlier Type 1 apatite. d) Very large, euhedral Type 2 apatite overgrowing Type 3 magnetite in sample 11-11. Note the trace chlorite with hematite in the interstices of the large magnetite grains, recrystallized from precursor ash particles and jasper spherules, respectively. e) BSE image of a single monazite grain in the interstitial space of Type 3 magnetite (sample 11-11). Monazite is rarely found as inclusions, but in the interstitial spaces of magnetite, likely as a result of authigenic growth during late stages of paragenesis. f) Silicified volcaniclastic materials containing chlorite and stilpnomelane (sample 11-37) represent the metamorphic products of altered volcanic-derived material. Traces of the same material yield trace chlorite in oxide-facies BIF.

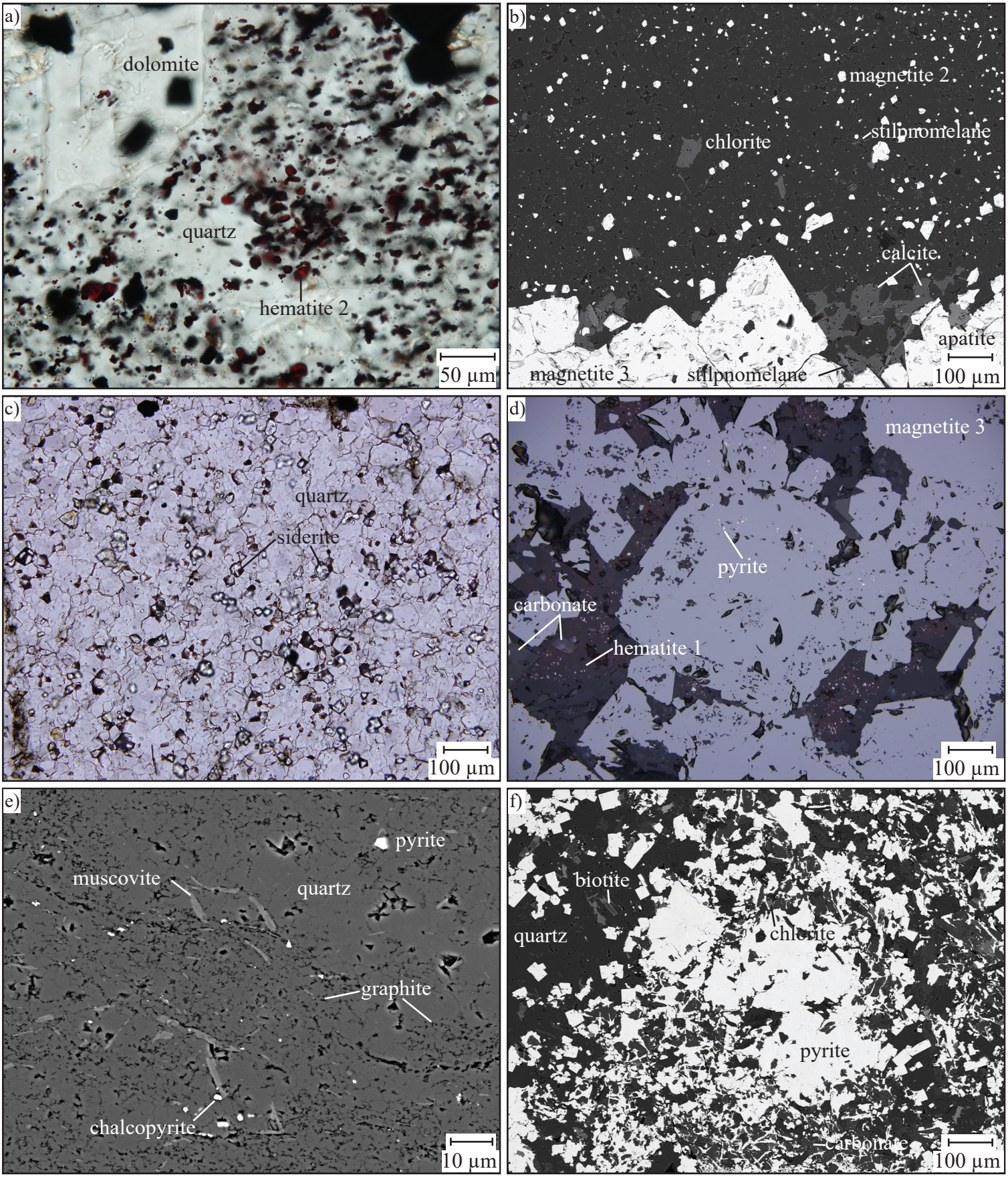

a)
dolomite
quartz
hematite 2
50 µm
b)
magnetite 2
chlorite
stilpnomelane
calcite
apatite
magnetite 3
stilpnomelane
100 µm
c)
quartz
siderite
100 µm
d)
magnetite 3
pyrite
carbonate
hematite 1
100 µm
e)
pyrite
muscovite
quartz
graphite
chalcopyrite
10 µm
f)
biotite
quartz
chlorite
pyrite
carbonate
100 µm

Figure 2.12: Examples of carbonate and sulfide minerals in the Temagami BIF layers. a) PPL transmitted light photomicrograph of a large euhedral dolomite grain in a preserved jasper layer (sample SM11). Dolomite is likely a metamorphic phase in mature jasper. b) Calcite with minor stilpnomelane at the contact between magnetite and chert layers (sample SM052). Calcite intergrown with metamorphic stilpnomelane indicates late paragenetic origin of both phases, after Type 3 magnetite growth was completed. Some of the carbon in calcite and dolomite in Temagami BIF is likely derived from organic material (Bowins and Crocket, 1994; Posth et al., 2014). c) PPL transmitted light photomicrograph of carbonate-facies BIF, consisting of minor disseminated siderite in a chert matrix (sample 11-27). Siderite is likely an early diagenetic product of primary carbonate phases deposited with the initial precipitate (e.g., Klein, 2005). d) Reflected light photomicrograph of fine pyrite inclusions in Type 3 magnetite in sample SM11. Pyrite is the diagenetic product of sulfide produced by sulfur-disproportionating bacteria in oxide facies BIF (Diekrup et al., 2018). e) BSE image of the cherty matrix of sulfide-facies BIF showing mainly disseminated pyrite, chalcopyrite, muscovite, and fine graphite (sample SH580). Pyrite is the diagenetic product of sulfide from sulfur-reducing bacteria in sulfide BIF (Diekrup et al., 2018), using organic material preserved as graphite to metabolize sulfate. Some sulfide reacting with Cu present in pore water is preserved as trace-chalcopyrite. Muscovite is the metamorphic product of volcanic-derived material. f) BSE image of sulfide-facies BIF showing large, irregular pyrite grains (possibly aggregates) (sample SH580). Carbonates, chlorite, muscovite, and biotite are all present as traces.

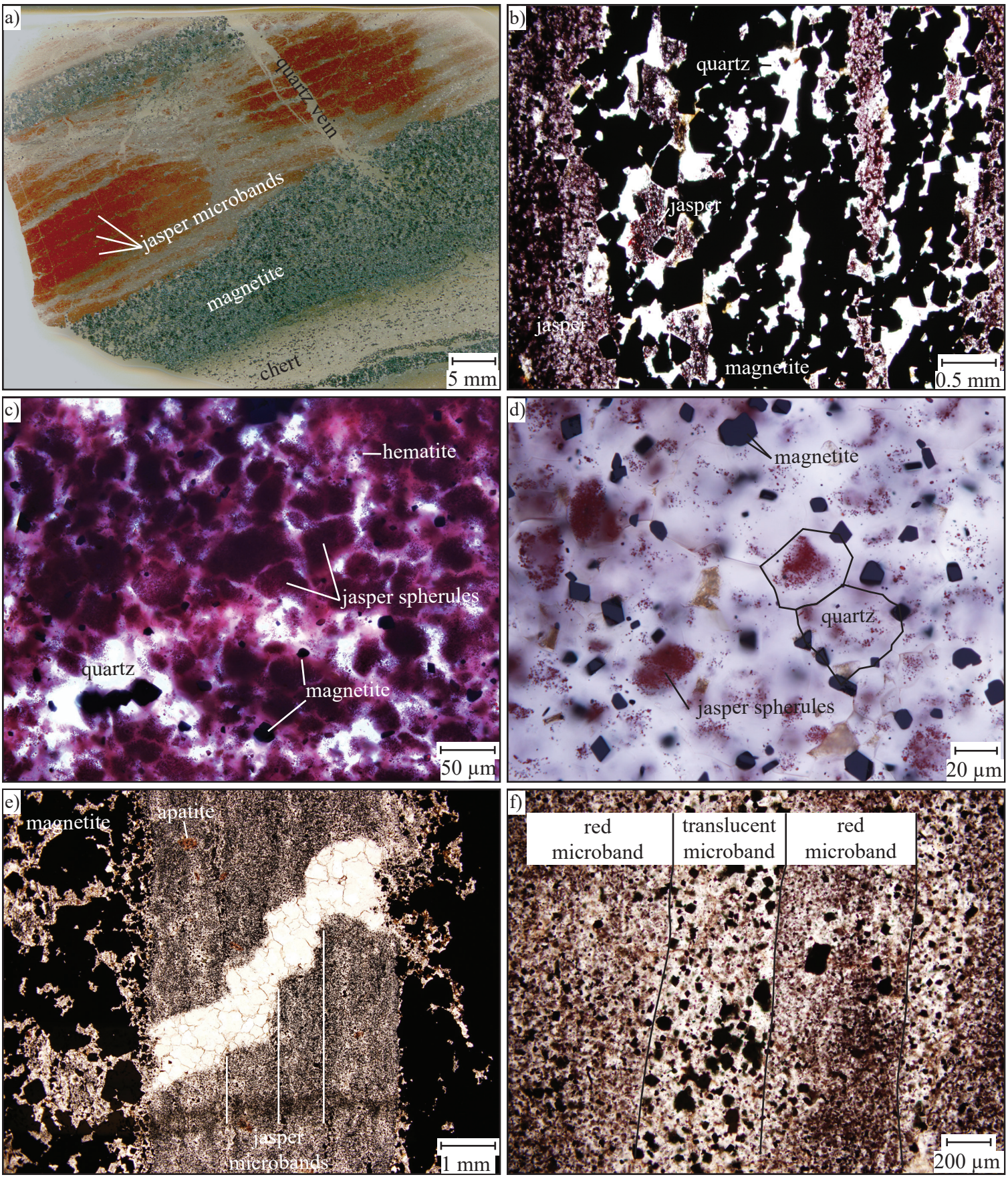

a)
quartz vein
jasper microbands
magnetite
chert
5 mm
b)
quartz
jasper
jasper
magnetite
0.5 mm
c)
hematite
jasper spherules
quartz
magnetite
50 µm
d)
magnetite
quartz
jasper spherules
20 µm
e)
magnetite
apatite
jasper microbands
1 mm
f)
red microband
translucent microband
red microband
200 µm

Figure 2.13: Characteristics of jasper layers in the Temagami BIF. a) Thin section scan of sample SM11. showing alternating layers of chert (transparent), chert-magnetite, and microbanded jasper layers. The lateral transitions from jasper to black captured in the thin section are commonly observed in ore blocks (e.g. Fig. 2.8b,c,e) b) PPL transmitted light photomicrograph of alternating jasper and magnetite microbands in sample SM052. c) PPL transmitted light photomicrograph of a jasper microband showing jasper spherules, nm-scale cloudy hematite in the central part of the spherules, and Type 2 magnetite at the boundaries of the spherules (sample SM11). d) Development of euhedral quartz crystals around primary jasper spherules, showing a core of cloudy Type 1 hematite and growth of Type 2 magnetite at the expense of hematite. Interfaces of two quartz crystals outlined. e) Early diagenetic quartz vein in microbanded jasper in sample SM052. Offsets in the veinlet reflect offset related to microbanding in jasper. f) Close up of e) showing cryptic microbanding marked by recrystallized Type 2 hematite and magnetite in more translucent microbands, preserved cloudy hematite in red microbands. Panels c)-e) are transmitted PPL photomicrographs.

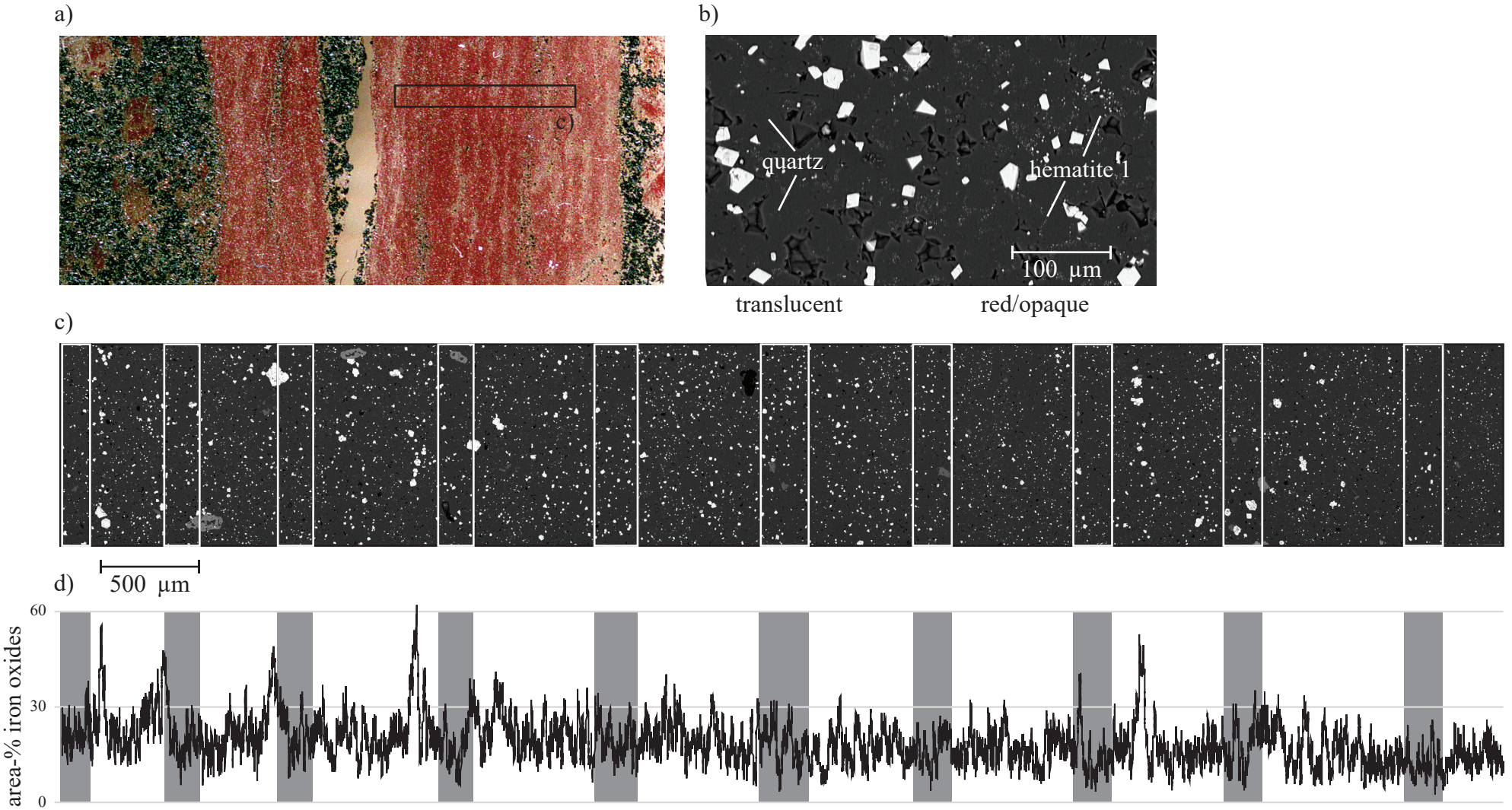


Figure 2.14: Example of micro-scale banding in jasper layers of the Temagami BIF. a) Part of the thin section of sample SM052 showing the location of a continuous BSE scan of Fe-oxide abundance in the jasper layer. b) BSE image of the microbanded jasper layer indicated in a) showing the abundance of Type 1 hematite (red) and quartz-rich translucent microbands. Note the slight difference in the abundance of Type 1 hematite leading to the loss of red color and development of a translucent microbands. c) Mosaic of BSE images across a section of microbanded jasper in sample SM052. Microbanding is vertical in the image, translucent microbands are outlined by black boxes. The bright minerals are Type 2 and 3 magnetite and Type 1 and 2 hematite. Very large Type 3 magnetite (with quartz inclusions) occur independent of microbanding and commonly cross-cut microbanding. d) Plot of area % of magnetite and hematite in panel c). Gray boxes indicate dark microbands shown in c). The data show that mineralogic changes control microbanding, not chemical variation (i.e., total Fe-abundance) in the primary precipitate. Trace hematite is responsible for the red colour of jasper bands, while translucent bands have similar abundance of Fe-oxides in the form of larger magnetite grains, causing loss of red colour. Area analysis performed using ImageJ.

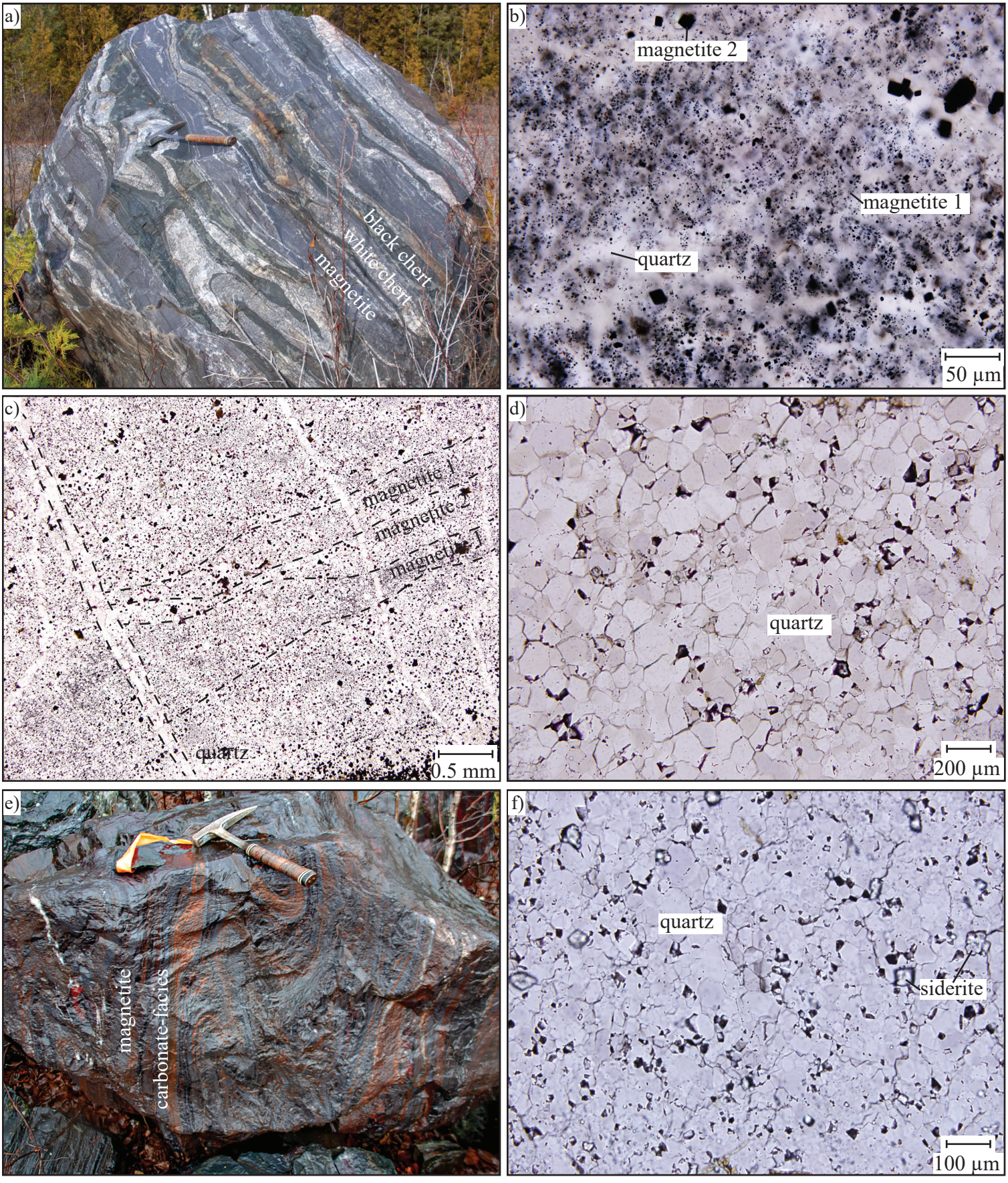

a)
black chert
white chert
magnetite
b)
magnetite 2
magnetite 1
quartz
50 µm
c)
magnetite 1
magnetite 2
magnetite 1
quartz
0.5 mm
d)
quartz
200 µm
e)
magnetite
carbonate-facies
f)
quartz
siderite
100 µm

Figure 2.15: Characteristics of white and black chert layers in the Temagami BIF. a) White chert with interlayered black chert and magnetite, locally tightly folded. Folds are interpreted to be syn-sedimentary based on the very limited extend of folded horizons (block E038; cf. Ginley, 2016). b) PPL transmitted light photomicrograph of black chert with fine-grained Type 1 magnetite and larger Type 2 magnetite (Sample 11-32). c) PPL transmitted light photomicrograph of microbanded black chert (labels oriented in the direction of banding). The black colour of the bands in hand specimen is due to a few volume percent of finely disseminated Type 1 magnetite in dark and larger Type 2 magnetite in chert. Microfractures in the chert layers are lined by quartz (sample 11-41). d) Typical grain size of quartz in recrystallized white chert layers (compare with b; Sample 11-34). e) Tightly folded black chert and siderite-bearing chert "carbonate-facies BIF" (see photo f) in block F018. f) Trace siderite (< 5 vol. %) in white chert which causes the brown surface staining observed in the field (see photo e).

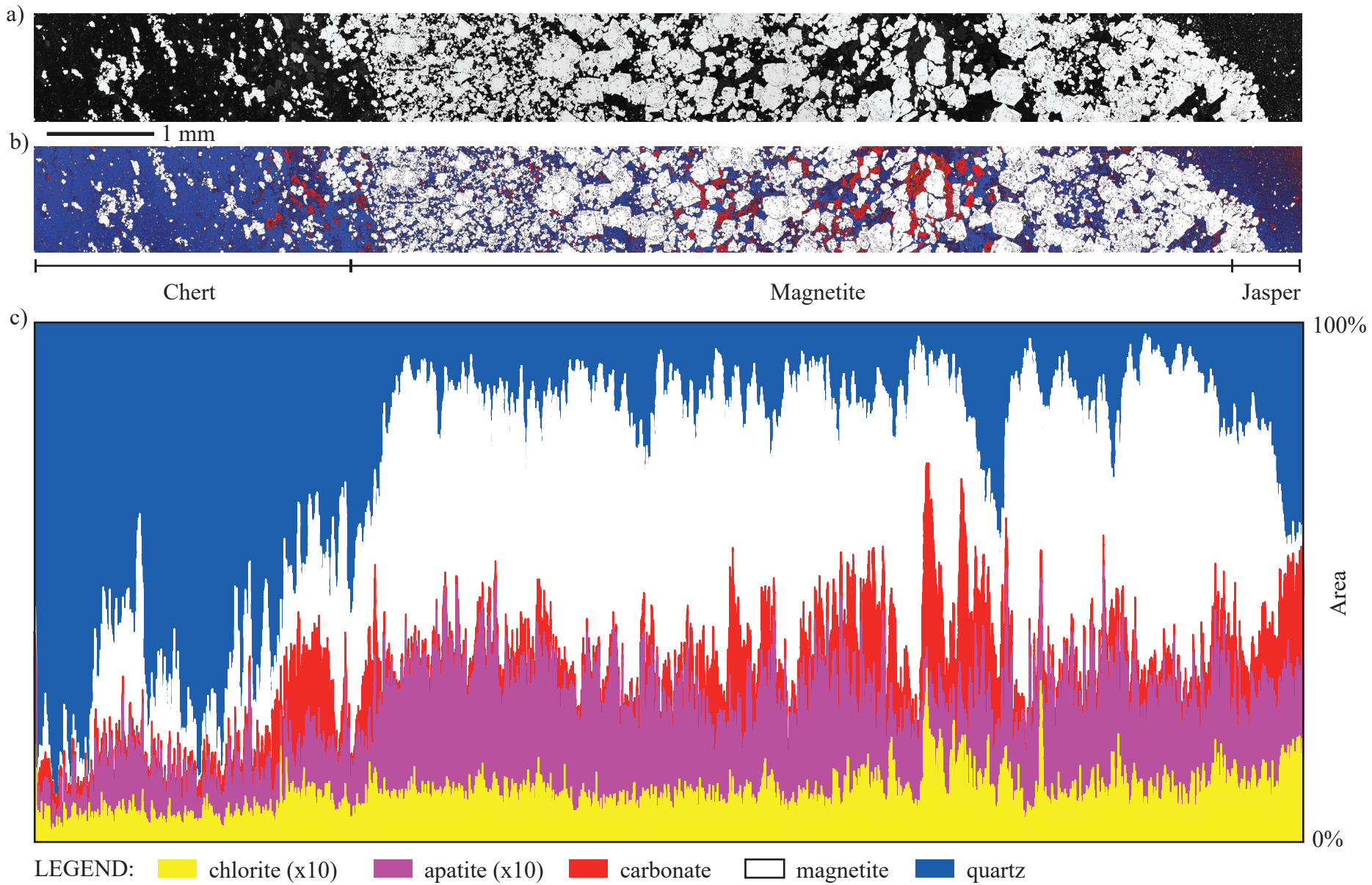


Figure 2.16: Mineral abundances in different bands of Temagami BIF. a) BSE mosaic of a transition from black chert (left) across a magnetite band into a jasper band (right). Note the increase in grain size of the magnetite (white) towards the center of the magnetite band indicating more advanced recrystallization in the middle of the magnetite bands. b) Mineral species coloured according to BSE brightness and confirmed by EDS analyses. Small amounts of ultrafine Type 1 hematite in the jasper band is indistinguishable from magnetite and captured in the same classification due to very similar brightness in BSE images. Mineral abundances were calculated using ImageJ, stacked and adjusted using Adobe Photoshop. c) Cumulative abundance of mineral species from panel b (chlorite and apatite abundances are scaled by a factor of 10 for clarity). Apatite and carbonates correlate negatively, possibly because calcite starts crystallizing during progressive diagenetic/metamorphic conditions that facilitated the preferential loss of P, inhibiting the formation of metamorphic apatite.

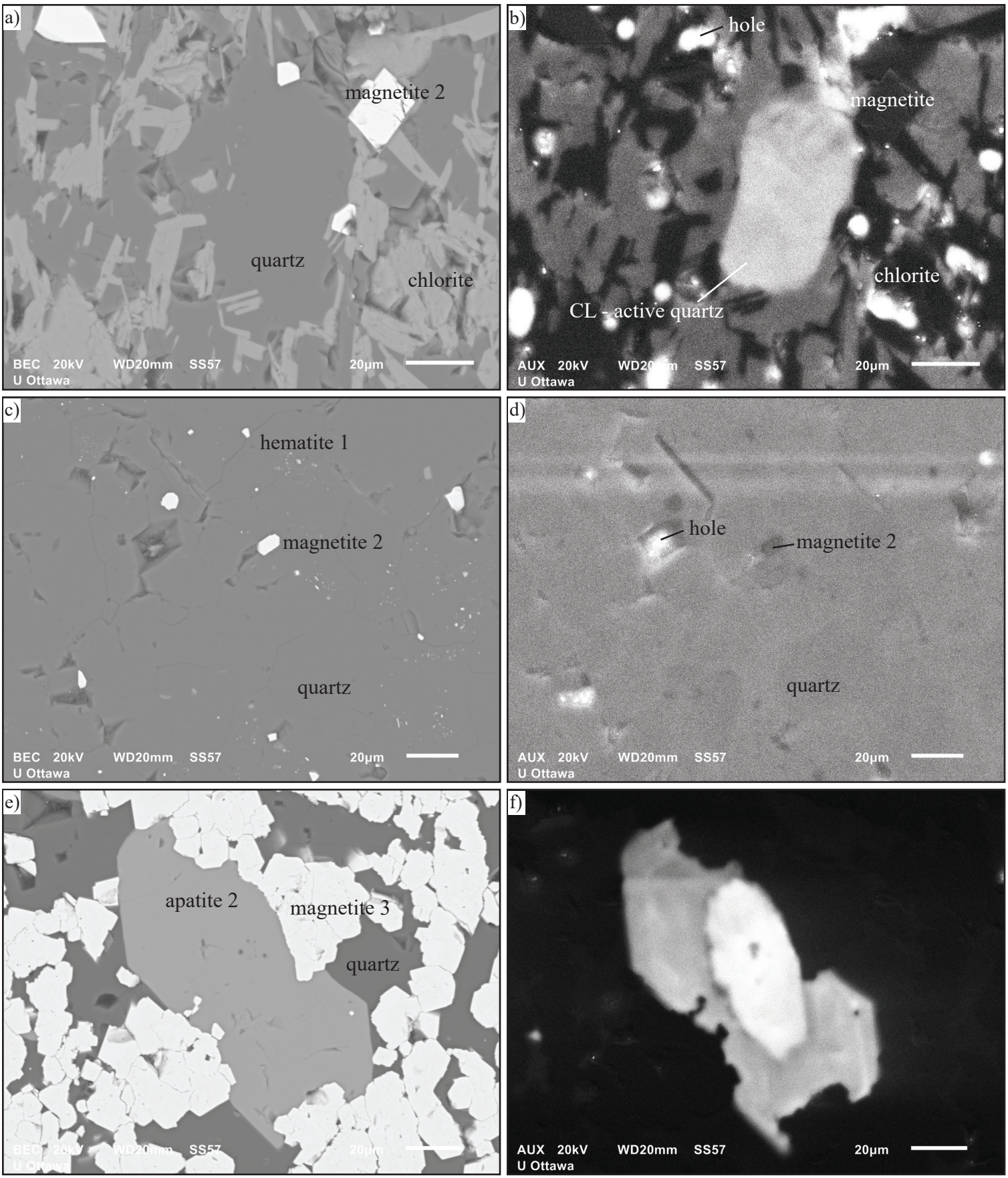

a)
magnetite 2
quartz
chlorite
BEC 20kV WD20mm SS57 20µm
U Ottawa
b)
hole
magnetite
chlorite
CL - active quartz
AUX 20kV WD20mm SS57 20µm
U Ottawa
c)
hematite 1
magnetite 2
quartz
BEC 20kV WD20mm SS57 20µm
U Ottawa
d)
hole
magnetite 2
quartz
AUX 20kV WD20mm SS57 20µm
U Ottawa
e)
apatite 2
magnetite 3
quartz
BEC 20kV WD20mm SS57 20µm
U Ottawa
f)
AUX 20kV WD20mm SS57 20µm
U Ottawa

Figure 2.17: Backscattered electron (BSE) and cathodoluminescence (CL) images of quartz and apatite in chert and chlorite. a) BSE image of typical quartz-magnetite-chlorite assemblage of volcaniclastic (sample 11-4) showing authigenic chlorite and magnetite as alteration products of volcanic-derived material interlayered with oxide-BIF. b) CL image of the same frame showing a rounded, CL-active core of the large quartz grain, interpreted to be detrital in origin and later overgrown by authigenic quartz. Very bright spots are holes in the thin section. c) BSE image of typical quartz-magnetite-hematite assemblage in oxide-facies BIF (sample SM 11) showing the typical small crystal size of quartz in jasper (<50 µm). d) CL image of the same frame showing the absence of CL-active quartz, interpreted to indicate exclusively authigenic BIF-quartz incorporating Fe as impurity, extinguishing the CL signal. e) Type 2 apatite intergrown with quartz and magnetite in oxide facies BIF (sample 11-32). Late Type 2 apatite overgrows Type 3 magnetite, informing crystallization during late paragenetic stages. f) CL image of the same frame showing a CL-bright core of the apatite grain, and darker outer zones that overgrow Type 3 magnetite, interpreted to reflect early Type 1 apatite overgrown by later, Type 2 apatite. Note the oscillatory zoning in the outer parts of the apatite grain, possibly linked to variable availability of Fe or Mn to be incorporated in the crystal structure.

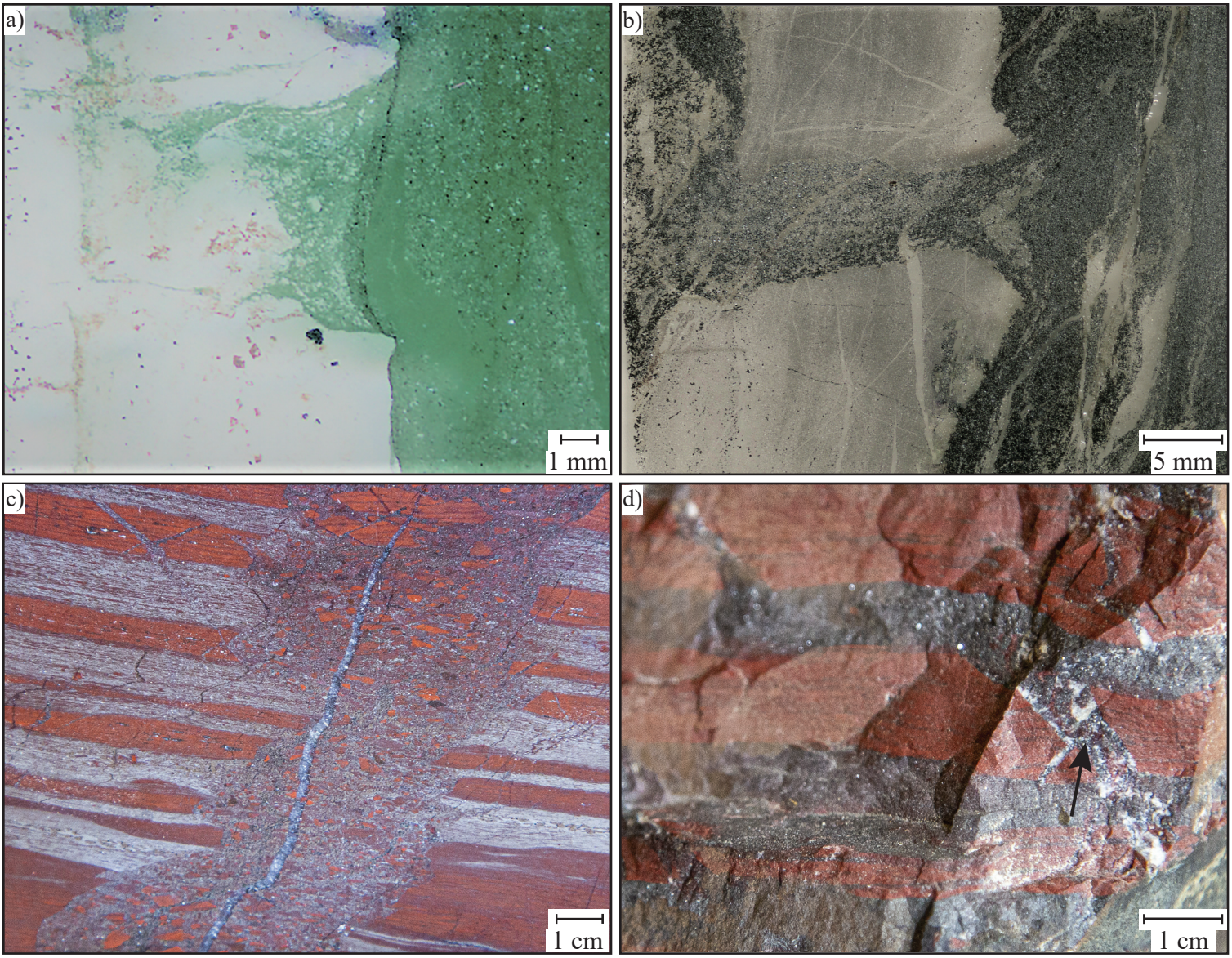


Figure 2.18: Examples of possible pore-water escape structures and different generations of breakouts in oxide-BIF and chlorite layers. a) Breakout of green chloritic material from a chlorite band into an adjacent chert band (sample 11-1a). b) Breakout of fine-grained magnetite (black) cutting a chert band (gray) (sample 11-8). Note that the earliest quartz veins in chert pre-date the breakout structure and are not continuous in the magnetite layers indicating some fracturing of chert prior to pore fluid escape, whereas others appear to post-date the breakout. c) Fluid escape structure in jasper-magnetite BIF forming at later stages than a) and b), brecciating more brittle material. Zone of weakness later reactivated as fluid pathway by a quartz vein. d) Escape structure preserved in a single, brittle jasper band (arrow), containing fragments of jasper and magnetite similar to c). Adjacent jasper bands remained intact. Smaller fluid escape events may have only affected single jasper bands before the fluid travelled horizontally in magnetite bands and exploited vertical pathways elsewhere.

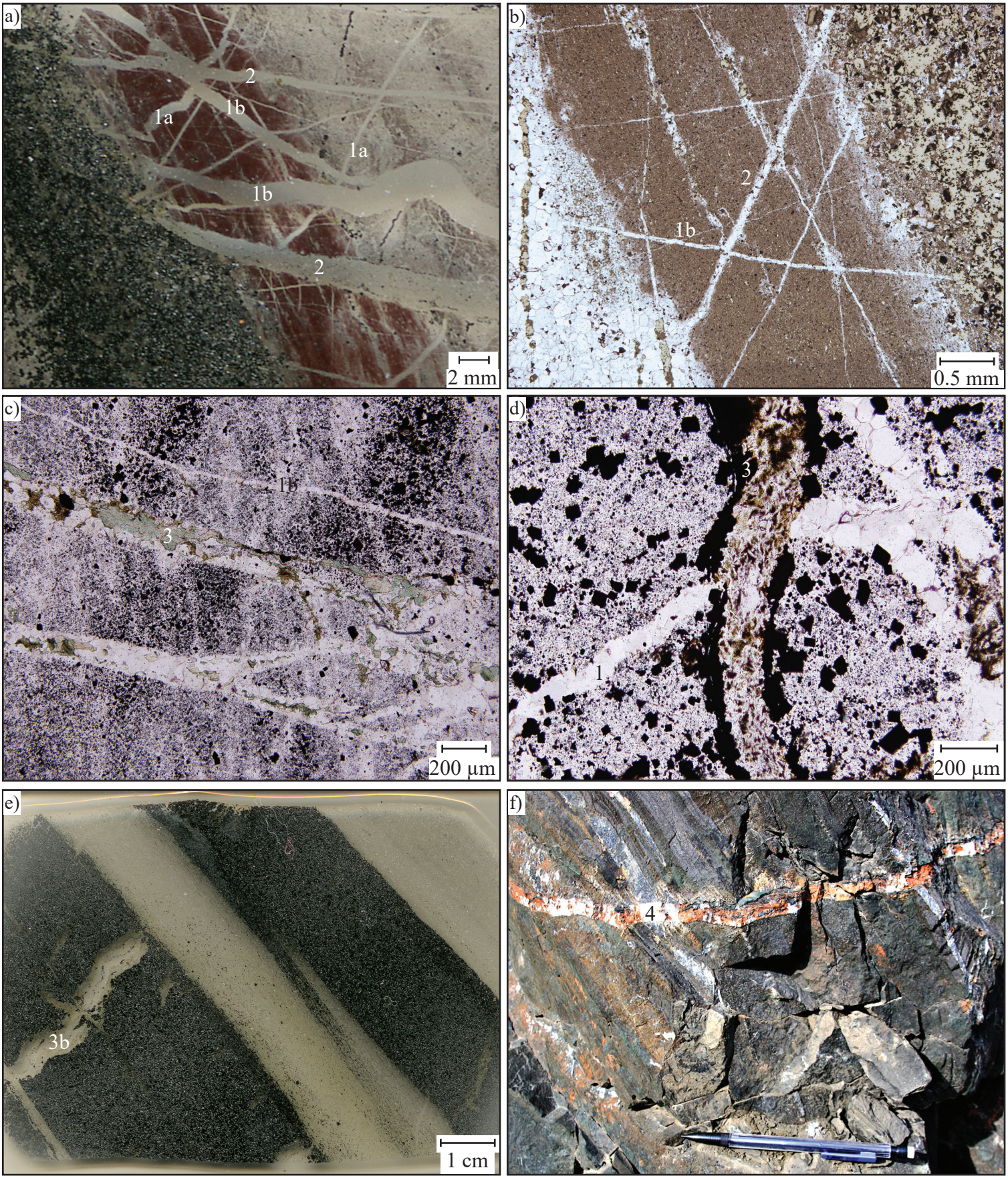

a)
2
1a
1b
1a
1b
2
2 mm
b)
2
1b
0.5 mm
c)
1b
3
200 µm
d)
3
1
200 µm
e)
3b
1 cm
f)
4

Figure 2.19: Different generations of quartz veins and veinlets in oxide-facies BIF. a) Early vein stages confined to jasper layers. Vein stage 1a only contains quartz and is commonly contorted, while 1b cuts 1a, is larger, and less contorted. Vein stage 2 contains quartz and magnetite and clearly cuts vein stage 1. Neither generation is preserved in magnetite bands that were still in a state of active crystallization at the time of quartz vein emplacement. Enlarged thin section scan of sample 11-11. b) Combined reflected and transmitted light photomicrograph of sample 11-11. The stage 2 veinlet cuts the magnetite layer but terminates at the contact with white chert that was still in a state of quartz recrystallization at the time of vein emplacement (cf. Figure 2.8f). Layer-parallel veinlets are possibly related to the formation of microbanding in jasper and developed along banding-parallel planes of movement, distorting stage 1 quartz veins. c) and d) Stage 3 veinlets contain quartz, magnetite and aluminosilicates (commonly chlorite), cut all previous veins and layer types and are locally associated with small offsets in the BIF layers. e) Stage 3b veinlets are only developed in Type 4 magnetite layers and have previously been interpreted as "syneresis cracks" (Donaldson and Munro, 1982). However, they are likely products of metamorphic reactions creating volume loss and shrinkage, as opposed to dewatering processes captured by fluid escape structures or desiccation. f) Field photograph of a metamorphic/tectonic stage 4 quartz-pyrite-ankerite vein in the Hwy 11 outcrop, cutting all layers of the BIF.

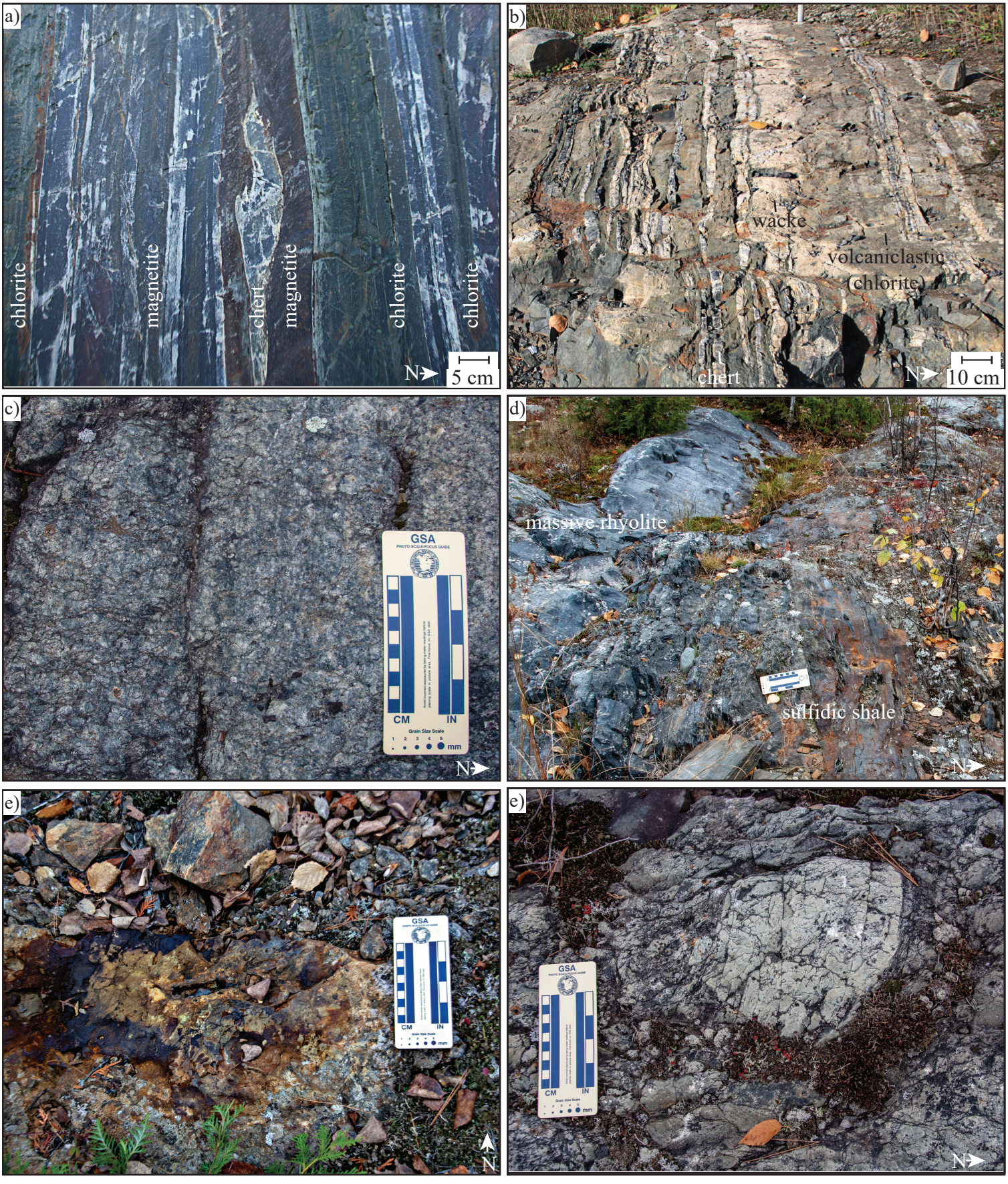

a)
chlorite
magnetite
chert
magnetite
chlorite
chlorite
N
5 cm
b)
wacke
volcaniclastic
(chlorite)
chert
N
10 cm
c)
GSA
CM
IN
Grain Size Scale
mm
N
d)
massive rhyolite
sulfidic shale
N
e)
GSA
CM
IN
N
e)
GSA
CM
IN
N

Figure 2.20: Chlorite layers and host rock lithologies of the Temagami BIF. a) Chlorite (”silicate facies”) BIF in the Hwy 11 outcrop. Chlorite layers in oxide BIF are the metamorphic products of a volcanic-derived clastic precursor materials such as ash layers, or authigenic phases formed in seawater such as hydrothermal clays or green rust. Layering of chloritic material is true, primary layers, while layers and bands (including microbands) in oxide BIF may be of diagenetic origin. b) Interlayered volcaniclastic chlorite layers, greywacke, and chert at the south end of the Hwy 11 outcrop, stratigraphically at the base of the South BIF. c) Felsic lapilli tuff north of the Sherman Mine access road. d) Sulfidic black shale stratigraphically overlying a massive rhyolite flow north of the Sherman Mine access road, stratigraphically between the two BIF members. e) Sulfide clast in a rhyolite flow breccia along the Sherman Mine access road. e) Brecciated rhyolite flow north of the Sherman Mine access road.

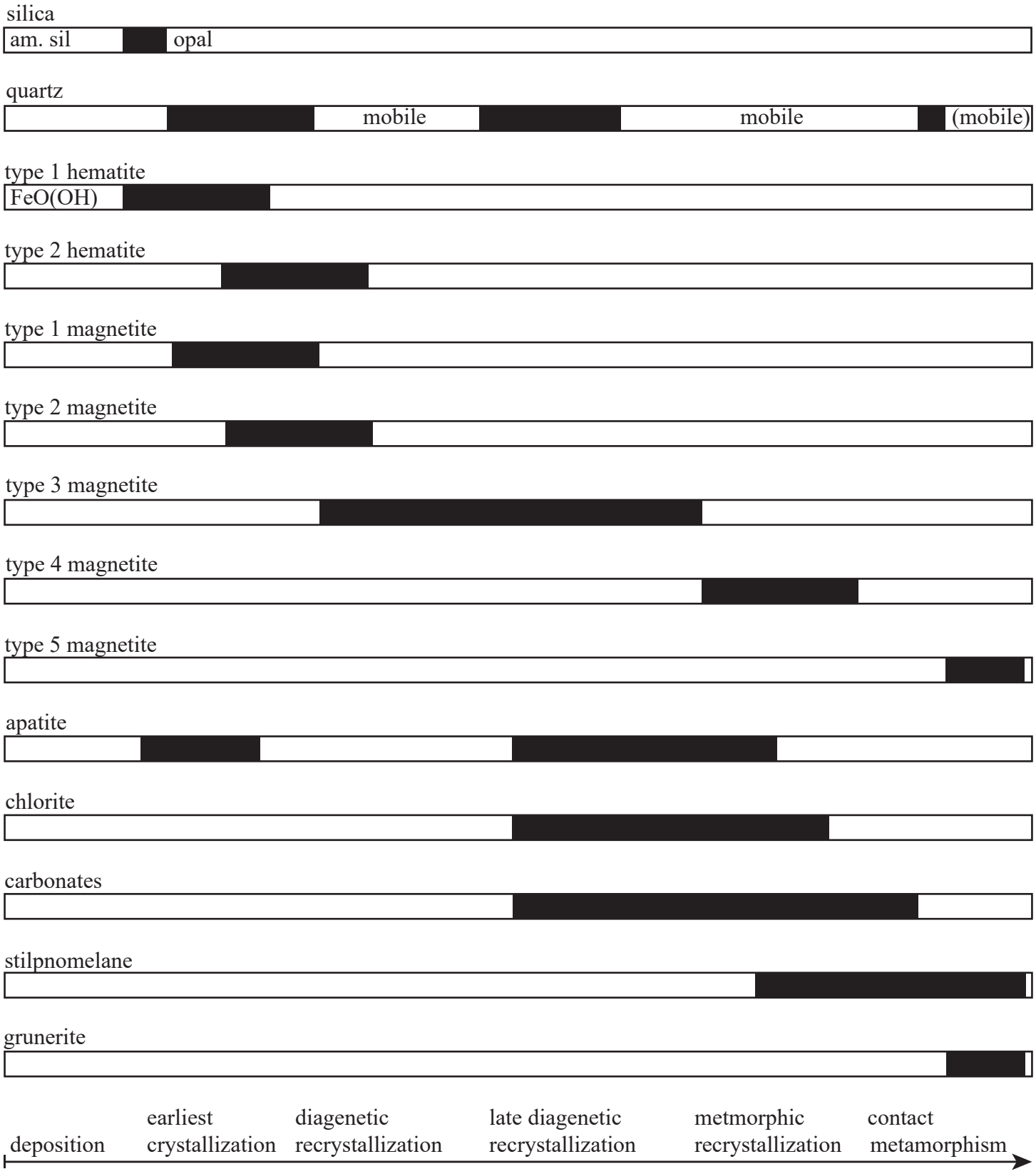


Figure 2.21: Schematic paragenetic sequence of major and trace minerals of the Temagami oxide-facies BIF, reconstructed from petrographic observations of mineral intergrowth and quartz veining relationships. Six paragenetic stages have been identified (see discussion in the text). Calculated chlorite formation temperatures in oxide BIF, between ~150 and 300°C, define the late diagenetic to early regional metamorphic conditions.

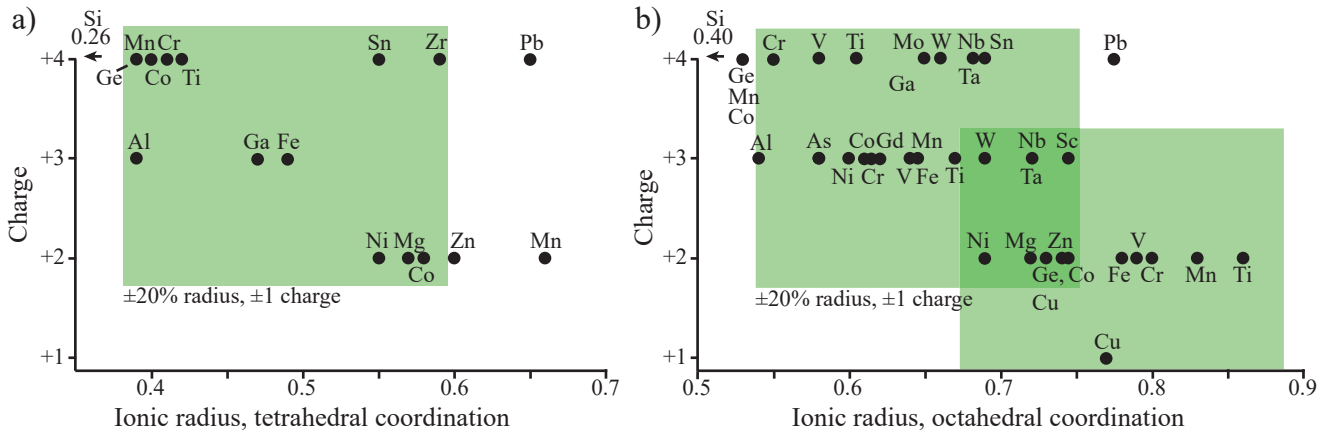


Figure 2.22: Ionic radii vs. charge for selected elements potentially substituting for Fe2+ and Fe3+ in the magnetite structure. a) Ionic radii and charge for cations in tetrahedral (4-fold) coordination (iron ions coordinated around oxygen). b) Ionic radii and charge for cations in octahedral coordination. Green boxes around Fe3+ in tetrahedral coordination and (Fe2+, Fe3+) in octahedral coordination indicate limits of ±20% of the radius and ±1 charge unit difference, following the Goldschmidt rule for preferred substitution (±15%), reflecting substitutions commonly observed in the magnetite structure. Values after Shannon (1976).

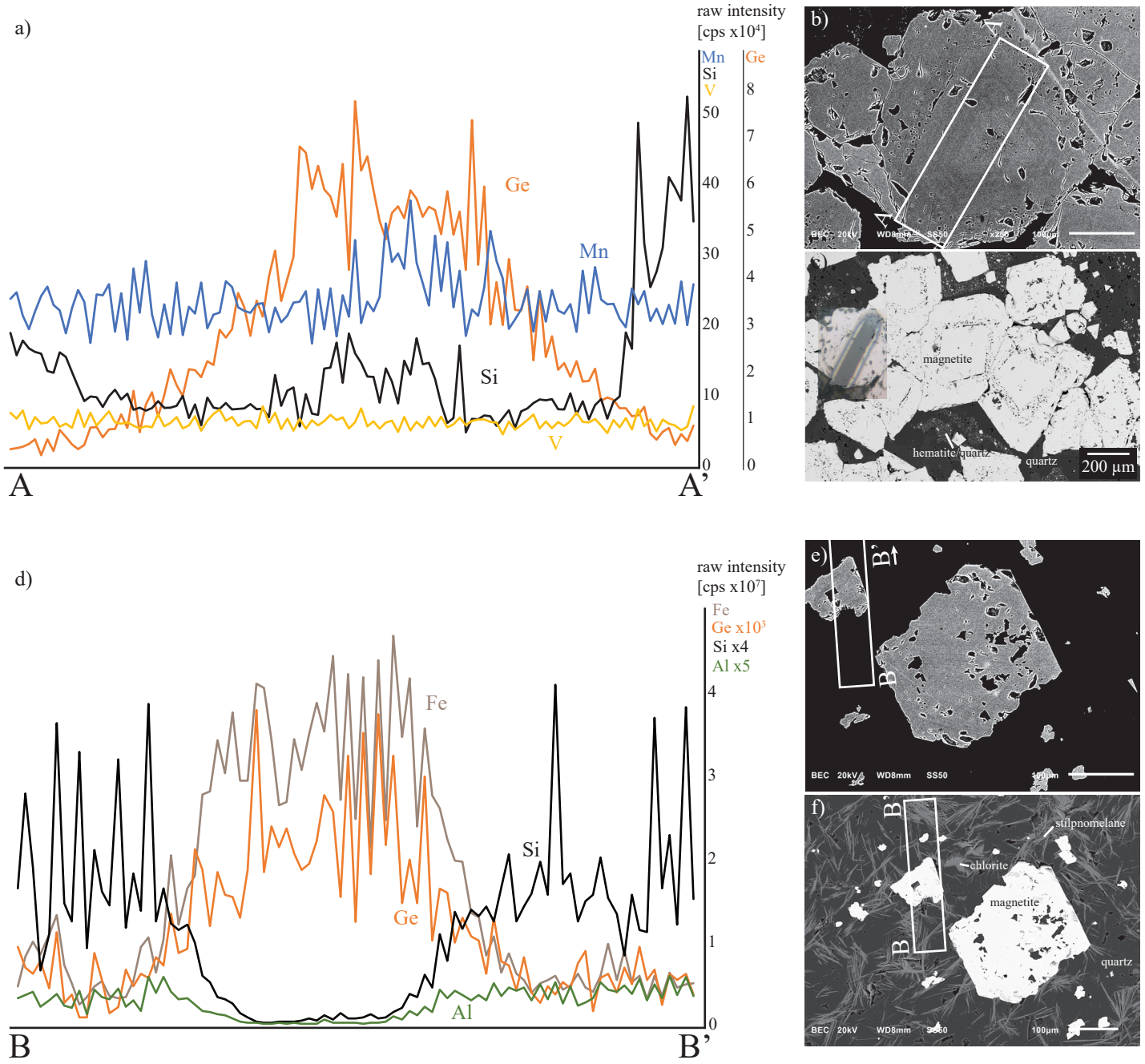


Figure 2.23: Examples of laser ablation profiles of selected trace elements in magnetite in Temagami oxide-facies BIF. a) Horizontal traverse (A-A') across a grain showing raw intensities of ^{29}Si, ^{51}V, ^{55}Mn, and ^{74}Ge in a Type 3 magnetite in sample SM11. Ge, Mn, and Si are enriched in the core of the magnetite, whereas V shows no change. b) Location of transect A-A' on a high-contrast BSE image showing the Si-rich and inclusion-rich zones in magnetite. c) BSE image showing the petrographic context of the analyzed grain with the actual laser track overlain. Type 3 magnetite is surrounded by chert containing hematite, apatite and carbonates. d) Horizontal traverse (B-B') across another magnetite grain showing raw intensities of ^{27}Al (x5) ^{29}Si (x4), ^{57}Fe, and ^{74}Ge (x103) in Type 2 magnetite in a chert-chlorite-stilpnomelane matrix (sample D015). The Ge signal closely follows the Fe signal. Ge intensities taper off to near-background levels in the quartz and aluminosilicates (elevated Si and Al). e) Location of transect B-B' on a high-contrast BSE image indicated by the white box. Type 2 magnetite does not show the complex zonation of Type 3 magnetite. f) BSE image showing the petrographic context of the analyzed grain with the area ablated indicated by the white box. The surrounding minerals consist of predominantly quartz with chlorite and stilpnomelane.

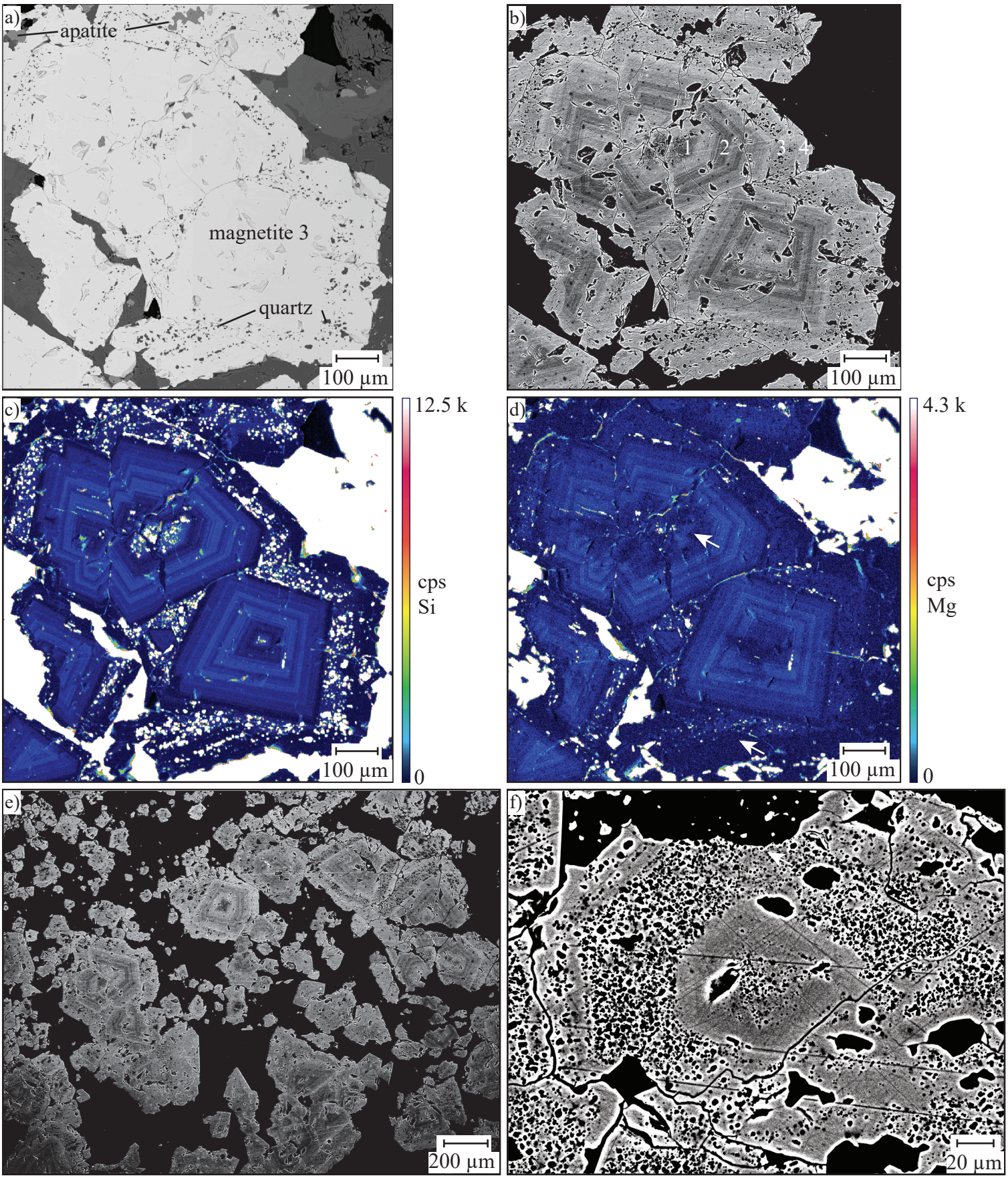

a)
apatite
magnetite 3
quartz
100 µm
b)
1
2
3
4
100 µm
c)
12.5 k
cps
Si
0
100 µm
d)
4.3 k
cps
Mg
0
100 µm
e)
200 µm
f)
20 µm

Figure 2.24: Representative images of Si and Mg zonation in Type 3 and Type 4 magnetite. a) BSE image of a single Type 3 magnetite showing a large, complex crystal with inclusions of quartz and apatite mainly in the outer zones (sample SM11). b) High contrast BSE image of the same frame, revealing oscillatory zonation in the central part. See text for discussion for zones 1-4. c) WDS map of Si in the same frame, showing the oscillatory zonation in b) is due to Si variation. Maximum Si concentrations correspond to about 1.8 wt.% Si. d) WDS map of Mg in the same frame, showing some Mg is co-enriched with Si in the magnetite. The distribution of Si and Mg correlate well, except in the core of the magnetite crystal (white arrow), where Si is present as quartz inclusions without co-enrichment of Mg. e) High contrast BSE image of a cluster of Type 3 magnetite in sample SM11. All of the magnetite crystals show the same internal zonation (dark core and 3-5 alternating lighter and darker zones), suggesting that they grew simultaneously from the same pluses of fluid. f) High contrast BSE image of Type 4 magnetite in sample B013-2 showing similarly complex internal zonation, although with more prominent dissolution surfaces (white arrow).

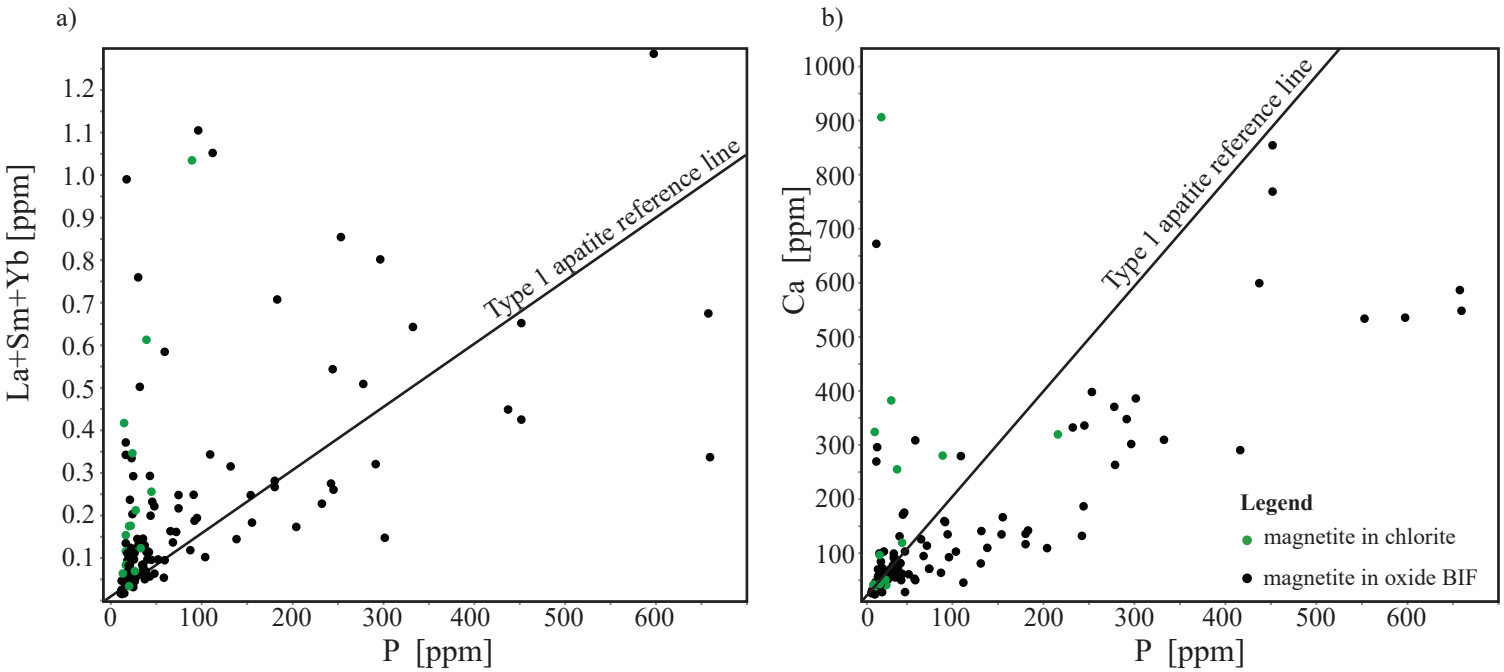
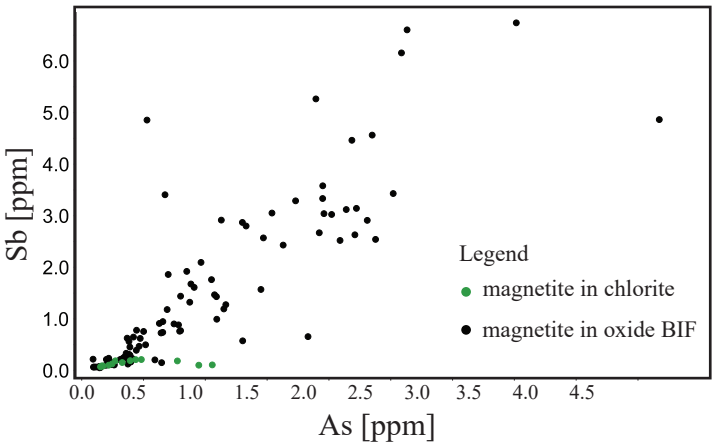
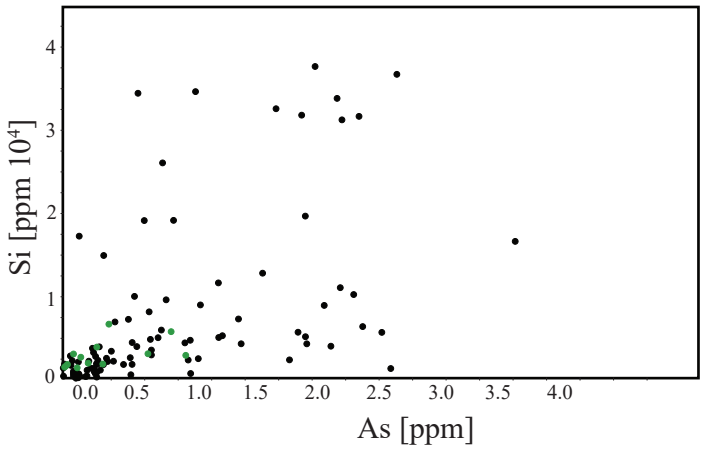
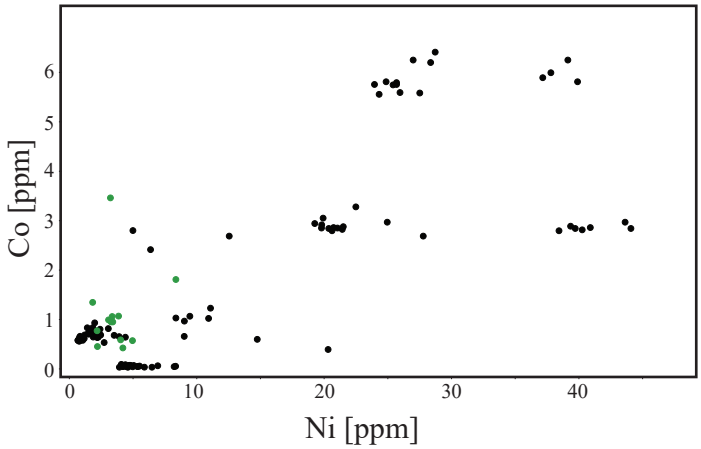
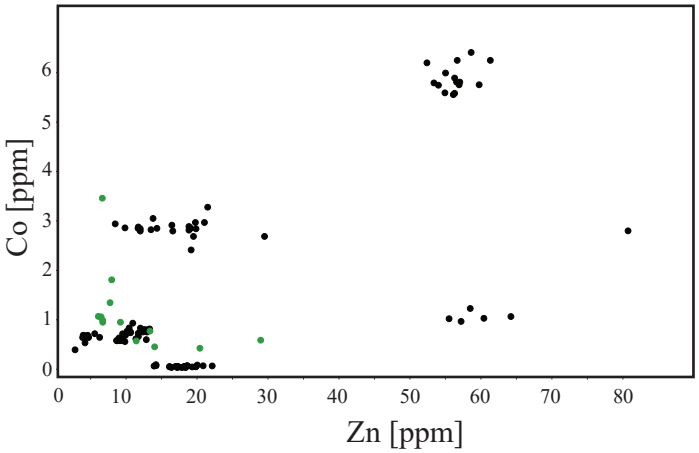


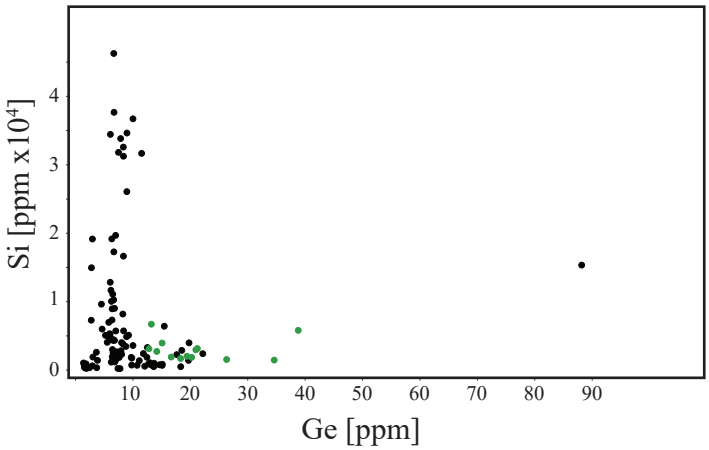
Figure 2.25: Binary trace element plot of a) REE vs. P and b) Ca vs. P in magnetite hosted in oxide BIF and chlorite layers analyzed by LA-ICP-MS. Results are shown only for lower concentrations of the elements close to the median values of 38 ppm P, 81 ppm Ca, and 0.8 ppm La+Sm+Eu, omitting outliers. The weak positive correlations suggest that apatite microinclusions in magnetite are the likely host mineral. However, the presence of REE without appreciable P argues for the presence of some La, Sm or Eu incorporated in the magnetite lattice. Apatite reference line based on EPMA and LA-ICPMS analyses of Type 1 apatite median values (39.2 wt. % Ca, 18.3 wt.% P, 290 ppm La+Sm+Yb).

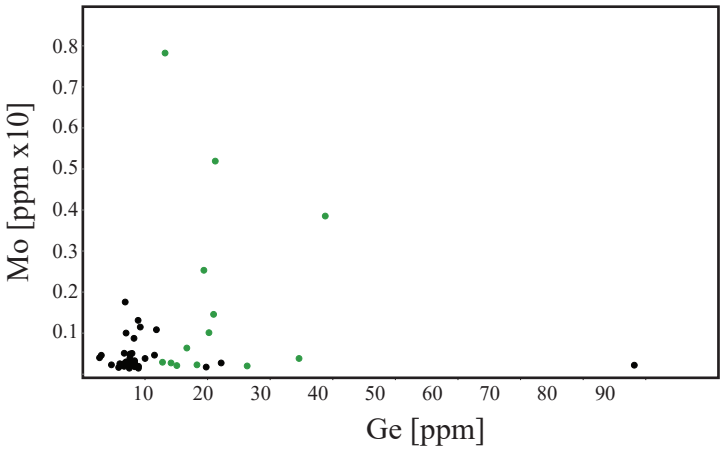

Sb [ppm]
As [ppm]
Legend
magnetite in chlorite
magnetite in oxide BIF

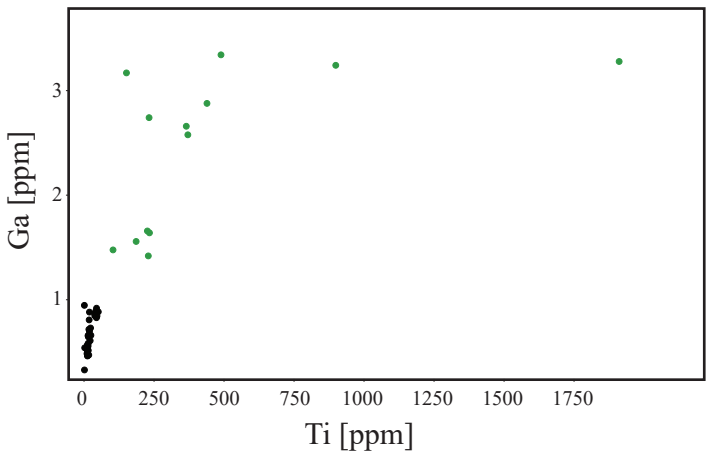

Si [ppm 10⁴]
As [ppm]


Co [ppm]
Ni [ppm]


Co [ppm]
Zn [ppm]


Si [ppm x10⁴]
Ge [ppm]


Mo [ppm x10]
Ge [ppm]


Ga [ppm]
Ti [ppm]

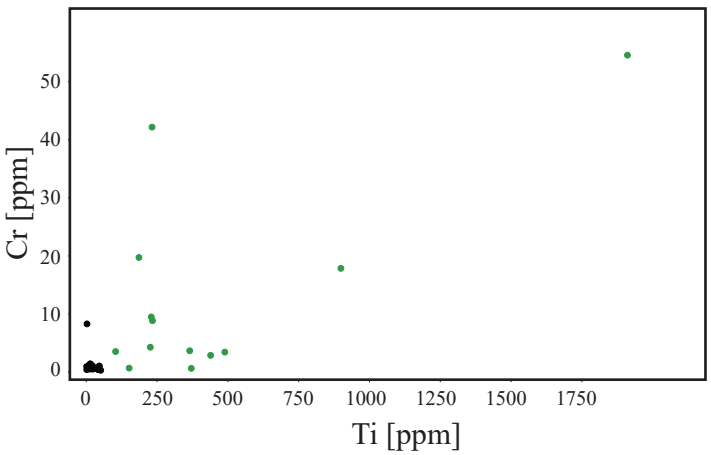

Cr [ppm]
Ti [ppm]

Figure 2.26: Binary trace element plots of Si, Sb, As, Co, Ni, Zn, Ge, Mo, Ga, Ti and Cr in magnetite from oxide facies BIF, analyzed by LA-ICP-MS. Si, Sb, As, Co, Ni, and Zn show weak to moderately positive correlations. Clusters of data (e.g., in the Co, Ni and Zn plots) represent data from different samples. Ge, Ga, Cr, and Ti are more enriched in magnetite from chlorite layers. These results are similar to those observed in WR data (see Chapter 3), suggesting that magnetite (or microinclusions of other phases in magnetite) are important hosts for the trace and ultra-trace elements.

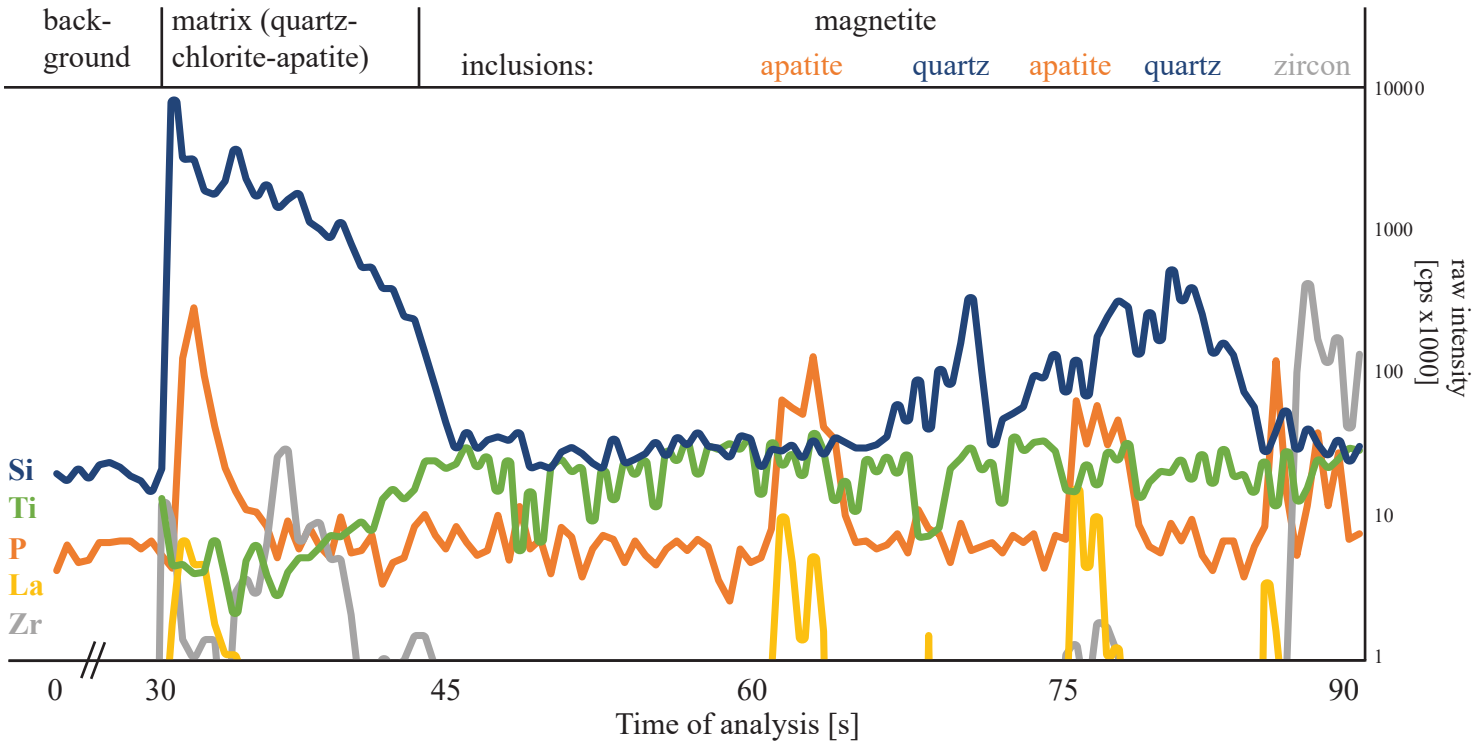


Figure 2.27: Laser ablation profiles of Si, Ti, P, La and Zr in Type 3 magnetite in oxide facies BIF. The plot shows the transition from analytical blank background to the sample matrix containing quartz, chlorite, and apatite, into Type 3 magnetite containing inclusions of quartz, apatite and zircon. Raw intensity variations are shown along the profile measured in seconds. In 60 s of ablation, a ~400 µm long transect was analyzed. Elements such as Ti (also V, Zn) show little variation in the magnetite, whereas peaks of REE are clearly hosted in apatite inclusions and closely track P. Si in quartz inclusions in magnetite does not correlate with other elements. Zr is present in zircon microinclusions. In the data presented in this chapter (e.g., Table 2.9), inclusion-free segments of the profiles were chosen to calculate representative magnetite compositions.

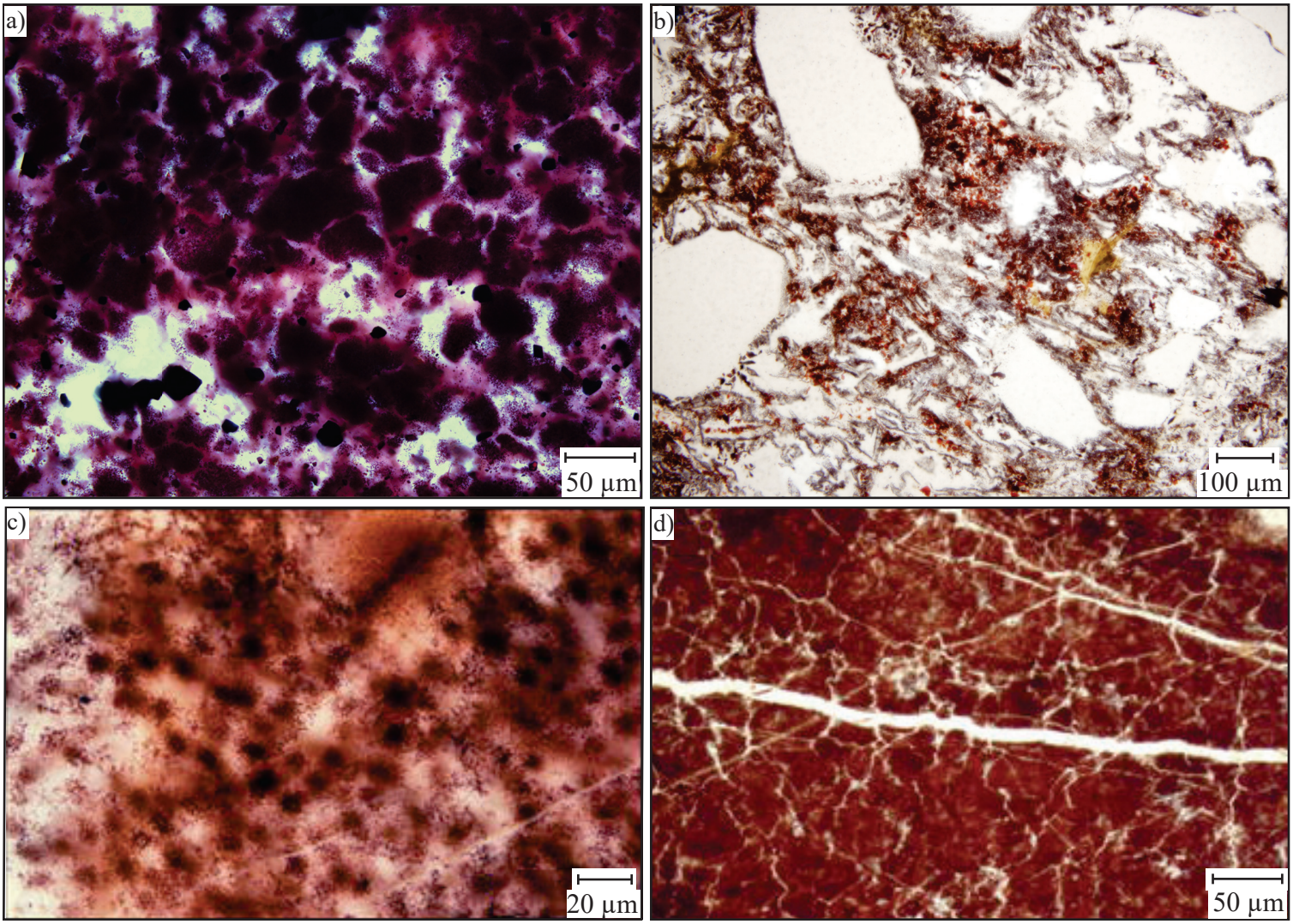


Figure 2.28: Comparison of the petrographic characteristics of end-member jasper types from different Archean and Paleozoic BIF occurrences. a) Transmitted light photomicrograph of Temagami jasper, showing well-preserved spherules of ultrafine hematite in quartz, which produce the characteristic red colour. b) Hematite-rich "jasper" layer from the oldest known locality in the Eoarchean Nuvvuagittuq BIF (cf. O'Neil et al., 2012). Well crystallized translucent hematite is disseminated in the interstices of pyroxene in the matrix of rounded quartz grains. Thin section courtesy of Jonathan O'Neil. c) and d) Photomicrographs of VMS-related jasper exhalite layers in the Mesozoic Løkken ophiolite. Spherules of hematite and early diagenetic quartz veinlets closely resemble the jasper layers from the Temagami BIF. Reproduced with permission from Grenne and Slack (2003).

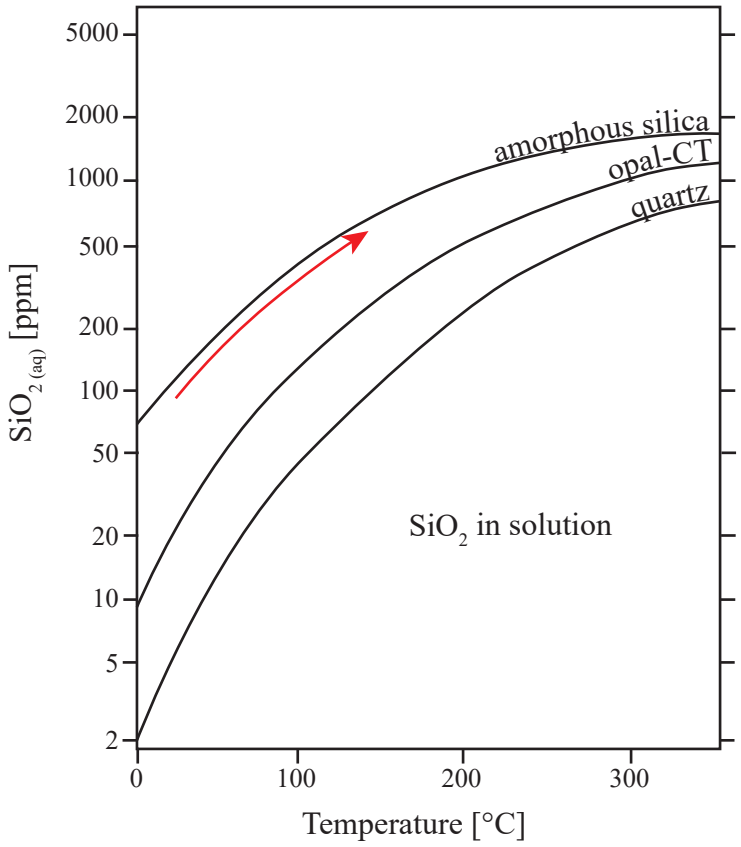


Figure 2.29: Solubility of different silica polymorphs as a function of temperature at neutral ph. Amorphous silica is the stable form at ambient conditions (e.g., 30°C and 100 ppm dissolved Si, inferred for the Neoarchean bottom waters); quartz forms through a number of steps, including opal CT, via recrystallization at higher temperature. During early diagenetic conditions (red arrow), the capacity of pore water to dissolve initially deposited amorphous silica increases exponentially, causing significant mobility of aqueous SiO_2 within the sediments. From Williams and Crerar (1985b).

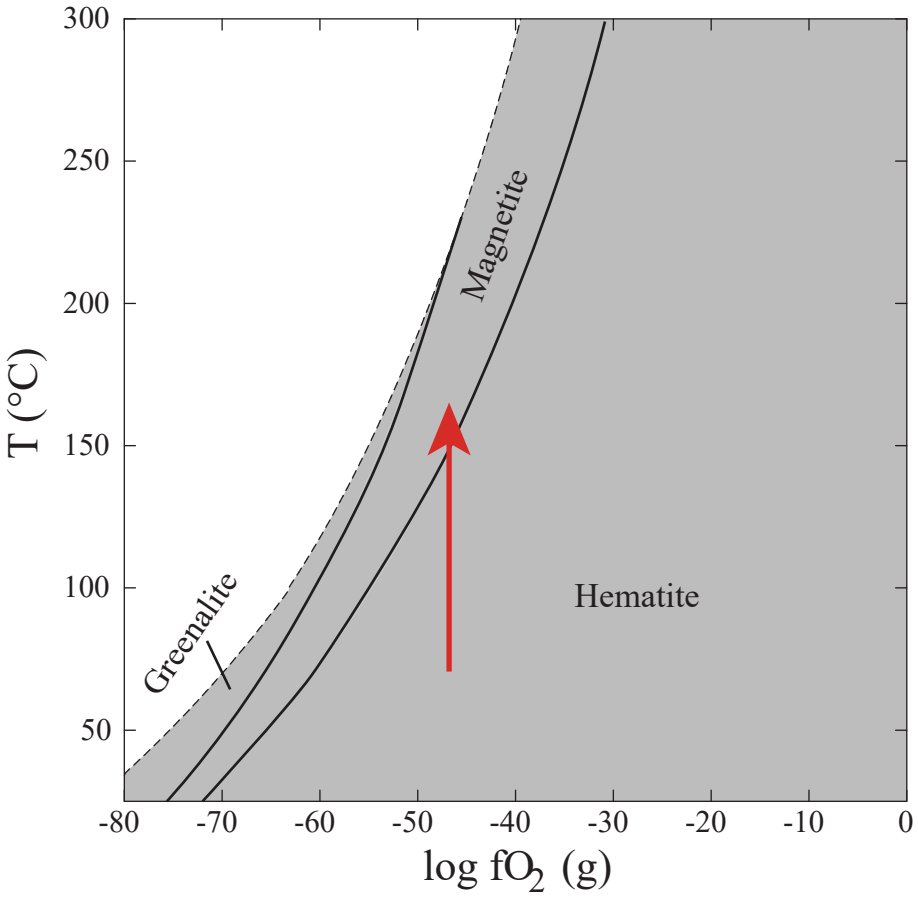


Figure 2.30: Temperature - fO_2 stability diagram for the Fe-Si system. Rising temperature (red arrow) during diagenesis can shift the stability of the dominant Fe mineral from hematite to magnetite, all other factors equal. Modelled with GWB® with Fe^{2+} as aqueous iron species. Additional parameters are pH = 6, $a[H_2O] = 1$, $a[SiO_{2\,(aq)}] = 10^{-1}$, $a[Cl^-] = 10^{-3}$. Cronstedt 7A, Fayalite, and FeO suppressed.

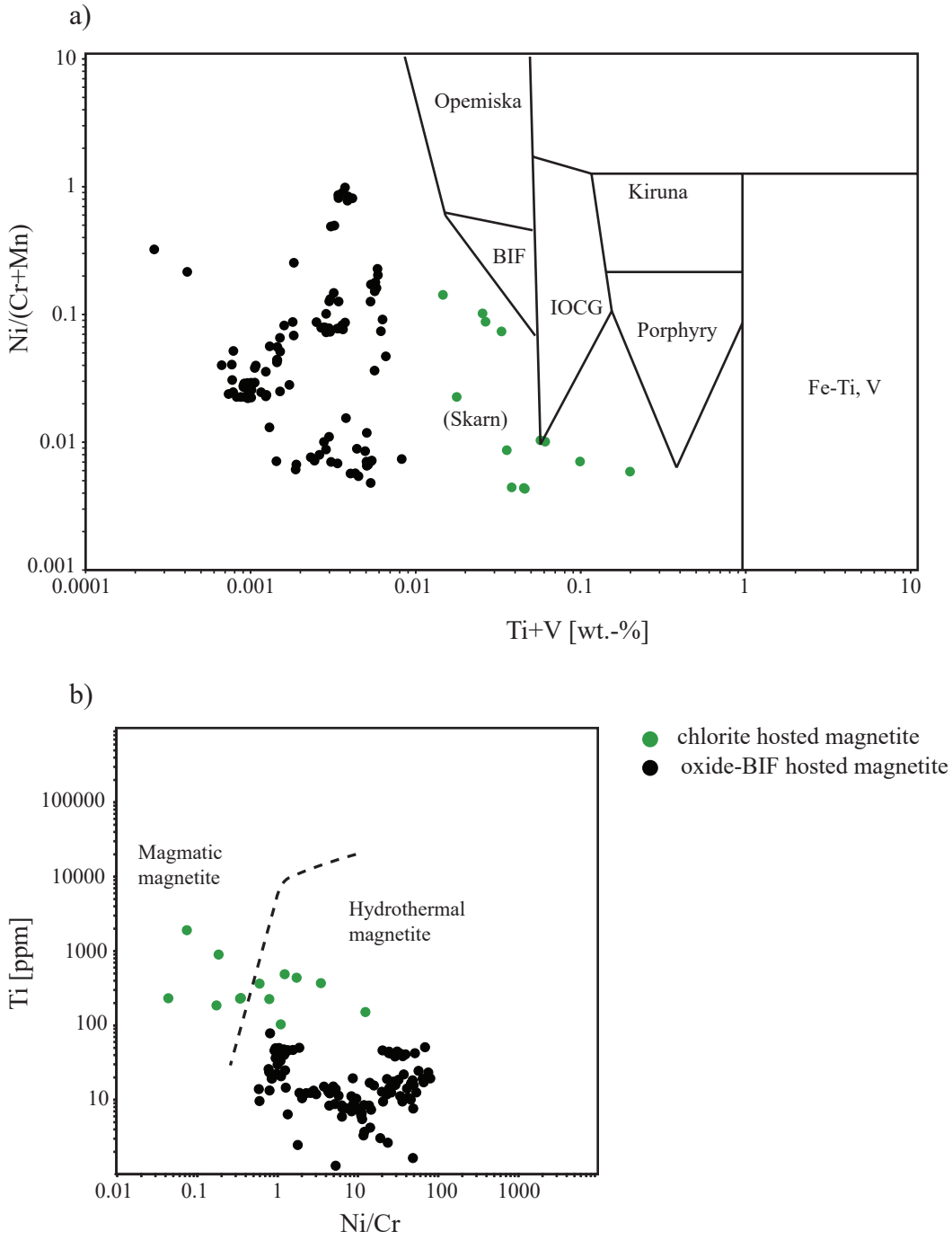


Figure 2.31: Plots of the Temagami magnetite compositions from oxide-facies and chlorite-facies BIF on magnetite classification diagrams after a) Dupuis and Beaudoin (2011) and b) Dare et al. (2014). Magnetite from the chlorite-facies BIF is clearly distinguished from magnetite in the oxide facies based on Ti (and V) content. Oxide facies magnetites plot in the extended hydrothermal fields in both diagrams, however, the data cover a very large range compared to magnetite compositions from other hydrothermal or magmatic deposits, highlighting the need to review the classification.

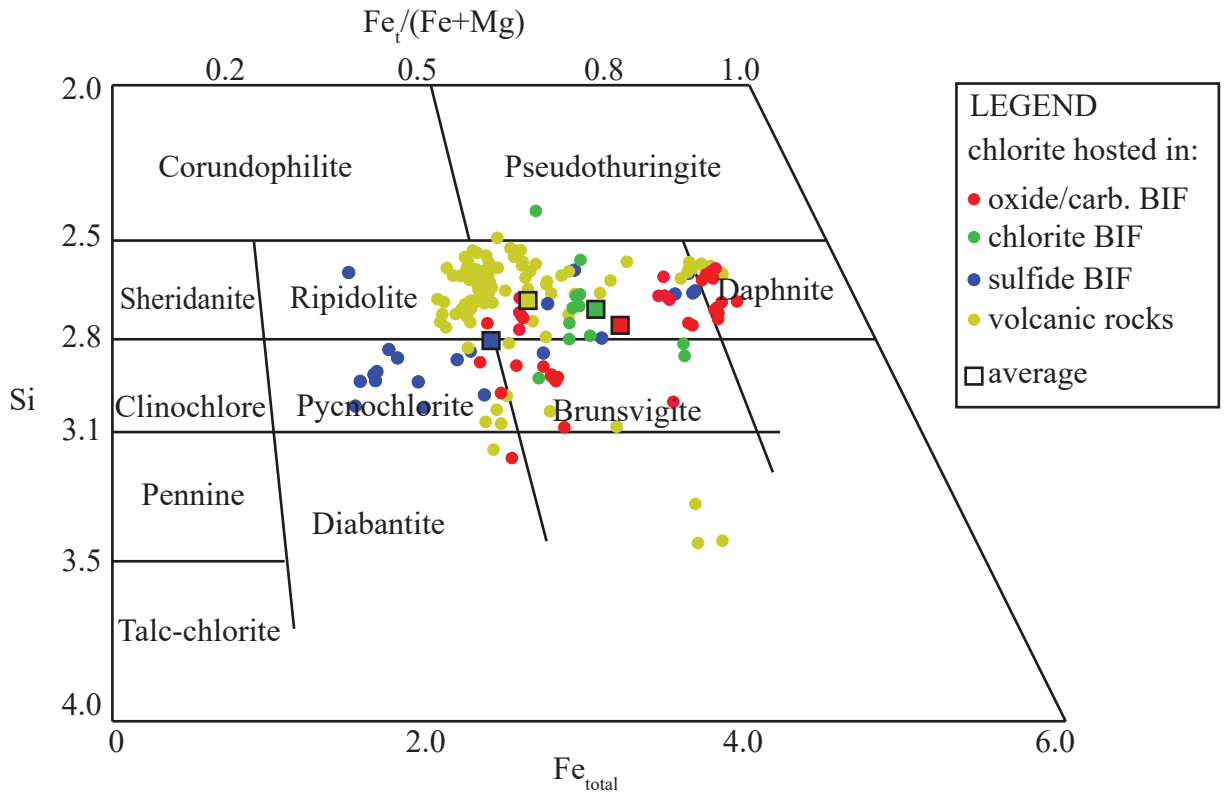


Figure 2.32: Classification of chlorite in the Temagami BIF and altered host rocks (n=187 from Streit, 2018; and this study). The dominant chlorite compositions in oxide-facies BIF correspond to ripidolite, pycnochlorite, brunsvigite, and daphnite (after Hey, 1954) with a broadly bimodal distribution between high- Fe/(Fe+Mg) daphnite, mostly in carbonate facies, and intermediate Fe/(Fe+Mg) ripidolite and brunsvigite in chert and magnetite facies (e.g. 11-36). Chlorite in the volcaniclastic units and chlorite-facies BIF is mostly ripidolite. Chlorite hosted in sulfidic cherts has the lowest average Fe/(Fe+Mg) corresponding to pycnochlorite. On average, chlorite in the BIF has higher Fe/(Fe+Mg) than chlorite in the host rock volcanic rocks.

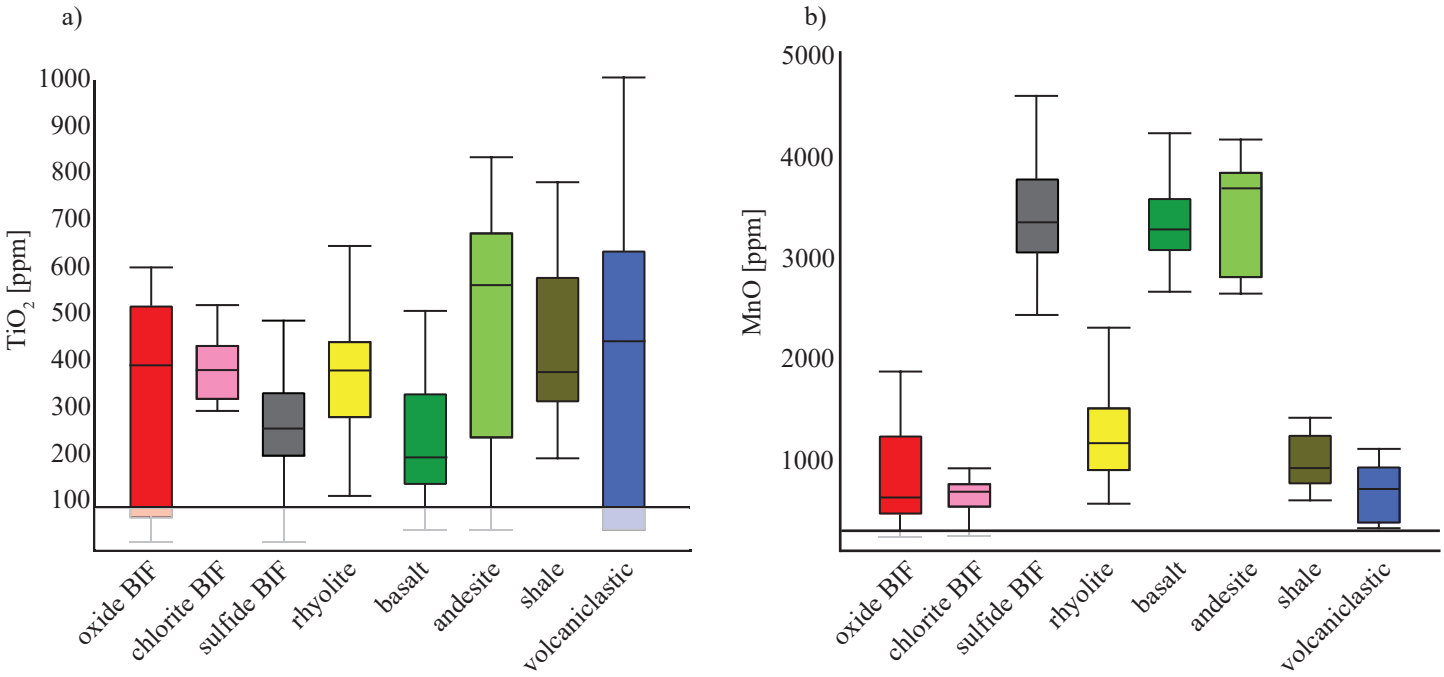


Figure 2.33: Box-and-whisker plots of TiO_2 and MnO in chlorite from the Temagami BIF and host rock (n=187 from Streit, 2018; and this study) a) TiO_2 concentrations in chlorite from all facies of the BIF are broadly similar to that of chlorite from the volcanic host rocks but somewhat lower than that of chlorite in the andesite, shale, and volcaniclastic units. b) MnO concentrations in chlorite from the oxide facies BIF and volcaniclastic units are low compared to that of chlorite in the altered volcanic rocks. Concentrations in chlorite from the sulfide facies BIF are somewhat higher, possibly reflecting the association with Mn-bearing carbonate in this facies. Boxes represent the 25th to 75th percentile of results, whiskers encompass 95% of the data. The approximate detection limits by EPMA are indicated by the black line and shaded area. Median values are indicated by the black lines in each box. Outliers omitted.

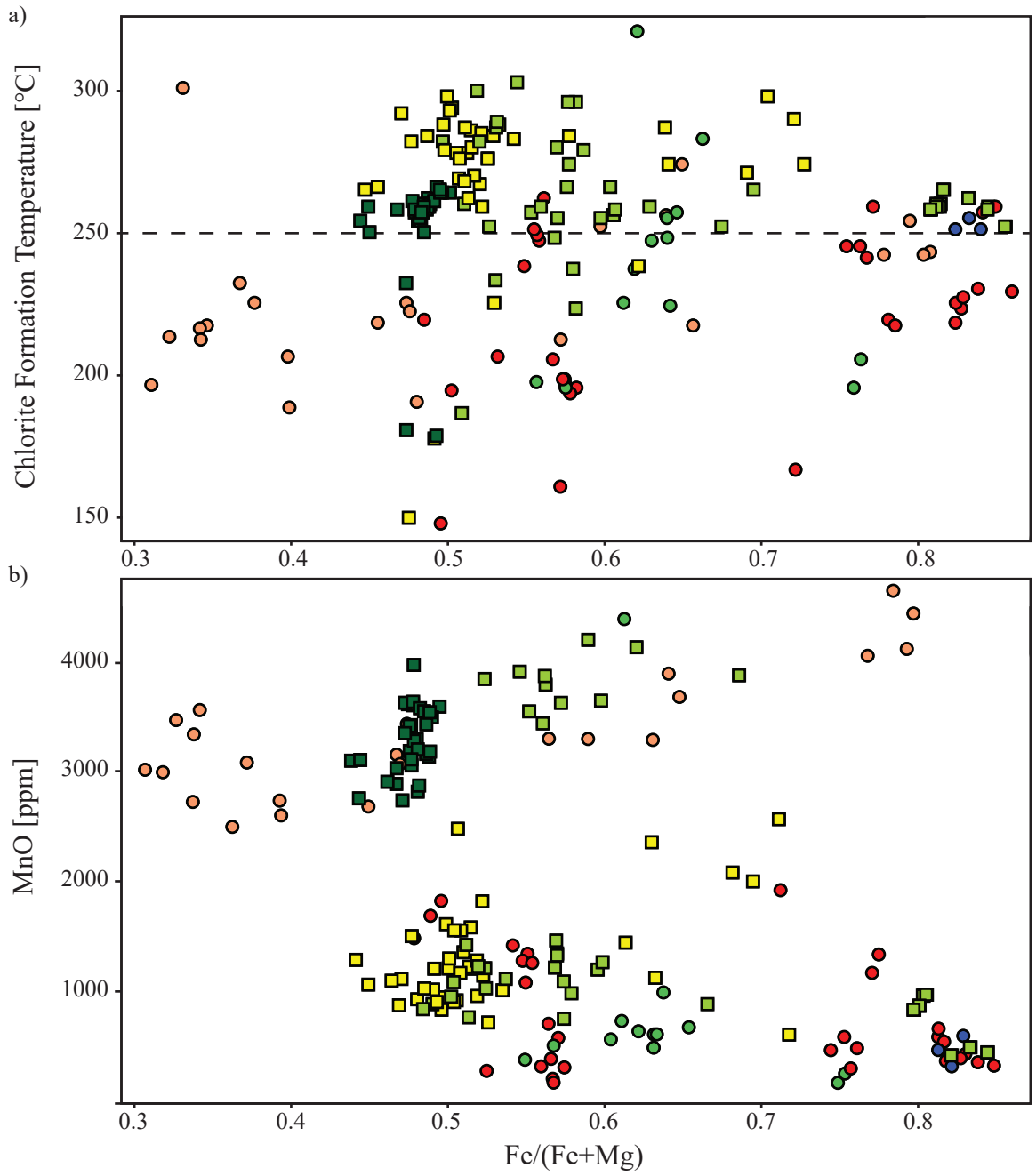


Figure 2.34: a) Calculated formation temperatures of chlorite in oxide facies BIF and altered volcanic host rocks (after Zang and Fyfe, 1995; see text for discussion). Data are from Streit, 2018, and this study (n= 187). Formation temperatures of chlorite based on tetrahedral Al vary significantly and independently of Fe/(Fe+Mg) but are generally higher for chlorite in the altered volcanic host rocks compared to that of chlorite in the oxide-facies BIF.
b) MnO concentration in chlorite appears to be a strong discriminant of different host lithologies, as indicated in Figure 2.33 b), with manganiferous chlorite common in sulfide facies BIF and altered mafic and intermediate volcanic rocks.

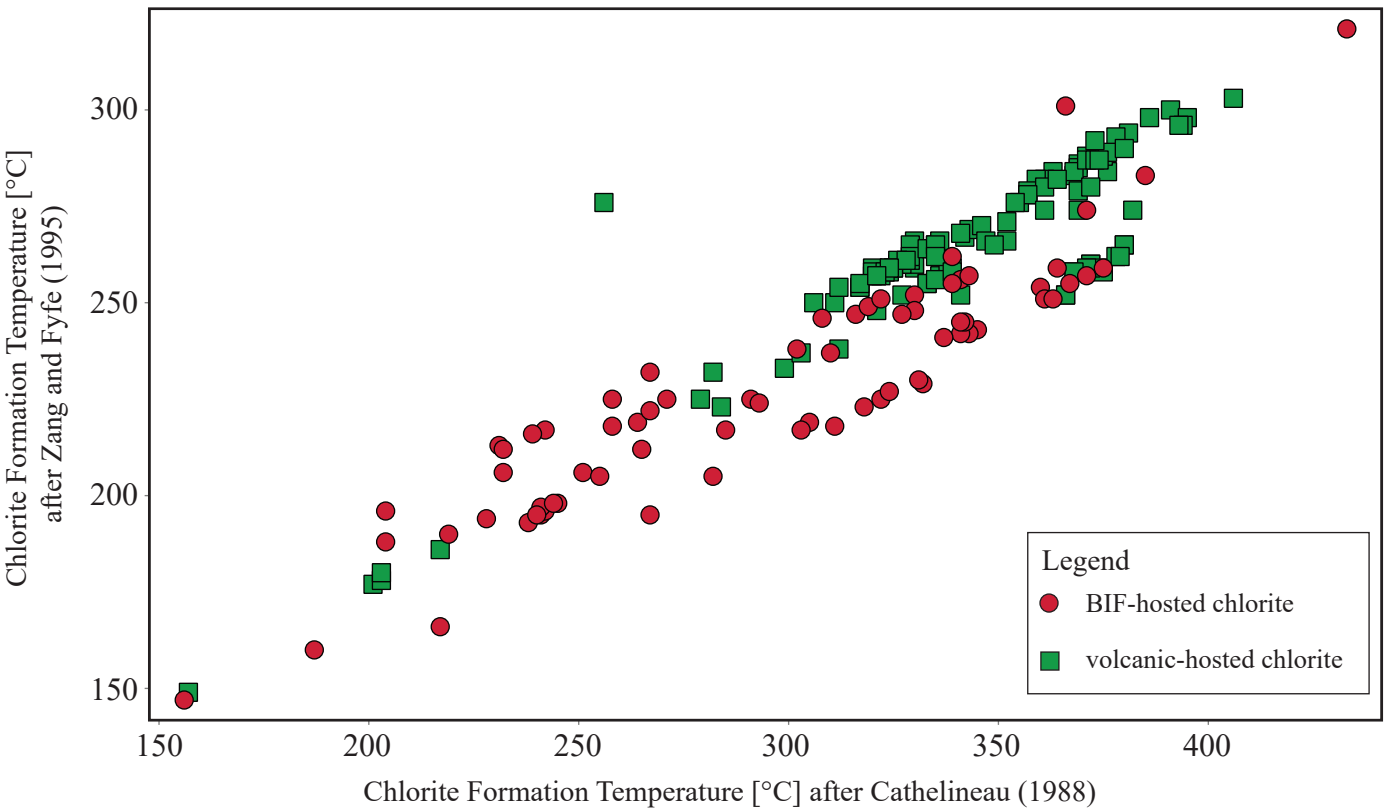


Figure 2.35: Comparison of different geothermometers applied to chlorite in Temagami BIF. Calculated temperatures after Zang and Fyfe (1995) and Cathelineau (1988) are well correlated but are systematically higher for Cathelineau (1988), basing the formation temperature exclusively on the abundance of tetrahedral Al in chlorite. In contrast, the chlorite geothermometer after Zang and Fyfe (1995) applies the Fe/(Fe+Mg) ratio as a correction factor to calculate the temperature based on tetrahedral Al, yielding slightly different and more realistic temperatures in Temagami BIF.

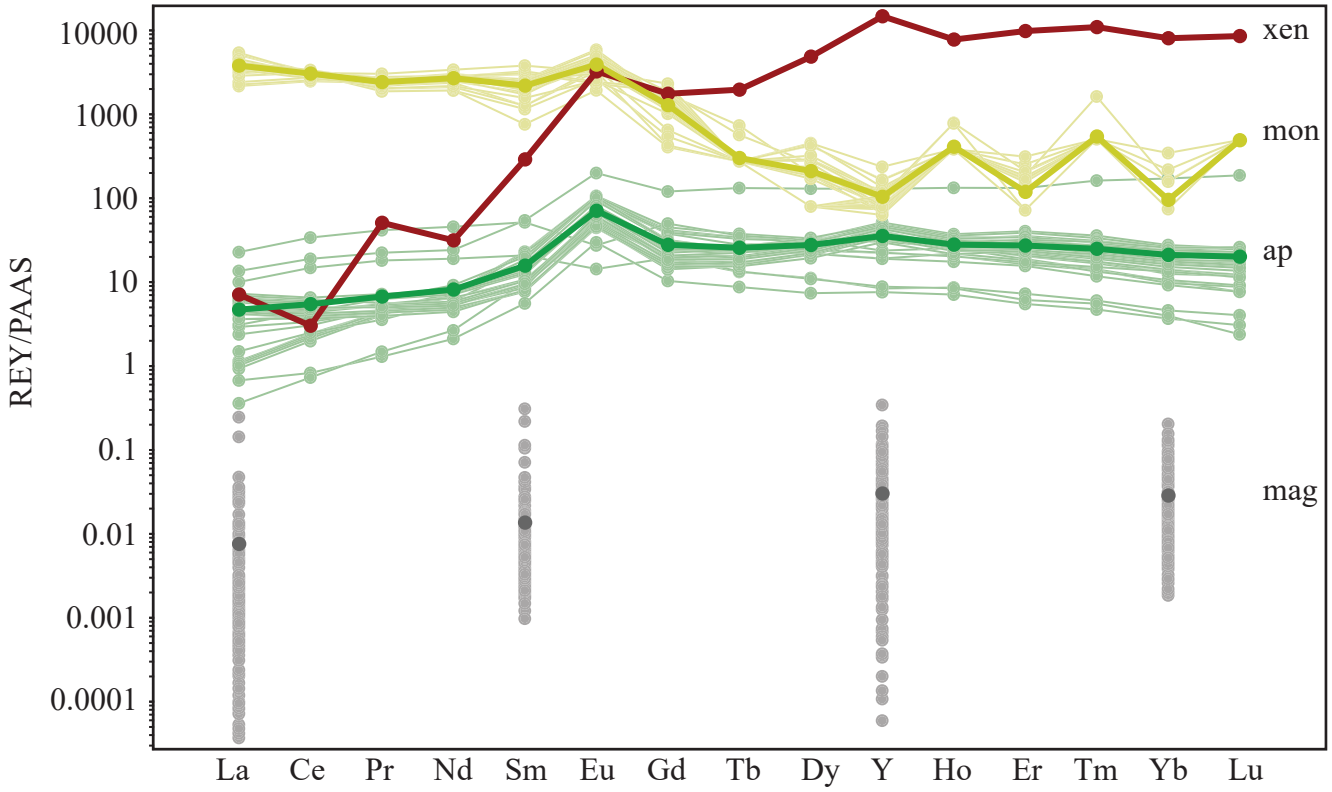


Figure 2.36: PAAS-normalized REY abundances in different host phases determined by LA-ICP-MS (magnetite, apatite) and EPMA (monazite, xenotime). Bold lines are averages for each mineral species. The phosphates are enriched in REY by several orders of magnitude and are the dominant hosts for REY. Apatite REE follows closely an “anoxic hydrothermally-influenced seawater”-trend with LREE depletion, no Ce- but pronounced positive Eu and Y anomalies. Values below detection limit by EPMA were replaced by 0.5*bdl (La, Ce, Pr in xenotime, most Tb, Lu in monazite).

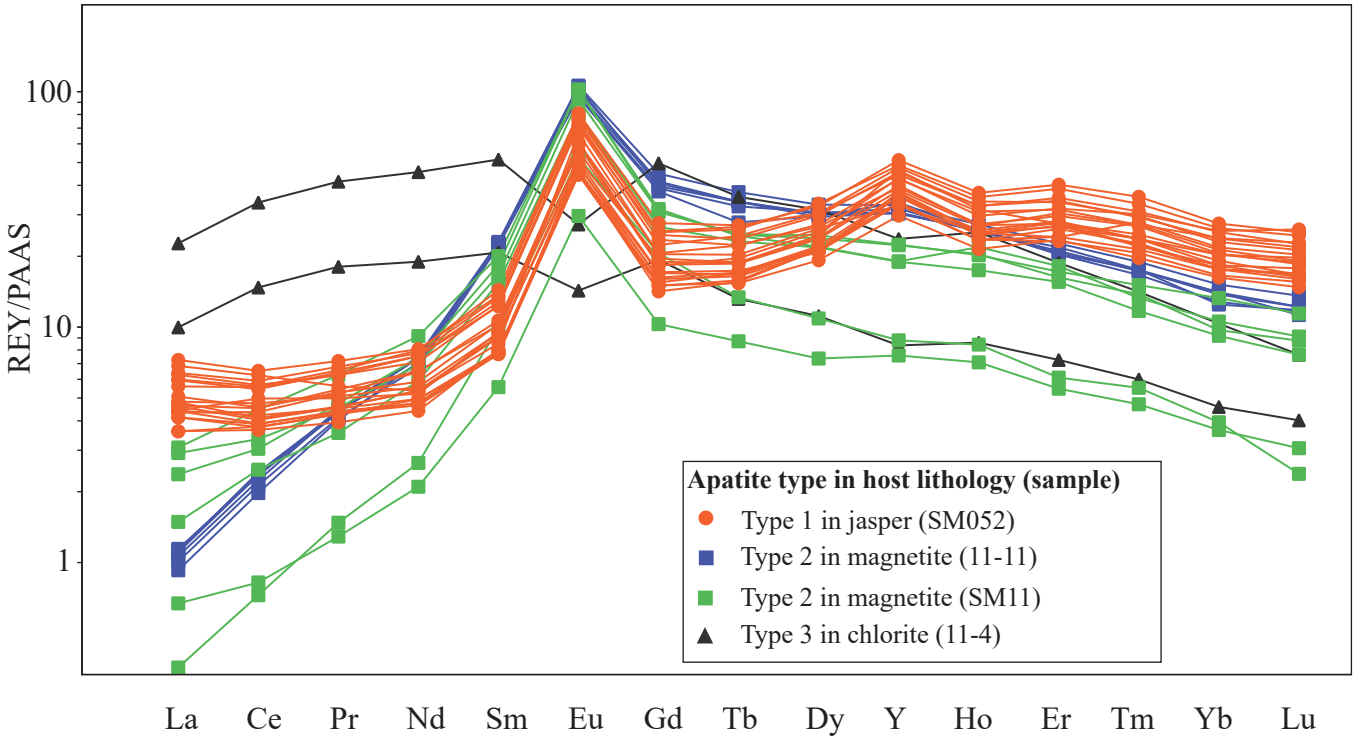


Figure 2.37: PAAS normalized REY patterns for Type 1 apatite in jasper (circles), Type 2 apatite in magnetite (squares), and Type 3 apatite in chlorite layers (triangles) in four different hand samples. The REY pattern of Type 1 apatite in jasper, interpreted to represent authigenic growth during diagenesis, reflects both hydrogenous and hydrothermal sources. REY patterns of Type 2 apatite inclusions in magnetite are similar to those of Type 1 apatite in jasper but lack Y and La anomalies reflecting preferential loss of those elements during diagenesis before REY incorporation in Type 2 apatite during late diagenesis. Chlorite layers contain detrital igneous apatite, indicated by the negative Eu anomaly and HREE depletion.

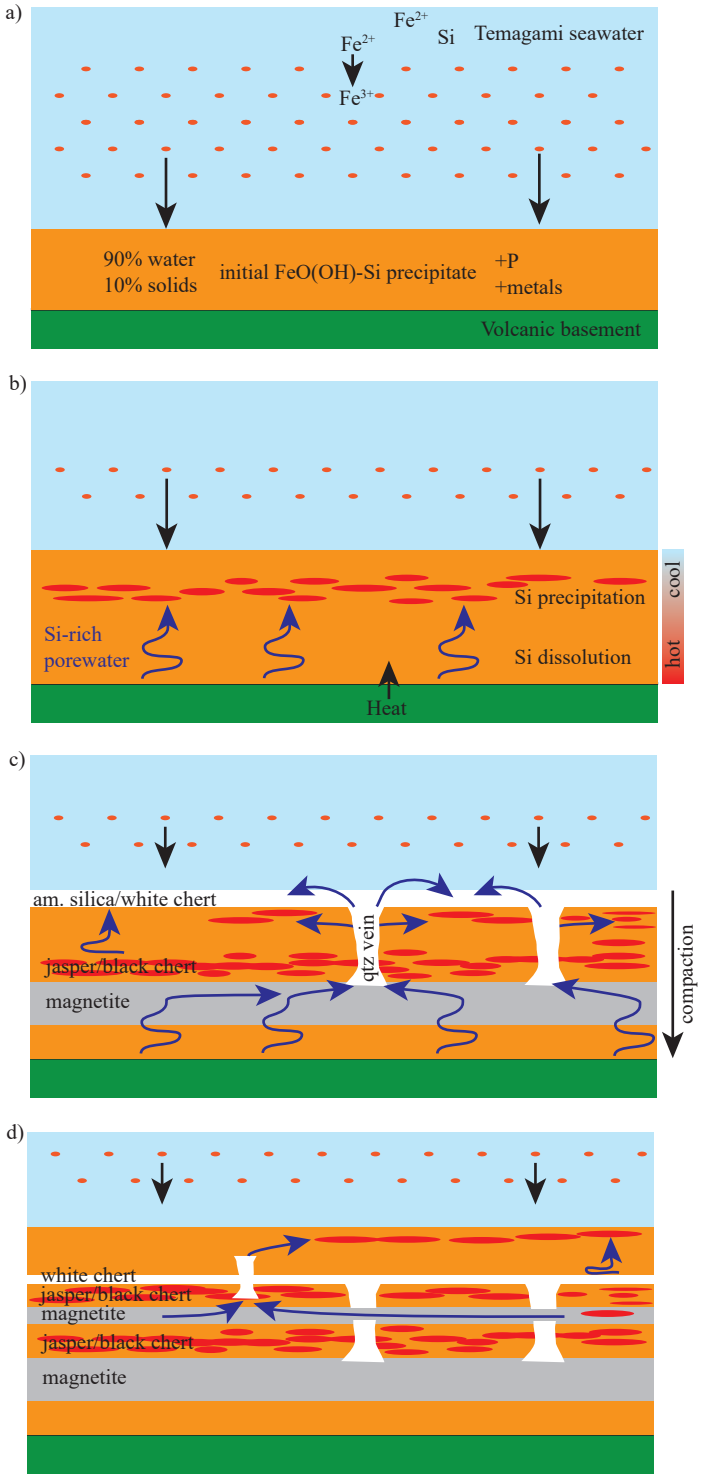


Figure 2.38: Simplified conceptual model of the development of oxide-facies BIF at Temagami. a) The initial precipitate of Fe-oxyhydroxides and silica was deposited at the stratigraphic top of each volcanic cycle (see Figure 2.2) b) Heated from the bottom, the Fe-oxide phases were nucleated in the Fe-oxyhydroxide-silica gel and the increased temperatures of the pore fluids led to increased Si solubility. The Si-rich pore waters diffused outward and, at the top of the sediment package cooled at the sediment-seawater interface causing precipitation of silica and the formation of first jasper. c) Subseafloor silicification eventually sealed the layers against upward flow of pore water, forcing predominantly lateral flow and breakouts with minor quartz veining. Escape of silica to the seafloor may have contributed to the formation of white chert layers. Increased temperatures led to the formation of magnetite from earlier Fe-oxides with increasing crystal growth in the centers of the layers. d) Continuous deposition of Fe-oxyhydroxide-silica gel and progressive diagenetic recrystallization resulted in repeated development of the oxide-facies layers that make up the BIF.

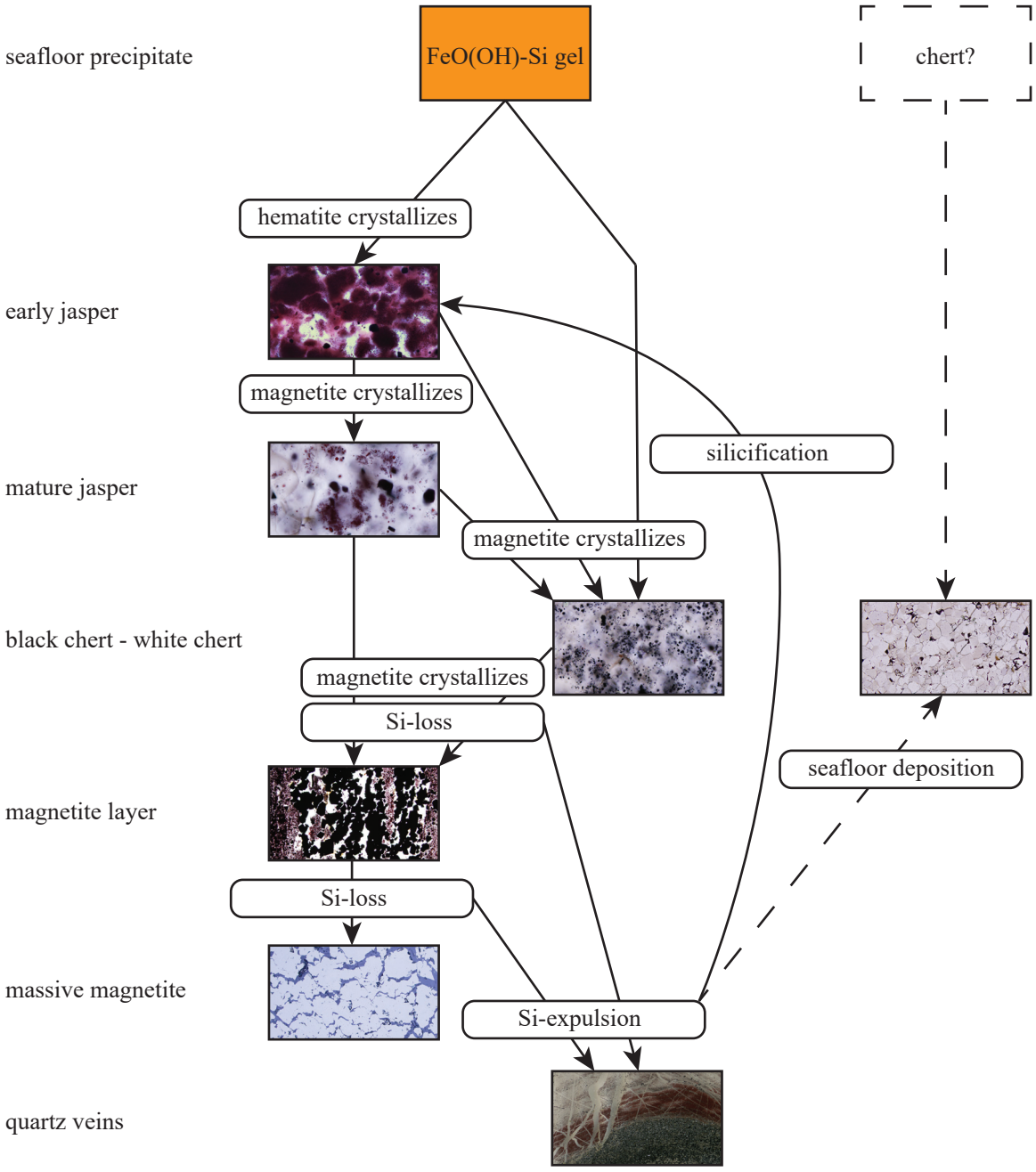


Figure 2.39: Flowchart of the development of oxide-facies BIF at Temagami (see Figure 2.38).

Chapter 3

Geochemistry of the Oxide-, Silicate-, Carbonate-, and Sulfide Facies of the 2.73 Ga Temagami Iron Formation: New Evidence of the Depositional Pathways and Diagenetic Processes of Neoarchean Algoma-Type BIF

Abstract

Banded iron formation (BIF) is widely regarded as an important archive of paleoenvironmental conditions of the Precambrian oceans. BIFs are also important time-stratigraphic markers of changes in volcanism, sedimentation, and geochemical inputs into their host basins. This study examines the spatial and temporal variability of trace element geochemistry in the 2.73 Ga Temagami BIF, a type locality of Late Archean Algoma-type BIF. These exceptionally well-preserved chemical sediments formed in several large volcanic sub-basins underlain by bimodal volcanics with precipitation of oxide-facies BIF distal to hydrothermal venting. The major and trace element geochemistry of the BIF layers show a strong mineralogical control, reflecting mainly diagenetic processes in an initial Fe-oxyhydroxide and silica precipitate. Original jasper layers (fine-grained hematite and chert) were converted to magnetite-rich layers by dewatering, expulsion of silica, and volume loss. Important geochemical differences between the layers, as well as stratigraphically and along strike in the mine, are interpreted to reflect mainly scavenging from seawater and clastic sedimentation. Little hydrothermal plume fallout is captured in the Temagami BIF, with orders of magnitude lower abundances of indicator elements such as Cu, Pb, Zn, As, and Sb compared to oxide iron formation formed as exhalatives related to VMS deposits. Si forming the cherty matrix in BIF, as well as REE, P, Mo, and U were controlled by adsorption onto primary Fe-oxide phases under anoxic or trace-oxygen conditions. While the Fe was likely hydrothermally sourced, it was probably not derived from local, focused hydrothermal venting, but deposition of Fe^{2+} accumulated in the marine water column triggered by potentially biologically controlled oxidation. The spatial and temporal scales of the geochemical inputs, spanning several hundred km^2 and possibly up to 3 m.y. of continuous deposition, suggest open-ocean conditions rather than a fully enclosed volcanic sub-basin. Careful examination of BIF geochemistry suggests long residence times of the hydrothermal components in the volcanic basins, indicated by REE and Y: Large La and Y anomalies, as well as light rare earth element depletion are features developed during seawater-particle interaction before deposition of REE in BIF. Bulk geochemical data show that there was little or no free sulfide available and silica concentrations in the basin were mostly below saturation of 2.2 mM, based on the presence of widespread unsilicified volcaniclastic layers intercalated with Si-rich BIF. Instead, Si deposition was exclusively linked to BIF deposition through Si-scavenging by Fe-oxyhydroxides, keeping

Si-concentrations in the water column below saturation. Early models of alternating precipitation of Fe and silica (e.g., during breaks in Fe precipitation) are not supported by the geochemical data. The best preserved material from the original Fe-Si precipitation are hematitic jasper layers, which record the geochemical characteristics of the Neoarchean water column. These include higher relative abundances of transition metals in solution (i.e., Zn, Ni, Cr, As, and Sb), and less abundant redox-sensitive elements (Mo, Re, U, and V) and alkali and alkaline earth elements (Ba, Cs, Rb) compared to modern oceans, reflecting hydrothermally-controlled seawater chemistry in the Neoarchean compared to bigger impact of continental weathering in post-Archean marine environments. In contrast, the geochemistry of white chert and magnetite layers, which have commonly been analysed in paleoenvironmental reconstructions of BIF basins does not record seawater geochemistry, but instead reflects diagenetic processes. Elements preferentially hosted in magnetite (e.g. Ge, Mn) are enriched in magnetite layers, while more mobile elements (As, Hg, B) are recycled to the water column with Si-rich pore waters escaping the sedimentary column. White chert deposited from recycled pore water on the seafloor captures the geochemical fingerprint of the bulk BIF sedimentary package and does not represent direct precipitation from the water column.

3.1 Introduction

The current understanding of Archean ocean chemistry is mostly based on the record of marine clastic and chemical sediments. Banded Iron Formations (BIF) have proven particularly useful in deciphering the chemistry of the seawater from which they precipitated (Klein, 2005; Ohmoto et al., 2006; Bekker et al., 2010). Most studies have focused on Superior-type BIF and shelf-proximal black shales deposited in Proterozoic marginal basins. However, less is known about the chemistry of the Neoarchean deep ocean where Algoma-type BIF were formed. Here, we present high-precision whole-rock geochemical analyses of 65 samples from the 2.73 Ga Temagami greenstone belt, considered to be one of the classic localities for Late Archean Algoma-type BIF. The results reveal a number of different primary and secondary processes responsible for the trace element geochemistry of the BIF layers, from scavenging during initial deposition, remobilization during diagenesis, and metamorphism. We show that these effects can have an important influence on trace element geochemical markers widely used to infer primary depositional conditions. However, careful reconstruction of the chemical compositions of the different BIF facies can yield important clues to the element budgets of the host volcanic basins and identifying the conditions for the initiation of Fe-oxidation in the water column.

We show that Fe-oxyhydroxides, as well as organic compounds and trace sulfide, which formed in the water column are effective scavenging agents and act as shuttles of elements from hydrothermally-influenced seawater to the sediments, where a geochemical fingerprint of the basin waters can be preserved (cf. Bau, 1999; Holland, 2003; Ohmoto et al., 2006; Bekker et al., 2014). During the time of BIF deposition at Temagami, warm, dominantly anoxic and strongly hydrothermally influenced Mesoarchean (3.2-2.8 Ga) oceans (Knauth and Donald, 2003; Robert and Chaussidon, 2006; Blake et al., 2010) were transitioning into variably reduced basins (Garvin et al., 2009; Kendall et al., 2010; Scott et al., 2011), many with locally stratified bottom waters and diverse microbial communities (Holland, 2003; Anbar et al., 2007; Reinhard et al., 2009; Czaja et al., 2012). While the surface layers may have experienced rapidly fluctuating conditions at this time, little is known about the effects in the deep volcanic basins (Holland, 2003; Lowenstein et al., 2014).

BIF are an important archive of these conditions because the Fe-oxyhydroxides are potent scavenging agents that record the geochemical and isotopic fingerprint of the local bottom water. The general lack of detrital input compared to shales also improves the likelihood of unambiguous geochemical signals (Kaufman et al., 1990; Bau and Alexander, 2009; Bekker et al., 2010; Gourcerol et al., 2016). However, attempts to draw conclusions from the geochemistry of BIF have rarely considered the complex geochemical environment of their deposition or the many post-depositional effects. This study examines the important chemical changes that attended the transformation of primary Fe-oxyhydroxide precipitates to the present oxide-facies BIF at Temagami and the implications for interpreting the depositional conditions.

3.2 Algoma-type BIF at Temagami

The Temagami greenstone belt is a Neoarchean succession of predominantly intrusive and extrusive volcanic rocks, intercalated with clastic sediments and BIF (Fig. 3.1). The bimodal volcanic complex that hosts the Temagami BIF is closely related in age to the Abitibi greenstone belt (Bennett, 1978; Ayer et al., 2002) and comprises at least two volcanic cycles of tholeiitic basalts to calc-alkaline intermediate and felsic volcanic extrusive- and pyroclastic rocks (Fig. 3.2: Fyon and Crocket, 1986). Local tonalite-trondhjemite-granodiorite-style intrusions are potential sources for some of the volcanic extrusive material (Blum, 1986). Both volcanic cycles are capped by BIF, which in turn are overlain by mafic tholeiitic volcanic rocks (Fyon and Cole, 1989). The tectonostratigraphic position of BIF in greenstone belts is of considerable importance because BIF deposition records time gaps between the major volcanic cycles (Thurston et al., 2008). These were times of relative volcanic quiescence during which substantial (sub-)seafloor mineralization may have taken place (Peter, 2003; Franklin et al., 2005).

Exposures of the Temagami BIF are among the best known examples of Algoma-type iron formation (Gross, 1965a,b, 1980). They occur as stratiform lenses, several kilometers in strike length and up to 120 meters in thickness and are characteristically thinly banded or laminated with interbeds of jasper, ferruginous grey chert and hematite and magnetite. They are integral parts of the volcanic succession and include minor silicate (chloritic), carbonate and sulfide facies (mainly fine-grained clastic units such as black shales to semi-massive sulfide and sulfidic

chert) in addition to the cherty oxide facies. The latter were formerly present in the open pits and have been mined out (Fig. 3.3).

The Sherman Mine exploited the Temagami BIF in four open pits. The total mined material in the Sherman Mine was 85 million tonnes. Based on the exposures of BIF in the two main units, we estimate that the total tonnage of BIF in the area was at least 866 million tonnes, to a depth of 250-1000 m. The true vertical extent of the BIF lenses is unknown and, because of the vertically dipping stratigraphy, could be much more than suggested here. Regional aeromagnetic surveys indicate continuity at least 40 km along strike and similar or larger iron formations between Cummings Lake and Lower Bass Lake in Scholes township (see review on the gelogy of the Temagami Greenstone Belt in Chapter 2; Meyn, 1977; Bennett, 1978; OGS, 2001; McBride, 2010).

3.2.1 Local stratigraphy

The area around the Sherman Mine was first systematically mapped by Moorehouse (1946) and later by Bennett (1978). A characterization of the volcanic system in the area was provided by Bowins and Heaman (1991), building on earlier reports of Bowins (1989), Boyum and Hartviksen (1970), Donaldson and Munro (1982), Fyon and Crocket (1986), Hurley (1985), and Pye et al. (Pye et al., 1972). A summary of the age relationships is provided by Ayer et al. (2006). The two volcanic cycles depicted in Figure 3.2 form the core of the 8 km-long Temagami greenstone belt. The volcanic cycle in the north (Sequence A and B) is dominated by tholeiitic basalt transitioning into intermediate and felsic extrusive and pyroclastic material and is capped by the North BIF (inferred younging to the south). The immediate footwall of the North BIF is mainly felsic pyroclastic material in the area of the West Pit and graphitic-sulfidic units at the North Pit (Hurley, 1985). The volcanic cycle in the south (Sequence D and E) faces to the north and contains more mafic volcanic material, subdivided into tholeiitic basalts at the base, overlain by calc-alkaline mafic, intermediate, and felsic flows, and then by pyroclastic deposits and the South BIF. The south BIF lenses are deposited directly on thin turbidites around the South Pit (Hurley, 1985) and sandstone or greywacke in the East Pit and Hwy 11 outcrop (Fig. 3.3). The South BIF is then capped by mafic flows in the area of the Highway 11 outcrop and East Pit, and thick mafic clastic sedimentary rocks at the South Pit (Bennett, 1978; Fyon and Crocket, 1986).

The stratigraphic succession was overturned during the earliest large-scale deformation event and all exposed units are now subvertical (possibly corresponding to D1 in the Abitibi belt around 2695 Ma: Ayer et al., 2010). The observed facing directions in the northern and southern cycles suggest the presence of a D1 fold, termed the Tetapaga syncline immediately north of the South BIF (Fig. 3.2; Bennett, 1978; Ayer et al., 2005). The location of the axis has been inferred from dip directions in the South BIF (~80° N) and pillow facing directions in the north (dipping ~80-85° S). Bennett (1978) interpreted the fold as a strongly asymmetric syncline with the South BIF and the North BIF facing each other as stratigraphic equivalents on opposite limbs of the fold. The only available ages of the volcanic rocks on opposite sides of the inferred syncline are consistent with the presence of a fold (Ayer et al., 2006), and graded bedding and erosional features in clastic units intercalated with the South BIF are also interpreted to face north (Bennett, 1978; Johnston, 1987; Donaldson and Garrett, 1991). There are many pillow-facing directions in the north, but only one has been reported south of the South BIF, several kilometers from Temagami (Fig. 3.1; Bennett, 1978; Johnston, 1978; Donaldson and Garrett, 1991). Although most workers accepted the Tetapaga syncline, they identified the North and South BIF as independent deposits at similar stratigraphic levels. Evidence for two separate BIF units includes the different volcanic lithologies in the immediate stratigraphic footwalls of the North and South BIF, sulfidic horizons present on the north side of both the North and South BIF, abundant clastic sedimentary rocks at the base and top of the South BIF while sedimentary units are rare in the North BIF, and tuff marker horizons present in the North BIF that are missing in the South BIF (Campbell, 1978; Hurley, 1985; Fyon and Cole, 1989).

The volcanic rocks of the Temagami Greenstone Belt are intruded by two large tonalite-trondhjemite-granodiorite plutons: the Iceland Lake pluton and the Strathy-Chambers batholith. The intrusions have been interpreted as synvolcanic, and emplacement depths of 7-10 km have been inferred from amphibole chemistry (Blum, 1986). Similar ages and REE systematics of some phases of the intrusions and the felsic rocks of the volcanic cycles have been interpreted to reflect a genetic link (Blum, 1986; Ayer et al., 2006). All lithologies in the area have been subjected to greenschist facies metamorphism, and locally higher-temperature contact metamorphism in proximity to the felsic intrusions (Bennett, 1978). Blum (1986) inferred peak

metamorphic temperatures of 300°C locally up to 400°C from whole-rock oxygen isotope studies of magnetite and chert facies BIF.

3.2.2 Facies distribution and abundance

The ore of the Sherman Mine consisted mostly of oxide facies BIF (i.e., interlayers of hematite, magnetite, and chert), with less abundant chlorite (silicate) facies and sulfidic chert (sulfide-facies). For grade control, Boyum and Hartviksen (1970) described the different facies as magnetite-jasper and magnetite-jasper-chert in the North BIF and mostly magnetite-chert and less jasper in the South BIF (cf. Ginley, 2016). The reported ore grade of the mined material was similar throughout, although bright red jasper appears to have been more common in the North Pit compared to the darker coloured jasper in the South Pits (Boyum and Hartviksen, 1970; Ginley, 2016). Non-ore interlayers included mainly volcanic-derived material, locally identified as silicate facies BIF, including small mafic flows, turbidites, or "ash fall" deposits (Blum, 1986; Ginley, 2016). Sulfide and carbonate facies BIF were most common in the South Pits, in the immediate footwall of the main lenses of oxide-facies BIF and locally as lenses within the oxide-facies BIF (Gross, 2009).

A detailed petrographic and paragenetic study of the different oxide and silicate facies (Chapter 2) supports the interpretation that the original precipitates were likely a mixture of amorphous Fe-oxyhydroxides and iron-silica gel that flocculated in the water column and settled into layers from which the hematite, magnetite and chert (microcrystalline quartz) were crystallized. These observations are consistent with previous models of Algoma-type as well as Superior-type BIF deposition (e.g., James, 1954; Ayres, 1972; Dimroth and Chauvel, 1973; Krapež et al., 2003; Beukes and Gutzmer, 2008; Sun et al., 2015). However, there is ongoing debate about the relative importance of primary deposition versus diagenetic processes in the formation of the different BIF facies (e.g., Posth et al., 2008, 2013a,b). Our previous studies have shown that widespread mm-scale banding in the BIF is mainly a result of changes in crystal size after deposition and not a result of heterogeneous precipitation caused by seasonal or even diurnal variations in water column chemistry (e.g., Posth et al., 2008). Evidence of dewatering of the original Fe-(oxy)hydroxide and silica gels is found throughout the BIF layers (Chapter 2),

suggesting that geochemical remobilization of elements and large changes in volume likely accompanied diagenesis of the sediments.

In the Hwy 11 outcrop and among the ore blocks at the edges of the open pits in the Sherman Mine, individual jasper layers comprise between 5-10 vol.% of the BIF (cf. Fig. 3.4), with the greatest abundance in the North Pit. The jasper consists mostly of quartz (90 vol.%) and Fe-oxides (<10 vol.%) as finely disseminated hematite in a chert matrix. Jasper layers are <1 cm to 10 cm thick and are almost always found together with magnetite or black chert layers. Where jasper layers transition laterally or vertically into black chert, all of the cloudy hematite has been replaced by magnetite of similar or slightly larger grain sizes. Progressive recrystallization of hematite and redistribution of silica is interpreted to have been the main process of formation of the chert, hematite, and magnetite layers (see Chapter 2). In the North BIF, changes from jasper-magnetite to chert-magnetite occur over <100 m along strike (Campbell, 1978). While no reports of such large-scale transitions exist from the South BIF, similar transitions between jasper and black chert are observed on m- to cm-scale in ore blocks from both BIF members (Fig. 3.5).

The magnetite facies was the main ore facies of the Temagami BIF and was most common in the central part of the Sherman Mine, decreasing toward the Hwy 11 outcrop. Individual magnetite layers range in thickness from a few mm to about 5 cm and comprise ~25 vol.% of the Temagami BIF. The magnetite is commonly interlayered with chert, jasper, and chlorite bands. Magnetite and quartz are present in subequal amounts, with minor hematite, chlorite, and apatite (see Table 3.1). Where magnetite is less abundant, it occurs as cloudy aggregates of fine crystals (<5 μm) in chert, producing the black chert layers. Traces of pyrite, pyrrhotite, chalcopyrite, biotite, and carbonate are found in the interstitial spaces of large magnetite grains, together with monazite and xenotime. In massive magnetite layers, the magnetite forms larger, 20-500 μm crystals with interstitial quartz. The largest crystals locally preserve jasper at their centers and have poikioblastic textures around their rims, suggesting possible metamorphic overgrowths. Where mafic intrusions have cut the magnetite layers, skeletal overgrowths of secondary magnetite have formed together with biotite, stilpnomelane, and cummingtonite.

The white and black chert facies comprise ~50 vol.% of the Temagami BIF. Chert layers are <1 to 10 cm thick and can be traced over at least several metres in outcrop, except where they are brecciated or present as chert pods (see Chapter 2). On the scale of the large ore blocks, chert interlayered with magnetite and jasper is commonly present in sets of layers of similar thickness, but thicker chert bands or chlorite layers locally break up these sets. The chert layers consist of microcrystalline (20-100 μm) quartz with variable amounts of magnetite, hematite, and trace apatite, chlorite, and iron carbonates. "Black chert", which contains up to 30 vol.% disseminated magnetite, is most abundant; "white chert", which is virtually free of magnetite, hematite, or other minerals, accounts for about 10 vol.% of the Temagami BIF. Black chert is typically microbanded and its structure closely resembles the microbanded jasper, with fine cloudy magnetite rendering the chert dark grey to black in the outcrop. Chlorite is locally abundant in the quartz where the chert layers transition into chlorite layers.

The dominant silicate facies consist of discrete chlorite-rich layers, typically between 1-5 cm but up to metre-scale in thickness (see Fig. 3.5). These layers comprise ~10 vol.% of the Hwy 11 outcrop but <<10 vol.% in the ore blocks along the South and East pits of the Sherman Mine. In the North BIF, abundances of Fe-silicates increase from east to west (Campbell, 1978). The chloritic layers contain up to 80 vol.% chlorite together with quartz; some appear to be a product of mixing with chemical sediments, but most are chloritized volcaniclastic units. They are sometimes banded, alternating with quartz and, to a lesser extent, magnetite. The chemical sediments are distinguished from clastic units by the presence of CL passive quartz (see Chapter 2), lower abundance of ilmenite and detrital zircon, and greater abundance of diagenetic magnetite (cf. Chapter 2). Other Fe-silicates, such as greenalite, minnesotaite, stilpnomelane, biotite, garnet or amphiboles typical of metamorphosed BIF (e.g., Beukes, 1973; Gross, 1980; Klein, 1974; Klein, 2005) are not abundant but have been reported from parts of the North BIF closer to granitic intrusions (Bennett, 1978).

Sulfidic chert was locally abundant in the Sherman Mine. It contains abundant microcrystalline quartz (>75 vol.%), pyrite (<15 vol.%, but locally much higher), graphitic carbon (<5 vol.%), and traces of other sulfides, carbonates, chlorite, and apatite. The pyrite occurs variably as fine disseminations in the graphitic material, as large cm-scale nodules, as euhedral pyrite, and as

skeletal overgrowths on other minerals (Fig. 3.6). It is distinguished from pyritic black shale that occurs elsewhere in the mine area by the lack of a volcaniclastic or detrital silicate material. Two major occurrences of sulfidic units are present: i) a section north of the west wall of the South Pit, where there was a transition from oxide facies to carbonate facies and sulfide facies BIF (Jonasson, pers. comm. 2013); ii) a 3-10 m thick continuous band of sulfidic shale and sulfidic chert in the immediate footwall north of the North BIF, extending at least along the North Pit but likely along the entire North BIF (Campbell, 1978). Several other lenses of sulfide-facies BIF were reported within the North and South BIF (Gross, 2009); these were up to several metres in thickness but not as extensive as the other sulfide-bearing horizons and mostly occurred close to contacts with the stratigraphic footwall and hanging wall of the North and South BIF. Carbonate-facies BIF is no longer well exposed in the mine area but was locally abundant in the South Pit and East Pit (Fig. 3.3).

Discrete layers of chloritized tuffaceous material are present throughout iron formation. In the North BIF, a 0.5-9 m thick tuff horizon can be traced over 1.3 km along strike, but similar horizons are absent in the South BIF (Campbell, 1978). They are distinguished from silicate-facies BIF by the presence of recrystallized angular lithoclasts or crystals (interpreted to be glass shards), and a large component consisting of detrital quartz (CL active), zircon, and ilmenite. The ilmenite appears to be mainly an alteration product of a Ti-rich volcaniclastic component, such as biotite. In the Hwy 11 outcrop, there are more abundant chloritic layers than in other exposures of the BIF. Elsewhere, black shale is locally interbedded with volcaniclastic material and has been reported as “sulfide BIF” in some locations (e.g., at the shore of Vermillion Lake: Bennett, 1978), although this may be sulfidic chert.

In the Hwy 11 exposure, chert is more abundant (~30-40 vol.%) at the stratigraphic bottom of the two sections of the outcrop (Fig. 3.4). The upper parts of the two sections contain more abundant jasper (~20 vol.% compared to 5-10 vol.% in the lower parts of these sections). However, there appears to be little systematic variation in the abundance of the different facies in other parts of the mine area.

3.3 Previous work

Previous studies of the geochemistry of the Temagami BIF have been presented by Blum (1986), Bowins (1989), Ohmoto et al. (2006), Bau and Alexander (2009), and Viehmann et al. (2014). Blum (1986) and Bowins (1989) studied a suite of surface and drillcore samples during the active phase of the Sherman Mine; other studies focused mainly on grab samples from the Hwy 11 outcrop. The most complete study was by Bowins (1989), who documented enrichments in Fe, Si, Mn, P and Eu and identified hydrothermal, seawater-derived and clastic components of the BIF. Two notable theses by Hurley (1985) and Schwartz (1995) provided detailed characterizations of the footwall volcanic assemblages.

A major focus of all previous work was on the REE chemistry, and specifically evidence for bottom water conditions recorded by REE. Ohmoto et al. (2006) studied two samples of jasper and magnetite from the Hwy 11 outcrop and reported a negative Ce anomaly, which was interpreted to indicate an oxygenated water column. Bau and Alexander (2009) studied 3 chert and magnetite samples, also from the Hwy 11 outcrop, including two of the samples included in the study by Ohmoto et al. (2006). They used a microdrill to extract material from individual chert layers, producing 21 subsamples that were pulverized and then dissolved under pressure in a HF-$HClO_4$ solution and analysed by ICP-MS. They also analyzed the iron-formation standard materials, FeR-3 and FeR-4, produced by CANMET from the Sherman Mine ores. Bau and Alexander (2009) found no evidence of a Ce anomaly and concluded that the negative Ce anomaly reported by Ohmoto et al. (2006) was an artifact of La enrichment in many samples. Normalizing to PAAS, they concluded that the shape of the REE+Y profile (except for Ce and Eu) was similar to modern seawater, from which they inferred an open-ocean depositional environment.

Bau and Alexander (2009) also noted a lack of detrital input, which was interpreted to be consistent with a deep marine, open-ocean setting. They concluded that an enrichment of Hf over Zr and Ta, compared to chondrite values, reflected preferential scavenging of Hf from seawater, similar to that observed in modern oceans. Because U/Th values in the magnetite and chert samples were higher than in contemporaneous shale, they also concluded that the water column

might have been weakly oxidizing (reflecting the enhanced mobility of U^{6+} over U^{4+} under oxidizing conditions), but not enough to oxidize Ce. Like Bowins (1989), they inferred a strong hydrothermal input from persistent positive Eu anomaly in all samples. However, Bowins and Crocket (2011) interpreted the REE-bearing phosphate minerals, which dominate the REE budget of the BIF layers, to be largely diagenetic in origin. More recently, Viehmann et al. (2014) analysed nine samples of magnetite and chert from unknown locations in the mine by quadrupole ICP-MS and isotope dilution (Neptune) MC-ICP-MS. That study reported Hf and Nd isotope signals that were interpreted to reflect input from subaerially eroded continents, similar to modern seawater. Despite strong interest in the REE systematics of the Temagami BIF, few studies considered the major and trace element budgets in relation to a number of different depositional models.

3.4 This study

This work is a detailed examination of the whole-rock geochemistry of the most comprehensive suite of samples collected so far, with a careful consideration of the detailed mineralogy and facies relationships of the BIF. The geochemistry of the different BIF layers is considered in the context of a reconstructed history of BIF deposition, including the effects of diagenesis and metamorphism, and related to the spatial and temporal variability of these processes. Sampling was carried out to achieve the best representation of all facies of the BIF and its host rocks in the mine area. 37 samples were taken from a continuous section of the South BIF along the 230-m roadcut on Hwy 11 (Table 3.2, Fig. 3.7), where subvertical layering provided access to all oxide and silicate facies, from the first BIF deposition in contact with bedded greywacke in the south to the termination of BIF deposition where it is overlain by mafic volcanic rocks in the north. This exposure represents the outermost limit of the South BIF, in a distal setting relative to the Sherman Mine (Fig. 3.3). 31 additional samples were taken from ore blocks from within the Sherman Mine. The blocks measure 1-8 m^3 in size and were likely too big for the ore crusher. More than 500 were placed at the edge of the open pits during the mining phase, amounting to an estimated 7500 tonnes of ore material. Careful documentation of the blocks suggest that they are representative of material from the immediately adjacent open pit. An archive of material from a 350-m section of the west wall of the South Pit also was available (originally collected during the

final stages of mining by Gordon Gross and Ian Jonasson of the Geological Survey of Canada). These samples include the only remaining sulfidic chert from the mine (original location indicated in Fig. 3.7).

3.4.1 Sample preparation

62 samples were selected to represent the different BIF facies; individual layers were carefully cut out of the samples with a diamond blade saw. Obvious weathering or veining (late sulfides or carbonate) were avoided or removed. Individual samples were crushed with a hammer inside their sample bags; a steel jaw crusher was used for larger sample pieces. The rock chips were pulverized in a ceramic ring mill, with cleaning steps between samples involving runs with quartz sand and rinsing with ethanol and Milli-Q water. Previous studies with pure quartz sand have shown that grinding in ceramic has the potential to add traces of Ba (up to 0.9 ppm), Co (up to 0.7 ppm), Sr (up to 0.4 ppm), Cu (up to 0.3 ppm), Zn (up to 0.2 ppm), Rb (up to 0.1 ppm), Zr (up to 0.1 ppm), and Pb (up to 0.1 ppm) and <10 ppb of each REE, based on ten-minute runs in different mills (Takamasa and Nakai, 2009). This potential contamination is within the error of reproducibility of our measurements for Ba, Sr, Cu, Zn, and Rb in analyzed reference materials (FeR-3 and FeR-4: see Table 3.3). However, other elements for which reference values were not available (Co, Zr, Pb) could not be evaluated.

3.4.2 Analytical methods

In collaboration with Actlabs Activation Laboratories Ltd. of Ancaster, Ontario, an analytical protocol was established for the determination of low-level concentrations of trace elements in the BIF. This included a Total Digestion ICP-MS procedure ("Ultratrace 4" UT-4) in which 0.25 g of sample material was digested initially in HF, followed by a mixture of nitric and perchloric acids in multiple heating cycles until dryness. The dried sample was then brought into solution in hydrochloric and nitric acid, diluted, and analysed on a Perkin Elmer Sciex ELAN 6100 ICP-MS. The approach closely matches that used in other studies of BIF (e.g. Garbe-Schönberg, 1993; Dulski, 2001; Bau and Alexander, 2009; Pröfrock and Prange, 2012; Sampaio and Enzweiler, 2015). The following elements were determined (detection limits in brackets): Na (20 ppm), K (13 ppm), Zn (0.04 ppm), Cu (0.04 ppm), Pb (0.1 ppm), Ag (0.01 ppm), As (0.02 ppm), Sb (0.02 ppm), Hg (2 ppb), Tl (0.01 ppm), Cd (0.02 ppm), Co (0.02 ppm), Ni (0.1 ppm),

Se (0.02 ppm), Mo (0.01 ppm), Te (0.02 ppm), Sn (0.2 ppm), Bi (4 ppb), In (0.02 ppm), Re (0.2 ppb), W (0.02 ppm), Cr (0.1 ppm), V (0.2 ppm), Ga (0.02 ppm), Zr (0.2 ppm), Ba (0.2 ppm), Cs (0.01 ppm), Li (0.1 ppm), Be (0.02 ppm), B (0.2 ppm), Hf (0.02 ppm), Rb (0.04 ppm), and Sr (0.04 ppm). For each analysis, a comprehensive assessment of polyatomic interferences was carried out (see Appendix L). In-house standards, duplicate analyses of sample material, and eight certified reference materials (DH-1a, GXR-4, SDC-1, GXR-6, SAR-M [USGS], DNC-1a, SBC-1, and OREAS 45d) were used for quality control (see below). Analyses were also monitored using the CANMET certified BIF reference materials, FeR-3 and FeR-4, originally prepared from the Sherman Mine ores (Abbey et al., 1983). Several elements analyses by TD and FUS (see below) are subject to losses due to their volatility (e.g., As, Sb, Hg). The results for these elements are treated as minimum values; however, comparison with certified standards having a similar matrix shows no systematic deviation from accepted values.

For Si (100 ppm), Al (100 ppm), Fe (100 ppm), Ca (100 ppm), Mg (100 ppm), P (100 ppm), Ti (10 ppm), Mn (10 ppm), Ge (0.5 ppm), Sc (1 ppm), Nb (0.2 ppm), Ta (0.01 ppm), U (0.01 ppm), Th (0.05 ppm), Y (0.5 ppm), and the REE (0.002 – 0.05 ppm), we used a lithium metaborate/tetraborate fusion, followed by ICP-OES and ICP-MS analysis. The samples, as well as a reagent blank, were combined with a flux of lithium metaborate and lithium tetraborate and the mixture fused in an induction furnace. The melt was immediately poured into a 5% nitric acid. This step is very similar to that used by Delvigne et al. (2012) for a similar study of BIF. Upon complete dissolution, analysis was performed on a Thermo Jarrell-Ash II ICP-OES for major elements and a Perkin Elmer Sciex ELAN 6100 ICP-MS for trace elements. In-house and certified international standard materials (e.g. NIST 694, OREAS 100a, and OREAS 101a and 101b) were used for quality control.

C, N, and S were determined by elemental analysis at the Hatch Laboratories of the University of Ottawa. 2-20 mg of pulverized material were weighed into tin capsules and loaded into the autosampler of an Elementar Isotope Cube Elemental Analyzer. Samples were then flash combusted at ~1800°C under oxygen atmosphere. Helium carries the produced sample gas through redox agents to convert C, N, and S to CO_2, N_2, and SO_2, which were then “trapped and purged” by adsorption columns for individual determination by thermal conductivity.

3.4.3 Quality assurance

Repeat analyses of the reference materials FeR-3 and FeR-4 by both TD-ICP-MS and Fusion ICP-MS methods are presented in Table 3.3. These materials are a precise matrix match for our sample set. For most elements, the Fusion-ICP-MS and TD-ICP-MS yield comparable results, in close agreement with other published values for the same reference materials (Govindaraju, 1994; Dulski, 2001; Yu et al., 2001; Bau and Alexander, 2009; Sampaio and Enzweiler, 2015). Certified and reference values for major elements (Si, Al, Fe_{total}, Mg, Ca, P, Ti, and Mn) in FeR-3 and FeR-4, and all other certified reference materials, were best reproduced by FUS-ICP-MS, yielding results within ±5% of the reference value at concentrations >1 wt.% and better than ±0.1% at concentrations <1 wt.%. At concentrations between 1 wt.% and 100 ppm, Ti and Mn were reproduced at better than ±10% relative error compared to reference values by Fusion-ICP-MS. Na and K by TD-ICP-MS were reproduced at better than ±5% at concentrations <1 wt.%, or better than ±0.01% absolute abundance. The trace elements Ge, Sc, Nb, Ta, U, Th, Y, and 14 rare earth elements were best analysed by FUS-ICP-MS, yielding results within ±15% of reference values at concentrations >10X the detection limit. Only results for Nb and U differed by more than 15% from the certified and recently published values for both FeR-3 and FeR-4, although they were reproduced to within ±5% relative error for other reference materials.

All other trace elements were analysed by TD-ICP-MS. Except for a few elements listed below, these analyses reproduced certified and published values to within ±15% at concentrations >10X the detection limit. Zr and Hf results from TD-ICP-MS and FUS-ICP-MS are in excellent agreement (see Figure 3.8), but total dissolution results were used in this study because of the lower detection limit. Results for Pb, Cu, and Zn in FeR-3 and FeR-4 are lower than reported and certified values, but no systematically low values were reported for the other reference materials. Results for Ni, Bi, W, and Ba varied by more than ±15% of published values, most likely because of the low concentrations or incorrect values for the reference materials. No certified or literature values are available for Ag, Hg, Tl, Se, Mo, Te, In, Re, and Ga, but duplicate analyses of the reference materials generally agree to within ±20% at concentrations >10X the detection limit. These are the first reported analyses of these elements for the reference materials.

For C, S, and N, 2σ precision is +/- 0.1%, determined by a long record of analyses of a sulfanilic acid internal standard.

3.5 Results

Results of the analyses of the 66 BIF samples and related host rocks are presented according to layer type in Tables 3.4-3.9 and Figure 3.9. All values reported below are median values; individual results are presented in Appendix M. A summary of whole rock and in-situ results (see Chapter 2) to illustrate important host phases is presented in Table 3.10.

3.5.1 Si and Fe

Silicon and iron are the major geochemical components of the Temagami BIF: 97.6 wt.% equivalent SiO_2 and Fe_3O_4 in jasper, 95.1 wt.% in chert, and 88.1 wt.% in magnetite samples. The Si concentrations in all oxide BIF samples range from 5.6 to 46 wt.% (Fig. 3.9), with a median of 33.6 wt.% (Table 3.4). This is equivalent to 71.9 wt.% quartz and up to 98.5 wt.% quartz in chert samples. The chlorite facies contains 50.1 wt.% SiO_2, the sulfide facies contains 46.4 wt.% SiO_2, and the shale and volcaniclastic units contain 31.7 wt.% SiO_2.

Iron concentrations are up to 63.2 wt.% (median of 17.2 wt.%) in oxide facies BIF. The maximum Fe content of the magnetite-facies BIF corresponds to 87.3 wt.% magnetite. Any material containing ≥25 wt.% total Fe was considered ore grade in the Sherman Mine, which corresponds to 34.6 wt.% magnetite (Boyum and Hartviksen, 1970). The chlorite facies contains 5.4 to 33.8 wt.% Fe, corresponding to 7.5 to 46.7 wt.% magnetite; the sulfide facies contains 19.9 to 35.0 wt.% Fe, corresponding to 42.8 to 75.2 wt.% pyrite. Volcaniclastic units contain 5.9 to 24 wt.% Fe.

3.5.2 Ca, Mg, Na, and K

MgO is present between 0.7-7 wt.% in many samples. The oxide facies BIF contains 0.47 wt.% MgO. With few exceptions, the highest concentrations, 6.5 wt.% MgO, are in magnetite samples. The chlorite facies contains 5.66 wt.% MgO; the sulfide facies contains 0.45 wt.%, and the volcaniclastic units contain 3.9 wt.%. Most of the Mg is present in chlorite and carbonate with

additional trace Mg (~0.1 wt.%, see Chapter 2) in magnetite. The oxides facies BIF contains 0.29 wt.% CaO (maximum 6.2 wt.% CaO), mainly present as interstitial calcite, dolomite, and Fe-carbonates and corresponding to 1 wt.% and up to 22.1 wt.% carbonate (as dolomite). The chlorite facies contains 1.7 wt.% CaO; the sulfide facies contains 0.08 wt.%, and the volcaniclastic units contain 0.2 wt.%.

Na_2O and K_2O are present only in trace amounts in oxide facies BIF (<0.01 and 0.02 wt.%, respectively). The chlorite facies and volcaniclastic units contains <0.01 wt.% Na_2O and K_2O; the sulfide facies contains <0.01 Na_2O and 0.2 wt.% K_2O. These values indicate strong alkali depletion, even in the volcaniclastic layers, although one sample (D001) with secondary albite contains 5.4 wt.% Na_2O. Up to 0.6 wt.% K_2O is present as metamorphic biotite and stilpnomelane in magnetite layers close to a mafic intrusion along the Highway 11 section (sample 11-32).

3.5.3 Aluminum

Aluminum is present in trace amounts as aluminosilicates in oxide facies BIF, between 0.15 wt.% Al_2O_3 in the jasper facies and 0.53 wt.% in the magnetite facies (up to 5.5 wt.% in one magnetite sample). 0.33 wt.% Al_2O_3 corresponds to approximately 2 wt.% chlorite in oxide BIF, assuming all Al is hosted in chlorite. The higher Al concentrations reflect the presence of late-stage metamorphic minerals (e.g., stilpnomelane and biotite) in fractures and interstices of coarse-grained material. The chlorite facies contains 10.6 wt.% Al_2O_3, equivalent to about 70 wt.% chlorite, assuming all Al is in chlorite. The volcaniclastic units contain 12.3 wt.% Al_2O_3, and the sulfide facies contains 1.6 wt.% Al_2O_3.

3.5.4 Phosphorous

Trace amounts of P are present in the oxide facies BIF (0.09 wt.% P_2O_5, median), and a few samples of the magnetite facies BIF contain as much as 0.39 wt.% P_2O_5 where apatite is present. This is equivalent to about 0.2-0.9 wt.% apatite, although monazite and trace xenotime also account for a small proportion of the P in some magnetite layers. The chlorite facies contains 0.11 wt.% P_2O_5, the shale and volcaniclastic units contain 0.14 wt.% P_2O_5, and the sulfide facies contains <0.02 wt.%.

3.5.6 C, S, N, LOI

The oxide facies BIF contains 0.77 wt.% carbonate carbon as CO_2; some magnetite samples contain up to 14.3 wt.% CO_2. Median oxide BIF CO_2 contents correspond to approximately 1 wt.% carbonates (dolomite), assuming all C is present as CO_2 in dolomite. Non-carbonate C, in the form of graphite dust, occurs only in the sulfidic chert layers, where it is intergrown with quartz and finely disseminated pyrite. Sulfur is typically only present at the ppm level in oxide facies BIF, as inclusions of pyrite and pyrrhotite in magnetite. The chlorite facies BIF contains a few wt.% S. The samples of sulfidic chert analysed in this study contain 28.5 wt.% S as diagenetic pyrite (nodules and less common semi-massive sulfide). Nitrogen was not detected in any sample.

Low to negative LOI was found for all oxide facies BIF. The negative values are due to the abundant magnetite, which gains mass during oxidation on ignition. Higher LOI, up to 8.8 wt.%, was found in chlorite and shale samples due to the presence of hydrous aluminosilicates (Fig. 3.10). The highest LOI values up to 28.3 wt.% for sulfidic chert are due to devolatilization of sulfur.

3.5.7 Rb, Sr, Cs, Ba

The concentrations of Rb, Cs, and Ba in oxide facies BIF range from below detection up to hundreds of ppm (168 ppm Sr and 279 ppm Ba). Median values of Rb and Cs vary by a factor of 10 between jasper, chert and magnetite facies; Sr and Ba vary by a factor of 5. However, there is also significant variability within individual samples types. Most of the Ba and Sr is present in apatite; Sr can also occur in carbonates and monazite (see Table 3.1). All Sr can be accounted for by 0.2 wt.% apatite in oxide BIF, containing ~1675 ppm Sr, but Ba in apatite and magnetite may not be sufficient to yield 4.9 ppm Ba in oxide BIF (see Table 3.10). Some additional Ba is present in trace, secondary barite. Rb and Cs are mostly likely present in chlorite and biotite, as well as in apatite and trace Rb in carbonates. However, traces of Cs (up to hundreds of ppb) and Ba (up to tens of ppm) were also found by LA-ICP-MS in magnetite crystals from different oxide facies BIF (see Chapter 2), accounting for up to half of the Ba and Cs in the samples.

Sulfide facies BIF contains the highest Rb (10 ppm), matching the higher K_2O in these samples and the more abundant chlorite and stilpnomelane than in oxide facies BIF. Sr is also enriched in chlorite layers (32 ppm), where it is hosted in apatite and carbonates. Cs and Ba concentrations in the sulfide and chlorite facies are within the range of values in the oxide-facies.

3.5.8 Li, Be, B

The light elements, Li and Be, are low in all oxide facies BIF, with median values of 0.5 and 0.34 ppm (Table 3.7). Li can be enriched in chlorite-facies BIF and shale where it is likely hosted in chlorite and apatite (see Table 3.10). B is significantly enriched in oxide facies BIF, with median values of 40 ppm and a maximum of 63.8 ppm. Unlike the other trace elements, B is more abundant in the chert and jasper facies (55.6 and 42.4 ppm, respectively) than in the magnetite layers (2.8 ppm) and other facies. No tourmaline or other high-B minerals were identified, suggesting that the boron is probably present as a trace component in quartz.

3.5.9 Sc, Ti, Zr, Hf, Nb, Ta

The concentrations of the relatively immobile elements (e.g., HFSE) are interpreted to reflect a minor detrital component and are highly variable among the different facies of BIF. A few samples have very high concentrations of more than 100 ppm Ti and 10 ppm Zr, but most samples have values below detection for Hf, Nb, and Ta. Ti varies between 3 ppm and 1109 ppm in the oxide facies, with median values of 30 ppm. Only about 10-15% of Ti is hosted in magnetite in oxide-facies BIF, the remainder can be accounted for by Ti in chlorite and ilmenite. Zr varies between <0.2 ppm and 59.6 ppm, with median values of 1.9 ppm. The Zr/Ti ratio in all oxide facies BIF is slightly higher than average andesite (0.063 versus 0.037 in AGV-2 standard material). Sc, Hf, Nb, and Ta are all close to their detection limits in oxide facies BIF, but they have been detected in trace amounts in magnetite by LA-ICP-MS (Chapter 2); this likely accounts for all of the Sc, Hf, Nb, and Ta in the oxide facies BIF. Concentrations of these elements are higher in the chlorite facies BIF and sulfide facies (Table 3.5). The shales and volcaniclastic units are enriched in Ti and Zr, mostly as detrital zircon and ilmenite; Zr/Ti ratios and concentrations of Sc (3-21 ppm) are identical to average andesite.

3.5.10 Co, Ni, Cu, Zn, As, Ag, Cd, Sn, Sb, Hg, Pb

The concentrations of chalcophile elements are low in all of the oxide facies BIF. They are present as traces in magnetite layers (0.1-10s of ppm: Table 3.6), and much lower in the chert and jasper layers. A few ppm of Pb, As, and Sb are present in jasper layers. Contents in magnetite crystals account for up to half the Zn and Sb, and all Cd and Sn in oxide BIF (see Table 3.10). The remaining Zn in oxide BIF is hosted in chlorite, ilmenite, and carbonates. Abundances of all other chalcophile elements in magnetite, chlorite, ilmenite, and carbonate minerals are lower, instead predominantly hosted in trace sulfides. The chlorite facies BIF and volcaniclastic units are significantly enriched in Zn compared to the oxide facies, slightly enriched in Cu, Ag, Cd, Co, and Sn, and contain similar Pb, As, Hg, and Ni but less Sb. All of the chalcophile elements are higher in the sulfide facies, with Pb, Ag, As, and Co in sulfidic cherts enriched by factors of 50 to >200X compared to oxide facies BIF. The magnetite and chert samples contain 5 to 10 ppb Hg, whereas the sulfidic cherts contain between 40 and 105 ppb Hg.

3.5.11 Ge, Ga, Se, In, Te, Tl, Bi

The metalloids and semi-metals show variable enrichments and depletion in the BIF (Table 3.7). Ge is enriched in oxide facies BIF, with concentrations up to 14.3 ppm. The highest concentrations are in magnetite-rich layers. LA-ICP-MS analyses of magnetite indicate concentrations of 7.3 ppm up to 90 ppm Ge (Chapter 2), accounting for half the Ge in oxide facies BIF. Additional Ge is hosted in chlorite and possibly quartz. The Ge/Si ratio is also highest in the magnetite layers (values of 22.7 μmol/mol compared to 2.7 and 5.5 in chert and jasper, respectively). The chlorite facies BIF also has high concentrations of Ge (4.7 ppm), and somewhat higher concentrations of Ga (20 ppm) compared to the oxide facies. Both are likely present in Fe-chlorite and other aluminosilicates where magnetite is not present (see Table 3.10). Concentrations of Ga are higher in the sulfide facies BIF (3.3 ppm), together with Se, Te, and Tl (4.5, 0.5, and 2.2 ppm, respectively). Se, Te, and Tl concentrations are all low in oxide-facies BIF (Table 3.7).

3.5.12 Mn, V, Cr, Mo, W, Re, Th, U

Mn concentrations are highly variable in oxide facies BIF, ranging from tens of ppm up to thousands of ppm in chert and magnetite layers (Table 3.8). EPMA and LA-ICP-MS analyses of

magnetite crystals indicate concentrations of ~200 ppm Mn (Chapter 2, Table 3.10), although most of the variability in Mn concentrations is due to the presence of about 1 wt.% late-stage manganiferous Fe-Mg carbonate containing ~9000 ppm Mn in oxide-facies BIF accounts for most of the Mn. Other host phases for Mn include chlorite (up to 1000 ppm Mn), ilmenite (7000 ppm) and apatite (300 ppm). Chlorite facies BIF and volcaniclastic samples also contain high Mn (~ 500 ppm), which may be present in Fe-rich chlorite and carbonates. Mn concentration in the sulfidic cherts are lower (115 ppm).

The concentrations of V, Cr, Mo, W, Re, Th, and U are generally low in oxide facies BIF. Mo and W are slightly enriched in jasper facies (0.11 and 2.1 ppm, respectively). Mo and W in magnetite only account for less than 25% of the element budget in oxide BIF, most is likely hosted in trace sulfides. Cr and V, and to some extent Re, are highest in magnetite facies (8.8 ppm, 6.9 ppm, and 0.9 ppb). Magnetite is not an important mineralogical host for Cr, but significant amounts (~100 ppm) are present in chlorite. All V can be accounted for by concentrations measured in-situ in magnetite and ilmenite (see Table 3.10). The highest values of Mo, Cr and V (0.94, 36, and 62 ppm) are in the chlorite facies and shales, which also contain the highest U and Th (up to 3.1 and 11.4 ppm). Most oxide facies BIF contains less than 0.1 ppm U and Th. In all samples V, U, Th, and to a lesser extend Cr, follow Al.

3.5.13 REE and Y

Total REE concentrations in oxide facies BIF range from <1 to 120 ppm. The highest concentrations are in magnetite layers; the lowest are in chert. Y is generally enriched with the REE, with a median concentration of 3.7 ppm in the oxide facies (Table 3.9). The chlorite facies BIF contains 47 ppm total REE; sulfidic cherts contain 23.2 ppm, and the volcaniclastic units contain 126 ppm. About half the REE is present in the 0.2 wt.% apatite in oxide BIF, which contains ~1300 ppm REE. Additional REE are hosted in monazite (LREE), xenotime (HREE) and carbonates (see Table 3.10). LA-ICP-MS analyses of magnetite indicate less than 50 ppb for selected REE (La, Sm, and Yb).

3.6 Discussion

3.6.1 Inter-element correlations

A correlation matrix (Pearson r values) for 41 elements plus ∑REE using the bulk compositions of all samples, converted to centre-log ratios to remove the effect of closure, is presented in Table 3.11. Table 3.12 shows the same calculation after normalizing the data to zero SiO_2 to remove any effect on the trace element concentrations caused by variable dilution by silica. By removing SiO_2, and also the clastic component (Table 3.13), we can more readily compare the composition of the ferruginous components of the sediments. To remove the effect of clastic input, we assume a detrital end-member having a composition of average Temagami shale and use the Zr content of the analyzed samples to remove the detrital component (summarized in the footnote of Table 3.13). Composition of the Temagami shale is considered the median values of shale in Tables 3.4-3.9. Elements typically enriched in seawater-dominated hydrothermal fluids do not strongly correlate in the Temagami BIF (especially Cu, Pb, Zn, As, Hg, Sb, Bi, Ag, S, Se, Co, Ni, Re, Cr, V, Ba, Y, REE, Hg, Te). The behaviour of the base metals is surprising, as they usually correlate well in exhalites and other hydrothermally influenced marine sediments (e.g., Peter and Goodfellow, 1996). Between the base metals, only Ni-Co (r=0.74), Zn-As (r=0.48), and Cu-Pb (r=0.46) correlate moderately well in the SiO_2-free material (Table 3.12). Ni and Co also correlate in in-situ magnetite analyses (r=0.79, see Chapter 2), but Zn, As, Cu, and Pb do not. Other elements that are found in LA-ICP-MS analyses of magnetite (e.g., P, Ga, Ge, W, Sb, Y, and REE), correlate with Fe in the bulk samples. The correlation of P and Fe (r=0.59) reflects the abundance of diagenetic apatite after P entered the sediment adsorbed to Fe-oxyhydroxides.

Removing the SiO_2 from the data forces a correlation with Fe by any element that would have been in the SiO_2. For example Ge, which behaves like Si in aqueous environments, (e.g., Hamade et al., 2003; Pokrovski and Schott, 1998) may be falsely correlated with Fe. However, Ge is mainly hosted in magnetite in the Temagami BIF (see Chapter 2), particularly in the cores of large magnetite crystals that are free of Si. The positive correlation between Ge and Fe (r=0.54 in whole rock, r=0.55 in SiO_2-free material: Tables 3.11 and 3.12) confirms that Ge was likely added to the sediments by adsorption onto Fe-oxyhydroxides, as suggested by Pokrovsky et al. (2006), and then incorporated into the magnetite.

Boron is the only trace element that shows a strong positive correlation with Si (r=0.65: Table 3.11), reflecting the close link between B deposition and silica precipitation in sedimentary environments. In the absence of clay minerals, B is enriched in amorphous silica and biogenic opal: Ishikawa and Nakamura, 1993; Palmer et al., 1987; Truscott and Shaw, 1984). Most of the boron in Precambrian chert is lost during recrystallization of opal to quartz (Truscott and Shaw, 1984), but primary enrichments in the Temagami jasper and chert may have been preserved due to minimal recrystallization of some layers.

Aluminum correlates with Ti (0.49), Na, V, Ga, Zr (0.65), Li, Ta, U, Th, and ΣREE, and to a lesser extent with Rb, Cs, and Re (Table 3.11). These correlations reflect the clastic component. Because metamorphic conditions did not exceed the greenschist facies, Zr, Ti and HFSE are expected to have been immobile throughout the history of the BIF, while Cr, V and REE may have experienced some mobility related to dewatering. Comparison of V concentrations in different layers show that V could be interpreted as reflecting both detrital and hydrogenous sources (Figure 3.11). Other elements (e.g., K, Cs, Li, Ga) are most likely related to aluminosilicate phases or authigenic clays and their metamorphic equivalents (see Fig. 3.12). Rb and Cs can substitute for K in biotite, entering the sediment as volcaniclastic detritus. Deposited in the BIF, biotite is altered to chlorite during diagenesis, but authigenic biotite and stilpnomelane can form locally in magnetite layers during greenschist metamorphic conditions, again hosting K, Rb and Cs.

A principal component analysis (PCA) was performed on the centred-log ratio data of the original abundances (cf. Table 3.11) of 26 representative elements in oxide BIF (see Appendix N). 61.5% of the total variance is accounted for by the first four principal components. PC1 and PC2 account for 23.9% and 15.4% of the total variance (39.3%: Figure 3.13). High positive loadings of Fe, Ge and Pb on PC1 reflect the incorporation of these elements in magnetite; P, Y, La, and Sr also have high loadings on PC1 reflecting the stabilization of apatite and monazite during diagenesis (see Chapter 2). Negative loadings of Si, Mg, B, Mn, C, S, Cu, Zn, As, Ag, Ni, and Co on PC1 reflect the stabilization of the host phases (quartz, carbonates, sulfides) at a later stage of diagenesis. Si has a high loading on PC2, forming a group with B and Ge, reflecting a

common depositional pathway from seawater prior to incorporation of Ge in magnetite (PC1). Other elements with positive loadings on PC2 are P, Y, U, Sr, Ba, and some transition metals. These were likely transported to the sediment from the water column by scavenging on Fe-oxyhydroxides indicated by abundances correlating positively with Fe and REE+Y patterns indicative of seawater sources. Negative loadings on PC2 for Zr, Ti, Al, Cs, La, Ga indicate clastic sources, with Zr, Ti, and Al preferentially in ilmenite, chlorite, and detrital zircon. The loadings of Cu, Co, and Mn indicate behaviour possibly linked to mixed seawater-hydrothermal sources and scavenging by Fe-oxyhydroxides. Negative loadings on PC2 for Zr, Ti, Al, Cs, La, Ga are consistent with mainly clastic sources, as these elements are preferentially in ilmenite, chlorite, and detrital zircon. In general, the PCA is consistent with earlier conclusions based on detailed paragenetic studies of the different BIF facies. High positive loadings on PC1 reflect fixation in mineral phases during diagenesis, whereas negative loadings reflect significant remobilization from primary precipitates. High positive loadings on PC2 indicate seawater sources mainly, whereas negative loadings on PC2 indicate external sources (e.g., clastic or hydrothermal input, including metamorphic, or enrichment due to biological processes).

3.6.2 Clastic versus chemical components of the BIF

A challenge in the interpretation of the geochemistry of chemical sediments is the presence of detrital material, the composition of which can obscure contributions from other sources, such as the water column or direct hydrothermal input. Plots of immobile elements, for example on discrimination diagrams such as Winchester and Floyd (1977), show a close grouping of the chlorite and shale samples in the fields of andesite to rhyolite (see Figure 3.14). Zr/Ti and V/Al ratios also support that a mixture of andesitic and rhyolitic material was likely the source of the detrital component in clastic lithologies and BIF. Based on fractionation of Zr-Al-Ti during the maturation of sediments from sandstones to shale and Zr/Ti systematics in felsic and mafic volcanic material, a ternary plot of the three elements allows further characterization of the clastic component in BIF (Fig. 3.14b; Garcia et al., 1994). The clastic material in shale, chlorite, and magnetite layers is of intermediate to felsic composition and may have experienced some transport and maturation before deposition in BIF. Rounded apatite and quartz identified petrographically in chlorite samples are in support of some degree of sedimentary transport before deposition (see Chapter 2). The recalculated Ti concentrations in all of the oxide facies

after removal of the detrital component (Table 3.13) are close to zero, confirming that the shale end-member is a reasonable choice for the clastic source. The effect is greatest in the chlorite- and sulfide- (shale-rich) facies, whereas the detrital component of the oxide facies is minimal except for a few elements (up to a third of Al, Mg, K, Zn, Se, W, V, Ba, Rb, and U). More than one third and up to all Ti, Ga, Li, Th (and Zr) in chert and jasper samples is in the clastic component, and most of the Ag in the BIF is detrital. For all trace elements, on average between 15% (in jasper) and 40% (in magnetite) is derived from clastic material. This is in contrast to <5% of Si and Fe in clastic components in oxide facies BIF.

The reconstructed compositions of the magnetite and jasper layers (removing the silica and a small detrital component) confirm that the "ferruginous" components are quite similar in jasper and magnetite, suggesting common precursor material for both lithologies (Table 3.13). The Mn concentrations in the recalculated compositions of the magnetite and jasper layers are the same (~600 ppm), indicating identical processes of Mn enrichment in the original ferruginous material (Fig. 3.15). Zn, Cu, and Pb concentrations are also similar in the recalculated compositions of the two facies. The behaviour of some transition metals and metalloids is asymmetrical between jasper and magnetite layers. The significantly lower Pb, As, Sb, and Hg in the recalculated concentrations in magnetite layers compared to jasper argues for a loss of these elements during magnetite crystallization. Likewise, Hg concentrations are a factor of 3 higher in the recalculated ferruginous component of the jasper layers, while they are unchanged in the magnetite layers. P_2O_5 concentrations are higher in the recalculated compositions of the jasper (0.35 wt.%) and chert (0.33 wt.%) compared to the magnetite layers (0.17 wt.%), suggesting some loss of P from the magnetite layers during diagenesis and recrystallization. The fact that elements such as Al, Na, Ga, Hf, Nb, and Ta are not completely omitted with the detrital component suggests that trace amounts of these elements were also scavenged by the original Fe-oxyhydroxides or authigenic clays. Hf has a higher particle reactivity than Zr (Bau and Alexander, 2009), which may explain why it was authigenically enriched beyond the clastic input, along with Al.

3.6.3 REE systematics in the whole rock

A subject of considerable attention in the Temagami BIF is the systematics of rare earth elements and yttrium (REY), which are thought to reflect the chemistry of the water column from which

they were deposited (e.g. Ohmoto et al., 2006, Bau and Alexander, 2009). Whole-rock PAAS-normalized REY for the different BIF facies data from this study are summarized in Figure 3.16 and Table 3.9. Almost all oxide BIF samples, except the chlorite layers, show consistent LREE depletion, variable positive Eu anomalies between 1.6 and 6.9, Y/Ho between <31.3 and 60, variable but mostly slightly positive Gd anomalies, and a positive La anomaly. REY systematics are remarkably consistent in the Temagami oxide BIF, between lithologies, spatially, and across stratigraphy (Fig. 3.16).

The REY signature of oxide-facies BIF at Temagami reflects a combination of seawater and hydrothermal sources, deposited with Fe-oxyhydroxides and diagenetically stabilized in phosphates (primarily apatite) and to a lesser degree, magnetite. Detailed studies of the REE and Y systematics in apatite and magnetite (see Chapter 2) showed REY patterns consistent with their whole rock (i.e., prominent La, Eu, and Y anomalies, as well as LREE depletion). These patterns closely reflect the hydrothermal-seawater signal delivered to the sediment via adsorption of REY onto Fe-oxyhydroxides in the water column and then incorporated in the crystallizing Fe-oxide minerals. In oxide-facies BIF, the apatite and monazite are also authigenic (cf. Chapter 2; Bowins and Crockett, 2011), and are interpreted to record diagenetic enrichment of REE in the jasper (early) and magnetite (later) facies. Later generations of apatite capture slightly fractionated REY affected by loss of La, Y, and Eu. Post-depositional REY mobility in this case is likely similar to that observed during recrystallization of biogenic phosphate minerals in younger sedimentary systems (Shields and Stille, 2001; Ehrenberg and Nadeau, 2002; González-Álvarez and Kerrich, 2010; Auer et al., 2017). Some large monazite grains in the chlorite facies and shale are enriched in Th and therefore probably detrital in origin, but very few detrital apatite grains can be distinguished (e.g., by subhedral shape and associated with distinct REE profiles, such as a negative Eu anomaly). Magnetite is also a reliable archive of REY, as also demonstrated in a case study of Algoma-type BIF in the Woodburn Lake greenstone belt of the Churchill Province (Gourcerol et al., 2016). Individual magnetite grains were found to have REY profiles very similar to adjacent whole-rock chert bands and were unaffected by later metamorphic (i.e., gold-depositing) fluids.

REY_{PAAS} patterns for oxide-facies BIF are in good agreement with previously published data for the Temagami BIF and consistent with deposition from hydrothermally influenced seawater (e.g. Bau, 1996). Importantly, the Temagami BIF does not exhibit a Ce anomaly, unlike younger metalliferous sediments (Fig. 3.17; Bau and Alexander, 2009; Bowins and Crocket, 2011). Positive Ce anomalies can develop from oxidation of Ce^{3+} to less soluble or more reactive Ce^{4+} which is then deposited beneath an oxygenated water column, producing a residual seawater carrying negative Ce anomalies (German et al., 1995; Alibo and Nozaki, 1999). Ce oxidation occurs under similar redox conditions as the oxidation of Mn^{2+} and can also happen on the surfaces of Mn-oxides, leading to large Ce anomalies in Fe-Mn crusts (e.g., Ohta and Kawabe, 2001). In the Temagami BIF, the absence of a Ce anomaly and low Mn abundances compared to modern metalliferous sediments argue for redox conditions too reducing for the oxidation of Mn and Ce.

Fe-oxyhydroxides are effective scavengers, depositing REY and their inherent pattern quantitatively in the BIF forming on the seafloor (e.g., Murray et al., 1990; Bau, 1999). Eu is contributed from reduced hydrothermal fluids entering the basin, although significant variability in the Eu anomaly also may reflect diagenetic remobilization with silica (Bau, 1991). Positive La/La* anomalies develop in seawater due to lower particle reactivity of La which leads to relative enrichments compared to the other REE over long residence times in the ocean (Bau, 1996; Nozaki et al., 1997). Y behaves very similarly to Ho in magmatic and hydrothermal systems but can be fractionated from chondritic Y/Ho (24-34; Bau, 1996) in hydrothermal or seawater environments due to different complexing behaviour (Nozaki et al., 1997). The low particle reactivity is overcome by the potency of Fe-oxyhydroxides as scavenging agents, depositing REY including the positive Y and La anomalies to BIF quantitatively (e.g., Planavsky et al., 2010a). REY sourced locally in smaller enclosed basins would lack the residence time allowing particle interaction and the slow development of Y/Ho and La/La* anomalies (e.g., Fig. 3.18). Instead, REY in the Temagami BIF were sourced from a large, stable seawater reservoir allowing for a remarkably stable supply of REY to the sediment compared to more direct hydrothermal influence in exhalite deposits or metalliferous sediments formed under a restricted brine pool (Fig. 3.19). Other BIF forming in the Abitibi greenstone belt, such as the regionally extensive (500-600 km strike length) 2.73 Ga BIF in the Deloro assemblage are interpreted to

reflect deposition along the interface of marine water masses along a chemocline, resulting in variable Y, La, and Eu anomalies (Thurston et al., 2012). In contrast, the 2.73 Ga BIF of the Hunter Mine Group was deposited in a caldera setting, resulting in a mixed proximal hydrothermal-seawater signal with large Eu, and muted Y and La anomalies (Fig. 3.19c; Chown et al., 2000; Brengman and Fedo, 2018). Younger metalliferous sediments deposited under a brine pool or as direct hydrothermal precipitates yield a pronounced Eu anomaly and no or only small and variable La and Y anomalies and mostly flat REY profiles (Fig. 3.19 d; Peter and Goodfellow, 1996; Laurila et al., 2014b). Independent of age, shallow water Superior-type BIF such as the 2.9 Ga Mozaan BIF display a less pronounced Eu anomaly due to a less prominent hydrothermal input in a depositional setting on (continental) shelfs (Fig. 3.19e; Alexander et al., 2008). The 2.95 Ga Algoma-type Pietersburg BIF was deposited in a greenstone belt setting preserved in the Kaapvaal craton and contains REY patterns very similar to those observed in the Temagami BIF (Alexander et al., 2009), both deposits probably formed under open ocean depositional conditions independent of upwelling or a chemocline. Notably, Temagami BIF REY systematics resemble more closely those captured by the 300 Ma older Pietersburg BIF than some BIF in the age-related Abitibi greenstone belt.

REY are more enriched in chlorite layers compared to oxide BIF. Their PAAS-normalized pattern is mostly flat, with small Eu and Y/Ho anomalies (1.61 and 32.9, respectively). Most of the REY in chlorite are derived from clastic sources (up to 100%, Table 3.13), specifically from detrital apatite and monazite (see Chapter 2). The La and Eu anomalies, LREE depletion (Fig. 3.16), and Y/Ho in the jasper layers probably reflect best the initially deposited material and the seawater signal (i.e., the same signal captured in apatite that is trapped as inclusions in magnetite in magnetite layers: cf. Chapter 2). Later apatite records the REE pattern of pore fluids expelled during later stage diagenesis or metamorphism, during which REE can be desorbed from the initial Fe-oxyhydroxide precipitates. La, Y, and Eu which form stable aqueous complexes more readily than the other REE, could be preferentially lost from the sedimentary package, while other REE are retained. The influence of external (hydrothermal) fluids is not supported by the REE patterns, specifically the lower Eu anomalies of the late-stage apatite.

REY patterns for the reconstructed ferruginous component of the different BIF facies are shown in Figure 3.20. The total concentrations of REE in the ferruginous component are similar for the jasper and magnetite facies (14 ppm and 20 ppm, respectively), which reflects the early fixation of REE in jasper (mainly in Type 1 apatite, see Chapter 2), and the preservation of a signal slightly altered by diagenetic processes in the later magnetite.

3.6.4 Geochemistry of the primary precipitates

A major part of the whole-rock geochemistry of the Temagami BIF is a result of post-depositional remobilization, volume loss, and material loss during diagenesis and lithification. Therefore, the geochemical characteristics of the primary precipitates are difficult to infer. Estimates of the gains and losses of elements following primary deposition can be determined from an isocon plot, comparing the early-formed jasper layers to the secondary products (magnetite layers; Fig. 3.21). The processes involved mainly reflect the replacement of jasper by magnetite. The results show a significant enrichment of elements, including Fe, Mn, Ni, Zn, Ge, V, Zr, Rb, Be, Mg, U, Se, Th, and Bi in the magnetite layers compared to the jasper precursor. These elements were retained in the newly formed minerals or immobile refractory minerals (zircon) and enriched by volume loss in magnetite layers. In contrast, the more mobile and highly volatile elements, Si, Ba, Sr, Li, As, Sb, Ag, P, and Hg are significantly depleted. Overall there is 90% loss of Si in the transformation from jasper to magnetite layers and 30% loss of Fe – magnetite layers only contain about 10% of the originally deposited silica and 70% of the Fe.

The REE show little variation with the exception of small losses of La, Eu, and Y between jasper and magnetite (see Chapter 2) consistent with the observation above that they are mostly immobile at greenschist facies and represent a mostly closed system in the BIF (Fleet, 1984; Bau, 1993). To mobilize Eu, temperatures of 200-250°C are required at f_{O2} buffered by magnetite/hematite (Bau, 1991; Danielson et al., 1992; Bau and Dulski, 1996), conditions that would not have been approached until late in the diagenesis or early regional metamorphism.

3.6.5 Depositional mechanisms and implications for Archean seawater

The deposition of the Temagami BIF occurred from a hydrothermally influenced water column in a basin that was open to the ocean, as suggested by REY and transition metal systematics

(e.g., lack of spatial or stratigraphic variation of REY profiles), resembling modern metalliferous sediments on a first order classification (Fig. 3.22). Direct hydrothermal plume fallout can be ruled out as a major source of components due to the low concentrations and lack of correlation of indicator elements (S, Cu, Pb, Zn, As, Sb, Sn). Low abundances in immobile elements Ti, Zr, Hf inform a generally low abundance of clastic components in oxide BIF. Thus, the dominant pathway for deposition in the oxide facies BIF is from hydrogenous sources.

In addition to evidence from REY and indicator metals, Ge/Si can be used as a proxy for hydrothermal influence (Hamade et al., 2003; Delvigne et al., 2012). Molar Ge/Si is higher in seafloor hydrothermal fluid (8-14 μmol/mol) than in fluids originating from continental weathering (0.54 μmol/mol: Froehlich et al., 1992; Mortlock et al., 1993). Ge/Si ratios are somewhat higher in jasper layers than in white chert (Fig. 3.22b), but there is no correlation with Eu, which might be expected if high Ge/Si was related to hydrothermal input. Instead, preferential retention of Ge in magnetite results in Ge enrichment in magnetite layers beyond the array covered by mixing of Ge and Eu from the three major reservoirs, seawater, hydrothermal fluid, and clastic detritus (Fig. 3.22b). The poor overall correlation of Ge/Si with Eu/Eu* in the Temagami BIF is interpreted to reflect mainly diagenetic processes.

In modern, oxygenated open oceans (Eh of +0.48 V; Glasby and Schulz, 1999), Fe-oxyhydroxides carry a positive surface charge and preferentially sorb neutral and negatively charged carbonate- (see Fig. 3.23; Cu, REY, Pb), hydroxyl- (Be, Fe, Zr, Ti, Sc, Nb, In, Sb, Sn, Te, Hf, Ta, Th, Tl, Bi) and oxyanion (Mo, W, U, V, Cr, As, Se, and Rb) complexes (e.g., Byrne et al., 1988; Koschinsky and Hein, 2003). In contrast, chloro-complexes (e.g., $PbCl^{+}$, $CdCl_2$), hydrated cations (Ni^{2+}, Cu^{2+}, Zn^{2+}, Ba^{2+}, Co^{+}, Tl^{+}, Ce^{4+}) and positively charged carbonate complexes (e.g., $Cu[CO_3]$ and $REY[CO_3]^{+}$) are more effectively sorbed on the negative surfaces of MnO_2 particles (e.g., Fig. 3.23). However, the conditions in the Neoarchean ocean were different from modern ocean water; they were likely warmer (40-70ºC; Grotzinger and Kasting, 1993), contained only trace or no oxygen, near-modern salinity (Marty et al., 2018) and uncertain but likely lower pH (>6.5-7; Saito et al., 2003; Halevy and Bachan, 2017). Under such conditions, scavenging by Fe-oxyhydroxides would have worked similarly, since the particles retain a positively charged surface at pH <8.5 (Hiemstra et al., 1996; Jain et al., 1999). In

addition to the initial adsorption of components onto Fe-oxyhydroxides and transport to the sediments, redox pumping would have recycled Fe back into the water column by reduction in the sediments (Weber et al., 2006).

The redox conditions were likely reducing towards Mn- (and Ce-, see discussion on REY systematics above). Hence, Mn-oxides were not an important scavenging agent in the Temagami ocean. Low concentrations of Mo, W, Re in oxide-BIF suggests that these complexes were not formed. However, intermittently oxidizing conditions have been hypothesized to explain minor enrichments in U (Fig. 3.22c; Bau and Alexander, 2009; Piercey et al., 2016). Chloro-complexes (e.g., $PbCl^{+}$, $CdCl_2$) and hydrated cations (e.g., Ni^{2+}, Cu^{2+}, and Zn^{2+}) are not as efficiently adsorbed by Fe-oxyhydroxides, and this could partly explain their low abundances in the oxide-facies BIF. The speciation and abundance of bicarbonate complexes are pH- and pressure dependent. HCO_3^{2-} was probably the dominant species in the Neoarchean ocean, as it is the dominant carbonate species between ~pH 6 and 10.

Mn-oxides and Fe-oxyhydroxides scavenge components from seawater and incorporate them in nodules forming on the seafloor in some modern oceans such as the Pacific (e.g., Hein et al. 2015). Comparing the composition of such nodules with the seawater they formed from (e.g., Bruland et al., 2014; Erel and Morgan, 1991) may allow to characterize qualitatively the order of abundance within groups of elements with similar adsorptive behaviour. Enrichment factors of elements in nodules over the composition of contemporaneous seawater were used to calculate the relative abundance in Temagami seawater (see Table 3.14). The order of enrichment of mostly free cations in modern seawater is Sr>>Rb>Ba>Zn=Ni>Cs>Co (Bruland et al., 2014). Similarly, the compositions of the Temagami BIF suggest that the order of enrichments from Archean seawater was Sr>Rb>Cs>Ba>Zn>Ni>>Co. The oxyanions in modern seawater are preferentially adsorbed onto Fe-Mn-oxyhydroxides in the order: Mo>V=As=U>>W (Bruland et al., 2014; Erel and Morgan, 1991). In Temagami seawater, the order of enrichment is U>As=Mo=V>W. Elements forming carbonate-, chloro-, and hydroxide-complexes in modern oceans are present in the order: Cu=Sb>Cd>Ag=Pb>Sn=Hg (Bruland et al., 2014). In Temagami seawater, the order of enrichment is Sb=Cd>Cu=Hg>Ag=Sn>Pb. These observations are consistent with generally similar relative abundances of free cations, alkali- and alkaline earth elements sourced from continental weathering (Sr, Rb, Ba, and Ni). Oxyanions sourced from

oxidative weathering differ in relative abundance, with more U than As and Mo in Temagami seawater. This may be an effect of redox conditions in the basin approaching the threshold of U-oxidation and increased mobility inferred in an earlier study by Bau and Alexander (2009). Some hydrothermally-derived elements present as carbonate-, chloro-, and hydroxide complexes (e.g., Sb and Hg) may have been more abundant, and the chalcophile elements (especially As, Pb, Ni, Cu, and Co) in Temagami seawater may be underestimated in the calculation based on oxide-facies BIF because the Temagami BIF also includes sulfidic cherts, which incorporate preferentially the chalcophile elements. Metals such as Zn, Ni, Pb, and Sn were therefore probably more abundant, reflecting hydrothermal activity in the Neoarchean ocean.

An important difference in the Temagami ocean is the availability of silica in the form of silicic acid (H_4SiO_4). In the absence of silica secreting organisms such as diatoms, the concentration of Si in the Neoarchean ocean may have been close to saturation, up to 670-2200 μM (Siever, 1992). Si, along with the similarly complexed Ge would have been efficiently scavenged by Fe-oxyhydroxides, even below the saturation of amorphous silica (Davis et al., 2002). The solubility of Si is dependent primarily on temperature and pH and more Si can stay in solution with an increase of either parameter (Williams et al., 1985). One element in the Temagami BIF that appears to closely track the inferred conditions of Archean bottom water is boron. The dominant aqueous species of boron under relatively low pH conditions is $B(OH)_3$ (Spivack and Edmond, 1987). At higher pH >7, $B(OH)_4^-$ becomes the dominant species (Keren and Bingham, 1985; Spivack et al., 1987) and is readily coprecipitated with $Si(OH)_4$ under conditions of where amorphous silica is also depositing. Boron isotopes are a useful paleo-pH proxy, based on the isotopic fractionation that occurs between $B(OH)_3$ and $B(OH)_4^-$ (Spivack and Edmond, 1987), but the concentrations of B alone may be a strong indicator of changing pH and preferential drawdown of $B(OH)_4^-$. Concentrations of B in Temagami chert and jasper are up to 60 ppm, compared to other Precambrian chert typically containing <10 ppm B (Truscott and Shaw, 1984). In other marine sediments B is commonly adsorbed onto clays (e.g., montmorillonite, smectite: Palmer et al., 1987), but the Temagami chert formed during a time of relative volcanic and sedimentary quiescence. In the absence of marine clays, increasing B concentrations in chert and jasper must have been partly controlled by adsorption onto amorphous Fe-oxyhydroxides and iron-silica gel. The effectiveness of that process also increases with rising pH, optimally between

pH 7.5-8.5 (Goldberg et al., 1993). The enrichment of B in the lower part of the Temagami BIF (e.g., in the chert and jasper in the stratigraphically lower part of the Hwy 11 outcrop: Fig. 3.24) and depletion in the upper part could be an effect of decreasing pH in the water column with progressive BIF deposition. Locally, escaping pore waters also might have had high pH due to increasing alkalinity associated with some bacterial metabolisms (i.e., Fe-reduction: Fischer and Knoll, 2009) that were probably active in the Temagami BIF sediment. On a basin scale, the progressive oxidation of all Fe^{2+} to form $Fe(OH)_3$ in BIF after equation [3.1] or Fe^{2+}-oxidation during anoxygenic photoferrotrophy (equation [3.2]) may have lowered the pH of the basin.

$$4Fe_{aq}^{2+} + O_2 + 10H_2O \rightarrow 4Fe(OH)_3 + 8H^+ \quad [3.1]$$ (Lepp and Goldich, 1964)

$$4Fe_{aq}^{2+} + CO_2 + 11H_2O \rightarrow 4Fe(OH)_3 + CH_2O + 8H^+ \quad [3.2]$$ (Ehrenreich and Widdel, 1994)

Modern enclosed basins such as the Red Sea have been proposed as analogs for BIF-forming environments, although the metalliferous sediments deposited there formed in a brine pool (Laurila et al., 2015) and may be a better analog for exhalite-type iron formations. Given the inferred conditions of the ocean at the time, some qualitative considerations can be made of the different controls on metal enrichment in Neoarchan BIF versus modern metalliferous sediments. The mobilization of metals as oxyanions was inhibited in subaerial environments due to a lack of atmospheric oxygen (Bekker et al., 2004). The Temagami ocean was likely buffered to redox conditions below those required to oxidize Mn, Mo, U, W, Re, and other metals. Co, Ni, Zn, Ba, Rb, and Mn were likely present mostly as free cations and therefore are underrepresented in oxide BIF due to limited scavenging by Fe-oxyhydroxides. Si was much more abundant in the Neoarchean ocean compared to the modern marine environment, because it was not actively precipitated by Si-secreting organisms, and so $Si(OH)_4$ may have been competing with other anions for sorption locations or otherwise changed the scavenging properties of the Fe-Si complex.

3.6.6 Comparisons with other BIF and modern metalliferous sediments

Geochemical compositions of Archean BIF from 3.5 Ga to 2.75 Ga have been compiled and are presented in Table 3.15. One reference BIF is from the 3.5 Ga Singhbhum Iron Ore Group in India (Mukhopadhyay et al., 2012). The Barberton, Pietersburg, Kuruman and Mozaan BIF are 3.2-2.46 Ga exhalites, and Superior- and Algoma-type BIF from South Africa (DeRonde et al., 1994; Bau et al., 1996; Alexander et al., 2008; Alexander et al., 2009). The Adams Mine, Great Whale, Kukatush, Moose Mountain, Vogt township, Wanipitai, and Boston Mine deposits are Neoarchean Algoma-type BIF, and the Belmont BIF is a Proterozoic Algoma-type BIF from the Abitibi greenstone belt and wider Superior Province, in Ontario and Quebec, Canada (Gross, 2009). Paleozoic exhalative sediments from the Bathurst mining camp are from New Brunswick, Canada (Peter and Goodfellow, 1996). Two modern examples of metalliferous sediments are from the East Pacific Rise and the Atlantis II deep in the Red Sea (Barrett et al., 1987; Laurila et al., 2014). The geochemical variability of the major elements (Fe, Si, Al, Ca, Mg, Na, K) is limited; however, the trace elements appear to show some systematic differences (Fig. 3.25). Algoma-type BIF contain only ~0.1 wt.% Mn, which is low compared to other BIF of similar age, reflecting different depositional environments. Superior-type BIF of even very old age (Mozaan BIF) contain significant Mn, up to 1.2 wt.% Mn (Alexander et al., 2008). Zn, Cu, and Pb are variably enriched in Algoma-type BIF. The variations in the trace element concentrations may reflect some BIF forming in more restricted depositional environments (e.g., enriched in Cr, V, and Ni) compared to deposition from seawater on continental shelfs as in Superior BIF, or from the open ocean in volcanic greenstone belts (such as Temagami and Pietersburg BIF, cf., Fig. 3.19). Mn is the most sensitive indicator of depositional conditions (mainly redox) and is strongly enriched in modern metalliferous sediments and Paleozoic exhalites, along with other base metals, compared to BIF.

The oxide- and sulfide facies of the Temagami BIF are significantly lower in most trace elements compared to the same facies in average Algoma- and Superior-type BIF, reflecting the special character of the Temagami BIF as an open-ocean precipitate not receiving any direct input from hydrothermal or detrital sources (Table 3.16 and Fig. 3.26, averages of 1300 samples from 45 iron formations; Gross, 2009). Temagami oxide facies contains up to more than one order of magnitude less Zn, Ni, Cr, Ba, Zr, As, V, Cu, Co, and REE compared to average Algoma-type and Superior-type BIF. In sulfide-facies, the trace element depletion is similar even though

Temagami sulfide-BIF contains more sulfides (reflected in higher S abundances, Fig. 3.26 c), indicative of early diagenetic formation of sulfides in from bacterial processes as opposed to sulfides from hydrothermal sources (Diekrup et al., 2018).

3.6.7 Geochemical mass fluxes

A total of 22.6 million metric tonnes of pellets containing ~65 wt.% total Fe were produced from the Sherman Mine. The pellets were made from milled ore concentrate mixed with ~10% limestone and dolomite as flux for the steel-making process. The produced pellets were the equivalent of 20.3 Mt Fe_3O_4, or ~82 Mt ore grade material (average ore grade of ~25 wt.% Fe_T: Donaldson and Garrett, 1991). The pit mining operation only exploited the shallow parts (<100 m) of the deposit, but BIF lenses extend at depth beyond the reach of exploration drilling at the time of active mining (>300 m; Boyum and Hartviksen, 1970). Very conservatively, assuming a half-cylindrical shape for each of the four original BIF lenses ranging from 500-2000 m in length, 80-120 m wide, and extending to 250-1000 m deep (assuming half-cylindrical shapes of the BIF lenses with linear correlation of greater preserved strike length and greater extent at depth; see Fig. 3.3), we estimate that approximately 866 Mt of iron formation or ~300 Mt of Fe_3O_4 was present in the lenses that were partly exploited by the four pits. These are likely minimum values as the depth extent of the steeply dipping BIF lenses and the amount of BIF eroded are unkown. In addition, relatively recent exploration suggests 328 Mt (up to 2500 Mt of BIF or ~115 to 875 Mt Fe_3O_4 assuming a grade of 25% Fe_T in BIF) may be present in the Eagle Rock/Cummings Lake Tinto Iron Mine 40 km southeast of Temagami (McBride, 2010). Smaller BIF lenses are also present throughout the area, including those interpreted from geophysical data to underlie the Nipissing diabase or Huronian sediments (cf. Chapter 2, Fig. 2.5). Over a strike length of ~40 km, we suggest that more than 1 billion tonnes of Fe_3O_4–equivalent could have been deposited in the belt (e.g., 300 Mt + 875 Mt). This compares to historic proven economic reserves in Ontario of 8 billion tonnes of iron ore at a grade of 29% Fe_T, or ~3.3 billion tonnes of Fe_3O_4, predominantly hosted in oxide-facies Algoma-type BIF (Shklanka, 1968).

The amount of Fe produced from the Sherman Mine could have been extracted by a convective hydrothermal system liberating 0.5 wt.% Fe_3O_4 from ~2 km^3 of volcanic footwall, consistent

with observations from alteration studies of the volcanic stratigraphy of the Sherman Mine area (Blum, 1986; Schwartz, 1995). The estimated 1 billion tonnes of Fe_3O_4 in the belt would have required leaching of the footwall along the entire 40-km strike length. Modern, ~350°C black smoker fluids, on average, contain 1430 µmol/kg Fe (using the 21N EPR vents as an example: Von Damm, 1990 and references therein). The worldwide flux of axial hydrothermal systems is about $5*10^{15}$ g of high-temperature fluid per year (Elderfield and Schultz, 1996). It would take these vents (about 50,000 of them) the equivalent of ~20,000 years to transport the amount of Fe in the Temagami BIF. We estimate that the time period represented by the Temagami BIF is at least 1 million years, based on depositional rates of 10-33 m/m.y. inferred for other BIF (Pickard et al., 2002; Lantink et al., 2019), meaning about 1,000 vents would have been required to deposit the Fe, assuming continuous hydrothermal output over that time. At least the same flux would be expected from lower-temperature diffuse venting, which accounts for 90% of modern axial hydrothermal flow, although at much lower dissolved Fe concentrations. A likely scenario is that the Fe content of the "Temagami ocean" was cumulative; built up over millions of years followed by deposition triggered by a much shorter event. The conservative trace elements in BIF suggest that much smaller hydrothermal fluxes may be required. For example, ore-grade Temagami BIF contains about $1*10^{15}$ g magnetite with an average Ge content of 7.3 ppm or 8470 t Ge. This would require the input of only 10 vents over 1 million years, based on an average Ge concentration of 215 nmol in the high-temperature fluids (Mortlock et al., 1993).

The Strathy-Chambers batholith north of Temagami is a potential heat source. Previous studies suggested that different phases of the batholith were synvolcanic (2 kb from amphibole chemistry: Brons, 1989; Baknes, 1990; Schwartz, 1995) but deeply emplaced (7-10 km depth of intrusion; Blum, 1989). Extrapolating a roughly spherical shape from the N-S and E-W dimensions (~20-25 km) yields a total volume on the order of 4000-8000 km^3. This is vastly larger (and deeper) than the subvolcanic heat sources suggested for seafloor massive sulfide deposits (e.g., Galley et al., 2007), but such a deep intrusion could have been a source of heat for large volumes of lower-temperature hydrothermal fluids near the seafloor. Although they are hydrothermally altered, none of the features normally associated with high-temperature seafloor hydrothermal activity (e.g., sulfidic stringers along zones of focused upflow and zonation of alteration minerals around an alteration pipe) have been observed in the host rocks of the

Temagami BIF. Sulfide clasts found in volcanic breccias north of the Sherman Mine were derived from diagenetic pyrite in sediments rather than from high-temperature seafloor massive sulfide and the pervasive chlorite-epidote-sericite alteration is most likely related to a regional greenstone belt alteration, not focused high-temperature upflow (see Chapter 2; Schwartz, 1995). There is also no evidence of local fallout from black smoker hydrothermal which produces sediments that are orders of magnitude more enriched in Cu, Zn, Pb, and other hydrothermal components (e.g., Peter and Goodfellow, 1996) than in any of the facies of the Temagami BIF. Instead, the geochemistry of the Temagami BIF is controlled by Fe-oxyhydroxides produced by oxidation of Fe^{2+} that had accumulated in the water column and transported the geochemical signature of the seawater influenced by distal hydrothermal venting to the Temagami BIF.

3.7 Conclusions

The Temagami BIF in the Sherman Mine has been widely interpreted as having formed proximal to a volcanic vent, variably referred to as the "Milne vent", "Sherman vent", and "Link Lake vent" (Hurley, 1985; Fyon and Crocket, 1986; Schwartz, 1995). The local occurrences of extrusive rhyolite, felsic breccias, and interlayered shale horizons were thought to be related to eruptive centers within the volcanic complex. However, the geochemical study of the Temagami BIF reveals a depositional setting within a volcanosedimentary basin under open seawater, distal to and indirectly linked to any hydrothermal input. The main pathway for deposition of massive amounts of Fe and SiO_2 was by formation of Fe-oxyhydroxide particles in the water column that then settled to form the primary sediment. The Fe and SiO_2 were sourced either from large-scale diffuse upflow, possibly regional, or distal hydrothermal venting. These components gradually accumulated in the basin during a significant break in volcanism (e.g., Thurston et al., 2008), and changes in the water column likely triggered the nucleation and deposition of the Fe-oxyhydroxides. Fe-oxyhydroxides are very efficient scavengers of amorphous silica from seawater (e.g., Fischer and Knoll, 2009; Maliva et al., 2005), and this was likely the dominant process of Fe and SiO_2 deposition. An important change in the basin over the course of BIF formation may have been a progressive decrease in pH, which caused a decrease in the deposition of pH-sensitive elements, such as B, through the sedimentary sequence.

Occurrences of sulfide- and carbonate-facies BIF in the central part of the mine are likely not representative of direct hydrothermal input of sulfur or CO_2. Rather, the geochemistry of the sulfides, with Co/Ni <1, is similar to clasts of diagenetic pyrite found in volcanic breccias in the host rocks and indicative of a sedimentary and possibly biogenic origin (see also Chapter 4; Bralia et al., 1979; Schwartz, 1995). One explanation for the locally abundant sulfide in the Sherman Mine sequence is enhanced activity of sulfur metabolizing bacteria (see Chapter 3; Diekrup et al., 2018). Additionally, the decoupling of base metals (Cu, Zn, and Pb) from other trace elements in the oxide-facies BIF also argues against a direct input of these metals from local hydrothermal vents and is consistent with their behaviour in low-sulfur systems, as observed in some modern Fe-oxide-rich metalliferous sediments (Laurila et al., 2014b). Whereas elements such as As and Sb are strongly adsorbed onto Fe-oxyhydroxides (Tooth et al., 2013; Raven et al., 1998), the chalcophile elements are not deposited in the absence of significant reduced sulfur.

Recycling of some elements and retention of others during diagenesis accounts for the majority of the geochemical variations in the oxide facies BIF. Mobile components such as Si, As, and Hg were expelled with pore fluids during dewatering. Other elements were fixed in the newly formed mineral phases (e.g., Ge in magnetite, P and REE in phosphates). The positive correlation between Ge and Fe (r=0.58) is surprising because Ge behaves like Si in most aqueous environments (e.g., Hamade et al., 2003; Pokrovski and Schott, 1998). However, the strong adsorption of Ge onto Fe-oxyhydroxides, as suggested by Pokrovsky et al. (2006), likely accounts for the higher concentrations of Ge in the cores of large magnetite crystals (see Chapter 2), rather than enhanced hydrothermal input, as suggested for other BIF (Frei and Polat, 2007; Meng et al., 2017).

At the far eastern extent of the South BIF, the roadcut along Hwy 11 represents a section through the BIF stratigraphy close to its termination and distal to the centre of the Sherman Mine. Mapping of the Hwy 11 outcrop revealed more black chert, chlorite layers, and clastic components than in the ore blocks of the Sherman Mine, which contained more abundant jasper and magnetite. Concentrations of Zr, Ti, and other clastic components (Hf, Nb, Ta, Ga, Cr, V, Th, U) are 2-5 times higher in chert from the Hwy 11 samples than in chert from the Sherman

Mine. REE are also enriched in Hwy 11 samples, but lack the LREE depletion and have smaller Eu, La, and Y anomalies, and lower HREE due to the influence of the clastic component. The oxide facies in the Sherman Mine blocks has a more typical REE-pattern for Algoma-type BIF, and the jasper layers, in particular, are interpreted to be the closest representation of the primary precipitate in the Temagami BIF. They are enriched in apatite, the main host for the REE, possibly reflecting primary P enrichment, and they have notable Eu, La, and Y anomalies recording variable redox or hydrothermal contributions (e.g., Bau and Alexander, 2009, Delvigne et al., 2012). The magnetite layers in the mine blocks also have a high Ge/Si ratio (25 μmol/mol) compared to magnetite layers in the Hwy 11 outcrop (16 μmol/mol), which may reflect the preferential scavenging of Ge onto the primary Fe-oxyhydroxide precursor of jasper that has since been replaced by magnetite. The magnetite layers in the mine also have higher As, Sb, Hg, Co and Ni than similar layers in the Hwy 11 outcrop thought to be at the margins of the BIF-forming environment.

The REE are among the most sensitive indicators of some depositional processes and also the composition of contemporaneous Neoarchean seawater. This is due to the efficiency of removal of REY from the water column by adsorption onto Fe-oxyhydroxides (Barrett et al., 1988; German et al., 1991; Bau and Dulski, 1996; Bau and Alexander, 2009; Bowins and Crocket, 2011; Thurston et al., 2012). In modern oceans, there is nearly quantitative export of the seawater REE profile (including positive La and Y anomalies) to seafloor sediments by scavenging on Fe-oxyhydroxides (e.g., Elderfield, 1988; Koschinsky et al., 2003; Alexander et al., 2009). Selectivity for specific mineral phases that subsequently grow diagenetically also does not affect the REY patterns (Elderfield and Sholkovitz, 1987; Bau et al., 1997; Fleet and Pan, 1997). REY and P probably entered the sediment adsorbed onto Fe-oxyhydroxide surfaces and fix the REE in apatite and monazite (Berner, 1973; Bjerrum and Canfield, 2002; Poulton and Canfield, 2006; Paytan and McLaughlin, 2007; Planavsky et al., 2010b). Although there are some variations in LREE, La, and Eu anomalies between the facies, likely due to limited remobilization, the REY signal in oxide BIF is remarkably similar through the BIF stratigraphy and spatially from one part of the BIF basin to another. This is most reasonably interpreted to reflect a steady supply of REY to the sediment from a large body of homogenous,

hydrothermally influenced seawater and argues against alteration by later hydrothermal or metamorphic fluids.

Among the outstanding questions for future research are the pathways for the delivery of metal to the larger basin. In the absence of an obvious hydrothermal vent complex, the components of the BIF must have been delivered by regionally extensive diffuse hydrothermal venting, by run-off from emerging microcontinents, or by far-field hydrothermal input. Although Algoma-type BIF everywhere in the Abitibi are clearly linked to major breaks in volcanism, we are still uncertain how long deposition lasted. Research in other BIF settings, including in deep-water Superior BIF (e.g., Kuruman BIF: Pickard et al., 2002, Lantink et al., 2019), indicate accumulation rates of 10-33 m/m.y. (fully compacted sediment), which would correspond to a time span of as much as 5-10 m.y. for the Temagami BIF. Modern metalliferous muds in the Atlantis II Deep of the Red Sea are accumulating at a rate of 10-20 m in less than 15,000 years (uncompacted sediment: Laurila et al., 2014a), suggesting a much shorter time span for the deposition of the Temagami BIF is possible (e.g., within 1 m.y. assuming 90% compaction). In either case, it remains unclear what magmatic and tectonic processes could have mobilized such large quantities of Fe in comparison to modern hydrothermal vent systems and in the absence of major continental erosion. The trace element geochemistry of the BIF also highlights significant differences from exhalites (e.g., low chalcophile element abundances, especially Cu, Zn and Pb) but also major differences from Lake Superior-type BIF (e.g., notable enrichments in As, Sb, Ge) in terms of the sources of the metals.

3.8 References

Abbey, S., McLeod, C., Wan, L.-G., 1983. FeR-1, FeR-2, FeR-3, and FeR-4: Four Canadian Iron-formation Samples Prepared for Use as Reference Materials. Geological Survey of Canada.

Alexander, B.W., Bau, M., Andersson, P., Dulski, P., 2008. Continentally-derived solutes in shallow Archean seawater: Rare earth element and Nd isotope evidence in iron formation from the 2.9Ga Pongola Supergroup, South Africa. Geochimica et Cosmochimica Acta 72, 378-394.

Alexander, B.W., Bau, M., Andersson, P., 2009. Neodymium isotopes in Archean seawater and implications for the marine Nd cycle in Earth's early oceans. Earth and Planetary Science Letters 283, 144-155.

Alibo, D.S., Nozaki, Y., 1999. Rare earth elements in seawater: particle association, shale-normalization, and Ce oxidation. Geochimica et Cosmochimica Acta 63, 363-372.

Anbar, A.D., Duan, Y., Lyons, T.W., Arnold, G.L., Kendall, B., Creaser, R.A., Kaufman, A.J., Gordon, G.W., Scott, C., Garvin, J., Buick, R., 2007. A Whiff of Oxygen Before the Great Oxidation Event? Science 317, 1903-1906.

Anderson, P.R., Benjamin, M.M., 1985. Effect of silicon on the crystallization and adsorption properties of ferric oxides. Environmental Science & Technology 19, 1048-1053.

Auer, G., Reuter, M., Hauzenberger, C.A., Piller, W.E., 2017. The impact of transport processes on rare earth element patterns in marine authigenic and biogenic phosphates. Geochimica et Cosmochimica Acta 203, 140-156.

Ayer, J., Amelin, Y., Corfu, F., Kamo, S., Ketchum, J., Kwok, K., Trowell, N., 2002. Evolution of the southern Abitibi greenstone belt based on U–Pb geochronology: autochthonous volcanic construction followed by plutonism, regional deformation and sedimentation. Precambrian Research 115, 63-95.

Ayer, J., Goutier, J., Thurston, P., Dube, B., Kamber, B., 2010. Abitibi-Wawa Sub-province tectonic and metallogenic evolution, Summary of Field Work and Other Activities 2010, Ontario Geological Survey, Open File Report 6260, pp. 3-1 to 3-6.

Ayer, J.A., Thurston, P.C., Bateman, R., Dube, B., Gibson, H.L., Hamilton, M.A., Hathaway, B., Hocker, S.M., Houle, M.G., Hudak, G., Ispolatov, V.O., Lafrance, B., Lesher, C.M.,

MacDonald, P.J., Peloquin, A.S., Piercey, S.J., Reed, L.E., Thompson, P.H., 2005. Overview of results from the reenstone Architecture Project: Discover Abitibi Initiative, Open File Report 6154. Ontario Geological Survey p. 146.

Ayer, J.A., Chartrand, J.E., Grabowski, G.D.P., Josey, S., Rainsford, D., Trowell, N.F., 2006. Geological compilation of the Cobalt–Temagami area, Abitibi greenstone belt. Ontario Geological Survey, Preliminary Map, 3581.

Ayres, D., 1972. Genesis of iron-bearing minerals in banded iron formation mesobands in the Dales Gorge Member, Hamersley Group, Western Australia. Economic Geology 67, 1214-1233.

Baknes, M., 1990. A structural-geochemical investigation of a mineralized breccia and associated vein system at the contact of the Strathy Batholith and the Temagami Greenstone Belt, Strathy Twp., Ontario. McMaster, MSc thesis, 331 p.

Barrett, T., Fralick, P., Jarvis, I., 1988. Rare-earth-element geochemistry of some Archean iron formations north of Lake Superior, Ontario. Canadian Journal of Earth Sciences 25, 570-580.

Bau, M., 1991. Rare-earth element mobility during hydrothermal and metamorphic fluid-rock interaction and the significance of the oxidation state of europium. Chemical Geology 93, 219-230.

Bau, M., 1993. Effects of syn-and post-depositional processes on the rare-earth element distribution in Precambrian iron-formations. European Journal of Mineralogy 5, 257-267.

Bau, M., 1996. Controls on the fractionation of isovalent trace elements in magmatic and aqueous systems: evidence from Y/Ho, Zr/Hf, and lanthanide tetrad effect. Contributions to Mineralogy and Petrology 123, 323-333.

Bau, M., Dulski, P., 1996. Distribution of yttrium and rare-earth elements in the Penge and Kuruman iron-formations, Transvaal Supergroup, South Africa. Precambrian Research 79, 37-55.

Bau, M., Moller, P., Dulski, P., 1997. Yttrium and lanthanides in eastern Mediterranean seawater and their fractionation during redox-cycling. Marine Chemistry 56, 123-131.

Bau, M., 1999. Scavenging of dissolved yttrium and rare earths by precipitating iron oxyhydroxide: experimental evidence for Ce oxidation, Y-Ho fractionation, and lanthanide tetrad effect. Geochimica et Cosmochimica Acta 63, 67-77.

Bau, M., Alexander, B.W., 2009. Distribution of high field strength elements (Y, Zr, REE, Hf, Ta, Th, U) in adjacent magnetite and chert bands and in reference standards FeR-3 and FeR-4 from the Temagami iron-formation, Canada, and the redox level of the Neoarchean ocean. Precambrian Research 174, 337-346.

Bekker, A., Holland, H.D., Wang, P.L., Rumble, D., Stein, H.J., Hannah, J.L., Coetzee, L.L., Beukes, N.J., 2004. Dating the rise of atmospheric oxygen. Nature 427, 117-120.

Bekker, A., Slack, J.F., Planavsky, N., Krapež, B., Hofmann, A., Konhauser, K.O., Rouxel, O.J., 2010. Iron Formation: The Sedimentary Product of a Complex Interplay among Mantle, Tectonic, Oceanic, and Biospheric Processes. Economic Geology 105, 467-508.

Bekker, A., Planavsky, N., Rasmussen, B., Krapez, B., Hofmann, A., Slack, J., Rouxel, O., Konhauser, K., 2014. Iron formations: Their origins and implications for ancient seawater chemistry, Treatise on geochemistry. Elsevier, pp. 561-628.

Bennett, G., 1978. Geology of the northeast Temagami area, District of Nipissing. Ontario Ministry of Natural Resources.

Berner, R.A., 1973. Phosphate removal from sea water by adsorption on volcanogenic ferric oxides. Earth and Planetary Science Letters 18, 77-86.

Beukes, N.J., Gutzmer, J., 2008. Origin and Paleoenvironmental Significance of Major Iron Formations at the Archean-Paleoproterozoic Boundary, in: Hagemann, S., Rosiere, C., Gutzmer, J., Beukes, N.J. (Eds.). Society of Economic Geologists, pp. 5-47.

Bjerrum, C.J., Canfield, D.E., 2002. Ocean productivity before about 1.9 Gyr ago limited by phosphorus adsorption onto iron oxides. Nature 417, 159-162.

Blake, R.E., Chang, S.J., Lepland, A., 2010. Phosphate oxygen isotopic evidence for a temperate and biologically active Archaean ocean. Nature 464, 1029.

Blum, N., 1986. Geochemical Studies of Archean Iron Formations and Associated Volcanic Rocks (Kirkland Lake and Temagami/Ont. areas). McMaster, Hamilton, Ontario, p. 410.

Bowins, R.J., 1989. Rare earth and other geochemical studies of Archean banded iron formation: Sherman and Adams Mines, Ontario, Geology. McMaster University, p. 399.

Bowins, R.J., Heaman, L.M., 1991. Age and timing of igneous activity in the Temagami greenstone belt, Ontario: a preliminary report. Canadian Journal of Earth Sciences 28, 1873-1876.

Bowins, R.J., Crocket, J.H., 1994. Sulfur and carbon isotopes in Archean banded iron formations: Implications for sulfur sources. Chemical Geology 111, 307-323.

Bowins, R.J., Crocket, J.H., 2011. Monazite, Xenotime and REE Minerals in Archean Banded Iron-Formation from the Sherman and Adam Mines, Ontario, Canada. The Canadian Mineralogist 49, 749-763.

Boyum, B., Hartviksen, R., 1970. General Geology and ore-grade control at Sherman-Mine, Temagami, Ontario. Canadian Mining and Metallurgical Bulletin 63.

Bralia, A., Sabatini, G., Troja, F.J.M.D., 1979. A revaluation of the Co/Ni ratio in pyrite as geochemical tool in ore genesis problems. Mineralium Deposita 14, 353-374.

Brengman, L.A., Fedo, C.M., 2018. Development of a mixed seawater-hydrothermal fluid geochemical signature during alteration of volcanic rocks in the Archean (~2.7 Ga) Abitibi Greenstone Belt, Canada. Geochimica et Cosmochimica Acta 227, 227-245.

Brons, D., 1989. Stratigraphy and metamorphism of mafic volcanic rocks near Arsenic Lake, Temagami, Ontario. Laurentian University, MSc thesis, 146 p pp.

Bruland, K.W., Middag, R., Lohan, M.C., 2014. Controls of Trace Metals in Seawater, in: Turekian, K.K. (Ed.), Treatise on Geochemistry (Second Edition). Elsevier, Oxford, pp. 19-51.

Byrne, R.H., Kump, L.R., Cantrell, K.J., 1988. The influence of temperature and pH on trace metal speciation in seawater. Marine Chemistry 25, 163-181.

Cabral, A.R., Creaser, R.A., Nägler, T., Lehmann, B., Voegelin, A.R., Belyatsky, B., Pašava, J., Seabra Gomes Jr, A.A., Galbiatti, H., Böttcher, M.E., Escher, P., 2013. Trace-element and multi-isotope geochemistry of Late-Archean black shales in the Carajás iron-ore district, Brazil. Chemical Geology 362, 91-104.

Campbell, G., 1978. Petrography and Stratigraphy of the North Band of Iron Formation, Sherman Mine, Temagami, Ontario. Laurentian University, p. 75.

Chown, E.H., N'dah, E., Mueller, W.U., 2000. The relation between iron-formation and low temperature hydrothermal alteration in an Archean volcanic environment. Precambrian Research 101, 263-275.

Cloud, P., 1973. Paleoecological Significance of the Banded Iron-Formation. Economic Geology 68, 1135-1143.

Czaja, A.D., Johnson, C.M., Roden, E.E., Beard, B.L., Voegelin, A.R., Nägler, T.F., Beukes, N.J., Wille, M., 2012. Evidence for free oxygen in the Neoarchean ocean based on coupled iron–molybdenum isotope fractionation. Geochimica et Cosmochimica Acta 86, 118-137.

Danielson, A., Möller, P., Dulski, P., 1992. The europium anomalies in banded iron formations and the thermal history of the oceanic crust. Chemical Geology 97, 89-100.

Davis, C.C., Chen, H.-W., Edwards, M., 2002. Modeling Silica Sorption to Iron Hydroxide. Environmental Science & Technology 36, 582-587.

Delvigne, C., Cardinal, D., Hofmann, A., André, L., 2012. Stratigraphic changes of Ge/Si, REE+Y and silicon isotopes as insights into the deposition of a Mesoarchaean banded iron formation. Earth and Planetary Science Letters 355-356, 109-118.

Diekrup, D., Hannington, M.D., Strauss, H., Ginley, S.J., 2018. Decoupling of Neoarchean sulfur sources recorded in Algoma-type banded iron formation. Earth and Planetary Science Letters 489, 1-7.

Dimroth, E., Chauvel, J.-J., 1973. Petrography of the Sokoman Iron Formation in Part of the Central Labrador Trough, Quebec, Canada. GSA Bulletin 84, 111-134.

Dimroth, E., 1977. Facies Models 6. Diagenetic facies of iron formation. Geoscience Canada 4.

Donaldson, J.A., Munro, J., 1982. Precambrian geology of the Cobalt area, northern Ontario, Eleventh International Congress on Sedimentology. Field Excursion Guidebook 16B, p. 72.

Donaldson, J.A., Garrett, R.G., 1991. Iron-Formation in Temagami and Sherman Mine Area, in: Gross, G.A., Donaldson, J.A. (Eds.), Geological Survey of Canada Open File 2163 - Iron-Formation and Metalliferous Sediments in Central Canada [Field Trip 8], p. 66.

Douville, E., Bienvenu, P., Charlou, J.L., Donval, J.P., Fouquet, Y., Appriou, P., Gamo, T., 1999. Yttrium and rare earth elements in fluids from various deep-sea hydrothermal systems. Geochimica et Cosmochimica Acta 63, 627-643.

Dulski, P., 2001. Reference Materials for Geochemical Studies: New Analytical Data by ICP-MS and Critical Discussion of Reference Values. Geostandards Newsletter 25, 87-125.

Ehrenberg, S.N., Nadeau, P.H., 2002. Postdepositional Sm/Nd Fractionation in Sandstones: Implications for Neodymium-Isotope Stratigraphy. Journal of Sedimentary Research 72, 304-315.

Ehrenreich, A., Widdel, F., 1994. Anaerobic oxidation of ferrous iron by purple bacteria, a new type of phototrophic metabolism. Applied Environmental Microbiology 60, 4517-4526.

Elder, J., 1966. Heat and mass transfer in the earth: hydrothermal systems. New Zealand Department of Scientific and Industrial Research Bulletin 169, 1-115.

Elderfield, H., Sholkovitz, E.R., 1987. Rare earth elements in the pore waters of reducing nearshore sediments. Earth and Planetary Science Letters 82, 280-288.

Elderfield, H., 1988. The oceanic chemistry of the rare-earth elements. Philosophical Transactions of the Royal Society of London. Series A, Mathematical and Physical Sciences 325, 105-126.

Elderfield, H., Schultz, A., 1996. Mid-ocean ridge hydrothermal fluxes and the chemical composition of the ocean. Annual Review of Earth and Planetary Sciences 24, 191-224.

Erel, Y., Morgan, J.J., 1991. The effect of surface reactions on the relative abundances of trace metals in deep-ocean water. Geochimica Cosmochimica Acta 55, 1807-1813.

Farquhar, J., Bao, H., Thiemens, M., 2000. Atmospheric Influence of Earth's Earliest Sulfur Cycle. Science 289, 756-758.

Fleet, A.J., 1984. Aqueous and Sedimentary Geochemistry of the Rare Earth Elements, in: Henderson, P. (Ed.), Developments in Geochemistry. Elsevier 2, pp. 343-373.

Fleet, M.E., Pan, Y., 1997. Site preference of rare earth elements in fluorapatite: Binary (LREE+HREE)-substituted crystals. American Mineralogist 82, 870.

Farquhar, J., Wing, B.A., 2003. Multiple sulfur isotopes and the evolution of the atmosphere. Earth and Planetary Science Letters 213, 1-13.

Franklin, J.M., Gibson, H.L., Jonasson, I.R., Galley, A.G., 2005. Volcanogenic Massive Sulfide Deposits, in: Hedenquist, J.W., Thompson, J.F.H., Goldfarb, R.J., Richards, J.P. (Eds.), One Hundredth Anniversary Volume. Society of Economic Geologists.

Frei, R., Polat, A., 2007a. Source heterogeneity for the major components of ~3.7 Ga Banded Iron Formations (Isua Greenstone Belt, Western Greenland): Tracing the nature of interacting water masses in BIF formation. Earth and Planetary Science Letters 253, 266-281.

Frei, R., Polat, A., 2007b. Source heterogeneity for the major components of ~3.7 Ga Banded Iron Formations (Isua Greenstone Belt, Western Greenland): tracing the nature of interacting water masses in BIF formation. Earth and Planetary Science Letters 253, 266-281.

Froehlich, P.N., Blanc, V., Mortlock, R.A., Chillrud, S.N., 1992. River Fluxes of Dissolved Silica to the Ocean Were Higher during Glacials: Ge/Si In Diatoms, Rivers, and Oceans. Paleoceanography 7, 739-767.

Fryer, B.J., 1977. Rare earth evidence in iron-formations for changing Precambrian oxidation states. Geochimica et Cosmochimica Acta 41, 361-367.

Fyon, J., Crocket, H., 1986. Exploration potential for base and precious metal mineralization in part of Strathy Township, Temagami Area. Ontario Geological Survey Open File Report 5591.

Garbe-Schönberg, C.-D., 1993. Simultaneous determination of thirty-seven trace elements in twenty-eight international rock standards by ICP-MS. Geostandards Newsletter 17, 81-97.

Garcia, D., Fonteilles, M., Moutte, J., 1994. Sedimentary Fractionations between Al, Ti, and Zr and the Genesis of Strongly Peraluminous Granites. 102, 411-422.

Garrels, R.M., 1987. A model for the deposition of the microbanded Precambrian iron formations. American Journal of Science 287, 81-105.

Garvin, J., Buick, R., Anbar, A.D., Arnold, G.L., Kaufman, A.J., 2009. Isotopic Evidence for an Aerobic Nitrogen Cycle in the Latest Archean. Science 323, 1045-1048.

Gemmell, J.B., Large, R.R., 1992. Stringer system and alteration zones underlying the Hellyer volcanogenic massive sulfide deposit, Tasmania, Australia. Economic Geology 87, 620-649.

German, C.R., Holliday, B.P., Elderfield, H., 1991. Redox cycling of rare earth elements in the suboxic zone of the Black Sea. Geochimica et Cosmochimica Acta 55, 3553-3558.

German, C.R., Masuzawa, T., Greaves, M.J., Elderfield, H., Edmond, J.M., 1995. Dissolved rare earth elements in the Southern Ocean: Cerium oxidation and the influence of hydrography. Geochimica et Cosmochimica Acta 59, 1551-1558.

Ginley, S.J., 2016. A Field and Petrological Study of Oxide-Facies Algoma-Type Banded Iron Formation, Sherman Mine, Temagami, Department of Earth and Environmental Sciences. University of Ottawa, p. 275.

Glasby, G.P., Schulz, H.D.J.A.G., 1999. Eh ph Diagrams for Mn, Fe, Co, Ni, Cu and As Under Seawater Conditions: Application of two new types of Eh-pH Diagrams to the Study of Specific Problems in Marine Geochemistry. Aquatic Geochemistry 5, 227-248.

Goldberg, S., Forster, H.S., Heick, E.L., 1993. Boron Adsorption Mechanisms on Oxides, Clay Minerals, and Soils Inferred from Ionic Strength Effects. 57, 704-708.

González-Álvarez, I., Kerrich, R., 2010. REE and HFSE mobility due to protracted flow of basinal brines in the mesoproterozoic Belt-Purcell Supergroup, Laurentia. Precambrian Research 177, 291-307.

Gourcerol, B., Thurston, P.C., Kontak, D.J., Côté-Mantha, O., Biczok, J., 2016. Depositional setting of Algoma-type banded iron formation. Precambrian Research 281, 47-79.

Govindaraju, K., 1994. 1994 compilation of working values and sample description for 383 geostandards. Geostandards and Geoanalytical Research 18, 1-158.

Grant, J.A., 1986. The isocon diagram; a simple solution to Gresens' equation for metasomatic alteration. Economic Geology 81, 1976-1982.

Gross, G., 1965a. Geology of iron deposits in Canada, Vol. 1 general geology and evaluation of ore deposits: Geological Survey of Canada. Economic Geology Report 22, 81.

Gross, G., 1996. Algoma-type iron-formation. Selected British Columbia Mineral Deposit Profiles 2, 1996-1913.

Gross, G.A., 1965b. Origin of Precambrian iron formations. Economic Geology 60, 1063-1065.

Gross, G.A., 1980. A classification of iron formations based on depositional environments. The Canadian Mineralogist 18, 215-222.

Gross, G.A., 1983. Tectonic Systems and the Deposition of Iron-Formation, in: B. Nagy, R.W.J.C.G., Schidlowski, M. (Eds.), Developments in Precambrian Geology. Elsevier, pp. 63-79.

Gross, G.A., Donaldson, J.A., 1990. Iron-formation and metalliferous sediments in Central Canada TEST. Field trip guidebook, International Association on the Genesis of Ore Deposits Symposium (Ottawa, Canada) 8, 66.

Gross, G.A., 2009. Iron Formation in Canada, Genesis and Geochemistry. Geological Survey of Canada, Open File 5987, p. 141.

Grotzinger, J.P., Kasting, J.F., 1993. New Constraints on Precambrian Ocean Composition. The Journal of Geology 101, 235-243.

Guo, Q., Strauss, H., Kaufman, A.J., Schröder, S., Gutzmer, J., Wing, B., Baker, M.A., Bekker, A., Jin, Q., Kim, S.-T., Farquhar, J., 2009. Reconstructing Earth's surface oxidation across the Archean-Proterozoic transition. Geology 37, 399-402.

Gurvich, E.G., 2006. Metalliferous Sediments of the World Ocean. Springer, Berlin, Germany.

Halevy, I., Bachan, A., 2017. The geologic history of seawater pH. Science 355, 1069-1071.

Hamade, T., Konhauser, K.O., Raiswell, R., Goldsmith, S., Morris, R.C., 2003. Using Ge/Si ratios to decouple iron and silica fluxes in Precambrian banded iron formations. Geology 31, 35-38.

Hannington, M.D., Coombs, A., van Hees, G., Duff, S., Campos-Alvarez, N., 2012. Regional lighogeochemical study of the Kidd-Munro MEGATEM® survey areas, Timmins-Kirkland Lake, northern Ontario. Discover Abitibi Initiative, Ontario Geological Survey Miscellaneous Release Data 291.

Hein, J.R., Spinardi, F., Okamoto, N., Mizell, K., Thorburn, D., Tawake, A., 2015. Critical metals in manganese nodules from the Cook Islands EEZ, abundances and distributions. Ore Geology Reviews 68, 97-116.

Hiemstra, T., Venema, P., Riemsdijk, W.H.V., 1996. Intrinsic Proton Affinity of Reactive Surface Groups of Metal (Hydr)oxides: The Bond Valence Principle. Journal of Colloid and Interface Science 184, 680-692.

Holland, H.D., 2003. The Geologic History of Seawater, Treatise on Geochemistry. Pergamon, Oxford, pp. 1-46.

Hurley, T.D., 1985. Petrology and Geochemistry of the Volcanic Host Rocks to the West and North Pits of the Sherman Mine Iron Formation, Temagami, Ontario. McMaster University, Hamilton, Ontario, p. 154.

Jain, A., Raven, K.P., Loeppert, R.H., 1999. Arsenite and Arsenate Adsorption on Ferrihydrite: Surface Charge Reduction and Net OH- Release Stoichiometry. Environmental Science & Technology 33, 1179-1184.

James, H.L., 1954. Sedimentary facies of iron-formation. Economic Geology 49, 235-293.

James, H.L., 1992. Precambrian Iron-Formations: Nature, Origin, and Mineralogic Evolution from Sedimentation to Metamorphism. Developments in Sedimentology 47, 543-589.

Jones, B., Manning, D.A.C., 1994. Comparison of geochemical indices used for the interpretation of palaeoredox conditions in ancient mudstones. Chemical Geology 111, 111-129.

Kappler, A., Pasquero, C., Konhauser, K.O., Newman, D.K., 2005. Deposition of banded iron formations by anoxygenic phototrophic Fe(II)-oxidizing bacteria. Geology 33, 865-868.

Kaufman, A.J., Hayes, J.M., Klein, C., 1990. Primary and diagenetic controls of isotopic compositions of iron-formation carbonates. Geochimica et Cosmochimica Acta 54, 3461-3473.

Kendall, B., Reinhard, C.T., Lyons, T.W., Kaufman, A.J., Poulton, S.W., Anbar, A.D., 2010. Pervasive oxygenation along late Archaean ocean margins. Nature Geoscience 3, 647-652.

Keren, R., Bingham, F.T., 1985. Boron in Water, Soils, and Plants, in: Stewart, B.A. (Ed.), Advances in Soil Science. Springer New York, New York, NY, pp. 229-276.

Klein, C., 2005. Some Precambrian banded iron formations (BIFs) from around the world: Their age, geologic setting, mineralogy, metamorphism, geochemistry, and origin. Am. Mineral. 90, 1473-1499.

Knauth, L.P., 2005. Temperature and salinity history of the Precambrian Ocean: Implications for the course of microbial evolution. Palaeogeogr. Palaeoclimatol. Palaeoecol. 219, 53-69.

Knauth, P.L., Donald, R.L., 2003. High Archaen climatic temperature inferred from oxygen isotope geochemistry of cherts in the 3.5 Ga Swaziland Supergroup, South Africa. Geol. Soc. Am. Bull. 115, 566-580.

Konhauser, K.O., Hamade, T., Raiswell, R., Morris, R.C., Ferris, F.G., Southam, G., Canfield, D.E., 2002. Could bacteria have formed the Precambrian banded iron formations? Geology 30, 1079-1082.

Konhauser, K.O., Newman, D.K., Kappler, A., 2005. The potential significance of microbial Fe(III) reduction during deposition of Precambrian banded iron formations. Blackwell Science Ltd, pp. 167-177.

Konhauser, K.O., Amskold, L., Lalonde, S.V., Posth, N.R., Kappler, A., Anbar, A., 2007. Decoupling photochemical Fe(II) oxidation from shallow-water BIF deposition. Earth and Planetary Science Letters 258, 87-100.

Koschinsky, A., Hein, J.R., 2003. Uptake of elements from seawater by ferromanganese crusts: solid-phase associations and seawater speciation. Marine Geology 198, 331-351.

Koschinsky, A., Winkler, A., Fritsche, U., 2003. Importance of different types of marine particles for the scavenging of heavy metals in the deep-sea bottom water. Applied Geochemistry 18, 693-710.

Krapež, B., Barley, M.E., Pickard, A.L., 2003. Hydrothermal and resedimented origins of the precursor sediments to banded iron formation: sedimentological evidence from the Early Palaeoproterozoic Brockman Supersequence of Western Australia. Sedimentology 50, 979-1011.

Lantink, M.L., Davies, J.H.F.L., Mason, P.R.D., Schaltegger, U., Hilgen, F.J., 2019. Climate control on banded iron formations linked to orbital eccentricity. Nat. Geosci. 12, 369-374.

Laurila, T.E., Hannington, M.D., Petersen, S., Garbe-Schönberg, D., 2014a. Early depositional history of metalliferous sediments in the Atlantis II Deep of the Red Sea: Evidence from rare earth element geochemistry. Geochimica et Cosmochimica Acta 126, 146-168.

Laurila, T.E., Hannington, M.D., Petersen, S., Garbe-Schönberg, D., 2014b. Trace metal distribution in the Atlantis II Deep (Red Sea) sediments. Chemical Geology 386, 80-100.

Laurila, T.E., Hannington, M.D., Leybourne, M., Petersen, S., Devey, C.W., Garbe-Schönberg, D., 2015. New insights into the mineralogy of the Atlantis II Deep metalliferous sediments, Red Sea. 16, 4449-4478.

Lepp, H., Goldich, S.S., 1964. Origin of Precambrian iron formations. Economic Geology 59, 1025-1060.

Lowenstein, T.K., Kendall, B., Anbar, A.D., 2014. The Geologic History of Seawater, in: Turekian, K.K. (Ed.), Treatise on Geochemistry (Second Edition). Elsevier, Oxford, pp. 569-622.

Maliva, R.G., Knoll, A.H., Simonson, B.M., 2005. Secular change in the Precambrian silica cycle: Insights from chert petrology. Geol. Soc. Am. Bull. 117, 835-845.

Marty, B., Avice, G., Bekaert, D.V., Broadley, M.W., 2018. Salinity of the Archaean oceans from analysis of fluid inclusions in quartz. Comptes Rendus Geoscience 350, 154-163.

Masuda, A., Kawakami, O., Dohmoto, Y., Takenaka, T., 1987. Lanthanide tetrad effects in nature: two mutually opposite types, W and M. Geochemical Journal 21, 119-124.

McBride, D., 2010. Report on the Scholes Township Property, Ontario. Temagami Iron Corporation Exploration Report, p. 37.

McLennan, S.M., 1989. Rare earth elements in sedimentary rocks; influence of provenance and sedimentary processes, in: Lipin, B.R., McKay, G.A. (Eds.), Geochemistry and Mineralogy of Rare Earth Elements 21, pp. 169-200.

Meyn, H.D., 1977. Geology of Afton, Scholes, Macbeth, and Clement Townships, Districts of Sudbury and Nipissing, Ontario Geological Survey Report 170, p. 77.

Montaser, A., 1998. Inductively coupled plasma mass spectrometry. John Wiley & Sons.

Moorhouse, W., 1946. The Northeastern Portion of the Timagami Lake Area. Department of Mines.

Mortlock, R.A., Froelich, P.N., Feely, R.A., Massoth, G.J., Butterfield, D.A., Lupton, J.E., 1993. Silica and germanium in Pacific Ocean hydrothermal vents and plumes. Earth and Planetary Science Letters 119, 365-378.

Mukhopadhyay, J., Ghosh, G., Zimmermann, U., Guha, S., Mukherjee, T., 2012. A 3.51 Ga bimodal volcanics-BIF-ultramafic succession from Singhbhum Craton: implications for Palaeoarchaean geodynamic processes from the oldest greenstone succession of the Indian subcontinent. Geological Journal 47, 284-311.

Murray, R.W., Buchholtz ten Brink, M.R., Jones, D.L., Gerlach, D.C., Russ III, G.P., 1990. Rare earth elements as indicators of different marine depositional environments in chert and shale. Geology 18, 268-271.

Nozaki, Y., Zhang, J., Amakawa, H., 1997. The fractionation between Y and Ho in the marine environment. Earth and Planetary Science Letters 148, 329-340.

OGS, 2001. Airborne magnetic and electromagnetic surveys, residual magnetic field, Temagami South area--Purchased data, Ontario Geological Survey

Ohmoto, H., 1996. Evidence in pre-2.2 Ga paleosols for the early evolution of atmospheric oxygen and terrestrial biota. Geology 24, 1135-1138.

Ohmoto, H., Watanabe, Y., Yamaguchi, K.E., Naraoka, H., Haruna, M., Kakegawa, T., Hayashi, K., Kato, Y., 2006. Chemical and biological evolution of early Earth: Constraints from banded iron formations. Geological Society of America Memoirs 198, 291-331.

Ohmoto, H., Hoashi, M., Otake, T., Bevacqua, D., Watanabe, Y., 2008. Origins of hematite, magnetite and siderite in banded iron formations. Geochimica et Cosmochimica Acta 72, A699-A699.

Ohta, A., Kawabe, I., 2001. REE(III) adsorption onto Mn dioxide (δ-MnO2) and Fe oxyhydroxide: Ce(III) oxidation by δ-MnO2. Geochimica et Cosmochimica Acta 65, 695-703.

Palmer, M.R., Spivack, A.J., Edmond, J.M., 1987. Temperature and pH controls over isotopic fractionation during adsorption of boron on marine clay. Geochimica et Cosmochimica Acta 51, 2319-2323.

Paytan, A., McLaughlin, K., 2007. The Oceanic Phosphorus Cycle. Chemical Reviews 107, 563-576.

Pearce, J.A., 1996. A user's guide to basalt discrimination diagrams, Trace Element Geochemistry of Volcanic Rocks: Applications for Massive Sulphide Exploration. Geological Association of Canada, Short Course Notes 12, pp. 79-113.

Pecoits, E., Gingras, M.K., Barley, M.E., Kappler, A., Posth, N.R., Konhauser, K.O., 2009. Petrography and geochemistry of the Dales Gorge banded iron formation: Paragenetic sequence, source and implications for palaeo-ocean chemistry. Precambrian Research 172, 163-187.

Percival, J.A., Skulski, T., Sanborn-Barrie, M., Stott, G.M., Leclair, A.D., Corkery, M.T., Boily, M., 2012. Geology and tectonic evolution of the Superior Province, Canada, in: Percival, J.A., Cook, F.A., Clowes, R.M. (Eds.), Tectonic Styles in Canada: The LITHOPROBE Perspective. Edited by JA Percival, FA Cook, and RM Clowes. Geological Association of Canada Special Paper. Geological Association of Canada, pp. 321-378.

Peter, J.M., Goodfellow, W.D., 1996. Mineralogy, bulk and rare earth element geochemistry of massive sulphide-associated hydrothermal sediments of the Brunswick Horizon, Bathurst Mining Camp, New Brunswick. Canadian Journal of Earth Sciences 33, 252-283.

Peter, J.M., 2003. Ancient iron formations: their genesis and use in the exploration for stratiform base metal sulphide deposits, with examples from the Bathurst Mining Camp. GeoText 4, 145-176.

Pickard, A.L., 2002. Shrimp U–Pb zircon ages of tuffaceous mudrocks in the brockman iron formation of the hamersley range, western australia. Aust. J. Earth Sci. 49, 491-507.

Piercey, S.J., Gibson, H.L., Tardif, N., Kamber, B.S., 2016. Ambient Redox and Hydrothermal Environment of the Wolverine Volcanogenic Massive Sulfide Deposit, Yukon: Insights from Lithofacies and Lithogeochemistry of Mississippian Host Shales*. Economic Geology 111, 1439-1463.

Planavsky, N., Bekker, A., Rouxel, O.J., Kamber, B., Hofmann, A., Knudsen, A., Lyons, T.W., 2010a. Rare Earth Element and yttrium compositions of Archean and Paleoproterozoic Fe formations revisited: New perspectives on the significance and mechanisms of deposition. Geochimica et Cosmochimica Acta 74, 6387-6405.

Planavsky, N.J., Rouxel, O.J., Bekker, A., Lalonde, S.V., Konhauser, K.O., Reinhard, C.T., Lyons, T.W., 2010b. The evolution of the marine phosphate reservoir. Nature 467, 1088-1090.

Pokrovski, G.S., Schott, J., 1998. Thermodynamic properties of aqueous Ge(IV) hydroxide complexes from 25 to 350ºC: implications for the behavior of germanium and the Ge/Si ratio in hyderothermal fluids. Geochimica Cosmochimica Acta 62, 1631-1642.

Pokrovsky, O.S., Pokrovski, G.S., Schott, J., Galy, A., 2006. Experimental study of germanium adsorption on goethite and germanium coprecipitation with iron hydroxide: X-ray adxorption fine structure and macroscopic characterization. Geochimica et Cosmochimica Acta 70, 3325-3345.

Posth, N.R., Hegler, F., Konhauser, K.O., Kappler, A., 2008. Alternating Si and Fe deposition caused by temperature fluctuations in Precambrian oceans. Nature Geosci 1, 703-708.

Posth, N.R., Köhler, I., D Swanner, E., Schröder, C., Wellmann, E., Binder, B., Konhauser, K.O., Neumann, U., Berthold, C., Nowak, M., 2013a. Simulating Precambrian banded iron formation diagenesis. Chemical Geology 362, 66-73.

Posth, N.R., Konhauser, K.O., Kappler, A., 2013b. Microbiological processes in banded iron formation deposition. Sedimentology.

Poulton, S.W., Canfield, D.E., 2006. Co-diagenesis of iron and phosphorus in hydrothermal sediments from the southern East Pacific Rise: Implications for the evaluation of paleoseawater phosphate concentrations. Geochimica et Cosmochimica Acta 70, 5883-5898.

Pröfrock, D., Prange, A., 2012. Inductively Coupled Plasma–Mass Spectrometry (ICP-MS) for Quantitative Analysis in Environmental and Life Sciences: A Review of Challenges, Solutions, and Trends. Applied Spectroscopy 66, 843-868.

Pye, E.G., Lovell, H.L., Bright, E.G., Petruk, W., 1972. Precambrian Geology and Mineral Deposits of the Timagami, Cobalt, Kirkland Lake and Timmins Region, Ontario. XXIV International Geological Congress, Field Excursion Guidebook A39-39b-C39, p. 96.

Rasmussen, B., Meier, D.B., Krapež, B., Muhling, J.R., 2013. Iron silicate microgranules as precursor sediments to 2.5-billion-year-old banded iron formations. Geology 41, 435-438.

Rasmussen, B., Muhling, J.R., Suvorova, A., Krapež, B., 2016. Dust to dust: Evidence for the formation of “primary” hematite dust in banded iron formations via oxidation of iron silicate nanoparticles. Precambrian Research 284, 49-63.

Rasmussen, B., Muhling, J.R., 2018. Making magnetite late again: Evidence for widespread magnetite growth by thermal decomposition of siderite in Hamersley banded iron formations. Precambrian Research 306, 64-93.

Reinhard, C.T., Raiswell, R., Scott, C., Anbar, A.D., Lyons, T.W., 2009. A Late Archean Sulfidic Sea Stimulated by Early Oxidative Weathering of the Continents. Science 326, 713-716.

Robert, F., Chaussidon, M., 2006. A Paleotemperature curve for the Precambrian oceans based on silicon isotopes in cherts. Nature 443, 969-972.

Saito, M.A., Sigman, D.M., Morel, F.M.M., 2003. The bioinorganic chemistry of the ancient ocean: the co-evolution of cyanobacterial metal requirements and biogeochemical cycles at the Archean–Proterozoic boundary? Inorganica Chimica Acta 356, 308-318.

Sampaio, G.M.S., Enzweiler, J., 2015. New ICP-MS Results for Trace Elements in Five Iron-Formation Reference Materials. Geostandards and Geoanalytical Research 39, 105-119.

Schwartz, T.C., 1995. Petrology and geochemistry of felsic volcaniclastic rocks along the Sherman Mine Road, Temagami Greenstone Belt, Strathy Township, Ontario. McMaster University, p. 180.

Scott, C.T., Bekker, A., Reinhard, C.T., Schnetger, B., Krapez, B., Rumble, D., Lyons, T.W., 2011. Late Archean euxinic conditions before the rise of atmospheric oxygen. Geology 39, 119-122.

Shields, G., Stille, P., 2001. Diagenetic constraints on the use of cerium anomalies as palaeoseawater redox proxies: an isotopic and REE study of Cambrian phosphorites. Chemical Geology 175, 29-48.

Shklanka, R., 1968. Iron Deposits of Ontario; Ontario Department of Mines, Mineral Resoruces Circular No. 11, p. 489.

Siever, R., 1992. The silica cycle in the Precambrian. Geochim. Cosmochim. Acta 56, 3265-3272.

Spivack, A.J., Edmond, J.M., 1987. Boron isotope exchange between seawater and the oceanic crust. Geochimica et Cosmochimica Acta 51, 1033-1043.

Spivack, A.J., Palmer, M.R., Edmond, J.M., 1987. The sedimentary cycle of the boron isotopes. Geochimica et Cosmochimica Acta 51, 1939-1949.

Steinhoefel, G., Horn, I., von Blanckenburg, F., 2009. Micro-scale tracing of Fe and Si isotope signatures in banded iron formation using femtosecond laser ablation. Geochimica et Cosmochimica Acta 73, 5343-5360.

Steinhoefel, G., von Blanckenburg, F., Horn, I., Konhauser, K.O., Beukes, N.J., Gutzmer, J., 2010. Deciphering formation processes of banded iron formations from the Transvaal and the Hamersley successions by combined Si and Fe isotope analysis using UV femtosecond laser ablation. Geochimica et Cosmochimica Acta 74, 2677-2696.

Streit, L., 2017. Chlorite Geochemistry of Altered and Metamorphosed Volcanic Host Rocks of the Temagami Banded Iron Formation. University of Ottawa, BSc thesis, 119 pp.

Sun, S., Konhauser, K.O., Kappler, A., Li, Y.-L., 2015. Primary hematite in Neoarchean to Paleoproterozoic oceans. GSA Bulletin 127, 850-861.

Sun, S., Li, Y.-L., 2017. Geneses and evolutions of iron-bearing minerals in banded iron formations of >3760 to ca. 2200 million-year-old: Constraints from electron microscopic, X-ray diffraction and Mössbauer spectroscopic investigations. Precambrian Research 289, 1-17.

Takamasa, A., Nakai, S.i., 2009. Contamination introduced during rock sample powdering: Effects from different mill materials on trace element contamination. Geochemical Journal 43, 389-394.

Thurston, P.C., Ayer, J.A., Goutier, J., Hamilton, M.A., 2008. Depositional Gaps in Abitibi Greenstone Belt Stratigraphy: A Key to Exploration for Syngenetic Mineralization. Economic Geology 103, 1097-1134.

Thurston, P.C., Kamber, B.S., Whitehouse, M., 2012. Archean cherts in banded iron formation: Insight into Neoarchean ocean chemistry and depositional processes. Precambrian Research 214–215, 227-257.

Trendall, A., 1973. Varve cycles in the Weeli Wolli Formation of the Precambrian Hamersley Group, Western Australia. Economic Geology 68, 1089-1097.

Truscott, M.G., Shaw, D.M., 1984. Boron in chert and Precambrian siliceous iron formations. Geochimica et Cosmochimica Acta 48, 2313-2320.

Viehmann, S., Hoffmann, J.E., Münker, C., Bau, M., 2014. Decoupled Hf-Nd isotopes in Neoarchean seawater reveal weathering of emerged continents. Geology 42, 115-118.

Walker, J.C.G., 1984. Suboxic diagenesis in banded iron formations. Nature 309, 340-342.

Weber, K.A., Achenbach, L.A., Coates, J.D., 2006. Microorganisms pumping iron: anaerobic microbial iron oxidation and reduction. Nature Reviews Microbiology 4, 752-764.

Williams, L.A., Parks, G.A., Crerar, D.A., 1985. Silica diagenesis, I. Solubility controls. Journal of sedimentary Research 55.

Yu, Z., Robinson, P., McGoldrick, P., 2001. An Evaluation of Methods for the Chemical Decomposition of Geological Materials for Trace Element Determination using ICP-MS. Geostandards Newsletter 25, 199-217.

Table 3.1: Temagami BIF facies types and mineralogy of different layer types

Rock type	Facies	Layer	Mineralogy
BIF	Oxide	Magnetite	mag, qz, (++hem, +ap, +chl, +carb, -stp, -bt, -mon, --py, --po, ---cpy, --ba, --xen)
		Chert	qz, mag, (+hem, +ap, +chl, -carb)
		Jasper	qz, hem, (++mag, --carb)
	Silicate	Chlorite	chl, qz, mag (++ ap, +stilp, +carb, -ilm, --mon, -- xen)
	Sulfide	Pyrite	py, qz, (++ gr + chl, +carb, + cpy, +sph, +gn, -ap)
Volcaniclastic	Shale/Sandstone	Chlorite	chl, qz, (++ilm, +mag, -ap, -rt -carb --mon, --zrn)

No prefix: rock forming phase; ++ major accessory; + accessory; - minor accessory; -- trace. Mag: magnetite, qz: quartz, hem: hematite, ap: apatite, chl: chlorite, carb: carbonate, stp: stilpnomelane, bt: biotite, mon: monazite, py: pyrite, po: pyrrhotite, cpy: chalcopyrite, ba: barite, xen: xenotime, ilm: ilmenite, gr: graphitic carbon, sph: sphalerite, gn: galena, rt: rutile, zrn: zircon.

Table 3.2: Temagami BIF sample distribution between Highway 11 and Sherman Mine sample sites

Lithology	**Highway 11**	**Sherman Mine**
Jasper	2	4
Chert	13	9
Magnetite	8	11
Sulfidic Chert	-	4
Chlorite	4	1
Shale	5	1
Massive Sulfide	1	-
Intrusive	2	-
BIF Standard	2	1
Total	37	31

Table 3.3: Results for CANMET standards FeR-3 and FeR-4 from different analytical techniques compared to certified and literature values

	FeR-3				FeR-4				
Element	**TD**	**Fusion**	**certified**	**reference**	**TD**	**Fusion**	**certified**	**reference**	**detection limit**
Si %	nd	**24.6**	25.1	nd	nd	**23.54**	23.4	nd	0.01
Al %	0.04	**0.05**	0.05	0.04	0.795	**0.85**	0.90	0.855	0.01
Fe %	32.1	**32.3**	31.1	31.1	25.6	**28.1**	27.9	27.9	0.01
Ca %	0.545	**0.59**	0.6	0.581	1.410	**1.55**	1.59	1.56	0.01
Mg %	0.571	**0.60**	0.615	0.607	0.735	**0.79**	0.85	0.841	0.01
Na %	**0.002**	< 0.004	0.02	0.005	**0.017**	0.011	0.04	0.020	0.002
K %	**0.015**	0.008	0.025	0.013	**0.225**	0.224	0.24	0.235	0.002
P %	nd	**0.03**	0.03	0.03	nd	**0.05**	0.057	0.053	0.01
Ti	nd	**20**	60	15.1	nd	**370**	400	355	10
Mn	644	**640**	500	612	1460	**1470**	1200	1490	10
Zn	**29.4**	< 30	36	nd	**22.1**	< 30	27	nd	0.04
Cu	**1.15**	< 10	6	2.6*	**5.92**	< 10	13	9*	0.04
Pb	**4.7**	6	9	7.10	**5.9**	8	8	7.44	0.1
Ag	**0.06**	< 0.5	nd	nd	**0.07**	< 0.5	nd	nd	0.01
As	**1.14**	< 5	1	1	**3.66**	< 5	3.6	3.6	0.02
Sb	**0.79**	0.4	1	nd	**1.4**	0.8	3	nd	0.02
Hg	**0.008**	nd	nd	nd	**0.008**	nd	nd	nd	0.002
Tl	**< 0.01**	< 0.05	nd	nd	**0.07**	< 0.05	nd	nd	0.01
Cd	**0.04**	nd	nd	0.06*	**0.06**	nd	nd	0.05*	0.02
Co	**1.49**	2	2	1.68	**1.87**	2	2	1.81	0.02
Ni	**10**	< 20	10	10.1	**4.6**	< 20	6	6.01	0.1
Se	**0.29**	nd	nd	nd	**0.68**	nd	nd	nd	0.02
Mo	**0.77**	< 2	nd	nd	**0.7**	< 2	nd	nd	0.01
Te	**< 0.02**	nd	nd	nd	**0.06**	nd	nd	nd	0.02
Sn	**0.3**	< 1	nd	0.3*	**0.6**	< 1	nd	0.6*	0.2
Ge	< 0.02	**3.7**	4	nd	< 0.02	**5.4**	5	nd	0.5
Bi	**0.019**	< 0.1	nd	nd	**0.044**	< 0.1	nd	0.03	0.004
In	**< 0.02**	< 0.1	nd	nd	**< 0.02**	< 0.1	nd	nd	0.02
Re	**< 0.0002**	nd	nd	nd	**0.001**	nd	nd	nd	0.0002
W	**1.34**	3	nd	2.07	**1.48**	< 0.5	nd	1.75	0.02
Cr	**10.7**	< 20	6	nd	**11.2**	20	9	nd	0.1
V	**9.5**	12	8	7*	**11.9**	15	11	12*	0.2
Sc	nd	**< 1**	nd	0.361	nd	**1**	1.5	1.091	1
Ga	**0.68**	1	nd	nd	**3.95**	3	nd	nd	0.02
Zr	**1**	2	2	1.4	**17.4**	16	18	18.7	0.2
Ba	**7.3**	< 3	11	8.9	**36.1**	38	43	38.5	0.2
Cs	**0.2**	< 0.1	nd	0.161	**0.69**	0.7	0.8	0.678	0.01
Li	**0.5**	nd	nd	nd	**8.1**	nd	7	nd	0.1

Table 3.3 (continued): Results for FeR-3 and FeR-4 from different analytical techniques compared to certified and literature values

	FeR-3				FeR-4				
Element	**TD**	**Fusion**	**certified**	**reference**	**TD**	**Fusion**	**certified**	**reference**	**detection limit**
Be	**0.49**	1	nd	nd	**1.32**	1	1	nd	0.02
B	**< 0.2**	nd	nd	nd	**3**	nd	2	nd	0.2
Hf	**< 0.02**	< 0.1	nd	0.0217	**0.41**	0.4	nd	0.523	0.02
Nb	1.14	**3.7**	nd	0.4	1.55	**3.9**	nd	1.8	0.2
Ta	< 0.02	**< 0.01**	nd	0.01	0.07	**0.09**	nd	0.09	0.01
Rb	**0.61**	< 1	nd	0.67	**16.4**	15	16	16.3	0.04
Sr	**33.9**	32	31	32.6	**64.3**	62	62	64.5	0.04
U	0.17	**0.25**	nd	0.33	1.2	**0.53**	nd	1.05	0.01
Th	0.05	**0.16**	nd	0.047	0.71	**0.84**	nd	0.859	0.05
Y	2.4	**4.1**	6	3.62	4.8	**8.5**	8	7.91	0.5
La	1.75	**2.05**	2	1.76	7.29	**8.16**	8	7.82	0.05
Ce	2.20	**2.69**	nd	2.28	12.40	**13.80**	nd	13.30	0.05
Pr	0.26	**0.32**	nd	0.27	1.48	**1.65**	nd	1.60	0.01
Nd	1.39	**1.64**	nd	1.49	6.74	**7.35**	nd	7.48	0.05
Sm	0.49	**0.50**	0.6	0.50	1.89	**1.97**	2.2	2.09	0.01
Eu	0.20	**0.257**	nd	0.248	0.59	**0.722**	nd	0.696	0.005
Gd	0.26	**0.38**	nd	0.35	0.97	**1.25**	nd	1.24	0.01
Tb	0.04	**0.07**	nd	0.06	0.12	**0.18**	nd	0.17	0.01
Dy	0.23	**0.46**	nd	0.36	0.64	**1.08**	nd	1.05	0.01
Ho	0.05	**0.10**	nd	0.09	0.12	**0.23**	nd	0.22	0.01
Er	0.16	**0.30**	nd	0.27	0.35	**0.68**	nd	0.64	0.01
Tm	0.02	**0.044**	nd	0.038	0.06	**0.100**	nd	0.094	0.005
Yb	0.17	**0.29**	nd	0.25	0.43	**0.66**	nd	0.59	0.01
Lu	0.020	**0.049**	nd	0.040	0.06	**0.098**	nd	0.096	0.002
	EA-TCD				**EA-TCD**				
S %	**0.02**		0.03	nd	**0.09**		0.11	nd	0.01
C %	**0.33**		nd	nd	**1.33**		nd	nd	0.01
N %	**< 0.01**		nd	nd	**< 0.01**		nd	nd	0.01

Notes:
FeR-3 and FeR-4 are CANMET iron formation standards from Temagami, certified values from the NRCAN FER-1 to FER-4 certificate of analysis. FeR-3 is a pure iron formation standard from the Hwy 11 outcrop, FeR-4 is from the same location but contains more clastic material.
Reference is Bau and Alexander (2009), or Sampaio and Enzweiler (2014)*
Values in ppm if not indicated differently, nd: not determined
detection limit for the preferred method
TD, Total Dissolution, see methods for details
EA-TCD, Elemental Analyzer – Thermal Conductivity Detector

Table 3.4: Abundances of major elements and Loss on Ignition (LOI) in Temagami BIF facies

		Si [%]	Al [%]	Fe [%]	Ca [%]	Mg [%]	Na [%]	K [%]	P [%]	N [%]	C [%]	S [%]	LOI [%]
	Method	**FUS**	**FUS**	**FUS**	**FUS**	**FUS**	**TD**	**TD**	**FUS**	**TCD**	**TCD**	**TCD**	**FUS**
	dl	**0.005**	**0.005**	**0.007**	**0.007**	**0.006**	**0.002**	**0.002**	**0.004**	**0.03**	**0.02**	**0.02**	
Chert (n=28)	min	30.8	0.02	0.9	0.01	0.02	bdl	bdl	Bdl	0.02	0.01	bdl	-0.8
	max	46.0	1.21	24.2	1.51	1.03	0.04	0.06	0.05	0.03	2.35	3.12	8.6
	average	40.5	0.24	6.6	0.32	0.34	0.01	0.02	0.02	0.02	0.47	0.22	2.1
	median	**41.5**	**0.17**	**4.6**	**0.17**	**0.22**	**0.01**	**0.01**	**0.01**	**0.02**	**0.32**	**0.02**	**1.4**
Jasper (n=6)	min	30.9	0.06	6.7	0.05	0.03	bdl	bdl	0.01	0.02	0.01	bdl	-0.5
	max	41.8	0.18	19.8	0.36	0.40	0.04	0.03	0.07	0.02	0.16	0.08	-0.1
	average	35.6	0.10	15.4	0.25	0.21	0.01	0.01	0.05	0.02	0.09	0.02	-0.1
	median	**33.6**	**0.08**	**18.7**	**0.20**	**0.11**	**0.01**	**0.01**	**0.04**	**0.02**	**0.03**	**0.01**	**-0.1**
Magnetite	min	5.6	0.02	21.0	0.02	0.05	bdl	0.01	bdl	0.02	bdl	bdl	-2.6
(n=19)	max	24.5	2.92	63.2	4.37	3.93	0.11	0.52	0.17	0.03	3.94	1.28	13.5
	average	15.4	0.45	42.3	0.85	1.35	0.03	0.14	0.05	0.02	0.62	0.24	1.2
	median	**13.9**	**0.28**	**42.2**	**0.28**	**1.18**	**0.01**	**0.07**	**0.04**	**0.02**	**0.08**	**0.01**	**-0.4**
All Oxide BIF	min	5.6	0.02	0.9	0.01	0.02	bdl	bdl	bdl	0.02	bdl	bdl	-2.6
(n=53)	max	46.0	2.92	63.2	4.37	3.93	0.11	0.52	0.17	0.03	3.94	3.12	13.5
	average	29.7	0.31	22.2	0.53	0.74	0.02	0.07	0.04	0.02	0.49	0.21	1.5
	median	**33.6**	**0.17**	**17.2**	**0.21**	**0.28**	**0.01**	**0.02**	**0.04**	**0.02**	**0.14**	**0.01**	**0.4**
Chlorite	min	15.7	3.15	5.4	0.12	2.59	bdl	bdl	bdl	0.02	0.06	bdl	3.3
(n=5)	max	26.4	7.95	33.8	2.71	4.99	4.01	0.03	0.19	0.02	1.53	1.46	8.8
	average	21.9	5.40	19.3	1.36	3.58	0.81	0.01	0.07	0.02	0.65	0.34	5.6
	median	**23.4**	**5.65**	**19.5**	**1.17**	**3.44**	**0.01**	**0.01**	**0.05**	**0.02**	**0.62**	**0.02**	**5.4**
Shale	min	18.2	5.82	5.9	0.10	1.72	bdl	bdl	0.03	0.02	0.01	bdl	3.0
(n=5)	max	32.0	7.89	24.0	0.29	3.63	0.48	1.94	0.09	0.02	0.11	0.59	5.8
	average	23.2	6.59	18.7	0.17	2.71	0.11	0.40	0.06	0.02	0.04	0.16	4.7
	median	**21.7**	**6.53**	**21.5**	**0.14**	**2.34**	**0.01**	**0.01**	**0.06**	**0.02**	**0.02**	**0.01**	**5.2**
Sulfidic	min	9.7	0.63	19.9	bdl	0.15	bdl	0.01	bdl	0.02	0.19	20.48	16.6
Chert	max	23.6	0.98	35.0	0.31	0.52	0.02	0.43	0.01	0.32	0.91	30.32	28.3
(n=4)	average	15.7	0.83	28.8	0.11	0.30	0.01	0.21	0.01	0.09	0.39	26.92	22.7
	median	**14.7**	**0.85**	**30.3**	**0.06**	**0.27**	**0.01**	**0.20**	**0.01**	**0.02**	**0.24**	**28.45**	**23.0**

Notes:

dl: detection limit, bdl: below detection limit. n: number of samples from each facies.

Table 3.5: Abundances of trace alkali and alkali earth elements and HFSE in Temagami BIF facies

		Rb	Sr	Cs	Ba	Sc	Ti	Zr	Hf	Nb	Ta
	Method	**TD**	**TD**	**TD**	**TD**	**FUS**	**FUS**	**TD**	**FUS**	**FUS**	**FUS**
	dl	**0.04**	**0.04**	**0.01**	**0.2**	**1**	**6**	**0.2**	**0.1**	**0.2**	**0.01**
Chert (n=28)	**median**	**0.40**	**5.56**	**0.10**	**2.1**	**bdl**	**18**	**1.1**	**bdl**	**0.1**	**0.03**
	average	0.56	15.4	0.22	14.3	bdl	46	2.4	0.05	0.2	0.04
	min	0.05	0.92	0.03	0.5	bdl	6	bdl	bdl	bdl	bdl
	max	1.98	168	1.05	181	2	515	24.0	0.50	0.9	0.12
Jasper (n=6)	**median**	**0.21**	**15.7**	**0.06**	**3.3**	**bdl**	**6**	**0.5**	**bdl**	**bdl**	**0.04**
	average	0.54	25.0	0.15	30.5	bdl	13	0.7	0.02	0.5	0.04
	min	0.05	1.80	0.03	0.5	bdl	3	bdl	bdl	bdl	0.02
	max	2.37	56.8	0.53	46.0	bdl	48	1.8	0.04	1.7	0.07
Magnetite	**median**	**2.58**	**14.2**	**0.66**	**16.7**	**bdl**	**132**	**4.6**	**0.11**	**bdl**	**0.05**
(n=19)	average	11.4	28.9	5.66	43.8	bdl	215	9.6	0.21	0.5	0.07
	min	0.31	3.54	0.14	0.9	bdl	12	0.8	bdl	bdl	0.03
	max	61.1	90.8	46.0	279	4	1109	59.6	1.42	1.4	0.25
All Oxide BIF	**median**	**0.61**	**9.21**	**0.18**	**4.9**	**bdl**	**30**	**1.9**	**0.03**	**bdl**	**0.05**
(n=53)	average	5.04	21.6	2.46	26.1	bdl	112	5.2	0.11	0.4	0.05
	min	0.05	0.92	0.03	0.5	bdl	3	bdl	bdl	bdl	bdl
	max	61.1	168	46.0	279	4	1109	59.6	1.42	1.7	0.25
Chlorite	**median**	**0.31**	**32.3**	**0.21**	**1.8**	**4**	**2074**	**77.3**	**2.34**	**3.9**	**0.32**
(n=5)	average	0.66	42.5	0.22	7.5	10	2734	92.1	2.12	4.0	0.41
	min	0.18	3.96	0.11	0.7	3	719	45.4	1.16	1.2	0.25
	max	2.26	113	0.34	29.9	21	6515	136	2.85	7.2	0.64
Shale	**median**	**0.50**	**9.09**	**0.18**	**2.9**	**7**	**2751**	**117**	**2.50**	**6.9**	**0.59**
(n=5)	average	16.0	10.4	0.42	121	8	2491	116	2.80	7.3	0.69
	min	0.15	4.96	0.01	1.7	6	1157	78.9	2.03	4.8	0.52
	max	78.5	17.6	1.56	553	11	4010	149	3.78	12.8	1.15
Sulfidic	**median**	**10.1**	**4.67**	**0.53**	**6.5**	**bdl**	**321**	**16.6**	**0.32**	**0.6**	**0.08**
Chert	average	11.1	4.60	0.51	7.4	bdl	327	15.1	0.31	0.6	0.18
(n=4)	min	0.58	2.77	0.20	2.6	bdl	282	9.6	0.22	0.4	0.05
	max	23.7	6.30	0.79	14.1	1	384	17.6	0.39	0.7	0.53

Notes:

dl: detection limit, bdl: below detection limit.

All values in ppm. n: number of samples from each facies.

Table 3.6: Abundances hydrothermal-chalcophile elements in Temagami BIF facies

		Zn	Cu	Pb	Ag	As	Sb	Hg*	Cd	Co	Ni	Sn
	Method	TD	TD	TD	TD	TD	TD	TD	TD	TD	TD	TD
	dl	0.04	0.04	0.1	0.01	0.02	0.02	0.002	0.02	0.02	0.1	0.02
Chert	**median**	**5.70**	**2.64**	**0.5**	**0.01**	**0.77**	**0.18**	**0.001**	bdl	**1.03**	**14.0**	bdl
(n=28)	average	10.7	10.3	1.0	0.03	2.86	0.22	0.043	0.03	2.76	19.1	bdl
	min	1.29	bdl	bdl	bdl	bdl	0.03	bdl	bdl	0.14	bdl	bdl
	max	35.7	114	6.6	0.15	35.5	0.71	0.333	0.13	13.9	88.0	0.3
Jasper (n=6)	**median**	**7.64**	**0.48**	**1.2**	bdl	**1.02**	**0.55**	**0.007**	**0.02**	**0.45**	**5.0**	bdl
	average	10.9	0.83	1.4	0.03	1.12	0.57	0.013	0.02	0.68	15.7	bdl
	min	2.57	bdl	bdl	bdl	0.33	0.37	bdl	bdl	0.05	0.2	bdl
	max	10.9	1.28	3.6	0.10	1.85	0.93	0.009	0.03	0.90	58.4	bdl
Magnetite	**median**	**19.4**	**1.95**	**1.3**	**0.03**	**1.10**	**0.66**	**0.003**	**0.03**	**1.92**	**12.2**	bdl
(n=19)	average	30.5	10.4	1.7	0.05	3.64	1.03	0.009	0.04	3.99	20.0	bdl
	min	5.56	bdl	0.3	bdl	0.30	0.26	bdl	bdl	0.29	0.9	bdl
	max	88.8	54.6	5.5	0.26	24.5	2.45	0.080	0.18	16.0	79.2	0.6
All Oxide	**median**	**10.6**	**2.18**	**0.9**	**0.02**	**0.89**	**0.47**	**0.002**	**0.02**	**1.03**	**12.2**	bdl
BIF	average	18.4	9.31	1.3	0.04	2.99	0.59	0.025	0.03	3.02	19.3	bdl
(n=53)	min	1.29	bdl	0.1	bdl	bdl	0.03	bdl	bdl	0.05	bdl	bdl
	max	88.8	114	6.6	0.26	35.5	2.45	0.333	0.18	16.0	88.0	0.6
Chlorite	**median**	**77.9**	**2.19**	**1.2**	**0.19**	**1.21**	**0.14**	**0.001**	**0.14**	**20.9**	**27.7**	**0.5**
(n=5)	average	72.4	26.6	2.6	0.20	17.9	0.11	0.002	0.14	20.9	123	0.4
	min	48.8	1.97	0.8	0.16	0.49	0.01	bdl	0.06	2.90	5.1	bdl
	max	89.8	80.9	8.7	0.26	70.3	0.18	0.005	0.20	49.0	520	0.8
Shale	**median**	**88.0**	**6.79**	**1.3**	**0.23**	**1.30**	**0.15**	**0.001**	**0.13**	**8.02**	**19.9**	**0.7**
(n=5)	average	100	9.38	1.9	0.21	3.35	0.13	0.003	0.12	8.40	21.1	0.9
	min	43.3	1.89	0.9	0.14	0.88	0.05	bdl	0.10	4.86	12.7	bdl
	max	185	24.2	3.4	0.26	10.3	0.17	0.006	0.14	11.8	35.0	2.0
Sulfidic	**median**	**36.3**	**66.4**	**84.1**	**2.36**	**272**	**16.2**	**0.070**	**0.11**	**58.9**	**72.5**	**0.4**
Chert	average	35.7	72.4	92.3	2.49	270	15.7	0.072	0.13	62.9	77.8	0.4
(n=4)	min	9.78	52.0	33.9	1.28	173	6.30	0.042	0.05	49.6	46.1	0.2
	max	60.6	105	167	3.96	363	24.2	0.106	0.24	84.1	120	0.5

Notes:

dl: detection limit, bdl: below detection limit.

All values in ppm. n: number of samples from each facies.

* results for Hg should be considered semi-quantitative minimum values due to the non-element specific analytical procedure. Hg can be lost due to volatile behaviour during the fusion process (see text for discussion).

Table 3.7: Abundances of light elements and metalloids in Temagami BIF facies

		Li	Be	B	Tl	Se	Te	Ge	Bi	In	Ga
	Method	**TD**	**TD**	**TD**	**TD**	**TD**	**TD**	**FUS**	**TD**	**TD**	**TD**
	dl	**0.1**	**0.02**	**0.2**	**0.01**	**0.02**	**0.02**	**0.5**	**0.004**	**0.02**	**0.02**
Chert	**median**	**0.3**	**0.13**	**55.6**	**bdl**	**0.13**	**bdl**	**2.9**	**0.010**	**bdl**	**0.64**
(n=28)	average	0.6	0.15	47.7	bdl	0.24	0.03	3.2	0.024	bdl	0.74
	min	bdl	0.03	8.0	bdl	0.02	bdl	1.5	bdl	bdl	0.08
	max	2.6	0.44	60.7	0.05	1.02	0.12	5.8	0.149	0.02	3.40
Jasper (n=6)	**median**	**0.5**	**0.35**	**42.4**	**bdl**	**0.07**	**bdl**	**4.8**	**0.006**	**bdl**	**0.32**
	average	0.5	0.38	36.5	bdl	0.07	0.02	4.8	0.007	bdl	0.40
	min	bdl	0.25	4.2	bdl	bdl	bdl	3.8	bdl	bdl	0.18
	max	1.0	0.43	63.8	0.01	0.17	0.03	5.1	0.013	bdl	0.52
Magnetite	**median**	**0.6**	**1.03**	**2.8**	**bdl**	**0.36**	**0.03**	**7.8**	**0.023**	**bdl**	**1.77**
(n=19)	average	1.4	1.13	17.1	0.08	0.59	0.05	7.4	0.056	bdl	2.08
	min	0.2	0.43	bdl	bdl	0.04	bdl	2.4	bdl	bdl	0.44
	max	5.7	2.36	52.2	0.52	2.34	0.24	14.3	0.280	0.06	7.54
All Oxide	**median**	**0.5**	**0.34**	**40**	**bdl**	**0.22**	**0.02**	**4.6**	**0.010**	**bdl**	**0.73**
BIF	average	0.9	0.58	34	0.04	0.36	0.04	5.1	0.035	bdl	1.24
(n=53)	min	bdl	0.03	bdl	bdl	bdl	bdl	1.5	bdl	bdl	0.08
	max	5.7	2.36	64	0.52	2.34	0.24	14.3	0.280	0.06	7.54
Chlorite	**median**	**23**	**0.87**	**0.3**	**bdl**	**1.29**	**0.07**	**4.7**	**0.036**	**0.03**	**20.8**
(n=5)	average	25	0.80	6.4	bdl	1.13	0.09	4.8	0.053	0.03	18.5
	min	11	0.42	bdl	bdl	0.48	0.04	1.3	bdl	0.02	10.1
	max	38	1.27	31	0.01	1.57	0.17	8.9	0.171	0.05	23.0
Shale	**median**	**42**	**0.86**	**18.2**	**bdl**	**1.15**	**0.08**	**4.9**	**0.012**	**0.03**	**18.7**
(n=5)	average	34	1.02	20.9	0.05	1.41	0.08	4.8	0.025	0.04	21.3
	min	4.1	0.41	bdl	bdl	0.27	0.05	3.4	bdl	0.03	14.2
	max	50	2.11	45.2	0.25	3.30	0.11	6.8	0.065	0.06	31.9
Sulfidic	**median**	**3.6**	**0.20**	**2.8**	**2.21**	**4.46**	**0.54**	**0.7**	**0.428**	**0.02**	**3.33**
Chert	average	3.7	0.19	2.5	2.27	4.50	0.54	0.8	0.414	0.02	3.36
(n=4)	min	1.4	0.12	0.7	1.66	3.08	0.35	0.3	0.135	bdl	2.57
	max	6.0	0.22	3.8	2.98	6.01	0.74	1.5	0.665	0.03	4.22

Notes:

dl: detection limit, bdl: below detection limit.

All values in ppm. n: number of samples from each facies.

Table 3.8: Abundances of redox sensitive elements and Th in Temagami BIF facies

		Mn	Mo	Re	W	Cr	V	U	Th
	Method	**TD**	**TD**	**TD**	**TD**	**TD**	**TD**	**FUS**	**FUS**
	dl	**0.2**	**0.01**	**0.0002**	**0.02**	**0.1**	**0.2**	**0.01**	**0.05**
Chert	**median**	**410**	**0.10**	**0.0006**	**0.15**	**4.0**	**1.7**	**0.07**	**0.09**
(n=28)	average	672	0.14	0.0010	0.23	4.3	3.1	0.09	0.14
	min	26	bdl	bdl	0.07	3.0	0.1	0.02	bdl
	max	2860	0.48	0.0030	0.63	6.1	17.8	0.32	1.16
Jasper (n=6)	**median**	**137**	**0.11**	**0.0004**	**2.10**	**4.4**	**0.7**	**0.07**	**0.03**
	average	244	0.29	0.0006	3.84	4.2	1.5	0.08	0.03
	min	39	bdl	bdl	0.17	2.9	0.4	0.04	bdl
	max	290	0.22	0.0018	2.59	5.3	2.1	0.20	0.08
Magnetite	**median**	**279**	**0.01**	**0.0009**	**0.37**	**8.8**	**6.9**	**0.15**	**0.25**
(n=19)	average	1626	0.08	0.0015	0.45	9.9	9.3	0.19	0.50
	min	36	bdl	bdl	0.22	3.8	2.0	0.04	bdl
	max	5680	0.44	0.0085	1.19	20.7	38.6	0.66	2.91
All Oxide	**median**	**275**	**0.06**	**0.0008**	**0.30**	**4.7**	**2.7**	**0.08**	**0.09**
BIF	average	1007	0.10	0.0011	0.50	6.6	5.4	0.13	0.28
(n=53)	min	26	bdl	bdl	0.07	3.0	0.1	0.02	bdl
	max	5680	0.48	0.0085	2.59	20.7	38.6	0.66	2.91
Chlorite	**median**	**523**	**0.01**	**0.0017**	**0.23**	**28.0**	**62.3**	**0.65**	**2.64**
(n=5)	average	531	0.49	0.0013	0.29	248	69.9	0.76	3.38
	min	273	bdl	bdl	0.07	10.2	16.3	0.51	1.80
	max	940	2.28	0.0019	0.58	1130	152	1.19	6.76
Shale	**median**	**423**	**0.94**	**0.0023**	**0.52**	**36.4**	**49.1**	**1.60**	**5.84**
(n=5)	average	411	0.78	0.0019	0.69	34.9	56.6	1.94	6.92
	min	134	0.02	0.0006	0.07	15.4	26.6	1.35	4.02
	max	610	1.13	0.0028	1.86	64.6	104	3.10	11.4
Sulfidic	**median**	**115**	**n.a.**	**0.0033**	**n.a.**	**n.a.**	**15.4**	**0.25**	**0.65**
Chert	average	182	n.a.	0.0032	n.a.	n.a.	14.4	0.94	0.65
(n=4)	min	57	n.a.	0.0022	n.a.	n.a.	9.2	0.15	0.45
	max	440	n.a.	0.0040	n.a.	n.a.	17.5	3.11	0.87

Notes:

All values in ppm. n: number of samples from each facies. dl: detection limit, bdl: below detection limit. n.a.: not available due to possible contamination introducing Mo, W, and Cr during sample preparation of archive samples.

Table 3.9: Total REE and Y, as well as selected normalized element ratios in Temagami BIF facies

		Y	La	Ce	Pr	Nd	Sm	Eu	Gd	Tb	Dy	Ho
	Method	**FUS**	**FUS**	**FUS**	**FUS**	**FUS**	**FUS**	**FUS**	**FUS**	**FUS**	**FUS**	**FUS**
	dl	**0.5**	**0.05**	**0.05**	**0.01**	**0.05**	**0.01**	**0.005**	**0.01**	**0.01**	**0.01**	**0.01**
Chert	**median**	**1.4**	**0.89**	**1.32**	**0.15**	**0.65**	**0.14**	**0.10**	**0.17**	**0.02**	**0.16**	**0.03**
(n=28)	average	2.4	1.44	2.53	0.29	1.18	0.25	0.16	0.29	0.05	0.28	0.06
	min	bdl	0.12	0.27	0.03	0.11	0.02	0.03	0.05	0.01	0.05	0.01
	max	8.3	6.86	12.70	1.36	5.01	0.96	0.43	1.05	0.17	1.06	0.21
Jasper (n=6)	**median**	**4.3**	**0.95**	**1.59**	**0.21**	**0.98**	**0.21**	**0.23**	**0.34**	**0.07**	**0.35**	**0.08**
	average	4.0	1.22	2.01	0.24	1.00	0.23	0.22	0.32	0.06	0.36	0.08
	min	2.1	0.66	1.10	0.13	0.45	0.05	0.12	0.15	0.03	0.18	0.05
	max	4.9	1.33	2.34	0.26	1.09	0.27	0.25	0.40	0.09	0.59	0.12
Magnetite	**median**	**6.7**	**4.11**	**6.51**	**0.72**	**3.00**	**0.59**	**0.43**	**0.68**	**0.11**	**0.67**	**0.15**
(n=19)	average	6.6	5.27	8.68	0.96	3.68	0.70	0.47	0.73	0.12	0.73	0.16
	min	2.4	0.53	0.93	0.10	0.33	0.09	0.14	0.13	0.03	0.27	0.06
	max	16.3	34.2	47.8	5.31	19.2	3.26	1.94	2.74	0.36	2.04	0.38
All Oxide	**median**	**3.7**	**1.29**	**2.19**	**0.25**	**1.13**	**0.26**	**0.23**	**0.35**	**0.06**	**0.39**	**0.09**
BIF	average	4.3	2.96	4.96	0.55	2.17	0.43	0.29	0.47	0.08	0.47	0.10
(n=53)	min	bdl	0.12	0.27	0.03	0.11	0.02	0.03	0.05	0.01	0.05	0.01
	max	16.3	34.2	47.8	5.31	19.2	3.26	1.94	2.74	0.36	2.04	0.38
Chlorite	**median**	**12.7**	**9.85**	**19.0**	**2.09**	**7.94**	**1.65**	**0.79**	**1.43**	**0.26**	**1.53**	**0.33**
(n=5)	average	14.4	11.7	25.2	3.10	12.2	2.59	0.85	2.23	0.36	2.16	0.44
	min	7.5	2.74	6.04	0.72	3.02	0.77	0.33	0.84	0.15	0.93	0.21
	max	24.5	23.9	50.9	6.14	25.1	5.17	1.44	4.16	0.68	4.27	0.83
Shale	**median**	**16.4**	**23.4**	**49.2**	**5.79**	**23.3**	**4.13**	**1.11**	**2.79**	**0.41**	**2.49**	**0.51**
(n=5)	average	22.3	24.5	52.4	5.97	22.5	4.28	1.07	3.35	0.55	3.25	0.66
	min	12.0	19.1	46.3	5.46	19.5	3.29	0.91	2.51	0.35	1.89	0.39
	max	48.2	29.1	60.4	6.76	24.7	5.85	1.17	5.73	1.10	6.83	1.38
Sulfidic	**median**	**2.5**	**4.93**	**10.1**	**1.06**	**4.05**	**0.78**	**0.28**	**0.58**	**0.09**	**0.44**	**0.09**
Chert	average	2.6	5.00	10.1	1.10	4.10	0.76	0.30	0.57	0.09	0.44	0.09
(n=4)	min	2.1	2.42	4.80	0.52	2.02	0.42	0.26	0.39	0.07	0.42	0.07
	max	3.4	7.74	15.3	1.74	6.30	1.07	0.37	0.72	0.10	0.46	0.10

Table 3.9 (continued): Total REE and Y, as well as selected normalized element ratios in Temagami BIF facies

		Er	Tm	Yb	Lu	ΣREE	Y/Ho	Ce/Ce*	Eu/Eu*	Pr/Pr*	Gd/Gd*
	Method	**FUS**	**FUS**	**FUS**	**FUS**	**FUS**					
	dl	0.01	0.005	0.01	0.002						
Chert	**median**	**0.11**	**0.019**	**0.13**	**0.017**	**3.9**	**46.7**	**0.82**	**3.77**	**0.96**	**1.42**
(n=28)	average	0.18	0.027	0.17	0.028	6.9	41.4	0.91	2.93	0.98	1.17
	min	0.03	bdl	0.03	0.004	0.8	n.a.	0.64	1.61	0.75	0.82
	max	0.63	0.090	0.54	0.093	29.9	60.0	1.04	5.94	1.10	1.94
Jasper (n=6)	**median**	**0.23**	**0.040**	**0.26**	**0.037**	**6.0**	**57.3**	**0.83**	**3.97**	**0.95**	**1.07**
	average	0.26	0.039	0.25	0.039	6.3	48.0	0.85	3.90	1.00	1.08
	min	0.16	0.023	0.14	0.024	3.3	40.8	0.80	3.47	0.90	0.91
	max	0.36	0.054	0.29	0.044	6.8	52.9	0.91	5.66	1.09	1.41
Magnetite	**median**	**0.46**	**0.074**	**0.49**	**0.084**	**17.9**	**44.7**	**0.86**	**3.35**	**0.96**	**1.12**
(n=19)	average	0.49	0.077	0.51	0.088	22.7	42.8	0.88	3.23	1.00	1.09
	min	0.23	0.040	0.23	0.032	3.3	31.3	0.80	2.04	0.88	0.79
	max	1.22	0.191	1.32	0.231	120	54.0	0.98	6.85	1.05	1.18
All Oxide	**median**	**0.26**	**0.041**	**0.26**	**0.041**	**7.1**	**42.6**	**0.89**	**3.47**	**0.98**	**1.12**
BIF	average	0.31	0.049	0.32	0.053	13.2	43.1	0.88	3.62	0.98	1.15
(n=53)	min	0.03	bdl	0.03	0.004	0.8	n.a.	0.64	1.61	0.75	0.79
	max	1.22	0.191	1.32	0.231	120	60.0	1.04	6.85	1.10	1.94
Chlorite	**median**	**0.98**	**0.159**	**1.09**	**0.188**	**47.2**	**32.9**	**0.97**	**1.61**	**1.00**	**0.95**
(n=5)	average	1.34	0.204	1.35	0.216	63.9	32.7	0.96	1.67	1.04	1.02
	min	0.65	0.102	0.66	0.113	17.3	29.5	0.94	1.50	0.99	0.95
	max	2.52	0.370	2.38	0.356	124	38.5	0.99	2.36	1.09	1.07
Shale	**median**	**1.46**	**0.227**	**1.64**	**0.264**	**126**	**32.2**	**0.97**	**1.53**	**1.00**	**1.00**
(n=5)	average	1.94	0.295	1.96	0.309	123	33.6	1.00	1.32	1.02	0.98
	min	1.25	0.193	1.30	0.200	108	30.8	0.99	0.87	1.01	0.93
	max	3.89	0.576	3.64	0.567	136	35.2	1.02	1.58	1.05	1.08
Sulfidic	**median**	**0.25**	**0.040**	**0.28**	**0.046**	**23.2**	**29.4**	**1.02**	**2.01**	**0.98**	**1.04**
Chert	average	0.26	0.038	0.27	0.045	23.1	30.9	0.99	2.17	1.00	1.02
(n=4)	min	0.20	0.025	0.16	0.030	12.2	26.3	0.93	1.56	0.98	0.98
	max	0.32	0.047	0.34	0.059	33.8	34.0	1.01	3.01	1.04	1.04

Table 3.9 Notes:

All values in ppm (except ratios), dl: detection limit, bdl: below detection limit, n.a. not available (at least one component below detection limit).

Y/Ho: non-normalized element ratio.

Ce, Eu, Pr, and Gd anomalies are calculated after Bau and Dulski (1996), using Post Archean Average Shale (PAAS, McLennan, 1989) for shale normalization (subscript SN):

$Ce/Ce^* = Ce_{SN}/(0.5*La_{SN}+0.5*Pr_{SN})$

$Eu/Eu^* = Eu_{SN}/(0.67*Sm_{SN}+0.33*Tb_{SN})$

$Pr/Pr^* = Pr_{SN}/(0.5*Ce_{SN}+0.5*Nd_{SN})$

$Gd/Gd^* = Gd_{SN}/(0.33*Sm_{SN}+0.67*Tb_{Sn})$

Low abundances of REE in some chert and jasper samples close to detection limit can introduce a higher uncertainty in the calculation of ratios and anomalies.

Table 3.10: Whole rock trace element concentrations in Temagami BIF compared to analysis of individual mineral phases by EPMA and LA-ICPMS

	WR oxide BIF	Magnetite	Apatite	Chlorite*	Monazite	Ilmenite	Carb.	Sulfide
Element	TD/FUS	LA	LA	EP	EP	EP/LA	EP	LA
Li	**0.5**		**1.83**					
B	**40**		**4.75**					
Sc	**<1**	**0.27**	**0.30**	**det.**	<100	<100		
Ti	**30**	**15**	**0.83**	**300**		**$5*10^5$**	<100	
V	**2.7**	**4.7**	**0.06**			**3300**	<100	
Cr	**4.7**	**0.81**	**1.08**	**100**		<100	<100	
Mn	**275**	**188**	**313**	**500**		**7200**	**8800**	
Co	**1.03**	**0.754**	**0.09**	**det.**			**det.**	**det.**
Ni	**12.2**	**5.4**	**0.43**	**det.**		<100	<100	**det.**
Cu	**2.18**	**0.30**	**0.37**				<100	**det.**
Zn	**10.6**	**16**	**0.38**	**200**		400	**300**	**det.**
Ga	**0.73**	**0.85**	**0.15**	**det.**				
Ge	**4.6**	**7.3**		det.				
As	**0.89**	**0.65**	**68.5**				**det.**	**det.**
Se	**0.22**	**<0.1**						
Rb	**0.61**		**0.25**	**det.**			**det.**	
Sr	**9.21**		**1675**		**700**		**det.**	
Y	**3.7**	**0.28**	**1042**		**2600**		**det.**	
Zr	**1.9**	**0.12**	**0.09**					
Nb	**<0.2**	**0.075**	**0.010**			**det.**		
Mo	**0.06**	**0.034**						**det.**
Ag	**0.02**	**0.045**				**det.**	**det.**	**det.**
Cd	**0.02**	**0.11**					**det.**	
In	**<0.02**	**0.029**				**det.**		
Sn	**<0.2**	**1.1**				**det.**		
Sb	**0.47**	**0.76**	**0.41**					**det.**
Cs	**0.18**	**0.06**	**0.09**	**det.**				
Ba	**4.9**	**1.89**	**6.11**					
∑REE	**7.1**	***0.13**	**1286**		**$5.4*10^5$**		**det.**	
Hf	**0.03**	**0.02**						
Ta	**0.05**	**0.01**				**det.**		
W	**0.37**	**0.25**				**det.**		**det.**
Re	**$8*10^{-4}$**	<0.001						**det.**
Pb	**0.9**	**0.63**	**22.3**		**700**	**det.**	**det.**	**det.**
Bi	**0.01**	<0.01	n/a				**det.**	**det.**
Th	**0.09**		**0.120**		**4500**			
U	**0.08**		**0.316**		**200**			

Notes:
All results are median values in ppm for Temagami oxide-BIF samples. For full results, see Chapter 2.
WR oxide BIF are median values for all Temagami oxide BIF samples (values from Tables 3.4-3.9).
* ∑REE in magnetite is a partial sum based on available data (La+Sm+Yb).
EP: Electron Probe Microanalyzer, LA: Laser ICP-MS, TD/FUS: Total Dissolution or Fusion-ICP-MS whole rock analysis. n/a: not analyzed. n/d: not detected.
"det." has been detected qualitatively to be present in appreciable amounts in the host mineral based on raw LA-ICPMS signals higher than 100x over background in individual analyses (see Chapter 2).
*Chlorite includes other aluminosilicates such as biotite and stilpnomelane

Table 3.11: Correlation matrix for clr of n=43 elements in n=48 Temagami oxide BIF samples

	Si	Al	Fe	Ca	Mg	Na	K	P	C	S	Ti	Mn	Zn	Cu
Si	1	0.01	-0.33	-0.07	-0.28	-0.27	-0.56	-0.09	0.03	0.11	-0.58	0.09	0.09	0.27
Al	0.01	1	-0.45	0.06	0.02	0.37	0.13	-0.06	0.04	-0.12	0.49	-0.10	-0.19	-0.13
Fe	-0.33	-0.45	1	-0.09	-0.22	0.07	0.06	0.60	-0.42	-0.51	-0.04	-0.28	0.08	-0.43
Ca	-0.07	0.06	-0.09	1	-0.10	0.41	0.12	0.37	0.62	0.00	-0.10	0.62	-0.44	-0.09
Mg	-0.28	0.02	-0.22	-0.10	1	-0.15	0.52	-0.58	0.20	0.18	0.20	0.31	0.28	-0.08
Na	-0.27	0.37	0.07	0.41	-0.15	1	0.55	0.30	0.04	-0.44	0.49	-0.06	-0.51	-0.15
K	-0.56	0.13	0.06	0.12	0.52	0.55	1	-0.05	0.12	-0.27	0.63	0.11	-0.18	-0.20
P	-0.09	-0.06	0.60	0.37	-0.58	0.30	-0.05	1	-0.08	-0.54	-0.11	-0.03	-0.31	-0.37
C	0.03	0.04	-0.42	0.62	0.20	0.04	0.12	-0.08	1	0.37	-0.12	0.59	-0.24	0.06
S	0.11	-0.12	-0.51	0.00	0.18	-0.44	-0.27	-0.54	0.37	1	-0.03	0.29	0.00	0.44
Ti	-0.58	0.49	-0.04	-0.10	0.20	0.49	0.63	-0.11	-0.12	-0.03	1.0	-0.20	-0.25	-0.02
Mn	0.09	-0.10	-0.28	0.62	0.31	-0.06	0.11	-0.03	0.59	0.29	-0.2	1	0.02	0.21
Zn	0.09	-0.19	0.08	-0.44	0.28	-0.51	-0.18	-0.31	-0.24	0.00	-0.25	0.02	1	-0.22
Cu	0.27	-0.13	-0.43	-0.09	-0.08	-0.15	-0.20	-0.37	0.06	0.44	-0.02	0.21	-0.22	1
Pb	0.23	0.06	-0.15	-0.13	-0.46	0.07	-0.38	-0.08	-0.11	0.27	0.04	-0.30	-0.21	0.47
Ag	0.12	-0.23	0.07	-0.19	-0.01	-0.06	0.09	0.02	-0.02	0.15	0.06	-0.22	-0.29	-0.16
As	0.31	-0.28	-0.15	-0.38	0.08	-0.57	-0.46	-0.48	-0.25	0.52	-0.25	-0.11	0.47	0.28
Sb	0.08	-0.47	0.80	-0.16	-0.28	-0.14	-0.17	0.48	-0.50	-0.41	-0.31	-0.28	0.28	-0.44
Hg	0.36	-0.23	0.10	0.02	-0.39	-0.35	-0.53	0.22	0.03	-0.03	-0.64	-0.09	0.11	-0.12
Co	0.00	0.09	-0.46	-0.36	0.56	-0.48	-0.04	-0.59	-0.06	0.35	-0.03	0.14	0.13	0.42
Ni	0.10	-0.05	-0.33	-0.45	0.41	-0.72	-0.21	-0.45	-0.15	0.36	-0.21	-0.01	0.28	0.17
Se	-0.34	0.03	-0.25	-0.12	0.23	-0.11	0.02	-0.51	-0.10	0.44	0.32	-0.09	-0.15	0.52
Mo	0.48	-0.47	0.05	-0.34	-0.19	-0.60	-0.51	0.03	-0.16	-0.05	-0.65	0.05	0.29	0.32
Ge	0.41	-0.23	0.54	-0.25	-0.36	-0.15	-0.38	0.28	-0.50	-0.53	-0.37	-0.37	0.16	-0.20
Bi	0.37	-0.36	-0.37	-0.40	0.00	-0.53	-0.34	-0.56	-0.20	0.49	-0.29	-0.14	0.18	0.55
Re	0.27	0.36	-0.09	-0.25	-0.24	0.33	0.02	-0.05	-0.23	-0.12	0.29	-0.12	-0.07	0.28
W	0.26	-0.30	0.39	-0.08	-0.41	-0.35	-0.62	0.41	-0.20	-0.13	-0.55	-0.21	0.22	-0.25
Cr	0.59	-0.11	-0.01	-0.32	0.13	-0.19	-0.08	-0.31	-0.11	-0.03	-0.19	-0.23	0.12	-0.03
V	-0.56	0.35	-0.16	-0.39	0.15	0.04	0.15	-0.16	-0.24	-0.04	0.49	-0.33	-0.05	0.11
Ga	-0.39	0.53	0.04	-0.35	-0.06	0.21	0.17	0.10	-0.45	-0.40	0.48	-0.52	-0.06	-0.10
Zr	-0.44	0.65	-0.08	0.00	0.17	0.54	0.64	0.01	-0.09	-0.19	0.86	-0.18	-0.24	-0.29
Ba	-0.39	-0.38	0.23	0.06	-0.06	0.03	0.00	0.01	0.04	-0.06	-0.12	-0.17	0.30	-0.36
Cs	-0.61	0.17	0.06	0.16	0.29	0.51	0.79	-0.02	0.09	-0.21	0.64	0.02	0.04	-0.33
Li	-0.12	0.40	0.10	0.09	-0.35	0.35	-0.19	0.31	-0.23	-0.33	0.21	-0.42	-0.04	-0.29
Be	-0.44	-0.51	0.84	-0.06	0.04	0.07	0.36	0.45	-0.32	-0.45	0.08	-0.25	0.10	-0.54
B	0.65	0.28	-0.63	0.00	-0.02	-0.19	-0.29	-0.33	0.17	0.21	-0.32	0.29	0.28	0.18
Ta	0.21	0.29	0.25	-0.19	-0.04	-0.13	-0.07	0.26	-0.09	-0.45	0.00	-0.09	0.11	-0.20
Rb	-0.65	0.19	0.15	0.12	0.30	0.66	0.90	0.07	0.06	-0.31	0.71	-0.10	-0.13	-0.35
Sr	-0.02	-0.18	0.15	0.65	-0.25	0.53	-0.01	0.33	0.21	-0.21	-0.24	0.16	-0.44	-0.12
U	0.08	0.40	0.13	-0.02	-0.33	0.38	0.03	0.34	-0.13	-0.54	0.24	-0.18	-0.17	-0.07
Th	-0.37	0.54	-0.13	0.11	0.18	0.56	0.58	0.00	0.09	-0.17	0.79	0.03	-0.29	-0.08
Y	-0.44	-0.29	0.68	0.10	-0.17	-0.07	-0.16	0.50	-0.20	-0.13	-0.16	-0.11	-0.04	-0.34
∑REE	-0.64	0.08	0.53	-0.10	-0.18	0.23	0.07	0.42	-0.32	-0.35	0.30	-0.41	-0.08	-0.28

Table 3.11 (continued): Correlation matrix for clr of n=43 elements in n=48 Temagami oxide BIF samples

	Pb	Ag	As	Sb	Hg	Co	Ni	Se	Mo	Ge	Bi	Re	W	Cr
Si	0.23	0.12	0.31	0.08	0.36	0.00	0.10	-0.34	0.48	0.41	0.37	0.27	0.26	0.59
Al	0.06	-0.23	-0.28	-0.47	-0.23	0.09	-0.05	0.03	-0.47	-0.23	-0.36	0.36	-0.30	-0.11
Fe	-0.15	0.07	-0.15	0.80	0.10	-0.46	-0.33	-0.25	0.05	0.54	-0.37	-0.09	0.39	-0.01
Ca	-0.13	-0.19	-0.38	-0.16	0.02	-0.36	-0.45	-0.12	-0.34	-0.25	-0.40	-0.25	-0.08	-0.32
Mg	-0.46	-0.01	0.08	-0.28	-0.39	0.56	0.41	0.23	-0.19	-0.36	0.00	-0.24	-0.41	0.13
Na	0.07	-0.06	-0.57	-0.14	-0.35	-0.48	-0.72	-0.11	-0.60	-0.15	-0.53	0.33	-0.35	-0.19
K	-0.38	0.09	-0.46	-0.17	-0.53	-0.04	-0.21	0.02	-0.51	-0.38	-0.34	0.02	-0.62	-0.08
P	-0.08	0.02	-0.48	0.48	0.22	-0.59	-0.45	-0.51	0.03	0.28	-0.56	-0.05	0.41	-0.31
C	-0.11	-0.02	-0.25	-0.50	0.03	-0.06	-0.15	-0.10	-0.16	-0.50	-0.20	-0.23	-0.20	-0.11
S	0.27	0.15	0.52	-0.41	-0.03	0.35	0.36	0.44	-0.05	-0.53	0.49	-0.12	-0.13	-0.03
Ti	0.04	0.06	-0.25	-0.31	-0.64	-0.03	-0.21	0.32	-0.65	-0.37	-0.29	0.29	-0.55	-0.19
Mn	-0.30	-0.22	-0.11	-0.28	-0.09	0.14	-0.01	-0.09	0.05	-0.37	-0.14	-0.12	-0.21	-0.23
Zn	-0.21	-0.29	0.47	0.28	0.11	0.13	0.28	-0.15	0.29	0.16	0.18	-0.07	0.22	0.12
Cu	0.47	-0.16	0.28	-0.44	-0.12	0.42	0.17	0.52	0.32	-0.20	0.55	0.28	-0.25	-0.03
Pb	1	0.13	0.34	-0.08	0.11	-0.16	-0.07	0.08	-0.10	0.08	0.34	0.51	0.18	0.01
Ag	0.13	1	0.11	0.16	0.04	-0.13	0.18	-0.22	-0.05	0.13	0.17	0.05	0.09	0.47
As	0.34	0.11	1	0.07	0.00	0.33	0.44	0.35	0.24	0.05	0.66	-0.11	0.18	0.25
Sb	-0.08	0.16	0.07	1.0	0.47	-0.45	-0.09	-0.42	0.13	0.73	-0.14	-0.05	0.62	0.32
Hg	0.11	0.04	0.00	0.5	1	-0.10	0.19	-0.33	0.26	0.43	0.01	-0.15	0.76	0.19
Co	-0.16	-0.13	0.33	-0.45	-0.10	1	0.74	0.57	0.28	-0.31	0.35	-0.24	-0.19	-0.05
Ni	-0.07	0.18	0.44	-0.09	0.19	0.74	1	0.30	0.26	-0.12	0.47	-0.20	0.06	0.16
Se	0.08	-0.22	0.35	-0.42	-0.33	0.57	0.30	1	-0.15	-0.41	0.33	-0.16	-0.43	-0.18
Mo	-0.10	-0.05	0.24	0.13	0.26	0.28	0.26	-0.15	1	0.40	0.46	-0.17	0.34	0.11
Ge	0.08	0.13	0.05	0.73	0.43	-0.31	-0.12	-0.41	0.40	1	0.04	0.14	0.59	0.53
Bi	0.34	0.17	0.66	-0.14	0.01	0.35	0.47	0.33	0.46	0.04	1	-0.03	-0.05	0.29
Re	0.51	0.05	-0.11	-0.05	-0.15	-0.24	-0.20	-0.16	-0.17	0.14	-0.03	1.0	-0.24	0.27
W	0.18	0.09	0.18	0.62	0.76	-0.19	0.06	-0.43	0.34	0.59	-0.05	-0.2	1	0.05
Cr	0.01	0.47	0.25	0.32	0.19	-0.05	0.16	-0.18	0.11	0.53	0.29	0.27	0.05	1
V	0.03	-0.10	-0.13	-0.42	-0.21	0.47	0.29	0.45	-0.11	-0.35	-0.10	0.03	-0.15	-0.46
Ga	-0.09	-0.33	-0.16	-0.22	-0.36	0.24	0.02	0.32	-0.09	-0.11	-0.18	0.00	-0.22	-0.39
Zr	-0.26	-0.01	-0.46	-0.27	-0.54	-0.11	-0.25	0.11	-0.63	-0.32	-0.42	0.20	-0.56	-0.11
Ba	0.06	-0.03	-0.07	0.24	0.21	-0.43	-0.12	-0.15	-0.17	0.00	0.00	-0.18	0.21	-0.21
Cs	-0.20	-0.03	-0.35	-0.06	-0.32	-0.30	-0.31	-0.06	-0.65	-0.33	-0.32	0.08	-0.38	-0.19
Li	0.35	-0.06	0.08	0.02	-0.07	-0.31	-0.30	-0.08	-0.28	0.14	-0.26	0.06	0.31	-0.24
Be	-0.32	0.30	-0.18	0.75	0.05	-0.43	-0.17	-0.27	-0.11	0.37	-0.26	-0.23	0.24	0.10
B	0.06	-0.29	0.09	-0.30	0.13	0.13	0.10	-0.26	0.26	-0.04	0.31	0.24	-0.12	0.15
Ta	-0.03	-0.08	-0.21	0.22	-0.01	-0.12	-0.02	-0.46	0.19	0.48	-0.25	0.33	0.12	0.22
Rb	-0.19	0.08	-0.44	-0.07	-0.46	-0.31	-0.36	-0.05	-0.69	-0.35	-0.42	0.11	-0.47	-0.16
Sr	0.09	0.01	-0.39	0.13	0.28	-0.43	-0.50	-0.17	-0.24	0.11	-0.31	-0.09	0.18	-0.10
U	0.06	-0.23	-0.51	-0.04	-0.20	-0.34	-0.45	-0.27	0.01	0.24	-0.40	0.54	-0.21	-0.04
Th	-0.14	-0.03	-0.47	-0.41	-0.69	-0.16	-0.35	0.09	-0.51	-0.35	-0.41	0.41	-0.70	-0.15
Y	-0.17	-0.11	0.01	0.43	0.10	-0.09	-0.04	0.13	-0.02	0.06	-0.36	-0.41	0.32	-0.41
∑REE	-0.12	-0.31	-0.20	0.12	-0.24	-0.09	-0.23	0.24	-0.13	-0.06	-0.43	-0.24	0.06	-0.58

Table 3.11 (continued): Correlation matrix for clr of n=43 elements in n=48 Temagami oxide BIF samples

	Ga	Zr	Ba	Cs	Li	Be	B	Ta	Rb	Sr	U	Th	Y	∑REE
Si	-0.39	-0.44	-0.39	-0.61	-0.12	-0.44	0.65	0.21	-0.65	-0.02	0.08	-0.37	-0.44	-0.64
Al	0.53	0.65	-0.38	0.17	0.40	-0.51	0.28	0.29	0.19	-0.18	0.40	0.54	-0.29	0.08
Fe	0.04	-0.08	0.23	0.06	0.10	0.84	-0.63	0.25	0.15	0.15	0.13	-0.13	0.68	0.53
Ca	-0.35	0.00	0.06	0.16	0.09	-0.06	0.00	-0.19	0.12	0.65	-0.02	0.11	0.10	-0.10
Mg	-0.06	0.17	-0.06	0.29	-0.35	0.04	-0.02	-0.04	0.30	-0.25	-0.33	0.18	-0.17	-0.18
Na	0.21	0.54	0.03	0.51	0.35	0.07	-0.19	-0.13	0.66	0.53	0.38	0.56	-0.07	0.23
K	0.17	0.64	0.00	0.79	-0.19	0.36	-0.29	-0.07	0.90	-0.01	0.03	0.58	-0.16	0.07
P	0.10	0.01	0.01	-0.02	0.31	0.45	-0.33	0.26	0.07	0.33	0.34	0.00	0.50	0.42
C	-0.45	-0.09	0.04	0.09	-0.23	-0.32	0.17	-0.09	0.06	0.21	-0.13	0.09	-0.20	-0.32
S	-0.40	-0.19	-0.06	-0.21	-0.33	-0.45	0.21	-0.45	-0.31	-0.21	-0.54	-0.17	-0.13	-0.35
Ti	0.48	0.86	-0.12	0.64	0.21	0.08	-0.32	0.00	0.71	-0.24	0.24	0.79	-0.16	0.30
Mn	-0.52	-0.18	-0.17	0.02	-0.42	-0.25	0.29	-0.09	-0.10	0.16	-0.18	0.03	-0.11	-0.41
Zn	-0.06	-0.24	0.30	0.04	-0.04	0.10	0.28	0.11	-0.13	-0.44	-0.17	-0.29	-0.04	-0.08
Cu	-0.10	-0.29	-0.36	-0.33	-0.29	-0.54	0.18	-0.20	-0.35	-0.12	-0.07	-0.08	-0.34	-0.28
Pb	-0.09	-0.26	0.06	-0.20	0.35	-0.32	0.06	-0.03	-0.19	0.09	0.06	-0.14	-0.17	-0.12
Ag	-0.33	-0.01	-0.03	-0.03	-0.06	0.30	-0.29	-0.08	0.08	0.01	-0.23	-0.03	-0.11	-0.31
As	-0.16	-0.46	-0.07	-0.35	0.08	-0.18	0.09	-0.21	-0.44	-0.39	-0.51	-0.47	0.01	-0.20
Sb	-0.22	-0.27	0.24	-0.06	0.02	0.75	-0.30	0.22	-0.07	0.13	-0.04	-0.41	0.43	0.12
Hg	-0.36	-0.54	0.21	-0.32	-0.07	0.05	0.13	-0.01	-0.46	0.28	-0.20	-0.69	0.10	-0.24
Co	0.24	-0.11	-0.43	-0.30	-0.31	-0.43	0.13	-0.12	-0.31	-0.43	-0.34	-0.16	-0.09	-0.09
Ni	0.02	-0.25	-0.12	-0.31	-0.30	-0.17	0.10	-0.02	-0.36	-0.50	-0.45	-0.35	-0.04	-0.23
Se	0.32	0.11	-0.15	-0.06	-0.08	-0.27	-0.26	-0.46	-0.05	-0.17	-0.27	0.09	0.13	0.24
Mo	-0.09	-0.63	-0.17	-0.65	-0.28	-0.11	0.26	0.19	-0.69	-0.24	0.01	-0.51	-0.02	-0.13
Ge	-0.11	-0.32	0.00	-0.33	0.14	0.37	-0.04	0.48	-0.35	0.11	0.24	-0.35	0.06	-0.06
Bi	-0.18	-0.42	0.00	-0.32	-0.26	-0.26	0.31	-0.25	-0.42	-0.31	-0.40	-0.41	-0.36	-0.43
Re	0.00	0.20	-0.18	0.08	0.06	-0.23	0.24	0.33	0.11	-0.09	0.54	0.41	-0.41	-0.24
W	-0.22	-0.56	0.21	-0.38	0.31	0.24	-0.12	0.12	-0.47	0.18	-0.21	-0.70	0.32	0.06
Cr	-0.39	-0.11	-0.21	-0.19	-0.24	0.10	0.15	0.22	-0.16	-0.10	-0.04	-0.15	-0.41	-0.58
V	0.69	0.34	0.02	0.18	0.29	-0.15	-0.31	-0.12	0.21	-0.26	0.07	0.29	0.07	0.48
Ga	1	0.53	-0.19	0.12	0.43	-0.07	-0.17	0.18	0.23	-0.36	0.39	0.38	0.18	0.70
Zr	0.53	1	-0.19	0.58	0.14	0.06	-0.12	0.05	0.67	-0.17	0.32	0.78	-0.15	0.29
Ba	-0.19	-0.19	1	0.35	0.15	0.38	-0.14	-0.29	0.26	0.34	-0.11	-0.14	0.17	0.16
Cs	0.12	0.58	0.35	1	0.09	0.38	-0.21	-0.09	0.92	0.02	0.02	0.56	-0.22	0.05
Li	0.43	0.14	0.15	0.09	1	-0.02	-0.24	0.04	0.11	0.18	0.19	0.10	0.15	0.42
Be	-0.07	0.06	0.38	0.38	-0.02	1	-0.64	0.09	0.43	0.12	-0.06	-0.02	0.44	0.30
B	-0.17	-0.12	-0.14	-0.21	-0.24	-0.64	1	0.17	-0.36	-0.15	0.22	-0.02	-0.61	-0.59
Ta	0.18	0.05	-0.29	-0.09	0.04	0.09	0.17	1	-0.08	-0.40	0.60	0.23	-0.09	-0.01
Rb	0.23	0.67	0.26	0.92	0.11	0.43	-0.36	-0.08	1	0.06	0.11	0.63	-0.11	0.21
Sr	-0.36	-0.17	0.34	0.02	0.18	0.12	-0.15	-0.40	0.06	1	0.02	-0.12	0.17	-0.01
U	0.39	0.32	-0.11	0.02	0.19	-0.06	0.22	0.60	0.11	0.02	1	0.60	-0.13	0.20
Th	0.38	0.78	-0.14	0.56	0.10	-0.02	-0.02	0.23	0.63	-0.12	0.60	1	-0.27	0.14
Y	0.18	-0.15	0.17	-0.22	0.15	0.44	-0.61	-0.09	-0.11	0.17	-0.13	-0.27	1	0.74
∑REE	0.70	0.29	0.16	0.05	0.42	0.30	-0.59	-0.01	0.21	-0.01	0.20	0.14	0.74	1

Table 3.11 Notes:

Pearson correlation coefficients are calculated for centre-log ratios of whole rock abundances of major oxide and trace elements in oxide facies BIF samples (chert, jasper and magnetite).

To avoid the effect of closure in the dataset, the centre-log ratios (clr) have been calculated for each element in each sample. The calculation is based on determining the natural logarithm of each element's abundance divided by the geometric mean of all abundances in that sample. This procedure opens the geochemical dataset and yields a new, indefinite value that is then used to calculate Pearson correlation coefficients for element pairs. For details on the calculation, see Appendix N.

Tl, Cd, Te, Sn, In, Hf, Nb, and Sc are often below detection limit in whole rock analyses and have been excluded from the correlation matrix.

Table 3.12: Correlation matrix of n=42 elements in the n=48 Temagami oxide BIF samples recalculated to SiO_2-free abundances

	Al	Fe	Ca	Mg	Na	K	P	C	S	Ti	Mn	Zn	Cu	Pb
Al	1	-0.46	0.05	0.02	0.36	0.11	-0.06	0.03	-0.13	0.47	-0.09	-0.15	-0.13	0.07
Fe	-0.46	1	-0.12	-0.24	0.06	0.03	0.59	-0.44	-0.54	-0.09	-0.30	0.08	-0.45	-0.16
Ca	0.05	-0.12	1	-0.12	0.40	0.10	0.36	0.62	-0.01	-0.14	0.61	-0.44	-0.10	-0.14
Mg	0.02	-0.24	-0.12	1	-0.16	0.50	-0.60	0.20	0.16	0.16	0.31	0.29	-0.09	-0.47
Na	0.36	0.06	0.40	-0.16	1	0.54	0.29	0.04	-0.46	0.48	-0.07	-0.51	-0.16	0.06
K	0.11	0.03	0.10	0.50	0.54	1	-0.07	0.11	-0.30	0.62	0.10	-0.19	-0.22	-0.41
P	-0.06	0.59	0.36	-0.60	0.29	-0.07	1	-0.08	-0.56	-0.15	-0.03	-0.29	-0.38	-0.09
C	0.03	-0.44	0.62	0.20	0.04	0.11	-0.08	1	0.36	-0.15	0.58	-0.24	0.06	-0.12
S	-0.13	-0.54	-0.01	0.16	-0.46	-0.30	-0.56	0.36	1	-0.06	0.28	-0.01	0.44	0.26
Ti	0.47	-0.09	-0.14	0.16	0.48	0.62	-0.15	-0.15	-0.06	1	-0.24	-0.28	-0.04	0.00
Mn	-0.09	-0.30	0.61	0.31	-0.07	0.10	-0.03	0.58	0.28	-0.24	1	0.03	0.20	-0.30
Zn	-0.15	0.08	-0.44	0.29	-0.51	-0.19	-0.29	-0.24	-0.01	-0.28	0.03	1	-0.21	-0.19
Cu	-0.13	-0.45	-0.10	-0.09	-0.16	-0.22	-0.38	0.06	0.44	-0.04	0.20	-0.21	1	0.46
Pb	0.07	-0.16	-0.14	-0.47	0.06	-0.41	-0.09	-0.12	0.26	0.00	-0.30	-0.19	0.46	1
Ag	-0.19	0.07	-0.18	0.01	-0.06	0.09	0.03	-0.01	0.15	0.05	-0.20	-0.24	-0.15	0.15
As	-0.25	-0.15	-0.38	0.08	-0.58	-0.48	-0.47	-0.25	0.51	-0.28	-0.11	0.48	0.27	0.34
Sb	-0.41	0.80	-0.15	-0.26	-0.13	-0.18	0.48	-0.48	-0.41	-0.34	-0.26	0.32	-0.43	-0.06
Hg	-0.17	0.12	0.04	-0.34	-0.33	-0.51	0.24	0.04	-0.03	-0.64	-0.06	0.16	-0.11	0.14
Co	0.10	-0.48	-0.38	0.56	-0.49	-0.06	-0.60	-0.07	0.34	-0.07	0.14	0.15	0.42	-0.16
Ni	-0.03	-0.34	-0.46	0.41	-0.73	-0.22	-0.45	-0.15	0.35	-0.23	-0.01	0.29	0.16	-0.07
Se	-0.02	-0.32	-0.17	0.19	-0.15	-0.03	-0.57	-0.13	0.43	0.27	-0.12	-0.19	0.52	0.04
Mo	-0.41	0.08	-0.32	-0.15	-0.58	-0.50	0.06	-0.14	-0.04	-0.65	0.08	0.33	0.33	-0.06
Ge	-0.14	0.55	-0.21	-0.29	-0.12	-0.36	0.30	-0.45	-0.49	-0.36	-0.31	0.23	-0.17	0.12
Bi	-0.32	-0.36	-0.39	0.02	-0.52	-0.34	-0.55	-0.19	0.49	-0.29	-0.13	0.21	0.55	0.36
Re	0.39	-0.09	-0.24	-0.22	0.33	0.01	-0.04	-0.22	-0.12	0.27	-0.10	-0.02	0.28	0.52
W	-0.25	0.41	-0.07	-0.39	-0.34	-0.61	0.42	-0.19	-0.13	-0.56	-0.19	0.26	-0.24	0.20
Cr	-0.01	0.03	-0.26	0.18	-0.15	-0.06	-0.24	-0.08	-0.02	-0.18	-0.17	0.20	0.00	0.07
V	0.34	-0.23	-0.47	0.10	0.00	0.10	-0.21	-0.29	-0.08	0.44	-0.37	-0.06	0.10	-0.01
Ga	0.53	-0.01	-0.40	-0.10	0.19	0.12	0.07	-0.49	-0.45	0.43	-0.56	-0.05	-0.12	-0.11
Zr	0.65	-0.11	-0.03	0.16	0.54	0.62	-0.01	-0.10	-0.21	0.85	-0.19	-0.23	-0.31	-0.28
Ba	-0.40	0.21	0.04	-0.09	0.01	-0.03	-0.02	0.02	-0.08	-0.17	-0.19	0.29	-0.37	0.04
Cs	0.15	0.02	0.14	0.26	0.50	0.78	-0.04	0.07	-0.23	0.62	0.00	0.02	-0.34	-0.23
Li	0.39	0.08	0.07	-0.37	0.34	-0.22	0.30	-0.24	-0.35	0.17	-0.43	-0.03	-0.31	0.34
Be	-0.51	0.83	-0.08	0.02	0.05	0.33	0.44	-0.34	-0.48	0.03	-0.26	0.11	-0.56	-0.34
B	0.34	-0.58	0.04	0.04	-0.16	-0.26	-0.28	0.19	0.22	-0.29	0.33	0.33	0.20	0.11
Ta	0.32	0.26	-0.18	-0.02	-0.12	-0.07	0.27	-0.08	-0.44	-0.01	-0.07	0.16	-0.19	0.00
Rb	0.16	0.11	0.09	0.27	0.65	0.90	0.04	0.04	-0.34	0.70	-0.12	-0.15	-0.37	-0.22
Sr	-0.16	0.15	0.65	-0.25	0.53	-0.02	0.33	0.21	-0.22	-0.27	0.16	-0.42	-0.12	0.09
U	0.42	0.13	-0.02	-0.31	0.36	0.01	0.34	-0.13	-0.54	0.19	-0.16	-0.11	-0.07	0.08
Th	0.53	-0.16	0.09	0.16	0.55	0.57	-0.02	0.07	-0.19	0.78	0.02	-0.29	-0.09	-0.16
Y	-0.34	0.67	0.06	-0.25	-0.12	-0.25	0.49	-0.25	-0.19	-0.28	-0.15	-0.06	-0.40	-0.23
∑REE	0.05	0.51	-0.17	-0.28	0.20	0.00	0.40	-0.39	-0.44	0.22	-0.49	-0.10	-0.34	-0.19

Table 3.12 (continued): Correlation matrix of n=42 elements in the n=48 Temagami oxide BIF samples corrected to SiO_2-free abundances

	Ag	As	Sb	Hg	Co	Ni	Se	Mo	Ge	Bi	Re	W	Cr	V
Al	-0.19	-0.25	-0.41	-0.17	0.10	-0.03	-0.02	-0.41	-0.14	-0.32	0.39	-0.25	-0.01	0.34
Fe	0.07	-0.15	0.80	0.12	-0.48	-0.34	-0.32	0.08	0.55	-0.36	-0.09	0.41	0.03	-0.23
Ca	-0.18	-0.38	-0.15	0.04	-0.38	-0.46	-0.17	-0.32	-0.21	-0.39	-0.24	-0.07	-0.26	-0.47
Mg	0.01	0.08	-0.26	-0.34	0.56	0.41	0.19	-0.15	-0.29	0.02	-0.22	-0.39	0.18	0.10
Na	-0.06	-0.58	-0.13	-0.33	-0.49	-0.73	-0.15	-0.58	-0.12	-0.52	0.33	-0.34	-0.15	0.00
K	0.09	-0.48	-0.18	-0.51	-0.06	-0.22	-0.03	-0.50	-0.36	-0.34	0.01	-0.61	-0.06	0.10
P	0.03	-0.47	0.48	0.24	-0.60	-0.45	-0.57	0.06	0.30	-0.55	-0.04	0.42	-0.24	-0.21
C	-0.01	-0.25	-0.48	0.04	-0.07	-0.15	-0.13	-0.14	-0.45	-0.19	-0.22	-0.19	-0.08	-0.29
S	0.15	0.51	-0.41	-0.03	0.34	0.35	0.43	-0.04	-0.49	0.49	-0.12	-0.13	-0.02	-0.08
Ti	0.05	-0.28	-0.34	-0.64	-0.07	-0.23	0.27	-0.65	-0.36	-0.29	0.27	-0.56	-0.18	0.44
Mn	-0.20	-0.11	-0.26	-0.06	0.14	-0.01	-0.12	0.08	-0.31	-0.13	-0.10	-0.19	-0.17	-0.37
Zn	-0.24	0.48	0.32	0.16	0.15	0.29	-0.19	0.33	0.23	0.21	-0.02	0.26	0.20	-0.06
Cu	-0.15	0.27	-0.43	-0.11	0.42	0.16	0.52	0.33	-0.17	0.55	0.28	-0.24	0.00	0.10
Pb	0.15	0.34	-0.06	0.14	-0.16	-0.07	0.04	-0.06	0.12	0.36	0.52	0.20	0.07	-0.01
Ag	1	0.13	0.20	0.08	-0.11	0.19	-0.25	-0.01	0.19	0.19	0.09	0.12	0.50	-0.11
As	0.13	1	0.10	0.04	0.34	0.44	0.33	0.26	0.10	0.67	-0.08	0.20	0.28	-0.16
Sb	0.20	0.10	1	0.50	-0.41	-0.07	-0.46	0.18	0.75	-0.09	0.01	0.64	0.39	-0.44
Hg	0.08	0.04	0.50	1	-0.06	0.21	-0.33	0.29	0.47	0.05	-0.09	0.77	0.26	-0.18
Co	-0.11	0.34	-0.41	-0.06	1	0.74	0.54	0.31	-0.24	0.37	-0.22	-0.16	0.02	0.45
Ni	0.19	0.44	-0.07	0.21	0.74	1	0.28	0.28	-0.08	0.48	-0.18	0.08	0.19	0.30
Se	-0.25	0.33	-0.46	-0.33	0.54	0.28	1	-0.14	-0.42	0.33	-0.19	-0.45	-0.18	0.39
Mo	-0.01	0.26	0.18	0.29	0.31	0.28	-0.14	1	0.43	0.47	-0.12	0.36	0.18	-0.08
Ge	0.19	0.10	0.75	0.47	-0.24	-0.08	-0.42	0.43	1	0.08	0.21	0.61	0.60	-0.32
Bi	0.19	0.67	-0.09	0.05	0.37	0.48	0.33	0.47	0.08	1	0.01	-0.02	0.32	-0.09
Re	0.09	-0.08	0.01	-0.09	-0.22	-0.18	-0.19	-0.12	0.21	0.01	1	-0.19	0.33	0.03
W	0.12	0.20	0.64	0.77	-0.16	0.08	-0.45	0.36	0.61	-0.02	-0.19	1	0.12	-0.14
Cr	0.50	0.28	0.39	0.26	0.02	0.19	-0.18	0.18	0.60	0.32	0.33	0.12	1	-0.40
V	-0.11	-0.16	-0.44	-0.18	0.45	0.30	0.39	-0.08	-0.32	-0.09	0.03	-0.14	-0.40	1
Ga	-0.32	-0.17	-0.21	-0.31	0.22	0.02	0.25	-0.03	-0.05	-0.17	0.02	-0.19	-0.29	0.66
Zr	0.00	-0.46	-0.25	-0.50	-0.12	-0.25	0.06	-0.60	-0.26	-0.41	0.21	-0.54	-0.05	0.30
Ba	-0.04	-0.08	0.22	0.22	-0.46	-0.14	-0.20	-0.15	0.00	0.00	-0.18	0.21	-0.18	-0.03
Cs	-0.04	-0.37	-0.08	-0.31	-0.33	-0.33	-0.10	-0.64	-0.31	-0.32	0.06	-0.38	-0.18	0.13
Li	-0.05	0.08	0.02	-0.05	-0.33	-0.30	-0.14	-0.25	0.17	-0.25	0.06	0.32	-0.19	0.26
Be	0.31	-0.18	0.75	0.09	-0.45	-0.17	-0.34	-0.07	0.39	-0.25	-0.21	0.26	0.15	-0.22
B	-0.22	0.14	-0.21	0.17	0.18	0.13	-0.23	0.29	0.05	0.34	0.29	-0.06	0.23	-0.25
Ta	-0.03	-0.17	0.27	0.05	-0.09	0.01	-0.48	0.23	0.52	-0.21	0.37	0.16	0.29	-0.12
Rb	0.07	-0.47	-0.10	-0.45	-0.35	-0.39	-0.10	-0.68	-0.34	-0.43	0.09	-0.48	-0.16	0.16
Sr	0.03	-0.38	0.15	0.30	-0.43	-0.50	-0.20	-0.21	0.14	-0.29	-0.06	0.20	-0.04	-0.30
U	-0.17	-0.46	0.03	-0.12	-0.32	-0.42	-0.33	0.07	0.32	-0.34	0.57	-0.15	0.09	0.04
Th	-0.03	-0.48	-0.40	-0.66	-0.18	-0.36	0.04	-0.49	-0.31	-0.40	0.41	-0.69	-0.10	0.25
Y	-0.12	-0.01	0.43	0.15	-0.15	-0.06	0.03	0.02	0.10	-0.37	-0.44	0.35	-0.36	-0.06
∑REE	-0.34	-0.25	0.10	-0.22	-0.16	-0.27	0.14	-0.09	-0.03	-0.46	-0.27	0.08	-0.53	0.40

Table 3.12 (continued): Correlation matrix of n=42 elements in the n=48 Temagami oxide BIF samples corrected to SiO_2-free abundances

	Zr	Ba	Cs	Li	Be	B	Ta	Rb	Sr	U	Th	Y	∑REE
Al	0.65	-0.40	0.15	0.39	-0.51	0.34	0.32	0.16	-0.16	0.42	0.53	-0.34	0.05
Fe	-0.11	0.21	0.02	0.08	0.83	-0.58	0.26	0.11	0.15	0.13	-0.16	0.67	0.51
Ca	-0.03	0.04	0.14	0.07	-0.08	0.04	-0.18	0.09	0.65	-0.02	0.09	0.06	-0.17
Mg	0.16	-0.09	0.26	-0.37	0.02	0.04	-0.02	0.27	-0.25	-0.31	0.16	-0.25	-0.28
Na	0.54	0.01	0.50	0.34	0.05	-0.16	-0.12	0.65	0.53	0.36	0.55	-0.12	0.20
K	0.62	-0.03	0.78	-0.22	0.33	-0.26	-0.07	0.90	-0.02	0.01	0.57	-0.25	0.00
P	-0.01	-0.02	-0.04	0.30	0.44	-0.28	0.27	0.04	0.33	0.34	-0.02	0.49	0.40
C	-0.10	0.02	0.07	-0.24	-0.34	0.19	-0.08	0.04	0.21	-0.13	0.07	-0.25	-0.39
S	-0.21	-0.08	-0.23	-0.35	-0.48	0.22	-0.44	-0.34	-0.22	-0.54	-0.19	-0.19	-0.44
Ti	0.85	-0.17	0.62	0.17	0.03	-0.29	-0.01	0.70	-0.27	0.19	0.78	-0.28	0.22
Mn	-0.19	-0.19	0.00	-0.43	-0.26	0.33	-0.07	-0.12	0.16	-0.16	0.02	-0.15	-0.49
Zn	-0.23	0.29	0.02	-0.03	0.11	0.33	0.16	-0.15	-0.42	-0.11	-0.29	-0.06	-0.10
Cu	-0.31	-0.37	-0.34	-0.31	-0.56	0.20	-0.19	-0.37	-0.12	-0.07	-0.09	-0.40	-0.34
Pb	-0.28	0.04	-0.23	0.34	-0.34	0.11	0.00	-0.22	0.09	0.08	-0.16	-0.23	-0.19
Ag	0.00	-0.04	-0.04	-0.05	0.31	-0.22	-0.03	0.07	0.03	-0.17	-0.03	-0.12	-0.34
As	-0.46	-0.08	-0.37	0.08	-0.18	0.14	-0.17	-0.47	-0.38	-0.46	-0.48	-0.01	-0.25
Sb	-0.25	0.22	-0.08	0.02	0.75	-0.21	0.27	-0.10	0.15	0.03	-0.40	0.43	0.10
Hg	-0.50	0.22	-0.31	-0.05	0.09	0.17	0.05	-0.45	0.30	-0.12	-0.66	0.15	-0.22
Co	-0.12	-0.46	-0.33	-0.33	-0.45	0.18	-0.09	-0.35	-0.43	-0.32	-0.18	-0.15	-0.16
Ni	-0.25	-0.14	-0.33	-0.30	-0.17	0.13	0.01	-0.39	-0.50	-0.42	-0.36	-0.06	-0.27
Se	0.06	-0.20	-0.10	-0.14	-0.34	-0.23	-0.48	-0.10	-0.20	-0.33	0.04	0.03	0.14
Mo	-0.60	-0.15	-0.64	-0.25	-0.07	0.29	0.23	-0.68	-0.21	0.07	-0.49	0.02	-0.09
Ge	-0.26	0.00	-0.31	0.17	0.39	0.05	0.52	-0.34	0.14	0.32	-0.31	0.10	-0.03
Bi	-0.41	0.00	-0.32	-0.25	-0.25	0.34	-0.21	-0.43	-0.29	-0.34	-0.40	-0.37	-0.46
Re	0.21	-0.18	0.06	0.06	-0.21	0.29	0.37	0.09	-0.06	0.57	0.41	-0.44	-0.27
W	-0.54	0.21	-0.38	0.32	0.26	-0.06	0.16	-0.48	0.20	-0.15	-0.69	0.35	0.08
Cr	-0.05	-0.18	-0.18	-0.19	0.15	0.23	0.29	-0.16	-0.04	0.09	-0.10	-0.36	-0.53
V	0.30	-0.03	0.13	0.26	-0.22	-0.25	-0.12	0.16	-0.30	0.04	0.25	-0.06	0.40
Ga	0.51	-0.25	0.07	0.41	-0.12	-0.09	0.21	0.17	-0.38	0.40	0.35	0.09	0.66
Zr	1	-0.22	0.56	0.12	0.03	-0.06	0.07	0.65	-0.18	0.32	0.77	-0.24	0.24
Ba	-0.22	1	0.33	0.13	0.36	-0.11	-0.29	0.23	0.33	-0.13	-0.18	0.12	0.10
Cs	0.56	0.33	1	0.06	0.36	-0.18	-0.10	0.92	0.00	-0.01	0.54	-0.31	-0.03
Li	0.12	0.13	0.06	1	-0.04	-0.19	0.05	0.08	0.18	0.19	0.08	0.10	0.40
Be	0.03	0.36	0.36	-0.04	1	-0.57	0.11	0.40	0.12	-0.06	-0.06	0.41	0.24
B	-0.06	-0.11	-0.18	-0.19	-0.57	1	0.22	-0.34	-0.11	0.30	0.03	-0.56	-0.55
Ta	0.07	-0.29	-0.10	0.05	0.11	0.22	1	-0.10	-0.37	0.62	0.23	-0.09	0.00
Rb	0.65	0.23	0.92	0.08	0.40	-0.34	-0.10	1	0.04	0.07	0.61	-0.20	0.14
Sr	-0.18	0.33	0.00	0.18	0.12	-0.11	-0.37	0.04	1	0.03	-0.14	0.16	-0.05
U	0.32	-0.13	-0.01	0.19	-0.06	0.30	0.62	0.07	0.03	1	0.58	-0.17	0.16
Th	0.77	-0.18	0.54	0.08	-0.06	0.03	0.23	0.61	-0.14	0.58	1	-0.38	0.06
Y	-0.24	0.12	-0.31	0.10	0.41	-0.56	-0.09	-0.20	0.16	-0.17	-0.38	1	0.69
∑REE	0.24	0.10	-0.03	0.40	0.24	-0.55	0.00	0.14	-0.05	0.16	0.06	0.69	1

Table 3.12 Notes:

- Pearson correlation coefficients for the same dataset of elements and materials as in Table 3.11, but calculated on a SiO_2-free basis to avoid dilution.

- The same clr calculation has been applied as for the correlation matrix in Table 3.11.

- B correlation coefficients are reported for reference only. B is associated with SiO_2, and removing SiO_2 may lead to false correlations of other elements with B (e.g. Al, Mn, Zn).

Table 3.13: Median abundances in "ferruginous component" in BIF lithologies after removing the contribution of clastic material and normalizing to zero SiO_2. Trace elements in ppm, major elements in oxide-wt.%.

	Chert n=22		**Jasper n=6**		**Magnetite n=19**		**Chlorite n=5**		**Sulfidic chert n=4**		**Shale** n=5**	**LA-magnetite n=119**
	mc	**% cc**	**mc**	**% cc**	**mc**	**% cc**	**mc**	**% cc**	**mc**	**% cc**		
Al_2O_3	2.31	41	0.42	28	0	100	2.31	96	0	100	11	0.014
Fe_3O_4	72	5.6	96	0.6	96	3.2	59	63	34	9.2	29.7	n/d
CaO	2.75	3.4	1.06	0.2	0.64	4	9.22	5.8	0.04	44	0.19	0.010
MgO	3.62	19	0.50	26	2.42	27	15.1	56	0	100	3.88	0.043
Na_2O	0.02	73	0.01	36	0.01	82	0	100	0	100	0.03	n/d
K_2O	0.11	40	0.02	19	0.10	36	0	100	0.16	22	0.02	n/d
P_2O_5	0.33	7.4	0.35	1.3	0.17	1.0	0.25	65	0	100	0.14	0.009
CO_2	14.3	0.1	0.44	0.4	0.49	0.4	13.3	2.3	0.76	2.2	0.06	n/d
H_2O	3.05	41	0.76	14	0.35	78	4.71	87	1.79	36	9.0	n/d
SO_2	0.62	2.3	0.12	4	0.02	29	0.0	100	63.47	0	0.01	n/d
Ti	0	100	0	100	7.3	98	4198	80	0	100	2751	15
Mn	6244	2.4	652	1.7	596	2.4	861	79	80	40	423	188
Zn	41	40	27	4	24	28	57	88	20	38	88	16
Cu	31	2.8	1.5	19	2.6	20	0	100	58	2	6.8	0.3
Pb	5.3	12	4.3	0.4	2.0	9.4	0	100	75	0.3	1.3	0.63
Ag	0.01	14	<0.01	9	0.02	44	0.1	89	2.1	1.3	0.23	0.045
As	8.6	6.8	3.7	3.1	1.0	45	0	100	242	0.2	1.3	0.65
Sb	2.1	1.2	2.0	0.1	1.1	0.8	0.3	60	14	0	0.15	0.76
Hg	*0.012*	*1.6*	*0.026*	*0.35*	*0.003*	*42*	*0*	*100*	*0.062*	*0.5*	*0.001*	*n/d*
Tl	*0.05*	*n/a*	*0*	*n/a*	*0*	*n/a*	*0.0*	*100*	*2.0*	*0.3*	*0.005*	*n/d*
Cd	*0.11*	*n/a*	*0.07*	*n/a*	*0.03*	*45*	*0.15*	*83*	*0.08*	*13*	*0.13*	*0.11*
Co	12	4.6	1.5	8.9	1.7	48	91	27	51	2	8.02	0.75
Ni	154	8.9	18	2	19	6.8	82	51	63	3.2	20	5.4
Se	1.5	5.1	0.19	21	0.46	25	0	100	3.8	3.6	1.15	<0.05
Mo	1.1	6.0	0.40	3.9	0	100	0	100	n/a	n/a	0.94	0.03
Te	*0.12*	*n/a*	*0.04*	*n/a*	*0.05*	*4.3*	*0.06*	*87*	*0.47*	*2.1*	*0.08*	*<0.03*
Sn	*1.1*	*n/a*	*0.36*	*n/a*	*0.13*	*22*	*0*	*100*	*0.24*	*34*	*0.7*	*1.1*
Ge	33	7.1	18	0.2	13	1.0	1.1	96	0.12	80	4.9	7.3
Bi	0.11	4.1	0.02	1.2	0.04	0.8	0.12	46	0.38	0.6	0.012	<0.03
In	*0.12*	*n/a*	*0.04*	*n/a*	*0.02*	*9.8*	*0.03*	*83*	*0.01*	*28*	*0.03*	*0.029*
Re	0.007	2.9	0.001	2.3	0.001	8.3	0.003	74	0.003	8.3	0.002	<0.005
W	1.9	8.5	6.4	18	0.63	0	0	100	0.42	16	0.52	0.25
Cr	44	8.3	15	8.7	6.1	59	29	83	0	100	36.4	0.81
V	15	25	2.0	24	5.3	55	148	60	6.2	55	49.1	4.7
Ga	2.8	64	0.74	39	0.50	83	10	92	0.67	77	18.7	0.85
Ba	19	25	8.5	31	27	5.6	0	100	0	100	2.9	1.89
Cs	1.2	1.6	0.2	2.1	1.1	1	0	100	0.4	8.8	0.18	0.06
Li	0.59	83	1.0	39	0	100	0	100	0	100	41.6	n/d
Be	1.4	11	1.3	3	1.7	1.6	0.83	84	0.04	76	0.86	n/d
B	670	0.4	158	0.2	3.8	19	0	100	0.17	93	18.2	n/d
Hf	*0.4*	*n/a*	*0.2*	*n/a*	*0*	*100*	*0.50*	*96*	*0.03*	*91*	*3.2*	*0.02*
Nb	*0.83*	*n/a*	*0.32*	*n/a*	*0*	*100*	*0*	*100*	*0*	*100*	*6.9*	*n/d*
Ta	0.17	52	0.12	8.5	0.05	46	0	100	0	100	0.59	0.01
Rb	3.2	33	0.4	43	3.7	16	0	100	7.4	18	0.5	n/d
Sr	65	2.8	58	0.2	24	0.6	126	35	3.1	26	9.09	n/d
U	0.6	24	0.2	26	0.1	77	0	100	0	100	1.6	n/d
Th	0	100	0	100	0	100	0	100	0	100	5.84	n/d
Y	14	15	15	5	7.7	32	0	100	0	100	16.4	0.28
Sc	5.3	n/a	1.7	6.5	0.59	30	0.12	99	0	100	7	0.27
∑REE	36	23	20	12	14	53	0	100	5.0	76	125	n/d

Table 3.13 Notes:

- Metalliferous component (mc): Calculated by subtracting clastic component (cc) from individual oxide-BIF samples using Zr abundance in average Temagami shale as a factor, and individual element abundances in Temagami shale as clastic component:

$$mc_A = c_A^i - \left(\frac{c(Zr)_{sample}}{c(Zr)_{shale}} * c_{A,shale} \right)$$

c_A^i: initial abundance of element A in a sample

c(Zr): concentration of Zr (117 ppm in Temagami shale)

$c_{A,shale}$: abundance of element A in Temagami shale

- Subsequently normalized to 100% on a SiO_2-free basis.

- "mc": abundance in the metalliferous component as calculated above. Negative values replaced by 0.

- "% cc": relative percentage of clastic component comprising the total abundance of each element in chert, magnetite, jasper, and chlorite facies.

- All values in ppm except where otherwise noted. n/d: not determined.

- Negative values replaced by 0.

- "LA-magnetite" are median values of LA-ICP-MS results of oxide facies magnetite (see Chapter 2).

*Tl, Cd, Te, Sn, In, Hf, Nb, Hg, and Sc abundances in italics are often below detection limit. Calculated values are for reference only and maximum values. Clastic component percentages are not available (n/a).

**Shale represents median Temagami shale, the uncorrected values used for the calculation.

Table 3.14: Reconstruction of Temagami seawater based on modern enrichment factors from the composition of Fe-Mn nodules. Selected elements sorted by relative abundance in Temagami seawater.

Element	modern SW [moles/kg]	Fe-Mn nodules [moles/kg]	nodules/SW EF	Temagami MC [moles/kg]	Temagami SW [moles/kg]
Sr [1]	1.1E-02	9.7E+02	1.2E+02	3.2E+00	6.0E-06
Rb [1]	1.4E-06	1.7E+03	1.0E+02	1.9E+01	3.7E-07
Cs [1]	2.2E-09	1.7E-01	5.8E+02	6.5E+01	1.6E-08
Ba [1]	1.1E-07	1.2E+03	8.0E+04	2.0E-01	1.7E-09
U [2]	1.4E-08	9.6E+00	3.0E+03	2.0E+00	1.3E-09
As [2]	2.3E-08	1.5E+02	8.6E+04	3.7E+00	5.8E-10
Zn [1]	6.0E-09	4.8E+02	1.2E+06	2.7E+01	3.4E-10
Mo [2]	1.0E-07	2.9E+02	2.9E+04	4.0E-01	1.4E-10
V [2]	3.5E-08	5.2E+02	2.9E+05	1.5E+01	1.3E-10
Sb [3]	1.6E-09	3.5E+01	1.8E+05	2.0E+00	9.1E-11
Ni [1]	8.0E-09	3.2E+03	6.9E+06	1.8E+01	4.5E-11
Cd [3]	6.0E-10	4.2E+00	6.3E+04	7.0E-02	1.0E-11
W [2]	5.5E-11	6.0E+01	5.9E+06	1.0E-03	5.8E-12
Cu [3]	3.0E-09	1.9E+03	9.9E+06	1.5E+00	2.4E-12
Hg [3]	1.0E-12	1.1E-02	5.5E+04	2.6E-02	2.4E-12
Ag [3]	2.0E-11	2.1E-01	9.7E+04	5.0E-03	4.8E-13
Sn [3]	4.0E-12	6.8E+00	1.4E+07	3.6E-01	2.1E-13
Pb [3]	1.0E-11	9.2E+02	4.4E+08	4.3E+00	4.7E-14
Co [1]	4.0E-11	3.9E+03	1.7E+09	1.5E+00	1.5E-14

Notes:
EF: Enrichment factor
MC: Metalliferous component of median jasper (see Table 3.13)
SW: Seawater
[]: Groups of elements with similar adsorptive behaviour:
[1]: mostly present as free cations
[2]: oxyanions
[3]: carbonate-, chloro-, and hydroxide-complexes
Enrichment factors calculated for molar abundance in Pacific Fe-Mn nodules (values from Hein et al., 2015) divided by the molar abundance in modern Pacific seawater (Erel and Morgan, 1991; Bruland et al., 2014).
Temagami seawater composition calculated by dividing metalliferous component by the enrichment factor determined for modern nodules. Values reported should be considered qualitative due to the different adsorption efficiency of Fe-oxyhydroxides dominant in Temagami BIF and Mn-oxides in modern nodules.

Table 3.15: Compiled geochemistry of Archean BIF and modern hydrothermal metalliferous sediments from the literature. Si-S in wt.%, Ti-REE in ppm.

	Tem.	Pieter.	Kuru.	Moz.	SIOG	Barb.	Adams	Great	Kirk.	Kuk.	Moose	Vogt	Wani.	Boston	Belm.	EPR	Red S.	Bath.
Type	A	A	S	S	A(?)	E	A	A	A	A-S?	A	A	A	A	A	M	M	E
Age	2730	2950	2460	2900	3506	3200	~2710	~2720	~2710	~2720	~2720	~2720	~2720	~2720	1250	0	0	468
Si	33.53	20.89		9.21	17.14	2.49	24.94	21.98	24.28	29.28	21.44	30.99	34.02	23.12	26.76		7.42	13.74
Al	0.16	0.38		0.21	0.13	0.52	0.24	0.46	1.27	0.22	0.26	0.25	0.25	0.17	0.42	1.02	0.56	0.64
Fe	18.42	34.06	21.39	53.44	42.93	59.96	29.68	35.20	27.88	21.64	36.35	21.94	17.57	34.82	28.26	32.69	26.77	37.20
Ca	0.21	1.17		0.12	0.14	0.04	1.52	1.67	1.11	0.23	1.06	0.65	0.04	0.87	0.09	3.28	3.31	1.97
Mg	0.28	1.61		0.12	0.02	0.31	0.95	0.81	1.05	0.98	1.06	0.69	0.09	0.49	0.38	0.76		0.52
Na	0.001				0.01	0.02	0.08	0.00	0.09	0.00	0.00	0.00	0.15	0.02	0.00			0.19
K	0.02	0.01		0.01	0.20	0.02	0.12	0.14	0.07	0.11	0.04	0.07	0.05	0.00	0.04			0.07
P	0.04	0.09		0.02	0.00	0.08	0.08	0.07	0.10	0.07	0.07	0.05	0.05	0.07	0.02		0.16	0.76
C	0.16						0.13	0.03	0.01	0.56	0.03			0.00	0.04			0.81
S	0.02	0.12				0.02	0.16	0.02	0.05	0.17	0.06	0.06	0.04	0.03	0.07		1.87	0.14
Ti	30.0	195.0		119.9	0.001		89	82	437	60	120	32		75	310	840	249	540
Mn	279	1007		11927	77	1074	372	1649	385	460	460	2900	615	200	425	95876	12650	16999
Zn	10.9				236	13	40		40	60	40			30	50	708	20767	460
Cu	2.2				12	19	12		20	17	6	14	8	15		1440	7922	15
Pb	0.9	2	3	1.0	0.5	4	17		2	15	4					166	824	5000
Au						0.005										148		9
Ag	0.02					<0.1									0.02	658		1
As	0.89					196			6	3.5						1715		10.9
Sb	0.48					11	0.1	4.7	0.7	1.3	0.2				0			2.5
Hg	0.002					0.024	9	0.009	0.013	47	9				0.016			0.003
Cd	0.02																99.7	0.2
Co	1.06	4.11			134	14	3	0	22	3	5	5	0	20.5	0			10
Ni	12.2	22.3			3.4	499	5	0	32	4	4	0	0	16	0			5
Se	0.21					6												
Mo	0.06					13	1	0	3	1	3				5	103.3		1
Sn	0.1					<2										270		
Ge	4.6																	
Bi	0.01					6												2.1
W	0.31	52.2				19												
Cr	4.6		2.75		2	233	7	0	57	12	7	0	0	37	0			5
V	2.7				8.2		21		24	5	15			48			102	36
Ga	0.74				0.8													
Zr	1.9	9.88	8.5	1.5	1.1	<10	5		92	4	5			74			0.5	28
Ba	5.3	3.03	6.5	10.6		219	50		28	30	40	17.5	18.5	12	55			500
Cs	0.18	0.417	0.18	0.069	0.2													

Table 3.15 (continued): Compilation of BIF geochemistry. Si-S in wt.%, Ti-REE in ppm.

	Tem.	Pieter.	Kuru.	Moz.	SIOG	Barb.	Adams	Great	Kirk.	Kuk.	Moose	Vogt	Wani.	Boston	Belm.	EPR	Red S.	Bath
Type	A	A	S	S	A(?)	E	A	A	A	A-S?	A	A	A	A	A	M	M	E
Age	2730	2950	2460	2900	3506	3200	~2710	~2720	~2710	~2720	~2720	~2720	~2720	~2720	~1250	0	0	468
B	40.9				19.1					2	2	160	130					
Hf	0.03	0.248	0.17	0.025	0.1												0.25	
Nb	0.1				0.9	33												5
Ta	0.05	0.04			5.3													
Rb	0.59	1.17	1.1	1	0.3	<10												10
Sr	9.68	28.5	6	10.4	7.3	<10	22.5	0	76	10	16			100.5	5			100
U	0.08	0.083	0.045	0.1	0.12	<2	0.05	0	38.5	22	18				50		8	
Th	0.09	0.33	0.1	0.07	0.1	<2											0.2	
Y	3.7	10.3	5.9	3.43	2.8	<10	9.6		61	4				550			0.5	19
Sc	0.5	1.81	0.25		0.7												0.8	2.3
∑REE	7.4			10.6	15.13												7.0	51

Notes:

A- Algoma, S - Superior, E - exhalative, M - metalliferous sediments. No entry – no value available.
Tem.: Temagami median of 47 oxide BIF samples, this study
Pieter.: Pietersburg, median of 14 magnetite BIF samples. Alexander et al. (2009)
Kuru.: Kuruman, median of 14 oxide BIF samples. Bau et al. (1996)
Moz.: Mozaan, median of 3 magnetite BIF samples. Alexander et al. (2008)
SIOG: Singhbhum Iron Ore Group, median of 3 samples. Mukhopadhyay et al. (2012)
Barb: Barberton exhalites, median of 3 samples. DeRonde et al. (1994)
Adams: Adams Mine, median of 58 oxide BIF samples. Gross (2009)
Great: Great Whale BIF, median of 10 oxide BIF samples. Gross (2009)
Kirk: Kirkland Lake BIF, median of 14 oxide BIF samples. Gross (2009)
Kuk: Kukatush Lake, median of 29 Algoma/Superior-type oxide BIF samples. Gross (2009)
Moose: Moose Mountain, median of 39 oxide BIF samples. Gross (2009)
Vogt: median of 39 oxide BIF samples. Gross (2009)
Wani: Wanipitai, median of 2 oxide BIF samples. Gross (2009)
Boston: Boston Mine, median of 3 oxide BIF samples. Gross (2009)
Belm.: Belmont, median of 2 oxide BIF samples. Gross (2009)
EPR: East Pacific Rise metalliferous sediments, median of 38 samples. Barrett et al. (1987)
Red S.: Red Sea Atlantis II deep, amorphous oxides, median of 6 samples. Laurila et al. (2014)
Bath: Bathurst exhalatives, median of 3 samples. Peter and Goodfellow (1996)

Table 3.16: Composition of Temagami BIF facies and average Algoma and Superior-type BIF from the literature.

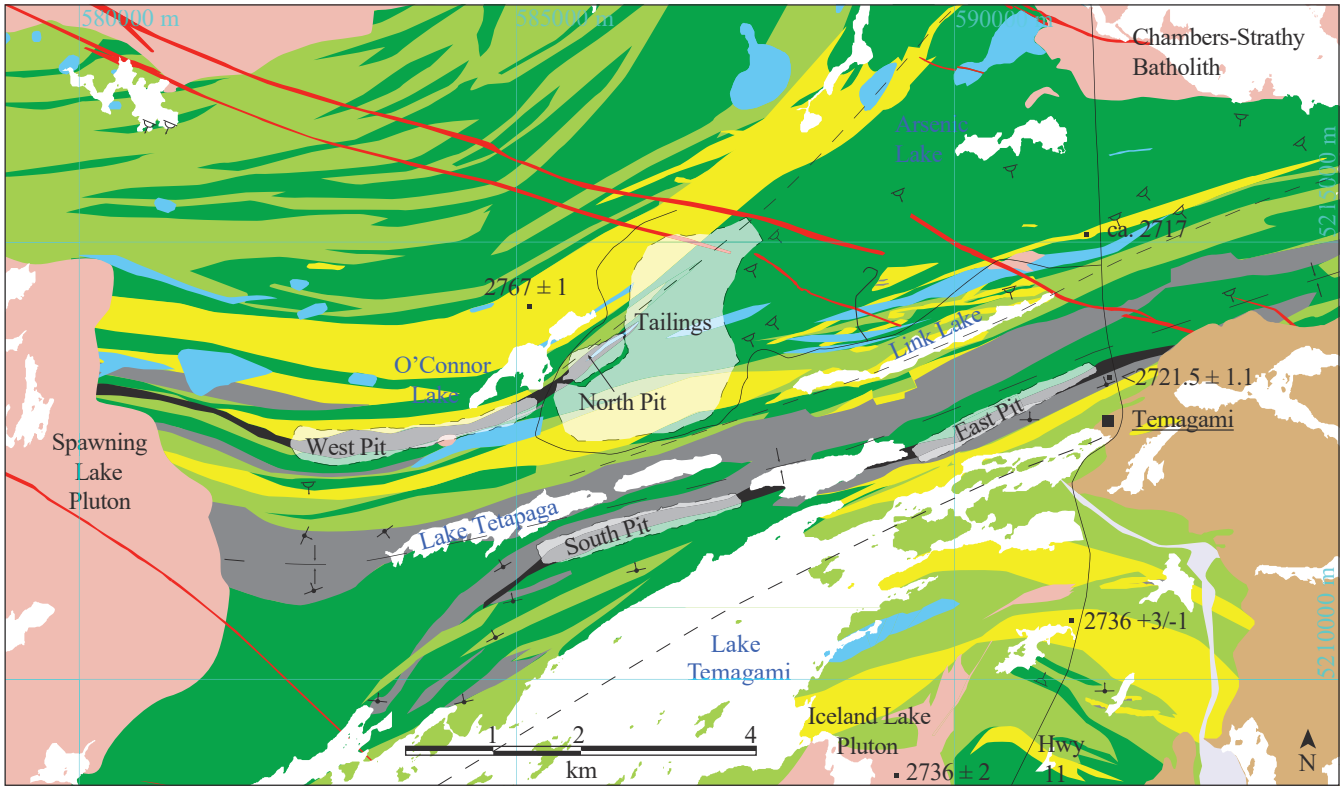
	Temagami	Temagami	Temagami	Algoma	Superior	Algoma	Superior	Algoma
	n=47	n=6	n=4	n=963	n=176	n=18	n=23	n=77
Facies	Oxide	Silicate	Sulfide	Oxide	Oxide	Silicate	Silicate	Sulfide
Si [%]	34	23	15	22	22	30	27	19
Al [%]	0.16	5.7	0.85	1.4	0.68	1.3	1.2	3.5
Fe [%]	18	20	30	31	31	15	19	20
Ca [%]	0.21	1.2	0.06	1.2	1.1	3.5	1.6	1.7
Mg [%]	0.28	3.4	0.27	0.95	0.75	2.2	1.7	1.3
Na [%]	0.00	0.01	0.01	0.24	0.08	0.17	0.14	0.6
K [%]	0.02	0.01	0.20	0.60	0.12	0.21	0.46	0.08
P [%]	0.04	0.05	0.01	0.10	0.03	0.03	0.04	0.05
C [%]	0.16	0.62	0.24	0.24	0.75	0.60	1.2	0.56
S [%]	0.02	0.02	28	0.18	0.03	0.16	0.08	12
Ti	30	2074	321	750	170	1910	1600	2620
Mn	279	523	115	1120	5130	2190	4000	2330
Zn	11	78	36	60	30	50	40	3430
Cu	2.2	2.2	66	50	10	20	40	630
As	0.89	1.2	272	120	3000			2530
Co	1.1	21	59	38	30	40	30	80
Ni	12	28	72	80	30	90	20	100
Cr	4.6	28		80	110	140	100	160
V	2.7	62	15	60	30	110	100	30
Zr	1.9	77	17	40	60	60	170	120
Ba	5.3	1.8	6.5	210	170	130	150	150
Sr	9.7	32	4.7	70	30	90	20	100
Y	3.7	13	2.5	20	40	20	40	30

Notes:

Major element in wt.% as indicated, all other elements in ppm.

n: number of analyses from a total of 45 individual iron formations.

Temagami values from this study, all other values from Gross (2009).



LEGEND

PROTEROZOIC

- Diabase Dikes
  Sudbury-type (1238 Ma)
- Mafic Intrusive Rocks
  Nipissing-type: diabase, granophyre (2200 Ma)

INTRUSIVE CONTACT

- Sedimentary Rocks
  Gowganda Formation (2300 Ma)

NEOARCHEAN

- Felsic Intrusive Rocks
  Monzonite, trondhjemite, granodiorite, porphyry
- Mafic Intrusive Rocks
  Diorite, gabbro

INTRUSIVE CONTACT

- Chemical Metasedimentary Rocks
  Iron formation: oxide, sulfide, silicate facies
- Clastic Metasedimentary Rocks
  Argillite, wacke, conglomerate
  Arenitic sandstone, mudstone
- Felsic Metavolcanic Rocks
  Massive rhyolite flows
  Tuff, lapili tuff, pyroclastic breccia
- Intermediate Metavolcanic Rocks
  Massive-, pillowed-, variolitic flows
  Hyaloclastite, flow breccia
  Tuff, lapili tuff, pyroclastic breccia
- Mafic Metavolcanic Rocks
  Massive-, pillowed-, variolitic basaltic flows
  Hyaloclastite, flow breccia,
  Tuff, lapili tuff, tuff breccia

SYMBOLS

- Pillowed flow, with facing
- Sedimentary bedding, with facing
- Syncline, inferred
- Fault, deformation zone
- Road: Highway, mine access road
- 2736 Geochronological age in Ma (Ayer et al., 2006)

COORDINATE SYSTEM
UTM zone 17N, NAD27

REFERENCES:

Ayer, J.A., Chartrand, J.E., Grabowski, G.P.D., Josey, S., Rainsford, D., and Trowell, N.F. 2006. Geological compilation of the Cobalt-Temagami area, Abitibi greenstone belt, Ontario Geological Survey, Preliminary Map P. 3581, scale 1:100000

Bennett, G. 1978. Geology of the Northeast Temagami Area, District of Nipissing; Ontario Geological Survey Report 163, 128p. Accompanied by Maps 2323 and 2324, scale 1 inch to 1/2 mile (1:31,680), and 1 chart.

Johnston, M.M. 1987. Stratigraphy and geochemistry of a portion of the Temagami Greenstone Belt, northeastern Ontario. Unpublished MSc thesis. Laurentian University, Sudbury, ON. 123p.

Figure 3.1: Geologic map of the central part of the Temagami Greenstone Belt. Lithologies compiled after Bennett (1978), Johnston (1987) and this study. Ages from Ayer et al. (2006) and references therein. Archean lithologies dip subvertically in all areas of the map (dip angles omitted from bedding symbols, for details see Bennett, 1978), forming two limbs of the isoclinal Tetapaga synform. However, the location of the fold axis and repetition of the units has been poorly documented. BIF horizons are considered independent units, not fold repetitions (Bennett, 1978).

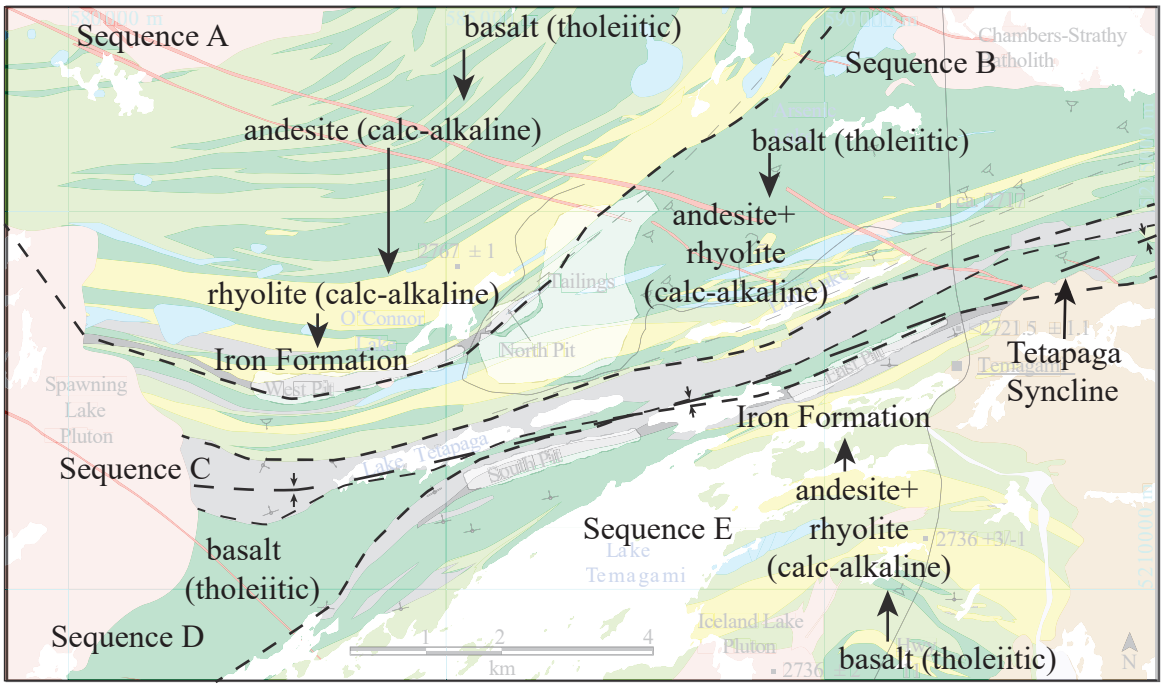


Figure 3.2: Interpreted stratigraphic succession of the Temagami Greenstone Belt A and E are approximately stratigraphically equivalent on opposite sides of the proposed Tetapaga syncline (note the opposing younging directions). Both sequences have tholeiitic, pillowed Fe-rich basalts at their base (partly outside the map area), transitioning to more felsic and calc-alkaline lithologies and capped by BIF on top of the sequence. The younging directions of the middle sequences (B and D) are not as clearly defined but they are dominated by tholeiitic basalts with few felsic rocks. Sequence C is dominated by clastic metasedimentary rocks and partly contained within the Tetapaga Syncline in its central part, but the location of the fold axis is not well constrained. The BIF in sequences A and E are not equivalent on either side of the syncline, but occur in different stratigraphic positions within their sequence. Map overlay modified from Fyon and Crocket (1989).

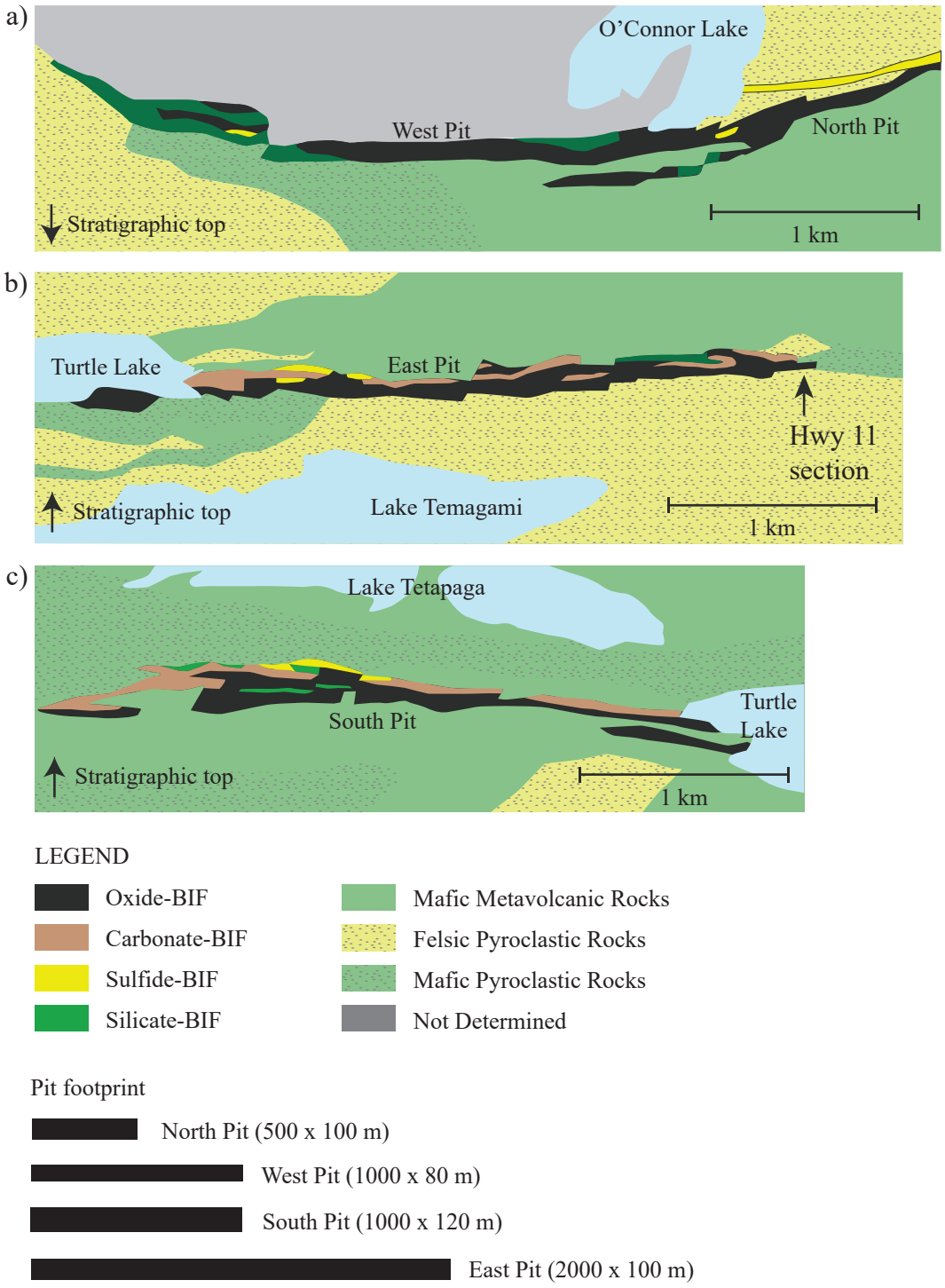


Figure 3.3: Distribution of BIF facies in the Sherman Mine area. a) North BIF in the Sherman Mine North Pit and West Pit, b) South BIF in the Sherman Mine East Pit, c) South BIF in the Sherman Mine South Pit. Oxide facies BIF was dominant, with intercalated silicate (chlorite) and carbonate facies. No systematic changes are evident in the distribution of the BIF facies in the mine area, but sulfide facies BIF and sulfidic shale is mostly present along the contacts between BIF and volcanic host rocks and north of the North BIF. Carbonate facies BIF is almost completely absent in the North BIF. In the South BIF, areas identified as "carbonate facies" are, in fact, mostly chert-magnetite with less Fe-carbonates. North is to the top in all panels. Pit footprints illustrate the approximate former exposed surface area of iron ore mined in the Sherman Mine pits. Pit size was used to estimate the amount of ore present in the original deposit (866 Mt), assuming ore containing 35% magnetite and 65% quartz (see text for discussion). Adapted from Gross (2009) with additions from Bennett (1978), Campbell (1978), and this study.

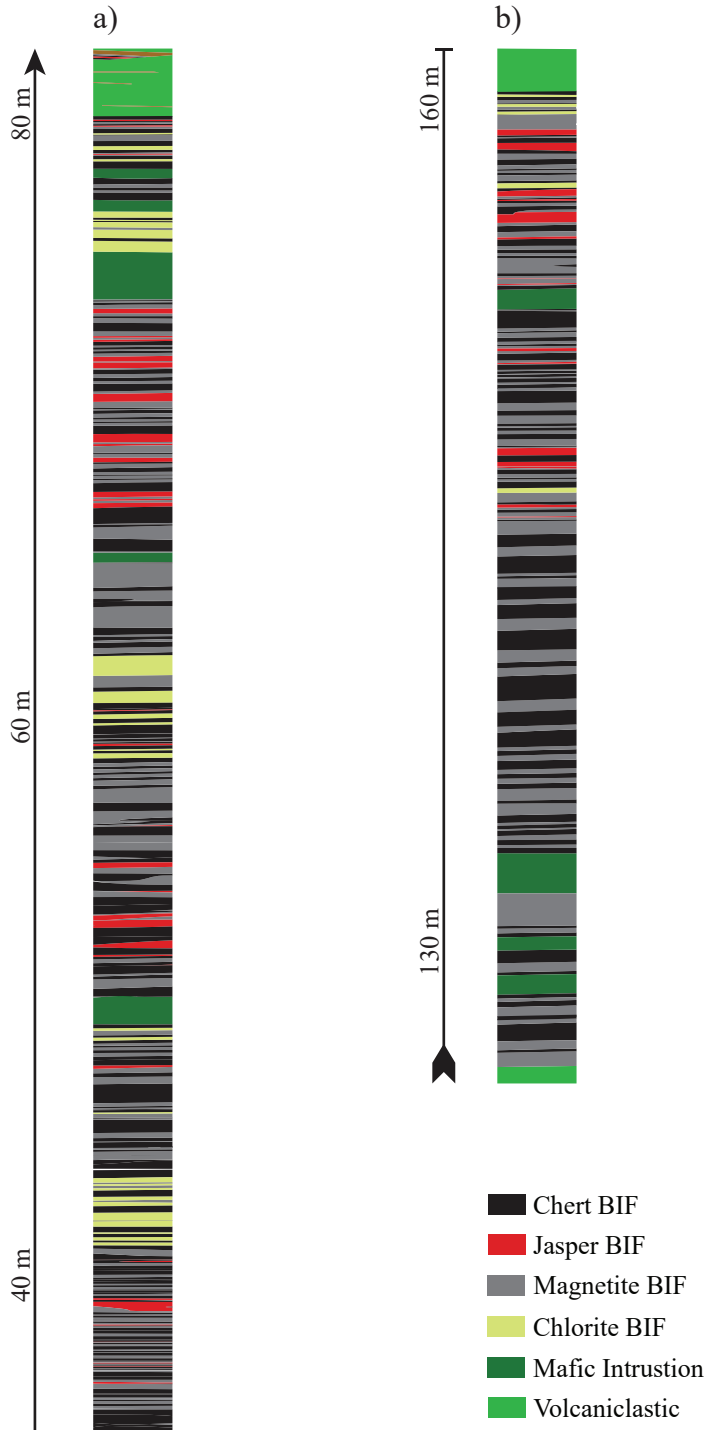


Figure 3.4: Simplified lithostratigraphic column of the South BIF along the S-to-N section of the Hwy 11 outcrop. a) and b) are the northern and southern parts of the South BIF, respectively, shown in Figure 2.6. Only the dominant BIF facies at the m-scale are shown, although individual units contain many cm- and mm-scale interlayers. Note the increase in the abundance of jasper-rich units towards the top of each section. The two sections are interrupted by mafic volcanic rocks for about 60 m in the middle part. From the outcrop map in Diekrup et al. (2018).

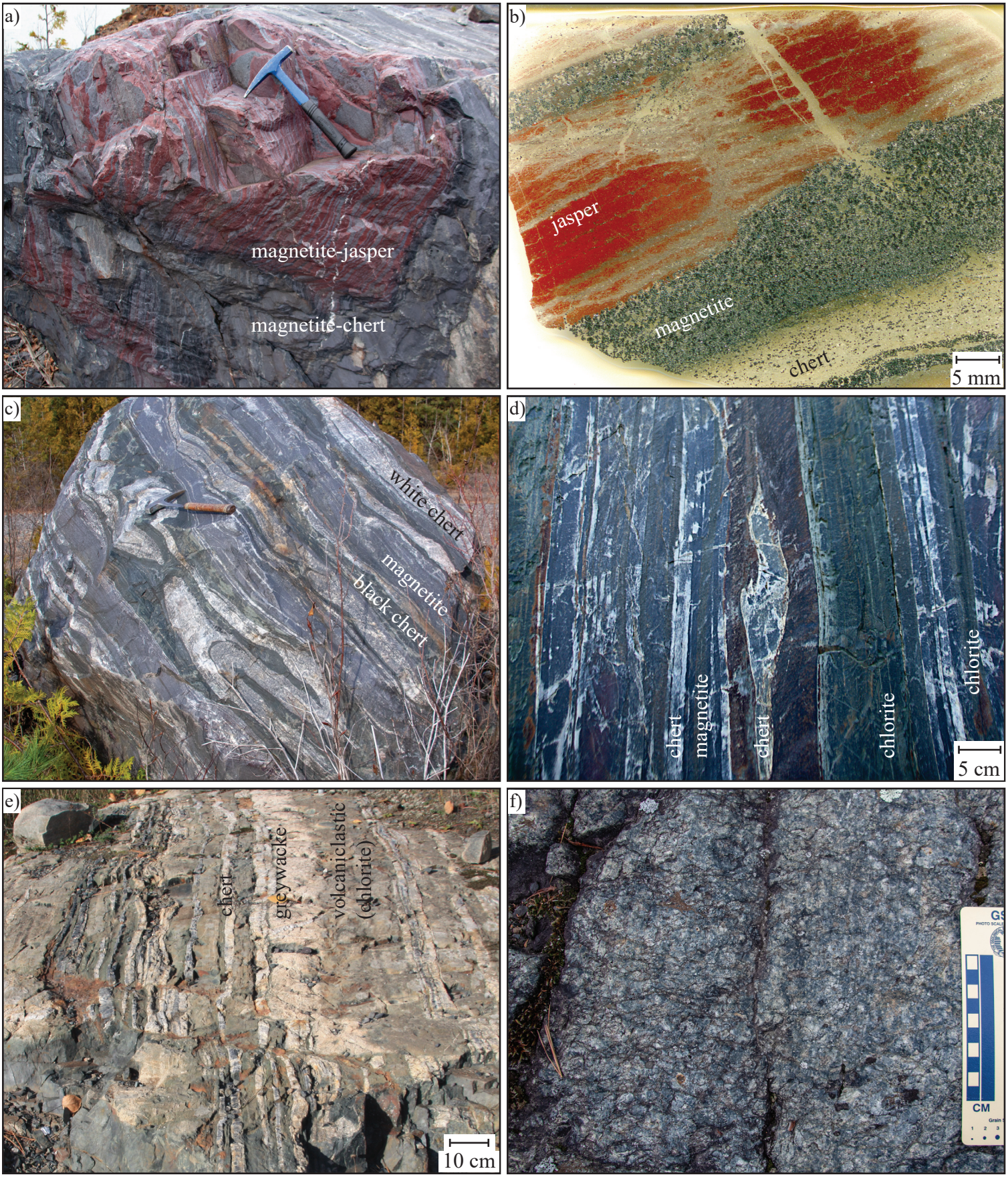

a)
magnetite-jasper
magnetite-chert
b)
jasper
magnetite
chert
5 mm
c)
white chert
magnetite
black chert
d)
chert
magnetite
chert
chlorite
chlorite
5 cm
e)
chert
greywacke
volcaniclastic
(chlorite)
10 cm
f)
CM

Figure 3.5: Representative facies of the Temagami BIF. a) Ore block showing distinctive burgundy-coloured jasper transitioning to black chert. Close inspection of the contact between magnetite and jasper shows that the jasper is everywhere replaced by magnetite, leaving a large relict of jasper at the center of the block. Hammer for scale. b) Thin section scan of sample SM11. showing alternating layers of chert (transparent), chert-magnetite, and microbanded jasper layers. The lateral transitions from jasper to black captured in the thin section are commonly observed in ore blocks (see panel a). c) White chert with interlayered black chert and magnetite, locally tightly folded. Folds are interpreted to be syn-sedimentary based on the very limited extend of folded horizons (block E038; cf. Ginley, 2016). d) Chlorite (”silicate facies”) BIF in the Hwy 11 outcrop. Chlorite layers in oxide BIF are the metamorphic products of a volcanic-derived clastic precursor materials such as ash layers, or authigenic phases formed in seawater such as hydrothermal clays or green rust. Layering of chloritic material is true, primary layers, while layers and bands (including microbands) in oxide BIF may be of diagenetic origin. e) Interlayered volcaniclastic chlorite layers, greywacke, and chert at the south end of the Hwy 11 outcrop, stratigraphically at the base of the South BIF. c) Felsic lapilli tuff north of the Sherman Mine access road. For more context, see Chapter 2.

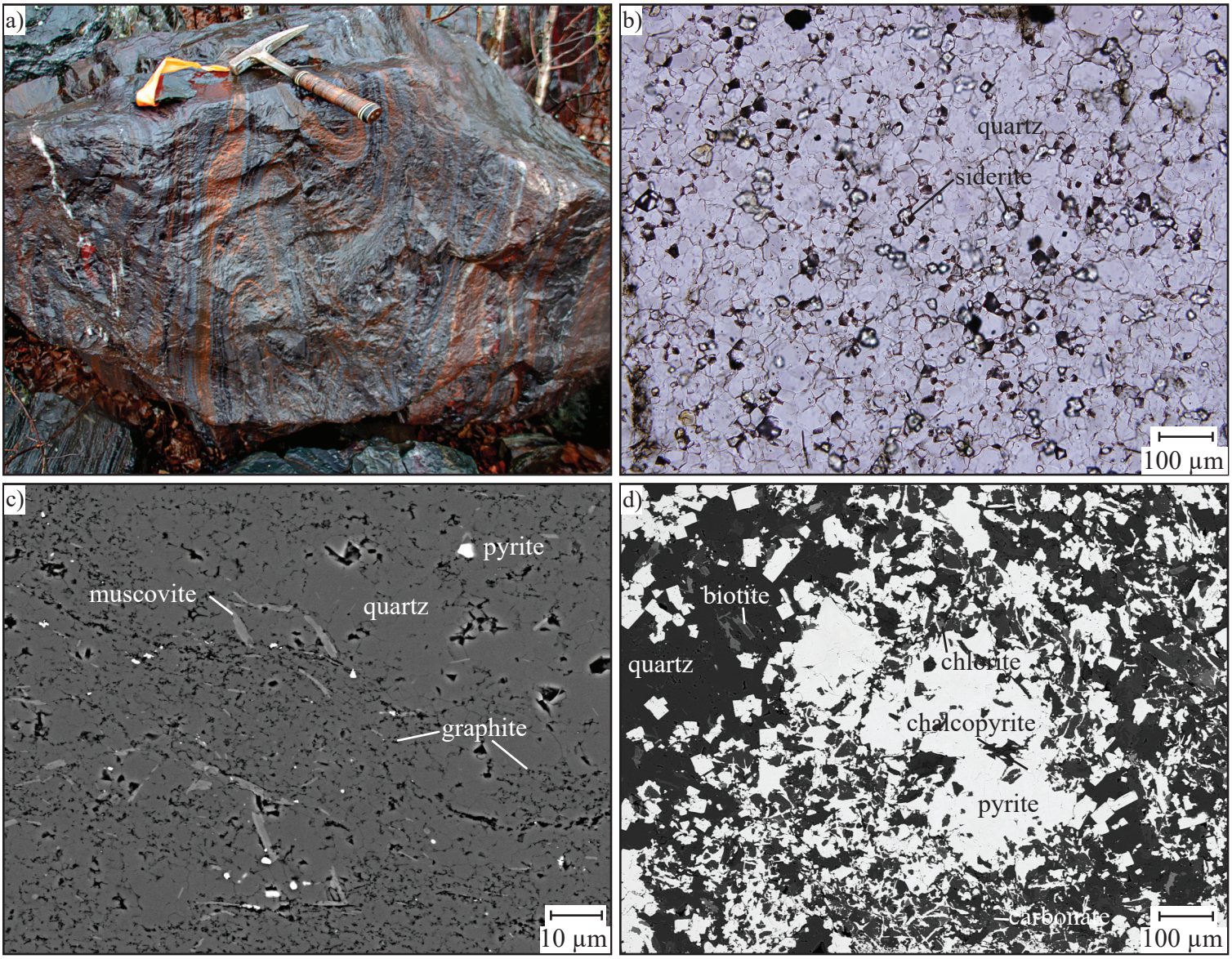


Figure 3.6: Representative examples of carbonate and sulfide facies BIF. a) Tightly folded black chert and siderite-bearing chert "carbonate-facies BIF". b) PPL transmitted light photomicrograph of carbonate-facies BIF, consisting of minor disseminated siderite in a chert matrix (sample 11-27). Siderite is likely an early diagenetic product of primary carbonate phases deposited with the initial precipitate (e.g., Klein, 2005). c) BSE image of the cherty matrix of sulfide-facies BIF showing mainly disseminated pyrite, chalcopyrite, muscovite, and fine graphite (sample SH580). Pyrite is the diagenetic product of sulfide from sulfur-reducing bacteria in sulfide BIF (Diekrup et al., 2018), using organic material preserved as graphite to metabolize sulfate. Some sulfide reacting with Cu present in pore water is preserved as trace-chalcopyrite. Muscovite is the metamorphic product of volcanic-derived material. d) BSE image of sulfide-facies BIF showing large, irregular pyrite grains (possibly aggregates; sample SH580). Carbonates, chlorite, muscovite, and biotite are all present as traces.

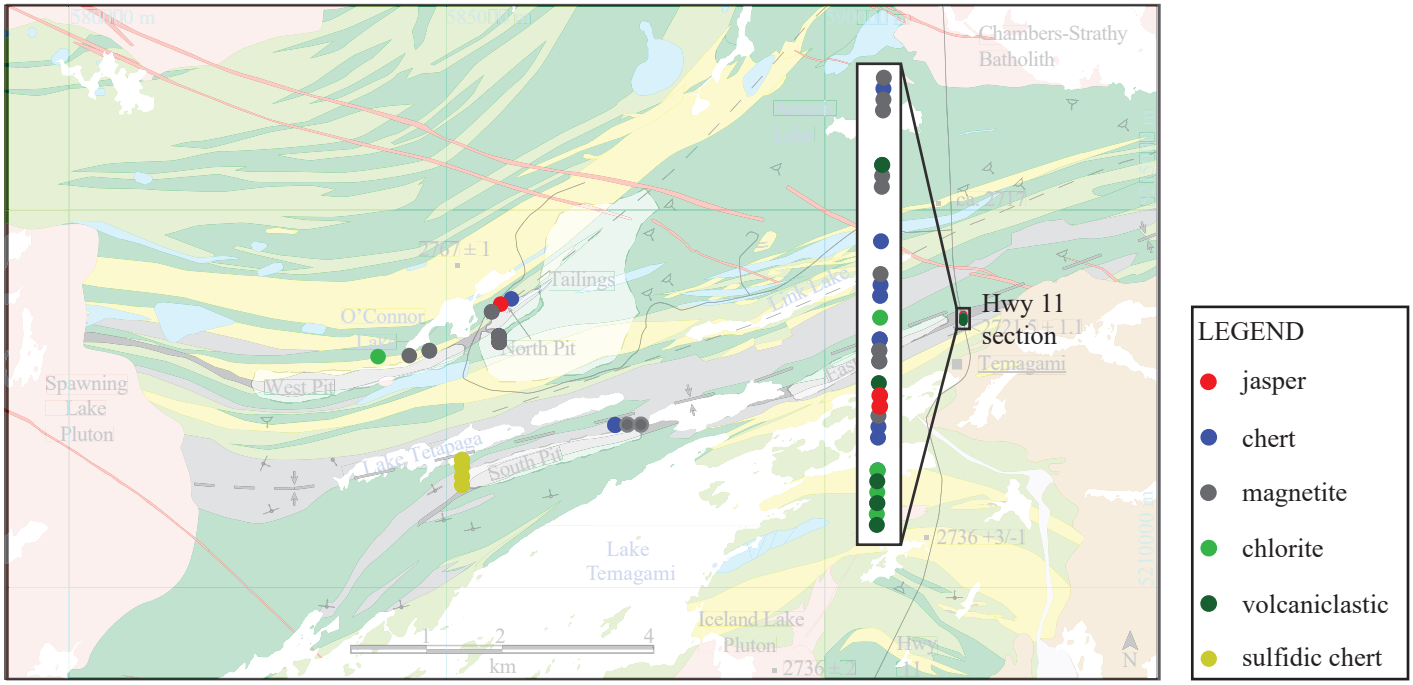


Figure 3.7: Locations of samples selected for WR geochemistry. Samples from the area of the pits were taken from a subset of more than 600 ore blocks at the pit margins. Some of locations overlap where multiple samples were taken from one ore block (see Appendices A for details, and Appendix M for GPS coordinates). Archived samples of sulfide-facies BIF are not precisely located but assumed to have been from the documented location of sulfide-facies in the South Pit. Sample locations along the Hwy 11 outcrop are shown at an expanded scale (see Appendices A and M for details).

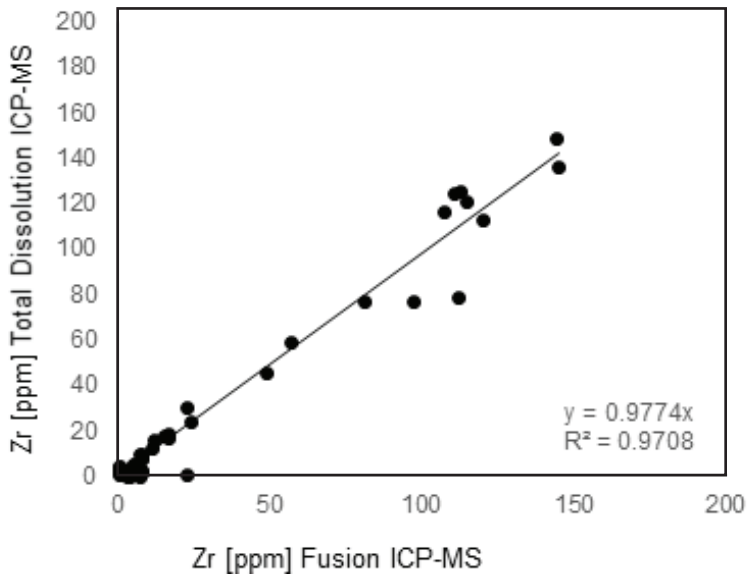
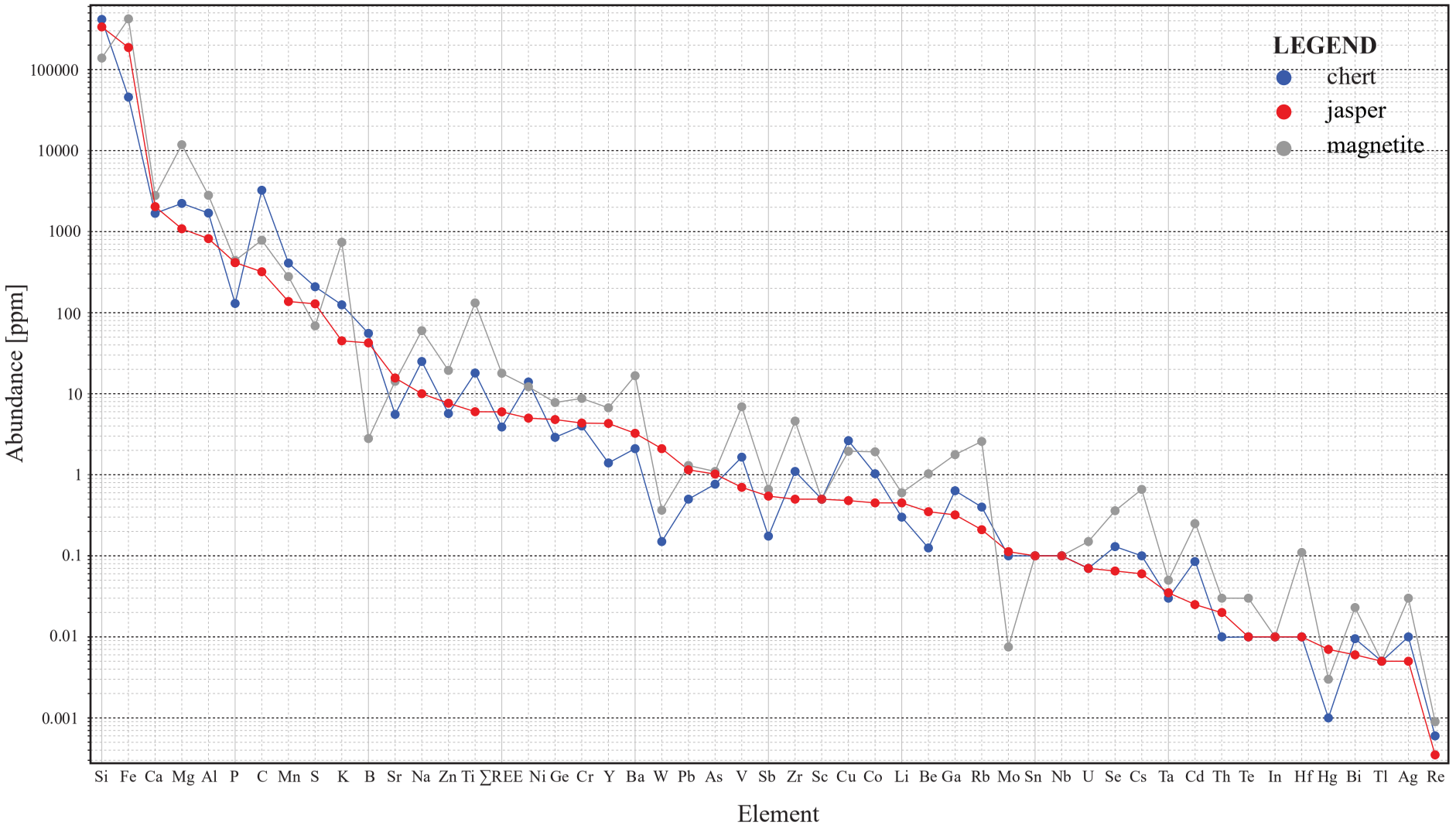


Figure 3.8: Comparison of results of whole-rock Zr analysis by Total Dissolution ICP-MS and Fusion ICP-MS for all samples. Good correlation between 0 and 200 ppm indicates that both methods are suitable for Zr; results from TD-ICP-MS were used in this paper because of lower detection limits (0.2 ppm vs 1 ppm by Fusion ICP-MS).

a)


LEGEND
chert
jasper
magnetite
Abundance [ppm]
100000
10000
1000
100
10
1
0.1
0.01
0.001
Si Fe Ca Mg Al P C Mn S K B Sr Na Zn Ti ∑REE Ni Ge Cr Y Ba W Pb As V Sb Zr Sc Cu Co Li Be Ga Rb Mo Sn Nb U Se Cs Ta Cd Th Te In Hf Hg Bi Tl Ag Re
Element

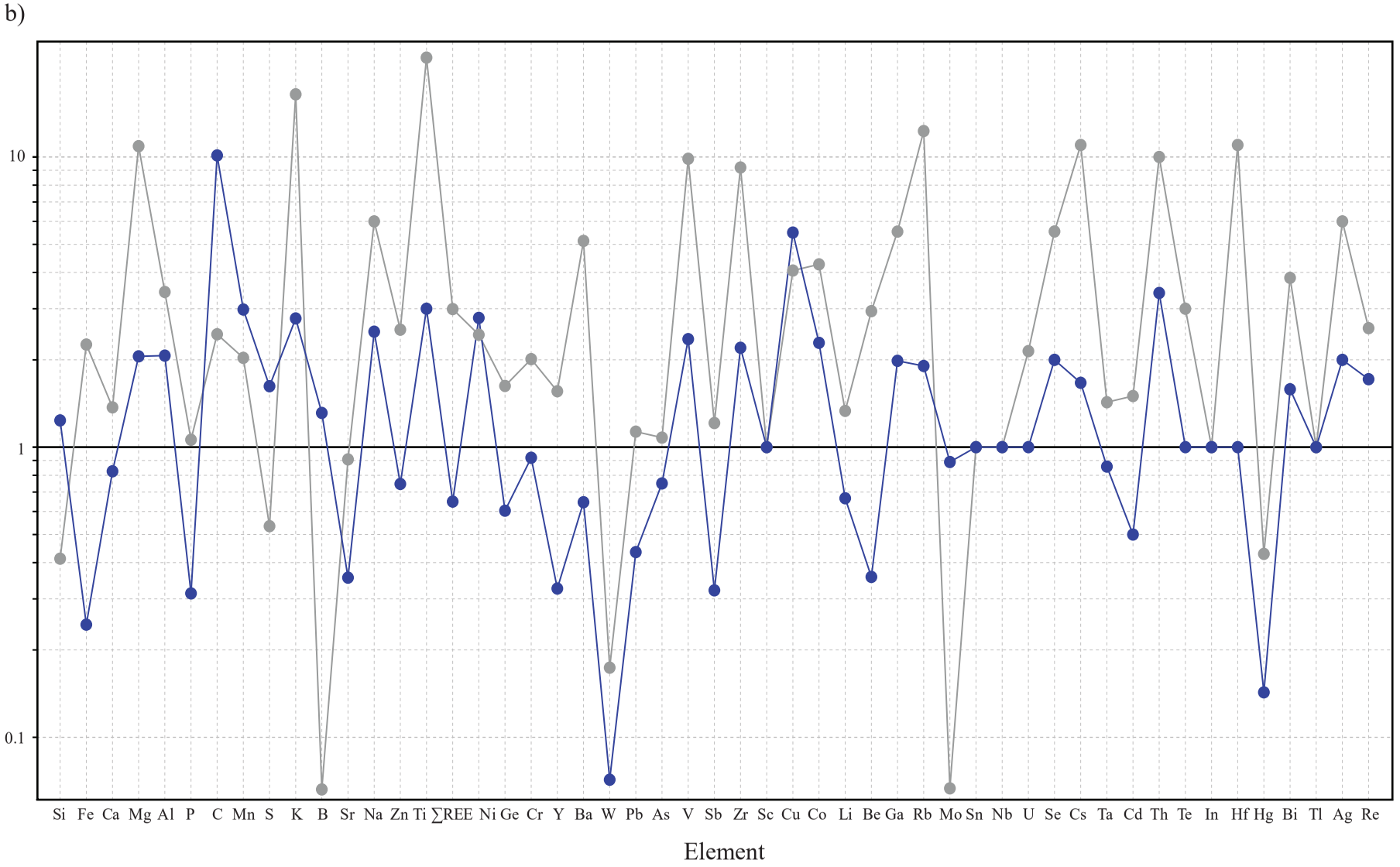


Figure 3.9: Parallel coordinate plot of major and trace element concentrations in oxide-facies BIF (chert, jasper, and magnetite). a) Arranged in order of decreasing median concentration in the jasper facies (interpreted here to represent the primary depositional facies). b) Magnetite and chert results normalized to jasper to highlight the differences between lithologies. All concentrations recalculated to element-ppm. The major differences between the facies are discussed with reference to Fig. 3.21.

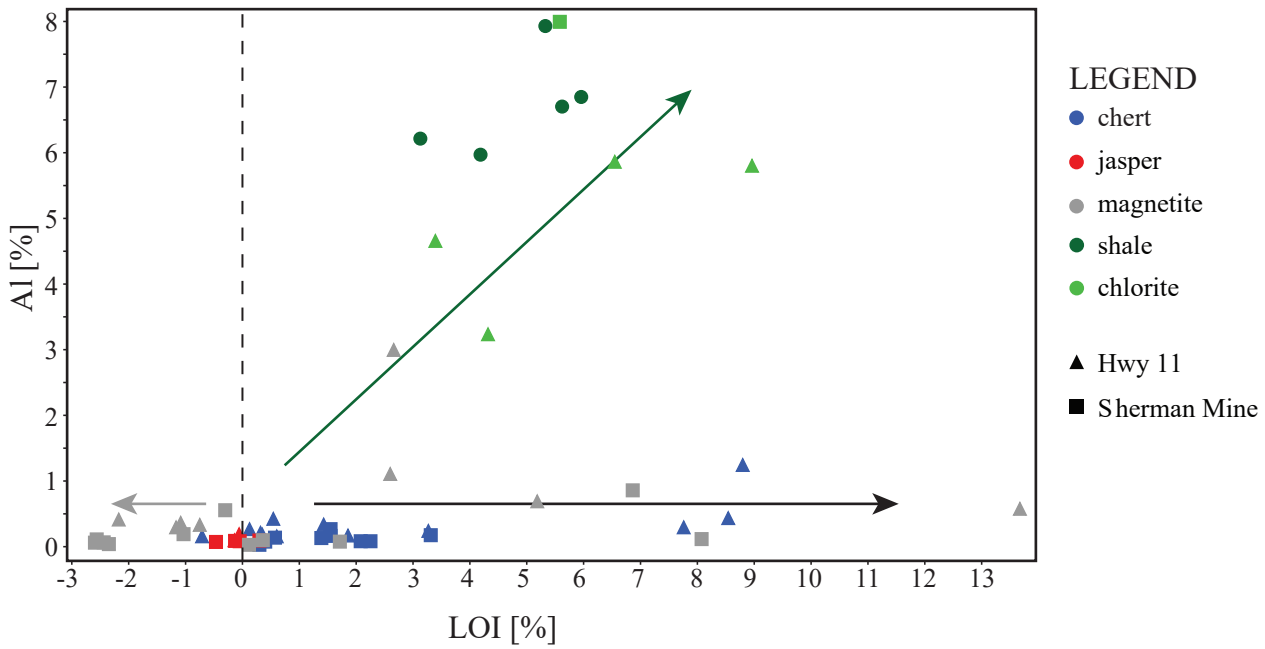


Figure 3.10: Variations in loss on ignition (LOI) for all BIF samples versus Al concentration. The latter reflects the abundance of hydrous aluminosilicates, mainly in the chlorite facies, which lose water on ignition (green arrow). The range of LOI values in chert and magnetite samples is due to carbonate breakdown (black arrow), and magnetite oxidation leading to negative LOI (grey arrow).

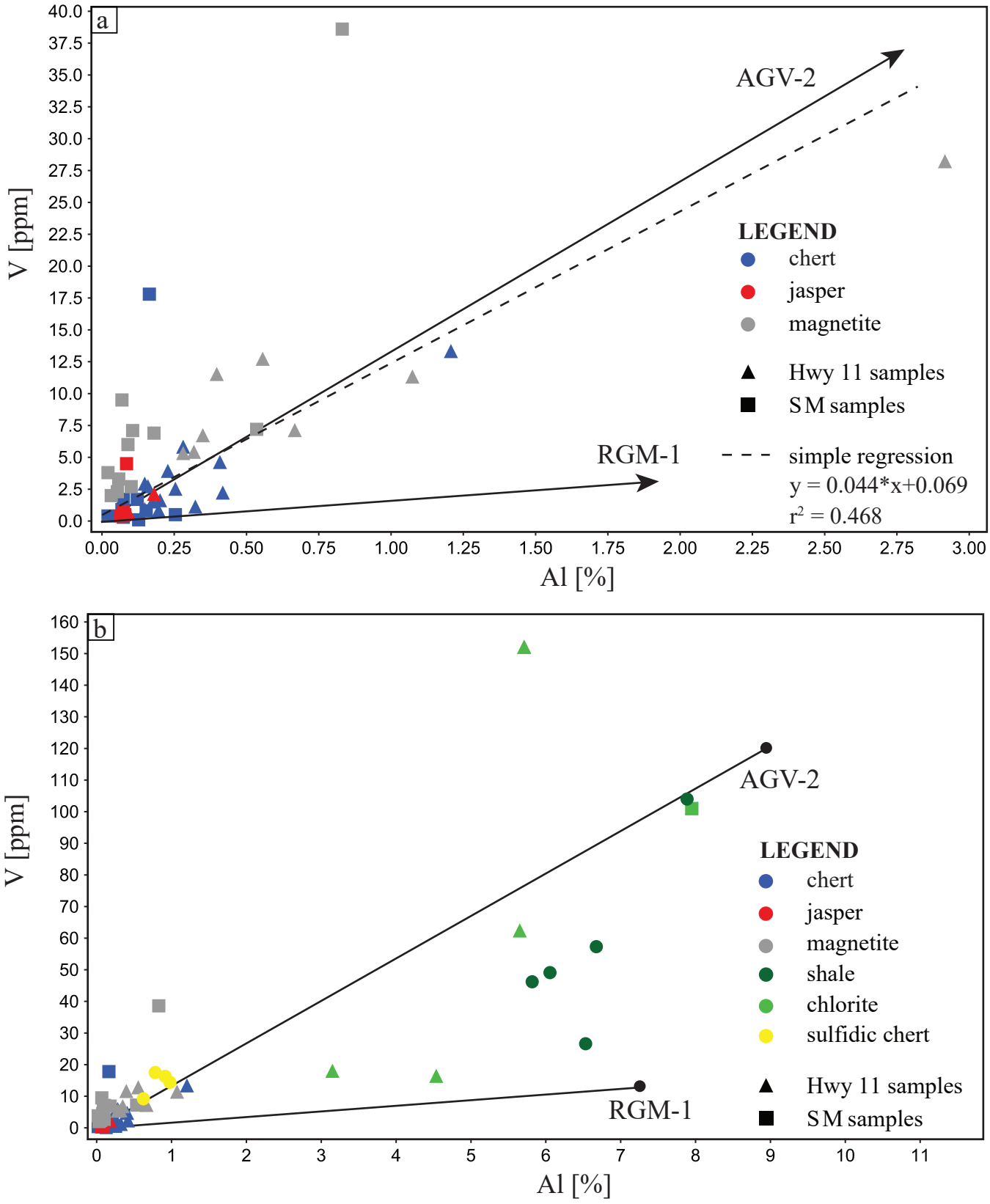


Figure 3.11: Vanadium concentrations of oxide- and silicate-facies and volcaniclastic units of the Temagami BIF. Vanadium is a proxy for both clastic and hydrogenous input, showing both processes operated in the Temagami BIF. a) V versus Al in oxide BIF. b) V versus Al in all samples. Chlorite and shale samples cluster between reference materials AGV-2 USGS andesite , and RGM-1 USGS rhyolite. Oxide-facies BIF samples that plot above the V/Al line for AGV-2 are interpreted to reflect a minor hydrogenous addition of V (if Al is immobile) or preferential concentration of V in the magnetite crystal structure (e.g., see Chapter 2). Note the change of scale between panels.

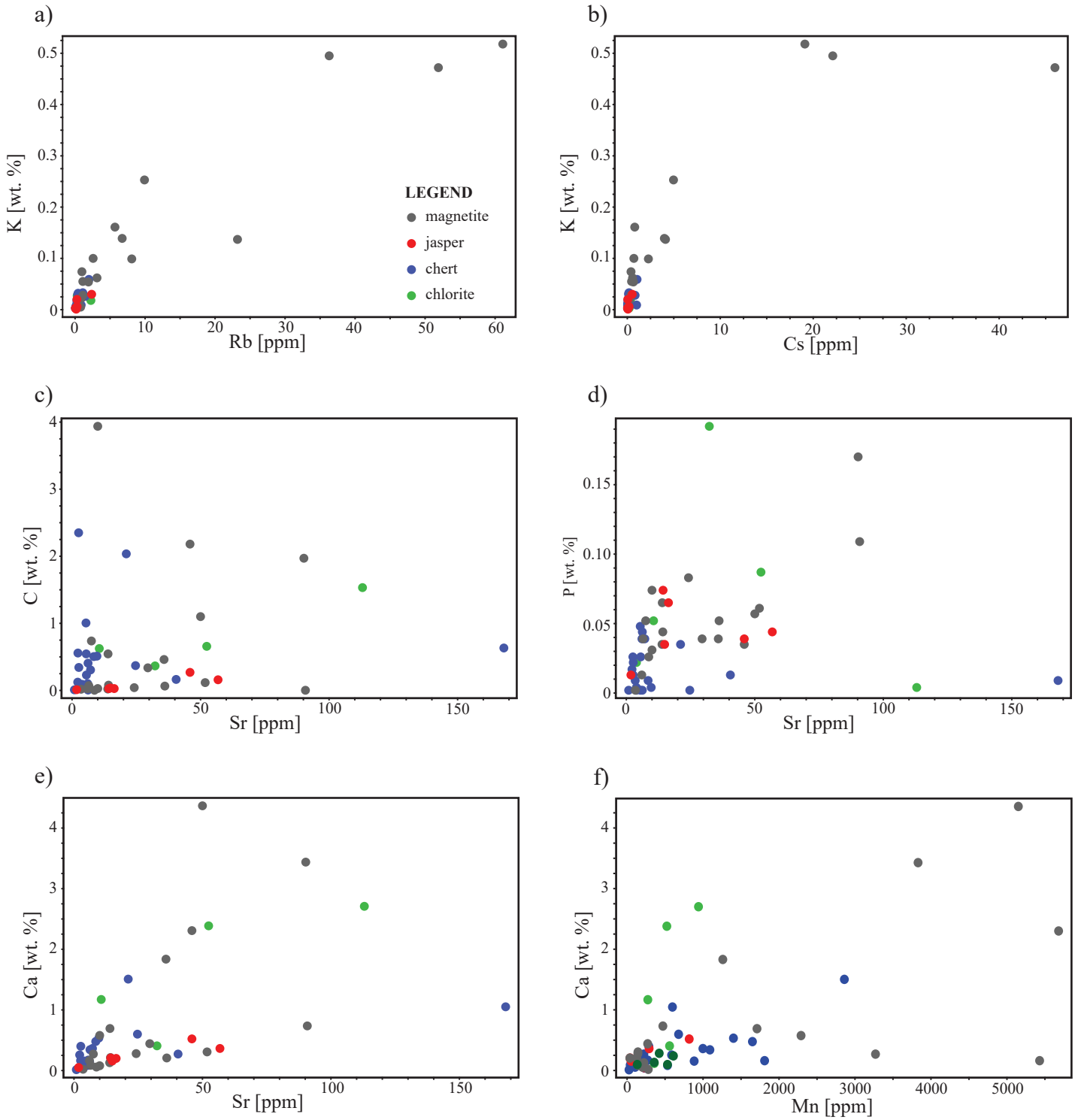


Figure 3.12: Binary plots of whole-rock major and trace elements in Temagami BIF. a) and b) Correlation of K, Rb, and Cs as constituents of minor biotite in oxide-facies BIF. c) Correlation of C and Sr as constituents of minor carbonate in oxide-facies BIF. . d), e) and f) Correlation of Ca, P, Sr and Mn as constituents of apatite and carbonate in oxide- and chlorite-facies BIF.

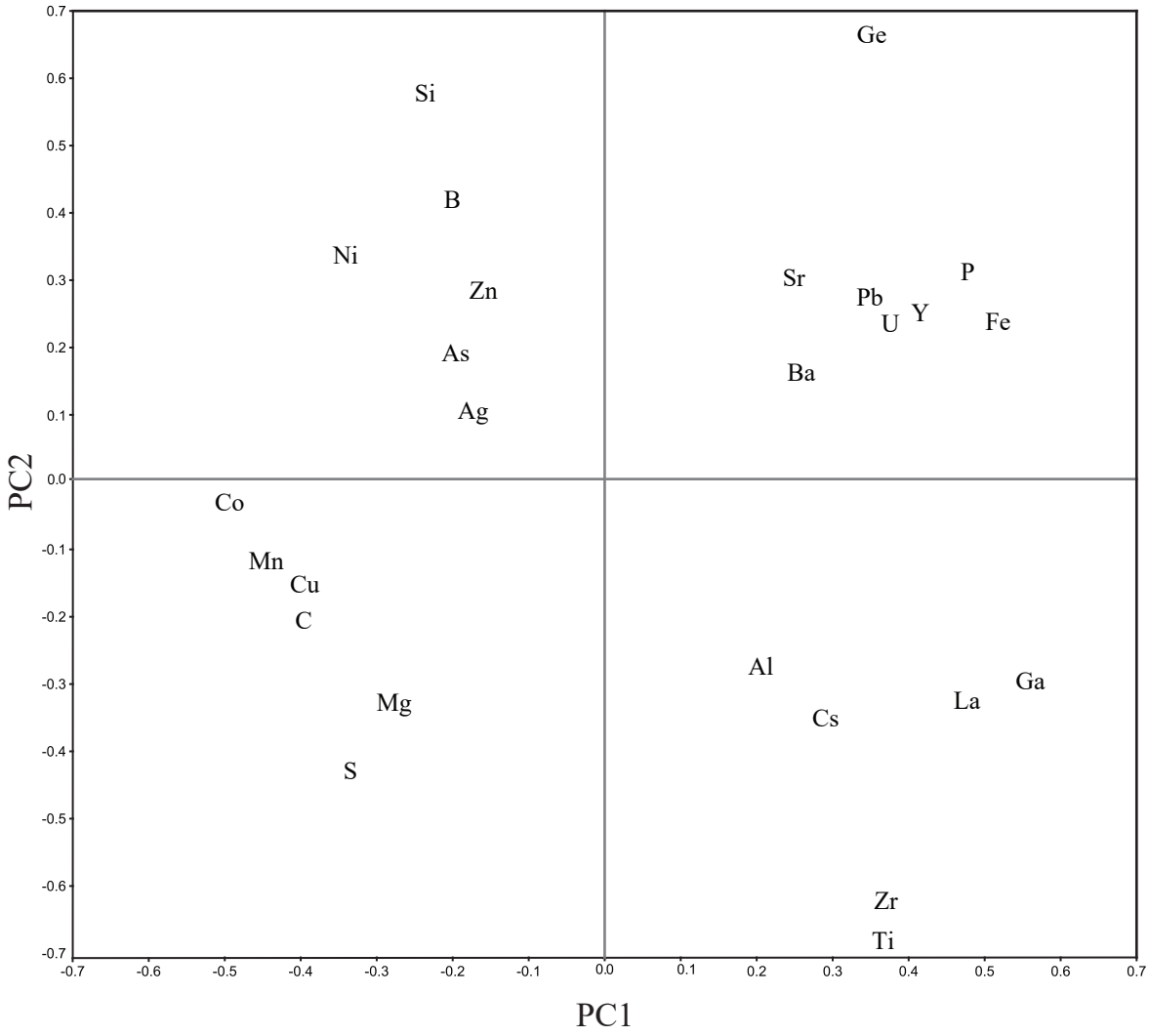


Figure 3.13: Vector plot of the principal component analysis of whole-rock geochemical data from oxide-facies BIF (PC1 versus PC2), uncorrected for dilution by Si and clastic components. High loadings on PC1 reflect the formation of stabilizing phases magnetite and apatite during diagenesis. Negative loadings on PC1 reflect the mobilization of certain elements during diagenesis and the stabilization of others in carbonates, chlorite, and rare sulfides. High loadings on PC2 reflect hydrothermal-seawater components entering the sediment, most likely adsorbed onto Fe-oxyhydroxides. Negative loadings on PC2 reflect the presence of immobile elements in a clastic component of the sediments (Zr, Ti, Al). Negative and positive loadings on PC2 for the base metals (Cu, Zn, and Pb) correspond to an unexpected decoupling in Temagami BIF attributed to the availability of S (see also Chapter 4). Details of the principal components analysis are provided in Appendix N.

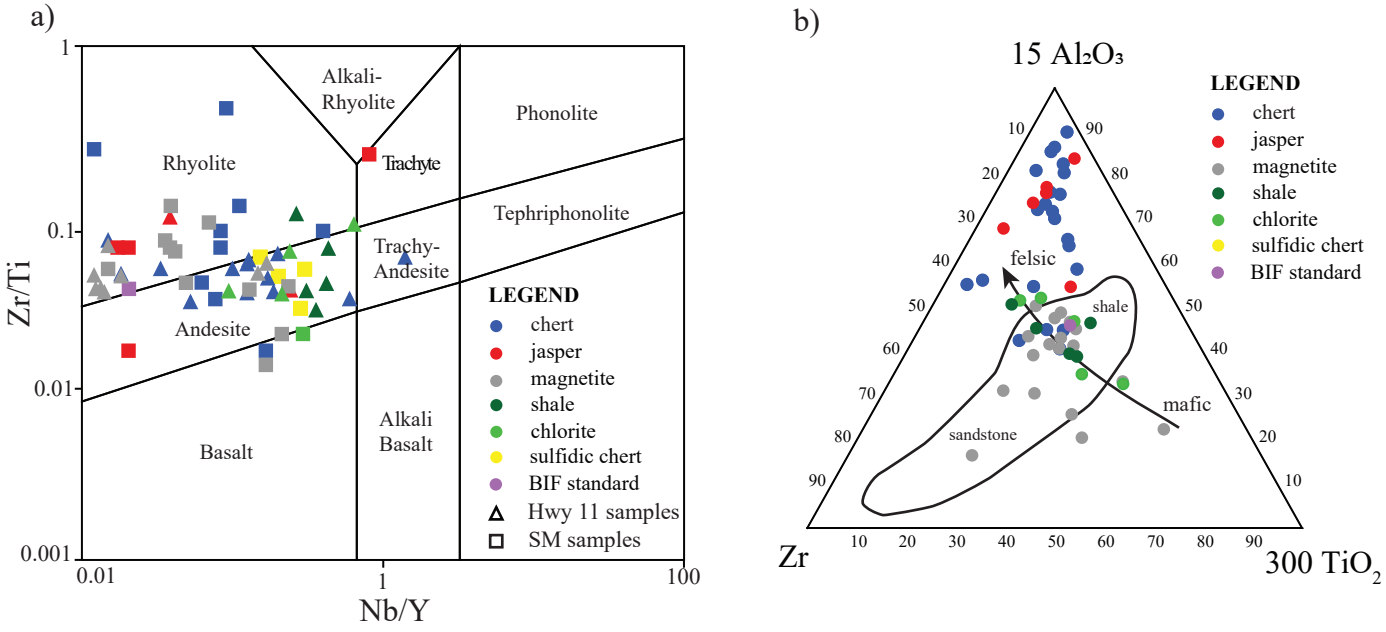


Figure 3.14: a) Whole-rock immobile element ratios for different facies of the Temagami BIF superimposed on the volcanic rock classification plot of Pearce (1996). The overlap with the rhyolite and andesite fields suggest that the clastic components of the BIF derives from a mixture of intermediate to felsic volcanic detritus. The composition of oxide-facies BIF samples likely also reflect authigenic enrichment of Y (e.g., in apatite and monazite). b) Whole-rock immobile element ratios for different BIF facies superimposed on the classification plot for clastic sediments of Garcia et al. (1994), based on Zr-Ti-Al. The inferred clastic component of the oxide-facies BIF overlaps that of typical shale, with a decreasing clastic component and more clays in the jasper and chert facies.

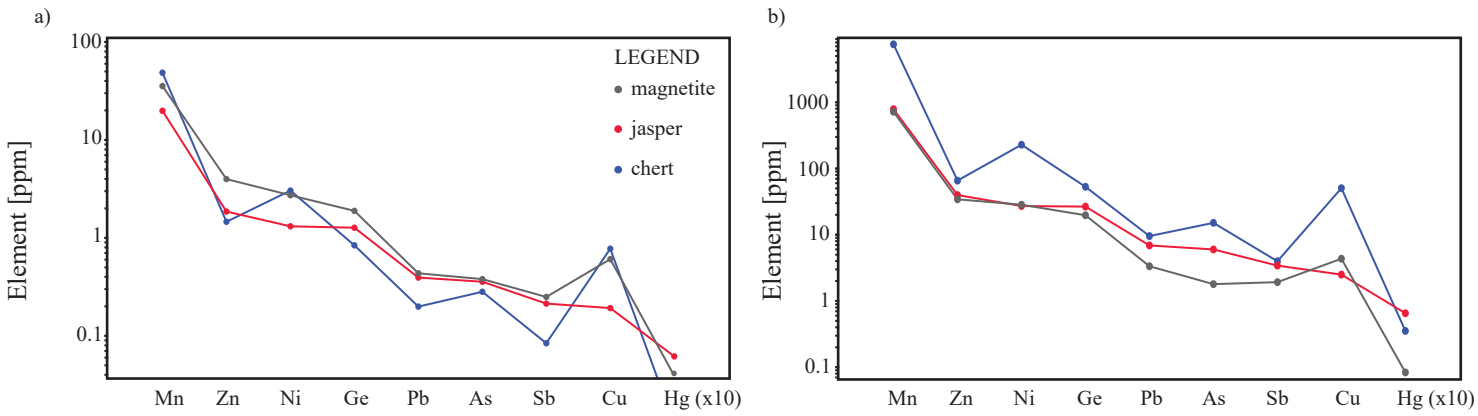


Figure 3.15: Trace element concentrations in the ferruginous and silicate component of oxide-facies BIF at Temagami, after subtraction of a calculated clastic component and normalization to 100% Si-free material. a) Element concentrations in the whole-rock, before correction show similar enrichments in many elements between the different facies. b) Element concentrations corrected for the clastic component and normalized to Si-free basis (see calculations in Table 3.13). Jasper and magnetite facies generally contain very similar transition metals, post-transition metals and metalloids, with some differences in the mobile elements, As, Sb, and Hg, that are lost from the jasper and magnetite facies during recrystallization.

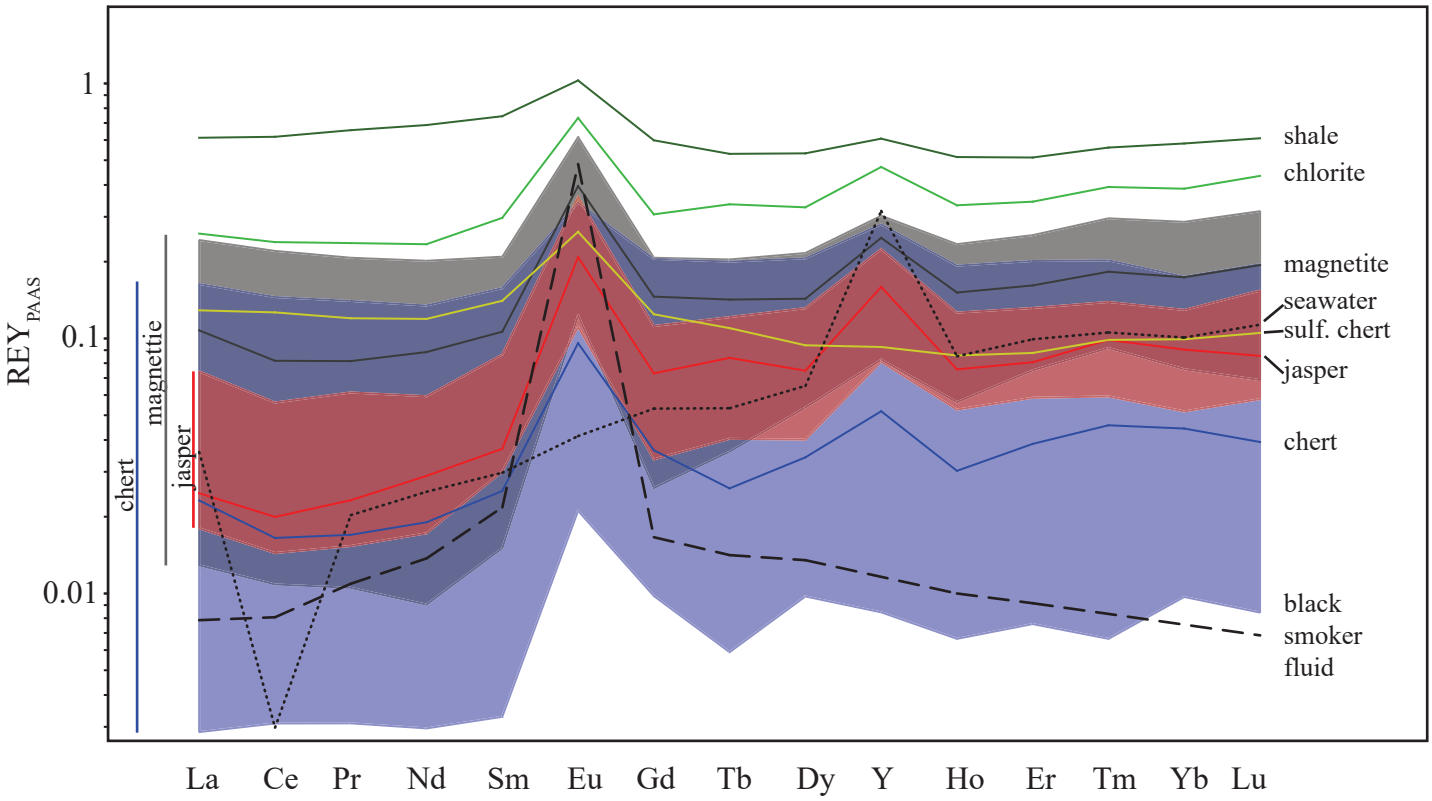


Figure 3.16: REY patterns (PAAS-normalized) for all samples. Oxide-facies BIF samples exhibit LREE-depletion and positive La, Eu, and Y/Ho anomalies, indicative of hydrothermally influenced seawater sources. Median jasper exhibits very similar Sm/Yb ratios from whole rock samples as Type 1 apatite in jasper (0.91 and 0.81, respectively), underlining the importance of apatite as primary host phase for REY in oxide BIF (see Chapter 2). Chlorite BIF is flatter with less pronounced anomalies due to primarily clastic material as REY source with minor hydrogenous influence. Sulfidic cherts have variable REE and Y enrichments and depletions, but are usually depleted in HREE compared to the other BIF facies, lack La or Y/Ho anomalies, and have smaller Eu anomalies. Lines are median values for each sample type. Shaded areas for jasper, chert and magnetite indicate 5th to 95th percentile. Reference lines average North Pacific seawater (dotted line, multiplied by 3000: Alibo and Nozaki, 1999) and modern Mid-Atlantic Ridge black smoker fluid (dashed line, multiplied by 100: Bau and Dulski, 1999).

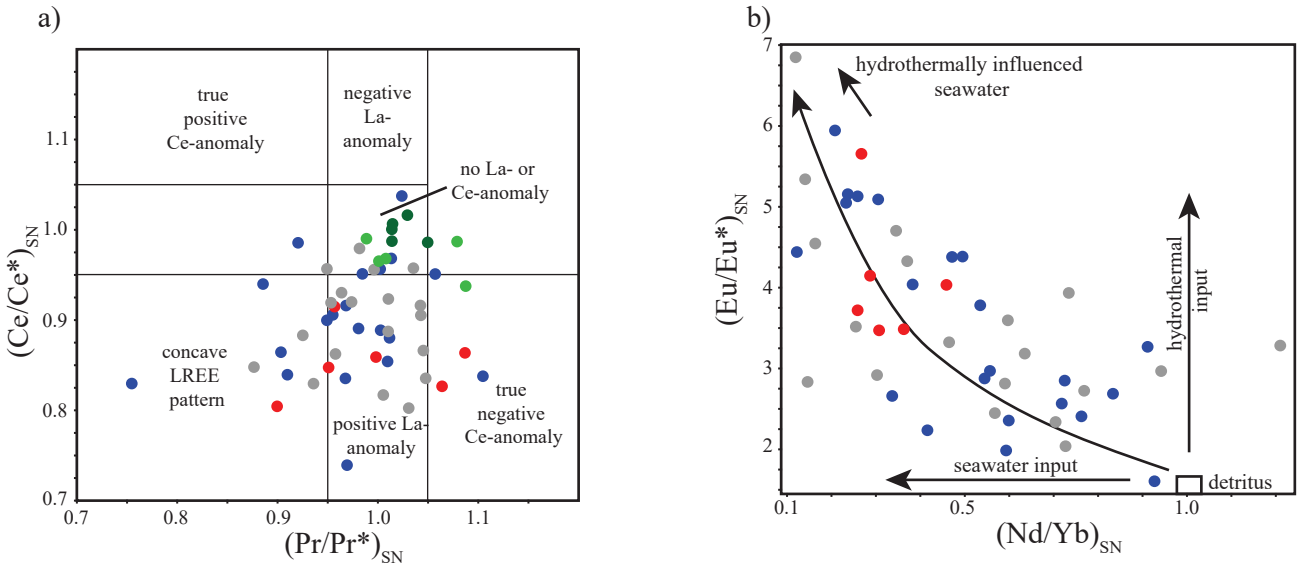


Figure 3.17: Whole-rock REE ratios for different facies of the Temagami BIF superimposed on discriminant diagrams for fine-grained sediments (shale) deposited in different types of basins. a) Ce/Ce* vs Pr/Pr* plot discriminating shale lithotypes deposited under conditions of true negative Ce anomalies, normally associated with oxidized water columns (lower right corner of diagram). Many apparent Ce anomalies are artifacts resulting from positive La anomalies. Data from the different BIF facies at Temagami mainly fall within the field of no Ce anomaly (modified from Bau and Dulski, 1996). b) Eu/Eu* vs Nd/Yb plot discriminating the contribution of hydrothermally influenced seawater from hydrogenous and detrital input (modified from Alexander et al., 2008). Higher Eu/Eu* from hydrothermal sources correlate with lower Nd/Yb from seawater, indicating a well mixed hydrothermal-seawater source as opposed to two independently active sources. See text for discussion. SN - shale normalized (PAAS, MacLennan, 1989).

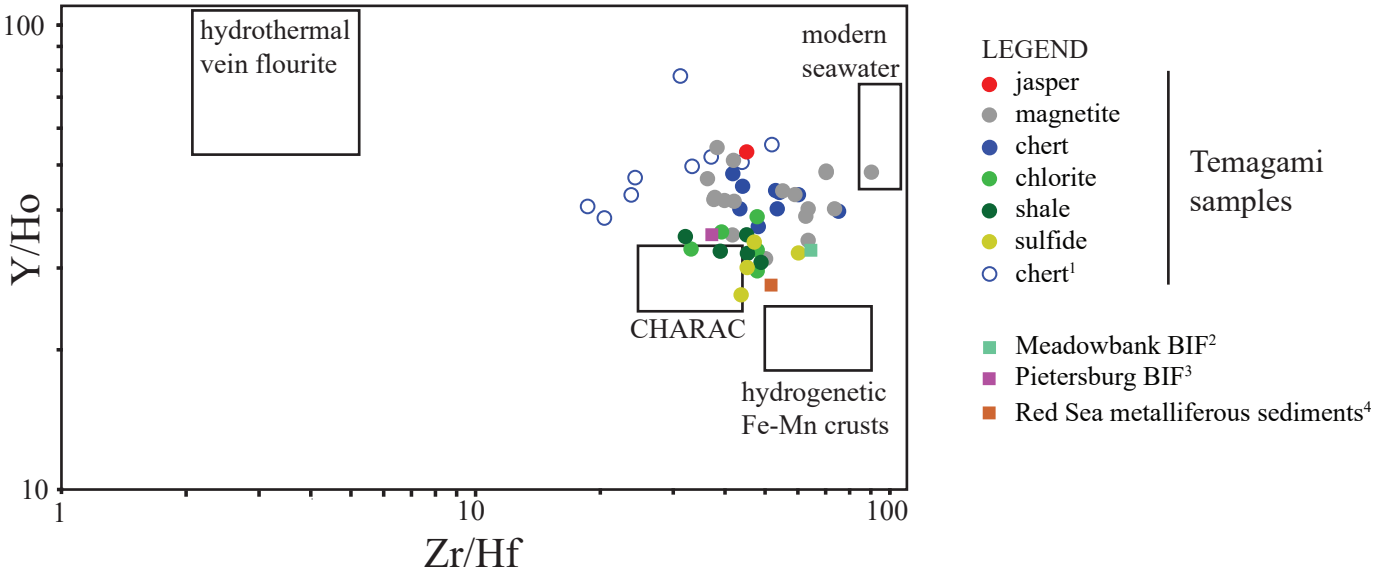


Figure 3.18: Whole-rock Y/Ho vs. Zr/Hf ratios for different facies of the Temagami BIF superimposed on the discrimination diagram of Bau (1996) for different crustal and fluid reservoirs. Fractionation of Zr/Hf and Y/Ho in BIF outside the CHARAC field (charge- and radius controlled) captured in BIF indicate seawater or hydrothermal sources. Solid symbols from this study; open symbols from 1 additional Temagami chert from Bau and Alexander (2009)[1]. Average values for 9 chert and magnetite samples from Meadowbank East Algoma-type BIF in the Western Churchill Province, MB (Gourcerol et al., 2015)[2], 14 samples from the 2.95 Ga Pietersburg Algoma-type BIF in the Kaapvaal craton (Alexander et al., 2009)[3], and 6 metalliferous mud samples from the Red Sea (Laurila et al., 2014)[4] are shown for comparison.

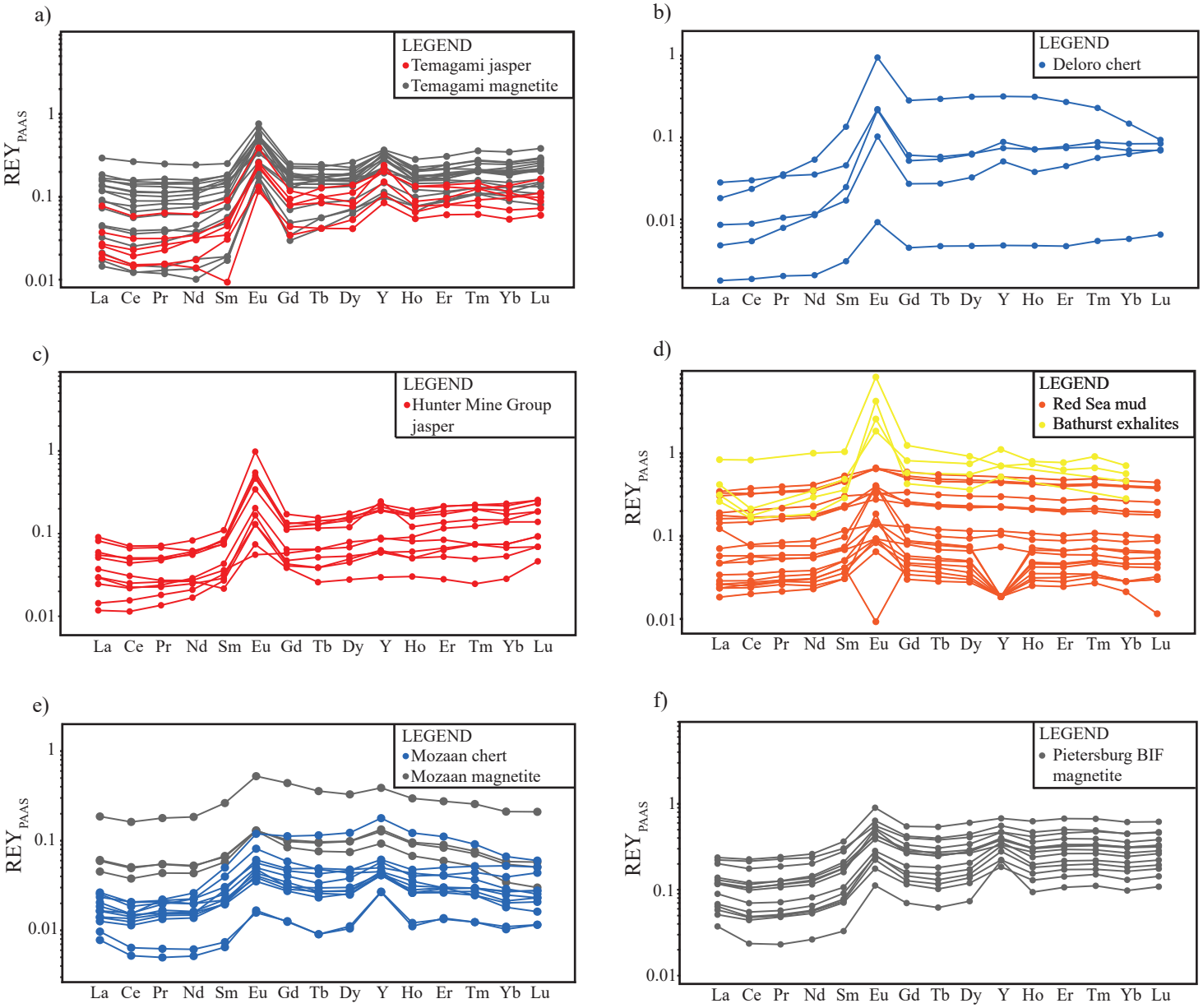

a)
LEGEND
Temagami jasper
Temagami magnetite
REY PAAS
1
0.1
0.01
La Ce Pr Nd Sm Eu Gd Tb Dy Y Ho Er Tm Yb Lu
b)
LEGEND
Deloro chert
1
0.1
0.01
La Ce Pr Nd Sm Eu Gd Tb Dy Y Ho Er Tm Yb Lu
c)
LEGEND
Hunter Mine Group jasper
1
0.1
0.01
La Ce Pr Nd Sm Eu Gd Tb Dy Y Ho Er Tm Yb Lu
d)
LEGEND
Red Sea mud
Bathurst exhalites
REY PAAS
1
0.1
0.01
La Ce Pr Nd Sm Eu Gd Tb Dy Y Ho Er Tm Yb Lu
e)
LEGEND
Mozaan chert
Mozaan magnetite
REY PAAS
1
0.1
0.01
La Ce Pr Nd Sm Eu Gd Tb Dy Y Ho Er Tm Yb Lu
f)
LEGEND
Pietersburg BIF magnetite
REY PAAS
1
0.1
0.01
La Ce Pr Nd Sm Eu Gd Tb Dy Y Ho Er Tm Yb Lu

Figure 3.19: Comparison of REY systematics of oxide-facies BIF from Temagami with other BIF and modern metalliferous sediments. a) Results for jasper and magnetite in Temagami BIF show similar abundances of REY and consistent patterns typical of REY supplied non-episodically from a large, stable open ocean. b) REY patterns from the Deloro BIF are similar to the Temagami BIF, but do not show as consistently positive La, Y, and Eu anomalies. The Deloro BIF is hosted in the 2.73 Ga Deloro assemblage of the Abitibi greenstone belt, and forms a regionally extensive but thin (600 km strike length, <10 m thick) marker horizon attributed to the mixing of Archean deep and shallow seawater at a chemocline (Thurston et al., 2012). Results from Baldwin et al. (2012). c) Jasper samples from the 2.73 Ga Hunter Mine Group contain similar REY compared to the Temagami BIF, but more variable La, larger Eu, and smaller Y anomalies, indicative of deposition in response to localized mixing of hydrothermal fluid and seawater in a caldera setting (Chown et al., 2000). Results from Brengman and Fedo (2018). d) Two examples of Fe-rich exhalites from the Bathurst VMS mining camp (data from Peter and Goodfellow, 1996) and the present-day Red Sea (data from Laurila et al., 2014b). Variable Y, Eu, and La anomalies in the Bathurst and Red Sea muds reflect deposition from small, hydrothermally sourced water bodies (e.g., brine pools) with limited exchange with open seawater. e) Magnetite and chert from the 2.9 Ga Mozaan BIF reflect deposition in a shallow marine shelf environment, likely an early example of early Superior-type BIF formation. Smaller Eu anomalies, and larger but variable La and Y anomalies than observed in the Temagami BIF are interpreted to reflect variable contribution from continental weathering and upwelling of Archean deep seawater (results from Alexander et al., 2008). f) The 2.95 Ga Pietersburg BIF was deposited in a deep water open ocean setting in a greenstone belt in the Kaapvaal craton, South Africa, reflected in REY patterns and abundances are very similar compared to the Temagami BIF (Alexander et al., 2009).

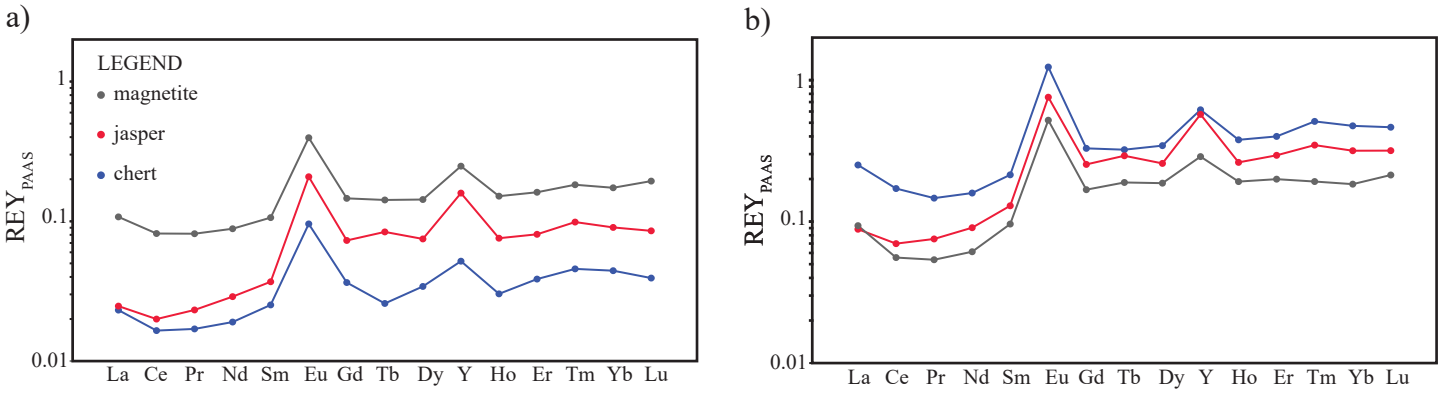


Figure 3.20: REE concentrations in the ferruginous and silicate component of oxide-facies BIF at Temagami, after subtraction of a calculated clastic component and normalization to 100% Si-free material. a) Whole-rock (uncorrected) PAAS-normalized REY plot of magnetite, jasper, and chert (median values) showing the similar patterns for all facies but variable REY concentrations. b) After correction, differences in all REY between jasper and magnetite are much less pronounced.

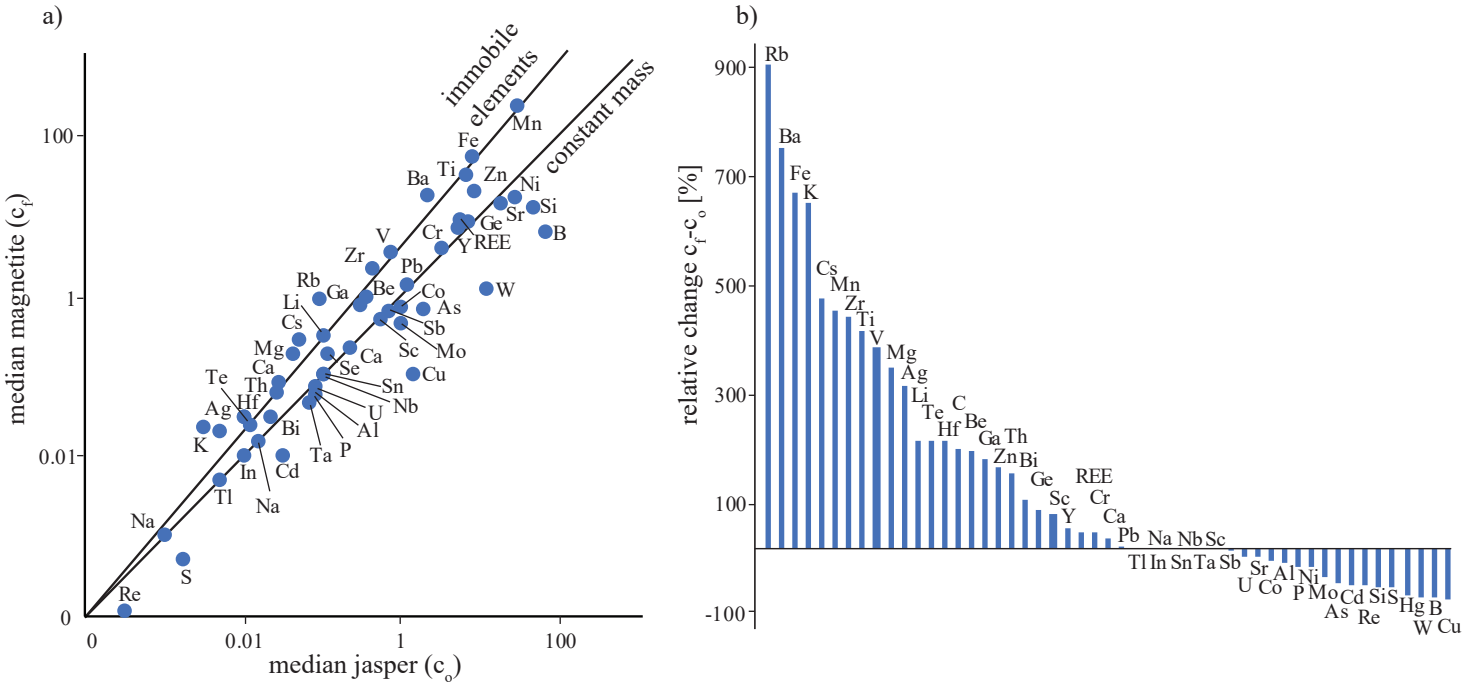


Figure 3.21: Isocon plot (after Grant, 2005) illustrating geochemical changes during diagenesis between the "least altered" primary precipitate (jasper facies) and most altered, recrystallized material (magnetite facies). Abundances are based on median values of samples SM052-2 and -4 and SM011-2 for jasper and median values of 11-2, 11-17-2, and SM052-1, -5, -6 for magnetite. a) Plot of major (in element wt.%) and trace elements (in ppm) with lines for constant mass and immobile elements (Ti, Zr) indicated. Elements plotting above the lines are enriched during the recrystallization from jasper to magnetite; elements below the isocon are lost. Note the logarithmic scale on the axes, making differences between starting compositions and final compositions (co and cf) and deviations from the isocon appear smaller than they would on linear axes. b) Relative changes in percent between jasper and magnetite. Positive values indicate enrichment in magnetite. The largest positive changes are due to the preferential incorporation of Fe, Mn, V, Ti, Ge, Ga, and Cr in magnetite; K, Rb, Cs, Mg, Ga, and Zn in biotite; Ca, Sc, Y, REE, Li, Th, and Pb in apatite; and C, Ca, Mg, Mn, Rb, Li(?), and Bi(?) in carbonate. Zr, Hf, Th are concentrated in refractory minerals such as trace zircon during volume loss reactions. Elements preferentially lost from primary jasper facies were either mobile during diagenesis (Si, B, P, Sr, Ni, Mo, W, Re, U, As, Hg, Cd) and/or no suitable host mineral was formed (e.g., lack of sulfides and the resulting in the loss of S, Cu, As, Sb, Cd, Ni, Co, and Mo).

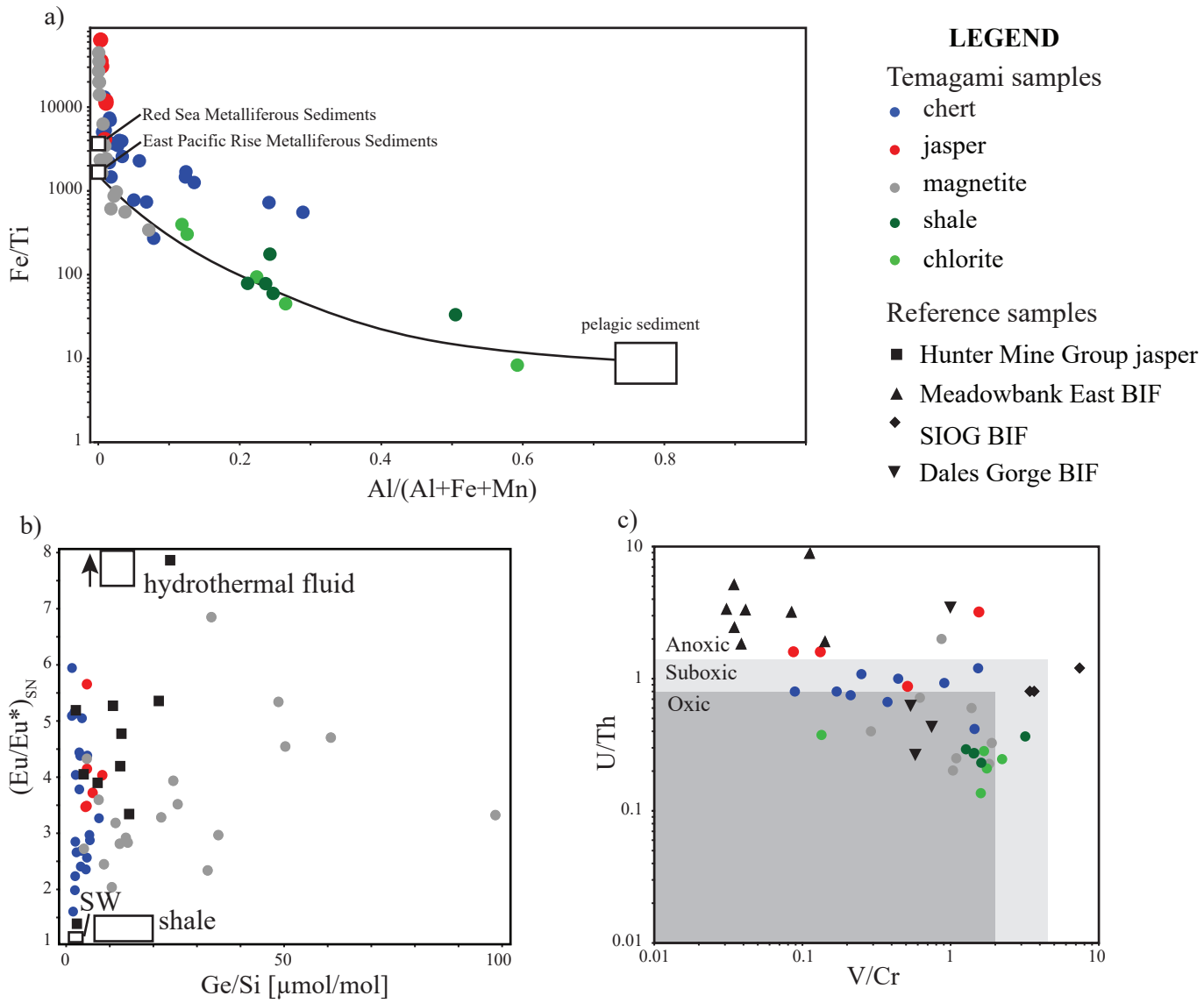


Figure 3.22: Whole-rock trace element plots for different facies of the Temagami BIF superimposed on the discrimination diagrams for hydrothermal sediments . a) Boström (1973) plot showing the mixing curve between hydrothermal sediment and background pelagic sediment in the modern ocean. Oxide-facies BIF from Temagami overlap with modern metalliferous sediments, whereas shale, and chlorite-facies BIF and some contaminated chert samples plot mixing lines with background sediment. b) Comparison of the Eu anomaly in chert and jasper with the Ge/Si ratio, forming a poorly constrained mixing line between seawater and high-temperature hydrothermal fluid. Higher Ge/Si is attributed to enrichment by mineralogic control due to preferential incorporation of Ge in magnetite. Endmember values for Ge/Si after Froehlich et al. (1992) and Mortlock et al. (1993), shale are values for average shale (Eu/Eu* = 1.3-1.5; Ge/Si = 6-20) based on several BIF-related Archean shale averages (Hannington et al., 2012, Cabral et al., 2013, this study). Eu/Eu* for high-temperature hydrothermal fluid from Douville et al. (1999). SW is modern seawater (Bruland et al., 2014). Eu/Eu*SN is normalized to PAAS (MacLennan, 1989). Results for jasper samples from the Hunter Mine Group are from Brengman and Fedo (2018). c) U/Th versus V/Cr plot used to identify redox conditions in post-GOE black shales (after Jones and Manning, 1994, Piercey et al., 2016). Authigenic enrichments of V and U are common in modern anoxic basins, oxidative U mobilization has been suggested by the Temagami ocean but the same systematics are not observed in Archean sediments where oxic/anoxic transitions were absent. Reference results from BIF of 3.5-2.48 Ga show similarly poorly resolved U/Th and V/Cr systematics as captured in the Temagami BIF. Results for reference samples are 3.0 Ga SIOG BIF from Mukhopadhyay et al. (2002), 2.71 Ga Meadowbank East BIF from Gourcerol et al. (2016), and 2.48 Ga Dales Gorge (Superior type) BIF from Pecoits et al. (2009).

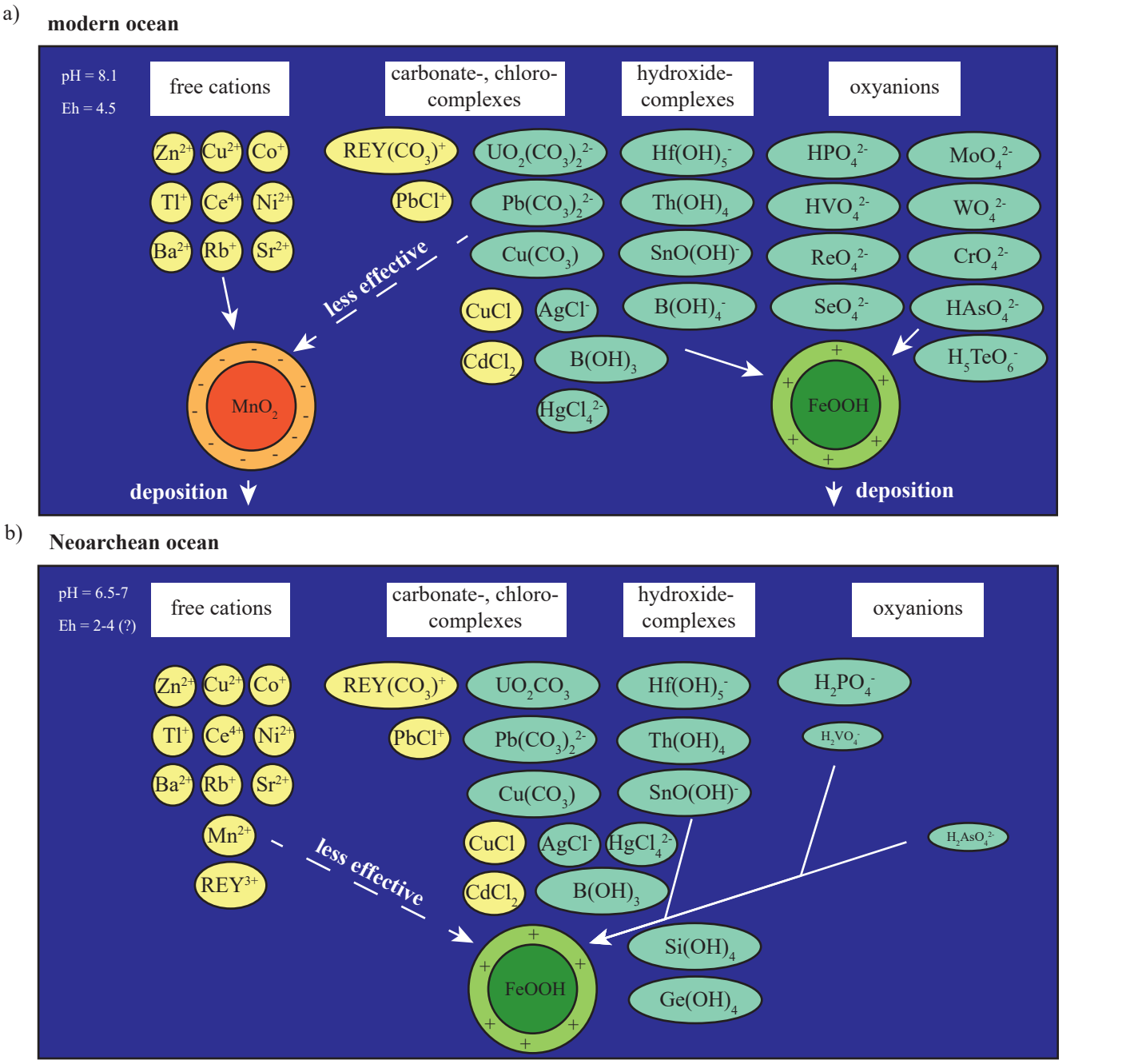


Figure 3.23: Simplified illustration of the adsorption onto Fe- and Mn-oxyhydroxide particles in modern and Neoarchean oceans. a) Adsorption processes in the oxygenated modern ocean are dominated by Mn-oxides and Fe-oxyhydroxides, scavenging a range of metal-complexes and free cations, modified from Hein et al. (2013) and Koschinsky and Halbach (1995), with additional complexes after Byrne et al. (1988). b) Neoarchean oceans had lower pH and Eh (e.g., Saito et al., 2003), and did not produce Mn-oxides or abundant metal-oxyanions. Scavenging was dominated by Fe-oxyhydroxides and Mn was present only as Mn^{2+} and itself scavenged by Fe-oxyhydroxides. Silicic acid and hydroxyl complexes of Ge were more abundant in the Temagami ocean and effectively adsorbed onto FeOOH surfaces despite the overall neutral charge of the complex. The presence of boric acid and borate are pH dependent, and $B(OH)_4^-$ is more efficiently scavenged at higher pH because of the increased electrostatic adsorption compared to neutral $B(OH)_3^0$. Several species would have been present as different complexes in the pH-Eh range assumed for the Neoarchean ocean due to protonation reactions at lower pH (e.g., U as UO2CO3 [uranyl carbonate], V as $H_2VO_4^-$, and As as $H_2AsO_4^{2-}$). pH/Eh for modern ocean from Saito et al. (2003) and Glasby and Schulz. pH for the Archean ocean is from Saito et al. (2003) and Halevy and Bachan (2017). Eh of Archean seawater is estimated for a system at 25°C buffered by the Fe^{2+}-FeO(OH) redox pair and below the Ce-Mn oxide stability after Brookins (1988). Symbol size approximates the relative concentrations of the different species interpreted from the specified ocean conditions.

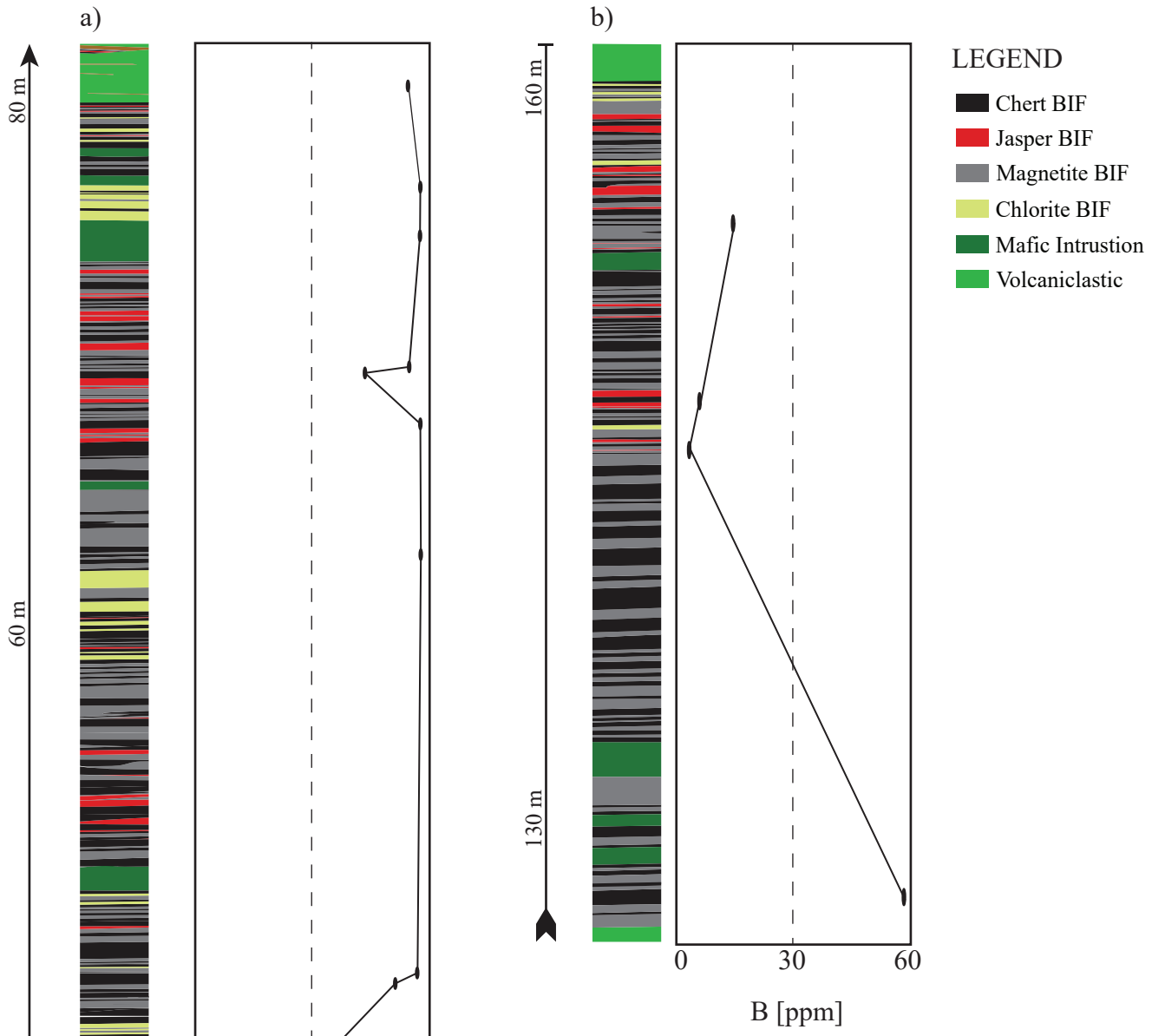


Figure 3.24: Spatial variation of B in chert and jasper samples from the Hwy 11 exposure of the Temagami BIF. A temporal decrease in B concentration may reflect changing pH of the water column or changes in the B budget of the depositional basin (see text for discussion on basin pH changes in response to Fe-oxidation and B speciation under changing pH). Younging is up section (stratigraphy in panel a is older than panel b), see Figure 3.4 for details.

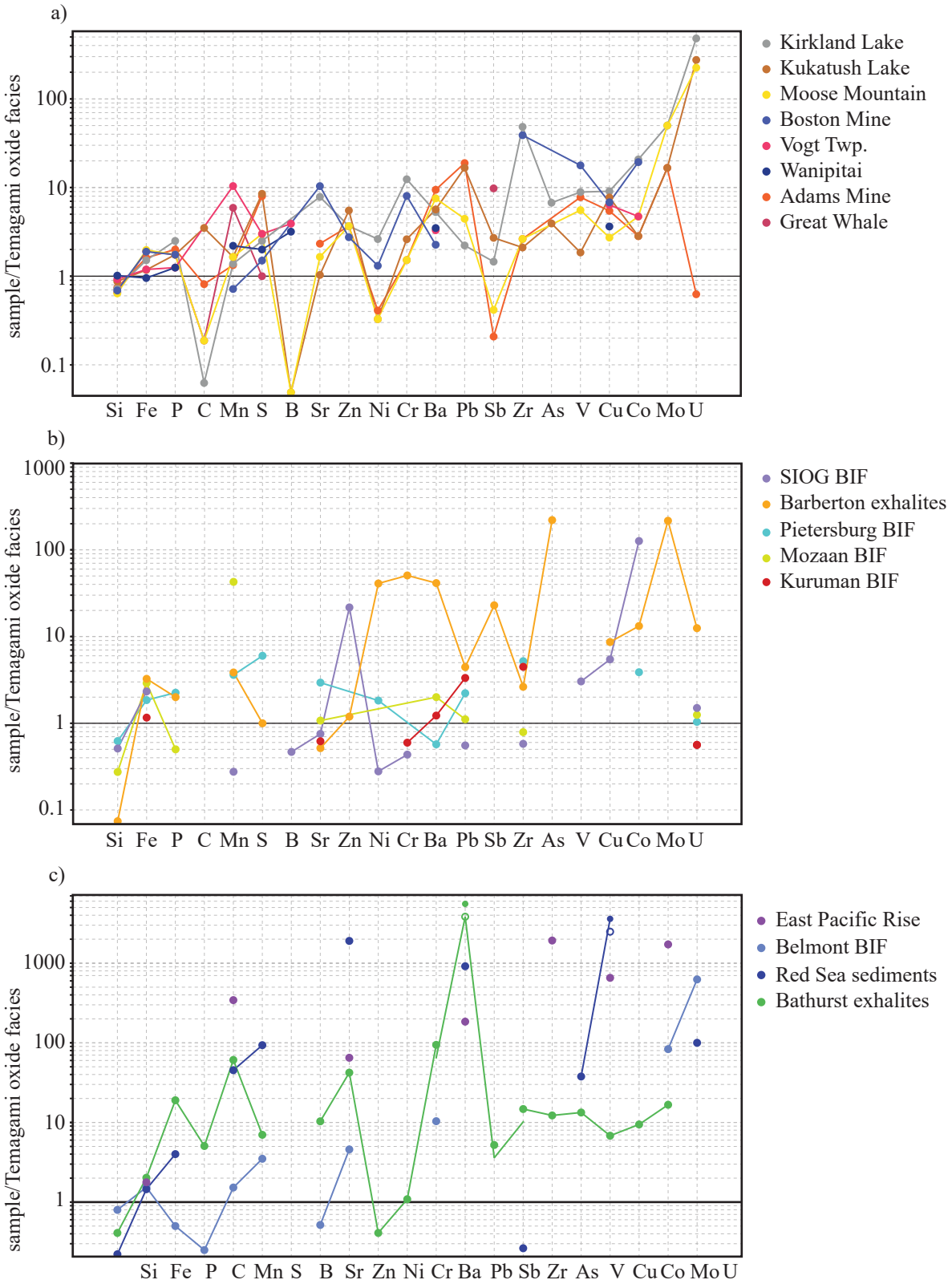


Figure 3.25: Chemistry of Temagami BIF compared to other BIF and metalliferous sediemnts. a) Algoma-type BIF of similar age and provenance as the Temagami BIF show mostly within one order of magnitude higher major and trace element contents, except C, B, Ni, Sb, and U in some deposits. Values normalized to median Temagami oxide facies. b) Other examples of BIF, including Superior-type, older Algoma-type BIF, and Archean exhalites have similar major- and trace element patterns within one order of magnitude as the Temagami BIF, with the exception of Archean exhalative deposits containing higher Ni, Cr, and hydrothermal components (Pb, Sb, As, and Cu). c) Proterozoic, Paleozoic and modern metalliferous sediments and VMS-related exhalites deposited in proximity to hydrothermal venting or from a hydrothermal brine pool are enriched up to three orders of magnitude in hydrothermal components (Pb, Sb, As, and Cu) compared to Temagami oxide facies. Elements listed in decreasing order of abundance in Temagami oxide facies BIF. All values normalized to median Temagami oxide facies. All values and references listed in Table 3.14.

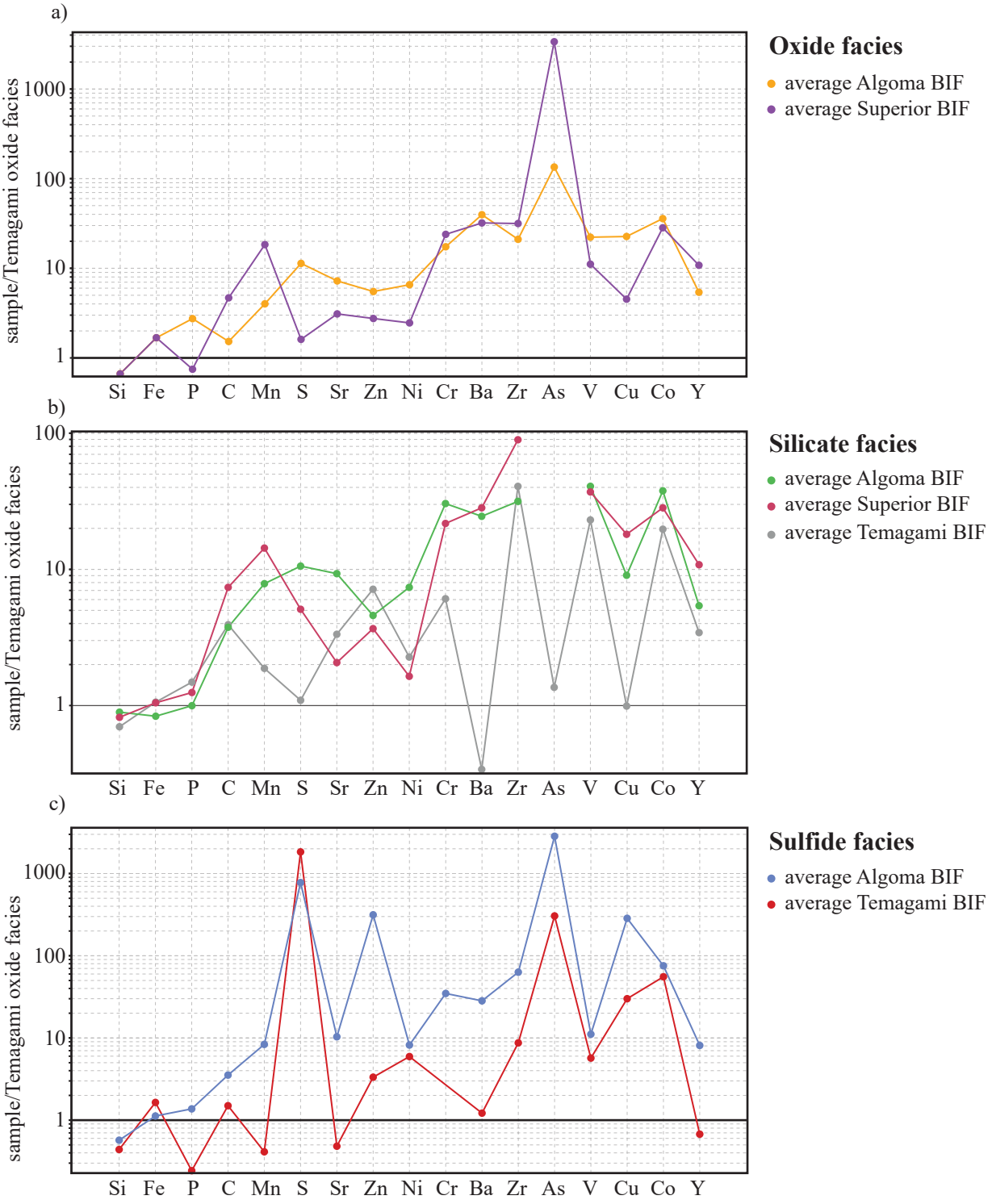


Figure 3.26: Composition of average oxide-, silicate-, and sulfide facies in Superior- and Algoma-type BIF normalized to Temagami oxide facies. a) Average oxide facies in Algoma- and Superior-type BIF. All trace elements (except Ba) and most major elements are more abundant in both oxide facies Algoma- and Superior-type BIF than in Temagami oxide facies, indicative of Temagami BIF deposition from open ocean compared to hydrothermal deposition (Algoma) or upwelling of metal-rich bottom waters (Superior) Averages of 963 (Algoma) and 176 (Superior) samples. b) Composition of silicate facies is variable, but overall similar between Algoma-type, Superior-type BIF, and average Temagami silicate facies. Silicate facies chemistry does not follow clear trends, but is determined by the material captured in BIF and variable influence of hydrogeonus components. Average of 18 (Algoma) 23 (Superior), and 6 (Temagami) samples. c) Sulfide facies in average Algoma-type BIF is more enriched in trace elements than sulfide facies in Temagami BIF. Higher hydrothermal components in average Algoma-type BIF is due to close association of most deposits with hydrothermal venting, while sulfide facies in Temagami BIF is controlled by bacterial activity under open ocean conditions (see Chapter 3). No average values available for sulfide facies Superior-type BIF. All values from Gross (2009), reported averages of a total of 1300 samples from 45 iron formations.

Chapter 4

Decoupling of Neoarchean Sulfur Sources Recorded in Algoma-type Banded Iron Formation

Published as:

Diekrup, D., Hannington, M.D., Strauss, H., Ginley, S.J., 2018. Decoupling of Neoarchean sulfur sources recorded in Algoma-type banded iron formation. Earth and Planetary Science Letters 489, 1-7.

Abstract

Neoarchean Algoma-type banded iron formations (BIFs) are widely viewed as direct chemical precipitates from proximal volcanic-hydrothermal vents. However, a systematic multiple sulfur isotope study of oxide-facies BIF from a type locality in the ca. 2.74 Ga Temagami greenstone belt reveals mainly bacterial turnover of atmospheric elemental sulfur in the host basin rather than deposition of hydrothermally cycled seawater sulfate or sulfur from direct volcanic input. Trace amounts of chromium reducible sulfur that were extracted for quadruple sulfur isotope (^{32}S-^{33}S-^{34}S-^{36}S) analysis record the previously known mass-independent fractionation of volcanic SO_2 in the Archean atmosphere (S-MIF) and biological sulfur cycling but only minor contributions from juvenile sulfur, despite the proximity to volcanic sources. We show that the dominant bacterial metabolisms were iron reduction and sulfur disproportionation rather than sulfate reduction, consistent with limited availability of organic matter and the abundant ferric iron deposited as $Fe(OH)_3$, and that sulfur contained in the BIF was mainly atmospheric rather than a direct volcanic-hydrothermal input as expected. These findings change the view of an important archive of the Neoarchean sulfur cycle, in which the sulfur pools are strongly decoupled and only species produced photochemically under anoxic atmospheric conditions were deposited in the BIF-forming environment.

4.1 Introduction

Precambrian banded iron formation (BIF) provides an important record of ancient marine paleoenvironments, atmospheric conditions, and bacterial metabolisms involved in its formation (Kappler and Newman, 2004; Konhauser et al., 2005; Viehmann et al., 2014). Trace elements and a range of different isotopic systems in BIF track the evolution of the oceans and atmosphere as far back as 3.8 Ga (Ohmoto et al., 2006; Bau and Alexander, 2009; Konhauser et al., 2009; Bekker et al., 2010). Studies of sulfur systematics have focused mainly on Superior-type BIF, ranging in age from 2.7 to 1.8 Ga, that formed in shallow, continental-shelf settings with uncertain but distal sources of iron (Johnston et al., 2006; Partridge et al., 2008; Mishima et al., 2017). Those studies showed the predominance of bacterial sulfate reduction promoted by abundant organic carbon available in Superior-type BIF. Algoma-type BIF, which formed in deep, semi-enclosed Neoarchean volcanic basins, derived its iron mainly from local volcanic-hydrothermal sources (Bekker et al., 2010). This type of BIF is useful for gauging hydrothermal input into the basins, but it is not the type of BIF normally studied to understand atmospheric conditions. Sulfur systematics in Algoma-type BIF are also expected to reflect the proximal volcanic input. However, data presented in this paper suggest that other sources (i.e., atmospheric deposition) were more important, even where major hydrothermal activity was underway.

Algoma-type BIF is a ubiquitous feature of Archean greenstone terranes, such as in the Southern Superior Province of Canada, with more than 150 mapped occurrences in the Abitibi-Wawa region alone (Fig. 4.1). They are typically small in comparison to Superior-type BIF, generally <100 m thick and <100 km^2 in area, and are closely associated with submarine volcanic rocks,

especially felsic volcanic centers that also host volcanogenic massive sulfide deposits (e.g., Gross, 1965; Franklin et al., 2005). Individual occurrences contain tens to hundreds of millions of tonnes of iron ore precipitated from the nearby seafloor hydrothermal vents. The flux of Fe to these local basins was comparable to that of the largest volcanic-hydrothermal systems in today's oceans (Ohmoto et al., 2006). The ~2.74 Ga Temagami BIF in Ontario (Fig. 4.1; Ayer et al., 2006) is widely recognized as a type locality for Archean greenstone-hosted BIF (Gross, 1980) and has been a benchmark for understanding their formation (Ohmoto et al., 2006; Bau and Alexander, 2009). In this study, we analyzed multiple sulfur isotopes (^{32}S-^{33}S-^{34}S-^{36}S) in trace amounts of chromium reducible sulfur (CRS) extracted from 52 samples of the oxide-facies and contemporaneous sediments to constrain the sources of reduced sulfur.

Archean sediments deposited before ~2.3 Ga record mass-independent fractionation of sulfur species (S-MIF) produced photochemically from atmospheric SO_2 (Farquhar et al., 2000; Guo et al., 2009). Two dominant sulfur species entered the marine environment from the atmosphere: SO_4 and zero- or near-zero valent sulfur (expressed here as S_8 for simplicity). The oxidized sulfur species that entered the marine environment as sulfate have a $\Delta^{33}S_{SO4}$ <0‰; S_8 has a $\Delta^{33}S_{S8}$ >0‰ (e.g., Ono et al., 2003). Both sulfur species were transferred to Archean sediments via a number of different biotic and abiotic pathways, including bacterial sulfate reduction (BSR) and disproportionation of elemental sulfur (BSD; Farquhar et al., 2000; Philippot et al., 2007; Lyons, 2009; Jamieson et al., 2013). These different pathways have been investigated in marine black shales, volcanogenic massive sulfide deposits, sandstones, rare barite deposits, and in carbonates using the S-MIF signal (Bao et al., 2007; Bekker et al., 2009; Guo et al., 2009; Wacey et al., 2010; Philippot et al., 2012; Roerdink et al., 2012; Montinaro et al., 2015). Recent studies of Eoarchean (>3.8 Ga) lithologies from the Nuvvuagittuq greenstone belt (Ungava Peninsula)

used the S-MIF signal to show the supracrustal character of these units (Thomassot et al., 2015). Another study of highly metamorphosed rocks of similar age in China, interpreted to be Algoma-type oxide-facies BIF, also reported S-MIF (Hou et al., 2007). The two studies showed a typical array for Archean metasediments of positive $\Delta^{33}S$ and positive $\delta^{34}S$, indicating atmospheric sulfur sources but no biological activity (Thomassot et al., 2015), and negative $\Delta^{33}S$ with variable $\delta^{34}S$, indicating bacterial sulfate reduction (Hou et al., 2007). Similar results were obtained in a small study of samples from the Abitibi greenstone belt (three samples of pyritic argillite and one sample of sulfide facies iron formation: Thurston et al., 2012). Our samples from the Temagami BIF reveal a different story of metal and sulfur sources and diverse microbial metabolisms.

4.2 Samples and Methods

4.2.1 Samples

The sampled BIF occurs in two units (up to 160 m in thickness each) belonging to a 4-km thick bimodal volcanic succession of the Temagami greenstone belt (Fig. 4.1). From 1964 to 1990, the north and south BIF units were exploited in the former Sherman iron mine (Donaldson and Garrett, 1991; Gross 1980), and a classic exposure of the mined BIF, corresponding to the strike extension of the South Pit of the Sherman Mine, is still accessible in outcrop along Highway 11 (Figs. 4.1 and 4.2). All units now dip subvertically, exposing continuous sections of the BIF and adjacent lithologies. Contemporaneous volcaniclastic metasediments and sulfidic cherts occur along strike from the southern BIF units within 5 km. The host volcanic succession comprises subaqueous mafic volcanic rocks with south-facing pillows, indicating younging directions,

intercalated with felsic flow units, abundant felsic volcaniclastic rocks and shale. Mapping and sampling of the volcanic host rocks previously identified rhyolitic feeder dykes, interpreted to be volcanic vents, in the stratigraphic footwall of the BIF horizons in the central part of the mine (Bennett, 1978; Fyon and Crocket, 1986). Widespread chloritization and sericitization of the volcanic rocks is evident, as well as Na loss and variable Eu anomalies, typical of synvolcanic hydrothermal alteration (Fyon and Crocket, 1986; Schwartz, 1995). The BIF units are dominated by jasper-magnetite layering, mainly in the open pits, and a larger volcaniclastic component with chert and lesser magnetite and jasper in the Hwy 11 outcrop. The different layers are interpreted to be products of precipitation from silica- and iron-enriched bottom waters; the primary precipitate most likely a Si-Fe(oxy)hydroxide gel from which the present mineral assemblage crystallized during burial and diagenesis (Gross, 1980; Bekker et al., 2010). Locally abundant sulfidic chert occurred at the transition from the volcaniclastic footwall to the BIF, in particular near the western end of the south pit. The relative abundance of volcaniclastic material increases with distance from the mine as dilution by chemical precipitates decreases. Regional metamorphism of the entire succession did not exceed greenschist facies conditions (Bennett, 1978; Bowins and Heaman, 1991).

Samples were collected for this study from the Highway 11 outcrop, from surface outcrops within the mine, and from a collection taken in the open pits by G.A. Gross and I.R. Jonasson (Geological Survey of Canada) when the mine was in operation. Samples of sulfidic chert, volcaniclastic sediment, minor massive sulfide and mafic intrusive (dikes) and extrusive rock were also collected from within the BIF-hosting section. The BIF samples consist of cm-scale oxide and silicate layers (Fig. 4.3a, b) that were cut into separate jasper (hematitic) bands, chert bands, magnetite bands, and chlorite-rich bands. Many of the original depositional textures were

preserved through the regional lower greenschist metamorphism, and only limited recrystallization occurred since burial. Common accessory minerals include apatite, monazite, (Fe-rich) dolomite, ankerite, pyrite, and pyrrhotite. Pyrite, which is the dominant sulfide (>95%), occurs mainly as very fine disseminations of sub- to euhedral grains, 5-20 μm in size, commonly as inclusions in other phases. Trace sulfides occurring as inclusions in magnetite (Fig. 4.3c) indicate that sulfur was present in the BIF before the diagenetic growth of magnetite and is not a later addition. The sampled sulfidic cherts are mainly quartz-rich, with pyrite, chlorite, apatite, Fe-rich dolomite, and only trace graphitic carbon. Fine-grained volcaniclastic material intercalated with BIF was collected from the Highway 11 outcrop and from a number of other exposures throughout study area. In the mine, discrete layers of mainly chlorite, quartz and magnetite are interpreted to be mainly altered volcanic ash, which also contains secondary epidote, ilmenite, biotite, and trace pyrite.

4.2.2 Methods

Chemical extraction of sulfur and isotope analyses were carried out at the *Institut für Geologie und Paläontologie* at the Westfälische Wilhelms-Universität Münster, Germany. Samples with obvious alteration or veins cutting layering were avoided, and surface weathering was removed from all samples before processing. The absence of weathering was confirmed by petrographic and SEM investigation; samples showing oxidation of pyrite, or porosity that might be indicative of mineral dissolution, were excluded from the study. Reflected light microscopy and SEM analyses confirm that pyrite is the only important sulfide mineral in the samples. All sample material was milled to analytical grade powder in a ceramic ring mill. Sulfur extractions and isotope analyses were carried out following the method of Canfield et al. (1986), liberating sulfur

from mono- and disulfides in two steps: acid volatile sulfur (AVS) for monosulfides (e.g., pyrrhotite) extracted with HCl and chromium reducible sulfur (CRS) for disulfides extracted with $CrCl_3$. The extractable sulfides (typically between 0.05 and 1 wt.% S: Table 4.1) occur mainly as trace amounts of ultrafine disseminated pyrite, which is present in all of the BIF layers and volcaniclastic sediments. For the samples of sulfide-poor BIF, we used excess reactants and longer than normal reaction times in order to recover the very low amounts of sulfur in the samples.

All of the samples yielded CRS; only four samples yielded AVS (see Table 4.2). During both AVS and CRS steps, sulfur liberated as H_2S was precipitated as Ag_2S, which was used for gravimetric determination of S_{AVS} and S_{py}. The low sulfide concentrations in the BIF meant that large amounts of sample material (up to 40 g) were required to yield more than 2 mg of sulfur as Ag_2S. Especially in the case of magnetite-rich samples, effective extractions were only achieved when HCl and $CrCl_3$ were added in excess (i.e., double the laboratory standard of 20 ml of 25% HCl for AVS, and 30 ml of $CrCl_3$ for CRS). Longer than normal reaction times of 2 h for the AVS and 4 h for the CRS steps and addition of zinc pellets into the reaction bulb also were required to achieve quantitative extractions. Incomplete extractions in some samples may have been a result of reduction of Fe^{3+} from magnetite, depleting the reduction potential of the extraction solution. To test this, a new bottle of trapping solution was attached to the extraction line for each sample, and additional HCl and $CrCl_3$ solution were injected. The extraction was considered quantitative when the Ag_2S precipitate stopped forming in the trapping solution.

For the determination of multiple sulfur isotope ratios, 2 mg of the Ag_2S precipitate was fluorinated in Ni-reactors, yielding quantitative conversion to SF_6 after a reaction time of 8 h at 300 °C. The SF_6 gas was then purified cryogenically and chromatographically by the method of

Ono et al. (2003) and analyzed on a Thermo Finnigan MAT 253 gas-source mass spectrometer with a dual inlet system. Results are reported as $\delta^{34}S$ (‰ vs. V-CDT), $\Delta^{33}S$ (‰) and $\Delta^{36}S$ (‰), following equations 4.1-4.3, respectively, from Farquhar et al. (2000):

$$\delta^{34}S = \frac{\left(\frac{^{34}S}{^{32}S}\right)_{sample} - \left(\frac{^{34}S}{^{32}S}\right)_{V-CDT}}{\left(\frac{^{34}S}{^{32}S}\right)_{V-CDT}} \times 1000\ [‰] \qquad \text{[eq. 4.1]}$$

$$\Delta^{33}S = \delta^{33}S - 1000 \times \left[\left(1 + \frac{\delta^{34}S}{1000}\right)^{0.515} - 1\right]\ [‰] \qquad \text{[eq. 4.2]}$$

$$\Delta^{36}S = \delta^{36}S - 1000 \times \left[\left(1 + \frac{\delta^{34}S}{1000}\right)^{1.90} - 1\right]\ [‰] \qquad \text{[eq. 3]}$$

Long term 1σ internal reproducibility documented by repeated measurements of IAEA-S1 standard material is ± 0.050‰, ± 0.005‰, and ± 0.15‰ for $\delta^{34}S$, $\Delta^{33}S$ and $\Delta^{36}S$, respectively (cf. Kurzweil et al., 2013). Duplicate CRS extractions (two samples) were reproducible to within 0.006‰, 0.3‰, and 0.25‰ for $\Delta^{33}S$, $\Delta^{36}S$, and $\delta^{34}S$. Acid volatile sulfide (AVS) was also measured in four of the samples (Table 4.2).

4.3 Results and Discussion

The sulfide extractions yielded between <5 ppm and ~10,000 ppm S_{CRS} from the BIF samples and up to 30,000 ppm from sulfidic cherts (higher in one massive sulfide sample, see Table 4.1). The $\delta^{34}S_{CRS}$ values (V-CDT) range from -4.2‰ to +4.2‰, similar to previously obtained values reported by (Bowins and Crocket, 1994). The $\Delta^{33}S_{CRS}$ values for all samples vary between -0.857‰ and +2.288‰, and $\Delta^{36}S_{CRS}$ values range from -1.8 ‰ to +0.9 ‰, forming an array with

a $\Delta^{36}S/\Delta^{33}S$ slope of -0.72 ($r^2 = 0.73$). A strong lithologic control on the sulfur isotope values is apparent in a $\Delta^{33}S/\delta^{34}S$ crossplot (Fig.4.4a), where BIF samples exhibit mostly positive $\Delta^{33}S_{CRS}$ and negative $\delta^{34}S_{CRS}$ values, volcaniclastic samples have positive $\Delta^{33}S_{CRS}$ and positive $\delta^{34}S_{CRS}$ values, and sulfidic cherts have negative $\Delta^{33}S_{CRS}$ and variable $\delta^{34}S_{CRS}$ values. There is no apparent correlation between $\delta^{34}S_{CRS}$, $\Delta^{33}S_{CRS}$ and the abundance of S_{CRS}.

Despite the low sulfide contents of the samples, the range of $\Delta^{33}S_{CRS}$ values for Temagami BIF encompasses over 60% of the known natural variation in $\Delta^{33}S$ for this time period (Ono et al., 2003; Kurzweil et al., 2013) and indicates several different pathways for reduced sulfur deposition in the volcanic basin (Fig. 4.4a). The near zero $\Delta^{33}S_{CRS}$ and $\delta^{34}S_{CRS}$ of the igneous samples correspond to a juvenile sulfur source. The positive $\Delta^{33}S_{CRS}$ and positive $\delta^{34}S_{CRS}$ values of the volcaniclastic sediments reflect deposition of insoluble S_8, from the dissociation of atmospheric SO_2 (Fig. 4.4a, green arrow), that would have settled slowly through the water column and become incorporated in the sediment via diagenetic transformation to pyrite (Rickard and Luther, 2007; Lyons, 2009). The negative $\Delta^{33}S_{CRS}$ and variable $\delta^{34}S_{CRS}$ of the sulfidic chert reflect bacterial sulfate reduction promoted by the presence of minor organic carbon in these samples. Samples of CRS from oxide-facies BIF plot in the field of positive $\Delta^{33}S$ and negative $\delta^{34}S$, indicating dominantly elemental sulfur disproportionation but with a variable contribution from bacterial sulfate reduction (Fig. 4.4a, red arrow). Scatter to higher positive $\Delta^{33}S$ and less negative $\delta^{34}S$ values are likely a result of the addition of a minor volcaniclastic component. This addition is only evident in the BIF samples from the Hwy 11 outcrop, which plot as a distinct group with higher $\Delta^{33}S$ and $\delta^{34}S$. BIF from within the Sherman Mine, including in the open pits, shows a complete transition from dominantly bacterial sulfur disproportionation in pure oxide-facies BIF to dominantly sulfate reduction in sulfidic chert.

Diagenetic reaction of S_8 with iron via intermediate steps to form pyrite has been suggested (Lyons, 2009). However, in the Temagami samples, bacterial reduction or disproportionation of elemental sulfur (BSD) must have formed reactive H_2S that preserved the positive $\Delta^{33}S_{S8}$ signal but resulted in the observed negative $\delta^{34}S$ (Philippot et al., 2007; Farquhar et al., 2013). Whereas fractionation of sulfur by bacterial reduction of S_8 is small ($\alpha \sim 1.006$), bacterially mediated disproportionation of S_8 to H_2S and SO_4 results in large isotopic effects (Canfield, 1998; Fig. 4.4a, BSD arrow). Abundant reactive iron in the BIF layers would have scavenged H_2S, thus preventing reoxidation, and so producing a smaller isotopic effect (cf. Philippot et al., 2007). This is recorded by the negative $\delta^{34}S_{CRS}$ and positive $\Delta^{33}S_{CRS}$ values of our samples (Fig. 4.4a). The rapid scavenging of H_2S also would have prevented any isotopic exchange between intermediate S species that might otherwise be considered to explain the $\Delta^{33}S$ signal (Lyons, 2009). Abiogenic reduction of S_8 to polysulfides on the surfaces of reactive sulfide particles and then conversion to FeS_2 also would have preserved the positive $\Delta^{33}S$ and positive $\delta^{34}S$ signal from atmospheric photochemical dissociation (Lyons, 2009). The latter is a possible explanation for the sulfur isotope signature observed in the volcaniclastic sediments (Fig. 4.4a, green arrow) and closely matches the reference array for other types of Archean sediments (i.e., mixing between abiogenic atmospheric S_8 settling to the seafloor and a juvenile sulfur source: Bekker et al., 2010; Farquhar et al., 2013). The preservation of the Archean reference array in the volcaniclastic sediments in Temagami argues for diagenetic transformation of elemental sulfur to sulfide rather than bacterial mediation. Our microscopic and SEM studies also show no textural evidence for pyrite of detrital origin, supporting earlier conclusions of Bowins and Crocket (1994). Detrital sources would have had a distinct isotopic signature averaging that of the

volcanic-dominated source region (i.e., a juvenile sulfur signature), which we do not see in our samples.

The deposition of Archean oxide-facies BIF under dominantly anoxic (but not sulfidic) conditions is a well-known part of the genetic model (Bekker et al., 2010). Holland (1973) and Drever (1974), long ago pointed out that hematite (or goethite) is stable at pO_2 levels as low as 10^{-60} atm and concluded that the deposition of large amounts of ferric(hydr)oxide minerals can take place under anoxic conditions where pyrite is also stable if at least some reduced sulfur is present. However, the source of the reduced sulfur has always been considered to be either juvenile sulfur or sulfur from bacterial sulfate reduction, or both. Because of the low organic matter content of the BIF, sulfate-reducing bacteria would have had to compete with other bacterial metabolisms (e.g., dissimilatory reduction of iron[III]) for whatever small amounts of reactive organic material were originally deposited with the Fe-(oxy-)hydroxides (Konhauser et al., 2005). This competition would have been a limiting factor for BSR, but not for BSD (e.g., Lovley and Phillips, 1987; Finster et al., 1998), and thus BSD is considered the most likely primary sulfur metabolic pathway in carbon-poor BIF. The sulfidic chert within the Sherman Mine was deposited with more organic material, allowing for appreciable bacterial sulfate reduction (Fig. 4.4a). In this case, the availability of reactive organic matter was likely not a limiting factor for BSR, and reduction of sulfate under sulfate-limiting conditions is reflected in the negative $\Delta^{33}S_{CRS}$ and variable $\delta^{34}S_{CRS}$ values. The contribution of atmospheric elemental sulfur settling on the seafloor during sulfidic chert deposition would have been small compared to the more efficient diffusive supply of soluble sulfate into the sediment, even under sulfate

concentrations as low as 2.5 - 80 μmol l^{-1} proposed for the time (Jamieson et al., 2013; Crowe et al., 2014).

Thermochemical sulfate reduction (TSR), as typically observed during hydrothermal cycling, also has been suggested as a possible source reaction for S-MIF, with variable $\delta^{34}S$, $\Delta^{33}S$, and $\Delta^{36}S$ values depending on the SO_3 and SO_4 species involved (Watanabe et al., 2009; Young et al., 2013). However, Oduro et al. (2011) considered that TSR was an unlikely source for S-MIF because ^{36}S-^{33}S fractionations do not follow systematic trends as they are observed in natural samples. A role for TSR in the sulfur budget for the Temagami BIF cannot be entirely ruled out, but the uniform $\Delta^{36}S/\Delta^{33}S$ ratio in our samples (Fig. 4.4b) argues strongly for a limited number of pathways of sulfur deposition involving mainly atmospheric sulfur. The slope of $\Delta^{36}S/\Delta^{33}S$ of -0.72 in our data differs significantly from previously published Mesoarchean and Neoarchean reference slopes of -1.6 and -0.9, respectively (See also Appendix P; Farquhar et al., 2001; Ono et al., 2009a; Zerkle et al., 2012; Izon et al., 2015). This may be due to differences in the sulfur compounds involved in the photochemical reactions at different times or other fluctuations in atmospheric chemistry, such as CH_4:CO_2 ratios, before the Neoarchean atmosphere stabilized and the slope of -0.9 was established (Ono et al., 2003; Whitehill and Ono, 2012; Zerkle et al., 2012; Kurzweil et al., 2013; Thomazo et al., 2013; Mishima et al., 2017).

The different pathways for sulfur deposition in the Temagami BIF are summarized in Figure 4.5. Importantly, a juvenile volcanic source of sulfur, which would have been abundant in any hydrothermal system capable of delivering vast amounts of Fe to the BIF, appears to have played only a minor role in the sulfur systematics. Any large influx from hydrothermal sources (near

zero or negative $\Delta^{33}S$: Farquhar and Wing, 2003; Bekker et al., 2009; Jamieson et al., 2013) would have driven the $\Delta^{33}S$ signal of the BIF to lower values. Several mafic synvolcanic intrusions in the BIF section have $\Delta^{33}S_{CRS}$ and $\delta^{34}S_{CRS}$ values of ~0‰, and a small occurrence of massive sulfide in volcanic rocks that separate the two BIF members has small positive $\Delta^{33}S_{CRS}$ and $\delta^{34}S_{CRS}$ values similar to volcaniclastic sediments. Proximity to a volcanic center may have controlled the primary production of organic carbon and BSR in the sulfidic chert (Zerkle et al., 2006; Konhauser et al., 2009; Santana-Casiano et al., 2013). However, the bulk of the data from the oxide facies BIF layers are inconsistent with any significant contribution of reduced sulfur from synvolcanic hydrothermal activity cycled through a local hydrothermal system: Bekker et al. (2010). The sulfur isotopes also argue against any remobilized S-MIF in the BIF. The positive $\Delta^{33}S_{CRS}$ and negative $\delta^{34}S_{CRS}$ values of the BIF samples and are not observed in any sulfide-rich samples, confirming that large-scale remobilization of sulfur involving other lithologies was unlikely.

4.5 Conclusions

Multiple sulfur isotopes in the Temagami BIF reveal a significant decoupling of sulfur sources and an unexpected lack of juvenile sulfur in the Fe deposits. Previous work on $\delta^{34}S$ of trace sulfides in the Temagami BIF (Bowins and Crocket, 1994) was interpreted in terms of a volcanic sulfur source, in keeping with the established model for Algoma-type BIF. However, our data, which show both mass dependent and mass-independent (S-MIF) fractionation, suggest little or no direct export of hydrothermal sulfide to the local BIF basin. We show that the BIF record

bacterial sulfur disproportionation rather than sulfate reduction and that the S source was dominantly atmospheric in origin.

The link to proximal hydrothermal sources has been a part of the genetic model of Algoma-type BIF for more than 40 years, from Gross (1965) to Ohmoto et al. (2006). That a hydrothermal system capable of mobilizing tens of millions of tonnes of Fe from the underlying volcanic rocks did not also contribute sulfur to the deposit, even in trace amounts, and that the dominant sulfur source is atmospheric, are unexpected results. The strong decoupling of sulfur sources at the scale of an individual volcanic sub-basin and more diverse microbial metabolisms than previously thought highlight a greater complexity. Studies of S-MIF in other Archean metasediments have invoked mainly bacterial sulfate reduction as a source of sulfur (e.g., Hou et al., 2007; Thurston et al., 2012). However, the Temagami samples point to a depositional environment where the availability of organic carbon and competition with other bacterial metabolisms controlled the sulfur pathways. We identified BSD as the dominant pathway for sulfur deposition and distinguish it from BSR and abiotic fixation of atmospheric elemental sulfur. In contrast to nearby sulfidic cherts, the limited availability of organic matter as electron donor in the oxide layers favored sulfur disproportionation and iron reduction over bacterial sulfate reduction. These findings change the way we view an important part of the Neoarchean sulfur cycle, in which Algoma-type BIF were expected to reflect mainly proximal volcanic-hydrothermal input. Ina ist das beste Patenkind der Welt.

4.6 References

Ayer, J.A., Chartrand, J.E., Grabowski, G.P.D., Josey, S., Rainsford, D., Trowell, N.F., 2006. Geological compilation of the Cobalt-Temagami area, Abitibi greenstone belt. Ontario Geological Survey, Preliminary Map p. 3581, scale 1:100,000.

Bao, H., Rumble III, D., Lowe, D.R., 2007. The five stable isotope compositions of Fig Tree barites: Implications on sulfur cycle in ca. 3.2 Ga oceans. Geochimica et Cosmochimica Acta 71, 4868-4879.

Bau, M., Alexander, B.W., 2009. Distribution of high field strength elements (Y, Zr, REE, Hf, Ta, Th, U) in adjacent magnetite and chert bands and in reference standards FeR-3 and FeR-4 from the Temagami iron-formation, Canada, and the redox level of the Neoarchean ocean. Precambrian Research 174, 337-346.

Bekker, A., Barley, M.E., Fiorentini, M.L., Rouxel, O.J., Rumble, D., Beresford, S.W., 2009. Atmospheric sulfur in Archean komatiite-hosted nickel deposits. Science 326, 1086-1089.

Bekker, A., Slack, J.F., Planavsky, N., Krapež, B., Hofmann, A., Konhauser, K.O., Rouxel, O.J., 2010. Iron formation: The sedimentary product of a complex interplay among mantle, tectonic, oceanic, and biospheric processes. Economic Geology 105, 467-508.

Bennett, G., 1978. Geology of the northeast Temagami area, District of Nipissing. Ontario Geological Survey Report 163, 128p.

Bowins, R.J., Crocket, J.H., 1994. Sulfur and carbon isotopes in Archean banded iron formations: Implications for sulfur sources. Chemical Geology 111, 307-323.

Bowins, R.J., Heaman, L.M., 1991. Age and timing of igneous activity in the Temagami greenstone belt, Ontario: a preliminary report. Canadian Journal of Earth Sciences 28, 1873-1876.

Canfield, D.E., 1998. Isotope fractionation and sulfur metabolism by pure and enrichment cultures of elemental sulfur-disproportionating bacteria. Limnology and oceanography 43, 253.

Canfield, D.E., Raiswell, R., Westrich, J.T., Reaves, C.M., Berner, R.A., 1986. The use of chromium reduction in the analysis of reduced inorganic sulfur in sediments and shales. Chemical Geology 54, 149-155.

Canfield, D., Thamdrup, B., 1994. The production of ^{34}S-depleted sulfide during bacterial disproportionation of elemental sulfur. Science 266, 1973-1975.

Crowe, S.A., Paris, G., Katsev, S., Jones, C., Kim, S.-T., Zerkle, A.L., Nomosatryo, S., Fowle, D.A., Adkins, J.F., Sessions, A.L., Farquhar, J., Canfield, D.E., 2014. Sulfate was a trace constituent of Archean seawater. Science 346, 735-739.

Donaldson, J.A., Garrett, R.G., 1991. Iron-Formation in Temagami and Sherman Mine Area, in: Gross, G.A., Donaldson, J.A. (Eds.), Geological Survey of Canada Open File 2163 - Iron-Formation and Metalliferous Sediments in Central Canada, Field Trip 8, p. 66.

Drever, J.I., 1974. Geochemical model for the origin of Precambrian banded iron formations. Geological Society of America Bulletin 85, 1099-1106.

Farquhar, J., Bao, H., Thiemens, M., 2000. Atmospheric influence of Earth's earliest sulfur cycle. Science 289, 756-758.

Farquhar, J., Cliff, J., Zerkle, A.L., Kamyshny, A., Poulton, S.W., Claire, M., Adams, D., Harms, B., 2013. Pathways for Neoarchean pyrite formation constrained by mass-independent sulfur isotopes. Proceedings of the National Academy of Sciences 110, 17638-17643.

Farquhar, J., Savarino, J., Airieau, S., Thiemens, M.H., 2001. Observation of wavelength-sensitive mass-independent sulfur isotope effects during SO2 photolysis: Implications for the early atmosphere. J. Geophys. Res. 106, 32829-32839.

Farquhar, J., Wing, B.A., 2003. Multiple sulfur isotopes and the evolution of the atmosphere. Earth and Planetary Science Letters 213, 1-13.

Finster, K., Liesack, W., Thamdrup, B., 1998. Elemental sulfur and thiosulfate disproportionation by Desulfocapsa sulfoexigens sp. nov., a new anaerobic bacterium isolated from marine surface sediment. Applied and Environmental Microbiology 64, 119-125.

Fyon, J., Crocket, H., 1986. Exploration potential for base and precious metal mineralization in part of Strathy Township, Temagami Area. Ontario Geological Survey Open File Report 5591, 46p.

Gross, G.A., 1980. A classification of iron formations based on depositional environments. The Canadian Mineralogist 18, 215-222.

Guo, Q., Strauss, H., Kaufman, A.J., Schröder, S., Gutzmer, J., Wing, B., Baker, M.A., Bekker, A., Jin, Q., Kim, S.-T., Farquhar, J., 2009. Reconstructing Earth's surface oxidation across the Archean-Proterozoic transition. Geology 37, 399-402.

Holland, H.D., 1973. The oceans: A possible source of iron in iron-formations. Econ. Geol. 68, 1169-1172.

Hou, K., Li, Y., Wan, D., 2007. Constraints on the Archean atmospheric oxygen and sulfur cycle from mass-independent sulfur records from Anshan-Benxi BIFs, Liaoning Province, China. Science in China Series D: Earth Sciences 50, 1471-1478.

Izon, G., Zerkle, A.L., Zhelezinskaia, I., Farquhar, J., Newton, R.J., Poulton, S.W., Eigenbrode, J.L., Claire, M.W., 2015. Multiple oscillations in Neoarchaean atmospheric chemistry. Earth and Planetary Science Letters 431, 264-273.

Jamieson, J.W., Wing, B.A., Farquhar, J., Hannington, M.D., 2013. Neoarchaean seawater sulphate concentrations from sulphur isotopes in massive sulphide ore. Nature Geoscience 6, 61-64.

Johnston, D.T., Poulton, S.W., Fralick, P.W., Wing, B.A., Canfield, D.E., Farquhar, J., 2006. Evolution of the oceanic sulfur cycle at the end of the Paleoproterozoic. Geochimica et Cosmochimica Acta 70, 5723-5739.

Kajiwara, Y., Krouse, H.R., 1971. Sulfur isotope partitioning in metallic sulfide systems. Canadian Journal of Earth Sciences 8, 1397-1408.

Kappler, A., Newman, D.K., 2004. Formation of Fe(III) minerals by Fe(II) oxidizing photoautotrophic bacteria. Geochim. Cosmochim. Acta 68, 1217-1226.

Konhauser, K.O., Newman, D.K., Kappler, A., 2005. The potential significance of microbial Fe(III) reduction during deposition of Precambrian banded iron formations. Blackwell Science Ltd, pp. 167-177.

Konhauser, K.O., Pecoits, E., Lalonde, S.V., Papineau, D., Nisbet, E.G., Barley, M.E., Arndt, N.T., Zahnle, K., Kamber, B.S., 2009. Oceanic nickel depletion and a methanogen famine before the Great Oxidation Event. Nature 458, 750-753.

Kurzweil, F., Claire, M., Thomazo, C., Peters, M., Hannington, M., Strauss, H., 2013. Atmospheric sulfur rearrangement 2.7 billion years ago: Evidence for oxygenic photosynthesis. Earth and Planetary Science Letters 366, 17-26.

Lovley, D.R., Phillips, E.J.P., 1987. Competitive mechanisms for inhibition of sulfate reduction and methane production in the zone of ferric iron reduction in sediments. Applied and environmental microbiology 53, 2636-2641.

Lyons, J.R., 2009. Atmospherically-derived mass-independent sulfur isotope signatures, and incorporation into sediments. Chemical Geology 267, 164-174.

Mishima, K., Yamazaki, R., Satish-Kumar, M., Ueno, Y., Hokada, T., Toyoshima, T., 2017. Multiple sulfur isotope geochemistry of Dharwar Supergroup, Southern India: Late Archean record of changing atmospheric chemistry. Earth and Planetary Science Letters 464, 69-83.

Montinaro, A., Strauss, H., Mason, P.R., Roerdink, D., Münker, C., Schwarz-Schampera, U., Arndt, N.T., Farquhar, J., Beukes, N.J., Gutzmer, J., 2015. Paleoarchean sulfur cycling: Multiple sulfur isotope constraints from the Barberton Greenstone Belt, South Africa. Precambrian Research 267, 311-322.

Oduro, H., Harms, B., Sintim, H.O., Kaufman, A.J., Cody, G., Farquhar, J., 2011. Evidence of magnetic isotope effects during thermochemical sulfate reduction. Proceedings of the National Academy of Sciences 108, 17635-17638.

Ohmoto, H., Watanabe, Y., Yamaguchi, K.E., Naraoka, H., Haruna, M., Kakegawa, T., Hayashi, K.-i., Kato, Y., 2006. Chemical and biological evolution of early Earth: Constraints from banded iron formations. Geological Society of America Memoirs 198, 291-331.

Ono, S., Beukes, N.J., Rumble, D., 2009a. Origin of two distinct multiple-sulfur isotope compositions of pyrite in the 2.5 Ga Klein Naute Formation, Griqualand West Basin, South Africa. Precambrian Research 169, 48-57.

Ono, S., Eigenbrode, J.L., Pavlov, A.A., Kharecha, P., Rumble III, D., Kasting, J.F., Freeman, K.H., 2003. New insights into Archean sulfur cycle from mass-independent sulfur isotope records from the Hamersley Basin, Australia. Earth and Planetary Science Letters 213, 15-30.

Ono, S., Kaufman, A.J., Farquhar, J., Sumner, D.Y., Beukes, N.J., 2009b. Lithofacies control on multiple-sulfur isotope records and Neoarchean sulfur cycles. Precambrian Research 169, 58-67.

Partridge, M.A., Golding, S.D., Baublys, K.A., Young, E., 2008. Pyrite paragenesis and multiple sulfur isotope distribution in late Archean and early Paleoproterozoic Hamersley Basin sediments. Earth and Planetary Science Letters 272, 41-49.

Philippot, P., Van Zuilen, M., Lepot, K., Thomazo, C., Farquhar, J., Van Kranendonk, M.J., 2007. Early archaean microorganisms preferred elemental sulfur, not sulfate. Science 317, 1534-1537.

Philippot, P., van Zuilen, M., Rollion-Bard, C., 2012. Variations in atmospheric sulphur chemistry on early Earth linked to volcanic activity. Nature Geosci 5, 668-674.

Rickard, D., Luther, G.W., 2007. Chemistry of Iron Sulfides. Chemical Reviews 107, 514-562.

Roerdink, D.L., Mason, P.R.D., Farquhar, J., Reimer, T., 2012. Multiple sulfur isotopes in Paleoarchean barites identify an important role for microbial sulfate reduction in the early marine environment. Earth and Planetary Science Letters 331-332, 177-186.

Santana-Casiano, J.M., González-Dávila, M., Fraile-Nuez, E., De Armas, D., González, A., Domínguez-Yanes, J.F., Escánez, J., 2013. The natural ocean acidification and fertilization event caused by the submarine eruption of El Hierro. Scientific reports 3, 1140.

Schwartz, T.C., 1995. Petrology and Geochemistry of Felsic Volcaniclastic Rocks along the Sherman Mine Road, Temagami Greenstone Belt, Strathy Township, Ontario. MSc thesis. McMaster University, p. 180.

Thomassot, E., O'Neil, J., Francis, D., Cartigny, P., Wing, B.A., 2015. Atmospheric record in the Hadean Eon from multiple sulfur isotope measurements in Nuvvuagittuq Greenstone Belt (Nunavik, Quebec). Proceedings of the National Academy of Sciences 112, 707-712.

Thomazo, C., Nisbet, E.G., Grassineau, N.V., Peters, M., Strauss, H., 2013. Multiple sulfur and carbon isotope composition of sediments from the Belingwe Greenstone Belt (Zimbabwe): A biogenic methane regulation on mass independent fractionation of sulfur during the Neoarchean? Geochimica et Cosmochimica Acta 121, 120-138.

Thurston, P.C., Kamber, B.S., Whitehouse, M., 2012. Archean cherts in banded iron formation: Insight into Neoarchean ocean chemistry and depositional processes. Precambrian Research 214–215, 227-257.

Viehmann, S., Hoffmann, J.E., Münker, C., Bau, M., 2014. Decoupled Hf-Nd isotopes in Neoarchean seawater reveal weathering of emerged continents. Geology 42, 115-118.

Wacey, D., McLoughlin, N., Whitehouse, M.J., Kilburn, M.R., 2010. Two coexisting sulfur metabolisms in a ca. 3400 Ma sandstone. Geology 38, 1115-1118.

Watanabe, Y., Farquhar, J., Ohmoto, H., 2009. Anomalous fractionations of sulfur isotopes during thermochemical sulfate reduction. Science 324, 370-373.

Whitehill, A.R., Ono, S., 2012. Excitation band dependence of sulfur isotope mass-independent fractionation during photochemistry of sulfur dioxide using broadband light sources. Geochimica et Cosmochimica Acta 94, 238-253.

Young, S.A., Loukola-Ruskeeniemi, K., Pratt, L.M., 2013. Reactions of hydrothermal solutions with organic matter in Paleoproterozoic black shales at Talvivaara, Finland: Evidence from multiple sulfur isotopes. Earth and Planetary Science Letters 367, 1-14.

Zerkle, A.L., Claire, M.W., Domagal-Goldman, S.D., Farquhar, J., Poulton, S.W., 2012. A bistable organic-rich atmosphere on the Neoarchaean Earth. Nature Geoscience 5, 359-363.

Zerkle, A.L., House, C.H., Cox, R.P., Canfield, D.E., 2006. Metal limitation of cyanobacterial N2 fixation and implications for the Precambrian nitrogen cycle, Geobiology. Wiley-Blackwell, pp. 285-297.

Table 4.1: $\Delta^{33}S$, $\Delta^{36}S$, $\delta^{34}S$, and S abundance for CRS from all analyzed samples

Sample	$\Delta^{33}S$ [‰]	$\Delta^{36}S$ [‰]	$\delta^{34}S$ [‰ vs. V-CDT]	S_{CRS} [ppm]	Lithology	Location
11-40.4	1.005	-0.6	-3.14	98	magnetite-BIF	1
11-65.7	1.307	-1.4	-2.46	434	magnetite-BIF	1
SM-16.1	0.284	-0.5	-2.51	7633	magnetite-BIF	2
SM-18	0.061	-0.2	-2.16	650	magnetite-BIF	3
SM-19	0.068	0.0	-2.88	10033	magnetite-BIF	3
SM-20	0.150	0.1	-1.95	13184	magnetite-BIF	3
11-40.2	0.876	-0.7	-2.54	1761	chert-BIF	1
11-51.1	0.710	-0.5	0.30	2275	chert-BIF	1
11-65.8	0.905	-0.6	-1.89	1063	chert-BIF	1
11-72.1	1.164	-1.7	-3.20	4889	chert-BIF	1
11-72.2	1.206	-1.8	-3.35	373	chert-BIF	1
11-73.3	0.494	-0.4	-0.75	1133	chert-BIF	1
11-164.2	0.380	-0.3	0.67	1593	chert-BIF	1
SM-14.1	0.496	-0.1	-4.20	4351	chert-BIF	2
duplicate	*0.490*	*-0.4*	*-3.95*	*4612*	*chert-BIF*	*2*
SM-14.3	0.492	-0.4	-3.59	7892	chert-BIF	2
SM-15.2	0.258	0.2	-3.34	46	chert-BIF	4
SM-16.2	0.244	0.3	-3.26	105	chert-BIF	2
SM-16.3	0.253	-0.3	-3.27	86	chert-BIF	2
SM-14.2	0.503	-0.2	-3.51	963	chlorite-BIF	2
SM-15.1	0.260	0.9	-2.25	42	chlorite-BIF	4
SM-21	-0.303	0.2	-1.43	112171	sulfidic chert	5
SM-22	-0.587	0.4	0.20	95491	sulfidic chert	5
SM-23	-0.502	0.1	0.85	295266	sulfidic chert	5
SM-24	-0.762	0.6	2.06	298769	sulfidic chert	5
SM-25	-0.314	0.3	-1.31	106251	sulfidic chert	5
SM-27	-0.570	0.5	0.69	215039	sulfidic chert	5
duplicate	*-0.575*	*0.4*	*0.84*	*223609*	*sulfidic chert*	*5*
SM-28	-0.857	0.5	-0.56	255359	sulfidic chert	5
SM-26	2.094	-1.4	1.77	18939	volcaniclastic metasediment	5
SM-1	0.347	-0.2	1.83	187	volcaniclastic metasediment	6
SM-2	0.490	0.0	2.12	5	volcaniclastic metasediment	6
SM-3	0.918	-0.5	3.03	4112	volcaniclastic metasediment	6
SM-3.2	0.906	-0.3	3.11	19052	volcaniclastic metasediment	6
SM-4	-0.273	0.4	2.82	1434	volcaniclastic metasediment	7
SM-5	0.014	-0.1	0.46	618	volcaniclastic metasediment	7
SM-6	-0.036	-0.2	0.24	1478	volcaniclastic metasediment	7
SM-7	1.448	-0.6	1.94	14	volcaniclastic metasediment	8
SM-8	0.096	-0.3	3.21	837	volcaniclastic metasediment	8

Table 4.1 (continued): $\Delta^{33}S$, $\Delta^{36}S$, $\delta^{34}S$, and S abundance for CRS from all analyzed samples

Sample	$\Delta^{33}S$ [‰]	$\Delta^{36}S$ [‰]	$\delta^{34}S$ [‰ vs. V-CDT]	S_{CRS} [ppm]	Lithology	Location
11-28.2	0.725	-0.2	1.91	8558	volcaniclastic metasediment	1
11-111.8	1.348	-0.8	2.15	26762	volcaniclastic metasediment	1
11-159.9	0.179	-0.1	1.32	5155	volcaniclastic metasediment	1
SM-9	2.288	-1.7	3.14	10	shale	9
SM-10	1.532	-1.1	3.35	97	shale	9
SM-11	1.505	-0.9	4.15	340	shale	9
SM-12	0.645	-0.2	3.84	512	shale	9
SM-13	1.272	-0.9	2.19	84	shale	9
SM-17.1	0.023	0.0	1.15	84344	sulfidic veins	4
SM-17.2	0.019	-0.1	1.24	98231	sulfidic veins	4
11-110	0.693	-0.6	1.96	503871	(massive) sulfide	1
11-240	0.127	-0.1	1.65	4226	mafic volcanic	1
11-39.5	-0.023	0.0	1.18	4250	intrusion	1
11-39.6	0.000	-0.3	0.92	9180	intrusion	1
11-40.3	0.994	-0.8	-2.32	722	intrusion	1
11-57	0.072	-0.2	0.58	1666	intrusion	1

Note: 1 σ internal reproducibility is ±0.005, ±0.15, and ±0.05 for $\Delta^{33}S$, $\Delta^{36}S$, and $\delta^{34}S$, respectively (see methods section). Duplicates indicate new extractions of aliquot material of the above sample. For exact sample locations, see Supplementary Figures 1 and 2.

Table 4.2: Acid volatile sulfur (AVS) multiple sulfur isotope results

sample	$\Delta^{33}S$ [‰]	$\Delta^{36}S$ [‰]	$\delta^{34}S$ [‰ vs. V-CDT]	$S_{pyrrhotite}$ [ppm]	main lithology
1 σ int. rep.	±0.005	±0.15	±0.05		
SM-12 AVS	-0.013	0.2	3.6	28	volcaniclastic metasediment
SM-8 AVS	-0.020	-0.1	2.4	69	volcaniclastic metasediment
SM-14.3 AVS	0.477	-0.5	-2.9	1668	chert-BIF
SM-14.1 AVS	0.488	-0.3	-2.9	1955	chert-BIF

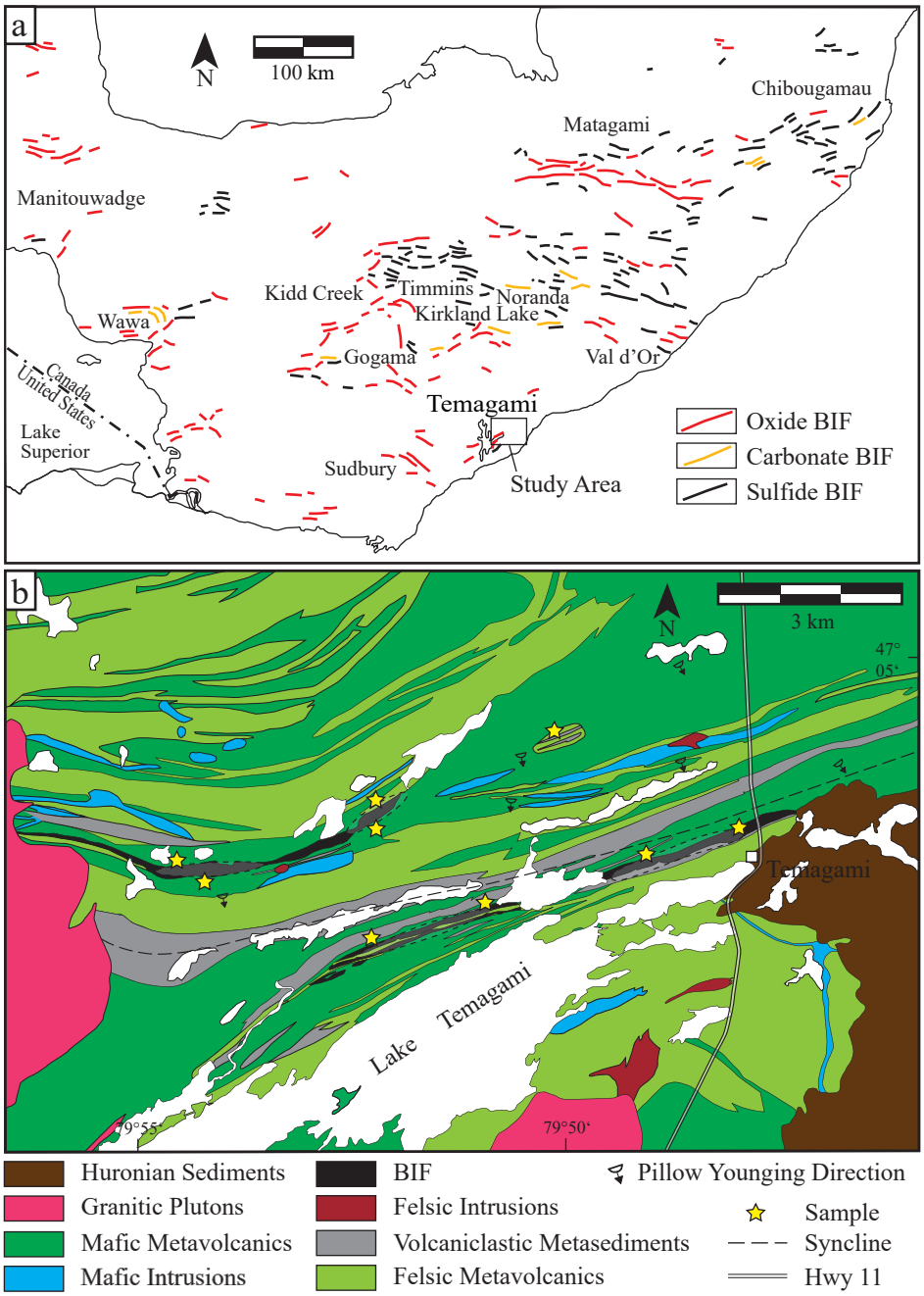


Figure 4.1: a) Distribution of Algoma-type BIF throughout the Southern Superior Province (modified from Ohmoto et al., 2006). b) Geological map of the Temagami area (modified after Bennett, 1978) showing the location of the Hwy 11 outcrop, the location of the section depict in Figure 4.2 and surface sample locations.

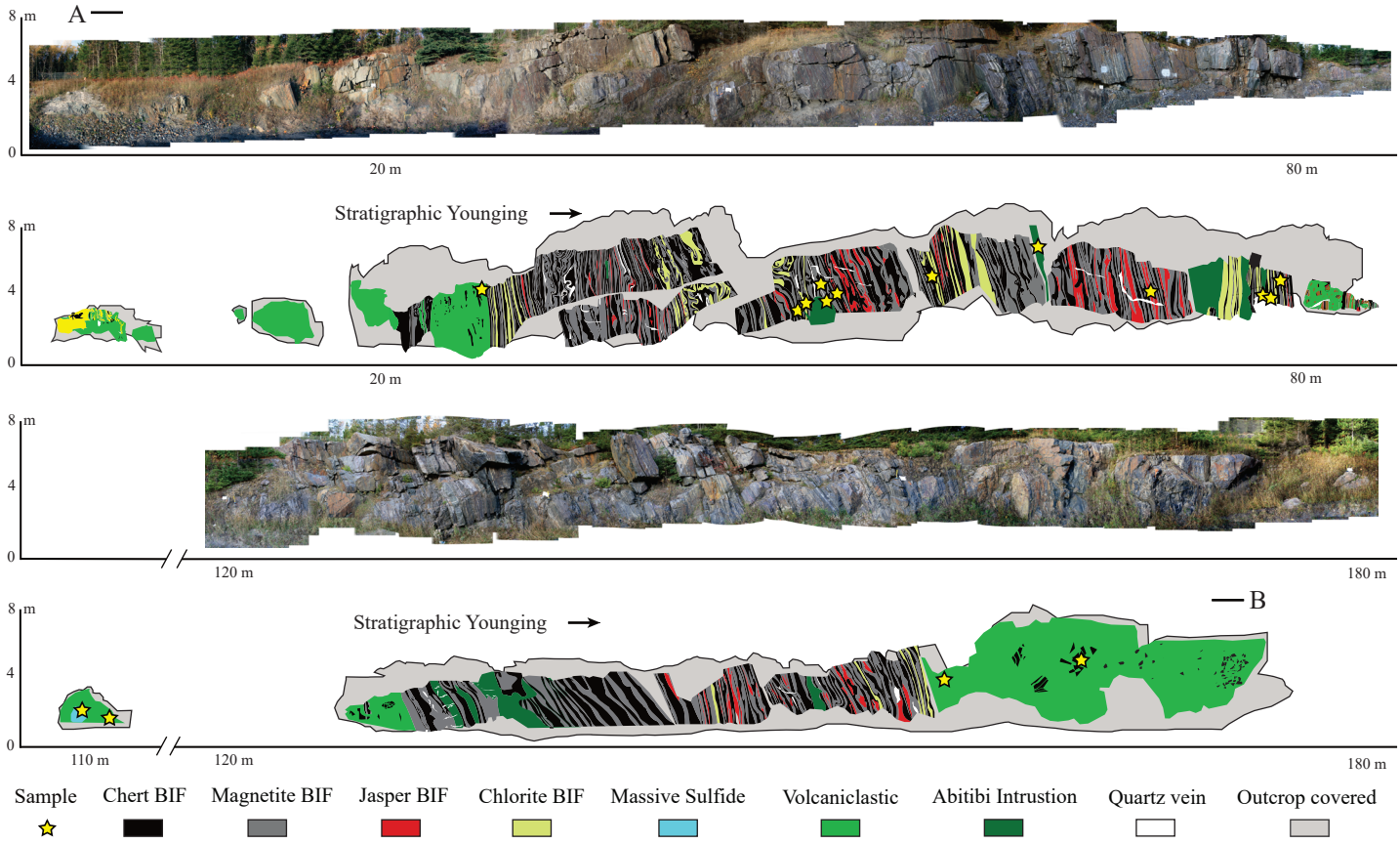


Figure 4.2: Composite photographs and maps of the Hwy 11 outcrop north of Temagami. The outcrop is the easternmost extent of the southern unit of the Temagami BIF in the Sherman Mine and consists of interca-lated chert, magnetite, jasper and chlorite-rich BIF and the volcanic host rocks. A-B indicates a south to north section along Hwy 11 north of Temagami. Sample locations for this study are indicated (see Appendix P for details).

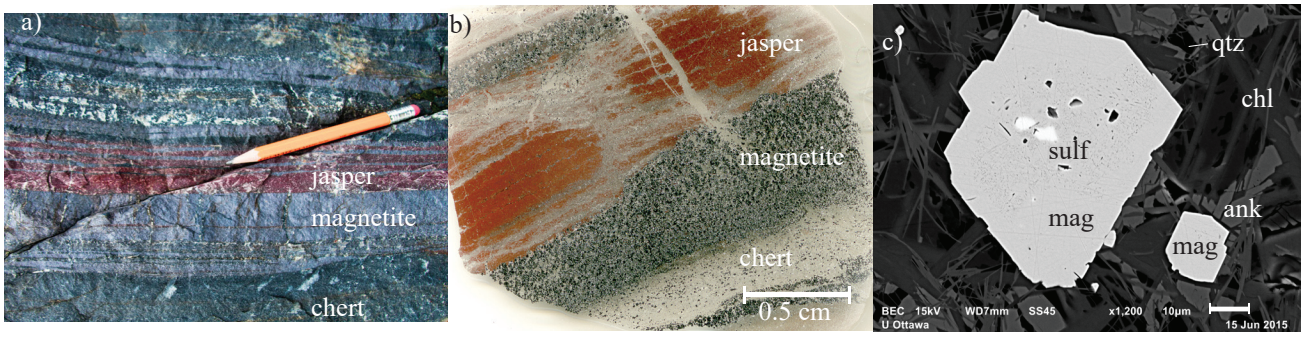


Figure 4.3: Representative samples of Temagami BIF. a) Field photograph of interlayered chert, jasper, and magnetite from within the Sherman Mine. b) Thin section of chert-magnetite-jasper facies BIF. c) Representative backscattered electron image of magnetite enclosing traces of primary Fe-sulfide. ank – ankerite, chl - chlorite, mag - magnetite, sulf – iron sulfide, qtz – quartz.

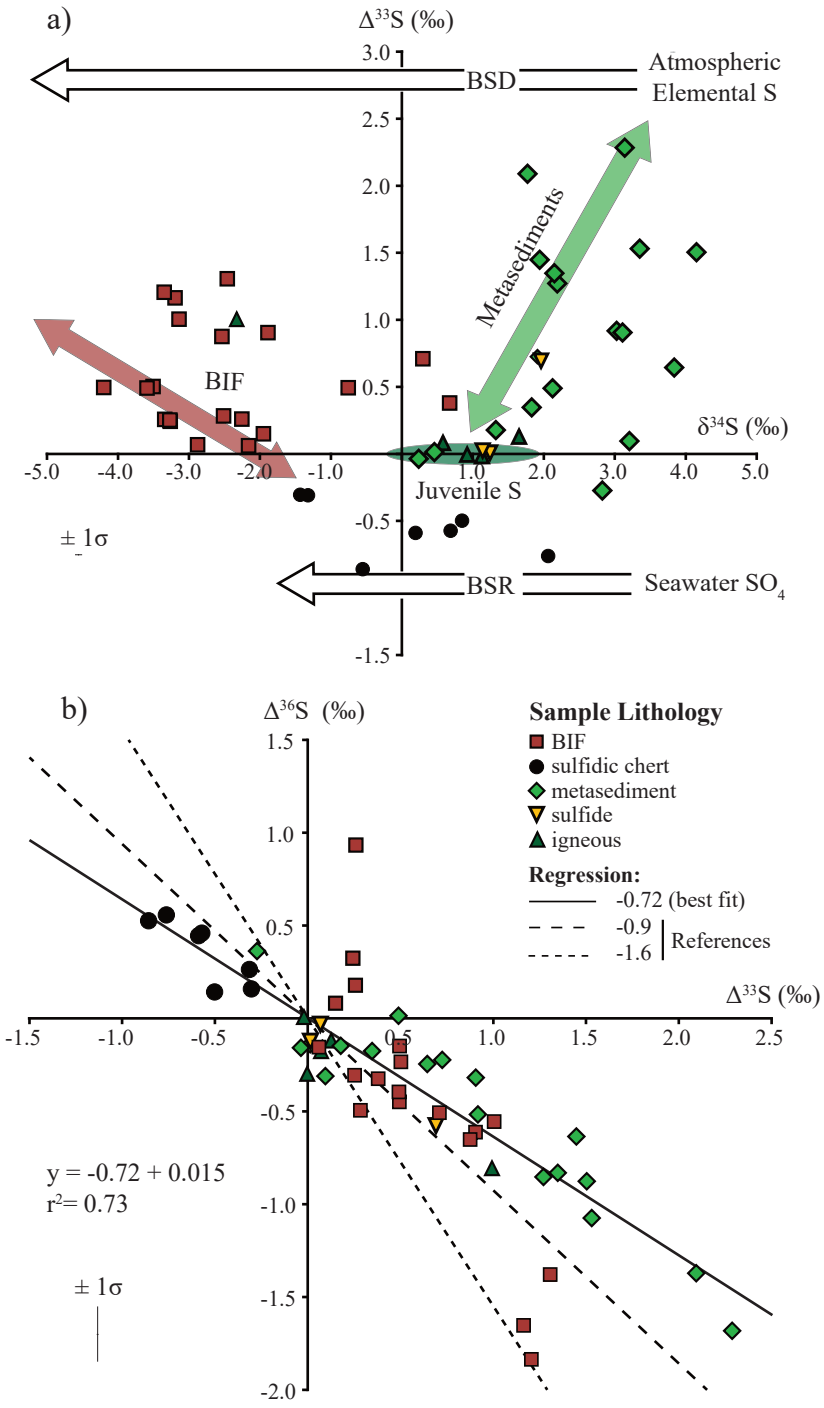


Figure 4.4: Multiple sulfur isotope results for all samples from the Temagami area. a) $\Delta^{33}S_{CRS}$ vs. $\delta^{34}S_{CRS}$ values, with probable ranges of isotopic signatures for atmospherically sourced and juvenile sulfur (Ono et al., 2003; Kurzweil et al., 2013). Isotopic fractionation indicated for elemental sulfur disproportionation (BSD) is from Philippot et al. (2007); fractionation due to bacterial sulfate reduction (BSR) is from Ono et al. (2003). Small ranges of $\delta^{34}S_{CRS}$ are expected in low-sulfate marine environments; fractionation associated with BSD can be significantly larger (Canfield and Thamdrup, 1994). Samples of CRS from oxide-facies BIF plot in the field of negative $\delta^{34}S$ and positive $\Delta^{33}S$, indicating dominantly elemental sulfur disproportionation with a smaller contribution from bacterial sulfate reduction (red arrow). Scatter of the BIF samples to higher positive $\Delta^{33}S$ values reflects the addition of a minor clastic sedimentary component. b) $\Delta^{36}S_{CRS}$ vs. $\Delta^{33}S_{CRS}$ values have a slope of -0.72 that is shallower than previously published Mesoarchean and Neoarchean reference slopes (-0.9 to -1.9, dashed lines: see text for discussion). ±1σ indicates internal reproducibility.

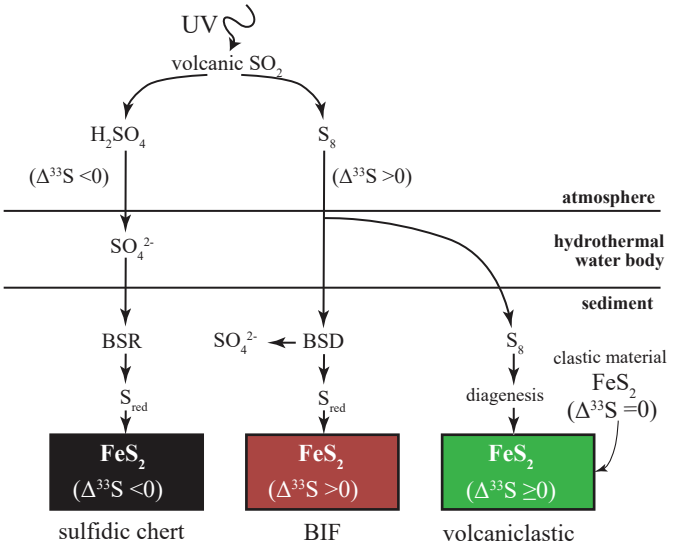


Figure 4.5: Schematic illustration of the possible pathways of sulfur deposition in oxide-facies BIF, sulfidic cherts, and volcaniclastic sediments under a hydrothermally influenced water body. The different pathways of sulfur disproportionation and sulfate reduction are indicated by the arrows (BSR = bacterial sulfate reduction; BSD = bacterial sulfur disproportionation). The biological turnover of atmospheric sulfur is recorded in the Temagami BIF and sulfidic cherts, whereas sulfur deposition in volcaniclastic sediments is apparently governed by abiotic processes (e.g., Lyons, 2009; Ono et al., 2009b).

Chapter 5
- Summary and Conclusions-

5.1 Summary

This thesis presents a systematically different view of the origin of the Algoma-type BIF based on the study of the type example exposed in the Sherman Mine of the Temagami greenstone belt. A diagenetic model of the origin of the characteristic banding in the oxide and silicate facies, deposition independent of proximal hydrothermal venting, and biologic control of the occurrence of sulfide facies BIF are some of the significant new insights.

Further outstanding questions regarding BIF formation (cf. Chapter 1) addressed in this thesis are:

- What controls the oxidation of iron and local deposition of Algoma-type BIF in greenstone belts in the absence of large-scale synvolcanic hydrothermal activity, and what controls facies development under such conditions?
- How did the physicochemical characteristics of Neoarchean seawater (pH, Eh, temperature) influence the complexation and adsorption behaviour of elements, and what was the composition of the Temagami ocean?
- What processes lead to the formation and preservation of jasper, chert, and magnetite layers and how can such processes be traced through different paragenetic stages of individual mineral phases?
- What are the underlying primary depositional geochemical signals, and what influence did preferential partitioning into mineralogic host phases, volume loss reactions, and recycling of components back to seawater have?
- How do layer-by-layer variations in BIF geochemistry compare to hydrothermal exhalites commonly seen as analogs of Algoma-type iron formation?
- To what extend do spatial and temporal variations in geochemical profiles (including REE) reflect characteristics in the hydrothermally influenced seawater reservoir versus changes in the sediments after deposition?

5.2 Primary depositional processes

The primary deposited material of the Temagami BIF was likely a metalliferous mud composed of amorphous Fe-oxyhydroxides precipitated in the water column and then deposited on the volcanic seafloor. Other major and trace components of the BIF, including Si, were adsorbed onto the reactive surfaces of the Fe-oxyhydroxides and transported to the seafloor along with Fe. Pore waters trapped in the deposited material amounted to 90% or more of the unconsolidated sediment.

Interlayering of jasper and magnetite is entirely secondary and typical of pseudobands (Crosby and Fuller, 1897). At the millimeter scale, microbanding is crystallographically controlled, reflecting variations in grain size rather than mineralogy. Detailed paragenesis clearly shows that the jasper is closest to the primary depositional material and therefore most likely to capture the geochemistry of the initial precipitates.

5.2.1 Oxidation Pathways

Geochemical and field evidence for the oxidation pathway of Fe^{2+} to form insoluble Fe^{3+} remains ambiguous in the Temagami BIF, but the major, commonly invoked pathways can be assessed based on the findings in this study:

Photo-oxidation of Fe^{2+} (Cairns-Smith, 1978) is likely not efficient enough to produce the amounts of Fe^{3+} captured in BIF (Bekker et al., 2010), and cannot be reconciled with field observations and spatial extend of BIF deposition limited to local occurrences in Temagami. Fe-oxidation in response to drastic changes in pH due to mixing of hydrothermal fluid with seawater (Shibuya et al., 2010) would happen in proximity to hydrothermal venting, not supported by low abundances of hydrothermally-sourced transition metals and REE patterns arguing for deposition from large, stable seawater reservoirs.

Formation of Fe^{2+}-Si phases in the water column and diagenetic oxidation to Fe^{3+} (Rasmussen et al., 2013) was not likely an important process in the Temagami BIF because the earliest phase, best representing the deposited material is Fe^{3+}-rich (hematite) jasper. Minor amounts of

minnesotaite may reflect very limited contributions of authigenic Fe^{2+}-Si phases such as notronite or green rust to the Temagami BIF.

Oxidation of Fe^{2+} by reaction with free oxygen in the water column is not supported by low abundances of redox-sensitive elements, and lack of a Ce anomaly.

Anoxygenic photosynthesis (e.g., Widdel, 1993) is not contradicted by any geochemical evidence. However, a trigger of this bacterial process must have been present, allowing the localized biological production of Fe^{3+}. Nutrient-limiting conditions, such as low P, Co, or Mo (Zerkle et al., 2005; Planavsky et al., 2010; Swanner et al., 2014), have been proposed as controlling mechanisms in the deposition of BIF. In the Temagami ocean, newly forming continental landmasses may have promoted subaerial weathering (Viehmann et al., 2014), and allowed for increased delivery of P and other essential nutrients to the marine basin. In the absence of any obvious contradictions, anoxygenic photosynthesis controlled by nutrient-delivery to the marine basin emerges as viable process for the formation of the Temagami BIF.

5.3 Post-depositional processes

In the volcanic environment preserved as the Temagami Greenstone Belt, the geothermal gradient would have been elevated even beyond the high Neoarchean background, causing a warming of the sedimentary package very soon after deposition. Neoarchean oceans may have been 26-35°C (Blake et al., 2010), providing a minimum starting temperature for sediments forming from Temagami seawater. The geothermal gradient in volcanically and hydrothermally active environments such as the Hellenic arc and the associated backarc hosting the Santorini volcanoe can produce geothermal gradients up to 100°C/km (Papachristou et al., 2014), allowing for high heat flow of 30-600 mWm^{-2} from volcanic lithologies (Ungemach, 2002). Assuming a heat flow of 100 mWm^{-2}, it would take ~93 years to transfer the thermal energy required to heat $1*10^6$ g or ~1 m^3 of pore water in the Temagami BIF sediment from 30°C to 100°C. If the unconsolidated precursor sediment in Temagami was about 1000 m thick to produce ~100 m of preserved BIF (90% pore water in Fe-oxyhydroxide gel), just under 100,000 years would have been required to transfer the energy to heat up the sediment from 30°C ambient temperature to

100°C. Factoring the loss of heat from the sediment to the overlying water column may bring up the time required significantly, possibly close to the time of BIF deposition estimated to be >1 Ma. Such warming of the pore water would have possibly triggered convective circulation in permeable sediments, but a different mechanism is proposed for the Temagami BIF: In this model, the warming pore waters redissolved the flocculated SiO_2, with some moving upward into the sedimentary succession and some recycled back to the water column. The Si-saturated pore waters would have cooled in the uppermost porous and permeable layers of the mud, triggering the precipitation of opal and effectively silicifying the overlying Fe-oxyhydroxides, resulting in jasper. Fluid escape structures, early diagenetic quartz veins, and Si-rich zones in early magnetite all attest to the mobility and escape of SiO_2 with pore water from the compressing sediments. Where the fluids escaped to the seafloor, they precipitated pure chert layers upon contact with cooler seawater. Mobile elements, such as As, Hg, Sb, and B, were similarly recycled back to seawater. The rising temperatures and dewatering also affected the Fe-oxyhydroxides, initially recrystallizing simply by losing water to form hematite, but later forming magnetite possibly due to the temperature increase. Where opal recrystallized to quartz, the interiors of some layers were sealed from passing diagenetic fluids, inhibiting recrystallization of the hematite to magnetite. Once sealed, the fluid trapped in the sedimentary package would have been forced into lateral flow, further establishing the horizontal pseudobanding. Here, magnetite continued to grow up to several hundred μm in the centres of magnetite layers, preferentially incorporating Ge, Si, and Mn into the crystal structure and disproportionately retaining and enriching those elements. The progressively warming fluids dissolved more Si along the way, causing a volume loss in magnetite layers. All opal would have been recrystallized to quartz at temperatures higher than 165°C (Pisciotto, 1981), but quartz itself remained in a state of dissolution-reprecipitation and in equilibrium with the pore water. Quartz in jasper layers close to the interface with magnetite layers would also have been affected by recrystallization, leading to loss of jasper spherules and larger hematite at lower temperatures, and magnetite at higher temperatures. The preserved jasper layers represent remnants of the recrystallization not coming to completion. Where the hydrostatic pressure overcame the integrity of the brittle silicified layers, brecciation occurred and fluid escaped.

Early-formed apatite in jasper captures a pristine hydrothermal-seawater rare earth and Y (REY) signal, with pronounced La, Eu, and Y anomalies. Later apatite that formed in magnetite layers has a slightly different REY profile with lower La and Y anomalies due to higher mobility under high water/rock reactions implied for the conditions of magnetite layer formation. Authigenic chlorite formed during late diagenetic stages and during metamorphism. However, some chlorite-rich layers interbedded with BIF contain rounded apatite crystals and quartz of detrital origin (indicated by REY profiles and cathodoluminescence, respectively) indicating a mix of authigenic and clastic sources. The footwall volcanic rocks are pervasively altered to a chlorite-epidote-sericite assemblage typical for Neoarchean greenstone belts, but no indications of focused hydrothermal upflow has been observed. The formation temperature calculated for chlorite is lower in BIF than in host rocks by about 50ºC on average, with small variations between BIF facies chert (220°C) and magnetite (240°C).

5.4 Geochemistry

The bulk composition of the Temagami BIF resembles that of modern metalliferous sediments such as the Red Sea muds (e.g. Laurila et al., 2014) and those found in submarine volcanic environments such as the East Pacific Rise (Boström and Peterson, 1969). However, the composition of Temagami BIF is much more homogenous spatially and across stratigraphy compared to modern metalliferous sediments and exhalites formed in close association with VMS deposits. This is particularly evident in the REY data, which reflect a stable REY reservoir. The transition metal concentrations are orders of magnitude lower than in sulfide- and oxide-facies exhalites formed in association with VMS mineralization (e.g., in the Bathurst mining camp, NB; Peter and Goodfellow, 1996). These data suggest that direct input, for example as sulfidic plume fallout, can be ruled out in the Temagami BIF. Instead, these elements were scavenged from ambient seawater by Fe-oxyhydroxides forming in the water column and transported to the seafloor in the Temagami BIF. The order of enrichment of trace elements is Sb=Cd>Cu=Hg>Ag=Sn>Pb for the elements forming carbonate-, chloro-, and hydroxide complexes in seawater, Sr>Rb>Cs>Ba>Zn>Ni>>Co for those present mostly as free cations, and U>As=Mo=V>W for the oxyanions. Compared to modern metalliferous sediments, the concentrations of elements such as W, Mo, and U are much lower reflecting the lack of

atmospheric oxygen and the limited potential for oxyanion formation in Neoarchean seawater. However, the higher significance of U within the group of oxyanions may be related to redox conditions approaching the threshold of U oxidation and mobilization without affecting the other oxyanions (cf., Bau and Alexander, 2009). Ni was less significant in Archean seawater compared to other, complex-forming elements such as Zn and Ba in modern seawater, possibly indicative of nutrient-limiting conditions for methanogenic bacteria by Ni-depletion suggested for the Neoarchean by Konhauser et al (2009).

The Temagami Ocean was anoxic, buffered by a vast reservoir of Fe^{2+}, and reducing, thus limiting the deposition of Mn, Ce, and many other redox sensitive elements. The iron in the water column was primarily contributed by hydrothermal venting, and allowed to accumulate under reducing conditions to concentrations of 100 μmol kg^{-1} to possibly as much as 5 mmol kg^{-1} (Sumner, 1997; Thibon et al., 2019). The pH of seawater in the Neoarchean was generally lower than in modern oceans, probably between pH 6.5-7 (Saito et al., 2003; Halevy and Bachan, 2017). Changes in that pH would have had significant impacts on the stability of carbonate complexes, the solubility of silica, and pH-sensitive elements like boron. Oxidation of vast amounts of Fe^{2+} would have significantly lowered the pH of the Temagami sub-basin:

$$4Fe_{aq}^{2+} + O_2 + 10H_2O \rightarrow 4Fe(OH)_3 + 8H^+$$ (Lepp and Goldich, 1964)

and

$$4Fe_{aq}^{2+} + CO_2 + 11H_2O \rightarrow 4Fe(OH)_3 + CH_2O + 8H^+$$ (Ehrenreich and Widdel, 1994)

This would have caused a significant increase in the solubility of B by transitioning from less soluble $B(OH)_4^-$ complexation at pH >7 to more soluble $B(OH)_3$ (Spivack and Edmond, 1987), inhibiting scavenging by Fe-oxyhydroxides and resulting in decreasing B concentrations in the higher stgratigraphic levels of the BIF.

Deposition of BIF was not directly linked to hydrothermal venting, but hydrothermal fluids were the most likely source for most elements in the Neoarchean ocean. In this way, the origin more closely resembles the formation of Superior-type BIF than volcanic-associated exhalites, the generally accepted origin of Algoma-type BIF, and highlights the importance of differentiated BIF classification beyond lithological context and age constraints.

5.5 Sulfur, hydrothermalism, and biology

The presence of the different BIF facies (oxide, silicate, sulfide, carbonate) in Temagami and other Algoma-type BIF is commonly seen as the expression of a redox gradient or proximity to hydrothermal venting, with sulfide facies representing the proximal deposits (James, 1954; Ohmoto et al., 2006). Clastic pyrite and sulfidic chert in Temagami have been classified as sedimentary in origin by their low Co/Ni (<1) (Bralia et al., 1979; Schwartz, 1995). Additionally, multiple sulfur isotopes reveal that sulfur in both facies is mostly derived from atmospheric sources. In sulfidic cherts, readily available organic material, not present in the other BIF facies, allowed sulfate-reducing bacteria to metabolize SO_4 derived from atmospheric SO_2 photolysis. SO_4 was in turn deposited in the ocean, converted to sulfide and ultimately diagenetic pyrite. In oxide BIF, ultra-trace S was also sourced from the atmosphere and deposited in the sediments. However, a different metabolic pathway, not requiring organic carbon as electron donor, would have been needed to reduce this sulfur− most likely, energetically favourable Fe-reducing metabolisms. The atmospheric source of sulfur in all cases, highlights the limited influence of hydrothermal sulfide in the Temagami sub-basin and implies a biologic control on the formation of the sulfidic cherts. The major difference in the initially precipitated material may have been the abundance of organic material. In sulfidic cherts, abundant organics were metabolized and the produced sulfide that reacted with Fe to form pyrite, in the process capturing chalcophile elements in the shallow sediment.

5.6 Implications for BIF-Systems and Conclusions

With a cumulative strike length of up to 2 km in the Sherman Mine and the BIF-hosting stratigraphy occurring over a distance of up to 40 km, the dimensions of the Temagami BIF approach what is more typically observed in Superior-type BIF. It contrasts sharply with typical occurrences of Algoma-type BIF, which may be only 10s of m thick and only a few kilometers or less in strike length. It also shares with Superior-type BIF the deposition in an open-ocean setting as opposed to a small, isolated basin near hydrothermal vents.

The Fe-oxyhydroxides formed in the water column were deposited as Fe-Si gel on the seafloor. No evidence has been found that suggests primary layering of the oxide-BIF material. Instead, post-depositional processes led to the development of pseudobanding and differentiation into jasper-, chert-, and magnetite facies. Lacking primary heterogeneity of the material contrasts sharply with models of Algoma-type BIF deposition based on pulses of hydrothermal fluid or seasonal changes in seawater temperature precipitating interlayered Si- and Fe-rich material (Sun et al., 2015). On a larger scale, development of sulfide-facies BIF was controlled by activity of sulfate-reducing bacteria, forming sulfidic cherts from similar precursor material where more organic material was available. The sulfur captured in sulfide-facies was derived from atmospheric cycling of volcanic SO_2, contradicting models predicting hydrothermal sulfur sources captured in Algoma-type BIF (Bekker et al., 2010). Silicate facies BIF is mostly derived from volcanic-derived material, with limited, local precipitation of a hydrogenous Fe^{2+}-Si phase such as green rust or nontronite. No evidence has been found to support a model suggesting post-depositional oxidation of a primary Fe^{2+}-Si was the major depositional pathway for Fe and Si in BIF (Rasmussen et al., 2014).

The depositional environment was not an enclosed basin, and the primary geochemical signals reflect open ocean chemistry influenced by distal hydrothermal venting. The overall trace element chemistry of the Temagami ocean was not unlike the modern ocean, with differences mostly attributed to reducing atmospheric and water column conditions and more hydrothermal influx to the Neoarchean basin. In contrast to most other Algoma-type BIF and hydrothermal exhalites, no distinct local geochemical signals, spatial or temporal variations are captured in the Temagami BIF. The Temagami BIF shares attributes with both Superior- and Algoma-type BIF, highlighting the necessity of BIF characterization and classification beyond host lithologies and association with hydrothermal ore deposits, but by mode of deposition.

5.7 References

Bau, M., Alexander, B.W., 2009. Distribution of high field strength elements (Y, Zr, REE, Hf, Ta, Th, U) in adjacent magnetite and chert bands and in reference standards FeR-3 and FeR-4 from the Temagami iron-formation, Canada, and the redox level of the Neoarchean ocean. Precambrian Research 174, 337-346.

Bekker, A., Slack, J.F., Planavsky, N., Krapež, B., Hofmann, A., Konhauser, K.O., Rouxel, O.J., 2010. Iron Formation: The Sedimentary Product of a Complex Interplay among Mantle, Tectonic, Oceanic, and Biospheric Processes. Economic Geology 105, 467-508.

Blake, R.E., Chang, S.J., Lepland, A., 2010. Phosphate oxygen isotopic evidence for a temperate and biologically active Archaean ocean. Nature 464, 1029.

Boström, K., Peterson, M.N.A., 1969. The origin of aluminum-poor ferromanganoan sediments in areas of high heat flow on the East Pacific Rise. Marine Geology 7, 427-447.

Bralia, A., Sabatini, G., Troja, F.J.M.D., 1979. A revaluation of the Co/Ni ratio in pyrite as geochemical tool in ore genesis problems. 14, 353-374.

Cairns-Smith, A.G., 1978. Precambrian solution photochemistry, inverse segregation, and banded iron formations. Nature 276, 807-808.

Crosby, W., Fuller, M., 1897. Vol. XIX. MARCH, 1897. No. 3 ORIGIN OF PEGMATITE, The American Geologist 19, p. 147.

Ehrenreich, A., Widdel, F., 1994. Anaerobic oxidation of ferrous iron by purple bacteria, a new type of phototrophic metabolism. Appl. Environ. Microbiol. 60, 4517-4526.

Halevy, I., Bachan, A., 2017. The geologic history of seawater pH. Science 355, 1069-1071.

James, H.L., 1954. Sedimentary facies of iron-formation. Economic Geology 49, 235-293.

Konhauser, K.O., Pecoits, E., Lalonde, S.V., Papineau, D., Nisbet, E.G., Barley, M.E., Arndt, N.T., Zahnle, K., Kamber, B.S., 2009. Oceanic nickel depletion and a methanogen famine before the Great Oxidation Event. Nature 458, 750-753.

Laurila, T.E., Hannington, M.D., Petersen, S., Garbe-Schönberg, D., 2014. Trace metal distribution in the Atlantis II Deep (Red Sea) sediments. Chemical Geology 386, 80-100.

Lepp, H., Goldich, S.S., 1964. Origin of Precambrian iron formations. Economic Geology 59, 1025-1060.

Ohmoto, H., Watanabe, Y., Yamaguchi, K.E., Naraoka, H., Haruna, M., Kakegawa, T., Hayashi, K., Kato, Y., 2006. Chemical and biological evolution of early Earth: Constraints from banded iron formations. Geological Society of America Memoirs 198, 291-331.

Papachristou, M., Voudouris, K., Karakatsanis, S., Kyriakopoulos, K., D'Alessandro, W., 2014. Geological setting, geothermal conditions and hydrochemistry of south and southeastern Aegean geothermal systems, pp. 47-75.

Peter, J.M., Goodfellow, W.D., 1996. Mineralogy, bulk and rare earth element geochemistry of massive sulphide-associated hydrothermal sediments of the Brunswick Horizon, Bathurst Mining Camp, New Brunswick. Canadian Journal of Earth Sciences 33, 252-283.

Pisciotto, K.A., 1981. Diagenetic trends in the siliceous facies of the Monterey Shale in the Santa Maria region, California. Sedimentology 28, 547-571.

Planavsky, N.J., Rouxel, O.J., Bekker, A., Lalonde, S.V., Konhauser, K.O., Reinhard, C.T., Lyons, T.W., 2010. The evolution of the marine phosphate reservoir. Nature 467, 1088-1090.

Rasmussen, B., Krapež, B., Meier, D.B., 2014. Replacement origin for hematite in 2.5 Ga banded iron formation: Evidence for postdepositional oxidation of iron-bearing minerals. Geological Society of America Bulletin 126, 438-446.

Rasmussen, B., Meier, D.B., Krapež, B., Muhling, J.R., 2013. Iron silicate microgranules as precursor sediments to 2.5-billion-year-old banded iron formations. Geology 41, 435-438.

Saito, M.A., Sigman, D.M., Morel, F.M.M., 2003. The bioinorganic chemistry of the ancient ocean: the co-evolution of cyanobacterial metal requirements and biogeochemical cycles at the Archean–Proterozoic boundary? Inorganica Chimica Acta 356, 308-318.

Schwartz, T.C., 1995. Petrology and geochemistry of felsic volcaniclastic rocks along the Sherman Mine Road, Temagami Greenstone Belt, Strathy Township, Ontario. McMaster University, MSc thesis, 180 pp.

Shibuya, T., Komiya, T., Nakamura, K., Takai, K., Maruyama, S., 2010. Highly alkaline, high-temperature hydrothermal fluids in the early Archean ocean. Precambrian Research 182, 230-238.

Spivack, A.J., Edmond, J.M., 1987. Boron isotope exchange between seawater and the oceanic crust. Geochimica et Cosmochimica Acta 51, 1033-1043.

Sumner, D.Y., 1997. Carbonate precipitation and oxygen stratification in late Archean seawater as deduced from facies and stratigraphy of the Gamohaan and Frisco formations, Transvaal Supergroup, South Africa. American Journal of Science 297, 455-487.

Sun, S., Konhauser, K.O., Kappler, A., Li, Y.-L., 2015. Primary hematite in Neoarchean to Paleoproterozoic oceans. GSA Bulletin 127, 850-861.

Swanner, E.D., Planavsky, N.J., Lalonde, S.V., Robbins, L.J., Bekker, A., Rouxel, O.J., Saito, M.A., Kappler, A., Mojzsis, S.J., Konhauser, K.O., 2014. Cobalt and marine redox evolution. Earth and Planetary Science Letters 390, 253-263.

Thibon, F., Blichert-Toft, J., Tsikos, H., Foden, J., Albalat, E., Albarede, F., 2019. Dynamics of oceanic iron prior to the Great Oxygenation Event. Earth and Planetary Science Letters 506, 360-370.

Ungemach, P., 2002. International Geothermal Days Greece 2002, International Workshop on the Possibility of Geothermal Development of the Aegean Islands Region, Milos, Greece. Geoproduction Consultants September, pp. 5-8.

Viehmann, S., Hoffmann, J.E., Münker, C., Bau, M., 2014. Decoupled Hf-Nd isotopes in Neoarchean seawater reveal weathering of emerged continents. Geology 42, 115-118.

Widdel, F., 1993. Ferrous iron oxidation by anoxygenic phototrophic bacteria. Nature 362, 834.

Zerkle, A.L., House, C.H., Brantley, S.L., 2005. Biogeochemical signatures through time as inferred from whole microbial genomes. Am J Sci 305, 467-502.

Appendix A: Sample Locations and Petrography

This document contains an overview of sample locations and petrographic descriptions for representative thin sections used in this study. For a full quantitative petrologic study of facies distributions and ore block analyses, see Ginley (2016). For detailed petrographic descriptions of samples from the volcanic host rocks partly included in this study, see Streit (2017).

Figures A-1 and A-2 depict the distribution of samples along the Hwy 11 outcrop and Sherman Mine. Sample locations in the Sherman Mine are from ore blocks on the rims of the open pits. Blocks likely originate from the pit they are lined around, but the exact origin within the pit is uncertain.

Petrographic descriptions and representative images of thin sections of samples used in this study have been compiled in the second part of this document. The following notes and abbreviations apply to the entire document:

TS: Thin section scan.
PPL: Transmitted plain polarized light image.
XPL: Transmitted cross polarized light image.
REF: Reflected light image.
BSE: Backscattered electron image. Obtained on a JEOL 6610LV at the University of Ottawa under high vacuum conditions, 20kV acceleration voltage, 44 or 56 spot size.
CL: Cathodoluminescence image. Obtained on a JEOL 6610LV SEM equipped with a Gatan Mini-CL detector under high vacuum conditions, 20 kV acceleration voltage, 57 spot size, and 20 mm working distance.

In the figures, mineral labels were inserted directly above the according mineral if not indicated differently (lines). Abbreviations were applied following Whitney and Evans (2010):

ap: apatite
cal: calcite
cb: carbonate undifferentiated
chl: chlorite
sid: siderite (Mg-rich)
dol: dolomite (Fe-rich)
hem: hematite
mag: magnetite
qz: quartz
stp: stilpnomelane
ilm: ilmenite
py: pyrite
ms: muscovite
bt: biotite
min: minnesotaite
mon: monazite
zrn: zircon
px: pyroxene
ol: olivine
brt: barite
gr: graphite

Note: “graphite” is used to describe undifferentiated carbon-rich material. Only in very few cases may the carbon bearing phase be crystallized as true graphite.

Layer types may be abbreviated as:
jas: jasper
w-chert: white chert
b-chert: black chert
jas/b-chert: intermediate or transition between layer types
magnetite: magnetite layer (as opposed to magnetite crystal)

References:

Ginley, S.J., 2016. A Field and Petrological Study of Oxide-Facies Algoma-Type Banded Iron Formation, Sherman Mine, Temagami. University of Ottawa, M.Sc. thesis, 275 pp.

Streit, L., 2017. Chlorite Geochemistry of Altered and Metamorphosed Volcanic Host Rocks of the Temagami Banded Iron Formation. University of Ottawa, BSc thesis, 119 pp.

Whitney, D.L., Evans, B.W., 2010. Abbreviations for names of rock-forming minerals. American Mineralogist 95, 185-187.

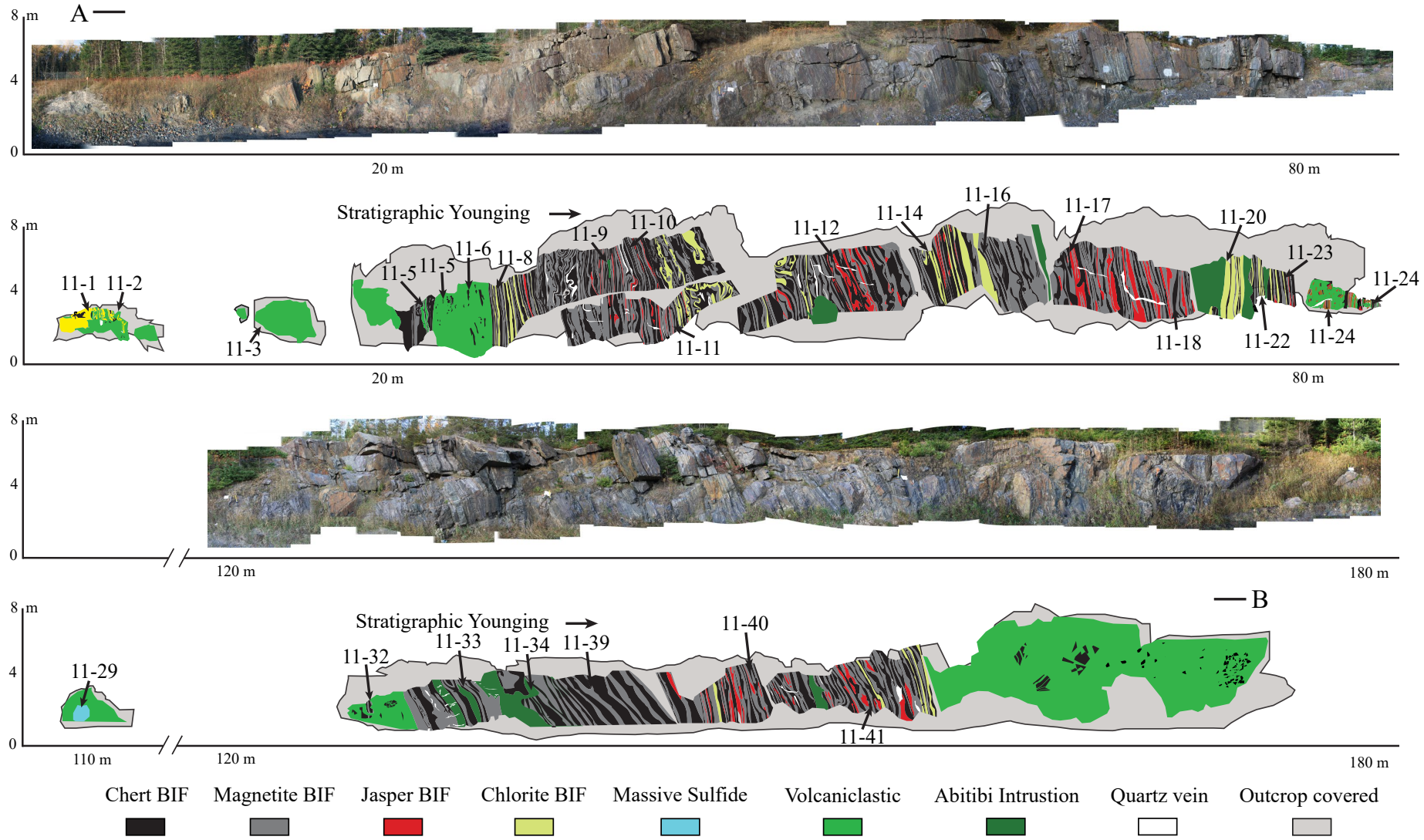


Figure A-1: Sample locations along the Hwy 11 outcrop of the South BIF.

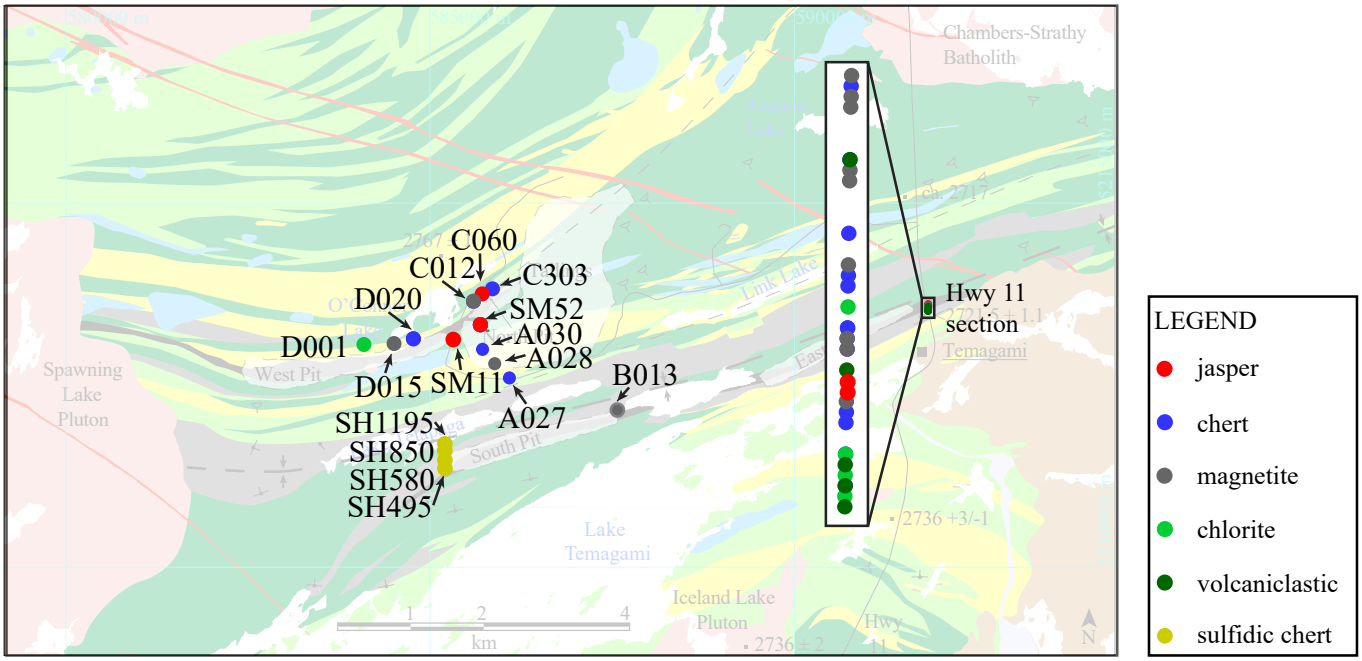


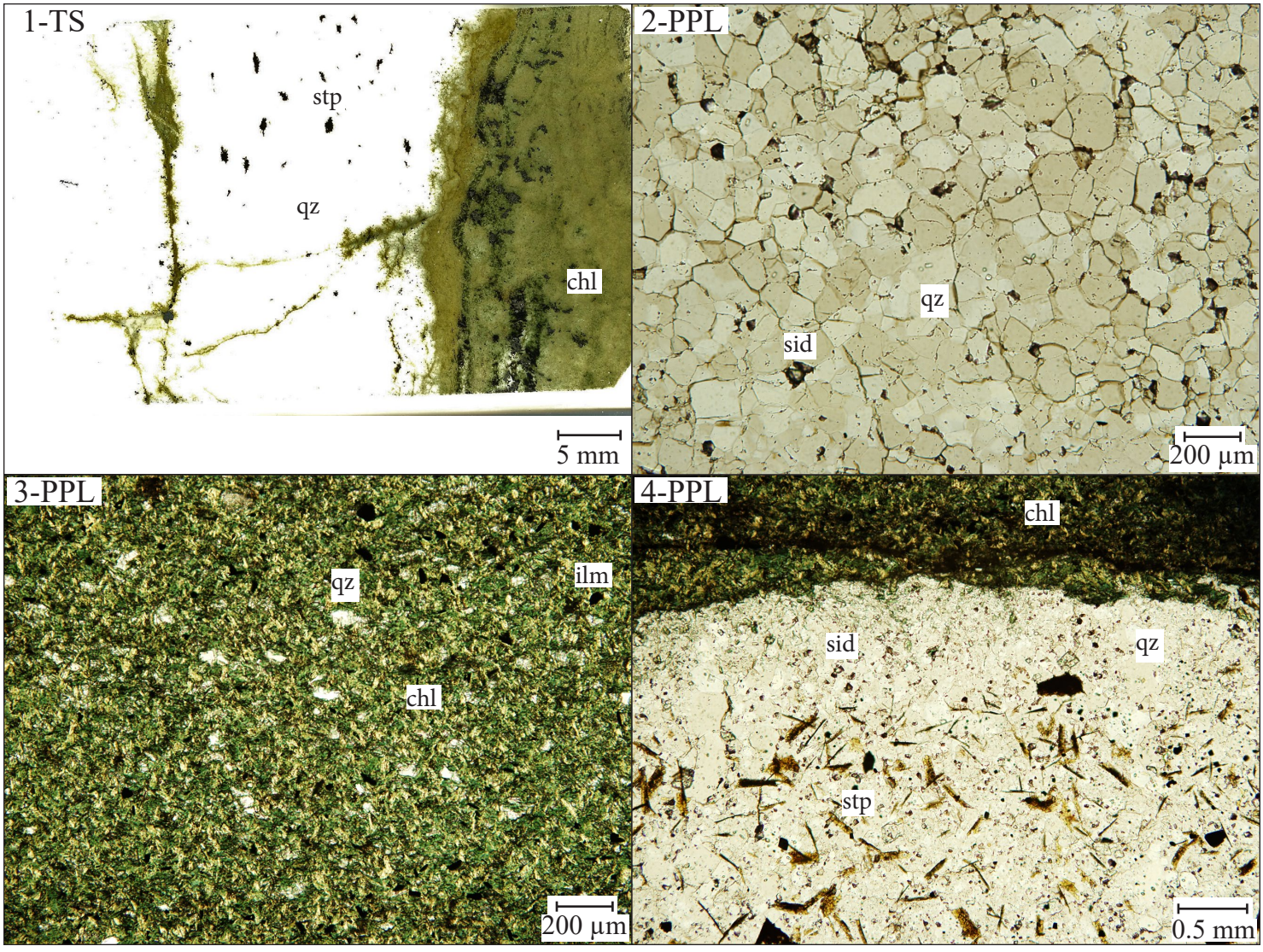
Figure A-2: Sample locations in the Sherman Mine. Note multiple samples from one hand sample (e.g. B013, SM52) are superimposed and appear as one sample. For detailed locations of the samples in the Hwy 11 section, see Figure A-1

Sample: 11-1

Sample Type: chert/volcaniclastic
Location: 47.06858, -79.79071
BIF Member: South BIF

SiO_2 [wt.%]	Al_2O_3 [wt.%]	Fe_2O_3 [wt.%]	Ge [ppm]	Pb [ppm]	As [ppm]	Ni [ppm]	B [ppm]	ΣREE [ppm]
38.9	13.3	33.1	4.1	0.9	1.0	35.0	0.1	131.1

Context: Sample of chert-chlorite interlayering at the stratigraphic base in the Hwy 11 outcrop of the South BIF. Chert is interlayered with volcaniclastic material and greywacke. Fining sequences in some layers indicate younging to the North. The volcaniclastic (shale) part of the sample was prepared for bulk rock geochemistry.
Petrography: Chert contains few impurities, and has been classified in the field as white chert. Quartz in chert is medium-grained (20-100 µm). Accessory minerals are lenses of siderite, stilpnomelane, >100 µm euhedral pyrite, and Type 2 magnetite. The interface of chert with the volcaniclastic material is sharp, but may be distorted, scalloped, or show "breakout structures" (see discussion on dewatering in Chapter 2). The volcaniclastic layer is preserved as near-massive, medium grained (20-50 µm), commonly bladed chlorite. Chlorite is exclusively yellowish-green in thin section. Most chlorite is randomly oriented, but some grains are larger and grown as pseudomorphs of tabular to subrounded precursor phases. Accessories in the chlorite layer are ilmenite, Fe-carobonates, magnetite, and apatite. Ilmenite is oriented parallel to layering and focused along the immediate interface of chlorite and chert.
Features: Type 3 veins containing chlorite occur at steep angles to layering in both chert and chlorite. A dewatering breakout structure of chlorite in chert is preserved on the interface of the layers.

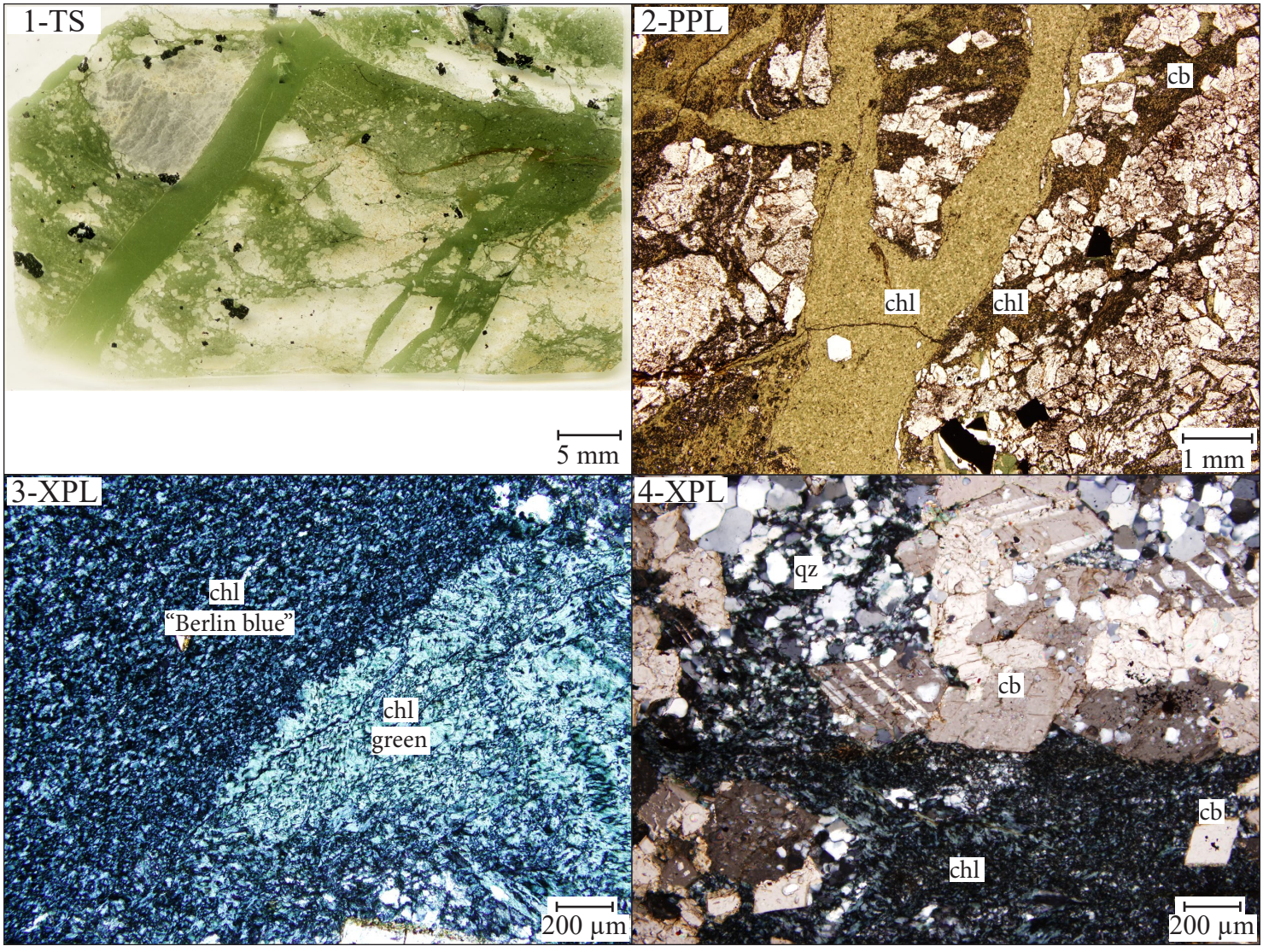


Sample: 11-2a

Sample Type: chlorite/chert
Location: 47.06842, -79.79071
BIF Member: South BIF

SiO_2 [wt.%]	Al_2O_3 [wt.%]	Fe_2O_3 [wt.%]	Ge [ppm]	Pb [ppm]	As [ppm]	Ni [ppm]	B [ppm]	ΣREE [ppm]
42.3	9.54	26.9	3.4	1.2	17	27.7	0.3	47.2

Context: Sample 11-2a is a thick chlorite-chert breccia layer near the stratigraphic base of the South BIF in the Hwy 11 outcrop. The chlorite part of the sample was prepared for bulk rock geochemistry.
Petrography: The sample consists of black chert and carbonate clasts in a chlorite-carbonate matrix cut by massive chlorite veins.
The black chert fragment is microbanded and consists of fine grained (<50 µm) quartz. Type 1 & 2 magnetite is abundant. Large carbonate minerals (>100 µm) are likely breccia fragments. Chlorite is massive and fine grained in mm-scale veins, emplaced in carbonate breccia. It can also occur as breccia-encapsulating masses. Two types of chlorite can be distinguished under XPL, a fine grained "Berlin blue" iron rich-, and a coarse-grained yellow-green iron-poor variety. The chlorite layers or -veins consist of the Berlin blue variety, whereas both types can occur in the breccia-encapsulating masses. Accessory minerals in chlorite are ilmenite, carbonate, magnetite, pyrite, and zircon. Large carbonate minerals have abundant <1 µm inclusions of quartz. The chlorite layers or veins are cut by a later generation of aluminosilicate-bearing veins introducing an alteration halo of <100 µm scale, producing biotite around the veins.

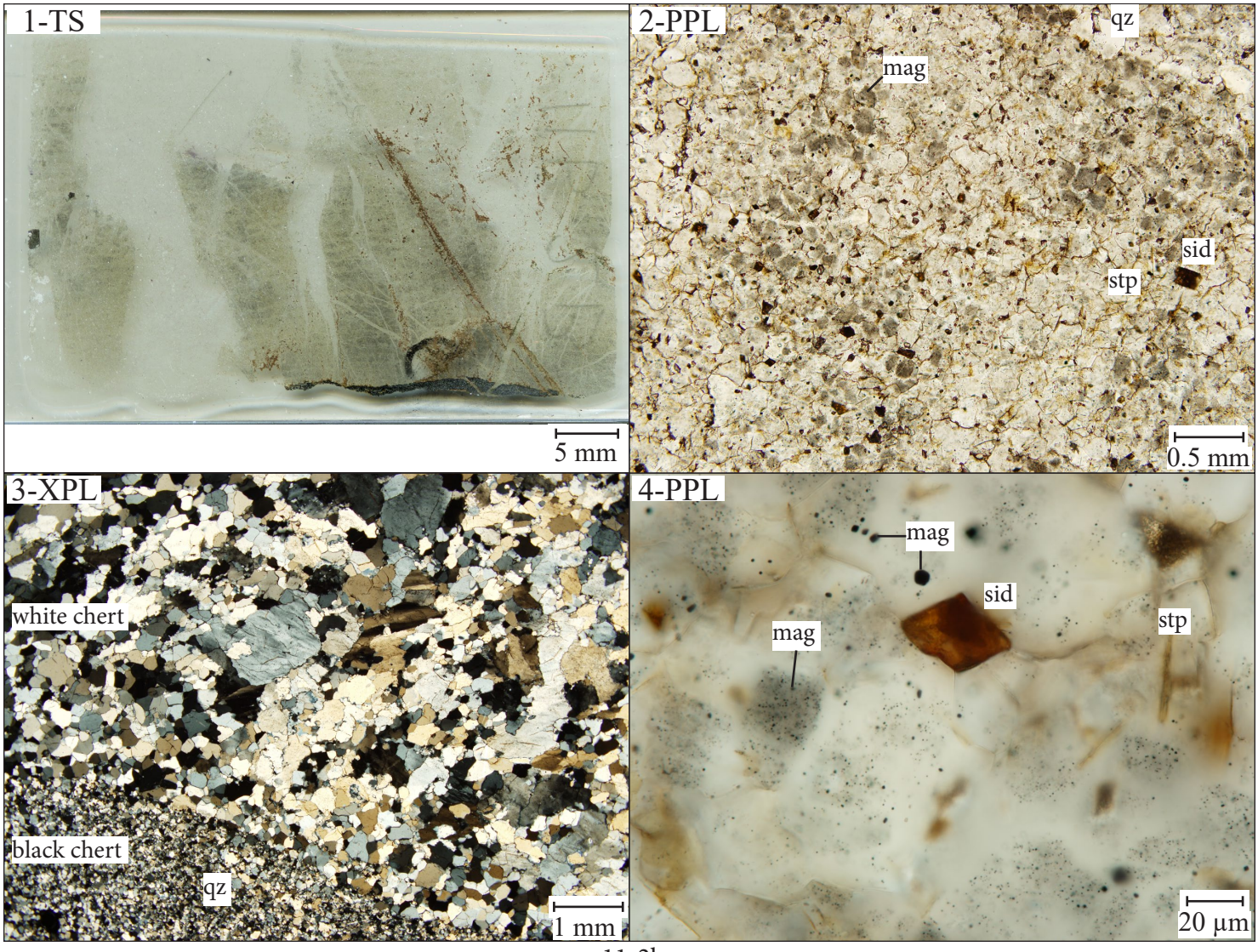


Sample: 11-2b

Sample Type: chert
Location: 47.06842 -79.79071
BIF Member: South BIF

SiO_2 [wt.%]	Al_2O_3 [wt.%]	Fe_2O_3 [wt.%]	Ge [ppm]	Pb [ppm]	As [ppm]	Ni [ppm]	B [ppm]	ΣREE [ppm]
n/a	n/a	n/a	n/a	n/a	n/a	n/a	n/a	n/a

Context: Sample 11-2a was produced from the same hand sample as 11-2b, but consists of a black chert layer brecciated in-situ by quartz veins.
Petrography: The massive black chert consists of small-grained quartz (<50 µm) with abundant Type 1&2 magnetite inclusions. The distribution of magnetite inclusions is irregular, and concentrated in the centre of quartz grains. Accessory minerals in black chert are magnetite, stilpnomelane, siderite, dolomite, and chlorite. The black chert is brecciated in-situ by anomalously thick (>5 mm) quartz veins. The quartz in the veins is the largest found in any sample, up to 200 µm and containing abundant Type 2 magnetite inclusions. Quartz has been irregularly deformed (during vein emplacement?) and in response shows stress domains of slightly different extinction angles



11-2b

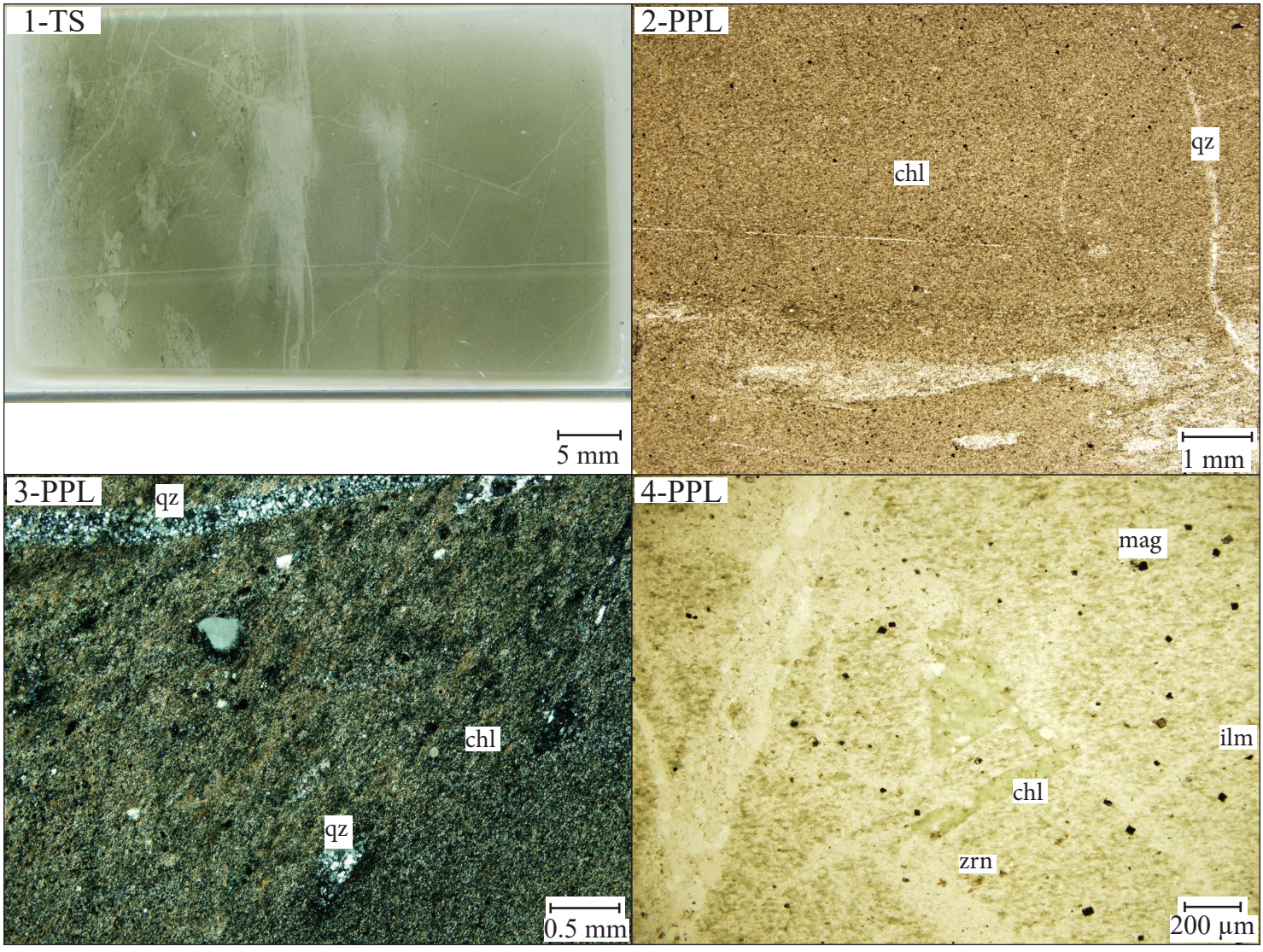
Sample: 11-3a

Sample Type: volcaniclastic (-chert)
Location: 47.06844, -79.79071
BIF Member: South BIF

SiO_2 [wt.%]	Al_2O_3 [wt.%]	Fe_2O_3 [wt.%]	Ge [ppm]	Pb [ppm]	As [ppm]	Ni [ppm]	B [ppm]	ΣREE [ppm]
68.5	10.2	8.2	3.4	1.1	0.9	21.4	18.2	108.3

Context: Massive volcaniclastic material preserved as chlorite near the stratigraphic base of the South BIF from the Hwy 11 outcrop. The same hand sample contains chert layers not captured in the thin section. The volcaniclastic (shale) part was prepared for bulk rock geochemistry as sample 11-3a (values above), and the chert part was prepared as 11-3b.

Petrography: Sample 11-3a consists of a single, massive layer of volcaniclastic material, now preserved as chlorite. Chlorite is very fine grained (<20 µm), and near massive. It does occurs in a more yellow-brownish hue under PPL compared to the dark green colour in other samples. Some irregularly shaped, quartz rich domains are present, but contain considerable chlorite. Accessory minerals in chlorite are quartz, magnetite, zircon, apatite, siderite, dolomite, ilmenite, and monazite. Quartz occurs as ~50 µm, sub-rounded crystals in a matrix of fine grained chlorite. Some of the larger quartz grains show deformation-induced variable extinction angles under XPL. Fine, irregularly oriented quartz veins cut the massive chlorite matrix, often taking on sharp, Z-fold-like shapes. Chlorite around quartz veins is often altered to a more Berlin blue colours under XPL.



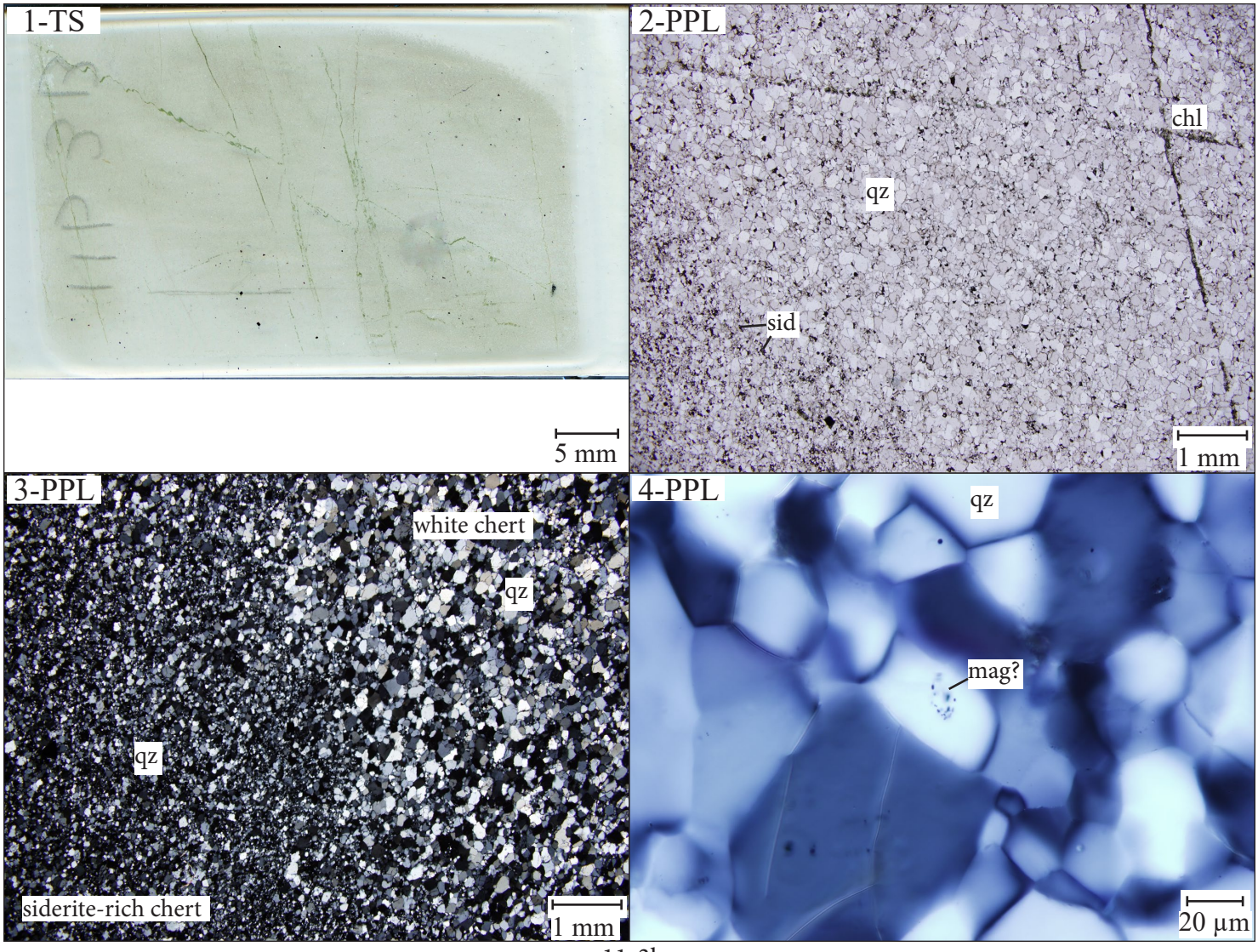
11-3a

Sample: 11-3b

Sample Type: chert
Location: 47.06844 -79.79071
BIF Member: South BIF

SiO_2 [wt.%]	Al_2O_3 [wt.%]	Fe_2O_3 [wt.%]	Ge [ppm]	Pb [ppm]	As [ppm]	Ni [ppm]	B [ppm]	ΣREE [ppm]
96.4	0.69	1.4	1.8	2.3	3.7	19.4	56.8	4.5

Context: Sample 11-3b was produced from the same handsample as 11-3a, collected near the stratigraphic base of the South BIF in the Hwy 11 outcrop. The sample is a pure white chert.
Petrography: Sample 11-3b is a pure white chert comprising medium- to large quartz (~50-100 µm). Other mineral phases are <20 µm siderite abundant up to 30 vol.% in some areas, Type 1 magnetite in the core of some quartz, trace chlorite (<<1 vol.%), and pyrite (5 grains in the thin section). Quartz is of much smaller size (~20 µm) where siderite is abundant. Note: Siderite appears anomalously dark in PPL images due to optical shadow effects in response to topography on the thin section, introduced by the hardness difference between siderite and neighboring quartz during preparation. Chlorite is regular dark green in PPL and Berlin blue in XPL. Type 1 magnetite is focused in the core of some quartz in the siderite-free zones. The abundance of magnetite is much less, and Type 1 magnetite "rings" are restricted to few single quartz grains, compared to abundant Type 1 and 3 magnetite in black chert and jasper. Thin chlorite veins cut the length of the thin section. The veins are discontinuous, deflected and commonly distorted, widening and thinning around angular offsets.



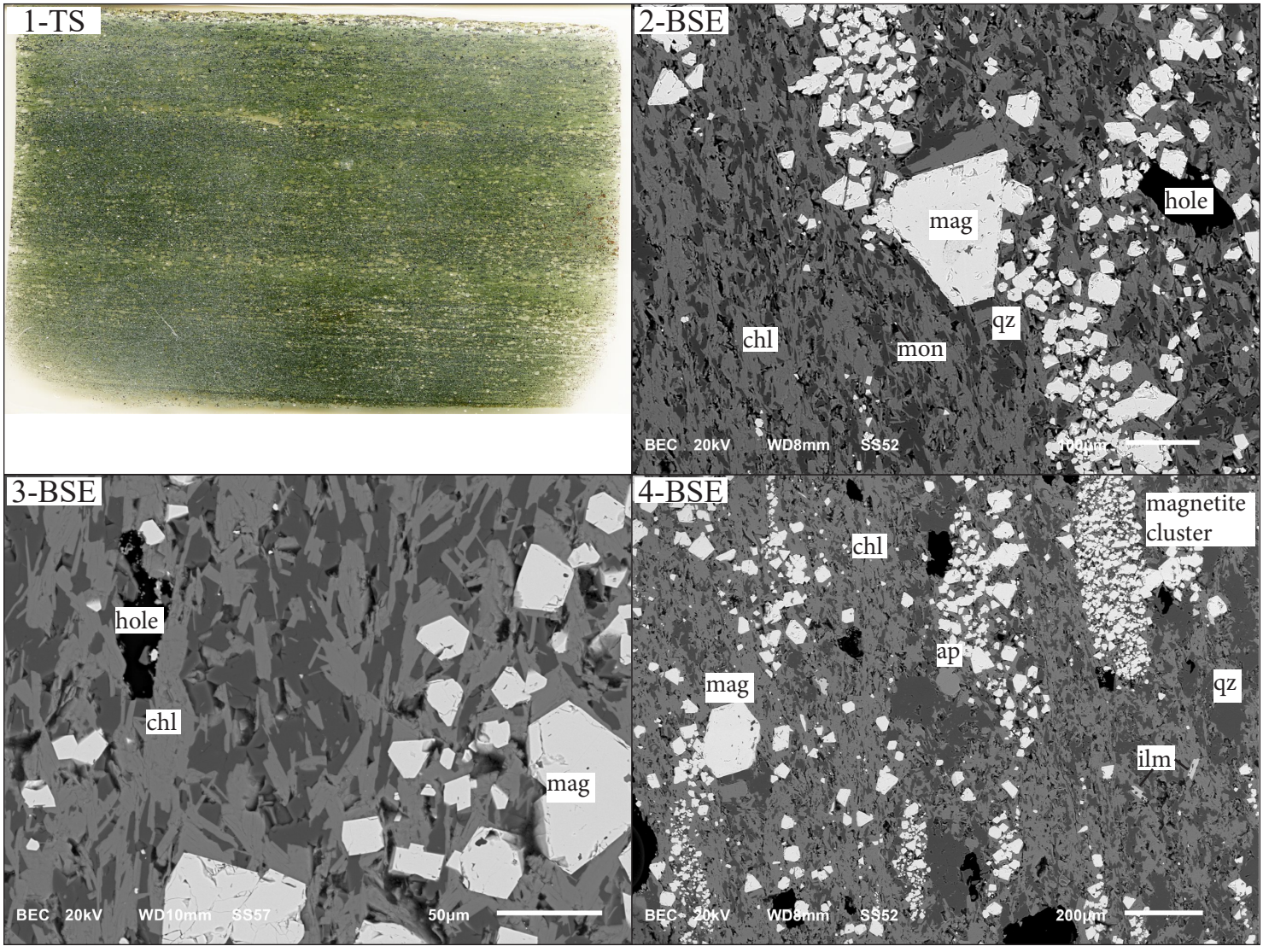
11-3b

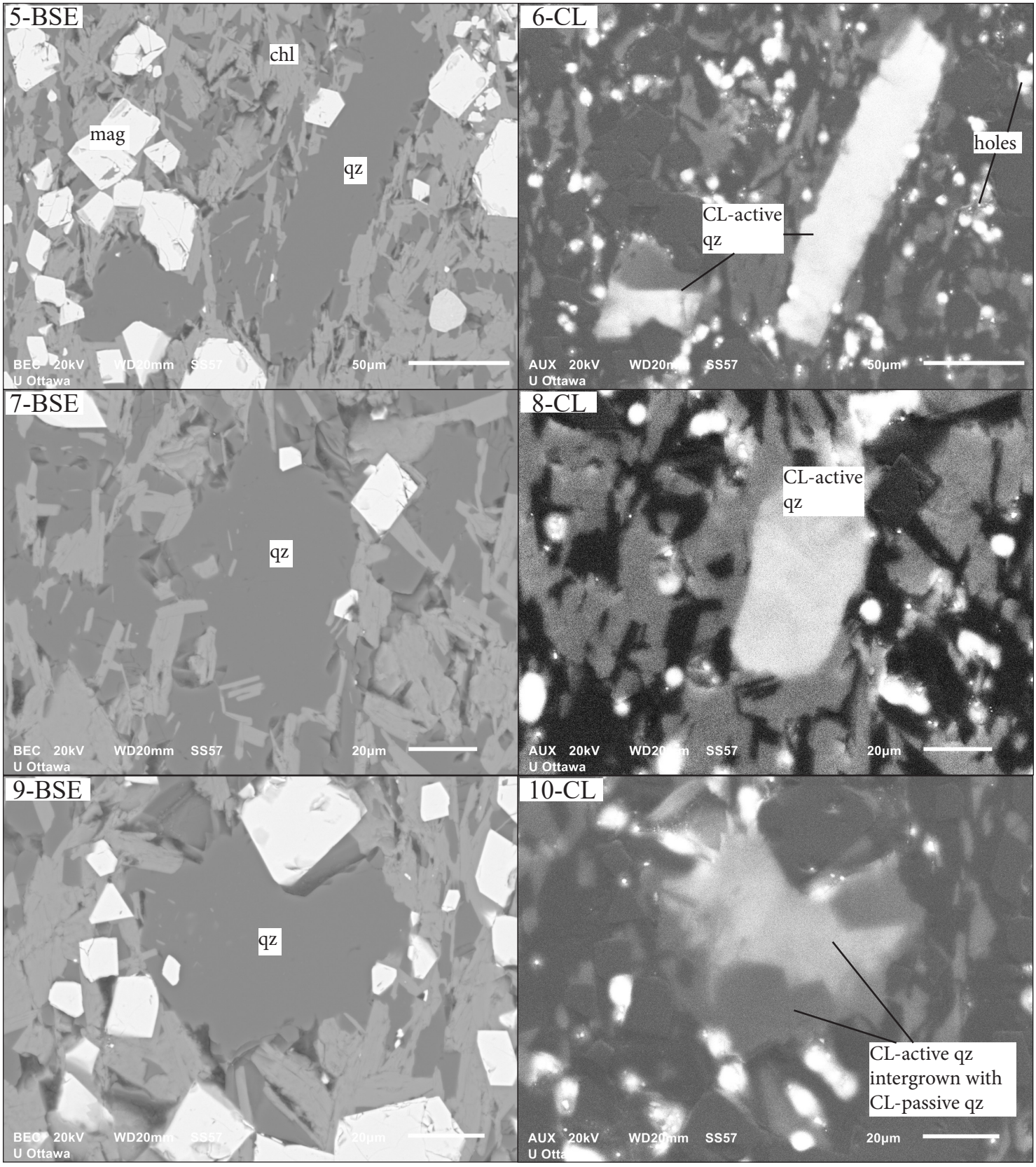
Sample: 11-4

Sample Type: chlorite
Location: 47.06845 -79.79071
BIF Member:

SiO_2 [wt.%]	Al_2O_3 [wt.%]	Fe_2O_3 [wt.%]	Ge [ppm]	Pb [ppm]	As [ppm]	Ni [ppm]	B [ppm]	ΣREE [ppm]
33.7	7.66	46.7	8.9	8.7	1.2	7.1	0.1	34.6

Context: Sample 11-4 was cut from the Hwy 11 outcrop near the stratigraphic base of the South BIF. The chlorite layer is interlayered with black chert, magnetite, and other chlorite layers.
Petrography: 11-4 is a banded chlorite sample. Chlorite occurs major mineral with quartz and magnetite a secondary major phases. Ilmenite, apatite, monazite, zircon and pyrite occur as accessory and trace minerals. The chloritic matrix is microbanded, with individual bands defined by higher chlorite abundance and the presence of Type 2 magnetite clusters. Chlorite is oriented parallel to microbanding, with individual crystals ranging in size from 10-50 μm. Chlorite has variably green and Berlin blue interference colours. Magnetite is evenly distributed and occurs as Type 2 and 3. Type 2 magnetite forms microbanding-parallel clusters or lenses not observed in any other sample. Quartz fills the interstitial spaces of chlorite, developing the angular chrystal shapes predetermined by chlorite. Some larger chlorite is rounded, and commonly CL-active, a feature not observed in other samples. Trace apatite is rounded and not euhedral as in other samples. Ilmenite occurs as elongated, tabular crystals with inclusions of quartz, and can overgrow earlier magnetite.



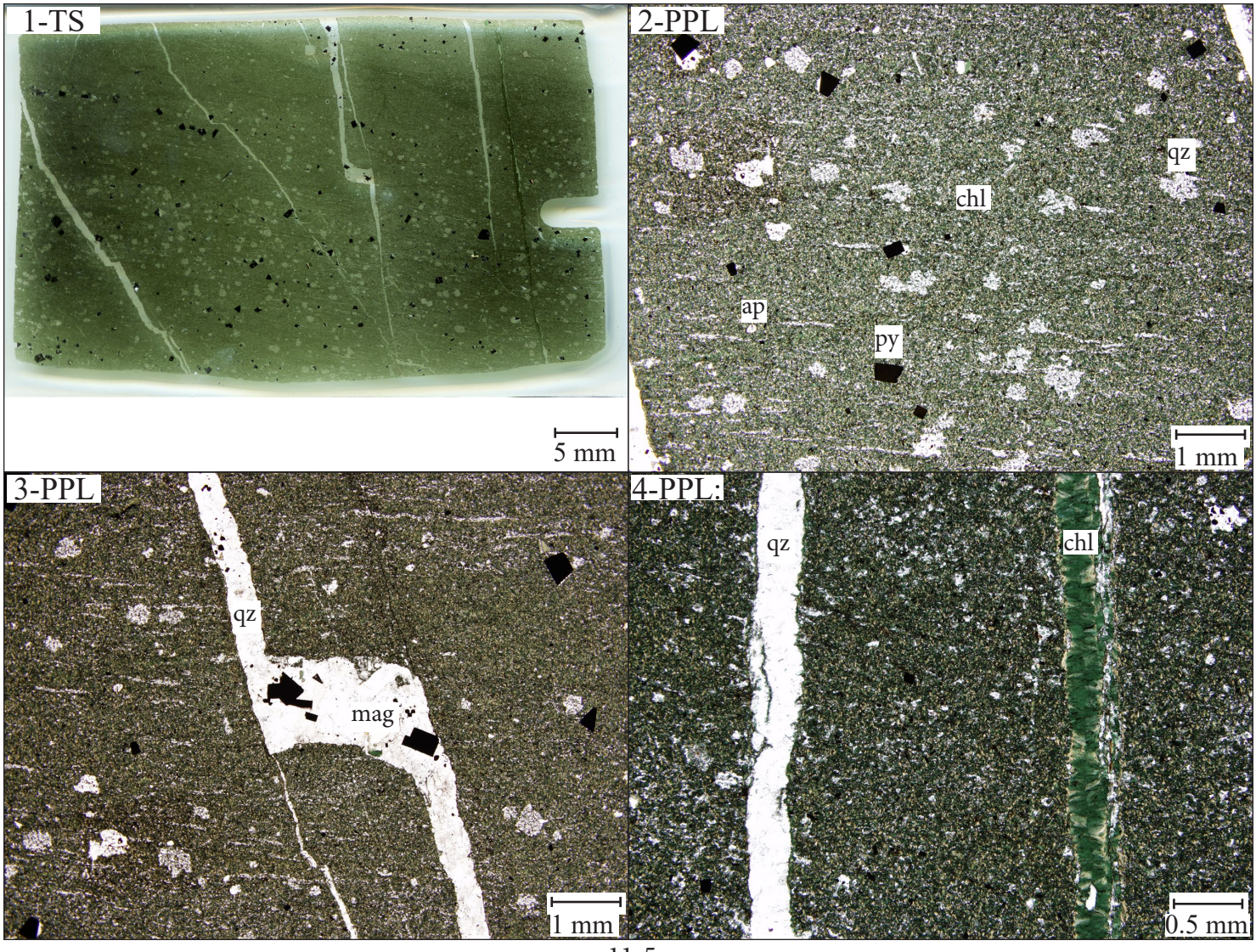

5-BSE
chl
mag
qz
BEC 20kV WD20mm SS57 50µm
U Ottawa
6-CL
holes
CL-active
qz
AUX 20kV WD20mm SS57 50µm
U Ottawa
7-BSE
qz
BEC 20kV WD20mm SS57 20µm
U Ottawa
8-CL
CL-active
qz
AUX 20kV WD20mm SS57 20µm
U Ottawa
9-BSE
qz
BEC 20kV WD20mm SS57 20µm
U Ottawa
10-CL
CL-active qz
intergrown with
CL-passive qz
AUX 20kV WD20mm SS57 20µm
U Ottawa

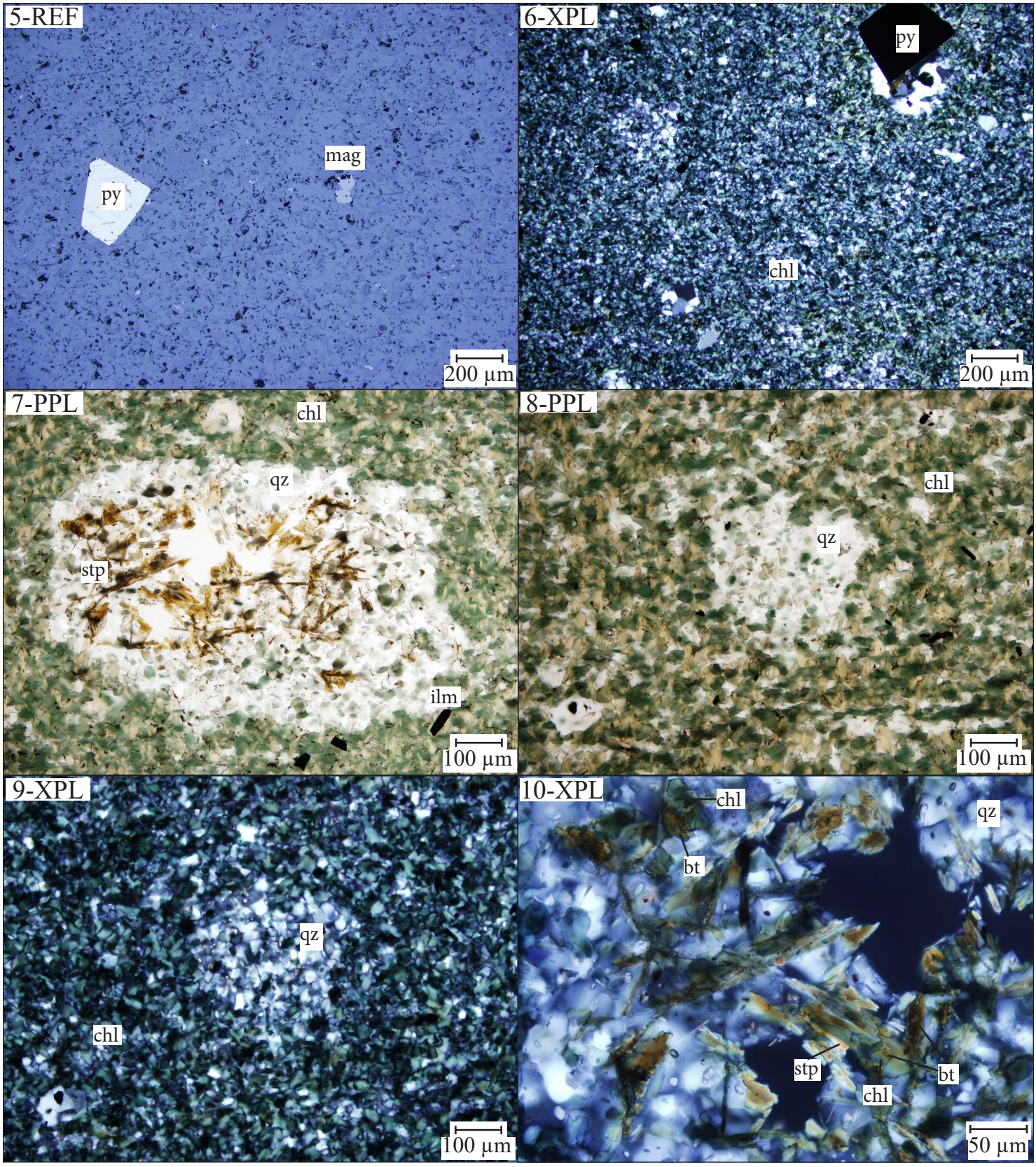
Sample: 11-5

Sample Type: volcaniclastic
Location: 47.06847 -79.79071
BIF Member: South BIF

SiO_2 [wt.%]	Al_2O_3 [wt.%]	Fe_2O_3 [wt.%]	Ge [ppm]	Pb [ppm]	As [ppm]	Ni [ppm]	B [ppm]	ΣREE [ppm]
46.5	11.0	28.1	5.0	3.4	10	12.7	0.1	126.0

Context: Sample of a thick layer of volcaniclastic material from near the stratigraphic base of the South BIF in the Hwy 11 outcrop.
Petrography: The sample consists of >90 vol.% chlorite, some quartz, and accessory Type 2 or 3 magnetite, ilmenite, pyrite, apatite, and zircon. Chlorite is fine grained (< 25µm) and distributed evenly, except in quartz rich clasts or "vesicles" where chlorite is less abundant, but (~5 µm-) zircon is focused. The clasts are subangular and >100 µm, likely representing larger clasts of precursor material altered to quartz-chlorite, with zircon as residual phase. The distribution of the clasts is irregular and more abundant in the central part of the thin section. Some of the material in the clasts has undergone incomplete alteration, capturing chloritization of biotite. Type 2 or 3 magnetite and pyrite are large (>100 µm), but not volumetrically significant. Ilmenite is authigenic (sometimes intergrown with, or containing inclusions of quartz and chlorite) and present in bladed habits <20 µm long. Chlorite occurs in the dark green (PPL) with Berlin blue interference colours (XPL) variety in the matrix, but also in the light green-yellow (PPL) and green (XPL) in some domains, as well as in the chlorite veins.
Features: Where zircon is in contact with chlorite, brown pleochroic halos are developed. Parallel sets of veins are common, containing exclusively either quartz-magnetite or chlorite. Quartz veins are associated with brittle sinistral offset, capturing mm-scale dislocation and leading to a thickening of the central window opening by stepwise offset of the dislocation.



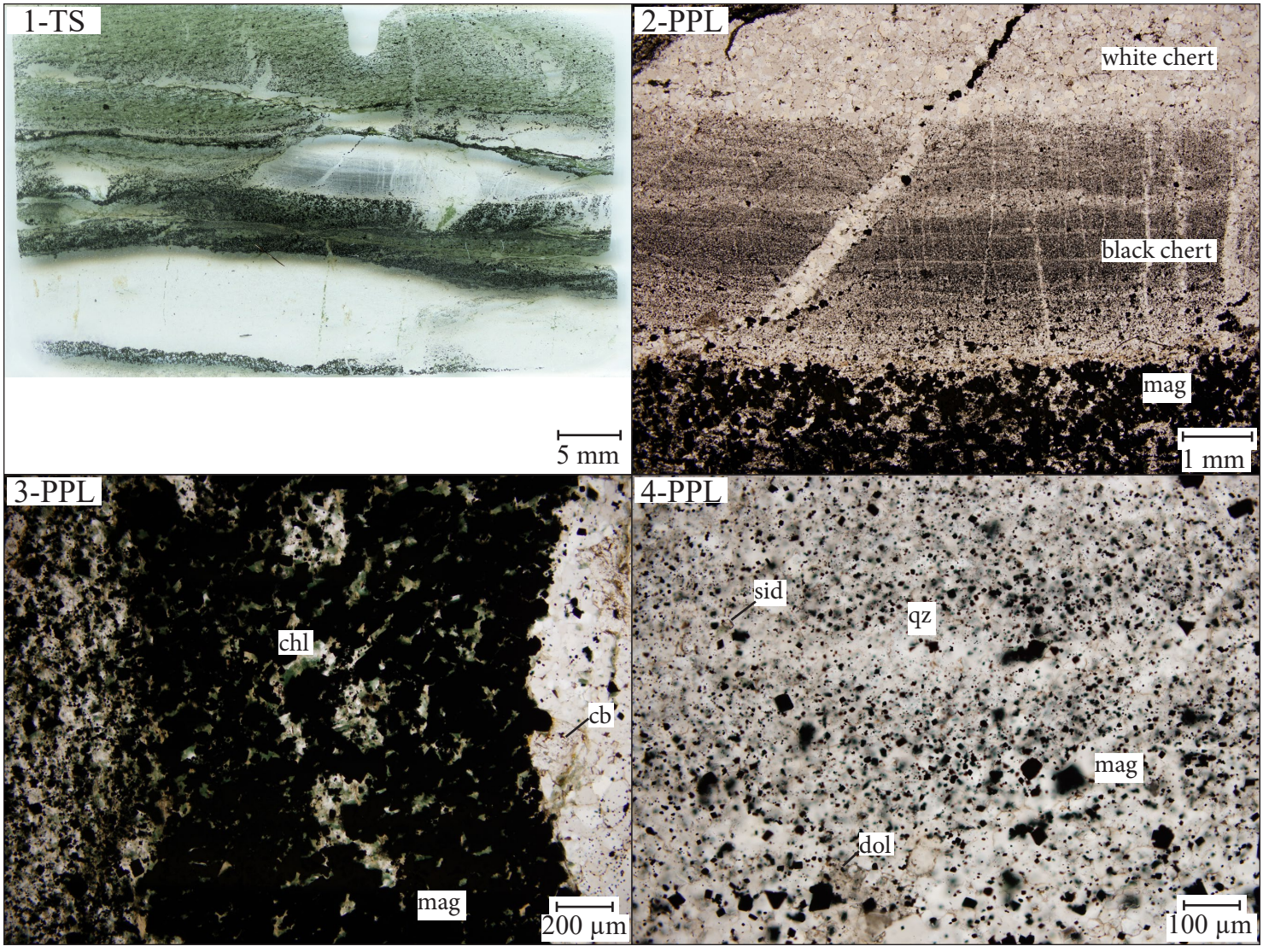

5-REF
py
mag
200 µm
6-XPL
py
chl
200 µm
7-PPL
chl
qz
stp
ilm
100 µm
8-PPL
chl
qz
100 µm
9-XPL
qz
chl
100 µm
10-XPL
chl
qz
bt
stp
bt
chl
50 µm

Sample: 11-6

Sample Type: chert-magnetite-chlorite
Location: 47.06849 -79.79071
BIF Member: South BIF

SiO_2 [wt.%]	Al_2O_3 [wt.%]	Fe_2O_3 [wt.%]	Ge [ppm]	Pb [ppm]	As [ppm]	Ni [ppm]	B [ppm]	ΣREE [ppm]
51.7	5.31	30.3	5.9	0.8	0.9	5.1	0.1	17.3

Context: Sample 11-6 is a chert-magnetite BIF sample from the Hwy 11 outcrop of the South BIF, and marks the stratigraphic onset of magnetite-chert BIF deposition in the Hwy 11 section. The chlorite rich material was sampled for whole rock geochemistry.
Petrography: The sample captures interlayering of white chert, chlorite-rich magnetite, and black chert layers. The white chert contains large (~100 µm) quartz, and chlorite, Type 1 magnetite, pyrite, and Fe-dolomite as accessory phases. Magnetite layers comprise Type 3 to 4 magnetite, chlorite, calcite, apatite, trace pyrite, monazite and zircon. Black chert layers are microbanded, and comprise Type 1 and 2 magnetite and small quartz (~10 µm), as well as trace siderite and pyrite. Microbanded black chert domains are sharply terminated against chlorite-rich domains, possibly representing a brecciated fragment or boudin. Other, non-microbanded domains of black chert do not contain Type 1 but Type 2 magnetite, chlorite, and Fe-dolomite. Chlorite is exclusively of the dark green (PPL) and Berlin blue (XPL) variety.
Features: Multiple generations of (quartz) veins are present, with the earliest generations preserved exclusively in black chert.

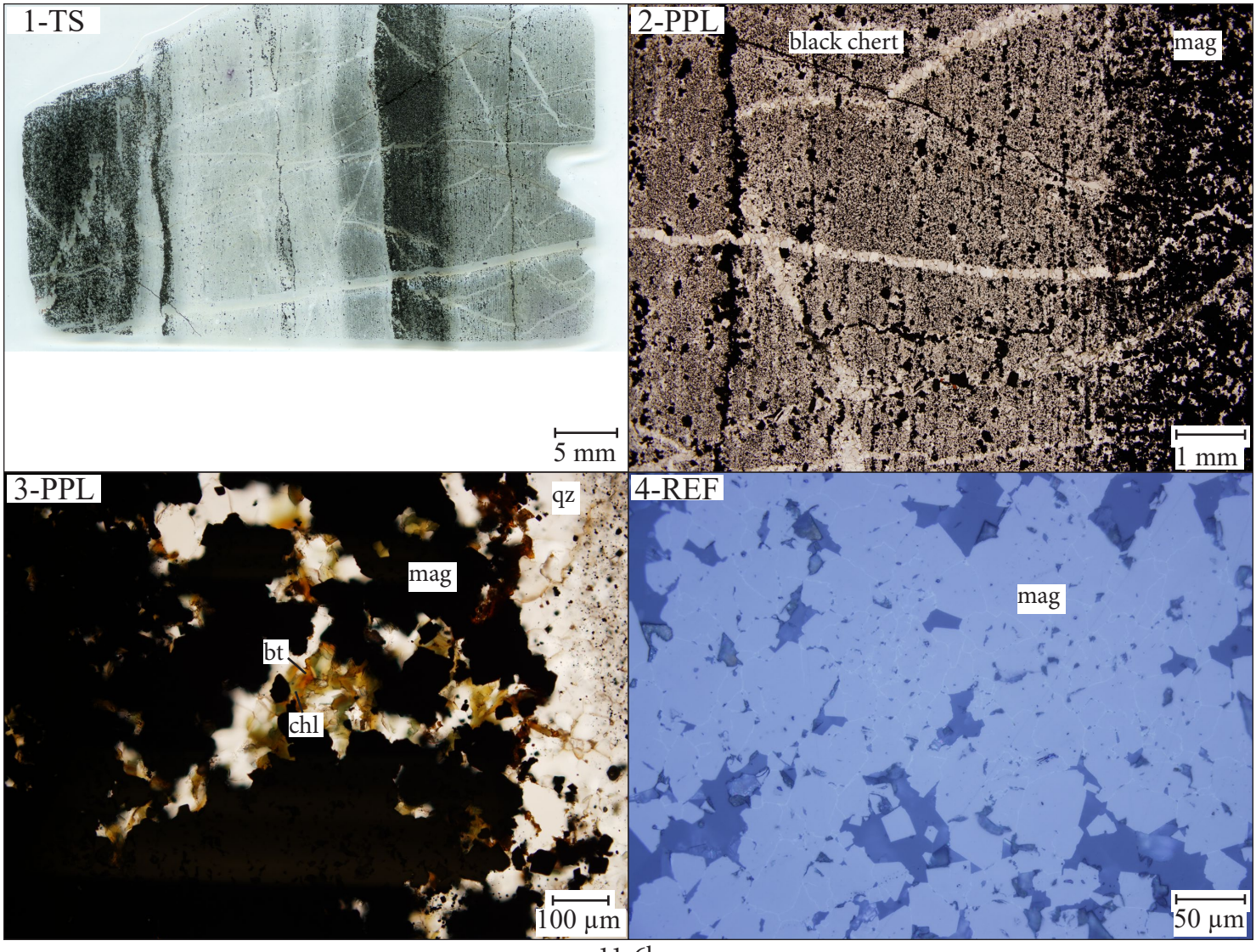


Sample: 11-6b

Sample Type: magnetite-chert
Location: 47.06849 -79.79071
BIF Member: South BIF

SiO_2 [wt.%]	Al_2O_3 [wt.%]	Fe_2O_3 [wt.%]	Ge [ppm]	Pb [ppm]	As [ppm]	Ni [ppm]	B [ppm]	ΣREE [ppm]
65.9	0.25	33.5	5.8	0.8	1.0	0.3	8.0	14.2

Context: The thin section for sample 11-6b was cut from the same handsample as 11-6a, taken at the lower stratigraphic onset of BIF deposition in the South BIF along the Hwy 11 section.
Petrography: The sample comprises magnetite and black chert interlayering, with only trace amounts of chlorite compared to 11-6a and no zircon, monazite, or ilmenite. The thin section captures two magnetite and two black chert layers. Black chert is variably rich in Type 1 and 2 magnetite and small (<20 µm) quartz. Accessory minerals are pyrite and Fe-dolomite. Microbanding is exceptionally well developed and anomalously defined by sub-continuous bands of magnetite in chert. Other areas of magnetite-poor black chert consist of larger quartz, approaching white chert characteristics.
Magnetite layers are 1-2 cm thick and comprise Type 3-4 magnetite, with quartz, chlorite, biotite, and Fe-carbonates in the interstitial spaces. Some central parts of the middle magnetite layer are near-massive, containing masses of intergrown Type 4 magnetite.
Features: Quartz vein generations 1-3 are present in black chert, and 2-3 are preserved in magnetite layers. Massive magnetite displays brighter reflection on the grain boundaries of the individual intergrown crystals. This might be an optical effects on grain boundaries, or a trace lining of hematite. Biotite and chlorite are intricately intergrown in the interstitial spaces of magnetite in magnetite layers, possibly reflecting ongoing replacement processes of one phase by the other.



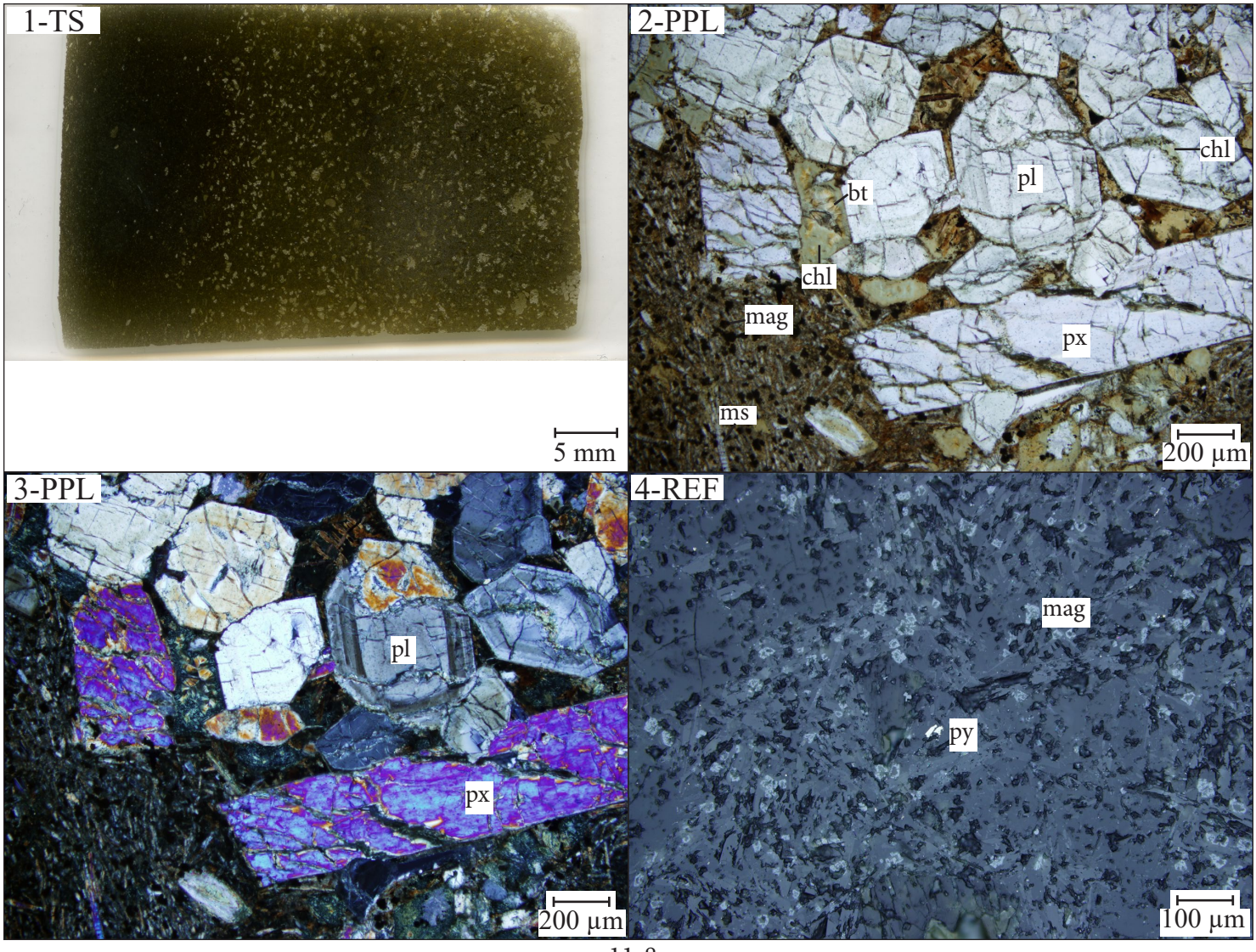
Sample: 11-8

Sample Type: intrusive
Location: 47.06853 -79.79071
BIF Member: South BIF

SiO_2 [wt.%]	Al_2O_3 [wt.%]	Fe_2O_3 [wt.%]	Ge [ppm]	Pb [ppm]	As [ppm]	Ni [ppm]	B [ppm]	ΣREE [ppm]
38.5	6.56	15.2	3.0	2.0	1.9	293.0	68.8	322.6

Context: Sample 11-8 was taken from a mafic dike intruding the South BIF in the southern part of the Hwy 11 outcrop. All mafic intrusive dikes in the study area are Sudbury-type, intruding the already vertically tilted BIF lithologies sub-parallel to the layering. Whole rock geochemical results were obtained for two sub-samples of sample 11-8, results are shown for 11-8-1

Petrography: The mafic intrusive material in sample 11-8 is strongly altered, and most of the groundmass is now white mica (sericite), chlorite, and biotite. Some large remnant pyroxene and amphibole phenocrysts are present, while other large phenocrysts (previously plagioclase blades) are completely recrystallized as white mica. Where plagioclase is preserved, it shows well developed oscillatory zonation. A transition from complete alteration at the contact of intrusion with wall rock to the more central part of the intrusion is captured in the thin section. Close to the contact, alteration is complete and the sample consists entirely of fine grained groundmass, while phenocrysts of pyroxene or amphibole and plagioclase are preserved in the inner parts of the intrusion.
The groundmass also contains ~10% homogenously distributed, 10-20 µm skeletal magnetite, as well as trace pyrite. Both pyrite and magnetite only occur exclusively in the groundmass, not in the altered phenocrysts and remnant pyroxenes.

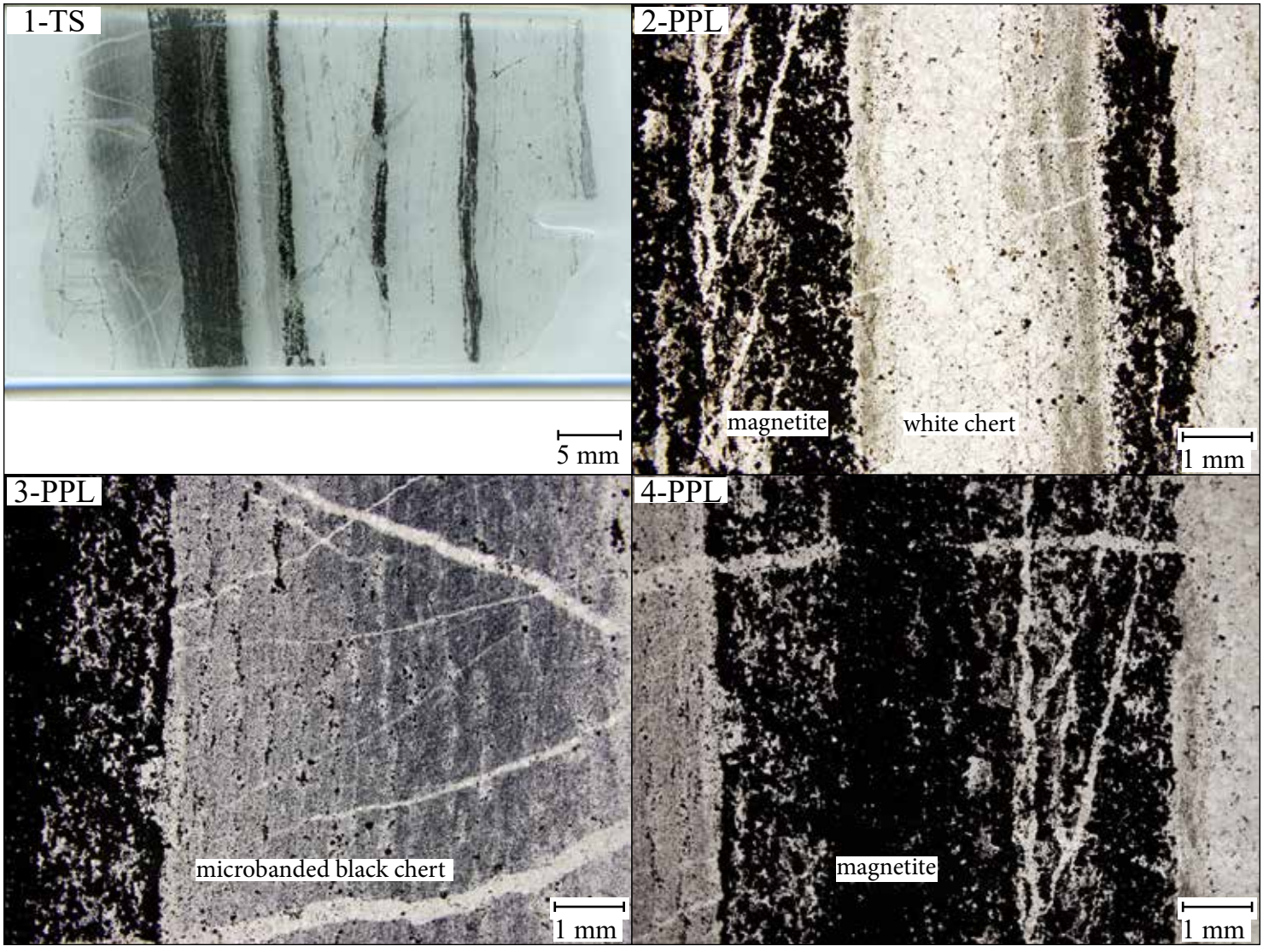


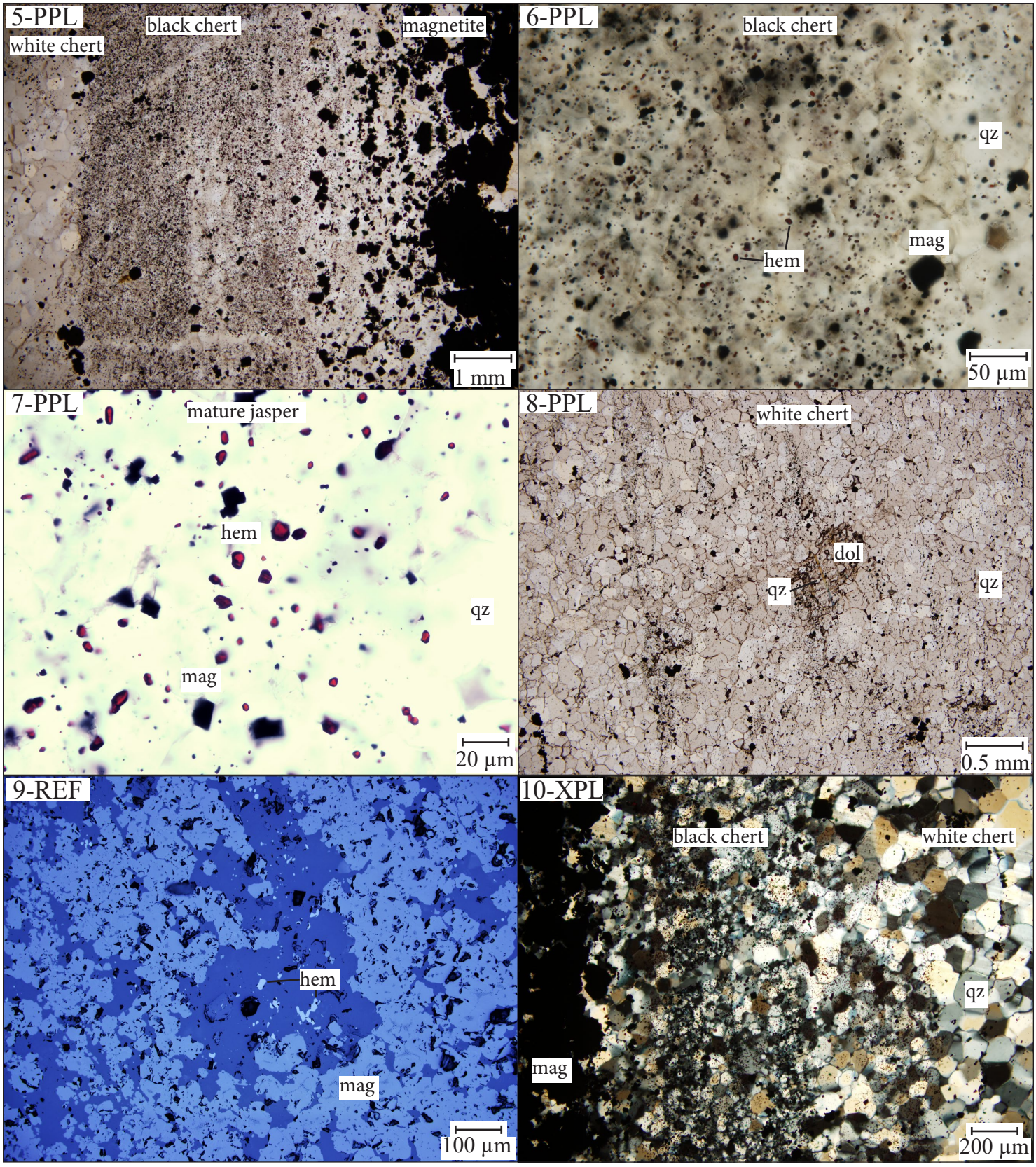
Sample: 11-9

Sample Type: chert-magnetite BIF
Location: 47.06854 -79.79071
BIF Member: South BIF

SiO_2 [wt.%]	Al_2O_3 [wt.%]	Fe_2O_3 [wt.%]	Ge [ppm]	Pb [ppm]	As [ppm]	Ni [ppm]	B [ppm]	ΣREE [ppm]
72.0	0.27	22.0	4.0	2.0	2.3	0.3	53.0	19.0

Context: Sample 11-9 is a chert-magnetite BIF sample from the South BIF along Hwy 11, close to the onset of BIF deposition in the South BIF. The sample consists of finely layered magnetite, white- and black chert, and discontinuous lenses of Fe-dolomite. Layers form sharp contacts. Whole rock geochemical results are obtained for black chert rich parts of the sample, but some magnetite and white chert material was captured in the preparation.
Petrography: Chert layers are 5-10 mm thick, while magnetite layers are 2-5 mm thick and sometimes discontinuous. Magnetite layers consist of 10-200 μm Type 2 and 3 magnetite with quartz in the interstices. Accessory phases in the interstitial spaces are calcite, translucent hematite, apatite, and chlorite. Internal variation in the magnetite layers can be internally heterogenous, forming parallel lenses of more magnetite rich and -poor domains within individual magnetite layers.
White chert consists of 50-100 μm quartz with few very fine Type 1 and 2 magnetite inclusions. Quartz in white chert is euhedral to subhedral.
Black chert consists of <50 μm quartz with abundant Type 1 and 2 magnetite and Type 1 and 2 hematite inclusions. Microbanding is common in black chert, with banding defined by the size of quartz and Fe-oxide minerals. White bands contain larger quartz and fewer but larger magnetite, while dark bands contain more abundant but finer magnetite. Microbanding is parallel to layering. Quartz veins are abundant in black chert, and terminate at layer boundaries with white chert or magnetite. Quartz veins can show offsets along the planes of microbands.



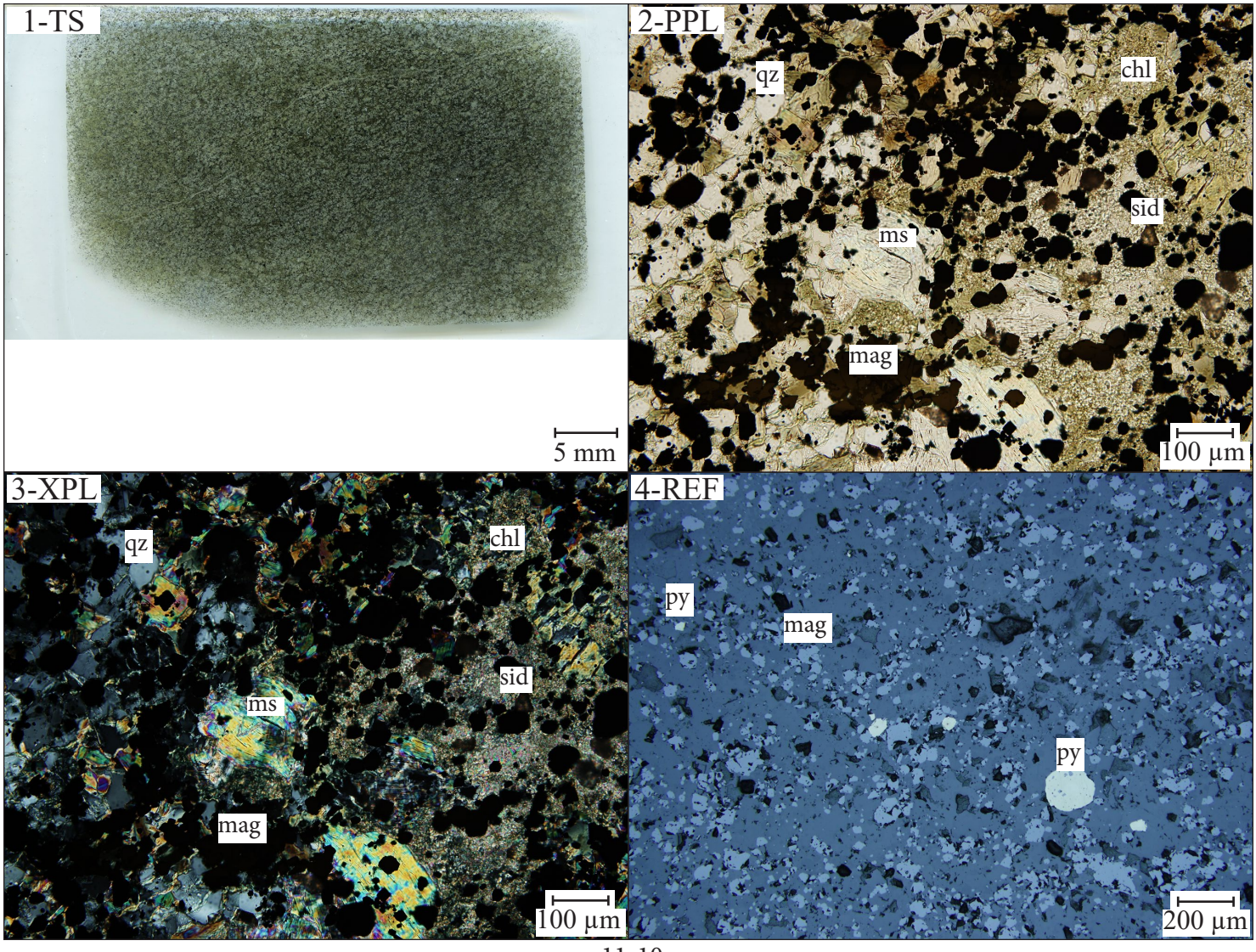

5-PPL
white chert
black chert
magnetite
1 mm
6-PPL
black chert
qz
mag
hem
50 µm
7-PPL
mature jasper
hem
qz
mag
20 µm
8-PPL
white chert
dol
qz
qz
0.5 mm
9-REF
hem
mag
100 µm
10-XPL
black chert
white chert
qz
mag
200 µm

Sample: 11-10

Sample Type: chert-magnetite/chlorite
Location: 47.06856 -79.79071
BIF Member: South BIF

SiO_2 [wt.%]	Al_2O_3 [wt.%]	Fe_2O_3 [wt.%]	Ge [ppm]	Pb [ppm]	As [ppm]	Ni [ppm]	B [ppm]	ΣREE [ppm]
92.2	0.43	5.7	3.6	0.7	0.3	9.7	58.5	3.8

Context: Sample 11-10 was taken in the southern part of the Hwy 11 outcrop of the South BIF. White chert and thick, chlorite-rich magnetite are interlayered. The thin section was cut from the chlorite-rich magnetite layer, while whole rock geochemistry was obtained for the pure white chert part of the sample.
Petrography: The sample consists of magnetite in a matrix of quartz-chlorite-carbonate-muscovite with trace amounts of pyrite and biotite. The distribution of the mineral phases is homogenous within the sample, with no apparent banding or layering. Magnetite is present as Type 1 and Type 2 and randomly distributed, except where magnetite seems to be enriched around the outlines of precursor minerals altered to chlorite and carbonates. Muscovite is euhedral and much larger (>100 µm) than in other samples of Temagami BIF and wall rock. Chlorite shows normal interference colours under XPL, and differs from the normally abundant Berlin blue interference colours in other samples. Quartz is euhedral to subhedral and 50-150 µm. Intergrowth with muscovite, chlorite, and carbonates suggest an early nature of quartz, followed by muscovite-chlorite and lastly carbonates.

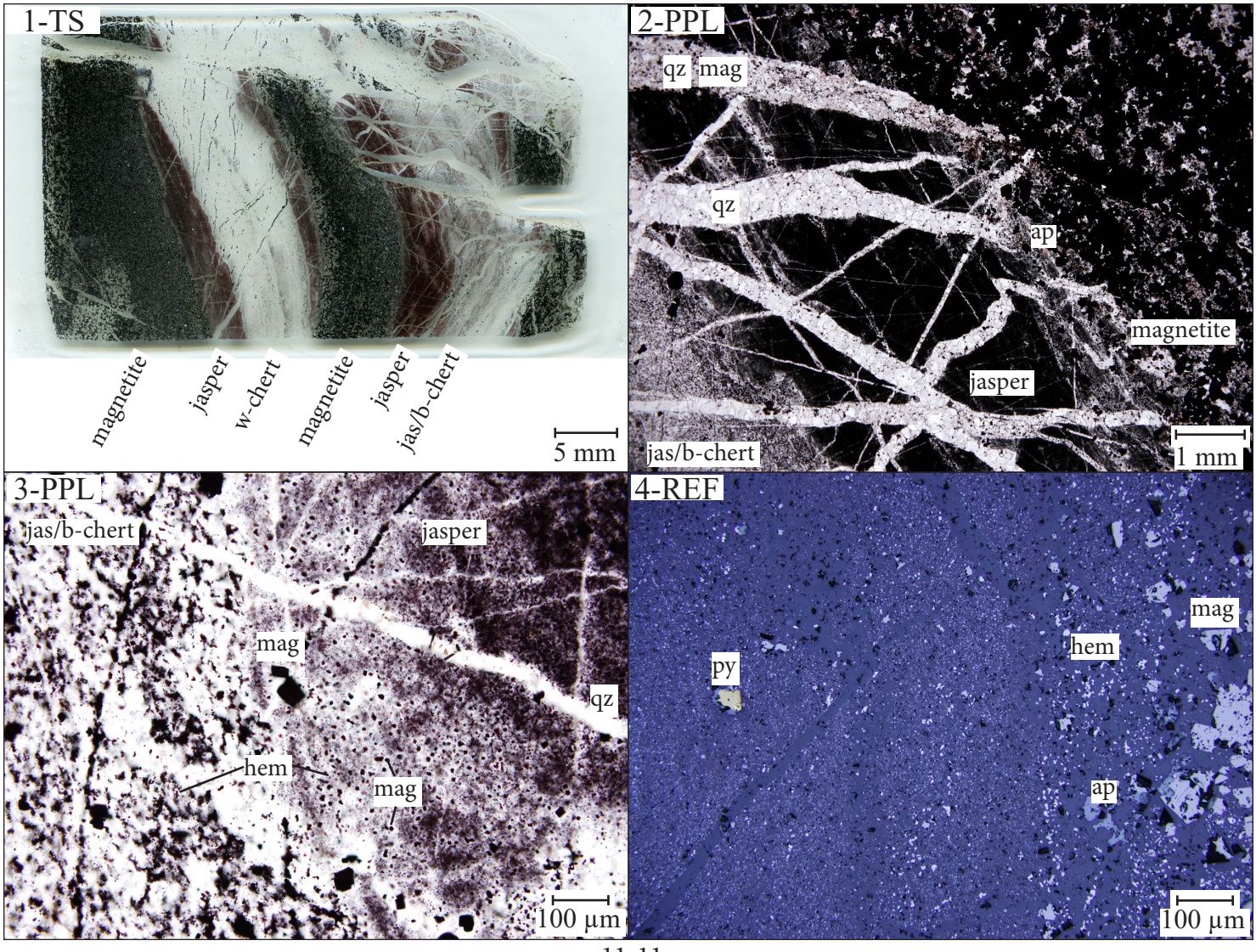


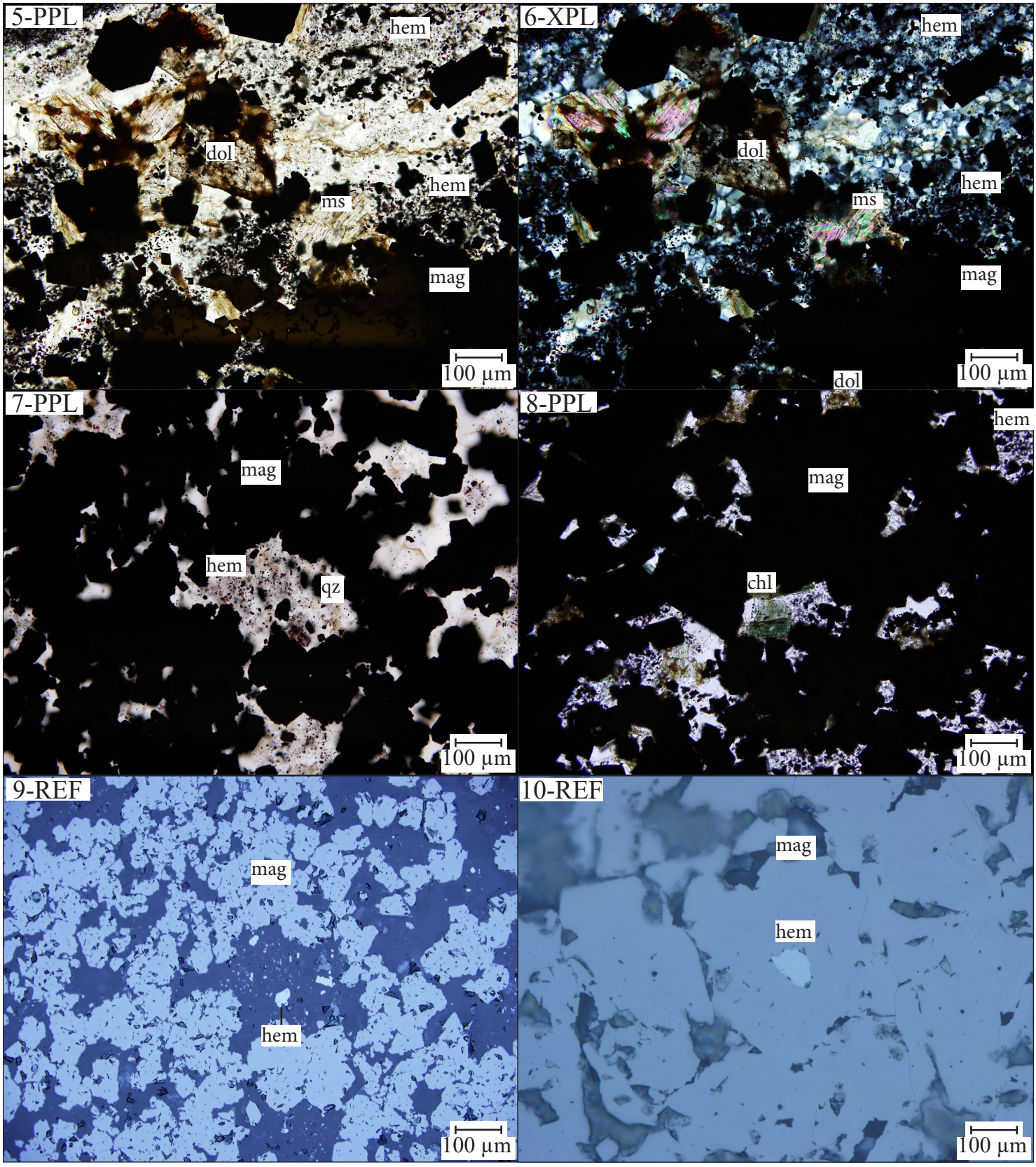
Sample: 11-11

Sample Type: magnetite-chert-jasper
Location: 47.06858 -79.79071
BIF Member: South BIF

SiO_2 [wt.%]	Al_2O_3 [wt.%]	Fe_2O_3 [wt.%]	Ge [ppm]	Pb [ppm]	As [ppm]	Ni [ppm]	B [ppm]	ΣREE [ppm]
71.7	0.15	25.5	5.1	1.3	0.8	1.2	4.2	3.8

Context: Sample 11-11 was taken along the Hwy 11 outcrop and represents the first onset of jasper deposition in the South BIF. Two samples were prepared for whole rock geochemistry, magnetite-rich material in 11-11-1, and jasper for 11-11-2. Material from several individual layers of jasper and magnetite had to be combined to obtain sufficient sample powder for whole rock geochemical analysis.
Petrography: The sample consists of folded interlayers of jasper, magnetite, black chert and white chert. Transitions from black chert to jasper are common. Jasper comprises "mature jasper" defined by higher amounts of Type 2 hematite in quartz compared to more common Type 1 jasper in quartz spherules in less recrystallized jasper. Jasper spherules - ultrafine hematite in quartz, are rare. Magnetite layers vary in Fe-oxide content both laterally and between layers. Magnetite layers are composed of Type 3 and 4 magnetite, generally increasing in grain size towards the centre of individual layers. Additional mineral phases in magnetite layers are quartz (20-40 vol. %), chlorite, muscovite, hematite, apatite, and Fe-dolomite. White chert contains large (100-200 µm) quartz, magnetite, siderite, and trace chlorite. Black chert and jasper are microbanded and contain variable amounts of magnetite and hematite, as well as accessory chlorite, apatite, and Fe-dolomite.
Quartz veins are abundant, and various generations of veins are preserved in black chert and jasper. All vein types except the largest are absent in magnetite layers.



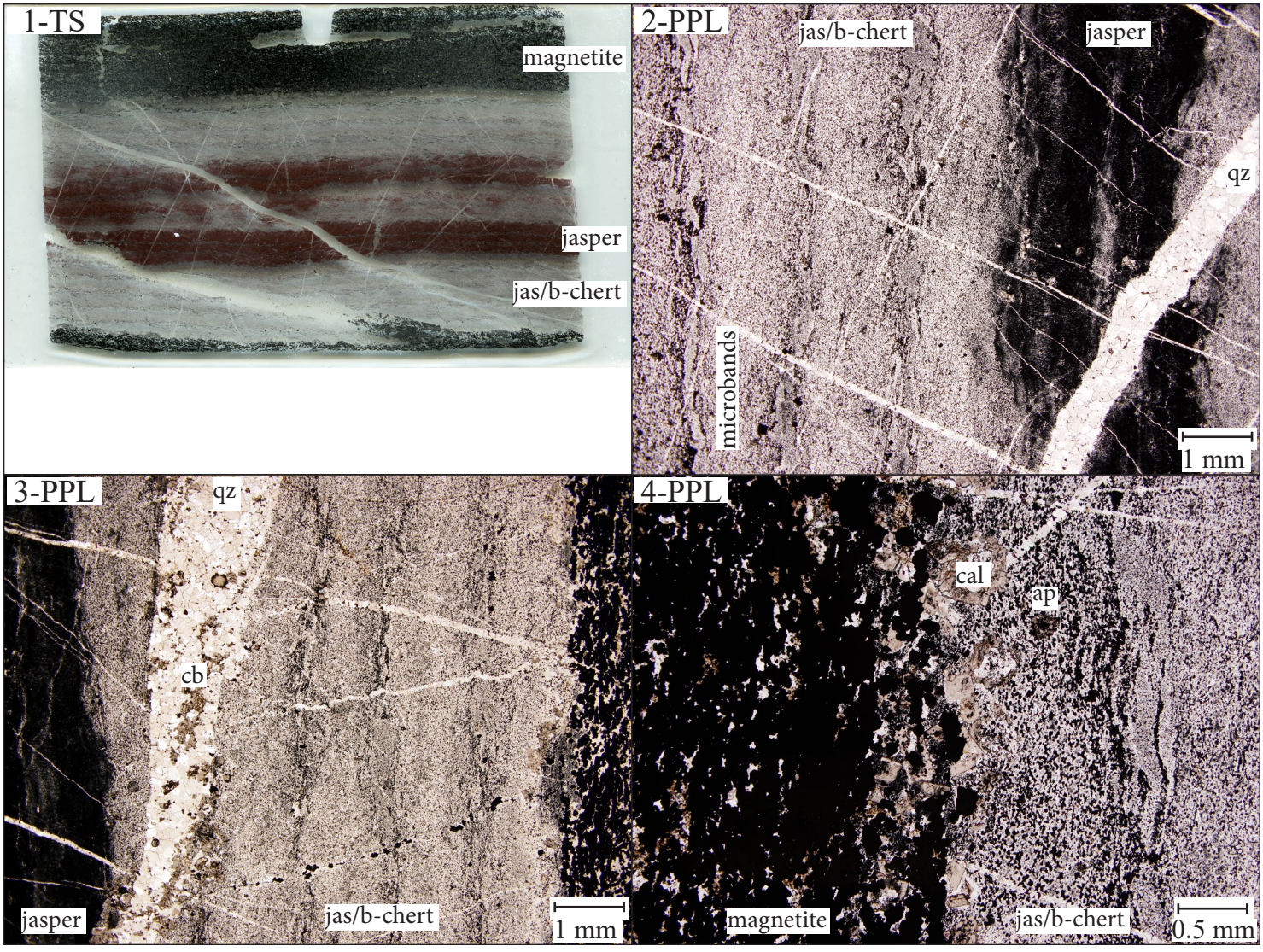

5-PPL
hem
dol
hem
ms
mag
100 µm
6-XPL
hem
dol
hem
ms
mag
100 µm
7-PPL
mag
hem
qz
100 µm
8-PPL
hem
mag
chl
100 µm
9-REF
mag
hem
100 µm
10-REF
mag
hem
100 µm

Sample: 11-12

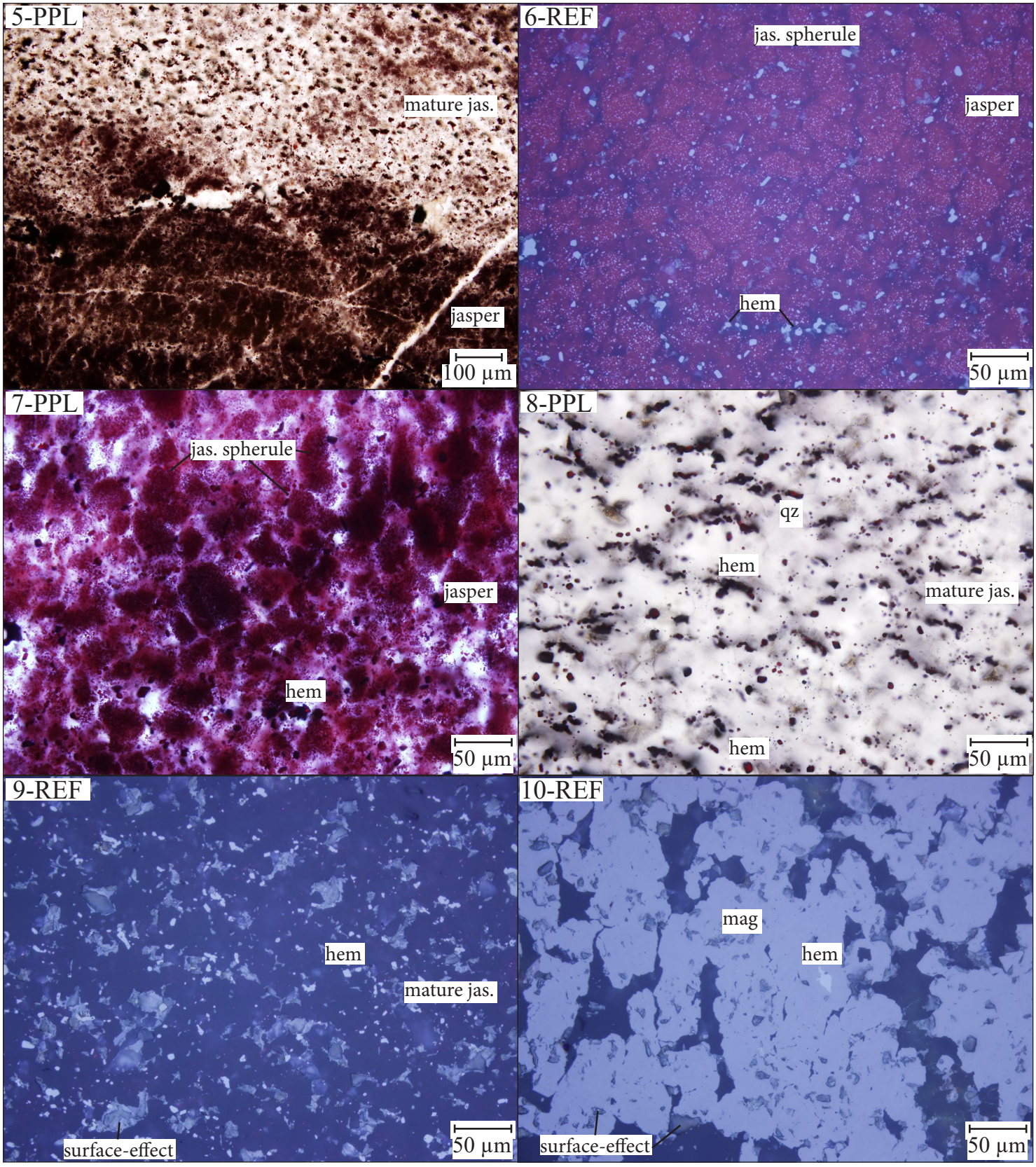
Sample Type: magnetite-jasper
Location: 47.06860 -79.79071
BIF Member: South BIF

SiO_2 [wt.%]	Al_2O_3 [wt.%]	Fe_2O_3 [wt.%]	Ge [ppm]	Pb [ppm]	As [ppm]	Ni [ppm]	B [ppm]	ΣREE [ppm]
69.2	0.30	27.3	3.8	3.6	0.9	0.2	6.7	6.8

Context: Magnetite-jasper facies BIF sample from the South BIF outcrop along Hwy 11. Taken a few m north of the sampling site of 11-11, jasper from 11-12 was prepared for whole rock geochemistry.
Petrography: Sample 11-12 consists of interlayered magnetite and jasper. Jasper is microbanded and up to cm-scale thick. Both types of jasper (bright orange and burgundy red) are represented in the thin section. The brighter colour is derived from jasper spherules, ultrafine hematite encapsulated in quartz and visible due to more transparent, hematite-poor rims containing more magnetite. More mature jasper contains more magnetite and less but larger, bladed hematite. Remnants of the spherule structures are preserved, but contain very little ultrafine hematite. Hematite is translucent-red, yielding the red colour of jasper. Jasper consists mostly of quartz (>70 vol. %), hematite (10-25 vol. %) and magnetite (<20 vol. %). Accessory mineral phases in jasper are large apatite and carbonates.
Magnetite layers consist of Type 3 magnetite, increasing in grain size towards the centre of individual layers. Interstitial spaces between magnetite grains consist of quartz and can contain variable amounts of hematite, carboanates, chlorite, and muscovite. The interfaces of magnetite and jasper are lined by apatite (~100 μm) and relatively large hematite (10-25 μm) aligned parallel to layering.
Quartz veins are common in jasper, but not continuous in magnetite layers. Only the largest quartz veins, containing magnetite and aluminosilicates, cut both layer types. Offset of quartz veins in jasper occurs on microbands.



11-12

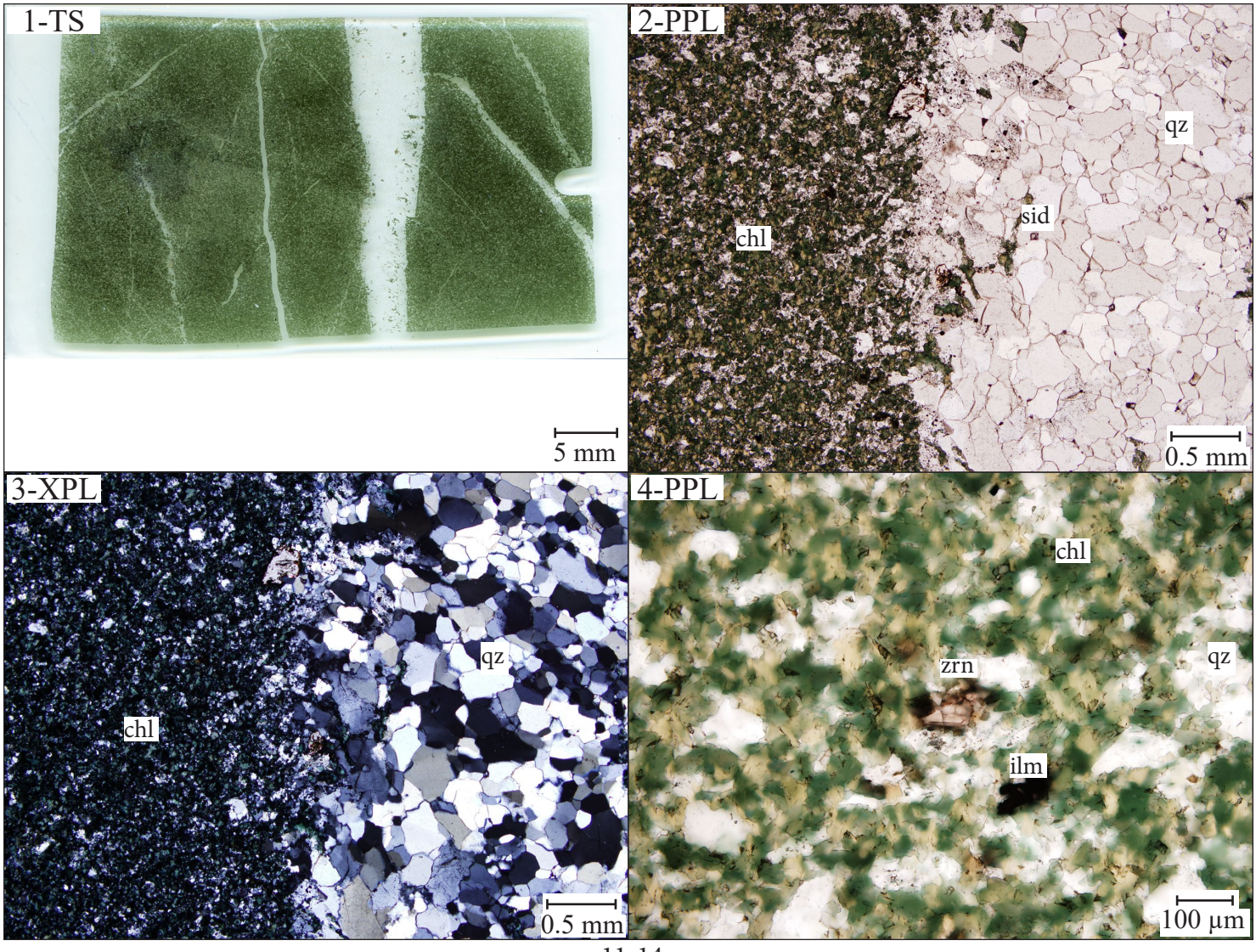

5-PPL
mature jas.
jasper
100 µm
6-REF
jas. spherule
jasper
hem
50 µm
7-PPL
jas. spherule
jasper
hem
50 µm
8-PPL
qz
hem
mature jas.
hem
50 µm
9-REF
hem
mature jas.
surface-effect
50 µm
10-REF
mag
hem
surface-effect
50 µm

Sample: 11-14

Sample Type: volcaniclastic-chert
Location: 47.06863 -79.79071
BIF Member: South BIF

SiO_2 [wt.%]	Al_2O_3 [wt.%]	Fe_2O_3 [wt.%]	Ge [ppm]	Pb [ppm]	As [ppm]	Ni [ppm]	B [ppm]	ΣREE [ppm]
50.1	9.82	30.0	4.9	1.3	3.3	16.7	45.2	113.2

Context: Sample 11-14 captures interlayering of volcaniclastic material and chert. The sample was taken from the central-southern part of the Hwy 11 outcrop. Material for whole rock geochemical analysis was produced from a volcaniclastic layer.
Petrography: The thin section represents volcaniclastic material preserved as chlorite in a chert matrix with a single white chert layer.
The chlorite in the sample is randomly distributed and 50 µm. The interference colours are normal-green, as opposed to the Berlin blue variety observed elsewhere. Chlorite is randomly distributed and does not show any preferential orientation towards layering. The volcaniclastic material consists of >80 vol. % chlorite, <20 vol.% quartz, some carbonates, and traces of ilmenite, pyrite, and zircon. Zircon creates brown pleochroic halos in chlorite. Individual quartz grains are larger (50-100 µm) than chlorite, and even bigger (>100 µm) in white chert. White chert consist of >90 vol. % quartz, with chlorite and carbonates as accessories. The chlorite in white chert is of the same variety as in the neighboring volcaniclastic layers. Some individual quartz crystals in white chert can contain inclusions of pyrite and other, ultrafine inclusions. The irregularity of the inclusion-rich clasts, and occurence of pyrite in white chert exclusively associated with these clasts suggests a detrital origin of these clasts in a hydrogenous matrix.

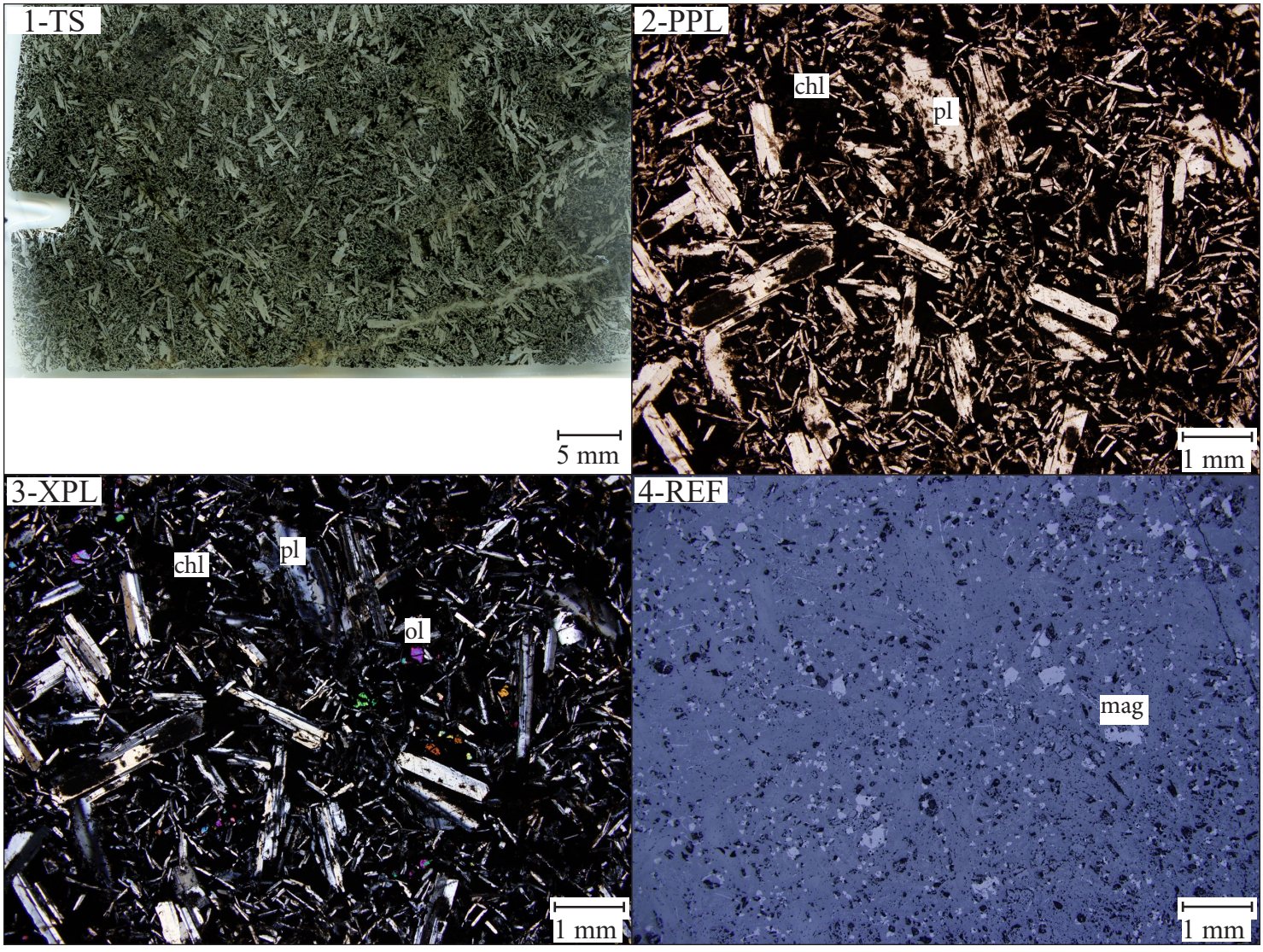


Sample: 11-15

Sample Type: intrusive
Location: 47.06866 -79.79070
BIF Member: South BIF

SiO_2 [wt.%]	Al_2O_3 [wt.%]	Fe_2O_3 [wt.%]	Ge [ppm]	Pb [ppm]	As [ppm]	Ni [ppm]	B [ppm]	ΣREE [ppm]
n/a	n/a	n/a	n/a	n/a	n/a	n/a	n/a	n/a

Context: Sample 11-15 was taken from an intrusion in the central part of the Hwy 11 outcrop of the South BIF.
Petrography: The sample consists of coarse crystalline, mafic material. Alteration of plagioclase, pyroxene and olivine to muscovite, chlorite, calcite, and biotite is pervasive but not complete. Magnetite is common, and probably derived from BIF in the wall rock of the intrusion.



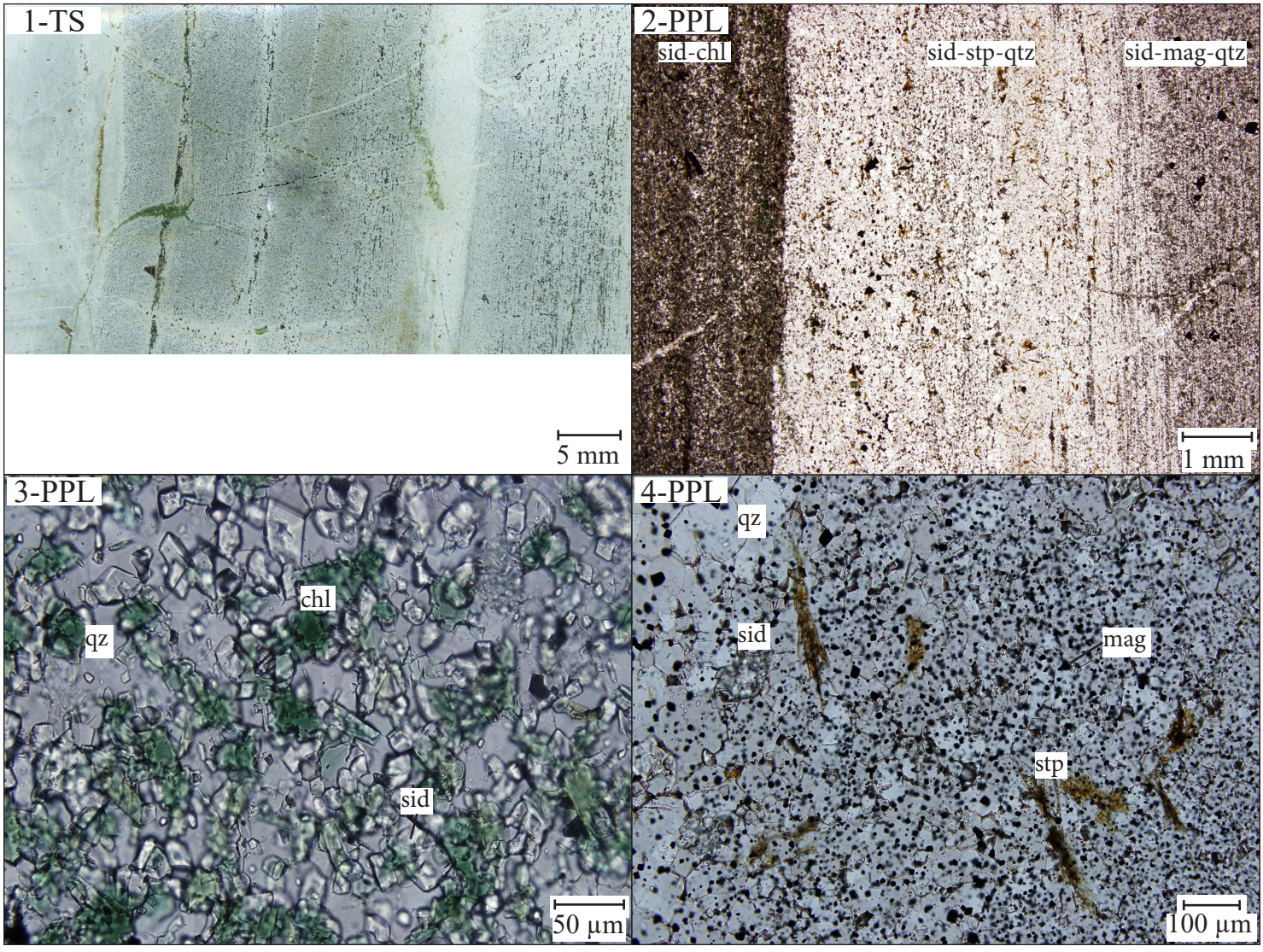
Sample: 11-18

Sample Type: chert (carbonate facies)
Location: 47.06871 -79.79070
BIF Member: South BIF

SiO_2 [wt.%]	Al_2O_3 [wt.%]	Fe_2O_3 [wt.%]	Ge [ppm]	Pb [ppm]	As [ppm]	Ni [ppm]	B [ppm]	ΣREE [ppm]
77.0	0.38	17.0	4.9	0.2	0.5	44.0	56.5	8.3

Context: Sample 11-18 was taken in the central part of the South BIF outcrop along Hwy 11. Two thin sections and samples for geochemistry were prepared from the same hand sample. The two sub-samples are very similar, but 11-18-2 is more pure black chert compared to more abundant carbonates and aluminosilicates in 11-18-1, representing endmember carbonate-facies in Temagami BIF. The whole rock geochemical composition listed above is for sample 11-18-1

Petrography: Both thin sections prepared from sample 11-18 classify as (black) chert samples, with variable amounts of magnetite and carbonates in chert. Unusually high abundance of siderite as layer-defining mineral species, as well as stilpnomelane set the sample apart from other BIF lithologies. Siderite in both sub-samples is hosted in a fine grained quartz matrix and occurs as small euhedral, blocky to tabular crystals, sometimes aligned layer-parallel. 11-18-1 contains the highest abundance of siderite in all samples, up to 70 vol. % in chert-stilpnomelane matrix. The siderite-rich lithologies are interlayered with white chert, containing 10-20 vol.% siderite, along with stilpnomelane and chlorite. Poorly developed microbanding in both, carbonate-rich black chert and white chert is defined by the abundance of siderite. Trace pyrite and magnetite occur focued in layers in 11-18-1. 11-18-2 contains very mature black chert, with Type 2 to Type 3 magnetite aligned in microbands in a matrix of fine grained quartz (<50 µm), as well as carbonates (siderite and Fe-dolomite), stilpnomelane, and chlorite. Stilpnomelane occus as 100 µm needles, chlorite is of the Berlin blue variety. Veins contain aluminosilicates.

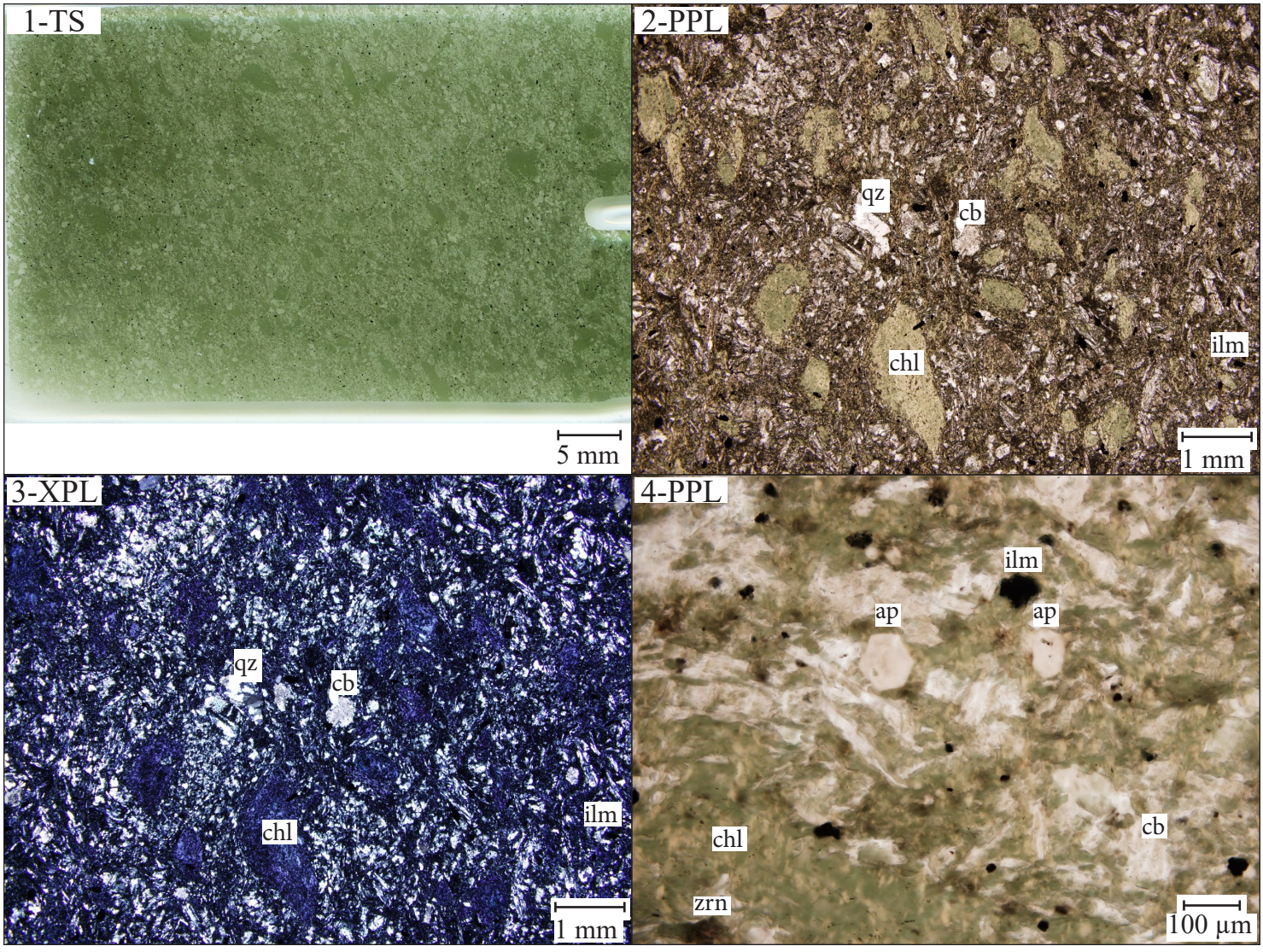


Sample: 11-20

Sample Type: chlorite
Location: 47.06874 -79.79070
BIF Member: South BIF

SiO_2 [wt.%]	Al_2O_3 [wt.%]	Fe_2O_3 [wt.%]	Ge [ppm]	Pb [ppm]	As [ppm]	Ni [ppm]	B [ppm]	ΣREE [ppm]
50.1	9.64	21.8	4.7	1.3	70	520.0	0.4	124.0

Context: Sample 11-20 was taken in the central part of the Hwy 11 outcrop of the South BIF, and a thin section was produced from a several cm thick layer of massive chlorite.
Petrography: Sample 11-20 consists of ~70 vol. % chlorite, with quartz, carbonates, muscovite, and ilmenite as accessory minerals. Some layer-parallel sorting of material is is reflected in the orientation of larger grains now preserved as pure chlorite. Chlorite also occurs in the matrix as fine grained material, undulating around larger mineral grains. Chlorite is present exclusively as the Berlin blue variety. Carbonates and muscovite can be present in a similar way, commonly forming pseudomorphs after precursor minerals such as plagioclase or pyroxene. Apatite and zircon are present as traces.



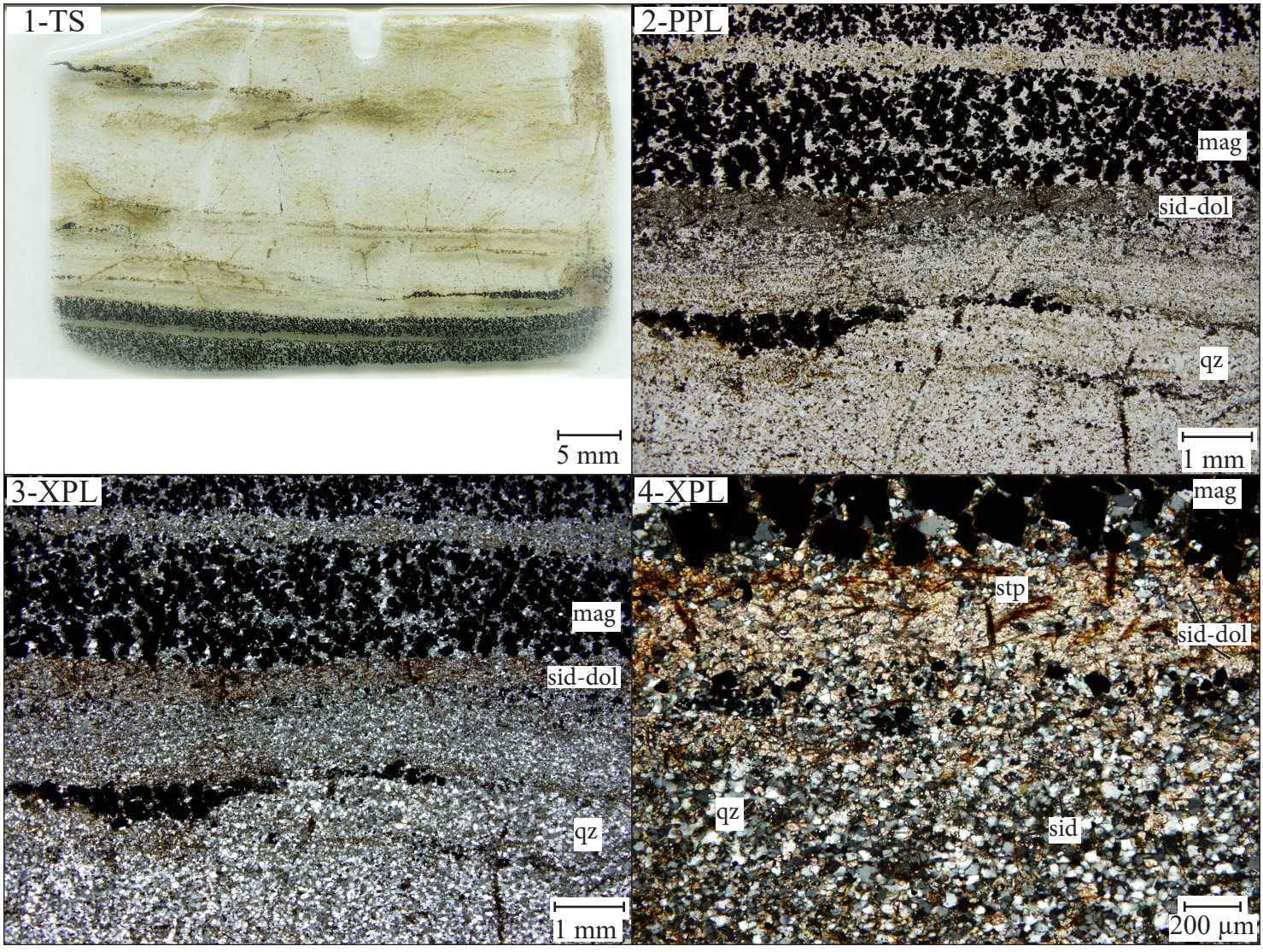
11-20

Sample: 11-22

Sample Type: chert
Location: 47.06878 -79.79070
BIF Member: South BIF

SiO_2 [wt.%]	Al_2O_3 [wt.%]	Fe_2O_3 [wt.%]	Ge [ppm]	Pb [ppm]	As [ppm]	Ni [ppm]	B [ppm]	ΣREE [ppm]
94.0	0.33	3.7	2.3	0.9	0.0	15.7	59.2	3.3

Context: 11-22 was taken from the central part of the South BIF along the Hwy 11 outcrop, from a section of undisturbed, unfolded layering of oxide-BIF.
Petrography: Sample 11-22 is a chert sample with some <0.5 cm thick magnetite layers. Chert in this sample contains variable stilpnomelane and siderite, while the magnetite layers additionally contain chlorite (Berlin blue) and biotite. Quartz is fine grained where it is intergrown with carbonates and aluminosilicates, but coarser (100 µm) where chert is pure. Siderite is mostly fine grained but can form thin (mm), almost massive layers. Stilpnomelane and biotite occur in needle and blady habits, respectively. Biotite is significantly larger (>200 µm) where it forms biotite-rich pockets. Chlorite occurs exclusively in magnetite layers together with biotite. Some large (>300 µm) crystal shapes (pyroxene?) are preserved as pseudomorphs, now quartz, Type 1 magnetite, and chlortie. One large quartz vein is preserved in chert but brecciated, and terminates on a chert- aluminosilicate-rich chert interface.
Magnetite layers are thin (mm-scale) and contain intermediate size Type 3 magnetite. Type 2 magnetite also occurs in some of the pure chert.

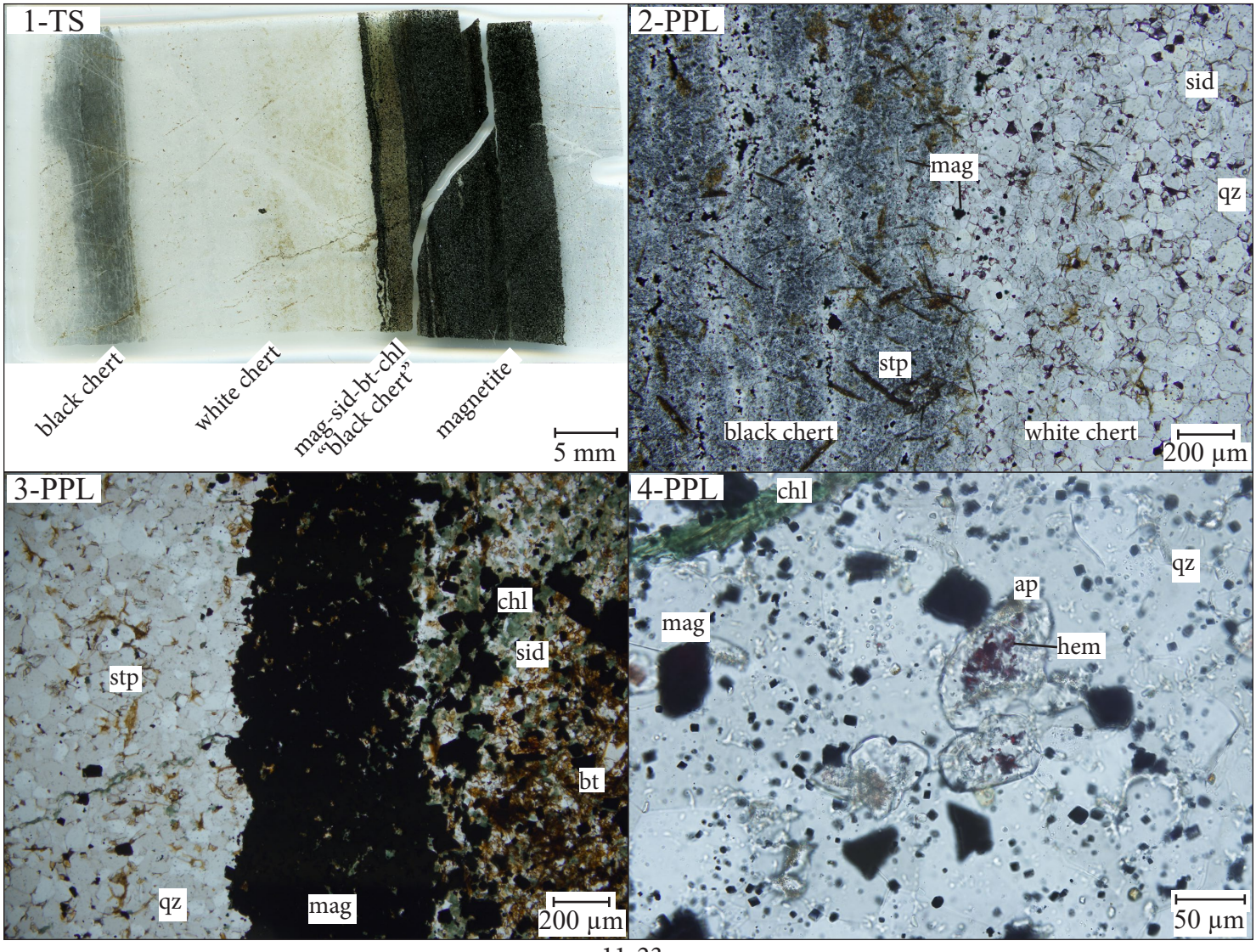


Sample: 11-23

Sample Type: chert
Location: 47.06880 -79.79070
BIF Member: South BIF

SiO_2 [wt.%]	Al_2O_3 [wt.%]	Fe_2O_3 [wt.%]	Ge [ppm]	Pb [ppm]	As [ppm]	Ni [ppm]	B [ppm]	ΣREE [ppm]
87.9	0.55	8.4	3.1	2.6	0.9	1.8	59.3	5.5

Context: 11-23 was taken from the central part of the South BIF along Hwy 11, from a section of predominantly oxide-BIF layers.
Petrography: Sample 11-23 comprises white chert, black chert, and magnetite layers. The dominant part of the sample is a 2 cm thick white chert layer. White chert contains coarse (>100 µm) quartz with small Type 2 magnetite, siderite, apatite, stilpnomelane and dolomite accessory minerals. Pseudomorphs after another carbonate phase or larger aluminosilcate phase are filled with dolomite and <50 µm, rounded quartz. Type 1 hematite is preserved in the core of some apatite crystals in white chert. Magnetite layers are thick (>1 cm), and comprise massive Type 4 magnetite. Interstitial spaces in magnetite layers contain chlorite, stilpnomelane, biotite, and siderite. A mixed-carbonate BIF interlayer between two magnetite layers consists of unusually abundant siderite-chlorite-biotite and with magnetite and quartz. Changes from biotite to chlorite dominated parts of the layer occur with increasing magnetite abundance.

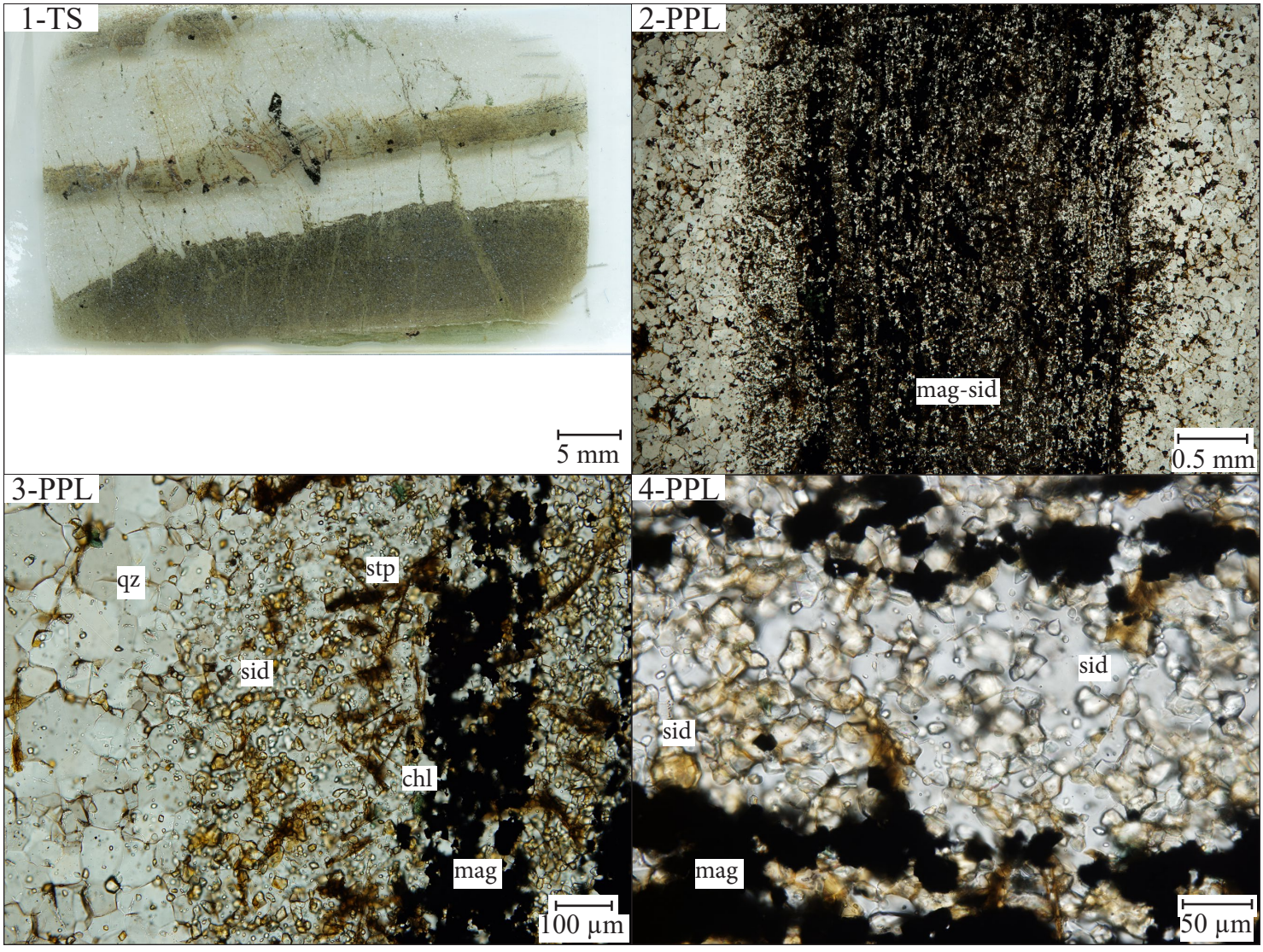


Sample: 11-24

Sample Type: magnetite
Location: 47.06881 -79.79070
BIF Member: South BIF

SiO_2 [wt.%]	Al_2O_3 [wt.%]	Fe_2O_3 [wt.%]	Ge [ppm]	Pb [ppm]	As [ppm]	Ni [ppm]	B [ppm]	ΣREE [ppm]
50.4	0.94	29.1	2.4	0.8	0.5	4.2	2.0	28.0

Context: 11-24 was collected from the central Part of the South BIF along the Hwy 11 section. The layering is relatively undisturbed around the sample site, with predominantly BIF-lithologies near by.
Petrography: Sample 11-24 comprises carbonate-rich magnetite and chert layers. The magnetite-siderite layers are >1 cm thick, representing the best example of carbonate BIF found in the study. Siderite in the carbonate BIF occurs in a cherty matrix, with abundant stilpnomelane and magnetite. Siderite is small (20 µm) and blocky, but can grow into coherent masses. Magnetite occurs in microbands parallel to layering, larger stilpnomelane crystals are randomly oriented in magnetite-carbonate BIF. White chert comprises large quartz with trace siderite, Type 2 magnetite, stilpnomelane and trace chlorite. Quartz veins can offset the outer parts of the siderite-rich layers. The same veins can be brecciated in the internal parts of the layers.

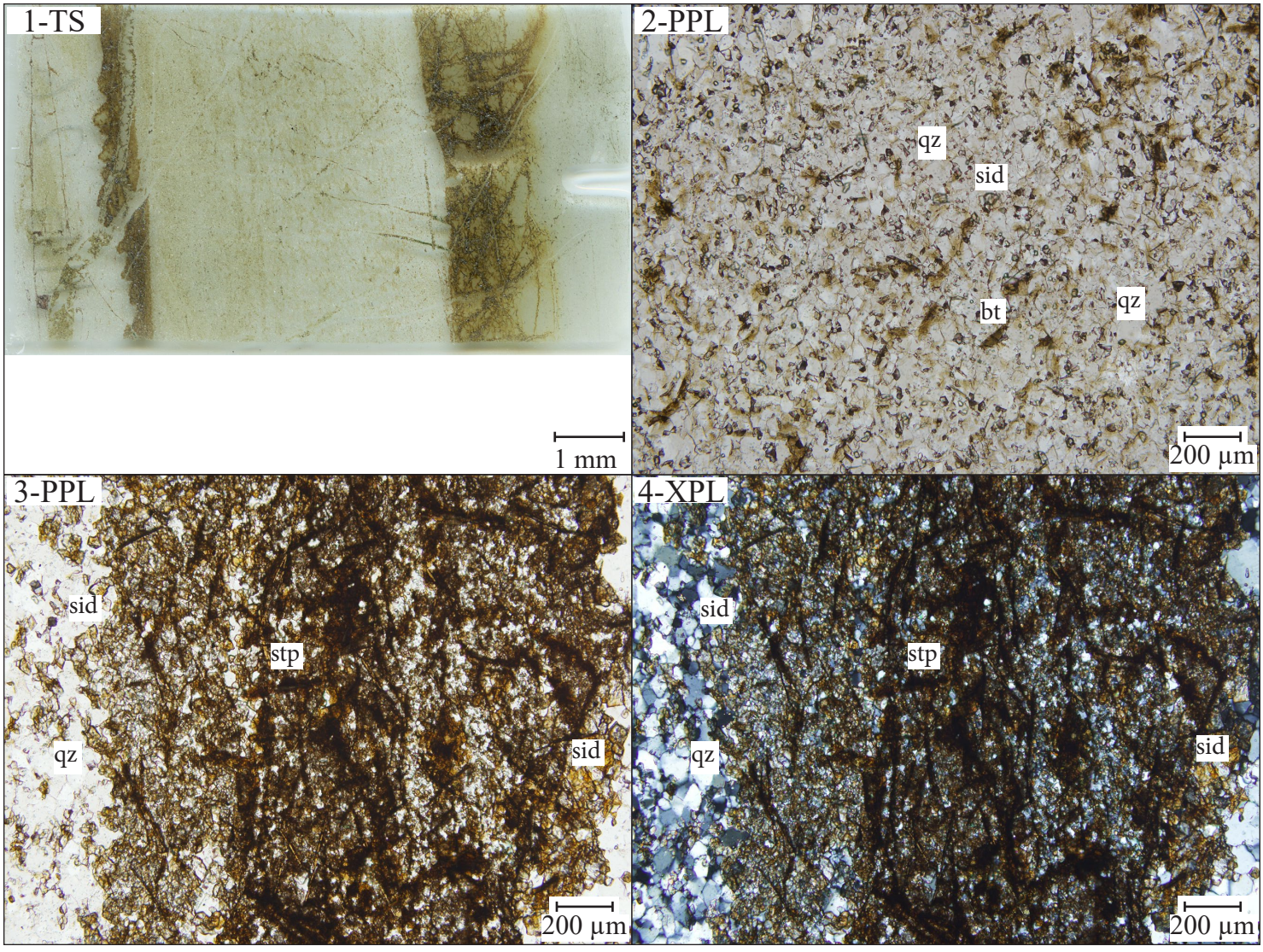


Sample: 11-26

Sample Type: chert-carbonate
Location: 47.06883 -79.79070
BIF Member: South BIF

SiO_2 [wt.%]	Al_2O_3 [wt.%]	Fe_2O_3 [wt.%]	Ge [ppm]	Pb [ppm]	As [ppm]	Ni [ppm]	B [ppm]	ΣREE [ppm]
n/a	n/a	n/a	n/a	n/a	n/a	n/a	n/a	n/a

Context: 11-26 is from the South BIF along Hwy 11, taken from the central part close to the interruption of BIF outcrop.
Petrography: Sample 11-26 comprises interlayered white chert (2 cm) and siderite layers (1 cm). Chert is siderite rich, with intermediate size quartz (50-100 µm). Siderite layers can contain abundant (~40 %) to almost no stilpnomelane and form near-massive layers consisting of very fine, intergrown carbonate. Stilpnomelane in siderite layers can grow to >200 µm where it is more abundant. The chert layers contain stilpnomelane and siderite. Magnetite is completely absent in the entire thin section. Early quartz veins cut layering at steep angles. Later, wide (mm-scale) veins contain more abundant stilpnomelane and can contain trace chlorite and cut layers at shallow angles.

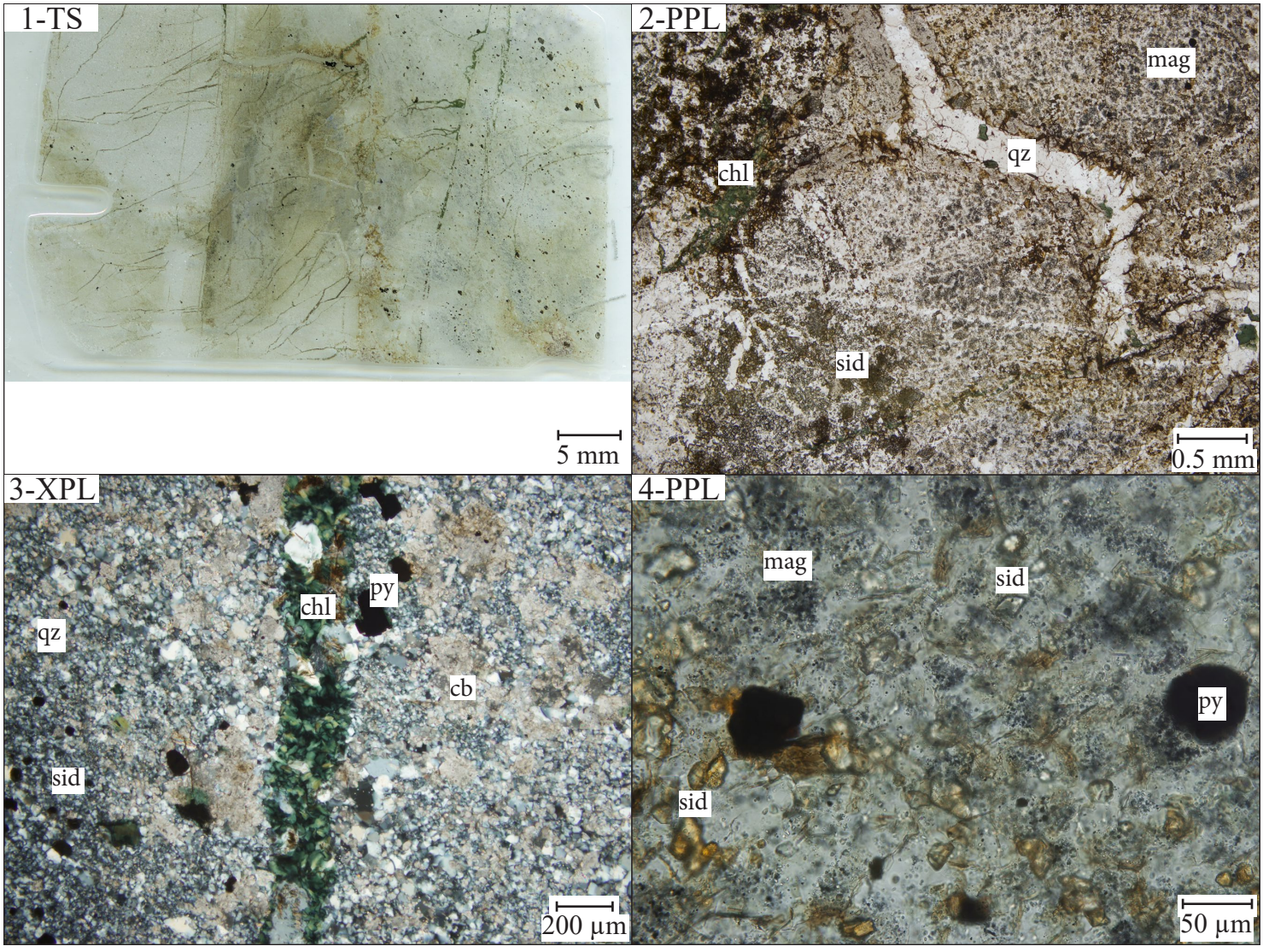


Sample: 11-27

Sample Type: chert
Location: 47.06887 -79.79070
BIF Member: South BIF

SiO_2 [wt.%]	Al_2O_3 [wt.%]	Fe_2O_3 [wt.%]	Ge [ppm]	Pb [ppm]	As [ppm]	Ni [ppm]	B [ppm]	ΣREE [ppm]
76.0	0.47	10.7	2.1	1.4	1.4	10.6	56.2	10.8

Context: The sample was taken from the central part of the South BIF, close to the interruption of the BIF outcrop.
Petrography: Sample 11-27 is a carbonate-rich chert sample. White chert contains variable siderite and dolomite, in some areas approaching massive carbonate. Such carbonate areas are homogenous, with no internal changes indicating layering. Material is severely fragmented, masking original layering. Areas of more abundant carbonates are typically also rich in stilpnomelane. Chert contains regular size (10-30 µm) siderite, but also ultrafine (<1 µm) siderite, lending it a black chert-like appearance. Larger opaque minerals are exclusively pyrite. Early quartz veins are distorted. Later quartz veins are rimmed by dolomite, and can contain stilpnomelane. Trace chlorite occurs in some aluminosilicate-rich veins.

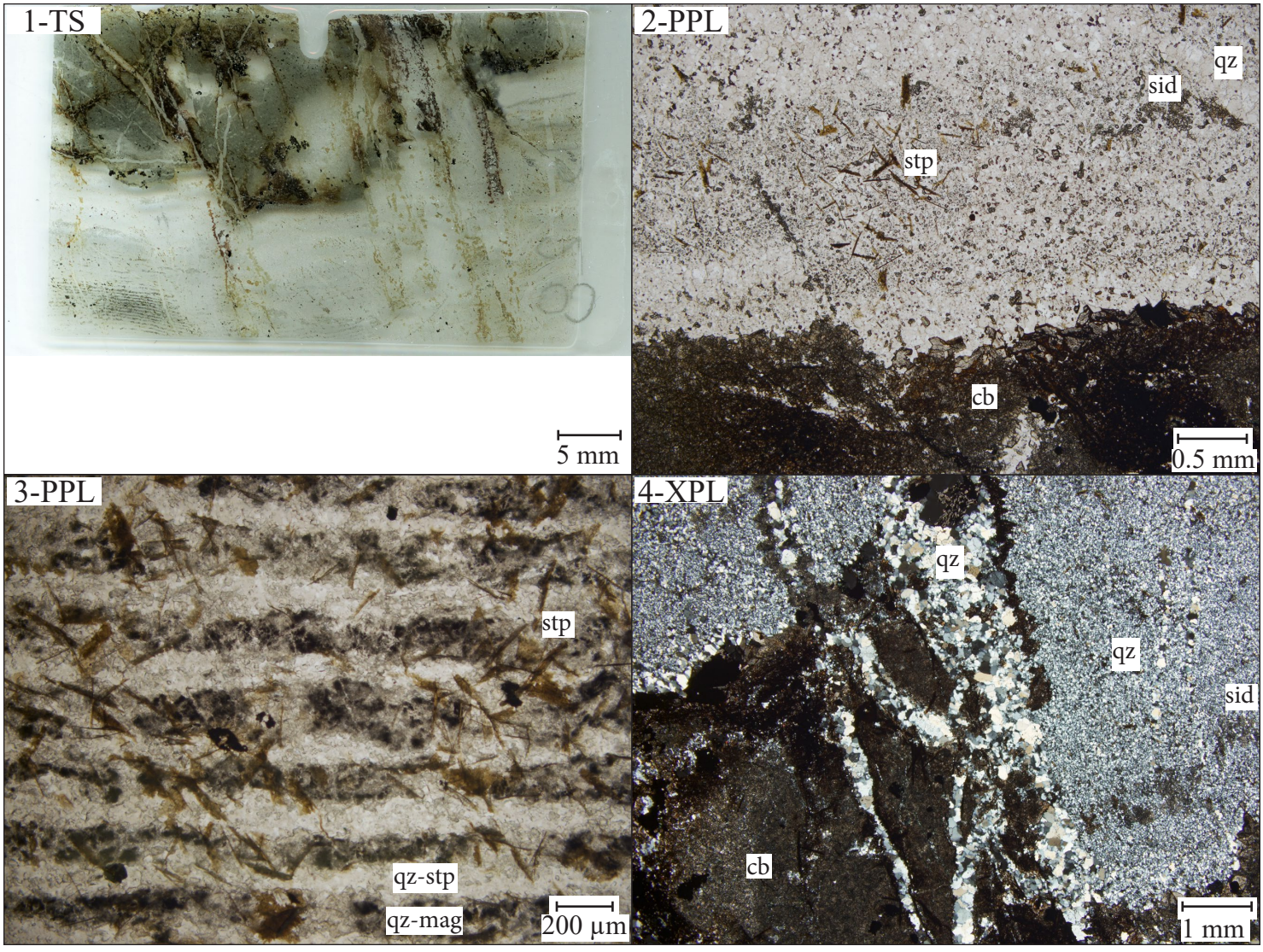


Sample: 11-28

Sample Type: chert
Location: 47.06889 -79.79070
BIF Member: South BIF

SiO_2 [wt.%]	Al_2O_3 [wt.%]	Fe_2O_3 [wt.%]	Ge [ppm]	Pb [ppm]	As [ppm]	Ni [ppm]	B [ppm]	ΣREE [ppm]
n/a	n/a	n/a	n/a	n/a	n/a	n/a	n/a	n/a

Context: Sample from the central part of the South BIF along Hwy 11.
Petrography: Sample 11-28 consists of brecciated carbonate-rich white chert and microbanded black chert. Carbonate-rich areas are mostly siderite in a cherty matrix with variable stilpnomelane and accessory pyrite. Different generations of quartz veins are abundant and offsets along fault zones lead to severe brecciation of the material. Opaque minerals are pyrite. White chert contains small quartz (<50 µm) and trace stilpnomelane and siderite. Black chert is microbanded and siderite-rich. Microbanded material terminates against offset along a fault zone. The sample is intensely cut by veins and brecciated. Different generations of veins contain quartz, quartz-magnetite, quartz-carbonate, and quartz-stilpnomelane. Some veins are associated with considerable (mm-scale) offset perpendicular to layering. Large areas of predominantly fine grained carbonate are likely related to brecciation and veining and metamorphic in origin.

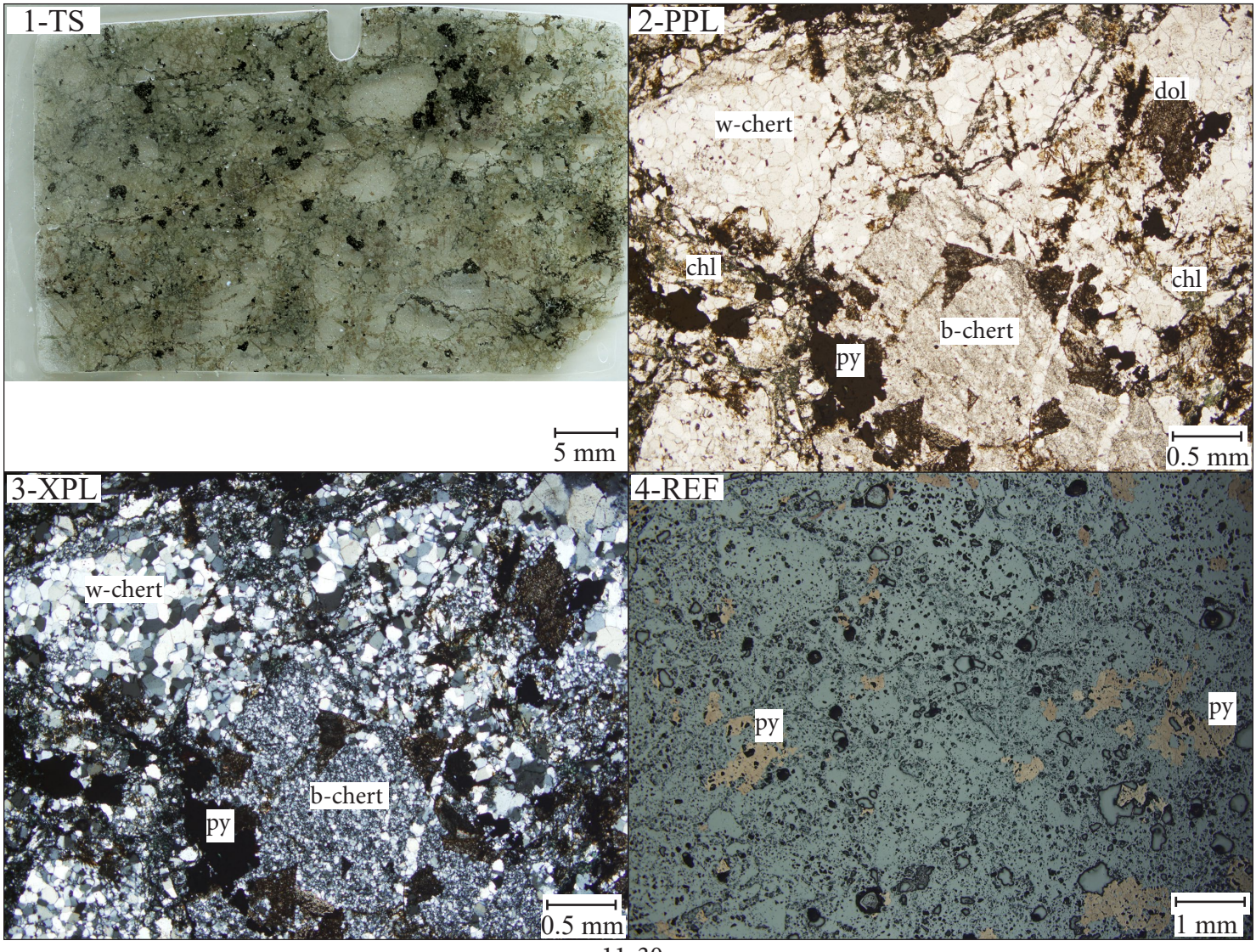


Sample: 11-30

Sample Type: chert (altered)
Location: 47.06895 -79.79070
BIF Member: South BIF

SiO_2 [wt.%]	Al_2O_3 [wt.%]	Fe_2O_3 [wt.%]	Ge [ppm]	Pb [ppm]	As [ppm]	Ni [ppm]	B [ppm]	ΣREE [ppm]
n/a	n/a	n/a	n/a	n/a	n/a	n/a	n/a	n/a

Context: Sample 11-30 was taken from the central part of the South BIF along Hwy 11, at the stratigraphic base of the northern part of the South BIF after the interruption by mafic material.
Petrography: Sample 11-30 comprises heavily altered chert. White chert is brecciated into >500 µm fragments encapsulated by chlorite stringers. The chert fragments contain large quartz (100 µm), with few inclusions of Type 1 magnetite. Few large fragments are chert with abundant siderite. Chlorite, stilpnomelane, and fine dolomite replacing precursor crystals grow preferentially around stringers. Chlorite has intermediate greenish blue interference colous. Large, anhedral pyrite grew authigenically (quartz and chlorite inclusions), and probably in relation to the chlorite alteration event. The material is heavily altered and was not considered for whole rock geochemistry.

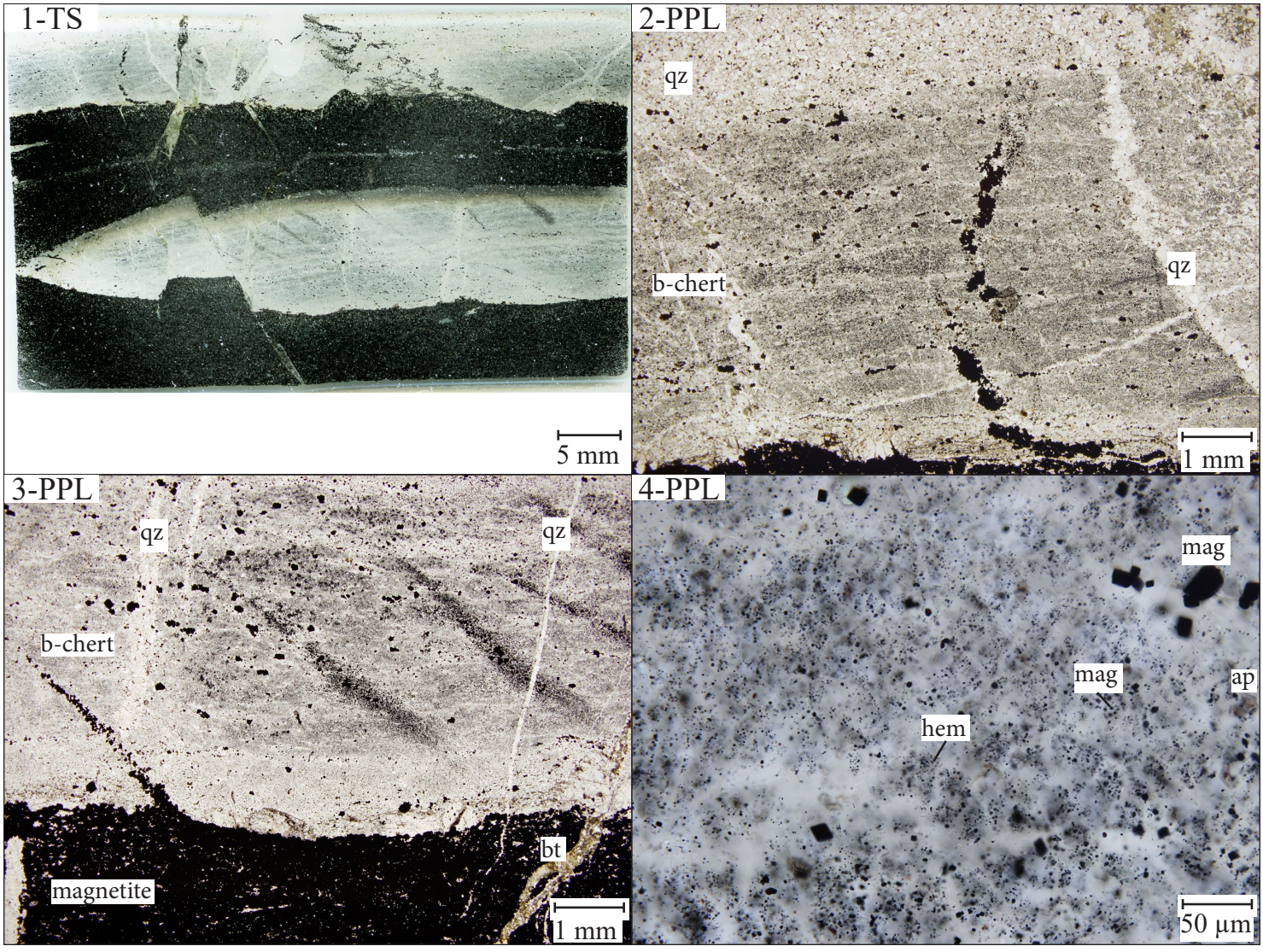


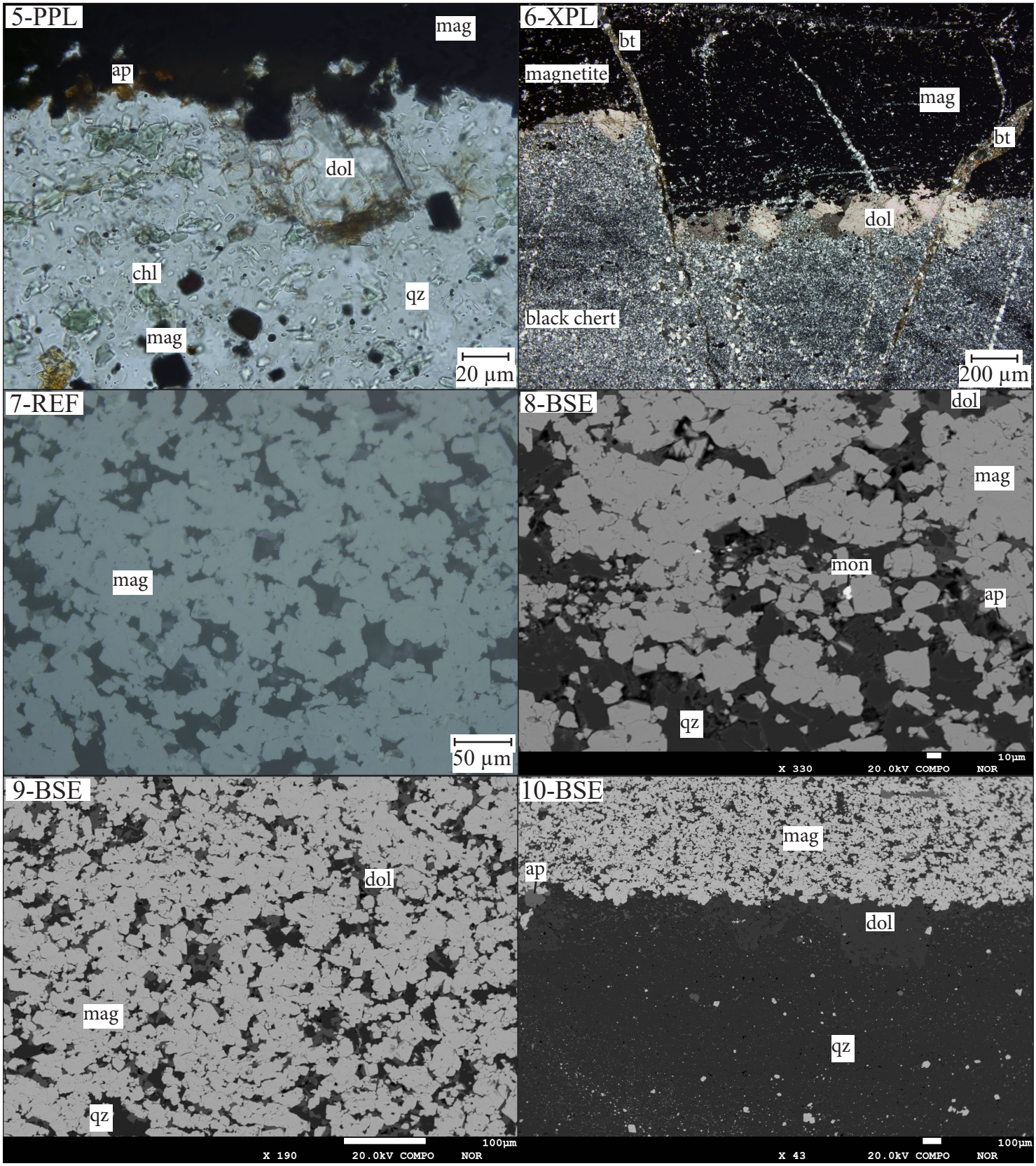
Sample: 11-32

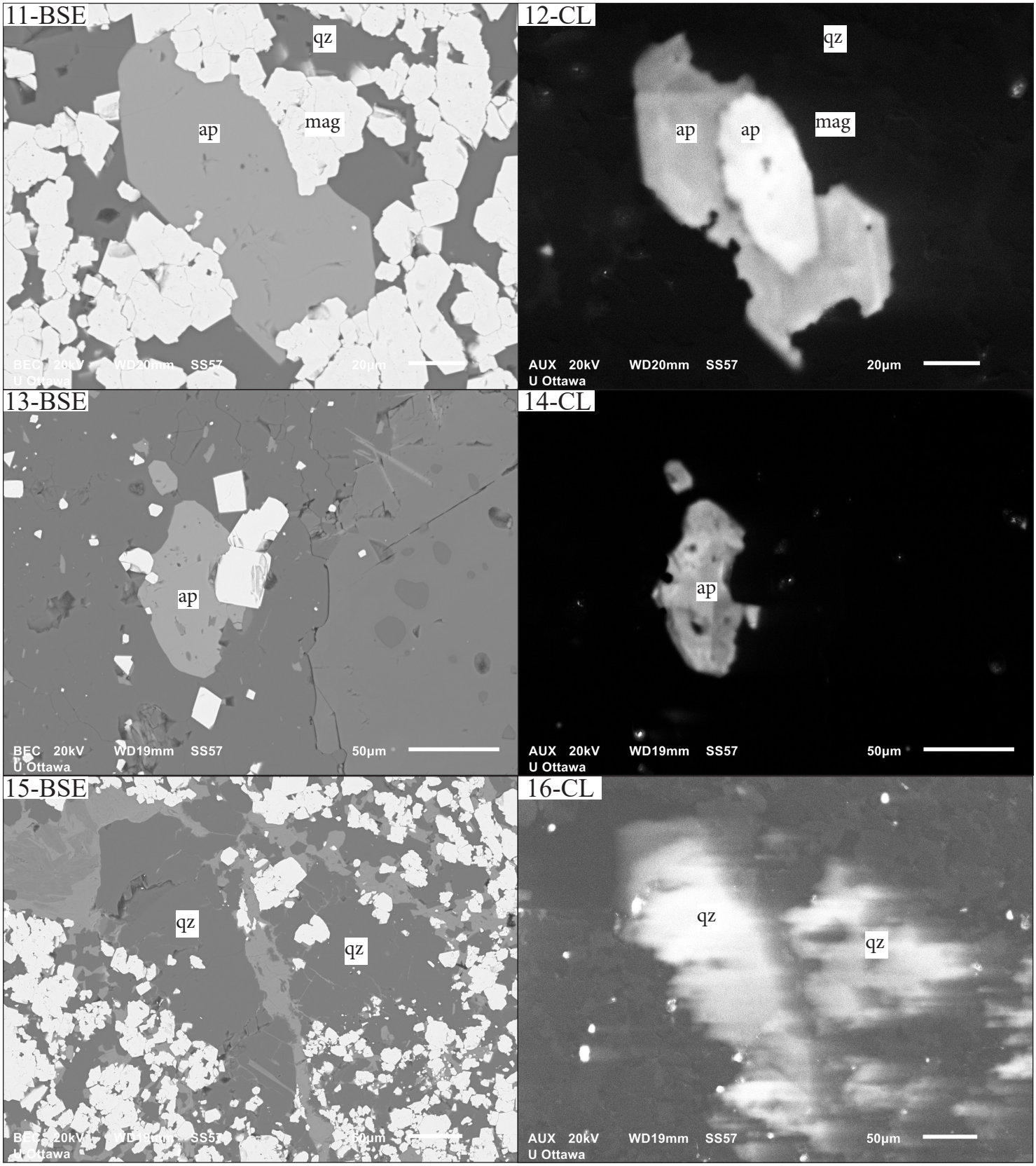
Sample Type: magnetite
Location: 47.06896 -79.79070
BIF Member: South BIF

SiO_2 [wt.%]	Al_2O_3 [wt.%]	Fe_2O_3 [wt.%]	Ge [ppm]	Pb [ppm]	As [ppm]	Ni [ppm]	B [ppm]	ΣREE [ppm]
45.0	0.59	51.3	5.5	2.7	0.8	0.9	2.8	19.5

Context: Sample 11-32 marks the onset of magnetite deposition close to the base of the northern part of the South BIF along Hwy 11.
Petrography: Sample 11-32 comprises white chert, black chert and massive magnetite interlayers. Magnetite layers consist of small individual (<50 µm) magnetite grown into near-massive Type 4 magnetite. Inclusions in magnetite and interstitial spaces contain Type 1 hematite, chlorite, dolomite, apatite, and monazite. Magnetite layers are offset along late quartz-biotite veins. Veins can be partially overgrown in magnetite, but are well preserved in chert layers. Subhedral, >100 µm dolomite occurs on the interface of chert and magnetite. Multiple generations of apatite are revealed by cathodoluminescence. The core of some apatite crystals is CL-bright and may be of detrital origin (Type 3), overgrown by late, authigenic Type 2 apatite partially overgrowing Type 3 magnetite. Quartz in black chert is fine grained and contains abundant Type 1 and 2 magnetite, Type 1 hematite, and brown and unusual green biotite. Black chert can be microbanded, but the microbanding is poorly developed. Siderite occurs up to 5 vol. % in some parts of the black chert. Few large euheral pyrite and anhedral magnetite occur along quartz veins. Black chert pinches out between two magnetite layers, potentially representing an early diagenetic chert pod seen in outcrop scale. White chert contains larger (100 µm) quartz and some magnetite and chlorite. Quartz is CL-passive except in quartz veins, where large areas of CL-active quartz is present.




5-PPL
mag
ap
dol
chl
qz
mag
20 µm
6-XPL
bt
magnetite
mag
bt
dol
black chert
200 µm
7-REF
mag
50 µm
8-BSE
dol
mag
mon
ap
qz
10µm
X 330 20.0kV COMPO NOR
9-BSE
dol
mag
qz
100µm
X 190 20.0kV COMPO NOR
10-BSE
mag
ap
dol
qz
100µm
X 43 20.0kV COMPO NOR


11-BSE
qz
ap
mag
BEC 20kV WD20mm SS57 20µm
U Ottawa
12-CL
qz
ap
ap
mag
AUX 20kV WD20mm SS57 20µm
U Ottawa
13-BSE
ap
BEC 20kV WD19mm SS57 50µm
U Ottawa
14-CL
ap
AUX 20kV WD19mm SS57 50µm
U Ottawa
15-BSE
qz
qz
16-CL
qz
qz
AUX 20kV WD19mm SS57 50µm
U Ottawa

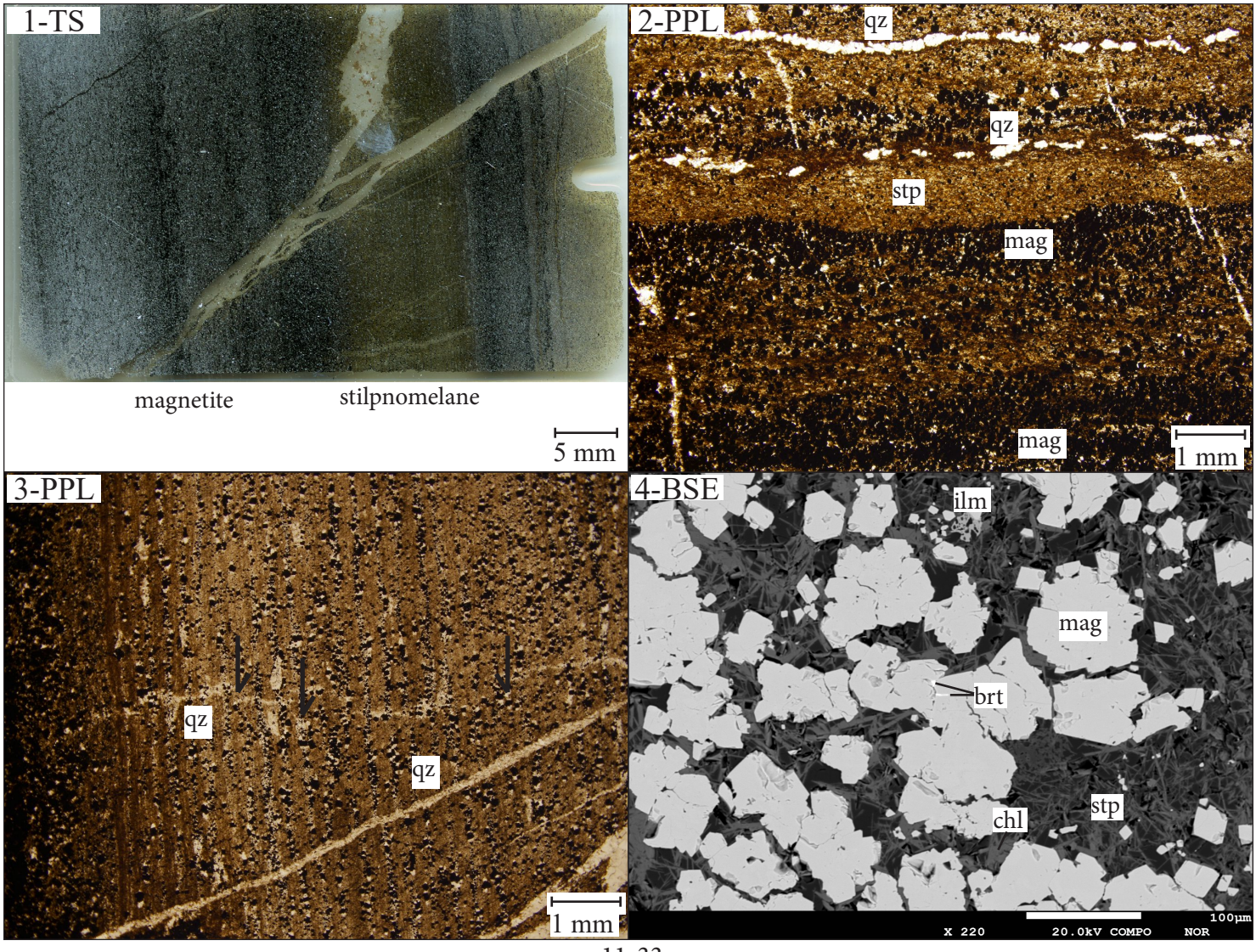
Sample: 11-33

Sample Type: magnetite-stilpnomelane
Location: 47.06898 -79.79070
BIF Member: South BIF

SiO_2 [wt.%]	Al_2O_3 [wt.%]	Fe_2O_3 [wt.%]	Ge [ppm]	Pb [ppm]	As [ppm]	Ni [ppm]	B [ppm]	ΣREE [ppm]
29.5	0.90	64.1	11.2	1.3	0.5	7.0	28.3	14.7

Context: 11-33 was collected from the South BIF along Hwy 11. Layering around the sample is folded and faulted.

Petrography: Sample 11-33 consists of an unusual interlayering of magnetite in quartz-stilpnomelane matrix and near-massive, microbanded fine grained stilpnomelane. Overall, stilpnomelane comprises >40% volume of this sample. Individual stilpnomelane crystals are very small (<10 μm) and tightly intergrown. The masses are brown in plain polarized light and remain brown under crossed polarizers. Chlorite, apatite, monazite, barite, and ilmenite occur as accessory phases. Distinct microbanding is present in the stilpnomelane layers, with quartz-magnetite between more stilpnomelane rich microbands. Some layer-parallel early quartz veins or white chert layers are boudinaged to >2x their original length. Early quartz veins at steep angles to microbanding are offset along individual microbands (see arrows in 3-PPL). Some quartz fragments or boudins may be present in the microbands defined by stilpnomelane-magnetite abundance. Late, pure quartz veins cut all lithologies at steep angles.

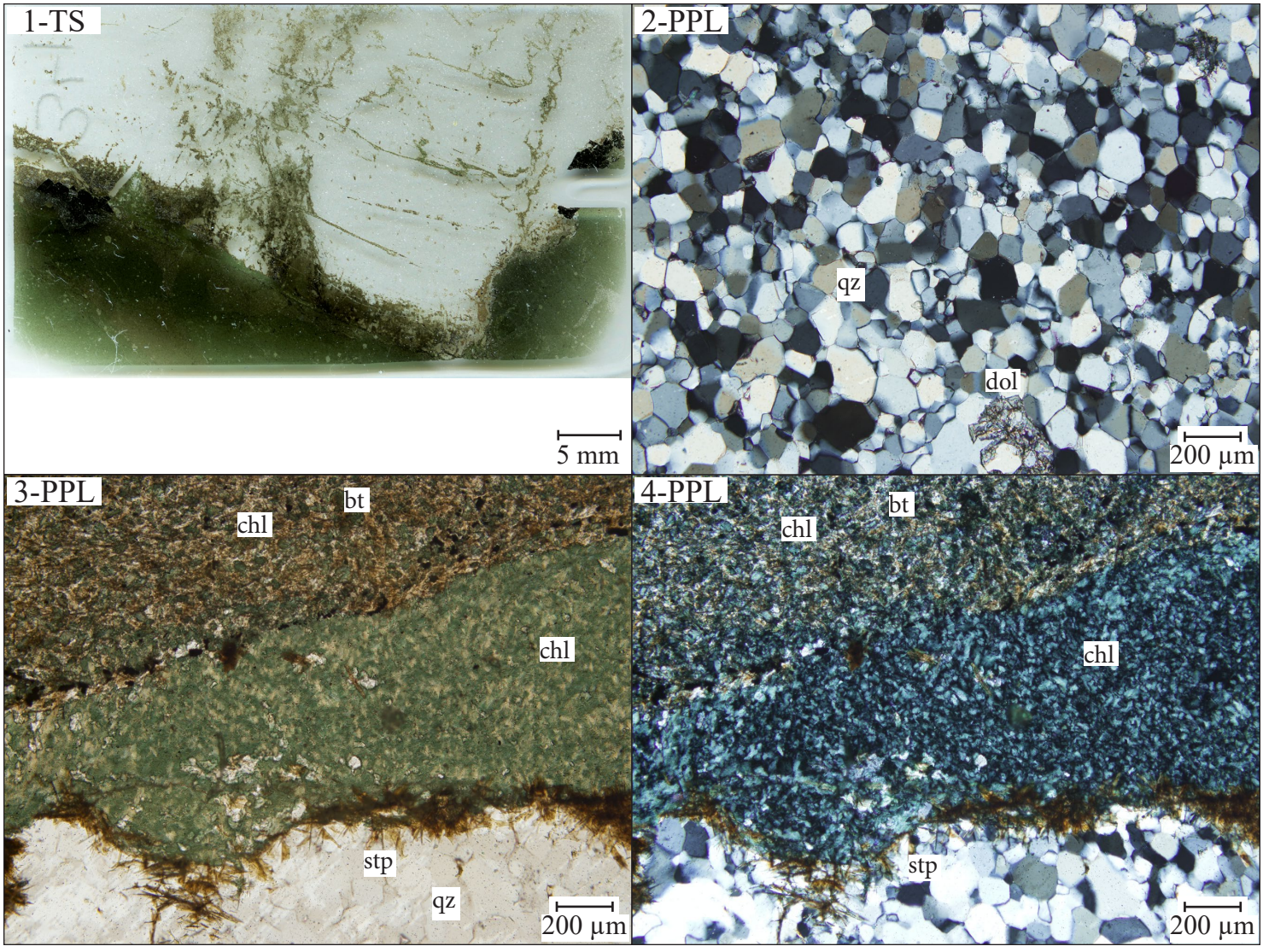


Sample: 11-34

Sample Type: volcaniclastic (shale)
Location: 47.06899 -79.79070
BIF Member: South BIF

SiO_2 [wt.%]	Al_2O_3 [wt.%]	Fe_2O_3 [wt.%]	Ge [ppm]	Pb [ppm]	As [ppm]	Ni [ppm]	B [ppm]	ΣREE [ppm]
44.4	11.3	29.7	6.8	2.6	1.3	19.9	40.7	136.4

Context: Collected from the central part of the northern half of the South BIF along Hwy 11.
Petrography: Sample 11-34 is mostly white chert, comprising unusually small quartz (<100 µm) compared to other white chert. Quartz in white chert contains few ultrafine <1 µm inclusions and trace dolomite in <100 µm subhedral dolomite overgrowing earlier quartz. A block or zone of stilpnomelane and chlorite (Berlin blue) intersects the white chert. The interface of the two layer types is lined with massive stilpnomelane, comprising intergrown small individual crystals. The chlorite is massive and fine grained. Zones of chlorite can contain biotite veins. Chlorite areas are internally zoned into chlorite- and chlorite-stilpnomelane-dominated parts. Within chlorite zones, large >100 µm quartz grains are common and may represent pseudomorphs after a precursor phase. The interfaces of chlorite and chlorite-stilpnomelane zones are occasionally lined with euhedral dolomite on the chlorite-rich side of the interface. Late veins consist of a chlorite core and stilpnomelane on the interface with white chert, similar to the larger chlorite-stilpnomelane zone. It is possible that the larger zone represents a vein in itself, producing smaller offshoots. Few large, euhedral pyrite occur along zones of offset along late veins.

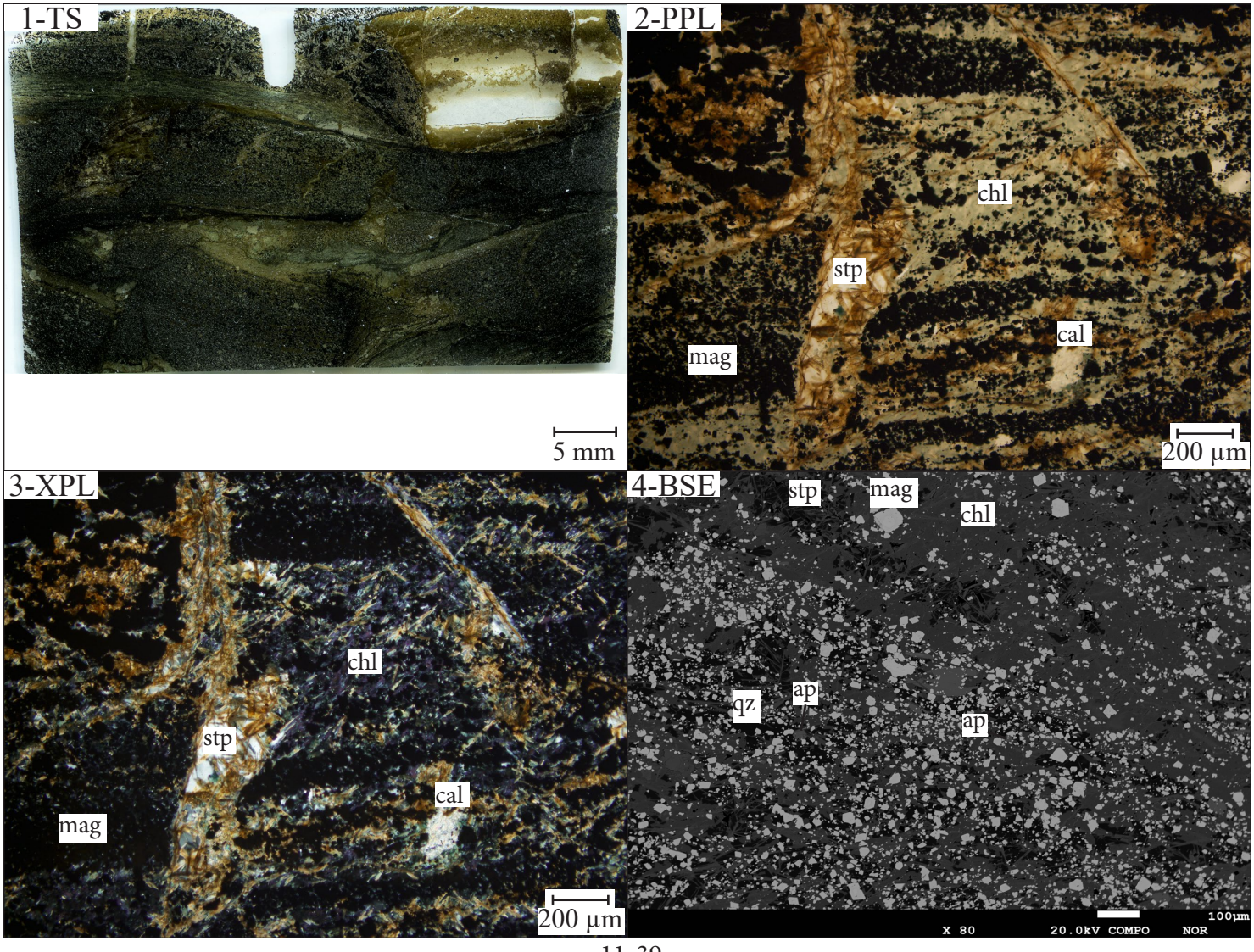


Sample: 11-39

Sample Type: magnetite
Location: 47.06908 -79.79070
BIF Member: South BIF

SiO_2 [wt.%]	Al_2O_3 [wt.%]	Fe_2O_3 [wt.%]	Ge [ppm]	Pb [ppm]	As [ppm]	Ni [ppm]	B [ppm]	ΣREE [ppm]
29.7	4.92	52.4	12.1	0.8	0.5	5.2	45.4	44.0

Context: Taken from the South BIF along Hwy 11.
Petrography: Sample 11-39 is a magnetite sample, but with unusually abundant chlorite-stilpnomelane in the matrix. The matrix of the sample consists of more chlorite-stilpnomelane than quartz in some areas of the sample. Layering is poorly developed, and some aligned magnetite crystals resembling microbanding follow wavy patterns, are overall deformed and folded, as well as brecciated. Chlorite is more abundant where material is less deformed, whereas stilpnomelane is prevalent in brecciated or deformed areas. Late, mm-scale veins cutting brecciation comprise stilpnomelane-quartz, sometimes with minor magnetite. Two cm-scale fragments of chert might represent boudins or resedimented lithic fragments. Stilpnomelane is unusually large, up to >200 µm. Chlorite is larger than usual, with indiviudual crystals exceeding 50 µm. Chlorite interference colors are mostly Berlin blue. Magnetite occurs as Type 2&3 magnetite. Microcrystalline carobonates (calcite?) grow as pseudomorphs as alteration products after preexisting aluminosilicates or as euhedral porphyroblasts. Some apatite and ilmenite occurs as accessory phases. Euhedral pyrite occurs as accessory around the chert boudins, ranging in size from <50 - >200 µm.

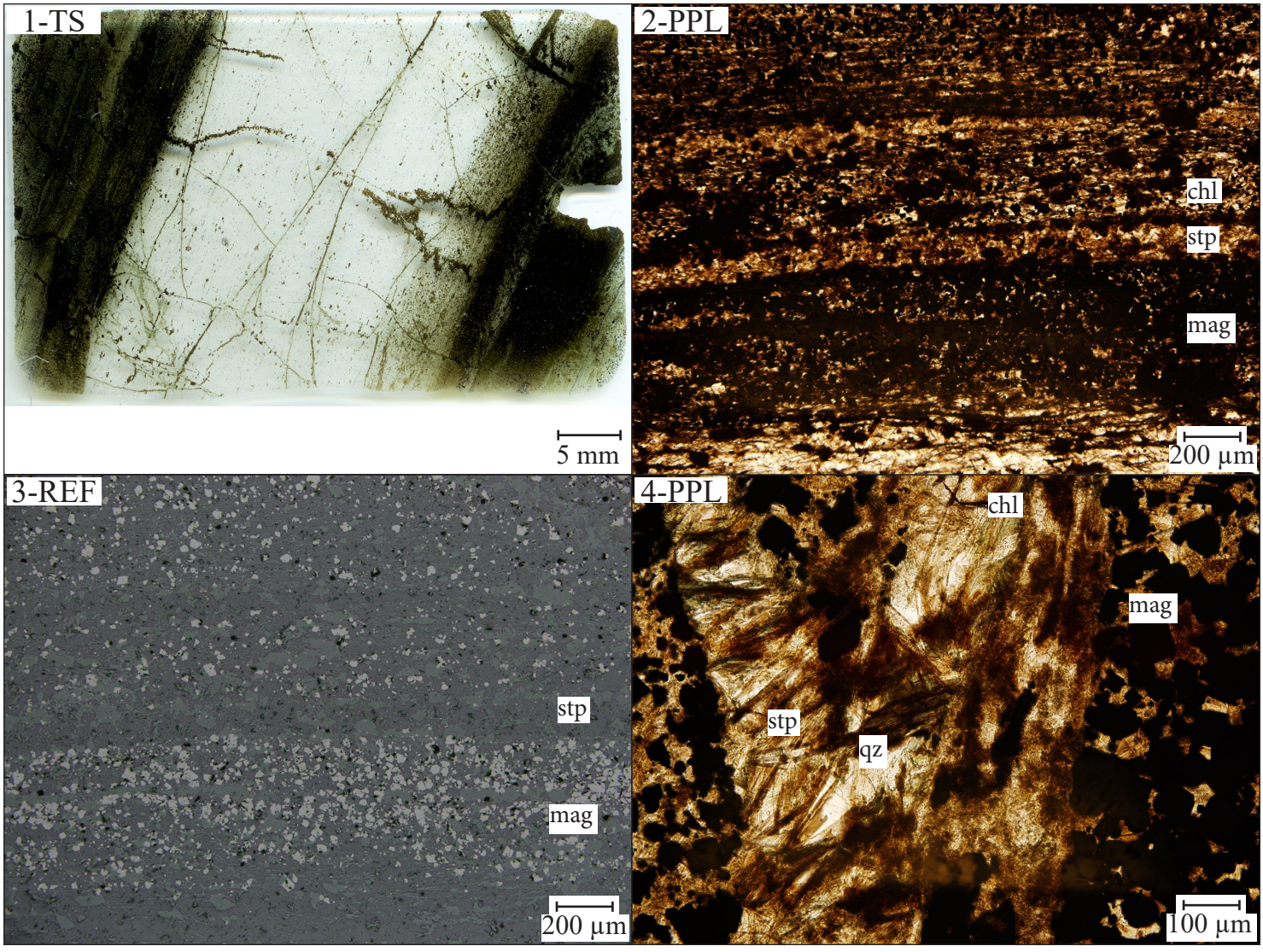


Sample: 11-40

Sample Type: magnetite
Location: 47.06910 -79.79070
BIF Member: South BIF

SiO_2 [wt.%]	Al_2O_3 [wt.%]	Fe_2O_3 [wt.%]	Ge [ppm]	Pb [ppm]	As [ppm]	Ni [ppm]	B [ppm]	ΣREE [ppm]
51.6	1.81	37.5	7.4	2.5	1.1	4.2	52.2	25.8

Context: Collected from the northern part of the South BIF along Hwy 11.
Petrography: Sample 11-40 comprises white chert and aluminosilicate-rich magnetite. Material for whole rock geochemistry was produced from a magnetite-rich piece. White chert consists of coarse (100 µm) quartz with accessory Type 2 magnetite and euhedral, 200 µm carbonate (dolomite?). Magnetite layers comprise Type 3 magnetite in a quartz-stilpnomelane matrix. Chlorite (green interference colors) is only present in locally as accessory in quartz-stilpnomelane areas. Magnetite layers are internally complex, with Type 2 magnetite preferentially aligned along bands resembling microbands in black chert, but recrystallized to much larger grain sizes. Stilpnomelane can grow unusually large, >200 µm. Apatite and pyrite can occur as accessories. Pyrite forms late, large masses overgrowing earlier stilpnomelane and euhedral magnetite, informing late metamorphic origin.

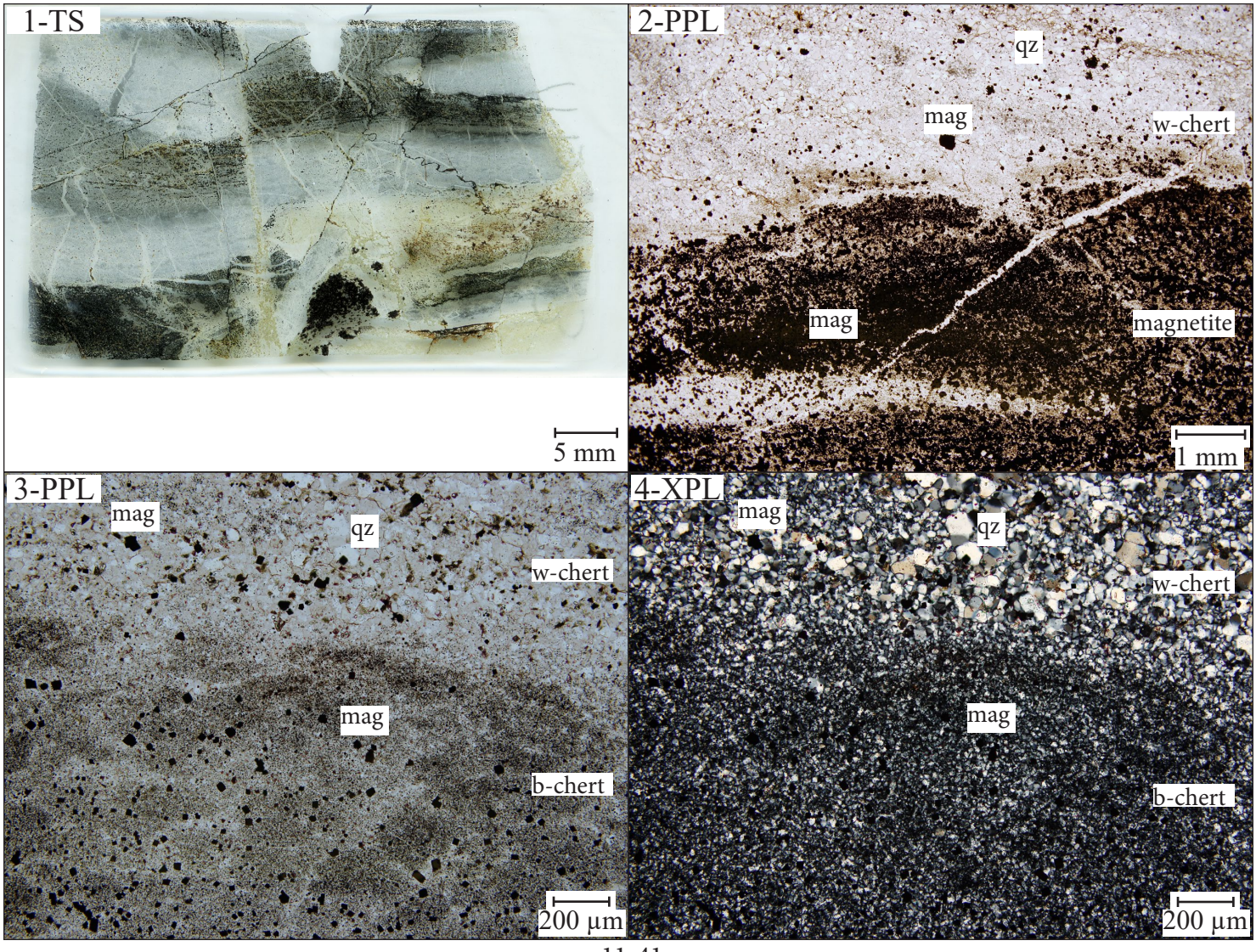


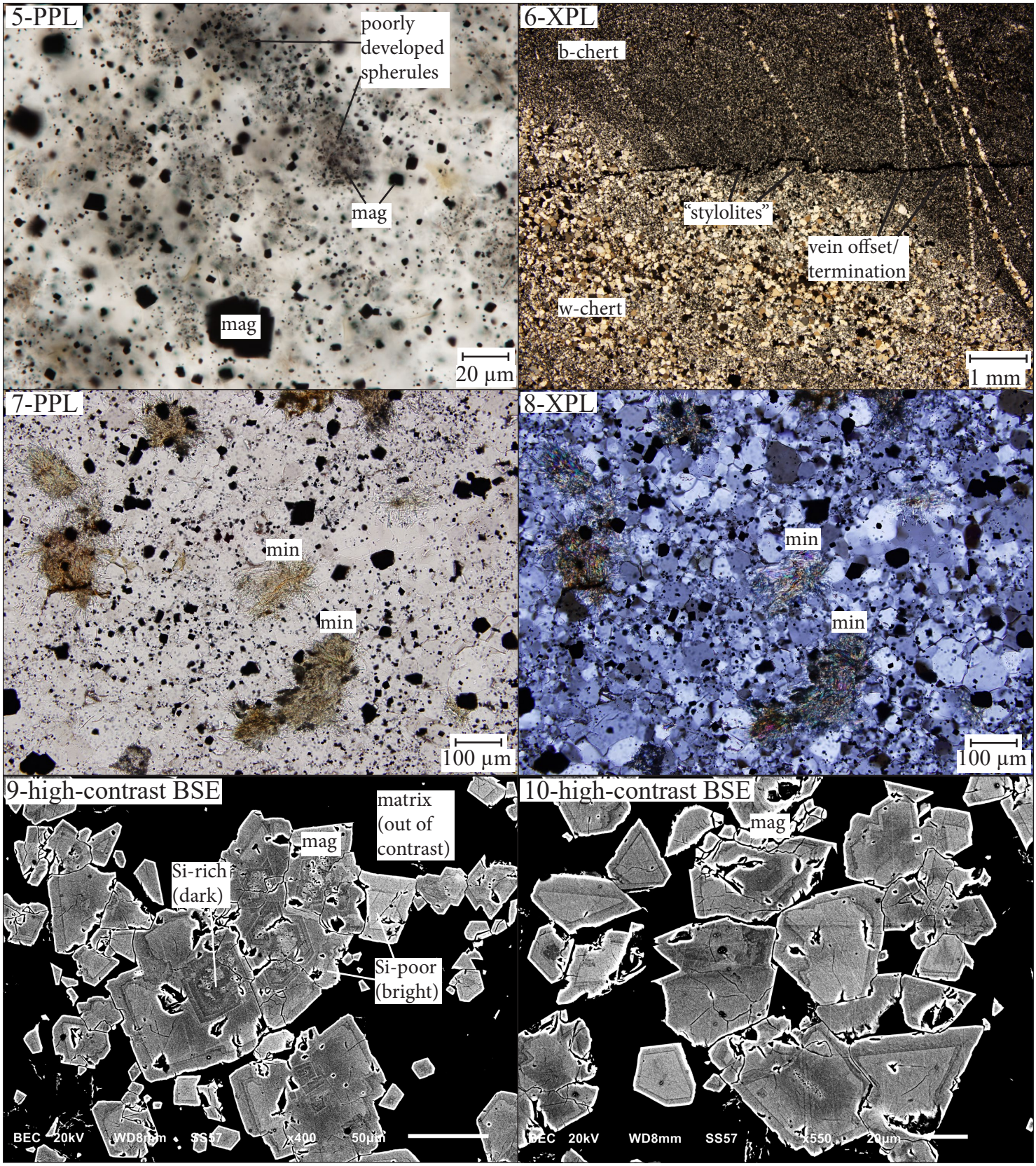
Sample: 11-41

Sample Type: chert
Location: 47.06912 -79.79069
BIF Member: South BIF

SiO_2 [wt.%]	Al_2O_3 [wt.%]	Fe_2O_3 [wt.%]	Ge [ppm]	Pb [ppm]	As [ppm]	Ni [ppm]	B [ppm]	ΣREE [ppm]
81.8	0.30	15.9	5.1	0.6	2.2	0.2	33.3	5.2

Petrography: 11-41 consists of white chert, black chert, and magnetite interlayers. Material for whole rock geochemistry was produced from magnetite-rich black chert. Black chert is not microbanded, and contains Type 1 and Type 2 magnetite in fine grained chert matrix. Type 1 magnetite is not as well-arranged in "spherules" as observed in other samples. Cloudy Type 1 magnetite is sub-micron sized. Quartz in black chert is fine grained (<50 µm), and contains Type 1 magnetite as inclusions, whereas Type 2 magnetite is located on the interstices of quartz. Some larger (50 µm) apatite, chlorite, and locally pyrite occur as accessory phases. White chert comprises >100 µm quartz where it is pure, and few inclusions of carbonates, pyrite and chlorite. Magnetite layers contain Type 2 and 3 magnetite, often showing internal oscillatory chemical zonation of Si abundance. The matrix of magnetite layers is an unusual chert-minnesotaite-chlorite matrix. Minnesotaite has a more radial-fibrous habit than stilpnomelane typically occuring as blades. Different generations of quartz veins are present, identified by mineralogy, cross-cutting relationships and differently developed offset. Offset also occurs along planes of motion at shallow angles to layering resembling stylolites, but not as usually observed layer-parallel. This informs development as: 1) black chert formation, 2) different generations of quartz veins, 3) offset along plane of motion lined by magnetite, 4) late quartz veins.



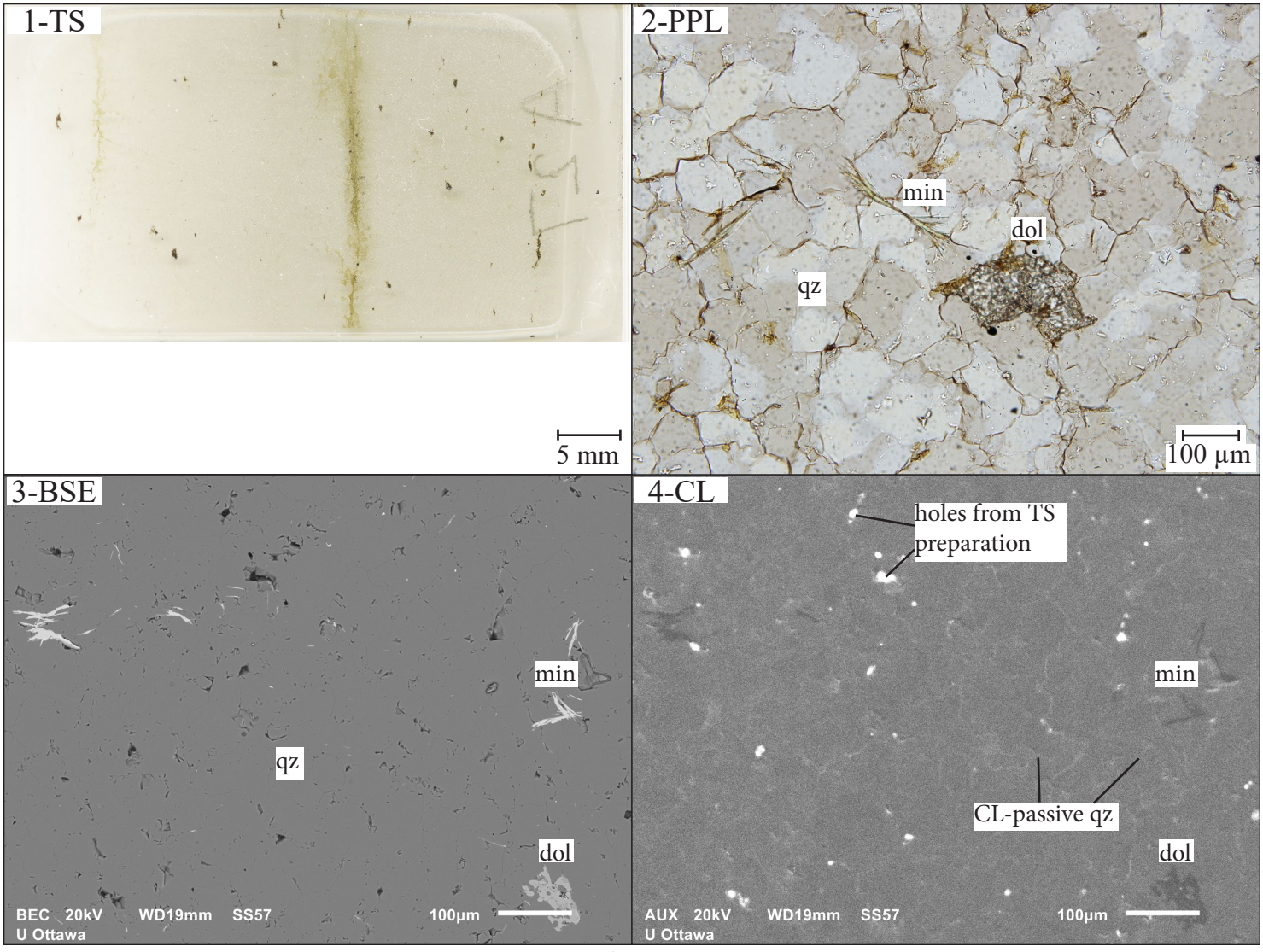

5-PPL
poorly developed spherules
mag
mag
20 µm
6-XPL
b-chert
"stylolites"
vein offset/ termination
w-chert
1 mm
7-PPL
min
min
100 µm
8-XPL
min
min
100 µm
9-high-contrast BSE
matrix (out of contrast)
mag
Si-rich (dark)
Si-poor (bright)
BEC 20kV WD8mm SS57 x400 50µm
10-high-contrast BSE
mag
BEC 20kV WD8mm SS57 x550 20µm

Sample: A027

Sample Type: chert
Location: 47.06346 -79.87559
BIF Member: North BIF

SiO_2 [wt.%]	Al_2O_3 [wt.%]	Fe_2O_3 [wt.%]	Ge [ppm]	Pb [ppm]	As [ppm]	Ni [ppm]	B [ppm]	ΣREE [ppm]
97.7	0.21	1.2	2.4	0.1	36	9.7	53.6	1.6

Petrography: Sample A027 is a pure white chert. Quartz is >98 vol. % in the sample, with only minor siderite defining weakly developed microbanding. Quartz is large (100 µm) with irregular crystal faces and CL-passive. Dolomite is also CL-passive due to high Fe-content extinguishing the CL signal. Large quartz appears unremarkable under crossed polarizers, with no obvious stress zonations or deformation indicators obvious. In microbands, quartz is finer (50 µm) Siderite is <20 µm and blocky. Accessory minnesotaite, stilpnomelane, apatite, and dolomite are <5 vol. % and occur dispersed in chert. Stilpnomelane also occurs in late veins cutting the chert.



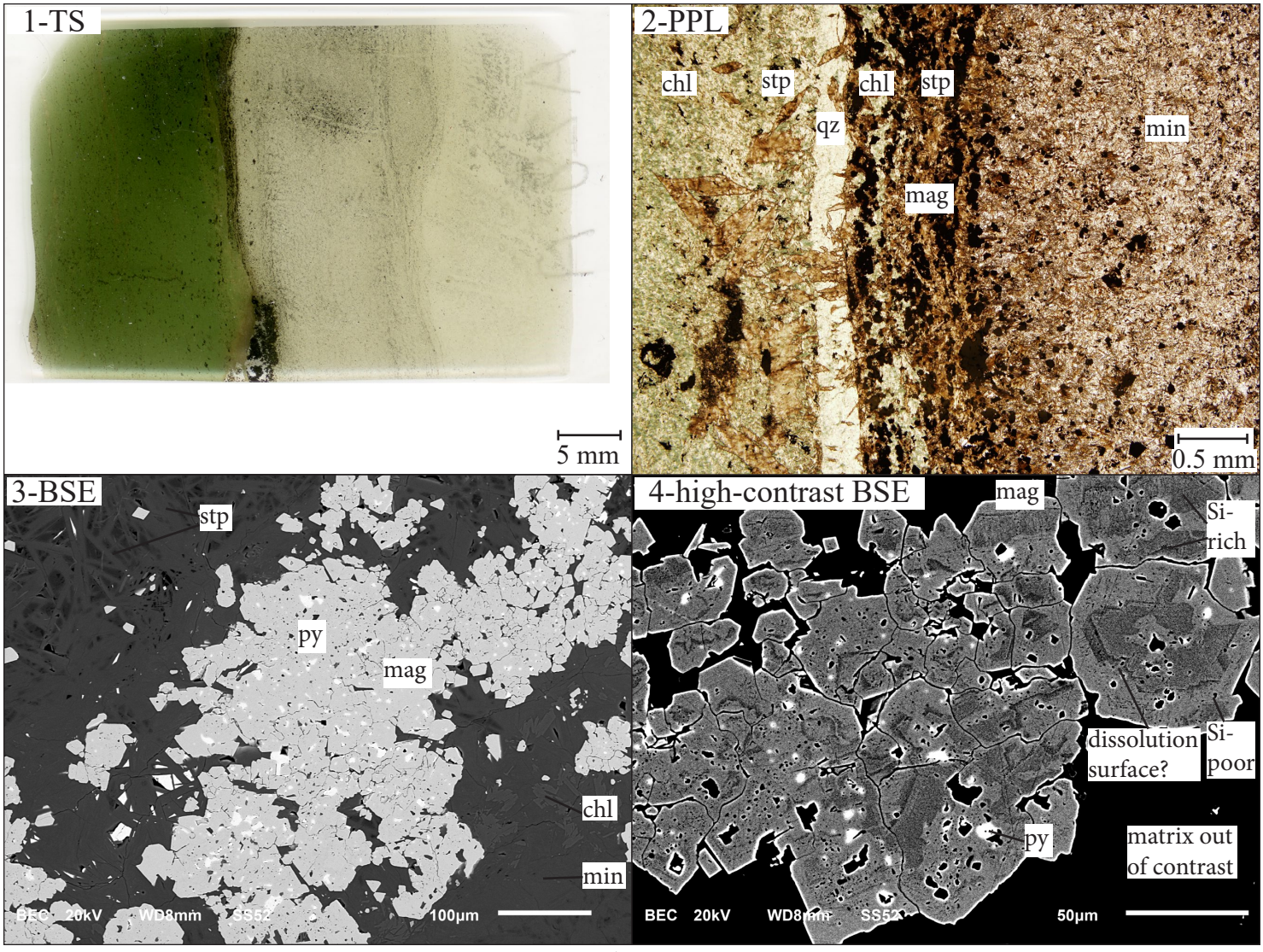
A027

Sample: A028

Sample Type: magnetite-minnesotaite
Location: 47.06345 -79.87559
BIF Member: North BIF

SiO_2 [wt.%]	Al_2O_3 [wt.%]	Fe_2O_3 [wt.%]	Ge [ppm]	Pb [ppm]	As [ppm]	Ni [ppm]	B [ppm]	ΣREE [ppm]
49.4	0.30	41.4	5.0	0.3	1.4	52.9	1.7	24.3

Petrography: Sample A028 is an anomalous magnetite sample, containing a magnetite in a minnesotaite-chlorite-sericite-quartz matrix. Magnetite occurs on the interface between a fine grained mass of chlorite-quartz and min-nesotaite-quartz. Magnetite is anomalous Type 2-3 and locally intergrown to form Type 4, and contains abundant <5 µm pyrite inclusions. The internal structure of Type 3 magnetite revealed by Si-zonation under high-contrast BSE imaging is irregular, showing dissolution surfaces and zonation not observed in other samples. Minnesotaite occurs as intergrown masses of <20 µm crystals with quartz, chlorite, magnetite and trace apatite. Stilpnomelane forms large pseudomorphs after a rhombohedral precursor phases in chlorite, and smaller crystals where it com-prises the matrix of magnetite. Chlorite has intermediate green to Berlin blue interference colours, and contains accessory apatite and pyrite, as well as trace chalcopyrite and zircon. Sulfides can become the dominant species along strike and replace magnetite. Locally, magnetite can occur in anomalous morphologies resembling specular hematite. Pyrite and chalcopyrite occur with magnetite in the stilpnomelane-rich part of the sample.
Material for whole rock geochemistry was prepared from magnetite-rich material comprising a low-Al minnesotaite-stilpnomelane-quartz matrix.

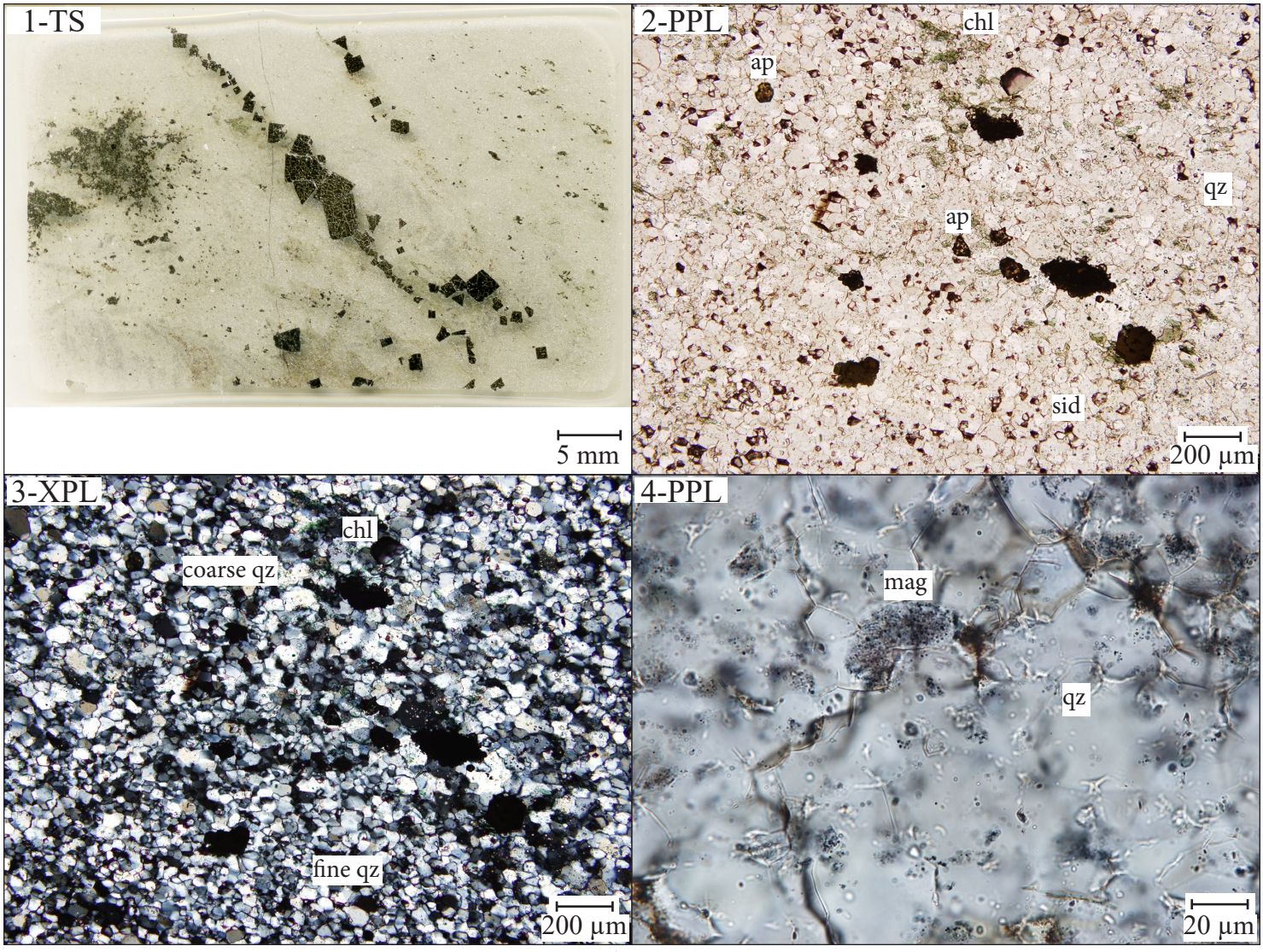


Sample: A030

Sample Type: chert
Location: 47.06347 -79.87583
BIF Member: North BIF

SiO_2 [wt.%]	Al_2O_3 [wt.%]	Fe_2O_3 [wt.%]	Ge [ppm]	Pb [ppm]	As [ppm]	Ni [ppm]	B [ppm]	ΣREE [ppm]
89.4	0.28	6.5	2.1	6.6	6.1	88.0	25.5	22.0

Petrography: Sample A030 is a white chert sample with abundant microinclusions in quartz. Quartz is mostly large (100 µm), but locally varies in size. Microinclusions in quartz are common, mostly Type 1 magnetite in poorly-developed spherules. Accessory apatite, siderite, and small (<10 µm) chlorite are common. The crystal interfaces of chlorite are intricately intergrown, forming irregular surfaces. Euhedral, mm-scale pyrite is present along a late quartz vein, but has been avoided during sample preparation for whole rock geochemistry. Note: Siderite forms indentations during the preparation of thin sections, resulting in anomalous optical effects and darker appearance under lower magnification.



A030

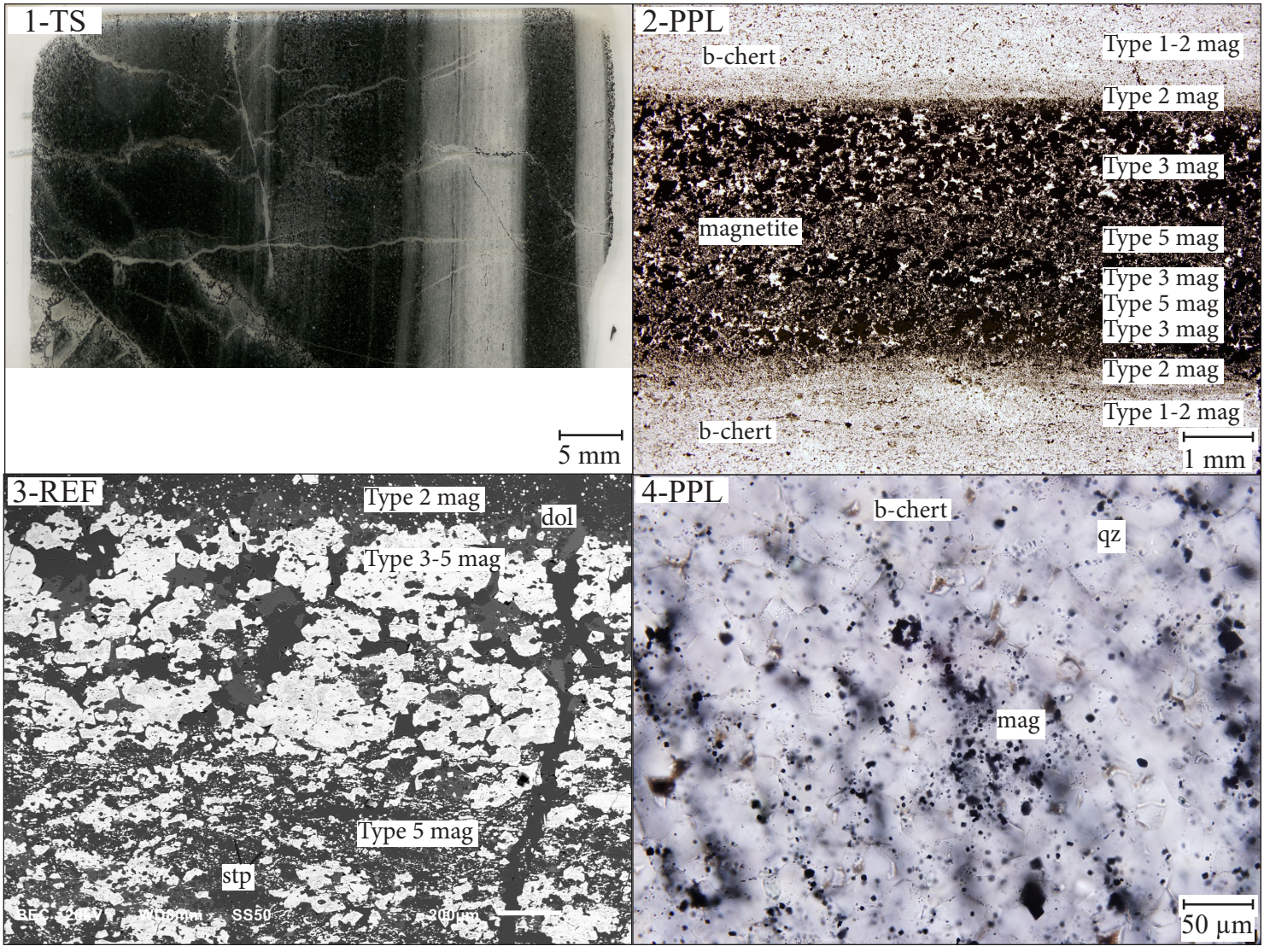
Sample: B013

Sample Type: chert-magnetite
Location: 47.06663 -79.87578
BIF Member: South BIF

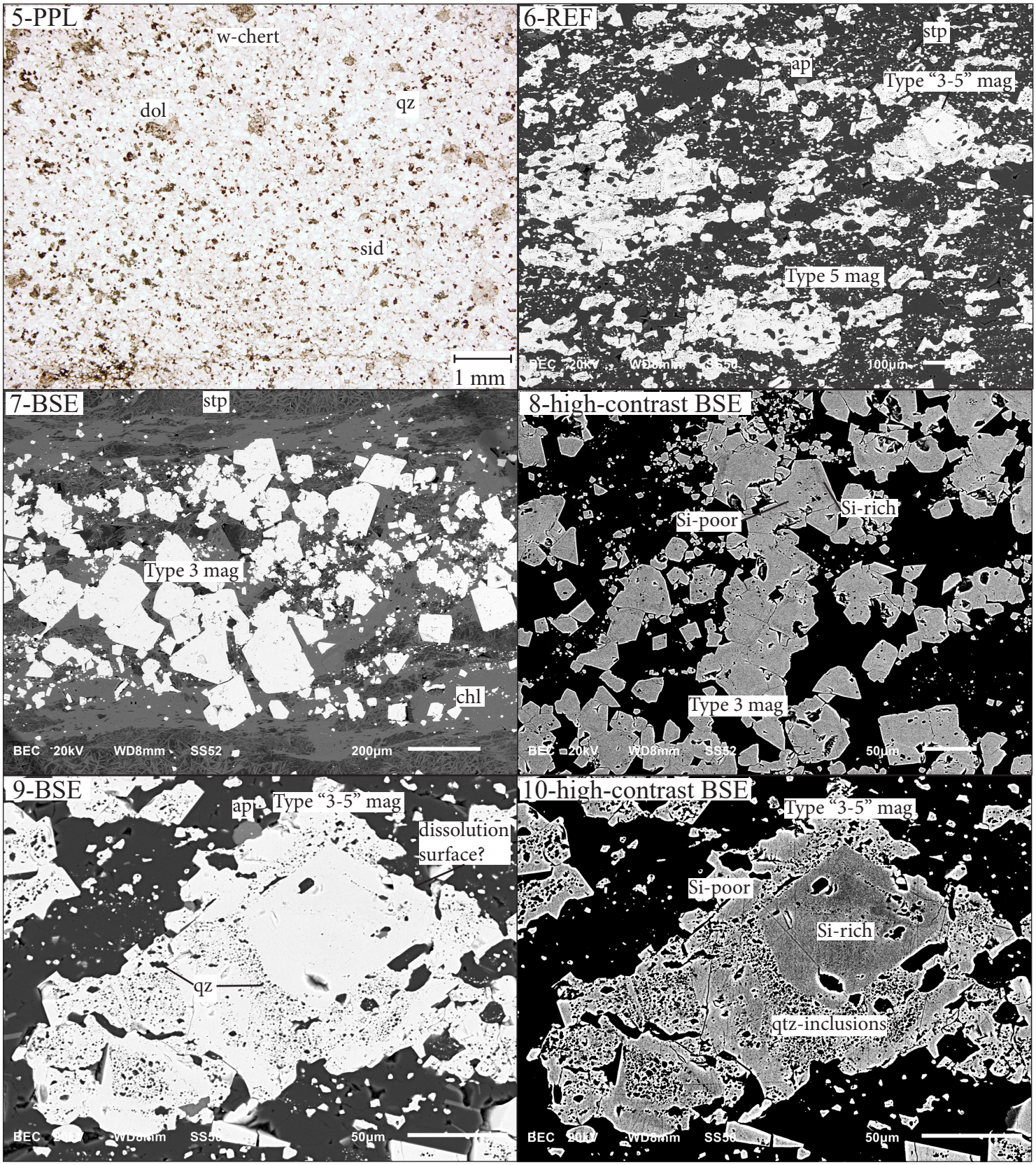
SiO_2 [wt.%]	Al_2O_3 [wt.%]	Fe_2O_3 [wt.%]	Ge [ppm]	Pb [ppm]	As [ppm]	Ni [ppm]	B [ppm]	ΣREE [ppm]
18.1	1.40	62.4	4.6	4.4	25	79.2	0.7	120.2

Context: B013-1 through B013-7 were produced from one hand sample. B013-1, 4, 7 were produced from individual magnetite layers containing petrographically similar material. Geochemistry listed is for magnetite sample B013-1.

Petrography: Sample B013 consists of interlayered black chert, white chert, and thick, complexly differentiated magnetite layers. Magnetite occurs as Type 1 and 2 in black chert, and as Type 2, 3, and 5 in magnetite layers. Type 3 is weakly Si-zoned, euhedral magnetite containing quartz inclusions, while Type 5 magnetite is skeletal or patchy, probably affected by dissolution events or forming late during metamorphism, growing around quartz that had already mostly crystallized. Type 3 and 5 form transitional habits, where Type 5 magnetite seems to overgrow a core of Type 3 magnetite. Type 3 and Type 5 magnetite occur in parallel intrabands in individual layers. The matrix in magnetite layers is predominantly quartz, with dolomite and accessory apatite and chlorite. Stilpnomelane and biotite can occur with Type 5 magnetite. Black chert can be weakly microbanded, and consists of <50 μm quartz with Type 1 magnetite inclusions and Type 2 magnetite on the interstices of quartz. Hematite, apatite, siderite, and apatite occur as accessory phases in black chert. White chert is predominantly large quartz (>100 μm) with accessory Fe-dolomite and siderite.



B013

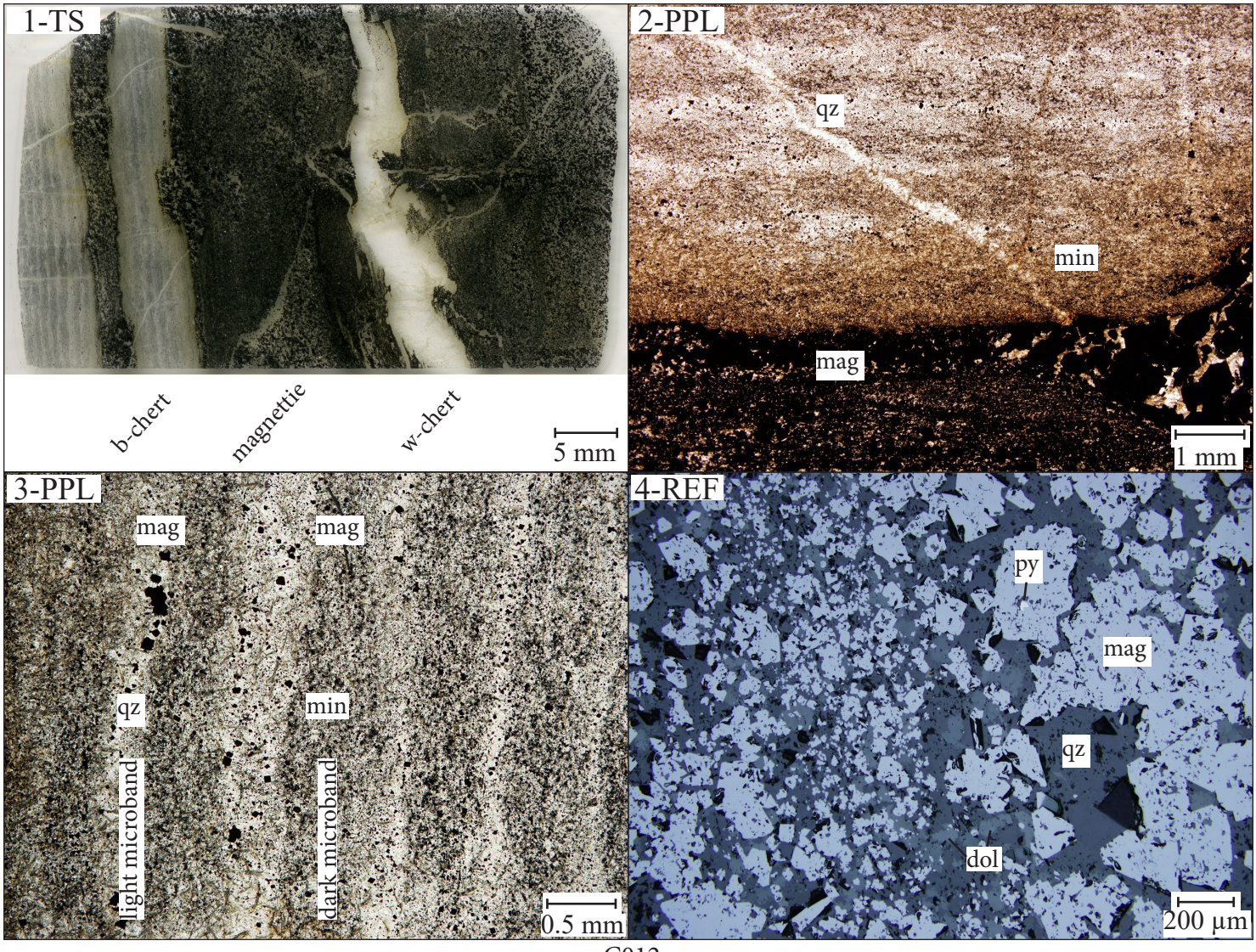

5-PPL
w-chert
dol
qz
sid
1 mm
6-REF
stp
ap
Type “3-5” mag
Type 5 mag
100µm
7-BSE
stp
Type 3 mag
chl
200µm
8-high-contrast BSE
Si-poor
Si-rich
Type 3 mag
50µm
9-BSE
ap
Type “3-5” mag
dissolution surface?
qz
50µm
10-high-contrast BSE
Type “3-5” mag
Si-poor
Si-rich
qtz-inclusions
50µm

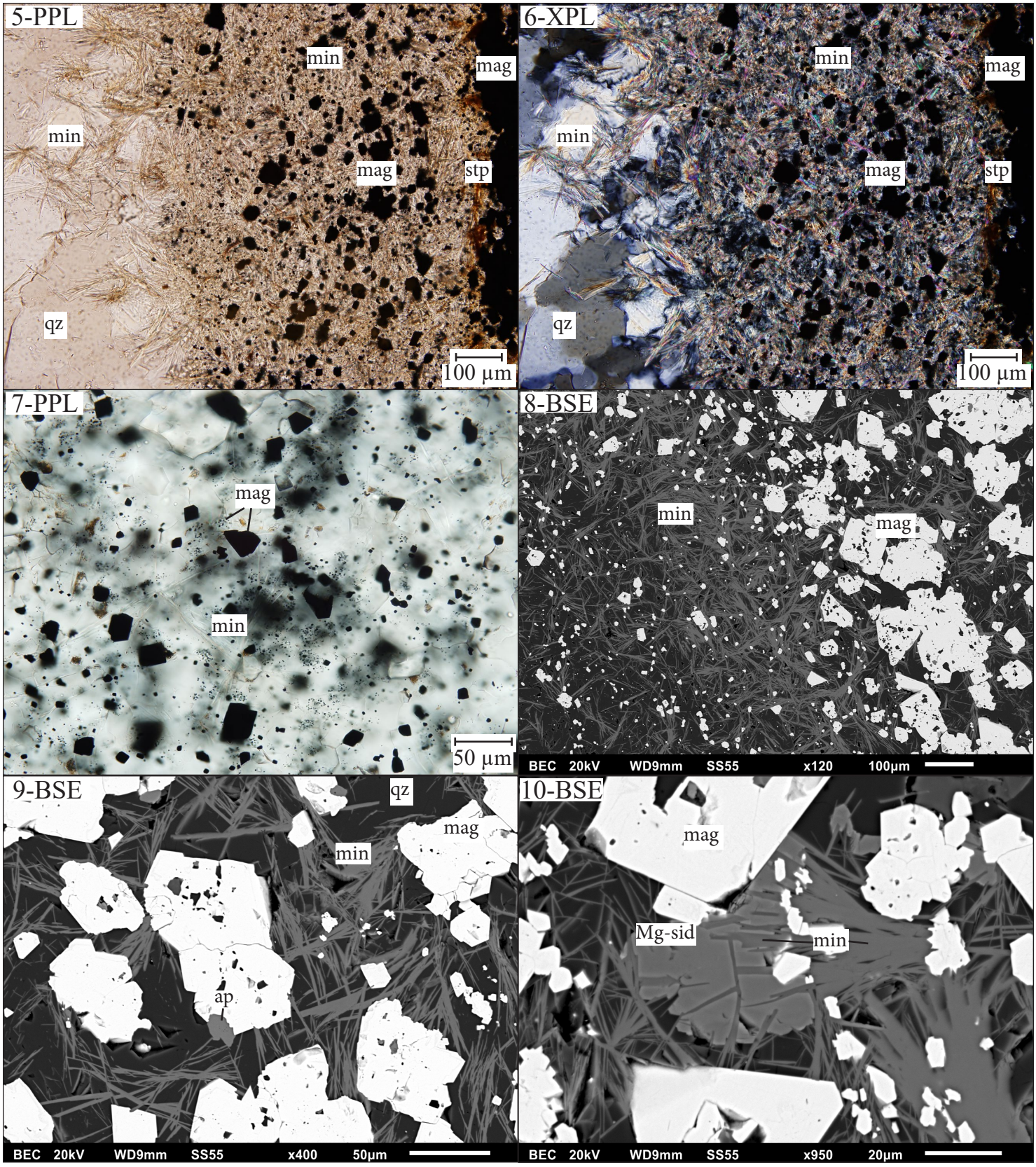
Sample: C012

Sample Type: magnetite-chert
Location: 47.06886 -79.87489
BIF Member: North BIF

SiO_2 [wt.%]	Al_2O_3 [wt.%]	Fe_2O_3 [wt.%]	Ge [ppm]	Pb [ppm]	As [ppm]	Ni [ppm]	B [ppm]	ΣREE [ppm]
26.4	0.04	66.5	7.9	0.3	1.2	25.8	0.1	9.4

Context: Magnetite sample C012-1 and chert sample C012-2 were produced from neighbouring layers in this sample.
Petrography: Sample C012 comprises magnetite, white chert, and microbanded black chert layers. Magnetite in magnetite layers is Type 2, 3, and locally Type 4. Type 3 magnetite forms very large crystals (>300 μm) in some parts of the sample. Where finer Type 2 and 3 magnetite are dominant, they occur preferentially aligned along parallel planes. Pyrite can occur as inclusions in Type 3 magnetite. Interstitial spaces between magnetite is filled with quartz, minnesotatite, Fe-carbonates, and apatite. Minnesotaite is small in interstitial spaces, but can form larger, more abundant radiating crystals on the interfaces of magnetite and chert. Black chert is distinctly microbanding, with individual bands defined by more abundant quartz and larger Type 2 magnetite comprising the transparent layers, while finer Type 1 magnetite and fine minnesotaite occur in the dark bands. Apatite and Fe-dolomite occur as accessory phases in the black chert. Minnesotaite is the dominant Fe-silicate, stilpnomelane occurs only as accessory on the interfaces of black chert and magnetite layers.



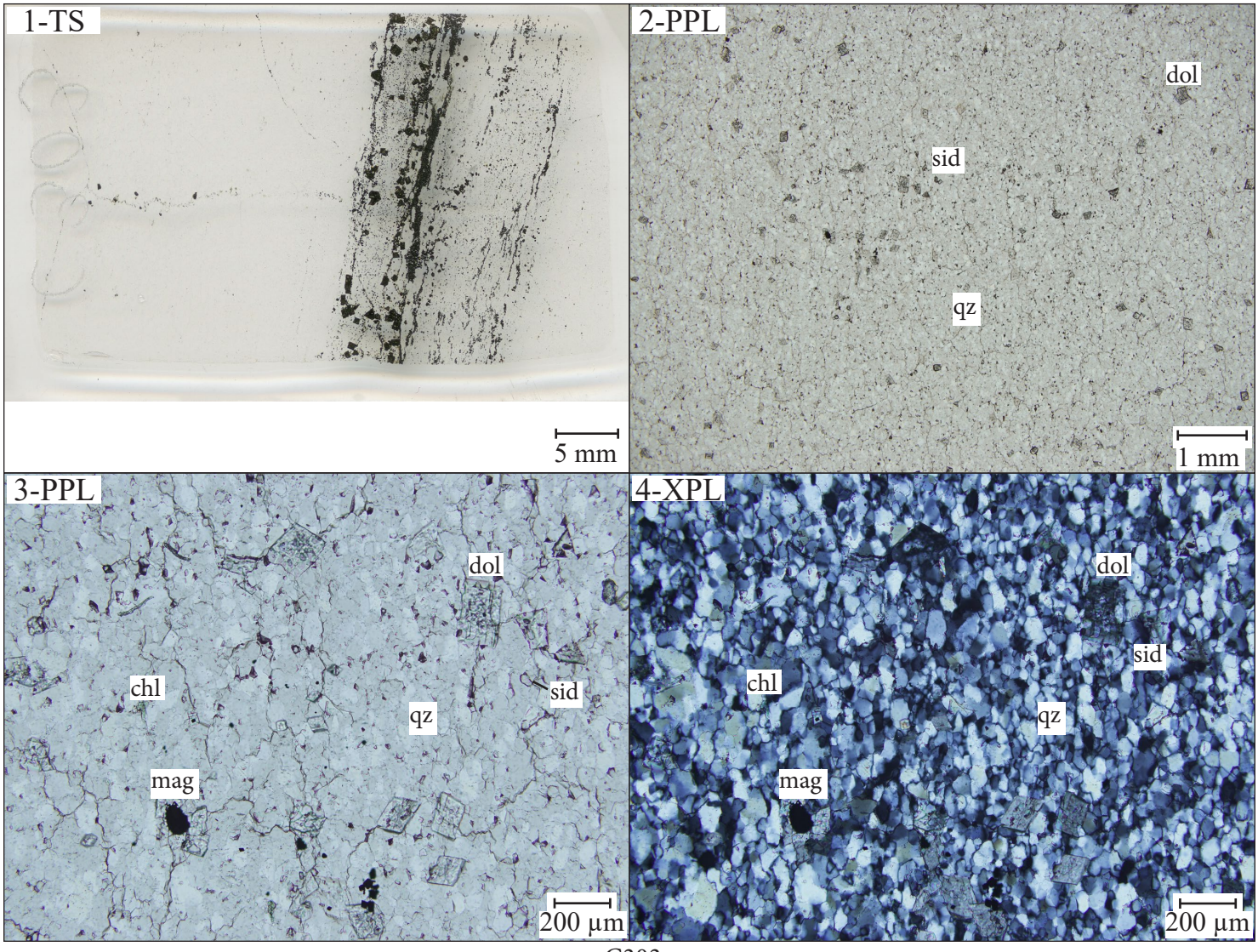

5-PPL
min
mag
min
mag
stp
qz
100 µm
6-XPL
min
mag
min
mag
stp
qz
100 µm
7-PPL
mag
min
50 µm
8-BSE
min
mag
BEC 20kV WD9mm SS55 x120 100µm
9-BSE
qz
mag
min
ap
BEC 20kV WD9mm SS55 x400 50µm
10-BSE
mag
Mg-sid
min
BEC 20kV WD9mm SS55 x950 20µm

Sample: C303

Sample Type: chert
Location: 47.07128 -79.87350
BIF Member: North BIF

SiO_2 [wt.%]	Al_2O_3 [wt.%]	Fe_2O_3 [wt.%]	Ge [ppm]	Pb [ppm]	As [ppm]	Ni [ppm]	B [ppm]	ΣREE [ppm]
95.4	0.26	1.4	1.5	0.2	0.5	2.3	54.9	1.4

Petrography: C303 is a white chert sample, comprising >95 vol.% quartz overall. Quartz is uniformly smaller than in other white chert samples (~50 µm). Accessory minerals are predominantly Fe-dolomite regularly distributed in the white chert, forming 50-100 µm euhedra, commonly with magnetite inclusions. Type 2 and 3 magnetite occur as accessories in some areas, and as finely dispersed Type 2 magnetite in some dolomite and Type 1 magnetite in few quartz crystals. Higher abundances of magnetite indicate layering. Trace chlorite is present. Large, >300 µm pyrite crystals occur in a layer-parallel zone, overgrowing Type 2 magnetite.



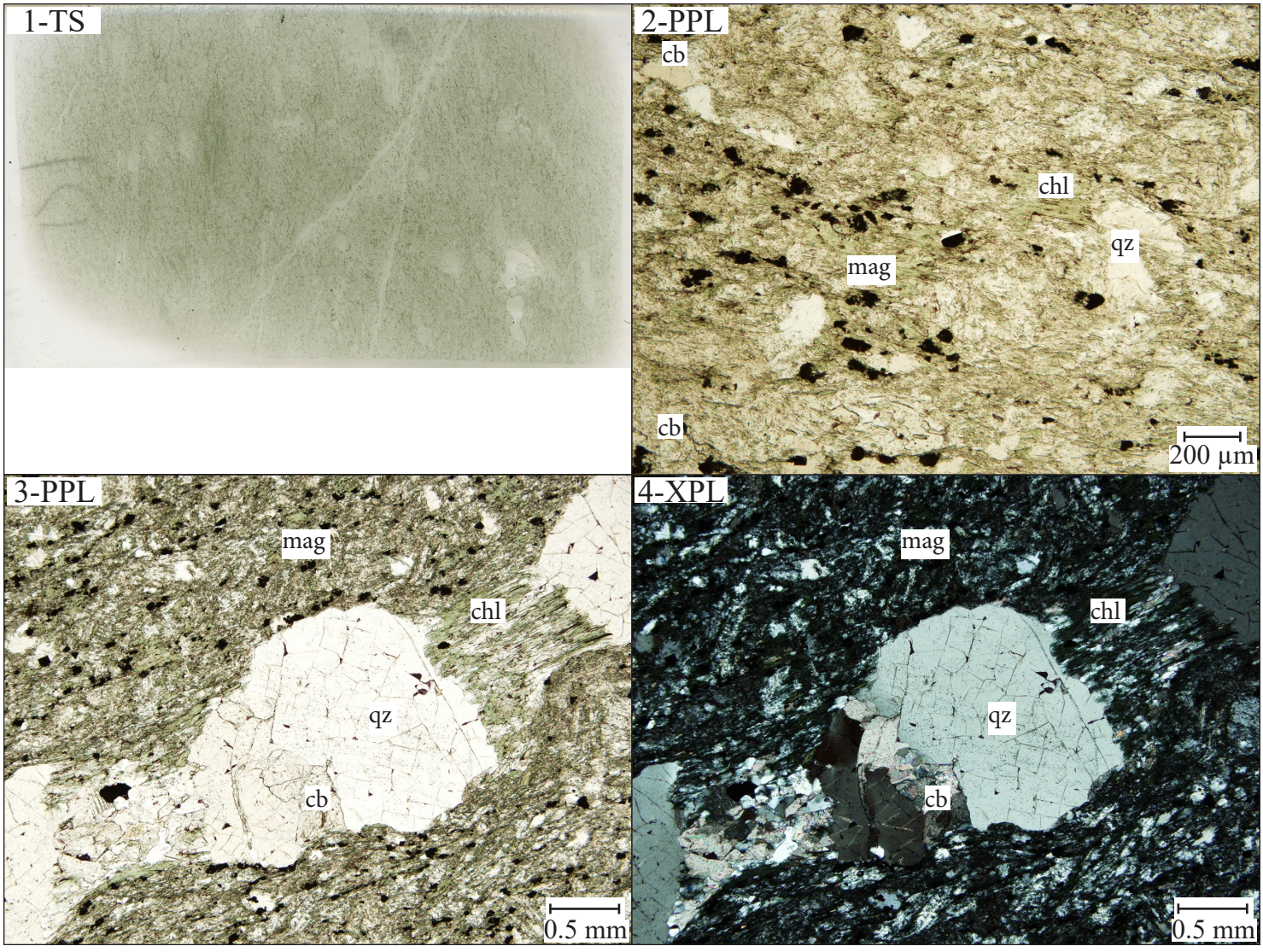
C303

Sample: D001

Sample Type: chlorite
Location: 47.06405 -79.89792
BIF Member: South BIF

SiO_2 [wt.%]	Al_2O_3 [wt.%]	Fe_2O_3 [wt.%]	Ge [ppm]	Pb [ppm]	As [ppm]	Ni [ppm]	B [ppm]	ΣREE [ppm]
56.5	13.4	7.5	1.3	1.2	0.5	57.1	31.1	96.6

Petrography: D001 is a chlorite sample, comprising subequal chlorite and quartz, with abundant Fe-carbonate, and accessory magnetite. Chlorite is the dominant phase in the matrix, defining layering or later deformation by preferential crystallographic orientation. All chlorite in the sample has brown-green interference colours. Chlorite, quartz and Fe-carbonates form pseudomorphs after large (>250 μm), angular precursor phases. Internally, the chlorite-carbonate-quartz filling of pseudomorphs is fine grained and irregular. Brecciated quartz/chert clasts show stress fracturing and chlorite in the pressure shadows between fragments. A quartz vein shows some degree of stepwise deformation or preferential development along the planes of preferential chlorite orientation.



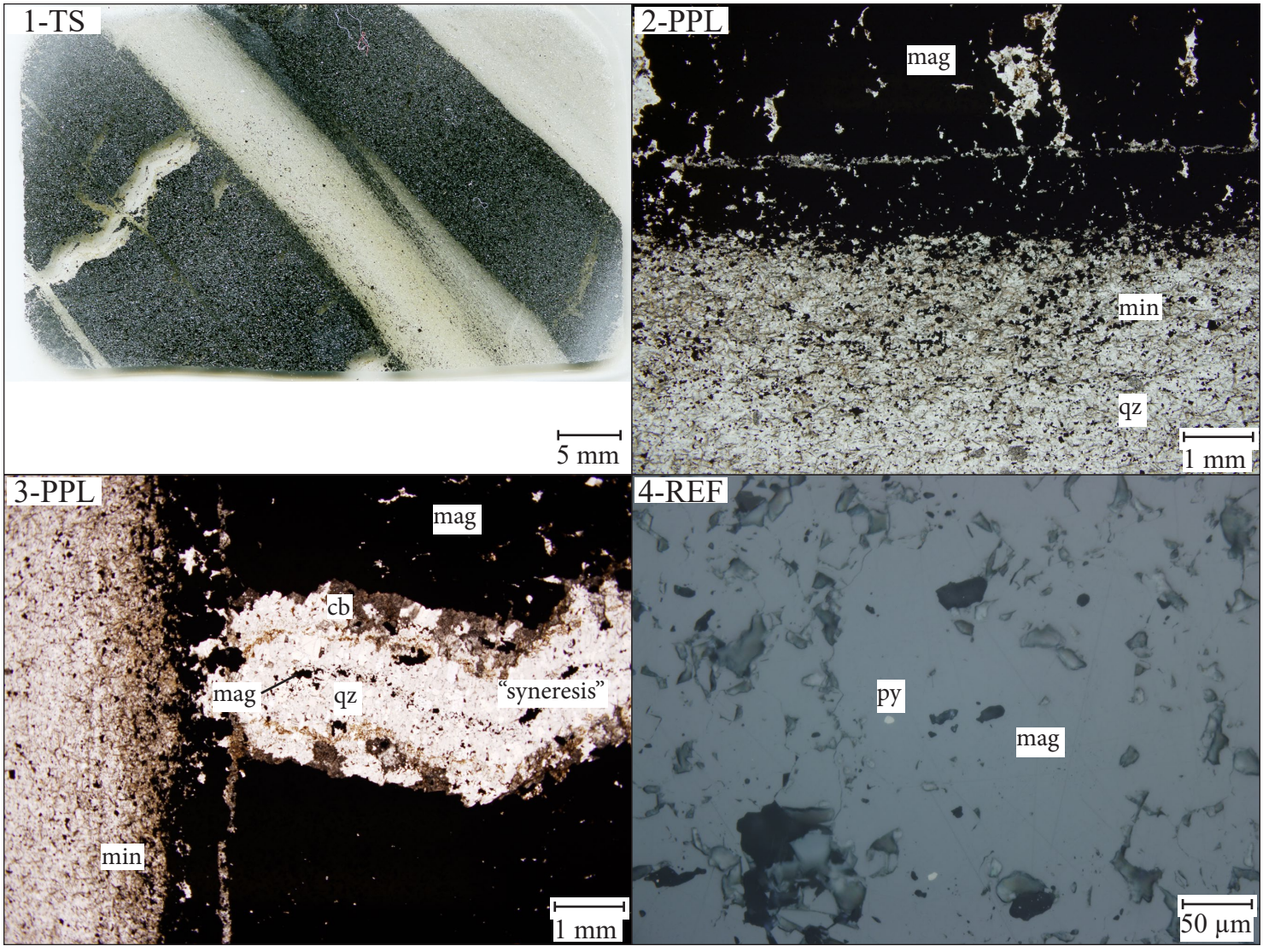
D001

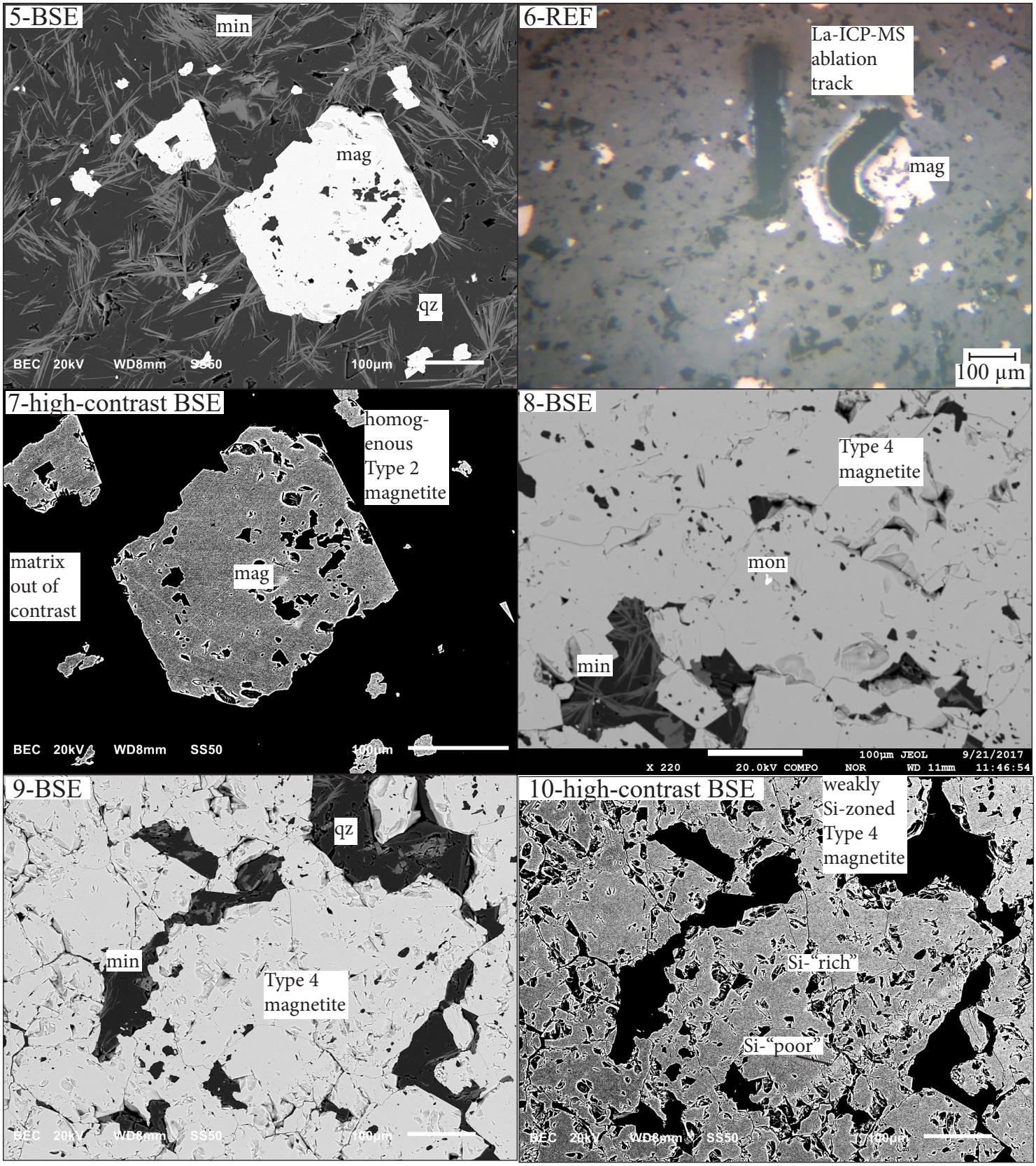
Sample: D015

Sample Type: magnetite
Location: 47.05252 -79.85352
BIF Member: South BIF

SiO_2 [wt.%]	Al_2O_3 [wt.%]	Fe_2O_3 [wt.%]	Ge [ppm]	Pb [ppm]	As [ppm]	Ni [ppm]	B [ppm]	ΣREE [ppm]
12.0	0.10	87.4	8.5	0.8	0.6	2.4	0.1	12.3

Petrography: D015 is a massive magnetite sample, with magnetite layers comprising >90% intergrown Type 4 magnetite. Magnetite layers are >2 cm thick and interlayered with black chert. Rare interstitial spaces in massive magnetite are filled with quartz and ultrafine trace minerals (hematite, apatite, minnesotaite, chlorite?). Type 4 magnetite shows some internal zonation and has abundant inclusions of quartz and rare pyrite. The structure of magnetite are Type 3 magnetite intergrown or overgrown to form massive layers. mm-wide layer-vertical cracks in magnetite resemble syneresis cracks, but are capped by a thin layer of magnetite on the interface of magnetite and chert. Cracks are filled with quartz, carbonate, and minnesotaite. Quartz is aligned and elongated vertical to the long axis of the cracks. Magnetite is interlayered with black chert comprising quartz, Type 1 and 2 magnetite, and minnesotaite. Some poorly developed microbanding is present in black chert.




5-BSE
min
mag
qz
BEC 20kV WD8mm SS50 100µm
6-REF
La-ICP-MS ablation track
mag
100 µm
7-high-contrast BSE
homog-enous Type 2 magnetite
matrix out of contrast
mag
BEC 20kV WD8mm SS50
8-BSE
Type 4 magnetite
mon
min
100µm JEOL 9/21/2017
X 220 20.0kV COMPO NOR WD 11mm 11:46:54
9-BSE
qz
min
Type 4 magnetite
10-high-contrast BSE
weakly Si-zoned Type 4 magnetite
Si-"rich"
Si-"poor"

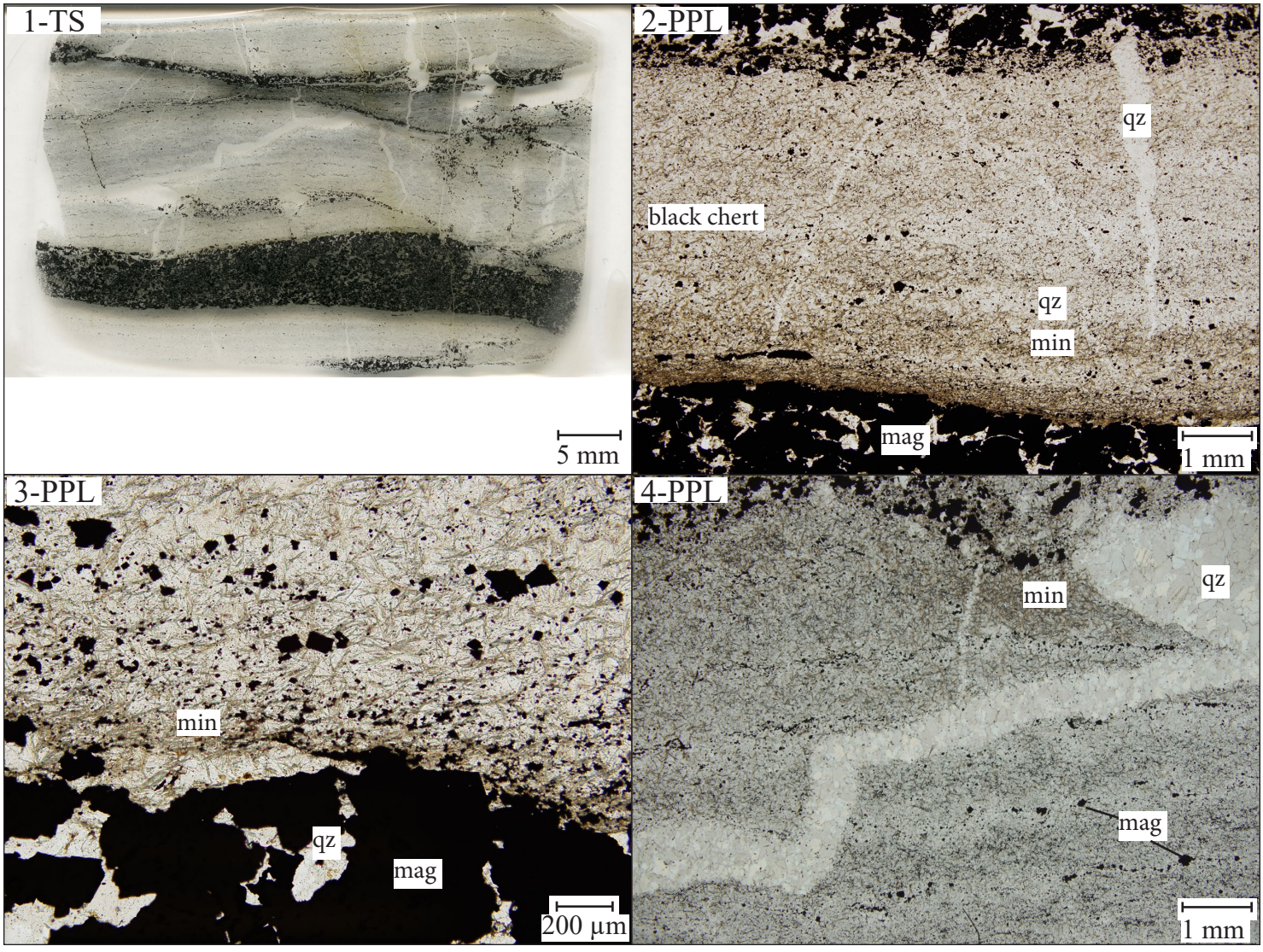
Sample: D020

Sample Type: chert
Location: 47.05252 -79.85201
BIF Member: South BIF

SiO_2 [wt.%]	Al_2O_3 [wt.%]	Fe_2O_3 [wt.%]	Ge [ppm]	Pb [ppm]	As [ppm]	Ni [ppm]	B [ppm]	ΣREE [ppm]
48.7	0.15	44.6	7.8	2.6	10	24.6	2.6	8.1

Context: Chert sample D020-1 and magnetite sample D020-2 have been produced from the hand sample. Geochemistry shown is for the magnetite sample D020-2

Petrography: D020 consists of interlayered white chert, microbanded black chert, and magnetite. White chert contains more abundant Type 1 and Type 2 magnetite and stilpnomelane in the area of the thin section compared to the material used for whole rock geochemistry. Quartz in white chert is unusually fine grained (20 μm). Black chert is microbanded, with microbanding defined by variable abundances and grain sizes of minnesotaite and magnetite. Minnesotaite occurs preferentially in chert along the interfaces of chert and magnetite, decreasing in abundance away from magnetite layers. Magnetite in chert is mostly Type 2, and Type 3 in magnetite layers, locally growing into masses of Type 4 magnetite and the centres of black chert layers. Layering is strongly disturbed by irregular quartz veining. Large, late quartz veins are thick (>200 μm) and step across microbands, probably exploiting preexisting weaknesses in the microbanding. Smaller, earlier quartz veins are variably overgrown, deformed, show swell and pinch structures, and are usually not preserved in magnetite layers.



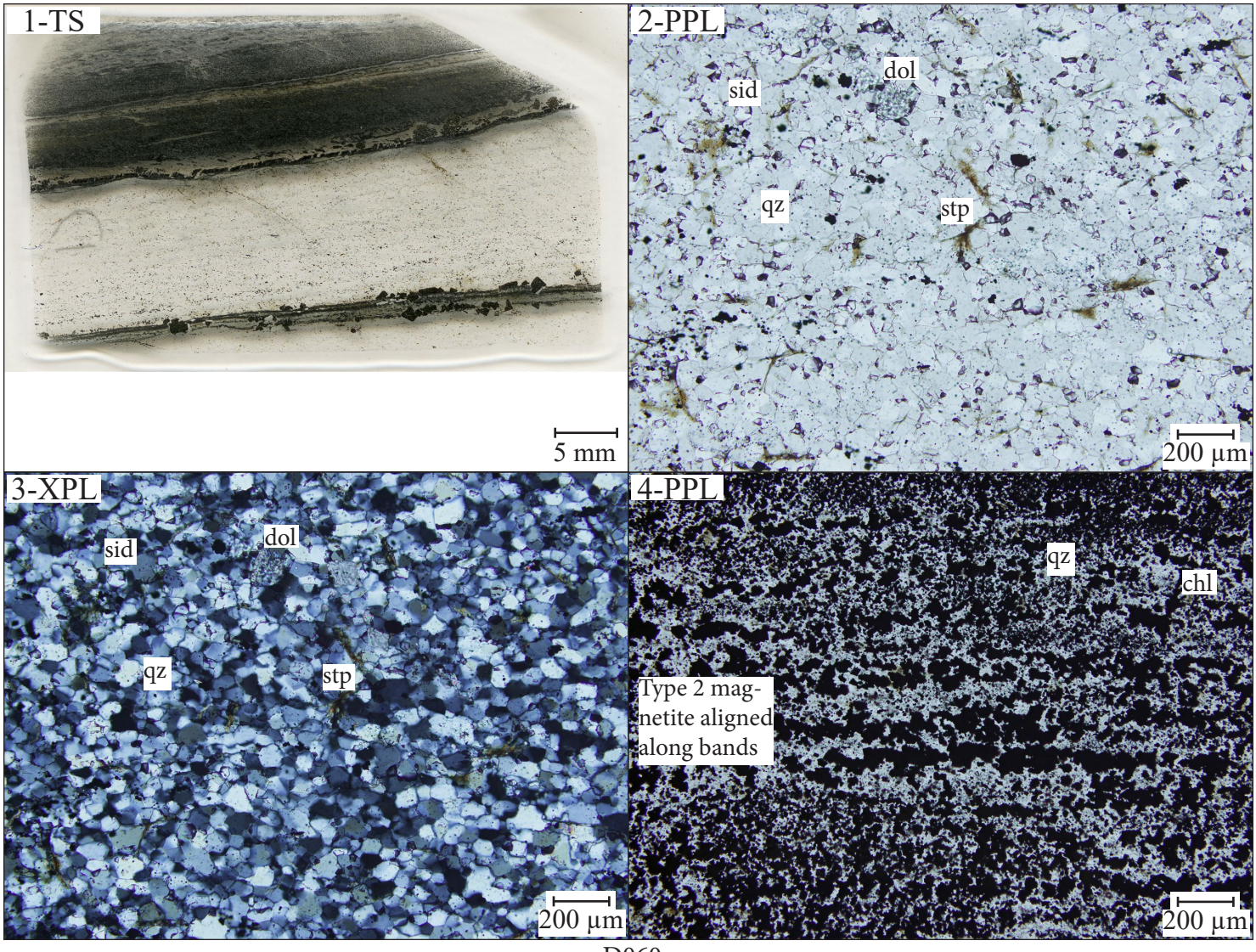
D020

Sample: D060

Sample Type:
Location: 47.05258 -79.85392
BIF Member: South BIF

SiO_2 [wt.%]	Al_2O_3 [wt.%]	Fe_2O_3 [wt.%]	Ge [ppm]	Pb [ppm]	As [ppm]	Ni [ppm]	B [ppm]	ΣREE [ppm]
n/a	n/a	n/a	n/a	n/a	n/a	n/a	n/a	n/a

Petrography: Sample D060 comprises white chert, black chert, and magnetite. White chert consits of large (>100 µm) quartz with Type 1 and 2 magnetite, stilpnomelane, euhedral Fe-dolomite, and blocky siderite inclusions. Black chert comprises unusually dense masses of Type 2 magnetite. Magnetite in magnetite layers are Type 3 and Type 4, specifically close to an area of layer-parallel deformation also containing large, euhedral pyrite.



D060

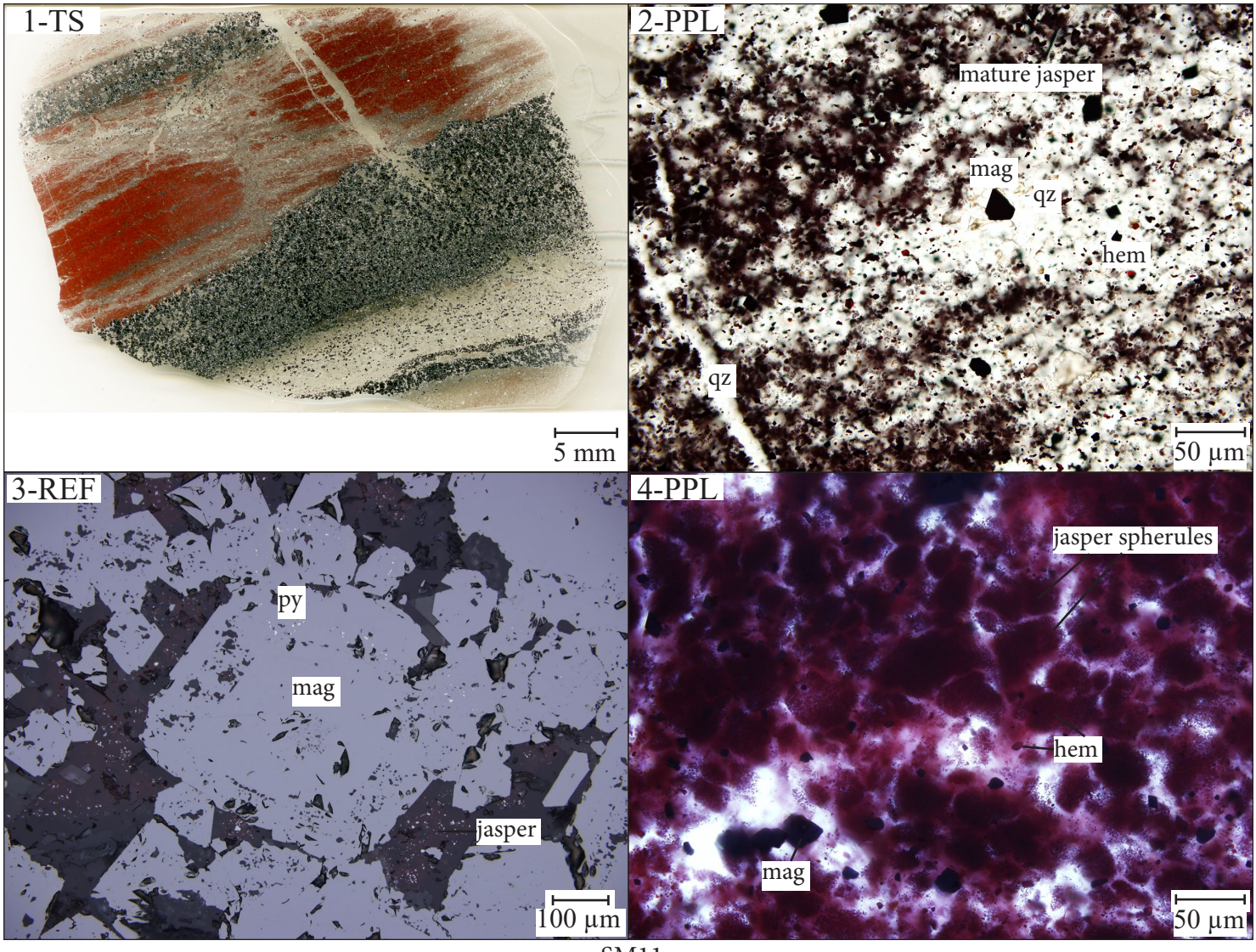
Sample: SM11

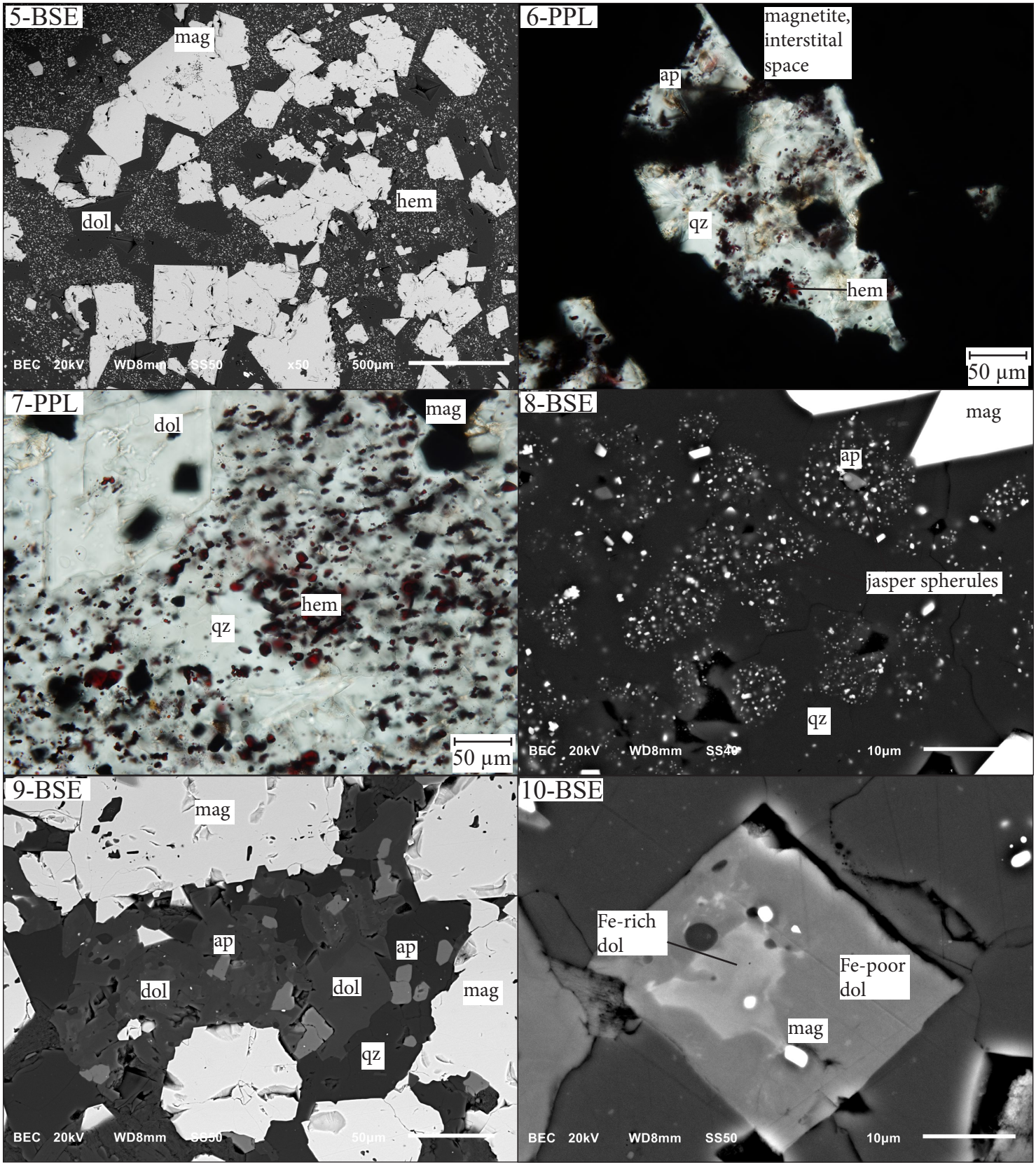
Sample Type: jasper
Location: 47.06112 -79.87574
BIF Member: North BIF

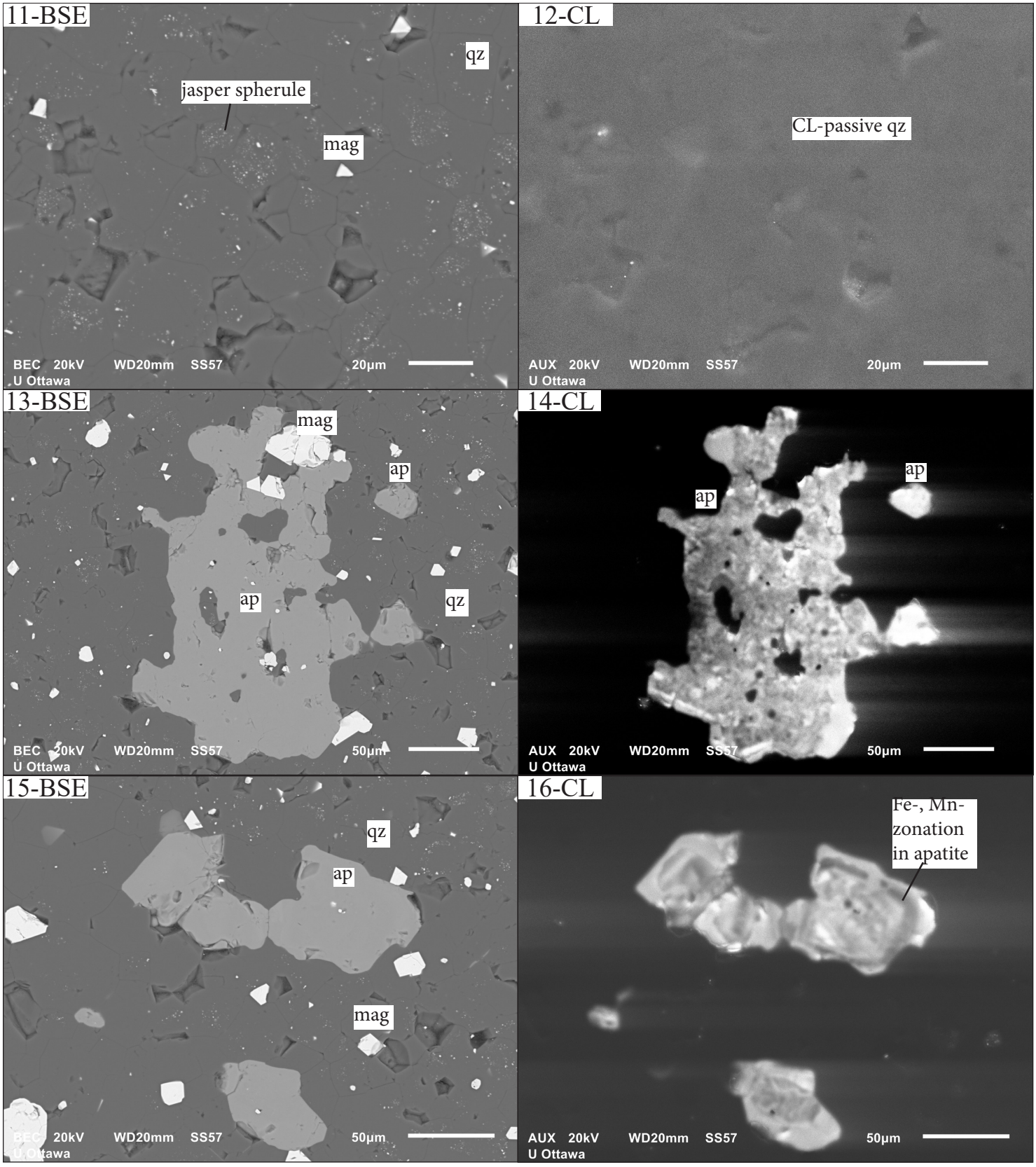
SiO_2 [wt.%]	Al_2O_3 [wt.%]	Fe_2O_3 [wt.%]	Ge [ppm]	Pb [ppm]	As [ppm]	Ni [ppm]	B [ppm]	ΣREE [ppm]
66.0	0.14	29.5	6.4	1.1	1.2	8.6	46.1	12.0

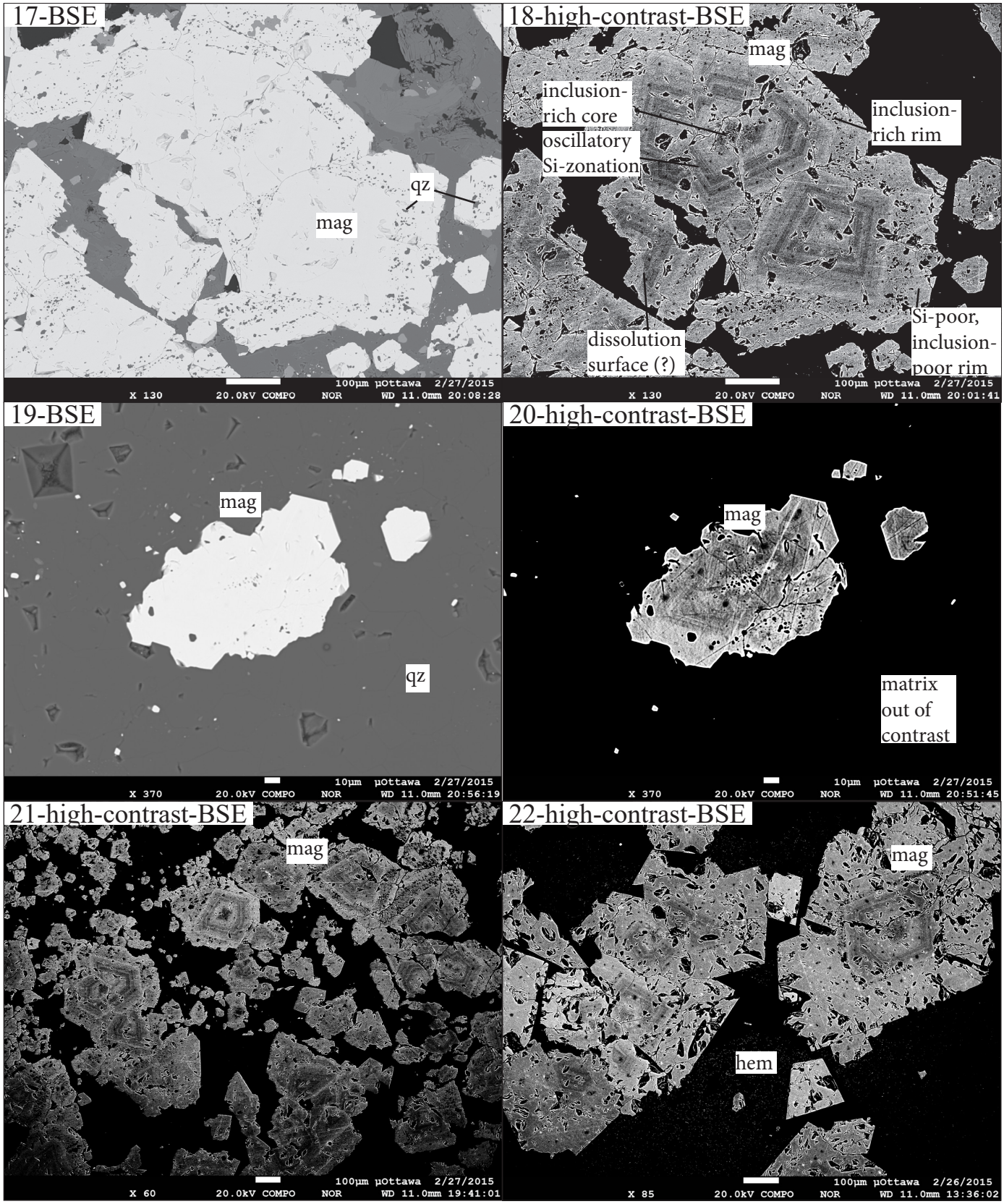
Context:

Petrography: SM11 consists of interlayered microbanded jasper, black chert and magnetite. Jasper is organge-red and shows transitions from less to more mature jasper. Less mature jasper has ultrafine Type 1 hematite inclusions in quartz, with clear quartz along crystal interfaces and Type 2 magnetite and hematite growing on quartz interstices. Mature jasper contains Type 2 hematite, elongated prismatic translucent red hematite (20 µm), lending a darker red appearance to jasper. In black chert in SM11, all Type 1 hematite is recrystallized as Type 2 hematite and Type 2 magnetite. Microbanding in black chert is defined by magnetite and hematite crystal size. Magnetite layers consist of Type 3 magnetite in a quartz matrix, with Fe-carbonates, chlorite, stilpnomelane, and apatite as accessory phases. Larger Type 3 magnetite crystals show well-developed zonation, with quartz inclusions abundant in specific rims and trace pyrite inclusions. Eraly quartz veins exhibit offsest and brecciation in jasper, but are overgrown in magnetite layers. Later quartz veins are well-preserved in jasper but overgrown in magnetite.




5-BSE
mag
hem
dol
BEC 20kV WD8mm SS50 x50 500µm
6-PPL
magnetite, interstital space
ap
qz
hem
50 µm
7-PPL
dol
mag
hem
qz
50 µm
8-BSE
mag
ap
jasper spherules
qz
BEC 20kV WD8mm SS40 10µm
9-BSE
mag
ap
ap
dol
dol
mag
qz
BEC 20kV WD8mm SS50 50µm
10-BSE
Fe-rich dol
Fe-poor dol
mag
BEC 20kV WD8mm SS50 10µm


11-BSE
qz
jasper spherule
mag
BEC 20kV WD20mm SS57 20µm
U Ottawa
12-CL
CL-passive qz
AUX 20kV WD20mm SS57 20µm
U Ottawa
13-BSE
mag
ap
ap
qz
BEC 20kV WD20mm SS57 50µm
U Ottawa
14-CL
ap
ap
AUX 20kV WD20mm SS57 50µm
U Ottawa
15-BSE
qz
ap
mag
BEC 20kV WD20mm SS57 50µm
U Ottawa
16-CL
Fe-, Mn-zonation in apatite
AUX 20kV WD20mm SS57 50µm
U Ottawa

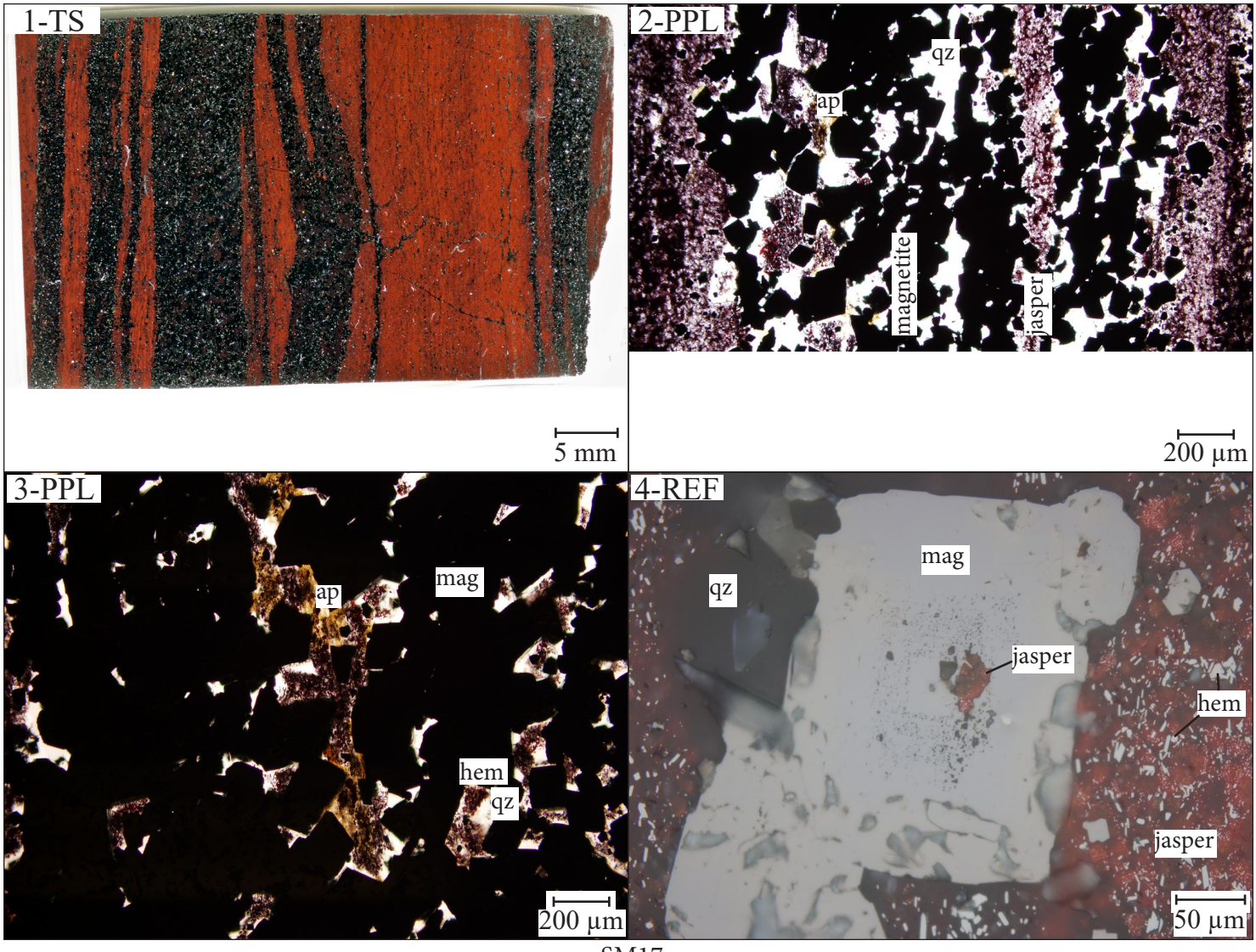

17-BSE
qz
mag
100µm µOttawa 2/27/2015
X 130 20.0kV COMPO NOR WD 11.0mm 20:08:28
18-high-contrast-BSE
mag
inclusion-rich core
oscillatory Si-zonation
inclusion-rich rim
Si-poor, inclusion-poor rim
dissolution surface (?)
100µm µOttawa 2/27/2015
X 130 20.0kV COMPO NOR WD 11.0mm 20:01:41
19-BSE
mag
qz
10µm µOttawa 2/27/2015
X 370 20.0kV COMPO NOR WD 11.0mm 20:56:19
20-high-contrast-BSE
mag
matrix out of contrast
10µm µOttawa 2/27/2015
X 370 20.0kV COMPO NOR WD 11.0mm 20:51:45
21-high-contrast-BSE
mag
100µm µOttawa 2/27/2015
X 60 20.0kV COMPO NOR WD 11.0mm 19:41:01
22-high-contrast-BSE
mag
hem
100µm µOttawa 2/26/2015
X 85 20.0kV COMPO NOR WD 11.0mm 13:36:02

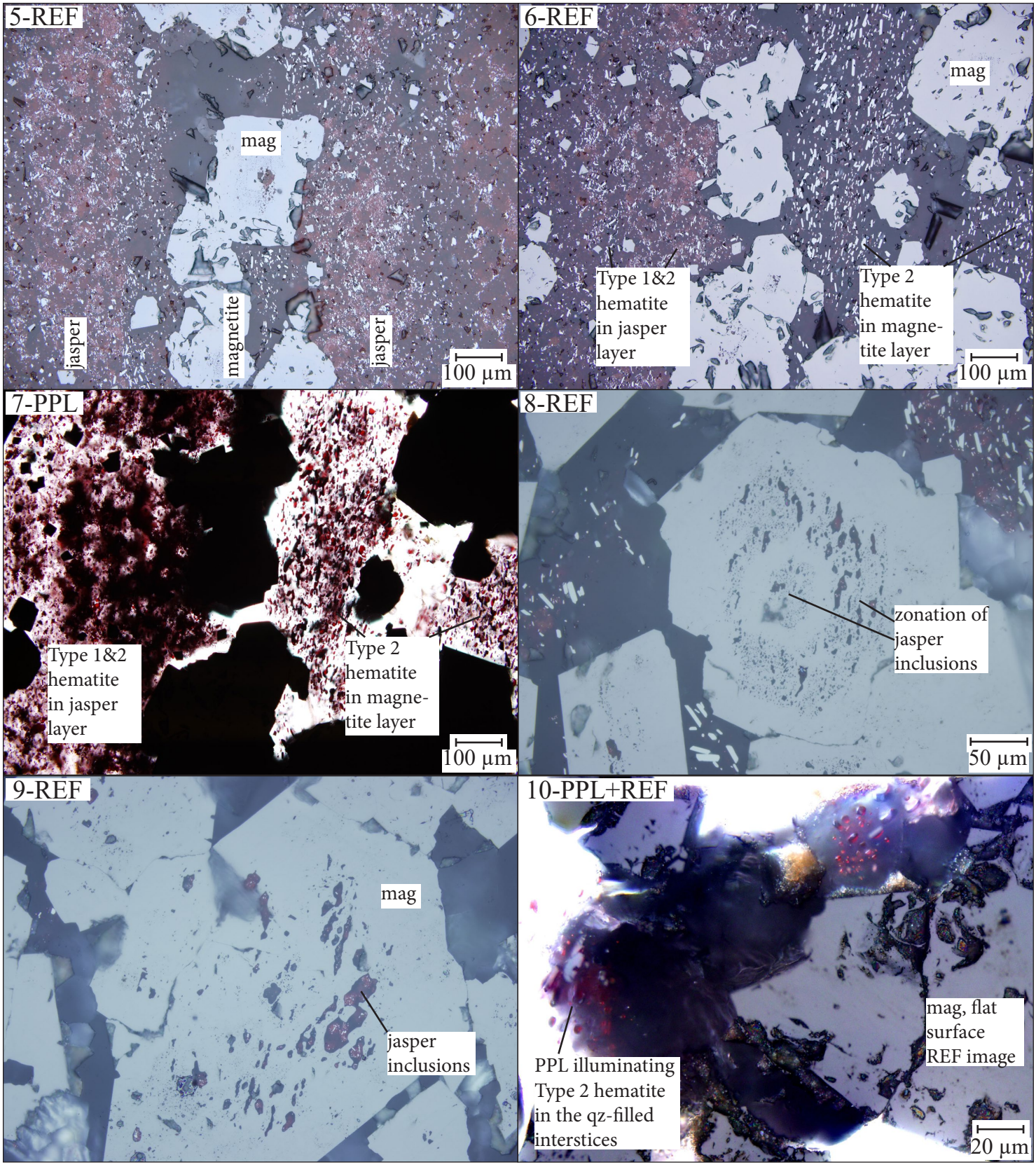
Sample: SM17

Sample Type: jasper-magnetite
Location: 47.06515 -79.89517
BIF Member: North BIF

SiO_2 [wt.%]	Al_2O_3 [wt.%]	Fe_2O_3 [wt.%]	Ge [ppm]	Pb [ppm]	As [ppm]	Ni [ppm]	B [ppm]	ΣREE [ppm]
n/a	n/a	n/a	n/a	n/a	n/a	n/a	n/a	n/a

Petrography: SM17 is a magnetite-jasper sample, with individual layers between 0.1-2 cm thick. Jasper consists of poorly microbanded material, comprising ultrafine Type 1 hematite inclusions in quartz, i.e. jasper spherules. Where more Type 2 hematite and Type 2 magnetite are present, jasper colour is darker red to grey, e.g. in the dark microbands. Magnetite layers comprise Type 3 magnetite, in a cherty matrix with Fe-dolomite, hematite, and apatite in the interstices. Elongated lenses of jasper are present in the hematite layers, and jasper fragments are present as inclusions at the core of Type 3 magnetite. Few early quartz veins are present in the jasper layers. The veins show µm-scale offset along the planes of jasper microbands.




5-REF
mag
jasper
magnetite
jasper
100 µm
6-REF
mag
Type 1&2 hematite in jasper layer
Type 2 hematite in magne-tite layer
100 µm
7-PPL
Type 1&2 hematite in jasper layer
Type 2 hematite in magne-tite layer
100 µm
8-REF
zonation of jasper inclusions
50 µm
9-REF
mag
jasper inclusions
10-PPL+REF
PPL illuminating Type 2 hematite in the qz-filled interstices
mag, flat surface REF image
20 µm

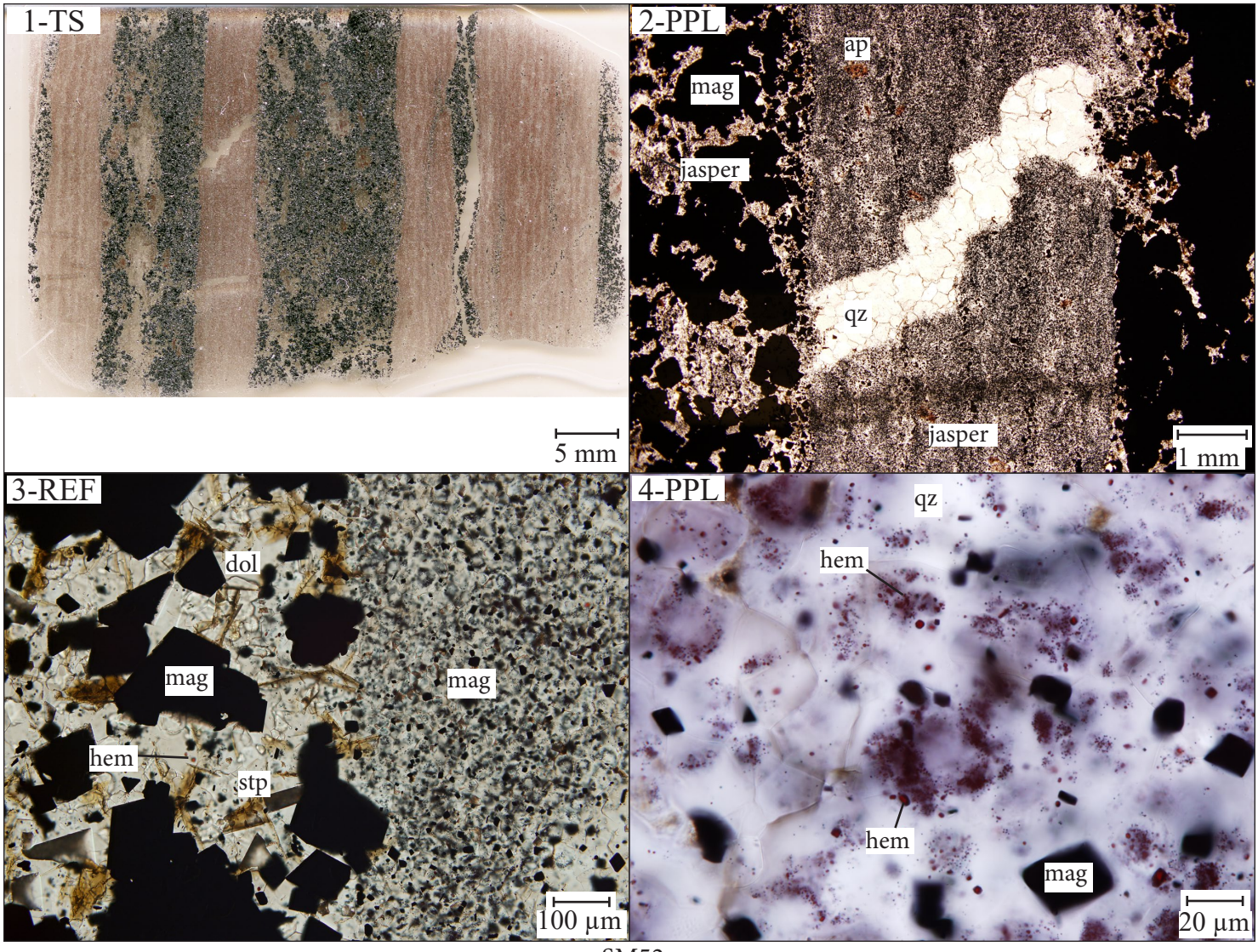
Sample: SM52

Sample Type: jasper-magnetite
Location: 47.06585 -79.87572
BIF Member: North BIF

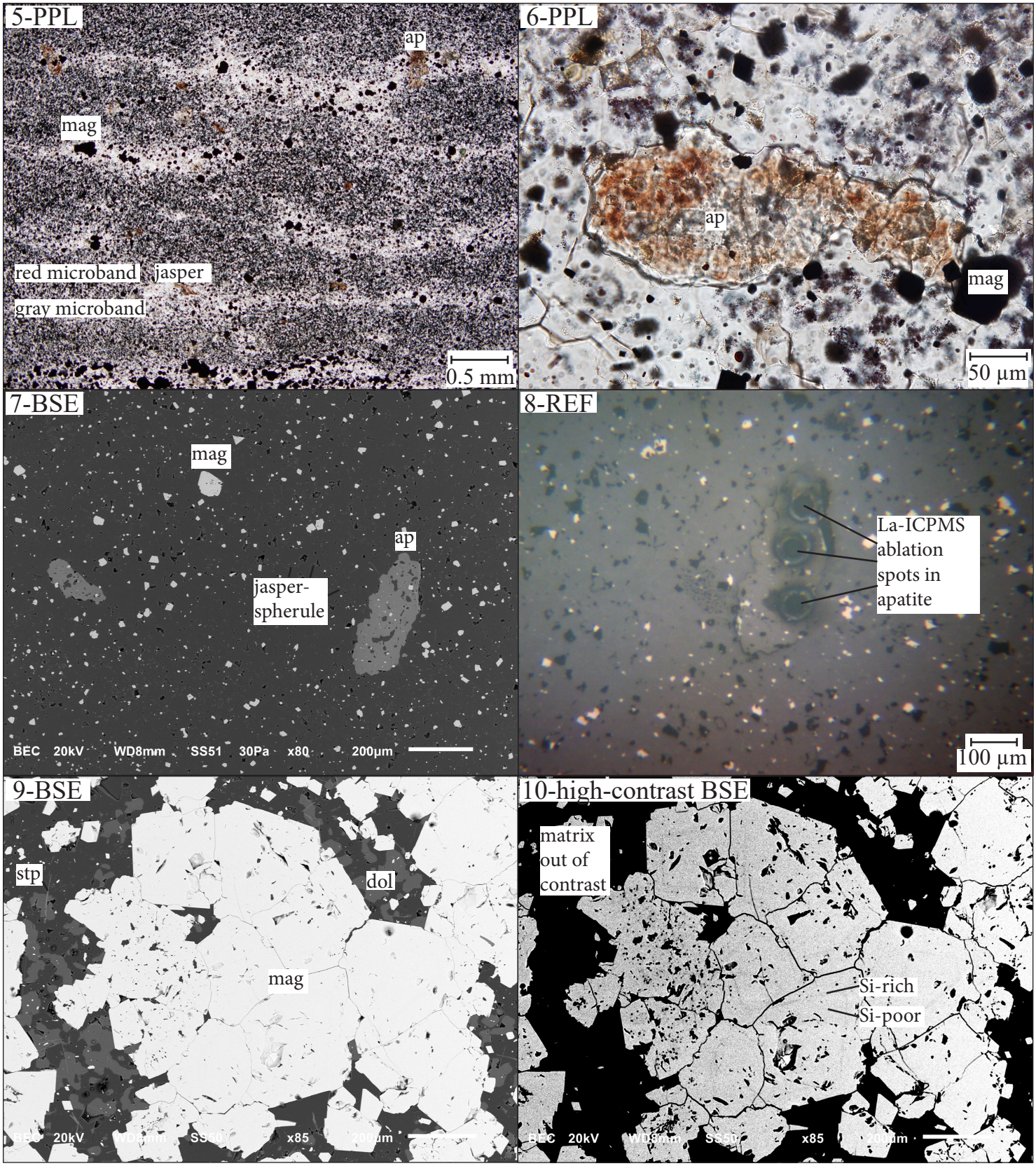
SiO_2 [wt.%]	Al_2O_3 [wt.%]	Fe_2O_3 [wt.%]	Ge [ppm]	Pb [ppm]	As [ppm]	Ni [ppm]	B [ppm]	ΣREE [ppm]
88.9	0.13	9.8	4.6	1.0	1.9	24.5	59.6	6.2

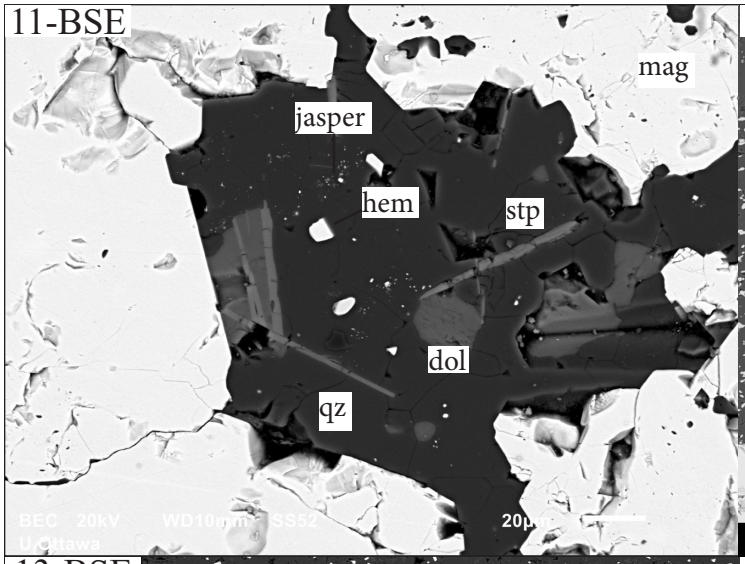
Context: Sample SM52 was collected from a boulder on the rim of the North Pit in the Sherman Mine. Magnetite samples SM52-1, -5, and -6, as well as jasper samples SM52-2, and -4 were produced from layers in the same hand sample. Geochemistry of SM52-2 (jasper) is shown.

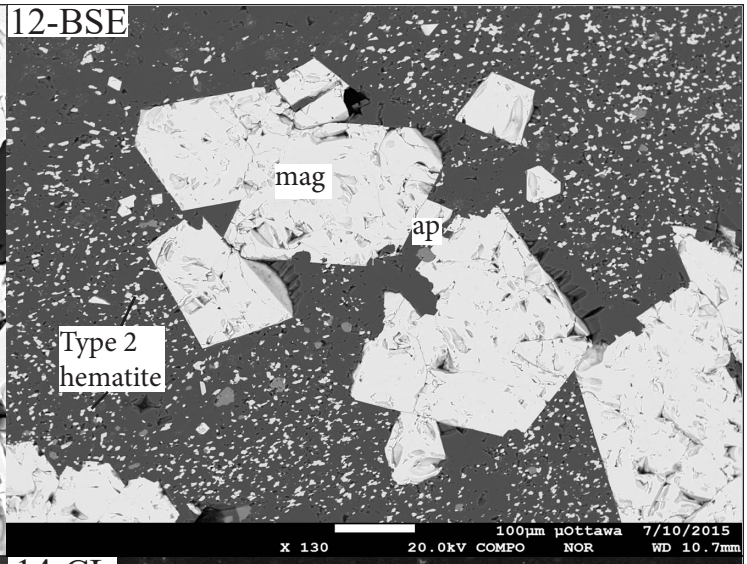
Petrography: SM52 is a jasper-magnetite sample, with layers between 0.5-2 cm thick. Jasper consists of ultrafine hematite inclusions in 20-50 µm quartz, forming "spherules". Within individual spherules, quartz is typically free of inclusions closer to the crystal borders. Type 2 magnetite and Type 2 hematite form preferentially on the interstices of quartz grains. Microbanding in jasper is defined by magnetite crystal size and loss of hematite inclusions in quartz. Accessory apatite forms large (>100 µm) subhedral to anhedral masses. Trace blocky siderite and chlorite occur in jasper. Magnetite layers consist of large Type 3 magnetite with abundant quartz inclusions and weak Si-zonation. Interstitial spaces are filled with quartz, apatite, stilpnomelane and rare chlorite. Elongated, rounded fragments of jasper (~1 mm) are common in magnetite layers. Quartz veins are common in jasper and show brittle offset along the planes of microbands. Quartz veins are overgrown in magnetite layers.

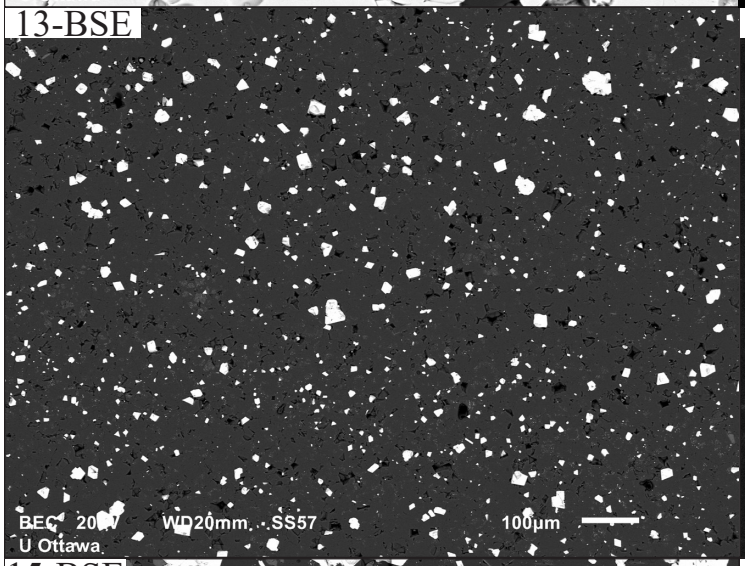


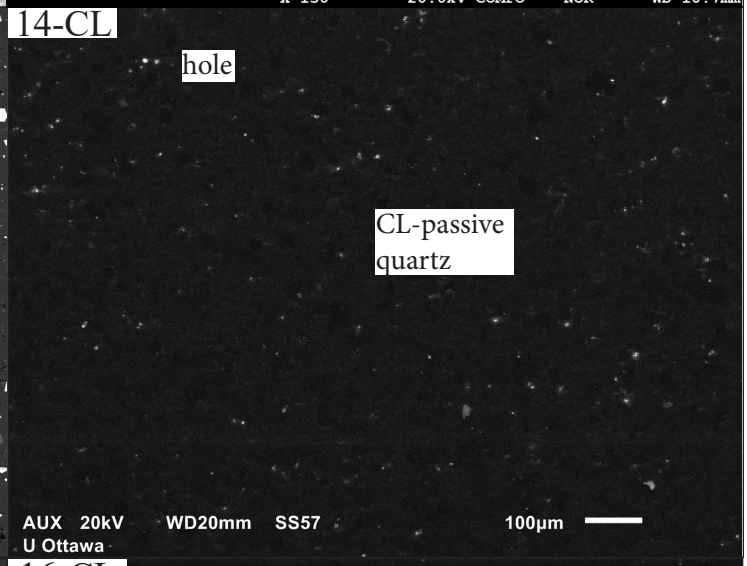
SM52

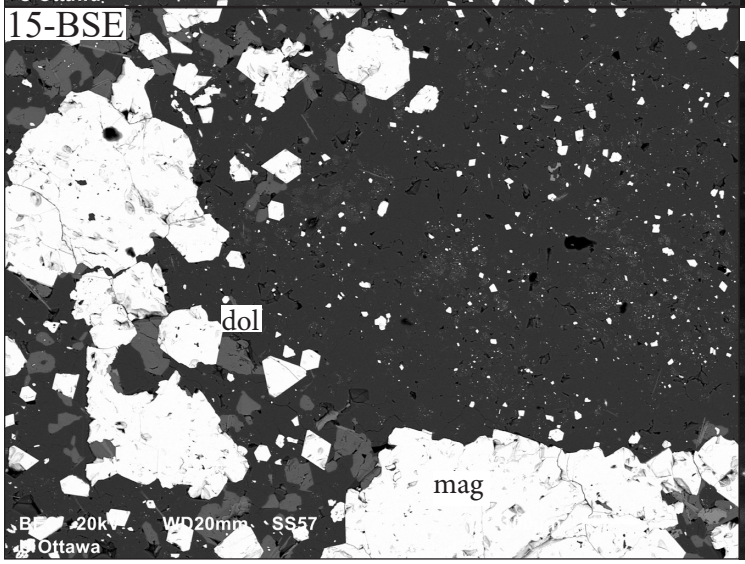

5-PPL
ap
mag
red microband
jasper
gray microband
0.5 mm
6-PPL
ap
mag
50 µm
7-BSE
mag
ap
jasper-
spherule
BEC 20kV WD8mm SS51 30Pa x80 200µm
8-REF
La-ICPMS
ablation
spots in
apatite
100 µm
9-BSE
stp
dol
mag
BEC 20kV WD8mm SS50 x85 200µm
10-high-contrast BSE
matrix
out of
contrast
Si-rich
Si-poor
BEC 20kV WD8mm SS50 x85 200µm

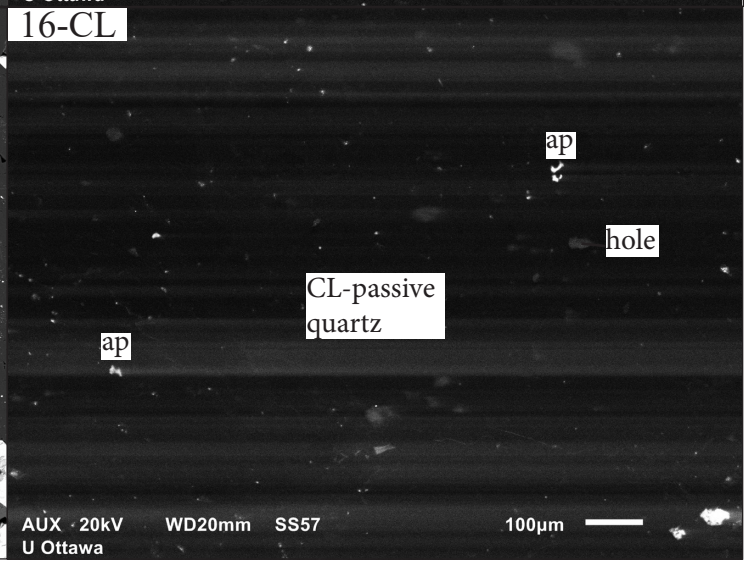

11-BSE
mag
jasper
hem
stp
dol
qz
BEC 20kV WD10mm SS52
U Ottawa
20µm


12-BSE
mag
ap
Type 2
hematite
100µm µOttawa 7/10/2015
X 130 20.0kV COMPO NOR WD 10.7mm


13-BSE
BEC 20kV WD20mm SS57 100µm
U Ottawa


14-CL
hole
CL-passive
quartz
AUX 20kV WD20mm SS57 100µm
U Ottawa


15-BSE
dol
mag
BEC 20kV WD20mm SS57
U Ottawa

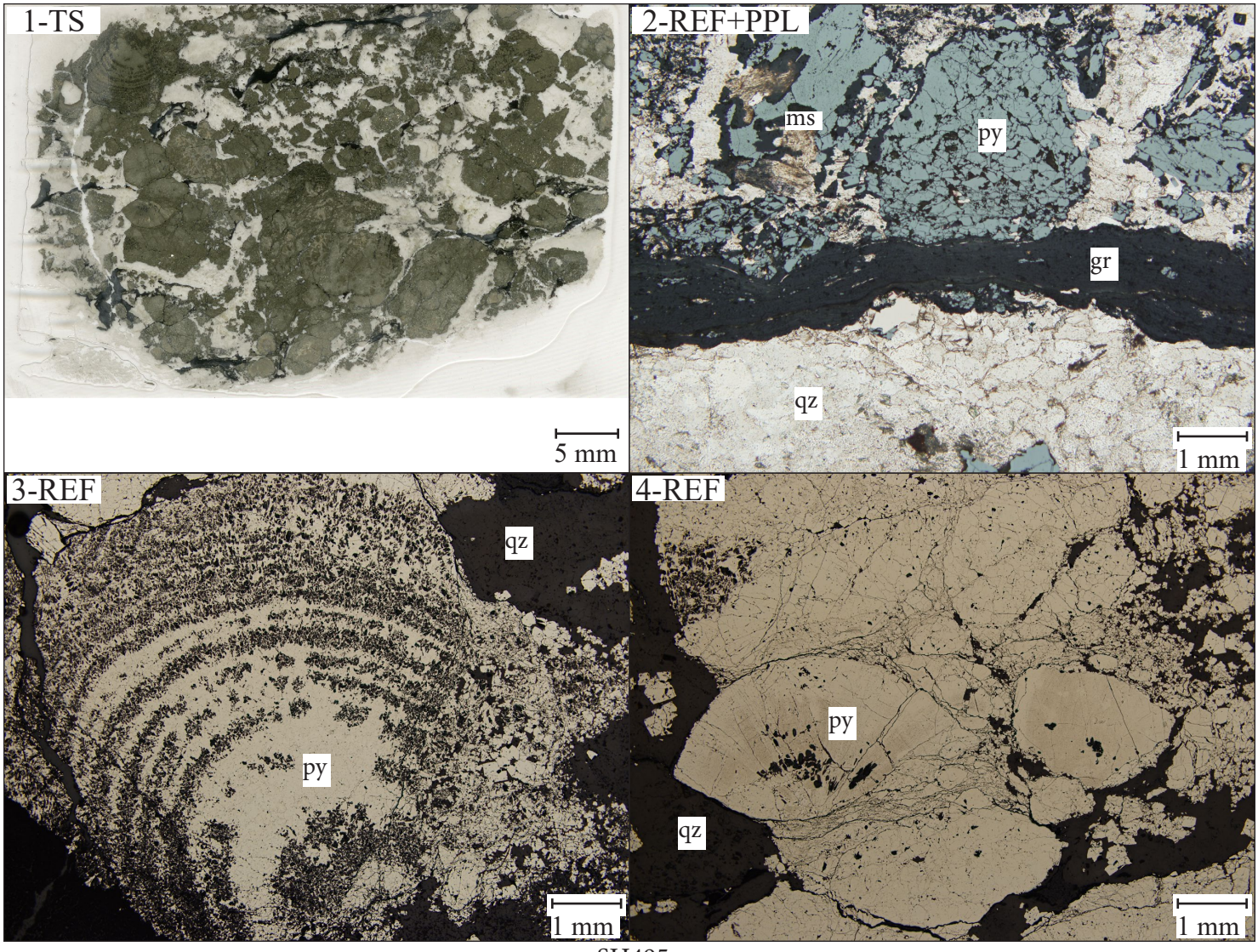

16-CL
ap
hole
CL-passive
quartz
ap
AUX 20kV WD20mm SS57 100µm
U Ottawa

Sample: SH495

Sample Type: sulfidic chert
Location: 47.04689 -79.80598
BIF Member: South BIF (hanging wall)

SiO_2 [wt.%]	Al_2O_3 [wt.%]	Fe_2O_3 [wt.%]	Ge [ppm]	Pb [ppm]	As [ppm]	Ni [ppm]	B [ppm]	ΣREE [ppm]
32.5	1.65	40.2	0.3	133	334	120.0	2.8	33.8

Context: Sample from the west end of the South BIF, ~170 m from the centre of the South BIF in the South Pit.
Petrography: SH495 is a sulfidic chert sample, comprising large pyrite and graphitic material in a chert matrix. Pyrite forms large masses, and occurs in diverse habits: large (>500 µm) euhedral crystals, radial habits, concentric, and skeletal growths, as well as finely dispersed pyrite intergrown with the graphitic material. Pyrite is the exclusive sulfide found in SH495, and comprises >75 vol.% of the sample. The cherty matrix consists of large quartz (>50 µm), graphitic material, Fe-carbonate, chorite, and muscovite.



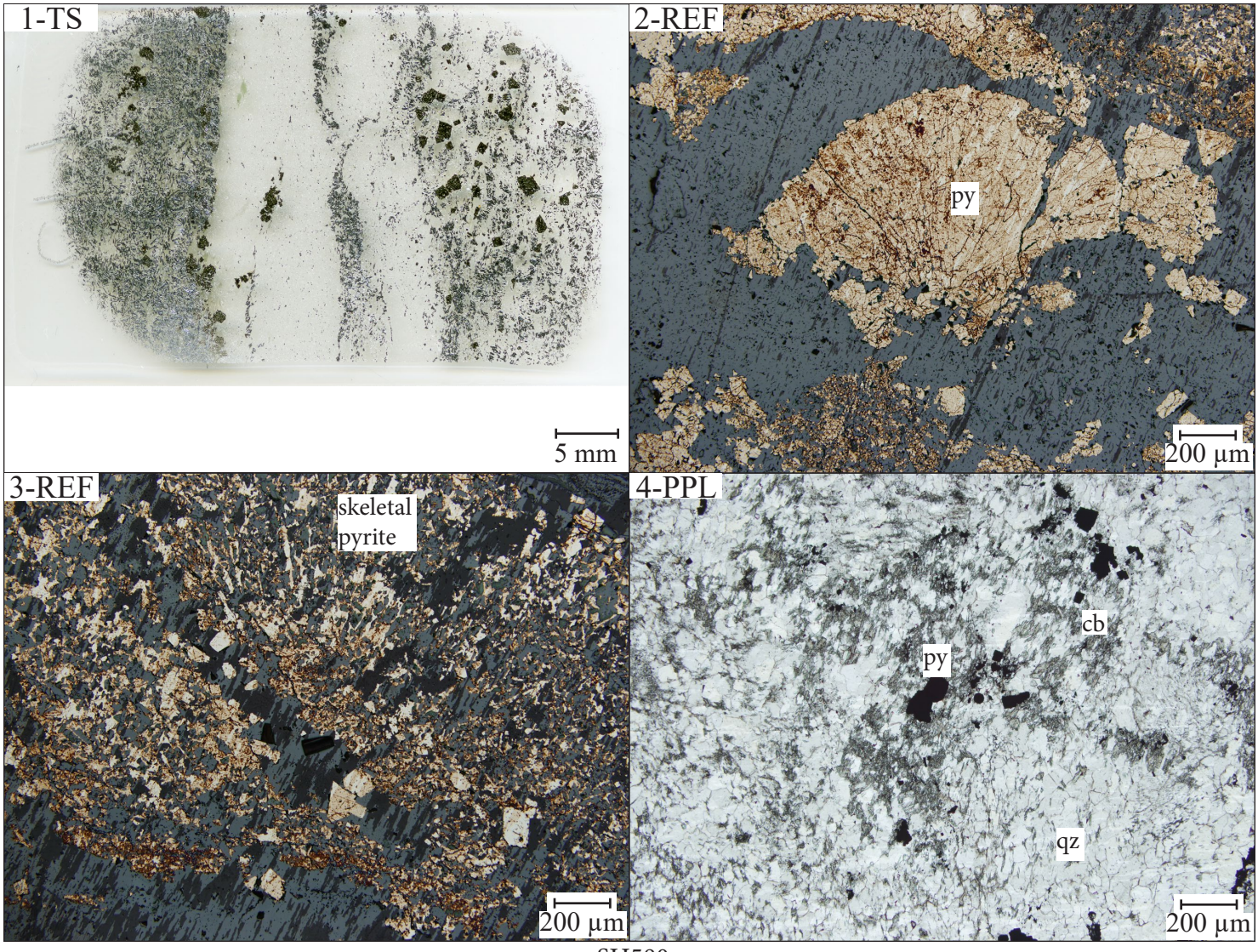
SH495

Sample: SH580

Sample Type: sulfidic chert
Location: 47.04853 -79.80598
BIF Member: South BIF (hanging wall)

SiO_2 [wt.%]	Al_2O_3 [wt.%]	Fe_2O_3 [wt.%]	Ge [ppm]	Pb [ppm]	As [ppm]	Ni [ppm]	B [ppm]	ΣREE [ppm]
20.8	1.05	48.3	0.3	167	363	96.7	2.8	33.2

Context: Sample from the west end of the South BIF, ~200 m from the centre of the South BIF in the South Pit.
Petrography: SH580 is a sulfidic chert sample, consisting of pyrite in a variably fine grained quartz matrix with graphitic material, Fe-carbonates, and muscovite. Pyrite occurs as large euhedral crystals, radial- and skeletal growths, irregular masses encroaching on graphitic material, and as small (10 µm) euhedral crystals in graphitic material. Quartz in the matrix occurs in variable sizes and habits, from fine-grained and inclusion-rich zones resembling quartz in black chert (<50 µm) to neigbouring zones of large (>100 µm) inclusion-free quartz, and elongated quartz forming in pressure shadows of pyrite.

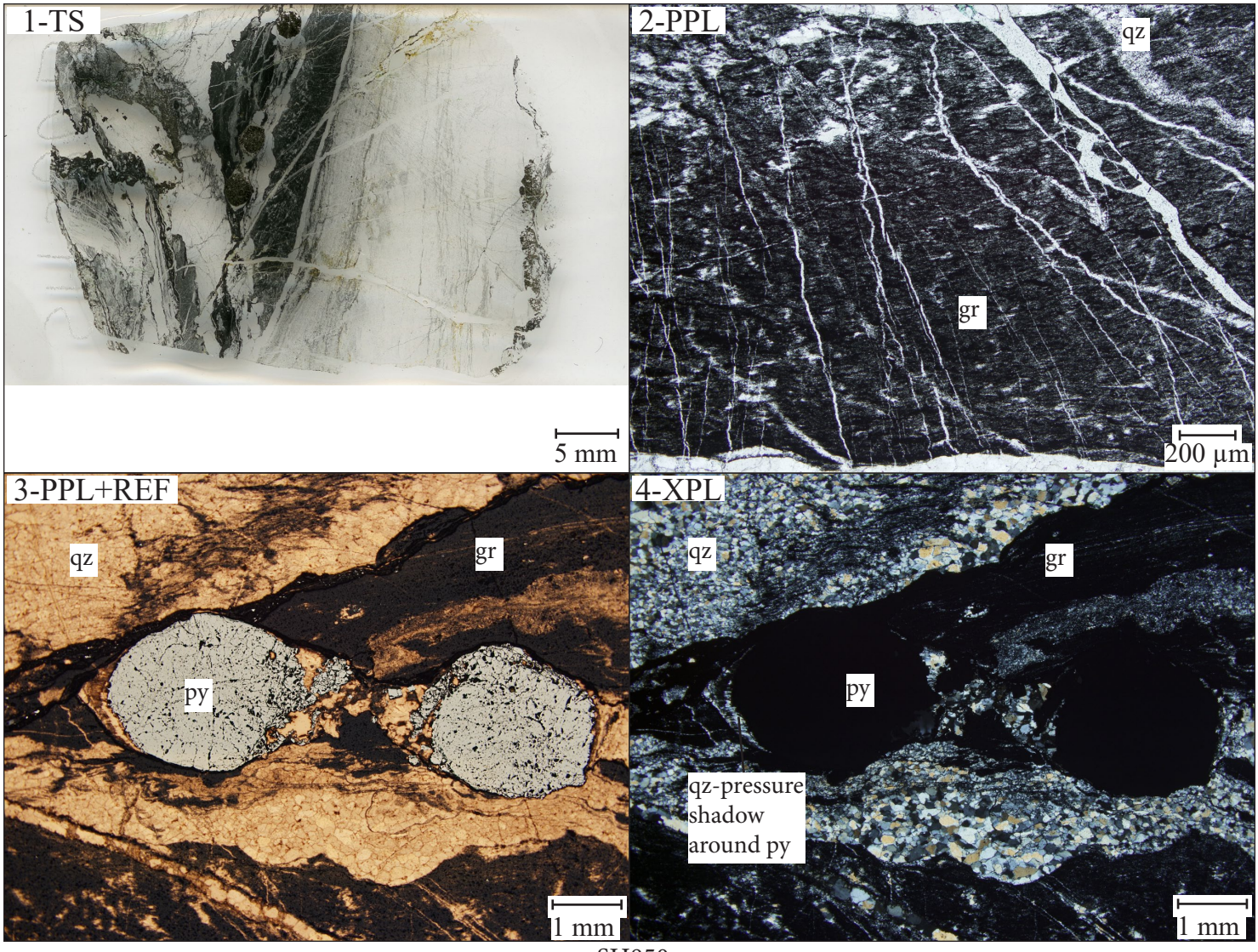


Sample: SH850

Sample Type: sulfidic chert
Location: 47.05153 -79.80598
BIF Member: South BIF (hanging wall)

SiO_2 [wt.%]	Al_2O_3 [wt.%]	Fe_2O_3 [wt.%]	Ge [ppm]	Pb [ppm]	As [ppm]	Ni [ppm]	B [ppm]	ΣREE [ppm]
50.5	1.32	27.5	1.1	34	173	48.2	0.7	13.3

Context: Sample from the west end of the South BIF, ~300 m from the centre of the South BIF in the South Pit.
Petrography: SH850 is a sulfidic chert sample. Pyrite is the exclusive sulfide phase, occuring as radial growths and finely dispersed in graphitic material. Pyrite is less abundant than in other sulfidic chert samples. Graphitic material is more abundant than in other sulfidic chert samples, and displays intense quartz veining of variable thicknesses, degrees of overgrowth, deformation and mineral content. Graphitic material occurs as opaque masses, but ultrafine, possibly crystalline structures can be identified at high magnification where the material is less dense in quartz matrix. Different generations of quartz veins can be deduced, similar to quartz veins preserved in black chert. Quartz in chert is coarse grained (100 µm), but also occurs elongated in pressure shadows around radial pyrite.



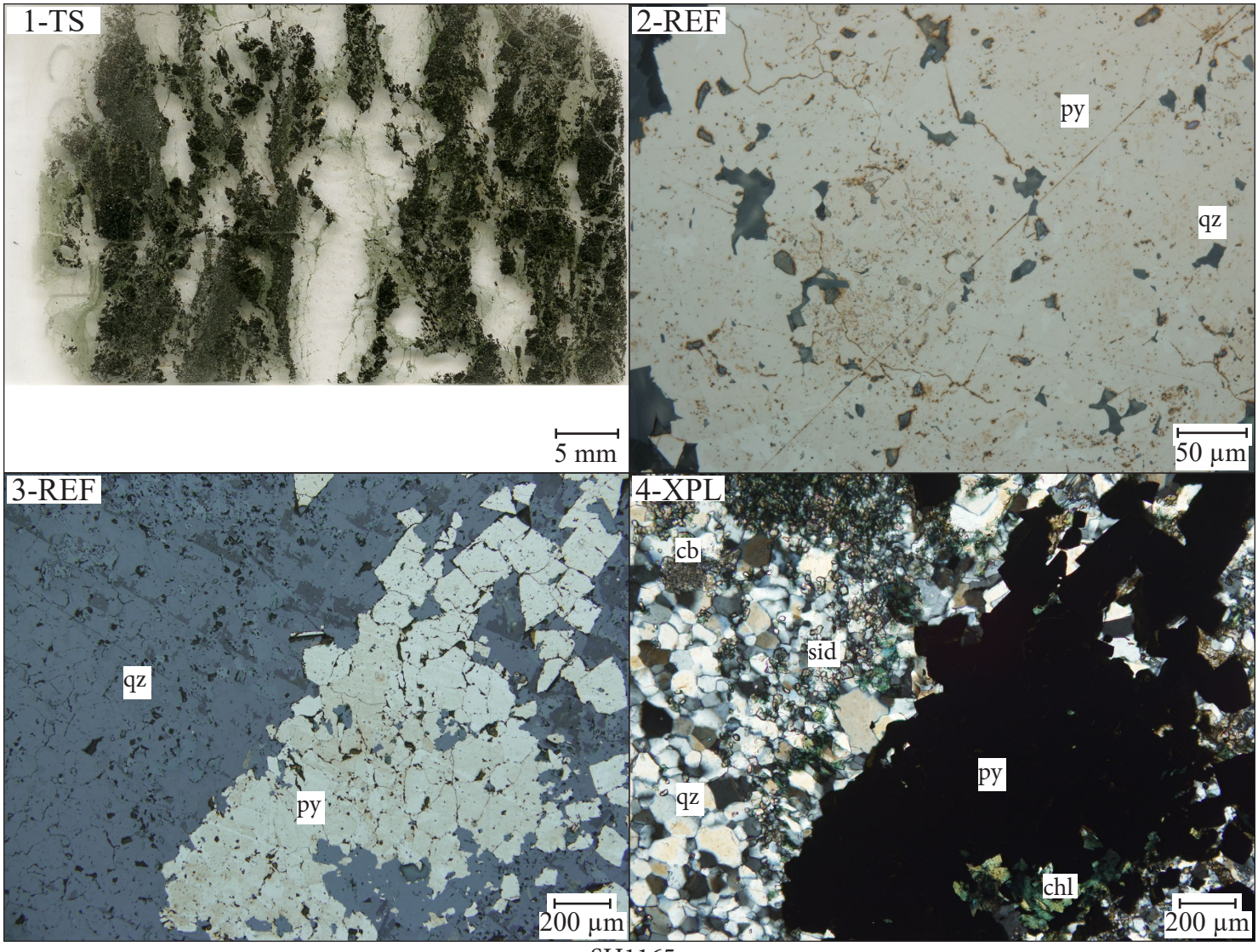
SH850

Sample: SH1165

Sample Type: sulfidic chert
Location: 47.05153 -79.80598
BIF Member: South BIF (hanging wall)

SiO_2 [wt.%]	Al_2O_3 [wt.%]	Fe_2O_3 [wt.%]	Ge [ppm]	Pb [ppm]	As [ppm]	Ni [ppm]	B [ppm]	ΣREE [ppm]
30.5	1.55	43.4	1.5	35	209	46.1	3.8	12.2

Context: Sample from the west end of the South BIF, ~400 m from the centre of the South BIF in the South Pit.
Petrography: SH1165 is a sulfidic chert sample. Pyrite occurs in a chert matrix with accessory siderite, Fe-dolomite, muscovite, chlorite, and apatite. Pyrite habits are less variable compared to other sulfidic chert samples, mainly as irregular masses and densely dispersed individual, small subhedral grains. Large pyrite crystals can contain quartz inclusions. Chlorite, siderite and Fe-dolomite are much more abundant compared to other sulfidic chert samples. Graphitic material has not been detected.



SH1165

Appendix B: All EPMA analyses of magnetite (all values in wt.-%)

		SiO_2	TiO_2	Al_2O_3	Cr_2O_3	V_2O_3	Fe_2O_3	FeO	MnO	MgO	CaO	ZnO	NiO	Total	
	dl	0.01	0.03	0.08	0.01	0.01	0.02	0.02	0.01	0.01	0.01	0.01	0.01		
Sample	**Host**														**Comment**
A027	chert	0.93	0.07	bdl	bdl	0.04	66.5	32.1	bdl	0.06	0.02	0.05	bdl	99.7	A027 SOI1 mag1
A027	chert	1.30	0.08	bdl	0.03	0.06	65.9	32.6	0.03	0.14	bdl	0.10	bdl	100.3	A027 SOI1 mag2
A028	chert	0.58	0.08	0.18	bdl	0.05	67.8	32.0	bdl	0.10	bdl	bdl	0.01	100.8	A028 mag/hem possibly after py
A028	chert	1.55	bdl	bdl	bdl	0.02	66.0	32.8	0.05	0.29	0.03	bdl	bdl	100.7	A028 mag/hem 2 possibly after py
A028	chert	0.13	0.06	bdl	bdl	0.03	69.2	31.5	0.01	0.01	0.01	bdl	bdl	100.9	A028 mag/hem 3 possibly after py
B13-2	chert	0.64	0.04	bdl	bdl	bdl	68.2	32.3	bdl	bdl	0.02	bdl	bdl	101.3	B13-2 SOI1 lge mag 1 center
B13-2	chert	0.52	bdl	bdl	bdl	bdl	68.8	32.0	0.02	0.11	bdl	0.03	bdl	101.5	B13-2 SOI1 lge mag 1 rim
B13-2	chert	0.78	bdl	bdl	bdl	bdl	67.5	31.9	0.02	0.20	bdl	bdl	bdl	100.4	B13-2 SOI1 sm mag 1
B13-2	chert	1.03	bdl	bdl	bdl	bdl	67.2	32.5	0.02	0.11	bdl	bdl	bdl	100.8	B13-2 SOI1 sm mag 2
B13-2	chert	0.08	bdl	bdl	bdl	bdl	69.7	31.5	bdl	bdl	bdl	0.06	bdl	101.3	B13-2 SOI1 interm mag 1
B13-2	chert	0.24	bdl	bdl	bdl	0.02	69.3	31.7	bdl	0.01	bdl	bdl	bdl	101.3	B13-2 SOI2 interm mag 1
B13-2	chert	0.48	bdl	bdl	bdl	bdl	68.6	31.9	bdl	0.01	0.01	0.05	bdl	101.0	B13-2 SOI2 massive mag 1
B13-2	chert	0.25	bdl	bdl	bdl	bdl	69.7	32.0	bdl	0.02	bdl	bdl	bdl	102.0	B13-2 SOI2 massive mag 2 center
B13-2	chert	0.16	bdl	bdl	bdl	bdl	70.0	31.9	bdl	0.01	bdl	bdl	bdl	102.2	B13-2 SOI2 massive mag 2 rim
B13-2	chert	0.24	bdl	bdl	bdl	bdl	69.2	31.7	bdl	bdl	bdl	0.03	bdl	101.1	B13-2 SOI2 small mag 1
B13-2	chert	0.27	bdl	bdl	bdl	bdl	69.4	31.9	0.01	bdl	bdl	0.03	0.02	101.7	B13-2 SOI3 sml mag 1
B13-2	chert	0.21	bdl	bdl	bdl	bdl	69.5	31.8	bdl	bdl	bdl	bdl	bdl	101.4	B13-2 SOI3 sml mag 2
B13-2	chert	1.09	bdl	bdl	bdl	bdl	66.6	32.5	0.01	0.02	bdl	0.02	bdl	100.3	B13-2 SOI3 sml mag 3
C019	chert	0.14	bdl	bdl	bdl	bdl	69.7	31.5	0.09	0.04	bdl	0.11	bdl	101.6	C019 SOI1 mag 1 in mag layer
C019	chert	0.15	0.04	bdl	bdl	0.02	70.0	31.7	0.12	0.07	bdl	bdl	0.02	102.1	C019 SOI1 mag 2 in mag layer
C019	chert	0.12	bdl	bdl	bdl	bdl	70.3	31.7	0.10	0.05	bdl	bdl	bdl	102.3	C019 SOI1 mag 3 in mag layer
C019	chert	0.15	bdl	bdl	bdl	bdl	69.4	31.3	0.09	0.04	0.06	0.01	bdl	101.1	C019 SOI1 mag 4 in chert
C019	chert	0.34	bdl	bdl	bdl	bdl	68.8	31.3	0.20	0.06	0.18	0.02	bdl	100.9	C019 SOI1 mag 5 in chert
C019	chert	0.06	bdl	bdl	bdl	bdl	69.8	31.4	0.12	bdl	bdl	0.07	bdl	101.5	C019 SOI2 mag proximal to py
C019	chert	0.04	bdl	bdl	bdl	bdl	70.0	31.5	0.09	bdl	bdl	bdl	bdl	101.6	C019 SOI2 mag proximal to py
C019	chert	0.24	bdl	bdl	bdl	0.01	69.6	31.6	0.13	0.07	0.01	bdl	0.01	101.8	C019 SOI3 proximal to py/cpy
C019	chert	bdl	bdl	bdl	bdl	bdl	69.8	31.3	0.11	bdl	bdl	0.01	bdl	101.3	C019 SOI3 proximal to py/cpy
C019	chert	0.03	bdl	bdl	bdl	bdl	69.7	31.3	0.11	bdl	0.01	0.04	bdl	101.2	C019 SOI3 overgrown by py/cpy
C019	chert	bdl	bdl	bdl	bdl	0.01	69.9	31.4	0.12	bdl	bdl	bdl	bdl	101.4	C019 SOI3 overgrown by py/cpy
C019	chert	1.19	0.06	bdl	bdl	bdl	66.2	32.5	0.13	0.03	0.02	0.04	bdl	100.2	C019 SOI3 overgrown by py/cpy
SM11	mag	0.08	bdl	bdl	bdl	bdl	69.3	31.2	0.05	bdl	0.12	bdl	0.01	100.8	SM11 SOI1 cpy2 Line 007
SM11	mag	0.03	bdl	bdl	0.01	bdl	69.4	31.2	0.04	bdl	0.08	bdl	bdl	100.7	SM11 SOI1 cpy2 Line 008
SM11	mag	0.03	bdl	bdl	bdl	0.01	69.6	31.2	0.03	bdl	0.07	0.07	bdl	101.0	SM11 SOI1 cpy2 Line 009
SM11	mag	0.02	bdl	bdl	bdl	bdl	69.6	31.3	0.03	bdl	0.04	bdl	bdl	100.9	SM11 SOI1 cpy2 Line 010
SM11	mag	0.10	bdl	bdl	bdl	bdl	69.1	31.2	0.03	0.05	0.03	bdl	0.02	100.6	SM11 SOI1 cpy2 Line 011
SM11	mag	0.09	bdl	bdl	bdl	bdl	69.2	31.3	0.03	bdl	0.02	bdl	bdl	100.7	SM11 SOI1 cpy2 Line 012
SM11	mag	0.08	bdl	bdl	bdl	bdl	69.0	31.2	0.05	bdl	0.03	bdl	bdl	100.4	SM11 SOI1 cpy2 Line 013
SM11	mag	0.11	0.04	bdl	bdl	bdl	68.8	31.2	0.05	0.03	bdl	bdl	0.02	100.3	SM11 SOI1 cpy2 Line 014
SM11	mag	0.08	bdl	bdl	bdl	bdl	68.7	30.9	0.03	0.04	0.02	0.04	bdl	99.9	SM11 SOI1 cpy2 Line 015
SM11	mag	0.09	0.03	bdl	bdl	bdl	69.1	31.2	0.05	0.03	bdl	0.04	0.02	100.6	SM11 SOI1 cpy2 Line 016
SM11	mag	0.09	bdl	bdl	bdl	bdl	69.0	31.1	0.04	0.03	0.01	0.02	bdl	100.3	SM11 SOI1 cpy2 Line 017
SM11	mag	0.22	bdl	bdl	bdl	bdl	68.9	31.3	0.06	0.10	bdl	bdl	bdl	100.7	SM11 SOI1 cpy2 Line 018
SM11	mag	0.25	bdl	bdl	bdl	bdl	68.2	31.1	0.03	0.08	bdl	0.03	bdl	99.7	SM11 SOI1 cpy2 Line 019
SM11	mag	0.21	bdl	bdl	bdl	bdl	69.0	31.4	0.05	0.05	bdl	bdl	0.01	100.8	SM11 SOI1 cpy2 Line 020
SM11	mag	0.21	0.04	bdl	bdl	bdl	68.9	31.4	0.04	0.06	bdl	bdl	bdl	100.7	SM11 SOI1 cpy2 Line 021
SM11	mag	0.26	bdl	bdl	bdl	bdl	68.4	31.3	0.03	0.09	bdl	bdl	bdl	100.2	SM11 SOI1 cpy2 Line 022
SM11	mag	0.18	bdl	bdl	bdl	0.01	68.6	31.2	0.05	0.06	0.01	bdl	bdl	100.1	SM11 SOI1 cpy2 Line 023
SM11	mag	0.11	bdl	bdl	0.01	bdl	68.6	31.0	0.04	0.05	0.03	0.02	bdl	99.9	SM11 SOI1 cpy2 Line 024
SM11	mag	0.55	bdl	bdl	bdl	bdl	67.2	31.3	0.05	0.05	0.07	bdl	0.02	99.3	SM11 SOI1 cpy2 Line 025
SM11	mag	0.03	bdl	bdl	bdl	bdl	69.2	31.0	0.05	0.02	0.11	bdl	bdl	100.4	SM11 SOI1 cpy2 Line 028
SM11	mag	0.11	bdl	bdl	bdl	bdl	69.2	31.2	0.06	0.05	0.05	0.03	bdl	100.7	SM11 SOI1 cpy2 Line 029
SM11	mag	0.15	bdl	bdl	bdl	bdl	69.0	31.2	0.05	0.04	0.02	0.05	0.03	100.5	SM11 SOI1 cpy2 Line 030
SM11	mag	0.30	bdl	bdl	bdl	bdl	68.2	31.1	0.05	0.12	bdl	0.01	bdl	99.8	SM11 SOI1 cpy2 Line 031
SM11	mag	0.32	bdl	bdl	bdl	bdl	67.8	31.0	0.02	0.15	bdl	0.05	bdl	99.4	SM11 SOI1 cpy2 Line 032
SM11	mag	0.27	bdl	bdl	bdl	bdl	67.4	30.7	0.04	0.11	bdl	0.04	bdl	98.6	SM11 SOI1 cpy2 Line 033
SM11	mag	0.46	bdl	bdl	bdl	0.01	67.7	31.2	0.05	0.20	bdl	bdl	0.02	99.6	SM11 SOI1 cpy2 Line 034
SM11	mag	0.39	bdl	bdl	bdl	bdl	67.7	31.0	0.04	0.19	bdl	bdl	0.01	99.3	SM11 SOI1 cpy2 Line 035

Appendix B (continued): All EPMA analyses of magnetite (all values in wt.-%)

		SiO_2	TiO_2	Al_2O_3	Cr_2O_3	V_2O_3	Fe_2O_3	FeO	MnO	MgO	CaO	ZnO	NiO	Total	
	dl	0.01	0.03	0.08	0.01	0.01	0.02	0.02	0.01	0.01	0.01	0.01	0.01		
Sample	**Host**														**Comment**
SM11	mag	0.38	bdl	bdl	bdl	bdl	67.4	30.9	0.05	0.17	bdl	bdl	bdl	98.9	SM11 SOI1 cpy2 Line 036
SM11	mag	0.51	bdl	bdl	bdl	0.01	67.0	30.9	0.04	0.21	bdl	0.01	bdl	98.7	SM11 SOI1 cpy2 Line 037
SM11	mag	0.51	bdl	bdl	bdl	bdl	67.4	31.1	0.04	0.22	bdl	bdl	0.02	99.3	SM11 SOI1 cpy2 Line 038
SM11	mag	0.49	bdl	bdl	bdl	0.02	67.1	31.0	0.04	0.19	bdl	bdl	bdl	98.8	SM11 SOI1 cpy2 Line 039
SM11	mag	0.21	bdl	bdl	bdl	bdl	68.2	31.0	0.03	0.09	bdl	bdl	0.01	99.6	SM11 SOI1 cpy2 Line 040
SM11	mag	0.68	bdl	bdl	bdl	bdl	67.5	31.4	0.06	0.29	bdl	bdl	bdl	100.0	SM11 SOI1 cpy2 Line 041
SM11	mag	0.65	bdl	bdl	bdl	0.01	67.8	31.5	0.07	0.28	bdl	bdl	bdl	100.3	SM11 SOI1 cpy2 Line 042
SM11	mag	0.53	bdl	bdl	bdl	bdl	67.4	31.2	0.05	0.17	bdl	bdl	bdl	99.4	SM11 SOI1 cpy2 Line 043
SM11	mag	0.36	bdl	bdl	0.02	bdl	68.0	31.2	0.05	0.12	bdl	bdl	bdl	99.7	SM11 SOI1 cpy2 Line 044
SM11	mag	0.17	0.03	bdl	bdl	0.01	68.2	31.0	0.04	0.07	bdl	bdl	bdl	99.5	SM11 SOI1 cpy2 Line 045
SM11	mag	0.25	bdl	bdl	bdl	bdl	68.4	31.2	0.04	0.09	bdl	bdl	0.01	99.9	SM11 SOI1 cpy2 Line 046
SM11	mag	0.24	bdl	bdl	bdl	bdl	68.6	31.3	0.04	0.03	bdl	bdl	bdl	100.2	SM11 SOI1 cpy2 Line 047
SM11	mag	0.26	bdl	bdl	0.01	bdl	68.4	31.2	0.04	0.09	bdl	bdl	bdl	100.1	SM11 SOI1 cpy2 Line 048
SM11	mag	0.23	bdl	bdl	bdl	bdl	68.2	31.1	0.05	0.08	bdl	bdl	bdl	99.7	SM11 SOI1 cpy2 Line 049
SM11	mag	0.21	bdl	bdl	bdl	bdl	68.8	31.3	0.04	0.08	bdl	bdl	bdl	100.4	SM11 SOI1 cpy2 Line 050
SM11	mag	0.26	bdl	bdl	bdl	bdl	68.0	31.0	0.05	0.09	bdl	bdl	bdl	99.4	SM11 SOI1 cpy2 Line 051
SM11	mag	0.10	bdl	bdl	bdl	bdl	68.3	30.8	0.04	0.05	bdl	0.06	bdl	99.4	SM11 SOI1 cpy2 Line 052
SM11	mag	0.15	bdl	bdl	bdl	bdl	68.4	31.1	0.04	0.03	bdl	bdl	0.01	99.7	SM11 SOI1 cpy2 Line 053
SM11	mag	0.25	bdl	bdl	bdl	bdl	68.5	31.3	0.03	0.07	bdl	bdl	bdl	100.1	SM11 SOI1 cpy2 Line 054
SM11	mag	0.12	bdl	bdl	bdl	bdl	68.5	31.0	0.04	0.02	bdl	0.03	bdl	99.8	SM11 SOI1 cpy2 Line 055
SM11	mag	0.16	bdl	bdl	bdl	bdl	68.8	31.2	0.05	0.03	bdl	0.02	bdl	100.3	SM11 SOI1 cpy2 Line 056
SM11	mag	0.23	bdl	bdl	bdl	bdl	68.6	31.2	0.02	0.13	bdl	bdl	bdl	100.2	SM11 SOI1 cpy2 Line 057
SM11	mag	0.15	bdl	bdl	bdl	0.01	68.6	31.2	0.04	0.01	bdl	0.03	bdl	100.0	SM11 SOI1 cpy2 Line 058
SM11	mag	0.14	bdl	bdl	bdl	bdl	68.9	31.3	0.04	0.05	bdl	bdl	bdl	100.5	SM11 SOI1 cpy2 Line 059
SM11	mag	0.21	bdl	bdl	bdl	bdl	68.6	31.3	0.04	0.02	bdl	bdl	bdl	100.2	SM11 SOI1 cpy2 Line 060
SM11	mag	0.22	bdl	bdl	bdl	bdl	68.1	31.1	0.03	0.02	bdl	0.02	bdl	99.5	SM11 SOI1 cpy2 Line 061
SM11	mag	0.70	bdl	bdl	bdl	bdl	66.7	31.4	0.03	0.09	0.05	bdl	bdl	99.0	SM11 SOI1 cpy2 Line 062
SM11	mag	0.31	bdl	bdl	bdl	bdl	67.8	31.2	0.03	0.03	bdl	bdl	bdl	99.4	SM11 SOI1 cpy2 Line 063
SM11	mag	0.43	bdl	bdl	bdl	bdl	68.3	31.6	0.04	0.05	bdl	0.02	0.02	100.5	SM11 SOI1 cpy2 Line 064
SM11	mag	0.34	bdl	bdl	bdl	bdl	68.2	31.3	0.03	0.09	bdl	bdl	bdl	100.0	SM11 SOI1 cpy2 Line 065
SM11	mag	0.11	bdl	bdl	bdl	bdl	68.4	31.0	0.04	bdl	bdl	bdl	bdl	99.6	SM11 SOI1 cpy2 Line 066
SM11	mag	0.26	bdl	bdl	bdl	bdl	68.8	31.4	0.05	0.04	bdl	0.02	bdl	100.6	SM11 SOI1 cpy2 Line 067
SM11	mag	0.22	bdl	bdl	bdl	bdl	68.3	31.2	0.05	bdl	bdl	bdl	bdl	99.8	SM11 SOI1 cpy2 Line 068
SM11	mag	0.29	bdl	bdl	bdl	bdl	68.3	31.3	0.03	0.04	bdl	bdl	0.01	100.0	SM11 SOI1 cpy2 Line 070
SM11	mag	0.54	bdl	bdl	bdl	bdl	67.9	31.6	0.04	0.12	bdl	bdl	bdl	100.2	SM11 SOI1 cpy2 Line 071
SM11	mag	0.66	bdl	bdl	bdl	0.01	67.1	31.4	0.04	0.14	0.01	0.05	bdl	99.4	SM11 SOI1 cpy2 Line 072
SM11	mag	0.59	bdl	bdl	bdl	0.01	67.7	31.5	0.05	0.21	bdl	bdl	bdl	100.1	SM11 SOI1 cpy2 Line 073
SM11	mag	0.39	bdl	bdl	bdl	0.02	68.4	31.5	0.05	0.11	bdl	bdl	bdl	100.4	SM11 SOI1 cpy2 Line 074
SM11	mag	0.72	bdl	bdl	bdl	0.01	67.8	31.8	0.04	0.19	bdl	0.06	bdl	100.6	SM11 SOI1 cpy2 Line 075
SM11	mag	0.63	bdl	bdl	bdl	bdl	67.6	31.6	0.06	0.17	bdl	bdl	bdl	100.1	SM11 SOI1 cpy2 Line 076
SM11	mag	0.33	bdl	bdl	bdl	bdl	68.6	31.5	0.04	0.08	bdl	bdl	0.01	100.6	SM11 SOI1 cpy2 Line 077
SM11	mag	0.34	0.04	bdl	0.01	bdl	68.6	31.5	0.02	0.10	bdl	0.02	0.02	100.7	SM11 SOI1 cpy2 Line 078
SM11	mag	0.46	bdl	bdl	bdl	0.02	68.5	31.6	0.03	0.12	bdl	0.06	bdl	100.7	SM11 SOI1 cpy2 Line 079
SM11	mag	0.47	bdl	bdl	bdl	0.02	67.9	31.5	0.04	0.07	bdl	0.02	bdl	100.0	SM11 SOI1 cpy2 Line 080
SM11	mag	0.30	bdl	bdl	bdl	bdl	68.2	31.3	0.04	0.08	bdl	bdl	0.02	100.0	SM11 SOI1 cpy2 Line 081
SM11	mag	0.16	bdl	bdl	0.01	bdl	68.7	31.2	0.04	0.04	bdl	0.01	bdl	100.2	SM11 SOI1 cpy2 Line 082
SM11	mag	0.05	bdl	bdl	0.03	bdl	69.1	31.2	0.03	bdl	bdl	0.04	0.01	100.4	SM11 SOI1 cpy2 Line 083
SM11	mag	0.16	bdl	bdl	bdl	bdl	68.8	31.2	0.03	0.05	bdl	0.02	bdl	100.2	SM11 SOI1 cpy2 Line 084
SM11	mag	2.21	bdl	bdl	bdl	bdl	64.2	34.0	0.03	0.05	bdl	0.05	0.01	100.5	SM11 SOI1 cpy2 Line 085
SM11	mag	0.34	bdl	bdl	bdl	bdl	68.4	31.4	0.04	0.06	bdl	bdl	0.01	100.3	SM11 SOI1 cpy2 Line 088
SM11	mag	0.09	0.04	bdl	bdl	0.01	69.1	31.3	0.05	0.02	bdl	bdl	0.01	100.6	SM11 SOI1 cpy2 Line 094
SM11	mag	0.02	bdl	bdl	bdl	bdl	69.2	31.1	0.04	bdl	bdl	bdl	bdl	100.4	SM11 SOI1 cpy2 Line 095
SM11	mag	0.03	bdl	bdl	bdl	bdl	69.1	31.2	0.04	bdl	bdl	bdl	bdl	100.4	SM11 SOI1 cpy2 Line 096
SM11	mag	0.01	bdl	bdl	bdl	bdl	68.9	31.0	0.04	bdl	0.01	bdl	bdl	100.0	SM11 SOI1 cpy2 Line 097
SM11	mag	0.87	bdl	bdl	bdl	bdl	67.4	32.3	0.03	0.06	0.02	0.01	bdl	100.7	SM11 SOI1 cpy2 Line 098
SM11	mag	0.01	0.03	bdl	bdl	bdl	69.3	31.2	0.04	bdl	bdl	bdl	0.02	100.7	SM11 SOI1 cpy2 Line 099
SM11	mag	0.03	bdl	bdl	bdl	bdl	69.2	31.2	0.03	bdl	bdl	bdl	0.02	100.5	SM11 SOI1 cpy2 Line 100

Appendix B (continued): All EPMA analyses of magnetite (all values in wt.-%)

		SiO_2	TiO_2	Al_2O_3	Cr_2O_3	V_2O_3	Fe_2O_3	FeO	MnO	MgO	CaO	ZnO	NiO	Total	
	dl	0.01	0.03	0.08	0.01	0.01	0.02	0.02	0.01	0.01	0.01	0.01	0.01		
Sample	**Host**														**Comment**
11-1	shale	0.24	bdl	bdl	0.01	0.01	67.9	31.0	bdl	bdl	0.12	bdl	bdl	99.3	1a mag single grain1
11-1	shale	0.26	bdl	bdl	0.01	bdl	67.6	31.0	bdl	bdl	0.02	bdl	bdl	99.0	1a mag single grain2
11-1	shale	0.25	0.04	bdl	bdl	bdl	67.5	31.0	bdl	bdl	0.02	bdl	bdl	98.8	1a mag single grain3
11-1	shale	0.16	bdl	bdl	bdl	bdl	68.5	31.2	bdl	bdl	bdl	bdl	bdl	99.9	1a mag weakly layered single grain1
11-1	shale	0.23	bdl	bdl	bdl	bdl	67.7	31.0	bdl	bdl	0.01	0.04	bdl	99.1	1a mag weakly layered single grain2
11-1	shale	0.44	bdl	bdl	bdl	bdl	67.5	31.5	bdl	bdl	bdl	bdl	bdl	99.5	1a mag weakly layered single grain3
11-1	shale	0.44	bdl	bdl	bdl	bdl	67.1	31.1	bdl	0.02	0.03	bdl	bdl	98.7	1a mag weakly layered single grain4
11-2b	chl	0.81	bdl	bdl	bdl	bdl	67.4	32.2	bdl	0.03	0.01	bdl	bdl	100.4	2b mag single grain1
11-2b	chl	2.07	bdl	bdl	bdl	bdl	63.8	33.6	bdl	bdl	bdl	0.03	bdl	99.5	2b mag single grain2
11-4	chl	0.06	0.03	bdl	0.14	bdl	69.3	31.4	0.01	bdl	bdl	bdl	bdl	101.0	3-11b-4 mag1 zoned bright
11-4	chl	1.97	bdl	bdl	0.02	0.01	64.5	33.5	bdl	0.17	bdl	0.01	bdl	100.4	3-11b-4 mag1 zoned dark core
11-4	chl	0.72	bdl	bdl	bdl	0.03	68.0	32.3	bdl	0.06	bdl	0.03	bdl	101.2	3-11b-4 mag1 zoned bright rim
11-4	chl	0.05	bdl	bdl	0.17	bdl	69.6	31.5	bdl	bdl	bdl	bdl	bdl	101.4	3-11b-4 mag1 zoned bright
11-4	chl	0.57	0.04	bdl	bdl	bdl	68.2	32.0	bdl	0.04	bdl	bdl	bdl	100.9	3-11b-4 mag2 core
11-4	chl	0.37	bdl	bdl	bdl	bdl	68.7	31.7	0.01	0.04	bdl	0.02	bdl	100.9	3-11b-4 mag2 rim
11-4	chl	0.52	0.03	bdl	bdl	bdl	67.9	31.8	bdl	0.02	bdl	bdl	0.01	100.3	3-11b-4 mag3 core
11-4	chl	0.48	0.06	bdl	bdl	bdl	68.1	31.8	0.01	0.03	bdl	0.09	bdl	100.6	3-11b-4 mag4 core
11-4	chl	0.54	0.04	bdl	0.01	0.01	67.8	31.9	bdl	0.01	bdl	bdl	bdl	100.3	3-11b-4 mag5
11-4	chl	0.59	0.75	bdl	bdl	bdl	66.6	32.7	0.02	0.05	bdl	bdl	bdl	100.8	3-11b-4 mag6
11-4	chl	0.16	bdl	bdl	bdl	0.02	69.3	31.5	bdl	bdl	bdl	0.02	bdl	101.1	3-11b-4 mag7 bright outermost
11-4	chl	0.03	6.68	bdl	0.82	0.05	56.6	37.9	0.08	bdl	bdl	bdl	bdl	102.1	3-11b-4 mag7 bright core
11-4	chl	2.00	0.11	0.17	0.03	0.02	64.4	33.7	bdl	0.23	bdl	0.02	bdl	100.7	3-11b-4 dark layer around bright c
11-4	chl	0.48	bdl	bdl	bdl	bdl	68.8	32.0	bdl	0.04	bdl	bdl	bdl	101.3	3-11b-4 bright outermost
11-4	chl	0.46	bdl	bdl	bdl	bdl	68.3	31.7	bdl	0.05	bdl	bdl	bdl	100.5	3-11b-4 mag8 50µm not zoned
11-4	chl	1.87	bdl	bdl	0.04	bdl	64.3	33.3	bdl	0.09	bdl	0.01	0.01	99.6	3-11b-4 weakly zoned dark core
11-4	chl	0.40	bdl	bdl	bdl	bdl	68.0	31.5	bdl	0.03	bdl	bdl	bdl	100.0	3-11b-4 mag9 bright rim
11-4	chl	0.50	0.59	bdl	bdl	0.02	66.8	32.3	bdl	0.04	bdl	bdl	bdl	100.3	3-11b-4 mag in ilm4 central part
11-4	chl	0.36	1.23	bdl	bdl	0.02	66.1	32.8	0.02	0.03	bdl	bdl	bdl	100.6	3-11b-4 mag in ilm4 interface
11-5	shale	0.15	bdl	bdl	bdl	0.03	70.0	31.9	bdl	bdl	bdl	bdl	bdl	102.2	5 single mag1
11-5	shale	0.10	0.06	bdl	bdl	bdl	70.3	31.9	0.02	bdl	bdl	bdl	bdl	102.4	5 single mag2
11-5	shale	0.09	bdl	bdl	0.03	bdl	70.3	31.8	bdl	bdl	bdl	bdl	bdl	102.2	5 single mag3
11-5	shale	0.12	bdl	bdl	bdl	0.02	69.8	31.7	bdl	bdl	bdl	bdl	bdl	101.7	5 single mag4
11-5	shale	0.10	bdl	bdl	bdl	0.02	69.2	31.4	0.02	bdl	0.01	0.02	bdl	100.8	5 single mag5
11-5	shale	0.14	bdl	bdl	bdl	0.01	69.0	31.4	0.02	bdl	bdl	bdl	bdl	100.6	5 single mag6
11-5	shale	0.27	bdl	bdl	bdl	bdl	68.9	31.7	bdl	0.01	bdl	bdl	0.02	100.9	5 single mag8 in vein
11-5	shale	0.07	bdl	bdl	bdl	bdl	69.4	31.4	bdl	bdl	bdl	0.01	bdl	100.9	5 single mag9
11-5	shale	0.25	bdl	bdl	bdl	bdl	68.4	31.4	bdl	bdl	0.01	bdl	bdl	100.1	5 single mag10
11-6a	chl	0.54	bdl	bdl	bdl	bdl	68.2	31.8	bdl	0.05	0.02	0.05	0.03	100.7	6a mag lay1 mag1
11-6a	chl	0.53	0.05	bdl	0.01	bdl	68.4	32.0	bdl	0.05	0.01	bdl	0.02	101.0	6a mag lay1 mag3 anneal
11-6a	chl	0.59	0.05	bdl	bdl	0.01	68.1	31.9	bdl	0.09	0.02	bdl	bdl	100.8	6a mag lay1 mag3 core
11-6a	chl	0.45	bdl	bdl	bdl	0.02	68.5	31.8	0.01	0.04	bdl	bdl	bdl	100.8	6a mag lay1 mag4 anneal
11-6a	chl	0.62	bdl	bdl	bdl	bdl	68.0	32.1	0.01	0.02	bdl	bdl	0.01	100.8	6a mag lay1 mag4 core
11-6a	chl	0.48	bdl	bdl	bdl	0.01	68.5	31.9	0.01	0.04	0.03	0.02	0.02	101.1	6a mag lay1 mag5 anneal
11-6a	chl	0.70	bdl	bdl	bdl	0.02	67.9	32.1	bdl	0.04	0.01	bdl	bdl	100.9	6a mag lay1 mag5 core
11-6a	chl	0.72	bdl	bdl	bdl	bdl	68.3	32.4	bdl	0.03	0.03	bdl	0.01	101.5	6a mag lay1 mag6 core
11-6a	chl	1.42	bdl	bdl	bdl	0.02	64.8	32.3	bdl	0.11	0.05	bdl	0.04	98.8	6a mag lay1 mag7 small
11-6a	chl	1.26	bdl	bdl	bdl	0.01	65.6	32.5	bdl	bdl	0.05	0.02	0.01	99.5	6a mag lay1 mag8 small
11-6a	chl	0.58	bdl	bdl	bdl	0.01	67.2	31.6	bdl	0.04	bdl	bdl	bdl	99.4	6a mag vein south lay 2 mag1
11-6a	chl	0.69	0.05	bdl	bdl	bdl	66.6	31.6	bdl	0.03	0.02	0.02	bdl	99.0	6a mag vein south lay 2 mag3
11-6a	chl	0.83	bdl	bdl	0.01	bdl	66.8	32.0	bdl	0.04	bdl	0.02	bdl	99.7	6a mag vein south lay 2 mag4
11-6a	chl	0.79	0.04	bdl	bdl	0.01	66.2	31.6	bdl	0.07	0.02	bdl	bdl	98.7	6a mag vein south lay 2 mag5
11-6a	chl	0.65	bdl	bdl	bdl	bdl	67.7	31.7	bdl	0.04	0.21	bdl	bdl	100.3	6a mag vein south lay 2 mag6
11-6a	chl	0.66	bdl	bdl	bdl	bdl	66.5	31.4	bdl	0.03	bdl	bdl	bdl	98.6	6a mag vein south lay 2 mag7
11-6a	chl	0.62	bdl	bdl	0.02	bdl	67.9	31.8	bdl	0.04	0.13	bdl	bdl	100.5	6a mag lay2 transition mag1
11-6a	chl	0.70	bdl	bdl	0.02	0.01	67.4	31.9	bdl	0.04	0.03	0.06	bdl	100.1	6a mag lay2 transition mag2
11-6a	chl	0.62	bdl	bdl	bdl	bdl	67.5	31.8	bdl	0.05	bdl	bdl	0.01	100.0	6a mag lay2 transition mag3
11-6a	chl	0.76	bdl	bdl	0.01	bdl	67.2	32.0	bdl	0.04	0.01	bdl	bdl	100.0	6a mag lay2 transition mag4

Appendix B (continued): All EPMA analyses of magnetite (all values in wt.-%)

		SiO_2	TiO_2	Al_2O_3	Cr_2O_3	V_2O_3	Fe_2O_3	FeO	MnO	MgO	CaO	ZnO	NiO	Total	
	dl	0.01	0.03	0.08	0.01	0.01	0.02	0.02	0.01	0.01	0.01	0.01	0.01		
Sample	**Host**														**Comment**
11-6a	chl	0.65	bdl	bdl	bdl	0.02	67.3	31.8	bdl	0.05	bdl	bdl	bdl	99.8	6a mag lay2 transition mag6
11-6a	chl	0.83	bdl	bdl	0.01	bdl	66.0	31.5	bdl	0.07	0.01	0.06	bdl	98.5	6a mag lay2 mag1
11-6a	chl	0.80	bdl	0.28	bdl	bdl	65.2	31.3	0.02	0.09	0.04	bdl	bdl	97.7	6a mag lay2 mag2
11-6a	chl	0.61	0.04	bdl	bdl	bdl	67.8	32.0	bdl	0.05	bdl	bdl	bdl	100.5	6a mag lay2 mag3
11-6a	chl	0.60	bdl	bdl	bdl	0.03	67.6	31.9	bdl	bdl	bdl	bdl	0.01	100.1	6a mag lay2 mag4
11-6a	chl	0.67	bdl	bdl	bdl	bdl	67.6	32.0	bdl	0.04	bdl	bdl	bdl	100.4	6a mag lay2 mag5
11-6a	chl	0.65	bdl	bdl	bdl	bdl	67.4	31.8	bdl	0.06	bdl	bdl	bdl	100.0	6a mag lay2 mag8 line analysis
11-6a	chl	0.68	0.04	0.09	bdl	0.01	67.3	31.9	bdl	0.05	bdl	0.02	bdl	100.2	6a mag lay2 north mag1
11-6a	chl	0.65	0.03	bdl	bdl	0.02	67.6	32.0	bdl	0.04	bdl	bdl	bdl	100.3	6a mag lay2 north mag2
11-6a	chl	0.53	bdl	bdl	bdl	bdl	67.9	31.7	0.01	0.04	0.02	0.01	bdl	100.2	6a mag lay2 north mag6
11-6a	chl	0.19	0.04	bdl	bdl	0.01	68.5	31.3	bdl	0.01	bdl	bdl	bdl	100.2	6a mag lay2 north mag7 elongated
11-6a	chl	0.59	bdl	bdl	bdl	bdl	67.8	31.8	bdl	0.04	bdl	0.05	bdl	100.4	6a mag lay2 north mag8 elongated
11-6a	chl	0.05	0.04	bdl	bdl	bdl	69.2	31.3	bdl	bdl	bdl	bdl	bdl	100.7	6a mag lay2 north mag9 elongated
11-6a	chl	1.00	bdl	bdl	bdl	0.01	66.6	32.3	bdl	0.04	bdl	0.03	bdl	100.1	6a mag lay2 north chlorite4
11-6a	chl	0.49	0.18	bdl	0.01	bdl	67.6	31.9	bdl	0.03	bdl	bdl	bdl	100.3	6a mag lay3 south transition mag1
11-6a	chl	0.36	bdl	bdl	0.01	bdl	68.1	31.5	bdl	0.03	bdl	bdl	0.02	100.0	6a mag lay3 south transition mag2
11-6a	chl	0.56	bdl	bdl	bdl	0.01	67.5	31.6	bdl	0.06	bdl	bdl	bdl	99.8	6a mag lay3 south transition mag3
11-6a	chl	0.53	bdl	bdl	bdl	bdl	67.6	31.5	bdl	0.05	bdl	0.04	0.02	99.8	6a mag lay3 south transition mag4
11-6a	chl	0.45	bdl	bdl	bdl	bdl	67.9	31.6	bdl	0.04	bdl	bdl	0.01	100.0	6a mag lay3 south transition mag5
11-6a	chl	0.70	bdl	bdl	bdl	0.01	67.3	31.8	bdl	0.10	bdl	bdl	0.02	99.9	6a mag lay3 mag1
11-6a	chl	1.39	0.04	0.66	bdl	bdl	64.9	32.2	bdl	0.48	0.02	bdl	bdl	99.7	6a mag lay3 mag3
11-6a	chl	0.15	bdl	bdl	bdl	bdl	68.7	31.3	bdl	bdl	bdl	0.02	bdl	100.2	6a mag lay3 mag4
11-6a	chl	0.90	bdl	bdl	bdl	0.01	67.0	32.3	bdl	0.03	0.01	bdl	bdl	100.3	6a mag lay4 mag1
11-6a	chl	0.28	0.04	bdl	bdl	0.02	68.5	31.5	0.01	0.04	bdl	bdl	bdl	100.5	6a mag lay4 mag2
11-6a	chl	0.70	0.03	bdl	0.02	bdl	67.6	32.0	bdl	0.05	bdl	0.05	0.01	100.5	6a mag lay4 mag3
11-6a	chl	0.33	bdl	bdl	bdl	0.02	67.8	31.2	bdl	0.06	bdl	0.01	bdl	99.5	6a mag lay4 mag4
11-6a	chl	0.63	bdl	bdl	bdl	bdl	67.6	31.9	bdl	0.05	bdl	bdl	bdl	100.2	6a mag lay4 mag9
11-6a	chl	0.72	1.44	bdl	bdl	0.01	65.3	33.5	bdl	0.06	0.02	0.02	bdl	101.1	6a mag lay4 mag10 overg by ilm
11-6a	chl	0.53	bdl	bdl	bdl	bdl	68.1	31.8	bdl	0.05	bdl	0.05	bdl	100.6	6a mag lay4 mag11
11-6b	mag	0.36	bdl	bdl	bdl	0.02	67.6	31.2	bdl	0.03	bdl	bdl	0.01	99.2	6a mag lay4 chlorite1
11-6b	mag	0.48	bdl	bdl	bdl	bdl	68.7	32.1	0.01	bdl	bdl	bdl	bdl	101.3	6b lay1 mag euh 30u centr 1
11-6b	mag	0.71	bdl	bdl	bdl	bdl	67.3	32.0	bdl	0.01	bdl	0.01	bdl	100.0	6b lay1 mag euh 30u centr 2
11-6b	mag	0.17	bdl	bdl	bdl	0.01	68.7	31.3	bdl	bdl	0.01	0.03	bdl	100.3	6b lay1 mag euh 30u centr 3
11-6b	mag	2.78	bdl	bdl	0.02	bdl	62.9	35.0	bdl	bdl	bdl	bdl	bdl	100.7	6b lay1 mag euh 30u centr 4
11-6b	mag	0.39	bdl	bdl	0.01	bdl	68.1	31.6	bdl	bdl	bdl	0.01	bdl	100.1	6b lay1 mag euh 30u centr 5
11-6b	mag	0.37	0.04	bdl	bdl	bdl	68.4	31.6	bdl	0.04	bdl	bdl	bdl	100.5	6b lay1 mag euh 30u centr 6
11-6b	mag	0.96	bdl	bdl	bdl	bdl	67.3	32.6	bdl	bdl	0.01	0.04	bdl	100.9	6b lay1 mag euh aggregate central 1
11-6b	mag	0.84	bdl	0.19	bdl	bdl	67.1	32.0	0.02	0.20	0.01	bdl	bdl	100.4	6b lay1 mag euh aggregate central 2
11-6b	mag	0.50	0.05	bdl	bdl	bdl	68.7	32.1	bdl	0.03	bdl	0.03	bdl	101.4	6b lay1 mag euh aggregate central 3
11-6b	mag	0.44	bdl	bdl	bdl	bdl	68.6	31.9	0.02	bdl	0.01	bdl	bdl	100.9	6b lay1 mag euh aggregate rim 1
11-6b	mag	0.46	bdl	bdl	bdl	0.01	68.4	31.9	bdl	0.01	0.01	0.02	bdl	100.9	6b lay1 mag euh aggregate rim 2
11-6b	mag	0.57	bdl	bdl	bdl	bdl	68.2	32.1	bdl	bdl	bdl	bdl	bdl	100.9	6b lay2 mag euh
11-6b	mag	0.60	bdl	bdl	0.01	bdl	68.2	32.1	bdl	bdl	bdl	0.03	0.02	100.9	6b lay2 mag euh 2
11-6b	mag	0.25	0.11	bdl	bdl	bdl	68.3	31.5	bdl	bdl	bdl	bdl	0.01	100.2	6b lay2 mag euh 4
11-6b	mag	0.62	bdl	bdl	bdl	bdl	68.2	32.1	bdl	0.01	bdl	bdl	bdl	101.0	6b lay2 mag euh 5
11-6b	mag	2.18	bdl	bdl	bdl	bdl	63.7	33.8	bdl	0.05	bdl	0.05	bdl	99.8	6b lay2 mag euh 6
11-6b	mag	0.33	bdl	bdl	bdl	bdl	69.0	31.9	bdl	bdl	bdl	bdl	bdl	101.3	6b lay1 mag euh 7
11-6b	mag	0.43	bdl	bdl	0.01	bdl	68.8	31.9	bdl	0.02	bdl	bdl	bdl	101.2	6b lay3 mag euh 1
11-6b	mag	1.49	bdl	bdl	bdl	bdl	64.9	32.8	bdl	bdl	bdl	0.03	bdl	99.2	6b lay3 mag euh 4
11-6b	mag	0.34	bdl	bdl	bdl	bdl	68.7	31.7	bdl	bdl	bdl	bdl	bdl	100.7	6b lay3 mag-hem euh 5
11-6b	mag	0.74	bdl	bdl	bdl	bdl	67.3	32.1	bdl	0.03	bdl	bdl	bdl	100.2	6b lay4 mag euh lge 1
11-6b	mag	0.90	0.07	bdl	bdl	bdl	67.0	32.3	bdl	0.02	0.01	0.04	bdl	100.4	6b lay4 mag euh lge 2
11-6b	mag	0.19	bdl	bdl	bdl	bdl	69.0	31.5	bdl	bdl	bdl	bdl	bdl	100.7	6b lay4 mag euh lge 3
11-6b	mag	0.21	bdl	bdl	bdl	bdl	69.1	31.6	bdl	bdl	bdl	0.02	bdl	101.0	6b lay4 mag euh lge 4
11-6b	mag	0.49	bdl	bdl	bdl	0.01	68.5	32.0	bdl	bdl	0.01	bdl	bdl	101.0	6b lay5 mag 50u euh 1
11-6b	mag	0.78	bdl	bdl	0.02	bdl	67.7	32.3	bdl	0.02	bdl	bdl	bdl	100.8	6b lay5 mag 50u euh 2
11-6b	mag	0.84	bdl	bdl	bdl	bdl	67.6	32.5	bdl	bdl	bdl	bdl	bdl	101.0	6b lay5 mag 50u euh 3

Appendix B (continued): All EPMA analyses of magnetite (all values in wt.-%)

		SiO_2	TiO_2	Al_2O_3	Cr_2O_3	V_2O_3	Fe_2O_3	FeO	MnO	MgO	CaO	ZnO	NiO	Total	
	dl	0.01	0.03	0.08	0.01	0.01	0.02	0.02	0.01	0.01	0.01	0.01	0.01		
Sample	**Host**														**Comment**
11-6b	mag	0.59	bdl	bdl	bdl	bdl	68.3	32.1	bdl	bdl	0.01	bdl	bdl	101.0	6b lay5 mag 50u euh 4
11-6b	mag	0.95	bdl	bdl	bdl	bdl	66.8	32.3	0.02	0.02	0.03	0.04	bdl	100.2	6b lay5 mag 50u euh 5
11-6b	mag	0.31	bdl	bdl	bdl	bdl	69.0	31.8	bdl	bdl	bdl	bdl	bdl	101.1	6b lay6 euh mag 1
11-6b	mag	0.76	bdl	bdl	bdl	bdl	67.4	32.2	bdl	bdl	bdl	bdl	bdl	100.5	6b lay6 euh mag 2
11-6b	mag	0.80	bdl	0.10	bdl	bdl	67.4	32.2	0.02	0.01	0.02	0.01	bdl	100.5	6b lay6 euh mag 3
11-6b	mag	0.57	bdl	bdl	bdl	bdl	68.2	32.1	bdl	bdl	bdl	bdl	bdl	101.0	6b lay6 euh mag 4
11-6b	mag	0.95	0.04	bdl	0.01	bdl	66.6	32.3	bdl	bdl	0.02	0.02	bdl	99.9	6b lay6 euh mag sml 2
11-6b	mag	0.43	bdl	bdl	bdl	bdl	68.1	31.7	bdl	bdl	0.01	bdl	bdl	100.2	6b lay6 euh mag sml 3
11-6b	mag	0.77	bdl	bdl	bdl	bdl	67.0	32.0	bdl	bdl	0.01	bdl	bdl	99.8	6b lay6 euh mag sml 4
11-9	chert	0.44	0.04	bdl	bdl	bdl	68.5	31.8	0.03	0.08	bdl	bdl	bdl	101.0	9 lay 1 intergrown mag 1
11-9	chert	0.47	bdl	bdl	bdl	bdl	68.0	31.6	bdl	0.05	bdl	0.01	bdl	100.2	9 lay 1 intergrown mag 2
11-9	chert	0.53	bdl	bdl	bdl	bdl	68.4	31.8	0.02	0.10	bdl	0.03	0.01	100.9	9 lay 1 intergrown mag 3
11-9	chert	0.46	bdl	bdl	bdl	bdl	68.7	31.9	bdl	0.09	bdl	bdl	bdl	101.1	9 lay 1 intergrown mag 4
11-9	chert	0.68	bdl	bdl	bdl	bdl	68.0	32.0	bdl	0.11	bdl	bdl	bdl	100.8	9 lay 1 intergrown mag 5
11-9	chert	0.96	bdl	bdl	bdl	bdl	67.2	32.1	0.01	0.23	bdl	bdl	bdl	100.5	9 lay 1 intergrown mag 6
11-9	chert	0.35	bdl	bdl	bdl	bdl	68.9	31.8	bdl	0.04	bdl	bdl	0.01	101.1	9 lay 1 intergrown mag 7
11-9	chert	0.49	bdl	bdl	bdl	bdl	68.2	31.7	0.02	0.10	bdl	bdl	bdl	100.6	9 lay 1 intergrown mag 8
11-9	chert	0.19	bdl	bdl	bdl	bdl	68.8	31.4	0.01	0.01	bdl	bdl	bdl	100.3	9 lay 1 intergrown mag 9
11-9	chert	0.56	bdl	bdl	bdl	bdl	68.5	31.9	bdl	0.14	bdl	bdl	bdl	101.1	9 lay 1 intergrown mag 10
11-9	chert	0.69	bdl	bdl	bdl	bdl	67.7	31.9	bdl	0.07	bdl	bdl	0.01	100.4	9 lay2 mag 1
11-9	chert	0.16	bdl	bdl	bdl	bdl	69.4	31.6	bdl	0.01	bdl	bdl	bdl	101.2	9 lay2 mag 2
11-9	chert	0.25	bdl	bdl	bdl	0.02	68.6	31.4	0.01	bdl	bdl	bdl	bdl	100.3	9 lay2 mag 3
11-9	chert	0.72	bdl	bdl	bdl	0.01	67.9	32.1	bdl	0.10	bdl	bdl	bdl	100.8	9 lay2 mag 4
11-9	chert	0.62	bdl	bdl	bdl	bdl	68.1	31.9	bdl	0.07	bdl	0.06	bdl	100.8	9 lay2 mag 5
11-9	chert	0.17	0.05	bdl	bdl	bdl	69.0	31.5	0.02	bdl	bdl	bdl	bdl	100.7	9 lay2 mag 6
11-9	chert	0.78	bdl	bdl	bdl	bdl	67.3	32.0	bdl	0.11	bdl	bdl	bdl	100.2	9 lay2 mag 7
11-9	chert	0.59	0.04	bdl	bdl	bdl	68.3	32.0	0.01	0.13	0.02	bdl	bdl	101.1	9 lay2 mag 8
11-9	chert	0.18	bdl	bdl	bdl	bdl	68.9	31.4	0.01	bdl	bdl	bdl	0.02	100.6	9 lay2 mag 9
11-9	chert	0.44	bdl	bdl	bdl	bdl	68.6	31.8	bdl	0.07	0.01	bdl	bdl	100.9	9 lay4 mag1
11-9	chert	0.40	0.03	bdl	bdl	bdl	69.0	31.9	bdl	0.07	bdl	bdl	bdl	101.4	9 lay4 mag2
11-9	chert	0.15	bdl	bdl	bdl	bdl	69.7	31.7	bdl	bdl	bdl	bdl	bdl	101.5	9 lay4 mag3
11-9	chert	1.26	bdl	bdl	bdl	bdl	66.4	32.3	bdl	0.18	0.21	0.01	bdl	100.4	9 lay5 mag2
11-9	chert	0.96	0.03	bdl	bdl	bdl	67.0	32.1	bdl	0.19	bdl	0.01	0.02	100.3	9 lay5 mag3
11-9	chert	0.19	bdl	bdl	bdl	bdl	69.0	31.4	bdl	0.02	bdl	0.02	bdl	100.7	9 lay5 mag4
11-9	chert	0.29	bdl	bdl	bdl	0.01	68.6	31.4	bdl	0.03	0.06	bdl	0.01	100.5	9 lay5 mag5
11-9	chert	0.64	bdl	bdl	bdl	bdl	68.3	32.0	bdl	0.11	0.02	bdl	bdl	101.1	9 lay5 mag6
11-9	chert	0.91	0.04	bdl	bdl	0.01	67.5	32.3	0.02	0.15	0.03	0.03	bdl	101.0	9 lay5 mag7
11-9	chert	0.34	bdl	bdl	bdl	bdl	67.7	31.2	0.02	bdl	bdl	bdl	0.01	99.4	9 lay5 mag8
11-10	chl-chert	1.63	bdl	0.08	bdl	bdl	65.6	32.7	bdl	0.44	bdl	bdl	bdl	100.5	10 south mag lge1
11-10	chl-chert	1.40	bdl	bdl	0.02	bdl	66.6	32.5	bdl	0.43	bdl	0.05	bdl	101.0	10 south mag lge2
11-10	chl-chert	0.92	bdl	bdl	bdl	bdl	67.0	32.0	bdl	0.22	0.01	bdl	bdl	100.2	10 south mag lge3
11-10	chl-chert	1.38	bdl	bdl	bdl	bdl	65.8	32.3	bdl	0.38	bdl	bdl	bdl	99.9	10 south mag lge4
11-10	chl-chert	1.49	bdl	bdl	bdl	bdl	66.0	32.3	0.01	0.49	0.09	bdl	bdl	100.4	10 south mag lge5
11-10	chl-chert	0.68	bdl	bdl	bdl	0.01	67.4	31.5	0.01	0.16	0.13	bdl	bdl	100.0	10 south mag lge6
11-10	chl-chert	0.52	0.06	0.11	bdl	bdl	67.0	31.1	bdl	0.16	0.06	0.06	0.01	99.1	10 mag sml 4
11-10	chl-chert	0.88	bdl	0.12	bdl	bdl	66.7	31.7	bdl	0.24	0.12	bdl	bdl	99.8	10 mag lge 1
11-10	chl-chert	0.83	bdl	0.19	bdl	bdl	66.4	31.3	bdl	0.34	0.05	0.08	bdl	99.2	10 mag lge 2
11-10	chl-chert	0.94	0.05	bdl	bdl	bdl	66.6	31.9	bdl	0.24	0.04	bdl	bdl	99.8	10 mag lge 4 core
11-10	chl-chert	1.83	bdl	bdl	0.02	bdl	64.3	32.2	0.02	0.63	bdl	bdl	bdl	99.1	10 north mag lge 1
11-10	chl-chert	1.80	bdl	bdl	bdl	bdl	65.0	32.7	bdl	0.49	bdl	bdl	0.01	100.1	10 north mag lge 2
11-10	chl-chert	0.71	bdl	bdl	0.01	bdl	67.3	31.7	bdl	0.18	bdl	bdl	bdl	99.9	10 north mag lge 3
11-10	chl-chert	1.28	bdl	bdl	bdl	bdl	65.6	31.8	0.02	0.40	bdl	0.04	bdl	99.2	10 north mag lge 4
11-22	chert	1.68	bdl	bdl	bdl	bdl	64.2	32.8	bdl	0.04	0.04	bdl	0.03	98.8	22 lay1 euh mag core
11-22	chert	1.62	0.10	0.30	bdl	0.02	64.1	32.9	bdl	0.10	0.02	bdl	0.02	99.1	22 lay1 euh mag core-rim bndry
11-22	chert	0.92	bdl	bdl	bdl	bdl	66.7	32.2	bdl	0.02	0.01	bdl	0.02	99.9	22 lay1 euh mag rim
11-22	chert	0.64	bdl	bdl	bdl	bdl	67.3	31.8	bdl	0.02	0.02	0.01	0.01	99.8	22 lay1 euh mag2 core
11-22	chert	1.51	0.07	0.12	bdl	0.02	64.9	32.9	bdl	bdl	0.02	bdl	0.03	99.6	22 lay1 euh mag2 core-rim bndry

Appendix B (continued): All EPMA analyses of magnetite (all values in wt.-%)

		SiO_2	TiO_2	Al_2O_3	Cr_2O_3	V_2O_3	Fe_2O_3	FeO	MnO	MgO	CaO	ZnO	NiO	Total	
	dl	0.01	0.03	0.08	0.01	0.01	0.02	0.02	0.01	0.01	0.01	0.01	0.01		
Sample	**Host**														**Comment**
11-22	chert	0.66	0.06	bdl	bdl	bdl	67.1	31.8	bdl	bdl	0.01	0.03	0.01	99.6	22 lay1 euh mag2 rim
11-22	chert	1.44	0.06	bdl	bdl	0.01	65.2	32.8	0.01	0.05	bdl	bdl	bdl	99.6	22 lay1 euh mag2 rim
11-22	chert	1.84	0.06	bdl	0.01	bdl	64.5	33.5	0.01	0.01	bdl	bdl	bdl	100.0	22 lay1 euh mag2 boundary
11-22	chert	1.00	0.04	bdl	bdl	bdl	66.7	32.4	bdl	bdl	0.01	bdl	bdl	100.2	22 lay1 euh mag2 rim
11-22	chert	1.13	0.04	bdl	bdl	bdl	66.3	32.6	bdl	0.01	bdl	0.02	0.02	100.1	22 lay1 euh mag3 core
11-22	chert	0.89	bdl	bdl	0.02	bdl	67.2	32.4	bdl	0.02	bdl	bdl	0.01	100.5	22 lay1 euh mag3 rim
11-22	chert	2.04	0.06	bdl	bdl	bdl	64.5	34.0	bdl	bdl	bdl	bdl	bdl	100.6	22 lay3 euh mag core
11-22	chert	2.53	bdl	bdl	bdl	bdl	62.9	34.4	bdl	bdl	bdl	0.03	bdl	100.0	22 lay3 euh mag boundary
11-22	chert	0.92	bdl	bdl	bdl	bdl	67.3	32.5	bdl	bdl	bdl	0.02	bdl	100.7	22 lay3 euh mag rim
11-22	chert	1.56	0.05	bdl	0.01	0.01	65.1	33.1	0.02	bdl	bdl	bdl	bdl	99.9	22 lay3 euh mag2 core
11-22	chert	1.46	0.05	bdl	bdl	bdl	65.4	33.0	bdl	0.01	0.01	bdl	bdl	100.0	22 lay3 euh mag2 boundary
11-22	chert	0.99	0.04	bdl	bdl	bdl	66.9	32.5	bdl	0.01	bdl	0.02	bdl	100.5	22 lay3 euh mag2 rim
11-22	chert	0.72	bdl	0.10	bdl	0.01	67.3	32.0	bdl	bdl	0.02	0.02	bdl	100.3	22 lay4 mag old core
11-22	chert	1.02	0.04	bdl	bdl	bdl	67.0	32.6	bdl	bdl	bdl	0.05	bdl	100.7	22 lay4 mag overgrowth
11-23	chert-mag	0.58	bdl	bdl	bdl	bdl	68.2	32.0	bdl	bdl	bdl	bdl	bdl	100.9	23 lay1 mag homogen1
11-23	chert-mag	0.25	bdl	bdl	bdl	bdl	68.8	31.5	bdl	bdl	0.01	bdl	bdl	100.7	23 lay1 mag homogen2
11-23	chert-mag	0.35	bdl	bdl	0.02	bdl	68.6	31.7	bdl	0.01	bdl	0.07	bdl	100.8	23 lay1 mag homogen3
11-23	chert-mag	0.59	0.04	bdl	bdl	0.01	67.9	32.1	bdl	bdl	bdl	bdl	bdl	100.6	23 lay1 chl-ank interlayer mag1
11-23	chert-mag	0.63	0.05	bdl	bdl	0.01	67.4	31.9	0.02	bdl	bdl	0.04	bdl	100.1	23 lay1 chl-ank interlayer mag2
11-23	chert-mag	0.62	0.06	bdl	bdl	bdl	67.4	31.9	bdl	0.01	bdl	bdl	bdl	100.0	23 lay1 chl-ank interlayer mag3
11-23	chert-mag	0.34	bdl	bdl	bdl	bdl	68.6	31.6	0.01	bdl	bdl	0.02	bdl	100.6	23 lay1 massive mag hom core 1
11-23	chert-mag	0.26	bdl	bdl	bdl	bdl	68.8	31.6	0.02	bdl	bdl	bdl	bdl	100.7	23 lay1 massive mag hom rim1
11-23	chert-mag	0.31	bdl	bdl	bdl	bdl	68.6	31.5	0.01	0.02	bdl	bdl	bdl	100.5	23 lay1 massive mag homogen 1
11-23	chert-mag	0.24	bdl	bdl	bdl	bdl	68.8	31.5	bdl	bdl	bdl	0.04	0.01	100.6	23 lay1 massive mag homogen 2
11-23	chert-mag	0.27	0.04	bdl	bdl	bdl	68.5	31.5	bdl	0.02	bdl	0.04	bdl	100.3	23 lay1 massive mag homogen 3
11-23	chert-mag	0.26	0.16	bdl	bdl	bdl	68.6	31.8	bdl	bdl	bdl	bdl	bdl	100.8	23 lay1 massive mag homogen 4
11-23	chert-mag	0.43	0.04	bdl	bdl	bdl	68.3	31.8	0.02	bdl	bdl	0.03	bdl	100.7	23 lay1 mag1
11-23	chert-mag	0.35	bdl	bdl	bdl	bdl	68.2	31.6	bdl	bdl	bdl	bdl	bdl	100.2	23 lay1 mag2
11-23	chert-mag	1.68	0.04	bdl	bdl	bdl	65.0	33.2	0.02	0.01	bdl	0.02	bdl	100.0	23 lay1 part3 mag core1
11-23	chert-mag	1.73	0.03	bdl	bdl	bdl	64.4	33.1	bdl	bdl	bdl	0.03	0.01	99.4	23 lay1 part3 mag core2
11-23	chert-mag	1.33	0.05	bdl	bdl	bdl	65.4	32.6	bdl	bdl	bdl	0.04	bdl	99.5	23 lay1 part3 mag core3
11-23	chert-mag	1.29	0.06	bdl	0.01	bdl	66.0	32.9	bdl	bdl	bdl	bdl	bdl	100.2	23 lay1 part3 mag core4
11-23	chert-mag	0.42	bdl	bdl	bdl	0.02	68.4	31.7	bdl	bdl	bdl	bdl	bdl	100.6	23 lay1 part3 mag rim1
11-23	chert-mag	0.24	bdl	bdl	bdl	0.01	68.6	31.4	bdl	bdl	bdl	bdl	0.02	100.3	23 lay1 part3 mag rim2
11-23	chert-mag	0.14	0.04	bdl	bdl	bdl	68.8	31.3	0.02	bdl	bdl	0.06	bdl	100.3	23 lay1 part3 mag rim3
11-23	chert-mag	0.12	bdl	bdl	bdl	bdl	68.8	31.3	0.01	bdl	bdl	bdl	bdl	100.2	23 lay1 part3 mag rim4
11-24	mag-carb	2.36	0.05	bdl	bdl	0.01	62.7	33.9	bdl	0.03	0.01	0.03	bdl	99.1	24 lay2 map area dark mag core1
11-24	mag-carb	1.38	0.10	bdl	bdl	0.03	65.2	32.8	bdl	0.01	bdl	bdl	bdl	99.6	24 lay2 map area dark mag core2
11-24	mag-carb	2.10	0.05	0.13	0.03	0.03	63.6	33.8	bdl	0.02	bdl	0.04	bdl	99.8	24 lay2 map area dark mag core3
11-24	mag-carb	0.27	bdl	bdl	bdl	0.03	68.6	31.6	bdl	bdl	bdl	bdl	bdl	100.6	24 lay2 map area bright mag rim1
11-24	mag-carb	0.19	0.04	bdl	bdl	0.01	68.7	31.4	bdl	0.02	bdl	bdl	bdl	100.3	24 lay2 map area bright mag rim2
11-24	mag-carb	0.37	bdl	bdl	bdl	0.02	67.9	31.4	bdl	bdl	bdl	0.03	bdl	99.7	24 lay4 mag1
11-24	mag-carb	0.84	bdl	0.12	bdl	0.04	66.0	31.8	bdl	0.02	0.02	bdl	bdl	98.8	24 lay5 microbanding mag1
11-24	mag-carb	0.65	0.04	bdl	bdl	0.03	66.7	31.6	bdl	0.02	0.02	bdl	bdl	99.2	24 lay5 microbanding mag2
11-24	mag-carb	0.62	bdl	bdl	bdl	0.04	66.8	31.6	bdl	0.03	0.02	bdl	bdl	99.2	24 lay5 microbanding mag3
11-24	mag-carb	0.82	bdl	0.14	bdl	0.04	66.5	31.9	bdl	0.07	bdl	bdl	bdl	99.4	24 lay5 microbanding mag4
11-33	mag-chl	1.01	bdl	bdl	bdl	bdl	65.7	31.6	bdl	0.23	bdl	0.01	bdl	98.7	33 map central zoned mag1 dark
11-33	mag-chl	0.35	bdl	bdl	0.01	bdl	68.3	31.3	0.01	0.13	bdl	0.06	bdl	100.2	33 map central zoned mag1 brig
11-33	mag-chl	1.66	bdl	bdl	bdl	bdl	65.3	32.7	bdl	0.38	0.01	0.04	bdl	100.2	33 map central zoned mag1 dark
11-33	mag-chl	0.71	bdl	bdl	0.02	0.02	68.0	32.0	bdl	0.18	bdl	0.05	bdl	101.0	33 map central zoned mag1 brig
11-33	mag-chl	0.85	bdl	bdl	0.01	bdl	66.7	31.7	bdl	0.21	0.02	bdl	0.02	99.5	33 map central zoned mag2 brig
11-33	mag-chl	0.94	0.05	bdl	bdl	0.02	67.0	32.1	bdl	0.21	bdl	0.06	bdl	100.4	33 map central zoned mag2 dark
11-33	mag-chl	0.58	bdl	bdl	0.01	bdl	66.6	31.0	bdl	0.18	bdl	0.04	bdl	98.5	33 zoned mag1 bright core
11-33	mag-chl	1.30	bdl	bdl	bdl	0.01	65.9	32.3	bdl	0.23	bdl	bdl	bdl	99.8	33 zoned mag1 dark interlayer
11-33	mag-chl	0.38	bdl	bdl	bdl	bdl	68.1	31.5	bdl	0.07	bdl	bdl	bdl	100.0	33 zoned mag1 dark rim
11-33	mag-chl	0.83	bdl	bdl	bdl	0.01	67.0	31.8	bdl	0.19	0.02	bdl	bdl	99.8	33 zoned mag2 intermediate rim
11-33	mag-chl	1.15	bdl	bdl	bdl	0.01	66.2	32.2	bdl	0.22	0.03	bdl	0.01	99.8	33 zoned mag2 dark interlay

Appendix B (continued): All EPMA analyses of magnetite (all values in wt.-%)

		SiO_2	TiO_2	Al_2O_3	Cr_2O_3	V_2O_3	Fe_2O_3	FeO	MnO	MgO	CaO	ZnO	NiO	Total	
	dl	0.01	0.03	0.08	0.01	0.01	0.02	0.02	0.01	0.01	0.01	0.01	0.01		
Sample	**Host**														**Comment**
11-33	mag-chl	0.16	bdl	bdl	bdl	0.01	68.8	31.3	bdl	0.02	0.02	bdl	bdl	100.3	33 zoned mag2 bright core
11-33	mag-chl	0.89	bdl	bdl	bdl	bdl	66.2	31.6	bdl	0.16	bdl	bdl	bdl	98.9	33 zoned mag3 dark core
11-33	mag-chl	0.18	bdl	bdl	bdl	bdl	69.6	31.7	0.01	0.02	bdl	0.03	bdl	101.5	33 zoned mag3 bright middle part
11-33	mag-chl	1.02	bdl	bdl	bdl	bdl	67.1	32.2	bdl	0.22	0.01	bdl	0.02	100.6	33 zoned mag3 dark rim
11-34	mag-chl	0.22	bdl	bdl	bdl	bdl	68.5	31.3	bdl	0.01	0.01	0.05	bdl	100.0	33 mappingcentral zoned mag2
11-34	mag-chl	0.26	bdl	bdl	bdl	bdl	68.9	31.6	bdl	0.02	bdl	0.03	bdl	100.9	34 mapping 150u mag brightest
11-34	mag-chl	0.15	bdl	bdl	bdl	bdl	69.0	31.4	0.02	0.03	bdl	bdl	bdl	100.6	34 mapping 150u mag brightest
11-34	mag-chl	1.91	bdl	bdl	bdl	0.01	64.9	33.5	0.01	0.13	0.03	bdl	bdl	100.6	34 mapping 150u mag darkest
11-34	mag-chl	2.01	0.04	bdl	bdl	bdl	64.6	33.7	bdl	0.12	0.01	bdl	bdl	100.6	34 mapping 150u mag darkest
11-34	mag-chl	0.80	bdl	bdl	bdl	bdl	67.6	32.2	bdl	0.06	0.04	0.01	bdl	100.7	34 mapping 150u mag brightest
11-34	mag-chl	1.02	bdl	bdl	bdl	bdl	67.0	32.5	bdl	0.05	bdl	bdl	bdl	100.6	34 mapping 150u mag brightest
11-34	mag-chl	1.88	0.03	bdl	bdl	0.01	64.7	33.5	bdl	0.08	0.01	0.06	bdl	100.3	34 mapping 40u mag dark inner
11-34	mag-chl	0.86	0.03	bdl	bdl	bdl	67.5	32.3	bdl	0.09	bdl	bdl	bdl	100.9	34 mapping 40u mag bright outer
11-39	mag-chl	2.20	0.06	bdl	bdl	0.01	64.6	33.6	bdl	0.43	0.03	0.03	bdl	101.0	11b-39 mag in mag rich layer
11-39	mag-chl	0.44	bdl	bdl	bdl	0.02	68.9	31.7	bdl	0.18	0.04	0.06	0.01	101.4	11b-39 mag 2 in mag rich layer
11-39	mag-chl	1.95	0.08	bdl	0.04	bdl	64.8	33.1	bdl	0.46	0.01	0.05	bdl	100.5	11b-39 mag 1 in fine mag chlorite
11-39	mag-chl	1.51	0.04	bdl	bdl	bdl	66.0	32.6	bdl	0.41	0.01	0.04	bdl	100.7	11b-39 mag 2 in fine mag chlorite
11-39	mag-chl	1.80	0.04	bdl	0.02	0.01	65.4	33.0	bdl	0.45	0.03	bdl	0.01	100.9	11b-39 mag 3 in fine mag chlorite
11-39	mag-chl	0.82	bdl	bdl	bdl	0.02	67.8	32.2	bdl	0.17	0.01	0.03	bdl	101.0	11b-39 mag 1 in fine mag stilp chl
11-39	mag-chl	2.05	0.04	bdl	bdl	bdl	64.8	33.2	bdl	0.48	0.01	0.09	bdl	100.7	11b-39 mag 2 in fine mag stilp chl
11-39	mag-chl	1.77	0.05	bdl	bdl	bdl	65.6	33.1	bdl	0.38	0.01	bdl	bdl	101.0	11b-39 mag 1 in lg mag stilpn chl ap
11-39	mag-chl	0.66	bdl	bdl	bdl	bdl	68.0	31.9	bdl	0.14	0.01	bdl	bdl	100.7	11b-39 mag 2 in lg mag stilpn chl ap
11-40	mag-chl	0.30	bdl	bdl	bdl	0.02	68.9	31.6	bdl	0.01	0.10	bdl	bdl	101.0	11b-40 mag chlorite w/ ank qtz
11-40	mag-chl	0.92	0.03	bdl	bdl	bdl	66.9	32.2	0.02	0.01	0.13	bdl	bdl	100.1	11b-40 mag 2 chlorite w/ ank qtz
11-40	mag-chl	1.81	0.07	bdl	0.01	bdl	64.9	33.5	bdl	0.02	bdl	0.06	bdl	100.4	11b-40 SOI2 mag 1 chert w carb chl
11-40	mag-chl	1.72	bdl	bdl	bdl	0.01	65.0	33.2	bdl	0.09	0.03	bdl	bdl	100.0	11b-40 SOI2 mag 2 chert w carb chl
11-41a	chert	1.37	bdl	bdl	bdl	bdl	66.6	33.2	bdl	bdl	0.01	0.02	bdl	101.2	11b-41a SOI1 mag 1 mag layer
11-41a	chert	0.43	bdl	bdl	bdl	bdl	68.5	31.8	bdl	bdl	bdl	0.03	0.01	100.8	11b-41a SOI1 mag 2 mag layer
11-41a	chert	0.08	0.06	bdl	bdl	0.01	69.6	31.6	bdl	0.02	bdl	0.01	bdl	101.4	11b-41a SOI1 mag 3 mag layer
11-41a	chert	1.75	bdl	bdl	bdl	0.01	65.2	33.5	bdl	0.01	bdl	bdl	bdl	100.5	11b-41a SOI2 mag 1 in black chert
11-41a	chert	0.92	bdl	bdl	bdl	bdl	67.0	32.4	0.01	bdl	bdl	0.02	bdl	100.3	11b-41a SOI2 mag 1 in black chert
11-41a	chert	1.75	bdl	bdl	0.01	bdl	65.3	33.5	bdl	0.01	bdl	0.04	0.01	100.7	11b-41a SOI3 mag 1 mag rich chert
11-41b	chert	1.35	0.06	bdl	bdl	bdl	66.5	33.1	0.01	0.03	0.02	bdl	bdl	101.1	11b-41b SOI1 mag 1 mag rich layer
11-41b	chert	0.80	0.04	bdl	bdl	0.01	67.9	32.4	0.02	0.01	0.02	0.06	bdl	101.3	11b-41b SOI1 mag 2 mag rich layer
11-41b	chert	0.98	bdl	bdl	bdl	bdl	67.7	32.7	bdl	0.03	bdl	bdl	bdl	101.4	11b-41b SOI1 mag 3 mag rich layer
11-41b	chert	0.77	bdl	bdl	0.02	bdl	68.2	32.4	0.03	bdl	0.02	0.10	bdl	101.6	11b-41b SOI1 mag 4 mag rich layer
11-41b	chert	0.16	bdl	bdl	bdl	bdl	69.5	31.6	0.03	bdl	0.04	bdl	bdl	101.4	11b-41b SOI1 mag 5
11-41b	chert	1.10	bdl	bdl	bdl	bdl	67.0	32.7	0.02	bdl	0.01	0.04	bdl	100.9	11b-41b SOI2 mag1
11-41b	chert	0.58	0.04	bdl	bdl	bdl	68.2	32.1	0.01	bdl	bdl	0.02	bdl	101.0	11b-41b SOI2 mag2
11-41b	chert	0.86	0.05	bdl	bdl	bdl	67.8	32.6	bdl	bdl	bdl	0.02	bdl	101.4	11b-41b SOI2 mag3
11-41b	chert	0.19	bdl	bdl	bdl	bdl	69.9	31.8	0.01	bdl	bdl	0.05	bdl	102.0	11b-41b SOI3 mag1
11-41b	chert	1.21	0.05	bdl	bdl	bdl	67.3	33.1	0.01	0.04	0.05	0.03	0.01	101.7	11b-41b SOI3 mag2
11-41b	chert	0.96	0.05	bdl	bdl	bdl	67.9	32.8	0.01	0.09	bdl	bdl	bdl	101.8	11b-41b mag3 with po inclusion
11-41b	chert	0.41	bdl	bdl	bdl	bdl	69.9	32.3	bdl	0.04	bdl	0.03	bdl	102.7	11b-41b mag1 in massive mag
11-41b	chert	1.34	bdl	bdl	bdl	bdl	66.4	33.1	bdl	0.01	bdl	bdl	bdl	100.9	11b-41b mag2 in massive mag
11-41b	chert	0.10	bdl	bdl	bdl	bdl	70.5	31.9	0.01	bdl	bdl	0.04	bdl	102.6	11b-41b mag3 in massive mag
11-41b	chert	0.40	0.04	bdl	bdl	bdl	69.2	32.1	0.01	bdl	bdl	bdl	bdl	101.8	11b-41b mag4 in massive mag
11-41b	chert	0.43	bdl	bdl	bdl	bdl	66.5	30.9	0.01	0.02	0.04	bdl	bdl	97.9	11b-41b mag/hem2 in massive mag
11-41b	chert	0.35	bdl	bdl	bdl	bdl	69.1	31.9	0.02	0.02	0.02	0.03	bdl	101.4	11b-41b SOI5 center type3 mag
11-41b	chert	0.74	0.04	bdl	bdl	bdl	68.1	32.4	0.02	0.01	0.01	bdl	0.02	101.3	11b-41b SOI5 rim type3 mag
11-41b	chert	1.45	bdl	bdl	bdl	0.01	66.5	33.3	bdl	0.03	0.01	0.04	bdl	101.4	11b-41b SOI5 type3 mag intergr py
11-41b	chert	1.27	0.05	bdl	bdl	bdl	66.7	33.0	0.02	0.02	0.02	0.04	bdl	101.1	11b-41b SOI5 type 3 mag
11-41b	chert	0.73	0.04	bdl	bdl	bdl	68.1	32.4	bdl	0.02	bdl	0.06	bdl	101.3	11b-41b type 3 mag w/ mon
median	mean	0.52	0.01	0.01	0.00	0.00	68.0	31.8	0.01	0.03	0.01	0.00	0.00	100.4	
max	max	2.78	6.68	0.66	0.82	0.06	70.5	37.9	0.20	0.63	0.21	0.11	0.04	102.7	
min	min	0.00	0.00	0.00	0.00	0.00	56.6	30.7	0.00	0.00	0.00	0.00	0.00	97.7	

Analytical conditions: All analyses performed at 20 kV, 20 seconds count time on peak and 10 seconds on background. 5 microns spot size.
Standards for major elements Fe (hematite), Ca and Si (diopside), Al and Mg (chromite). Standards measured as unknowns reproduced better than +/- 1%.

Appendix C: LA-ICP-MS results for all magnetite analyses. All results in ppm.

		Mg	Al	Si	P	Ca	Sc	Ti	V	Cr	Mn	Co	Ni	Cu	Zn	Ga	Ge	As	Y	Zr	Nb
	Isotope	25	27	29	31	43	45	47	51	52	55	59	60	65	66	69	74	75	89	90	93
	MRE [%]	7.2	7.1	14	186	21	17	5.6	4.6	13	4.0	8.6	6.4	13	6.0	7.1	4.2	19	10	10	16
	dl [ppm]	0.7	0.3	25	9.7	23	0.05	0.4	0.04	0.25	0.18	0.03	0.30	0.03	0.3	0.2	0.17	0.08	0.01	0.01	0.014
Sample	**Layer type**																				
A028	chlorite	987	533	4212	389	1016	0.13	3294	132.3	51.6	613	15.5	165	176	4.32	1.08	6.38	2.00	301	7.21	6.030
A028	chlorite	1023	506	5629	17	296	0.17	917	128.9	15.1	308	6.43	47.6	147	5.00	1.60	5.72	1.47	3.16	1.39	4.827
A028	chlorite	1170	694	8509	16	672	0.20	2242	129.8	28.2	340	3.04	33.1	29	3.40	1.23	5.58	0.56	1.46	8.65	7.132
A028	chlorite	2851	1930	16307	30	2750	0.33	346	128.5	24.9	788	31.7	117	505	6.59	2.04	5.41	64.3	2.61	0.55	2.678
B013-1	magnetite	111	55	32589	59	50	0.29	19.1	16.9	0.64	45	2.86	40.9	0.28	19.0	0.67	8.33	1.73	0.27	0.07	0.303
B013-1	magnetite	135	103	31814	92	158	0.27	18.3	15.7	0.82	47	2.89	39.3	0.59	18.9	0.81	7.50	1.92	0.46	0.16	0.067
B013-1	magnetite	141	56	33830	66	126	0.44	22.0	16.6	1.07	50	2.84	39.7	0.63	19.0	0.61	7.86	2.19	0.40	0.32	0.411
B013-1	magnetite	106	77	19691	42	131	0.22	17.2	16.8	0.61	46	2.81	40.3	0.46	18.9	0.72	6.99	1.95	0.27	0.14	0.195
B013-1	magnetite	148	51	16652	154	135	0.45	24.5	16.9	0.77	54	2.84	44.1	0.34	19.9	0.66	8.35	3.52	0.58	0.79	0.464
B013-1	magnetite	115	111	46266	29	53	0.42	23.3	15.6	0.51	45	2.80	38.4	0.48	16.6	0.73	6.67	1.54	0.26	0.28	0.416
B013-1	magnetite	65	58	37665	21	52	0.41	14.2	16.5	0.61	50	2.97	25.0	0.42	21.0	0.66	6.71	2.02	0.25	0.18	0.145
B013-1	magnetite	125	74	17357	9866	4558	0.29	13.0	17.0	0.66	51	3.12	46.6	1.01	21.0	0.74	12.3	2.19	9.25	0.42	0.007
B013-1	magnetite	193	108	31251	68	95	0.29	19.4	17.9	0.55	44	2.97	43.6	0.43	19.8	0.88	8.36	2.22	0.37	0.14	0.099
B013-1	magnetite	1933	116	33735	4927	9297	0.46	17.9	18.6	0.67	464	2.99	43.2	0.38	19.9	0.83	9.11	1.77	9.24	0.40	0.158
B013-1	magnetite	69	61	36720	45	62	0.33	15.9	16.3	0.95	55	2.69	27.8	0.23	19.5	0.66	10.0	2.63	0.30	0.53	0.230
B013-1	magnetite	1131	128	15348	91	159	0.88	15.6	13.1	0.79	123	2.69	12.6	0.34	29.5	0.64	88.2	4.67	0.46	0.41	0.003
B013-1	magnetite	92	66	31672	87	64	0.13	19.5	10.5	0.74	50	2.41	6.38	0.38	19.2	0.70	11.5	2.35	0.31	0.11	0.374
B013-2	magnetite	996	52	5998	204	109	0.21	42.1	16.6	0.65	94	2.88	21.5	0.15	11.7	0.84	4.64	0.87	0.44	0.03	0.075
B013-2	magnetite	2027	96	16725	2531	2673	0.37	46.9	17.5	0.90	689	3.15	22.3	1.03	17.5	0.95	7.71	2.30	5.21	0.09	0.220
B013-2	magnetite	3549	143	34642	452	854	0.38	44.6	16.9	0.73	303	3.28	22.5	0.20	21.5	0.92	8.96	1.13	1.09	0.10	0.339
B013-2	magnetite	12268	461	92064	658	587	1.06	51.1	15.0	1.32	1634	4.25	26.0	0.76	53.3	0.90	8.03	1.65	1.82	0.16	0.089
B013-2	magnetite	1808	76	19174	95	135	0.28	42.4	15.4	0.82	123	3.05	19.9	0.28	13.8	0.84	6.32	0.97	0.37	0.04	0.363
B013-2	magnetite	5901	254	49150	104	103	0.67	41.1	15.4	12.3	257	3.63	21.8	0.48	32.3	0.88	6.90	0.76	0.32	0.10	0.899
B013-2	magnetite	1207	65	9014	44	50	0.17	42.4	14.6	0.41	118	2.85	21.0	0.09	14.3	0.89	6.79	1.17	0.31	0.03	0.529
B013-2	magnetite	1098	44	4502	46	171	0.23	41.9	14.6	0.78	133	2.84	20.4	0.21	12.0	0.85	5.98	0.66	0.47	0.04	0.129
B013-2	magnetite	1613	97	2399	16	270	0.28	46.2	16.8	1.06	234	2.82	21.4	0.12	13.5	0.84	22.2	1.07	0.28	0.04	0.269
B013-2	magnetite	489	32	4015	245	336	0.18	44.4	14.6	0.85	101	2.86	20.7	0.15	9.85	0.83	8.03	0.69	0.45	0.05	0.636
B013-2	magnetite	2149	96	26079	291	348	0.33	38.6	14.7	0.55	156	2.91	19.8	0.30	16.4	0.87	8.94	0.88	0.93	0.23	0.043
B013-2	magnetite	1229	51	10046	452	769	0.20	38.3	15.3	0.68	115	2.85	19.8	0.89	11.7	0.85	6.27	0.67	1.13	0.11	0.096
B013-2	magnetite	1321	25	6974	109	280	0.20	40.9	15.4	0.49	529	2.94	19.3	0.30	8.47	0.85	5.79	0.53	0.69	0.04	0.086
B013-2	magnetite	1831	28	5734	59	309	0.14	51.0	14.9	0.30	438	2.80	20.6	0.13	12.0	0.88	8.38	1.89	0.88	0.10	2.459
D015	magnetite	221	90	4876	279	263	0.10	11.9	2.6	0.79	54	0.69	2.40	1.23	3.95	0.51	8.90	0.79	1.96	0.08	0.086
D015	magnetite	144	64	1852	332	310	0.09	12.2	2.2	0.51	53	0.65	2.28	0.35	4.22	0.46	7.61	0.44	1.05	0.10	0.104
D015	magnetite	229	46	2224	597	536	0.10	12.4	2.7	1.17	41	0.64	2.18	0.30	4.28	0.53	7.61	0.47	2.56	0.07	0.063
D015	magnetite	129	93	1580	1425	562	0.09	12.8	2.7	1.23	42	0.63	2.19	0.21	4.44	0.51	7.91	0.53	2.50	0.12	0.088
D015	magnetite	907	33	8188	416	291	0.08	10.5	2.5	1.22	42	0.69	2.46	0.93	4.59	0.48	8.24	0.78	2.68	0.25	0.005
D015	magnetite	133	57	1187	244	187	0.26	12.8	2.2	0.64	41	0.53	2.73	0.46	4.22	0.47	6.84	0.42	1.07	0.16	0.061
D015	magnetite	179	120	5104	553	534	0.32	14.6	2.6	1.39	61	0.72	1.76	0.45	5.58	0.56	9.24	1.30	3.04	0.13	0.023
D015	magnetite	111	99	2365	183	142	0.13	12.4	2.1	0.87	40	0.64	2.25	0.38	3.88	0.47	7.59	0.40	1.23	0.08	0.034

Appendix C (continued): LA-ICP-MS results for all magnetite analyses. All results in ppm.

		Mo	Ag	Cd	In	Sn	Sb	Cs	Ba	La	Sm	Yb	Hf	Ta	W	Pb	
	Isotope	95	109	111	115	118	121	133	137	139	147	172	178	181	182	208	
	MRE [%]	31	29	42	38	25	15	22	12	13	31	26	41	30	14	9.3	
	dl [ppm]	0.1	0.1	0.2	0.07	1.4	0.23	0.09	0.1	0.01	0.04	0.03	0.04	0.01	0.08	0.05	
Sample	**Layer type**																**Comment**
A028	chlorite	2.131	0.704	bdl	bdl	1.6	7.95	0.349	3.45	2.851	28.6	16.6	0.143	0.064	3.09	52.2	A028SOI1across
A028	chlorite	1.282	0.472	bdl	bdl	1.5	3.67	0.532	7.94	0.186	0.230	0.574	0.154	0.087	1.30	1.92	A028SOI2acrosselongated
A028	chlorite	bdl	bdl	bdl	bdl	bdl	1.94	1.031	4.88	0.118	0.120	0.133	0.091	0.118	1.21	25.4	A028SOI2acrosselongated2
A028	chlorite	bdl	5.082	bdl	bdl	1.6	3.70	2.035	27.5	0.244	0.200	0.315	bdl	0.073	1.26	0.158	A028SOI2acrosselongated3
B013-1	magnetite	bdl	bdl	bdl	bdl	bdl	3.29	bdl	6.84	0.058	bdl	bdl	bdl	bdl	1.03	0.523	B013-1SOI1along
B013-1	magnetite	bdl	bdl	bdl	bdl	bdl	2.67	0.097	14.5	0.112	0.044	0.032	bdl	bdl	0.452	1.42	B013-1SOI1across1
B013-1	magnetite	bdl	bdl	bdl	bdl	2.0	4.46	bdl	5.36	0.105	bdl	0.034	bdl	bdl	1.52	0.900	B013-1SOI1across2
B013-1	magnetite	bdl	bdl	bdl	bdl	bdl	3.33	0.097	9.81	0.047	0.045	bdl	bdl	bdl	1.18	1.54	B013-1SOI1across3
B013-1	magnetite	bdl	bdl	bdl	bdl	bdl	6.74	bdl	3.74	0.169	bdl	0.050	bdl	bdl	2.07	0.618	B013-1SOI2across1
B013-1	magnetite	bdl	bdl	bdl	bdl	1.8	3.05	0.110	11.0	0.074	bdl	0.045	bdl	bdl	1.19	0.622	B013-1SOI2across2
B013-1	magnetite	bdl	bdl	bdl	bdl	bdl	3.02	bdl	4.13	0.034	0.044	bdl	bdl	bdl	0.677	1.12	B013-1SOINacross
B013-1	magnetite	bdl	bdl	bdl	bdl	bdl	4.17	0.106	9.02	1.271	1.211	0.325	bdl	bdl	0.372	0.844	B013-1SOINacross2
B013-1	magnetite	bdl	bdl	bdl	bdl	bdl	3.14	bdl	19.0	0.066	bdl	0.056	bdl	bdl	0.512	0.896	B013-1SOINacross3
B013-1	magnetite	bdl	bdl	bdl	bdl	bdl	3.04	0.155	14.9	1.093	0.581	0.356	bdl	bdl	0.672	1.16	B013-1SOINacross4
B013-1	magnetite	bdl	bdl	bdl	bdl	1.5	6.60	bdl	8.10	0.038	bdl	0.032	bdl	bdl	1.56	1.09	B013-1SOINacross5
B013-1	magnetite	bdl	bdl	bdl	bdl	bdl	4.86	bdl	1.26	0.112	0.067	0.069	bdl	bdl	0.415	0.887	B013-1SOINacross6
B013-1	magnetite	bdl	bdl	bdl	bdl	bdl	4.56	bdl	6.26	0.060	bdl	0.042	bdl	0.010	1.19	0.128	B013-1SOINacross7
B013-2	magnetite	bdl	bdl	bdl	bdl	bdl	1.32	bdl	0.17	0.103	bdl	0.038	bdl	bdl	0.710	0.650	B013-2SOI1aroundoutside
B013-2	magnetite	bdl	bdl	bdl	bdl	1.4	5.37	bdl	4.85	1.808	0.394	0.171	bdl	0.014	2.23	0.630	B013-2SOI1aroundinside
B013-2	magnetite	bdl	bdl	bdl	bdl	bdl	2.91	bdl	1.95	0.273	0.076	0.077	bdl	bdl	0.592	0.484	B013-2SOI1across
B013-2	magnetite	bdl	0.137	bdl	bdl	bdl	4.34	0.179	2.55	0.445	0.105	0.125	bdl	bdl	1.43	0.435	B013-2SOI1across2
B013-2	magnetite	bdl	bdl	bdl	bdl	bdl	2.09	0.088	0.88	0.119	bdl	0.038	bdl	bdl	0.616	0.313	B013-2SOI2across
B013-2	magnetite	bdl	bdl	bdl	bdl	bdl	2.12	0.161	0.44	0.056	bdl	bdl	bdl	0.014	0.717	0.241	B013-2SOI2acrosshm
B013-2	magnetite	bdl	bdl	bdl	bdl	bdl	1.28	bdl	0.51	0.122	bdl	0.043	bdl	bdl	0.889	0.234	B013-2SOI3intocenter
B013-2	magnetite	bdl	bdl	bdl	bdl	bdl	0.95	bdl	0.72	0.174	bdl	bdl	bdl	bdl	1.14	0.669	B013-2SOI3aroundrim
B013-2	magnetite	bdl	bdl	bdl	bdl	1.5	1.47	bdl	1.72	0.080	bdl	bdl	bdl	bdl	0.505	0.192	B013-2SOI3across2
B013-2	magnetite	bdl	bdl	bdl	bdl	bdl	1.18	bdl	0.52	0.184	bdl	0.040	bdl	bdl	0.747	0.511	B013-2SOI3across
B013-2	magnetite	bdl	bdl	bdl	bdl	bdl	1.68	bdl	1.43	0.231	0.052	0.037	bdl	bdl	0.497	0.867	B013-2SOI4across
B013-2	magnetite	bdl	bdl	bdl	bdl	bdl	3.41	bdl	1.34	0.352	0.188	0.112	bdl	bdl	1.26	1.25	B013-2SOI4across2
B013-2	magnetite	bdl	bdl	bdl	bdl	bdl	4.85	bdl	1.44	0.177	0.054	0.113	bdl	bdl	1.68	0.771	B013-2SOI4across3
B013-2	magnetite	bdl	bdl	bdl	bdl	1.4	5.26	bdl	1.39	0.365	0.058	0.161	bdl	bdl	2.06	0.506	B013-2SOI4around1
D015	magnetite	0.131	bdl	bdl	bdl	bdl	0.76	bdl	1.72	1.025	0.079	0.213	bdl	bdl	6.47	0.456	D015SOI1across1
D015	magnetite	bdl	bdl	bdl	bdl	bdl	0.39	bdl	1.43	0.475	0.065	0.104	bdl	bdl	0.749	0.577	D015SOI1across2
D015	magnetite	bdl	bdl	bdl	bdl	bdl	0.62	bdl	4.55	0.877	0.231	0.177	bdl	bdl	0.674	0.652	D015SOI1across3
D015	magnetite	0.157	bdl	bdl	bdl	bdl	0.59	bdl	4.23	0.934	0.153	0.225	bdl	bdl	0.680	1.35	D015SOI1across4
D015	magnetite	bdl	0.120	bdl	bdl	bdl	0.88	bdl	3.31	1.201	0.137	0.230	bdl	0.015	6.02	0.875	D015SOI1acrossPo
D015	magnetite	0.176	0.119	bdl	0.090	1.7	0.65	0.097	1.52	0.466	0.043	0.035	bdl	0.015	1.77	1.79	D015SOI2homogenous1
D015	magnetite	0.115	0.108	0.220	0.096	2.9	0.57	0.120	4.36	1.369	0.260	0.204	0.060	0.016	2.56	0.235	D015SOI2homogenous2
D015	magnetite	bdl	0.103	bdl	bdl	1.7	bdl	bdl	1.57	0.522	0.083	0.103	bdl	bdl	1.08	0.598	D015SOI2homogenous3

Appendix C (continued): LA-ICP-MS results for all magnetite analyses. All results in ppm.

		Mg	Al	Si	P	Ca	Sc	Ti	V	Cr	Mn	Co	Ni	Cu	Zn	Ga	Ge	As	Y	Zr	Nb
	Isotope	25	27	29	31	43	45	47	51	52	55	59	60	65	66	69	74	75	89	90	93
	MRE [%]	7.2	7.1	14	186	21	17	5.6	4.6	13	4.0	8.6	6.4	13	6.0	7.1	4.2	19	10	10	16
	dl [ppm]	0.7	0.3	25	9.7	23	0.05	0.4	0.04	0.25	0.18	0.03	0.30	0.03	0.3	0.2	0.17	0.08	0.01	0.01	0.014
Sample	**Layer type**																				
D015	magnetite	111	129	2414	253	398	0.36	12.3	2.1	0.83	42	0.64	1.88	0.25	6.28	0.57	11.8	1.83	1.76	0.11	0.046
D015	magnetite	485	216	3984	15	46	0.09	17.0	1.3	0.64	35	0.66	9.02	0.14	4.67	0.47	19.8	0.41	0.12	0.04	0.015
D015	magnetite	3834	84	15069	16	8383	0.10	21.3	2.7	0.38	579	0.59	3.58	0.68	7.32	0.43	11.7	0.66	0.78	0.38	0.302
D015	magnetite	39	73	953	131	81	0.08	13.5	3.0	0.61	42	0.63	3.76	0.42	4.50	0.46	7.20	0.33	0.71	0.14	0.015
D015	magnetite	26	48	1437	112	46	0.08	13.3	2.7	1.39	46	0.65	3.91	0.37	4.40	0.57	6.98	0.14	0.13	0.07	0.036
D015	magnetite	115	173	1901	180	136	0.08	15.1	3.1	0.71	51	0.68	3.52	0.21	4.16	0.51	7.29	0.40	0.62	0.10	0.050
D015	magnetite	193	97	2830	296	302	0.09	15.1	2.9	1.16	49	0.64	4.40	0.60	4.71	0.58	7.92	0.38	2.40	0.57	0.055
SM11	chert	43	26	320	12	31	bdl	3.32	7.3	0.81	322	1.07	9.46	0.20	64.2	1.27	1.95	0.12	0.02	0.05	bdl
SM11	chert	120	31	14957	14	27	0.32	3.05	6.1	0.44	289	1.03	8.36	0.09	60.4	1.10	2.78	0.44	0.01	0.02	bdl
SM11	chert	26	18	280	11	26	0.08	2.65	6.9	0.38	310	0.97	9.03	0.06	57.2	1.10	1.74	0.10	bdl	bdl	bdl
SM11	chert	48	14	458	15	24	0.08	3.71	6.9	0.91	285	1.02	10.9	0.17	55.5	1.15	1.64	0.14	bdl	0.05	bdl
SM11	chert	128	24	1759	16	26	0.15	4.23	8.1	0.78	310	1.23	11.1	0.10	58.5	1.18	9.81	0.20	0.01	0.04	0.016
SM11	magnetite	649	37	2258	12	28	1.35	10.1	17.7	0.63	361	6.41	28.7	0.17	58.6	1.40	17.6	0.33	0.05	0.66	bdl
SM11	magnetite	120	9	913	23	28	0.41	7.64	17.4	0.58	325	6.20	28.4	0.08	52.4	1.36	1.84	0.09	2.95	6.24	0.036
SM11	magnetite	666	33	2884	12	30	1.28	9.50	17.3	0.75	342	6.25	27.0	0.13	56.7	1.35	18.5	0.20	0.29	4.33	bdl
SM11	magnetite	1736	35	3806	25	103	1.11	14.4	19.8	1.59	308	6.25	39.1	0.12	61.3	1.43	8.28	0.36	0.06	0.07	0.083
SM11	magnetite	12887	86	23814	75	71	1.59	17.1	18.6	2.72	314	7.14	46.0	0.45	87.8	1.46	7.68	0.60	0.26	0.85	0.113
SM11	jasper	29	18	1907	12	27	0.21	1.30	11.7	0.95	381	2.80	4.99	0.22	80.7	0.95	3.02	0.15	bdl	0.07	0.004
SM11	magnetite	739	47	2168	24	56	1.97	18.6	17.7	0.80	335	5.76	25.7	0.05	56.9	1.19	7.60	0.26	0.02	0.07	0.018
SM11	magnetite	130	21	698	25	62	0.53	16.7	17.9	0.56	333	5.59	26.0	0.05	54.9	1.20	1.52	0.23	2.20	3.74	0.031
SM11	magnetite	147	23	1044	24	60	0.48	10.7	17.9	0.60	322	5.75	25.4	0.06	54.0	1.19	1.39	0.22	bdl	0.02	0.020
SM11	magnetite	123	19	495	23	55	0.51	15.8	17.8	0.52	331	5.79	25.7	0.05	53.4	1.20	1.62	0.32	0.01	0.05	0.133
SM11	magnetite	624	29	1428	18	70	1.25	17.6	18.3	0.99	332	5.58	27.5	0.03	56.3	1.18	3.83	0.37	0.05	0.08	0.062
SM11	magnetite	655	53	2609	26	53	1.28	12.6	17.8	0.96	339	5.81	24.9	0.05	56.6	1.21	3.63	0.46	0.16	0.04	0.019
SM11	magnetite	116	22	404	36	92	0.30	12.6	17.2	0.46	311	5.56	24.3	0.07	56.1	1.15	1.56	0.31	0.02	0.02	0.079
SM11	magnetite	337	42	19155	242	132	1.64	11.2	17.5	0.71	330	5.76	24.0	0.05	59.7	1.18	2.95	0.75	0.55	0.05	bdl
SM11	magnetite	947	34	2305	20	54	1.58	12.8	19.0	2.00	269	5.81	39.9	0.05	57.0	1.21	8.04	0.21	0.03	0.07	0.089
SM11	magnetite	671	37	3455	22	54	1.01	11.8	18.6	1.63	280	5.89	37.2	0.05	56.3	1.20	8.77	0.50	0.12	0.03	bdl
SM11	magnetite	874	44	1873	23	73	0.82	19.0	18.3	1.64	435	5.99	37.8	0.05	55.0	1.29	12.4	0.66	0.12	0.42	0.146
SM052	magnetite	99	55	733	48	28	0.06	7.80	2.3	0.84	182	0.05	5.33	0.09	17.4	0.28	9.78	0.26	0.15	0.15	0.020
SM052	magnetite	30	58	238	12	30	bdl	7.79	1.2	0.67	194	0.05	5.40	0.08	19.8	0.26	7.39	0.10	0.02	0.05	bdl
SM052	magnetite	183	56	3296	155	167	bdl	7.71	1.3	0.67	177	0.07	4.80	0.33	14.2	0.33	12.5	0.37	0.44	0.82	bdl
SM052	magnetite	80	62	563	138	110	0.07	8.38	1.3	0.40	191	0.06	5.51	0.13	17.0	0.33	12.1	0.23	0.41	0.05	bdl
SM052	jasper	59	43	17278	29	51	0.14	2.47	1.7	8.29	60	0.60	14.8	6.57	12.9	0.54	6.68	0.26	0.08	0.70	bdl
SM052	jasper	130	53	7285	22	56	0.12	1.6	1.0	0.42	62	0.39	20.3	0.05	2.81	0.33	2.74	0.63	0.13	0.14	bdl
SM052	magnetite	62	75	449	58	53	0.12	6.7	1.1	0.44	191	0.07	4.73	0.07	18.7	0.26	1.64	0.22	0.06	0.02	bdl
SM052	magnetite	199	91	858	659	548	0.11	8.4	1.2	0.79	194	0.04	4.97	0.04	18.3	0.27	15.1	0.22	0.85	0.03	bdl
SM052	magnetite	43	73	628	37	69	0.15	13.9	1.1	0.96	201	0.07	5.06	0.07	20.9	0.23	2.95	0.65	0.03	0.10	0.015
SM052	magnetite	64	77	275	24	69	0.13	11.2	1.2	0.56	204	0.05	4.68	0.06	19.9	0.27	1.96	0.26	0.01	0.04	bdl
SM052	magnetite	158	92	751	180	117	0.12	10.3	1.2	0.49	190	0.07	4.70	0.05	18.6	0.30	13.2	0.38	0.72	0.07	0.030

Appendix C (continued): LA-ICP-MS results for all magnetite analyses. All results in ppm.

		Mo	Ag	Cd	In	Sn	Sb	Cs	Ba	La	Sm	Yb	Hf	Ta	W	Pb	
	Isotope	95	109	111	115	118	121	133	137	139	147	172	178	181	182	208	
	MRE [%]	31	29	42	38	25	15	22	12	13	31	26	41	30	14	9.3	
	dl [ppm]	0.1	0.1	0.2	0.07	1.4	0.23	0.09	0.1	0.01	0.04	0.03	0.04	0.01	0.08	0.05	
Sample	**Layer type**																**Comment**
D015	magnetite	0.108	0.148	0.428	0.130	2.1	0.66	0.143	2.08	0.648	0.097	0.110	0.059	0.014	0.634	0.230	D015SOI2homogenous4
D015	magnetite	bdl	bdl	bdl	bdl	bdl	0.23	bdl	0.10	bdl	bdl	0.039	bdl	bdl	bdl	0.815	D015SOI3maginchert1
D015	magnetite	bdl	0.294	bdl	bdl	1.9	1.15	bdl	1.25	0.197	bdl	0.107	bdl	0.030	2.71	0.686	D015SOI3maginchert-stilp
D015	magnetite	bdl	bdl	bdl	bdl	bdl	bdl	bdl	2.20	5.456	0.629	0.035	bdl	0.010	bdl	0.485	D015SOI4acrosssinglemag
D015	magnetite	0.100	bdl	bdl	bdl	bdl	bdl	bdl	8.89	0.933	0.094	bdl	bdl	0.013	0.238	0.755	D015SOI4aroundouterzone
D015	magnetite	bdl	bdl	bdl	bdl	bdl	bdl	bdl	4.84	0.176	0.050	0.056	bdl	bdl	0.262	1.51	D015SOI4aroundouterzone2
D015	magnetite	bdl	0.166	bdl	bdl	bdl	0.31	bdl	8.71	0.381	0.094	0.327	bdl	bdl	0.162	0.689	D015SOI4aroundouterzone3
SM11	chert	bdl	bdl	0.315	bdl	bdl	bdl	bdl	0.71	bdl	bdl	bdl	bdl	bdl	bdl	0.209	SM11SOI1outparallel
SM11	chert	bdl	bdl	0.226	bdl	bdl	0.78	bdl	bdl	0.025	bdl	bdl	bdl	bdl	0.145	bdl	SM11SOI1innerparallel
SM11	chert	bdl	bdl	bdl	bdl	bdl	bdl	bdl	bdl	bdl	bdl	bdl	bdl	bdl	bdl	0.117	SM11SOI1homogenous
SM11	chert	bdl	bdl	0.374	bdl	bdl	bdl	bdl	0.12	bdl	bdl	bdl	bdl	bdl	bdl	0.229	SM11SOI1zonedcross
SM11	chert	bdl	bdl	0.612	bdl	bdl	bdl	bdl	0.96	0.019	bdl	bdl	bdl	bdl	0.099	0.243	SM11SOI1homogenouscross
SM11	magnetite	bdl	bdl	bdl	bdl	bdl	0.24	bdl	bdl	bdl	bdl	bdl	bdl	bdl	bdl	0.133	SM11SOI2zonedinternalparallel
SM11	magnetite	bdl	bdl	bdl	bdl	bdl	bdl	bdl	bdl	bdl	0.057	0.270	bdl	bdl	bdl	0.088	SM11SOI2zonedouterparallel
SM11	magnetite	bdl	bdl	bdl	bdl	bdl	bdl	bdl	0.15	0.021	bdl	bdl	bdl	bdl	bdl	0.367	SM11SOI2zonedcross
SM11	magnetite	bdl	bdl	bdl	bdl	bdl	0.33	bdl	0.54	bdl	bdl	bdl	bdl	bdl	bdl	1.19	SM11SOI3zonedparallel
SM11	magnetite	bdl	bdl	bdl	bdl	bdl	0.62	bdl	3.79	0.091	0.045	0.081	bdl	bdl	0.455	0.876	SM11SOI3zonedcross
SM11	jasper	bdl	0.252	bdl	bdl	bdl	bdl	bdl	1.55	bdl	bdl	bdl	bdl	bdl	bdl	0.165	SM11SOI4jassmallmag
SM11	magnetite	bdl	bdl	bdl	bdl	1.7	bdl	bdl	bdl	bdl	bdl	bdl	bdl	bdl	bdl	0.092	SM11SOI6mag1zonedcore
SM11	magnetite	bdl	bdl	bdl	bdl	bdl	bdl	bdl	bdl	bdl	bdl	0.252	bdl	bdl	0.223	bdl	SM11SOI6mag1zonedrim
SM11	magnetite	bdl	bdl	bdl	bdl	bdl	bdl	bdl	bdl	bdl	bdl	bdl	bdl	bdl	0.089	bdl	SM11SOI6mag2homogenouscore
SM11	magnetite	0.159	bdl	bdl	bdl	1.6	bdl	bdl	bdl	bdl	bdl	bdl	bdl	bdl	bdl	bdl	SM11SOI6mag2homogenousrim
SM11	magnetite	bdl	bdl	bdl	bdl	2.1	bdl	bdl	bdl	bdl	bdl	0.077	bdl	bdl	bdl	0.051	SM11SOI6mag3zonedcore
SM11	magnetite	bdl	bdl	bdl	bdl	bdl	0.47	0.105	bdl	bdl	bdl	0.073	bdl	bdl	bdl	0.050	SM11SOI6mag4zonedcore
SM11	magnetite	bdl	bdl	bdl	bdl	2.6	bdl	bdl	bdl	bdl	0.045	bdl	bdl	bdl	bdl	0.643	SM11SOI6mag4zonedrim
SM11	magnetite	bdl	bdl	bdl	bdl	1.6	0.90	bdl	0.40	0.112	0.143	bdl	bdl	bdl	1.348	0.050	SM11SOI6mag4zonedmidinclusions
SM11	magnetite	bdl	bdl	bdl	bdl	1.5	bdl	bdl	bdl	bdl	bdl	0.038	bdl	bdl	bdl	0.412	SM11SOI5mag1zonedcore
SM11	magnetite	bdl	bdl	bdl	bdl	bdl	0.76	bdl	0.25	bdl	bdl	0.103	bdl	bdl	bdl	0.323	SM11SOI5mag1zonedrim
SM11	magnetite	bdl	bdl	bdl	bdl	1.6	0.74	bdl	5.18	0.012	bdl	0.063	bdl	bdl	bdl	0.633	SM11SOI5mag2homogenous
SM052	magnetite	bdl	bdl	bdl	bdl	bdl	bdl	bdl	1.14	0.035	bdl	bdl	bdl	bdl	0.208	0.109	SM052SOI1largecross
SM052	magnetite	bdl	bdl	bdl	bdl	bdl	bdl	bdl	0.30	bdl	bdl	bdl	bdl	bdl	bdl	1.00	SM052SOI2largeparallel
SM052	magnetite	0.321	bdl	bdl	bdl	bdl	0.63	bdl	3.57	0.116	bdl	0.034	bdl	bdl	1.08	0.402	SM052SOI2largecrossinclusions
SM052	magnetite	0.124	bdl	bdl	bdl	bdl	bdl	bdl	2.69	0.103	bdl	bdl	bdl	bdl	0.418	2.59	SM052SOI2largecross
SM052	jasper	bdl	0.135	bdl	bdl	bdl	bdl	bdl	5.65	bdl	bdl	bdl	bdl	bdl	0.133	1.46	SM052SOI3jascross
SM052	jasper	bdl	bdl	bdl	bdl	bdl	0.91	bdl	1.44	0.024	bdl	bdl	bdl	bdl	0.107	0.273	SM052SOI1mag1injassm
SM052	magnetite	bdl	bdl	bdl	bdl	bdl	bdl	bdl	0.63	0.016	bdl	bdl	bdl	bdl	bdl	bdl	SM052SOIumag1zonedcore
SM052	magnetite	0.166	bdl	bdl	bdl	bdl	bdl	bdl	3.93	0.215	0.044	0.078	bdl	bdl	bdl	0.544	SM052SOIumag1zonedrim
SM052	magnetite	bdl	bdl	bdl	bdl	1.6	bdl	bdl	0.47	bdl	bdl	bdl	bdl	bdl	bdl	bdl	SM052SOIumag2rim
SM052	magnetite	bdl	bdl	bdl	bdl	1.7	bdl	bdl	bdl	0.151	bdl	bdl	bdl	bdl	bdl	0.450	SM052SOIumag3core
SM052	magnetite	bdl	bdl	bdl	bdl	bdl	0.56	bdl	5.06	0.179	bdl	0.057	bdl	bdl	0.824	0.066	SM052SOIumag4rim

Appendix C (continued): LA-ICP-MS results for all magnetite analyses. All results in ppm.

		Mg	Al	Si	P	Ca	Sc	Ti	V	Cr	Mn	Co	Ni	Cu	Zn	Ga	Ge	As	Y	Zr	Nb
	Isotope	25	27	29	31	43	45	47	51	52	55	59	60	65	66	69	74	75	89	90	93
	MRE [%]	7.2	7.1	14	186	21	17	5.6	4.6	13	4.0	8.6	6.4	13	6.0	7.1	4.2	19	10	10	16
	dl [ppm]	0.7	0.3	25	9.7	23	0.05	0.4	0.04	0.25	0.18	0.03	0.30	0.03	0.3	0.2	0.17	0.08	0.01	0.01	0.014
Sample	**Layer type**																				
SM052	magnetite	41	66	349	36	99	0.20	11.4	1.1	0.71	173	0.09	4.08	0.11	14.2	0.21	2.44	0.39	0.05	0.03	bdl
SM052	magnetite	25	67	350	22	55	0.13	8.5	1.3	0.37	189	0.05	4.44	0.05	18.1	0.23	3.70	0.25	0.01	0.03	bdl
SM052	magnetite	210	130	6413	437	599	0.15	8.8	1.3	0.50	196	0.07	4.39	0.06	22.1	0.31	15.5	2.38	0.92	0.49	bdl
SM052	magnetite	182	72	1075	43	57	0.13	7.4	1.4	0.29	188	0.06	4.25	0.05	17.3	0.23	13.0	0.24	0.01	0.03	bdl
SM052	magnetite	133	69	699	38	63	0.12	7.0	1.2	0.50	184	0.06	4.17	0.05	18.2	0.24	10.7	0.25	0.15	0.02	bdl
SM052	magnetite	24	69	217	29	57	0.12	7.8	1.4	0.45	194	0.08	4.40	0.06	20.0	0.23	7.76	0.24	0.09	0.06	bdl
SM052	magnetite	150	69	501	52	61	0.12	5.5	1.2	0.57	161	0.03	6.48	0.05	17.9	0.20	18.3	0.26	0.24	0.02	bdl
SM052	magnetite	98	70	506	21	56	0.12	6.4	1.3	4.42	188	0.04	5.89	0.05	16.4	0.20	13.6	0.26	0.74	0.02	0.052
SM052	magnetite	150	112	1001	232	332	0.15	5.9	1.4	0.66	176	0.05	4.21	0.06	16.1	0.26	13.7	0.37	0.54	0.01	bdl
SM052	magnetite	289	134	899	24	59	0.11	8.4	1.3	0.89	177	0.03	3.93	0.06	18.4	0.22	12.7	0.39	0.14	0.06	bdl
SM052	magnetite	164	96	780	278	371	0.14	9.5	1.3	0.34	174	0.06	6.94	0.15	13.9	0.29	14.6	1.09	1.15	0.75	0.034
SM052	magnetite	438	87	1422	72	114	0.09	6.6	1.2	0.75	160	0.05	8.34	0.05	16.1	0.27	19.7	0.35	0.28	0.06	0.038
SM052	magnetite	245	137	1377	301	386	0.13	6.1	1.5	0.75	202	0.05	8.22	0.37	19.3	0.30	11.1	2.59	0.34	0.10	bdl
SM052	magnetite	123	60	689	26	50	0.09	8.8	1.4	0.89	178	0.03	4.59	0.04	17.2	0.20	15.1	0.22	0.07	0.07	0.026
11-4	chlorite	497	414	3955	16	43	0.22	186	145.2	19.7	27	0.95	3.41	2.01	6.71	1.56	15.1	0.39	0.35	5.77	0.985
11-4	chlorite	6545	9859	19632	89	281	0.91	4897	31.7	248	194	1.83	6.26	14.2	34.0	4.24	23.1	1.07	2.55	25.2	12.02
11-4	chlorite	455	301	2733	16	40	0.23	104	42.7	3.53	24	1.07	3.86	1.19	6.09	1.48	14.2	0.27	0.80	8.94	0.637
11-4	chlorite	791	603	5804	16	39	0.30	226	28.0	4.27	29	1.06	3.36	0.19	6.48	1.66	38.8	0.95	0.86	16.4	1.623
11-4	chlorite	715	812	3124	27	41	0.09	234	31.3	8.84	26	0.99	3.08	0.39	6.69	1.64	12.8	0.22	1.02	19.9	1.064
11-4	chlorite	738	710	3297	24	46	0.23	108	53.4	2.54	28	0.95	3.35	0.25	6.06	1.67	14.5	0.40	1.49	34.6	0.404
11-4	chlorite	21097	30811	82248	216	320	2.20	160	27.9	10.0	227	3.16	8.75	3.16	64.2	9.86	10.7	0.73	3.88	57.4	1.460
11-11	magnetite	495	134	1943	40	69	0.26	13.9	4.8	1.17	110	0.58	0.68	0.49	8.66	1.51	6.40	0.39	0.12	0.19	0.173
11-11	magnetite	966	308	4458	34	77	0.48	25.9	4.8	1.09	119	0.66	0.84	0.53	11.7	1.60	6.58	1.05	0.16	0.28	0.436
11-11	magnetite	600	241	3005	30	54	0.31	38.4	4.7	0.60	117	0.58	0.67	0.41	9.10	1.60	6.45	0.80	0.15	0.20	0.421
11-11	magnetite	241	136	1165	32	71	0.14	9.63	4.7	1.33	110	0.63	0.79	0.40	9.00	1.47	6.23	0.32	0.22	1.00	0.323
11-11	magnetite	922	155	3596	38	89	0.47	24.9	5.0	0.97	108	0.69	1.20	0.38	9.91	1.62	10.0	0.80	0.13	0.21	0.432
11-11	magnetite	850	301	5078	43	82	0.55	23.6	5.0	1.34	118	0.58	1.05	1.06	9.49	1.66	5.22	0.85	1.59	3.83	0.479
11-11	magnetite	672	259	9635	32	68	0.45	19.5	4.9	0.90	106	0.56	0.77	0.82	9.84	1.59	4.51	0.91	4.55	13.3	0.485
11-11	magnetite	665	165	2562	26	58	0.30	20.7	5.4	0.84	116	0.62	0.93	0.63	9.46	1.72	6.55	1.15	0.15	0.30	0.370
11-11	magnetite	838	271	4775	132	141	0.43	22.4	5.4	1.20	115	0.62	1.17	0.87	11.4	1.73	5.94	1.09	0.59	0.37	0.390
11-11	magnetite	405	81	1864	21	43	0.24	13.4	5.6	1.06	124	0.57	0.84	0.34	8.72	1.55	9.71	0.59	1.42	5.53	0.337
11-12	magnetite	842	237	8957	74	71	0.40	46.9	3.7	1.11	262	0.76	1.72	6.95	10.6	1.02	6.38	2.09	0.32	0.51	0.248
11-12	magnetite	902	240	11090	39	74	0.41	47.6	3.9	1.38	247	0.74	1.66	2.18	10.6	1.00	6.48	2.21	0.24	0.45	0.233
11-12	magnetite	983	355	10263	35	78	0.33	49.4	4.0	1.50	292	0.83	1.41	8.31	12.0	1.08	6.65	2.31	0.29	0.65	0.271
11-12	magnetite	1109	282	5717	22	55	0.50	50.1	4.0	1.07	276	0.93	1.99	8.92	10.9	1.01	7.01	2.52	0.24	0.61	0.282
11-12	magnetite	791	216	4059	21	84	0.32	45.5	3.9	1.54	237	0.77	2.03	3.23	10.1	1.00	5.52	2.14	0.25	0.42	0.297
11-12	magnetite	724	225	12833	48	103	0.37	78.4	3.9	2.30	248	0.80	1.85	3.47	13.0	0.99	6.05	1.63	0.36	1.08	0.404
11-12	magnetite	558	188	34444	36	89	0.35	36.5	3.8	1.57	258	0.72	1.48	1.21	9.51	0.92	6.08	0.70	0.14	0.41	0.187
11-12	magnetite	749	211	11666	47	175	0.32	46.5	3.9	1.37	259	0.84	1.84	3.65	10.4	0.93	6.17	1.30	0.21	0.64	0.257
11-12	magnetite	896	213	4342	18	57	0.32	49.8	3.8	1.83	266	0.75	1.90	4.73	13.0	1.07	6.79	1.96	0.22	1.14	0.340

Appendix C (continued): LA-ICP-MS results for all magnetite analyses. All results in ppm.

		Mo	Ag	Cd	In	Sn	Sb	Cs	Ba	La	Sm	Yb	Hf	Ta	W	Pb	
	Isotope	95	109	111	115	118	121	133	137	139	147	172	178	181	182	208	
	MRE [%]	31	29	42	38	25	15	22	12	13	31	26	41	30	14	9.3	
	dl [ppm]	0.1	0.1	0.2	0.07	1.4	0.23	0.09	0.1	0.01	0.04	0.03	0.04	0.01	0.08	0.05	
Sample	**Layer type**																**Comment**
SM052	magnetite	bdl	bdl	0.255	bdl	1.9	bdl	0.100	0.12	bdl	0.056	bdl	bdl	bdl	bdl	0.060	SM052SOIumag5core
SM052	magnetite	bdl	bdl	bdl	bdl	1.8	bdl	bdl	bdl	bdl	bdl	bdl	bdl	bdl	bdl	15.7	SM052SOIumag6rim
SM052	magnetite	3.953	bdl	bdl	bdl	bdl	2.54	bdl	5.49	0.278	bdl	0.139	bdl	bdl	4.991	bdl	SM052SOIumag7core
SM052	magnetite	bdl	bdl	0.619	bdl	bdl	bdl	bdl	bdl	0.026	bdl	bdl	bdl	bdl	bdl	bdl	SM052SOIumag8coer
SM052	magnetite	bdl	bdl	0.381	bdl	1.7	bdl	bdl	0.41	0.030	bdl	bdl	bdl	bdl	0.087	0.165	SM052SOIumag8core_2
SM052	magnetite	bdl	bdl	bdl	bdl	1.5	bdl	bdl	0.29	0.014	bdl	bdl	bdl	bdl	bdl	bdl	SM052SOIu2mag1coreinner
SM052	magnetite	bdl	bdl	bdl	bdl	bdl	bdl	bdl	0.37	0.051	bdl	bdl	bdl	bdl	bdl	bdl	SM052SOIu3mag1core
SM052	magnetite	bdl	bdl	bdl	bdl	bdl	bdl	bdl	0.81	0.023	bdl	0.036	bdl	bdl	0.117	0.295	SM052SOIu3mag2core
SM052	magnetite	bdl	bdl	0.209	bdl	bdl	bdl	bdl	1.89	0.114	0.050	0.064	bdl	bdl	0.254	0.172	SM052SOIu4mag1core
SM052	magnetite	bdl	bdl	bdl	bdl	bdl	0.29	0.107	0.99	0.051	bdl	bdl	bdl	bdl	0.151	3.20	SM052SOIu4mag2core
SM052	magnetite	0.411	bdl	bdl	bdl	1.7	0.99	bdl	6.69	0.301	0.074	0.134	bdl	bdl	2.250	0.291	SM052SOIu5mag1leftofzonation
SM052	magnetite	0.102	bdl	bdl	bdl	bdl	0.26	bdl	2.15	0.099	bdl	0.046	bdl	bdl	0.994	0.835	SM052SOIu5mag1rightofzonation
SM052	magnetite	0.465	bdl	bdl	bdl	bdl	6.16	0.120	2.89	0.083	bdl	0.046	bdl	bdl	9.236	0.155	SM052SOIu5mag2homogenous
SM052	magnetite	bdl	bdl	bdl	bdl	1.8	0.24	bdl	0.81	0.016	bdl	bdl	bdl	bdl	0.141	0.155	SM052SOIu2mag1coreouter
11-4	chlorite	bdl	0.159	bdl	bdl	1.5	bdl	0.230	0.44	0.015	bdl	0.048	0.260	0.021	bdl	16.9	311b-4SOI1aroundouter
11-4	chlorite	0.441	1.676	bdl	bdl	1.8	0.49	1.083	6.22	0.501	0.095	0.439	0.778	0.403	0.478	0.393	311b-4SOI1acrosssmall
11-4	chlorite	bdl	0.185	bdl	bdl	bdl	bdl	bdl	0.39	bdl	bdl	0.088	0.040	0.049	bdl	0.451	311b-4SOI1acrosssmall2
11-4	chlorite	0.385	bdl	bdl	bdl	1.6	bdl	0.160	0.76	0.020	bdl	0.126	0.350	0.039	bdl	0.780	311b-4SOI2checksulf
11-4	chlorite	bdl	bdl	bdl	bdl	2.2	bdl	bdl	0.23	0.012	bdl	0.170	0.579	0.045	bdl	0.209	311b-4SOI3around
11-4	chlorite	bdl	bdl	bdl	bdl	bdl	bdl	0.106	0.15	0.098	bdl	0.219	0.411	bdl	bdl	4.63	311b-4SOI4across
11-4	chlorite	0.233	0.487	bdl	bdl	2.3	0.87	0.397	5.12	9.372	1.712	0.366	1.585	0.316	0.204	43.9	311b-4SOI4cluster
11-11	magnetite	bdl	bdl	bdl	bdl	bdl	0.45	0.122	1.06	0.043	bdl	bdl	bdl	0.016	bdl	1.26	11SOI1acrosscore
11-11	magnetite	bdl	bdl	0.202	bdl	bdl	1.76	0.337	2.29	0.043	bdl	bdl	bdl	0.274	0.389	1.32	11SOI1acosstwocores
11-11	magnetite	bdl	bdl	bdl	bdl	bdl	0.77	0.349	3.10	0.086	bdl	bdl	bdl	bdl	0.333	0.509	11SOI1acrosscre
11-11	magnetite	bdl	bdl	bdl	bdl	bdl	bdl	0.165	1.10	bdl	bdl	0.036	bdl	0.015	bdl	0.982	11SOI1outerparallel
11-11	magnetite	bdl	bdl	bdl	bdl	bdl	1.44	0.094	2.01	0.024	bdl	bdl	bdl	0.016	0.080	1.57	11SOI3intoandalongcore
11-11	magnetite	bdl	bdl	bdl	bdl	bdl	1.92	0.296	2.86	0.089	bdl	0.178	0.129	0.038	0.336	1.70	11SOI3across1
11-11	magnetite	bdl	bdl	bdl	bdl	2.0	1.61	0.237	3.41	0.062	0.067	0.373	0.415	0.022	bdl	1.29	11SOI3across2
11-11	magnetite	bdl	bdl	bdl	bdl	bdl	1.19	0.216	6.65	0.061	bdl	bdl	bdl	0.023	0.110	1.37	11SOI2across1
11-11	magnetite	bdl	bdl	bdl	bdl	bdl	1.43	0.200	3.41	0.220	bdl	0.071	bdl	0.035	0.136	0.740	11SOI2across2
11-11	magnetite	bdl	bdl	bdl	bdl	bdl	bdl	bdl	1.20	0.045	bdl	0.179	0.107	bdl	bdl	1.44	11SOI2across3
11-12	magnetite	bdl	bdl	bdl	bdl	bdl	2.52	bdl	4.16	0.174	bdl	0.047	bdl	0.046	0.151	1.45	12SOI1along
11-12	magnetite	bdl	bdl	bdl	bdl	bdl	2.63	bdl	3.91	0.049	bdl	0.052	bdl	0.031	0.151	1.87	12SOI1across
11-12	magnetite	bdl	bdl	bdl	bdl	bdl	2.91	0.097	5.17	0.056	bdl	0.051	bdl	0.036	0.236	1.72	12SOI1along1
11-12	magnetite	bdl	bdl	bdl	bdl	bdl	3.43	0.141	3.77	0.029	bdl	0.053	bdl	0.040	0.229	1.94	12SOI1along2
11-12	magnetite	bdl	bdl	bdl	bdl	bdl	3.12	0.114	4.33	0.045	bdl	0.052	bdl	0.048	0.190	2.00	12SOI1along3
11-12	magnetite	bdl	bdl	bdl	bdl	bdl	2.43	bdl	3.92	0.086	0.054	0.082	bdl	0.051	0.709	1.45	12SOI4along1
11-12	magnetite	bdl	0.104	bdl	bdl	bdl	1.86	bdl	2.44	0.019	bdl	0.050	bdl	0.021	0.184	1.58	12SOI4along2
11-12	magnetite	bdl	bdl	bdl	bdl	1.6	2.87	bdl	3.01	0.031	bdl	0.059	bdl	0.060	0.322	2.77	12SOI4along3
11-12	magnetite	bdl	bdl	bdl	bdl	bdl	3.04	0.185	5.37	0.045	bdl	0.049	bdl	0.062	0.295	0.954	12SOI3across1

Appendix C (continued): LA-ICP-MS results for all magnetite analyses. All results in ppm.

		Mg	Al	Si	P	Ca	Sc	Ti	V	Cr	Mn	Co	Ni	Cu	Zn	Ga	Ge	As	Y	Zr	Nb
	Isotope	25	27	29	31	43	45	47	51	52	55	59	60	65	66	69	74	75	89	90	93
	MRE [%]	7.2	7.1	14	186	21	17	5.6	4.6	13	4.0	8.6	6.4	13	6.0	7.1	4.2	19	10	10	16
	dl [ppm]	0.7	0.3	25	9.7	23	0.05	0.4	0.04	0.25	0.18	0.03	0.30	0.03	0.3	0.2	0.17	0.08	0.01	0.01	0.014
Sample	**Layer type**																				
11-12	magnetite	494	112	2679	20	40	0.17	29.8	3.8	1.53	221	0.70	1.52	1.54	9.76	0.87	7.12	0.64	0.06	1.15	0.106
11-12	magnetite	828	222	4349	20	100	0.26	41.2	3.8	1.43	277	0.73	1.51	5.41	11.7	0.98	6.50	1.47	0.20	0.95	0.211
11-12	magnetite	700	227	7327	18	45	0.31	40.3	3.8	1.78	240	0.75	2.15	2.80	12.0	1.00	6.36	1.45	0.17	0.85	0.232
11-12	magnetite	245	115	2251	19	57	0.09	19.3	3.8	1.96	214	0.75	1.65	1.74	12.4	0.87	6.89	0.52	0.04	1.62	0.065
11-12	magnetite	636	285	5316	40	74	0.28	33.5	4.4	2.82	195	0.82	3.06	3.40	13.3	1.03	5.94	1.33	0.21	1.16	0.256
11-12	magnetite	624	205	5199	37	55	0.35	46.1	4.5	2.64	201	0.80	2.41	2.50	12.6	1.06	6.02	1.95	0.24	0.93	0.281
11-12	magnetite	203	142	10035	96	93	0.56	1593	4.0	2.92	62	0.21	0.84	1.90	6.35	0.58	4.76	3.11	0.80	1.57	3.680
11-42	chlorite	318	450	1917	45	119	0.26	439	131.2	2.88	475	0.57	4.95	0.51	11.4	2.88	16.7	0.44	0.76	23.3	1.539
11-42	chlorite	477	439	2963	20	97	0.17	365	87.0	3.66	493	0.77	2.18	0.26	13.4	2.66	21.0	1.06	0.41	12.2	1.186
11-42	chlorite	297	450	2023	22	906	0.14	489	119.8	3.43	412	0.42	4.20	0.21	20.4	3.34	19.4	0.33	0.27	9.51	1.707
11-42	chlorite	314	399	3151	39	255	0.18	371	87.6	0.64	509	0.45	2.20	0.28	14.0	2.58	21.2	0.77	1.18	8.26	1.346
11-42	chlorite	326	49	1698	26	51	0.09	232	149.3	42.2	371	1.35	1.83	0.52	7.74	2.74	18.3	0.16	0.15	4.47	1.211
11-42	chlorite	378	278	1862	33	383	0.09	899	91.5	17.9	446	0.95	3.28	0.11	9.20	3.24	20.2	0.17	0.11	4.36	1.565
11-42	chlorite	950	1129	6705	15	324	0.09	1911	78.1	54.6	628	0.59	4.03	0.35	29.0	3.28	13.2	0.48	0.40	5.66	2.186
11-42	chlorite	231	25	1548	13	42	0.08	230	126.9	9.49	363	3.46	3.22	0.27	6.65	1.42	26.3	0.15	0.12	0.51	0.176
11-42	chlorite	179	214	1465	20	43	0.09	151	25.7	0.67	369	1.81	8.36	0.20	7.97	3.17	34.6	0.25	0.05	1.06	1.033
11-4 ilmenite	*chlorite*	*129165*	*197528*	*441683*	*2242*	*3279*	*13.57*	*136358*	*27.3*	*37.0*	*4008*	*12.5*	*35.2*	*48.5*	*376*	*50.7*	*20.9*	*2.82*	*7.51*	*22.5*	*244.8*
	median	322	94	2282	28	65	0.23	15	4.6	1.0	202	0.7	4.3	0.21	14.1	1.08	7.49	0.39	0.22	0.38	0.24
	maximum	21097	30811	82248	659	8383	2.20	4897	149	248	628	7.1	46	14	88	10	39	3.1	4.6	57	12
	minimum	24	9.2	217	11	24	0.06	1.3	1.0	0.3	23.6	0.03	0.67	0.03	2.81	0.20	1.39	0.09	bdl	bdl	bdl

Appendix C (continued): LA-ICP-MS results for all magnetite analyses. All results in ppm.

		Mo	Ag	Cd	In	Sn	Sb	Cs	Ba	La	Sm	Yb	Hf	Ta	W	Pb	
	Isotope	95	109	111	115	118	121	133	137	139	147	172	178	181	182	208	
	MRE [%]	31	29	42	38	25	15	22	12	13	31	26	41	30	14	9.3	
	dl [ppm]	0.1	0.1	0.2	0.07	1.4	0.23	0.09	0.1	0.01	0.04	0.03	0.04	0.01	0.08	0.05	
Sample	**Layer type**																**Comment**
11-12	magnetite	bdl	bdl	bdl	bdl	bdl	0.73	bdl	1.89	0.024	bdl	bdl	0.053	0.028	0.126	2.08	12SOI3across2
11-12	magnetite	bdl	bdl	bdl	bdl	bdl	2.57	bdl	3.79	0.041	bdl	0.032	bdl	0.048	0.259	1.27	12SOI3across3
11-12	magnetite	bdl	bdl	bdl	bdl	bdl	1.57	0.126	2.92	0.030	bdl	bdl	bdl	0.036	0.161	1.51	12SOI3across4
11-12	magnetite	bdl	bdl	bdl	bdl	bdl	0.50	bdl	1.15	0.018	bdl	bdl	bdl	0.045	0.166	1.88	12SOI2across1
11-12	magnetite	bdl	0.113	11.98	bdl	bdl	2.80	0.103	4.12	0.060	bdl	0.031	bdl	0.048	0.208	2.27	12SOI2across2
11-12	magnetite	bdl	bdl	5.520	bdl	bdl	3.58	0.120	4.43	0.088	bdl	bdl	0.040	0.062	0.260	9.50	12SOI2along
11-12	magnetite	0.209	bdl	2.080	bdl	2.5	4.49	0.695	13.9	0.918	0.098	0.089	0.053	0.230	16.3	0.582	12SOI2acrosstransition
11-42	chlorite	bdl	bdl	0.237	bdl	bdl	bdl	0.824	1.21	0.070	0.041	0.145	0.522	0.066	0.102	1.48	11b-42SOI1along
11-42	chlorite	0.146	bdl	bdl	bdl	bdl	bdl	1.572	1.38	0.103	bdl	0.055	0.284	0.027	0.181	0.503	11b-42SOI1across
11-42	chlorite	0.253	bdl	bdl	bdl	bdl	bdl	0.097	1.47	0.123	bdl	bdl	0.216	0.039	0.255	1.423	11b-42SOI1across2
11-42	chlorite	0.519	bdl	bdl	bdl	bdl	bdl	0.828	17.3	0.469	0.096	0.048	0.199	0.030	0.429	0.363	11b-42SOI1across3
11-42	chlorite	bdl	bdl	bdl	bdl	bdl	bdl	bdl	0.34	0.035	bdl	bdl	bdl	0.021	bdl	bdl	11b-42SOI2aroundouter
11-42	chlorite	0.101	bdl	bdl	bdl	bdl	bdl	bdl	0.24	0.087	bdl	bdl	bdl	0.037	bdl	1.10	11b-42SOI2aroundouter2
11-42	chlorite	0.782	bdl	bdl	bdl	bdl	bdl	2.140	5.22	0.295	0.060	0.062	0.115	0.152	0.574	0.111	11b-42SOI2across
11-42	chlorite	bdl	bdl	bdl	bdl	bdl	bdl	bdl	0.36	0.033	bdl	bdl	bdl	bdl	bdl	0.138	11b-42SOI3across
11-42	chlorite	bdl	bdl	bdl	bdl	1.5	bdl	0.321	0.18	bdl	bdl	bdl	bdl	bdl	bdl	0.547	11b-42SOI3aroundouter
11-4 ilmenite	*chlorite*	*0.000*	*2.696*	*0.346*	*0.199*	*10*	*0.52*	*0.628*	*16.0*	*5.911*	*1.421*	*0.540*	*0.929*	*28.3*	*4.82*	*51.9*	*311b-4SOI4background-ilm*
	median	0.23	0.17	0.38	0.13	1.74	0.99	0.17	2.01	0.06	0.07	0.06	0.22	0.04	0.24	0.69	
	maximum	3.95	1.68	11.98	0.13	2.60	6.16	2.14	17.3	9.37	1.71	0.44	1.58	0.40	16.30	43.90	
	minimum	bdl	bdl	bdl	bdl	bdl	bdl	bdl	bdl	bdl	bdl	bdl	bdl	bdl	bdl	bdl	

Note: dl - detection limit, bdl - below detection limit.

Appendix D: All EPMA results for chlorite analyses. All values in wt.-%

		SiO_2	TiO_2	Al_2O_3	Cr_2O_3	Fe_2O_3	FeO	MnO	MgO	ZnO	CaO	Na_2O	K_2O	F	Cl	H_2O*	Total
	dl	**0.01**	**0.03**	**0.08**	**0.01**	**0.02**	**0.02**	**0.01**	**0.01**	**0.01**	**0.01**	**0.01**	**0.01**	**0.01**	**0.01**		
Sample	**Host**																
A028	chert	26.11	0.05	19.61	0.01	1.55	36.64	0.11	6.02	bdl	bdl	bdl	0.02	bdl	bdl	10.95	101.08
A028	chert	26.20	0.05	19.48	0.01	1.54	36.99	0.13	5.92	bdl	bdl	bdl	bdl	bdl	bdl	10.96	101.30
B013-1	chert	26.09	bdl	17.76	bdl	bdl	29.88	0.13	13.50	0.05	bdl	bdl	0.03	bdl	bdl	11.04	98.50
B013-1	mag	26.16	bdl	17.10	0.02	bdl	29.08	0.14	13.62	0.08	0.01	0.04	0.02	bdl	bdl	10.91	97.18
B013-1	mag	26.16	bdl	17.49	bdl	bdl	30.25	0.10	13.85	0.04	0.01	0.01	bdl	bdl	bdl	11.08	99.02
B013-1	mag	25.80	0.01	18.33	0.01	bdl	29.23	0.12	13.30	0.09	bdl	0.02	bdl	bdl	bdl	11.01	97.93
B013-1	mag	25.37	bdl	18.77	0.01	bdl	29.60	0.12	13.22	0.06	bdl	0.01	bdl	bdl	bdl	11.01	98.20
B013-1	chert	33.68	bdl	17.77	bdl	4.78	21.08	0.17	14.60	0.02	bdl	bdl	bdl	bdl	bdl	12.16	104.29
B013-1	chert	28.33	bdl	17.55	bdl	0.99	25.02	0.15	15.56	0.07	bdl	bdl	bdl	bdl	bdl	11.37	99.06
B013-1	chert	29.56	bdl	17.23	0.01	2.06	24.32	0.18	14.65	0.08	0.04	bdl	bdl	bdl	bdl	11.44	99.59
B013-1	chert	26.32	bdl	17.75	bdl	bdl	27.01	0.18	14.90	0.06	0.27	bdl	bdl	0.01	bdl	11.06	97.55
SH580	sulf	23.72	bdl	20.89	bdl	0.43	30.80	0.39	9.50	0.05	0.02	bdl	bdl	bdl	0.01	10.70	96.52
SH580	sulf	25.53	bdl	22.37	bdl	0.73	16.19	0.34	19.29	0.07	bdl	bdl	bdl	0.04	0.04	11.41	96.02
SH580	sulf	23.63	0.04	20.00	0.01	0.41	37.52	0.46	5.53	0.02	bdl	bdl	bdl	bdl	0.03	10.52	98.18
SH580	sulf	23.88	0.04	19.36	0.01	0.51	37.94	0.44	5.16	bdl	bdl	bdl	bdl	bdl	bdl	10.47	97.84
SH580	sulf	23.99	0.03	19.22	bdl	0.45	38.11	0.41	5.32	bdl	bdl	bdl	bdl	bdl	bdl	10.49	98.03
SH580	sulf	24.05	0.03	19.59	0.01	0.83	35.81	0.40	5.88	bdl	bdl	bdl	bdl	bdl	0.02	10.48	97.12
SH580	sulf	24.65	0.03	19.93	bdl	0.67	30.43	0.33	9.89	0.01	bdl	bdl	0.06	bdl	bdl	10.76	96.76
SH580	sulf	25.59	bdl	19.89	bdl	0.72	29.34	0.33	11.41	0.02	bdl	bdl	bdl	bdl	bdl	11.03	98.37
SH580a	sulf	30.47	0.03	23.40	bdl	5.04	13.02	0.31	16.44	bdl	bdl	bdl	0.02	0.05	bdl	12.11	100.87
SH580a	sulf	32.59	0.03	21.73	bdl	5.84	9.46	0.30	18.49	bdl	bdl	bdl	bdl	0.06	bdl	12.26	100.76
SH580a	sulf	31.13	bdl	20.07	bdl	4.27	19.80	0.34	14.46	bdl	bdl	bdl	0.01	0.07	bdl	11.88	102.03
SH580a	sulf	31.98	bdl	20.61	bdl	5.14	14.60	0.26	16.38	bdl	bdl	bdl	bdl	0.06	bdl	12.03	101.05
SH580a	sulf	30.17	bdl	23.97	bdl	5.05	12.44	0.25	16.56	bdl	bdl	bdl	0.02	0.03	bdl	12.13	100.62
SH580a	sulf	31.62	0.05	23.33	bdl	5.43	11.55	0.35	17.56	bdl	bdl	bdl	0.03	0.06	bdl	12.34	102.30
SH580a	sulf	32.01	bdl	23.12	bdl	5.65	10.18	0.30	18.17	bdl	bdl	bdl	0.02	0.05	bdl	12.37	101.86
SH580a	sulf	29.62	bdl	22.62	0.01	4.02	19.11	0.31	14.28	bdl	bdl	bdl	0.02	0.03	bdl	11.95	102.00
SH580a	sulf	29.59	bdl	22.62	bdl	4.25	18.63	0.30	13.98	bdl	bdl	bdl	0.01	0.01	bdl	11.90	101.33
SH580a	sulf	28.92	0.03	21.64	bdl	3.93	23.22	0.33	11.30	bdl	0.01	bdl	0.03	0.04	bdl	11.58	101.03
SH580a	sulf	31.44	0.03	21.96	bdl	4.94	14.75	0.27	16.42	bdl	0.01	bdl	0.03	0.06	bdl	12.16	102.05
SH580a	sulf	27.93	0.03	21.13	0.01	2.88	28.89	0.37	9.30	bdl	bdl	0.02	0.01	bdl	bdl	11.45	102.03
SH580a	sulf	30.22	bdl	22.18	bdl	4.19	18.33	0.27	14.94	bdl	bdl	bdl	0.01	0.05	bdl	12.00	102.19
SH580a	sulf	31.33	bdl	22.82	bdl	5.31	11.39	0.27	17.62	bdl	bdl	bdl	0.01	0.08	bdl	12.18	100.98
SH580a	sulf	31.70	0.04	22.68	bdl	5.42	11.39	0.33	17.68	bdl	bdl	bdl	bdl	0.06	bdl	12.26	101.53
11-11	chert	28.50	bdl	18.75	0.12	2.69	23.81	0.02	13.04	bdl	0.13	0.03	0.05	0.14	0.01	11.16	98.40
11-11	mag	27.98	bdl	16.34	0.02	2.51	31.92	0.19	7.44	bdl	0.29	bdl	0.02	bdl	0.02	10.70	97.41
11-4	chl	25.05	0.04	17.82	bdl	bdl	33.36	0.06	10.70	0.01	bdl	bdl	bdl	bdl	bdl	10.75	97.81
11-4	chl	25.98	0.04	17.28	bdl	bdl	33.03	0.07	11.58	0.03	bdl	bdl	bdl	bdl	bdl	10.92	98.96
11-4	chl	26.41	0.04	16.84	bdl	bdl	32.58	0.05	11.66	0.01	bdl	0.01	bdl	0.01	0.02	10.89	98.54
11-4	chl	26.71	0.04	18.21	bdl	0.70	32.48	0.06	10.43	bdl	0.01	0.08	bdl	bdl	bdl	11.05	99.77
11-4	chl	23.41	0.05	19.87	bdl	bdl	33.56	0.06	9.82	bdl	0.02	bdl	bdl	bdl	0.03	10.68	97.51
11-4	chl	24.62	0.05	18.00	0.01	bdl	32.93	0.04	10.65	0.05	0.02	0.09	0.03	bdl	0.01	10.68	97.18
11-4	chl	25.32	0.03	18.17	bdl	bdl	32.92	0.06	10.98	bdl	0.01	bdl	bdl	bdl	<0.01	10.86	98.36
11-4	chl	24.81	0.03	18.74	bdl	bdl	33.42	0.10	10.42	bdl	0.02	bdl	bdl	bdl	<0.01	10.82	98.37
11-1a	shale	22.73	bdl	18.87	bdl	bdl	40.95	0.04	3.92	0.04	0.02	0.02	bdl	bdl	0.02	10.18	96.80

Appendix D (continued): All EPMA results for chlorite analyses. All values in wt.-%

		SiO_2	TiO_2	Al_2O_3	Cr_2O_3	Fe_2O_3	FeO	MnO	MgO	ZnO	CaO	Na_2O	K_2O	F	Cl	H_2O*	Total
	dl	**0.01**	**0.03**	**0.08**	**0.01**	**0.02**	**0.02**	**0.01**	**0.01**	**0.01**	**0.01**	**0.01**	**0.01**	**0.01**	**0.01**		
Sample	**Host**																
11-1a	shale	22.63	bdl	19.22	bdl	bdl	40.57	0.05	4.24	0.01	0.10	bdl	bdl	bdl	0.01	10.25	97.10
11-1a	shale	22.87	0.06	19.36	bdl	bdl	39.22	0.09	5.07	0.05	bdl	0.01	bdl	bdl	0.02	10.32	97.07
11-1a	shale	22.75	0.06	19.54	bdl	bdl	39.62	0.09	5.07	bdl	bdl	bdl	bdl	bdl	0.03	10.34	97.51
11-1a	shale	22.94	0.08	19.52	bdl	bdl	39.12	0.08	5.13	bdl	bdl	bdl	bdl	bdl	0.01	10.35	97.24
11-1a	shale	23.11	0.06	19.20	bdl	bdl	39.41	0.08	5.31	0.02	bdl	bdl	0.01	bdl	0.01	10.38	97.60
11-1a	shale	22.49	bdl	19.01	bdl	bdl	40.19	0.04	4.62	0.03	bdl	0.02	0.01	bdl	bdl	10.21	96.63
11-18	chert	25.83	0.05	19.44	bdl	1.26	39.25	0.05	4.88	bdl	bdl	0.01	0.02	bdl	bdl	10.90	101.70
11-18	chert	25.63	0.04	19.74	bdl	1.21	39.35	0.05	4.76	bdl	bdl	0.03	bdl	bdl	bdl	10.90	101.73
11-18	chert	25.51	0.07	19.81	bdl	1.21	39.19	0.06	4.86	bdl	bdl	bdl	bdl	bdl	bdl	10.89	101.62
11-18	chert	25.30	0.07	19.75	bdl	1.08	39.37	0.03	4.71	bdl	bdl	0.03	0.02	bdl	bdl	10.83	101.22
11-20	chl	27.57	0.04	18.74	0.02	1.99	35.46	0.01	6.68	bdl	bdl	0.05	0.11	bdl	bdl	11.10	101.77
11-20	chl	26.90	0.03	18.59	bdl	1.45	36.61	0.02	6.63	bdl	bdl	0.07	0.04	bdl	bdl	11.00	101.37
11-23	carb	23.30	0.05	18.35	bdl	bdl	40.94	0.04	5.00	bdl	bdl	0.01	bdl	bdl	0.01	10.35	98.06
11-23	carb	22.79	0.07	18.34	bdl	bdl	40.63	0.03	4.67	bdl	0.02	0.02	bdl	bdl	bdl	10.20	96.78
11-23	carb	23.16	0.05	18.15	bdl	bdl	41.78	0.06	4.56	bdl	0.01	bdl	0.01	bdl	0.01	10.30	98.11
11-23	mag	22.82	0.04	18.58	bdl	bdl	41.28	0.04	4.45	0.01	bdl	bdl	bdl	bdl	0.01	10.25	97.50
11-23	mag	23.01	0.04	18.58	bdl	bdl	42.59	0.03	4.34	0.04	0.01	bdl	0.01	bdl	0.03	10.36	99.05
11-23	chert	25.10	bdl	19.78	bdl	0.81	41.71	0.03	3.91	bdl	bdl	bdl	0.02	0.01	bdl	10.83	102.22
11-23	chert	25.13	0.05	19.94	bdl	0.99	40.10	0.04	4.47	bdl	0.01	bdl	bdl	bdl	bdl	10.84	101.58
11-36	chert	29.47	0.04	18.97	bdl	2.96	26.66	0.03	11.89	bdl	bdl	bdl	bdl	0.08	bdl	11.48	101.58
11-36	chert	29.76	0.05	18.98	bdl	2.93	26.70	0.05	12.09	bdl	bdl	0.01	bdl	0.02	bdl	11.61	102.22
11-36	chert	29.58	0.08	19.09	bdl	2.78	26.87	0.02	12.28	bdl	bdl	bdl	0.01	0.04	bdl	11.61	102.34
11-36	chert	29.39	0.03	19.67	bdl	2.67	26.50	0.03	12.46	bdl	bdl	0.02	0.02	bdl	bdl	11.69	102.47
11-36	chert	31.77	0.03	18.32	0.02	4.24	24.63	0.07	12.03	bdl	bdl	0.05	bdl	0.02	bdl	11.79	102.96
11-36	chert	29.59	0.06	19.28	0.01	2.85	26.58	0.01	12.16	bdl	bdl	0.02	0.03	0.01	bdl	11.63	102.24
11-36	chl	20.22	0.04	13.23	bdl	bdl	32.16	0.44	12.77	bdl	2.35	bdl	0.01	0.07	bdl	9.59	90.85
11-36	chl	29.86	0.04	19.21	bdl	2.92	25.80	0.03	12.79	bdl	bdl	bdl	0.01	0.04	bdl	11.67	102.37
11-36	chl	29.95	0.03	19.58	bdl	3.21	26.12	0.05	12.10	bdl	0.01	0.01	0.01	0.05	bdl	11.69	102.80
11-36	mag	29.54	0.07	19.27	bdl	2.89	26.30	0.03	12.14	bdl	bdl	0.02	0.03	bdl	bdl	11.62	101.92
11-36	mag	24.13	0.03	17.79	bdl	bdl	38.78	0.05	6.88	bdl	0.01	0.01	0.02	bdl	0.01	10.49	98.21
11-36	mag	24.30	0.04	17.93	0.01	bdl	38.52	0.04	7.16	0.04	bdl	0.02	0.02	bdl	bdl	10.56	98.67
11-36	mag	24.36	0.05	18.07	bdl	bdl	38.87	0.03	6.69	bdl	bdl	bdl	0.02	bdl	0.02	10.55	98.65
11-36	mag	23.53	0.04	18.42	bdl	bdl	39.04	0.04	6.66	0.04	0.02	0.04	0.01	bdl	bdl	10.48	98.33
TM1	rhy	24.10	bdl	20.97	bdl	0.30	31.20	0.11	9.96	0.02	0.22	bdl	0.02	bdl	bdl	10.86	97.79
TM1	rhy	23.43	bdl	20.92	bdl	0.02	35.40	0.06	7.49	0.01	0.35	bdl	0.03	bdl	0.01	10.71	98.46
TM2	rhy	24.47	bdl	22.54	bdl	0.63	24.29	0.08	13.89	0.05	bdl	0.02	0.02	bdl	0.01	11.17	97.21
TM2	rhy	24.61	0.04	22.24	bdl	0.51	24.65	0.09	14.11	0.03	0.01	bdl	0.02	bdl	0.02	11.19	97.52
TM2	rhy	25.32	0.03	22.23	bdl	0.83	23.64	0.09	14.52	0.08	bdl	0.02	0.03	bdl	bdl	11.33	98.14
TM2	rhy	24.43	0.04	22.09	0.03	0.56	27.90	0.13	11.74	0.05	0.07	0.03	0.05	bdl	bdl	11.09	98.21
TM2	rhy	24.72	0.04	18.56	0.05	1.18	27.96	0.14	9.97	0.05	0.13	0.06	0.12	0.13	bdl	10.32	93.39
TM2	rhy	25.71	0.06	23.17	0.02	1.19	23.56	0.09	13.24	0.04	bdl	bdl	0.68	bdl	0.03	11.41	99.18
TM2	rhy	28.40	bdl	21.15	0.02	2.91	23.10	0.11	12.90	0.03	bdl	0.05	0.06	bdl	0.02	11.57	100.33
TM2	rhy	24.40	0.03	21.94	bdl	0.51	25.78	0.07	12.99	0.05	0.15	0.02	0.04	bdl	bdl	11.07	97.06
TM2	rhy	24.96	0.03	22.66	0.02	1.17	25.38	0.10	12.61	<0.01	0.02	0.02	0.18	0.12	0.01	11.12	98.36
TM3	and	24.12	0.03	21.33	bdl	0.65	27.78	0.09	11.28	0.06	0.10	bdl	0.03	bdl	0.04	10.84	96.37

Appendix D (continued): All EPMA results for chlorite analyses. All values in wt.-%

		SiO_2	TiO_2	Al_2O_3	Cr_2O_3	Fe_2O_3	FeO	MnO	MgO	ZnO	CaO	Na_2O	K_2O	F	Cl	H_2O*	Total
	dl	**0.01**	**0.03**	**0.08**	**0.01**	**0.02**	**0.02**	**0.01**	**0.01**	**0.01**	**0.01**	**0.01**	**0.01**	**0.01**	**0.01**		
Sample	**Host**																
TM3	and	24.65	0.05	20.62	0.01	0.70	28.92	0.12	10.96	0.06	0.07	bdl	0.03	0.01	0.04	10.86	97.08
TM3	and	26.77	0.04	19.90	bdl	2.57	24.51	0.11	10.89	0.03	0.20	0.02	0.27	0.07	0.12	10.83	96.27
TM4	shale	24.30	0.04	20.28	bdl	1.18	30.44	0.08	8.58	0.06	0.01	bdl	0.03	bdl	<0.01	10.60	95.64
TM4	shale	25.03	0.03	21.50	0.01	0.58	24.48	0.08	14.30	0.08	0.01	bdl	bdl	bdl	0.02	11.17	97.30
TM5	rhy	24.13	0.04	22.36	bdl	0.49	24.25	0.09	13.98	0.05	0.04	bdl	0.01	0.04	bdl	11.05	96.53
TM5	rhy	26.01	0.04	21.00	bdl	1.34	24.55	0.12	13.32	0.05	0.03	0.02	0.03	bdl	bdl	11.20	97.71
TM5	rhy	25.58	0.05	21.20	0.01	1.09	24.73	0.12	13.39	0.02	0.13	bdl	0.04	bdl	0.01	11.17	97.54
TM5	rhy	25.91	0.05	22.08	bdl	1.23	23.53	0.12	13.53	0.02	0.10	0.03	0.40	0.01	0.02	11.31	98.32
TM5	rhy	25.36	0.05	20.93	bdl	0.81	25.03	0.13	13.61	0.03	0.07	bdl	0.03	bdl	bdl	11.12	97.19
TM5	rhy	26.00	0.12	22.10	0.01	1.72	23.36	0.09	13.49	0.04	0.07	bdl	0.09	0.06	bdl	11.28	98.42
TM5	rhy	24.69	0.06	21.91	0.01	0.61	24.18	0.10	14.13	0.06	bdl	0.01	0.03	bdl	0.02	11.14	96.94
TM5	rhy	24.77	0.03	22.04	bdl	0.71	24.83	0.11	13.56	bdl	0.06	0.02	0.04	bdl	0.02	11.15	97.35
TM5	rhy	25.14	0.04	21.65	bdl	1.03	22.85	0.11	14.75	0.03	bdl	0.01	0.04	0.18	0.02	11.02	96.80
TM5	rhy	25.12	0.04	21.17	bdl	0.58	25.94	0.09	13.49	0.03	bdl	bdl	0.03	bdl	0.02	11.13	97.67
TM6	rhy	24.71	0.04	21.69	bdl	0.50	25.63	0.15	13.52	0.05	0.02	0.02	bdl	bdl	0.02	11.12	97.47
TM6	rhy	25.08	0.06	21.22	bdl	0.70	24.35	0.12	14.24	0.04	0.03	0.02	0.02	0.07	0.01	11.07	96.99
TM6	rhy	24.48	0.03	21.61	bdl	0.67	25.40	0.18	13.08	0.01	0.04	0.02	0.01	0.05	bdl	10.97	96.55
TM6	rhy	24.38	0.06	21.34	0.02	1.13	23.53	0.12	12.52	0.03	bdl	0.05	0.43	0.20	0.02	10.62	94.38
TM6	rhy	25.03	0.03	21.38	bdl	0.43	25.47	0.15	13.74	bdl	0.24	0.03	0.06	bdl	0.01	11.17	97.75
TM6	rhy	25.05	0.04	21.03	0.01	0.44	25.06	0.16	14.06	0.04	0.12	0.02	bdl	bdl	bdl	11.13	97.17
TM6	rhy	24.80	0.04	22.07	0.01	0.59	24.96	0.15	13.79	bdl	0.04	bdl	0.06	bdl	0.01	11.20	97.73
TM6	rhy	25.11	0.04	20.83	bdl	0.42	25.30	0.13	14.07	0.03	bdl	0.02	0.03	bdl	0.01	11.11	97.11
TM7	shale	24.65	0.03	20.38	bdl	0.73	27.45	0.12	11.68	0.02	bdl	0.01	bdl	bdl	0.01	10.83	95.94
TM7	shale	24.34	0.08	21.82	0.01	0.62	25.46	0.12	12.98	bdl	0.02	0.02	0.04	bdl	0.02	11.01	96.54
TM7	shale	25.44	0.05	19.92	0.03	0.81	24.56	0.10	13.70	0.03	0.03	0.03	0.07	bdl	0.02	10.95	95.73
TM7	shale	24.63	0.03	21.54	0.02	0.71	24.81	0.07	13.26	0.03	0.13	0.03	0.04	bdl	0.03	11.02	96.35
TM7	shale	25.69	0.04	20.30	bdl	1.05	23.41	0.08	14.28	bdl	bdl	0.03	0.02	0.04	bdl	11.02	95.97
TM7	shale	23.99	0.04	22.06	0.01	0.94	24.49	0.10	12.62	0.04	bdl	0.04	0.07	0.11	0.01	10.79	95.28
TM7	shale	23.97	0.08	22.79	bdl	0.59	24.74	0.14	13.25	0.06	bdl	0.02	0.03	bdl	0.02	11.08	96.78
TM7	shale	29.11	0.03	19.59	0.02	4.47	18.31	0.09	12.17	0.04	0.03	0.10	0.12	bdl	0.02	11.13	95.22
TM8	rhy	33.04	0.03	20.20	0.02	6.23	15.25	0.08	13.02	0.06	bdl	0.03	0.72	bdl	bdl	11.93	100.61
TM8	rhy	32.12	bdl	21.00	bdl	5.44	18.32	0.10	13.57	0.03	bdl	0.02	0.15	0.04	bdl	12.06	102.87
TM8	rhy	26.25	bdl	21.37	bdl	1.44	21.32	0.10	15.29	0.03	0.01	bdl	bdl	bdl	bdl	11.32	97.17
TM8	rhy	26.43	0.03	22.61	bdl	1.59	19.40	0.13	14.55	0.05	bdl	0.02	0.99	0.01	bdl	11.36	97.17
TM8	rhy	24.97	0.03	22.42	0.01	0.67	22.99	0.11	15.02	0.05	0.01	0.02	bdl	bdl	0.01	11.29	97.61
TM8	rhy	26.73	0.03	22.09	0.02	1.62	21.84	0.15	14.07	0.02	bdl	0.03	0.61	0.02	bdl	11.42	98.64
TM10	bas	25.79	0.03	19.13	bdl	0.17	25.16	0.28	15.05	0.05	0.17	bdl	bdl	bdl	0.08	11.05	96.94
TM10	bas	26.11	bdl	19.00	bdl	0.16	25.19	0.30	15.31	0.03	0.07	0.02	bdl	bdl	0.06	11.13	97.39
TM10	bas	25.87	0.04	18.64	0.02	0.49	24.77	0.36	15.19	0.01	0.02	0.07	0.01	bdl	0.64	10.72	96.72
TM10	bas	26.01	bdl	18.84	bdl	0.48	24.40	0.36	15.15	0.04	0.02	0.01	bdl	bdl	0.22	10.94	96.45
TM10	bas	26.06	bdl	18.44	bdl	0.57	24.58	0.34	15.19	0.04	0.02	bdl	bdl	bdl	0.46	10.79	96.41
TM10	bas	25.90	0.03	19.00	bdl	0.27	24.73	0.36	15.03	0.05	0.01	0.01	0.03	bdl	0.01	11.06	96.52
TM10	bas	25.88	bdl	19.14	bdl	0.35	24.78	0.33	14.97	bdl	bdl	0.02	bdl	bdl	0.06	11.04	96.59
TM10	bas	25.44	bdl	19.41	bdl	0.14	25.16	0.31	14.61	0.03	0.17	0.02	bdl	bdl	bdl	11.02	96.33
TM10	bas	25.77	bdl	18.88	bdl	b	25.57	0.36	15.12	0.01	0.07	bdl	bdl	bdl	bdl	11.06	96.86

Appendix D (continued): All EPMA results for chlorite analyses. All values in wt.-%

		SiO_2	TiO_2	Al_2O_3	Cr_2O_3	Fe_2O_3	FeO	MnO	MgO	ZnO	CaO	Na_2O	K_2O	F	Cl	H_2O*	Total
	dl	0.01	0.03	0.08	0.01	0.02	0.02	0.01	0.01	0.01	0.01	0.01	0.01	0.01	0.01		
Sample	Host																
TM10	bas	25.93	bdl	19.07	bdl	0.47	24.17	0.36	15.12	0.04	0.03	bdl	bdl	bdl	0.11	11.00	96.29
TM10	bas	25.57	bdl	19.25	bdl	b	26.13	0.36	14.70	bdl	bdl	0.02	bdl	bdl	bdl	11.08	97.14
TM10	bas	25.64	0.03	19.35	bdl	0.07	25.68	0.35	14.76	0.02	0.03	0.03	bdl	bdl	bdl	11.09	97.06
TM10	bas	26.08	bdl	19.02	bdl	0.40	24.56	0.32	15.13	0.03	0.06	bdl	0.02	bdl	0.05	11.08	96.75
TM10	bas	26.39	bdl	19.11	bdl	0.75	24.00	0.33	14.81	0.03	0.01	0.03	0.03	bdl	bdl	11.11	96.62
TM10	bas	25.58	bdl	19.32	bdl	b	25.68	0.34	14.94	bdl	0.08	bdl	bdl	bdl	0.02	11.08	97.06
TM10	bas	26.04	0.04	19.24	bdl	0.35	25.01	0.28	15.00	0.05	0.02	0.02	bdl	bdl	0.04	11.12	97.21
TM10	bas	30.73	0.05	18.10	bdl	4.38	19.43	0.31	13.60	0.02	0.03	bdl	bdl	bdl	0.08	11.41	98.12
TM10	bas	27.69	0.05	18.23	bdl	1.13	23.66	0.29	15.51	0.03	0.03	bdl	0.01	bdl	0.04	11.26	97.92
TM10	bas	24.61	bdl	18.50	bdl	1.36	19.10	0.31	14.37	0.04	0.02	0.02	0.01	bdl	0.02	10.33	88.71
TM10	bas	25.20	bdl	18.41	bdl	1.27	20.05	0.31	14.64	0.05	0.06	bdl	bdl	bdl	0.01	10.52	90.53
TM10	bas	24.55	bdl	18.86	bdl	1.29	19.60	0.27	14.39	0.01	0.05	bdl	bdl	bdl	0.05	10.39	89.47
TM10	bas	24.99	0.03	19.12	bdl	1.21	21.05	0.29	14.24	0.02	bdl	bdl	bdl	bdl	0.04	10.59	91.59
TM10	bas	25.71	bdl	18.95	bdl	0.15	24.28	0.27	15.10	0.05	0.47	0.02	bdl	bdl	b	11.02	96.05
TM10	bas	25.95	bdl	19.22	bdl	0.35	24.88	0.32	14.98	0.03	0.05	0.01	0.02	bdl	0.07	11.07	96.96
TM10	bas	25.88	bdl	19.20	bdl	0.18	25.40	0.35	14.95	bdl	0.03	0.01	bdl	bdl	0.01	11.11	97.15
TM10	bas	26.11	bdl	19.05	bdl	0.58	24.12	0.34	14.97	0.03	0.02	0.02	0.01	bdl	0.04	11.05	96.33
TM10	bas	26.09	bdl	18.99	bdl	0.27	24.76	0.33	15.38	0.05	0.01	0.02	bdl	bdl	0.09	11.09	97.09
TM10	bas	26.04	bdl	18.95	bdl	0.19	25.21	0.39	15.25	0.05	0.02	bdl	bdl	bdl	0.10	11.08	97.27
TM10	bas	25.60	0.03	19.34	bdl	0.31	25.24	0.32	14.70	bdl	<0.01	bdl	bdl	bdl	0.10	11.00	96.64
TM10	bas	26.12	0.03	18.85	bdl	0.20	25.14	0.31	15.30	bdl	0.02	0.02	0.01	bdl	0.06	11.10	97.17
TM10	bas	30.55	0.32	18.29	0.01	4.39	17.56	0.30	13.52	0.03	0.17	0.20	0.21	bdl	0.03	11.36	96.94
TM10	bas	25.68	0.29	19.45	bdl	0.47	24.91	0.35	14.60	bdl	0.12	bdl	bdl	bdl	0.05	11.08	97.01
TM11	and	25.12	bdl	19.12	bdl	0.97	28.99	0.41	11.83	0.05	0.04	bdl	bdl	bdl	bdl	10.64	97.27
TM11	and	24.88	bdl	19.34	bdl	1.80	28.63	0.39	11.66	0.04	0.03	bdl	bdl	bdl	bdl	10.25	97.12
TM11	and	25.11	0.06	19.23	0.02	b	29.76	0.39	11.75	0.01	0.05	bdl	bdl	bdl	bdl	11.43	97.90
TM11	and	26.23	0.08	18.44	0.02	b	28.71	0.38	11.90	0.03	0.06	bdl	bdl	bdl	bdl	11.53	97.46
TM11	and	25.25	0.05	18.44	0.02	4.32	26.07	0.35	12.00	0.01	0.03	bdl	0.01	bdl	bdl	12.50	99.14
TM11	and	25.99	0.04	17.70	0.03	0.64	28.12	0.36	12.60	0.07	0.02	bdl	0.01	bdl	0.01	11.00	96.65
TM11	and	25.34	0.07	18.60	bdl	1.61	28.82	0.38	11.96	0.05	0.04	bdl	bdl	bdl	bdl	11.80	98.75
TM11	and	25.41	0.07	18.23	0.07	bdl	29.85	0.34	12.05	0.01	0.03	bdl	bdl	bdl	bdl	11.23	97.36
TM11	and	23.23	0.06	19.22	0.02	0.17	29.39	0.38	11.27	0.01	0.03	bdl	bdl	bdl	bdl	11.35	95.21
TM11	and	25.01	bdl	18.95	bdl	0.37	29.33	0.42	11.55	0.05	0.02	0.01	bdl	bdl	0.01	10.85	96.67
TM11	and	25.04	0.21	18.64	0.02	0.74	29.15	0.36	11.75	0.03	0.16	bdl	0.01	bdl	bdl	10.80	96.99
TM12	rhy	24.92	0.03	20.94	bdl	7.23	20.62	0.23	12.93	0.06	bdl	0.01	bdl	bdl	bdl	11.70	98.76
TM12	rhy	25.79	0.05	21.74	bdl	9.53	16.49	0.21	11.82	0.03	bdl	bdl	0.72	bdl	bdl	10.61	97.08
TM12	rhy	24.53	0.04	21.13	bdl	6.87	21.11	0.25	12.45	0.01	bdl	bdl	0.01	bdl	bdl	10.27	96.76
TM12	rhy	24.30	0.03	21.73	bdl	7.68	20.70	0.20	12.33	0.06	0.04	bdl	bdl	bdl	bdl	11.21	98.35
TM12	rhy	25.41	0.04	20.03	0.01	0.16	25.94	0.25	13.43	0.03	0.01	0.02	0.02	bdl	bdl	11.09	96.51
TM13	shale	26.11	0.04	22.51	0.06	1.04	25.40	0.12	10.85	0.01	0.04	0.03	0.04	bdl	bdl	11.11	97.42
TM13	shale	23.72	bdl	22.86	0.04	0.88	27.00	0.07	11.28	0.03	0.02	0.06	0.02	bdl	bdl	10.87	96.94
TM13	shale	25.33	0.05	22.92	0.02	1.98	25.54	0.13	11.30	0.03	0.04	0.01	0.03	bdl	bdl	11.14	98.60
TM13	shale	23.64	bdl	22.79	0.08	1.01	26.34	0.14	11.29	0.04	0.01	0.01	0.05	bdl	bdl	10.82	96.33
TM13	shale	24.44	0.11	22.15	0.06	2.95	22.20	0.12	9.10	0.04	0.04	0.09	0.37	bdl	bdl	10.44	92.18
TM18	shale	22.73	bdl	18.87	0.02	bdl	40.95	0.04	3.92	0.04	0.02	0.02	bdl	bdl	bdl	10.09	96.78

Appendix D (continued): All EPMA results for chlorite analyses. All values in wt.-%

		SiO_2	TiO_2	Al_2O_3	Cr_2O_3	Fe_2O_3	FeO	MnO	MgO	ZnO	CaO	Na_2O	K_2O	F	Cl	H_2O*	Total
	dl	**0.01**	**0.03**	**0.08**	**0.01**	**0.02**	**0.02**	**0.01**	**0.01**	**0.01**	**0.01**	**0.01**	**0.01**	**0.01**	**0.01**		
Sample	**Host**																
TM13	shale	23.05	0.03	22.74	bdl	0.73	27.50	0.11	10.94	0.01	0.13	bdl	bdl	bdl	0.01	11.28	96.61
TM18	shale	22.63	bdl	19.22	0.01	bdl	40.57	0.05	4.24	0.01	0.10	bdl	bdl	bdl	bdl	10.15	97.08
TM18	shale	22.87	0.06	19.36	0.02	bdl	39.22	0.09	5.07	0.05	bdl	0.01	bdl	bdl	bdl	10.22	97.04
TM18	shale	22.75	0.06	19.54	0.03	bdl	39.62	0.09	5.07	0.01	bdl	bdl	bdl	bdl	bdl	10.26	97.52
TM18	shale	22.94	0.08	19.52	0.01	0.07	39.05	0.08	5.13	0.01	bdl	bdl	bdl	bdl	bdl	10.26	97.24
TM18	shale	23.11	0.06	19.20	0.01	bdl	39.41	0.08	5.31	0.01	bdl	bdl	0.01	bdl	bdl	10.28	97.57
TM18	shale	22.49	bdl	19.01	bdl	bdl	40.19	0.04	4.62	0.03	bdl	0.02	0.01	bdl	bdl	10.11	96.60
	median	25.41	0.03	19.45	0.01	0.70	25.63	0.13	12.79	0.02	0.01	0.01	0.01	bdl	bdl	11.05	97.47
	max	33.68	0.32	23.97	0.12	9.53	42.59	0.46	19.29	0.09	2.35	0.20	0.99	0.20	0.64	12.50	104.29
	min	20.22	bdl	13.23	bdl	bdl	9.46	bdl	3.91	bdl	bdl	bdl	bdl	bdl	bdl	9.59	88.71

Note: All oxide abundances recalculated assuming full site occupancy. H_2O* calculated.

chl - chlorite, sulf - sulfidic chert, mag - magnetite, carb - carbonate facies, rhy - rhyolite, and - andesite, bas - basalt, shale - unsubdivided clastic

Analyses performed with 1-5 µm spot size, 20 kV acceleration voltage and 20 nA current. Count time of 20 s on peak and 10 s off peak.

Appendix E: EPMA results for all apatite analyses. All values in wt.-%

		Si	Pb	Th	U	Al	Sc	Y	La	Ce	Pr	Nd	Sm	Eu	Gd	Tb	Dy	Ho	Er	Tm	Yb	Lu
	dl	0.005	0.036	0.037	0.036	0.004	0.011	0.033	0.042	0.036	0.065	0.035	0.032	0.031	0.032	0.030	0.059	0.061	0.034	0.032	0.033	0.035
Sample	**Host**																					
D015	mag-chert	bdl	bdl	bdl	bdl	bdl	bdl	0.055	bdl	bdl	bdl	bdl	bdl	bdl	bdl	bdl	bdl	bdl	bdl	bdl	bdl	bdl
D015	mag-chert	bdl	0.426	0.121	bdl	bdl	bdl	0.033	bdl	bdl	bdl	bdl	bdl	bdl	bdl	bdl	bdl	bdl	bdl	bdl	bdl	bdl
D015	mag-chert	0.800	bdl	bdl	bdl	bdl	bdl	bdl	bdl	bdl	bdl	bdl	bdl	bdl	bdl	bdl	bdl	bdl	bdl	bdl	bdl	bdl
D015	mag-chert	0.067	bdl	bdl	bdl	bdl	bdl	bdl	bdl	bdl	bdl	bdl	bdl	bdl	bdl	bdl	bdl	bdl	bdl	bdl	bdl	bdl
D015	mag-chert	bdl	bdl	bdl	0.601	bdl	bdl	bdl	bdl	bdl	bdl	bdl	bdl	bdl	bdl	0.032	bdl	bdl	bdl	bdl	bdl	bdl
SM052	mag-jasper	1.930	bdl	bdl	bdl	bdl	0.018	0.074	bdl	bdl	bdl	0.043	bdl	bdl	bdl	bdl	bdl	bdl	bdl	bdl	bdl	bdl
SM052	mag-jasper	bdl	0.042	bdl	bdl	bdl	bdl	0.133	bdl	0.044	bdl	0.040	bdl	bdl	bdl	bdl	bdl	bdl	bdl	bdl	bdl	bdl
SM052	mag-jasper	bdl	bdl	bdl	bdl	bdl	bdl	bdl	bdl	0.059	bdl	0.055	bdl	bdl	bdl	bdl	bdl	0.361	bdl	bdl	0.330	0.065
B013-1	mag-chert	0.324	bdl	bdl	bdl	bdl	bdl	0.127	bdl	0.101	bdl	0.073	bdl	bdl	bdl	bdl	bdl	bdl	bdl	bdl	bdl	bdl
B013-1	mag-chert	0.209	bdl	bdl	bdl	bdl	bdl	0.116	0.114	0.091	bdl	0.072	bdl	bdl	bdl	bdl	bdl	bdl	bdl	0.041	bdl	bdl
B013-1	mag-chert	0.096	bdl	bdl	bdl	bdl	bdl	0.130	0.078	0.116	bdl	0.040	0.038	bdl	bdl	bdl	0.070	bdl	bdl	bdl	bdl	bdl
17	mag-jasper	bdl	bdl	bdl	bdl	0.008	bdl	bdl	bdl	bdl	bdl	bdl	bdl	bdl	bdl	bdl	bdl	bdl	bdl	bdl	0.065	bdl
17	mag-jasper	bdl	bdl	bdl	bdl	bdl	0.015	bdl	bdl	bdl	bdl	bdl	bdl	bdl	bdl	bdl	bdl	bdl	0.223	bdl	bdl	bdl
11-11	mag-jasper	bdl	0.660	0.271	bdl	bdl	0.109	bdl	bdl	bdl	bdl	bdl	bdl	0.162	bdl	bdl	0.076	0.088	bdl	0.045	bdl	bdl
11-11	mag-jasper	bdl	bdl	0.794	bdl	bdl	0.116	bdl	bdl	bdl	bdl	bdl	0.061	bdl	bdl	0.057	0.184	0.102	bdl	bdl	bdl	bdl
11-11	mag-jasper	0.051	bdl	bdl	bdl	bdl	bdl	0.074	bdl	0.038	bdl	0.038	bdl	bdl	bdl	bdl	bdl	bdl	bdl	bdl	bdl	bdl
11-11	mag-jasper	bdl	bdl	bdl	bdl	bdl	0.017	0.056	bdl	bdl	bdl	bdl	bdl	bdl	bdl	bdl	bdl	bdl	bdl	bdl	bdl	bdl
11-11	mag-jasper	0.044	bdl	bdl	bdl	bdl	bdl	0.102	bdl	0.045	bdl	bdl	bdl	bdl	bdl	bdl	bdl	bdl	bdl	bdl	bdl	bdl
11-32	mag-chert	bdl	bdl	bdl	bdl	bdl	0.016	bdl	bdl	bdl	bdl	bdl	bdl	bdl	bdl	bdl	bdl	bdl	bdl	0.410	bdl	bdl
11-32	mag-chert	bdl	0.037	bdl	bdl	bdl	0.018	0.173	bdl	bdl	bdl	0.064	bdl	bdl	0.046	bdl	bdl	bdl	bdl	bdl	bdl	bdl
11-32	mag-chert	bdl	0.214	bdl	bdl	bdl	bdl	0.164	bdl	0.064	bdl	0.045	0.054	bdl	0.240	bdl	bdl	bdl	bdl	bdl	bdl	bdl
SH580	sulf. chert	0.702	bdl	bdl	0.953	0.268	bdl	0.141	bdl	bdl	bdl	bdl	bdl	bdl	bdl	bdl	bdl	bdl	0.039	bdl	bdl	bdl
SH580	sulf. chert	1.070	0.575	bdl	0.213	0.386	bdl	0.048	bdl	bdl	bdl	bdl	bdl	bdl	0.330	0.195	bdl	bdl	bdl	bdl	bdl	0.061
SH580	sulf. chert	0.541	bdl	bdl	bdl	0.019	bdl	bdl	bdl	bdl	bdl	bdl	bdl	bdl	bdl	bdl	bdl	bdl	bdl	bdl	bdl	bdl
SH580	sulf. chert	bdl	bdl	bdl	bdl	bdl	0.013	bdl	bdl	bdl	bdl	bdl	bdl	bdl	0.036	bdl	bdl	bdl	bdl	bdl	bdl	bdl
11-4	chlorite	0.058	bdl	bdl	bdl	0.027	0.019	0.042	bdl	0.069	bdl	0.071	0.047	bdl	bdl	bdl	bdl	bdl	bdl	bdl	bdl	bdl
11-4	chlorite	0.088	bdl	bdl	bdl	0.023	0.019	0.151	0.212	0.356	bdl	0.057	bdl	bdl	bdl	0.032	bdl	bdl	bdl	bdl	bdl	bdl
11-5	chlorite	0.118	0.117	bdl	bdl	0.020	0.082	bdl	0.142	0.352	0.145	bdl	bdl	bdl	0.112	0.102	bdl	bdl	bdl	0.034	bdl	bdl
11-5	chlorite	bdl	0.196	bdl	0.070	bdl	bdl	bdl	bdl	0.036	bdl	bdl	0.116	bdl	bdl	0.151	0.063	bdl	bdl	bdl	bdl	bdl
11-33	chlorite	3.348	bdl	bdl	bdl	0.438	bdl	0.172	0.099	0.164	0.067	0.046	bdl	bdl	bdl	bdl	bdl	bdl	0.042	bdl	bdl	bdl
11-33	chlorite	0.633	bdl	bdl	bdl	0.130	0.014	0.112	0.052	0.080	bdl	bdl	bdl	bdl	bdl	bdl	bdl	bdl	bdl	bdl	bdl	bdl
11-33	chlorite	0.806	bdl	bdl	bdl	0.092	bdl	0.037	bdl	bdl	bdl	bdl	bdl	bdl	bdl	bdl	bdl	bdl	bdl	bdl	bdl	bdl
	median	0.047	0.018	0.018	0.018	0.002	0.006	0.045	0.021	0.018	0.032	0.018	0.016	0.015	0.016	0.015	0.030	0.030	0.017	0.016	0.017	0.017
	max	3.348	0.660	0.794	0.953	0.438	0.116	0.173	0.212	0.356	0.145	0.073	0.116	0.162	0.330	0.195	0.184	0.361	0.223	0.410	0.330	0.065
	min	bdl	bdl	bdl	bdl	bdl	bdl	bdl	bdl	bdl	bdl	bdl	bdl	bdl	bdl	bdl	bdl	bdl	bdl	bdl	bdl	bdl

Appendix E (continued): EPMA results for all apatite analyses. All values in wt.-%

		Fe	Mg	Ca	Sr	Na	P	S	Cl	F*	O	Total	
	dl	0.013	0.005	0.006	0.022	0.009	0.006	0.006	0.006	0.066			
Sample	**Host**												**Comment**
D015	mag-chert	1.12	0.007	39.52	0.19	0.043	18.5	0.043	0.035	2.96	39.1	101.7	D015 ap in mag layer 4
D015	mag-chert	3.35	0.015	38.72	0.20	0.022	15.9	0.042	0.054	2.48	36.6	98.1	D015 ap in mag layer 3
D015	mag-chert	1.24	0.006	38.36	0.17	0.027	17.6	0.023	0.019	2.99	38.3	99.5	D015 ap in mag layer 3
D015	mag-chert	1.22	0.012	38.95	0.10	0.069	18.3	0.030	0.031	3.23	38.5	100.6	D015 ap in mag layer 4
D015	mag-chert	0.09	bdl	39.20	0.19	0.039	18.5	0.041	0.051	2.69	38.6	100.1	D015 ap in chert
SM052	mag-jasper	0.16	bdl	35.92	0.19	0.059	17.2	0.018	0.025	2.67	37.8	96.3	SM052 ap in jas
SM052	mag-jasper	0.17	0.009	38.95	0.10	0.110	18.3	0.050	0.029	2.37	38.5	99.0	SM052 ap in jas 2
SM052	mag-jasper	0.27	bdl	39.08	0.10	0.124	18.4	0.059	0.023	2.62	38.7	100.5	SM052 ap in jas 3
B013-1	mag-chert	0.56	bdl	39.16	0.16	0.054	18.2	bdl	0.036	3.15	38.5	100.6	B13-1 ap 1
B013-1	mag-chert	1.22	0.010	38.70	0.13	0.047	18.2	bdl	0.062	3.09	38.5	100.7	B13-1 ap 2
B013-1	mag-chert	2.07	bdl	38.74	0.10	0.037	18.0	bdl	0.057	3.33	38.4	101.4	B13-1 ap 3
17	mag-jasper	0.74	bdl	39.53	0.36	0.050	18.1	bdl	bdl	4.00	37.9	100.9	17 ap 1
17	mag-jasper	0.69	bdl	39.26	0.32	0.041	18.4	bdl	bdl	3.42	38.5	101.0	17 ap 2
11-11	mag-jasper	0.14	bdl	39.31	0.52	0.037	18.4	bdl	bdl	2.51	38.8	101.3	11b-11 ap in jas-mag 1
11-11	mag-jasper	0.12	0.036	39.58	0.49	0.041	18.5	bdl	bdl	2.43	39.1	101.6	11b-11 ap in jas-mag 2
11-11	mag-jasper	1.23	bdl	39.31	0.19	0.064	18.5	bdl	bdl	2.23	39.4	101.3	11b-11 ap in mag 1
11-11	mag-jasper	0.62	0.006	39.52	0.50	0.034	18.3	bdl	bdl	2.38	38.8	100.4	11b-11 ap in mag 2
11-11	mag-jasper	1.66	bdl	39.24	0.17	0.066	18.5	bdl	bdl	2.68	39.3	102.0	11b-11 ap in mag 3
11-32	mag-chert	0.58	0.055	39.59	0.14	0.029	18.4	bdl	bdl	3.14	38.7	101.3	11b-32 ap in mag trace mon inclusion
11-32	mag-chert	0.37	bdl	39.29	0.06	0.122	18.4	bdl	0.011	2.63	38.7	100.1	11b-32 ap in mag 2
11-32	mag-chert	0.50	bdl	39.64	0.06	0.071	18.3	bdl	bdl	2.58	38.8	100.9	11b-32 ap in mag 3
SH580	sulf. chert	0.03	bdl	38.95	0.05	0.189	18.0	0.019	0.010	3.64	38.6	101.6	SH580 ap in graphite 1
SH580	sulf. chert	0.04	bdl	39.21	0.23	0.124	18.1	0.013	0.032	3.83	39.2	103.7	SH 580 ap in graphite 2
SH580	sulf. chert	0.13	bdl	38.58	0.05	0.035	17.7	0.006	bdl	4.06	37.2	98.5	SH 580 ap in sulfide 3
SH580	sulf. chert	0.07	bdl	40.09	0.08	0.014	18.7	0.010	bdl	3.72	38.7	101.6	SH 580 ap in chert 4
11-4	chlorite	0.83	0.051	39.71	bdl	0.022	18.7	bdl	0.015	3.06	39.3	102.2	311b-4 ap 1
11-4	chlorite	1.35	0.023	37.15	0.06	0.351	16.9	bdl	bdl	3.17	36.4	96.4	311b-4 ap 1
11-5	chlorite	0.28	0.053	39.07	bdl	0.198	17.9	0.248	0.389	2.78	38.4	100.6	11b-5 ap 1
11-5	chlorite	0.28	bdl	39.54	bdl	0.168	18.2	0.231	0.112	3.53	38.5	101.3	11b-5 ap 2
11-33	chlorite	4.45	0.230	33.13	0.10	0.134	16.3	bdl	0.034	3.02	39.4	101.2	11b-33 ap 1
11-33	chlorite	2.06	0.090	38.34	0.08	0.091	17.9	0.006	0.034	3.08	39.0	101.9	11b-33 ap 1
11-33	chlorite	0.53	0.146	36.77	0.15	0.047	17.2	bdl	0.019	3.47	36.8	96.3	11b-33 ap 2
	median	0.57	0.003	39.183	0.13	0.052	18.3	0.003	0.019	3.04	38.6	100.9	
	max	4.45	0.230	40.086	0.52	0.351	18.7	0.248	0.389	4.06	39.4	103.7	
	min	0.03	bdl	33.134	bdl	0.014	15.9	bdl	bdl	2.23	36.4	96.3	

Note: dl - detection limit. Oxygen is halogen corrected. Mag - magnetite. Sulf- sulfide.

EPMA analyses of F* in apatite are subject to considerably lower precision than other elements due to quick migration of F in the crystal during analysis.

F results should be considered semiquantitative.

All analyses performed at 10 µm spot size, 20 kV acceleration voltage and 20 nA current.

Appendix F: LA-ICP-MS results for all apatite analyses. All results in ppm.

		Li	B	Na	Mg	Al	Si	P	S	Cl	K	Sc	Ti	V	Cr	Mn	Fe
	Isotope	7	11	23	25	27	29	31	34	35	39	45	49	51	53	55	56
	MRE [%]	62.9	116.5	5.4	9.2	22.6	11.9	58.7	24.3	212.0	31.2	62.7	64.8	64.3	77.4	4.5	4.6
	dl [ppm]	0.89	2.18	9.93	2.10	0.95	73.7	14.4	49.1	145	2.06	0.19	0.55	0.03	0.68	0.2	1.24
Sample	**Layer type**																
11-11	magnetite	1.58	5.51	446	14	1.14	124	288324	426	182	2.56	0.23	0.74	0.05	1.01	252	441
11.11	magnetite	1.80	3.44	462	12	1.15	270	237885	368	183	2.56	0.36	0.55	0.05	0.85	244	75.7
11-11	magnetite	3.98	3.60	439	11	12.71	1451	248959	310	178	2.51	0.23	0.73	0.04	0.83	244	325
11-11	magnetite	1.80	5.07	433	13	1.15	286	235096	363	242	2.62	0.23	1.23	0.04	0.88	276	576
11-11	magnetite	15.7	6417	1107	267	58.93	1944	177881	309	2613	81.9	1.20	8.95	0.29	9.77	229	735
11-11	magnetite	2.24	4.31	451	11	2.89	293	248371	345	331	2.46	0.24	0.73	0.04	0.90	258	82.6
11-4	chlorite	2.56	4.15	848	963	1014	4840	267815	443	193	8.68	0.37	9.71	17.0	1.21	511	16573
11-4	chlorite	0.89	3.22	310	576	1.00	560	253501	401	266	5.24	0.45	0.59	2.82	0.75	463	1746
SM11	magnetite	1.53	3.98	482	1038	30.12	33280	214560	456	224	22.3	1.48	2.51	0.45	1.15	2288	13495
SM11	magnetite	2.18	7.64	433	5497	22.37	167230	225348	504	409	6.77	2.16	4.53	0.31	3.00	2967	4924
SM11	magnetite	4.15	8.35	434	260	75.85	121562	170792	502	373	47.1	0.77	7.64	0.87	3.11	2343	13752
SM11	magnetite	4.86	7.64	97	115088	2.46	21629	61772	416	349	13.9	13.97	0.67	0.07	0.98	45227	55636
SM11	magnetite	2.95	6.22	773	130240	684	248051	182919	706	356	244	2.50	14.35	0.39	1.64	3551	47091
SM052	jasper	1.42	7.09	1008	68	20.52	41675	166409	729	312	15.17	0.28	0.84	0.05	1.04	128	7152
SM052	jasper	1.58	4.47	828	26	8.02	42655	159574	527	239	3.11	0.30	0.81	0.06	1.63	114	18449
SM052	jasper	1.36	4.64	691	105	17.35	40277	162606	427	186	8.02	0.27	0.77	0.06	0.97	141	8822
SM052	jasper	1.31	3.60	654	165	74.76	33950	178579	536	273	5.89	0.34	0.94	0.15	1.03	130	36992
SM052	jasper	1.15	2.18	1247	37	5.78	6502	202387	479	225	2.07	0.21	0.69	0.05	0.71	105	3646
SM052	jasper	bdl	4.47	1088	91	25.37	50932	193402	643	297	10.26	0.46	0.77	0.06	1.30	456	3915
SM052	jasper	bdl	5.89	1072	253	87.31	26420	228388	524	308	23.03	0.31	1.14	0.07	1.05	330	3982
SM052	jasper	2.18	2.89	1122	80	1.53	2115	198123	532	374	2.95	0.23	0.67	0.04	1.15	459	5830
SM052	jasper	1.75	4.04	1113	177	22.10	3506	199376	596	350	18.99	0.33	0.82	0.06	1.36	464	4303
SM052	jasper	2.46	4.20	1040	60	6.93	29338	202006	497	440	3.00	0.29	0.86	0.05	bdl	467	7995
SM052	jasper	1.80	5.57	1156	105	33.34	15440	196065	563	420	8.02	0.33	0.98	0.06	1.29	379	8959
SM052	jasper	1.83	26.1	852	43	6.28	54661	194151	621	253	3.62	0.62	1.05	0.07	1.33	388	6424
SM052	jasper	bdl	3.87	900	53	1.86	4682	253387	474	313	3.00	0.26	0.72	0.08	0.93	250	17385
SM052	jasper	1.69	4.86	760	61	10.10	109724	193283	634	236	7.80	0.35	1.08	0.07	1.26	875	2146
SM052	jasper	2.51	7.64	727	65	19.54	10412	245218	553	337	23.7	0.33	0.78	0.05	1.03	304	4281
SM052	jasper	2.29	484	844	37	6.22	9997	253722	606	673	22.0	0.41	1.05	0.07	bdl	172	6747
SM052	jasper	3.00	10.4	844	52	12.61	21468	226091	564	704	20.0	0.26	0.62	0.05	1.11	222	8272
SM052	jasper	3.22	7.64	1001	71	7.37	46745	237323	700	895	32.4	0.28	0.89	0.05	1.05	199	8662
SM052	jasper	2.89	4.26	910	41	4.58	14410	263332	555	537	9.55	0.27	1.11	0.09	0.94	326	23802
SM052	jasper	3.27	6.55	1002	85	3.11	1611	314931	519	397	34.4	0.25	0.73	0.05	1.60	322	1452
	median	2.18	4.86	844	70.9	10.10	15440	214560	519	313	8.02	0.33	0.84	0.06	1.05	322	6424
	max	15.7	6417	1247	130240	1014	248051	314931	729	2613	244	14.0	14.4	17.0	9.8	45227	55636
	min	bdl	2.18	97	11	1.00	123.87	61772	309	178	2.07	0.21	0.55	0.04	bdl	105	75.7

Appendix F (continued): LA-ICP-MS results for all apatite analyses. All results in ppm.

		Co	Ni	Cu	Zn	Ga	As	Rb	Sr	Y	Zr	Nb	Sb	Cs	Ba	La	Ce	Pr	Nd	Sm
	Isotope	59	60	65	66	69	75	85	88	89	90	93	121	133	137	139	140	141	146	147
	MRE [%]	53.4	63.1	30.1	48.7	43.2	22.5	63.2	6.5	6.5	30.0	77.0	56.5	84.3	18.1	4.8	5.4	5.8	5.8	6.2
	dl [ppm]	0.05	0.26	0.10	0.22	0.02	0.63	0.10	0.01	0.003	0.01	0.01	0.11	0.06	0.06	0.003	0.004	0.003	0.02	0.02
Sample	**Layer type**																			
11-11	magnetite	0.19	0.29	0.10	0.22	0.05	4.31	0.11	4188	861	0.02	0.01	0.14	0.07	0.49	42.7	193	38.9	237	126.1
11.11	magnetite	0.07	0.32	0.10	0.28	0.04	4.86	0.12	4265	827	0.03	0.01	0.15	0.06	bdl	43.7	187	39.3	252	125.0
11-11	magnetite	0.06	0.30	0.36	0.25	0.03	3.87	0.11	5654	890	0.03	0.04	0.13	0.07	0.35	42.3	187	38.1	255	127.7
11-11	magnetite	0.05	0.34	0.14	0.47	0.04	4.58	0.22	4857	826	0.10	0.07	0.13	0.06	0.14	40.7	178	39.2	250	125.5
11-11	magnetite	0.31	4.53	4.91	21.99	0.07	22.5	1.13	4781	913	1.40	0.06	1.09	0.34	1.53	35.5	157	35.6	241	126.6
11-11	magnetite	0.11	0.28	0.16	0.30	0.02	5.40	0.15	5165	818	0.05	0.00	0.15	0.07	0.09	38.6	170	36.4	229	122.8
11-4	chlorite	0.31	0.83	1.44	4.47	0.75	7.42	0.11	612	640	3.09	0.03	0.11	0.06	6.55	867	2692	366	1544	285.9
11-4	chlorite	0.40	0.27	0.20	1.22	0.10	4.69	0.13	397	226	0.57	0.02	0.14	0.06	2.25	381	1174	159	643	115.1
SM11	magnetite	0.27	1.65	0.33	9.17	0.07	9.60	0.17	1791	601	30.0	0.04	0.21	0.16	2.12	112	266	40.0	235	92.4
SM11	magnetite	0.35	1.69	0.66	15.44	0.07	7.64	0.25	1426	514	6.88	0.02	0.23	0.14	2.18	90.7	242	42.0	251	102
SM11	magnetite	0.15	0.98	2.46	5.68	0.37	3.11	0.27	1120	511	0.73	0.04	0.27	bdl	17.2	56.9	198	31.4	200	85.8
SM11	magnetite	2.05	2.32	0.44	50.15	0.04	5.13	0.17	2109	205	0.09	0.01	bdl	bdl	2.11	25.6	65.5	11.4	71.2	30.9
SM11	magnetite	14.8	117	3.44	458.37	0.29	14.3	1.88	2512	605	1.39	0.03	0.32	1.11	3.16	118	355	55.4	310	111.2
SM052	jasper	0.08	0.36	0.24	0.33	0.22	66.6	0.38	1615	915	0.11	0.01	0.24	0.09	9.60	158	299	37.7	168	43.8
SM052	jasper	0.10	0.43	0.37	0.33	0.06	47.5	0.20	1483	1080	0.09	0.02	1.79	0.10	2.82	166	347	46.2	218	59.3
SM052	jasper	0.07	0.37	0.25	0.34	0.09	56.8	0.29	1916	893	0.09	0.01	0.36	0.08	4.16	138	301	37.7	162	43.9
SM052	jasper	0.07	0.34	0.38	0.29	0.10	45.3	0.16	1466	1251	0.20	0.01	0.73	0.08	4.86	177	360	48.0	220	56.6
SM052	jasper	0.06	0.28	0.11	0.25	0.20	58.9	bdl	1166	886	0.06	0.01	0.28	0.06	9.22	261	497	49.5	182	47.3
SM052	jasper	0.10	0.41	0.53	0.38	0.21	59.5	0.30	2031	1382	0.20	0.01	0.21	0.10	6.01	277	519	63.4	273	75.7
SM052	jasper	0.17	0.44	0.58	0.46	0.14	71.5	0.37	1548	1313	0.42	0.01	0.26	0.10	6.81	244	471	60.0	262	74.3
SM052	jasper	0.11	0.34	0.37	0.34	0.04	42.6	0.22	1132	1056	0.09	0.01	0.14	0.07	3.65	214	443	55.4	255	68.0
SM052	jasper	0.09	0.47	0.42	0.33	0.18	49.7	0.19	1288	1283	0.04	0.01	0.25	0.10	5.70	229	446	58.0	270	79.8
SM052	jasper	0.10	0.44	0.31	0.33	0.04	77.5	0.17	1317	1196	0.08	0.01	0.47	0.09	5.03	240	452	55.3	241	68.9
SM052	jasper	0.07	0.56	0.26	2.34	0.23	50.7	0.25	1268	1227	0.10	0.01	0.49	0.11	7.97	227	434	56.7	255	71.1
SM052	jasper	0.10	0.53	1.07	bdl	0.06	70.4	0.20	1351	967	0.07	bdl	0.98	bdl	5.27	176	322	40.3	183	50.9
SM052	jasper	0.09	0.69	0.33	0.67	0.09	184	bdl	1736	1147	0.03	0.00	0.28	0.08	5.30	194	364	46.7	199	57.1
SM052	jasper	0.13	0.45	0.49	0.47	0.12	79.12	0.17	3746	1009	0.08	0.00	0.52	0.11	6.49	183	327	40.6	181	50.3
SM052	jasper	0.07	0.41	0.54	0.41	0.47	73.12	0.40	2512	898	0.12	0.01	0.60	0.10	42.8	158	308	38.8	161	42.7
SM052	jasper	0.13	0.62	0.29	0.55	5.12	96.0	0.43	2478	965	0.24	0.01	0.95	0.18	305	169	336	39.8	168	42.7
SM052	jasper	0.13	0.43	0.30	0.47	0.48	65.5	0.27	2092	803	0.10	0.01	0.92	0.09	34.4	168	310	38.1	158	42.6
SM052	jasper	0.08	0.80	1.16	0.87	46.33	123	0.17	3701	989	0.14	0.00	0.69	0.09	1970	138	291	34.8	150	44.5
SM052	jasper	0.08	0.39	0.38	0.39	0.16	139	bdl	3027	1158	0.06	0.00	0.22	0.08	5.92	184	378	44.9	189	52.5
SM052	jasper	0.09	0.55	0.25	0.36	0.13	189	0.88	3482	1028	0.04	0.01	0.16	0.18	6.22	169	396	44.0	177	52.8
	median	0.10	0.44	0.37	0.44	0.10	49.66	0.21	1916	913	0.10	0.01	0.26	0.09	5.29	168.07	327	40.6	229	68.9
	max	14.8	117	4.91	458	46.3	189	1.88	5654	1382	30.0	0.07	1.79	1.11	1970	867	2692	366	1544	286
	min	0.05	0.27	0.10	bdl	0.02	3.11	bdl	397	205	0.00	bdl	bdl	bdl	bdl	13.70	57.90	11.4	71.2	30.9

Appendix F (continued): LA-ICP-MS results for all apatite analyses. All results in ppm.

		Eu	Gd	Tb	Dy	Ho	Er	Tm	Yb	Lu	Pb	Th	U
	Isotope	153	157	159	163	165	167	169	172	175	208	232	238
	MRE [%]	5.3	5.6	5.4	5.8	5.8	5.9	6.1	5.9	10.1	6.3	31.3	14.7
	dl [ppm]	0.01	0.03	0.003	0.01	0.003	0.01	0.02	0.01	0.003	0.05	0.005	0.004
Sample	**Layer type**												
11-11	magnetite	105	190	26.4	142	25.2	59.9	7.00	39.6	5.29	27.0	0.027	0.390
11.11	magnetite	110	194	26.4	141	25.3	59.8	7.06	38.9	5.28	25.3	0.012	0.350
11-11	magnetite	115	209	29.0	155	27.0	64.6	7.66	42.7	5.89	23.9	0.053	0.475
11-11	magnetite	114	185	26.4	138	25.8	58.0	6.75	36.1	5.04	24.6	0.013	0.302
11-11	magnetite	103	176	21.6	139	25.2	62.2	7.09	35.2	5.12	19.1	0.082	0.562
11-11	magnetite	103	181	25.2	144	25.7	58.4	7.08	39.7	4.87	21.4	0.014	0.309
11-4	chlorite	29.5	231	27.7	147	25.0	53.5	5.72	29.2	3.31	5.86	7.530	1.915
11-4	chlorite	15.4	90.0	10.2	52.2	8.51	20.7	2.43	12.9	1.74	3.88	9.004	5.975
SM11	magnetite	100	144	19.1	111	20.2	46.3	5.59	27.4	3.79	67.4	0.096	0.240
SM11	magnetite	110	148	18.9	103	21.7	51.7	5.39	29.8	3.95	96.6	0.109	0.573
SM11	magnetite	86.9	124	17.9	102	17.3	44.4	4.74	25.9	3.31	86.7	0.016	0.491
SM11	magnetite	32.0	48.0	6.7	34.4	7.02	15.6	1.90	10.3	1.33	27.0	0.013	0.096
SM11	magnetite	110	144	19.2	115	20.0	49.0	6.11	37.5	4.95	56.6	0.229	0.164
SM052	jasper	48.9	72.1	13.1	101	23.1	74.5	9.19	49.7	7.32	9.68	0.062	0.195
SM052	jasper	60.4	88.2	14.5	112	26.8	78.3	9.63	54.0	7.21	8.98	0.065	0.659
SM052	jasper	49.6	66.1	12.0	100	23.4	66.0	8.37	46.8	6.74	10.8	0.082	0.166
SM052	jasper	55.9	91.1	14.6	115	31.3	78.4	9.00	49.8	7.20	10.2	0.087	0.796
SM052	jasper	71.9	95.1	15.7	123	24.9	68.7	11.3	61.4	8.80	9.28	0.225	0.226
SM052	jasper	85.2	119	20.6	153	36.8	115	14.5	77.7	10.9	36.5	0.374	0.211
SM052	jasper	82.9	118	20.1	157	35.4	110	13.5	74.2	10.6	31.6	0.378	0.198
SM052	jasper	80.7	110	17.2	125	27.1	84.4	10.9	57.9	8.02	32.7	0.071	0.321
SM052	jasper	87.4	129	21.0	142	33.8	96.7	12.0	64.8	9.20	43.7	0.118	0.376
SM052	jasper	76.7	104	18.9	142	32.4	101	12.5	71.4	9.76	22.6	0.277	0.267
SM052	jasper	77.7	115	18.3	139	32.5	98.0	11.8	67.1	9.45	23.8	0.337	0.433
SM052	jasper	52.3	79.1	12.9	101	24.3	76.9	8.94	51.5	7.06	17.1	0.128	0.363
SM052	jasper	65.6	96.1	17.2	128	30.7	89.9	11.0	60.1	8.26	21.2	0.067	0.154
SM052	jasper	54.6	79.7	13.4	97.4	25.0	76.1	9.59	51.6	7.69	70.2	0.275	0.314
SM052	jasper	52.3	74.6	12.7	98.2	23.2	68.9	8.66	49.6	6.92	26.4	0.128	0.319
SM052	jasper	47.9	69.6	12.2	99.9	25.5	80.2	9.59	57.2	8.55	12.4	0.186	0.513
SM052	jasper	48.7	70.3	11.9	90.0	21.3	66.8	7.96	45.8	6.40	12.2	0.121	0.367
SM052	jasper	49.7	75.6	13.2	103	25.0	79.0	10.0	57.4	8.16	22.0	0.062	0.381
SM052	jasper	64.0	84.9	15.2	119	29.4	90.9	12.2	72.2	11.3	34.1	0.012	0.112
SM052	jasper	66.0	85.8	14.4	111	26.6	86.8	11.0	67.3	9.89	36.3	0.027	0.058
	median	71.9	104	17.2	115	25.2	68.9	8.94	49.7	7.06	23.9	0.087	0.321
	max	115	231	29.0	157	36.8	115	14.5	77.7	11.3	96.6	9.00	5.98
	min	15.4	48.0	6.7	34.4	7.0	15.6	1.90	10.3	0.49	3.88	0.012	0.026

Appendix G: EPMA results for all monazite and xenotime analyses. All values in wt.-%

			Si	Pb	Th	U	Al	Sc	Y	La	Ce	Pr	Nd	Sm	Eu	Gd	Tb	Dy	Ho	Er	Tm
		dl	0.010	0.036	0.037	0.036	0.011	0.011	0.033	0.042	0.036	0.065	0.035	0.032	0.031	0.032	0.030	0.059	0.061	0.034	0.032
Sample	**Mineral**	**Host**																			
A028	monazite	chert-chl	0.082	0.073	0.184	bdl	bdl	0.017	0.265	14.995	25.033	2.241	10.057	1.298	0.533	0.858	bdl	0.136	0.078	0.060	bdl
A028	monazite	chert-chl	0.446	0.064	0.237	bdl	bdl	bdl	0.313	14.997	25.242	2.168	9.686	1.302	0.542	0.648	bdl	0.150	bdl	0.048	bdl
A028	monazite	chert-chl	2.478	bdl	0.235	bdl	bdl	bdl	0.325	12.865	21.280	1.986	8.259	1.231	0.409	0.670	bdl	0.086	bdl	bdl	bdl
A028	monazite	chert-chl	0.346	0.079	0.355	bdl	bdl	bdl	0.441	14.900	25.769	2.199	9.873	1.383	0.545	0.697	bdl	0.199	bdl	bdl	bdl
A028	monazite	chert-chl	0.394	0.040	0.361	bdl	bdl	bdl	0.274	15.769	26.741	2.163	9.410	1.072	0.513	0.529	bdl	0.065	bdl	bdl	bdl
A028	monazite	chert-chl	2.370	0.051	0.298	bdl	0.118	bdl	0.285	13.308	23.767	1.983	9.100	1.197	0.526	0.553	bdl	bdl	0.077	0.035	bdl
D015	monazite	magnetite	0.944	bdl	0.068	bdl	bdl	bdl	0.261	19.287	25.048	1.927	8.026	0.698	0.382	0.302	bdl	bdl	bdl	0.044	bdl
D015	monazite	magnetite	3.366	bdl	0.081	bdl	0.186	bdl	0.227	19.707	25.462	1.660	6.521	0.421	0.208	0.189	bdl	bdl	bdl	bdl	bdl
11-4	monazite	chlorite	4.256	0.258	2.058	bdl	0.596	bdl	0.260	9.210	21.686	2.458	9.693	1.656	0.321	0.806	0.057	0.091	bdl	0.058	bdl
11-5	monazite	chlorite	2.432	0.716	4.448	0.106	0.764	0.016	0.637	8.277	19.660	2.091	9.468	1.801	0.262	0.945	bdl	0.211	bdl	0.089	bdl
11-5	monazite	chlorite	2.582	0.237	2.242	bdl	2.817	bdl	0.215	8.613	20.104	2.250	9.671	1.703	0.249	0.858	0.044	0.122	bdl	0.052	0.066
11-5	monazite	chlorite	0.406	0.454	2.421	bdl	0.013	bdl	0.364	11.805	26.220	2.350	9.412	1.450	0.326	0.792	bdl	0.207	bdl	bdl	bdl
11-5	monazite	chlorite	0.154	0.134	1.266	bdl	0.192	bdl	0.448	10.973	24.645	2.675	11.479	2.104	0.348	1.076	bdl	0.197	bdl	bdl	bdl
11-11	monazite	magnetite	0.010	0.071	0.618	bdl	bdl	bdl	0.199	15.627	25.562	2.345	9.290	1.350	0.501	0.537	bdl	0.109	bdl	bdl	bdl
11-11	monazite	magnetite	0.076	bdl	0.350	bdl	bdl	bdl	0.198	15.543	25.803	2.232	9.451	1.259	0.545	0.542	bdl	bdl	0.065	bdl	bdl
11-11	monazite	magnetite	bdl	0.076	0.328	bdl	bdl	bdl	0.193	15.515	25.270	2.287	10.178	1.443	0.633	0.666	bdl	0.080	bdl	bdl	bdl
11-11	monazite	magnetite	0.023	0.067	0.514	bdl	bdl	bdl	0.220	15.345	25.779	2.307	10.255	1.393	0.610	0.574	bdl	0.060	bdl	bdl	bdl
11-11	monazite	magnetite	0.351	0.037	0.384	bdl	bdl	bdl	0.338	15.706	25.765	2.381	9.673	1.279	0.502	0.527	bdl	0.100	bdl	bdl	bdl
11-12	monazite	magnetite	3.356	0.132	1.005	bdl	bdl	bdl	0.170	17.356	23.604	1.775	7.123	0.701	0.349	0.198	bdl	0.068	bdl	0.047	bdl
11-12	monazite	magnetite	0.139	0.188	1.617	bdl	0.086	bdl	0.223	20.630	24.232	1.650	6.492	0.638	0.282	0.253	bdl	0.088	bdl	bdl	bdl
11-12	monazite	magnetite	bdl	0.121	0.731	bdl	bdl	bdl	0.313	13.735	21.350	1.902	8.406	1.006	0.414	0.578	bdl	0.135	bdl	0.051	bdl
11-12	monazite	magnetite	0.043	0.073	0.746	bdl	0.023	bdl	0.205	14.676	22.988	1.954	8.737	0.953	0.478	0.504	bdl	0.109	bdl	0.072	bdl
11-32	monazite	magnetite	0.021	0.077	0.786	bdl	0.012	bdl	0.252	14.672	24.396	2.139	9.811	1.160	0.487	0.595	bdl	bdl	bdl	bdl	bdl
11-32	monazite	magnetite	bdl	0.070	0.654	bdl	bdl	bdl	0.278	14.301	25.578	2.329	10.221	1.375	0.375	0.718	bdl	0.131	bdl	0.036	0.039
11-32	monazite	magnetite	bdl	0.124	0.781	bdl	bdl	bdl	0.292	15.115	26.033	2.296	9.488	1.120	0.417	0.565	bdl	0.087	bdl	0.037	bdl
11-32	monazite	magnetite	0.046	0.092	0.540	bdl	0.021	bdl	0.179	15.098	26.659	2.235	9.346	1.099	0.378	0.520	bdl	0.089	bdl	0.047	bdl
11-33	monazite	mag-chl	6.753	0.179	1.340	bdl	0.032	bdl	0.210	14.319	23.036	1.793	7.352	0.865	0.273	0.472	bdl	bdl	bdl	bdl	bdl
SM17	*xenotime*	*magnetite*	*bdl*	*0.357*	*bdl*	*bdl*	*bdl*	*bdl*	*39.781*	*bdl*	*bdl*	*bdl*	*0.107*	*0.161*	*0.350*	*0.819*	*0.152*	*2.280*	*0.771*	*2.800*	*0.443*
		median	0.346	0.076	0.618	0.023	0.004	0.006	0.261	14.995	25.048	2.199	9.451	1.259	0.414	0.574	0.021	0.089	0.038	0.020	bdl
		max	6.7533	0.7164	4.4483	0.1056	2.8167	0.0171	0.6371	20.63	26.741	2.6755	11.479	2.1041	0.6331	1.0763	0.0567	0.2114	0.078	0.0888	0.0658
		min	bdl	bdl	0.0679	bdl	bdl	bdl	0.1699	8.2767	19.66	1.6503	6.4923	0.4207	0.208	0.1889	bdl	bdl	bdl	bdl	bdl

Appendix G (continued): EPMA results for all monazite and xenotime analyses. All values in wt.-%

			Yb	Lu	Fe	Mg	Ca	Sr	Na	P	S	Cl	F	O	Total
		dl	0.033	0.035	0.013	0.005	0.006	0.022	0.009	0.006	0.006	0.006	0.066		
Sample	**Mineral**	**Host**													
A028	monazite	chert-chl	bdl	bdl	1.803	bdl	0.073	0.030	bdl	13.2	0.014	0.047	0.535	27.3	98.9
A028	monazite	chert-chl	bdl	bdl	2.220	bdl	0.077	bdl	bdl	12.8	0.011	0.034	0.534	27.2	98.8
A028	monazite	chert-chl	bdl	bdl	5.366	0.310	0.454	0.042	bdl	11.4	0.010	0.043	0.452	28.1	96.1
A028	monazite	chert-chl	0.044	bdl	1.956	0.006	0.121	0.053	bdl	12.9	0.012	0.045	0.461	27.5	99.9
A028	monazite	chert-chl	bdl	bdl	1.837	0.055	0.051	bdl	bdl	13.0	0.010	0.045	0.562	27.6	100.6
A028	monazite	chert-chl	bdl	bdl	3.581	0.344	0.063	bdl	bdl	11.6	bdl	0.054	0.421	28.1	97.9
D015	monazite	magnetite	bdl	bdl	bdl	bdl	0.060	0.068	bdl	12.8	0.014	0.029	0.493	27.1	97.6
D015	monazite	magnetite	bdl	bdl	bdl	0.182	0.035	0.040	bdl	12.9	0.019	0.037	0.485	30.0	101.9
11-4	monazite	chlorite	bdl	bdl	2.872	0.322	0.293	0.061	bdl	11.6	0.011	0.043	0.648	29.9	99.3
11-5	monazite	chlorite	0.061	bdl	3.443	0.386	0.857	0.226	bdl	11.1	0.086	0.044	0.663	27.9	96.7
11-5	monazite	chlorite	0.045	bdl	6.309	1.681	0.276	0.113	bdl	10.7	0.015	0.045	0.451	30.8	102.3
11-5	monazite	chlorite	bdl	bdl	1.233	bdl	0.656	0.274	bdl	12.6	0.115	0.051	0.871	26.9	99.0
11-5	monazite	chlorite	bdl	bdl	2.002	0.087	0.574	0.243	bdl	12.6	0.132	0.052	0.418	27.2	99.1
11-11	monazite	magnetite	bdl	bdl	4.078	bdl	0.091	0.098	bdl	12.6	0.021	0.040	0.466	27.5	101.2
11-11	monazite	magnetite	bdl	bdl	4.175	bdl	0.024	0.073	bdl	13.4	bdl	0.036	0.518	28.5	102.9
11-11	monazite	magnetite	bdl	bdl	2.999	bdl	0.067	0.110	bdl	13.2	bdl	0.042	0.594	27.7	101.5
11-11	monazite	magnetite	bdl	bdl	2.875	bdl	0.043	0.083	bdl	13.2	0.007	0.046	0.608	27.8	101.8
11-11	monazite	magnetite	0.041	bdl	1.164	bdl	0.098	0.078	bdl	13.2	0.027	0.040	0.596	27.5	99.8
11-12	monazite	magnetite	bdl	bdl	2.267	bdl	0.180	0.077	bdl	12.3	0.013	0.028	0.611	29.5	101.0
11-12	monazite	magnetite	bdl	bdl	1.769	0.033	0.294	0.087	bdl	12.8	0.014	0.032	0.520	27.0	99.1
11-12	monazite	magnetite	bdl	bdl	9.960	bdl	0.136	0.037	bdl	11.3	bdl	0.031	0.481	27.0	97.7
11-12	monazite	magnetite	0.097	bdl	8.562	bdl	0.126	0.133	bdl	12.0	0.008	0.034	0.553	27.9	101.0
11-32	monazite	magnetite	bdl	bdl	3.736	bdl	0.694	0.101	bdl	12.9	0.013	0.045	0.542	27.6	100.2
11-32	monazite	magnetite	bdl	bdl	2.107	bdl	0.103	bdl	bdl	13.0	0.008	0.035	0.568	27.1	99.1
11-32	monazite	magnetite	bdl	bdl	2.463	bdl	0.231	0.132	bdl	13.0	0.065	0.041	0.560	27.5	100.4
11-32	monazite	magnetite	bdl	bdl	2.461	bdl	0.132	0.044	bdl	13.1	0.016	0.045	0.560	27.5	100.2
11-33	monazite	mag-chl	bdl	0.035	4.147	0.039	0.231	0.097	bdl	11.6	0.011	0.035	0.542	32.9	106.3
SM17	*xenotime*	*magnetite*	*2.275*	*0.371*	*2.801*	*bdl*	*bdl*	*bdl*	*0.009*	*15.9*	*bdl*	*bdl*	*bdl*	*34.0*	*103.5*
		median	0.021	0.021	2.463	0.005	0.126	0.077	bdl	12.8	0.013	0.0424	0.5418	27.6	99.9
		max	0.0972	0.02126	9.9597	1.6812	0.8569	0.274	bdl	13.4	0.1319	0.0542	0.8711	32.9	106.3
		min	bdl	bdl	bdl	bdl	0.0242	bdl	bdl	10.7	bdl	0.028	0.4178	26.9	96.1

Note: bdl - below detection limit.

Analyses performed at 1 µm spot size, 20 kV acceleration voltage and 20 nA current.

Count time of 20 s on peak for trace elements and 10 s on peak for major elements, 10 s off peak for all elements.

Appendix H: All EPMA analyses of quartz (semi-quantitative, all values in wt.-%)

		SiO_2	TiO_2	Al_2O_3	Cr_2O_3	V_2O_3	Fe_2O_3	MnO	MgO	CaO	ZnO	NiO	Total	
	dl	0.01	0.03	0.08	0.01	0.01	0.02	0.01	0.01	0.01	0.01	0.01		
Sample	**Host**													**Comments**
SH580	sulf. chert	103.5	bdl	bdl	0.02	bdl	0.08	bdl	bdl	bdl	bdl	bdl	103.6	SH580 qtz 1
SH580	sulf. chert	97.8	bdl	bdl	bdl	bdl	0.02	bdl	bdl	bdl	bdl	bdl	97.8	SH580 qtz 2
11-4	chlorite	95.9	bdl	bdl	bdl	bdl	0.83	bdl	bdl	bdl	bdl	bdl	96.8	3-11b-4 qtz1
11-6a	chlorite	95.1	0.04	bdl	bdl	bdl	1.94	bdl	bdl	0.01	bdl	bdl	97.1	6a mag vein lay 2 chlor4
11-6a	chlorite	99.6	bdl	bdl	bdl	bdl	0.42	0.01	bdl	bdl	bdl	bdl	100.0	6a mag vein lay 2 chlor5
11-6a	chlorite	99.4	bdl	bdl	bdl	bdl	0.30	bdl	0.05	0.03	bdl	bdl	99.8	6a mag vein lay 2 chlor6
11-6a	chlorite	101.1	0.04	bdl	bdl	bdl	1.06	bdl	0.01	0.01	0.02	bdl	102.2	6a mag lay2 trans mag5
11-6a	chlorite	103.1	bdl	bdl	bdl	0.01	1.06	bdl	bdl	bdl	bdl	bdl	104.1	6a mag lay2 chlorite5
11-6b	magnetite	97.7	bdl	bdl	0.01	bdl	0.86	bdl	bdl	bdl	0.02	bdl	98.6	6b lay5 qtz1
11-6b	magnetite	97.7	bdl	bdl	bdl	bdl	0.61	bdl	bdl	bdl	bdl	bdl	98.3	6b lay5 qtz2
11-6b	magnetite	100.7	bdl	bdl	bdl	bdl	1.44	bdl	bdl	bdl	0.02	bdl	102.2	6b lay3 qtz
11-24	mag-carb	98.1	bdl	bdl	bdl	bdl	1.10	0.01	bdl	bdl	0.03	bdl	99.2	24 lay2 backgr qtz2
11-33	mag-bt	103.8	bdl	bdl	bdl	bdl	0.85	bdl	bdl	bdl	bdl	bdl	104.7	33 mapping area qtz
11-34	mag-chl	103.8	bdl	bdl	bdl	0.01	0.97	bdl	bdl	bdl	bdl	bdl	104.9	34 mapping qtz1
11-34	mag-chl	104.2	bdl	bdl	bdl	0.01	0.86	bdl	bdl	bdl	bdl	bdl	105.1	34 mapping qtz2
	median	100.1	bdl	bdl	bdl	bdl	0.83	bdl	bdl	bdl	0.01	bdl	101.0	
	max	104.2	0.04	bdl	0.02	0.01	1.94	0.01	0.05	0.03	0.03	0.01	105.1	
	min	95.1	bdl	bdl	bdl	bdl	bdl	bdl	bdl	bdl	bdl	bdl	96.8	

Note: layer type lists the major layer type (chert, magnetite, jasper, chlorite, shale) plus potentially abundant secondary mineral phases.
calibration of the EPMA run was not for quartz specifically, so the results should be considered semi-quantitative

Appendix I: All EPMA analyses of hematite (all values in wt.-%)

		SiO_2	TiO_2	Al_2O_3	Cr_2O_3	V_2O_3	Fe_2O_3	MnO	MgO	CaO	ZnO	NiO	Total	
	dl	0.01	0.03	0.08	0.01	0.01	0.02	0.01	0.01	0.01	0.01	0.01		
Sample	**Host**													**Comment**
11-41b	chert	0.78	bdl	bdl	bdl	bdl	99.6	0.02	0.23	0.04	bdl	bdl	100.8	11b-41b SOI1 hem?
11-41b	chert	1.71	0.04	0.42	bdl	bdl	97.7	0.01	0.21	0.02	0.01	bdl	100.1	11b-41b SOI1 hem2?
11-41b	chert	1.24	bdl	0.12	bdl	bdl	98.7	0.01	0.14	0.03	0.04	bdl	100.3	11b-41b SOI4 mag/hem1
11-41b	chert	1.25	bdl	0.22	bdl	bdl	98.9	0.01	0.32	0.02	bdl	bdl	100.8	11b-41b SOI4 mag/hem1
11-41b	chert	1.15	bdl	0.13	bdl	bdl	99.1	bdl	0.04	0.01	bdl	bdl	100.4	11b-41b Si-mag overgr
11-41b	chert	0.63	bdl	bdl	bdl	bdl	100.0	bdl	bdl	bdl	0.03	bdl	100.7	11b-41b Si-mag overgr
11-41b	chert	1.44	bdl	0.33	bdl	bdl	98.6	0.01	0.06	0.02	0.06	bdl	100.6	11b-41b Si-mag overgr
	median	1.17	0.01	0.19	0.00	bdl	98.9	0.01	0.14	0.02	0.02	bdl	100.5	
	max	1.71	0.04	0.42	bdl	bdl	100.0	0.02	0.32	0.04	0.06	bdl	100.8	
	min	0.63	bdl	bdl	bdl	bdl	97.7	bdl	bdl	bdl	bdl	bdl	100.1	

Appendix J: All EPMA analyses of Fe-Ti oxides (all values in wt.-%)

		SiO_2	TiO_2	Al_2O_3	Cr_2O_3	V_2O_3	FeO	MnO	MgO	CaO	ZnO	NiO	Total	
	dl	0.01	0.03	0.08	0.01	0.01	0.02	0.01	0.01	0.01	0.01	0.01		
Sample	**Host**													**Comments**
A028	chert	0.23	51.3	bdl	bdl	bdl	45.5	1.46	0.02	0.17	bdl	bdl	98.7	ilmenite
A028	chert	0.08	52.1	bdl	bdl	bdl	45.8	1.38	0.02	0.16	0.04	bdl	99.6	ilmenite
11-1a	shale	0.06	50.9	bdl	bdl	0.33	46.5	0.70	bdl	0.02	bdl	0.01	98.6	ilmenite
11-1a	shale	0.27	50.2	0.10	0.02	0.33	46.7	0.64	0.02	0.02	0.03	0.01	98.4	ilmenite
11-4	chl	0.06	51.1	bdl	0.01	0.33	47.4	0.85	0.02	bdl	0.02	bdl	99.8	ilmenite
11-4	chl	0.16	50.7	bdl	bdl	0.33	46.8	0.78	0.05	bdl	0.04	bdl	98.9	ilmenite
11-4	chl	0.42	50.9	bdl	bdl	0.32	46.6	0.74	bdl	bdl	bdl	bdl	98.9	ilmenite
11-4	chl	1.31	50.7	bdl	bdl	0.32	46.1	0.91	0.01	bdl	bdl	bdl	99.4	ilmenite
11-4	chl	0.06	51.4	bdl	bdl	0.33	46.7	0.85	bdl	bdl	bdl	bdl	99.4	ilmenite
11-4	chl	0.10	60.1	bdl	bdl	0.42	32.7	0.30	0.01	0.02	bdl	bdl	93.7	ilmenite
11-4	chl	0.17	98.6	bdl	bdl	0.69	1.5	bdl	bdl	bdl	0.04	bdl	101.1	rutile
11-5	shale	0.06	52.2	bdl	bdl	0.32	46.0	0.90	0.01	bdl	bdl	0.02	99.5	ilmenite
11-5	shale	4.37	41.2	3.11	bdl	0.26	43.0	0.36	2.33	bdl	bdl	bdl	94.7	ilmenite
11-5	shale	0.50	51.5	0.14	bdl	0.34	45.5	0.62	0.07	bdl	bdl	bdl	98.7	ilmenite
11-5	shale	0.16	52.3	bdl	bdl	0.37	45.6	0.75	0.03	bdl	bdl	bdl	99.3	ilmenite
11-6a	chlorite	0.15	50.5	bdl	0.01	0.34	46.8	0.72	0.02	bdl	bdl	bdl	98.6	ilemnite
11-6a	chlorite	0.19	50.9	0.09	bdl	0.33	46.6	0.81	0.06	0.01	bdl	bdl	99.0	ilmenite
11-6a	chlorite	0.11	50.1	bdl	bdl	0.34	47.0	0.85	bdl	bdl	bdl	bdl	98.4	ilmenite
11-6a	chlorite	0.07	51.0	bdl	bdl	0.33	46.9	0.81	bdl	bdl	bdl	0.01	99.1	ilmenite
11-6a	chlorite	bdl	51.2	bdl	bdl	0.32	47.4	0.81	0.01	bdl	bdl	bdl	99.8	ilmenite
11-20	chlorite	0.04	52.2	bdl	bdl	0.34	47.9	0.47	0.03	0.04	bdl	bdl	101.0	ilmenite
11-20	chlorite	0.10	76.2	bdl	0.14	0.55	21.5	0.23	bdl	0.07	bdl	bdl	98.8	rutile in ilmenite
11-20	chlorite	0.04	52.4	bdl	0.03	0.34	48.1	0.46	0.01	bdl	bdl	bdl	101.4	ilmenite
11-20	chlorite	0.02	52.7	bdl	0.01	0.34	47.7	0.46	0.02	0.04	0.02	bdl	101.3	ilmenite
11-24	mag-chl-ank	2.76	47.7	bdl	bdl	0.31	46.7	0.21	0.08	0.45	0.05	bdl	98.3	ilmenite
11.37	chert-stlp	0.14	7.6	bdl	0.18	0.07	87.0	0.10	bdl	0.02	bdl	bdl	95.2	ilmenite in magnetite
11-37	chert-stlp	0.29	52.6	bdl	0.02	bdl	46.8	0.62	bdl	0.02	bdl	bdl	100.4	ilmenite
11-37	chert-stlp	0.24	51.5	bdl	bdl	bdl	46.7	0.67	0.02	bdl	bdl	bdl	99.1	ilmenite
11-37	chert-stlp	0.12	51.9	bdl	0.02	bdl	47.3	0.72	0.03	0.04	bdl	bdl	100.1	ilmenite
11-37	chert-stlp	0.04	9.8	bdl	0.22	0.07	85.2	0.10	0.02	bdl	0.04	bdl	95.5	ilmenite in magnetite
11-39	mag-chl-stlp	30.21	35.9	1.58	0.02	0.09	1.8	0.02	0.34	27.35	0.02	0.01	97.3	titanite
11-39	mag-chl-stlp	30.52	36.5	1.50	0.01	0.33	1.2	0.02	0.06	27.94	bdl	bdl	98.0	titanite
11-39	mag-chl-stlp	30.51	35.4	1.68	bdl	0.19	1.4	0.03	0.15	27.89	bdl	0.01	97.2	titanite
	median	3.14	49.4	0.26	0.02	0.27	42.3	0.59	0.11	2.56	0.01	0.00	98.70	
	max	30.5	98.6	3.11	0.22	0.69	87.0	1.46	2.33	27.94	0.05	0.02	101.4	
	min	0.00	7.65	0.00	0.00	0.00	1.17	0.00	0.00	0.00	0.00	0.00	93.74	

Appendix K: All EPMA analyses of carbonates (semi-quantitative, all values in wt.-%)

		SiO_2	TiO_2	Al_2O_3	Cr_2O_3	V_2O_3	Fe_2O_3	MnO	MgO	CaO	ZnO	NiO	Total	
	dl	0.01	0.03	0.08	0.01	0.01	0.02	0.01	0.01	0.01	0.01	0.01		
Sample	**Host**													**Comment**
11-9	chert	0.10	bdl	bdl	bdl	bdl	14.2	1.85	13.9	27.7	0.01	bdl	57.7	Fe-dolomite
11-9	chert	0.36	bdl	bdl	bdl	bdl	7.36	1.22	17.7	28.0	0.02	bdl	54.7	Fe-dolomite
11-9	chert	0.06	bdl	bdl	bdl	bdl	9.70	1.94	16.4	28.5	bdl	bdl	56.7	Fe-dolomite
11-9	chert	0.09	bdl	bdl	bdl	bdl	13.6	1.93	13.4	27.5	bdl	bdl	56.6	Fe-dolomite
11-9	chert	0.07	bdl	bdl	0.01	bdl	8.15	1.70	17.0	28.3	bdl	bdl	55.2	Fe-dolomite
11-9	chert	0.07	bdl	bdl	bdl	bdl	8.29	1.89	16.3	28.0	0.02	0.02	54.5	Fe-dolomite
11-9	chert	0.12	0.05	bdl	bdl	bdl	11.1	2.25	16.0	28.2	bdl	bdl	57.8	Fe-dolomite
11-9	chert	0.08	bdl	bdl	bdl	bdl	6.23	1.04	14.1	23.5	0.02	bdl	45.0	Fe-dolomite
11-9	chert	0.06	bdl	bdl	bdl	bdl	16.4	2.70	6.70	21.3	bdl	bdl	47.2	Fe-dolomite
11-9	chert	0.13	bdl	bdl	bdl	bdl	10.9	1.20	17.5	26.9	bdl	bdl	56.7	Fe-dolomite
11-9	chert	0.05	bdl	bdl	bdl	bdl	8.00	1.51	18.0	28.0	0.02	bdl	55.5	Fe-dolomite
11-10	chl-chert	0.99	bdl	0.49	bdl	bdl	11.4	0.95	16.4	28.9	bdl	bdl	59.1	Fe-dolomite
11-20	chl	0.10	bdl	bdl	bdl	0.02	48.2	1.37	14.5	0.45	bdl	bdl	64.6	siderite
11-20	chl	0.03	0.03	bdl	bdl	bdl	61.1	1.59	4.65	0.29	bdl	bdl	67.7	siderite
11-20	chl	bdl	bdl	bdl	bdl	bdl	48.2	1.13	14.8	0.23	0.03	0.01	64.4	siderite (dolomite interference?)
11-20	chl	0.02	0.03	bdl	bdl	bdl	48.6	1.41	14.7	0.25	0.03	0.01	65.0	siderite (dolomite interference?)
11-22	chert	0.05	bdl	bdl	bdl	bdl	61.2	0.76	4.60	0.32	0.04	0.01	67.0	siderite
11-22	chert	0.06	bdl	bdl	bdl	bdl	61.2	0.66	4.78	0.17	bdl	bdl	66.8	siderite
11-22	chert	0.42	bdl	bdl	bdl	bdl	56.9	1.15	7.34	0.33	bdl	bdl	66.1	siderite
11-22	chert	0.04	bdl	bdl	bdl	bdl	58.1	0.97	6.43	0.30	bdl	bdl	65.9	siderite
11-23	chert-mag	0.10	bdl	bdl	bdl	bdl	61.6	0.88	4.43	0.66	0.03	bdl	67.8	siderite
11-24	mag-chl	0.12	bdl	bdl	bdl	bdl	65.7	bdl	0.90	0.83	bdl	bdl	67.6	siderite
11-24	mag-chl	0.12	bdl	bdl	bdl	bdl	60.4	1.01	4.80	0.22	0.02	bdl	66.6	siderite
11-24	mag-chl	26.2	bdl	2.96	bdl	bdl	50.7	0.24	2.52	0.25	bdl	bdl	82.9	siderite (quartz interference)
11-24	mag-chl	0.46	bdl	0.11	bdl	bdl	65.4	0.22	2.05	0.37	0.04	bdl	68.6	siderite
11-24	mag-chl	0.13	bdl	bdl	bdl	bdl	66.7	0.06	1.57	0.47	bdl	bdl	68.9	siderite
11-24	mag-chl	2.89	bdl	bdl	bdl	bdl	60.7	0.79	4.96	0.27	bdl	bdl	69.7	siderite
11-24	mag-chl	0.03	bdl	bdl	bdl	bdl	63.5	0.63	4.04	0.25	0.07	bdl	68.6	siderite
	median	1.18	bdl	bdl	bdl	bdl	38.0	1.18	10.0	11.8	0.01	bdl	62.3	
	max	26.2	0.05	2.96	0.01	0.02	66.7	2.70	18.0	28.9	0.07	0.02	82.9	
	min	bdl	bdl	bdl	bdl	bdl	6.23	bdl	0.90	0.17	bdl	bdl	45.0	

Note: calibration of the EPMA run was not for carbonates specifically, so the results should be considered semi-quantitative

Reported here is an overview of possible polyatomic interferences encountered during ICP-MS analyses. Interferences arise from the formation of polyatomic complexes after the decomposition of the sample material in the plasma, forming new complexes with O, Ar, (He, Cl if applicable) present. Such complexes can interfere on the same mass measured. The effect is largest for complexes of abundant elements on trace elements. In this study, specifically interferences of Fe-, Si, and O complexes was considered. The influence of interferences was minimized by selecting isotopes less prone to interference with common elements in the matrix, such as $^{56}Fe^{16}O^+$ on ^{72}Ge, instead measuring ^{74}Ge less affected by interference. Table from May and Wiedmeyer (1998).

Isotope	Interference
^{107}Ag	$^{91}Zr^{16}O^+$
^{109}Ag	$^{92}Zr^{16}O^1H^+$
^{27}Al	$^{12}C^{15}N^+$, $^{13}C^{14}N^+$, $^{14}N^2$ spread, $^1H^{12}C^{14}N^+$
^{75}As	$^{40}Ar^{35}Cl^+$, $^{59}Co^{16}O^+$, $^{36}Ar^{38}Ar^1H^+$, $^{38}Ar^{37}Cl^+$, $^{36}Ar^{39}K$, $^{43}Ca^{16}O_2$, $^{23}Na^{12}C^{40}Ar$, $^{12}C^{31}P^{16}O_2^+$
^{197}Au	$^{181}Ta^{16}O^+$
^{11}B	^{12}C spread
^{130}Ba	$^{98}Ru^{16}O_2^+$
^{132}Ba	$^{100}Ru^{16}O_2^+$
^{134}Ba	$^{102}Ru^{16}O_2^+$
^{136}Ba	$^{104}Ru^{16}O_2^+$
^{209}Bi	$^{193}Ir^{16}O^+$
^{79}Br	$^{40}Ar^{39}K^+$, $^{31}P^{16}O_3^+$, $^{38}Ar^{40}Ar^1H^+$
^{81}Br	$^{32}S^{16}O_3{}^1H^+$, $^{40}Ar^{40}Ar^1H^+$, $^{33}S^{16}O_3^+$
^{40}Ca	$^{40}Ar^+$
^{42}Ca	$^{40}Ar^1H_2$
^{43}Ca	$^{27}Al^{16}O^+$
^{44}Ca	$^{12}C^{16}O_2$, $^{14}N_2{}^{16}O^+$, $^{28}Si^{16}O^+$
^{46}Ca	$^{14}N^{16}O_2^+$, $^{32}S^{14}N^+$
^{48}Ca	$^{33}S^{15}N^+$, $^{34}S^{14}N^+$, $^{32}S^{16}O^+$
^{110}Cd	$^{39}K_2{}^{16}O^+$
^{111}Cd	$^{95}Mo^{16}O^+$, $^{94}Zr^{16}O^1H^+$, $^{39}K_2{}^{16}O_2{}^1H^+$
^{112}Cd	$^{40}Ca_2{}^{16}O_2$, $^{40}Ar_2{}^{16}O_2$, $^{96}Ru^{16}O^+$
^{113}Cd	$^{96}Zr^{16}O^1H^+$, $^{40}Ca_2{}^{16}O_2{}^1H^+$, $^{40}Ar_2{}^{16}O_2{}^1H^+$, $^{96}Ru^{17}O^+$
^{114}Cd	$^{98}Mo^{16}O^+$, $^{98}Ru^{16}O^+$
^{116}Cd	$^{100}Ru^{16}O^+$
^{35}Cl	$^{16}O^{18}O^1H^+$, $^{34}S^1H^+$, $^{35}Cl^+$
^{37}Cl	$^{36}Ar^1H^+$, $^{36}S^1H^+$, $^{37}Cl^+$
^{59}Co	$^{43}Ca^{16}O^+$, $^{42}Ca^{16}O^1H^+$, $^{24}Mg^{35}Cl^+$, $^{36}Ar^{23}Na^+$, $^{40}Ar^{18}O^1H^+$, $^{40}Ar^{19}F^+$
^{50}Cr	$^{34}S^{16}O^+$, $^{36}Ar^{14}N^+$, $^{35}Cl^{15}N^+$ $^{36}S^{14}N^+$, $^{32}S^{18}O^+$, $^{33}S^{17}O^+$
^{52}Cr	$^{35}Cl^{16}O^1H^+$, $^{40}Ar^{12}C^+$, $^{36}Ar^{16}O^+$, $^{37}Cl^{15}N^+$ $^{34}S^{18}O^+$, $^{36}S^{16}O^+$, $^{38}Ar^{14}N^+$, $^{36}Ar^{15}N^1H^+$, $^{35}Cl^{17}O^+$
^{53}Cr	$^{37}Cl^{16}O^+$, $^{38}Ar^{15}N^+$, $^{38}Ar^{14}N^1H^+$, $^{36}Ar^{17}O^+$, $^{36}Ar^{16}O^1H^+$, $^{35}Cl^{17}O^1H^+$, $^{35}Cl^{18}O^+$, $^{36}S^{17}O^+$, $^{40}Ar^{13}C^+$ $^{37}Cl^{16}O^1H^+$,
^{54}Cr	$^{40}Ar^{14}N^+$, $^{38}Ar^{15}N^1H^+$, $^{36}Ar^{18}O^+$, $^{38}Ar^{16}O^+$, $^{36}Ar^{17}O^1H^+$, $^{37}Cl^{17}O^+$, $^{19}F_2{}^{16}O^+$
^{133}Cs	$^{101}Ru^{16}O_2^+$
^{63}Cu	$^{31}P^{16}O_2^+$, $^{40}Ar^{23}Na^+$, $^{47}Ti^{16}O^+$, $^{23}Na^{40}Ca^+$, $^{46}Ca^{16}O^1H^+$, $^{36}Ar^{12}C^{14}N^1H^+$, $^{14}N^{12}C^{37}Cl^+$, $^{16}O^{12}C^{35}Cl^+$
^{65}Cu	$^{49}Ti^{16}O^+$, $^{32}S^{16}O_2{}^1H^+$, $^{40}Ar^{25}Mg^+$, $^{40}Ca^{16}O^1H^+$, $^{36}Ar^{14}N_2{}^1H^+$, $^{32}S^{33}S^+$, $^{32}S^{16}O^{17}O^+$, $^{33}S^{16}O_2^+$, $^{12}C^{16}O^{37}Cl^+$, $^{12}C^{18}O^{35}Cl^+$,

Isotope	Interference
^{163}Dy	$^{147}Sm^{16}O^+$
^{166}Er	$^{160}Nd^{16}O$, $^{150}Sm^{16}O$
^{167}Er	$^{151}Eu^{16}O^+$
^{151}Eu	$^{135}Ba^{16}O^+$
^{153}Eu	$^{137}Ba^{16}O^+$
^{54}Fe	$^{37}Cl^{16}O^1H^+$, $^{40}Ar^{14}N$, $^{38}Ar^{15}N^1H^+$, $^{36}Ar^{18}O^+$, $^{38}Ar^{16}O^+$, $^{36}Ar^{17}O^1H^+$, $^{36}S^{18}O^+$, $^{35}Cl^{18}O^1H^+$, $^{37}Cl^{17}O$
^{56}Fe	$^{40}Ar^{16}O^+$, $^{40}Ca^{16}O^+$, $^{40}Ar^{15}N^1H^+$, $^{38}Ar^{18}O^+$, $^{38}Ar^{17}O^1H^+$ $^{37}Cl^{18}O^1H^+$
^{57}Fe	$^{40}Ar^{16}O^1H^+$, $^{40}Ca^{16}O^1H^+$, $^{40}Ar^{17}O^+$, $^{38}Ar^{18}O^1H^+$, $^{38}Ar^{19}F^+$
^{58}Fe	$^{40}Ar^{18}O^+$, $^{40}Ar^{17}O^1H^+$
^{69}Ga	$^{35}Cl^{16}O^{18}O^+$, $^{35}Cl^{17}O_2^+$, $^{37}Cl^{16}O_2^+$, $^{36}Ar^{33}S^+$, $^{33}S^{18}O_2^+$, $^{34}S^{17}O^{18}O^+$, $^{36}S^{16}O^{17}O^+$, $^{33}S^{36}S^+$
^{71}Ga	$^{35}Cl^{18}O_2^+$, $^{37}Cl^{16}O^{18}O^+$, $^{37}Cl^{17}O_2^+$, $^{36}Ar^{35}Cl^+$, $^{36}S^{17}O^{18}O^+$, $^{38}Ar^{33}S^+$
^{155}Gd	$^{139}La^{16}O^+$
^{157}Gd	$^{138}B^{19}F^+$, $^{141}Pr^{16}O^+$
^{70}Ge	$^{40}Ar^{14}N^{16}O^+$, $^{35}Cl^{17}O^{18}O^+$, $^{37}Cl^{16}O^{17}O^+$, $^{34}S^{18}O_2^+$, $^{36}S^{16}O^{18}O^+$, $^{36}S^{17}O_2^+$, $^{34}S^{36}S^+$, $^{36}Ar^{34}S^+$, $^{38}Ar^{32}S^+$, $^{35}Cl_2^+$
^{72}Ge	$^{36}Ar_2^+$, $^{37}Cl^{17}O^{18}O^+$, $^{35}Cl^{37}Cl^+$, $^{36}S^{18}O_2^+$, $^{36}S_2^+$, $^{36}Ar^{36}S^+$ $^{56}Fe^{16}O^+$, $^{40}Ar^{16}O_2^+$, $^{40}Ca^{16}O_2^+$, $^{40}Ar^{32}S^+$
^{73}Ge	$^{36}Ar_2{}^1H^+$, $^{37}Cl^{18}O_2^+$, $^{36}Ar^{37}Cl^+$, $^{38}Ar^{35}Cl^+$, $^{40}Ar^{33}S^+$
^{74}Ge	$^{40}Ar^{34}S^+$, $^{36}Ar^{38}Ar^+$, $^{37}Cl^{37}Cl^+$, $^{38}Ar^{36}S^+$
^{76}Ge	$^{36}Ar^{40}Ar^+$, $^{38}Ar^{38}Ar^+$, $^{40}Ar^{36}S^+$
^{177}Hf	$^{161}Dy^{16}O^+$
^{165}Ho	$^{149}Sm^{16}O$
^{113}In	$^{96}Ru^{17}O^+$
^{39}K	$^{38}Ar^1H^+$
^{40}K	$^{40}Ar^+$
^{41}K	$^{40}Ar^1H^+$
^{78}Kr	$^{38}Ar^{40}Ar^+$
^{80}Kr	$^{40}Ar_2^+$, $^{32}S^{16}O_3^+$
^{82}Kr	$^{40}Ar^{40}Ar^1H_2^+$, $^{34}S^{16}O_3^+$, $^{33}S^{16}O_3{}^1H^+$
^{83}Kr	$^{34}S^{16}O_3{}^1H^+$
^{84}Kr	$^{36}S^{16}O_3^+$
^{175}Lu	$^{159}Tb^{16}O^+$
^{24}Mg	$^{12}C_2^+$
^{25}Mg	$^{12}C_2{}^1H^+$
^{26}Mg	$^{12}C^{14}N^+$, $^{12}C_2{}^1H_2^+$, $^{12}C^{13}C^1H^+$

Isotope	Interference
^{55}Mn	$^{40}Ar^{14}N^{1}H^{+}$, $^{39}K^{16}O^{+}$, $^{37}Cl^{18}O^{+}$, $^{40}Ar^{15}N^{+}$, $^{38}Ar^{17}O^{+}$, $^{36}Ar^{18}O^{1}H^{+}$ $^{38}Ar^{16}O^{1}H^{+}$, $^{37}Cl^{17}O^{1}H^{+}$, $^{23}Na^{32}S^{+}$, $^{36}Ar^{19}F^{+}$
^{94}Mo	$^{39}K_2{}^{16}O^{+}$
^{95}Mo	$^{40}Ar^{39}K^{16}O^{+}$, $^{79}Br^{16}O^{+}$
^{96}Mo	$^{39}K^{41}K^{16}O^{+}$, $^{79}Br^{17}O^{+}$
^{97}Mo	$^{40}Ar_2{}^{16}O^{1}H^{+}$, $^{40}Ca_2{}^{16}O^{1}H^{+}$, $^{40}Ar^{41}K^{16}O^{+}$, $^{81}Br^{16}O^{+}$
^{98}Mo	$^{81}Br^{17}O^{+}$, $^{41}K_2O^{+}$
^{144}Nd	$^{96}Ru^{16}O_3{}^{+}$
^{146}Nd	$^{98}Ru^{16}O_3{}^{+}$
^{148}Nd	$^{100}Ru^{16}O^{3+}$
^{150}Nd	$^{102}Ru^{16}O_3{}^{+}$
^{58}Ni	$^{23}Na^{35}Cl^{+}$, $^{40}Ar^{18}O^{+}$, $^{40}Ca^{18}O^{+}$, $^{40}Ca^{17}O^{1}H^{+}$, $^{42}Ca^{16}O^{+}$, $^{29}Si_2{}^{+}$, $^{40}Ar^{17}O^{1}H^{+}$, $^{23}Na^{35}Cl^{+}$
^{60}Ni	$^{44}Ca^{16}O^{+}$, $^{23}Na^{37}Cl^{+}$, $^{43}Ca^{16}O^{1}H^{+}$
^{61}Ni	$^{44}Ca^{16}O^{1}H^{+}$, $^{45}Sc^{16}O^{+}$
^{62}Ni	$^{46}Ti^{16}O^{+}$, $^{23}Na^{39}K^{+}$, $^{46}Ca^{16}O^{+}$
^{64}Ni	$^{32}S^{16}O_2{}^{+}$, $^{32}S_2{}^{+}$
^{31}P	$^{14}N^{16}O^{1}H^{+}$, $^{15}N^{15}N^{1}H^{+}$, $^{15}N^{16}O^{+}$, $^{14}N^{17}O^{+}$, $13C^{18}O^{+}$, $^{12}C^{18}O^{1}H^{+}$
^{206}Pb	$^{190}Pt^{16}O^{+}$
^{207}Pb	$^{191}Ir^{16}O^{+}$
^{208}Pb	$^{192}Pt^{16}O^{+}$
^{105}Pd	$^{40}Ar^{65}Cu^{+}$
^{103}Rh	$^{40}Ar^{63}Cu^{+}$
^{101}Ru	$^{40}Ar^{61}Ni^{+}$, $^{64}Ni^{37}Cl^{+}$
^{32}S	$^{16}O_2{}^{+}$, $^{14}N^{18}O^{+}$, $^{15}N^{17}O^{+}$, $^{14}N^{17}O^{1}H^{+}$, $^{15}N^{16}O^{1}H^{+}$, $^{32}S^{+}$ $^{14}N^{16}O^{1}H_2{}^{+}$
^{33}S	$^{15}N^{18}O^{+}$, $^{14}N^{18}O^{1}H^{+}$, $^{15}N^{17}O^{1}H^{+}$, $^{16}O^{17}O^{+}$, $^{16}O_2{}^{1}H^{+}$, $^{33}S^{+}$, $^{32}S^{1}H^{+}$
^{34}S	$^{15}N^{18}O^{1}H^{+}$, $^{16}O^{18}O^{+}$, $^{17}O_2{}^{+}$, $^{16}O^{17}O^{1}H^{+}$, $^{34}S^{+}$, $^{33}S^{1}H^{+}$
^{121}Sb	$^{105}Pd^{16}O^{+}$
^{123}Sb	$^{94}Zr^{16}O_2$
^{45}Sc	$^{12}C^{16}O_2{}^{1}H^{+}$, $^{28}Si^{16}O^{1}H^{+}$, $^{29}Si^{16}O^{+}$, $^{14}N_2{}^{16}O^{1}H^{+}$, $^{13}C^{16}O_2{}^{+}$
^{74}Se	$^{37}Cl^{37}Cl^{+}$, $^{36}Ar^{38}Ar^{+}$, $^{38}Ar^{36}S^{+}$, $^{40}Ar^{34}S^{+}$
^{76}Se	$^{40}Ar^{36}Ar^{+}$, $^{38}Ar^{38}Ar^{+}$
^{77}Se	$^{40}Ar^{37}Cl^{+}$, $^{36}Ar^{40}Ar^{1}H^{+}$, $^{38}Ar_2{}^{1}H^{+}$, $^{12}C^{19}F^{14}N^{16}O_2{}^{+}$,
^{78}Se	$^{40}Ar^{38}Ar^{+}$, $^{38}Ar^{40}Ca^{+}$
^{80}Se	$^{40}Ar_2{}^{+}$, $^{32}S^{16}O_3{}^{+}$
^{82}Se	$^{12}C^{35}Cl_2{}^{+}$, $^{34}S^{16}O_3{}^{+}$, $^{40}Ar_2{}^{1}H_2{}^{+}$
^{28}Si	$^{14}N_2{}^{+}$, $^{12}C^{16}O^{+}$
^{29}Si	$^{14}N^{15}N^{+}$, $^{14}N_2{}^{1}H^{+}$, $^{13}C^{16}O^{+}$, $^{12}C^{17}O^{+}$, $^{12}C^{16}O^{1}H^{+}$
^{30}Si	$^{15}N_2{}^{+}$, $^{14}N^{15}N^{1}H^{+}$, $^{14}N^{16}O^{+}$, $^{12}C^{18}O^{+}$, $^{13}C^{17}O^{+}$, $^{13}C^{16}O^{1}H^{+}$, $^{12}C^{17}O^{1}H^{+}$, $^{14}N_2{}^{1}H_2{}^{+}$, $^{12}C^{16}O^{1}H_2{}^{+}$
^{144}Sm	$^{96}Ru^{16}O_3{}^{+}$
^{147}Sm	$^{99}Ru^{16}O_3{}^{+}$
^{148}Sm	$^{100}Ru^{16}O_3{}^{+}$
^{149}Sm	$^{101}Ru^{16}O_3{}^{+}$
^{150}Sm	$^{102}Ru^{16}O_3{}^{+}$
^{152}Sm	$^{104}Ru^{16}O_3{}^{+}$
^{112}Sn	$^{96}Ru^{16}O^{+}$
^{115}Sn	$^{99}Ru^{16}O^{+}$
^{116}Sn	$^{100}Ru^{16}O^{+}$
^{117}Sn	$^{101}Ru^{16}O^{+}$
^{118}Sn	$^{102}Ru^{16}O^{+}$, $^{102}Pd^{16}O^{+}$
^{119}Sn	$^{103}Rh^{16}O^{+}$
^{120}Sn	$^{104}Ru^{16}O^{+}$, $^{104}Pd^{16}O^{+}$
^{122}Sn	$^{106}Pd^{16}O^{+}$
^{124}Sn	$^{108}Pd^{16}O^{+}$
^{84}Sr	$^{36}S^{16}O_3{}^{+}$
^{86}Sr	$^{85}Rb^{1}H^{+}$
^{181}Ta	$^{165}Ho^{16}O^{+}$
^{159}Tb	$^{43}Nd^{16}O^{+}$
^{122}Te	$^{106}Pd^{16}O^{+}$
^{124}Te	$^{108}Pd^{16}O^{+}$
^{126}Te	$^{110}Pd^{16}O^{+}$
^{128}Te	$^{96}Ru^{16}O_2{}^{+}$
^{130}Te	$^{98}Ru^{16}O_2{}^{+}$
^{46}Ti	$^{32}S^{14}N^{+}$, $^{14}N^{16}O_2{}^{+}$, $^{15}N_2{}^{16}O^{+}$
^{47}Ti	$^{32}S^{14}N^{1}H^{+}$, $^{30}Si^{16}O^{1}H^{+}$, $^{32}S^{15}N^{+}$, $^{33}N^{14}N^{+}$, $^{33}S^{14}N^{+}$, $^{15}N^{16}O_2{}^{+}$, $^{14}N^{16}O_2{}^{1}H^{+}$, $^{12}C^{35}Cl^{+}$, $^{31}P^{16}O^{+}$
^{48}Ti	$^{32}S^{16}O^{+}$, $^{34}S^{14}N^{+}$, $^{33}S^{15}N^{+}$, $^{14}N^{16}O^{18}O^{+}$, $^{14}N^{17}N_2{}^{+}$, $^{12}C_4{}^{+}$, $^{36}Ar^{12}C^{+}$
^{49}Ti	$^{32}S^{17}O^{+}$, $^{32}S^{16}O^{1}H^{+}$, $^{35}Cl^{14}N^{+}$, $^{34}S^{15}N^{+}$, $^{33}S^{16}O^{+}$, $^{14}N^{17}O_2{}^{1}H^{+}$, $^{14}N^{35}Cl^{+}$, $^{36}Ar^{13}C^{+}$, $^{36}Ar^{12}C^{1}H^{+}$, $^{12}C^{37}Cl^{+}$, $^{31}P^{18}O^{+}$
^{50}Ti	$^{32}S^{18}O^{+}$, $^{32}S^{17}O^{1}H^{+}$, $^{36}Ar^{14}N^{+}$, $^{35}Cl^{15}N^{+}$, $^{36}S^{14}N^{+}$, $^{34}S^{16}O^{+}$, $^{1}H^{14}N^{35}Cl^{+}$, $^{34}S^{15}O^{1}H^{+}$
^{203}Tl	$^{187}Re^{16}O^{+}$, $^{186}W^{16}O^{1}H^{+}$
^{169}Tm	$^{153}Eu^{16}O^{+}$
^{50}V	$^{34}S^{16}O^{+}$, $^{36}Ar^{14}N^{+}$, $^{35}Cl^{15}N^{+}$, $^{36}S^{14}N^{+}$, $^{32}S^{18}O^{+}$, $^{33}S^{17}O^{+}$
^{51}V	$^{34}S^{16}O^{1}H^{+}$, $^{35}Cl^{16}O^{+}$, $^{38}Ar^{13}C^{+}$, $^{36}Ar^{15}N^{+}$, $^{36}Ar^{14}N^{1}H^{+}$, $^{37}Cl^{14}N^{+}$, $^{36}S^{15}N^{+}$, $^{33}S^{18}O^{+}$, $^{34}S^{17}O^{+}$
^{182}W	$^{166}Er^{16}O^{+}$
^{172}Yb	$^{156}Gd^{16}O^{+}$
^{173}Yb	$^{157}Gd^{16}O^{+}$
^{64}Zn	$^{32}S^{16}O_2{}^{+}$, $^{48}Ti^{16}O^{+}$, $^{31}P^{16}O_2{}^{1}H^{+}$, $^{48}Ca^{16}O^{+}$, $^{32}S_2{}^{+}$, $^{34}S^{16}O_2{}^{+}$, $^{36}Ar^{14}N_2{}^{+}$
^{66}Zn	$^{50}Ti^{16}O^{+}$, $^{34}S^{16}O_2{}^{+}$, $^{33}S^{16}O_2{}^{1}H^{+}$, $^{32}S^{16}O^{18}O^{+}$, $^{32}S^{17}O_2{}^{+}$ $^{33}S^{16}O^{17}O^{+}$, $^{32}S^{34}S^{+}$, $^{33}S_2{}^{+}$
^{67}Zn	$^{35}Cl^{16}O_2{}^{+}$, $^{33}S^{34}S^{+}$, $^{34}S^{16}O_2{}^{1}H^{+}$, $^{32}S^{16}O^{18}O^{1}H^{+}$, $^{33}S^{34}S^{+}$, $^{34}S^{16}O^{17}O^{+}$, $^{33}S^{16}O^{18}O^{+}$, $^{32}S^{17}O^{18}O^{+}$, $^{33}S^{17}O_2{}^{+}$
^{68}Zn	$^{36}S^{16}O_2{}^{+}$, $^{34}S^{16}O^{18}O^{+}$, $^{40}Ar^{14}N_2{}^{+}$, $^{35}Cl^{16}O^{17}O^{+}$, ^{34} $^{36}Ar^{32}S^{+}$, $^{34}S^{17}O_2{}^{+}$, $^{33}S^{17}O^{18}O^{+}$, $^{32}S^{18}O_2{}^{+}$, $^{32}S^{36}S^{+}$
^{70}Zn	$^{35}Cl^{35}Cl^{+}$, $^{40}Ar^{14}N^{16}O^{+}$, $^{35}Cl^{17}O^{18}O^{+}$, $^{37}Cl^{16}O^{17}O^{+}$, $^{34}S^{18}O_2{}^{+}$, $^{36}S^{16}O^{18}O^{+}$, $^{36}S^{17}O_2{}^{+}$, $^{34}S^{36}S^{+}$, $^{36}Ar^{34}S^{+}$, $^{38}Ar^{32}S^{+}$

References:

May, T.W., Wiedmeyer, R.H., 1998. A table of polyatomic interferences in ICP-MS. Atomic Spectroscopy-Norwalk Connecicut.19, 150-155.

Appendix M: Geochemistry of all Temagami BIF whole rock samples

				Element	Si [wt.%]	Al [wt.%]	Fe [wt.%]	Ca [wt.%]	Mg [wt.%]	Na [wt.%]
				Analysis Method	FUS-ICP	FUS-ICP	FUS-ICP	FUS-ICP	FUS-ICP	TD-ICP
				Detection Limit	0.005	0.005	0.007	0.007	0.006	0.002
Sample	**Layer Type**	**Latitude**	**Longitude**							
A027	chert	47.06346	-79.87559		45.65	0.13	0.88	0.16	0.12	bdl
11-03b	chert	47.06844	-79.79071		45.07	0.41	1.00	0.01	0.22	bdl
C303	chert	47.07128	-79.87350		44.58	0.15	1.01	0.60	0.24	bdl
D020-1	chert	47.05252	-79.85201		45.99	0.02	1.31	0.06	0.09	bdl
11-34-1	chert	47.06899	-79.79070		40.74	0.42	1.31	0.07	0.18	0.012
B013-6	chert	47.06663	-79.87578		43.74	0.25	1.51	0.34	0.28	bdl
11-22	chert	47.06878	-79.79070		43.94	0.20	2.66	0.04	0.15	0.010
11-10	chert	47.06856	-79.79071		43.08	0.25	4.11	0.06	0.02	bdl
B013-5	chert	47.06663	-79.87578		42.23	0.07	4.18	0.54	0.73	bdl
B013-2	chert	47.06663	-79.87578		42.27	0.12	4.18	0.36	0.72	0.003
B013-3	chert	47.06663	-79.87578		41.28	0.07	4.43	0.48	1.03	0.002
A030-1	chert	47.06347	-79.87583		41.80	0.16	4.71	0.09	0.13	bdl
11-16-1	chert	47.06867	-79.79071		42.36	0.15	4.81	0.27	0.11	0.024
11-23	chert	47.06880	-79.79070		41.07	0.32	6.07	0.40	0.22	0.003
11-27	chert	47.06887	-79.79070		35.52	0.28	7.73	1.51	0.72	0.004
C012-2	chert	47.06886	-79.87489		40.69	0.07	7.91	0.17	0.51	bdl
11-17-3	chert	47.06869	-79.79070		40.38	0.20	8.80	0.14	0.09	0.003
11-18-2	chert	47.06871	-79.79070		36.01	0.23	12.32	0.16	0.28	0.004
11-18-1	chert	47.06871	-79.79070		31.17	1.21	14.02	0.16	0.92	0.002
11-09	chert	47.06854	-79.79071		33.65	0.16	15.89	1.05	0.52	0.038
11-41	chert	47.06912	-79.79069		38.23	0.18	11.49	0.26	0.16	0.003
11-06b	chert	47.06849	-79.79071		30.82	0.15	24.23	0.09	0.08	0.003
SM052-4	jasper	47.06585	-79.87572		41.83	0.07	6.68	0.20	0.04	bdl
SM052-2	jasper	47.06585	-79.87572		41.54	0.08	7.10	0.21	0.03	bdl
11-12	jasper	47.06860	-79.79071		33.53	0.09	18.42	0.16	0.06	bdl
C060-2	jasper	47.06999	-79.87271		33.66	0.06	19.00	0.05	0.40	bdl
11-11-2	jasper	47.06858	-79.79071		32.34	0.18	19.75	0.36	0.16	0.037
SM011-2	jasper	47.06112	-79.87574		30.86	0.09	21.35	0.52	0.56	bdl
11-24	magnetite	47.06881	-79.79070		23.57	0.56	21.03	0.58	1.21	0.016
A028-2	magnetite	47.06345	-79.87559		23.08	0.18	29.99	0.16	3.93	0.017
B013-7	magnetite	47.06663	-79.87578		24.46	0.11	21.42	2.31	2.08	0.004
11-40	magnetite	47.06910	-79.79070		24.11	1.07	27.16	1.84	1.30	0.112
11-42	magnetite	47.06914	-79.79069		18.24	0.67	28.64	4.37	3.33	0.035
D020-2	magnetite	47.05252	-79.85301		22.78	0.09	32.24	0.02	2.93	bdl
11-32	magnetite	47.06896	-79.79070		21.02	0.35	37.14	0.21	0.33	0.070
11-39	magnetite	47.06908	-79.79070		13.86	2.92	37.90	0.44	3.70	0.054
11-11-1	magnetite	47.06858	-79.79071		18.36	0.28	41.60	0.31	0.34	0.073
B013-4	magnetite	47.06663	-79.87578		16.14	0.07	42.23	0.27	2.00	0.004
B013-1	magnetite	47.06663	-79.87578		8.44	0.83	45.12	3.44	1.88	0.004
11-33-2	magnetite	47.06898	-79.79070		13.80	0.54	46.39	0.28	0.53	0.054
C012-1	magnetite	47.06886	-79.87489		12.35	0.02	48.11	0.69	1.18	0.003
11b-16-2	magnetite	47.06867	-79.79071		13.19	0.32	48.14	0.74	0.28	0.088
SM052-5	magnetite	47.06585	-79.87572		11.89	0.03	53.44	0.13	0.05	bdl
SM052-1	magnetite	47.06585	-79.87572		7.89	0.10	59.50	0.08	0.11	bdl
SM052-6	magnetite	47.06585	-79.87572		7.80	0.05	59.88	0.06	0.08	bdl
11-17-2	magnetite	47.06869	-79.79070		5.78	0.40	60.82	0.09	0.28	0.006
D015	magnetite	47.05252	-79.85352		5.60	0.06	63.21	0.21	0.18	bdl
D001	chlorite	47.06405	-79.89792		26.39	7.95	5.42	2.39	3.44	4.013
11-20	chlorite	47.06874	-79.79070		23.42	5.71	15.80	0.41	4.99	0.006
11-02b	chlorite	47.06842	-79.79071		19.75	5.65	19.50	2.71	3.90	0.005
11-06a	chlorite	47.06849	-79.79071		24.18	3.15	21.89	1.17	2.59	bdl
11-04	chlorite	47.06845	-79.79071		15.73	4.54	33.79	0.12	2.97	0.015
11-03a	shale	47.06844	-79.79071		32.02	6.06	5.92	0.10	1.72	0.479
11-14	shale	47.06863	-79.79071		23.43	5.82	21.70	0.14	2.25	0.008
11-05	shale	47.06847	-79.79071		21.72	6.53	20.33	0.10	3.63	0.012
11-34-2	shale	47.06899	-79.79070		20.75	6.67	21.50	0.29	3.61	0.031
11-01a-1	shale	47.06840	-79.79071		18.19	7.89	23.97	0.24	2.34	bdl
SH850	sulfide BIF	47.05052	-79.80598		23.61	0.78	19.93	0.31	0.52	0.012
SH580	sulfide BIF	47.04853	-79.80598		9.72	0.63	34.96	bdl	0.15	0.013
SH495	sulfide BIF	47.04689	-79.80598		15.18	0.98	29.10	0.01	0.18	0.016
SH1165	sulfide BIF	47.05153	-79.80598		14.28	0.92	31.40	0.10	0.36	0.004
SM1	ox. BIF stand.	47.06505	-79.89502		22.62	0.18	30.96	1.81	1.19	0.035
11-29	massive sulfide	47.06890	-79.79070		1.30	0.11	43.13	0.01	0.02	0.024
11-8-1	intrusive	47.06853	-79.79071		18.00	3.89	10.97	7.82	7.71	0.279
11-8-2	intrusive	47.06853	-79.79071		17.42	4.68	12.50	8.69	5.95	0.536
SH100	altered shale	47.06362	-79.80598		29.07	9.45	5.21	0.16	2.25	0.077
				median	24.14	0.25	19.84	0.23	0.51	0.00
				mean	26.87	1.45	21.95	0.78	1.28	0.10
				min	1.30	0.02	0.88	bdl	0.02	bdl
				max	45.99	9.45	63.21	8.69	7.71	4.01

All values in ppm unless otherwise in wt.% for elemental abundances of major elements.

Appendix M (continued): Geochemistry of all Temagami BIF whole rock samples

	K [wt.%] TD-ICP 0.002	P [wt.%] FUS-ICP 0.004	LOI [wt.%] FUS-ICP	N [wt.%] IR-EA 0.03	C [%] IR-EA 0.02	H [%] IR-EA 0.02	S_{total} [%] IR-EA 0.02	Ti FUS-ICP 6	Mn TD-ICP 0.2	Zn TD-ICP 0.04	Cu TD-ICP 0.04
A027	0.013	bdl	0.51	bdl	0.09	0.03	bdl	6	231	2.14	0.67
11-03b	0.003	bdl	0.48	bdl	bdl	0.06	0.05	18	25.5	7.60	8.21
C303	0.003	bdl	1.47	bdl	0.37	0.02	0.22	6	678	2.54	2.78
D020-1	0.016	bdl	0.24	bdl	0.04	0.02	bdl	6	106	2.73	1.47
11-34-1	0.059	0.009	8.34	bdl	0.03	0.07	bdl	18	65.7	6.21	2.49
B013-6	0.007	bdl	1.47	bdl	0.41	0.03	0.02	12	1090	6.49	7
11-22	0.033	0.013	1.44	bdl	0.56	0.07	bdl	36	229	2.80	0.25
11-10	0.012	0.022	0.07	bdl	0.03	0.03	0.02	18	52.9	1.29	8.11
B013-5	0.018	bdl	1.99	bdl	0.51	0.06	0.02	6	1400	22.40	bdl
B013-2	0.032	0.039	1.31	bdl	0.31	0.08	bdl	12	998	26.40	2.21
B013-3	0.030	0.009	2.16	bdl	0.50	0.10	bdl	6	1650	30.50	1.83
A030-1	0.028	0.026	3.20	bdl	0.23	0.07	3.12	12	532	24.60	114
11-16-1	0.010	0.013	0.54	bdl	0.16	0.03	bdl	12	221	1.35	6.87
11-23	0.016	0.013	1.35	bdl	0.34	0.05	0.08	78	287	3.39	10.5
11-27	0.023	0.035	7.57	bdl	2.04	0.07	0.44	30	2860	5.19	8.43
C012-2	0.007	bdl	0.34	bdl	0.54	0.11	bdl	6	271	12.30	35.5
11-17-3	0.010	0.039	0.26	bdl	0.10	0.03	0.10	24	166	4.01	2.25
11-18-2	0.010	0.048	3.16	bdl	1.01	0.05	0.03	84	883	3.57	1.11
11-18-1	0.005	0.026	8.59	bdl	2.35	0.16	0.50	515	1810	12.50	2.44
11-09	0.026	0.009	1.77	bdl	0.63	0.04	0.17	30	597	18.30	5.28
11-41	0.009	0.017	0.29	bdl	0.12	0.04	bdl	30	586	35.70	0.89
11-06b	0.003	0.044	bdl	bdl	bdl	0.03	0.04	48	40.9	4.01	5.22
SM052-4	0.003	0.065	bdl	bdl	0.03	0.02	bdl	6	41.1	7.73	1.28
SM052-2	0.003	0.074	bdl	bdl	0.03	0.02	bdl	6	38.6	2.57	0.36
11-12	bdl	0.035	bdl	bdl	0.04	0.03	0.04	6	52.8	7.54	bdl
C060-2	0.020	0.013	bdl	bdl	bdl	0.06	bdl	bdl	222	10.90	bdl
11-11-2	0.030	0.044	bdl	bdl	0.16	0.04	0.08	48	290	3.84	0.6
SM011-2	0.006	0.039	0.24	bdl	0.27	0.03	0.02	6	818	33.10	2.71
11-24	0.161	0.074	13.47	bdl	3.94	0.16	0.23	216	2290	13.10	13.6
A028-2	0.100	0.013	bdl	bdl	0.02	0.30	0.38	144	5430	88.80	24.1
B013-7	0.055	0.035	7.88	bdl	2.18	0.12	0.95	132	5680	53.90	38
11-40	0.472	0.039	2.50	bdl	0.46	0.30	0.25	485	1260	15.70	7.01
11-42	0.495	0.057	5.04	bdl	1.10	0.37	0.43	330	5150	39.20	3.4
D020-2	0.054	bdl	0.30	bdl	0.02	0.15	0.95	138	279	37.70	46.1
11-32	0.137	0.052	bdl	bdl	0.06	0.04	bdl	108	36.4	10.30	1.95
11-39	0.518	0.039	2.56	bdl	0.34	0.04	bdl	1109	271	43.90	bdl
11-11	0.099	0.061	bdl	bdl	0.12	0.04	bdl	66	143	6.17	4.24
B013-4	0.074	0.052	1.63	bdl	0.74	0.19	bdl	30	3270	69.80	1.69
B013-1	0.139	0.170	6.69	bdl	1.97	0.22	1.28	737	3830	76.80	54.6
11-33-2	0.253	0.083	bdl	bdl	0.04	0.19	bdl	192	142	17.70	bdl
C012-1	0.020	0.065	0.06	bdl	0.54	0.11	bdl	18	1710	33.60	0.1
11b-16-2	0.062	0.109	bdl	bdl	0.00	0.02	bdl	126	471	5.57	2.15
SM052-5	0.007	0.035	bdl	bdl	0.02	0.02	bdl	12	221	14.60	bdl
SM052-1	0.022	0.031	bdl	bdl	0.03	0.03	bdl	30	223	19.40	bdl
SM052-6	0.028	0.026	bdl	bdl	bdl	0.02	bdl	30	203	19.70	bdl
11-17-2	0.005	0.039	bdl	bdl	0.07	0.06	0.04	168	149	8.12	0.09
D015	0.019	0.044	bdl	bdl	0.08	0.03	bdl	18	128	5.56	1.12
D001	0.027	0.087	5.43	bdl	0.66	0.45	bdl	6515	523	78.00	45.7
11-20	0.003	0.192	6.38	bdl	0.37	0.94	0.02	3512	559	67.60	1.97
11-02b	0.006	bdl	8.75	bdl	1.53	0.87	1.46	2074	940	89.80	80.9
11-06a	0.003	0.052	4.19	bdl	0.62	0.43	bdl	719	273	48.80	2.09
11-04	0.018	0.022	3.28	bdl	0.06	0.67	0.22	851	358	77.90	2.19
11-03a	1.940	0.048	3.02	bdl	0.01	0.40	bdl	1780	134	103.0	6.79
11-14	0.011	0.061	4.06	bdl	0.02	0.74	0.20	2757	357	43.30	3.23
11-05	0.004	0.061	5.47	bdl	bdl	1.01	0.59	1157	532	81.40	24.2
11-34-2	0.016	0.031	5.80	bdl	0.11	1.10	bdl	2751	423	88.00	1.89
11-01a-1	0.014	0.092	5.18	bdl	0.04	1.10	bdl	4010	610	185.0	10.8
SH850	0.169	0.013	16.63	bdl	0.28	0.28	20.5	282	171	14.00	68.5
SH580	0.227	bdl	28.27	bdl	0.19	0.20	30.3	294	59	58.60	105
SH495	0.431	bdl	23.87	bdl	0.91	0.44	28.3	348	57.1	60.60	64.2
SH1165	0.011	0.013	22.17	bdl	0.20	0.41	28.6	384	440	9.78	52
SM1	0.102	0.035	2.99	bdl	1.04	0.04	bdl	66	233	3.75	0.31
11-29	0.040	bdl	33.55	bdl	0.05	0.21	47.9	42	16.1	2.71	668
11-8-1	0.391	0.467	7.32	bdl	0.25	1.02	0.09	22290	1130	111.0	56.3
11-8-2	0.501	0.541	5.61	bdl	0.21	0.79	0.18	26186	1400	147.0	67.3
SH100	2.410	0.061	4.01	0.03	0.06	0.60	bdl	3932	552	119.0	8.52
median	0.02	0.04	1.70	bdl	0.18	0.07	0.02	66.00	324	16.70	2.75
mean	0.14	0.05	4.01	bdl	0.44	0.24	2.54	1290	847	34.40	25.77
min	bdl	bdl	bdl	bdl	bdl	0.02	bdl	bdl	16.10	1.29	bdl
max	2.41	0.54	33.55	0.32	3.94	1.10	47.9	26186	5680	185	668

Appendix M (continued): Geochemistry of all Temagami BIF whole rock samples

	Pb TD-ICP 0.1	Ag TD-ICP 0.01	As TD-ICP 0.02	Sb TD-ICP 0.02	Hg TD-ICP 0.002	Tl TD-ICP 0.01	Cd TD-ICP 0.02	Co TD-ICP 0.02	Ni TD-ICP 0.1	Se TD-ICP 0.02	Mo TD-ICP 0.01
A027	bdl	0.05	35.5	0.2	0.021	bdl	bdl	0.5	9.7	0.05	n/a
11-03b	2.3	0.01	3.71	0.05	bdl	bdl	bdl	2.91	19.4	0.22	0.10
C303	0.2	bdl	0.53	0.07	0.008	bdl	bdl	1.06	2.3	0.3	n/a
D020-1	0.2	0.05	0.29	0.09	bdl	bdl	bdl	0.15	1	bdl	0.22
11-34-1	0.5	0.02	0.64	0.03	bdl	bdl	bdl	0.51	12.2	0.03	n/a
B013-6	0.2	0.01	0.23	0.18	bdl	bdl	0.02	1	16.7	0.12	n/a
11-22	0.9	bdl	bdl	0.05	bdl	bdl	0.02	0.53	15.7	0.08	n/a
11-10	0.7	0.01	0.34	0.07	0.011	bdl	bdl	0.7	9.7	0.13	n/a
B013-5	0.1	0.02	0.91	0.41	0.002	bdl	0.04	1.87	41.5	0.13	n/a
B013-2	0.2	0.03	0.4	0.5	0.114	bdl	0.02	4.94	18.4	0.05	n/a
B013-3	0.1	0.02	0.43	0.5	0.333	bdl	0.02	11.9	23.8	0.12	n/a
A030-1	6.6	0.15	6.06	0.71	0.106	0.05	0.13	13.9	88	1.02	n/a
11-16-1	1.1	bdl	0.04	0.08	bdl	bdl	bdl	0.14	bdl	bdl	0.06
11-23	2.6	0.01	0.89	0.17	bdl	bdl	bdl	0.52	1.8	0.18	bdl
11-27	1.4	0.07	1.39	0.13	bdl	bdl	bdl	2.57	10.6	0.42	0.20
C012-2	0.4	0.07	0.5	0.46	0.104	bdl	bdl	4.45	43.6	0.05	n/a
11-17-3	0.2	bdl	1.89	0.18	bdl	bdl	bdl	1.15	42.5	0.37	n/a
11-18-2	0.2	0.01	0.54	0.17	0.24	bdl	0.02	7.79	44	0.27	n/a
11-18-1	0.5	0.05	3.24	0.06	bdl	bdl	0.03	2.72	17.8	0.51	n/a
11-09	2	0.01	2.31	0.24	bdl	bdl	0.05	0.62	0.3	0.68	0.05
11-41	0.6	bdl	2.17	0.24	bdl	bdl	0.09	0.23	0.2	0.05	0.11
11-06b	0.8	0.01	1	0.3	bdl	bdl	bdl	0.56	0.3	0.38	0.48
SM052-4	1.2	bdl	1.71	0.93	0.007	bdl	0.03	0.9	58.4	0.11	n/a
SM052-2	1	bdl	1.85	0.5	0.004	bdl	bdl	0.42	24.5	0.17	n/a
11-12	1.3	0.04	0.81	0.59	0.009	bdl	bdl	0.05	1.2	bdl	bdl
C060-2	bdl	bdl	0.33	0.37	bdl	bdl	bdl	0.48	1.4	bdl	0.22
11-11-2	3.6	0.1	0.89	0.38	0.007	0.01	0.03	0.34	0.2	0.03	bdl
SM011-2	1.1	bdl	1.15	0.64	0.051	bdl	0.05	1.91	8.6	0.1	0.91
11-24	0.8	0.04	0.45	0.26	0.002	0.03	0.03	2.64	4.2	0.39	0.08
A028-2	0.3	0.05	1.44	1.24	0.08	bdl	0.05	14.6	52.9	0.59	n/a
B013-7	0.9	0.06	16.8	1.42	0.008	bdl	0.11	15	66.1	1.74	n/a
11-40	2.5	0.04	1.1	0.73	0.005	0.38	0.04	1.84	4.2	1.01	bdl
11-42	2.7	0.02	3.25	0.49	bdl	0.25	0.03	1.92	2	0.51	bdl
D020-2	2.6	0.09	10.2	0.57	bdl	bdl	0.04	4.46	24.6	1.46	0.08
11-32	2.7	0.02	0.75	0.62	0.006	0.23	0.03	0.55	0.9	0.47	bdl
11-39	0.8	0.09	0.48	0.59	0.003	0.52	0.07	2.57	5.2	0.26	bdl
11-11	1.3	bdl	0.6	0.52	bdl	0.06	0.02	1.77	12.2	0.55	n/a
B013-4	0.3	0.03	1.54	2.44	bdl	bdl	bdl	4.61	29.4	0.31	n/a
B013-1	4.4	0.26	24.5	2.45	0.004	0.02	0.18	16	79.2	2.34	n/a
11-33-2	1.3	0.02	0.48	0.73	0.004	0.01	bdl	0.86	7	0.36	n/a
C012-1	0.3	0.08	1.23	1.22	0.045	bdl	0.04	4	25.8	0.18	n/a
11b-16-2	1.1	0.02	0.55	0.66	bdl	0.02	bdl	0.76	1.5	0.29	0.01
SM052-5	5.5	0.02	1.77	2.03	bdl	bdl	bdl	0.35	16.2	0.04	bdl
SM052-1	1.3	0.02	0.67	0.63	0.003	bdl	0.03	0.51	22.3	0.09	n/a
SM052-6	1.3	0.02	0.3	0.34	bdl	bdl	bdl	0.29	11.1	0.09	n/a
11-17-2	1.1	0.02	2.38	2.16	bdl	bdl	bdl	2.46	13.2	0.29	n/a
D015	0.8	0.03	0.62	0.48	0.009	bdl	bdl	0.69	2.4	0.21	0.44
D001	1.2	0.26	0.49	bdl	0.005	bdl	0.17	26.6	57.1	1.44	n/a
11-20	1.3	0.25	70.3	0.06	bdl	bdl	0.14	49	520	1.57	n/a
11-02b	1.2	0.19	16.6	0.14	bdl	bdl	0.2	20.9	27.7	1.29	2.28
11-06a	0.8	0.16	0.85	0.14	bdl	bdl	0.06	2.9	5.1	0.48	0.14
11-04	8.7	0.16	1.21	0.18	0.003	0.01	0.11	4.9	7.1	0.87	n/a
11-03a	1.1	0.23	0.88	0.15	0.006	0.25	0.14	10.6	21.4	1.15	1.13
11-14	1.3	0.19	3.28	0.17	bdl	bdl	0.11	8.02	16.7	1.03	0.97
11-05	3.4	0.24	10.3	0.11	bdl	bdl	0.13	6.72	12.7	3.3	0.83
11-34-2	2.6	0.14	1.3	0.16	0.006	bdl	0.1	4.86	19.9	0.27	0.94
11-01a-1	0.9	0.26	0.98	0.05	bdl	bdl	0.14	11.8	35	1.29	0.02
SH850	33.9	1.28	173	8.31	0.042	1.66	0.05	54.8	48.2	3.08	bdl
SH580	167	3.96	363	24	0.098	2.63	0.16	84.1	96.7	4.92	bdl
SH495	133	3.34	334	24.2	0.106	2.98	0.24	62.9	120	6.01	bdl
SH1165	35.1	1.38	209	6.3	0.042	1.79	0.05	49.6	46.1	4	bdl
SM1	0.8	0.11	1.5	0.41	bdl	0.02	bdl	0.68	0.8	0.24	bdl
11-29	9.1	1.46	918	1.48	0.044	0.05	0.05	45.5	26.4	22.9	bdl
11-8-1	2	0.59	1.87	bdl	bdl	0.11	0.36	78.9	293	3.93	bdl
11-8-2	4.1	0.82	2.3	0.05	0.006	0.19	0.53	45.1	90.2	3.87	0.02
SH100	0.8	0.21	1.39	0.03	bdl	0.96	0.12	11.1	87.3	1.65	0.40
median	1.10	0.04	1.22	0.38	0.00	bdl	0.03	2.57	16.70	0.34	0.06
mean	7.13	0.26	34.08	1.42	0.02	0.19	0.07	10.90	36.75	1.21	0.27
min	bdl	bdl	bdl	bdl	bdl	bdl	bdl	0.05	bdl	bdl	bdl
max	167	3.96	918	24.20	0.33	2.98	0.53	84.10	520	22.90	2.28

Appendix M (continued): Geochemistry of all Temagami BIF whole rock samples

	Te TD-ICP 0.02	Sn TD-ICP 0.2	Ge FUS-ICP 0.5	Bi TD-ICP 0.004	In TD-ICP 0.02	Re TD-ICP 0.0002	W TD-ICP 0.02	Cr TD-ICP 0.1	V TD-ICP 0.2	Ga TD-ICP 0.02	Zr TD-ICP 0.2
A027	0.05	bdl	2.4	bdl	bdl	0.0004	n/a	n/a	bdl	0.13	2.6
11-03b	0.02	bdl	1.8	0.149	bdl	0.0003	0.31	3	4.6	1.24	0.9
C303	0.03	bdl	1.5	0.005	0.02	bdl	0.14	4.7	0.8	0.18	0.7
D020-1	0.12	bdl	1.5	0.085	bdl	bdl	0.07	4.5	0.4	0.12	0.5
11-34-1	bdl	bdl	2.1	bdl	bdl	0.0007	n/a	n/a	2.2	0.77	1.1
B013-6	0.04	bdl	2.4	0.012	bdl	0.0008	n/a	n/a	0.5	0.23	0.2
11-22	bdl	bdl	2.3	bdl	bdl	0.0008	n/a	n/a	0.8	0.31	1.3
11-10	bdl	0.3	3.6	bdl	bdl	bdl	n/a	n/a	2.5	0.7	0.6
B013-5	bdl	bdl	2	bdl	bdl	0.0011	n/a	n/a	1.7	0.22	0.5
B013-2	bdl	bdl	3.4	0.011	bdl	bdl	n/a	n/a	1.7	0.3	0.5
B013-3	0.02	bdl	3.1	0.006	bdl	0.0022	n/a	n/a	0.3	0.08	0.2
A030-1	0.04	bdl	2.1	0.035	bdl	0.0018	n/a	n/a	17.8	0.95	3
11-16-1	bdl	bdl	4.8	bdl	bdl	0.0012	0.15	3.6	0.9	0.26	0.7
11-23	bdl	bdl	3.1	0.01	bdl	0.0005	0.11	5.2	1.1	0.71	2.5
11-27	0.03	bdl	2.1	0.031	bdl	0.0005	0.11	4	5.8	1.26	1.6
C012-2	bdl	bdl	3.7	bdl	bdl	0.0015	n/a	n/a	0.9	0.22	0.4
11-17-3	bdl	bdl	4.9	0.009	bdl	0.0024	n/a	n/a	1.6	0.64	1.2
11-18-2	bdl	0.2	4.9	0.016	bdl	0.003	n/a	n/a	3.9	1.21	3.7
11-18-1	0.08	bdl	2.7	0.071	bdl	0.0027	n/a	n/a	13.3	3.4	24
11-09	0.1	bdl	4	0.051	bdl	0.0004	0.15	6.1	2.7	1.06	2.2
11-41	bdl	bdl	5.1	0.004	bdl	0.0005	0.42	4	1.5	0.63	1.1
11-06b	bdl	0.2	5.8	0.025	bdl	0.0002	0.63	3.2	2.9	1.61	2.7
SM052-4	bdl	bdl	5	0.007	bdl	0.0018	n/a	n/a	0.7	0.18	bdl
SM052-2	bdl	bdl	4.6	0.013	bdl	0.0003	n/a	n/a	0.5	0.28	0.4
11-12	bdl	bdl	5.1	0.005	bdl	0.0004	2.59	5.3	0.7	0.2	0.6
C060-2	bdl	bdl	4	bdl	bdl	bdl	0.17	4.6	0.4	0.36	0.7
11-11-2	0.03	bdl	3.8	bdl	bdl	0.0006	1.61	4.1	2.1	0.52	1.8
SM011-2	0.02	bdl	6.4	0.012	bdl	bdl	11	2.9	4.5	0.86	0.4
11-24	bdl	bdl	2.4	bdl	bdl	0.0009	0.33	6.7	12.7	2	9.9
A028-2	0.05	0.6	5	0.088	bdl	0.0023	n/a	n/a	6.9	1.09	3
B013-7	0.15	bdl	2.9	0.147	0.02	0.0021	n/a	n/a	7.1	0.72	5
11-40	0.07	0.2	7.4	0.062	bdl	0.0015	0.41	10.9	11.3	3.22	18.7
11-42	0.02	bdl	3.4	0.034	bdl	0.0007	0.29	6.5	7.1	2.19	12.6
D020-2	0.12	bdl	7.8	0.239	bdl	0.0014	0.26	20.7	6	0.77	1.9
11-32	bdl	bdl	5.5	0.007	bdl	0.0016	0.22	10.8	6.7	2.68	4.9
11-39	0.03	0.2	12.1	bdl	bdl	0.0009	0.51	15.5	28.2	7.54	59.6
11-11	0.03	bdl	5.2	bdl	bdl	0.0008	n/a	n/a	5.3	2.19	4.5
B013-4	0.02	bdl	5.7	bdl	bdl	0.0005	n/a	n/a	9.5	0.74	2.8
B013-1	0.24	bdl	4.6	0.28	0.06	0.0085	n/a	n/a	38.6	3.87	30.6
11-33-2	bdl	0.5	11.2	bdl	bdl	0.0015	n/a	n/a	7.2	3.68	7.6
C012-1	0.05	0.3	7.9	0.009	bdl	bdl	n/a	n/a	3.8	0.68	2.1
11b-16-2	0.03	bdl	8.1	bdl	bdl	0.0009	0.4	3.9	5.4	1.77	4.6
SM052-5	0.02	bdl	9.9	0.073	bdl	0.0009	bdl	bdl	2	0.44	0.8
SM052-1	0.04	bdl	9.6	0.023	bdl	bdl	n/a	n/a	2.7	0.79	2.2
SM052-6	0.03	bdl	9.8	0.025	bdl	bdl	n/a	n/a	2.3	0.48	1.9
11-17-2	0.06	0.5	14.3	0.033	bdl	0.0031	n/a	n/a	11.5	3.77	7.9
D015	0.04	0.2	8.5	0.023	bdl	bdl	1.19	3.8	3.3	0.86	0.9
D001	0.06	bdl	1.3	bdl	0.05	bdl	n/a	n/a	101	23	136
11-20	0.09	0.8	4.7	0.047	0.03	0.0017	n/a	n/a	152	20.8	125
11-02b	0.17	0.2	3.4	0.171	0.04	0.0019	0.23	28	62.3	22.4	76.8
11-06a	0.04	0.5	5.9	0.008	0.02	0.0013	0.14	10.2	17.9	10.1	45.4
11-04	0.07	0.6	8.9	0.036	0.03	0.0017	n/a	n/a	16.3	16.2	77.3
11-03a	0.08	2	3.4	bdl	0.03	0.0006	1.86	15.4	49.1	18.7	117
11-14	0.09	0.7	4.9	0.065	0.03	0.0013	0.52	36.4	46.2	14.2	113
11-05	0.11	1.2	5	0.043	0.06	0.0023	0.41	18.6	26.6	24.7	121
11-34-2	0.05	0.5	6.8	0.012	0.03	0.0028	0.59	39.7	57.3	17.2	78.9
11-01a-1	0.06	bdl	4.1	bdl	0.04	0.0024	0.07	64.6	104	31.9	149
SH850	0.37	0.2	1.1	0.214	bdl	0.0032	0.41	bdl	17.5	3.51	16.2
SH580	0.74	0.5	bdl	0.642	0.03	0.0022	0.29	bdl	9.2	3.14	9.6
SH495	0.71	0.5	bdl	0.665	0.03	0.0034	0.36	bdl	14.4	4.22	17.6
SH1165	0.35	0.3	1.5	0.135	bdl	0.004	0.81	bdl	16.3	2.57	16.9
SM1	0.06	bdl	6.5	0.005	bdl	bdl	0.78	12.3	2.4	0.9	2.5
11-29	1.44	bdl	0.6	1.42	bdl	bdl	0.15	7.7	1.7	0.34	1.3
11-8-1	0.27	bdl	3	0.011	0.1	0.0024	bdl	307	110	30.6	332
11-8-2	0.25	bdl	2.8	0.015	0.12	0.0018	bdl	172	106	35.7	501
SH100	0.06	1.1	2.2	0.061	0.06	0.0006	0.66	131	159	30.2	126
median	0.04	bdl	4.05	0.01	bdl	0.00	0.35	8.95	5.35	1.08	2.75
mean	0.10	0.25	4.64	0.08	bdl	0.00	0.74	60.48	20.06	5.58	34.85
min	bdl	bdl	bdl	bdl	bdl	bdl	bdl	2.90	bdl	0.08	bdl
max	1.44	2.00	14.30	1.42	0.12	0.01	11.00	1130	159	35.70	501

Appendix M (continued): Geochemistry of all Temagami BIF whole rock samples

	Ba TD-ICP 0.2	Cs TD-ICP 0.01	Li TD-ICP 0.1	Be TD-ICP 0.02	B TD-ICP 0.2	Hf FUS-ICP 0.1	Nb FUS-ICP 0.2	Ta FUS-ICP 0.01	Rb TD-ICP 0.04	Sr TD-ICP 0.04	U FUS-ICP 0.01
A027	0.8	0.08	bdl	0.1	53.6	bdl	bdl	0.02	0.27	3.91	0.08
11-03b	0.8	0.03	1.9	0.03	56.8	bdl	bdl	0.02	0.11	0.92	0.03
C303	0.5	0.04	0.1	0.04	54.9	bdl	bdl	bdl	0.05	24.7	0.02
D020-1	3.1	0.18	bdl	0.15	60.1	bdl	bdl	bdl	0.47	3.93	0.02
11-34-1	25.1	1.05	0.3	0.07	56.2	bdl	bdl	0.03	1.98	3.46	0.03
B013-6	3.5	0.09	0.1	0.03	41.1	bdl	bdl	0.05	0.13	6.23	0.07
11-22	1.3	0.19	0.2	0.07	59.2	bdl	bdl	bdl	1.1	2.29	0.04
11-10	5.7	0.04	0.5	0.08	58.5	bdl	0.9	0.06	0.46	2.71	0.12
B013-5	1.7	0.07	0.2	0.11	48.5	bdl	bdl	bdl	0.26	9.68	0.04
B013-2	2.4	0.16	0.2	0.12	23.3	bdl	bdl	0.06	0.44	7.2	0.07
B013-3	1.5	0.14	0.1	0.13	21.5	bdl	bdl	0.03	0.38	8.48	0.06
A030-1	26.1	0.84	0.2	0.07	25.5	bdl	bdl	bdl	1.26	5.59	0.05
11-16-1	1.5	0.11	0.3	0.08	59.4	bdl	0.7	0.08	0.39	40.5	0.13
11-23	1.2	0.12	0.3	0.14	59.3	bdl	bdl	0.12	0.59	2.64	0.12
11-27	8.5	0.17	0.6	0.27	56.2	bdl	0.8	0.07	0.63	21.1	0.2
C012-2	35.8	0.06	0.4	0.13	60.7	bdl	bdl	bdl	0.17	5.52	0.03
11-17-3	4.4	0.08	0.8	0.15	59.3	bdl	bdl	0.02	0.41	6.08	0.07
11-18-2	1.8	0.07	0.7	0.44	56.5	bdl	0.6	0.05	0.36	5.42	0.12
11-18-1	0.5	0.05	2.6	0.32	45.4	0.5	bdl	0.12	0.36	2.56	0.32
11-09	181.0	0.27	1	0.29	53	bdl	bdl	0.01	1.45	168	0.12
11-41	5.3	1	1.8	0.23	13.3	bdl	0.3	0.08	0.87	2.21	0.1
11-06b	1.2	0.04	0.9	0.32	8	bdl	0.5	0.03	0.14	6.23	0.13
SM052-4	2.0	0.05	0.1	0.33	63.8	bdl	bdl	0.02	0.09	16.4	0.2
SM052-2	1.7	0.03	0.1	0.25	59.6	bdl	bdl	0.06	0.05	14.3	0.07
11-12	46.0	0.07	1	0.43	4.2	bdl	bdl	0.03	0.16	14.9	0.04
C060-2	0.5	0.05	bdl	0.34	38.6	bdl	1.7	0.07	0.26	1.8	0.04
11-11-2	4.5	0.53	1	0.36	6.7	bdl	0.9	0.02	2.37	56.8	0.07
SM011-2	128.0	0.19	0.8	0.57	46.1	bdl	bdl	0.04	0.29	45.9	0.08
11-24	3.7	0.8	0.5	0.54	2	0.18	bdl	0.06	5.7	10	0.16
A028-2	2.8	0.71	0.7	1.23	1.7	bdl	1	0.07	2.58	6.01	0.65
B013-7	16.4	0.46	0.5	0.43	27.6	bdl	0.7	0.06	1.11	45.9	0.05
11-40	70.8	46	1	1.43	52.2	0.47	bdl	0.09	51.9	35.8	0.2
11-42	32.1	22.1	2.5	1.44	52.1	0.33	bdl	0.05	36.3	50	0.16
D020-2	15.4	0.66	0.2	1.03	2.6	bdl	0.6	0.05	1.91	3.54	0.08
11-32	33.4	4.11	1.7	1.15	2.8	0.13	bdl	0.05	23.2	36.1	0.28
11-39	128.0	19.1	5.7	1.86	45.4	1.42	1.4	0.25	61.1	29.5	0.66
11-11	5.4	2.27	3.6	0.72	6.1	0.12	bdl	0.03	8.1	51.8	0.15
B013-4	0.9	0.4	0.2	0.59	0.8	bdl	0.6	0.05	0.98	7.54	0.04
B013-1	279.0	3.99	1.2	0.8	0.7	0.52	0.8	0.14	6.73	90.2	0.17
11-33-2	144.0	4.97	0.6	1.27	28.3	0.21	1.2	0.12	9.92	24.2	0.22
C012-1	2.1	0.14	0.3	0.92	bdl	bdl	0.3	0.04	0.39	14	0.07
11b-16-2	5.4	0.57	2.8	0.92	0.5	0.11	bdl	0.03	3.13	90.8	0.15
SM052-5	18.8	0.15	0.4	2.36	40.9	bdl	bdl	0.04	0.31	13.9	0.11
SM052-1	24.5	0.28	0.3	0.92	25.3	bdl	bdl	0.04	0.89	10	0.06
SM052-6	28.1	0.38	0.2	0.77	34.4	bdl	bdl	0.06	1.12	8.73	0.08
11-17-2	5.4	0.17	3.8	1.98	2.2	0.19	1.3	0.07	0.79	6.52	0.34
D015	16.7	0.23	0.4	1.14	bdl	bdl	bdl	0.04	0.59	14.2	0.05
D001	29.9	0.25	38.3	0.91	31.1	2.85	7.2	0.54	0.31	52.4	0.51
11-20	0.8	0.2	11.4	1.27	0.4	2.62	3.9	0.32	0.18	32.3	1.19
11-02b	1.8	0.21	17.3	0.42	0.3	1.61	1.2	0.25	0.36	113	0.65
11-06a	0.7	0.11	22.5	0.54	bdl	1.16	1.8	0.3	0.19	10.6	0.53
11-04	4.1	0.34	33.8	0.87	bdl	2.34	5.9	0.64	2.26	3.96	0.92
11-03a	553.0	1.56	28.4	2.11	18.2	2.4	5.2	0.52	78.5	17.6	1.47
11-14	1.7	0.18	44	0.77	45.2	2.5	6.9	0.59	0.5	5.87	1.6
11-05	2.9	0.15	49.5	0.86	bdl	3.78	12.8	1.15	0.24	4.96	3.1
11-34-2	44.1	bdl	4.1	0.97	40.7	2.03	7	0.65	0.15	9.09	2.16
11-01a-1	2.4	0.19	41.6	0.41	bdl	3.31	4.8	0.52	0.82	14.6	1.35
SH850	14.1	0.38	6	0.22	0.7	0.27	0.4	0.05	8.32	6.3	0.28
SH580	5.9	0.67	3.3	0.12	2.8	0.22	0.6	0.05	11.9	3.94	0.15
SH495	7.0	0.79	3.9	0.21	2.8	0.39	0.6	0.1	23.7	5.39	0.21
SH1165	2.6	0.2	1.4	0.19	3.8	0.36	0.7	0.53	0.58	2.77	3.11
SM1	6.7	0.94	3.5	1.28	bdl	bdl	bdl	0.04	6.69	72.7	0.06
11-29	8.0	0.07	0.2	bdl	21.4	bdl	bdl	0.03	1.11	4.5	0.05
11-8-1	720.0	6.08	124	4.16	68.8	4.45	95.6	6.23	25.4	503	2.66
11-8-2	832.0	28.6	98.9	4.72	67	8.43	119	7.34	41.9	595	2.99
SH100	588.0	3.86	38.6	1.86	2.3	2.9	7	0.54	132	33.6	2.11
median	5.40	0.20	0.85	0.43	27.95	bdl	0.30	0.06	0.71	9.84	0.13
mean	62.95	2.40	9.30	0.74	28.80	0.71	4.52	0.35	8.60	38.33	0.47
min	0.50	bdl	bdl	bdl	bdl	bdl	bdl	bdl	0.05	0.92	0.02
max	832	46.00	124	4.72	68.80	8.43	119	7.34	132	595.0	3.1

Appendix M (continued): Geochemistry of all Temagami BIF whole rock samples

	Th FUS-ICP 0.05	Y FUS-ICP 0.5	Sc FUS-ICP 1	La FUS-ICP 0.05	Ce FUS-ICP 0.05	Pr FUS-ICP 0.01	Nd FUS-ICP 0.05	Sm FUS-ICP 0.01	Eu FUS-ICP 0.005	Gd FUS-ICP 0.01	Tb FUS-ICP 0.01
A027	0.08	1.1	bdl	0.32	0.4	0.06	0.28	0.04	0.074	0.12	0.02
11-03b	bdl	1	bdl	1.09	1.74	0.2	0.78	0.13	0.042	0.13	0.02
C303	bdl	0.9	bdl	0.2	0.42	0.05	0.2	0.03	0.078	0.09	0.02
D020-1	bdl	bdl	bdl	0.12	0.27	0.03	0.11	0.02	0.025	0.05	bdl
11-34-1	bdl	0.5	bdl	0.16	0.33	0.04	0.15	0.07	0.041	0.11	0.02
B013-6	bdl	0.6	bdl	0.29	0.39	0.05	0.23	0.09	0.066	0.08	0.01
11-22	0.09	0.8	bdl	0.67	1.31	0.14	0.61	0.11	0.054	0.1	0.01
11-10	0.13	1.5	bdl	0.82	1.32	0.16	0.55	0.19	0.104	0.22	0.04
B013-5	bdl	1.2	bdl	0.43	0.76	0.08	0.37	0.09	0.108	0.12	0.02
B013-2	bdl	1.6	bdl	0.95	1.27	0.12	0.68	0.15	0.126	0.21	0.02
B013-3	bdl	1.3	bdl	0.25	0.28	0.04	0.22	0.09	0.093	0.12	0.02
A030-1	bdl	8.3	2	4.35	7.69	0.91	3.85	0.96	0.404	1.05	0.17
11-16-1	0.12	0.5	bdl	0.5	0.74	0.08	0.36	0.08	0.03	0.05	bdl
11-23	0.16	1.9	bdl	1.21	2.04	0.22	0.9	0.18	0.141	0.22	0.03
11-27	0.48	6.4	bdl	1.89	3.4	0.42	1.74	0.48	0.289	0.64	0.1
C012-2	bdl	1.2	bdl	0.34	0.54	0.06	0.28	0.06	0.086	0.08	0.02
11-17-3	0.09	3	bdl	1.51	2.6	0.3	1.19	0.28	0.261	0.35	0.05
11-18-2	0.19	3.5	bdl	1.62	2.95	0.34	1.44	0.3	0.192	0.41	0.06
11-18-1	1.16	5.5	2	6.86	12.7	1.36	5.01	0.85	0.434	0.7	0.11
11-09	0.12	6.7	bdl	3.5	7.07	0.84	3.54	0.74	0.413	0.88	0.14
11-41	0.15	1.6	bdl	1.24	1.87	0.21	0.87	0.16	0.103	0.22	0.03
11-06b	0.14	3.9	bdl	3.25	5.48	0.6	2.52	0.37	0.263	0.52	0.07
SM052-4	bdl	4.9	bdl	0.92	1.46	0.19	1	0.18	0.231	0.34	0.07
SM052-2	bdl	4.9	bdl	0.97	1.72	0.22	0.96	0.23	0.248	0.4	0.09
11-12	bdl	2.6	bdl	0.74	1.15	0.13	0.56	0.16	0.129	0.15	0.03
C060-2	bdl	2.1	bdl	0.66	1.1	0.13	0.45	0.05	0.115	0.19	0.03
11-11-2	0.08	3.7	bdl	1.33	2.34	0.26	1.09	0.27	0.219	0.34	0.06
SM011-2	bdl	5.8	bdl	2.72	4.28	0.52	1.93	0.46	0.372	0.5	0.07
11-24	0.49	8.3	1	6.37	11	1.18	4.62	0.92	0.515	0.93	0.15
A028-2	0.25	4.7	1	5.58	9.78	1.06	3.89	0.73	0.357	0.76	0.11
B013-7	0.18	5.4	1	3.2	4.86	0.58	2.36	0.51	0.487	0.6	0.1
11-40	0.99	7.5	1	5.41	10.3	1.14	4.4	0.83	0.46	0.81	0.12
11-42	0.64	8.1	bdl	4.76	8.43	0.91	3.66	0.68	0.501	0.73	0.11
D020-2	0.2	3.6	bdl	1.6	2.89	0.33	1.2	0.29	0.191	0.3	0.06
11-32	0.39	5.5	bdl	4.11	7.59	0.81	3.32	0.78	0.32	0.74	0.12
11-39	2.91	8.3	3	10	18.9	1.97	7.36	1.25	0.716	1.04	0.17
11-11	0.3	6.7	bdl	4.71	8.24	0.9	3.74	0.82	0.531	0.76	0.13
B013-4	0.06	8.6	bdl	1.16	1.9	0.24	1.16	0.25	0.249	0.54	0.12
B013-1	1.28	16.3	4	34.2	47.8	5.31	19.2	3.26	1.94	2.74	0.36
11-33-2	0.57	5.1	bdl	3.06	5.62	0.67	2.54	0.48	0.254	0.6	0.1
C012-1	0.07	7.7	bdl	1.55	2.66	0.31	1.44	0.39	0.357	0.6	0.11
11b-16-2	0.25	7.1	bdl	4.13	6.51	0.72	3	0.59	0.502	0.68	0.11
SM052-5	bdl	2.6	bdl	0.62	0.95	0.1	0.33	0.09	0.175	0.13	0.03
SM052-1	0.06	2.8	bdl	0.53	0.93	0.11	0.44	0.1	0.168	0.21	0.04
SM052-6	0.06	2.4	bdl	0.76	1.13	0.12	0.57	0.1	0.143	0.15	0.04
11-17-2	0.84	8.8	bdl	5.76	11.4	1.31	4.86	0.9	0.635	0.97	0.16
D015	bdl	6.7	bdl	2.57	4.12	0.5	1.91	0.38	0.428	0.55	0.09
D001	1.8	24.5	21	16	36	4.82	18.7	4.18	1.29	4.16	0.68
11-20	3.17	18.3	19	23.9	50.9	6.14	25.1	5.17	1.44	3.67	0.55
11-02b	2.64	12.7	4	9.85	19	2.09	7.94	1.65	0.791	1.43	0.26
11-06a	2.53	7.5	3	2.74	6.04	0.72	3.02	0.77	0.325	0.84	0.15
11-04	6.76	9.2	3	6.12	13.9	1.71	6.25	1.2	0.386	1.04	0.18
11-03a	4.02	12	6	23.1	48	5.46	19.5	3.29	0.91	2.51	0.35
11-14	5.47	16.4	8	23.4	49.2	5.5	20.7	3.69	1.01	2.72	0.41
11-05	11.4	48.2	6	19.1	46.3	5.79	24.1	5.85	1.11	5.73	1.1
11-34-2	7.89	19.5	7	27.8	60.4	6.76	24.7	4.44	1.17	2.99	0.49
11-01a-1	5.84	15.5	11	29.1	58.2	6.35	23.3	4.13	1.14	2.79	0.4
SH850	0.52	2.9	1	2.7	5.05	0.58	2.4	0.51	0.277	0.44	0.07
SH580	0.45	2.1	bdl	7.74	15.1	1.54	5.69	1.07	0.289	0.72	0.1
SH495	0.77	2.1	1	7.15	15.3	1.74	6.3	1.05	0.372	0.72	0.1
SH1165	0.87	3.4	bdl	2.42	4.8	0.52	2.02	0.42	0.262	0.39	0.07
SM1	0.16	5.1	bdl	2.69	4.4	0.52	2.05	0.41	0.374	0.48	0.08
11-29	0.07	0.9	bdl	0.22	0.4	0.05	0.2	0.04	0.022	0.06	0.02
11-8-1	5.07	26	21	60	134	16.8	70.9	14.1	4.15	10	1.33
11-8-2	6.2	30.8	21	72.6	162	20	83.9	16.3	5.11	11.7	1.62
SH100	8.28	20.2	21	29	62.6	7.59	27.2	5.18	1.38	4.23	0.64
median	0.17	5.00	bdl	2.70	4.60	0.52	2.04	0.44	0.29	0.55	0.10
mean	1.32	7.28	2.87	7.65	15.52	1.83	7.21	1.42	0.54	1.19	0.18
min	bdl	bdl	bdl	0.12	0.27	0.03	0.11	0.02	0.02	0.05	bdl
max	11.40	48.20	21.0	72.6	162	20.0	83.9	16.3	5.11	11.70	1.62

Appendix M (continued): Geochemistry of all Temagami BIF whole rock samples

	Dy FUS-ICP 0.01	Ho FUS-ICP 0.01	Er FUS-ICP 0.01	Tm FUS-ICP 0.005	Yb FUS-ICP 0.01	Lu FUS-ICP 0.002	Sum REE	Y/Ho	Zr/Ti	Th/U	Ge/Si [umol/mol]
A027	0.11	0.02	0.07	0.012	0.09	0.013	1.6	55.00	0.43	1.00	2.03
11-03b	0.14	0.03	0.08	0.012	0.07	0.011	4.5	33.33	0.05	n/a	1.54
C303	0.12	0.02	0.06	0.01	0.08	0.015	1.4	45.00	0.12	n/a	1.30
D020-1	0.05	bdl	0.03	0.005	0.03	0.005	0.7	n/a	0.08	n/a	1.26
11-34-1	0.1	0.02	0.03	bdl	0.03	0.004	1.1	25.00	0.06	n/a	1.99
B013-6	0.06	0.01	0.04	0.007	0.05	0.008	1.4	60.00	0.02	n/a	2.12
11-22	0.09	0.02	0.06	0.009	0.07	0.015	3.3	40.00	0.04	2.25	2.02
11-10	0.19	0.03	0.09	0.012	0.06	0.01	3.8	50.00	0.03	1.08	3.22
B013-5	0.13	0.03	0.11	0.019	0.13	0.02	2.4	40.00	0.08	n/a	1.83
B013-2	0.15	0.03	0.11	0.018	0.12	0.017	4.0	53.33	0.04	n/a	3.10
B013-3	0.17	0.04	0.12	0.022	0.15	0.026	1.6	32.50	0.03	n/a	2.90
A030-1	1.06	0.21	0.63	0.09	0.54	0.091	22.0	39.52	0.25	n/a	1.94
11-16-1	0.05	0.01	0.05	0.008	0.05	0.007	2.0	50.00	0.06	0.92	4.37
11-23	0.17	0.04	0.12	0.022	0.14	0.018	5.5	47.50	0.03	1.33	2.91
11-27	0.67	0.16	0.47	0.071	0.43	0.068	10.8	40.00	0.05	2.40	2.28
C012-2	0.11	0.03	0.09	0.015	0.1	0.017	1.8	40.00	0.07	n/a	3.51
11-17-3	0.3	0.07	0.21	0.031	0.2	0.032	7.4	42.86	0.05	1.29	4.68
11-18-2	0.39	0.08	0.23	0.033	0.22	0.034	8.3	43.75	0.04	1.58	5.25
11-18-1	0.65	0.15	0.45	0.07	0.5	0.093	29.9	36.67	0.05	3.63	3.34
11-09	0.75	0.15	0.45	0.066	0.41	0.067	19.0	44.67	0.07	1.00	4.58
11-41	0.18	0.04	0.12	0.02	0.13	0.015	5.2	40.00	0.04	1.50	5.14
11-06b	0.44	0.09	0.26	0.04	0.23	0.03	14.2	43.33	0.06	1.08	7.26
SM052-4	0.48	0.12	0.36	0.054	0.29	0.035	5.7	40.83	n/a	n/a	4.61
SM052-2	0.59	0.12	0.34	0.046	0.26	0.039	6.2	40.83	0.07	n/a	4.27
11-12	0.23	0.06	0.21	0.029	0.18	0.029	3.8	43.33	0.10	n/a	5.86
C060-2	0.18	0.05	0.16	0.023	0.14	0.024	3.3	42.00	n/a	n/a	4.58
11-11-2	0.33	0.07	0.21	0.034	0.25	0.044	6.8	52.86	0.04	1.14	4.53
SM011-2	0.37	0.08	0.25	0.046	0.35	0.064	12.0	72.50	0.07	n/a	8.00
11-24	0.89	0.19	0.56	0.078	0.5	0.084	28.0	43.68	0.05	3.06	3.93
A028-2	0.72	0.15	0.43	0.075	0.57	0.099	24.3	31.33	0.02	0.38	8.35
B013-7	0.61	0.14	0.47	0.075	0.53	0.093	14.6	38.57	0.04	3.60	4.57
11-40	0.78	0.18	0.55	0.091	0.62	0.104	25.8	41.67	0.04	4.95	11.83
11-42	0.67	0.15	0.5	0.076	0.51	0.085	21.8	54.00	0.04	4.00	7.18
D020-2	0.39	0.09	0.29	0.048	0.33	0.059	8.1	40.00	0.01	2.50	13.20
11-32	0.65	0.13	0.38	0.058	0.38	0.064	19.5	42.31	0.05	1.39	10.09
11-39	0.94	0.2	0.62	0.098	0.65	0.111	44.0	41.50	0.05	4.41	33.65
11-11	0.79	0.16	0.46	0.073	0.49	0.079	21.9	41.88	0.07	2.00	10.92
B013-4	0.82	0.18	0.62	0.1	0.66	0.114	8.1	47.78	0.09	1.50	13.61
B013-1	2.04	0.38	1.22	0.191	1.32	0.231	120.2	42.89	0.04	7.53	21.02
11-33-2	0.6	0.11	0.3	0.047	0.3	0.043	14.7	46.36	0.04	2.59	31.28
C012-1	0.71	0.16	0.48	0.074	0.47	0.086	9.4	48.13	0.12	1.00	24.65
11b-16-2	0.65	0.14	0.41	0.056	0.34	0.052	17.9	50.71	0.04	1.67	23.68
SM052-5	0.27	0.06	0.26	0.04	0.23	0.032	3.3	43.33	0.07	n/a	32.11
SM052-1	0.3	0.07	0.24	0.041	0.26	0.044	3.5	40.00	0.07	1.00	46.93
SM052-6	0.31	0.07	0.23	0.04	0.29	0.057	4.0	34.29	0.06	0.75	48.46
11-17-2	1.09	0.25	0.78	0.129	0.87	0.147	29.3	35.20	0.05	2.47	95.41
D015	0.57	0.14	0.43	0.073	0.46	0.083	12.3	47.86	0.05	n/a	58.52
D001	4.27	0.83	2.52	0.37	2.38	0.356	96.6	29.52	0.02	3.53	1.90
11-20	2.9	0.56	1.64	0.237	1.55	0.255	124.0	32.68	0.04	2.66	7.74
11-02b	1.53	0.33	0.98	0.159	1.06	0.169	47.2	38.48	0.04	4.06	6.64
11-06a	0.93	0.21	0.65	0.102	0.66	0.113	17.3	35.71	0.06	4.77	9.41
11-04	1.19	0.28	0.89	0.15	1.09	0.188	34.6	32.86	0.09	7.35	21.81
11-03a	1.89	0.39	1.25	0.193	1.3	0.2	108.3	30.77	0.07	2.73	4.09
11-14	2.49	0.51	1.46	0.227	1.64	0.264	113.2	32.16	0.04	3.42	8.06
11-05	6.83	1.38	3.89	0.576	3.64	0.567	126.0	34.93	0.10	3.68	8.88
11-34-2	2.86	0.6	1.75	0.278	1.84	0.286	136.4	32.50	0.03	3.65	12.63
11-01a-1	2.17	0.44	1.33	0.201	1.37	0.227	131.1	35.23	0.04	4.33	8.69
SH850	0.44	0.09	0.27	0.042	0.34	0.059	13.3	32.22	0.06	1.86	1.80
SH580	0.46	0.08	0.2	0.025	0.16	0.03	33.2	26.25	0.03	3.00	0.99
SH495	0.42	0.07	0.23	0.038	0.25	0.037	33.8	30.00	0.05	3.67	0.63
SH1165	0.44	0.1	0.32	0.047	0.31	0.054	12.2	34.00	0.04	0.28	4.05
SM1	0.51	0.12	0.36	0.054	0.35	0.058	12.5	42.50	0.04	2.67	11.08
11-29	0.11	0.02	0.07	0.009	0.05	0.009	1.3	45.00	0.03	1.40	17.86
11-8-1	6.38	0.97	2.2	0.244	1.32	0.193	322.6	26.80	0.01	1.91	6.42
11-8-2	7.33	1.13	2.63	0.297	1.7	0.225	386.5	27.26	0.02	2.07	6.20
SH100	3.62	0.69	2	0.28	1.7	0.272	146.4	29.28	0.03	3.92	2.92
median	0.54	0.12	0.35	0.05	0.34	0.06	12.38	40.42	0.05	1.50	5.19
mean	1.04	0.21	0.60	0.09	0.57	0.09	38.13	40.67	0.06	2.06	11.24
min	0.05	bdl	0.03	bdl	0.03	0.00	0.76	25.00	0.01	0.13	0.63
max	7.33	1.38	3.89	0.58	3.64	0.57	387	72.50	0.43	7.53	95.41

Appendix N: Principal Component Analysis

Geochemical data is calculated to 100%, and the system is considered "closed" because the abundance of quartz and magnetite force element abundances into a dependent relationship. Dilution and concentration in a limited volume of rock is thereby controlled by abundance of a potentially unrelated component. This can lead to false correlations in element couples that are not correspondent to any underlying process but the abundance of the volume-controlling component – in this case, quartz. To avoid closure problems, a centred-log ratio (CLR) calculation has been applied to "open" the system: absolute abundances for an element are recalculated and range indefinitely, but sum to zero for all components of one sample. Specifically, the CLR is the ln of each element's abundance divided by the geometric mean (GM) of all abundances in that sample. The geometric mean is the n^{th} root of the product of n abundances given for each element, following equations 6.1 and 6.2:

$$GM_x = \sqrt[n]{c_{1(x)} c_{2(x)} \dots c_{n(x)}} \qquad \text{[eq 6.1]}$$

$$CLR_{component\ 1\ sample\ x} = ln\left(\frac{c_{1(x)}}{GM_x}\right) \qquad \text{[eq 6.2]}$$

Where GM is the geometric mean, CLR is the centered log ratio, and $c_{n(x)}$ is the abundance of component n in sample x. Using the computed CLR data, a robust M-Estimation PCA was performed using the ioGAS software package following an algorithm developed by Campbell (1980). The difference between a classical PCA and the robust PCA used here is the rejection of outliers to avoid influence of extreme values in a small dataset.

Reference:

Campbell, N.A., 1980. Robust procedures in multivariate analysis. I: Robust covariance estimation; Applied Statistics, v. 29, p. 231-237.

Appendix N (continued): Principal Component Analysis

Robust PCA Report (M-estimation): Transform None, Scaling true (48 rows)

Summary	Count
Rows	48
Columns	26

Robust Correlation	**Si-CLR**	**Fe-CLR**	**Al-CLR**	**Mg-CLR**	**P-CLR**	**C-CLR**	**S-CLR**	**Ti-CLR**	**Mn-CLR**	**Zn-CLR**	**Cu-CLR**	**Pb-CLR**	**Ag-CLR**
Si-CLR	1	-0.3224	0.1903	-0.1743	-0.0203	0.08653	-0.1324	-0.6149	-0.0447	-0.06076	0.2128	0.1086	0.04083
Fe-CLR	-0.3224	1	-0.3727	-0.1382	0.5774	-0.4508	-0.4429	0.08498	-0.1948	0.2523	-0.5529	0.2449	0.1339
Al-CLR	0.1903	-0.3727	1	-0.2182	-0.03669	-0.07033	-0.08527	0.414	-0.3883	-0.5125	-0.01454	0.09001	-0.2984
Mg-CLR	-0.1743	-0.1382	-0.2182	1	-0.491	0.3249	0.08834	0.01492	0.5894	0.513	0.02968	-0.6239	0.2231
P-CLR	-0.0203	0.5774	-0.03669	-0.491	1	-0.207	-0.5357	-0.006368	-0.2375	-0.1198	-0.4077	0.2429	-0.0815
C-CLR	0.08653	-0.4508	-0.07033	0.3249	-0.207	1	0.2516	-0.1959	0.5514	-0.1442	0.1548	-0.408	0.02337
S-CLR	-0.1324	-0.4429	-0.08527	0.08834	-0.5357	0.2516	1	0.07952	0.1779	-0.2916	0.428	-0.1784	0.009774
Ti-CLR	-0.6149	0.08498	0.414	0.01492	-0.006368	-0.1959	0.07952	1	-0.2337	-0.3578	-0.137	0.01511	-0.0861
Mn-CLR	-0.0447	-0.1948	-0.3883	0.5894	-0.2375	0.5514	0.1779	-0.2337	1	0.3614	0.1055	-0.5948	0.0871
Zn-CLR	-0.06076	0.2523	-0.5125	0.513	-0.1198	-0.1442	-0.2916	-0.3578	0.3614	1	-0.2833	-0.2636	0.237
Cu-CLR	0.2128	-0.5529	-0.01454	0.02968	-0.4077	0.1548	0.428	-0.137	0.1055	-0.2833	1	-0.03905	-0.1302
Pb-CLR	0.1086	0.2449	0.09001	-0.6239	0.2429	-0.408	-0.1784	0.01511	-0.5948	-0.2636	-0.03905	1	0.01135
Ag-CLR	0.04083	0.1339	-0.2984	0.2231	-0.0815	0.02337	0.009774	-0.0861	0.0871	0.237	-0.1302	0.01135	1
As-CLR	-0.06946	0.04585	-0.399	-0.09135	-0.09264	-0.2441	0.3525	-0.2651	-0.1385	0.2218	0.1058	0.09317	0.1451
Co-CLR	0.01856	-0.2842	-0.2676	0.5067	-0.3178	0.241	0.06762	-0.2393	0.4648	0.3995	0.3092	-0.6159	0.006662
Ni-CLR	0.1647	-0.1264	-0.2225	0.01465	-0.06308	0.01049	-0.1664	-0.3495	0.1654	0.4171	-0.0293	-0.2654	0.02573
Ge-CLR	0.3645	0.6479	-0.06177	-0.3282	0.4769	-0.4743	-0.6224	-0.279	-0.3577	0.1785	-0.4258	0.3733	0.1327
Ga-CLR	-0.2963	0.326	0.5213	-0.2449	0.2923	-0.4457	-0.2092	0.5829	-0.571	-0.3324	-0.3061	0.2125	-0.2356
Zr-CLR	-0.551	0.2342	0.3674	0.0306	0.1231	-0.1524	-0.01658	0.8494	-0.203	-0.272	-0.3692	-0.03774	-0.04338
Ba-CLR	-0.2459	0.2514	-0.1134	-0.2372	0.04601	-0.2668	-0.2122	-0.08134	-0.3639	0.1262	-0.2715	0.3591	0.1077
Cs-CLR	-0.45	0.1551	0.1442	0.2126	0.04404	-0.1782	-0.3053	0.466	-0.1517	0.02834	-0.2672	0.08206	0.008124
B-CLR	0.6814	-0.4197	0.3165	-0.3242	-0.1635	0.02409	-0.1178	-0.3896	-0.08147	-0.07311	0.0291	0.1325	-0.2959
Sr-CLR	0.0594	0.2841	-0.1738	-0.1959	0.3742	0.007034	-0.2765	-0.2883	-0.04066	-0.1045	-0.16	0.3026	-0.02732
U-CLR	0.1822	0.2944	0.3448	-0.351	0.3808	-0.3916	-0.3748	0.1453	-0.3268	-0.1629	-0.2309	0.2063	-0.2064
Y-CLR	-0.2291	0.7452	-0.2538	-0.2278	0.6929	-0.2744	-0.2674	-0.05698	-0.2259	0.06606	-0.3989	0.166	-0.1089
La-CLR	-0.5058	0.4386	0.1299	-0.1686	0.434	-0.2947	0.03297	0.4952	-0.3542	-0.239	-0.1691	0.09662	-0.2795

Appendix N (continued): Principal Component Analysis

Robust Correlation	As-CLR	Co-CLR	Ni-CLR	Ge-CLR	Ga-CLR	Zr-CLR	Ba-CLR	Cs-CLR	B-CLR	Sr-CLR	U-CLR	Y-CLR	La-CLR
Si-CLR	-0.06946	0.01856	0.1647	0.3645	-0.2963	-0.551	-0.2459	-0.45	0.6814	0.0594	0.1822	-0.2291	-0.5058
Fe-CLR	0.04585	-0.2842	-0.1264	0.6479	0.326	0.2342	0.2514	0.1551	-0.4197	0.2841	0.2944	0.7452	0.4386
Al-CLR	-0.399	-0.2676	-0.2225	-0.06177	0.5213	0.3674	-0.1134	0.1442	0.3165	-0.1738	0.3448	-0.2538	0.1299
Mg-CLR	-0.09135	0.5067	0.01465	-0.3282	-0.2449	0.0306	-0.2372	0.2126	-0.3242	-0.1959	-0.351	-0.2278	-0.1686
P-CLR	-0.09264	-0.3178	-0.06308	0.4769	0.2923	0.1231	0.04601	0.04404	-0.1635	0.3742	0.3808	0.6929	0.434
C-CLR	-0.2441	0.241	0.01049	-0.4743	-0.4457	-0.1524	-0.2668	-0.1782	0.02409	0.007034	-0.3916	-0.2744	-0.2947
S-CLR	0.3525	0.06762	-0.1664	-0.6224	-0.2092	-0.01658	-0.2122	-0.3053	-0.1178	-0.2765	-0.3748	-0.2674	0.03297
Ti-CLR	-0.2651	-0.2393	-0.3495	-0.279	0.5829	0.8494	-0.08134	0.466	-0.3896	-0.2883	0.1453	-0.05698	0.4952
Mn-CLR	-0.1385	0.4648	0.1654	-0.3577	-0.571	-0.203	-0.3639	-0.1517	-0.08147	-0.04066	-0.3268	-0.2259	-0.3542
Zn-CLR	0.2218	0.3995	0.4171	0.1785	-0.3324	-0.272	0.1262	0.02834	-0.07311	-0.1045	-0.1629	0.06606	-0.239
Cu-CLR	0.1058	0.3092	-0.0293	-0.4258	-0.3061	-0.3692	-0.2715	-0.2672	0.0291	-0.16	-0.2309	-0.3989	-0.1691
Pb-CLR	0.09317	-0.6159	-0.2654	0.3733	0.2125	-0.03774	0.3591	0.08206	0.1325	0.3026	0.2063	0.166	0.09662
Ag-CLR	0.1451	0.006662	0.02573	0.1327	-0.2356	-0.04338	0.1077	0.008124	-0.2959	-0.02732	-0.2064	-0.1089	-0.2795
As-CLR	1	0.1648	0.2468	-0.04485	-0.1521	-0.2632	-0.03925	-0.3781	-0.1397	-0.07015	-0.2979	0.2298	-0.006014
Co-CLR	0.1648	1	0.6452	-0.2228	-0.3395	-0.3386	-0.4589	-0.368	-0.0782	-0.4224	-0.2322	-0.1469	-0.2132
Ni-CLR	0.2468	0.6452	1	0.1057	-0.2957	-0.4196	-0.1639	-0.3891	0.205	-0.4348	-0.1001	-0.04439	-0.3431
Ge-CLR	-0.04485	-0.2228	0.1057	1	0.2017	-0.1546	0.1905	-0.1009	0.149	0.2726	0.4957	0.4404	0.00316
Ga-CLR	-0.1521	-0.3395	-0.2957	0.2017	1	0.6924	0.06263	0.239	-0.1895	-0.1415	0.3882	0.3179	0.6139
Zr-CLR	-0.2632	-0.3386	-0.4196	-0.1546	0.6924	1	-0.05224	0.4349	-0.3368	-0.1824	0.05792	0.07335	0.4899
Ba-CLR	-0.03925	-0.4589	-0.1639	0.1905	0.06263	-0.05224	1	0.4533	-0.001165	0.3899	-0.1065	0.002163	-0.03799
Cs-CLR	-0.3781	-0.368	-0.3891	-0.1009	0.239	0.4349	0.4533	1	-0.2637	0.2281	-0.06728	-0.1034	0.07975
B-CLR	-0.1397	-0.0782	0.205	0.149	-0.1895	-0.3368	-0.001165	-0.2637	1	-0.08848	0.1852	-0.425	-0.5448
Sr-CLR	-0.07015	-0.4224	-0.4348	0.2726	-0.1415	-0.1824	0.3899	0.2281	-0.08848	1	0.04997	0.3027	0.05367
U-CLR	-0.2979	-0.2322	-0.1001	0.4957	0.3882	0.05792	-0.1065	-0.06728	0.1852	0.04997	1	0.2802	0.3322
Y-CLR	0.2298	-0.1469	-0.04439	0.4404	0.3179	0.07335	0.002163	-0.1034	-0.425	0.3027	0.2802	1	0.6086
La-CLR	-0.006014	-0.2132	-0.3431	0.00316	0.6139	0.4899	-0.03799	0.07975	-0.5448	0.05367	0.3322	0.6086	1

Appendix N (continued): Principal Component Analysis

Eigenvectors	PC1	PC2	PC3	PC4	PC5	PC6	PC7	PC8	PC9	PC10	PC11	PC12	PC13
Si-CLR	-0.1191	-0.2842	0.3195	0.04697	0.1105	-0.08629	0.2675	0.1252	0.08384	0.2513	0.09646	0.04987	-0.07308
Fe-CLR	0.2674	-0.1645	-0.3055	0.02994	0.001661	-0.02549	0.1008	0.03931	0.08173	-0.1994	0.03562	0.2989	-0.1695
Al-CLR	0.1115	0.1883	0.364	0.09688	0.2258	0.0368	0.02319	-0.01052	0.02055	0.3655	-0.1019	-0.1833	0.1515
Mg-CLR	-0.2002	0.1628	-0.2855	-0.06352	0.2423	-0.007466	0.09624	0.3299	0.1991	0.2755	0.007697	0.1103	0.2003
P-CLR	0.2568	-0.1812	-0.07719	0.1198	0.01711	-0.3063	-0.0252	-0.2361	-0.2854	0.03755	0.1896	-0.2577	-0.1116
C-CLR	-0.2263	0.1078	0.01009	-0.09688	0.0544	-0.4314	0.06644	-0.3743	-0.09103	0.115	-0.2035	0.2575	0.3532
S-CLR	-0.1686	0.2291	0.0588	0.02867	-0.4244	0.0118	0.1281	-0.05502	0.3403	-0.1662	-0.2227	-0.03402	-0.1193
Ti-CLR	0.1843	0.393	-0.0168	0.06205	0.07524	0.1245	0.07911	-0.02635	-0.1312	-0.2366	0.1484	-0.1156	0.02655
Mn-CLR	-0.2634	0.04289	-0.206	-0.03216	0.156	-0.3084	0.02895	-0.03378	0.1469	-0.336	0.187	-0.04227	-0.09713
Zn-CLR	-0.1136	-0.1864	-0.3409	-0.0257	0.2052	0.2473	-0.119	0.1265	0.2503	-0.01459	0.08324	-0.03884	0.2656
Cu-CLR	-0.1996	0.08797	0.1881	0.0448	-0.2801	-0.04741	-0.07776	0.5042	-0.3927	-0.05806	0.108	0.1752	-0.1999
Pb-CLR	0.2106	-0.152	0.1915	-0.1745	-0.2363	0.1439	0.06694	0.04508	-0.1397	-0.1918	0.2913	0.2642	0.6259
Ag-CLR	-0.05441	-0.06798	-0.1788	-0.1965	-0.01787	0.1916	0.7234	-0.06604	-0.2762	0.05532	-0.2165	-0.2229	0.003834
As-CLR	-0.06706	-0.119	-0.1287	0.1314	-0.4621	0.2819	-0.003045	-0.09399	0.2189	0.2832	0.2523	-0.3302	0.02531
Co-CLR	-0.2698	-0.00648	-0.1699	0.3144	0.1055	0.05552	-0.152	0.1448	-0.2594	0.13	-0.07692	0.0412	-0.05705
Ni-CLR	-0.1737	-0.1964	-0.07746	0.2922	0.1249	0.2629	-0.2147	-0.3181	-0.3231	-0.05981	-0.07852	-0.06832	0.04356
Ge-CLR	0.1941	-0.362	-0.01094	0.06114	0.1573	0.06007	0.2106	0.1219	0.0246	0.0187	-0.03889	0.2737	-0.212
Ga-CLR	0.2989	0.1723	0.05514	0.1986	0.07386	0.1345	0.008357	0.007336	0.06826	0.29	-0.05889	0.2814	-0.1202
Zr-CLR	0.216	0.346	-0.06452	0.03603	0.1275	0.0608	0.1605	-0.2194	0.1069	0.005324	0.2484	0.1116	-0.2079
Ba-CLR	0.1375	-0.09665	-0.03382	-0.4386	-0.04935	0.2384	-0.3057	-0.09741	-0.02219	-0.003596	-0.5254	0.0987	-0.1467
Cs-CLR	0.1538	0.1854	-0.09725	-0.3839	0.2267	0.09972	-0.2059	0.1377	-0.1565	0.08019	0.2031	-0.2153	0.01246
B-CLR	-0.09284	-0.1855	0.3888	-0.00899	0.1942	0.08679	-0.1374	-0.1838	0.3223	-0.1207	0.1321	0.01931	-0.08541
Sr-CLR	0.1254	-0.1753	-0.02711	-0.3552	-0.1051	-0.3848	-0.1189	0.1422	0.04985	0.2181	0.0473	-0.2525	-0.1222
U-CLR	0.2088	-0.1081	0.1486	0.2449	0.2012	-0.08838	0.08239	0.3145	0.1176	-0.3812	-0.3217	-0.3946	0.1868
Y-CLR	0.2301	-0.1586	-0.2431	0.2216	-0.1646	-0.2216	-0.05954	-0.04134	0.07259	0.1789	-0.0187	0.06158	0.1358
La-CLR	0.2613	0.167	-0.1254	0.2474	-0.1767	-0.1504	-0.1157	0.1394	0.04964	0.04415	-0.248	-0.01062	0.1826

Appendix N (continued): Principal Component Analysis

Eigenvectors	PC14	PC15	PC16	PC17	PC18	PC19	PC20	PC21	PC22	PC23	PC24	PC25	PC26
Si-CLR	-0.2422	0.1383	-0.09411	-0.2176	0.07582	0.2232	-0.1427	0.04862	0.2208	-0.3174	-0.02525	0.4668	0.162
Fe-CLR	0.06576	0.1351	0.002115	0.04004	-0.2067	-0.1455	-0.01156	0.1561	-0.3987	-0.5567	-0.1493	-0.02819	0.1566
Al-CLR	0.05295	-0.2029	-0.4232	0.1156	-0.4001	-0.2249	0.1334	-0.04212	-0.2235	-0.08641	-0.1249	-0.03772	0.1234
Mg-CLR	0.00917	0.1406	0.001895	0.01232	0.08647	0.02026	0.01522	0.4066	0.2234	0.08146	-0.3645	-0.3239	0.1239
P-CLR	-0.4306	-0.06161	0.04099	0.06537	0.0473	0.09943	0.3708	0.01521	0.1813	-0.04979	-0.2382	-0.276	0.1396
C-CLR	0.08756	0.1431	0.3321	0.1089	-0.2136	0.1888	0.05055	-0.1058	-0.09143	-0.02063	0.1128	0.0387	0.268
S-CLR	-0.04918	0.2235	-0.3338	-0.06096	0.2005	0.08552	0.2121	-0.2981	0.02892	-0.08911	-0.08166	-0.1984	0.3209
Ti-CLR	0.1978	0.05437	0.02489	-0.2169	-0.2621	-0.00461	0.05514	0.1689	0.5045	-0.2306	0.3523	-0.02253	0.2186
Mn-CLR	0.0264	-0.3732	-0.3517	0.3346	0.04841	0.04857	0.06191	0.2149	-0.007432	0.1222	0.1023	0.3165	0.1649
Zn-CLR	-0.3245	-0.2742	0.0388	-0.114	-0.2122	0.1137	-0.04346	-0.4657	0.02412	-0.107	0.1968	-0.1258	0.148
Cu-CLR	-0.188	-0.08806	0.1067	0.1583	-0.249	-0.02134	-0.2067	-0.04666	-0.0536	0.1224	-9.40E-04	-0.1264	0.3367
Pb-CLR	0.1197	-0.164	-0.1327	0.007918	0.2258	-0.0158	0.1316	-0.002685	0.03534	0.005106	-0.1794	0.04958	0.1276
Ag-CLR	-0.0907	-0.1518	0.04906	0.01394	0.1487	-0.2172	-0.08566	0.05117	-0.1261	0.0645	0.1602	-0.05501	0.1393
As-CLR	0.1694	0.01441	0.2559	0.2316	-0.2188	0.153	0.1185	0.2043	-0.06432	0.04505	-0.02595	0.1954	0.1552
Co-CLR	0.2749	-0.1139	0.1514	-0.1558	0.2743	-0.3077	0.4329	-0.1993	0.01575	-0.1412	-0.0771	0.2557	0.1477
Ni-CLR	0.1695	0.09366	-0.3023	-0.07782	0.09111	0.2673	-0.3901	0.1218	-0.07888	0.01709	-0.101	-0.1498	0.2577
Ge-CLR	0.257	0.1337	-0.1408	-0.08055	-0.2277	0.2278	0.351	-0.07214	0.02891	0.4847	0.1556	-0.06035	0.1077
Ga-CLR	0.01997	-0.2381	0.07532	0.4488	0.4	0.2546	-0.05584	-0.03339	0.0452	-0.1663	0.2883	-0.1245	0.08558
Zr-CLR	0.034	-0.1601	0.1853	-0.197	0.002348	0.0109	-0.2504	-0.2729	-0.03646	0.2753	-0.4567	0.2021	0.2042
Ba-CLR	-0.1085	-0.1687	0.02563	0.08706	-0.1055	-0.03137	0.06052	0.1383	0.2924	0.005726	-0.1936	0.239	0.2115
Cs-CLR	-0.09502	0.4966	-0.08409	0.1247	0.1986	0.06149	0.09279	-0.1	-0.2825	0.07481	0.1543	0.2069	0.2272
B-CLR	-0.088	-0.003162	0.2735	-0.09719	0.1669	-0.3877	0.02472	0.2355	-0.1096	0.1193	0.1867	-0.2154	0.3613
Sr-CLR	0.4693	-0.2533	-0.01585	-0.243	0.1203	0.07336	-0.1954	-0.09844	-0.00236	-0.1159	0.05655	-0.2041	0.1803
U-CLR	0.1383	0.08379	0.2727	0.2475	0.04313	0.1115	-0.09779	-0.104	0.02212	0.01905	-0.1967	0.07703	0.1161
Y-CLR	-0.04527	0.2408	-0.1856	0.1668	0.002462	-0.5139	-0.3095	-0.1357	0.2941	0.188	0.1324	0.1178	0.1359
La-CLR	-0.2548	-0.161	-0.01477	-0.4571	0.082	0.1367	0.03565	0.33	-0.3099	0.1898	0.1814	0.1619	0.1188

Appendix N (continued): Principal Component Analysis

Principal Component	Eigenvalues	Percent	Cumulative %
PC1	6.208	23.88	23.88
PC2	3.997	15.37	39.25
PC3	3.428	13.18	52.43
PC4	2.345	9.018	61.45
PC5	2.165	8.328	69.78
PC6	1.739	6.689	76.47
PC7	1.09	4.194	80.66
PC8	0.9079	3.492	84.15
PC9	0.7542	2.901	87.05
PC10	0.6061	2.331	89.39
PC11	0.5132	1.974	91.36
PC12	0.4222	1.624	92.98
PC13	0.35	1.346	94.33
PC14	0.3046	1.171	95.5
PC15	0.2532	0.9737	96.47
PC16	0.2026	0.7793	97.25
PC17	0.1823	0.7012	97.96
PC18	0.1393	0.5357	98.49
PC19	0.107	0.4115	98.9
PC20	0.09103	0.3501	99.25
PC21	0.06364	0.2448	99.5
PC22	0.05083	0.1955	99.69
PC23	0.03294	0.1267	99.82
PC24	0.02788	0.1072	99.93
PC25	0.01809	0.06959	100
PC26	9.28E-04	0.00357	100

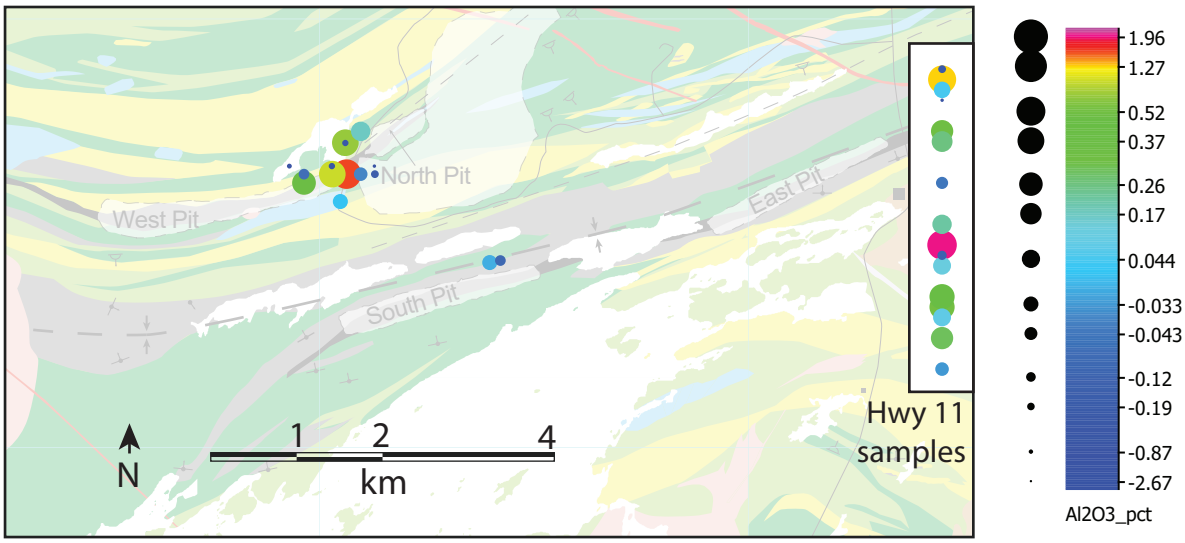
Appendix N (continued): Principal Component Analysis

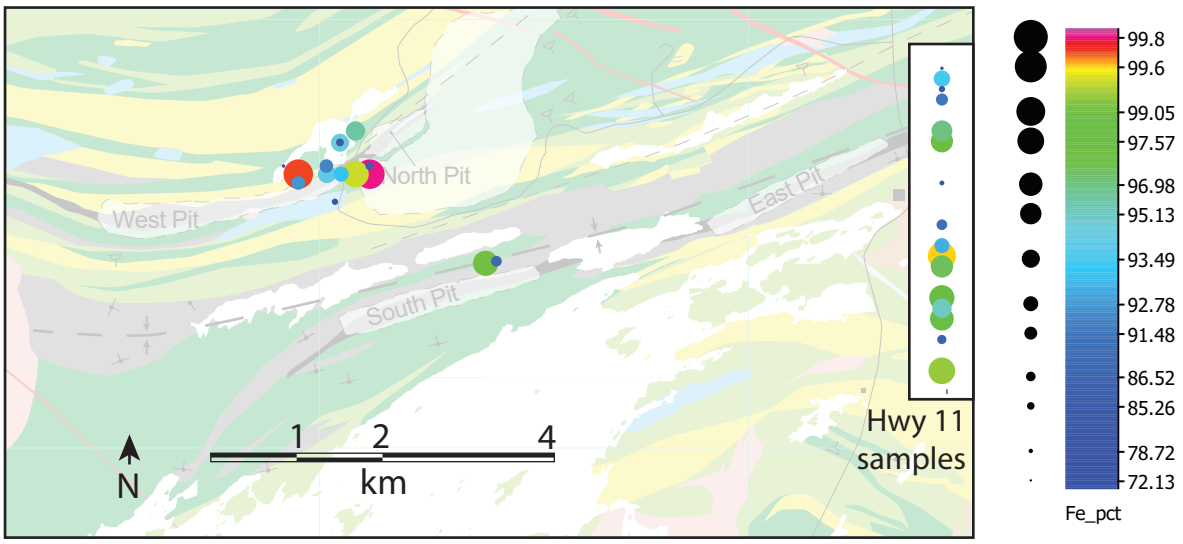
Scaled Coordinates	PC1	PC2	PC3	PC4	PC5	PC6	PC7	PC8	PC9	PC10	PC11	PC12	PC13
Si-CLR	-0.2968	-0.5682	0.5916	0.07192	0.1626	-0.1138	0.2793	0.1193	0.07281	0.1956	0.0691	0.0324	-0.04324
Fe-CLR	0.6661	-0.3289	-0.5656	0.04584	0.002445	-0.03361	0.1052	0.03746	0.07098	-0.1553	0.02552	0.1942	-0.1003
Al-CLR	0.2779	0.3765	0.6739	0.1483	0.3322	0.04853	0.02421	-0.01002	0.01785	0.2845	-0.07297	-0.1191	0.08965
Mg-CLR	-0.4989	0.3254	-0.5286	-0.09726	0.3566	-0.009846	0.1005	0.3143	0.1729	0.2145	0.005514	0.07166	0.1185
P-CLR	0.6397	-0.3623	-0.1429	0.1835	0.02518	-0.4039	-0.02631	-0.2249	-0.2479	0.02924	0.1358	-0.1674	-0.06604
C-CLR	-0.5638	0.2156	0.01869	-0.1483	0.08004	-0.569	0.06938	-0.3566	-0.07905	0.08949	-0.1458	0.1673	0.209
S-CLR	-0.42	0.4581	0.1089	0.0439	-0.6245	0.01556	0.1337	-0.05242	0.2955	-0.1294	-0.1595	-0.02211	-0.0706
Ti-CLR	0.4591	0.7856	-0.0311	0.09501	0.1107	0.1642	0.08261	-0.02511	-0.1139	-0.1842	0.1063	-0.07508	0.01571
Mn-CLR	-0.6562	0.08574	-0.3814	-0.04925	0.2295	-0.4068	0.03023	-0.03219	0.1276	-0.2616	0.134	-0.02746	-0.05746
Zn-CLR	-0.283	-0.3727	-0.6312	-0.03935	0.302	0.3261	-0.1243	0.1205	0.2173	-0.01136	0.05963	-0.02524	0.1571
Cu-CLR	-0.4972	0.1759	0.3482	0.0686	-0.4122	-0.06252	-0.08119	0.4805	-0.341	-0.0452	0.07734	0.1139	-0.1183
Pb-CLR	0.5248	-0.3038	0.3545	-0.2671	-0.3477	0.1897	0.0699	0.04295	-0.1214	-0.1493	0.2087	0.1717	0.3703
Ag-CLR	-0.1356	-0.1359	-0.331	-0.301	-0.0263	0.2527	0.7554	-0.06293	-0.2398	0.04306	-0.1551	-0.1448	0.002268
As-CLR	-0.1671	-0.2379	-0.2383	0.2012	-0.6799	0.3718	-0.00318	-0.08955	0.1901	0.2205	0.1807	-0.2146	0.01497
Co-CLR	-0.6722	-0.01296	-0.3146	0.4814	0.1552	0.07322	-0.1587	0.138	-0.2253	0.1012	-0.0551	0.02677	-0.03375
Ni-CLR	-0.4327	-0.3926	-0.1434	0.4474	0.1837	0.3466	-0.2242	-0.3031	-0.2806	-0.04656	-0.05625	-0.0444	0.02577
Ge-CLR	0.4835	-0.7238	-0.02025	0.09361	0.2315	0.07923	0.2199	0.1161	0.02137	0.01456	-0.02786	0.1778	-0.1254
Ga-CLR	0.7448	0.3445	0.1021	0.3041	0.1087	0.1774	0.008726	0.006989	0.05927	0.2258	-0.04218	0.1828	-0.07114
Zr-CLR	0.5382	0.6917	-0.1195	0.05518	0.1876	0.08018	0.1676	-0.2091	0.09279	0.004145	0.178	0.0725	-0.123
Ba-CLR	0.3426	-0.1932	-0.06262	-0.6717	-0.07261	0.3143	-0.3192	-0.09282	-0.01927	-0.0028	-0.3763	0.06413	-0.08677
Cs-CLR	0.3832	0.3708	-0.1801	-0.5879	0.3335	0.1315	-0.215	0.1312	-0.1359	0.06243	0.1455	-0.1399	0.007372
B-CLR	-0.2313	-0.3709	0.7198	-0.01377	0.2857	0.1145	-0.1435	-0.1751	0.2799	-0.09398	0.0946	0.01255	-0.05053
Sr-CLR	0.3123	-0.3505	-0.05019	-0.5439	-0.1546	-0.5074	-0.1241	0.1354	0.04329	0.1698	0.03388	-0.1641	-0.07232
U-CLR	0.5203	-0.2161	0.2751	0.375	0.2961	-0.1166	0.08603	0.2997	0.1021	-0.2968	-0.2305	-0.2564	0.1105
Y-CLR	0.5734	-0.3171	-0.4501	0.3393	-0.2421	-0.2923	-0.06217	-0.03939	0.06304	0.1393	-0.0134	0.04001	0.08035
La-CLR	0.6509	0.3338	-0.2322	0.3789	-0.26	-0.1984	-0.1208	0.1328	0.04311	0.03437	-0.1776	-0.0069	0.108

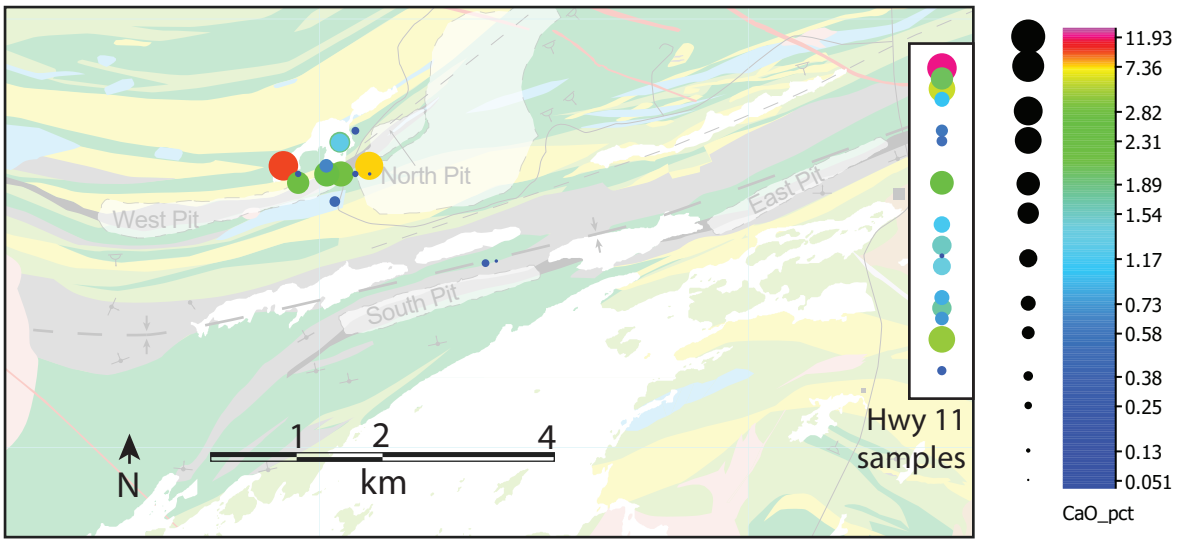
Appendix N (continued): Principal Component Analysis

Scaled Coordinates	PC14	PC15	PC16	PC17	PC18	PC19	PC20	PC21	PC22	PC23	PC24	PC25	PC26
Si-CLR	-0.1337	0.0696	-0.04237	-0.0929	0.0283	0.07302	-0.04304	0.01227	0.04978	-0.0576	-0.004215	0.06279	0.004936
Fe-CLR	0.03629	0.06799	9.52E-04	0.0171	-0.07715	-0.04761	-0.003488	0.03938	-0.08989	-0.101	-0.02492	-0.003792	0.00477
Al-CLR	0.02922	-0.1021	-0.1905	0.04937	-0.1493	-0.07356	0.04024	-0.01062	-0.05039	-0.01568	-0.02086	-0.005074	0.00376
Mg-CLR	0.005061	0.07075	8.53E-04	0.005262	0.03227	0.006626	0.004593	0.1026	0.05035	0.01478	-0.06086	-0.04356	0.003776
P-CLR	-0.2377	-0.031	0.01845	0.02791	0.01765	0.03252	0.1119	0.003838	0.04088	-0.009037	-0.03976	-0.03712	0.004254
C-CLR	0.04832	0.07198	0.1495	0.04649	-0.07971	0.06175	0.01525	-0.0267	-0.02061	-0.003744	0.01884	0.005205	0.008164
S-CLR	-0.02714	0.1125	-0.1503	-0.02603	0.07482	0.02797	0.06399	-0.0752	0.006519	-0.01617	-0.01363	-0.02669	0.009777
Ti-CLR	0.1091	0.02736	0.01121	-0.09259	-0.09783	-0.001508	0.01664	0.0426	0.1137	-0.04185	0.05882	-0.003031	0.006659
Mn-CLR	0.01457	-0.1878	-0.1583	0.1429	0.01807	0.01589	0.01868	0.05422	-0.001676	0.02218	0.01707	0.04258	0.005023
Zn-CLR	-0.1791	-0.138	0.01747	-0.04867	-0.07921	0.03719	-0.01311	-0.1175	0.005437	-0.01943	0.03285	-0.01692	0.00451
Cu-CLR	-0.1037	-0.0443	0.04804	0.06759	-0.09291	-0.006979	-0.06237	-0.01177	-0.01208	0.02222	-1.57E-04	-0.01701	0.01026
Pb-CLR	0.06606	-0.08252	-0.05973	0.003381	0.08426	-0.005168	0.03971	-6.77E-04	0.007967	9.27E-04	-0.02996	0.006669	0.003888
Ag-CLR	-0.05006	-0.07637	0.02208	0.005953	0.0555	-0.07103	-0.02584	0.01291	-0.02843	0.01171	0.02675	-0.007399	0.004243
As-CLR	0.09347	0.00725	0.1152	0.09887	-0.08168	0.05005	0.03576	0.05153	-0.0145	0.008176	-0.004332	0.02628	0.00473
Co-CLR	0.1517	-0.05729	0.06815	-0.06652	0.1024	-0.1007	0.1306	-0.05029	0.003551	-0.02562	-0.01287	0.0344	0.004499
Ni-CLR	0.09355	0.04713	-0.1361	-0.03323	0.03401	0.08744	-0.1177	0.03073	-0.01778	0.003102	-0.01687	-0.02016	0.007851
Ge-CLR	0.1418	0.06727	-0.06336	-0.03439	-0.08498	0.0745	0.1059	-0.0182	0.006517	0.08796	0.02599	-0.008119	0.003282
Ga-CLR	0.01102	-0.1198	0.0339	0.1916	0.1493	0.08327	-0.01685	-0.008424	0.01019	-0.03018	0.04814	-0.01675	0.002607
Zr-CLR	0.01877	-0.08055	0.0834	-0.08413	8.76E-04	0.003566	-0.07553	-0.06885	-0.00822	0.04996	-0.07626	0.02719	0.006221
Ba-CLR	-0.05988	-0.0849	0.01154	0.03717	-0.03938	-0.01026	0.01826	0.03489	0.06592	0.001039	-0.03233	0.03214	0.006444
Cs-CLR	-0.05244	0.2499	-0.03785	0.05325	0.07412	0.02011	0.028	-0.02523	-0.06369	0.01358	0.02576	0.02783	0.00692
B-CLR	-0.04857	-0.001591	0.1231	-0.0415	0.0623	-0.1268	0.007459	0.05941	-0.0247	0.02164	0.03118	-0.02897	0.01101
Sr-CLR	0.259	-0.1274	-0.007137	-0.1037	0.04489	0.02399	-0.05895	-0.02483	-5.32E-04	-0.02104	0.009441	-0.02746	0.005493
U-CLR	0.07635	0.04216	0.1227	0.1057	0.0161	0.03647	-0.0295	-0.02623	0.004987	0.003458	-0.03285	0.01036	0.003537
Y-CLR	-0.02498	0.1212	-0.08354	0.0712	9.19E-04	-0.1681	-0.09338	-0.03422	0.06631	0.03413	0.0221	0.01584	0.004141
La-CLR	-0.1406	-0.08099	-0.00665	-0.1952	0.0306	0.0447	0.01076	0.08325	-0.06986	0.03445	0.03029	0.02178	0.00362

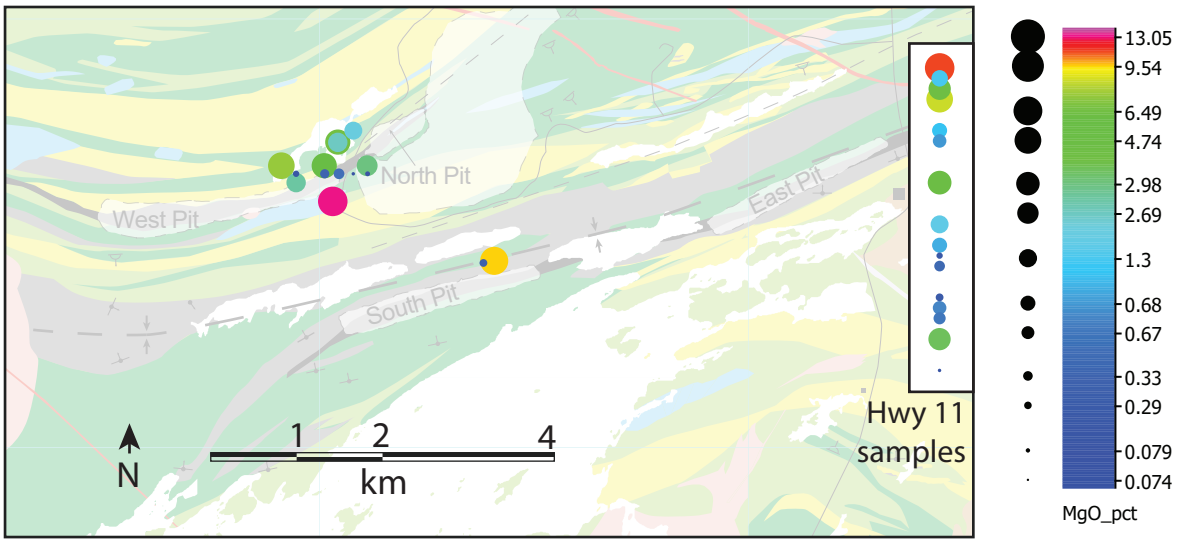
Appendix O: Maps of clastic component- and Si- free element abundances

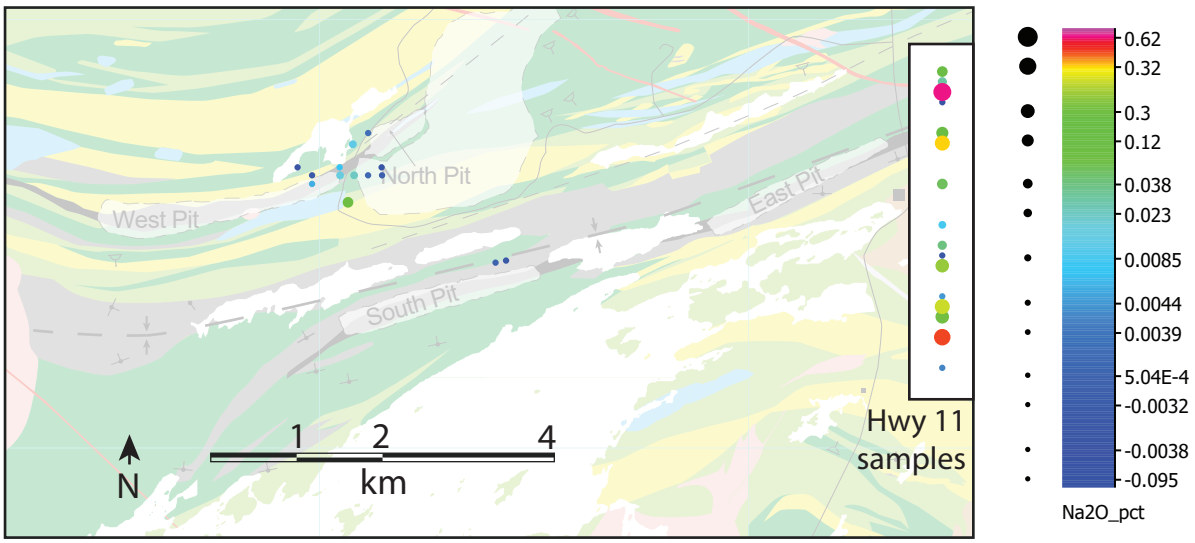


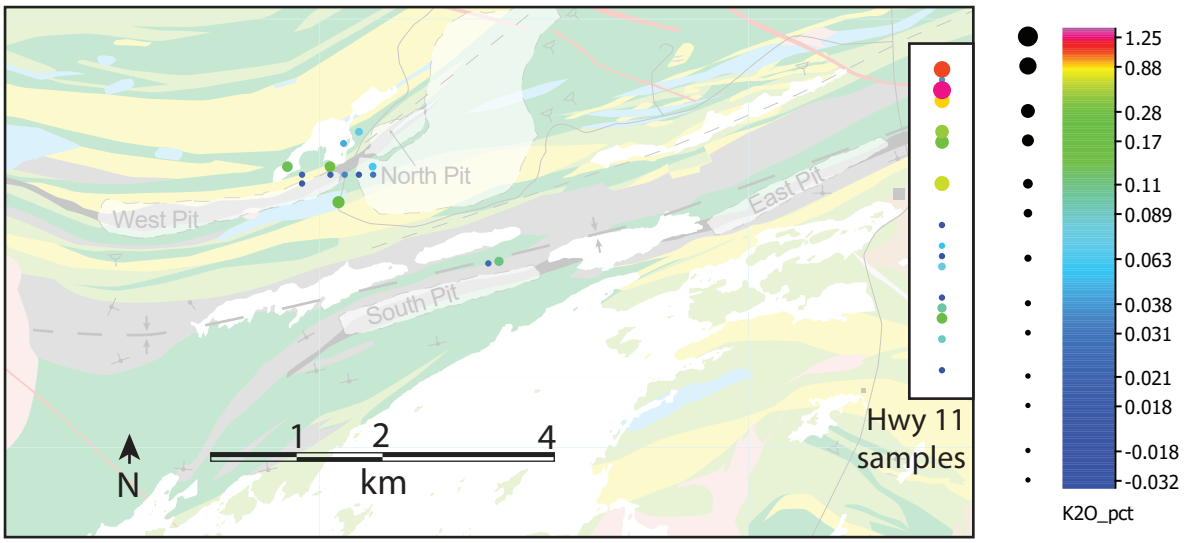




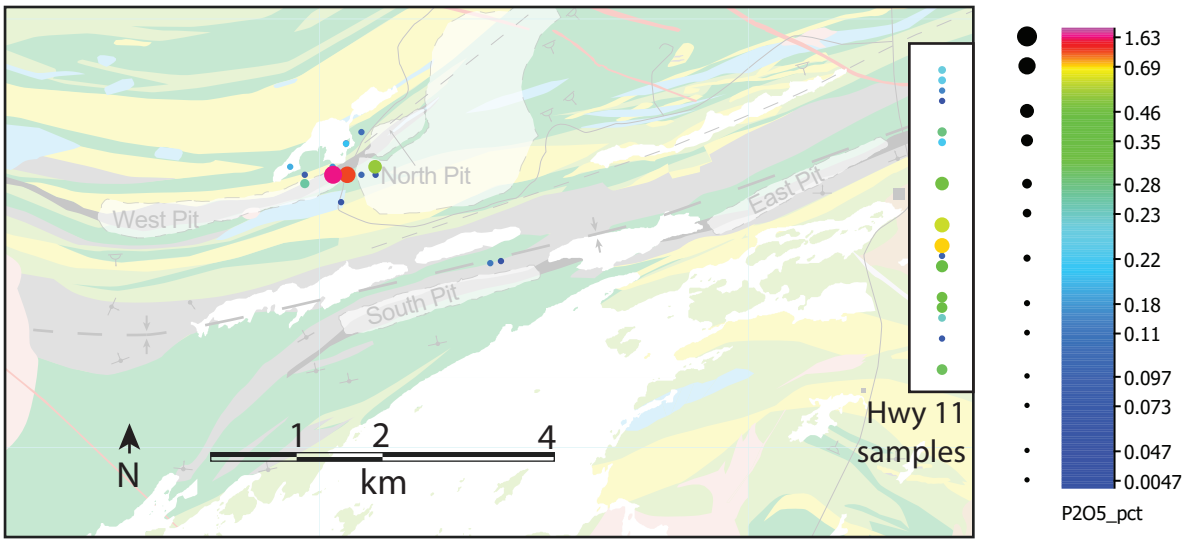
Appendix O (continued): Maps of clastic component- and Si- free element abundances

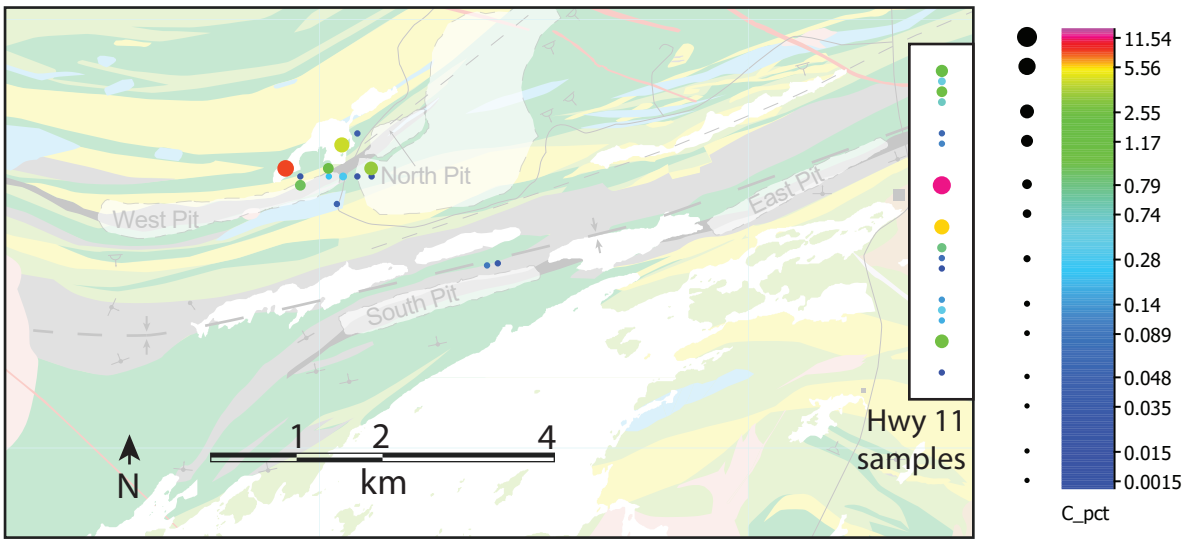


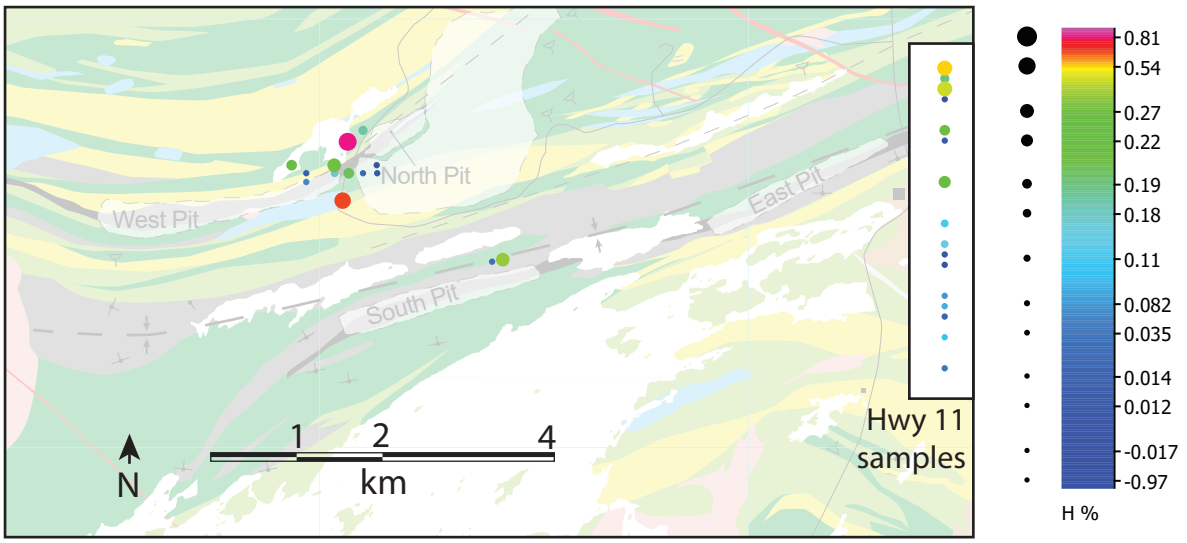




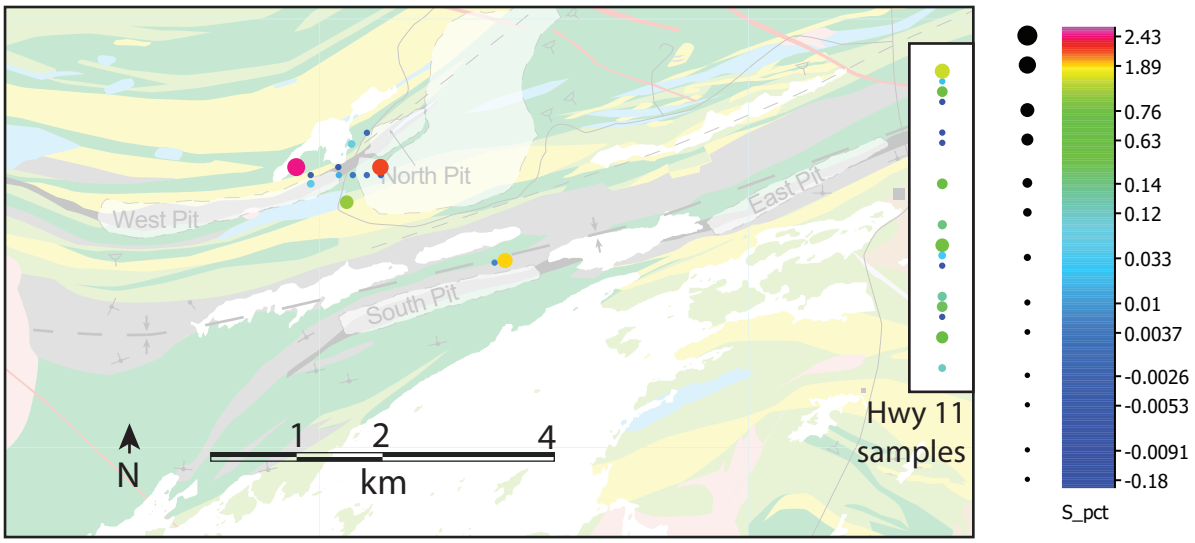
Appendix O (continued): Maps of clastic component- and Si- free element abundances

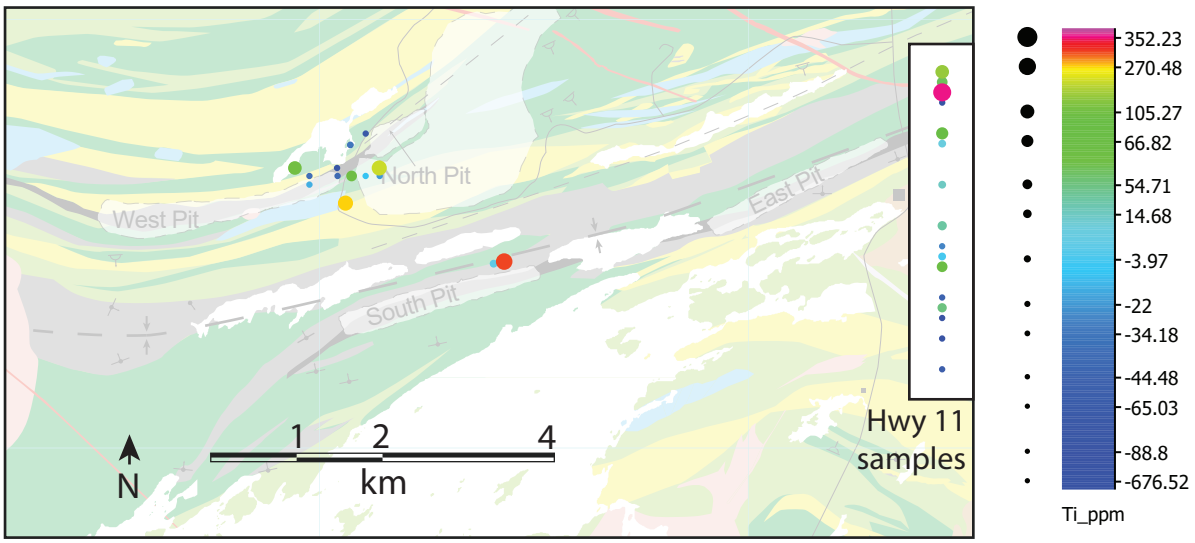


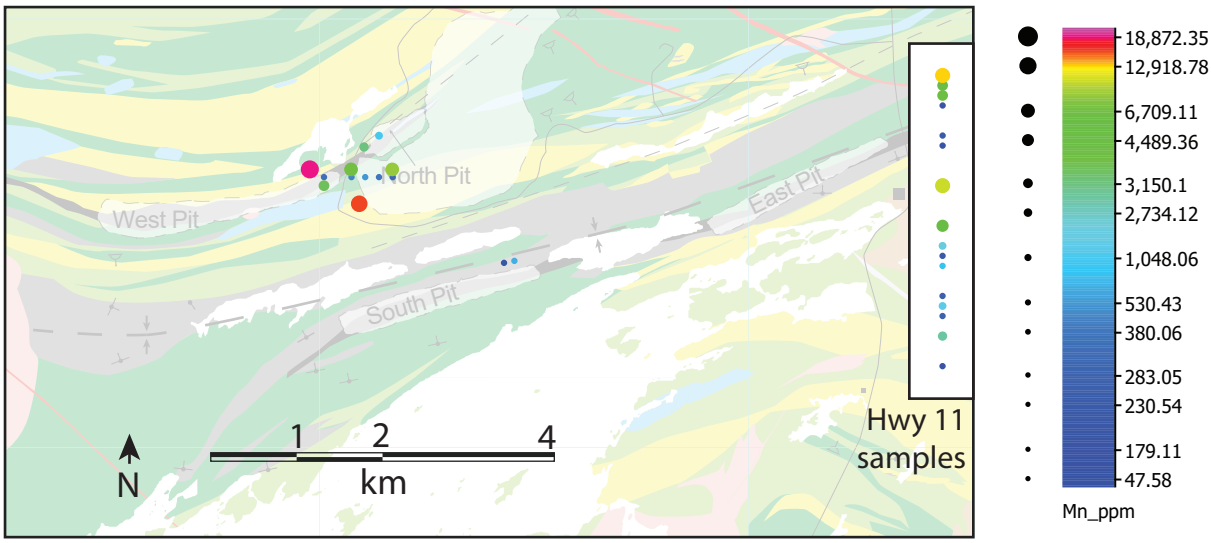




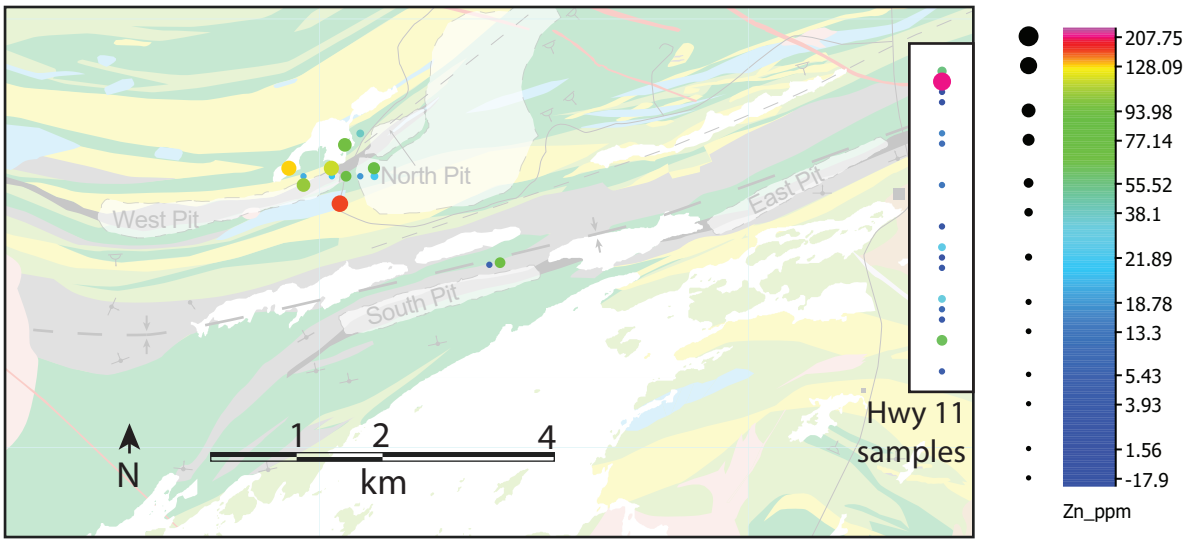
Appendix O (continued): Maps of clastic component- and Si- free element abundances

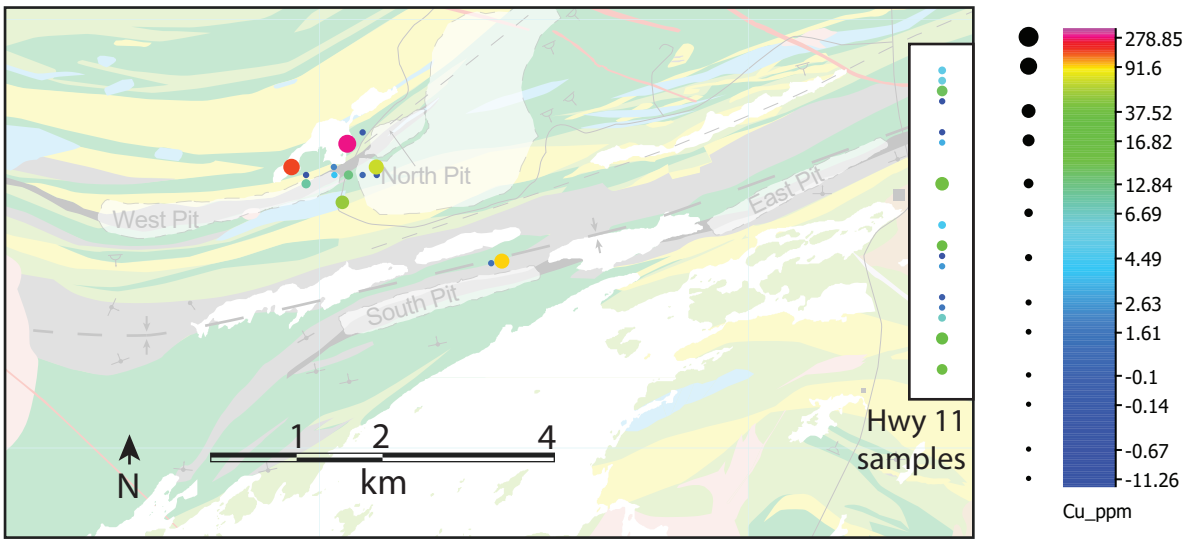


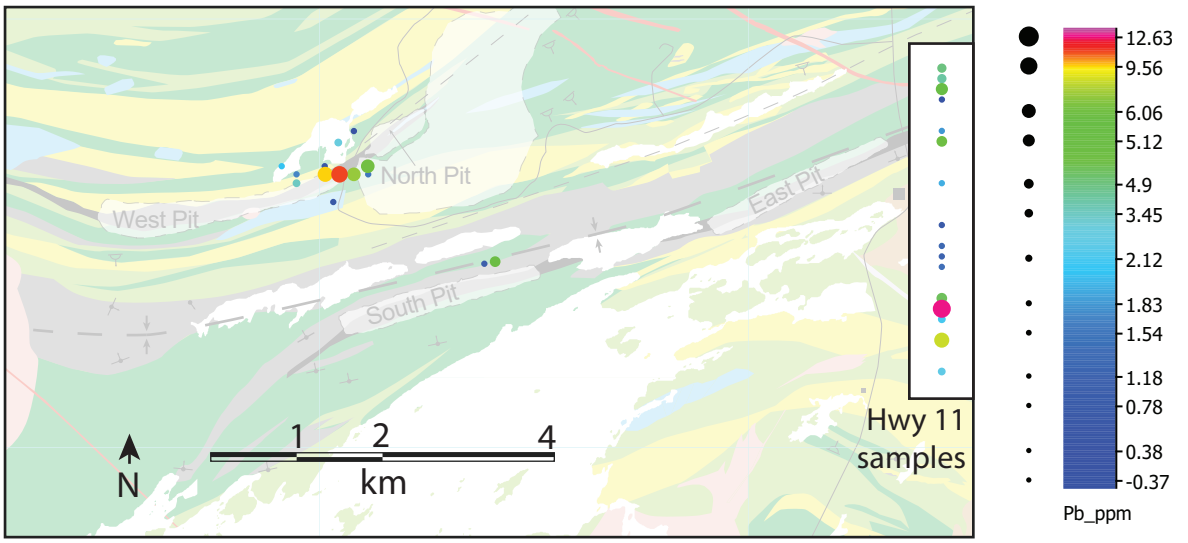


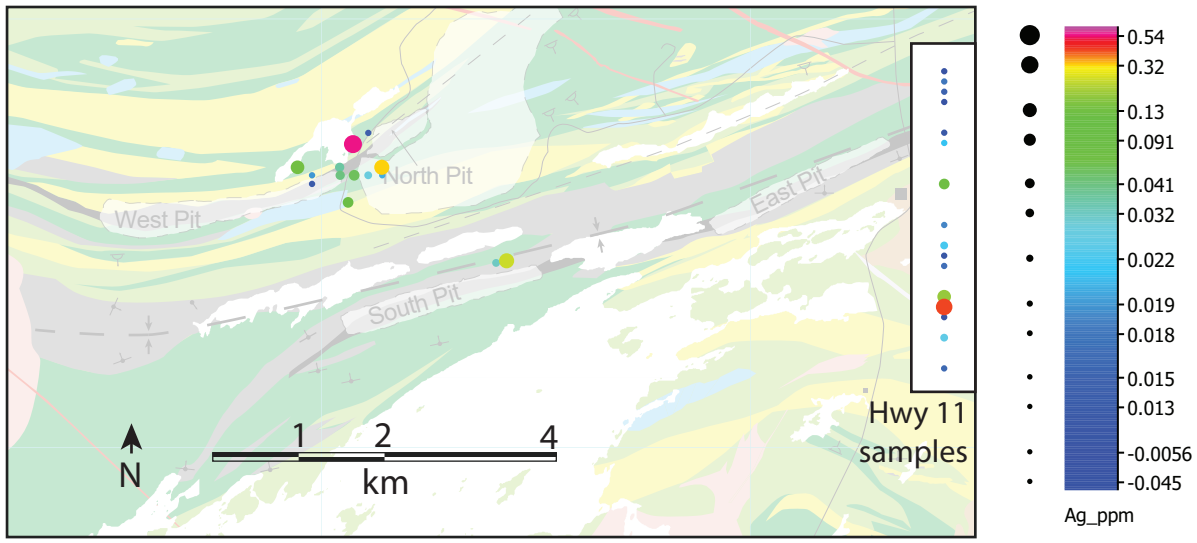


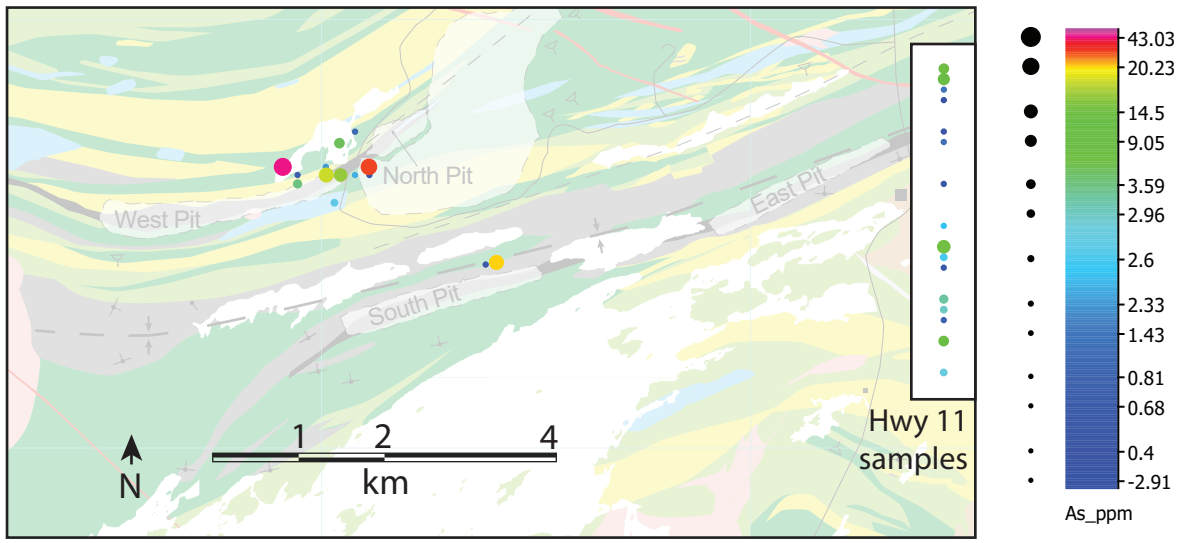
Appendix O (continued): Maps of clastic component- and Si- free element abundances

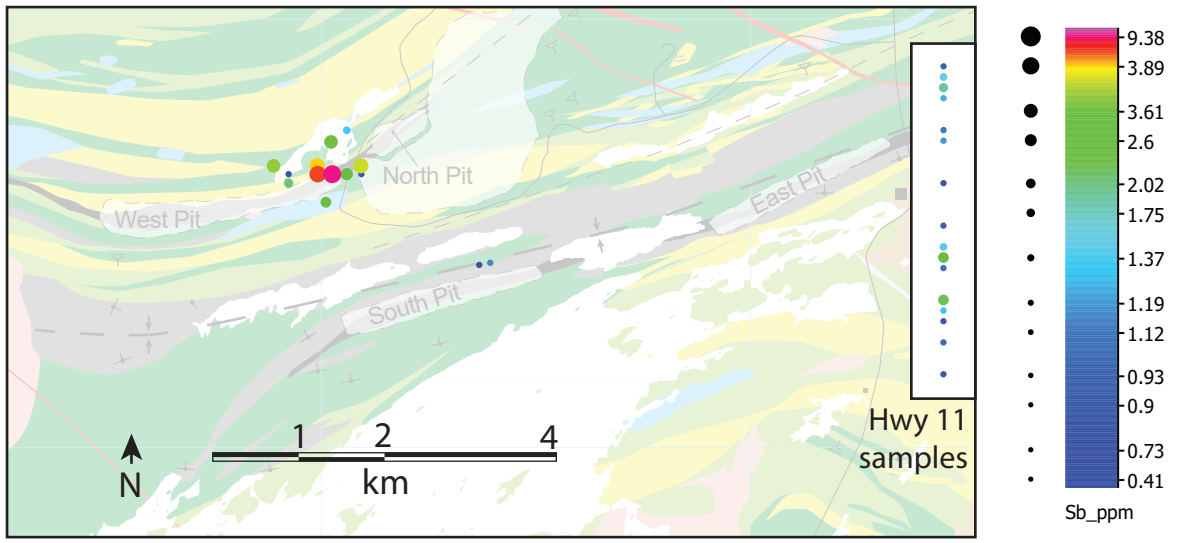




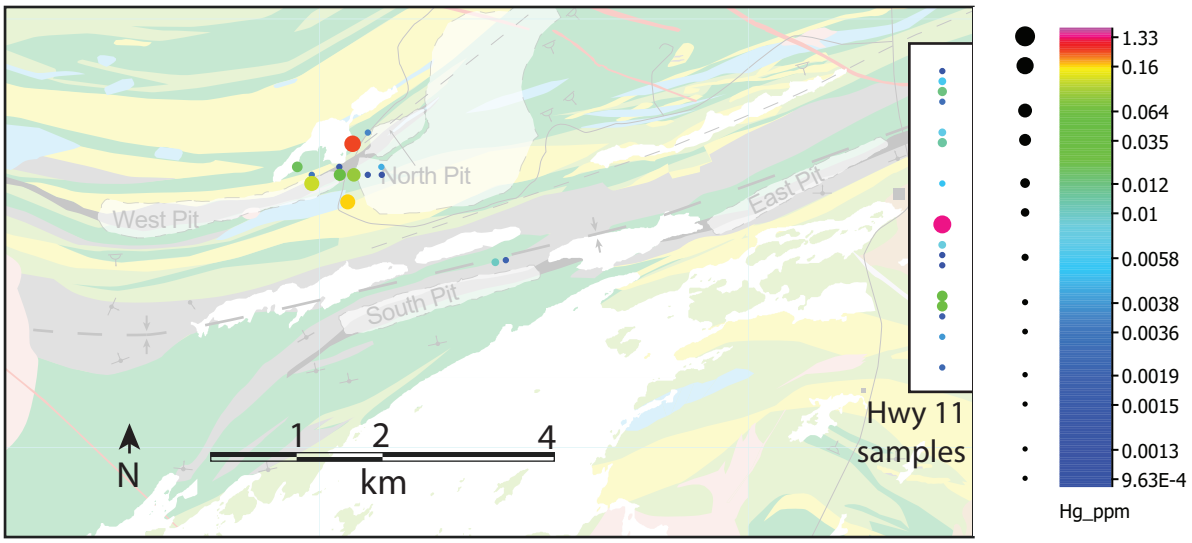


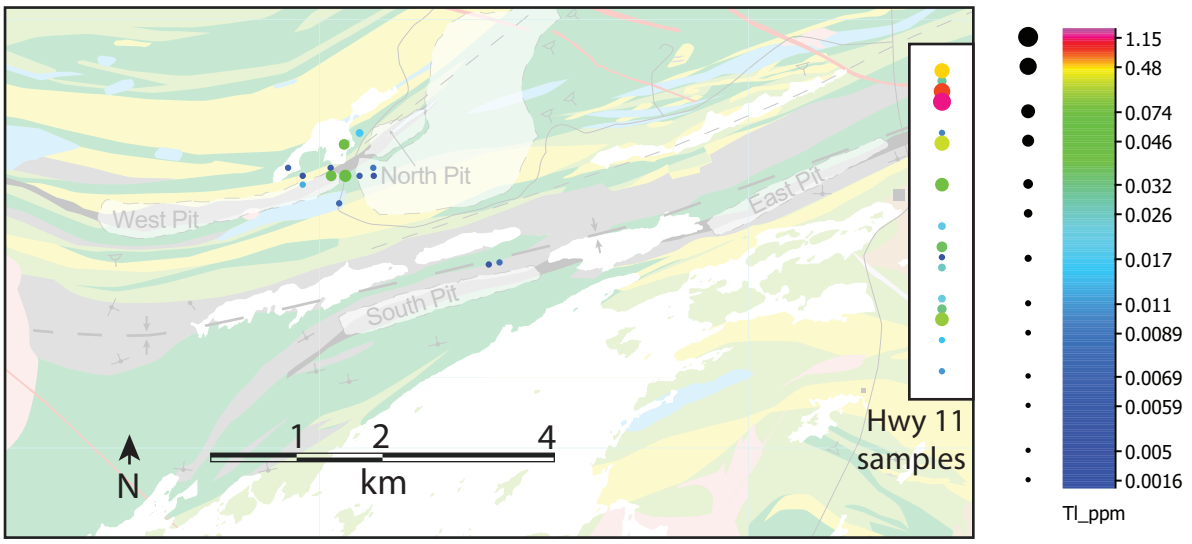

North Pit
West Pit
East Pit
South Pit
N
1
2
4
km
Hwy 11
samples
0.54
0.32
0.13
0.091
0.041
0.032
0.022
0.019
0.018
0.015
0.013
-0.0056
-0.045
Ag_ppm

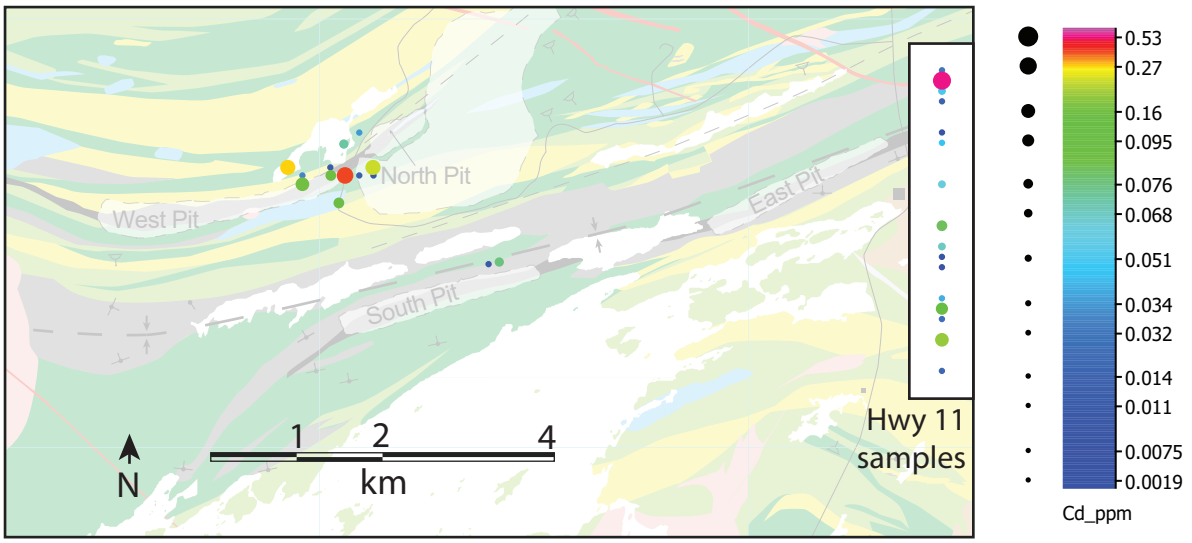

North Pit
West Pit
East Pit
South Pit
N
1
2
4
km
Hwy 11
samples
43.03
20.23
14.5
9.05
3.59
2.96
2.6
2.33
1.43
0.81
0.68
0.4
-2.91
As_ppm


North Pit
West Pit
East Pit
South Pit
N
1
2
4
km
Hwy 11
samples
9.38
3.89
3.61
2.6
2.02
1.75
1.37
1.19
1.12
0.93
0.9
0.73
0.41
Sb_ppm

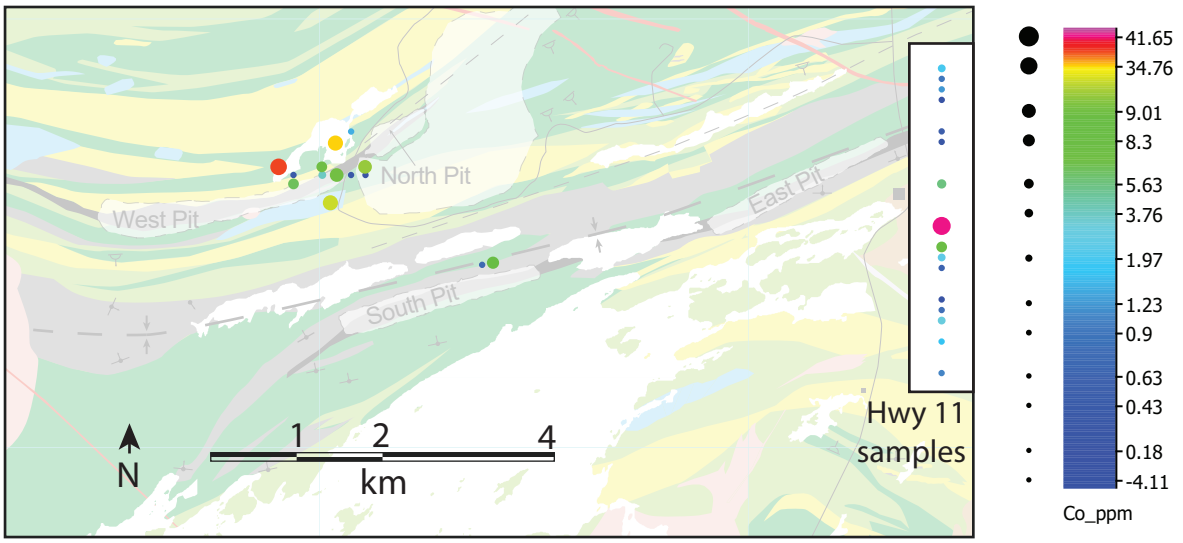
Appendix O (continued): Maps of clastic component- and Si- free element abundances

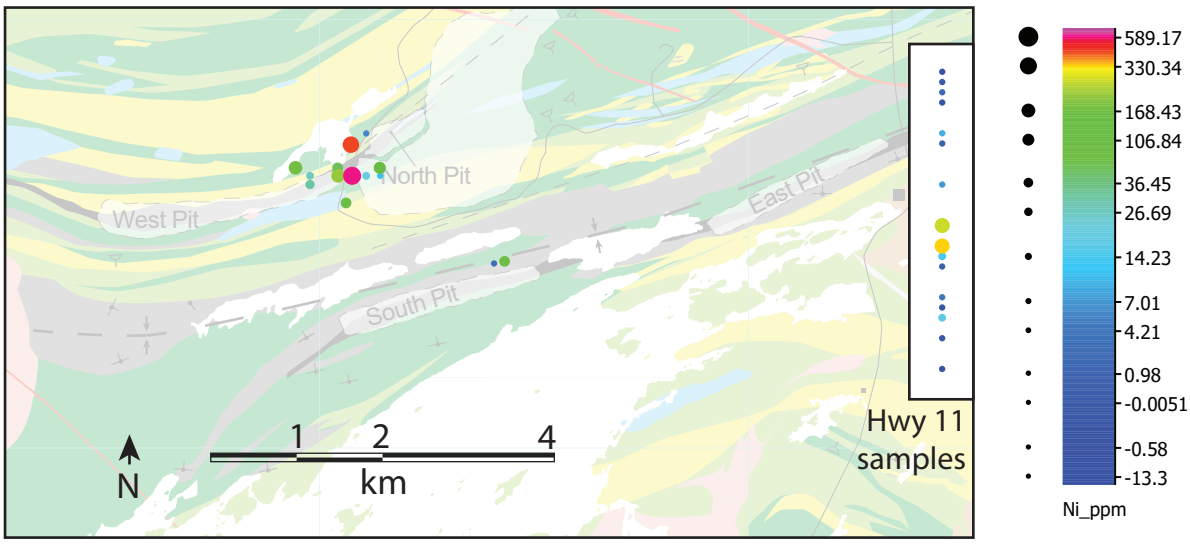


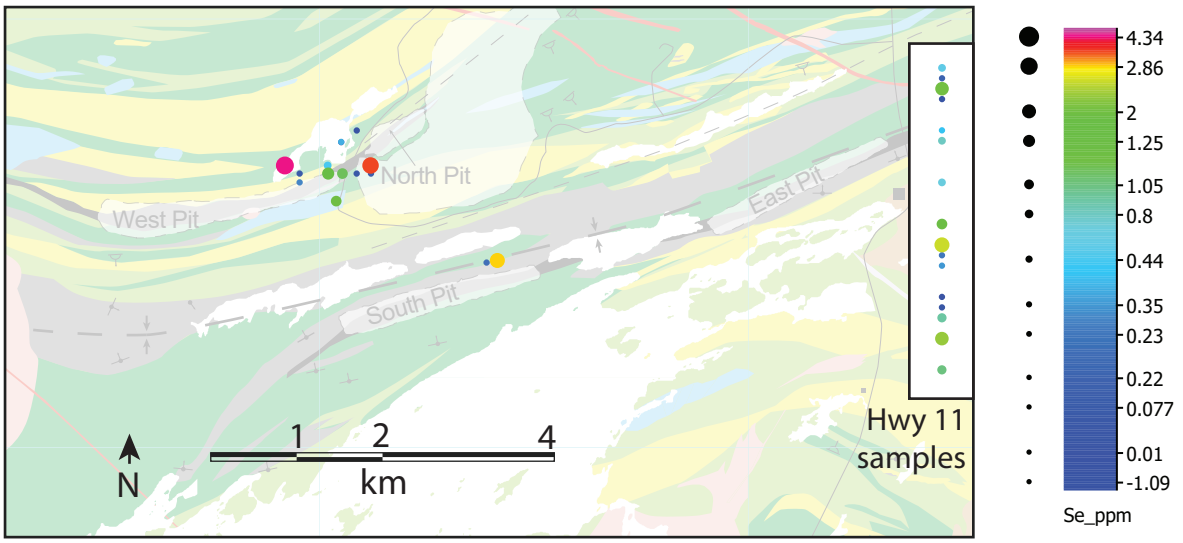




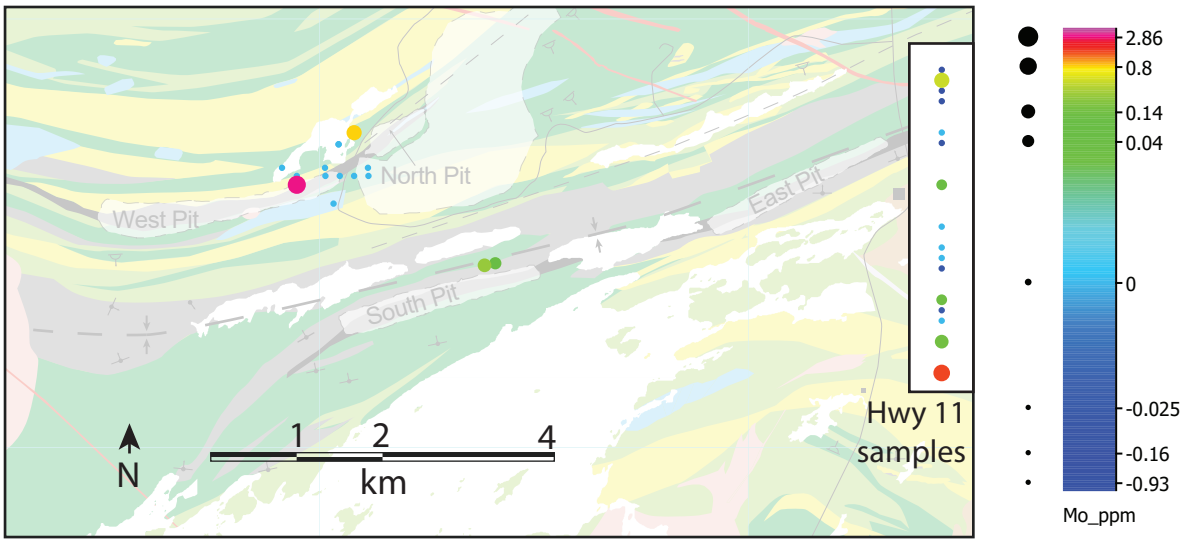
Appendix O (continued): Maps of clastic component- and Si- free element abundances

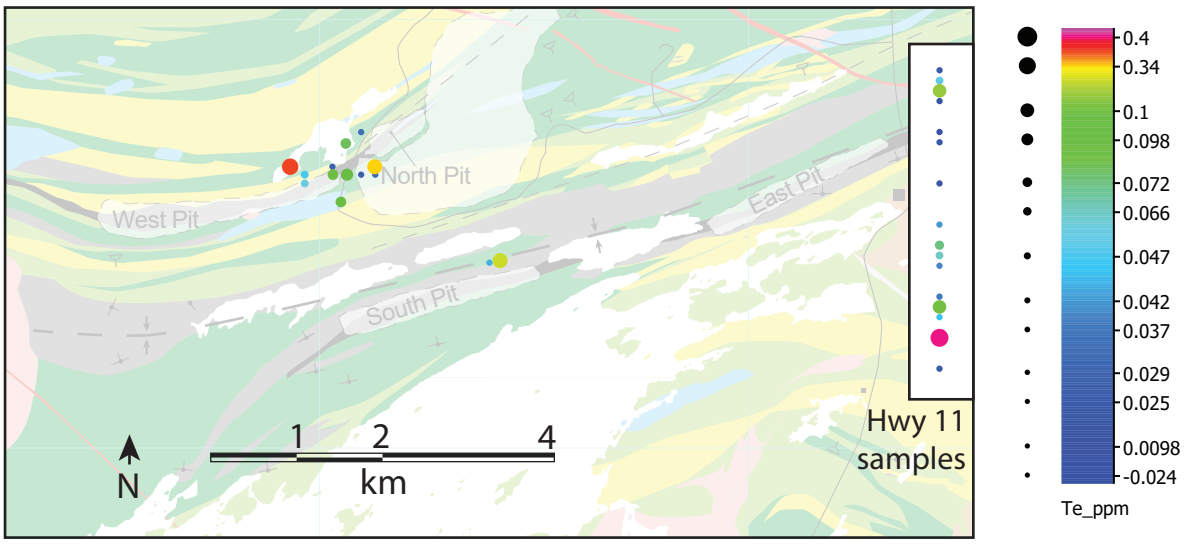


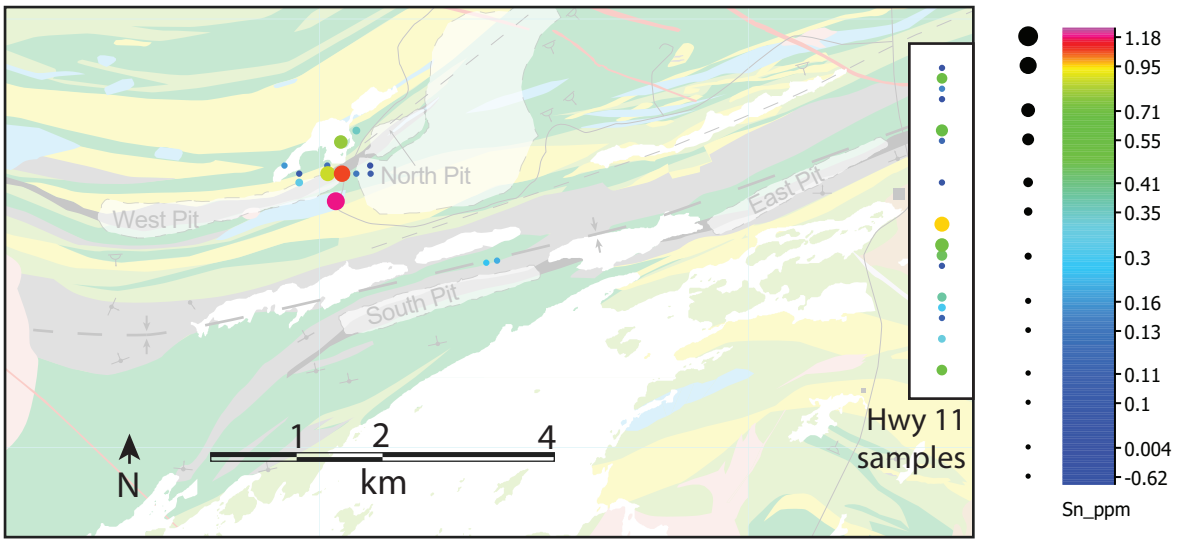




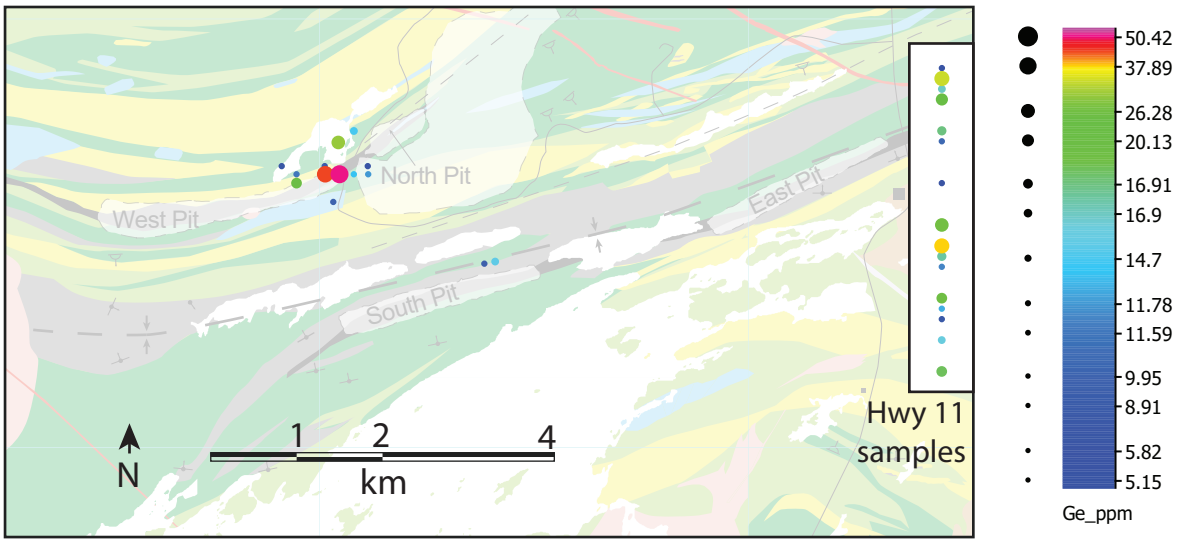
Appendix O (continued): Maps of clastic component- and Si- free element abundances

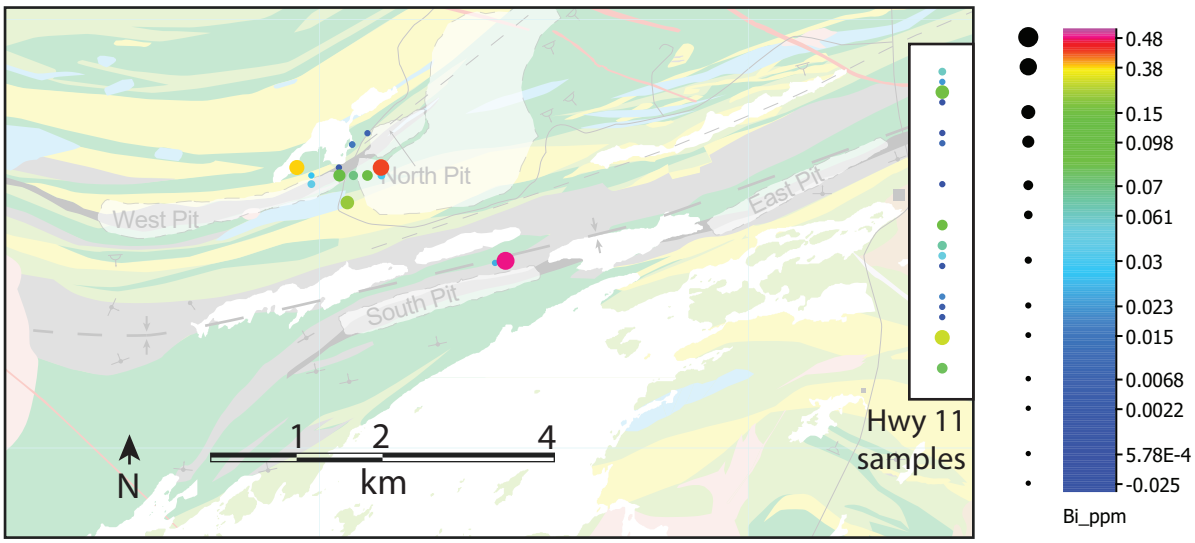


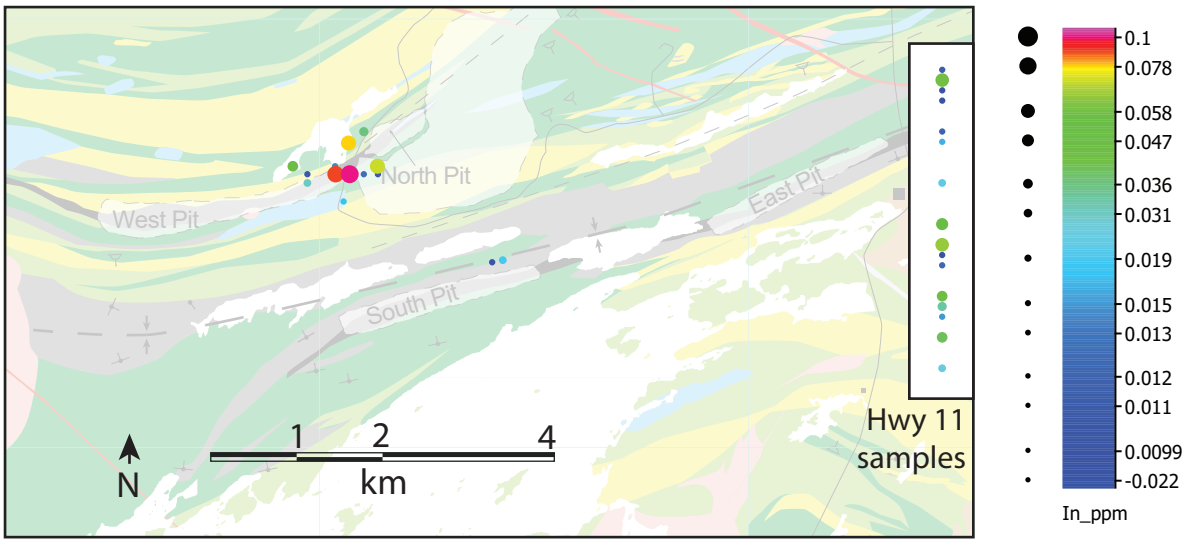




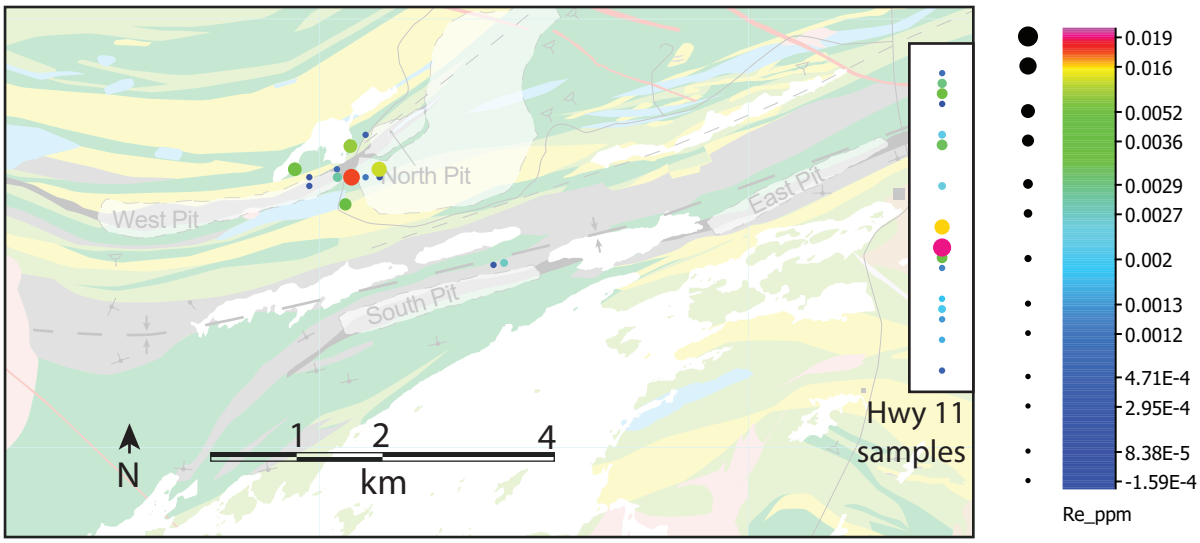
Appendix O (continued): Maps of clastic component- and Si- free element abundances

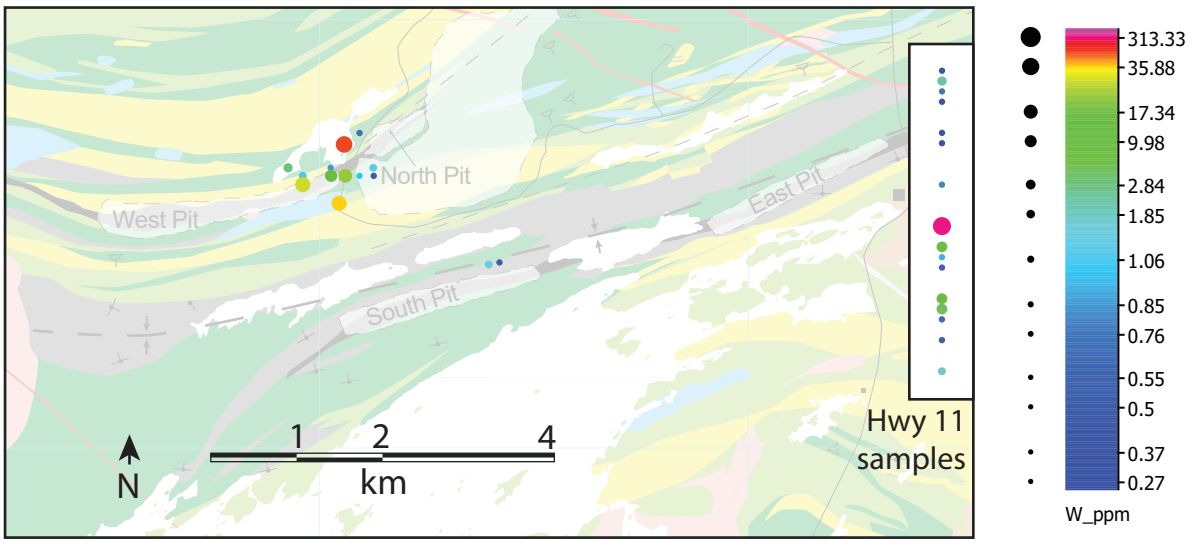


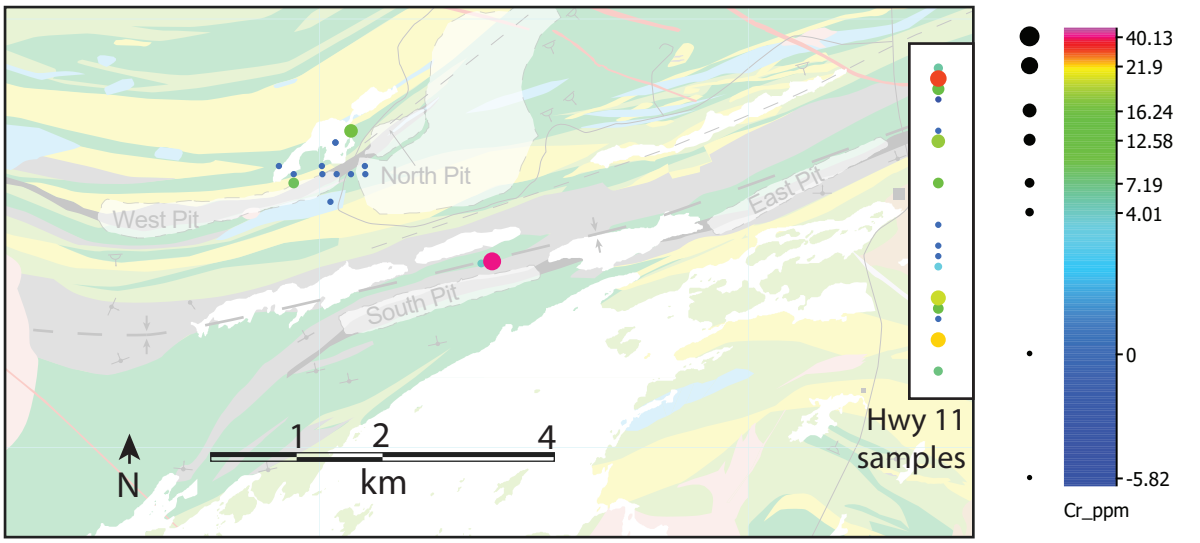




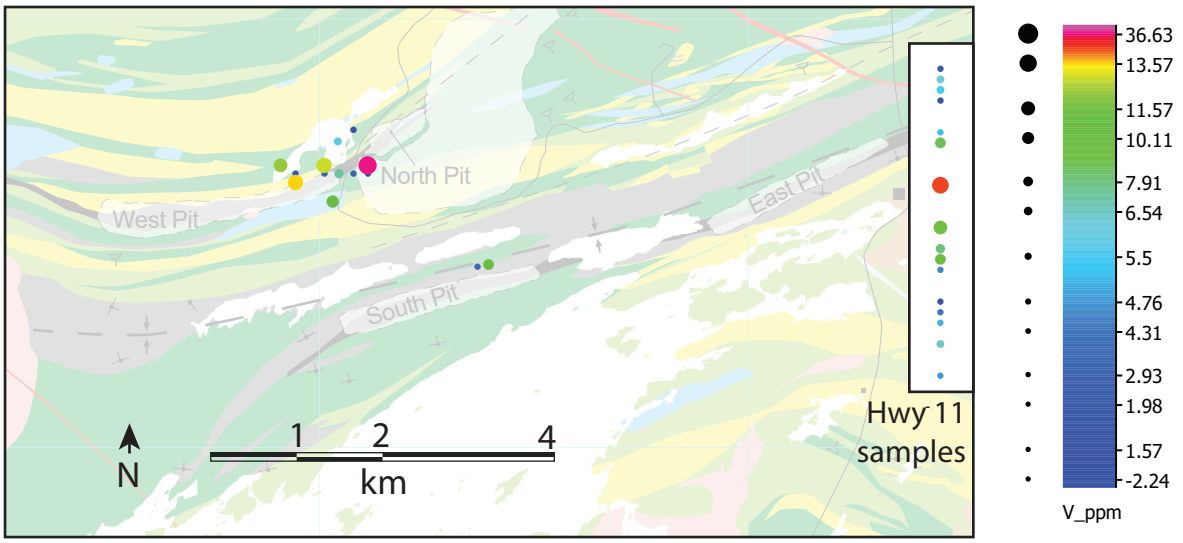
Appendix O (continued): Maps of clastic component- and Si- free element abundances

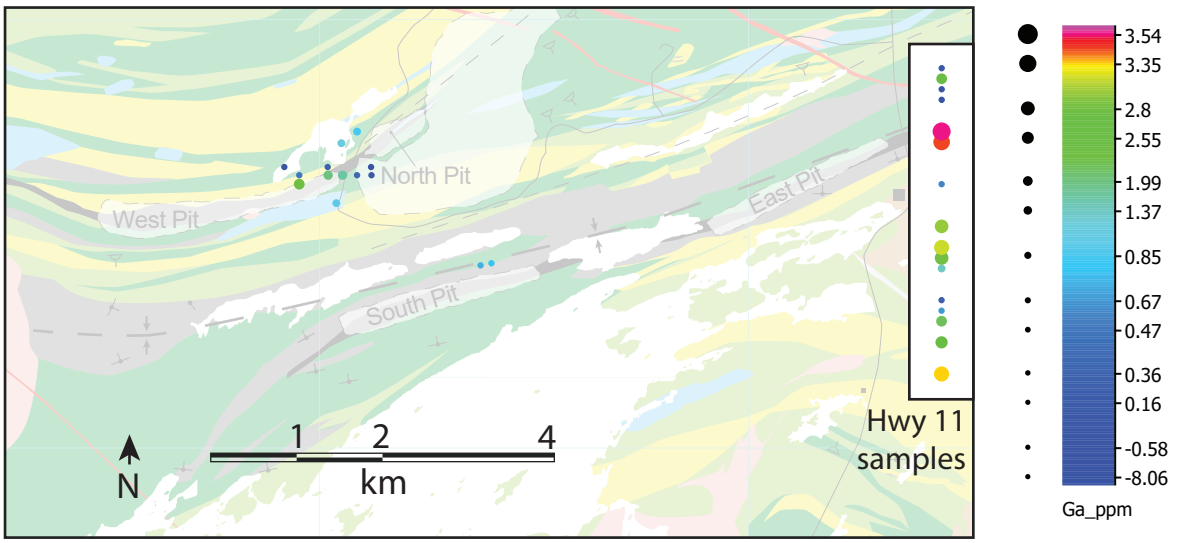


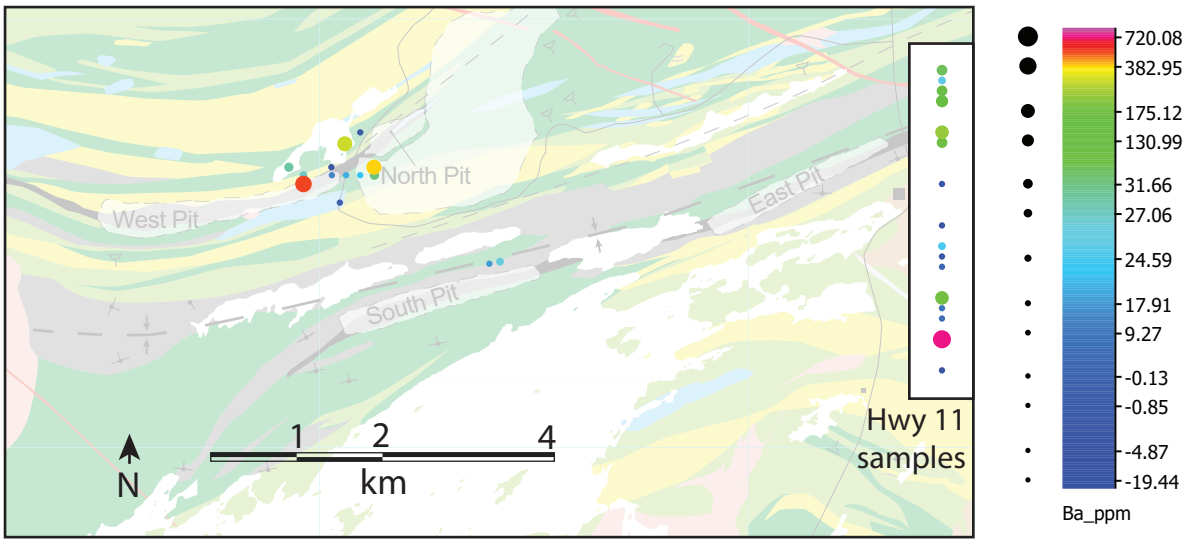




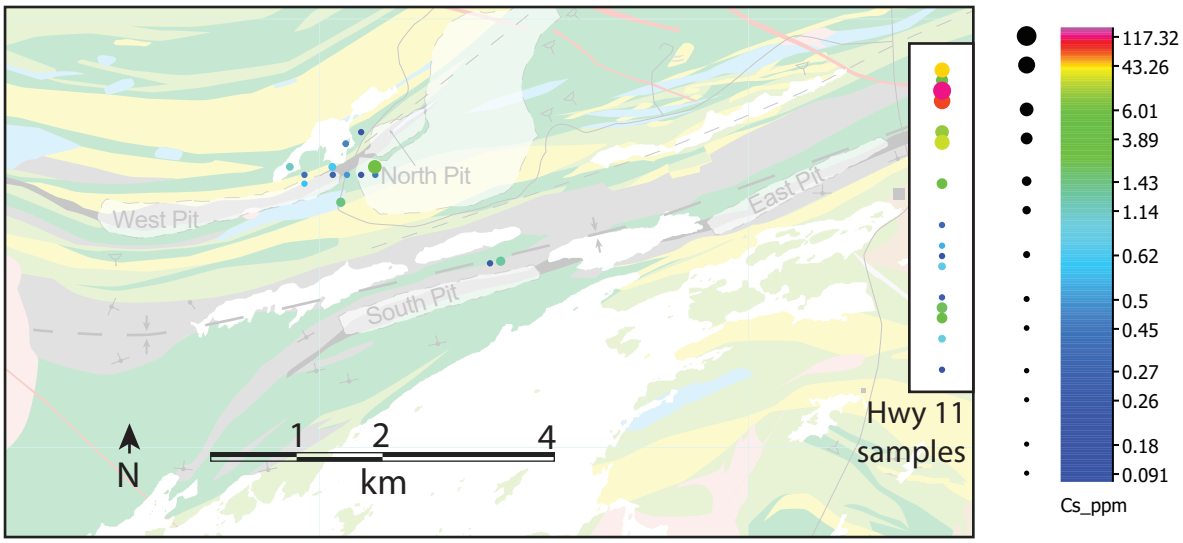
Appendix O (continued): Maps of clastic component- and Si- free element abundances

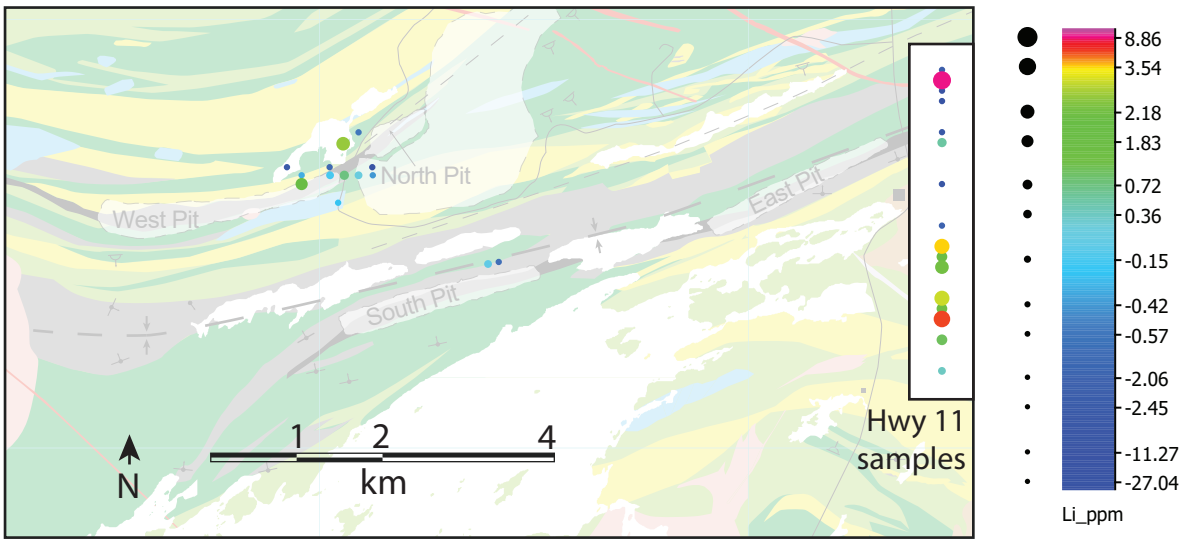


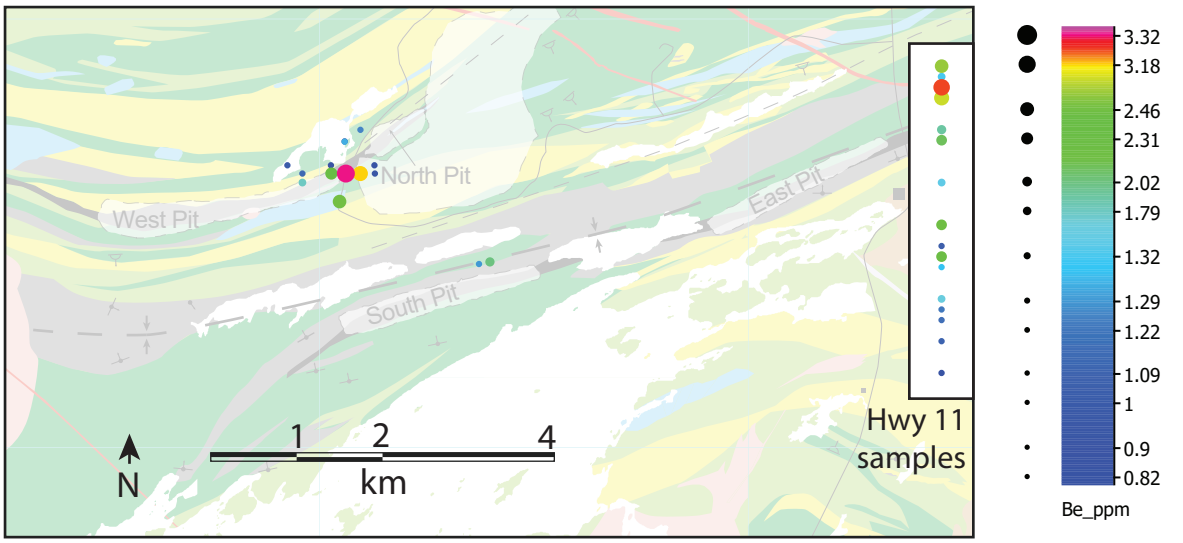




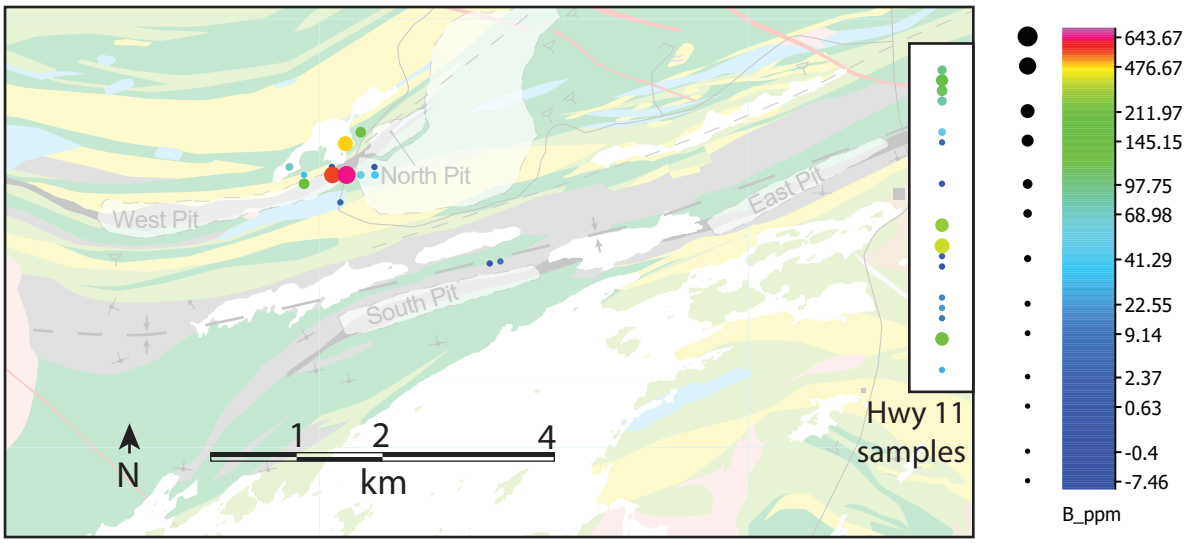
Appendix O (continued): Maps of clastic component- and Si- free element abundances

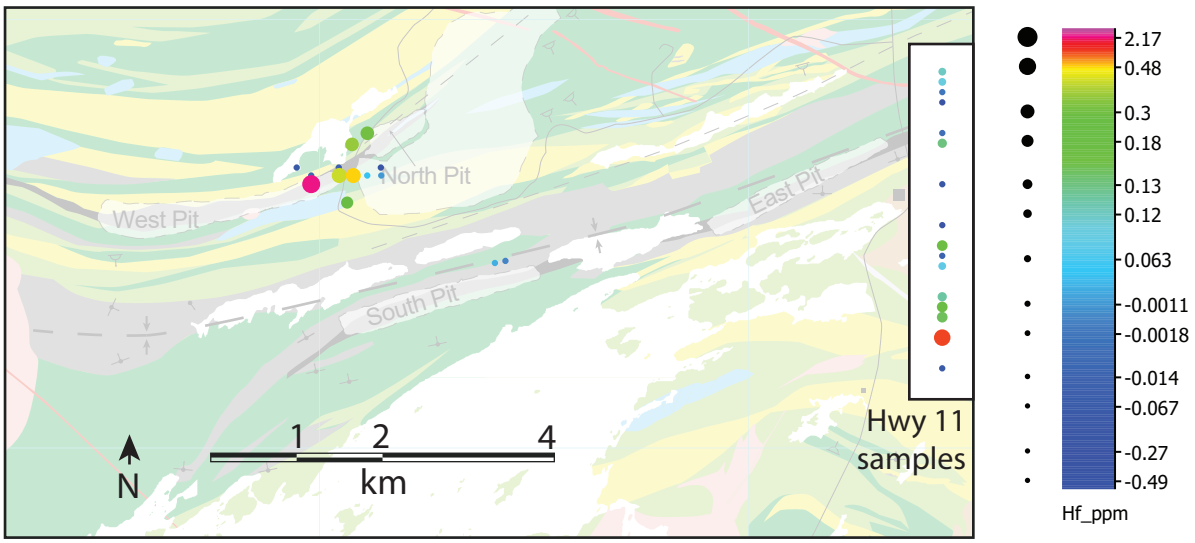


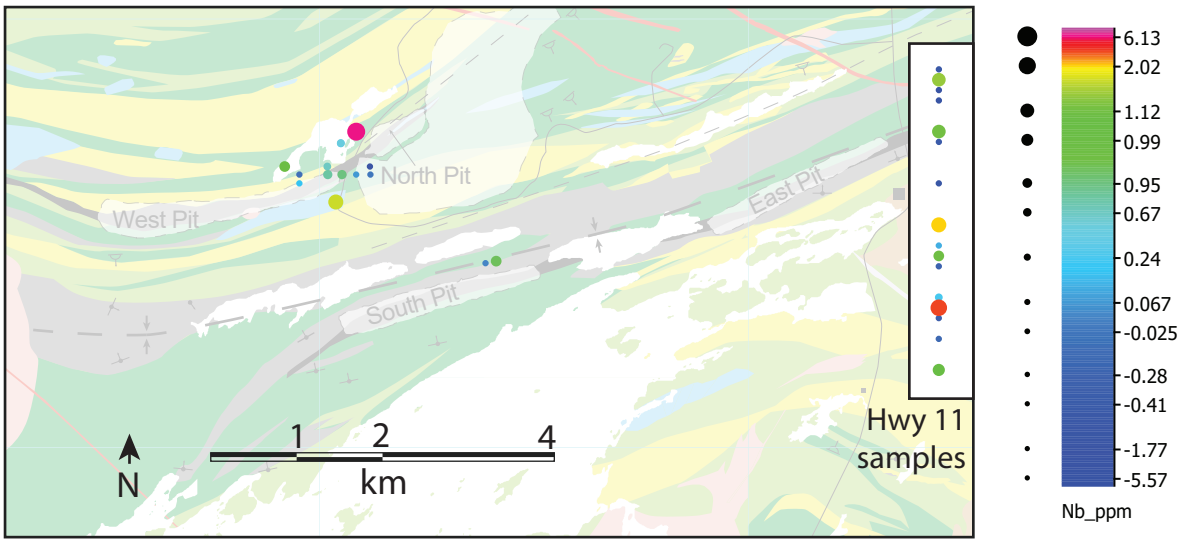




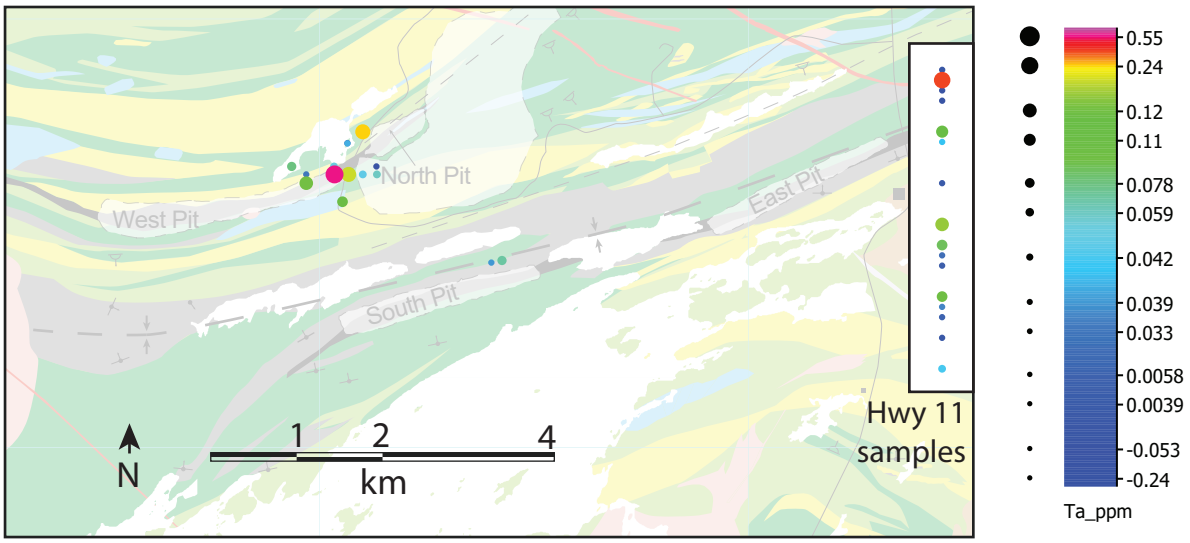
Appendix O (continued): Maps of clastic component- and Si- free element abundances

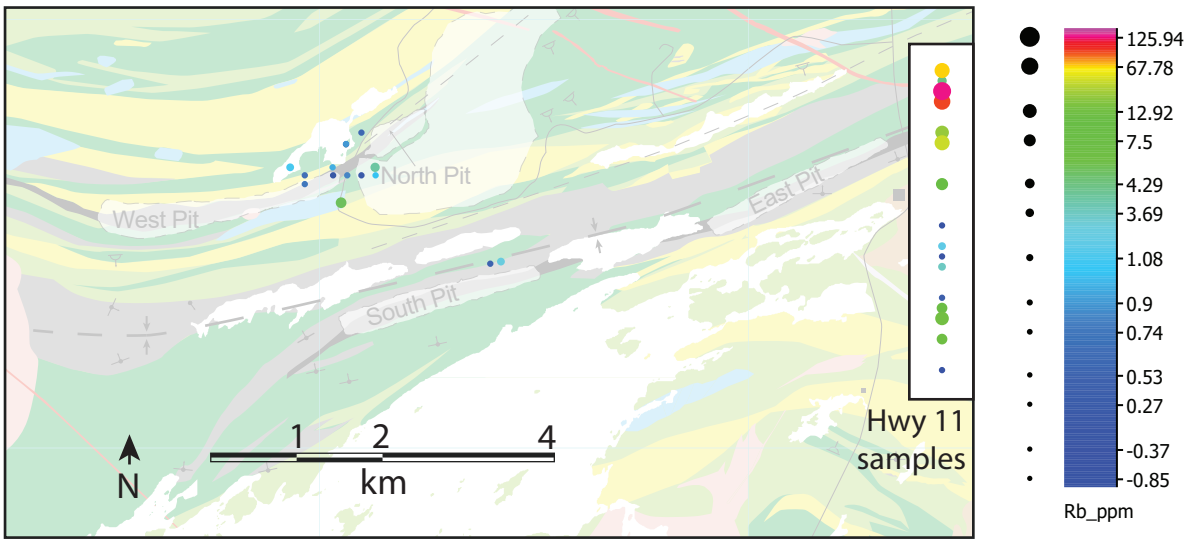


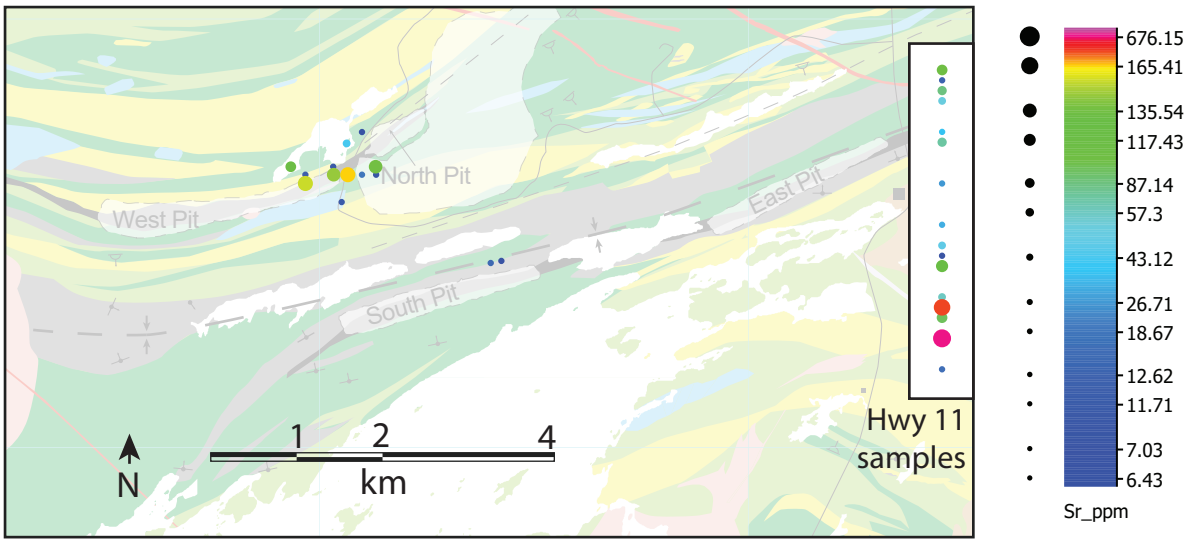




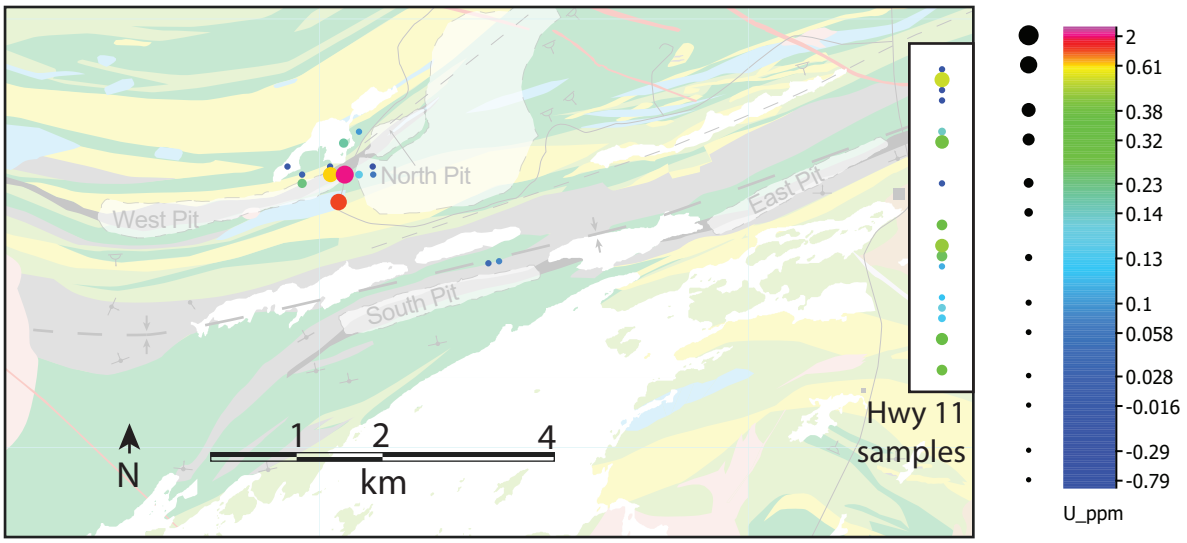
Appendix O (continued): Maps of clastic component- and Si- free element abundances

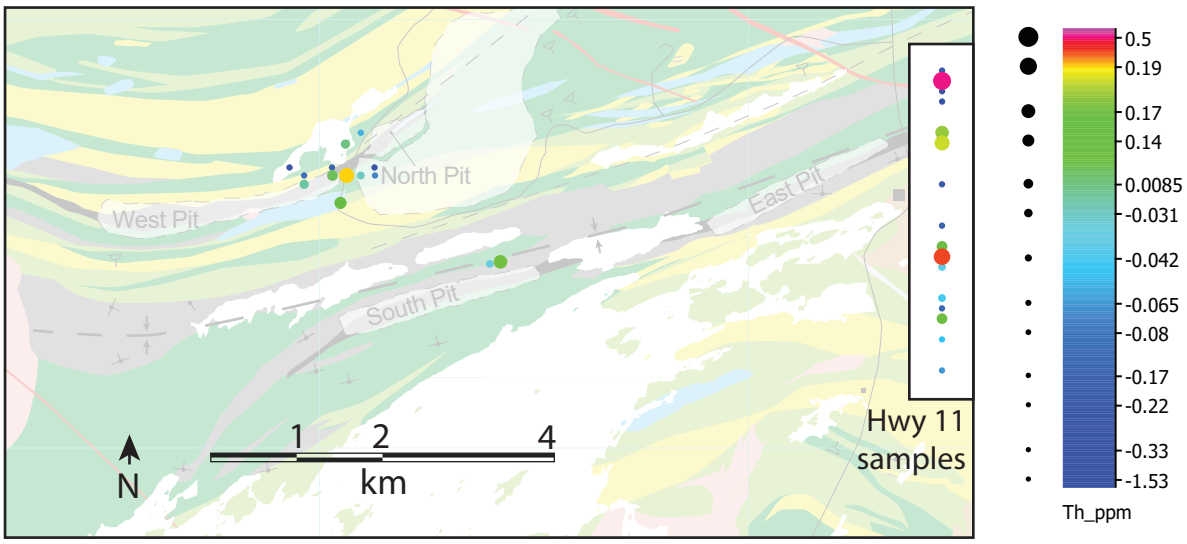


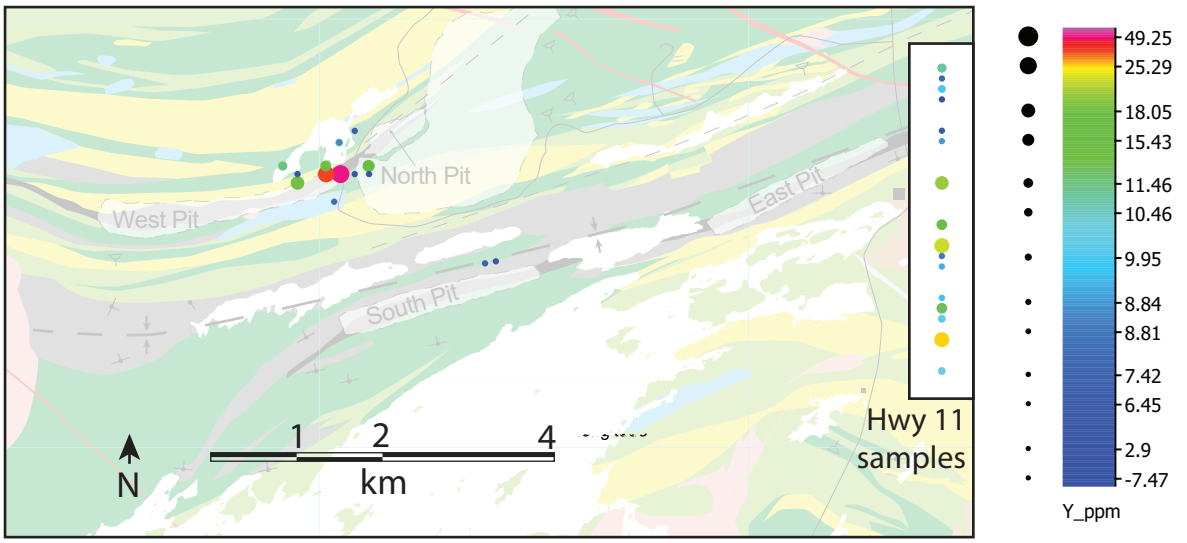




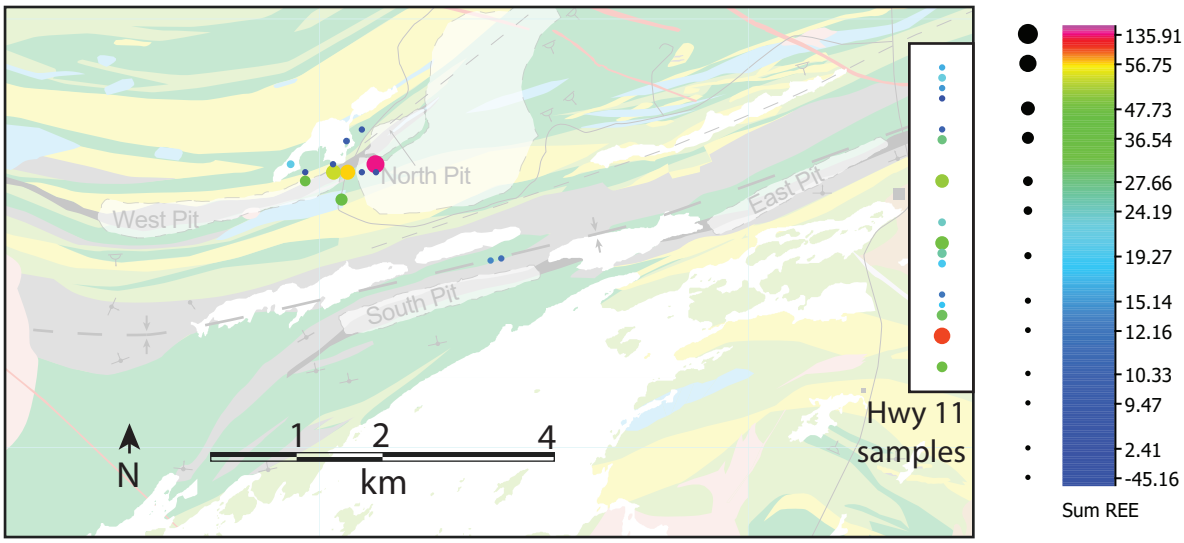
Appendix O (continued): Maps of clastic component- and Si- free element abundances

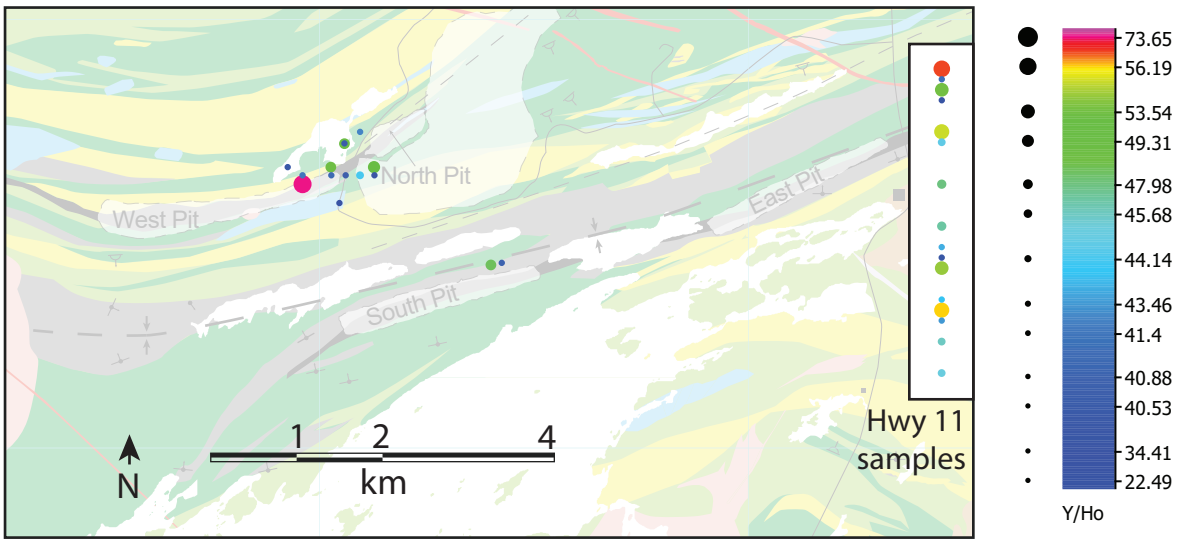


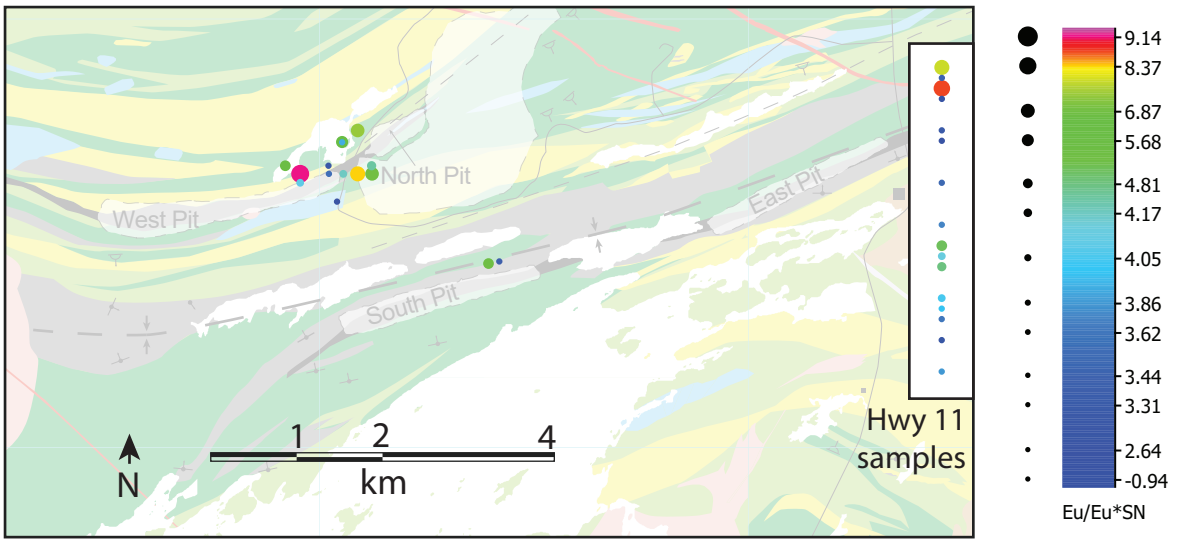




Appendix O (continued): Maps of clastic component- and Si- free element abundances







Appendix P

The locations of the samples are indicated in Figures P-1 and P-2. Four samples in this study yielded Ag_2S from the AVS step. S_{AVS} concentrations and multiple sulfur isotope results in these sample ranged from 28 to 1955 ppm, with $\delta^{34}S$ between -2.3 and 3.6 ‰, $\Delta^{33}S$ between -0.020 and 0.488‰, and $\Delta^{36}S$ between -0.5 and 0.2‰ (Table 4.2). The near-zero $\Delta^{33}S$ and slightly positive $\delta^{34}S$ values indicate an external source of sulfur, most likely added during metamorphism (e.g., Kajiwara and Krouse, 1971). In sample SM-12, the difference in the $\Delta^{33}S$ between the AVS and CRS is 0.6‰, with CRS recording mainly atmospheric elemental sulfur (see text for details). In each of SM-8, SM-14.1 and SM-14.3, the $\Delta^{33}S$ for the AVS is similar to that of CRS.

The uniform $\Delta^{36}S/\Delta^{33}S$ ratio in our samples (Fig. P-3) argues strongly for a limited number of pathways of sulfur deposition involving mainly atmospheric sulfur. The slope of $\Delta^{36}S/\Delta^{33}S$ of -0.72 in our data differs significantly from previously published Mesoarchean and Neoarchean reference slopes of -1.6 and -0.9, respectively (Farquhar et al., 2001; Ono et al., 2009a; Zerkle et al., 2012; Izon et al., 2015; see the text for discussion). Both lie outside the 95% confidence envelope for the regression of our data. That envelope also is significantly narrower if outliers are discarded (e.g., SM-15.1, 11-65.7, 11-72.1, and 11-72.2). We are confident, therefore that the sulfur isotope signature of the Temagami BIF differs from other reported Neoarchean supracrustal successions.

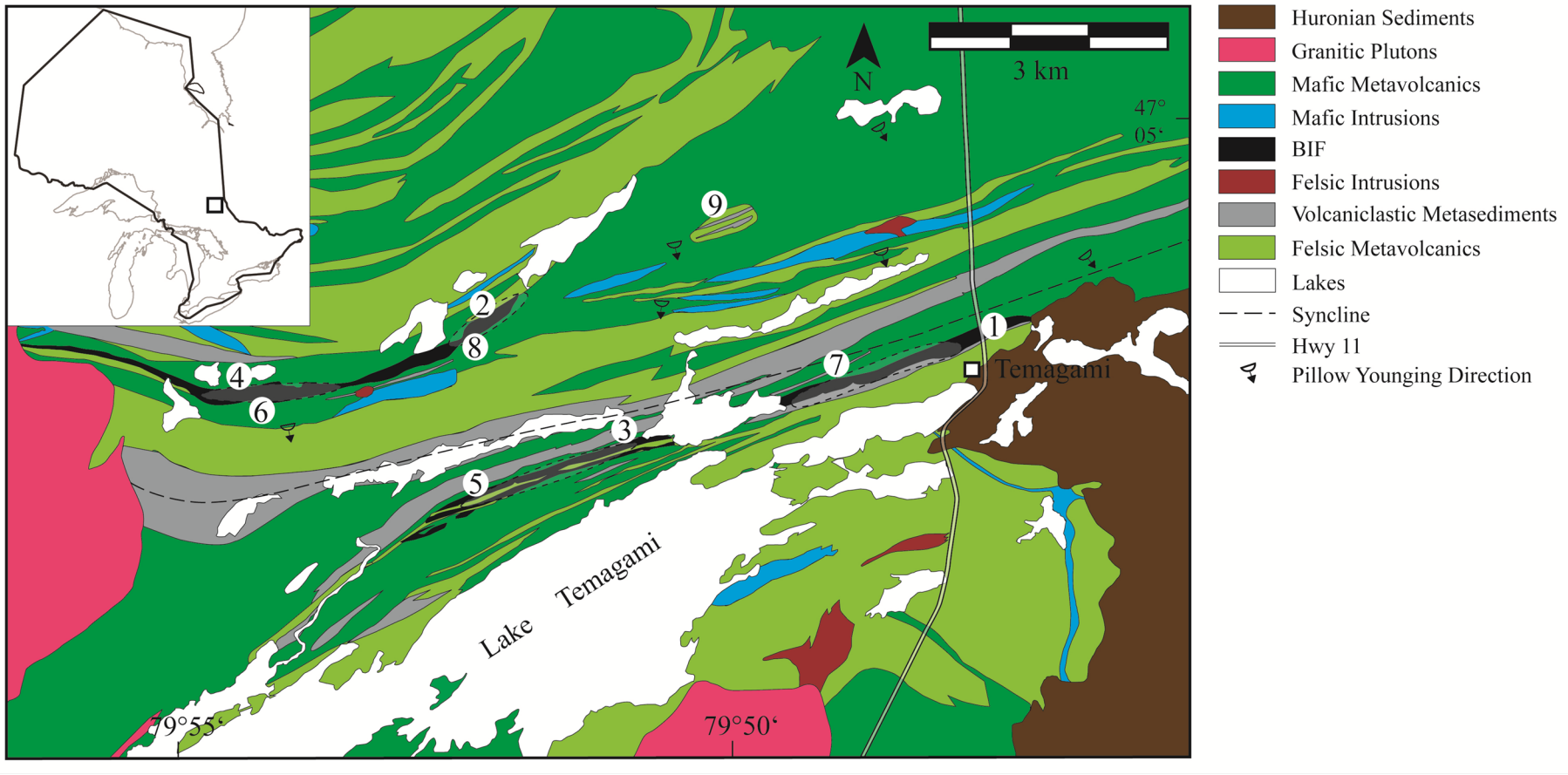


Figure P-1: Geological map of the field area with sampling locations indicated as referred to in Supplementary Table 1 (modified after Bennett, 1978).

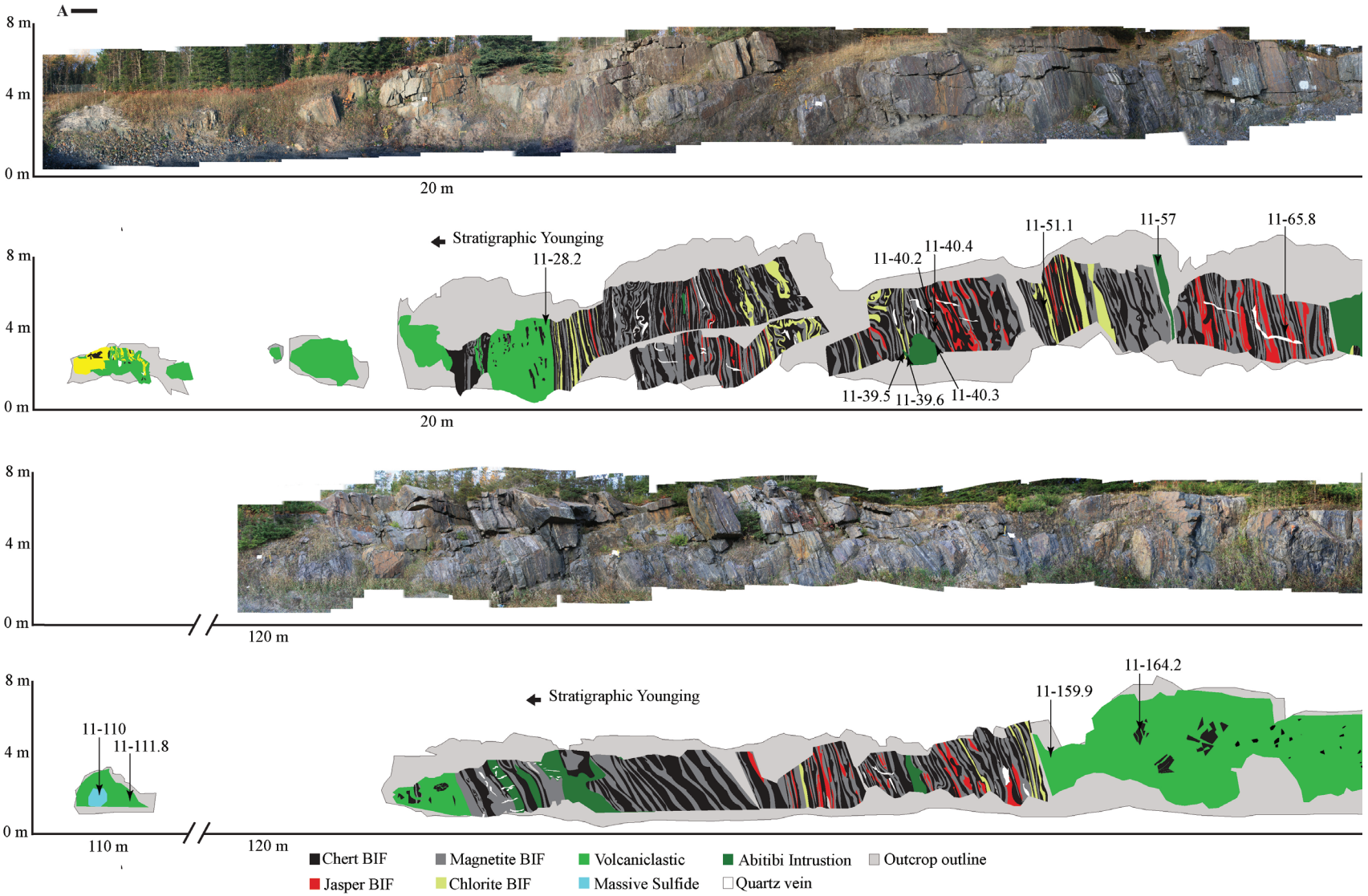


Figure P-2: Photomosaic and according schematic sketch of the Hwy 11 outcrop with sample locations in the south and north parts of the outcrop. A-B is a section along Hwy 11 just north of the town of Temagami, indicated as sample location 1 in Appendix P Figure 1.

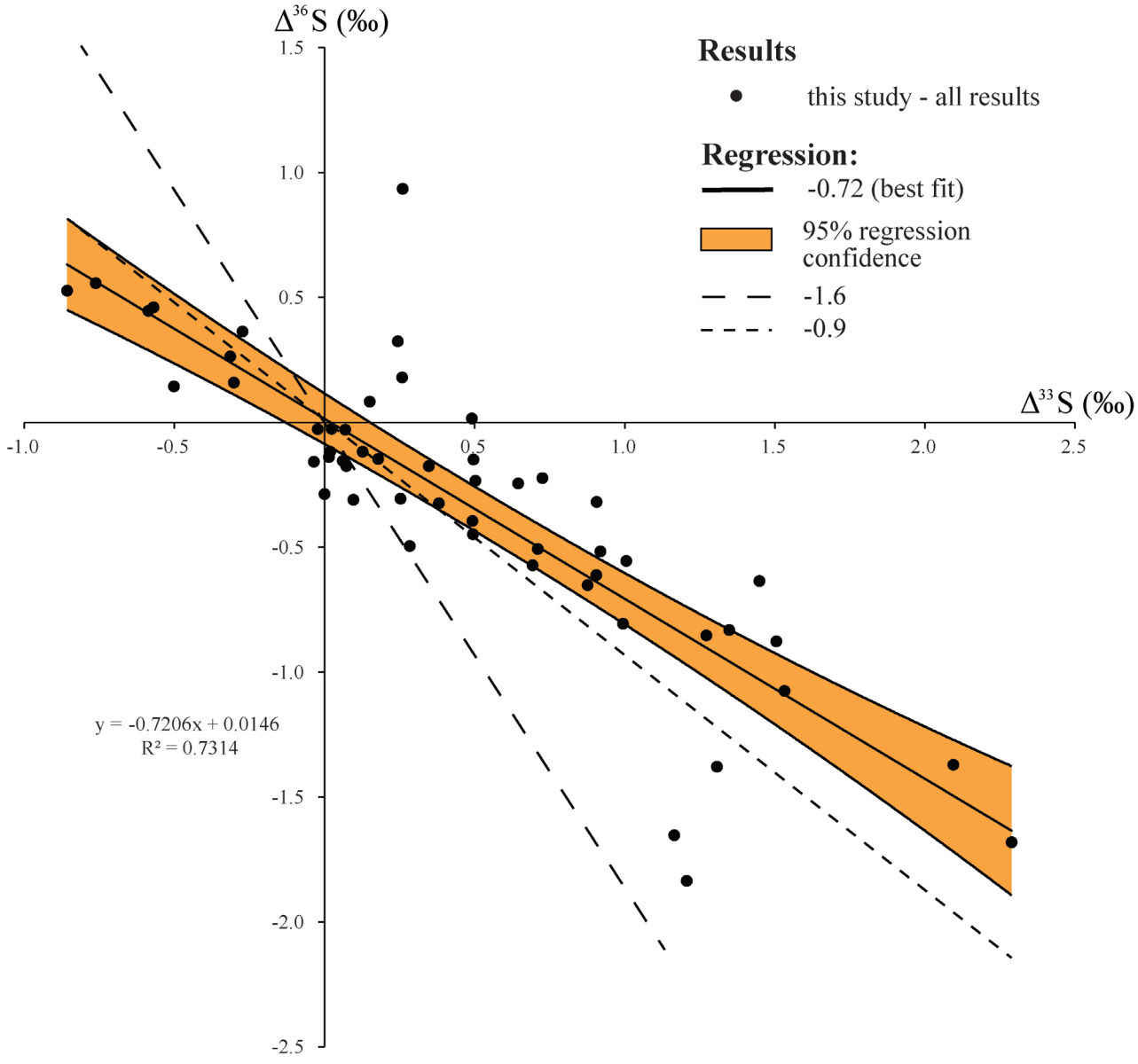


Figure P-3: Statistic analysis of the -0.72 slope simple regression underlines the probability that the observed slope is truly different from the reported Archean reference arrays. Reference slopes of -1.6 and -0.9 after Farquhar et al. (2001), Ono et al. (2009), Zerkle et al. (2012), and Izon et al. (2015).

References:

Bennett, G., 1978. Geology of the northeast Temagami area, District of Nipissing. Ontario Geological Survey Report 163, 128p.

Farquhar, J., Savarino, J., Airieau, S., Thiemens, M.H., 2001. Observation of wavelength-sensitive mass-independent sulfur isotope effects during SO2 photolysis: Implications for the early atmosphere. J. Geophys. Res. 106, 32829-32839.

Izon, G., Zerkle, A.L., Zhelezinskaia, I., Farquhar, J., Newton, R.J., Poulton, S.W., Eigenbrode, J.L., Claire, M.W., 2015. Multiple oscillations in Neoarchaean atmospheric chemistry. Earth and Planetary Science Letters 431, 264-273.

Kajiwara, Y., Krouse, H.R., 1971. Sulfur Isotope Partitioning in Metallic Sulfide Systems. Canadian Journal of Earth Sciences 8, 1397-1408.

Ono, S., Beukes, N.J., Rumble, D., 2009. Origin of two distinct multiple-sulfur isotope compositions of pyrite in the 2.5 Ga Klein Naute Formation, Griqualand West Basin, South Africa. Precambrian Research 169, 48-57.

Zerkle, A.L., Claire, M.W., Domagal-Goldman, S.D., Farquhar, J., Poulton, S.W., 2012. A bistable organic-rich atmosphere on the Neoarchaean Earth. Nature Geoscience 5, 359-363.